SOUTHWESTERN UNITED STATES GROUND MOTION CHARACTERIZATION SSHAC LEVEL 3

Technical Report

REVISION 2

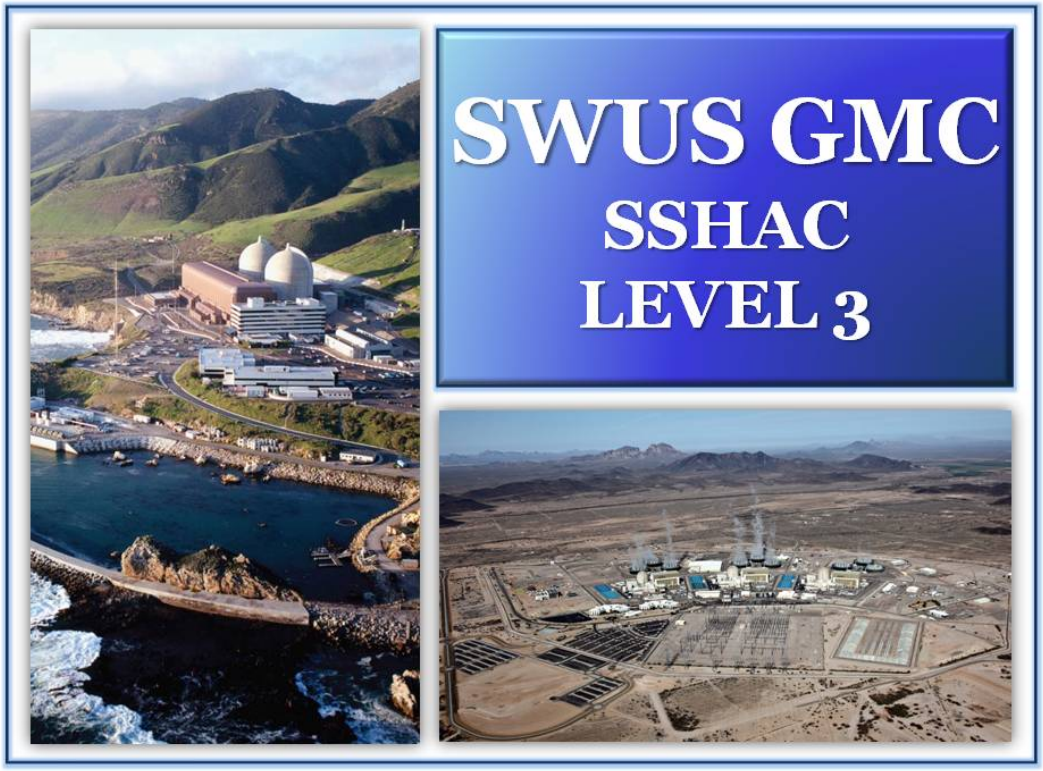

aps PG&E

GeoPentech
Geotechnical & Geoscience Consultants

SOUTHWESTERN UNITED STATES

GROUND MOTION CHARACTERIZATION

SSHAC LEVEL 3

Technical Report

March 10, 2015

Prepared for:

Arizona Public Service Company
Palo Verde Nuclear Generating Station
Wandell, Christopher J.
Senior Consulting "Chief" Civil Engineer
Phone: (623) 393-6741; E-mail: christopher.wandell@aps.com

Pacific Gas and Electric Company
Diablo Canyon Power Plant
Ferre, Kent
Manager Geosciences
Phone: (415) 973-5291; E-mail: KSF1@pge.com

Version: Rev. 2
Date: March 10, 2015

Citation: GeoPentech (2015). Southwestern United States Ground Motion Characterization SSHAC Level 3 – Technical Report Rev.2, March 2015

Prepared by:

Editor:

Carola Di Alessandro
GeoPentech, Inc.

The following individuals contributed to this Technical Report (alphabetical order):

Norman A. Abrahamson
Pacific Gas and Electric Company

Linda Al-Atik
Al Atik Consulting

Jeff Bayless
URS Corp.

Andrew Dinsick
GeoPentech, Inc.

Douglas S. Dreger
University of California – Berkeley

Nick Gregor
Nick Gregor Consulting

Nicolas Kuehn
University of California – Berkeley

Melanie Walling
Lettis Consultants International, Inc.

Jennie Watson-Lamprey
Watson-Lamprey Consulting

Kathrin Wooddell
Pacific Gas and Electric Company

Robert R. Youngs
AMEC Foster Wheeler

TABLE OF CONTENTS

LIST OF TABLES

LIST OF FIGURES

Acknowledgements

This report describes research sponsored by APS and PG&E, and conducted under the technical management of GeoPentech.

The project would like to acknowledge the Participatory Peer Review Panel (S. Day – Chairman, B. Chiou, K. Campbell, and T. Rockwell), who reviewed the technical and process aspects of the project.

Jennifer Donahue (Geosyntec Consultants) participated as part of the Technical Integration Team until Workshop #2, and her contribution to the project is kindly appreciated.

The ground-motion experts who participated in the March 19-21, 2013, Workshop #1 (Table 3.4-1), in the October 20-22, 2013 Workshop #2 (Table 3.5-1), and in the March 10-12, 2014 Workshop #3 (Table 3.7-1) are also acknowledged.

The quality of the GMC SWUS products was enhanced through productive cooperation with the Pacific Earthquake Engineering Research (PEER) Center, the Southern California Earthquake Center (SCEC), members of the U.S. Geological Survey (USGS), Virginia Tech and Pacific Engineering and Analysis (PEA).

The Management Team members (C. Di Alessandro, J.A. Barneich, A. Dinsick, A. Sarmiento and H. Boyd) of GeoPentech, Inc., are thanked for their assistance with the preparation of the report and with administrative support throughout the project duration.

EXECUTIVE SUMMARY

Introduction

This Technical Report describes the results of the Southwestern U.S. (SWUS) Ground-Motion Characterization (GMC) Project for the Palo Verde Nuclear Generating Station (PVNGS) in Arizona and the Diablo Canyon Power Plant (DCPP) in central coastal California. The study was conducted following the procedures for a SSHAC Level 3 study as described in NUREG/CR-6372 "Recommendations for Probabilistic Seismic Hazard Analysis: Guidance on Uncertainty and Use of Experts" (U.S. NRC, 1997). The approach used to meet the requirements for a SSHAC Level 3 is summarized in Chapter 2.

A SSHAC Level 3 study involves four components: (1) evaluation; (2) integration; (3) participatory peer review; and (4) documentation. The goal of any SSHAC study is to capture the center, body, and range (CBR) of the technically defensible interpretations (TDI) relevant to the seismic hazard at the site of interest. The GMC from a SSHAC study should represent the current state of knowledge for ground-motion models including the epistemic uncertainties, but it should also be focused on the model features that are important to the hazard at the sites of interest. Chapter 3 provides a summary of how the SSHAC Level 3 study was implemented for the SWUS project and describes the various experts involved in the project and their roles in the SSHAC study.

The GMC models for PVNGS and DCPP are both developed for a reference site condition with V_{S30} (travel-time-averaged shear wave velocity in the top 30 meters) of 760 m/s. For both sites, the site-specific rock has a higher V_{S30} than 760 m/s. This reference rock condition was selected because it is in the upper range of V_{S30} values for which the GMPEs are well constrained by the empirical data in active crustal regions. The reference rock ground motion will need to be adjusted to the site-specific conditions for the PVNGS and DCPP control points through site-response studies.

The GMC is a set of alternative models for the median and standard deviation of 5%-damped psuedo-spectral acceleration (PSA) for a given earthquake scenario. The alternative models are assigned weights based on the Technical Integrator (TI) Team's evaluation of the center, body, and range of the technically defensible interpretations of the ground motions for the relevant scenarios.

The hazard input documents (HIDs) in Appendix C for the DCPP and PVNGS sites provide all the information required to implement the SWUS GMC models in a probabilistic seismic hazard analysis (PSHA).

University Research

The SWUS GMC study received key input in the form of data and models from a suite of ground-motion projects that were relevant to the hazard evaluation for western U.S. sites. The first set of projects was conducted by the Pacific Earthquake Engineer Research (PEER) center and focused on empirical models. The PEER studies included the NGA-West2 project (Bozorgnia et al., 2014) which developed an expanded empirical ground-motion database that included key data from shallow crustal earthquakes in active regions around the world. The PEER NGA-West2 project also developed an updated set of proponent ground-motion prediction equations (GMPEs) that have been selected by the USGS for use in the national seismic hazard maps for the western U.S. In addition to the NGA-West2 studies, PEER also conducted studies for site characterization at seismic stations in Arizona including characterization of both the V_S profiles and the kappa (Kishida et al., 2014a). Finally, the PEER studies also included development of a simplified implementation of directivity effects (Watson-Lamprey, 2015).

The second set of projects was conducted by the Southern California Earthquake Center (SCEC) and focused on finite-fault simulations of ground motions using the SCEC broadband platform (BBP). These projects included a major validation exercise that evaluated which of the methods available on the BBP were considered to be ready for engineering applications (Dreger et al., 2013). The validation of the numerical simulation methods was organized in two parts described in details in Goulet et al. (2015), and addressed only the median pseudo spectral acceleration for the average horizontal component.

These two sets of university research projects provide the SWUS project with up-to-date data sets and ground-motion models for both empirical data and numerical simulations for the TI Team evaluation.

Seismotectonic Setting of Project Areas

Chapter 4 summarizes the regional tectonic setting for the DCPP and PVNGS sites. It also provides a brief description of the main controlling sources affecting the seismic hazard at the two nuclear power plant (NPP) sites and indentifies the range of sources that are included in the seismic source characterization (SSC) models (magnitudes, dips, mechanisms, and distances) for each site. Additionally, Chapter 4 summarizes the hazard contributions and deaggregation from previous hazard studies conducted for the two sites.

The Diablo Canyon Power Plant (DCPP) is located along the coastal margin of the San Luis Range in south-central California near San Luis Obispo. This region of California is characterized by transpressional deformation between the San Andreas Fault zone to the east and the Hosgri-San Simeon-San Gregorio system of near-coastal faults to the west (Figure EX-1). The earthquakes in this region are mainly strike-slip and reverse. Previous evaluations of the seismic hazard at the DCPP site have shown that, at low probability levels (10^{-3} to 10^{-6} Annual Frequency of Exceedance – AFE), the hazard is controlled by the four nearby (< 10 km) faults (Hosgri, Shoreline, Los Osos, and San Luis Bay faults). The DCPP site is located on the hanging-wall side of the nearby dipping faults. Based on the deaggregation, at low probability levels, the earthquakes with magnitudes between 5.5 and 7.0 at short distances (< 10 km) control the hazard at the high frequencies (> 5 Hz). For the low frequencies (< 1 Hz), the controlling earthquakes are shifted slightly to higher magnitudes (**M**6.0-**M**7.5), but are still at short distances (< 10 km).

The PVNGS site is located in the Sonoran Desert sub-province of the southern part of the Basin and Range (Figure EX-2). The earthquakes in the Basin and Range are mainly strike-slip and normal. The nearest active fault is the Sand Tank Fault located 40 km from PVNGS. The San Andreas Fault and other high activity sources in the Eastern California Shear-zone are located about 250 km east of the PVNGS site. Previous hazard studies for PVNGS (LCI, 2013) showed that, for hazard level of 10^{-4} Annual Frequency of Exceedance (AFE), the high-frequency hazard at the PVNGS site is controlled by **M**5 to **M**7 earthquakes in the areal source zones within 70 km of the site and the low-frequency hazard at the PVNGS site is controlled by the distant **M**7.5 to **M**8.5 earthquakes located in the southern California and Mexico region.

Ground-Motion Databases

Chapter 5 describes the ground-motion database used to evaluate the alternative ground-motion prediction equations (GMPE) for the median PSA relevant to the PVNGS and DCPP sites. The databases were also used to develop new models for the aleatory variability using the partially non-ergodic approach (single-station sigma and single-path region sigma).

The five main ground-motion databases used in the project are listed in Table EX-1. There are four empirical ground-motion databases and one numerical simulation ground-motion database. Many of the databases were used for multiple purposes. The uses of these five databases in the SWUS GMC project are listed in Table EX-1.

For PVNGS, four empirical ground-motion databases were used by the TI Team for evaluation of the alternative models for the median and aleatory variability. The first two databases, the PEER NGA-West2 database (Ancheta et al., 2014) and the Reference Database of Seismic Ground Motion in Europe

(RESORCE) described in Akkar et al. (2014c), are databases that have been used to derive GMPEs. Subsets of these databases, restricted to strike-slip and normal faulting earthquakes that control the hazard at PVNGS, are used to evaluate the alternative median GMPEs. The RESORCE database is used for PVNGS because it has a large number of recordings from normal-faulting earthquakes which are important for the hazard in the Basin and Range. The third database, the PEER Arizona database (Kishida et al., 2014a), includes both the recordings in Arizona from earthquakes in California and Mexico and recordings in Arizona from earthquakes in Arizona. It is used for two purposes: (1) to evaluate the path effects from median ground motion from the distant California earthquakes, and (2) to evaluate kappa for rock sites in Arizona. The PEER Arizona database is also used to develop the aleatory variability models for earthquakes in California and Mexico recorded in central Arizona (single-path region sigma models). The fourth database, consisting of ground-motion residuals from **M**4 to **M**6 earthquakes from Taiwan as described in Lin et al. (2011), is combined with the PEER NGA-West2 database for use in develop new models for the single-station sigma. The RESORCE database was also used to develop new model for the single-station sigma.

For DCPP, two empirical ground-motion and one finite-fault simulation databases were used by the TI Team for evaluation of the alternative models for the median and aleatory variability. The first empirical database is the PEER NGA-West2 database (Ancheta et al., 2014). A subset of this database, restricted to strike-slip and reverse-faulting earthquakes at short distance, that control the hazard at DCPP, are used to evaluate the alternative median GMPEs. The finite-fault simulation database is used to evaluate the median GMPEs and to provide insight into the scaling for complex and splay ruptures, and for hanging-wall effects. The second empirical databases is the Taiwanese Lin et al. (2011) database, which is combined with the PEER NGA-West2 database to develop the new models for single-station sigma.

In addition to the ground-motion databases, Chapter 5 also describes the selection of the candidate GMPEs for median ground motion. The candidate GMPEs are described in the database Chapter because they are used as inputs to the development of the proponent models for the median. In all, 19 GMPEs published between 2004 and 2014 were evaluated as potential candidate GMPEs for use at either DCPP or PVNGS. From this set of 19 GMPES, 8 candidate GMPEs were selected for DCPP, 6 candidate GMPEs were selected for PVNGS - Greater Arizona sources, and 5 candidate GMPEs were selected for PVNGS – California and Mexico sources.

Median Ground-Motion Models

Chapter 6 describes the selection of the candidate GMPEs for PVNGS and DCPP. Because the many of the alternative candidate GMPEs use similar data sets, particularly for large magnitudes at short distances, additional epistemic uncertainty is added to each candidate GMPE using the epistemic

uncertainty model of Al-Atik and Youngs (2014). The selected candidate GMPEs for DCPP and for PVNGS are listed in Table EX-2 for both the local sources and the distant sources.

Evaluation of the Median models using Sammon's maps

A key feature of the TI Team evaluation of the median ground-motion model is the use of the Sammon's map representation of the alternative magnitude and distance scaling of the GMPEs. In this approach, the selected candidate GMPEs are expanded to develop continuous distributions of the median GMPEs which can then be discretized into representative models that are approximately mutually exclusive and collectively exhaustive.

In the Sammon's map approach, a large suite of new common-form models are created from existing GMPEs which both interpolate between the existing GMPEs and extrapolate beyond the range of the existing GMPEs. Visualization techniques are used to map the suite of new models into a 2-D plane (Scherbaum et al., 2010). The Sammon's maps technique is used to calculate a two-dimensional representation of the model space. The model space can then be discretized into a small number of cells with representative models selected for each cell. Weights are then assigned to each cell based on the comparisons with hazard relevant data sets (empirical and/or simulated) and with the density of the suite of models within each cell, to represent the center, body and range of median predictions. A single representative model is selected for each cell. The process is repeated for each spectral period.

An example of a Sammon's map for PVNGS is shown in Figure EX-3. In this map, the original GMPEs (including the additional epistemic uncertainty) are shown by the colored dots. In these maps, the distance between two points on the map is the standard deviation of the difference between the natural log PSA values for a range of scenarios (magnitude and distances) that are relevant to the hazard at the PVNGS site. The cells used to discretize the model space (shown by the contours in the background) are shown by the lines. The contours in the background show the mean residual at each point (every model) computed from the selected database.

This new method allows the TI Team's evaluations to assign logic weights to the alternative GMPEs that directly represent the probability of each GMPE and not just the relative merit of each GMPE. The TI Team found that this method helped them to address center, body, and range of median GMPE predictions in a more systematic way than the traditional approach of evaluating the relative merits of the alternative candidate GMPEs because it addressed issues of the potential redundancy in some of the GMPEs and extended the alternative sets of GMPEs.

The representative suite of models envelop the range from the candidate GMPEs in the Sammon's map space, but because the Sammon's map uses a average measure of the differences between ground motion based on the selected representative earthquake scenarios, the selected representative models do not envelop the candidate GMPEs for every scenario. Although the ranges from the common-form

models do not bound the ranges from the GMPEs with additional epistemic uncertainty for all scenarios, the ranges of the 5th and 95th fractiles for the common-form models are, on average, wider than the ranges of the 5th and 95th fractiles for the GMPEs.

A key issue for the TI Team evaluation was to check if the representative suite of models lead to hazard curves that bounded the range of the hazard from the original candidate models. Because the hazard is a combination from many different scenarios, it samples the ground motions from a range of scenarios similar to the Sammon's maps. The TI Team checked the range from the hazard calculations and confirmed that the range of the hazard from the selected representative models captures the range of the hazard using the original candidate GMPEs including the additional epistemic uncertainty.

Ground-Motion Models for Distant Sources

The previous hazard studies, described in Chapter 4, showed that the distant sources for DCPP did not contribute significantly to the hazard, but the distant California and Mexico earthquakes could have a significant contribution to the low-frequency hazard at PVNGS. A key issue for the TI Team's evaluation of the candidate GMPEs for use in computing the low-frequency ground motions at PVNGS from these distant sources is the distance attenuation from California to central Arizona. In particular, is the distance scaling for earthquakes in California to sites in central Arizona different from the distance scaling for earthquakes and sites within California from which the GMPEs were derived?

A key feature of this study is the use of ground-motion data from these distant sources in California and Mexico recorded in Central Arizona to empirically constrain the path effects. Fourteen earthquakes in southern California recorded at sites in central Arizona are used to constrain the source-specific distance scaling for the low-frequency ground motions from two separate source regions in southern California and Mexico (called Region 1 and Region 2&3 in Figure EX-3). The epistemic uncertainty in the estimated path effects due to the limited number of earthquakes for these specific paths is estimated and is included in the PVNGS GMC model.

Hanging-Wall Effects

Hanging-wall (HW) effects refer to increase in the ground motion above the rupture surface of dipping earthquake ruptures compared to what would be expected for equivalent rupture distances on the footwall side of ruptures. Not all of the candidate GMPEs include HW effects. Although there are few empirical data to constrain the functional form of the HW factors, strong HW effects are seen in the available ground-motion data and they are also seen clearly in finite-fault simulations. Therefore, the TI Team judged that HW effects should be included in all of the models. To capture the uncertainty in the

HW effects, five alternative models for the HW effects were developed by the TI Team, based on the HW effects in the candidate GMPEs and from the finite-fault simulations.

Directivity Effects

Directivity refers to the dependence of the ground motion on the direction of the rupture (either toward the site, or away from the site). For sites at the same closest distance, the median of the ground motion will vary for different locations along strike depending on the direction of rupture. New models that parameterize the directivity effects have been developed, but there are significant issues related to their application. In particular, the directivity models may not be directly applicable to the candidate GMPE because their scaling is not centered on the GMPE.

Chiou and Youngs (2014) developed a directivity model that is centered on their GMPE. This model provides a factor on the median ground motion that is added to the median ground motion from the GMPE that depends on the hypocenter location on the rupture plane. Randomizing over the hypocenter location for the directivity implies variability in the median ground motions, which impacts the standard deviation. To simplify the application of the Chiou and Youngs (2014) directivity model, Watson-Lamprey (2015) developed scale factors that describe the change in the median and total standard deviation as a function of the position along strike (R_Y) and the distance perpendicular to the strike of the rupture (R_X). The application of the Watson-Lamprey model to the hazard estimates for the DCPP site-source geometry showed that there was only a small effect (< 2%) on the hazard for this geometry.

Because (1) the Watson-Lamprey model is still under review at PEER, (2) the effect on the hazard at DCPP is small, and (3) concern about the applicability of the CY14 centering and directivity models to other GMPEs, the TI Team judged that the Watson-Lamprey directivity model should not be applied to either DCPP or PVNGS. Excluding the directivity adjustment model in the logic trees for both sites has an implicit assumption that the median directivity effect is zero and the variability of the ground motion due to directivity is captured by the standard deviation by the GMPEs for the two sites. The small effect of directivity on the hazard at DCPP is captured through the large epistemic uncertainty in the median ground-motion models.

Splay and Complex Ruptures

The SSC for DCPP includes rupture scenarios that involve rupture of multiple fault segments including fault segments with major changes in the rake, dip, and rupture width (called complex ruptures), and ruptures of a splay fault off of a main rupture (called splay ruptures). While these complex and splay ruptures have very low rates of occurrence in the 2015 DCPP SSC and will, therefore, have little effect on the hazard, the hazard analysts require rules for implementing these ruptures using the GMPEs. For complex ruptures, the key issue is how to specify the style-of-faulting parameter which affects the

scaling, and how to specify the dip and rupture width which affects the HW scaling. Finite-fault simulations were used by the TI Team to evaluate alternative simplified methods for computing the ground motion for these cases. These simulations showed that treating the two sources as separate earthquakes in the GMPEs and then combining the resulting ground motions using the square root of the sum of the squares (SRSS) was the best approach.

Aleatory Variability Models

For both DCPP and PVNGS, the partially non-ergodic approach (Anderson and Brune, 1999) is used, which removes the systematic site term differences from the ground-motion residuals. This leads to the single-station within-event standard deviation is called ϕ_{SS}. The between-event standard deviation is referred to as τ.

Because the standard deviation of a GMPE represents the limitations of the GMPE to describe the observations, the standard deviations models are developed using empirical data. The TI Team evaluated the previously published models for ϕ_{SS} and τ, and concluded that new models should be developed that take advantage of the large increase in the empirical ground-motion databases that has occurred since the previously published models were developed.

Chapter 7 describes the development of a suite of new alternative models for the τ and ϕ_{SS} using different subsets of the databases listed in Table EX-1. The subsets include a global data set, a California only subset, and a European subset. The epistemic uncertainty of the τ and ϕ_{SS} for each subset is estimated based on the data set size.

GMC for Median Ground Motions for DCPP

Chapter 8 describes the logic trees for the median ground motions for DCPP. The TI Team's evaluation concluded that R_{RUP}-based models should be used for DCPP, but R_{JB}-based models should not be used for DCPP because of the potential for hanging-wall effects from a range of dip angles which are better captured by R_{RUP}-based models (Donahue and Abrahamson, 2014).

The Sammon's map approach is used to select a suite of about 30 representative common-form ground-motion models for each spectral period. The weights for the models are based on the consistency with the selected subsets of both empirical ground-motion data and simulated data (Table EX-1) and on the distribution from the candidate GMPEs with equal weights. One of five hanging-wall models is then randomly associated with each of the representative common-form models.

GMC for Median Ground Motions for PVNGS

Chapter 9 describes the logic trees for the median ground motions for PVNGS. For the Greater Arizona sources, the Sammon's map method is used, similar to the approach used for DCPP. The main difference is in the selection of the candidate models and the comparisons to the selected data sets (Table EX-1). For PVNGS, both the global data and the European data sets are used to increase the number of recordings from normal faulting earthquakes. Finite-fault simulations are not used as there are no known active faults close to PVNGS.

Because there are no nearby faults, hanging-wall effects are not large. The TI Team's evaluation concluded that both R_{RUP}-based models and R_{JB}-based models should be used for PVNGS. As with DCPP, the Sammon's map approach is used to select a suite of about 30 representative common-form ground-motion models for each spectral period. The weights for the models are based on the consistency with the selected subsets of data and on the distribution from the candidate GMPEs with equal weights. One of five hanging-wall models is then randomly associated with each of the common-form models.

GMC for Between-event Aleatory Variability for DCPP and PVNGS

Chapter 10 describes the logic trees for the between-event aleatory variability (τ) which is used for both PVNGS and DCPP. The weights for the alternative models are based on the statistical estimates of the uncertainty due to the limited number of earthquakes in each subset of data.

Single-Station Within-Event Aleatory Variability for DCPP

Chapter 11 describes the logic trees for the within-event aleatory variability for DCPP using the partially non-ergodic approach. For DCPP, the ϕ_{SS} logic tree captures the following uncertainties: the alternative datasets used to derive the model (global empirical data sets versus a smaller California only data set); the statistical uncertainty of the estimate of the ϕ_{SS} applicable to a single site based on sample size; and the alternative forms of the upper tail for the aleatory residual distribution (traditional normal distribution of the log PSA or the mixture model, which has fatter tails).

The mixture model represents a new approach that was developed for this project in response to the discussion at the SWUS Workshop #2 about the shape of the upper tails of the ground-motion distributions. An evaluation of the distribution of the traditional within-event residuals and single-station within-event residuals showed that the upper tail tended to be fatter than would be expected from a normal distribution at epsilon values greater than about 2.5. To capture this behavior, a new

model for the aleatory distribution of the log residual was developed, that is a combination (mixture) of two normal distributions. The upper tails of this mixture model was found to be consistent with the observed distribution of the residuals. Because this only affects the distribution at high epsilon values, it mainly affects the hazard at very low probability levels.

Within-event aleatory variability for PVNGS

Chapter 12 describes the logic trees for the within-event aleatory variability for PVNGS. As for DCPP, the partially non-ergodic approach is used. For PVNGS, two logic trees were developed depending on the source location: (1) a ϕ_{SS} and a ϕ_{SP-R} logic tree for sources located in Regions 1, and combined Regions 2&3 (distant California and Mexico sources) of Figure EX-3; and (2) a ϕ_{SS} logic tree for sources outside Regions 1, and 2&3 (called Greater Arizona sources). A different logic trees is used for the distant sources for PVNGS to take advantage of the availability of ground-motion data from distant California earthquakes recorded at a group of sites in the PVNGS region. These data allow the estimation of the repeatable path-to-region effects that are then removed from the ϕ_{SS} because of the improved median model predictions for these sources.

For the Greater Arizona sources, the ϕ_{SS} logic tree captures the following uncertainties: the alternative datasets used to derive the model (large global data sets versus smaller European data sets with a larger fraction of normal faulting earthquakes); the statistical uncertainty of the estimate of the ϕ_{SS} applicable to a single site based on sample size; and the alternative forms of the upper tail for the aleatory residual distribution (same mixture model as for DCPP).

For the distant California and Mexico sources, the ϕ_{SP-R} logic tree captures the following uncertainties: the statistical uncertainty of the estimate of the ϕ_{SP-R} applicable to a single site based on sample size; and the alternative forms of the upper tail for the aleatory residual distribution.

Total Sigma

Chapter 13 describes the development of the logic tree for the total single-station sigma (σ_{SS}) and the total single-path region sigma (ϕ_{SP-R}) by combining the logic trees for the between-event aleatory variability (τ) and the within-event aleatory variability (ϕ_{SS} or ϕ_{SP-R}). The reason for combining these two standard deviations into a single total standard deviation is to reduce in computation burden in

the PSHA calculation: the use of three alternative discrete values representing the composite continuous distribution for σ_{SS} instead of nine alternative discrete values representing the combination of three alternative discrete values for τ with three alternative discrete values for ϕ_{SS}.

Hazard Sensitivity

Hazard sensitivity feedback was provided throughout the project to focus the TI Team's evaluations on the uncertainties that are most important for the hazard at the two sites. The hazard sensitivity was conducted by isolating each node of the GMC logic trees. For the node of interest, one branch is given full weight and the mean hazard is computed by sampling every combination of branches for the other nodes.

The hazard sensitivity is displayed using "Tornado" plots which show the sensitivity of the ground-motion level at a given hazard. The summary tornado plots for spectral frequencies of 5 Hz and 0.5 Hz for the mean annual frequency of exceedance of 10^{-4} are shown in Figures EX-6 and EX-7 for DCPP and Figures EX-8 and EX-9 for PVNGS. For both DCPP and PVNGS, the largest single contributor to the uncertainty is the median GMPE model from the Sammon's map method, shown at the top of the plots. The next largest contributor to the uncertainty in hazard are the standard deviation models (ϕ_{SS} the and τ) except for the low-frequency hazard at PVNGS for which the uncertainty in the path terms is the second largest contributor to the uncertainties.

Model Applicability

The Ground-Motion (GM) Models for both sites are applicable to a reference site condition with V_{S30} = 760 m/s with a kappa value of 0.041 seconds.

The DCPP ground-motion models are separated into two sets: one set of models for the nearby faults and one set of models for the distant faults. The common-form models are optimized for large magnitues (**M**5.5 to **M**7.5) strike-slip and reverse events at short distances(< 10 km) that dominate the hazard at DCPP (Section 4.2.3). The common-form models are applicable to the following sources nearby DCPP (from Table 4.1-1): Hosgri fault, Shoreline fault, San Luis Bay fault, Oceano Fault, Wilmar fault, Los Osos fault, Oceano and SWBZ faults, and the Irish Hills background zone. The representative suite of common-form ground-motion models captures the CBR for the scenarios that dominate the hazard at the DCPP site, but they may not capture the full CBR for the very long distances. For the other more distant sources, the NGA-West2 GMPEs are applicable. These distant sources do not contribute significantly to the hazard at DCPP. The NGA-West2 GMPEs are used for these sources rather than the

common-form models because the common-form models were not well constrained for larger distances (the focus of the evaluation was on the short distances).

The PVNGS ground-motion models are separated into two types of sources: the earthquakes in the Greater Arizona regions, and the earthquakes in California and Mexico in Regions 1, 2 and 3.

For the Greater Arizona regions, the ground-motion models are optimized for magnitues **M**5.0 to **M**7.0 normal and strike-slip events at distance less that 70 km that dominate the hazard at PVNGS for the short periods; however, the GM models were constrained to extrapolate in a reasonable way for mangitudes up to **M**8.0, and for distances as large as 320 km. GM models are also applicable to reverse-faulting events.

For the sources in California and Mexico in Regions 1, 2 and 3, the GM models are optimized for the path effects from southern California to central Arizona. The GM model is based on the NGA-West2 GMPEs which can be extrapolated reasonably up to **M**8.5. The GM models capture the CBR for the scenarios that dominate the low-frequency hazard.

Table EX-1: Ground-motion databases and their application for the SWUS project.

	NGA-West2	RESORCE	PEER-Arizona	Lin et al (2011)	Finite-Fault Simulations
DCPP Median	SS and REV				SS and REV
DCPP complex & splay ruptures					SS and REV
PVNGS Median Greater AZ		SS and NML			
PVNGS Kappa for Arizona rock site			Earthquakes in Arizona		
PVNGS Median for CA/Mex sources			CA/Mex eqk 200-400 km		
DCPP Single-Station Sigma	X			X	
PVNGS Single-Station Sigma	X	X		X	
PVNGS Sigma for CA/Mex sources			CA/Mex eqk 200-400 km		
DCPP & PVNGS HW scaling					X

Table EX-2: Selected Candidate GMPEs for the median ground motion

GMPE	DCPP	DCPP Distant Sources	PVNGS - Greater Arizona Sources	PVNGS - Distant CA & MEX Sources
Abrahamson et al (2014)	X	X	X	X
Boore et al (2014)	X	X	X	X
Campbell and Bozorgnia (2014)	X	X	X	X
Chiou and Youngs (2014)	X	X	X	X
Idriss (2104)	X	X		X
Zhao et al (2014)	X			
Zhao and Lu (2011) adjustment to magnitude scaling	X			
Akkar et al (2014a, 2014b)	X		X	
Bindi et al (2014a, 2014b)			X	

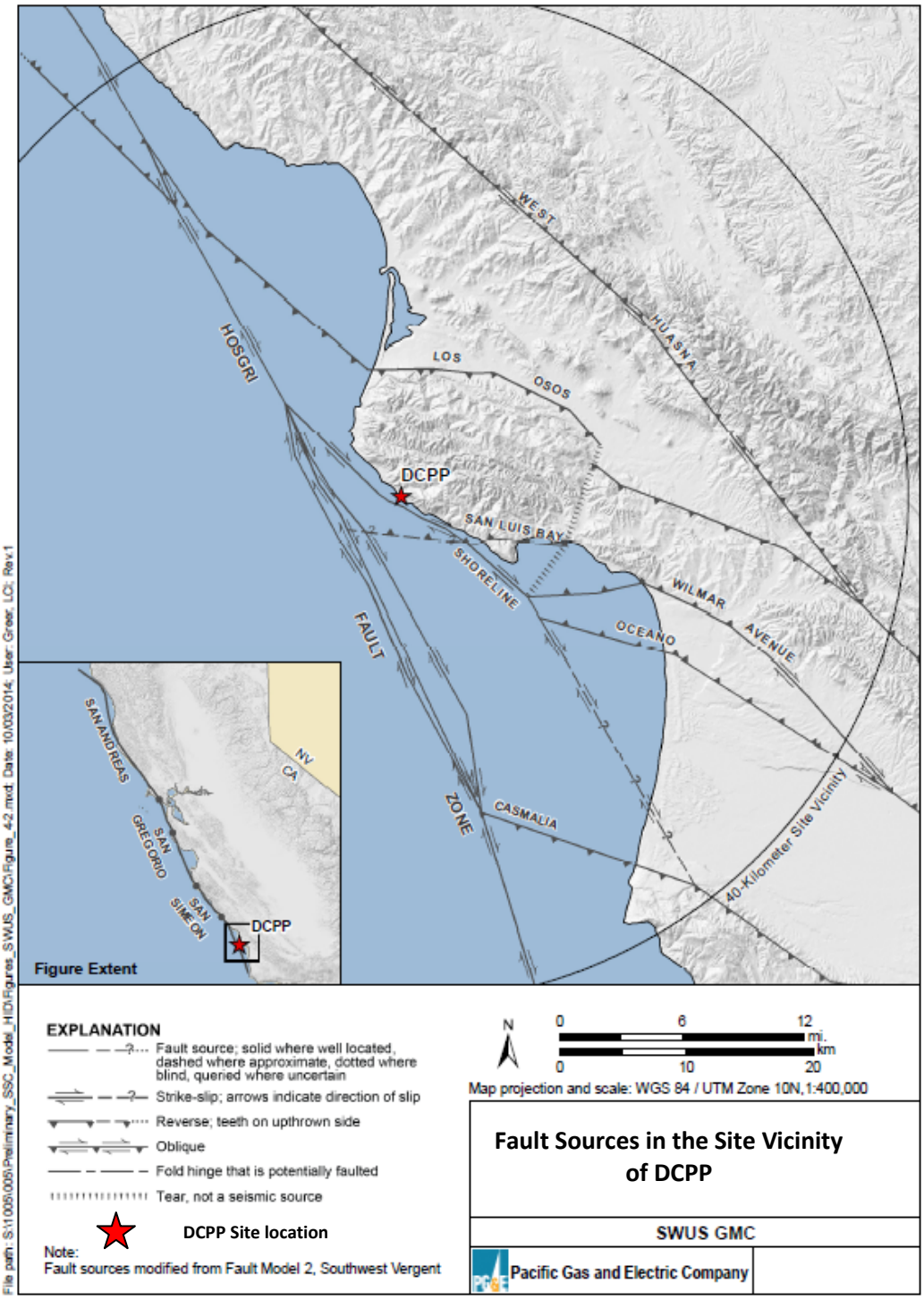

Figure EX-1: Fault sources in the seismotectonic alternative of the in the DCPP SSC model (PG&E, 2015). Star shows location of the DCPP site.

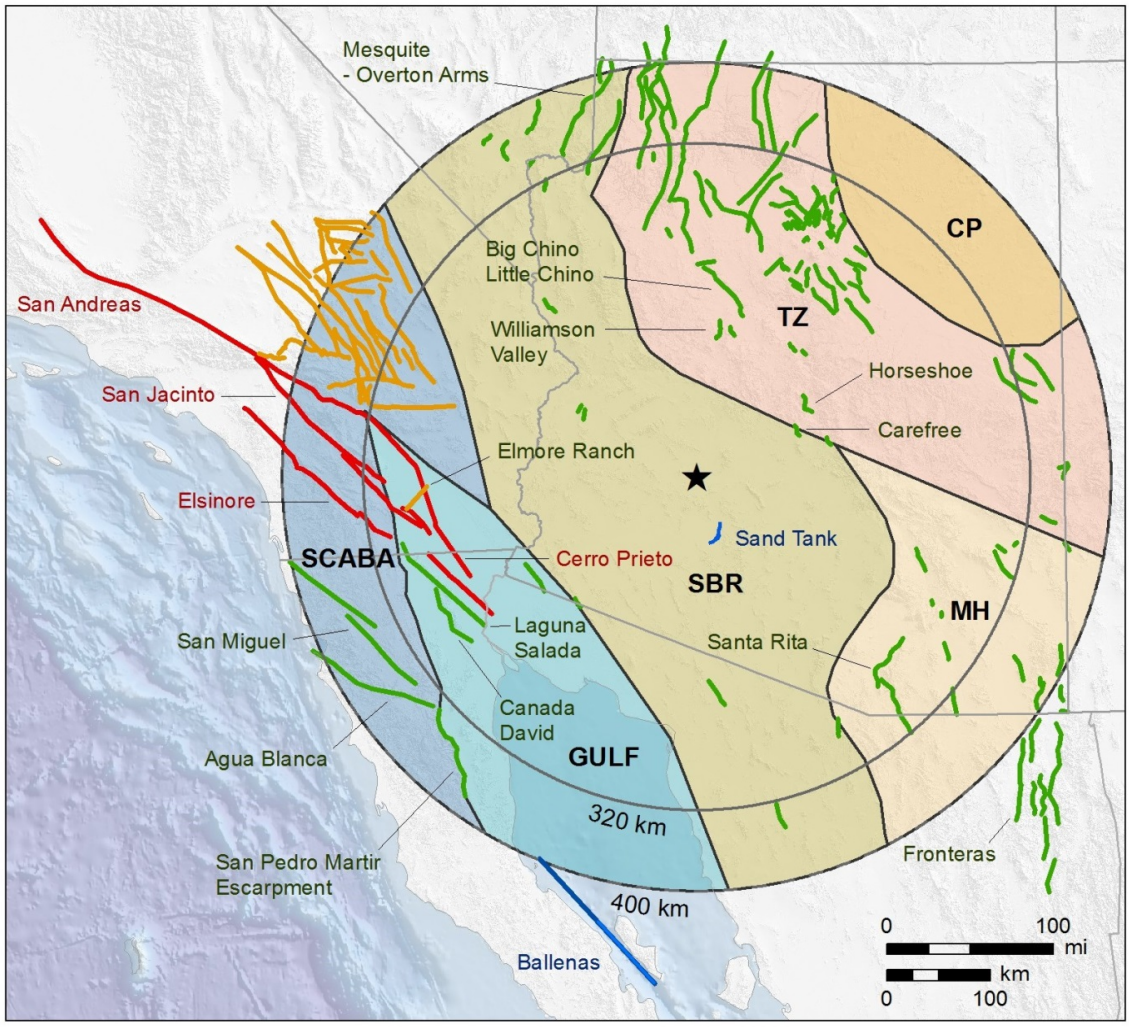

Figure EX-2: Areal and fault sources in the seismotectonic alternative of the in the PVNGS SSC model (LCI, 2014). Star shows location of the PVNGS site. The areal seismic sources are identified by their name in the PVNGS SSC model (LCI, 2014), where GULF refers to the Gulf of California zone, SCABA refers to the Southern California And Baja zone, SBR refers to the Southern Basin and Range zone, MH refers to the Mexican Highland zone, TZ refers to the Transition Zone, and CP refers to the Colorado Plateau zone. The fault sources are distinguished by the following color code: red = layered fault sources, yellow = other fault sources in California, green = fault sources in Arizona, Nevada, and Mexico, blue = unique fault sources (Sand Tank fault in Arizona and Ballenas Transform in the Gulf of California).

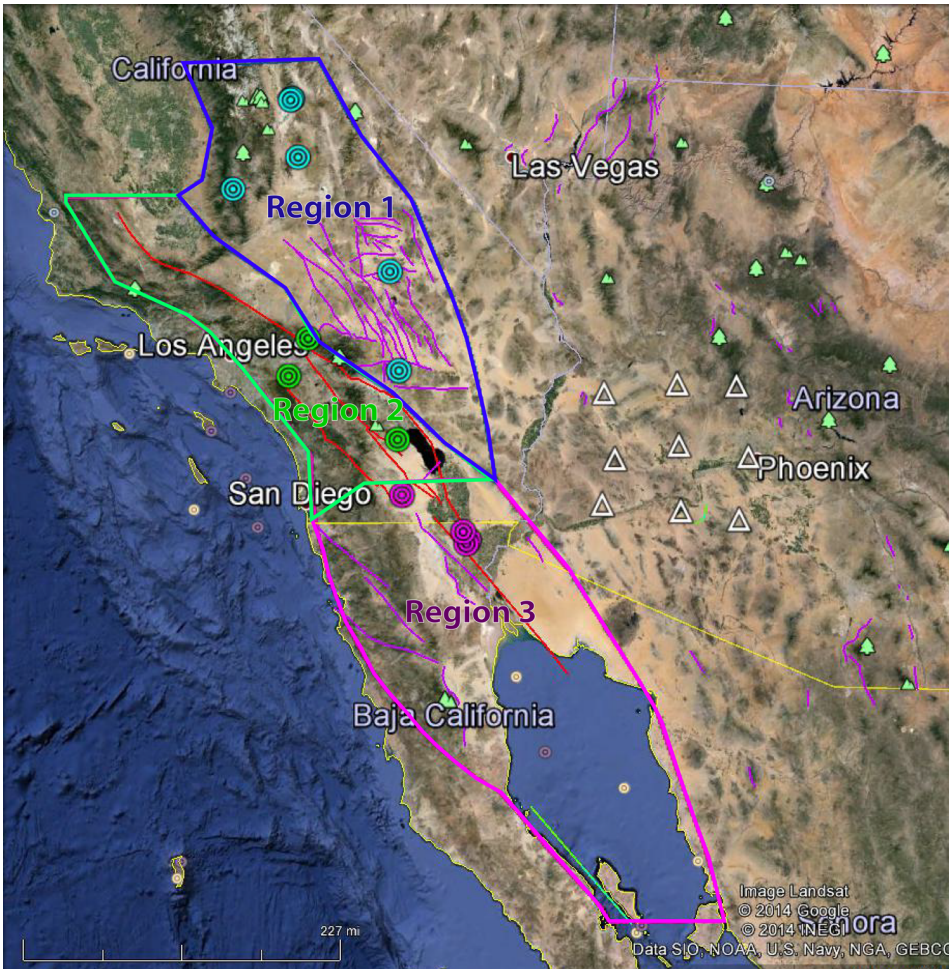

Figure EX-3: Geographic extensions of Region 1, Region 2, and Region 3 shown as blue, green, and purple closed polygons, respectively. Also plot are the NGA-West2 earthquakes selected for the path effect analysis (blue circles for the Region 1 earthquakes, green circles for the Region 2 earthquakes, and purple circles for the Region 3 earthquakes) and the selected Arizona Transportable Array recording stations (white triangles) used for the path effect analysis. Colored lines represent faults in PVNGS SSC Model (Workshop #3, Ross Hartleb, personal communication 2014).

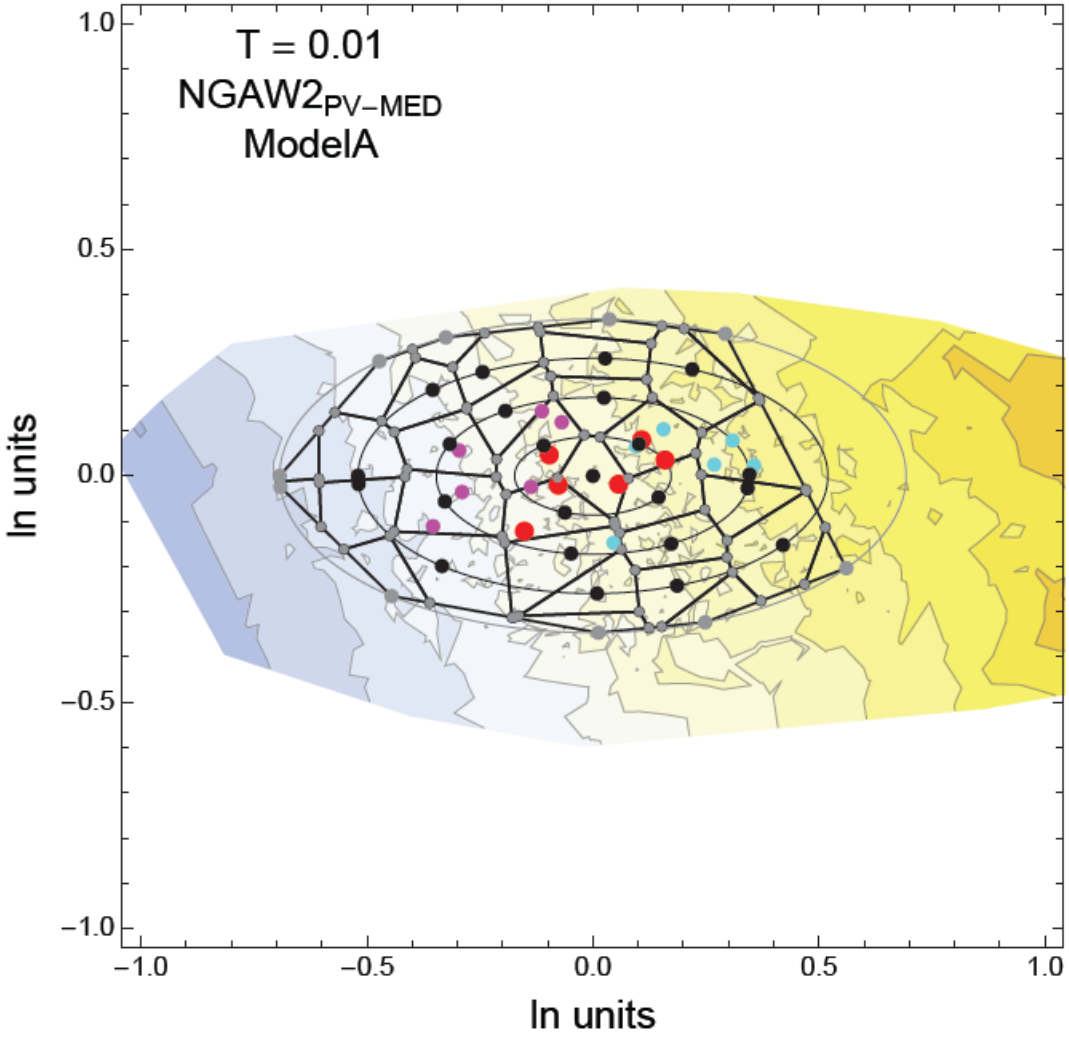

Figure EX-4: Example of a Sammon's map**.** Contour plot of mean between-event residuals for the weighted $NGAW2_{PV\text{-}MED}$ dataset (PVNGS, Model A, T = 0.01 sec). The Voronoi cells used for selecting and weighting models are shown as black lines. The candidate GMPEs are red dots, plus/minus uncertainty as magenta/cyan dots.

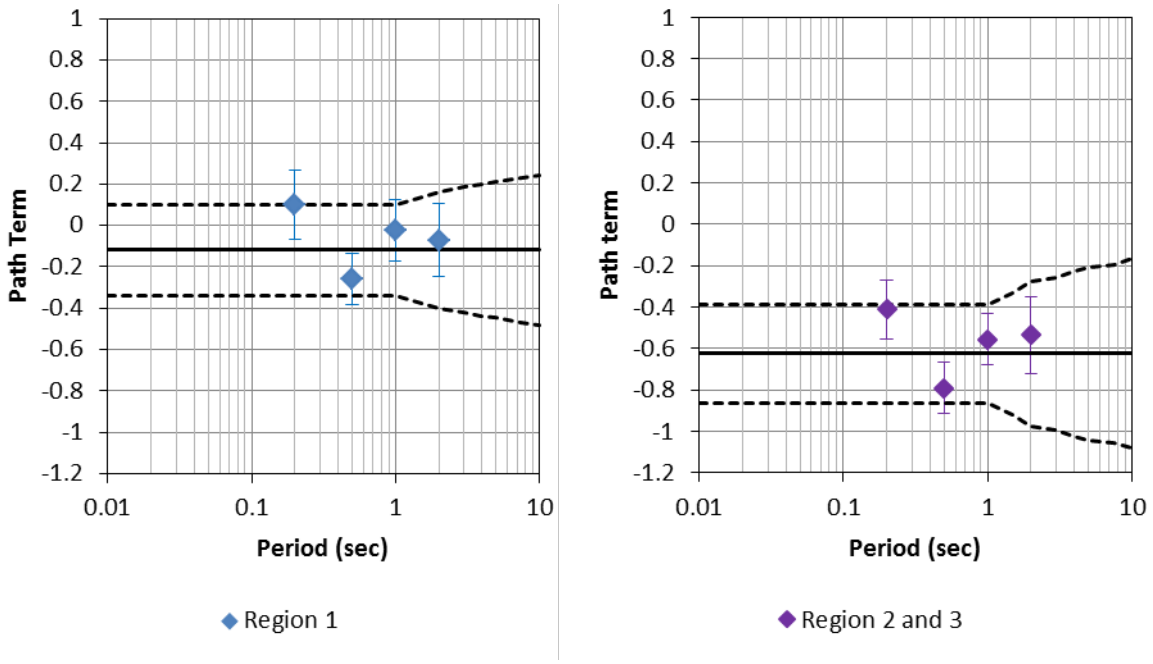

Figure EX-5: Central, high and low path terms for Regions 1 and 2&3. The differences in the central estimates lead to higher ground motions from sources in Region 2&3 by about a factor of 1.7 as compared to sources in Region 1 with the same magnitude and distance.

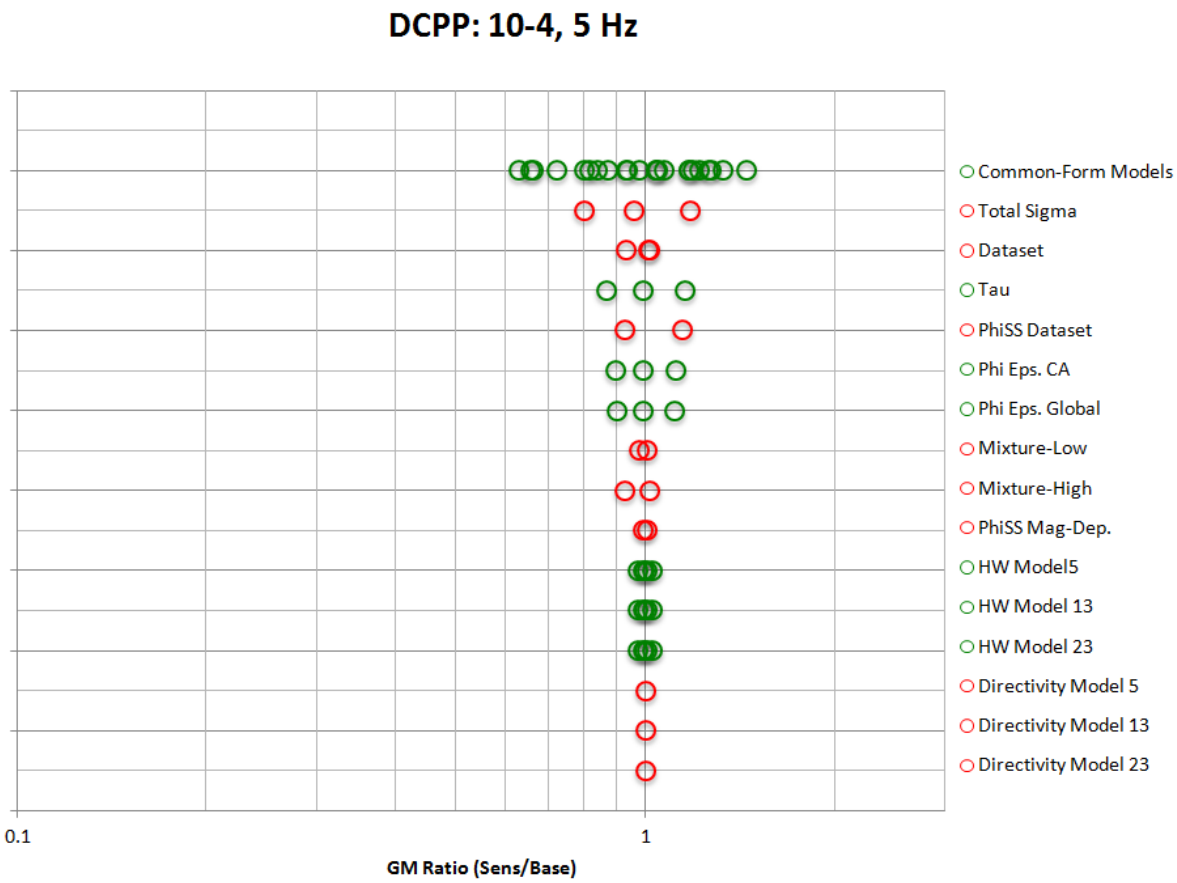

Figure EX-6: Summary tornado plot for DCPP for 5 Hz spectral acceleration at the 10^{-4} hazard level.

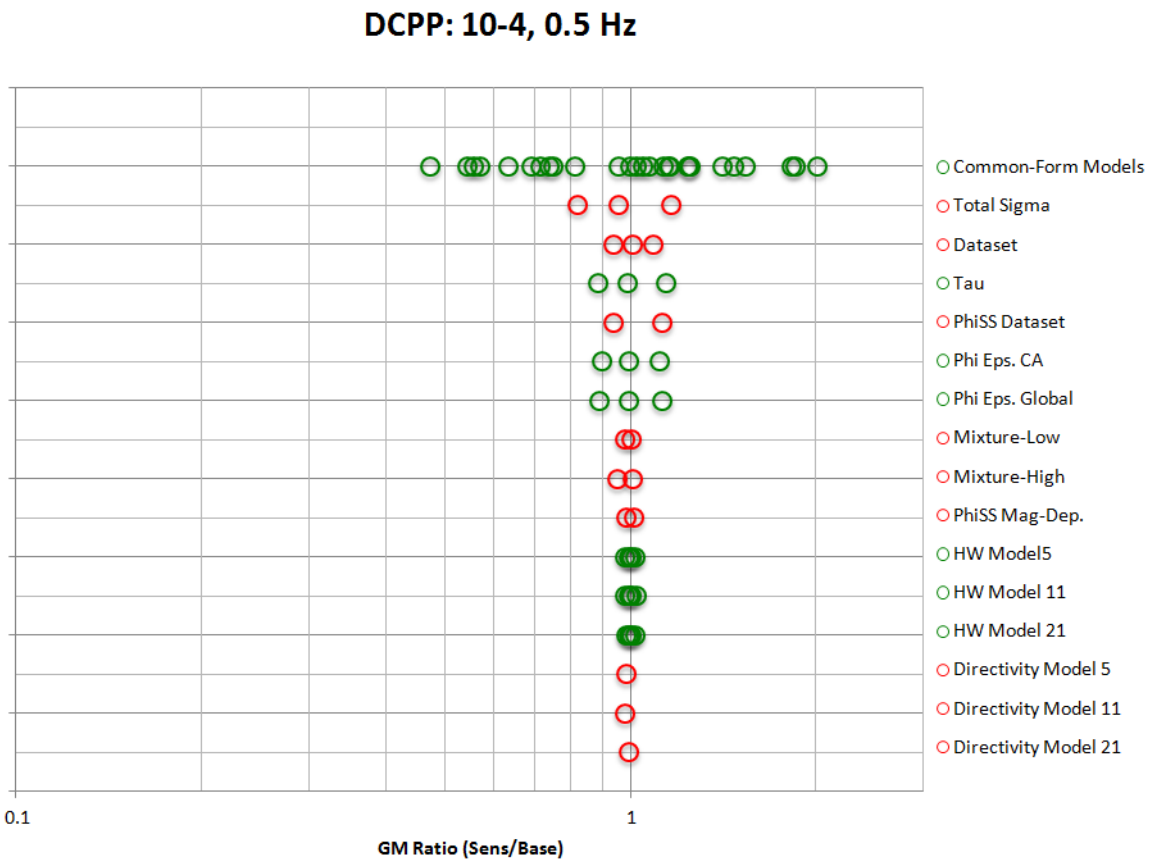

Figure EX-7: Summary tornado plot for DCPP for 0.5 Hz spectral acceleration at the 10^{-4} hazard level.

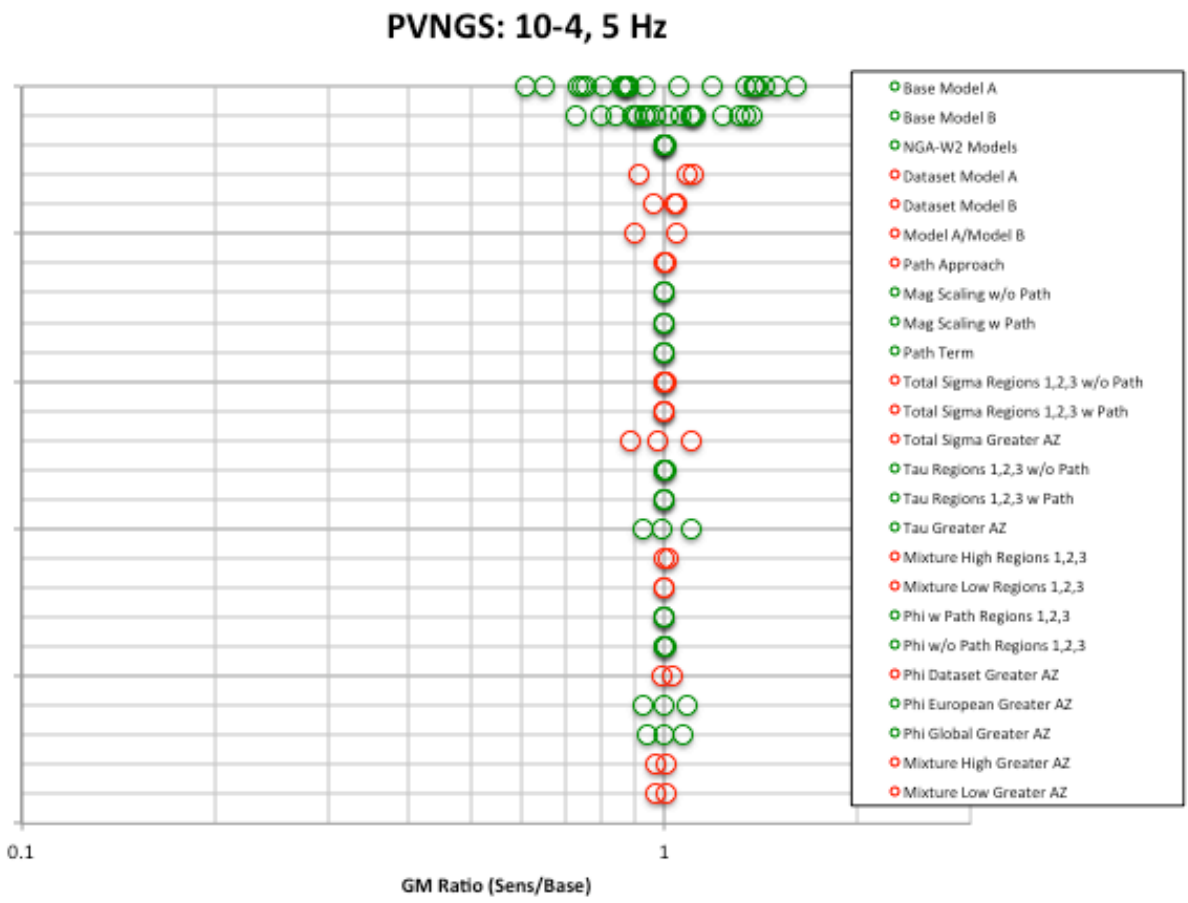

Figure EX-8: Summary tornado plot for PVNGS for 5 Hz spectral acceleration at the 10^{-4} hazard level.

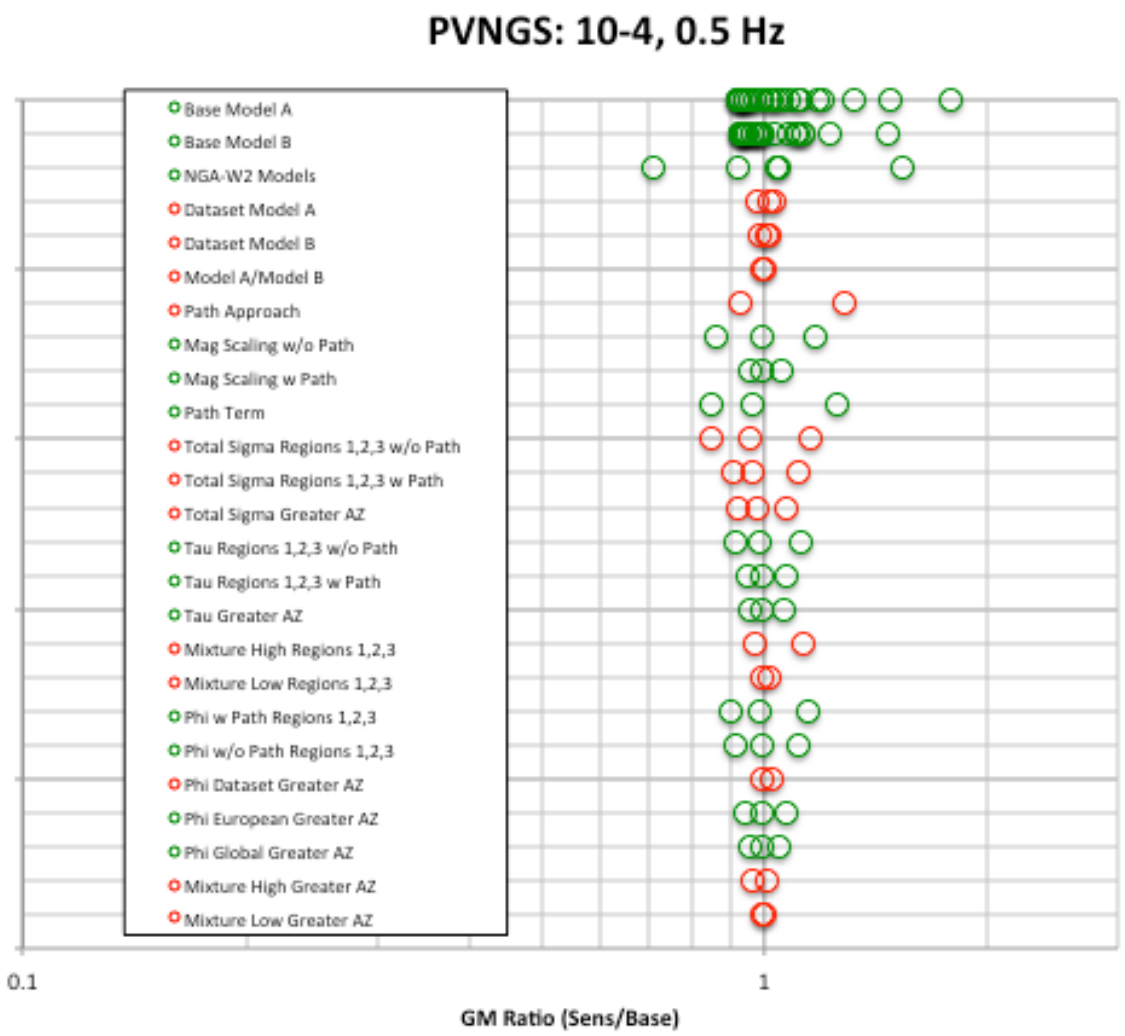

Figure EX-9: Summary tornado plot for PVNGS for 0.5 Hz spectral acceleration at the 10^{-4} hazard level.

LIST OF ABBREVIATIONS and COMMON ACRONYMS

1D	One-Dimensional
2D	Two-Dimensional
AB	Agua Blanca Fault
ABR	Arizona Basin and Range
ACR	Active Crustal Region
AFE	Annual Frequency of Exceedance
APS	Arizona Public Services
AS08	Abrahamson and Silva (2008) GMPE
ASB14	Akkar et al. (2014a, 2014b) GMPE
ASK14	Abrahamson et al. (2014) GMPE
AZ	Arizona
AZGS	Arizona Geological Survey
BA08	Boore and Atkinson (2008) GMPE
BCLC	Big Chino Little Chino Fault
Bi14	Bindi et al. (2014a, 2014b) GMPE
BBP	Broad-band Platform
BSL	Berkeley Seismological Laboratory
BSSA14	Boore et al. (2014) GMPE
CA	California
Caltech	California Institute of Technology
CB08	Campbell and Bozorgnia (2008) GMPE
CB14	Campbell and Bozorgnia (2014) GMPE
CBR	Center, Body, and Range
CD	Canada David Detachment
CDF	Cumulative Distribution Function
CEA	California Earthquake Authority
CEC	California Energy Commission

CEUS	Central and Eastern United States
CF	Carefree Fault Zone
CFM	Community Fault Models
CFR	Code of Federal Regulations
CGS	California Geological Survey
CH	Calico-Hidalgo Fault
CI	Closeness Index
COSMOS	Consortium of Organizations for Strong-Motion Observation Systems
CP	Colorado Plateau
CP - F	Cerro Prieto Fault
CPUC	California Public Utilities Commission
CV	Coefficient of Variation
CY08	Chiou and Youngs (2008) GMPE
CY14	Chiou and Youngs (2014) GMPE
DCPP	Diablo Canyon Power Plant
ΔDPP	Directivity Parameter in Chiou and Youngs (2013)
δS2S	Site-to-site Residual (also known as Site Term)
δWS	Singe-Site within-event Residual
EE	Evaluator Expert
EL	Elsinore Fault
$EUR_{PV\text{-}MED}$	Subset of European Database used to evaluate PVNGS GMPE weights
eqk	Earthquake
EXSIM	EXSIM FFS method
ϕ	Phi, Intra-event Standard Deviation
ϕ_{SP-R}	Single Path-to-Region Sigma
ϕ_{SS}	Single Station Sigma
FAS	Fourier Amplitude Spectrum
FF	Finite Fault
FFS	Finite Fault Simulations
FGF	Fragile Geological Feature
FN	Fault Normal

FP	Fault Parallel
FW	Footwall
GIL7	crustal velocity model of Pasyanos et al. (1996)
GIS	Geographic Information System
$GLOBAL_{DC\text{-}PHISS}$	Global Database used to evaluate DCPP Single-Station Sigma
$GLOBAL_{PV\text{-}PHISS}$	Global Database used to evaluate PVNGS Single-Station Sigma
GM	Ground Motion
GMC	Ground Motion Characterization
GMPE	Ground Motion Prediction Equation
GMRS	Ground Motion Response Spectrum
GP	Graves and Pitarka FFS method
GPS	Global Positioning System
GULF	Gulf of California
HA	Hazard Analyst
HID	Hazard Input Document
HC	Hazard Calculation
HS	Hurricane Fault (Southern)
HSL	Helendale-South Lockhart Fault
HW	Hanging Wall
Hz	Hertz
Id14	Idriss (2014) GMPE
IMP	Imperial Fault
IPRG	Independent Peer Review Group
ITC	Informed Technical Community
IRVT	Inverse Random Vibration Theory
JOS	Joshua Tree (refers to recording site)
κ	kappa (a measure of the observed high-frequency decay of Fourier amplitude spectra - FAS of ground motion)
κ_0	zero-distance kappa
κ_{AS}	kappa estimated using acceleration spectrum approach
κ_{BB}	kappa estimated using broadband approach
κ_{SD}	kappa estimated using displacement spectrum approach

κ_{obs}	kappa observed at a site from a given earthquake
κ_{source}	spectral decay due to source effect
κ_{path}	spectral decay due to site effect
κ_{site}	spectral decay due to site effect
km	Kilometer
L	Rupture length
LA	Landers Fault
LCI	Lettis Consultants International
LCN	Lucerne (refers to recording site)
LI	Libertad Fault
LiDAR	Light Detection and Ranging
LLOWS	Lenwood-Lockhart-Old Woman Springs Fault
ln	Natural Log
LS	Laguna Salada Fault
M	Moment Magnitude
MASW	Multi-channel Analysis of Surface Waves
MH	Mexican Highlands
MHBR	Mexican Highland Basin and Range
ms	Milliseconds
NASB	Northern Arizona Seismic Belt
NBR	Nevada Basin and Range
NE	Northeast-Vergent (refers to DCPP alternative fault geometry models)
NEHRP	National Earthquake Hazards Reduction Program
NGA	Next Generation Attenuation
NGA-West1	Project name for the five 2008 NGA models
NGA-West2	Project name for the 2014 update of the 2008 NGA models
$NGA\text{-}W2_{DC\text{-}MED}$	Subset of NGA-West2 Database used to evaluate DCPP GMPE weights
$NGA\text{-}W2_{PV\text{-}MED}$	Subset of NGA-West2 Database used to evaluate PVNGS GMPE weights
$NGA\text{-}W2_{CA\text{-}PHISS}$	Subset of NGA-West2 Database used to evaluate DCPP Single-Station Sigma
$NGA\text{-}W2_{PV\text{-}PHISS}$	Subset of NGA-West2 Database used to evaluate PVNGS Single-Station Sigma
NML	Normal (refers to normal faults and events)

NPP	Nuclear Power Plant
N_{REC}	Number of Recordings
NRC	Nuclear Regulatory Commission
NSHM	National Seismic Hazard Maps
NSHMP	National Seismic Hazard Mapping Program
NUREG	U.S. Nuclear Regulatory Commission Regulation
NV	Nevada
OBL	Oblique (refers to oblique faults and events)
OV	Outward-Vergent (refers to DCPP alternative fault geometry models)
PBMML	Pisgah-Bullion Mountain-Mesquite Lake Fault
PCA	Principal Component Analysis
PE	Proponent Expert
PE&A	Pacific Engineering and Analysis, Inc.
PEER	Pacific Earthquake Engineering Research Center
PEER-AZ_{PATH}	Subset of NGA-West2 Database used to evaluate PVNGS path terms
PEER-AZ_{KAPPA}	Subset of NGA-West2 Database used to evaluate PVNGS kappa term
PGA	Peak Ground Acceleration
PG&E	Pacific Gas & Electric
PKD	Parkfield (refers to recording site)
PM	Project Manager
PMF	Pinto Mountain Fault
PPRP	Participatory Peer Review Panel
PRP	Pegasos Refinement Project
PSA	Pseudo-spectral acceleration
PSHA	Probabilistic Seismic Hazard Analysis
PTI	Project Technical Integrator
PVNGS	Palo Verde Nuclear Generating Station
Q	Anelastic Attenuation
QA	Quality Assurance
Q-Q Plot	Quantile Plot
RE	Resource Expert
REV	Reverse (refers to reverse faults and events)

REV/OBL	Reverse/Oblique (refers to reverse faults and events)
RESORCE	Reference Database of Seismic Ground Motion in Europe
RG	Regulatory Guide
RMS	Root Mean-Squared Distance
R_{JB}	Joyner and Boore Distance
R_{RUP}	Rupture Distance
R_X	Horizontal Distance from Top of Rupture Measured Perpendicular to Fault Strike
R_Y	Horizontal Distance from End of Rupture Measured Parallel to Fault Strike
σ^2	Total Aleatory Variance
σ	Sigma (total aleatory standard deviations)
σ_{SP-R}	Single Path-to-Region Total Sigma
σ_{SS}	Single-Station Total Sigma
$\sigma^2_{CHANGE}(T)$	Difference in CY14 variance if directivity effects are explicitly included or excluded
SA	San Andreas Fault
SASW	Spectral Analysis of Surface Waves
SBR	Sonora Basin and Range
SC	Southern California
SCABA	Southern California and Baja
SCE	Southern California Edison
SCEC	Southern California Earthquake Center
SCFM	Statewide Community Fault Model
SCSN	Southern California Seismic Network
SD	Spectral Displacement
SD	Standard Deviation
SDSU	San Diego State University FFS method
sec	Seconds
SH	Superstition Hills Fault
$SIM_{Complex}$	SCEC BBP Simulations used to evaluate DCPP complex rupture ground motions
$SIM_{DC\text{-}MED}$	SCEC BBP Simulations used to evaluate DCPP GMPE weights
SIM_{HW}	SCEC BBP Simulations used to evaluate DCPP HW effects and Z_{TOR} scaling
SIM_{Splay}	SCEC BBP Simulations used to evaluate DCPP splay rupture ground motions

SJ	San Jacinto Fault
SM	San Miguel Fault
SOF	Style of Faulting
SONGS	San Onofre Nuclear General Station
SPME	San Pedro Martir Escarpment
SP-R	Similar Path-to-Region
SRSS	Square Root of the Sum of the Square
SS	Strike Slip (refers to strike slip faults and events)
SSC	Seismic Source Characterization
SSHAC	Senior Seismic Hazard Analysis Committee
SSRS	Square Root of the Sum of the Squares
SSS	Single-Station Sigma
ST	Sand Tank Fault
SW	Southwest-Vergent (refers to DCPP alternative fault geometry models)
SWUS	Southwestern United States
SZ	Subduction Zone
T	Period
τ	Tau, event-to-event standard deviation
TA	Transportable Array
TDI	Technically Defensible Interpretation
TI	Technical Integrator
TNSP	Thyspunt Nuclear Siting Project
TZ	Arizona Transition Zone
TZA	Arizona Transition Zone A
TZB	Arizona Transition Zone B
TZC	Arizona Transition Zone C
UCERF2	Uniform California Earthquake Rupture Forecast, Version 2
UCERF3	Uniform California Earthquake Rupture Forecast, Version 3
U.S.	United States
USArray	EarthScope Transportable Array
USGS	United States Geological Society
U.S.NRC	U.S. Nuclear Regulatory Commission

USR	Unified Structural Representation
VA	Vallecitos Fault
V_{S30}	Travel-time-averaged Shear Wave Velocity in the upper 30 meters
W	Down-dip rupture width (km)
WGCEP	Working Group on California Earthquake Probabilities
WidthDD	Down-Dip Width
WNA	Western North America
WUS	Western United States
WVG	Williamson Valley Grabes
χ^2	Chi-squared (refers to distribution)
ZH06	Zhao et al. (2006) GMPE
ZL11	Zhao and Lu (2011) GMPE implementation by GMC TI Team
Z_{TOR}	Depth to Top of Rupture

1 INTRODUCTION

This report describes the results of the Southwestern U.S. (SWUS) Ground-Motion Characterization (GMC) Project conducted from August 2012, to February, 2015. The results of this study are alternative sets of ground motion prediction equations (GMPEs) to be used in probabilistic seismic hazard analyses (PSHAs) by licensees of nuclear plants located in California and Arizona in developing their responses to the request for information from the Nuclear Regulatory Commission (NRC) regarding the near-term task force review of insights for the Fukushima Dai-Ichi accident, Recommendation 2.1: Seismic. This request for information was issued by the NRC on March 12, 2012 (U.S. NRC, 2012a).

Because many of the technical issues for ground motion are similar for Western U.S. sites, thee Western U.S. utilities, Arizona Public Sevice (APS), Pacific Gas and Electric (PG&E) Company, and Southern California Edison (SCE) Company, joined together to conduct a Western U.S. ground motion characterization study applicable to the Palo Verde Nuclear Generating Station (PVNGS), the Diablo Canyon Power Plant (DCPP), and the San Onofre Nuclear Generating Station (SONGS) sites. In September 2013, SCE withdrew from the project. As a result, the final report addresses the ground motion characterization for only two sites: DCPP and PVNGS.

The implementation of the project was consistent with the NRC's March 2012 letter which requires a Senior Seismic Hazard Analysis Committee (SSHAC) Level 3 approach for the development of the seismic source characterization (SSC) and ground motion characterization (GMC) for use in a PSHA.

1.1 Objective of the SWUS GMC Project

The objective of the SWUS GMC Project is to develop site-specific ground motion models for the median and the total aleatory standard deviation (sigma) for use in conducting probabilistic seismic hazard analyses (PSHAs) at the DCPP and PVNGS sites that meet the requirements for a SSHAC Level 3 study as described in NUREG/CR-6372 "Recommendations for Probabilistic Seismic Hazard Analysis: Guidance on Uncertainty and Use of Experts" (U.S. NRC, 1997). The NRC guidance for conducting a SSHAC Level 3 study is described in NUREG-2117 "Practical Implementation Guidelines for SSHAC Level 3 and 4 Hazard Studies" (U.S. NRC, 2012b).

The ground motion models are defined for a reference site condition described in section 1.1.2. The reference site condition is the same for the two sites. The site-specific aspects of the ground motion models are addressed by optimizing the ground motion models for the seismic sources that have significant contributions to the seismic hazard at each site.

1.1.1 Interface with SSC Models

The development of the SSC models at PVNGS and DCPP are site-specific efforts carried out in separate studies conducted by the two utilities. The GMC models have been developed to be applicable to all the relevant sources that have been characterized by the SSC studies. The interface with the SSC projects benefitted from several interactions among respective TI Team members, Project Managers, Project Technical Integrators and Hazard Analysts, to ensure that all the relevant sources were adequately characterized with respect to their ground motions.

For DCPP, the hazard is dominated by nearby strike-slip and reverses faults (within 10 km) with mangitudes in the range of **M**5.5 to **M**7.5. The DCPP site is on the hanging wall of the hazard significant dipping faults. Therefore, the ground motion model was optimized for near-fault ground motions including hanging-wall effects. In addition, linked ruptures, which are either complex ruptures (significant change in dip or rake along strike) or splay ruptures (synchronous rupture of over-lapping fault segments near the site), are being considered by the SSC so rules for using the GMPEs to compute the ground motion for these cases are also developed.

For PVNGS, the hazard is dominated by nearby strike-slip and normal faulting earthquakes in the host areal zone (local Arizona earthquakes) and by distant large magnitude earthquakes in California and Mexico. Two separate sets of ground motion models were developed for these two dominant sources. For the local sources, the ground motion models were optimized for predominately normal faulting earthquakes with magnitudes **M**5 to **M**7 at distances less than 50 km. For the distant California and Mexico sources, the ground motion models were developed for large magnitudes (**M**7.0 to **M**8.5) at large distances (200 to 300 km). For the distant California and Mexico sources, path-specific effects were included to capture the systematic differences between the path effects from California and Mexico earthquakes to sites in central Arizona from the average path effects in California.

1.1.2 Reference Site Conditions and Interface with Site Response Efforts

The GMC models for PVNGS and DCPP are both developed for a reference site condition with V_{S30} (travel-time-averaged shear wave velocity in the top 30 meters) of 760 m/s. For both sites, the site-specific rock has a higher V_{S30} than 760 m/s. This reference rock condition was selected because it is in the upper range of V_{S30} values for which the GMPEs are well constrained by the empirical data. The site response studies being conducted for PVNGS and DCPP will need to adjust the computed hazard from

the reference rock condition to the site-specific rock condition, in addition to computing the site amplification. The adjustment for the rock condition also needs to address the effect of differences in kappa (a measure of the observed high-frequency decay of Fourier amplitude spectra - FAS of ground motion) in addition to the difference in the V_{S30}. The site response studies are separate, site-specific efforts carried on by each utility and are not part of this report.

To have a consistent interface between the GMPEs for the reference rock site condition and the site-specific site amplification at PVNGS, guidelines addressing the key interface issues are given in Appendix L.

1.2 Ground Motion Models Used in Previous Seismic Hazard Studies

The most recent seismic hazard studies previously conducted at DCPP and PVNGS used published GMPEs with region and/or site-specific adjustments. The approaches used for the developing the GMPEs for DCPP and PVNGS in the previous studies are described below.

1.2.1 DCPP

The most recent seismic hazard study previously conducted for DCPP was in 2011 (PG&E, 2011). This study used the five 2008 Next Generation Attenuation models (now called NGA-West1) as the base models. The 2008 NGA-West1 median ground motion models were adjusted to account for additional epistemic uncertainty (Youngs, 2009) and to account for the site-specific amplification based on recorded ground motions at DCPP. The epistemic uncertainty in the median site-specific amplification was included. The standard deviation was based on the single-station sigma approach using the BCHydro (Addo et al., 2012) model.

1.2.2 PVNGS

The most recent seismic hazard study previously conducted for PVNGS was a SSHAC Level 2 PSHA Project conducted in 2012 (LCI, 2013). The rock ground motion models were based on four of the five NGA-West1 GMPEs (Abrahamson and Silva, 2008 – AS08; Boore and Atkinson, 2008 – BA08; Campbell and Bozorgnia, 2008 – CB08; and Chiou and Youngs, 2008 – CY08).

The large distance scaling for the medians of two of these GMPEs (AS08 and CB08) was evaluated to be inappropriate. The distance scaling beyond 200 km for these two models was modified to be consistent with the distance scaling of the CY08 model.

All four models were adjusted to account for differences in anelastic attenuation between Arizona and California. Two alternative models were used to capture the higher values of anelastic attenuation (Q) in Arizona. The first model assumed that the average Q for paths between California and Mexico sources and the PVNGS site is equal to that for the paths represented by the BA08 and CY08 GMPEs, so that the original BA08 and CY08 models are used. The second model assumed that the average Q for paths between California and Mexico sources and the PVNGS is 50 percent higher than that for the paths represented by the BA08 and CY08 models and the distance scaling coefficients for these models were adjusted to capture reduced attenuation.

The last modification accounted for additional epistemic uncertainty related to the limited size of the strong-motion data set. An intermediate value between the USGS (2008) model and the Youngs (2006) model for additional epistemic uncertainty was used.

1.3 Products of the Project

1.3.1 Ground Motion Characterization Models for Study Sites

The ground motion characterization (GMC) is a set of alternative models using a logic tree format for a reference rock site condition with V_{S30} of 760 m/s. The alternative models for the median and standard deviation of 5%-damped psuedo-spectral acceleration are assigned weights based on the Technical Integrator (TI) Team's assessment on the center, body, and range of the technically defensible interpretations for the ground motion.

A new method for developing a representative suite of models that represents a continuous distribution of GMPEs for the median based models was used (Section 6.4). With this new approach, the weights assigned to the branches of the logic tree for the median represent probabilities based on discretizing continuous distribution rather than relative merit weights for existing GMPEs.

For PVNGS, the GMPE median models include models for the difference in path attenuation between California and Mexico sources and central Arizona compared with the path attenuation within California.

The alternative models for the aleatory standard deviation are based on the single-station sigma approach (see Chapter 7).

1.3.2 Hazard Input Documents

The hazard input documents (HID) in Appendix C for the DCPP and PVNGS sites provide all the information required to implement the SWUS GMC models in a probabilistic seismic hazard analysis

(PSHA). The purpose of the HID is to ensure that the Hazard Analyst for each site receives accurate and unambiguous description of the TI Team's expert assessments.

1.3.3 Documentation of Technical Bases for the Assessments

The technical bases for the TI Team's evaluations are provided in this report. Chapter 6 provides the technical bases for the selection of the candidate models for the median ground motions. Chapter 7 provides the technical bases for the selection of the candidate models for the aleatory standard deviation motions. Chapters 8-13 provide the technical bases for the selection of the weights on each branch of the logic trees.

1.3.4 Application Guidelines and Limitations

The application guidelines and limitations are given in Chapter 15. Appendix L also provides guidelines for the site response studies at PVNGS to be consistent with the GMPEs developed in this study.

1.4 References

Abrahamson, N.A., and Silva, W. (2008). Summary of the Abrahamson & Silva NGA Ground-Motion Relations, *Earthquake Spectra*, Vol. 24(1), 67-97.

Addo, K.O., Abrahamson, N.A., and Youngs, R.R. (2012). Ground Motion Characterization (GMC) Model, *BC Hydro SSHAC Level 3 Probabilistic Seismic Hazard Analysis (PSHA) Report*, Vol.3, November 2012.

Boore, D.M., and Atkinson, G.M. (2008). Ground-Motion Prediction Equations for the Average Horizontal Component of PGA, PGV, and 5%-Damped PSA at Spectral Periods between 0.01s and 10.0s, *Earthquake Spectra*, Vol. 24(1), 99-138.

Campbell, K.W., and Bozorgnia, Y. (2008). NGA Ground Motion Model for the Geometric Mean Horizontal Component of PGA, PGV, PGD and 5% Damped Linear Elastic Response Spectra for Periods Ranging from 0.01 to 10 s, *Earthquake Spectra*, Vol. 24(1), 139-171.

Chiou, B.S-J., and Youngs, R.R. (2008). An NGA Model for the Average Horizontal Component of Peak Ground Motion and Response Spectra, *Earthquake Spectra*, Vol. 24(1), 173-215.

Lettis Consultants International – LCI (2013). Seismic Hazard Evaluation for the Palo Verde Nuclear Generating Station Wintersburg, Arizona, Final Report (Revision 4), Arizona Public Service Co., August 2013.

PG&E (2011). Report on the Analysis of the Shoreline Fault Zone, Central Coastal California, January 2011.

United States Geologic Survey – USGS (2008). Documentation for the 2008 update of the United States National Seismic Hazard Maps, prepared by Petersen, M.D., et al., *U.S. Geological Survey Open File Report* 2008-1128.

U.S. NRC (1997). Recommendations for probabilistic seismic hazard analysis: Guidance on uncertainty and use of experts, prepared by Senior Seismic Hazard Analysis Committee, Lawrence Livermore National Laboratory, Volume 1, Main Report, NUREG/CR-6372, UCRL-ID-122160, 280 pp.

U.S. NRC (2012a). Near-Term Task Force, "Request For Information Pursuant To Title 10 Of The Code Of Federal Regulations 50.54(F) Regarding Recommendations 2.1, 2.3, and 9.3, Of The Near-Term Task Force Review Of Insights From The Fukushima Dai-Ichi Accident."

U.S. NRC (2012b). Practical Implementation Guidelines for SSHAC Level 3 and 4 Hazard Studies, U.S.NRC NUREG-2117.

Youngs, R.R. (2006). Epistemic Uncertainty Model for Use of PEER-NGA Ground Motion Models in National Hazard Mapping. Presented to Next Generation Attenuation Relationships Workshop, PEER, Richmond, CA, September, available at http://earthquake.usgs.gov/hazards/about/workshops/nga_workshop/1D--Youngs_Epistemic.pdf (last accessed 8/05/2014).

Youngs, R.R. (2009). Epistemic uncertainty in the NGA models, Appendix D in Ground Motion Models for the Pacific Northwest, *Report to B.C. Hydro*, December 2010.

2 PROJECT ORGANIZATION

This Chapter addresses the organization and implementation of the SSHAC Level 3 assessment process, with particular emphasis to the fundamental goals and activities of the assessment process, i.e. evaluation and integration.

The description of the project organization is provided in Section 2.2, which also introduces the roles of the key project participants.

Key activities and explanation of how the assessment process adheres to the SSHAC guidelines are instead topics addressed in Chapter 3.

2.1 Goals and Activities of a SSHAC Assessment Process

As described in Section 1.1 of this report, a Senior Seismic Hazard Analysis Committee (SSHAC) methodology, as described in NUREG/CR-6372 "Recommendations for Probabilistic Seismic Hazard Analysis: Guidance on Uncertainty and Use of Experts" (U.S. NRC, 1997), is implemented to ensure that the ground-motion characterization (GMC) inputs to the probabilistic seismic hazard analysis (PSHA) properly and completely represent knowledge, data, and modeling uncertainties. A SSHAC Level 3 study is performed to develop the PSHA for the Western U.S. licensees consistent with the current practice, as described in NUREG-2117 “Practical Implementation Guidelines for SSHAC Level 3 and 4 Hazard Studies” (U.S. NRC, 2012b).

The fundamental goal of a SSHAC process is to provide a methodology for developing GMC models that “…represent the center, the body, and the range of technical interpretations that the larger informed technical community would have if they were to conduct the study” (U.S. NRC, 1997, p. 21). The terminology “center, body, and range (CBR)” refers to the complete characterization of uncertainty in both present-day technical knowledge and available data, while properly representing the uncertainty in the PSHA model. More recently, the NRC (U.S. NRC, 2012b) suggested replacing the terminology “informed technical community (ITC)” with “technically defensible interpretations (TDI)” of the available data, models and methods to more clearly reflect the intent of the SSHAC process.

By following the structured methodology of the SSHAC process, the intent is to provide reasonable regulatory assurance that the goal of representing the center, body, and range of the characterizations has been met, and thus provides the basis for developing seismic hazard estimates that are reproducible, defensible, transparent, and stable.

For the SWUS GMC Project, the SSHAC Level 3 study involves four components: (1) evaluation; (2) integration; (3) participatory peer review; and (4) documentation. These process components are described below.

2.1.1 Evaluation

Evaluation refers to the process of compiling, considering and evaluating relevant sets of data, alternative models/methods, and alternative interpretations proposed by the larger technical community that are relevant to the ground-motion model's hazard at any of the nuclear power plant (NPP) sites in the project.

The process of evaluation includes, but is not limited to, the: (a) identification of hazard-significant issues; (b) compilation of relevant data and models; and (c) evaluation of the data and models with respect to their impact on the GMC by means of sensitivity analyses.

2.1.2 Integration

Integration refers to the assessment process where the various data sets, models, and interpretations are combined into a representation of the CBR of the TDI for the GMC in light of the evaluation process.

The process of integration commonly includes: (a) development of a version of the GMC logic tree by the Technical Integrator (TI) Team; (b) hazard sensitivity analyses conducted by Hazard Analysts to document the impact of model parameters on the seismic hazard; (c) feedback from the Resource Experts, Proponent Experts, and Participatory Peer Review Panel (PPRP) members on the logic-tree models, and hazard sensitivity; and (d) the development of the next versions of the GMC logic tree. This process is iterated until final site-specific GMC logic trees are developed for each site.

The majority of the integration process occurs through informal working meetings and internal work. Among other purposes, the workshops are designed to present the models and sensitivity results, and to collect feedback.

2.1.3 Participatory Peer Review

Participatory peer review refers to review of the evaluation and integration process by a peer review panel capable of providing feedback, during the project, on technical aspects of the project and whether

the SSHAC Level 3 process was implemented appropriately. By receiving feedback from the peer review panel during the project, the TI Team can make necessary corrections before the project is complete. The overall goals of this review will be to ensure that the SSHAC process is adequately followed and that the technical results adequately characterize the CBR of the TDI.

2.1.4 Documentation

Documentation refers to the final reports produced by the project that document the technical results, the technical basis for the evaluation and assignment of weights on the logic tree, and how the SSHAC Level 3 process was implemented. In addition, the documentation provides the basis for review by any pertinent regulatory officials.

2.2 SWUS GMC Project Organization

As described by U.S. NRC (1997 and 2012b) and Hanks et al. (2009), specific roles and responsibilities of individuals within a SSHAC process have been clearly defined. The guided interaction between the different roles allows for the center, body, and range of the GMC to be robustly characterized. During the entire duration of the project, starting with the Kick-Off Workshop, all project participants have been informed of their roles, and were reminded of the importance of keeping to their assigned roles and responsibilities as appropriate.

The project organization is shown on Figure 2.2-1; specific roles of the SSHAC Project Team are described below. The basis for the selection of the project members is given in the SWUS GMC Project Plan (See Annex A of Appendix A).

2.2.1 Project Sponsors

According to the SSHAC approach, the Project Sponsors provide financial support and “own” the results of the study in the sense of property ownership.

Arizona Public Service (APS) and Pacific Gas and Electric Company (PG&E) jointly sponsored the SWUS GMC SSHAC Level 3 Project. Southern California Edison (SCE) was initially part of the joint sponsorship, but withdrew its participation before Workshop #2 as a result of San Onofre Nuclear Generating Station (SONGS) retirement.

Project Sponsors representatives attended all the formal workshops and key project meetings. Additionally, they interacted with the Project Management on a regular basis throughout the duration

of the project. The regular interactions supported the establishment of common goals and expectations, and facilitated tracking of progress and activities.

Additionally, the Sponsors reviewed and approved the Project Plan.

2.2.2 Progect Management

Project Management was responsible for the project logistics, including scope, schedule and budget. It also coordinated the execution of the project and ensured timely delivery of all the products.

In particular, the responsibilities associated to contract management were assigned to GeoPentech, which contracted with the Sponsors and the SWUS GMC Project participants, represented the main interface for contracts by securing adequate compliance, and provided support for workshops and technical meetings.

The responsibilities associated with maintaining clear lines of communication and main point of contact between Sponsors, the TI Team Lead and the PPRP were assigned to the SWUS GMC Project Manager, Carola Di Alessandro. Dr. Di Alessandro was selected by the Project Sponsors, and assisted GeoPentech in establishing and maintaining budgets and schedules, assured that the project plan was executed in accordance with the scope and timeline, and had the responsibility for the delivery of all technical products, including Project Plan, workshop documentation on public website, and project reports.

The Project Management was also responsible for preparing regular status reports on schedule, scope and budget for the Project Sponsors. Together with the TI Team Lead, the Project Management was involved in the organization of the formal workshops and working meetings, and reviewed technical documents delivered by the TI Team. Together with the TI Lead and some of the TI Team members, the Project Manager was also actively involved in the University Research Task (see Section 3.3) to keep abreast of the research development and to provide some technical evaluation on the impact of the research in the ground-motion at the NPP sites.

2.2.3 Technical Integrator (TI) Team

The Technical Integrator (TI) Team, led by Dr. Norman Abrahamson, was responsible for implementing the SSHAC Level 3 procedure, including the key evaluation and integration tasks. Accordingly, the TI Team was responsible for ensuring that: (1) the various data, models, and methods proposed by the larger technical community and relevant to the hazard analysis are considered in the evaluation; and (2) the final GMC models represent the center, body and range of the TDI. The members of the TI Team ultimately “own” the results of the study with respect to intellectual responsibility for the results. As such, they were accountable for the development of the GMC models, and for the clear and comprehensive documentation of all the associated technical bases and assessments. Specific

responsibilities of the TI Team included preparing the SWUS GMC Project Plan, performing evaluation and integration activities, leading the conduct of multiple working meetings, finding and assuring participation of suitable Resource and Proponent Experts, running workshops and ensuring that the participants clearly understand the workshop objectives, their individual roles, the required output from the workshops, and the implication to hazard. The TI Team members were also involved, together with the Project Manager, in responding to PPRP's comments and reviews throughout the duration of the project.

The TI Team members were selected with the goal of having a balance between senior members with extensive experience in SSHAC studies and younger members that have limited or no SSHAC experience. The purpose of including younger members was to build up the pool of ground-motion experts with SSHAC experience. Initially, a 5-member TI Team was selected for this project with three senior people and two younger people. After Workshop #2, one of the younger TI Team members was called to military service and had to drop out from the project. The TI Team members have experience with empirical data, ground-motion model development, and numerical simulations.

The TI Team was supported by a staff of Evaluator Experts that were not officially part of the TI Team but assisted the Team in developing new models during the data evaluation part of the project.

2.2.4 Project Technical Integrators (PTI)

The two PTIs were responsible for ensuring coordination and compatibility between the joint SWUS GMC Project and the seismic-source characterization (SSC) studies being conducted separately by the two utilities. Dr. Abrahamson and Dr. McGuire (assisted by Dr. Toro) were selected as PTI by PG&E and APS, respectively, to be responsible for the coordination of the SWUS GMC, the plant-specific SSC, and the site-specific site response efforts. The choice was consistent with the description of the PTI's requirements according to the SSHAC protocol, which defines the PTI as a technical expert with knowledge of the SSHAC process, both GMC and SSC studies, and the site-specific application for site response effects.

2.2.5 Specialty Contractors and Database Developers

Specialty contractors were involved during various stages of the project to provide certain technical products, including collection of ground-motion data in Arizona, shear wave velocity characterization of selected seismographic stations around PVNGS, analysis of spatial correlation effects on sigma, and preliminary estimates on the kappa sensitivity for PVNGS.

Database developers produced collections of ground motions and proponent models to be used in the evaluation process by the TI Team. The ground motions included both empirically recorded and

simulated data, and were mainly produced as part of the "University Research" Task described in Section 3.3.

2.2.5.1 Pacific Earthquake Engineering Research Center (PEER)

PEER was involved in a number of activities associated with Database Development, described in details in Section 3.2. The PEER NGA-West2 database was one of the primary empirical databases utilized in the SWUS GMC Project (see Chapter 5 for more details). With partial funding from the SWUS GMC Project, PEER was also involved in the Arizona Ground Motion Project (Kishida et al., 2014). This project led to the creation and dissemination of a new ground-motion database for Arizona, which included recordings from small magnitude earthquakes in Arizona recorded in the surrounding region of PVNGS, and recordings from moderate to large magnitude earthquakes in California and Mexico recorded in Arizona. The Arizona Ground Motion Project was also inclusive of two external technical contributions addressing the characterization of the recording stations around PVNGS in terms of kappa evaluation (by Dr. Olga Ktenidou – ISTerre Grenoble, France; and by Pacific Engineering and Analysis, Inc.), and in terms of V_{S30} and NEHRP classification (by Dr. Robert Kayen, UCLA and USGS). The results of the Arizona Ground Motion Project are published as a PEER report (Kishida et al., 2014) and are publicly available.

In terms of ground-motion database development, PEER also collected and processed ground motions from the Fukushima-Hamadori Japanese normal-faulting earthquake that occurred shortly after the Fukushima earthquake, as part of the NGA-Subduction ongoing effort (Bozorgnia - personal communication, 2015). The data are stored at the PEER website and are publicly available (Section 5.1.5.2).

Proponent NGA-West2 ground-motion prediction equations (GMPEs) evaluated in the SWUS GMC Project were developed as a PEER project. Proponent models for addressing directivity adjustments to median and sigma, for single station sigma, and for epistemic uncertainty through visualization techniques applied to GMPEs were also developed as PEER projects in coordination with the NGA-West2 effort, with partial funding from PG&E and SCE.

2.2.5.2 Southern California Earthquake Center (SCEC)

A part of the database compiled for the SWUS GMC Project includes suites of numerical finite-fault simulations (FFS) computed using the SCEC broadband platform. SCEC conducted a major systematic evaluation of the methods for numerical simulation of ground motion for engineering applications. In doing so, they developed a series of validation exercises designed to test the numerical simulation methods. SCEC has produced a report describing the evaluation process and recommending a set of simulations methods that pass the validation tests (Dreger et al., 2013). This set of proponent models are evaluated as part of the SWUS GMC study under the SSHAC process (Section 5.2). The SCEC validation study was partially supported with external funding from PG&E and SCE, whereas the

Broadband network cost to produce the simulations utilized by the SWUS GMC Project was shared among the Sponsors.

2.2.5.3 Other Studies (Virginia Tech, PE&A, etc)

Dr. Shrey Shahi, under the guidance of Prof. Adrian Rodriguez-Marek at Virginia Tech, evaluated the impact of spatial correlation to sigma (Shahi et al., 2015 – Attachment D). These results are evaluated by the TI Team under the SSHAC process (Section 13.4).

An additional specialty contract was assigned to Walt Silva at Pacific Engineering and Analysis, Inc. (PE&A) to estimate the sensitivity of the ground-motion amplification at PVNGS if the underlying bedrock kappa differs significantly from the kappa associated with the reference Western U.S. profile. The results of that sensitivity were presented at the SWUS Workshop #1 and indicated that the impact of the kappa difference between California and Arizona could be significant, thus prompting the PEER–led efforts to characterize kappa in the PVNGS surroundings.

2.2.6 Resource Experts

Resource Experts (RE) are one of the three experts categories identified in the SSHAC guidance, together with the Proponent Experts and the Evaluator Experts. A RE is an expert with a specialized knowledge of a particular data set, interpretation, or hypothesis who can present this information without a proponent bias. The REs provide their specialized knowledge to assist the TI Team in the evaluation but they do not take ownership or endorse the final GMC models.

The REs were identified as needed during the project. REs were generally invited to one or more workshops. Additionally, throughout the duration of the project, some REs attended working meetings with the TI Team to present and discuss their specialized knowledge regarding the strengths and weaknesses of alternative models and data sets.

2.2.7 Proponent Experts

In contrast to the RE, a Proponent Expert (PE) advocates a particular hypothesis or technical position. The PE's opinion may range from mainstream to extreme (outlier) views. PEs were identified as needed during the project, and were primarily GMPEs developers and FFS modelers. PEs were generally invited to one or more workshops and some provided post-workshop feedback or attended working meetings.

2.2.8 Hazard Calculation Team

The Hazard Analyst (HA) is a PSHA expert responsible for performing the PSHA calculations. Hazard Analysts are incorporated into all phases of the study (e.g., evaluation, integration) because they can

provide: (a) valuable insight into how to represent uncertainty for input into PSHA; and (b) hazard sensitivity feedback to identify the key parameters contributing to the hazard uncertainty.

Each utility provided its own Hazard Analyst, knowledgeable with the site-specific SSC, so that the hazard feedback addressed the key issues at the two NPP sites. The selected Hazard Analysts have technical expertise with hazard computation and analysis, have specific working knowledge of PSHA programs, and are able to perform hazard analysis under quality assurance (QA).

2.2.9 Participatory Peer Review Panel

The Participatory Peer Review Panel (PPRP) is a panel of experts with SSHAC methodology and/or PSHA experience that is involved throughout all phases of the project by providing continuous review of the project adherence to the SSHAC Level 3 process, and of the technical evaluations of the TI Team. The PPRP's review ensures that: (a) the range of technically defensible interpretations prevailing within the technical community has been captured and documented; (b) knowledge and uncertainties have been properly quantified and incorporated into the analysis, and (c) the technical bases and justifications have been clearly documented while properly implementing the SSHAC process.

The members of the PPRP serve as individuals and not as an affiliate of any organization. As panel members, they are serving as recognized experts in their respective fields and are selected so that, collectively, they have experience and specialized technical knowledge on: (a) empirical ground-motion models for active crustal regions; (b) numerical simulations of ground-motion models for active crustal regions, and (c) source characterizations in the Southwestern U.S. (for interface issues between SSC and GMC models).

Members of the PPRP fulfilled their responsibilities by: (a) reviewing and providing written comments on the SWUS GMC Project Plan; (b) attending all of the formal workshops and working meetings; (c) participating in selected technical meetings as suggested by the TI Team Lead, to keep abreast of the scientific work being developed in the technical community that would be used as input by the project; d) providing oral and written review comments on interim technical assessments or other products developed by the TI Team during the project; e) participating in the PPRP Closure Pre-Briefing and Briefing Meetings; f) reviewing the draft project report, and g) issuing commentary letters to improve the draft project report.

Additionally, members of the PPRP interacted individually with the TI Team and Project Manager in the role of Resource or Proponent Expert during selected meetings.

A concurrence letter report (after review comments were adequately addressed) was provided to the Project Manager for inclusion in the final project report (Appendix B).

2.3 Project Schedule

The schedule for completing the SWUS GMC SSHAC Level 3 Project is presented as Figure 2.3-1, which shows the major milestones of the project and the duration of the main work elements. The schedule also reflects major milestones associated with the University Research tasks conducted by PEER and SCEC for the SWUS GMC study.

Table 2.3-1 shows the dates that the main meetings which took place during the SWUS GMC study. The project commenced with Workshop 0 (Kick-Off Meeting) in August 2012, preceded by two planning meetings. Formal workshops were held at 6-month intervals in October and March during the study. Several working meetings were conducted during the project, in preparation and as follow-up to the three formal workshops. Members of the PPRP attended the workshops and working meetings. A two-day working meeting, referred to as Special Working Meeting, occurred in January 2014 where additional feedback from Workshop #2 REs and PEs was presented and discussed in the presence of the PPRP and additional observers. Also, internal communications among TI Team, PM, and relevant project participants occurred during informal Logic Tree Meetings held to develop the final GMC models. Two briefing meetings with PPRP were conducted after Workshop #3 (PPRP Closure Pre-Briefing and Closure Briefing in May and July 2014, respectively) to present the updated GMC models to the PPRP while capturing their verbal feedback.

2.4 References

Dreger, D.S., Beroza, G.C., Day, S.M., Goulet, C.A., Jordan, T. H., Spudich, P.A, and Stewart, J. P. (2013). Evaluation of SCEC Broadband Platform Phase 1 Ground Motion Simulation Results, 33 pp. plus Appendices, Report submitted to SCEC, Aug. 1 2013. Available at http://scec.usc.edu/scecpedia/SCEC_BBP_Phase_1_Evaluation.

Hanks, T.C., Abrahamson, N.A., Boore, D.M., Coppersmith, K.J., and Knepprath, N.E. (2009). Implementation of the SSHAC Guidelines for Level 3 and 4 PSHAs—Experience Gained from Actual Applications, U.S. Geological Survey, Open File Report 2009-1093, 66 pp.

Kishida, T., Kayen, R.E., Ktenidou, O.-J., Silva, W., Darragh, R., and Watson-Lamprey, J. (2014). PEER Arizona Strong Motion Database and GMPEs Evaluation, Pacific Earthquake Engineering Research Center *PEER Report 2014/09*, 135 pp.

Shahi, S.K., Baker, J.W., and Rodriguez-Marek, A. (2015). Effect of Spatial Correlation on the Standard Deviations of CY14 Model, Report submitted to GeoPentech, Inc., January 2015, 9 pp.

U.S. NRC (1997). Recommendations for probabilistic seismic hazard analysis: Guidance on uncertainty and use of experts, prepared by Senior Seismic Hazard Analysis Committee, Lawrence Livermore National Laboratory, Volume 1, Main Report, NUREG/CR-6372, UCRL-ID-122160, 280 pp.

U.S. NRC (2012b). Practical Implementation Guidelines for SSHAC Level 3 and 4 Hazard Studies, U.S.NRC NUREG-2117.

Table 2.3-1: Main meetings occurred during the SWUS GMC study

Title	Date	Invited Participants
Working Meeting #1 (Planning Meeting #1)	June 21, 2012	TI Team, PM, PPRP, HAs, PTIs, selected REs, TI Staff
Working Meeting #2 (Planning Meeting #2)	July 18, 2012	TI Team, PM, PPRP, HAs, PTIs, TI Staff
Kick-Off Meeting	August 27, 2012	TI Team, PM, PPRP, HAs, PTIs, Sponsors, TI Staff
Working Meeting #3	October 8, 2012	TI Team, PM, PPRP, HAs, PTIs, TI Staff
Working Meeting #4	December 20, 2012	TI Team, PM, PPRP, HAs, PTIs, TI Staff
Working Meeting #5	February 11, 2013	TI Team, PM, PPRP, HAs, PTIs, TI Staff
Workshop #1 (GMC Model 0)	March 19-21, 2013	TI Team, PM, PPRP, HAs, PTIs, , TI Staff, selected REs, selected PEs, Sponsors, other Observers
Working Meeting #6	April 12, 2013	TI Team, PM, PPRP, HAs, PTIs, TI Staff
Working Meeting #7	May 23, 2013	TI Team, PM, PPRP, HAs, PTIs, TI Staff
Working Meeting #8	June 24, 2013	TI Team, PM, PPRP, HAs, PTIs, TI Staff
Working Meeting #9	July 16, 2013	TI Team, PM, PPRP, HAs, PTIs, TI Staff
Working Meeting #10	August 21, 2013	TI Team, PM, PPRP, HAs, PTIs, TI Staff
Working Meeting #11	October 02, 2013	TI Team, PM, PPRP, HAs, PTIs, TI Staff
Working Meeting #12	October 15, 2013	TI Team, PM, PPRP, HAs, PTIs, TI Staff
Workshop #2 (GMC Model 1.0)	October 22-24, 2013	TI Team, PM, PPRP, HAs, PTIs, TI Staff, selected REs, selected PEs, Sponsors, other Observers
Working Meeting #13	November 26, 2013	TI Team, PM, PPRP, HAs, PTIs, TI Staff
Working Meeting #14	January 2, 2014	TI Team, PM, PPRP, HAs, PTIs, TI Staff
Special Working Meeting	January 28-29, 2014	TI Team, PM, PPRP, HAs, PTIs, TI Staff selected REs, selected PEs, Sponsors, other Observers
Logic Tree Meetings for Workshop #3	February 11, 12, 26 and 27, 2014	TI Team, PM, HAs, PTIs, TI Staff
Working Meeting #15	March 3, 2014	TI Team, PM, PPRP, HAs, PTIs, TI Staff
Workshop #3 (GMC Model 2.0)	March 10-12, 2014	TI Team, PM, PPRP, HAs, PTIs, selected REs, selected PEs, Sponsors, other Observers
Working Meeting #16	March 24, 2014	TI Team, PM, PPRP, HAs, PTIs, TI Staff
Logic Tree Meetings for Draft Preliminary GMC Model (GMC Model 3.0)	April 11 and 25, 2014	TI Team, PM, HAs, PTIs, TI Staff
PPRP Closure Pre-Briefing	May 14, 2014	TI Team, PM, PPRP, HAs, PTIs, TI Staff, Sponsors
Logic Tree Meetings for Preliminary GMC Model (GMC Model 3.1)	June 10, 2014; July 11, 2014	TI Team, PM, HAs, PTIs, TI Staff
PPRP Closure Briefing	July 17-18, 2014	TI Team, PM, PPRP, HAs, PTIs, TI Staff, Sponsors
Logic Tree Meetings for Final GMC Model (GMC Model 4.0)	August 6, 2014	TI Team, PM, HAs, PTIs, TI Staff

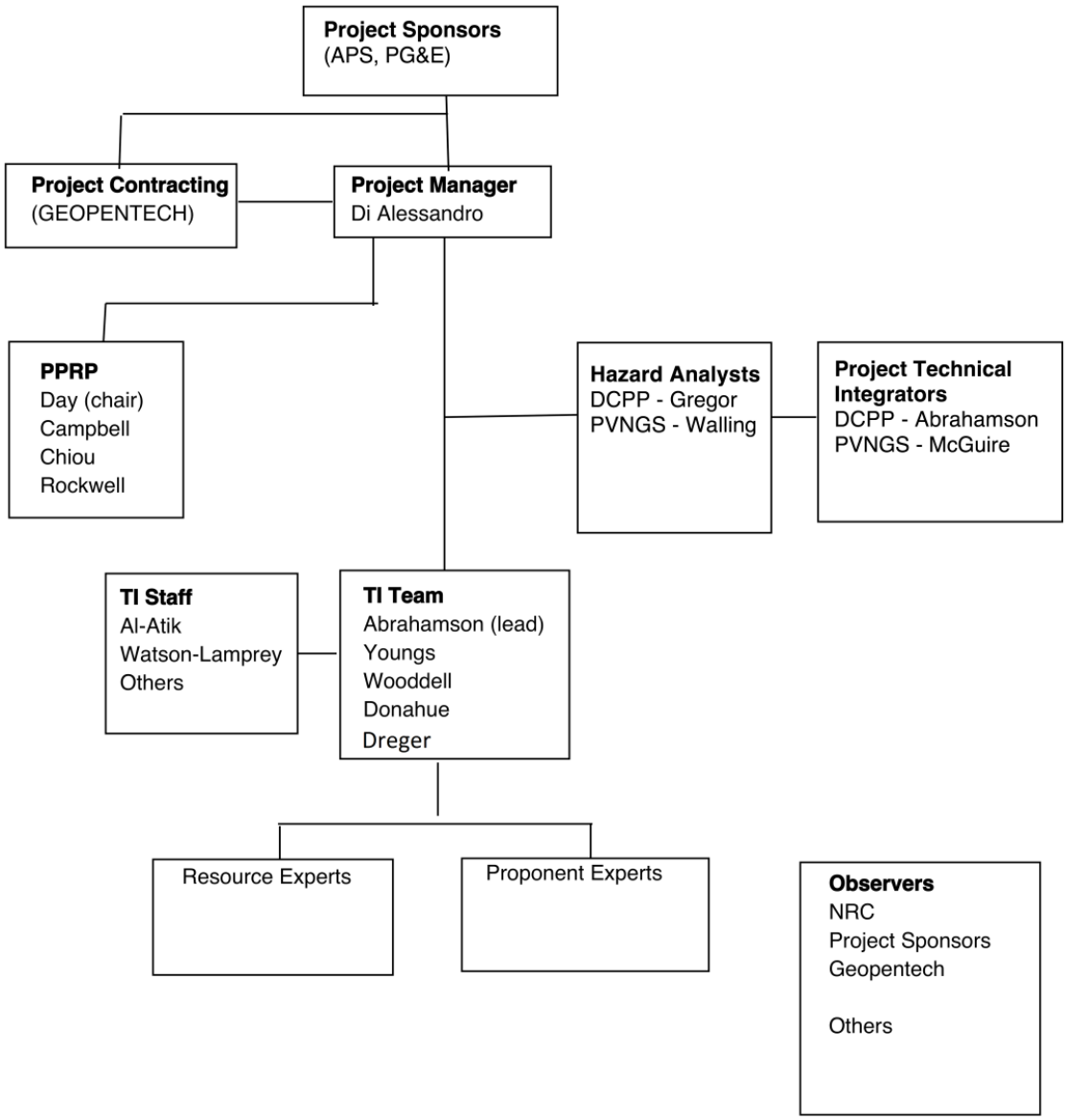

Figure 2.2-1: Southwestern U.S. Ground Motion Characterization Project Organization.

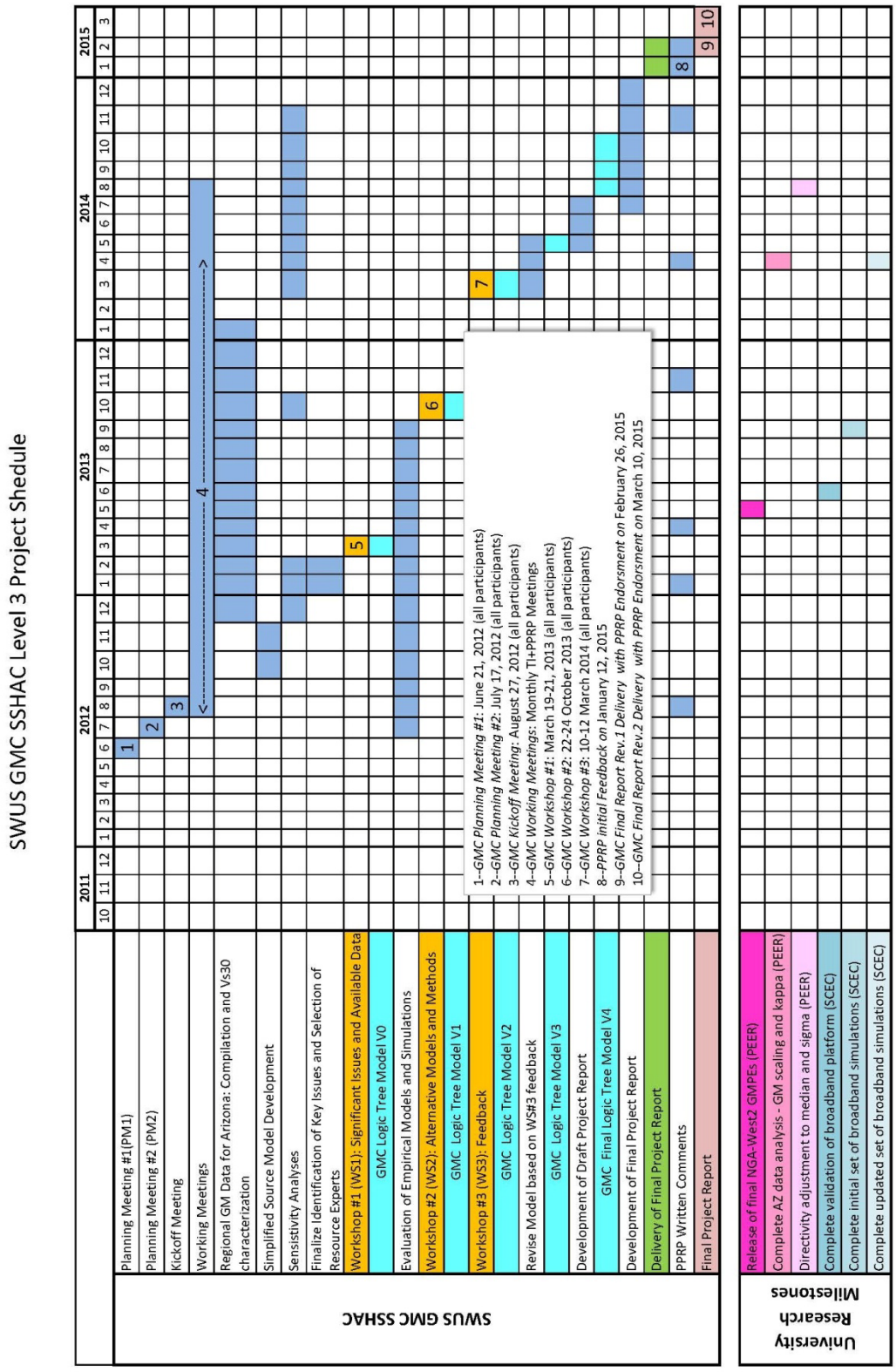

Figure 2.3-1: SWUS GMC Schedule and Major Milestones.

3 SWUS GMC WORK PLAN AND KEY STUDY TASKS

This Chapter discusses the key tasks that fulfill the main four components associated to the SWUS GMC Project and its SSHAC Level 3 study implementation (i.e. (1) evaluation, (2) integration, (3) participatory peer review, and (4) documentation) as described in Section 2.1.

3.1 Preparation of Project Plan and Kick-Off Meeting

The initial task for the SWUS GMC study was to prepare the Project Plan and hold a Workshop 0 (also known as the Kick-Off Meeting). The Technical Integration (TI) Team, Project Technical Integrators (PTIs), and Project Management (PM) developed the Project Plan. A draft Project Plan was provided to the Participatory Peer Review Panel (PPRP) prior to the August 2012 Kick-Off Meeting. The draft plan was reviewed at the Kick-Off Meeting that was attended by the Project Sponsors, PPRP, TI Team, Hazard Analyst (HA) from each utility, PTI from each utility, and the Project Management. Based on the discussions held during the Kick-Off Meeting and on the written comments received from the PPRP, the SWUS GMC Project Plan was revised and finalized in November 2012. The final TI Team composition and a contingency plan in case the broad-band platform (BBP) simulations were not usable for the SWUS GMC study was agreed upon with the PPRP's approval. The final Project Plan includes the PPRP letter documenting their review of the Project Plan.

In addition to reviewing the Project Plan, the purpose of the Kick-Off Meeting was also to discuss the roles of the project participants, and identify key interface issues (Seismic Source Characterization - SSC, GMC, and site response) for the nuclear power plant (NPP) sites in the project.

3.2 Database Development

The development of the SWUS GMC Project Database involved collecting data and models in support of the TI Team evaluation and integration tasks. The Project Database includes several databases, which were compiled according to their intended use. The compiled databases include ground-motion data and ground-motion models applicable to shallow crustal earthquakes in active regions for ranges of

magnitudes and distances that are relevant to the seismic hazard at the two NPP sites. The databases can be grouped into five main categories: 1) empirical ground-motion databases used to constrain the median models; 2) simulated ground-motion databases also used to constrain the median models; 3) empirical ground-motion databases used to constrain the aleatory variability models; 4) databases of existing candidate ground-motion models for the median ground motions; and 5) databases of existing candidate models for the aleatory variability of the ground motions. Details on the ground-motion databases selected for the project are provided in Chapter 5.

In addition to including the relevant ground-motion database, the SWUS GMC Project Database also includes a documentation repository which was maintained throughout the duration of the study to include PPRP final letters, working meetings material, and other reference documents relevant to the two NPPs. The reference documents include PEER reports describing the empirical ground-motion studies and SCEC reports describing the simulation methods and the validation study. Access to the project database was provided to TI team, PPRP members, and project sponsors. In particular, critical reference material was available prior to each workshop to allow adequate time for the PPRP to prepare for the workshops.

Additionally, a public project-specific website was developed to maintain a subset of the project documents. The web-page is managed by PG&E and allows public access to the SWUS GMC Project Plan, presentations from public workshops, workshop proceedings, and the final report.

3.3 University Research to Develop Proponent Models

Although not part of the formal SSHAC process, the SWUS GMC study received key input from two major ground-motion projects relevant to the hazard evaluation for western U.S. sites. These projects were conducted in a University-research framework, and resulted in a set of proponent models that were evaluated for their applicability to the two project sites as part of the SWUS GMC study under the SSHAC process.

The first study is the PEER NGA-West2 (Bozorgnia et al., 2014), which developed an updated set of ground-motion prediction equations (GMPEs), and released an expanded PEER database that included key data from shallow crustal earthquakes in active regions around the world. Other studies focusing on other aspects relevant to the ground-motion characterization were conducted in coordination with the NGA-West2 program. These studies include single-station sigma, kappa scaling, and near-fault fling effects. The Arizona Ground Motion Project (Kishida et al., 2014) was also conducted in coordination with NGA-West2 project.

The second study is the SCEC broadband platform (BBP) validation (Dreger et al., 2013), which comprised a major systematic evaluation of several methods for numerical simulation of ground motion

for engineering applications. The validation of the numerical simulation methods was organized in two parts described in details in Goulet et al. (2015), and addressed the median pseudo spectral acceleration for the average horizontal component.

3.4 Workshop #1: Hazard Significant Issues, Available Data, and Data Needs

A three-day Workshop #1 was held on March 19-21, 2013. The goal for the Workshop #1 was to: (1) review the ground rules for the conduct of SSHAC workshops and expert roles within the project; (2) identify the technical issues of highest significance to the hazard analysis; and (3) review available data that will be considered for constructing the GMC model. This includes identification of data, information and/or additional work required to address those issues.

The TI Team and the Project Manager developed the agenda for Workshop #1 and identified appropriate Resource Experts (REs). Letters were sent to selected REs one month before the workshop that include a set of focused questions related to topics and issues to be addressed at the workshop, with the objective of focusing the discussion on key issues related to a particular data set, including quality of data, expected use of data, and uncertainty or limitations in the data or interpretations. The agenda, list of REs, and draft focused questions were provided to the PPRP for their review prior to the workshop, to ensure that the technical discussions would adequately cover the topics for consideration at the Workshop #1.

Workshop #1 was attended by the TI Team, the PTIs, the PPRP, the Hazard Analysts, Resource Experts, the Project Management, and the Evaluator Experts supporting the TI Team. Members of the public attended the Workshop #1 as well, including representatives of the Project Sponsors, representatives of the regulators and other general observers. The list of Workshop #1 attendees is provided in Table 3.4-1

Prior to the Workshop #1, the TI Team identified the following topics to be addressed during the Workshop:

- Overview of existing or ongoing SSC studies for the project sites;
- Present sensitivity analysis to ground-motion models for project sites (GMC Model 0);
- Review new data and GMPEs from PEER, with special focus on their relevance and applicability to the hazard controlling sources;
- Review other GMPEs developed for extensional regimes outside of the U.S., such as from Japan, Taiwan, Italy, Turkey, and New Zealand;

- Identification of data needs or gaps and models to constrain the GMPEs in critical ranges, including near fault effects such as directivity, fling, and hanging wall effects (for DCPP);
- Identification of data needs or gaps and models to constrain the GMPEs for multi-fault ruptures and for splay ruptures (**M**6-**M**7.5 earthquakes at distances of 0 to 15 km - for DCPP);
- Identification of data needs or gaps and models to constrain the GMPEs for moderate (**M**5.5 to **M**6.5) earthquakes at distances less than 100 km from a site, for a variety of rupture mechanisms, including normal faulting (for PVNGS);
- Identification of data needs or gaps and models to constrain the GMPEs attenuation with distance in Arizona (for PVNGS), and to resolve geometrical spreading, anelastic attenuation, kappa, and stress-drop differences between California and central Arizona;
- Identification of data needs or gaps to derive path-specific corrections to GMPEs;
- Review use of simulations for the SWUS GMC Project, including the SCEC BBP validation effort;
- Review base rock characteristics (e.g. host-region V_{S30} and kappa) of available ground-motion models, and select the best representative reference condition that is consistent with the site response approaches envisioned for the project sites;
- Identification of data availability and needs for single station sigma.

Through the discussions with the REs, specific data sets' merits were discussed, and additional data were identified to address the hazard significant issues. In particular, three recommendations at the workshop were related to augmenting the sparse empirical data for normal faulting earthquakes. First, it was recommended to consider the **M**7.2 Fukushima-Hamadori event for its potential to help constrain the large magnitude scaling of GMPEs for normal style-of-faulting. Second, it was suggested to check the Bindi et al. (2011) data set for **M** ≥ 5 events recorded by stations within 50 km, which were not included in the PEER NGA-West2 database. Third, it was suggested to review the Wells, Nevada **M**6.0 event for possible use in constraining directivity models for normal faulting earthquakes. The sparse data for constraining hanging-wall effects from moderate (**M**5.0 to **M**6.0) earthquakes was also noted and it was suggested to examine the Japanese data set that Dr. Rodriguez-Marek was assembling for additional empirical data that could be used to constrain the hanging-wall scaling for moderate magnitudes. For evaluating ground-motion scaling in Arizona, it was suggested to look for historical intensities and additional recordings for the **M**7.2 El Mayor Cucapah earthquake recorded by stations at the VA Hospital and Roosevelt Dam to constrain the distance attenuation in Arizona. For the purpose of estimating kappa in central Arizona, it was discussed that the relevant recording sites' characterization be improved by in situ investigations.

Another key outcome of Workshop #1 was the identification of the scenarios to be implemented in the numerical simulations, and the definition of the scope of the numerical simulations to be conducted, including the selection of the simulation methods to be implemented.

A comprehensive summary of the discussion points that occurred during the workshop is provided in the Workshop #1 Proceedings (see Appendix E). The proceedings include a letter issued by the PPRP following the Workshop #1, documenting their observations of the workshop.

Table 3.4-1: Workshop #1 participants

Group	Individual	Affiliation
PPRP	Day, Steven	San Diego State University
	Campbell, Kenneth	Kenneth W Campbell Consulting
	Chiou, Brian	Brian Chiou Consulting
	Rockwell, Tom	San Diego State University
Project Management - GeoPentech	Barneich, John	GeoPentech, Inc.
	Di Alessandro, Carola	GeoPentech, Inc.
	Dinsick, Andrew	GeoPentech, Inc.
Project Management - Utilities	Arsene, Florin	Southern California Edison
	Horstman, William R. (*)	Pacific Gas and Electric Company
	Jahangir, Nozar	Pacific Gas and Electric Company
	Klimczak, Richard	Pacific Gas and Electric Company
	Malzahn, Mark	Southern California Edison
	Powell, Mike	Arizona Public Service
	Reidenbach, Nicholas	Arizona Public Service
	Wandell, Christopher	Arizona Public Service
Project Technical Integrator	Abrahamson, Norman A.	Pacific Gas and Electric Company
	McGuire, Robin	Lettis Consultants International, Inc.
	Moriwaki, Yoshi	GeoPentech, Inc.
Hazard Analysts	Dinsick, Andrew	GeoPentech, Inc.
	Gregor, Nick	Nick Gregor Consulting
	Walling, Melanie	Lettis Consultants International, Inc.
Technical Integrator Team	Abrahamson, Norman A.	Pacific Gas and Electric Company
	Donahue, Jennifer	Geosyntec Cons.
	Dreger, Doug	Univ. of California, Berkeley
	Wooddell, Katie	Pacific Gas and Electric Company
	Youngs, Bob	AMEC Geomatrix
Technical Integrator Support	Al Atik, Linda	Linda Alatik Consulting
	Watson-Lamprey, Jennie	Watson-Lamprey Consulting
Resource and Proponent Experts	Aagaard, Brad (*)	U.S. Geological Survey, Menlo Park
	Anderson, John	Univ. of Nevada, Reno
	Archuleta, Ralph	Univ. of California, Santa Barbara
	Baker, Jack	Stanford University, Palo Alto
	Baltay, Annemarie	U.S. Geological Survey, Menlo Park
	Bayless, Jeff	URS
	Boore, David	U.S. Geological Survey, Menlo Park
	Bozorgnia, Yousef	Univ. of California, Berkeley
	Brumbaugh, David (*)	Northern Arizona University
	Castro Escamilla, Raul (*)	CICESE, Baja California
	Darragh, Robert	Pacific Engineering and Analysis
	Freeman, Tom	GeoPentech, Inc.
	Goulet, Christine	Univ. of California, Berkeley
	Graves, Robert (*)	U.S. Geological Survey, Pasadena
	Hanks, Tom	U.S. Geological Survey, Menlo Park

Group – Continued	Individual	Affiliation
Resource and Proponent Experts	Hardebeck, Jeanne (*)	U.S. Geological Survey, Menlo Park
	Harris, Ruth (*)	U.S. Geological Survey, Menlo Park
	Heaton, Thomas	California Institute of Technology
	Helmberger, Donald	California Institute of Technology
	Jordan, Tom	SCEC, Univ. of Southern California
	Kalkan, Erol	U.S. Geological Survey, Menlo Park
	Kamai, Ronnie	Univ. of California, Berkeley
	Ktenidou, Olga-Joan	ISTerre, France
	Lettis, William	Lettis Consultants International, Inc.
	Lindvall, Scott	Lettis Consultants International, Inc.
	Maechling, Phil	SCEC, Univ. of Southern California
	Olsen, Kim	San Diego State University
	Rodriguez-Marek, Adrian	Virginia Tech
	Silva, Walt (*)	Pacific Engineering and Analysis
	Somerville, Paul	URS
	Stewart, Jonathan	Univ. of California, Los Angeles
	Thompson, Steve	Lettis Consultants International, Inc.
	Wang, Feng	SCEC, Univ. of Southern California
	Youngs, Jeri	Arizona Geological Survey
Regulatory Observers	Anderson, Robert	California Seismic Safety Commission
	Chen, Rui	California Geological Survey
	Gibson, Bruce (*)	San Luis Obispo County
	Graizer, Vladimir	US Nuclear Regulatory Commission
	Hale, Christie	US Nuclear Regulatory Commission - Region IV
	Johnsson, Mark J.	California Coastal Commission
	Kammerer, Annie (*)	US Nuclear Regulatory Commission
	Stamatakos, John	Center for Nuclear Waste
	Stirewalt, Gerry (*)	US Nuclear Regulatory Commission
	Walter, Joan	California Energy Commission
	Weaver, Casey	California Energy Commission
	Williams, Megan	US Nuclear Regulatory Commission - Region IV
	Wills, Chris J.	California Geological Survey
Other Observers	Carlton, Brian	Univ. of California, Berkeley
	Dabaghi, Mayssa	Univ. of California, Berkeley
	El Menchawi, Osman	Fugro Consultants, Inc.
	Hollenback, Justin	Univ. of California, Berkeley
	Lisle, Greg A.	Columbia Project - Energy Northwest
	Nigbor, Robert L.	Univ. of California, Los Angeles
	Pitarka, Arben	Lawrence Livermore National Laboratory
	Retson, Thomas P.	Blue Castle Project - EnergyPath Corporation
	Sewell, Rob	R.T. Sewell Associates
	Skarlatoudis, Andreas	URS

(*) Remote attendance

3.5 Workshop #2: Proponent Models and Alternative Interpretations

The TI Team and the Project Manager developed the agenda for Workshop #2 and identified appropriate Proponent Experts (PEs) and Resource Experts (REs). Letters were sent to selected PEs and REs one month before the workshop, including focused questions to orient the presentations and discussions to the merits of specific methods, models or perspective regarding key issues of highest significance to the hazard at the two sites in the project. Also, PEs were requested to present strengths and limitations of the method or model they advocate, and to explain the underlying technical bases for applicability of the method or perspective.

The agenda, list of PEs and REs, and draft focused questions were provided to the PPRP for their review prior to the workshop, to ensure that the technical discussions would adequately cover the topics for consideration at the Workshop #2.

A three-day Workshop #2 was held on October 22-24, 2013. The goal for the Workshop was to: (1) present, discuss, and debate alternative models, methods, and viewpoints regarding key GMC technical issues of highest significance to the hazard analysis; (2) identify the technical bases for the alternatives and discuss the associated uncertainties; and (3) provide a basis for the subsequent development of a preliminary GMC model that considers these alternatives. Additionally, as part of the Workshop #2, the TI Team's current evaluations and the tasks supporting the ongoing evaluation were reviewed, including the new data collection activities being performed after Workshop #1. Finally, interface considerations between the SSC and GMC models, including the data pertinent to both models were identified.

Workshop #2 was attended by the TI Team, the PTIs, the PPRP, the Hazard Analysts, Proponent Experts, Resource Experts, the Project Management, and the Evaluator Experts supporting the TI Team. Members of the public attended the Workshop #2 as well, including representatives of the Project Sponsors, representatives of the regulators and other general observers. The list of Workshop #2 attendees is provided in Table 3.5-1

Prior to the Workshop #2, the TI Team had reviewed hazard sensitivity analyses conducted by the Hazard Analysts using the alternative proponent models to help focus the discussion of the proponent models on those features that are most important to the hazard at the project sites. Accordingly, the following topics were identified to be addressed during the Workshop #2:

- Results of the hazard sensitivity analysis using GMC Model 1.0 logic trees and the available simplified SSC models;
- Strengths and weaknesses of the proponent models. The proponent models included current GMPEs for shallow crustal seismicity, simulation methods evaluated in the SCEC BBP validation

effort, novel visualization techniques for the epistemic uncertainty, and models for the aleatory variability.

- Proponent model for simplified approach to directivity adjustments for the median and standard deviation;
- Development of the TI Team models for adjusting or computing GMPEs for ruptures associated to multiple faults rupturing simultaneously (splay faulting) or to significant changes in rake and dip along strike (complex faulting);
- Development of TI Team models for hanging-wall scaling;
- Evaluation of the proponent models with comparisons to data, as appropriate, to deem their applicability to the project's sites;
- Identification of model gaps, i.e. cases that don't appear to be covered by current models, and how to cover those gaps;
- Results from new data collection activities in support of path-effects evaluation and kappa scaling;
- Definition of additional simulation scenarios to support the ground-motion scaling of hanging wall effects for small-to-moderate magnitudes (**M**5 to **M**6.5) and of splay or complex ruptures.

The information gained from the interactions with PEs and REs formed the basis for identifying other alternative models or technical issues that were not captured in the GMC Model 1.0 logic trees and that are needed to characterize the center, body and range (CBR) of the GMPEs.

In terms of median GMPE models, the concept of using the visualization of epistemic uncertainty approach received several recommendations for improvements, including suggestions to refine the approach by using hazard-based weighting functions for the magnitude-distance space, and to use alternative data sets to establish the CBR of the technically defensible interpretations (TDIs). Additionally, it was discussed how the concept of the magnitude scaling's absence above **M** of about 7, as suggested in Zhao and Lu (2011), was lacking in the current candidate GMPE. Accordingly, a need was identified to implement the Zhao and Lu (2011)'s concept into a new GMPE. Also, it was recommended to replace the Bindi et al. (2011) GMPE with the most recent version including pan-European data (Bindi et al., 2014a and 2014b). Finally, several of the focused questions were not completely addressed by the PEs, and some additional model-specific questions for the PEs were identified which were addressed by the PEs after the workshop.

In terms of numerical simulations, it was suggested to implement additional scenarios to capture the ground-motion scaling for splay and complex ruptures. Also, the need of a series of consistency checks

was discussed to compare the peak displacements of the simulations and the surface slip. Additionally, to be applicable for hanging-wall effect scaling at **M**5.5, it was recommended that the numerical simulations undergo an additional round of validation versus GMPEs.

In terms of the sigma model, the discussion of alternative models or technical issues included the need for a different distribution to describe the epistemic uncertainty, which might not be lognormal and symmetric.

Among the model gaps recognized at the time of the Workshop #2, the Idriss (2014) and EXSIM finite fault simulation methods could not be discussed due to the absence of their proponent modelers, or any designated representative. Also, the task associated to the development of path and directivity adjustment models for median and aleatory variability were not ready to be presented at the time of the Workshop #2.

A comprehensive summary of the discussion points that occurred during the workshop is provided in the Workshop #2 Proceedings (see Appendix F). The proceedings include a letter issued by the PPRP following the Workshop #2, documenting their observations of the workshop.

3.6 Working Meetings

Several working meetings were held during the project. As shown in Table 2.3-1, sixteen working meetings were held prior to and soon after the formal workshops. Those working meetings provided an informal framework for the TI Team's SSHAC evaluation and integration activities, outside of a workshop environment. The working meetings were held almost every month, and were attended by the TI Team, PPRP members, PM, PTIs, HAs, and Evaluator Experts supporting the TI Team. Working Meeting #1 and the January 2014 Special Working Meeting were attended also by selected REs and PEs. The first meeting (Working Meeting #1) served for planning purposes by gaining the input from REs on the hazard-significant issues, whereas the latter meeting (January 2014 Special Working Meeting) served to discuss additional feedback from the PEs and REs which were not addressed during Workshop #2. Tasks that were not completed by the time of the Workshop #2 were also discussed during the two-day Special Working Meeting that included the TI team, PPRP, REs, Sponsors' representative and other technical observers associated with the University Research task (see Section 3.3).

An agenda was prepared for each working meeting. Whenever applicable, relevant material supporting the TI Team's evaluation on one or more significant technical issue was also distributed prior to the meetings. Any action item or follow-up tasks identified during the working meetings were provided to the relevant project participants shortly after the meeting's conclusion.

Table 3.5-1: Workshop #2 participants

Group	Individual	Affiliation
PPRP	Day, Steve	San Diego State University
	Campbell, Kenneth	Kenneth W Campbell Consulting
	Chiou, Brian	Brian Chiou Consulting
	Rockwell, Tom	San Diego State University
Project Management - GeoPentech	Barneich, John	GeoPentech, Inc.
	Di Alessandro, Carola	GeoPentech, Inc.
	Dinsick, Andrew	GeoPentech, Inc.
Project Management - Utilities	Klimczak, Richard	Pacific Gas and Electric Company
	Horstman, William R. (*)	Pacific Gas and Electric Company
	Jahangir, Nozar	Pacific Gas and Electric Company
	Wandell, Chris	Arizona Public Service
Project Technical Integrator	Abrahamson, Norman A.	Pacific Gas and Electric Company
	McGuire, Robin	Lettis Consultants International. Inc.
Hazard Analysts	Gregor, Nick	Bechtel Corporation
	Walling, Melanie	Lettis Consultants International, Inc.
Technical Integrator Team	Abrahamson, Norman A.	Pacific Gas and Electric Company
	Donahue, Jennifer	Geosyntec Cons.
	Dreger, Doug	Univ. of California, Berkeley
	Wooddell, Katie	Pacific Gas and Electric Company
	Youngs, Bob	AMEC Geomatrix
Technical Integrator Support	Al Atik, Linda	Linda Alatik Consulting
Resource and Proponent Experts (Continues on following page)	Aagaard, Brad	U.S. Geological Survey, Menlo Park
	Akkar, Sinan	Middle East Technical University, Turkey
	Anderson, John (*)	Univ. of Nevada, Reno
	Archuleta, Ralph	Univ. of California, Santa Barbara
	Baker, Jack	Stanford University, Palo Alto
	Baltay, Annemarie (*)	U.S. Geological Survey, Menlo Park
	Bayless, Jeff	URS
	Boore, David	U.S. Geological Survey, Menlo Park
	Bozorgnia, Yousef	Univ. of California, Berkeley
	Goulet, Christine	Univ. of California, Berkeley
	Graves, Robert (*)	U.S. Geological Survey, Pasadena
	Hanks, Tom (*)	U.S. Geological Survey, Menlo Park
	Harris, Ruth (*)	U.S. Geological Survey, Menlo Park
	Heaton, Thomas	California Institute of Technology
	Kalkan, Erol	U.S. Geological Survey, Menlo Park

Group – Continued	Individual	Affiliation
Resource and Proponent Experts (Continues from previous page)	Ktenidou, Olga	ISTerre, France; Univ. of California, Berkeley
	Kuehn, Nicolas	Potsdam Univ, Germany; Univ. of California, Berkeley
	Lozos, Julian	Univ. of California, Berkeley
	Mayeda, Kevin	Univ. of California, Berkeley
	McLaren, Marcia	Pacific Gas and Electric Company
	Olsen, Kim	San Diego State University
	Pitarka, Arben	Lawrence Livermore National Laboratory
	Rodriguez-Marek, Adrian	Virginia Tech
	Somerville, Paul	URS
	Stewart, Jonathan	Univ. of California, Los Angeles
	Stirling, Mark	GNS Science, New Zealand
	Toro, Gabriel	Lettis Consultants International, Inc.
Regulatory Observers	Ake, Jon P.	US Nuclear Regulatory Commission
	Anderson, Robert	California Seismic Safety Commission
	Budnitz, Robert J.	Lawrence Livermore National Laboratory
	Chen, Rui	California Geological Survey
	Graizer, Vladimir	US Nuclear Regulatory Commission
	Hale, Christie	US Nuclear Regulatory Commission - Region IV
	Johnsson, Mark	California Coastal Commission
	McCarthy, Richard (*)	California Seismic Safety Commission
	Stamatakos, John	Center for Nuclear Waste
	Stirewalt, Gerry	US Nuclear Regulatory Commission
	Walter, Joan	California Energy Commission
	Weaver, Casey	California Energy Commission
	Wills, Chris J.	California Geological Survey
Other Observers (Continues on following page)	Abramson Ward, Hans	Lettis Consultants International. Inc.
	Ancheta, Timothy (*)	RMS
	Brumbaugh, David	Northern Arizona University
	Dabaghi, Mayssa	Univ. of California, Berkeley
	El Menchawi, Osman	Fugro Consultants, Inc.
	Ferre', Kent	Pacific Gas and Electric Company
	Geesman, John	A4NR
	Hamilton, Douglas	DHH Geoconsult
	Hardebeck, Jeanne (*)	U.S. Geological Survey, Menlo Park
	Kammerer, Annie	Bechtel Corporation
	Lettis, William (*)	Lettis Consultants International
	Lewis, Sherry	Mothers for Peace

Group – Continued	Individual	Affiliation
Other Observers (Continues from previous page)	Lin, Po-Shen	Sinotech, Taiwan
	Lisle, Greg A.	Columbia Project - Energy Northwest
	Liu, Hsun-Jen	Nat. Cent. for Res. on Earthq. Engin., Taiwan
	Renault, Philippe	PEGASOS Refinement Project - Swissnuclear
	Rowshandel, Badie	California Earthquake Authority
	Seyhan, Emel	Univ. of California, Berkeley
	Sewell, Rob	R.T. Sewell Associates
	Skarlatoudis, Andreas	URS
	Spudich, Paul (*)	U.S. Geological Survey, Menlo Park
	Thompson, Steve	Lettis Consultants International, Inc.
	Weisman, David	A4NR
	Wu, Chiun-lin	Nat. Cent. for Res. on Earthq. Engin., Taiwan

(*) Remote attendance

3.7 Workshop #3: Preliminary GMC Models and Hazard Feedback

A three-day Workshop #3 was held on March 10-12, 2014. Workshop #3 was preceded by a number of activities which followed Workshop #2's execution. In particular, the TI Team further evaluated the proponent models and integrated the information into GMC Model 2.0 version of the logic tree based on the feedback from Workshop #2. Modeling gaps identified at Workshop #2 were addressed by development of new models as appropriate. Several of these new models and evaluations were presented and discussed at the Special Working Meeting held in January 2014, which also served to obtain additional PEs/REs feedback.

The identification of technical issues and parameters to be discussed at Workshop #3 was aided by hazard sensitivities conducted for each site using the new GMC Model 2.0 and the existing SSC models. The hazard sensitivities highlighted the major contributors to the uncertainty, and the parameters having the greatest impact to the hazard at the two sites.

The goals for Workshop #3 were to: (1) review the tasks that the GMC TI Team have conducted after Workshop #2 as part of their evaluations; (2) present and discuss the TI Team's approach to obtain preliminary GMC models and calculations in a forum that provides the opportunity for feedback to the evaluators; (3) shed light on the most important technical issues through feedback given in the form of comments on hazard results and sensitivity analyses; (4) obtain PPRP feedback through extensive questions on the preliminary GMC models; and (5) discuss the path forward towards the finalization of the GMC models in light of Workshop #3 feedback.

In particular, it was planned that the emphasis of the TI Team presentations on the approach for the models be given to the manner in which alternative viewpoints and uncertainties have been incorporated. Discussions of the approach for obtaining preliminary models, the technical bases for the assessments and weights were also planned to allow for discussion of the implications and constraints provided by the available data. Also, sensitivity analyses and hazard calculations were prepared to aid discussion and insights into the hazard significance of the preliminary models.

The TI Team and the Project Manager developed the agenda for Workshop #3 and identified appropriate PEs and REs. Letters were sent to the selected PEs and REs one month before the Workshop identifying discussion topics for which their feedback was sought. Even though not formally required to deliver presentations, the REs and PEs were encouraged to participate to discussions pertaining to how the TI Team considered the views of the larger community and the manner in which their preliminary model represents current knowledge and uncertainties.

Prior to the Workshop #3, the PPRP met with the TI Team to review the agenda, the list of PEs and REs, and to obtain a preview of the topics, presentations and technical discussions planned to be addressed during Workshop #3. Feedback received during the preview secured an adequate planning of the topics for consideration at the Workshop #3.

Workshop #3 was attended by the TI Team, the PTIs, the PPRP, the Hazard Analysts, Proponent Experts, Resource Experts, the Project Management, and the Evaluator Experts supporting the TI Team. Members of the public attended the Workshop #3 as well, including representatives of the Project Sponsors, representatives of the regulators, and other general observers. The list of Workshop #3 attendees is provided in Table 3.7-1

The discussions and feedback were mainly related to the following topics:

- Summary of the key data and results from the January 2014 Special Working Meeting;
- Approach for median ground-motion models, including use of visualization techniques and alternative datasets for weights.
- Plans for the inclusions of hanging-wall effects and calibration of the adjustment scaling using finite-fault simulations;
- Evaluation and selection of models to compute ground motion for complex and splay ruptures for DCPP;
- Model to account for the effect of directivity to median and sigma for DCPP;
- TI Team model to account for path effects to median and sigma for PVNGS

- TI Team models for τ and ϕ;

- Other issues to be considered for building the aleatory variability model, including deviation from the standard assumption of lognormal distribution of residuals (for upper tail), and the potential effect of spatial correlation on ground motions on estimates of τ and ϕ.

One other outcome of the Workshop #3 was the need for a close interaction between the GMC group and the site response groups to secure consistent interface in handing kappa and site amplification. Another identified interface issue with the SSC groups was to make sure that all the source types being considered in the SSC models are captured by the ground-motion models.

In contrast to Workshops #1 and #2, the PPRP were active participants in Workshop #3 to fully query the technical basis for the GMC model including model parameters, level of documentation, uncertainty, and rationale in developing the model.

A comprehensive summary of the discussion points that occurred during the workshop is provided in the Workshop #3 Proceedings (see Appendix G). The proceedings include a letter issued by the PPRP following the Workshop #3, documenting their observations of the workshop.

Table 3.7-1: Workshop #3 participants

Group	Individual	Affiliation
PPRP	Day, Steven	San Diego State University
	Campbell, Kenneth	Kenneth W Campbell Consulting
	Chiou, Brian	Brian Chiou Consulting
	Rockwell, Tom	San Diego State University
Project Management - GeoPentech	Barneich, John	GeoPentech, Inc.
	Di Alessandro, Carola	GeoPentech, Inc.
	Dinsick, Andrew	GeoPentech, Inc.
Project Management - Utilities	Klimczak, Richard	Pacific Gas and Electric Company
	Jahangir, Nozar	Pacific Gas and Electric Company
	Powell, Michael	Arizona Public Service
	Wandell, Christopher	Arizona Public Service
Project Technical Integrator	Abrahamson, Norman A.	Pacific Gas and Electric Company
	McGuire, Robin (*)	Lettis Consultants International. Inc.
Hazard Analysts	Gregor, Nick	NG Consulting
	Walling, Melanie	Lettis Consultants International, Inc.
Technical Integrator Team	Abrahamson, Norman A.	Pacific Gas and Electric Company
	Dreger, Doug	Univ. of California, Berkeley
	Wooddell, Katie	Pacific Gas and Electric Company
	Youngs, Bob	AMEC Environment and Infrastructure
Technical Integrator Support	Al Atik, Linda	Linda Alatik Consulting
	Bayless, Jeff	URS Corporation
	Watson-Lamprey, Jennie	Watson-Lamprey Consulting
Resource and Proponent Experts (continues on next page)	Aagaard, Brad (*)	U.S. Geological Survey, Menlo Park
	Anderson, John (*)	Univ. of Nevada, Reno
	Archuleta, Ralph	Univ. of California, Santa Barbara
	Baker, Jack	Stanford University, Palo Alto
	Bozorgnia, Yousef	Univ. of California, Berkeley
	Goulet, Christine	Univ. of California, Berkeley
	Graves, Robert	U.S. Geological Survey, Pasadena
	Harris, Ruth (*)	U.S. Geological Survey, Menlo Park
	Heaton, Thomas	California Institute of Technology
	Idriss, IM	IM Idriss Consulting
	Kuehn, Nicolas	Univ. of California, Berkeley
	Lozos, Julian	Stanford Univ., Palo Alto
	Olsen, Kim	San Diego State University
	Pasyanos, Michael	Lawrence Livermore National Laboratory
	Pitarka, Arben	Lawrence Livermore National Laboratory

Group – Continued	Individual	Affiliation
Resource and Proponent Experts (continued from previous page)	Rodriguez-Marek, Adrian	Virginia Tech
	Somerville, Paul	URS Corporation
	Stewart, Jonathan	Univ. of California, Los Angeles
	Toro, Gabriel	Lettis Consultants International, Inc.
Regulatory Observers	Ake, Jon P.	US Nuclear Regulatory Commission
	Anderson, Robert	California Seismic Safety Commission
	Budnitz, Robert J.	Lawrence Livermore National Laboratory
	Chen, Rui	California Geological Survey
	Giacinto, Josef	US Nuclear Regulatory Commission
	Gibson, Bruce	San Luis Obispo County
	Graizer, Vladimir	US Nuclear Regulatory Commission
	Hale, Christie	US Nuclear Regulatory Commission - Region IV
	Johnsson, Mark	California Coastal Commission
	Stamatakos, John	Center for Nuclear Waste
	Walter, Joan	California Energy Commission
	Weaver, Casey	California Energy Commission
	Wills, Chris J.	California Geological Survey
Other Observers	AbramsonWard, Hans	Lettis Consultants International. Inc.
	Ancheta, Tim (*)	RMS
	Becker, Rochelle	A4NR
	Chao, Shu- Hsien	Nat. Cent. for Res. on Earthq. Engin., Taiwan
	Chang, Yu-Wen	Nat. Cent. for Res. on Earthq. Engin., Taiwan
	Ferre', Kent	Pacific Gas and Electric Company
	Geesman, John	A4NR
	Hamilton, Douglas	DHH Geoconsult
	Hardebeck, Jeanne (*)	U.S. Geological Survey, Menlo Park
	Hartleb, Ross	Lettis Consultants International
	Hollenback, Justin	Univ. of California, Berkeley
	Lewis, Sherry	Mothers for Peace
	Renault, Philippe	PEGASOS Refinement Project - Swissnuclear
	Silva, Fabio (*)	SCEC - Univ. of Southern California
	Thompson, Steve	Lettis Consultants International, Inc.
	Weisman, David	A4NR

(*) Remote attendance

3.8 Development of Final GMC Models

Following Workshop #3, the key project participants interacted during two internal meetings (referred to as logic tree meetings in Table 2.3-1) to resolve comments from the PPRP and REs/PEs. This process yielded to a Draft Preliminary GMC Model (GMC Model 3.0) which was presented to the PPRP during a briefing meeting occurred on May 14, 2014. Such meeting is referred to as PPRP Closure Pre-Briefing in Table 2.3-1.

The Preliminary GMC Model (GMC Model 3.1) was developed between May and July 2014. The model development was aided by two internal logic tree meetings where the TI Team, HAs, PTIs, Evaluator Experts supporting the TI Team and PM had the chance to interact internally. A provisional Hazard Input Document (HID) dated July 8, 2014, and describing the Preliminary GMC Model was transmitted to the PPRP. A short document dated July 16, 2014 describing the Preliminary GMC Model (preliminary draft report) was also provided to the PPRP. Both documents provided background material to facilitate the discussions at the PPRP Closure Briefing meeting held on July 17 and 18, 2014. The TI Team presented the Preliminary GMC Model for median and sigma, including the technical basis for the assessments of relative weights representing the CBR of the TDI. The hazard significance of the various branches in the Preliminary GMC Model was presented by means of hazard sensitivities and tornado plots. During the discussions that followed the presentations, the PPRP provided some recommendations which were recorded by the TI Team. Some of the PPRP comments addressed unclear documentation or inadequate justification associated to the technical bases and assessments; these comments were addressed in the development of the draft report (see Section 3.9). Other comments highlighted the need for improving some of the models. In the case of the generation of median model via visualization technique, among others, it was suggested to improve the magnitude-distance weighting approach, reconsider the approach to assign relative weights for alternative datasets, and resolve the skewed distribution of the selected median models for PVNGS as shown in the tornado plots. In the case of the adjustments to take into account directivity, it was suggested to explore an alternative hypocenter distribution (i.e. showing more concentrated or unilateral hypocentral distribution). In terms of sigma model, it was suggested for the TI Team to consider smoothing an apparent change in slope in single station ϕ_{SS} models at period T > 5 sec. Finally, a recent change in the development of the PVNGS SSHAC Level 3 SSC model was discussed. This prompted the need of a small change in regionalization for the path effects, with the associated revision of the path adjustments terms for both median and sigma.

Between July 2014 and September 2014 the TI Team continued working on improving the Preliminary GMC Model following the PPRP recommendations, and their results were documented in the draft report. The Final GMC Model 4.0 was developed and documented in the current report following the activities summarized below:

1. PPRP Letter N.1, dated December 13, 2014, summarizing the comments and recommendations for the aleatory variability models and associated documentation.
2. PPRP, TI Team and PM Conference Call (December 16, 2014)

3. Initial TI Team and PM responses to PPRP Letter N.1 (December 22, 2014) highlighting the plan to implement the PPRP comments.
4. PPRP Letter N.2, dated January 5, 2015, summarizing the comments and recommendations for the median models and associated documentation.
5. PPRP, TI Team and PM Conference Call (January 7, 2015), serving also to orally communicate the initial TI Team and PM responses to PPRP Letter N.2 highlighting the plan to implement the PPRP comments and refine the GMC models.
6. PPRP, TI Team and PM Conference Call (January 26, 2015), summarizing the modifications to the GMC models and to the documentation while addressing the PPRP comments.
7. PPRP, TI Team and PM Conference Call (February 9, 2015), highlighting unresolved issues on documentation and identified model limitations.
8. PPRP Letter N.3, dated February 20, 2015, summarizing the comments and recommendations for improving the completeness and clarity of the documentation.
9. PPRP Closure Letter, dated February 24, 2015, summarizing the review of the Final SWUS GMC Model, the associated technical justifications, and the adherence to the SSHAC procedure.
10. TI Team and PM responses to PPRP Closure Letter (February 26, 2015), and publication of Rev.1 Technical Report.
11. Updated PPRP Closure Letter, dated March 10, 2015, summarizing the review of the Final SWUS GMC Model, the updated associated technical justifications, and the adherence to the SSHAC procedure.
12. TI Team and PM responses to the Updated PPRP Closure Letter (March 10, 2015), and publication of Rev.2 Technical Report.

3.9 Documentation

The Final SWUS GMC Model, the associated technical justifications, and the assessments performed by the TI Team are documented in this project report. The essential elements of the GMC model are documented in the Hazard Input Documents (HID, see Appendix C), which provides clear instructions for the hazard analysts to correctly implement the model while avoiding the need to distill the info from the full report. As such, the TI Team technical justifications for the model are not included in the HID.

A preliminary draft project report was prepared in July 2014 to facilitate the PPRP Final Briefing. The draft project report (draft Rev. 0) was developed following the summer and early fall 2014 by the key project participants, including all the members of the TI Team, the Project Manager, the Hazard Analysts and selected Evaluator Experts supporting the TI Team. The draft report was designed to include complete documentation on the SSHAC methodology implemented throughout the project, the database used in the project, the final GMC model including all the technical bases for the assessments, and hazard sensitivities showing the GMC branches' contribution to the uncertainty. Several appendices

were included in the draft report, including the SWUS GMC Project Plan, key written communications with PPRP, formal workshops' proceedings, final HID, and project-specific documentation on models and data sets. Several attachments were also included in the draft report to provide key deliverables associated to the University Research and Specialty Contractors tasks (see Sections 2.5 and 3.2).

The draft report was provided to the PPRP in various installments between October and November 2014, with some parts provided in early January 2015. The PPRP reviewed the draft project report to check if the TI Team's technical assessments for the GMC model were adequately justified and completely documented, and if that documentation was clear, consistent and self-contained. Written comments were provided by the PPRP, which were addressed by the TI Team while revising the report. A Rev.0 report incorporating the critical PPRP's comments was issued on January 12, 2015. The draft Rev.1 report addressing the PPRP's request on augmented quality of documentation was provided to the PPRP at the end of January 2015. Logs collecting PPRP questions and TI Team-PM responses were also shared with the PPRP to facilitate their final review task on the draft Rev.1 report and on the Final GMC Model. A Rev.1 report addressing further PPRP questions was issued on February 26, 2015. To address the PPRP's comments on limitation of documentation in terms of completeness and clarity, a Rev.2 report was issued on March 10, 2015.

3.10 References

Bindi, D., Pacor, F., Luzi, L., Puglia, R., Massa, M., Ameri, G., and Paolucci, R. (2011). Ground motion prediction equations derived from the Italian strong motion database, *Bull. Earthquake Eng*., Vol. 9, 1899-1920.

Bindi D., Massa M., Luzi L., Ameri G., Pacor F., Puglia R., and Augliera, P. (2014a). Pan-European Ground-Motion Prediction Equations for the Average Horizontal Component of PGA, PGV, and 5%-Damped PSA at Spectral Periods up to 3.0 s using the RESORCE dataset, *Bull Earthquake Eng*., Vol. 12, 391–430, DOI: 10.1007/s10518-013-9525-5.

Bindi D., Massa M., Luzi L., Ameri G., Pacor F., Puglia R., and Augliera, P. (2014b). Erratum to: Pan-European Ground-Motion Prediction Equations for the Average Horizontal Component of PGA, PGV, and 5%-Damped PSA at Spectral Periods up to 3.0 s using the RESORCE dataset, *Bull Earthquake Eng*., Vol. 12, 432-448, DOI: 10.1007/s10518-014-9589-x.

Bozorgnia, Y., Abrahamson, N. A., Al Atik, L., Ancheta, T. D., Atkinson, G. M., Baker, J. W., Baltay, A., Boore, D. M., Campbell, K. W., Chiou, B. S.-J., Darragh, R., Day, S., Donahue, J., Graves, R. W., Gregor, N., Hanks, T., Idriss, I. M., Kamai, R., Kishida, T., Kottke, A., Mahin, S. A., Rezaeian, S., Rowshandel, B., Seyhan, E., Shahi, S., Shantz, T., Silva, W., Spudich, P., Stewart, J. P., Watson-Lamprey, J., Wooddell, K., and Youngs, R. (2014). NGA-West2 research project, *Earthquake Spectra,* Vol. 30(3), 973-987.

Dreger, D.S., Beroza, G.C., Day, S.M., Goulet, C.A., Jordan, T. H., Spudich, P.A, and Stewart, J. P. (2013). Evaluation of SCEC Broadband Platform Phase 1 Ground Motion Simulation Results, 33 pp. plus Appendices, Report submitted to SCEC, Aug. 1 2013. Available at http://scec.usc.edu/scecpedia/SCEC_BBP_Phase_1_Evaluation.

Goulet, C.A., Abrahamson, N.A., Somerville, P.G., and Wooddell, K.E. (2015). The SCEC Broadband Platform Validation Exercise: Methodology for Code Validation in the Context of Seismic-Hazard Analyses, *Seismological Research Lett*ers, Vol. 86, 17-26, DOI: 10.1785/0220140104.

Idriss, I.M. (2014). An NGA-West2 Empirical Model for Estimating the Horizontal Spectral Values Generated by Shallow Crustal Earthquakes, *Earthquake Spectra*, Vol. 30(3), 1155-1177, DOI: 10.1193/070613EQS195M.

Kishida, T., Kayen, R.E., Ktenidou, O.-J., Silva, W., Darragh, R., and Watson-Lamprey, J. (2014). PEER Arizona Strong Motion Database and GMPEs Evaluation, *PEER Report 2014/09*, Pacific Earthquake Engineering Research (PEER) Center, University of California, Berkeley, CA, 135 pp.

Zhao, J.X., and Lu, M. (2011). Magnitude-Scaling Rate in Ground-Motion Prediction Equations for Response Spectra from Large, Shallow Crustal Earthquakes, *Bull. Seism. Soc. Am*., Vol. 101, 2643-2661.

4 SEISMOTECTONIC SETTING OF PROJECT AREAS

This Chapter summarizes the regional tectonic setting for the DCPP and PVNGS sites. It also provides a brief description of the main controlling sources affecting the seismic hazard at the two nuclear power plant (NPP) sites and indentifies the range of sources that are included in the seismic source characterization (SSC) models (magnitudes, dips, mechanisms, and distances) for each site. Additionally, this Chapter summarizes the hazard contributions and deaggregation from previous hazard studies conducted for the two sites. The objective of this Chapter is to describe the range of sources for which the ground-motion models need to be applicable. The technical justifications for the SSC models are given in the respective SSC reports and are not addressed in this Chapter.

In terms of nomenclature, the term areal source is used throughout this report, noting that it can be used interchangeably with the term area source.

4.1 Seismotectonic Setting of DCPP

The Diablo Canyon Power Plant (DCPP) is located along the coastal margin of the San Luis Range in south-central California near San Luis Obispo. This region of California is characterized by transpressional deformation (Lettis and Unruh, 2009) between the San Andreas Fault zone to the east and the Hosgri-San Simeon-San Gregorio system of near-coastal faults to the west (Figure 4.1-1). Active fault sources within 320 km from the DCPP site location are considered for the purpose of hazard analysis (Figure 4.1-1). The controlling fault sources in the site vicinity (within 40 km radius from DCPP) are shown on Figure 4.1-2 and are described in Section 4.1.1.

Regional seismicity patterns and focal mechanisms from 1987 to 2008 (Hardebeck, 2010) show that earthquakes extend to a depth of 12 to 15 km. The 2003 **M**6.5 San Simeon earthquake (McLaren et al., 2008) is the largest event recorded in the region since the Ms 7.0 Lompoc earthquake of 1927 (McLaren and Savage, 2001; Figure 4.1-1).

4.1.1 Source Parameters for Nearby Faults

Previous evaluations of the seismic hazard at the DCPP site have shown that, at low probability levels (10^{-3} to 10^{-6} Annual Frequency of Exceedance – AFE), the hazard is controlled by faults that come within 10 km of the plant site (PG&E, 1988; PG&E, 2011). Specifically, the hazard at the site is controlled by the Hosgri, Shoreline, Los Osos, and San Luis Bay faults (Figure 4.1-2). Section 4.1.4 summarizes the hazard contribution of the sources characterized in the Shoreline Fault Report (PG&E, 2011), and the associated deaggregation by magnitude and distance ranges.

In the Shoreline Fault Report, the Hosgri and Shoreline faults are characterized as strike-slip faults, whereas the Los Osos and San Luis Bay faults are reverse or reverse-oblique slip faults. The DCPP site is located on the hanging-wall side of both of the reverse faults and on the hanging-wall side of the steeply dipping Hosgri fault.

The 2015 DCPP SSC model separates the ruptures into four groups: characteristic, linked, complex, and splay. The characteristic ruptures are based on the commonly used Youngs and Coppersmith (1985) magnitude density function for faults. The linked ruptures allow for multiple fault segments with the same style-of-faulting to rupture together into larger magnitude earthquakes. The complex ruptures allow for fault segments with different styles-of-faulting to rupture together. In addition, the complex ruptures also include multi-segment ruptures that have non-similar dips along strike (difference in dips greater than 15 degrees) for the parts of the ruptures that are close to the site (within 20 km of the site which could affect the calculation of the hanging-wall effect). The splay ruptures allow for ruptures from smaller secondary fault segments that are close to the site to rupture during the rupture of a larger segment. The splay ruptures lead to over-lapping ruptures near the site. For the purpose of ground-motion estimation, the characteristic and linked ruptures are grouped together because they do not require any special treatment for implementation in the ground-motion prediction equations (GMPEs). The complex and splay ruptures require a special treatment because only a single style-of-faulting class and a single dip angle can be entered in the GMPEs.

The range of magnitudes and dip angles for the nearby faults that dominate the hazard are listed in Tables 4.1-1 to 4.1-3. Some of the ruptures in the SSC model have changes in dip along strike and down dip. For these sources, the ranges of dips listed in Table 4.1-1 to 4.1-3 are measured over the top 5 km thickness of fault sections participating in the ruptures within 20 km from the NPP site. The fault sections are associated with the three alternative fault geometry models in the DCPP vicinity being considered by the 2015 DCPP SSC effort (i.e. Outward-Vergent – OV; NE-Vergent – NE; and SW-Vergent - SW).

Table 4.1-1 lists the range of magnitudes and dip angles for the characteristic and linked ruptures. For strike-slip earthquakes, the mean characteristic earthquakes are between **M**6.3 and **M**7.3 with maximum magnitudes from the linked ruptures reaching up to **M**8.5. For reverse-slip earthquakes, the

mean characteristic earthquakes are between **M**6.0 and **M**7.3 with maximum magnitudes from the linked ruptures reaching up to **M**7.55. The dip angles for the reverse-slip earthquakes range from 45 to 90 degrees with the DCPP site on the hanging-wall (HW) side of the dipping faults, so the ground-motion models need to be applicable to a wide range of dip angles for sites on the HW side of the rupture.

For the splay ruptures, the range of magnitudes and dip angles are listed in Table 4.1-2. The 2015 DCPP SSC model includes one scenario of a Strike-Slip (SS) splay rupture with a SS main rupture. In this case, the main rupture has a much larger magnitude (**M**7.7) than the splay rupture (**M**6.5). The SSC model includes three scenarios for Reverse-slip (REV) splay ruptures with a REV main rupture. In all three cases, the magnitudes of the main rupture and the splay rupture are similar to each other and are in the **M**6.1 to **M**6.6 range.

For the complex ruptures, the range of magnitudes and dip angles are listed in Table 4.1-3. The 2015 DCPP SSC model includes five complex rupture scenarios with SS and REV or REV/OBL slip segments rupturing together. Four of the five scenarios are for a large strike-slip rupture (**M**7.5 to **M**8.4) with a smaller REV or REV/OBL rupture (rows 1, 2, 4, and 5 in Table 4.1-3). One of the scenarios is for moderate strike-slip rupture (**M**6.5) with a large reverse-slip rupture (**M**7.5) (row 3 in Table 4.1-3).

4.1.2 Source Parameters for Host Areal Source Zone

The areal source zone near the site is modeled using virtual faults for strike-slip and reverse-slip earthquakes. The range of dips and the maximum magnitudes for the virtual faults from the 2015 DCPP SSC model are listed in Table 4.1-4. The maximum magnitudes (**M**7.2) and the range of dips (35-70) for reverse-slip earthquakes are similar to the range from the characterized faults. Therefore, the ground-motion models developed for the SSC scenarios will be applicable to the virtual faults and no additional focus on the scenarios captured by the virtual faults is needed for the ground-motion characterization.

4.1.3 Other Sources

The 2015 DCPP SSC model includes other faults out to a distance of 320 km. Previous hazard studies (PG&E, 2011) have shown that these regional faults do not have a significant impact on the hazard at the hazard levels of interest (10^{-3} to 10^{-6} AFE). These sources are included in the hazard calculation for completeness, but they are not the focus of the ground-motion model characterization and are not discussed in this report.

4.1.4 Hazard Contribution and Deaggregation from the Shoreline Fault Report (PG&E, 2011)

Figures 4.1-3 a) and b) show the hazard curves for 5 Hz and 1.0 Hz spectral acceleration resulting from the Shoreline Fault Report (PG&E, 2011). The figures show the individual contributions to the total hazard from the fault sources. The results in the Shoreline Fault Report study indicated that the main contribution to the total hazard is from the Hosgri fault for all hazard levels. The Los Osos, San Luis Bay, and Shoreline faults are similar in terms of their contribution to the hazard.

Figures 4.1-4 a) and b) show the deaggregation for the 10^{-4} AFE for the 5 Hz and 1 Hz spectral acceleration. The deaggregation results indicate that the earthquakes with magnitudes between 5.5 and 7.0 at short distances (< 10 km) control the hazard at the high frequencies (5 Hz). For the low frequencies (1 Hz), the controlling sources from the deaggregation are shifted slightly to higher magnitudes (**M**6.0 - **M**7.5), but are still at short distances (< 10 km).

4.2 Seismotectonic Setting of PVNGS

The PVNGS site is located in the Sonoran Desert sub-province of the southern part of the Basin and Range (Figure 4.2-1). The Southern Basin and Range zone (SBR) is the host zone and is generally characterized by an extensional deformation regime, bounded to the southwest by the obliquely oriented southern portion of the modern-day San Andreas Fault and other sources in the Eastern California Shear-zone, and by the actively spreading Gulf of California. To the northeast, the region is bounded by the Arizona Transition Zone which separates the Basin and Range province from the Colorado Plateau (Figure 4.2-1).

The fault sources from the Rev. 0 PVNGS SSC model (LCI, 2014) are also shown in Figure 4.2-1. Few mapped Quaternary faults lie within the SBR, with the Sand Tank Fault being the closest to PVNGS (60 km southwest of the NPP).

The Southern Basin and Range is generally characterized by a low rate of instrumentally recorded seismicity with earthquakes of small to moderate magnitudes that are usually not associated with known faults (LCI, 2013). A M_S 6.1 earthquake occurred south of Death Valley in 1916. Several other moderate-magnitude earthquakes have occurred within the northwestern portion of the southern Basin and Range. The largest historical earthquake associated with the central part of the Southern Basin and Range is a 1952 local magnitude (M_L) 5.1 earthquake that occurred just south of the U.S.-Mexico border. A historical surface-rupturing earthquake (1887 magnitude 7.5 Sonora; Castro et al., 2010) occurred in the southern part of the southern Basin and Range.

Sources generally within 400 km from the PVNGS site location are considered for the purpose of hazard analysis (Figure 4.2-1). Some fault sources shown in Figures 4.2-1 extend beyond the 400 km radius from PVNGS. All the sources in the PVNGS SSC model are associated with active crustal seismicity.

For the purpose of evaluating the potential source and path effects, the western sources (included in the areal zones SCABA and GULF in Figure 4.2-1) have been differentiated into three regions. The rationale for the extent of the three regions was to identify earthquakes whose ray-paths to southern Arizona cross through the Gulf of California/Baja California zone (Region 3), or cross the extensional zone of the Salton Trough located north of the Gulf of California (Region 2), or cross north of the extensional zone, including the Transverse Range (Region 1). The spatial extents of Regions 1, 2 and 3 are shown in Figure 4.2-2.

4.2.1 Q structure in Arizona

The regional Q (quality factor) structure can have a significant impact on attenuation of the seismic waves with distance. Several of the proponent GMPE models (Section 5.5) have used data out to distances of 400 km to constrain the distance scaling, but these GMPEs did not include ground-motion data from sites in Arizona.

Phillips et al. (2014) has shown that Q obtained from tomographic inversion of USArray Lg data was low for coastal regions in California and the Salton Trough, and high for the Mojave Desert and for more stable regions such as the Colorado Plateau. In general, Phillips et al. (2014)'s results showed that Q increases at higher frequencies, but that regional patterns remain similar for the different frequencies.

The comparison between Q associated with the NGA-West2 California data and Q associated with NGA-West2 events that originated in California and were recorded in Arizona (referred to as PEER-AZ_{PATH} data set, see Section 5.3.3 for more details) has been addressed in Chapter 5 of Kishida et al. (2014). In general, the Q values averaged over the paths from California to Arizona indicate that events from central California have higher Q, events from Baja California have lower Q, and events from southern California and the Transverse Ranges have intermediate Q.

4.2.2 Controlling Sources for PVNGS

Previous hazard studies for PVNGS (LCI, 2013) have shown that for hazard level of 10^{-4} annual frequency of exceedance (AFE), the high-frequency hazard at the PVNGS site is controlled by earthquakes in the areal source zones within 70 km of the site and the low-frequency hazard at the PVNGS site is controlled by the distant large magnitude sources located in the southern California region. Section 4.2.3 summarizes the hazard contribution of the sources characterized in the PVNGS SSHAC Level 2 Project (LCI, 2013), and the associated deaggregation by magnitude and distance ranges.

Based on the Rev. 0 Hazard Input Document (HID) for the PVNGS SSC model (LCI, 2014), the range of source parameters for the areal source zones is listed in Table 4.2-1. For the SBR zone, where few Quaternary-active faults are identified, the areal source zone is modeled by virtual faults with dips in the 50 ± 15 degree range for normal faults and the 80 ± 10 degree range for strike-slip faults. In the SBR, the sources are mainly normal mechanisms (80%) with some strike-slip mechanisms (20%). The PVNGS SSC model allows for magnitudes up to **M**7.9 in the areal zones. Therefore, the ground-motion models must extrapolate up to **M**7.9 at short distances in a reasonable way, although, these large magnitude earthquakes do not have a significant effect on the hazard at the PVNGS site (Chapter 14, Section 14.3).

The PVNGS SSC separates the faults into layered faults and individual faults. Layered fault models are developed for plate boundary fault sources for high slip rate, such as the San Andreas, San Jacinto, Elsinore, and Cerro Prieto faults, so that, in each layered model, a fault is divided into several rupture geometries (layers) with corresponding slip rates and magnitudes. Spatially overlapping layers sum to the full slip rate of the fault, and the different combinations of layers that exist along strike accommodate the along-strike variations in geologic slip rate (LCI, 2014). For the purpose of ground-motion estimation, there is no difference between these two types of fault sources and they are combined. The ranges of source parameters for the faults are listed in Table 4.2-2. For both the California and Mexico faults (referred to as Regions 1 and 2&3 in this Report) and the other faults (AZ, NM, NV, and Mexico – referred to as Greater Arizona sources), the range of mean characteristic earthquakes are similar (**M**5.7 to **M**8.0) and the largest maximum magnitudes are 8.25. Therefore, the ground-motion models need to be applicable to **M**5.5 to **M**8.25 earthquakes at large distances (240 to 400 km). In addition, for the normal faults in the SBR, they also need to be applicable to distances as short as 50 km for magnitudes up to 7.85. This short distance range overlaps with the important distances from the areal source zones.

4.2.3 Hazard Contribution and Deaggregation from the PVNGS SSHAC Level 2 Project (LCI, 2013)

Figures 4.2-3 a) and b) show the hazard curves for the PVNGS site for 10 Hz and 1.0 Hz spectral acceleration resulting from the PVNGS SSHAC Level 2 Project (LCI, 2013). The figures show the individual contributions to the total mean hazard from the sources (both areal and faults) characterized in LCI (2013). For the areal sources, the mean hazard is also shown from the two alternatives (i.e. coarse and fine zonation). In the coarse zonation, there are fewer areal sources in which spatial smoothing of seismicity is implemented. In the fine zonation, there are more areal sources in the seismicity rates are uniform through each areal source. For the fault sources, the mean hazard from detailed faults in Arizona and Mexico and Arizona is differentiated from the mean hazard from fault sources listed in the 2008 National Seismic Hazard Mapping project (NSHMP – USGS, 2008) for faults in Nevada and California (non-type A faults). The mean hazard from the detailed Type-A faults in California (San Andrea, San Jacinto and Elsinore faults) is show in Figure 4.2-4 a) and b) for 10 and 1.0 Hz spectral

acceleration, together with the mean hazard from other individual faults. The results in the PVNGS SSHAC Level 2 Project indicated that, at AFE of 10^{-4} to 10^{-6}, the local areal sources are the dominant contributor to hazard at the higher spectral frequencies and they contribute about 10% to 50% of the hazard at the low spectral frequencies with the larger contribution at the lower AFE range. The distant fault sources are the dominant contributor to hazard at lower spectral frequencies at an AFE of 10^{-4} and contribute about 50% of hazard at an AFE of 10^{-4}.

Figures 4.2-5 a) and b) show deaggregation results by magnitude and distance for spectral accelerations corresponding to AFE of 10^{-4} for high (5 to 10 Hz) and low (1 to 2.5 Hz) spectral frequencies, respectively. For high frequencies, local earthquakes dominate the hazard, with a broad contribution to the total hazard from magnitudes in the **M**5 to **M**7 range and from distances less than 70 km. For low frequencies, the deaggregation plots show that the main contributions are from sources associated to magnitudes **M**7.5 to **M**8.5 and located at distances of 200-300 km from the site. The LCI (2013) study associated those faults to the distant, large earthquake-capable San Andreas, San Jacinto, and Cerro Prieto Faults.

4.3 References

Castro, R.R., Shearer P.M., Astiz L., Suter M., Jacques-Ayala, C., and Vernon, F. (2010). The Long-Lasting Aftershock Series of the 3 May 1887 Mw 7.5 Sonora Earthquake in the Mexican Basin and Range Province, *Bull. Seismol. Soc. Am.*, Vol. 100(3), 1153-1164.

Hardebeck, J.L. (2010). Seismotectonics and fault structure of the California central coast, *Bull. Seismol. Soc. Am.,* Vol. 100, 1031-1050, DOI: 10.1785/0120090307.

Kishida, T., Kayen, R.E., Ktenidou, O-J., Silva, W.J., Darragh, R.B., and Watson-Lamprey, J. (2014). PEER Arizona Strong-Motion Database and GMPEs Evaluation, *PEER Report 2014/09*, Pacific Earthquake Engineering Research Center, University of California, Berkeley, CA, June 2014, 136 pp.

Lettis, W.R., and Unruh, J.R. (2009). Quaternary Tectonic Setting of South-Central Coastal California, SSA 2009 Annual Meeting Abstract, *Seismological Research Letters*, Vol. 80(2), 323.

Lettis Consultants International – LCI (2013). Seismic Hazard Evaluation for the Palo Verde Nuclear Generating Station Wintersburg, Arizona, Final Report (Revision 4), Arizona Public Service Co., August 2013.

Lettis Consultants International – LCI (2014). Hazard Input Document (HID) for Palo Verde Final SSC Model, PR No. PV001-PR-01 - Revision 0, November 7, 2014

McLaren, M.K., and W.U. Savage (2001). Seismicity of south-central coastal California: October 1987 through January 1997, *Bull. Seismol. Soc. Am.*, Vol. 91, 1629-1658.

McLaren, M.K., Hardebeck, J.L., van der Elst, N., Unruh, J.R., Bawden, G.W., and Blair, J.L. (2008). Complex faulting associated with the 22 December 2003 Mw 6.5 San Simeon, California, earthquake, aftershocks and postseismic surface deformation, *Bull. Seismol. Soc. Am*., Vol. 98, 1659-1680.

PG&E (1988). Final report of the Diablo Canyon long-term seismic program, U.S. Nuclear Regulatory Commission Docket No. 50-275 and No. 50-323.

PG&E (2011). Report on the Analysis of the Shoreline Fault Zone, Central Coastal California, January 2011.

Phillips, W.S., Mayeda, K.M., and Malagnini, L. (2014). How to Invert a Multi-Band, Regional Phase Amplitudes for 2-D Attenuation and Source Parameters: Tests Using the USArray, *PAGEOPH,* DOI: 10.1007/s00024-013-0646-1.

United States Geologic Survey – USGS (2008). Documentation for the 2008 update of the United States National Seismic Hazard Maps, prepared by Petersen, M.D., et al., *U.S. Geological Survey Open File Report* 2008-1128.

Youngs, R.R., and Coppersmith, K.J. (1985). Implications of fault slip rates and earthquake recurrence models to probabilistic hazard assessments, *Bull. Seismol. Soc. Am.*, Vol. 75, 934-964.

Table 4.1-1: Range of Source Parameters for the Nearby Faults (excluding splay ruptures and complex ruptures) for DCPP.

Style-of-Faulting	Nearest Segment (Ruptures)	Range of Dip Angles (*)	Range of Mean Char Mag	Largest Max Mag	HW/FW for Nearest Segment
SS	Hosgri	72-90	6.8-7.3	8.5	HW
SS	Shoreline	90	6.3-6.8	8.4	NA (vertical)
REV	San Luis Bay	74-84 (OV model) 45-55 (SW model)	6.0-7.0	7.25	HW
REV	Oceano	45 (SW model) 45 (NE model)	6.8-7.3	7.55	NA (off the end)
REV	Wilmar	45-67 (NE model) 50-65 (SW model)	6.2-6.5	6.75	NA (off end)
REV	Los Osos	50-67 (NE model)	6.1-6.8	7.05	HW
REV/OBL	Los Osos	60-90 (SW model) 60-80 (OV model)	6.5-7.0	7.25	NA (off the end)
REV/OBL	Oceano & SWBZ (**)	65 (OV model)	6.7-7.2	7.45	NA (off the end)

(*) Dip is for points of the rupture within 20 km and is measured over the top 5 km of the rupture.

(**) SWBZ is the segment starting at the southern end of the Oceano – Wilmar Avenue faults shown in Figure 4.1-2

Table 4.1-2: Range of Source Parameters for the DCPP Nearby Faults for Splay Ruptures.

Style-of-Faulting	Rupture Segments	Range of Dip Angles (*)	Range of Mean Char Mag	Largest Max Mag	HW/FW for Nearest Segment
SS	Hosgri - Main Shoreline - Splay	72-90 main 90 splay	7.7 main 6.5 splay	7.7	HW
REV	Los Osos - Main San Luis Bay - Splay	50-67 62-70 (NE model) 74-84 (OV model)	6.4- 6.5 main 6.1-6.2 splay	6.5	HW
REV	San Luis Bay - Main Los Osos - Splay	45-65 80 (SW model)	6.4 main 6.3 splay	6.4	HW
REV	Wilmar Ave - Main Los Osos - Splay	45-67 65-70 (NE model) 67-80 (SW model)	6.5-6.6 main 6.3 splay	6.6	HW

(*) Dip is for points of the rupture within 20 km and is measured over the top 5 km of the rupture.

Table 4.1-3: Range of Source Parameters for the DCPP Nearby Faults for Complex Ruptures.

Style-of-Faulting	Closest Rupture Segments	Range of Dip Angles (*)	Range of Mean Char Mag	Largest Max Mag	HW/FW for Nearest Segment
SS & REV	Shoreline (SS) San Luis Bay (REV) OV and NE models	90 (SS) 45-84 (REV)	6.0 - 7.0	8.2	HW
SS & REV/OBL	Hosgri (SS) Los Osos (REV/OBL) OV, SW and NE models	75-90 (SS) 60-90 (REV/OBL)	6.5-7.1	8.4	HW
SS & REV	Shoreline (SS) Oceano & SWBZ (REV) OV model	90 (SS) 65 (RV)	6.5-7.1	7.5	NA (off the end)
SS & REV	Hosgri (SS) San Luis Bay (REV) SW model	75-90 (SS) 45-55 (RV)	6.4-6.9	8.4	HW
SS & REV/OBL	Hosgri (SS) Los Osos (REV/OBL) SW and NE models	75-90 (SS) 50-90 (RV/OBL)	6.4-7.1	8.4	NA (off shore)

(*) Dip is for points of the rupture within 20 km and is measured over the top 5 km of the rupture.

Table 4.1-4: Range of Source Parameters for the Virtual Faults in the Host Areal Source Zone for DCPP.

Style-of-Faulting	Fraction of Earthquakes	Range of Dip Angles	Largest Max Mag
SS	0.70	65-90	7.1
REV	0.30	35-70	7.2

Table 4.2-1: Areal Sources Parameters for PVNGS.

Areal Source Name	Style-of-Faulting	Fraction of Events	Depth Range (km)	Range of Dip Angles	Largest Max Mag
SCABA	SS	0.90	12-18	80 ± 10 deg	7.9
	REV	0.10		45 ± 15 deg	
GULF	SS	0.70	12-16	80 ± 10 deg	7.9
	NML	0.30		50 ± 15 deg	
SBR & MH	SS	0.80	12-18	80 ± 10 deg	7.9
	NML	0.20		50 ± 15 deg	
TZ	SS	0.70	14-20	80 ± 10 deg	7.9
	NML	0.30		50 ± 15 deg	
CP	SS	0.70	15-25	80 ± 10 deg	7.9
	NML	0.30		50 ± 15 deg	

Table 4.2-2: Range of Faults Parameters for PVNGS

	Style-of-Faulting	Range of Dip Angles	Range of Mean Char Mag	Largest Max Mag	Minimum R_{RUP} (km)
CA and Mexico Faults (Regions 1, 2 and 3)	SS	67-90	5.7-8.0	8.25	240
	NML	37	7.1-7.5	7.75	250
	REV	41-49	6.6-7.3	7..55	350
AZ, NV, NM, & Mexico Faults (Greater Arizona sources)	NML	50	5.8 – 7.6	7.85	50
	SS	90	6.8 - 8.0	8.25	260
	REV	70	6.1 – 6.5	6.75	340

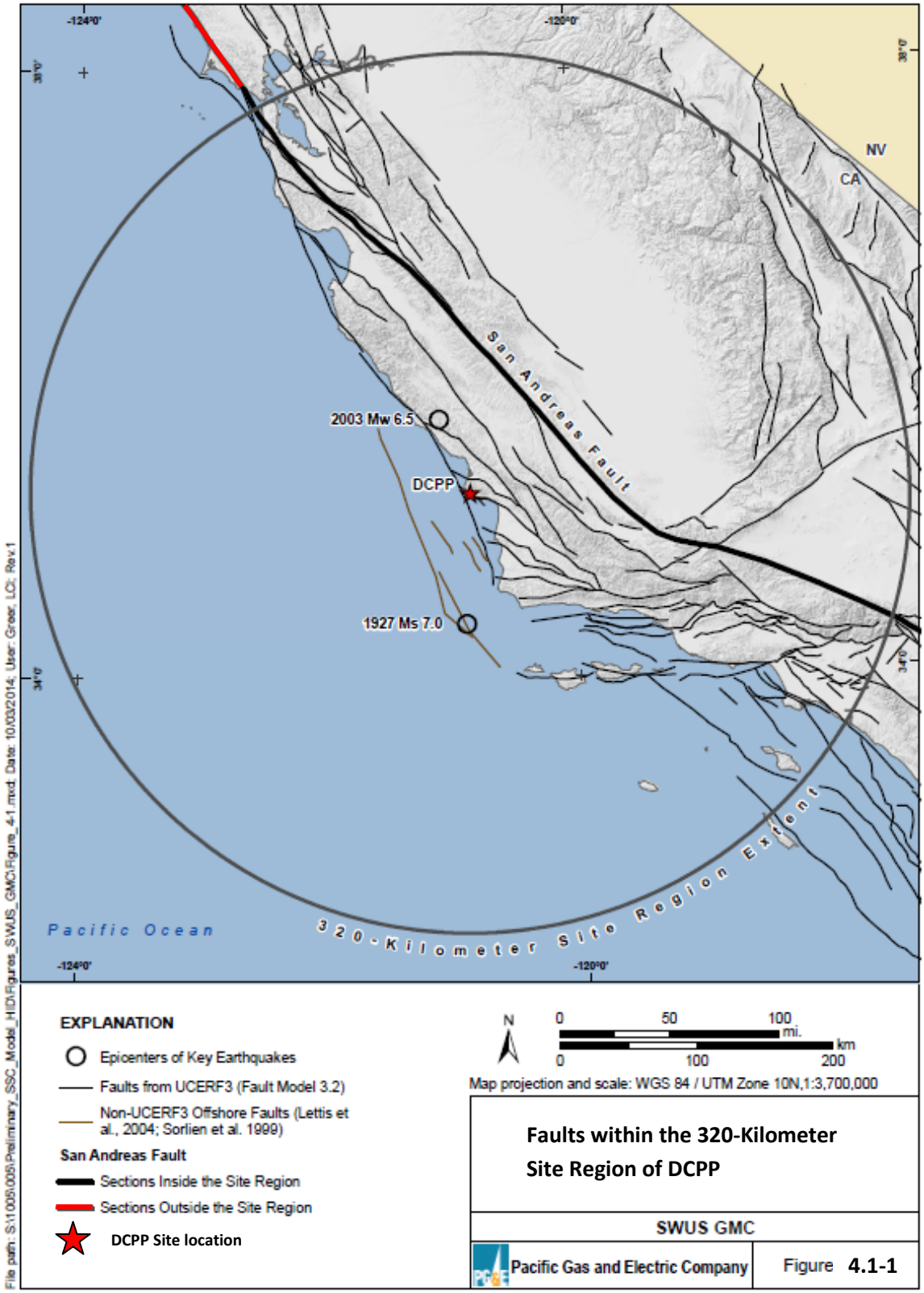
-124°0'
-120°0'
39°0'
34°0'
NV
CA
San Andreas Fault
2003 Mw 6.5
DCPP
1927 Ms 7.0
Pacific Ocean
320-Kilometer Site Region Extent
EXPLANATION
Epicenters of Key Earthquakes
Faults from UCERF3 (Fault Model 3.2)
Non-UCERF3 Offshore Faults (Lettis et al., 2004; Sorlien et al. 1999)
San Andreas Fault
Sections Inside the Site Region
Sections Outside the Site Region
DCPP Site location
N
0 50 100 mi.
0 100 200 km
Map projection and scale: WGS 84 / UTM Zone 10N,1:3,700,000
Faults within the 320-Kilometer Site Region of DCPP
SWUS GMC
Pacific Gas and Electric Company
Figure 4.1-1
File path: S:\1005\005\Preliminary_SSC_Model_HID\Figures_SWUS_GMC\Figure_4-1.mxd, Date: 10/03/2014, User: Greer, LC: Rev.1

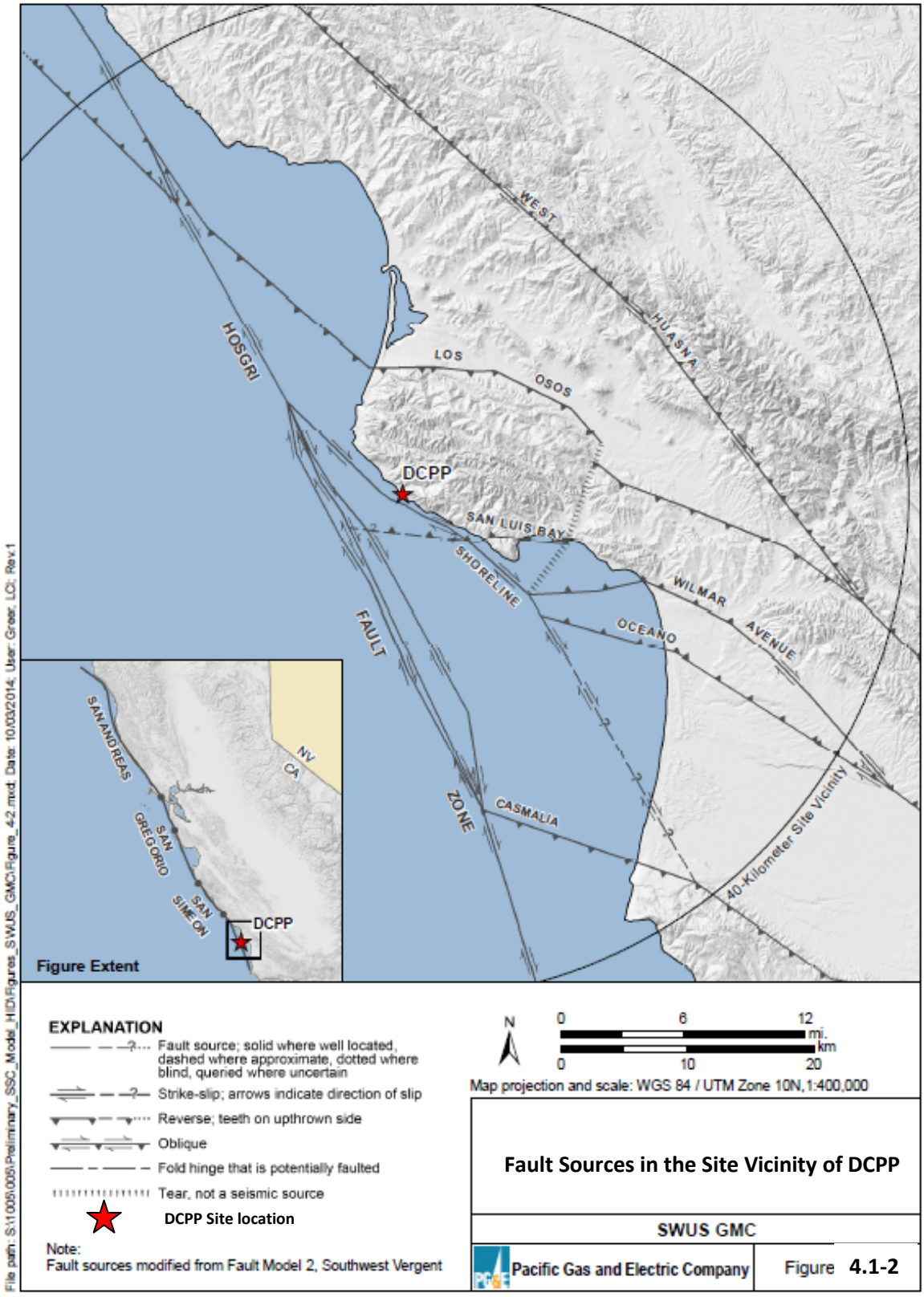
WEST
HUASNA
HOSGRI
LOS
OSOS
DCPP
SAN LUIS BAY
SHORELINE
FAULT
WILMAR
AVENUE
OCEANO
ZONE
CASMALIA
40-Kilometer Site Vicinity
SAN ANDREAS
SAN GREGORIO
SAN SIMEON
NV
CA
DCPP
Figure Extent
EXPLANATION
Fault source; solid where well located, dashed where approximate, dotted where blind, queried where uncertain
Strike-slip; arrows indicate direction of slip
Reverse; teeth on upthrown side
Oblique
Fold hinge that is potentially faulted
Tear, not a seismic source
DCPP Site location
Note:
Fault sources modified from Fault Model 2, Southwest Vergent
N
0 6 12 mi.
0 10 20 km
Map projection and scale: WGS 84 / UTM Zone 10N, 1:400,000
Fault Sources in the Site Vicinity of DCPP
SWUS GMC
Pacific Gas and Electric Company
Figure 4.1-2
File path: S:\1005\005\Preliminary_SSC_Model_HID\Figures_SWUS_GMC\Figure_4-2.mxd Date: 10/03/2014 User: Greer, LCI; Rev 1

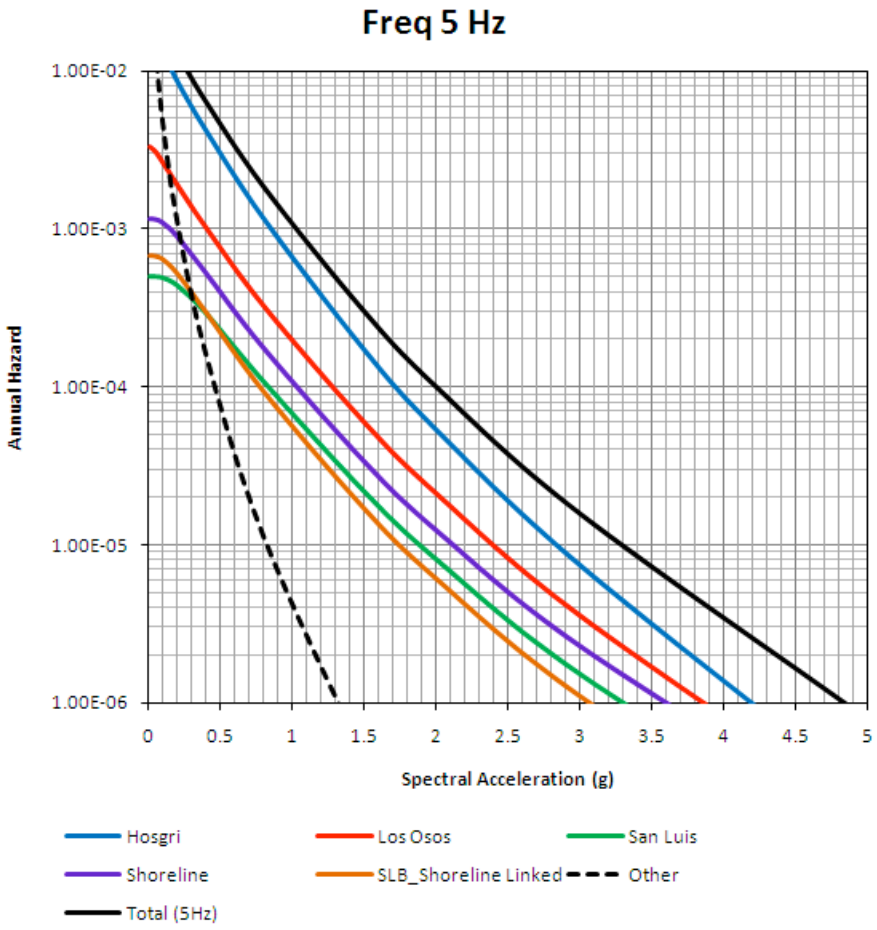

Figure 4.1-3a: Hazard by source for 5 Hz spectral acceleration at DCPP from the Shoreline Fault Report (PG&E, 2011, Figure 6-20b).

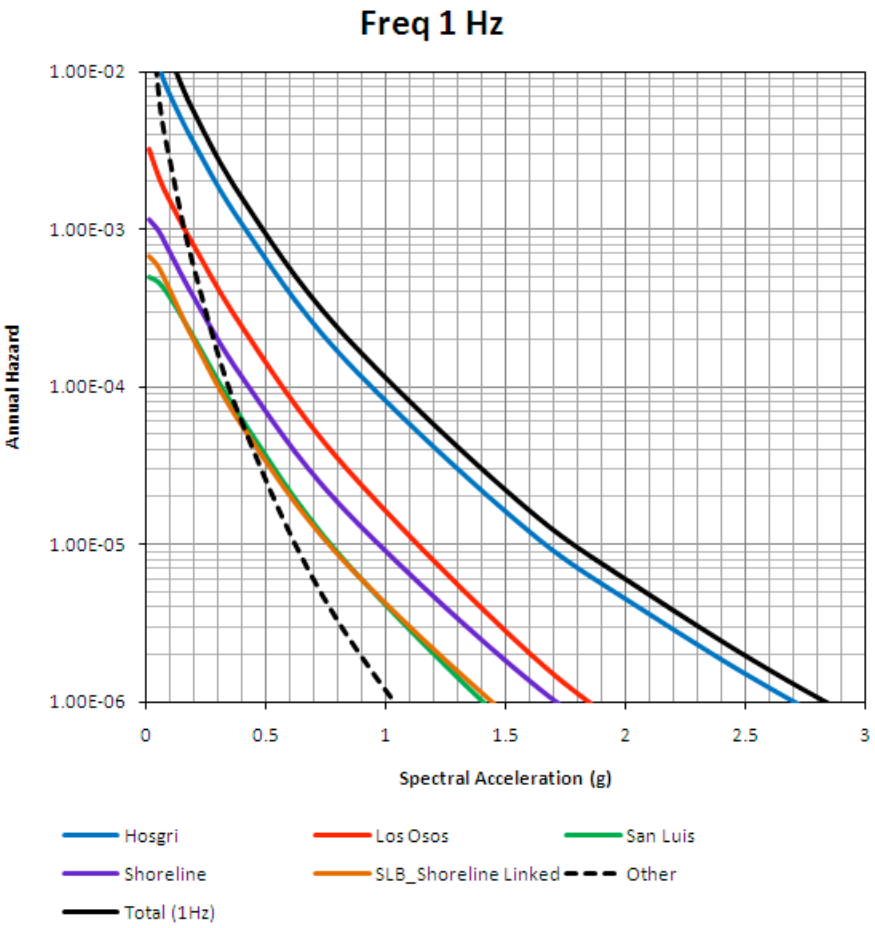

Figure 4.1-3b: Hazard by source for 1 Hz spectral acceleration at DCPP from the Shoreline Fault Report (PG&E, 2011, Figure 6-20c).

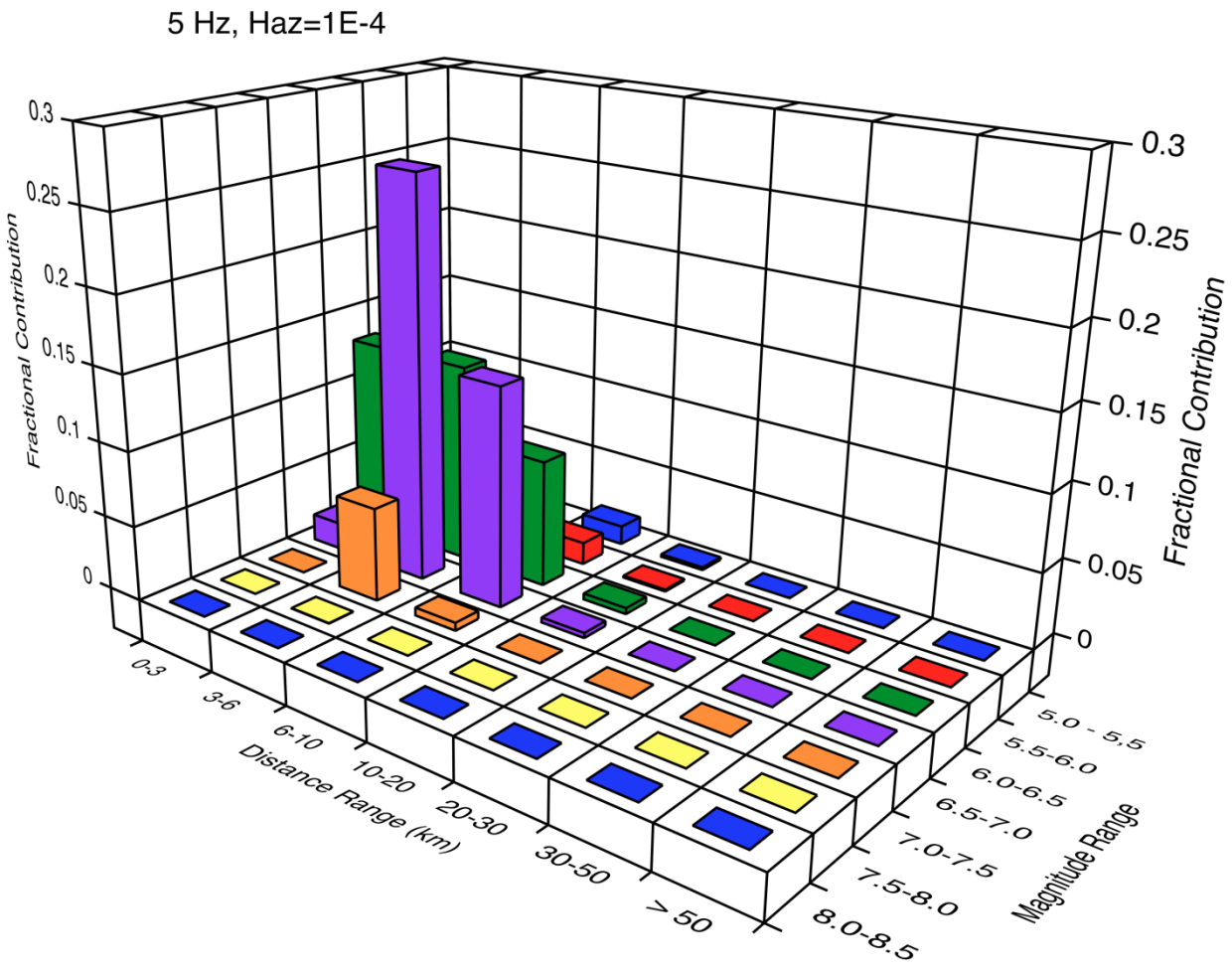

Figure 4.1-4a: Deaggregation for 5 Hz spectral acceleration at 10^{-4} hazard level for DCPP from the Shoreline Fault Report (PG&E, 2011, Figure 6-22b).

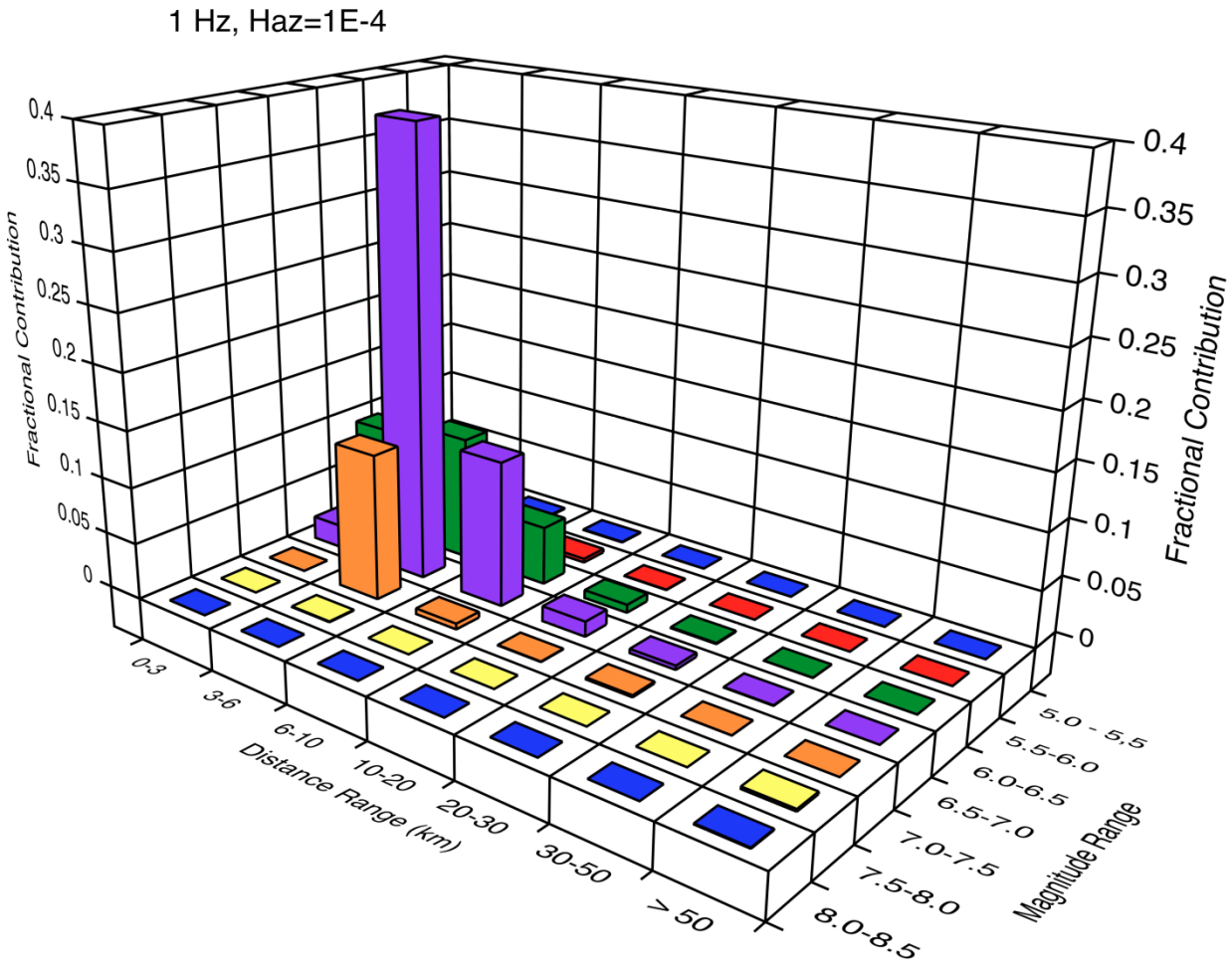

Figure 4.1-4b: Deaggregation for 1 Hz spectral acceleration at 10^{-4} hazard level for DCPP from the Shoreline Fault Report (PG&E, 2011, Figure 6-22c).

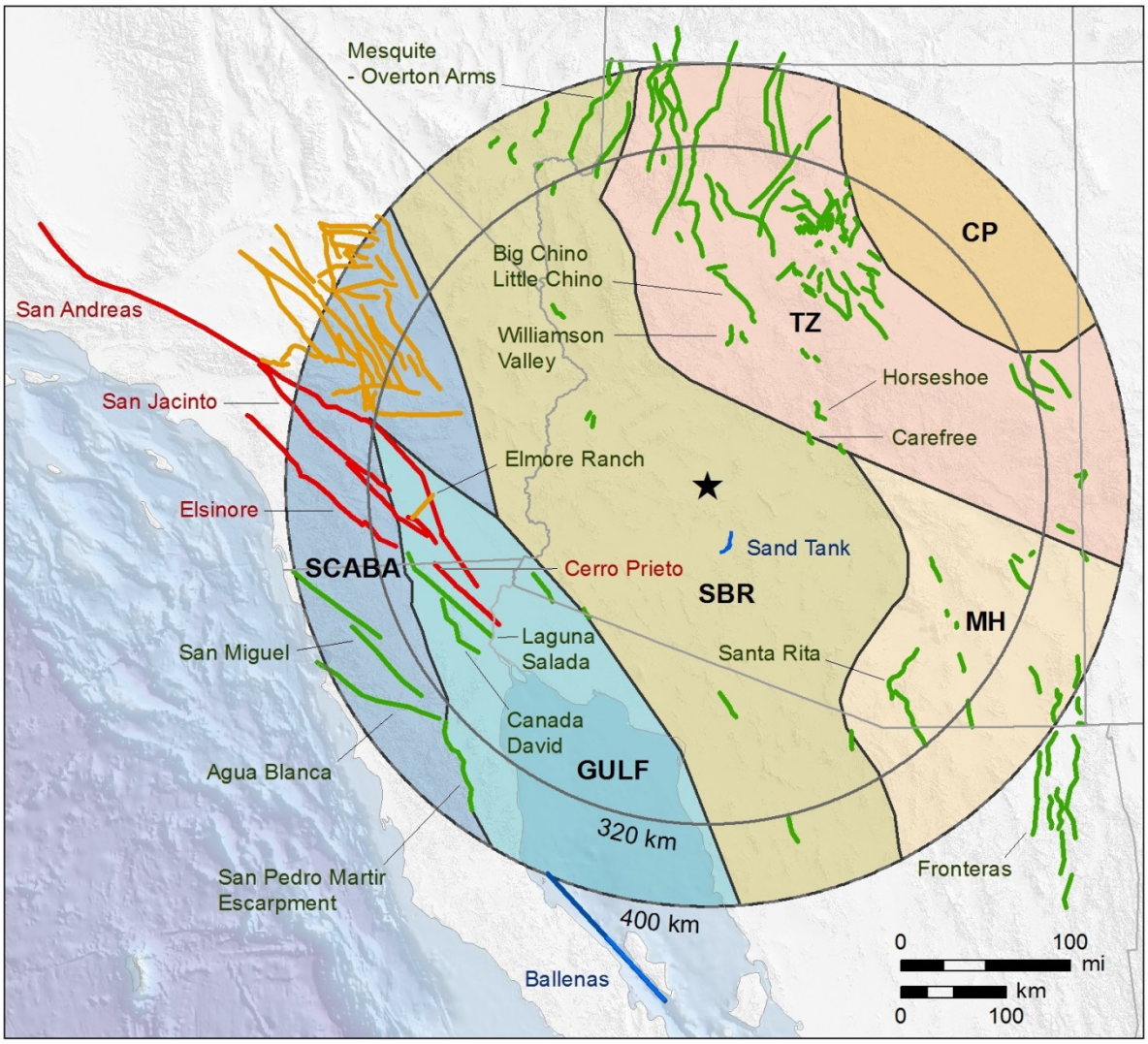

Figure 4.2-1: Areal and fault sources in the seismotectonic alternative of the in the PVNGS SSC model (LCI, 2014). Star shows location of the PVNGS site. The areal seismic sources are identified by their name in the PVNGS SSC model (LCI, 2014), where GULF refers to the Gulf of California zone, SCABA refers to the Southern California And Baja zone, SBR refers to the Southern Basin and Range zone, MH refers to the Mexican Highland zone, TZ refers to the Transition Zone, and CP refers to the Colorado Plateau zone. The fault sources are distinguished by the following color code: red = layered fault sources, yellow = other fault sources in California, green = fault sources in Arizona, Nevada, and Mexico, blue = unique fault sources (Sand Tank fault in Arizona and Ballenas Transform in the Gulf of California).

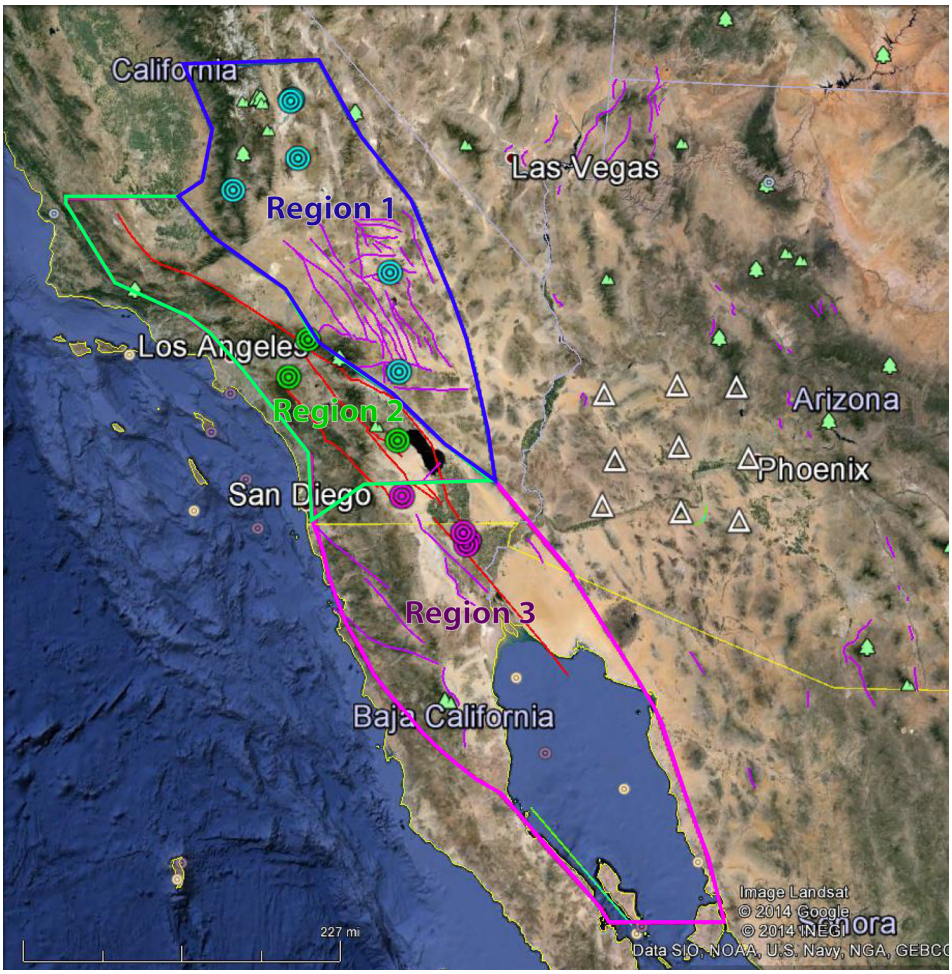

Figure 4.2-2: Geographic extensions of Region 1, Region 2, and Region 3 shown as blue, green, and purple closed polygons, respectively. Also plot are the NGA-West2 earthquakes selected for the path effect analysis (blue circles for the Region 1 earthquakes, green circles for the Region 2 earthquakes, and purple circles for the Region 3 earthquakes) and the selected Arizona Transportable Array recording stations (white triangles) used for the path effect analysis. Colored lines represent faults in PVNGS SSC Model (Workshop #3, Ross Hartleb, personal communication 2014).

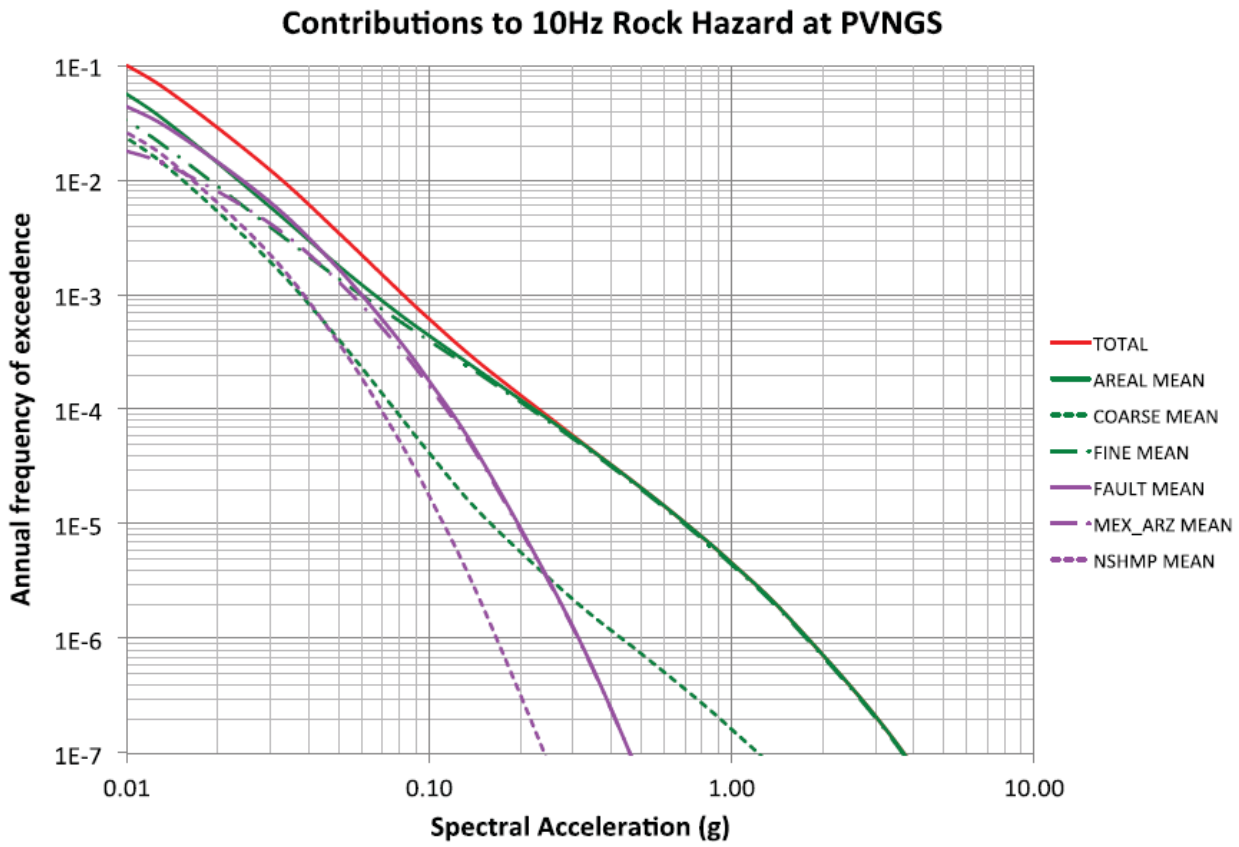

Figure 4.2-3a: 10 Hz spectral acceleration weighted mean rock hazard curves showing total hazard and contributions from coarse and fine areal sources, and from Mexico-Arizona faults and NSHMP faults characterized in the PVNGS SSHAC Level 2 Project (LCI, 2013, Figure 6.1).

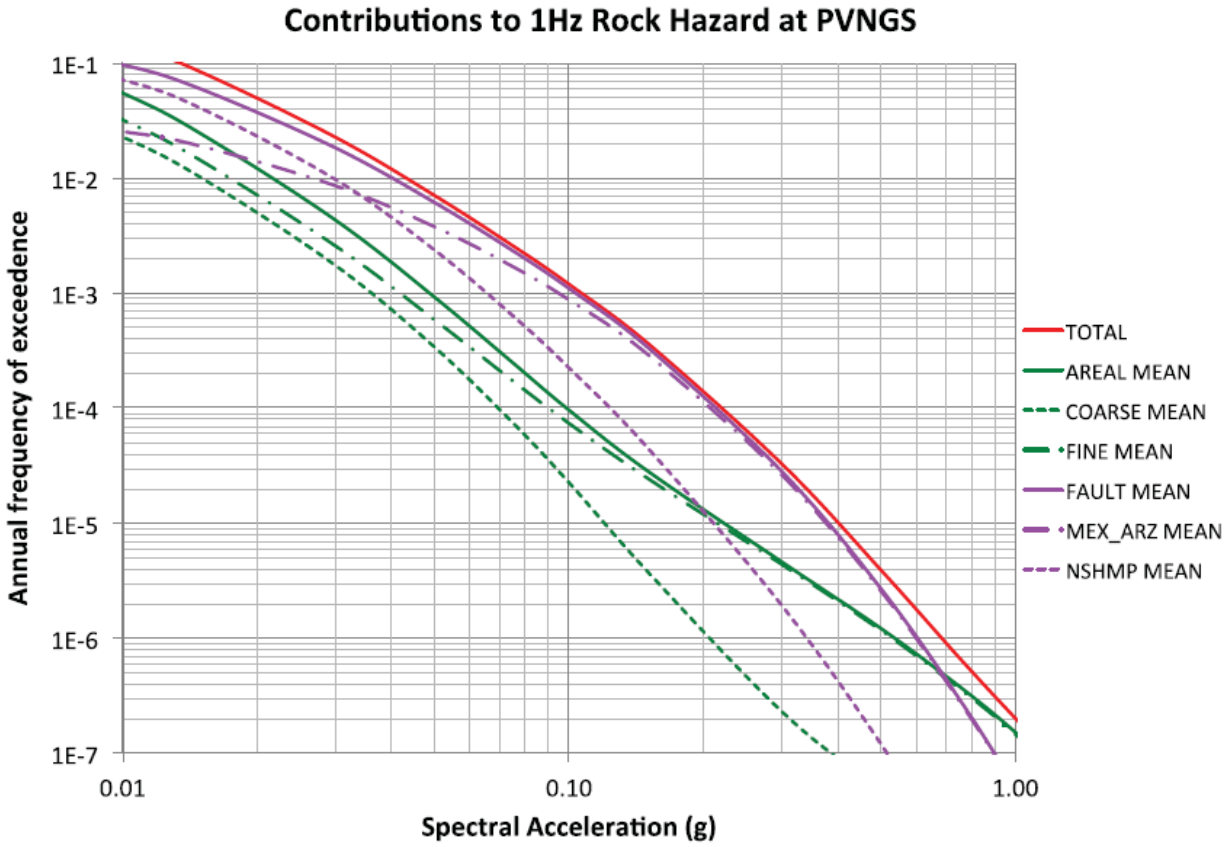

Figure 4.2-3b: 1 Hz spectral acceleration weighted mean rock hazard curves showing total hazard and contributions from coarse and fine areal sources, and from Mexico-Arizona faults and NSHMP faults characterized in the PVNGS SSHAC Level 2 Project (LCI, 2013, Figure 6.2).

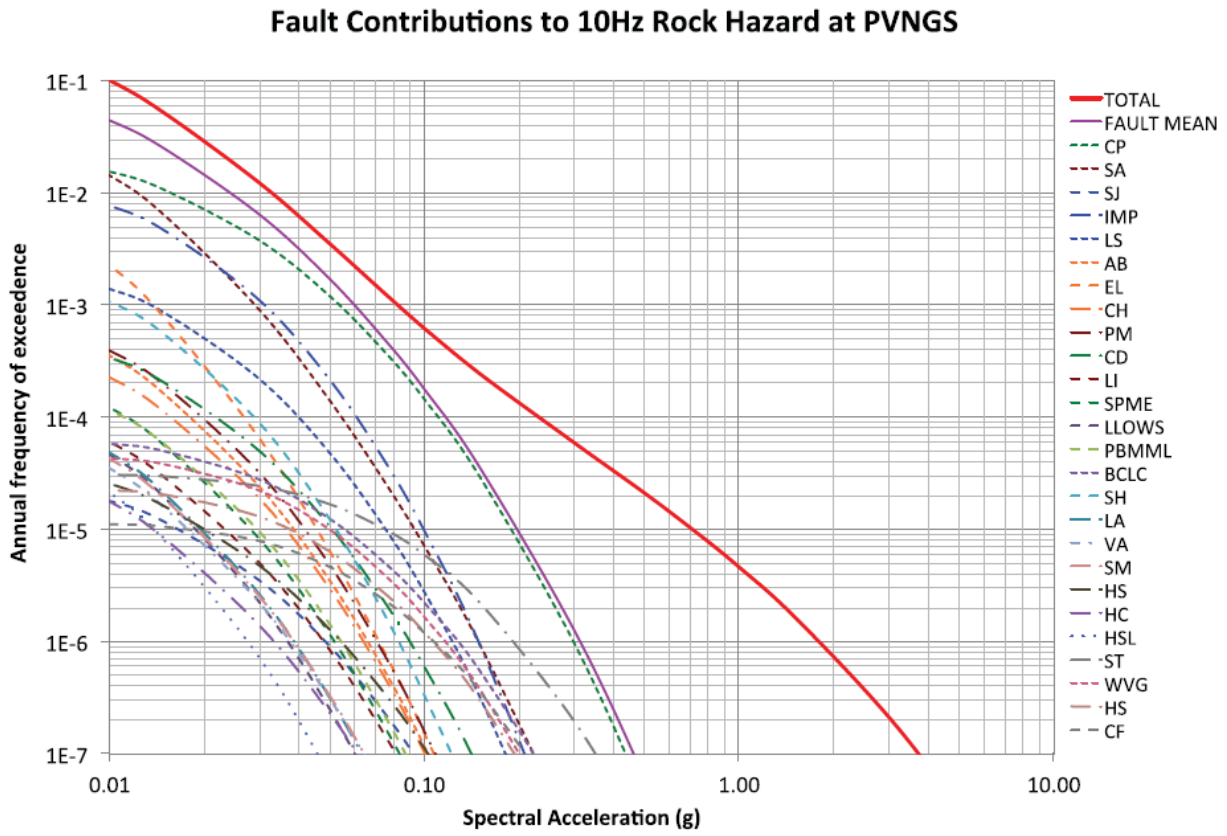

Figure 4.2-4a: 10 Hz spectral acceleration weighted mean rock hazard curves showing total hazard and contributions from individual fault sources. The dominant contributor to hazard is the Cerro Prieto (CP) fault from the Mexico-Arizona database, and the San Andreas (SA) and the San Jacinto (SJ) faults. The abbreviation of the individual faults is consistent with the one adopted in LCI (2013) and is not repeated here. LCI, 2013, Figure 6.7).

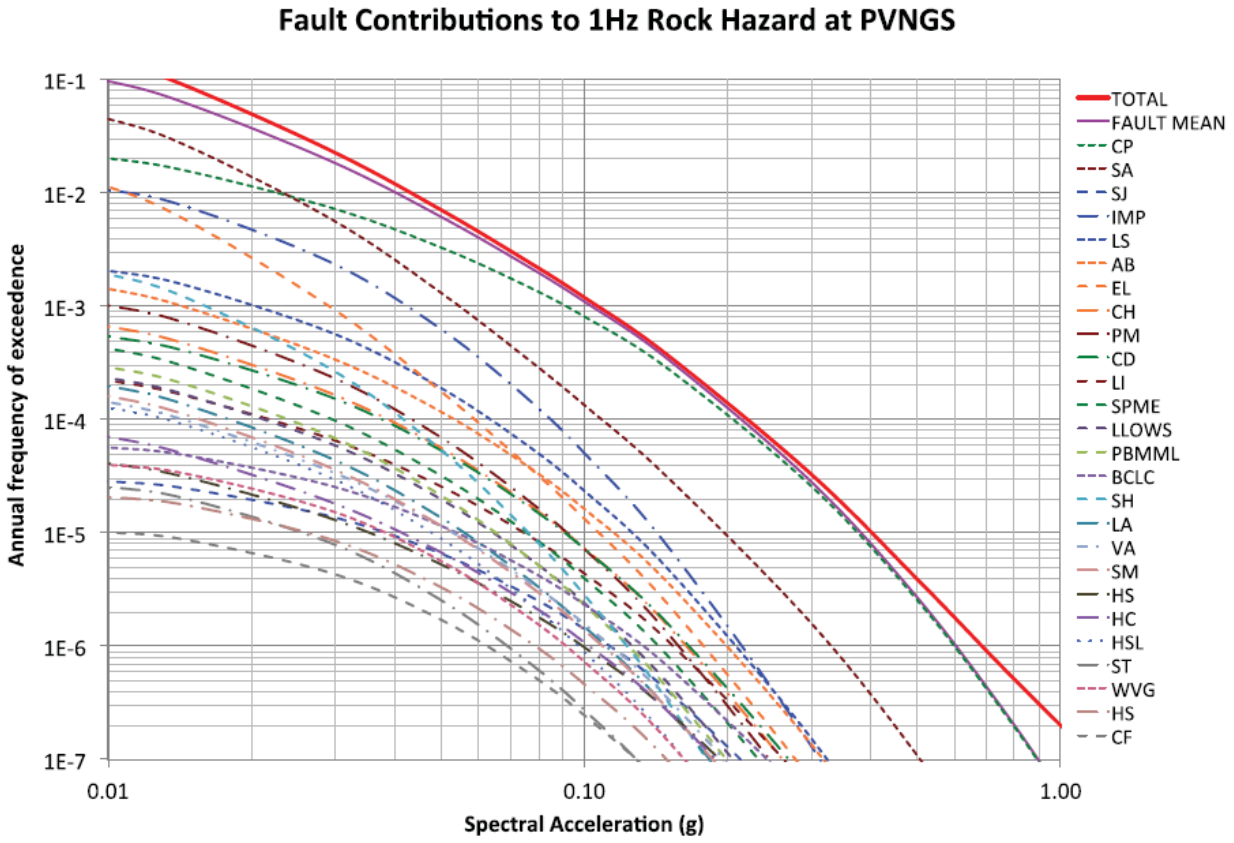

Figure 4.2-4b: 1 Hz spectral acceleration weighted mean rock hazard curves showing total hazard and contributions from individual fault sources. The dominant contributor to hazard is the Cerro Prieto (CP) fault from the Mexico-Arizona database, and the San Andreas (SA) and the San Jacinto (SJ) faults. The abbreviation of the individual faults is consistent with the one adopted in LCI (2013) and is not repeated here. (LCI, 2013, Figure 6.8).

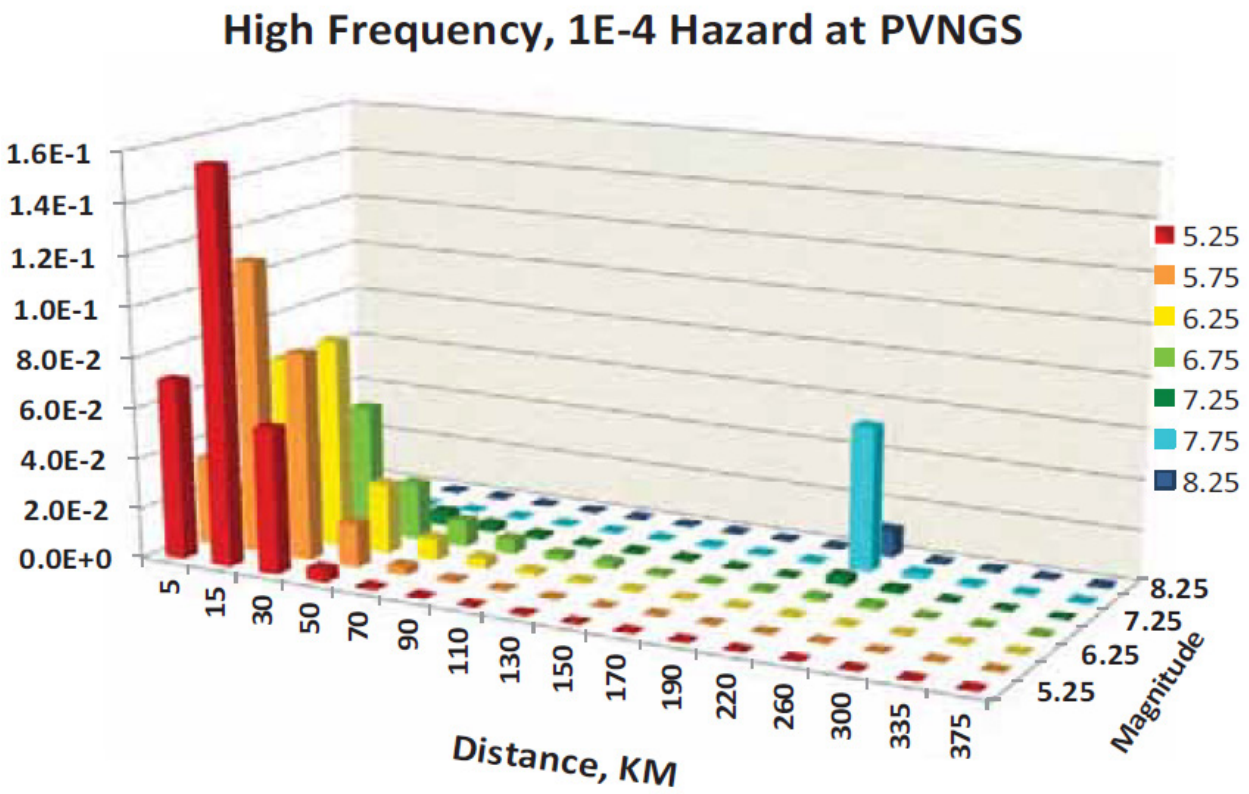

Figure 4.2-5a: Deaggregation of rock hazard for 10^{-4} mean annual frequency of exceedance at spectral frequencies of 5 and 10 Hz (taken from Figure 6.19 in LCI, 2013).

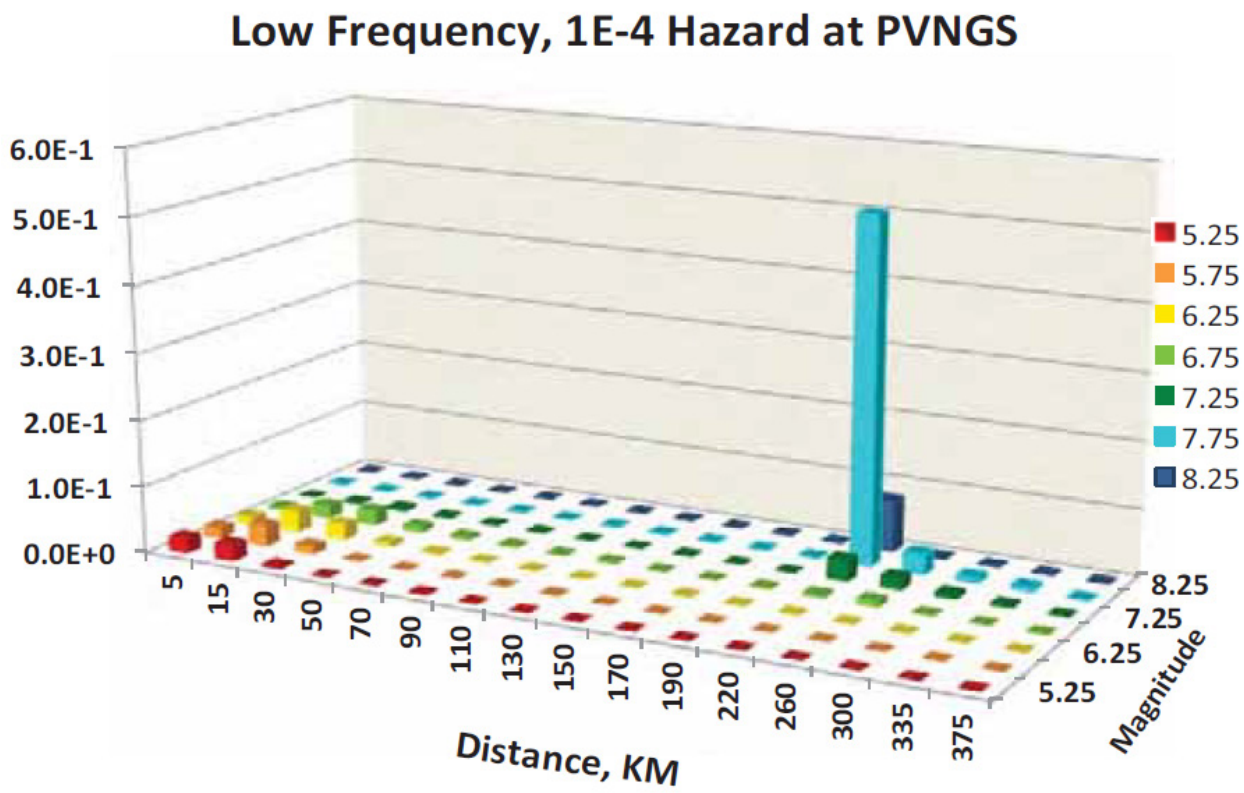

Figure 4.2-5b: Deaggregation of rock hazard for 10^{-4} mean annual frequency of exceedance at spectral frequencies of 1 and 2.5 Hz (taken from Figure 6.19 in LCI, 2013).

5 GROUND-MOTION DATABASES AND CANDIDATE MODELS FOR THE MEDIAN AND ALEATORY STANDARD DEVIATION

This Chapter describes the components of the database that were used for two purposes: to evaluate the existing ground-motion prediction equation (GMPE) models relevant to the DCPP and PVNGS sites, and to develop new GMPE models. The database consists of both empirical ground-motion data and simulated ground-motion data from finite-fault simulations.

In addition to the ground-motion databases, this Chapter also includes candidate models for median ground motion (GMPEs) and previously published models for the components of the aleatory standard deviation. The candidate GMPEs are described in this database Chapter because they are used as inputs to the development of the SWUS GMC median models as described in Chapter 6. The existing single-station sigma models are used for comparisons with new single-station sigma models developed for the SWUS GMC Project and described in Chapter 7.

5.1 Empirical Ground-Motion Database for Median Ground Motion

There are four primary empirical ground-motion databases used in the project: the PEER NGA-West2 database (Ancheta et al., 2014); the PEER Arizona database (Kishida et al., 2014a); the Reference Database of Seismic Ground Motion in Europe (RESORCE) described in Akkar et al. (2014c); and the ground-motion residuals from **M**4 to **M**6 earthquakes from Taiwan described in Lin et al. (2011). The four primary databases are summarized in Table 5.1-1, with the Arizona dataset separated into two parts: the recordings in Arizona from earthquakes in California and Mexico (Regions 1, 2, and 3 described in Section 4.2) and recordings in Arizona from earthquakes in Arizona.

In addition to these primary databases, ground motions from the **M**6.0 2008 Wells, Nevada and the **M**6.7 2011 Fukushima-Hamadori normal-faulting earthquakes were evaluated based on the recommendations at SWUS Workshop #1. These earthquakes were not included in any of the four primary ground-motion databases considered for this project. The Wells earthquake provides ground motions from a normal-faulting earthquake, if one should occur in the Southern Basin and Range, which

are not well represented in the NGA-West2 database. The Fukushima-Hamadori earthquake provides a large set of near-fault ground motions from a complex rupture normal-faulting earthquake.

Many different subsets of the data from the four primary databases are used in the various TI Team evaluations. Overviews of the various subsets used for the median pseudo-spectral acceleration (PSA), aleatory variability of PSA, and other cases (kappa and ground motion from complex and splay ruptures) are given in Tables 5.1-2, 5.1-4, and 5.1-3, respectively. To help keep track of the different subsets, each subset is given a unique name, which is listed in the first column of these tables. The second column lists the primary data base or bases from which the subset was selected. The third column describes the selection criteria that were applied. The fourth column describes how the subset is used by the TI Team. For the data sets used to evaluate the aleatory variability (Table 5.1-4), there are multiple versions of the dataset depending on which of the NGA-West2 GMPEs is used for the residuals, because different subsets of the NGA-West2 dataset were used by the different developers of the GMPEs. For these cases, the subset name includes the reference GMPE as well.

To summarize the attributes of the data sets, a common set of plots is used. As example, Figure 5.1.1-1 shows this common data set plot for the NGA-West2 database. The top frames show the distribution of the data in magnitude and Joyner-Boore distance (R_{JB}) space separated by the style-of-faulting classification. The middle frames show the effect of the limited frequency ranges for which the data are reliable in terms of the number of earthquakes with at least one reliable recording at a given period and the total number of recordings that are reliable at a given period. Finally, the bottom frames show how well the earthquakes were recorded in terms of the distributions for the number of recordings per earthquake, and number of recordings per site, and number of recordings per site conditions (V_{S30}).

5.1.1 PEER NGA-West2 Database

The NGA-West2 project database expanded the previous PEER (2008) NGA ground-motion database to include worldwide ground-motion data recorded from shallow crustal earthquakes in active tectonic regimes after 2003. In this expansion, the range of magnitudes included in the database was extended down to **M**3. One reason for including the smaller magnitudes is that it greatly increases the number of recordings per site for use in estimating site-specific site terms, which is required for estimation of single-station sigma.

Each NGA-West2 developer selected their own subsets from the full NGA-West2 data set. Part of the selection process was to remove recordings that had missing key metadata, had data that were judged to be unreliable (metadata or ground-motion data), or were not considered applicable to shallow crustal earthquakes in active tectonic regions. Other selection criteria were applied by some developers such as removing class 2 earthquakes (aftershocks). Of the five subsets selected, the ASK14 selection criteria was the most broad and the TI Team selected this data set as the base NGA-West2 subset for use in the

evaluations of the medians. For the aleatory variability, the individual subset for each developer was used because the evaluation of the aleatory variability requires use of the residuals from the developers.

The attributes of the ASK14 subset of the NGA-West2 dataset are shown in Figure 5.1.1-1. The majority of the earthquakes are either strike slip (57%) or reverse and reverse oblique (26%). Normal and normal oblique earthquakes make up 17% of the earthquakes but only 8% of the recordings. For **M** > 5, the distribution of earthquakes is similar: 49% strike-slip, 31% reverse (31%), and 20% normal.

The data coverage for the hanging-wall (HW) effects in the NGA-West2 data set is shown in Figure 5.1.1-2. This plot shows the subset of recordings that have the potential for significant HW effects: **M** ≥ 5, dip ≤ 80 degrees, R_{JB} < 5 km, and at least one recording on both the FW and HW sides of the rupture. This figure shows that there are sparse data for **M**5 to **M**6 earthquakes that can be used to constrain the HW scaling.

5.1.2 Arizona Ground-Motion Database

PEER compiled a database of ground motions recorded by 15 stations in Arizona produced by 26 earthquakes that occurred in Arizona, California, or Mexico after 2007. These recordings are listed in Table 5.1.2-1. Thirteen of the Arizona recording stations around the PVNGS site were part of the Earth Scope Transportable Array (USArray) deployment, and the other two were permanent stations managed by the USGS/CalTech Southern California Seismic Network. The PEER Arizona database is described in Kishida et al. (2014a). The PEER Arizona dataset consist of 12 small (**M** < 3.5) earthquakes in Arizona with hypocenter distances of 9 to 300 km, and 14 earthquakes in California and Mexico with R_{JB} distances between 150 and 600 km. The fourteen California and Mexico earthquakes had recordings in California that were included in NGA-West2 database, but the ground motions in Arizona were not included in the NGA-West2 database.

Figure 5.1.2-1 shows the attributes of the PEER-Arizona data set. The closest station to PVNGS (Z14A) is located 8 km away. The recordings were processed following the standard PEER processing procedure (Kishida et al., 2014b), and are publicly available at the PEER Website (http://peer.berkeley.edu/ngawest2/wp-content/uploads/2010/09/Arizona_Database.zip).

During SWUS Workshop #1, it was recommended that a search be made for additional recordings from the El Mayor Cucapah earthquake at the Veteran Administration (VA) Hospital in Phoenix and at Roosevelt Dam. A check of the strong motion databases for the National Strong Motion Program and for COSMOS did not show any additional recordings from this earthquake at either of these two sites.

5.1.2.1 V_{S30} for the Arizona Sites

The site conditions at the seismic stations in Arizona had not been previously characterized. Because knowledge of the site conditions is important to evaluating the ground-motion data from Arizona, the SWUS project sponsored a study to characterize the site conditions at the Arizona seismic stations. The shallow shear-wave velocity profiles for 10 of the 15 stations in the PVNGS region were measured using the spectral analysis of surface wave (SASW) dispersion technique. The SASW study is described in Chapter 3 of Kishida et al. (2014a). The 10 sites were selected on the basis of being the closest to the PVNGS location, having a sufficient number of recordings from Arizona and California events, and having acceptable accessibility for SASW measurements. For each of these sites, the detailed site velocity profile, the average velocity in the upper 30 m of the profile (V_{S30}), the average velocity for the entire profile ($V_{S,Z}$), and the NEHRP site classification were derived. Three independent inversion techniques were employed. The results showed that there were two typical site types: deep stiff soil (alluvium) sites and thin soil over rock sites. For sites situated on deep alluvium (8 stations), V_{S30} is typically in the range of 370 to 690 m/s, with usually gentle monotonic increasing velocity with depth. For sites situated on thin soil over rock, (2 stations), V_{S30} is in the range of 970-1240 m/s, with greater variance in the field dispersion data and greater variability between the inverted profiles than for the deep alluvium sites. Table 5.1.2-2 shows the V_{S30} values obtained by the SASW analyses for the characterized recording stations.

5.1.3 Akkar et al. Subset from RESORCE Database

The most recent pan-European earthquake strong-motion databank, called RESORCE (Reference Database for Seismic Ground-Motion in Europe), is one of the products of the Seismic Ground Motion Assessment (SIGMA; projet-sigma.com) project. The full RESORCE database set is described in Akkar et al. (2014c). The moment magnitude range covered by RESORCE is from **M**2.8 to **M**7.8, with the majority of the data at **M** < 5.5. The R_{JB} distances range from 0 to 587 km. The accelerograms were processed using a uniform methodology. The sampled periods for the response spectral values included in the Akkar dataset are between 0.01 sec and 4 sec.

The subset of the RESORCE database used by Akkar et al. (2014c) was used by the SWUS GMC project because this subset provided an initial evaluation of the more reliable data. The Akkar et al. database excluded recordings that did not have measured V_{S30} values, earthquakes with magnitudes less than 4.0, earthquakes with unknown style-of-faulting, hypocentral depth greater than 30 km, recordings at R_{JB} distances greater than 200 km, and events with only one recording. The Akkar et al. database includes 1,041 3-component recordings from 221 earthquakes recorded at 322 strong-motion stations.

The attributes of Akkar et al. database are summarized in Figure 5.1.3-1. The majority of earthquakes and accelerograms are from strike-slip events (38% of events and 36% of recordings) and normal events

(47% of events and 51% of recordings). The number of reverse-slip events and number of reverse-slip recordings in the Akkar et al. database are small compared to the other style-of-faulting classes (only 15% of the events and 13% of recordings are from reverse events). The Akkar et al. data set has good coverage for distances from 5 to 200 km and magnitudes from 4.5 to 6.0 for normal and strike-slip mechanisms. Most of the sites have V_{S30} values in the range of 250 to 750 m/s. There is sparse coverage for V_{S30} values greater than 750 m/s.

5.1.4 Lin et al. Database

The Lin et al. (2011) database was developed to study the components of the aleatory variability (site, path, and source terms) using the extensive data set of ground motions from Taiwan. Because of the large number of aftershocks from the 1999 Chi-Chi earthquake, there are many sites with large numbers of recordings per site. For the objective of evaluating the components of variability, Lin et al. restricted their data set to sites with at least 10 recordings per site. The attributes of the Lin et al. database are summarized in Figure 5.1.4-1. This data set is only used for the evaluation of the single-site within-event standard deviation, denoted ϕ_{SS}.

5.1.5 Additional Data from Normal Style-of-Faulting Earthquakes

As noted in section 5.1.1, only 8% of the recordings in the NGA-West2 data set are from normal-faulting earthquakes. The SWUS GMC project investigated if there were additional moderate to large magnitude normal-faulting earthquakes that could be added to the existing databases. Two events were identified: the 2008 Wells, Nevada earthquakes (**M**6) and the 2011 Fukushima-Hamadori, Japan earthquake (**M**6.7).

5.1.5.1 2008 Wells, Nevada Earthquake

The 2008 Wells, Nevada earthquake was located approximately 10 km northeast of the town of Wells, Nevada. This event had a moment magnitude of 6.0, a normal focal mechanism, and occurred on a previously unmapped fault (USGS, 2014). This Basin and Range earthquake is not part of the PEER NGA-West2 database. The ground motion and metadata from this earthquake were compiled and are summarized in Appendix I.

This earthquake occurred during the time in which the USArray was deployed in Arizona. There were 8 stations within 100 km of the epicenter (Figure 5.1.5-1), but the recordings at station M12A were clipped. For the seven sites with records that were not clipped, the V_{S30} values were inferred based on the surface geology from the USGS (2007) database and the correlation of V_{S30} and geology given by Wills and Clahan (2006). Table 5.1.5-1 shows the inferred V_{S30} values for the recording stations, as well as estimates of finite-fault distances (R_{JB}, R_{RUP} and R_X).

5.1.5.2 2011 Fukushima-Hamadori, Japan Earthquake

The Fukushima-Hamadori event is a crustal normal-faulting earthquake with **M**6.7, which occurred in eastern Tohoku, Japan, on 11 April 2011 and was apparently triggered by the 11 March 2011 Tohoku (**M**9.0) earthquake. A total of 598 records from K-net and KIK-net stations within 800 km from the epicenters were collected by PEER and processed following the same procedures as the NGA-West2 database. The flatfile containing the 5%-damped PSA values is available at: http://peer.berkeley.edu/ngawest2/wp-content/uploads/2010/09/Fukushima_Flatfile_RotD50_d050_04112014.zip

The Fukushima-Hamadori earthquake consisted of a complex rupture involving several faults. According to Shiba and Noguchi (2012) and Tanaka et al. (2014), the source was comprised of two rupture planes (the Itozawa fault and the Yunodake fault, see Figure 5.1.5-2). In Tanaka et al. (2014), the source parameters for the two rupture planes were derived using kinematic waveform inversion from observed data, and the total seismic moment is partitioned approximately equally between the two faults.

5.1.6 Additional Data for Hanging Wall Effects for Moderate Magnitudes

As noted in Workshop #1 (appendix E), the HW scaling in the NGA-West2 models is not well constrained for magnitudes less than 6.5. In general, there is a need for more empirical data to constrain the HW scaling for moderate magnitude earthquakes (**M**5–**M**6) in the GMPEs, and also to compare the HW scaling between the GMPEs and the scaling that comes out of finite-fault simulations. Following the recommendation from SWUS Workshop #1, recent Japanese data collected by Dawood et al. (2014) were reviewed by Dr. Di Alessandro to determine if there were ground-motion recordings that could be used to constrain the HW scaling for earthquakes in the **M**5 to **M**6 range.

The Dawood et al. (2014) data set contains 65 crustal earthquakes in the **M**5 to **M**6.2 range. To provide useful constraints on the HW scaling, multiple recordings at short distances (R_{JB} < 5km) on both the HW side and the FW side of the rupture are required. None of the 65 events had two or more recordings at short distances on both the HW and footwall (FW) sides of the rupture. Therefore, the Japanese earthquakes were deemed not to provide additional cases for empirically constraining the HW scaling for **M**5 to **M**6 earthquakes. Instead, numerical simulations, described in Section 5.2, are used to evaluate the magnitude dependence of the HW scaling for moderate magnitude earthquakes.

5.1.7 Kappa for the Arizona Sites

Previous region-specific estimates of kappa for rock sites in Arizona were not available. Because kappa can vary from region to region and kappa can have a large effect on the high-frequency ground motions, the SWUS GMC project sponsored PEER to estimate kappa for rock sites in Arizona.

The small magnitude local Arizona events were used to estimate kappa. The subset of data used for kappa consists of twelve earthquakes with hypocenter locations in Arizona (called the PEER-AZ_{KAPPA} subset). The hypocenter locations were provided by Jeri Young of the Arizona Earthquake Information Center (2013, personal communication). The events range in magnitude between 1.2 and 3.4, and were recorded by stations located at epicentral distances between 9 and 300 km. Eleven out of the twelve events occurred in three distinct clusters. Table 5.1.2-2 shows the number of recordings, the magnitude and distance ranges, and the V_{S30} range for the small magnitude subset. Figure 5.1.7-1 shows the attributes of the PEER-AZ_{KAPPA} dataset.

The zero-distance kappa (κ_0) values for the recording sites in the PVNGS region were estimated using three different methods: (1) the acceleration spectrum approach (Anderson and Hough, 1984); (2) the displacement spectrum approach (Biasi and Smith, 2001); and (3) the broadband approach (EPRI, 1993, and Silva et al., 1997). Following the nomenclature proposed by Ktenidou et al. (2014), the kappa values estimated using these three methods are called κ_{AS}, κ_{DS}, and $\kappa_{BB,}$ respectively. The details of the kappa evaluation are given in Kishida et al. (2014a). A summary of the kappa study is given below.

All of the recordings are from broadband velocity instruments with a sampling rate of 40 samples/sec and a Nyquist frequency of 20 Hz. The high-frequency limit is about 16 Hz. The limited high-frequency bandwidth for the USArray data severely limits the resolving power for κ.

Estimates of site kappa values are sensitive to the assessment of site amplification. If the evaluation does not account for the site amplification (e.g. amplification is set equal to unity), then the estimates of κ_0 can be reduced by about 35%. In Kishida et al. (2014a) site amplification is included for all of the kappa estimation methods.

Using a range of frequency-dependent Q models, the κ_{BB} method led to a mean κ_0 of 33 msec with a plus-minus one standard deviation range of 20-54 msec. Using a frequency-independent Q, the estimated κ_0 from the broadband method is 24 msec. The κ_0 for the frequency-independent Q assumption falls in the lower end of the range of κ_0 values from the κ_{AS} and κ_{BB} methods. Using method 1, κ_0 was estimated to be 33±14 msec. The κ_{DS} method for very small earthquakes led to a κ_0 of 50 msec. Because the κ_{DS} method tends to systematically larger kappa values than the κ_{AS} method, this 50 msec value is considered to be biased above the best estimate of the kappa term.

5.2 Finite-Fault Simulation Database for Median

A data base of ground motions from finite-fault simulations was developed using multiple simulation methods implemented on the SCEC Broadband Platform (BBP) as described in Maechling et al., (2015). The scenarios for simulations were selected to address four issues: magnitude and distance scaling of

near-fault ground motions, rules for estimating ground motions from complex ruptures, rules for estimating ground motions from splay ruptures, and magnitude scaling for HW effects for moderate magnitudes (**M**5 to **M**6). The simulation validation process, the construction of simulation scenarios, and the simulations processing for the projects objectives are described in detail in Appendix J.

5.2.1 Finite-Fault Simulations Methods

The SCEC BBP version 13.6 (Maechling et al., 2015) has implemented five different broadband, finite-source simulation methods: CSM composite source model (Zeng et al., 1994); UCSB method (Liu et al., 2006; Schmedes et al., 2010; and Schmedes et al., 2012); EXSIM (Motozedian and Atkinson, 2005; and Boore 2009); GP (Graves and Pitarka, 2010); and SDSU (Mai et al., 2010, and Mena et al., 2010). The five methods were subjected to a validation exercise and were evaluated by a SCEC BBP review panel (Dreger et al., 2013) for suitability for engineering applications for the median pseudo spectral acceleration (PSA). The peer review was documented in Dreger et al. (2013) (see Attachment B, also available at http://scec.usc.edu/scecpedia/SCEC_BBP_Phase_1_Evaluation), and in Dreger et al. (2015).

There were two parts to the validation: Part A included comparisons between the simulated and observed PSA for past earthquakes and Part B included comparisons between the simulated PSA and those computed using the NGA-West1 GMPEs for magnitudes and distances for which the GMPEs are reasonably well constrained by empirical data. During the validation, the authors of the methods made modifications to the methods to improve the comparisons for Part A and Part B.

Three methods passed the SCEC BBP review panel as described in Appendix J, Section J.1.1. The three selected methods are EXSIM, GP, and SDSU, and the modified forms are described in Atkinson and Assatourians (2015), Graves and Pitarka (2015) and Olsen and Takedatsu (2015), respectively. EXSIM is a purely stochastic approach utilizing a band-limited white-noise model. GP and SDSU are hybrid approaches that use stochastic motions for frequencies greater than 1 Hz, and deterministic motions for frequencies less than 1 Hz.

The results of the validation indicates that three methods are suitable for the simulation of PSA in the 0.01 to 3 seconds range, for the distance range between 0 to 200 km, and magnitudes from 5.5 to 7.2 (the range of validation event magnitudes including validation against GMPE). The panel noted that, for periods above 1 second, there is increased bias relative to recordings, and, above 3 seconds period, there are significant deviations from GMPEs. The panel concluded that further analysis will be required to understand the source of this additional bias. The review panel concluded that these three methods are also useable for evaluating relative ground-motions effects such as directivity, the effects of faulting geometrical complexity including splay and complex rupture scenarios, and for evaluating HW effects up to **M**8.

Based on the SCEC validation exercise, the TI team judged that the three finite-fault simulation methods that passed the SCEC validation represent technically defensible interpretations of ground motions that should be included in the evaluation of the near-fault ground motions for DCPP. These validation tests included the comparison of simulated and observed motions over a wide magnitude, distance and frequency range, the assessment of distance attenuation behavior, as well as verification of consistency with GMPE derived from much more extensive ground-motion data sets. Based on the positive results of these tests and published technical documentation of the methods, the TI Team judged that the simulation methods may be used to examine the magnitude and distance scaling of near-fault ground motions, the rules for estimating ground motions from complex ruptures, the rules for estimating ground motions from splay ruptures, and the magnitude scaling for HW effects for moderate magnitudes (**M**5 to **M**6).

5.2.1.1 Comparison of Fault Slip and Long Period Ground Motions

At SWUS Workshop #2 (Appendix F), one of the participants commented that long-period motions at sites close to the fault are most sensitive to nearby slip on the fault, and that if ground motions are simply scaled in terms of magnitude, rather than local slip, that this may oversimplify the problem. To examine this, simulated long-period transient motions, static displacement, and spectral displacement (SD) were compared to the fault slip in the source realizations. For this analysis, the GP simulations for the 1992 Landers earthquake (one of the validation earthquakes described in Dreger et al., 2013) at the two closest recording sites were used: Lucerne (LCN) and Joshua Tree (JOS).

The near-fault long-period ground motions (peak displacement, peak static, and spectral displacement) were compared to a suite of parameters: nearest surface slip, the geometric mean of the maximum radiation pattern weighted fault-parallel (FP) and fault-normal (FN) slip, and the geometric mean of the FP and FN radiation pattern weighted slip. It was found that the nearest surface slip alone (without radiation pattern weights) did not correlate well with the long-period ground-motion parameters, which is not surprising because there can be large contributions to the ground motions from nearby shallow regions of the fault. The aerial extent of the fault expected to contribute significantly to the FP and FN motions was studied via radiation pattern sensitivity. This sensitivity study showed that if radiation pattern weights are applied, then the weighted nearby slip is correlated with the long period ground motions.

Given that the nearby slip (with radiation pattern weighting) is important for determining the long period ground motion, the question then is whether the simulation procedure using multiple source realizations captures the possible variation of the nearby slip. To address this question, the geometric mean of the two horizontal components of SD for the 50 random source simulations at stations LCN and JOS were compared to the NGA-West2 GMPE relationships for SD. Figure 5.2.1-1 provides a comparison of the SD from the suite of simulations, the observed SD, and the SD from the GMPEs for station LCN.

The results of this evaluation show that the average and range of the SD values from the long-period simulations from the 50 finite-source slip realizations are consistent with the observed SD and the GMPE SD values.

More details and plots on this topic are available in Appendix J, section J.6.2.

5.2.2 1-D Velocity Structure for Simulations

The SCEC BBP currently implements 1D velocity models to compute Green's functions. There are two models that are being used, one based on average southern California structure and the other for northern California. Note that EXSIM does not explicitly use a velocity model to compute Green's functions and so is unaffected by the 1D approximation as currently implemented. Both GP and SDSU use deterministic Green's functions for periods longer than 1 second. For periods shorter than 1 second, both models use stochastic formulations that are not affected by the 1D model approximation.

5.2.2.1 Potential for Missing 3-D Effects

To examine the suitability of the BBP northern California velocity model for use in DCPP ground-motion simulations, broadband three-component waveforms with frequency-wavenumber synthetics were compared for a **M**4.7 San Simeon aftershock using four alternative S-wave velocity models, compared in Figure 5.2.2-1. The red curve is the velocity model used by the BBP, the two gray models have been proposed for the Central Coast Ranges (Walter and Mooney, 1982; McLaren and Savage, 2001), and the black curve, model GIL7 (defined in Stidham et al., 1999), was developed through broadband waveform modeling and is currently used by the Berkeley Seismological Laboratory (BSL) to routinely estimate seismic moment tensors in northern California (Pasyanos et al., 1996). The Walter and Mooney (1982) and McLaren and Savage (2001) models are P-wave models and a Poisson's ratio of 0.25 was assumed to scale S-wave velocities from the reported P-wave velocities. A density structure similar to the GIL7 model was also assumed in order to compute synthetic ground motions using a frequency-wavenumber approach. As Figure 5.2.2-1 shows, the BBP northern California model is similar to the other three central coast models in terms of: 1) the thickness of the crust, 2) the depth of a mid-crustal discontinuity (although there is variation in the size of the discontinuity), and 3) the presence of a pronounced velocity gradient in the shallow crust (less than 5 km depth).

In Figure 5.2.2-2, broadband synthetics (frequencies from 0 to 25 Hz) are compared with the observations recorded at the BSL PKD site, located 56.5 km from the earthquake. The strike, rake, dip, scalar seismic moment and source depth parameters (286°, 93°, 62°, 1.33e+23 dyne cm, 5.5 km) from the Berkeley Moment Tensor Catalog (http://ncedc.org) were assumed. The frequency-wavenumber Green's functions were convolved with a Brune (1970, 1971) source time function with a rise time of 0.3 seconds, which is appropriate for the **M**4.7 earthquake. The top row shows the transverse, radial and

vertical component data in black, and the GIL7 velocity model (e.g. Pasyanos et al., 1996). The other four rows compare synthetic seismograms for the four 1D models. On balance, the simulated waveforms based on the BBP northern California profile agree with the key features of the observed waveforms at least as well as those based on alternative available 1D models, and qualitatively fits the data in terms of the long-period P-wave on the radial and vertical components, the Love wave dispersion on the transverse component, and the Rayleigh wave dispersion on the radial and vertical components.

In Figure 5.2.2-3 the same data and synthetics are compared for frequencies less than 1 Hz, which is the passband where the GP and SDSU methods are using deterministic Green's functions to simulate PSA. At these frequencies the waveforms are essentially a point-source response for a **M**4.7 event, and as the figure shows, there is good agreement between the synthetic based on the BBP northern velocity model and the observations in terms of the waveform characteristics (phasing and duration). Based on the comparisons of the BBP 1D velocity model with others proposed for the region, and the test comparing point-source simulations with the broadband records for the **M**4.7 event, the TI Team judged that the use of the 1D velocity model simulation results for the ground-motion objectives of the project is justified.

5.2.3 Scenarios for Forward Simulations

Based on the findings of the SCEC BBP review panel, three methods (the stochastic EXSIM, and the hybrid GP and SDSU methods) were utilized for determining numerical, finite-fault median PSA for the four topics listed in Section 5.2. The following describes the setup and parameterization of the various rupture scenarios that were used.

5.2.3.1 Magnitude-Area Relations for Simulations

An issue for the simulations is defining the appropriate magnitude for a given rupture area and the down-dip width of the rupture. The GMC and SSC TI Teams discussed how to best define the scenarios for the simulations. The SSC models provide both the magnitude and rupture dimensions (length and width), but the BBP validation scenarios used rupture dimensions consistent with the Leonard (2010) scaling relations. As a result, the SSC scenarios are not always consistent with the magnitude scaling relations used in developing, testing, and validating the simulation methods.

The scaling relations for scenarios used in the forward application of the BBP should be consistent with the scaling relations used in the BBP validation. Therefore, the GMC TI Team defined the scenarios for the forward applications of the BBP to use magnitudes consistent with the range of magnitudes from the SSC model but with lengths and widths of the ruptures set to be consistent with the Leonard (2010) scaling relationships. In this way, the simulations are applicable to a given magnitude and distance. This

is similar to how GMPEs are applied: they are defined for a given magnitude and distance, not a specific rupture length and width.

The basic sets of relations from Leonard (2010) are:

$$M = \log_{10}(A) + 4 \qquad \text{(Eq. 5.2.3-1)}$$

$$W = C * L^{2/3} \qquad \text{(Eq. 5.2.3-2)}$$

where **M** = moment magnitude

A = rupture area in km^2 = L*W

L = fault length in km

W = down-dip fault width in km

C = empirically derived constant;

C = 1.75 for dip-slip faults

C = 1.5 for strike-slip faults up to **M** = 7.1,

for **M** > 7.1 fix W = 22km and use L = A/W to get length

Equation (5.2.3-1) is satisfied in all of the simulation cases. For all scenarios, the rupture width is computed using equation (5.2.3-2) except that, for strike-slip faults, the width saturates at 22km (this only applies to scenarios with **M** > 7.1).

For complex rupture scenarios which combine reverse and strike-slip segments, the magnitude-area scaling relations for strike-slip faults were assumed to apply to both the reverse and strike-slip segments.

5.2.3.2 Magnitude and Distance Scaling of Near-Fault Ground Motions

The ground motions for a suite of planar ruptures were simulated to constrain the magnitude and distance scaling of near-fault ground motions. Both reverse and strike-slip planar scenarios (different magnitude, dip, and Z_{TOR} cases) were computed on the SCEC Broadband Platform using each of the three methods that passed the SCEC validation exercise: GP, SDSU, and EXSIM. The simulated data are used as an alternative dataset in the model weighting scheme described in Section 6.4.5, analogous to the use of the empirical dataset described in Section 5.1.

Figure 5.2.3-1 shows the magnitude-distance distribution of the simulations used to evaluate the ground-motion models for DCPP for both the reverse and strike-slip scenarios.

For the strike-slip cases, four simple planar ruptures were defined: magnitudes 5.5, 6.0, 6.6, and 7.2; vertical fault dip; and Z_{TOR} between 0 and 14 km. For each scenario, there are 32 realizations of the hypocenters and slip models. For each realization, the ground motions are computed at 182 stations.

For reverse faulting scenarios, 35 simple planar ruptures were defined: magnitudes of 5.5, 6.0 and 6.5; depths to the top of the rupture (Z_{TOR}) of 2.5, 7.0, and 12.0 km; and fault dips of 10, 20, 30, 45, and 60 degrees. Not all of the combinations were implemented. The reverse rupture scenarios are listed in Table 5.2.3-1. For each scenario, there are 32 realizations of the hypocenters and slip models. For each realization, the ground motions are computed at 182 stations. Figure 5.2.3-2 shows the station layout with respect to the **M**5.5, **M**6.0, and **M**6.5 scenarios with a dip of 45 degrees.

5.2.3.3 Hanging-Wall Effects for Moderate Magnitudes (M5 to M6)

Donahue and Abrahamson (2014) used broadband finite-source simulations to develop a HW functional form. This form was then applied to implement HW terms in the ASK14 (Abrahamson et al., 2014) and CB14 (Campbell and Bozorgnia, 2014) GMPEs. The other NGA-West2 GMPE relationships (CY14: Chiou and Youngs, 2014) utilized HW terms informed from broadband simulations. These studies utilized simulations for **M** ≥ 6.5 and the limited data to constrain the HW terms. ASK14 and CB14 applied magnitude tapers, which produce HW effects for **M** ≥ 6.0, but the tapers reduced the HW terms to zero for **M** < 6.0.

The simulations for reverse earthquakes described in Section 5.2.3.2 and listed in Table 5.2.3 -1 are used for: 1) comparison with HW scaling in the published GMPEs to assess the applicability of the moderate magnitude tapers, and 2) to test a SWUS HW factor model developed by this project to be applied to the Common Functional Form median motion GMPE (Section 6.3).

Comparison of HW terms from proponent GMPEs with simulated data are presented and discussed in Appendix J.5.2.

5.2.3.4 Complex Ruptures Scaling

Working with the Diablo Canyon Seismic Source Characterization (SSC) project, two representative complex rupture scenarios were developed. Each complex rupture scenario consists of a combined rupture of two separate planar faults; Hosgri-Los Osos, and Shoreline-San Luis Bay. A schematic sketch for the two complex scenarios and the associated detailed parameters used to define the scenarios are provided in Figures 5.2.3-3 and 5.2.3-4, and listed in Tables 5.2.3-2, and 5.2.3-3, respectively.

The first scenario (Scenario 1) is representative of the Hosgri – Los Osos fault geometry. It involves two segments: one is strike-slip and the other is reverse. The site for which the TI Team wants to characterize the ground-motion scaling is closer to the reverse segment, on the HW side.

The second scenario (Scenario 2) is representative of the Shoreline – San Luis Bay fault geometry. It involves two segments: one is strike-slip and the other is reverse. The site for which the TI Team wants to characterize the ground-motion scaling is closer to the strike-slip segment.

Each scenario has three magnitude cases from which the dimensions were derived: **M** = 7.0, 7.2, and 7.4. To address the inconsistencies in the rupture lengths used for the simulations compared to the SSC lengths, the endpoint of the rupture closest to the DCPP site was fixed to the SSC point and the other end of the rupture was adjusted to yield the rupture length consistent with the Leonard (2010) scaling. This approach maintains the geometry of the rupture closest to the DCPP site.

5.2.3.5 Splay Ruptures Scaling

The terminology used to describe the splay ruptures is shown in Figure 5.2.3-5. Each scenario consists of a combined rupture of two separate planar faults (termed the primary and secondary segments), for which the TI Team has performed simulations. Working with the SSC project, two representative splay rupture scenarios were developed: one representative of the Hosgri fault primary strike-slip rupture with the Shoreline fault strike-slip secondary rupture (Figure 5.2.3-6); and one representative of the Los Osos fault primary reverse rupture with the San Luis Bay fault secondary reverse rupture in which they meet at depth Figure 5.2.3-7).

Details on how the geometries and fault parameters for the splay scenarios were defined are provided in Appendix J. In general, the scenarios are consistent with the Leonard (2010) scaling relationships.

Each scenario has three magnitude cases (on the primary segments) from which the dimensions were derived: **M** = 7.0, 7.2, and 7.4. The magnitudes for the secondary segments were determined using the process outlined in Appendix J, section J.2. The detailed parameters used to define the scenarios are listed in Tables 5.2.3-4 and 5.2.3-5.

5.3 Data Subsets for the Median Ground Motion

The subsets of the four primary empirical sets and the finite-fault simulations used for the evaluation of the median ground motion are summarized in Table 5.1-2. There are six subsets used for the median. These subsets are shown in this section for DCPP and PVNGS.

5.3.1 Subsets for DCPP Median

For DCPP, the hazard deaggregation from previous study (Section 4.1.4) showed that the important contributors to the hazard are strike-slip and reverse sources in the magnitude range **M**5.5 to **M**7.5 at rupture distances ranging from 0 to 15 km. As shown in Table 5.1-2, two datasets are developed for the evaluation of the DCPP median ground motion: one based on the NGA-West2 data (called NGA-$W2_{DC\text{-}MED}$) and one based on the finite-fault simulations (called $SIM_{DC\text{-}MED}$).

For the selection of the empirical dataset, the range of magnitudes and distances was expanded beyond the range of controlling sources from the deaggregation to maintain a large enough data set for the evaluation. The NGA-$W2_{DC\text{-}MED}$ dataset consists of strike-slip earthquakes and reverse/reverse-oblique earthquakes with **M** ≥ 5, with recordings at distances of -70km ≤ R_x ≤70 km, and with V_{S30} ≥ 250 m/s. Recordings with potentially strong HW effects are excluded because the HW effects are treated separately (Section 6.3). These sites with potentially large HW effects are sites with the following conditions: $R_x > 0$, $R_{JB} < 10$ km, and dip < 80 degrees. The V_{S30} lower limit was applied to avoid large amplitude scaling of motions that may have been affected by highly non-linear site response, which may be less well modeled by the simple V_{S30} scaling relationships in the empirical GMPEs.

Although the event terms can be estimated for earthquakes with just one recording using random effects, the subset was also restricted to earthquakes with at least 3 recordings to remove events with poorly constrained event terms. The minimum of 3 recordings per event was selected based on the sampling of recordings per earthquake of the original NGA-West2 data set shown in Figure 5.1.1-1 and the Akkar et al. data set shown in Figure 5.1.3-1. (Both data sets are considered to lead to a consistent minimum number of recordings per earthquake for both subsets.) The NGA-West2 data for **M** > 5, R_X < 70 km, and V_{S30} > 250 m/s have about 200 earthquakes with at least one recording, 110 earthquakes with at least three recordings, and 95 earthquakes with at least 5 recordings. The Akkar et al. data for **M** > 5, R_X < 70 km, and V_{S30} > 250 m/s have about 110 earthquakes with at least one recording, 45 earthquakes with at least three recordings, and 25 earthquakes with at least 5 recordings. Using a minimum of 5 recording per earthquake would leave too small of a subset for the Akkar et al dataset.

The NGA-$W2_{DC\text{-}MED}$ data set is for **M** > 5, R < 70 km, and V_{S30} > 250 m/s with a minimum of 3 recordings per earthquake. The attributes of the NGA-$W2_{DC\text{-}MED}$, are shown in Figure 5.3.1-1.

For the NGA-$W2_{DC\text{-}MED}$ subset, the pseudo-spectral acceleration (PSA) values are adjusted to 760 m/s using the V_{S30} scaling in the ASK14 model. The ASK14 scaling was selected because the NGA-West2 data subset was based on the ASK14 subset (Section 5.1.1). Therefore, the TI Team judged that the ASK14 V_{S30} scaling should be used to be most consistent with the selected subset.

The finite-fault simulation data set, $SIM_{DC\text{-}MED}$, consists of simulations from strike-slip earthquakes (**M**5.5 to **M**7.2) and reverse-slip earthquakes (**M**5.5 to **M**6.5) described in Section 5.2.3.2. For the strike-slip

simulations, the ground motions for stations at distances up to 70 km were simulated (see Figure 5.2.3-1). For the reverse simulations, the subset of simulated ground motions at stations located on the footwall at distances up to 20 km were selected. The simulations were computed for V_{S30} = 863 m/s. Based on the NGA-West2 GMPEs, the difference between V_{S30} of 760 m/s and 863 m/s leads to a difference in PSA between 5% and 14% depending on period. Given this difference, the TI Team judged that the simulations could be used for comparison with the ground motions for the reference V_{S30} of 760 m/s without correction. The magnitude and distance ranges of the simulations were shown in Figure 5.2.3-1. The DCPP datasets for the median are used to evaluate the weights for the alternative common-form GMPEs (Section 8.4.2).

5.3.2 Subsets for PVNGS Median for Greater Arizona Sources

The hazard deaggregation from previous studies in Section 4.2.3 showed that the high-frequency hazard at PVNGS is mainly controlled by normal fault sources within 70 km of the site and with 5 < **M** < 7, whereas the low-frequency hazard has significant contributions from both the local normal-faulting sources and from the distant California and Mexico sources. This section only addresses the subsets for the evaluation of the median ground motion for the Greater Arizona sources. The subsets for the California and Mexico sources are addressed in Section 5.3.3.

Two subsets are used for the median ground motion from the Greater Arizona sources: one based on the NGA-West2 database (called NGA-$W2_{PV\text{-}MED}$) and one based on the European data set used to derive the Akkar et al (2014a and 2014b) model (called $EUR_{PV\text{-}MED}$).

The NGA-$W2_{PV\text{-}MED}$ dataset consists of recordings from strike-slip and normal/normal-oblique earthquakes for **M** ≥ 5, -70km ≤ R_x ≤70 km, and V_{S30} ≥ 250 m/s. Using both the positive and negative R_X values includes both FW and HW sites. Unlike the DCPP subset described in Section 5.3.1, sites with potentially large HW effects are not removed from this subset. As explained in Section 6.3, HW effects are included as part of the PVNGS base model ground-motion characterization so the HW sites are maintained in the subset. The subset was also restricted to earthquakes with at least 3 recordings to remove events with poorly constrained event terms. The minimum of 3 recordings per event was selected based on the sampling of the original data set: using a higher threshold would remove too many of the earthquakes. The attributes of the NGA-$W2_{PV\text{-}MED}$ dataset are shown in Figure 5.3.2-1.

The $EUR_{PV\text{-}MED}$ dataset consists of recordings from strike-slip and normal/normal-oblique earthquakes for the same magnitude and distance range as used for the NGA-$W2_{PV\text{-}MED}$ dataset: **M** ≥ 5, -70km ≤ R_x ≤70 km, and V_{S30} ≥ 250 m/s. Again, the subset was also restricted to earthquakes with at least 3 recordings to remove events with poorly constrained event terms. The minimum of 3 recordings per event was selected based on the sampling of the original data set: using a higher threshold would remove too many of the earthquakes. The attributes of the $EUR_{PV\text{-}MED}$ dataset are shown in Figure 5.3.2-2.

As done for the DCPP (Section 5.3.1), the PSA values from these recordings were adjusted to the reference V_{S30} of 760 m/s. For the NGA-W2$_{PV\text{-}MED}$ dataset, the V_{S30} scaling from the ASK14 model is used to make the adjustment as discussed in Section 5.3.1. For the EUR$_{PV\text{-}MED}$ dataset, the V_{S30} scaling from ASB14 is used because this scaling was derived from the Akkar et al. data set.

5.3.3 Subsets for PVNGS Median for Earthquakes in Regions 1, 2, and 3

The distant California and Mexico events subset consists of 14 earthquakes previously included in the NGA-West2 database. Because this subset was used to compute path terms, they are called the PEER-AZ$_{PATH}$ subset. The events have magnitudes that range between **M** 4.26 and 7.2, and are recorded by stations at R_{JB} distances between 150 and 650 km.

As previously shown in Figure 5.1.2-1, all of the earthquakes had a minimum of 3 recordings and almost all had a minimum of 5 recordings. The number of recordings per event starts to drop off above 5. For evaluating the path effects, the data set was restricted to sites with at least 5 recording per site. The attributes of the PEER-AZ$_{PATH}$ dataset are shown in Figure 5.3.3-1. These data are used for the evaluation of the median path effects for PVNGS from sources in Regions 1, 2, and 3.

5.3.4 Subset for HW Scaling Evaluations

As part of the median ground-motion model, the TI Team developed a suite of HW scaling models as described in Section 6.3. As noted in Section 6.3, the magnitudes scaling of the HW factor for moderate magnitudes (**M**5.0 to **M**6) is not well constrained by the empirical data. A subset of the finite-fault simulations was selected to provide information that can be used to evaluate the magnitude scaling for the HW factor. This dataset, called SIM$_{HW\text{-}MED}$, consists of ground motions from reverse earthquakes with magnitude **M**5.5 to **M**6.5, and dips of 10 to 60 degrees with Z_{TOR} of 2.5 to 12 km, described in Section 5.2.3.3. This data set is used for the evaluation of the magnitude scaling of the HW model which is applied to both the DCPP and PVNGS common-form models.

5.4 Data Sets for the ϕ_{SS} and $\phi_{SP\text{-}R}$ Models

There are four types of the single-station sigma (ϕ_{SS}) models that are developed in Sections 7.3 and 7.4: (1) a short-distance global model based on European data, (2) a short-distance global model based on NGA-West2 and Lin et al. (2011) data, (3) a long-distance global model based on NGA-West2 data, and (4) two short-distance models based on California data in the NGA-West2 database. The data sets used to develop each of the single-station sigma models are described in Sections 5.4.1 to 5.4.4.

For the subsets used for ϕ_{SS}, only the data with a minimum of three recordings per earthquake and three recordings per site were selected. To have enough data with three recordings per site and to increase the reliability of estimated site terms, the site terms and single-site within-event residuals were computed using the entire datasets (all magnitudes and distances). Once the site terms were removed, then the subset was restricted to the larger magnitudes and distances that matter the most to the hazard, as indicated from the deaggregation results (Section 4.1.4 and 4.2.3). The ϕ_{SS} was then computed using this subset of single-site within-event residuals in the magnitude and distance range of interest.

Datasets are also used for the development of the single-path-to-region ϕ (ϕ_{SP-R}) models. These datasets are described in Section 5.4.5.

5.4.1 Subset for the Short-Distance ϕ_{SS} Model based on Global Data

The global data set is a combination of the NGA-West2 data and the Lin et al (2011) data. The within-event residuals for Taiwan (Lin et al., 2011) were combined with the NGA-West2 residuals after removing residuals from common recordings from Taiwan earthquakes included in both the NGA-West2 data set and the Lin et al dataset. The NGA-West2 developers used different subsets of the NGA-West2 as shown in Table 5.4.1-1. The Idriss 2014 (Id14) residuals are not used for the ϕ_{SS} evaluation because Idriss did not separate his residuals into between-event and within-event terms. A subset is developed for each of the four NGA-West2 GMPEs that separated the within-event and between-event residuals. The magnitude-distance distributions of the four datasets ($GLOBAL_{PHISS\text{-}ASK14}$, $GLOBAL_{PHISS\text{-}BSSA14}$, $GLOBAL_{PHISS\text{-}CY14}$, and $GLOBAL_{PHISS\text{-}CB14}$) are shown in Figures 5.4.1-1, 5.4.1-2, 5.4.1-3, and 5.4.1-4.

To derive the short-distance ϕ_{SS} model, magnitude and distance selection criteria (**M** ≥ 5.0 and R_{JB} < 50 km) are applied. Also, the data is selected so that there are at least three recordings per earthquake and at least three recordings per site prior to the magnitude limit (e.g. all magnitudes are used to constrain the site term, but only a subset of the site corrected residuals with **M** ≥ 5 and $R_{JB} \leq 50$ km are used to compute the ϕ_{SS} values.

Table 5.4.1-1 presents a summary of the data distribution for the four NGA-West2 datasets for the short-distance ϕ_{SS}. Table 5.4.1-1 shows that the California dataset comprises about 30% to 40% of the recordings and 40 to 60% of the earthquakes in the global dataset, while the Taiwanese data represent 50% to 70% of the number of recordings and 25% to 40% of the number of earthquakes.

5.4.2 Subsets for the Short-Distance ϕ_{SS} Model based on European Data

A subset of the Akkar et al. (2014a and 2014b) data set was selected to be used in developing the single-station sigma models for application to PVNGS for the Greater Arizona sources. To be consistent with the selection used for the global data (Section 5.4.1), the same magnitude and distance selection criteria are applied: **M** ≥ 5.0 and R_{JB} < 50 km. The same minimum number of recordings per earthquake and per site are also applied: at least three recordings per earthquake and at least three recordings per site prior to the magnitude limit (e.g. all magnitudes are used to constrain the site term, but only a subset of the site corrected residuals with **M** ≥ 5 and R_{JB} ≤ 50 km are used to compute the ϕ_{SS} values). The magnitude-distance distribution of the dataset (EUR_{PHISS}) is shown in Figure 5.4.2-1.

This subset consists of 223 recordings from 73 earthquakes (35 normal, 25 strike-slip, and 13 reverse events) recorded at 79 stations. Ground-motion data at periods greater than 4.0 seconds are not available for the European dataset.

5.4.3 Subsets for the Short-Distance ϕ_{SS} Models based on California Data

The California data sets used for evaluating ϕ_{SS} are the NGA-West2 residuals dataset for events that have occurred in California and were recorded by a minimum of three stations. The constraint of restricting stations with minimum three recordings per site is also applied. The full range of magnitudes and distances are used to estimate the site terms, but only the **M** > 5 and R < 50 km data are used for estimating ϕ_{SS}. The California dataset in this magnitude and distance range of interest consists of 342 - 672 recordings from 38-54 earthquakes, depending on the subset used by the NGA-West2 developers (Table 5.4.1-1).

Because each developer used their own subsets of the NGA-West2 data set to develop their models and compute their residuals, there are different versions of the California data sets used to compute the ϕ_{SS}, one for each developer: NGA-$W2_{CA\text{-}PHISS\text{-}ASK14}$, NGA-$W2_{CA\text{-}PHISS\text{-}BSSA14}$, NGA-$W2_{CA\text{-}PHISS\text{-}CB14}$, and NGA-$W2_{CA\text{-}PHISS\text{-}CY14}$. As noted in Section 5.4.1, the Idriss 2014 (Id14) model is not used for the ϕ_{SS} evaluation because Idriss did not separate his residuals into between-event and within-event terms. A random-effects regression was not applied to the Idriss (2014) model to estimate the within-event residuals as this would also change the median regression and change the model.

The magnitude-distance distribution of the datasets is shown in Figures 5.4.3-1 to 5.4.3-4 for the four NGA-West2 subsets. These datasets are used to develop ϕ_{SS} models for application to DCPP.

5.4.4 Subsets for the Long-Distance ϕ_{SS} Models based on Global Data

As shown in Section 4.2.3, the distant earthquakes in California and Mexico contribute to the PVNGS hazard at long periods. The controlling distance from the deaggregation is 200-300 km from large magnitudes (**M** > 7.5). This controlling magnitude distance range is broadened to **M** ≥ 5.5, distance 200-400 km to allow for enough data points for the evaluation of the ϕ_{SS} model.

The global data with magnitude greater than or equal to **M**5.5 and distances of 200 to 400 km lacks Taiwanese data in that range of interest. Furthermore, CB14 used mixed-effects regression to derive the anelastic attenuation term from data with R_{RUP} > 80 km, but allowed the source terms to vary from those with a maximum R_{RUP} distance of 80 km. Therefore, the Taiwan and CB14 sets were excluded from the ϕ_{SS} analysis, so that only three sets of NGA-West2 residuals were used to develop the ϕ_{SS} model for PVNGS – Distant California and Mexico sources.

The global dataset in this magnitude and distance range of interest (**M** ≥ 5.5, distance 200-400 km) consists of 264-415 recordings from 4 to 23 earthquakes (mostly from Japan), depending on the GMPE developer (Table 5.4.4-1). The magnitude-distance distributions by region of the datasets used to derive the ϕ_{SS} model (NGA-$W2_{LD\text{-}PHISS\text{-}ASK14}$, NGA-$W2_{LD\text{-}PHISS\text{-}BSSA14}$, NGA-$W2_{LD\text{-}PHISS\text{-}CY14}$) are shown in Figures 5.4.4-1, 5.4.4-2, and 5.4.4-3 for the three datasets. The number of recordings and earthquakes per region in the dataset is summarized in Table 5.4.4-1, which shows that the dataset in the distance range of 200 to 400 km is relatively small, consisting primarily of a few California and Japanese earthquakes.

5.4.5 Subsets for the Long-Distance $\phi_{SP\text{-}R}$ Model

A subset of the Arizona dataset (Section 5.1.2) was compiled to derive the magnitude-independent ϕ_{SP-R} and path-adjustment models for PVNGS. This dataset consists of earthquakes in California and Mexico that have been recorded at the 9 stations in the vicinity of PVNGS. From this dataset, 49 records from 11 earthquakes with rupture distances that range from 200 to 500 km are used to compute ϕ_{SP-R} for three regions: Region 1 (4 earthquakes), Region 2 (3 earthquakes), and Region 3 (3 earthquakes). Figure 5.4.5-1 shows the magnitude-distance distribution of the data by region.

5.5 Proponent Models for Median Ground Motions

5.5.1 Candidate GMPEs for Shallow Crustal Earthquakes in Active Regions

The development of the median ground-motion models for the DCPP and PVNGS sites is based, in part, on the range of predicted ground motions produced by current GMPEs for shallow crustal earthquakes in active crustal regions (ACRs).

The literature was reviewed to identify recently developed and published GMPEs for shallow crustal earthquakes in ACRs. Table 5.5.1-1 lists the GMPEs that were identified. They represent ground-motions models developed from world-wide databases such as the PEER NGA projects and models developed for specific regions, such as the ACR portions of Europe, individual areas within Europe and the Middle East, Japan, and New Zealand.

5.5.1.1 TI Team Model to Accommodate Zhao and Lu (2011) Magnitude Scaling

In addition to the published GMPEs, Zhao and Lu (2011) published a concept for alternative magnitude scaling at large magnitudes. While Zhao and Lu (2011) don't provide a complete GMPE, the proposed magnitude scaling is evaluated.

Zhao and Lu (2011) fit ground-motion data from **M**7.1 to **M**7.9 shallow crustal earthquakes with a functional form that allowed for an event specific geometric spreading, an event specific anelastic attenuation, and an event specific intercept. They found that the event specific differences in geometric spreading were not statistically significant, and as a result their final fitted model has magnitude independent geometric spreading. They found statistically significant event specific values of anelastic attenuation for some earthquake groups (Wenchuan, China; the Middle East; Alaska), indicating regional differences in anelastic attenuation. They also found statistically significant differences in the intercept only for the Wenchuan earthquake.

Zhao and Lu (2011) plotted the average residual from their model for each earthquake versus magnitude. Figures 5.5.1-1 and 5.5.1-2 shows their results for PSA at periods from 0.5 to 5 sec. The red curve shows a linear fit to the average residual for each earthquake versus magnitude excluding the Duzce earthquake and the blue dashed line shows a fit including Duzce. The black long dash line is the magnitude scaling from Chiou and Youngs (2008) at a distance of 100 km. From results like these, Zhao and Lu (2011) conclude that there is little to no magnitude scaling above **M** ~7 at longer spectral periods. J. Zhao (2013, written communication) suggested that the hinge point is at **M**7.1.

Implementation of the Zhao and Lu (2011) concept in combination with the Zhao et al. (2006) GMPE suggests that magnitude scaling be capped at a specific magnitude. The results shown in Figures 5.5.1-1 and 5.5.1-2 suggest that this saturation magnitude may be ~ **M**7.3 to **M**7.4, given that the average

residual for both earthquakes less than **M**7.2 are lower than those for higher magnitudes where the scaling appears magnitude independent. In addition, the crustal earthquake data used by Zhao et al. (2006) was limited above **M**7, as shown on Figure 5.5.1-3, suggesting that the magnitude scaling at large **M** may not be well constrained for shallow crustal earthquakes in the Zhao et al. (2006) GMPE.

Therefore, the TI Team developed a new GMPE that implemented the Zhao and Lu (2011) modification to cap the Zhao et al. (2006) ground-motion estimates at **M**7.3, and use these results for all larger magnitudes. This implementation would be consistent with both Zhao et al. (2006) data, and the Zhao and Lu (2011) results for crustal data. Based on the fact that Zhao and Lu (2011) show essentially zero magnitude scaling at a distance of 100 km and show no trend in their residuals with distance up to about 200 km, this modification to the Zhao (2006) model would apply at all distances.

5.5.2 Selection of Candidate Models

The set of relevant existing GMPEs that were identified in Section 5.5.1 and are listed in Table 5.5.1-1 are evaluated by the TI Team in this section. A subset of candidate models was selected based on the following seven criteria:

1. More recent published GMPEs by the same development team were selected over older GMPEs on the basis that the newer models would have benefited from more data and refinements to the approach. Thus, for example, the PEER NGA-West2 models are selected and the PEER NGA-West1 models are not. In the case of the modified magnitude scaling suggested by Zhao and Lu (2011), the Zhao et al. (2006) GMPE is selected along with a modified form based on Zhao and Lu (2011). The basis is that Zhao and Lu have not developed a full GMPE to replace Zhao et al. (2006).

2. Models that represent an adjustment of another model to fit data from a specific region which is not California or western Arizona were not selected (e.g. Bradley, 2013). The basis for rejecting these models is that they have been adjusted from one region to another and should not be adjusted back to the original region or to a third region.

3. Models that do not extrapolate well beyond the magnitude-distance range over which they were developed were not selected. For example, models that have only a single linear magnitude scaling term were not selected, as evaluations by many investigators of data sets containing a large range in magnitude have shown that a single linear magnitude scaling term does not capture the magnitude scaling over the range of magnitudes from **M**5 to **M**8.

4. Models that do not clearly separate shallow crustal earthquakes from those occurring as a part of subduction were not selected. The basis for rejecting these models is that the magnitude and distance scaling from subduction zone earthquakes is different than from crustal earthquakes.

5. Models developed as research tools were not selected. The basis for rejecting these models is that they have not developed to the point where they could be used for engineering application.

6. Models developed for a relatively small specific region different from the ones of interest (e.g. Italy) were not selected. The basis for rejecting these models is that the data from a single region may be too limited to capture scaling for the full range of magnitude and distance of interest and the specifics of the regional behavior may be different from California and western Arizona.

7. Models that have not been peer reviewed or vetted by the larger scientific community were not selected. For example, the Graizer and Kalkan model was rejected because was only published as a conference paper (Graizer 2014) during the project.

Table 5.5.1-1 indicates which models were selected for use in characterization of median ground motions and the reason the other models were not selected.

5.5.3 Host Kappa Values for Selected Candidate Models at Reference V_{S30}

For PVNGS, the planned site response analysis accounts for differences in the kappa implied for the candidate GMPEs and the kappa for rock sites in central Arizona. The kappa implied by the spectral shape of the GMPEs is called the "Host" kappa.

Under the direction of the TI Team, Dr. Al-Atik estimated the host kappa values for the seven candidate GMPEs selected for PVNGS (Table 5.5.1-1) using the IRVT approach (Al Atik et al., 2013) for the following for a reference V_{S30} of 760 m/sec: Abrahamson et al. (2014) (ASK14), Boore et al. (2014) (BSSA14), Campbell and Bozorgnia (2014) (CB14), Chiou and Youngs (2014) (CY14), Bindi et al. (2014a, 2014b) (Bi14), Akkar et al. (2014a, 2014b) (ASB14), and Zhao et al. (2006) (ZH06).

Because the estimate of kappa depends on the spectral shape, which can change for different scenarios, the host kappa values were derived for nine normal-faulting scenarios with a dip angle of 50 degrees, with magnitude 5.0, 6.0, and 7.0 and R_X distances of 5, 10, and 20 km on the footwall. Footwall scenarios were used because the hanging-wall factors also affect the high-frequency spectral shape, and would lead to bias in the kappa estimate. These magnitude, distance, and style-of-faulting scenarios were selected because of their significant contribution to the hazard at PVNGS, at large enough distance so that there is adequate data to constraint the spectral shape, but not such at large distances that the effect of the anelastic attenuation (Q) would become a dominant effect.

GMPE response spectra-compatible Fourier Amplitude Spectrum (FAS) were derived using the IRVT approach for the nine scenarios considered and then divided by the host site amplification factors compatible with the western U.S. (WUS) V_S profile of Kamai et al. (2013) with a V_{S30} of 760 m/sec (shown in Appendix M, Figure M-1), which was used as a representative V_S profile for the host region. Kappa

was estimated by fitting the Anderson and Hough (1984) exponential kappa scaling function to the FAS between the start and end frequencies (f_1 and f_2) over which log(FAS) versus frequency is approximately linear. Details on the host kappa derivation approach are provided in Appendix M.

Figures 5.5.3-1 shows an example of the high-frequency kappa fit to the derived FAS for the ASK14 GMPE for the **M**6.0 and R_X 10 km scenario. More plots are available in Appendix M.

Best estimate host kappa values were computed by averaging the estimated kappa values for the nine scenarios for each GMPE (Table 5.5.3-1). The best kappa estimate kappa values for the seven GMPEs range between 0.037 and 0.045 seconds, with a geometric mean of 0.041 seconds.

5.6 Previous Proponent Single-station Sigma Models and Datasets

5.6.1 Introduction

Following discussions with the PTIs for PVNGS and DCPP, the TI Team decided to use the single-station sigma approach which is a partially non-ergodic approach (Rodriguez-Marek et al., 2014) that removes the systematic site response effects from the traditional ergodic within-event standard deviation. The single-station sigma, σ_{SS}, is given by

$$\sigma_{SS} = \sqrt{\phi_{SS}^2 + \tau^2} \qquad \text{(Eq. 5.6.1-1)}$$

where ϕ_{SS}^2 is the standard deviation of the site-corrected within-event residual and τ is the standard deviation of the event terms. The single-station sigma approach was selected because it avoids double counting of the epistemic uncertainty of the site response that can occur if the traditional ergodic sigma is used, and the site response also addresses the epistemic uncertainty.

To develop empirical estimates of ϕ_{SS} requires data sets with multiple recordings per site. With the greatly expanded empirical data sets that are now available, multiple studies of empirical data have shown that there are significant systematic differences in the ground-motion scaling for individual sites, individual ray paths, and individual source regions: Chen and Tsai (2002) used the recordings from Taiwan to evaluate the site terms; Atkinson (2006) used data from limited source regions in southern California to estimate the standard deviation for a single path and site; Morikawa et al. (2008) used data from limited source regions in Japan to estimate the standard deviation for a single path and site; Lin et al. (2011) used data from Taiwan to estimate the standard deviations of the site terms, path terms, and source terms separately. Most recently, Rodriguez-Marek et al. (2013) combined the data sets used in previous studies and added additional data to develop a comprehensive global data set for estimating the single-station sigma for application to the Pegasos Refinement Project (PRP; Renault et al., 2010).

This model is described in Section 5.6.2. Slight modification of the Rodriguez-Marek et al. (2013) model have been proposed for application to the Thyspunt Nuclear Siting Project (TNSP; Bommer et al., 2013) in South Africa (Rodriguez-Marek et al., 2014), and to the Hanford PSHA project (Coppersmith et al., 2014). The latter is addressed in section 5.6.3. Finally, a constant single-station sigma model using Italian data has been recently developed by Luzi et al. (2014) and is described in Section 5.6.4.

5.6.2 Composite Model by Rodriguez-Marek et al. (2013)

Rodriguez-Marek et al. (2013) compiled ground-motion data with multiple recording per site from five regions: California, Taiwan, Japan, Switzerland, and Turkey. The distribution of the data in terms of magnitude and distance for each region is shown in Figure 5.6.2-1. The average ϕ_{SS} values for **M** > 4.5 and R < 200 km for each region are shown in Figure 5.6.2-2. The lower plot shows the traditional ergodic ϕ values and the upper plot shows the partially non-ergodic ϕ_{SS} values. The ϕ_{SS} values are mainly between 0.4 and 0.5 ln units and are much more consistent across regions than the ϕ values. The Rodriguez-Marek et al. (2013) model used residuals from the Chiou et al. (2010) evaluation of California data, which had access to only three spectral periods.

Based on the global data set shown in Figure 5.6.2-1, Rodriguez-Marek et al. (2013) developed four single-station sigma models: a distance-dependent model, a magnitude-dependent model, a magnitude- and distance-dependent model, and a constant (magnitude- and distance-independent) model. Two of these four models are shown in Figure 5.6.2-3 (distance-dependent), and Figure 5.6.2-4 (magnitude- and distance- dependent). The constant model is shown in Figure 5.6.4-2 as compared to the Luzi et al. (2014) ϕ_{SS} models.

The distance dependence is only observed for the smaller magnitude data and may reflect factors that are not applicable to larger magnitude events. There are several possible reasons for the observed distance dependence for small magnitudes: sensitivity to the location errors, systematic focal mechanism effects, geometrical spreading for small magnitudes, and magnitude dependence of the saturation ("fictitious depth" term). Based on recent evaluations of small magnitudes at short distances, motivated by the induced-seismicity issues in the central U.S., the limitations of the GMPEs for small magnitudes at short distances has been apparent. In particular, the "fictitious depth" models developed for larger magnitudes are not applicable to smaller magnitudes when used with R_{RUP} distance-based GMPEs (Atkinson, 2015).

The TNPS single-station model is a minor update of the Rodriguez-Marek et al. (2013) model and is also based on the PRP data. For the TNPS project the distance-dependence of ϕ_{SS} was rejected, reflecting the limitations of the ϕ_{SS} for small magnitude earthquakes noted in the previous section.

5.6.3 The Hanford Model

The Hanford ϕ_{SS} model represents a slight modification of the Rodriguez-Marek et al. (2013) model and uses the same PRP data. The model is also magnitude-dependent and corresponds to the intra-event standard deviation (ϕ) by Abrahamson and Silva (2008; AS08) scaled by 0.8. The rationale for adopting this model was that the ϕ_{SS} values closely resembled the scaled AS08 model. The Hanford ϕ_{SS} model is shown in Figure 5.6.3-1.

5.6.4 Single-Station Sigma Model for Italy by Luzi et al. (2014)

Luzi et al. (2014) compiled ground motion data from Italy using three alternative datasets, whose distribution in terms of magnitude and distance for each dataset is shown in Figure 5.6.4-1. The first dataset (BIea) comprises the data used to derive the Bindi et al. (2011) GMPE for Italy and corresponds to a well-recorded subset of the Italian strong-motion database (Pacor et al., 2011) in the period 1972‑2009. The second dataset (BIea2) is an extension of BIea to include all records in the 4.0‑6.9 magnitude range recorded from 1972 to 2011. The third dataset (ABR) is a subset of the BIea2, composed of the records related to the 2009 L'Aquila sequence, (local magnitude 3.5‑5.8). The ABR dataset was used to evaluate the single-station sigma for one seismic source zone (single-path sigma).

Tabulated ϕ_{SS} results for the three datasets are provided in Luzi et al. (2014). Although the authors discuss the dependency of their results with magnitude, distance and site conditions, they propose a constant ϕ_{SS} model for Italy. The Luzi et al (2014) ϕ_{SS} models are compared to the PRP constant ϕ_{SS} model in Figure 5.6.4-2. The ϕ_{SS} values for the Italian data are in the same range of 0.4 to 0.5 as seen for other global data sets.

5.7 REFERENCES

Abrahamson, N.A., and Youngs, R.R. (1992). A stable algorithm for regression analysis using the random effect model, *Bull. Seism. Soc. Am*., Vol. 82, 505-510.

Abrahamson, N.A., and Silva, W. (2008). Summary of the Abrahamson & Silva NGA Ground-Motion Relations, *Earthquake Spectra*, Vol. 24(1), 67-97.

Abrahamson, N.A., Silva, W.J., and Kamai, R. (2014). Summary of the AKS14 Ground-Motion Relation for Active Crustal Regions, *Earthquake Spectra*, Vol. 30(3), 1025-1055, DOI: 10.1193/070913EQS198M.

Akkar, S. and Bommer, J.J. (2010). Empirical Equations for the Prediction of PGA, PGV, and Spectral Accelerations in Europe, the Mediterranean Region, and the Middle East, *Seism. Res. Letters*, Vol. 81, 195-206.

Akkar, S. and Çagnan, Z. (2010). A Local Ground-Motion Predictive Model for Turkey, and Its Comparison with Other Regional and Global Ground-Motion Models, *Bull. Seism. Soc. Am.*, Vol. 100(6), 2978-2995.

Akkar, S., Sandikkaya, M.A., and Bommer, J.J. (2014a). Empirical ground-motion models for point- and extended-source crustal earthquake scenarios in Europe and the Middle East, *Bull. Earthquake Eng*., Vol. 12(1), 359-387, DOI: 10.1007/s10518-013-9461-4.

Akkar, S., Sandikkaya, M.A., and Bommer, J.J. (2014b). Erratum to: Empirical ground-motion models for point- and extended-source crustal earthquake scenarios in Europe and the Middle East, *Bull. Earthquake Eng.*, Vol. 12(1), 389-390, DOI: 10.1007/s10518-013-9508-6.

Akkar S., Sandıkkaya M.A., Şenyurt M., Azari Sisi A., Ay B.Ö., Traversa P., Douglas J., Cotton F., Luzi L., Hernandez B., Godey S. (2014c). Reference database for seismic ground-motion in Europe (RESORCE), *Bull. Earthquake Eng.*, Vol.12(1), 311-339, DOI 10.1007/s10518-013-9506-8.

Al Atik, L. Kottke, A., Abrahamson, N.A, and Hollenback, J. (2013). Kappa (κ) Scaling of Ground-Motion Prediction Equations Using an Inverse Random Vibration Theory Approach, *Bull. Seismol. Soc. Am.* Vol. 14, 336-346. DOI: 10.1785/0120120200.

Ancheta, T.D., Darragh, R.B, Stewart, J.P., Seyhan, E., Silva, W.J, Chiou, B.S-J., Wooddell, K.E., Graves, R.W., Kottke, A.R., Boore, D.M., Kishida, T., and Donahue J.L. (2014). NGA-West 2 Database. *Earthquake Spectra,* Vol. 30(3), 989-1005, DOI: 10.1193/070913EQS197M.

Anderson, J.G., and Hough, S.E. (1984). A model for the shape of the Fourier amplitude spectrum of acceleration at high frequencies, *Bull. Seismol. Soc. Am.,* Vol. 74, 1969-1993.

Atkinson, G.M. (2006). Single-station sigma, *Bull. Seismol. Soc. Am*., Vol. 96, 446–455.

Atkinson, G.M, and Assatourians, K. (2015). Implementation and validation of EXSIM (a stochastic finite-fault ground-motion simulation algorithm) on the SCEC broadband platform, *Seismol. Res. Letts Letts*., Vol. 86(1), 48-60, DOI: 10.1785/0220140097.

Atkinson, G.M. (2015). Ground-Motion Prediction Equation for Small-to-Moderate Events at Short Hypocentral Distances, with Application to Induced-Seismicity Hazards, *Bull. Seismol. Soc. Am*., Vol. 105, DOI: 10.1785/0120140142.

Biasi, G.P., and Smith K.D. (2001). Site effects for seismic monitoring stations in the vicinity of Yucca Mountain, Nevada, *MOL20011204.0045*, a report prepared for the US DOE/University and Community College System of Nevada (UCCSN) Cooperative Agreement.

Bindi, D., Pacor, F., Luzi, L., Puglia, R., Massa, M., Ameri, G., and Paolucci, R. (2011). Ground motion prediction equations derived from the Italian strong motion database, *Bull. Earthquake Eng*., Vol. 9, 1899-1920.

Bindi D., Massa M., Luzi L., Ameri G., Pacor F., Puglia R., and Augliera, P. (2014a). Pan-European Ground-Motion Prediction Equations for the Average Horizontal Component of PGA, PGV, and 5%-Damped PSA at Spectral Periods up to 3.0 s using the RESORCE dataset, *Bull. Earthquake Eng*., Vol. 12, 391-430, DOI: 10.1007/s10518-013-9525-5.

Bindi D., Massa M., Luzi L., Ameri G., Pacor F., Puglia R., and Augliera, P. (2014b). Erratum to: Pan-European Ground-Motion Prediction Equations for the Average Horizontal Component of PGA, PGV, and 5%-Damped PSA at Spectral Periods up to 3.0 s using the RESORCE dataset, *Bull. Earthquake Eng*., Vol. 12, 432-448, DOI: 10.1007/s10518-014-9589-x.

Bommer, J. J., K. J. Coppersmith, R. T. Coppersmith, K. L. Hanson, A. Mangongolo, J. Neveling, E. M. Rathje, A. Rodriguez-Marek, F. Scherbaum, R. Shelembe, P. Stafford, and F. O. Strasser (2013). A SSHAC Level 3 probabilistic seismic hazard analysis for a new build nuclear site in South Africa, *Earthquake Spectra*, DOI 10.1193/060913EQS145M, *in press.*

Boore, D.M., and Atkinson, G.M. (2008). Ground-Motion Prediction Equations for the Average Horizontal Component of PGA, PGV, and 5%-Damped PSA at Spectral Periods between 0.01s and 10.0s, *Earthquake Spectra*, Vol. 24(1), 99-138.

Boore, D.M. (2009). Comparing stochastic point-source and finite-source ground-motion simulations: SMSIM and EXSIM, *Bull. Seism. Soc. Am.*, Vol. 99(6), 3202-3216.

Boore, D.M., Stewart, J.P., Seyhan, E., and Atkinson, G.M. (2014). NGA-West 2 Equations for Predicting PGA, PGV, and 5%-Damped PSA for Shallow Crustal Earthquakes, *Earthquake Spectra*, Vol. 30(3), 1057-1085, DOI: 10.1193/070113EQS184M.

Bora, S.S., Scherbaum, F., Kuehn, N., and Stafford, P. (2013). Fourier spectral- and duration models for the generation of response spectra adjustable to different source-, propagation-, and site conditions, *Bull. Earthquake Eng.*, Vol. 12(1), 467-493, DOI: 10.1007/s10518-013-9482-z.

Bradley, B.A. (2013). A New Zealand-Specific Pseudospectral Acceleration Ground-Motion Prediction Equation for Active Shallow Crustal Earthquakes Based on Foreign Models, *Bull. Seism. Soc. Am.*, Vol. 103(3), 1801-1822, DOI: 10.1785/0120120021.

Brune, J. N. (1970). Tectonic stress and the spectra of seismic shear waves from earthquakes, *J. Geophys. Res*., Vol. 76, 4997-5009.

Brune, J. N. (1971). Correction, *J. Geophys. Res.,* Vol. 76, 5002.

Campbell, K.W., and Bozorgnia, Y. (2008). NGA Ground Motion Model for the Geometric Mean Horizontal Component of PGA, PGV, PGD and 5% Damped Linear Elastic Response Spectra for Periods Ranging from 0.01 to 10 s, *Earthquake Spectra*, Vol. 24(1), 139-171.

Campbell, K.W., and Bozorgnia, Y. (2014). NGA-West2 Ground Motion Model for the Average Horizontal Components of PGA, PGV, and 5%-Damped Linear Acceleration Response Spectra, *Earthquake Spectra*, Vol. 30(3), 1087-1115, DOI: 10.1193/062913EQS175M.

Chen, Y-H., and Tsai, C-C.P. (2002). A new method for estimation of the attenuation relationship with variance components, *Bull. Seism. Soc. Am*., Vol. 92, 1984-1991.

Chiou, B.S-J and Youngs, R.R. (2008). An NGA Model for the Average Horizontal Component of Peak Ground Motion and Response Spectra, *Earthquake Spectra*, Vol. 24(1), 173-215.

Chiou, B.S-J., and Youngs, R.R. (2014). Update of the Chiou and Youngs NGA Model for the Average Horizontal Component of Peak Ground Motion and Response Spectra, *Earthquake Spectra*, Vol. 30(3), 1117-1153, DOI: 10.1193/072813EQS219M.

Chiou, B.S-J., Youngs, R.R., Abrahamson, N.A., and Addo, K. (2010). Ground-Motion Attenuation Model for Small-To-Moderate Shallow Crustal Earthquakes in California and Its Implications on Regionalization of Ground-Motion Prediction Models, *Earthquake Spectra*, Vol. 26 (4), 907-926.

Coppersmith, K.J., Bommer, J., Hanson, K., Coppersmith, R., Unruh, J.R., Wolf, L., Youngs, R., Al Atik, L., Rodriguez-Marek, A., Toro, G., and Montaldo-Falero, V. (2014). Hanford Sitewide Probabilistic Seismic Hazard Analysis, *PNNL-23361*, Pacific Northwest National Laboratory, Richland Washington.

Dawood, H.M., Rodriguez-Marek, A., Bayless, J., Goulet, C., and Thompson E. (2014). The KiK-net database processed using an automated ground motion processing protocol. Available at https://nees.org/resources/7849.

Derras, B., Bard, P-Y, and Cotton, F. (2013) Towards fully data driven ground-motion prediction models for Europe, *Bull Earthquake Eng*., Vol. 12, 391–430, DOI: 10.1007/s10518-013-9481-0.

Donahue, J., and Abrahamson, N.A. (2014). Simulation-based HW Effects, *Earthquake Spectra*, Vol. 30(3), 1269-1284.

Dreger, D.S., Beroza, G.C., Day, S.M., Goulet, C.A., Jordan, T. H., Spudich, P.A, and Stewart, J. P. (2013). Evaluation of SCEC Broadband Platform Phase 1 Ground Motion Simulation Results, 33 pp. plus

Appendices, Report submitted to SCEC, Aug. 1 2013. Available at http://scec.usc.edu/scecpedia/SCEC_BBP_Phase_1_Evaluation.

Dreger, D. S., G. C. Beroza, S. M. Day, C. A. Goulet, T. H. Jordan, P. A. Spudich, and J. P. Stewart (2015). Validation of the SCEC broadband platform v14.3 simulation methods using pseudospectral acceleration data, *Seismol. Res. Lett.*, Vol. 86(1), 39-47, DOI: 10.1785/0220140118.

Electric Power Research Institute - EPRI (1993). Guidelines for determining design basis ground motions. Palo Alto, Calif: Electric Power Research Institute, Vol. 1-5, EPRI TR-102293.

Faccioli, E., Bianchini, A., and Villani, M. (2010). New ground motion prediction equations for T > 1 s and their influence on seismic hazard assessment, *Proc. Univ. Tokyo Sym. on Long-Period Ground Motion and Urban Disaster Mitigation*, March 17-18, 2010.

Graizer, V. (2014). Updated Graizer-Kalkan Ground-motion Prediction Equations for Western United States, *Proceedings for the 10th U.S. National Conference on Earthquake Engineering Frontiers of Earthquake Engineering*, July 21-25, 2014, Anchorage, Alaska, Paper ID 1097, 11 pp.

Graves, R. W. and Pitarka, A. (2010). Broadband Ground-Motion Simulation Using a Hybrid Approach, *Bull. Seism. Soc. Am.*, Vol. 100 (5a), 2095-2123.

Graves, R.W. and Pitarka, A. (2015). Refinements of the Graves and Pitarka (2010) Broadband Ground-Motion Simulation Method, *Seismol. Res. Letts.*, Vol. 86(1), 75-80, DOI: 10.1785/0220140101.

Hermkes, M., Kuehn, N.M., and Riggeslen, C. (2013). Simultaneous quantification of epistemic and aleatory uncertainty in GMPEs using Gaussian process regression, *Bull. Earthquake Eng.*, DOI: 10.1007/s10518-013-9507-7.

Idriss, I.M. (2008). An NGA Empirical Model for Estimating the Horizontal Spectral Values Generated By Shallow Crustal Earthquakes, *Earthquake Spectra*, Vol. 24(1), 217-242.

Idriss, I.M. (2014). An NGA-West2 Empirical Model for Estimating the Horizontal Spectral Values Generated by Shallow Crustal Earthquakes, *Earthquake Spectra*, Vol. 30(3), 1155-1177, DOI: 10.1193/070613EQS195M.

Kamai, R., Abrahamson, N.A., and Silva, W.J. (2013). Nonlinear Horizontal Site Response for the NGA-West2 Project, *PEER Report 2013/12*, Pacific Earthquake Engineering Research Center, University of California, Berkeley, CA, May 2013, 70 pp.

Kanno, T., Narita, A., Morikawa, N., Fujiwara, H. and Fukushima, Y. (2006) A New Attenuation Relation for Strong Ground Motion in Japan Based on Recorded Data, *Bull. Seism. Soc. Am.*, Vol. 96, 879-897.

Kishida, T., Kayen, R.E., Ktenidou, O.-J., Silva, W., Darragh, R., and Watson-Lamprey, J. (2014a). PEER Arizona Strong Motion Database and GMPEs Evaluation, Pacific Earthquake Engineering Research Center PEER Report 2014/09, 135 pp.

Kishida, T., Ktenidou, O.-J., Darragh, R., and Silva, W. (2014b). Data processing for Fourier amplitude spectrum (FAS) estimation from NGA-West2 processed accelerations, Chapter 7 in the PEER NGA-East Database Report Pacific Earthquake Engineering Research Center, pp. 50 (in review).

Ktenidou, O.-J., Cotton, F., Abrahamson, N., and Anderson, J.G. (2014). Taxonomy of kappa: a review of definitions and estimation methods targeted to applications. *Seismol. Res. Letts* Vol. 85(1), 135-146.

Leonard, M. (2010). Earthquake Fault Scaling: Self-Consistent Relating of Rupture Length, Width, Average Displacement, and Moment Release, *Bull. Seismol. Soc. Am.*, Vol. 100, 1971-1988.

Lin, P.-S., Chiou, B., Abrahamson, N., Walling, M., Lee, C.-T., and Cheng, C.-T. (2011). Repeatable source, site, and path effects on the standard deviation for empirical ground-motion prediction models, *Bull. Seismol. Soc. Am.,* Vol. 101(5), 2281-2295, DOI: 10.1785/012009031.

Liu, P., Archuleta, R.J., and Hartzell, S.H. (2006). Prediction of broadband ground-motion time histories: Hybrid low/high-frequency method with correlated random source parameters, *Bull. Seism. Soc. Am*., Vol. 96, 2118-2130, doi: 10.1785/0120060036.

Luzi, L., Bindi, D., Puglia, R., Pacor, F. and Oth, A. (2014). Single-Station Sigma for Italian Strong-Motion Stations, *Bull. Seism. Soc. Am*., Vol. 104(1), 467-483.

Maechling, P.J., Silva, F., Callaghan, S., and Jordan, T.H. (2015). Broadband Platform: System Architecture and Software Implementation, *Seismol. Res. Letts*., Vol. 86(1), 27-38, DOI:10.1785/0220140125

Mai, P.M., Imperatori, W., Olsen, K.B. (2010), Hybrid Broadband Ground-Motion Simulations: Combining Long-Period Deterministic Synthetics with High-Frequency Multiple S-to-S Backscattering, *Bull. Seism. Soc. Am*., Vol. 100(5A), 2124-2142.

McLaren, M.K., and W.U. Savage (2001). Seismicity of South-Central Coastal California: October 1987 through January 1997, *Bull. Seism. Soc. Am*., Vol. 91, 1629-1658.

McVerry, G.H., Zhao, J.X., Abrahamson, N.A., Somerville, P.G. (2006). New Zealand acceleration response spectrum attenuation relations for crustal and subduction zone earthquakes, *Bulletin of the New Zealand Society for Earthquake Engineering*, Vol. 39, 1-58.

Mena, B., Mai, P.M., Olsen, K.B., Purvance, M.D., and Brune, J.N. (2010). Hybrid Broadband Ground-Motion Simulation Using Scattering Green's Functions: Application to Large-Magnitude Events, *Bull. Seism. Soc. Am*., Vol. 100, 2143-2162.

Morikawa, N., Kanno, T., Narita, A., Fujiwara, H., Okumura, T., Fukushima, Y., and Guerpinar, A. (2008). Strong motion uncertainty determined from observed records by dense network in Japan. *J. Seismol.,* Vol. 12(4), 529–546.

Motozedian, D. and Atkinson, G.M. (2005). Stochastic finite-fault modeling based on a dynamic corner frequency, *Bull. Seism. Soc. Am*., Vol. 95(3), 995-1010.

Olsen, K. and Takedatsu, R. (2015). The SDSU Broadband Ground Motion Generation Module BBtoolbox Version 1.5, *Seismol. Res. Letts*., Vol. 86(1), 81-88, DOI: 10.1785/0220140102.

Pacor, F., Paolucci, R., Luzi, L., Sabetta, F., Spinelli, A., Gorini, A., Nicoletti, M., Marcucci, S., Filippi, L., and Dolce, M. (2011). Overview of the Italian strong motion database ITACA 1.0, *Bull. Earthq. Eng.,* Vol. 9(6), 1723–1739, DOI: 10.1007/s10518-011-9327-6.

Pankow, K.L., and Pechmann, C. (2004). The SEA99 ground-motion predictive relations for extensional tectonic regimes: Revisions and a new peak ground velocity relation, *Bull. Seism. Soc. Am*., Vol. 94(1), 341-348.

Pasyanos, M., Dreger, D.S., and Romanowicz, B. (1996). Toward real-time estimation of regional moment tensors, *Bull. Seism. Soc. Am*., Vol. 86, 12255-1269.

Renault, P., Heuberger, S., and Abrahamson, N.A. (2010). PEGASOS Refinement Project: An improved PSHA for Swiss nuclear power plants, *Proc. 14th European Conference of Earthquake Engineering*, Ohrid, Republic of Macedonia, 30 August-3 September 2010, Paper ID 991.

Rodriguez-Marek, A., Cotton, F., Abrahamson, N.A., Akkar, S., Al Atik, L., Edwards, B., Montalva, G.A., and Dawood, H. (2013). A model for single-station standard deviation using data from various tectonic regions*, Bull. Seismol. Soc. Am.,* Vol. 103, 3149-3163.

Rodriguez-Marek, A., Rathje, E.M., Bommer, J.J., Scherbaum, F., and Stafford, P.J. (2014). Application of Single-Station Sigma and Site-Response Characterization in a Probabilistic Seismic-Hazard Analysis for a New Nuclear Site, *Bull. Seismol. Soc. Am.,* Vol. 104, 1601-1619, DOI: 10.1785/0120130196.

Schmedes, J., Archuleta, R.J., and Lavallée, D. (2010). Correlation of earthquake source parameters inferred from dynamic rupture simulations, *J. Geophys. Res*., Vol. 115, B03304, DOI: 10.1029/2009JB006689.

Schmedes, J., Archuleta, R.J., and Lavallée, D. (2012). A kinematic rupture model generator incorporating spatial interdependency of earthquake source parameters, *Geophys. J. Int.*, Vol. 192(3), 1116-1131.

Shiba, Y., and Noguchi, S. (2012). Statistical characteristics of seismic source parameters controlling broadband strong ground motions -Investigation based on source inversion analysis. *CRIEPI REPORT.* N11054 (in Japanese with English abstract).

Silva, W.J., Abrahamson, N., Toro, G., and Costantino, C. (1997). Description and validation of the stochastic ground motion model, Report submitted to Brookhaven National Laboratory, Associated Universities, Inc., Upton, New York 11973, Contract No. 770573.

Spudich, P., Joyner, W.B., Lindh, A.G., Boore, D.M., Margaris, B.M., and Fletcer, J.B. (1999). SEA99: A revised ground motion prediction relation for use in extensional tectonic regimes, *Bull. Seism. Soc. Am*., Vol. 89(5), 1156-1170.

Stidham, C., Antolik, M., Dreger, D., Larsen, S., and Romanowicz, B. (1999). Three-Dimensional Structure Influences on the Strong Motion Wavefield of the 1989 Loma Prieta Earthquake, *Bull. Seism. Soc. Am.*, Vol. 89, 1184-1202.

Tanaka, M., Asano, K., Iwata, T., and Kubo, H. (2014). Source rupture process of the 2011 Fukushima-ken Hamadori earthquake: how did the two subparallel faults rupture? *Earth, Planets and Space*, Vol. 66:101, DOI:10.1186/1880-5981-66-101

United States Geological Survey – USGS (2007). Preliminary integrated geologic map databases for the United States: Western States, California, Nevada, Arizona, Washington, Oregon, Idaho, and Utah, Version 1.3, *Open File Report 2005-1305* available at [http://pubs.usgs.gov/of/2005/1305/]; updated December 2007.

United States Geological Survey – USGS (2014). Magnitude 6.0 – NEVADA: Earthquake Summary, available at [http://earthquake.usgs.gov/earthquakes/eqinthenews/2008/us2008nsa9/#summary]; page last modified July 2014.

Walter, A. W., and Mooney, W.D. (1982). Crustal structure of the Diablo Gabilan Ranges, Central California; a reinterpretation of existing data, *Bull. Seism. Soc. Am.*, Vol. 72, 1567-1590.

Wills, C.J., and Clahan, K.B. (2006). Developing a map of geologically defined site- condition categories for California, *Bull. Seismol. Soc. Am*., Vol. 96, 1483-1501.

Zeng, Y., Anderson, J.G. and Yu, G. (1994). A composite source model for computing realistic synthetic strong ground motions, *Geophysical Research Letters*, Vol. 21, 725-728.

Zhao, J.X., Zhang, J., Asano, A., Ohno, Y., Oouchi, T., Takahashi, T., Ogawa, H., Irikura, K., Thio, H.K., Somerville, P.G., Fukushima, Y., and Fukushima, Y. (2006). Attenuation Relations of Strong Ground Motion in Japan Using Site Classification Based on Predominate Period, *Bull. Seism. Soc. Am*., Vol. 96, 898-913.

Zhao, J.X., and Lu, M. (2011). Magnitude-Scaling Rate in Ground-Motion Prediction Equations for Response Spectra from Large, Shallow Crustal Earthquakes, *Bull. Seism. Soc. Am*., Vol. 101, 2643-2661.

Table 5.1-1: Primary Empirical Data Sets

DATASET	Magnitude Range	Distance Range (R_{JB} in km)	V_{S30} Range (m/s)	Dip Range (degrees)	Mechanisms by Earthquake
PEER NGA-West2	3.0 - 7.9	0 - 1532	89 - 2100	10 - 90	57% SS 17% NML 26% REV
Akkar Subset of Reference database of Seismic Ground Motion in Europe (RESORCE)	4.0 - 7.6	0-200	92-2165	2-90	38% SS 47% NML 15% REV
PEER Arizona (Regions 1, 2, and 3)	4.3 - 7.2	145 - 649	398 - 1312	40 - 86	93% SS 7% NML 0% REV
PEER Arizona (Central Arizona)	1.2 - 3.4	9 - 301	398 - 1237	Not Available	Not Available
Lin et al. (2011)	3.9 - 7.6	0.6 - 208	166 - 760	10-90	

Table 5.1-2: Data Sets Used for the Evaluation of the Median Ground Motions

DATASET	DATABASE OF ORIGIN	SUBSET	USE OF DATASET
NGA-W2$_{DC-MED}$	PEER NGA-West2	**M** ≥ 5.0 No HW sites* V_{S30} ≥ 250 m/s N_{REC}/eqk ≥ 3 Adjusted to V_{S30}=760 m/s	Evaluation of the median ground-motion model (for DCPP) for base FW model
NGA-W2$_{PV-MED}$	PEER NGA-West2	**M** ≥5.0 -70km ≤ Rx≤ 70 km for both SS and NML V_{S30} ≥ 250 m/s N_{REC}/eqk ≥ 3 Adjusted to V_{S30}=760 m/s	Evaluation of the median ground-motion model (for PVNGS)
EUR$_{PV-MED}$	Reference database of Seismic Ground Motion in Europe (RESORCE)	**M** ≥5.0 R_{JB}≤ 70 km for both SS and NML V_{S30} ≥ 250 m/s N_{REC}/eqk ≥ 3 Adjusted to V_{S30}=760 m/s	Evaluation of the median ground-motion model (for PVNGS)
PEER-AZ$_{PATH}$	PEER Arizona	Earthquakes from NGA-West2 in Regions 1 and 2&3 recorded at stations in Arizona N_{REC}/eqk ≥ 3 N_{REC}/station ≥ 5	Estimation of the median path terms for Regions 1 and 2&3 (for PVNGS)
SIM$_{DC-MED}$	SCEC simulations using the broad band platform	SS: **M**5.5, **M**6.0, **M**6.6, and **M**7.2 REV: **M**5.5, **M**6.0, and **M**6.5	Evaluation of the median ground-motion model (for DCPP)
SIM$_{HW}$	SCEC simulations using the broad band platform	REV: **M**5.5, **M**6.0, and **M**6.5 Dips: 10, 20, 30, 45, 60 Z_{TOR}: 2.5, 7.5, 12 km	Evaluation of the scaling of the HW effect for magnitudes between **M**5 and **M**6.5, and for Z_{TOR} scaling (for DCPP)

* Includes the following: 0 ≥ R_X ≥ -70 km for both SS and REV; 0 ≤ R_X ≤ 70 km & R_{JB} ≤ 10 km for SS; and 0 ≤ R_X ≤ 70 km for SS, & Dip ≥ 80 deg.

Table 5.1-3: Data Sets Used for the Evaluation of the Kappa and Ground Motions from Splay and Complex Ruptures

DATASET	DATABASE OF ORIGIN	SUBSET	USE OF DATASET
PEER-AZ_{KAPPA}	PEER Arizona	Earthquakes in Arizona recorded at stations in Arizona	Estimation of kappa for stations in central Arizona (for PVNGS)
SIM_{Splay}	SCEC simulations using the broadband platform	Main SS: **M**7.0 - **M**7.4 REV: **M**7.0 - **M**7.4 Splay: SS: **M**6.0-**M**6.4 REV: **M**6.4	Evaluation of the methods to compute ground motions for splay ruptures (for DCPP)
$SIM_{Complex}$	SCEC simulations using the broadband platform	SS: **M**6.7-**M**7.4 REV: **M**6.4-**M**7.0	Evaluation of the methods to compute ground motions for complex ruptures (for DCPP)

Table 5.1-4: Data Sets Used for the Evaluation of the Aleatory Standard Deviation

DATASET	DATABASE OF ORIGIN	SUBSET	USE OF DATASET
EUR_{PHISS}	Reference database of Seismic Ground Motion in Europe (RESORCE)	**M** ≥ 5 DIST ≤ 50 km N_{REC}/eqk ≥ 3 N_{REC}/site ≥ 3	1. Computation of residuals 2. Development of single-station sigma models based on European data for application to PVNGS sources in Greater Arizona (ϕ_{SS-EUR} model)
$GLOBAL_{PHISS-ASK14}$ $GLOBAL_{PHISS-BSSA14}$ $GLOBAL_{PHISS-CY14}$ $GLOBAL_{PHISS-CB14}$	PEER NGA-West2 and Lin et al (2011)	**M** ≥ 5 DIST ≤ 50 km N_{REC}/eqk ≥ 3 N_{REC}/site ≥ 3 Selection applied to the subset used by the GMPE developer	1. Use of residuals from GMPE developers 2. Development of single-station sigma models based on the global data for application to both DCPP and PVNGS sources in Greater Arizona. ($\phi_{SS-GLOBAL-R50}$ model)
$NGA\text{-}W2_{LD\text{-}PHISS\text{-}ASK14}$ $NGA\text{-}W2_{LD\text{-}PHISS\text{-}BSSA14}$ $NGA\text{-}W2_{LD\text{-}PHISS\text{-}CY14}$	PEER NGA-West2	**M** ≥ 5.5 200 ≤ Dist ≤ 400 km N_{REC}/eqk ≥ 3 N_{REC}/site ≥ 3 Selection applied to the subset used by the GMPE developer	1. Use of residuals from GMPE developers 2. Development of single-station sigma model based on large distance data for application to PVNGS sources in regions 1, and 2&3 ($\phi_{SS-GLOBAL-LD}$ model)
$NGA\text{-}W2_{CA\text{-}PHISS\text{-}ASK14}$ $NGA\text{-}W2_{CA\text{-}PHISS\text{-}BSSA14}$ $NGA\text{-}W2_{CA\text{-}PHISS\text{-}CY14}$ $NGA\text{-}W2_{CA\text{-}PHISS\text{-}CB14}$	PEER NGA-West2	California earthquakes with **M** ≥ 5 DIST ≤ 50 km N_{REC}/eqk ≥ 3 N_{REC}/site ≥ 3 Selection applied to the subset used by the GMPE developer	1. Use of residuals from GMPE developers 2. Development of single-station sigma models based on CA data for application to DCPP ($\phi_{SS-CA-1}$ & $\phi_{SS-CA-2}$ models)
$PEER\text{-}AZ_{PATH\text{-}ASK14}$ $PEER\text{-}AZ_{PATH\text{-}BSSA14}$ $PEER\text{-}AZ_{PATH\text{-}CY14}$ $PEER\text{-}AZ_{PATH\text{-}CB14}$	PEER Arizona	Earthquakes from NGA-West2 in Region 1 and Regions 2&3 recorded at stations in Arizona	1. Computation of residuals 2. Development of single-path sigma for application to PVNGS from earthquakes in Region 1 and Regions 2&3 ($\phi_{SP-R123}$ model)

Table 5.1.2-1: PEER-Arizona Data Set Earthquake Event Catalog (from Table 2.2 in Kishida et al., 2014a)

EQID	Earthquake Name	YEAR/MODY/HRMN	Mangitude (*)	Epicenter Latitude	Epicenter Longitude	Hypocentral Depth (km)
1267	NA	2008/0105/2345	3.10 ML	35.0230	-113.9140	1.00
1268	NA	2008/0117/2200	3.40 ML	35.0200	-113.9140	1.00
1269	NA	2008/0120/1728	2.10 ML	35.0260	-113.9290	1.00
1270	NA	2008/0724/1405	2.40 ML	34.1880	-113.8440	6.00
1271	NA	2008/0803/0953	2.00 ML	34.1880	-113.8620	7.00
1272	NA	2008/1129/0148	1.50 ML	32.9520	-112.7740	13.00
1273	NA	2008/1129/0710	1.50 ML	32.9530	-112.7740	13.00
1274	NA	2008/1129/0711	1.50 ML	32.9550	-112.7720	13.00
1275	NA	2008/1129/0722	1.50 ML	32.9550	-112.7710	13.00
1276	NA	2008/1129/1621	1.50 ML	32.9540	-112.7700	13.00
1277	NA	2008/1129/1622	1.20 ML	32.9550	-112.7700	13.00
1278	NA	2012/0203/0242	2.50 Md	33.5905	-111.0490	13.87
1028	10275733	2007/0902/1729	4.73 **M**	33.7328	-117.4921	10.02
1047	10321585	2008/0501/0811	4.43 **M**	35.4744	-118.4262	6.68
1053	14330056	2007/1024/1222	4.34 **M**	35.8373	-117.6780	6.86
1058	14285168	2007/0415/2257	4.41 **M**	32.7070	-116.0400	10.16
1067	10230869	2007/0209/0333	4.29 **M**	33.2262	-116.1472	10.89
1182	14517500	2009/1001/1001	5.00 **M**	36.3864	-117.8583	7.41
1186	14519780	2009/1003/0115	5.19 **M**	36.4034	-117.8499	9.42
280	El Mayor-Cucapah	2010/0404/2240	7.20 **M**	32.3000	-115.2670	0.00
1004	14346868	2008/0209/0712	5.10 **M**	32.4105	-115.3120	18.65
1005	14408052	2008/1206/0418	5.06 **M**	34.8118	-116.4227	9.33
1009	14462064	2009/0523/2258	4.73 **M**	36.4011	-117.8397	7.42
1017	10347253	2008/0905/2154	4.63 **M**	32.3362	-115.2425	17.16
1018	10370141	2009/0109/0349	4.45 **M**	34.1081	-117.3062	14.80
1020	14295640	2007/0602/0511	4.26 **M**	33.8776	-116.2019	10.06

* Moment magnitudes (**M**) for the NGA-West2 earthquakes are from Ancheta et al. 2014. The local magnitudes (M_L) and duration magnitude (Md) for the Arizona events are from Jeri Young (2013, personal communication), Arizona Earthquake Information Center.

Table 5.1.2-2: Arizona Data Set V_{S30} Values (from Table 3-1 of Kishida et al., 2014a).

Station	Number of Recordings	Magnitude Range	Distance Range (km)	V_{S30} (m/s)	Max Inversion Depth of V_S profile (m)	Used for Kappa
Z14A	11	1.2 – 3.4	50 - 206	490 - 524	108	Yes
115A	9	1.2 – 3.4	59 – 301	424 - 460	99	Yes
Y16A	4	1.5 – 1.5	158 - 159	970 - 1028	40	Yes
Y15A	8	1.5 – 3.4	119 - 189	499 - 566	40	Yes
Z15A	2	1.5 – 3.1	69 - 251	373 - 464	39	Yes
113A	7	1.5 – 3.4	96 - 250	1140 - 1237	38	Yes
Y14A	9	1.5 – 3.4	82 - 147	473 - 526	50	Yes
Y13A	5	2.0 – 3.4	42 - 135	532 - 560	50	Yes
114A	7	1.2 – 2.4	28 - 183	380 - 404	50	Yes
Z13A	5	1.5 – 2.4	88 - 111	652 - 689	50	Yes

Table 5.1.5-1: Recording Stations within 100 km of the Wells, Nevada Earthquake

Station	R_{JB} (km)	R_{RUP} (km)	R_X (km)	Inferred V_{S30} (m/s)
ELK	56.3	56.8	-56.3	750
M11A	81.7	82.1	-81.7	600
M13A	62.9	63.4	62.9	280
N11A	82	82.4	-82	450
N12A	37.7	38.5	-37.7	350
N13A	66.2	66.7	66.2	280
O12A	100.2	100.5	100.2	600

Table 5.2.3-1: Single Planar Fault Scenarios for Reverse Earthquakes.

SCENARIO	M	RAKE	DIP	Z_{TOR} (km)
00	5.5	90	10	2.5
01	5.5	90	10	7.0
02	5.5	90	10	12.0
03	5.5	90	20	2.5
04	5.5	90	20	7.0
05	5.5	90	20	12.0
06	5.5	90	30	2.5
07	5.5	90	30	7.0
08	5.5	90	30	12.0
09	5.5	90	45	2.5
10	5.5	90	45	7.0
11	5.5	90	45	12.0
12	5.5	90	60	2.5
13	5.5	90	60	7.0
14	5.5	90	60	12.0
15	6.0	90	10	2.5
16	6.0	90	10	7.0
17	6.0	90	10	12.0
18	6.0	90	20	2.5
19	6.0	90	20	7.0
20	6.0	90	20	12.0
21	6.0	90	30	2.5
22	6.0	90	30	7.0
23	6.0	90	30	12.0
24	6.0	90	45	2.5
25	6.0	90	45	7.0
26	6.0	90	45	12.0
27	6.0	90	60	2.5
28	6.0	90	60	7.0
29	6.0	90	60	12.0
30	6.5	90	10	0.0
31	6.5	90	20	0.0
32	6.5	90	30	0.0
33	6.5	90	45	0.0
34	6.5	90	60	0.0
35	7.0	90	45	0.0

Table 5.2.3-2: Parameters defining the Complex Scenario 1 for a strike-slip rupture and a reverse-slip rupture with similar magnitudes for the two ruptures (representative of the Hosgri-Los Osos complex scenarios).

Name	M total	Strike 1	Dip 1	Rake 1	Length 1	M 1	Strike 2	Dip 2	Rake 2	Length 2	M 2
Case 1A	7.0	338.14	90	180	16.27	6.66	115.25	50	90	33.20	6.88
Case 1B	7.2	338.14	90	180	38.84	7.02	115.25	50	90	33.20	6.98
Case 1C	7.4	338.14	90	180	80.98	7.30	115.25	50	90	33.20	7.02

Table 5.2.3-3: Parameters defining the Complex Scenario 2 for a strike-slip rupture and a reverse-slip rupture with a smaller magnitude for the reverse rupture part (representative of the Shoreline-San Luis Bay complex scenarios).

Name	M total	Strike 1	Dip 1	Rake 1	Length 1	M 1	Strike 2	Dip 2	Rake 2	Length 2	M 2
Case 2A	7.0	299.86	90	180	41.67	6.96	273.19	70	90	7.80	6.42
Case 2B	7.2	299.86	90	180	64.24	7.18	273.19	70	90	7.80	6.47
Case 2C	7.4	299.86	90	180	106.38	7.39	273.19	70	90	7.80	6.51

Table 5.2.3-4: Parameters defining the Splay Scenario 1 for strike-slip ruptures (representative of the Hosgri-Shoreline splay rupture scenarios).

	Segment	**M**	**Strike**	**Rake**	**Dip**	**Z_{TOR}**	**L**	**W**
Case 1A	Main	7.0	334.2	180	90	0	49.47	20.21
	Splay	6.05	305.7	180	90	0	13.26	8.4
Case 1B	Main	7.2	334.2	180	90	0	72.04	22.0
	Splay	6.22	305.7	180	90	0	16.86	9.86
Case 1C	Main	7.4	334.2	180	90	0	114.18	22.0
	Splay	6.43	305.7	180	90	0	22.44	11.93

Table 5.2.3-5: Parameters defining the Splay Scenario 2 for reverse ruptures (representative of the Los Osos-San Luis Bay splay rupture scenarios).

	Segment	**M**	**Strike**	**Rake**	**Dip**	**Z_{TOR}**	**L**	**W**
Case 2A	Main	7.00	115.4	90	60	0	44.82	22.08
	Splay	6.39	295.4	90	70	0	19.55	12.7
Case 2B	Main	7.20	115.4	90	60	0	59.26	26.6
	Splay	6.39	295.4	90	70	0	19.55	12.7
Case 3B	Main	7.40	115.4	90	60	0	78.19	32.0
	Splay	6.39	295.4	90	70	0	19.55	12.7

Table 5.4.1-1: Number of recordings and earthquakes in the global dataset (**M** ≥ 5, R < 50km) for four of the NGA-West2 models for the short-distance ϕ_{SS}.

	ASK14		**BSSA14**		**CB14**		**CY14**	
Region	Nb Recs	Nb Eqks	Nb Recs	Nb Eqks	Nb Recs	Nb Eqks	Nb Recs	Nb Eqks
CA	672	54	630	48	342	38	349	41
Taiwan	846	28	846	28	846	28	846	28
Japan	65	3	65	3	0	0	63	3
Italy	69	15	62	11	6	4	0	0
China	10	2	102	26	17	4	0	0
Total	1,662	102	1,705	116	1,211	74	1,258	72

Table 5.4.4-1: Number of recordings and earthquakes in the global dataset (**M** ≥ 5.5, R = 200 to 400km) for three of the NGA-West2 models

	ASK14		**BSSA14**		**CY14**	
Region	Nb Recs	Nb Eqks	Nb Recs	Nb Eqks	Nb Recs	Nb Eqks
CA	133	1	209	4	160	2
Japan	131	3	157	4	129	4
China	0	0	49	15	0	0
Total	264	4	415	23	289	6

Table 5.5.1-1: Existing GMPEs Considered for the Development of Median Ground-Motion Models (continues on the following page).

GMPE	Comments	Candidate for DCPP	Candidate for PVNGS Greater Arizona Sources	Candidate for PVNGS Distant California Sources
Abrahamson et al. (2014)	Update of Abrahamson and Silva (2008)	Yes	Yes	Yes
Akkar and Cagnan (2010)	Regional for Turkey	No, superseded by pan-Europe/Middle East ACR GMPEs	No, superseded by pan-Europe/Middle East ACR GMPEs	No, superseded by pan-Europe/Middle East ACR GMPEs plus non California/Western Arizona attenuation
Akkar et al. (2013a, 2014)	Update of Akkar and Bommer (2010)	Yes	Yes	No, non California/Western Arizona attenuation
Bindi et al. (2014a, 2014b)	Update of Bindi et al. (2011)	No, extrapolation above **M**7 problematic at some periods	Yes, **M** > 7 not a significant contributor to hazard	No, extrapolation above **M**7 problematic at some periods
Boore et al. (2014)	Update of Boore and Atkinson (2008)	Yes	Yes	Yes
Bora et al. (2013)	RESORCE Experimental Model	No, experimental	No, experimental	No, experimental
Bradley (2013)	Modification of Chiou et al. (2010) for New Zealand	No, regional adjustment to other model included in study	No, regional adjustment to other model included in study	No, regional adjustment to other model included in study
Campbell and Bozorgnia (2014)	Update of Campbell and Bozorgnia (2008)	Yes	Yes	Yes
Chiou and Youngs (2014)	Update of Chiou and Youngs (2008) and Chiou et al. (2010)	Yes	Yes	Yes
Derras et al. (2013)	RESORCE Experimental Model	No, experimental	No, experimental	No, experimental
Faccioli et al. (2010)	Global data, primarily Japan	No, single linear magnitude scaling over entire range	No, single linear magnitude scaling over entire range	No, single linear magnitude scaling over entire range

GMPE	Comments	Candidate for DCPP	Candidate for PVNGS Greater Arizona Sources	Candidate for PVNGS Distant California Sources
Graizer (2014)	NGA West 1 database plus 2004 Parkfield and 2005 San Simeon	No, not published in a peer-reviewed journal	No, normal fault not specifically studied	No, not published in a peer-reviewed journal
Hermkes et al. (2013)	RESORCE Experimental Model	No, experimental	No, experimental	No, experimental
Idriss (2014)	Update of Idriss (2008)	Yes, not used for R_{RUP} < 3km	No, normal fault not specifically studied	Yes
Kanno et al. (2006)	Used only depth for separation of event type	No, no clear separation of ACR from SZ interface earthquakes	No, not relevant to tectonics	No, no clear separation of ACR from SZ interface earthquakes, plus non California/Western Arizona attenuation
McVerry et al. (2006)	Regional for New Zealand	No, specific to New Zealand, superseded by global models that use recent New Zealand earthquake data	No, specific to New Zealand, superseded by global models that use recent New Zealand earthquake data	No, specific to New Zealand, superseded by global models that use recent New Zealand earthquake data
Pankow and Pechmann (2004)	Update of Spudich et al. (1999)	No, not relevant to tectonics	No, superseded by more recent models (e.g. NGA-West2)	No, not relevant to tectonics
Zhao and Lu (2011)	Proposed change in magnitude scaling above ~ **M**7.1	Yes	No, not relevant to tectonics	No, non California/Western Arizona attenuation
Zhao et al. (2006)	Mostly Japan data, ACR and SZ with separate factors	Yes	No, not relevant to tectonics	No, non California/Western Arizona attenuation

Table 5.5.3-1: Host kappa values for the seven candidate GMPEs for PVNGS Greater Arizona sources for a reference V_{S30} of 760 m/sec.

GMPE	ASK14	BSSA14	CB14	CY14	ASB14	Bi14	ZH06
Host Kappa (sec)	0.045	0.038	0.037	0.041	0.042	0.045	0.042

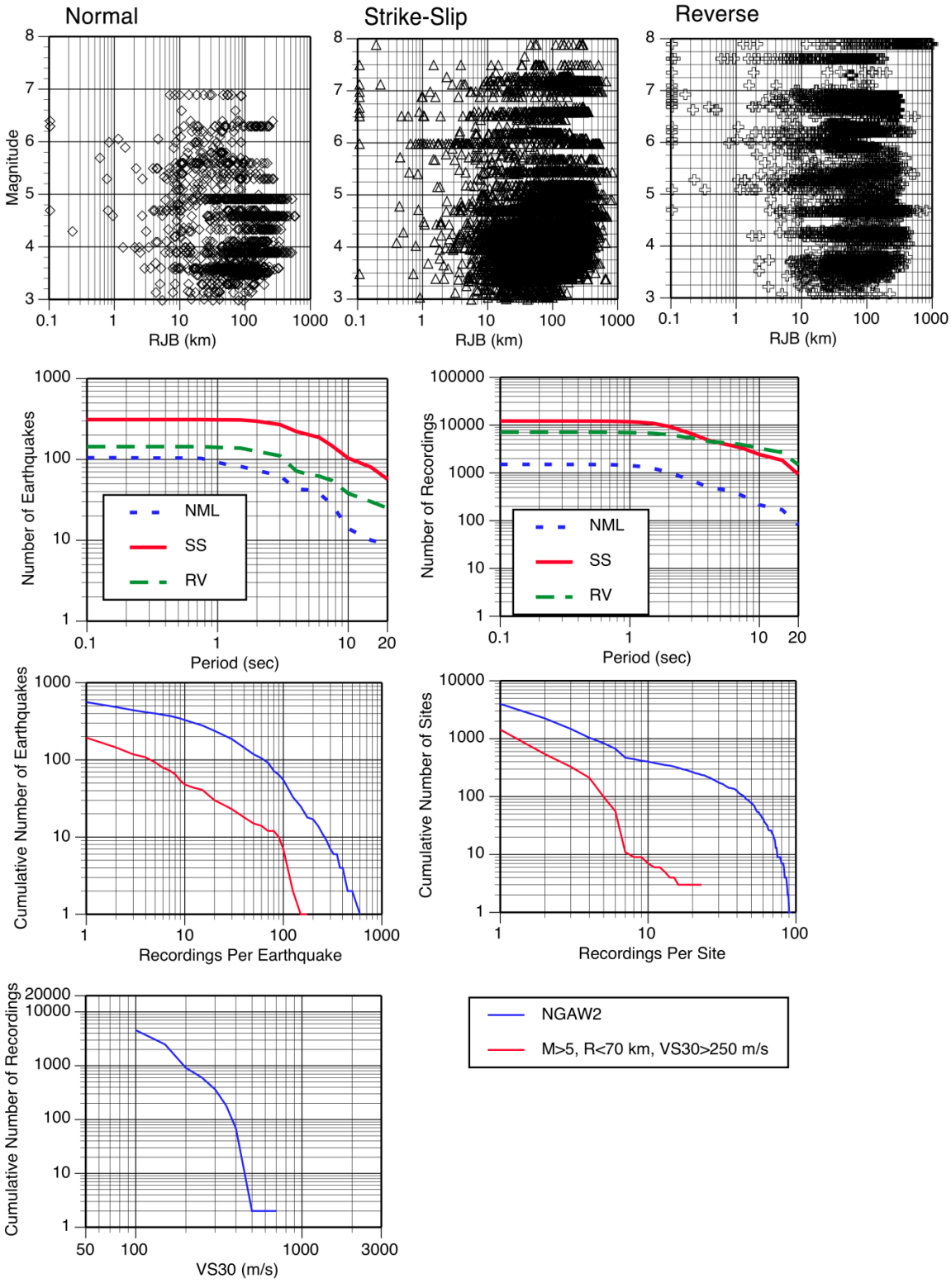

Figure 5.1.1-1: Summary of the data distribution of the NGA-West2 database using the subset of reliable data selected by ASK14.

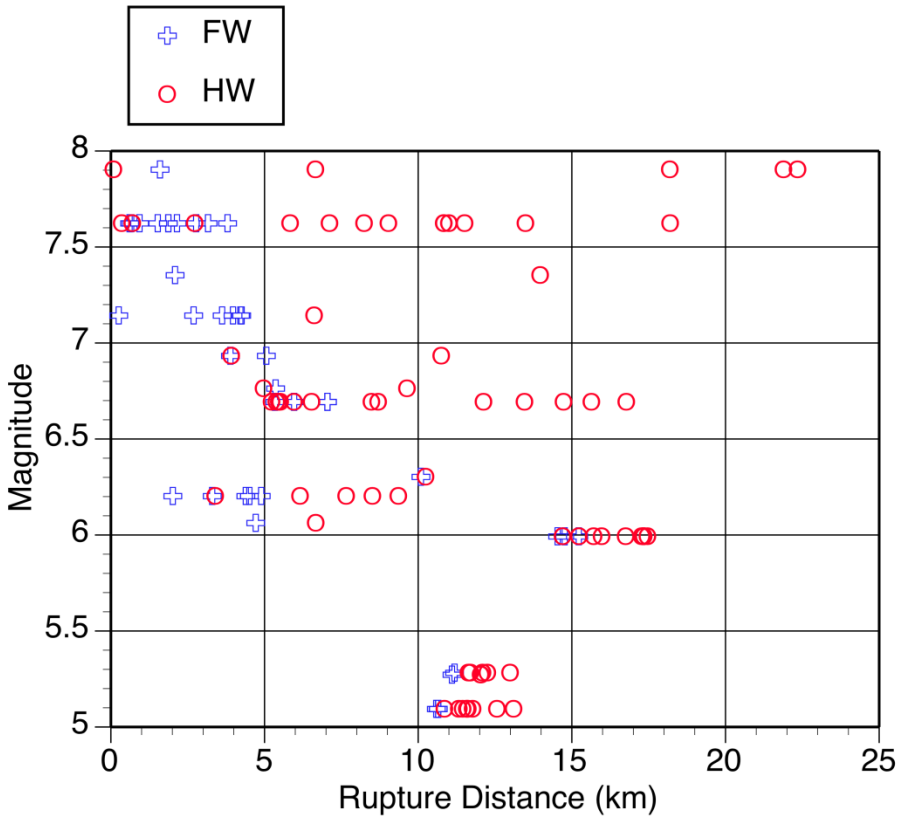

Figure 5.1.1-2: NGA-West2 data with at least one recording on both the FW and HW for sites with R_{JB} distance less than 5 km, and dip < 80 degrees.

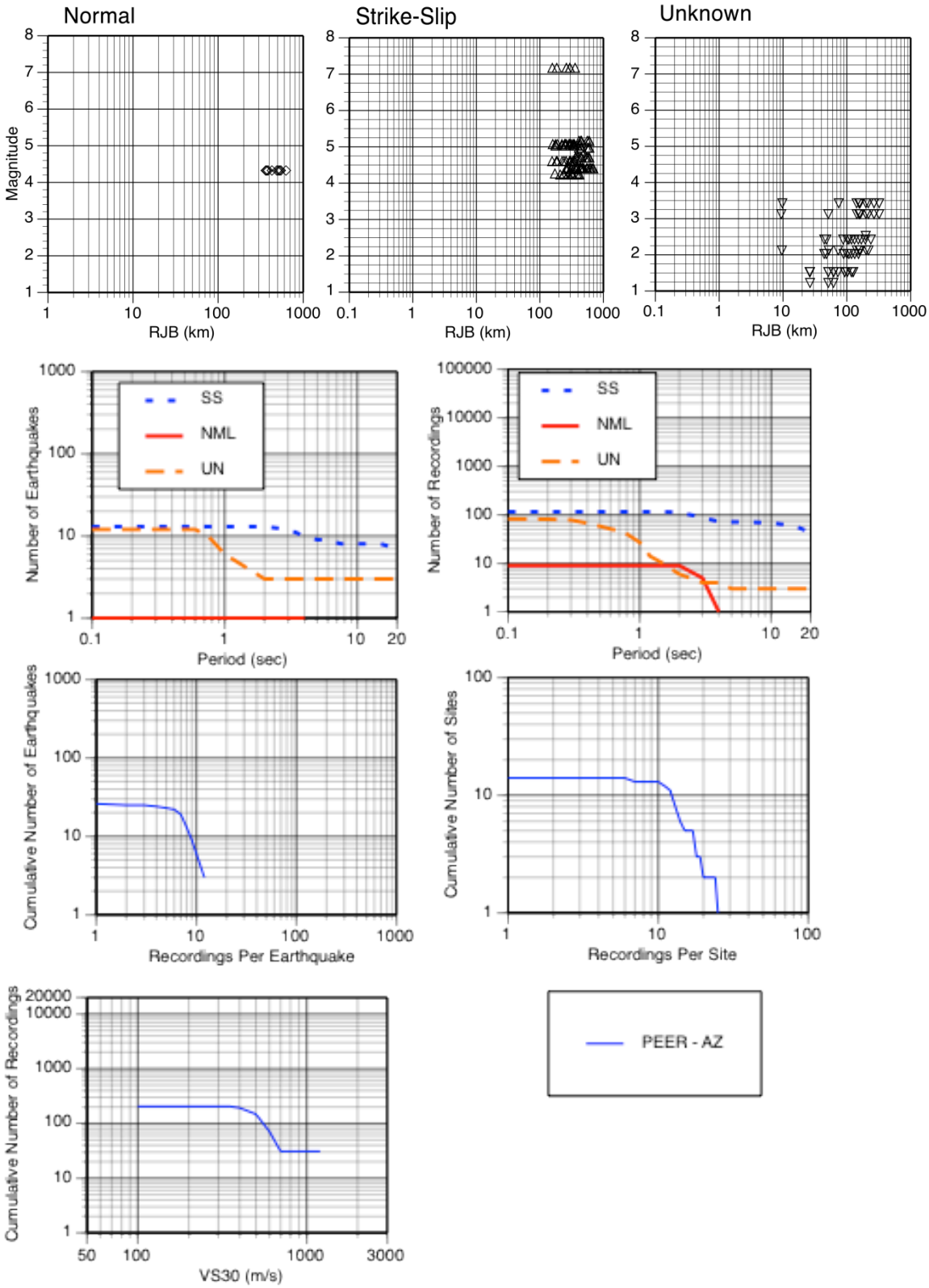

Figure 5.1.2-1: Summary of the data distribution of the PEER-Arizona database.

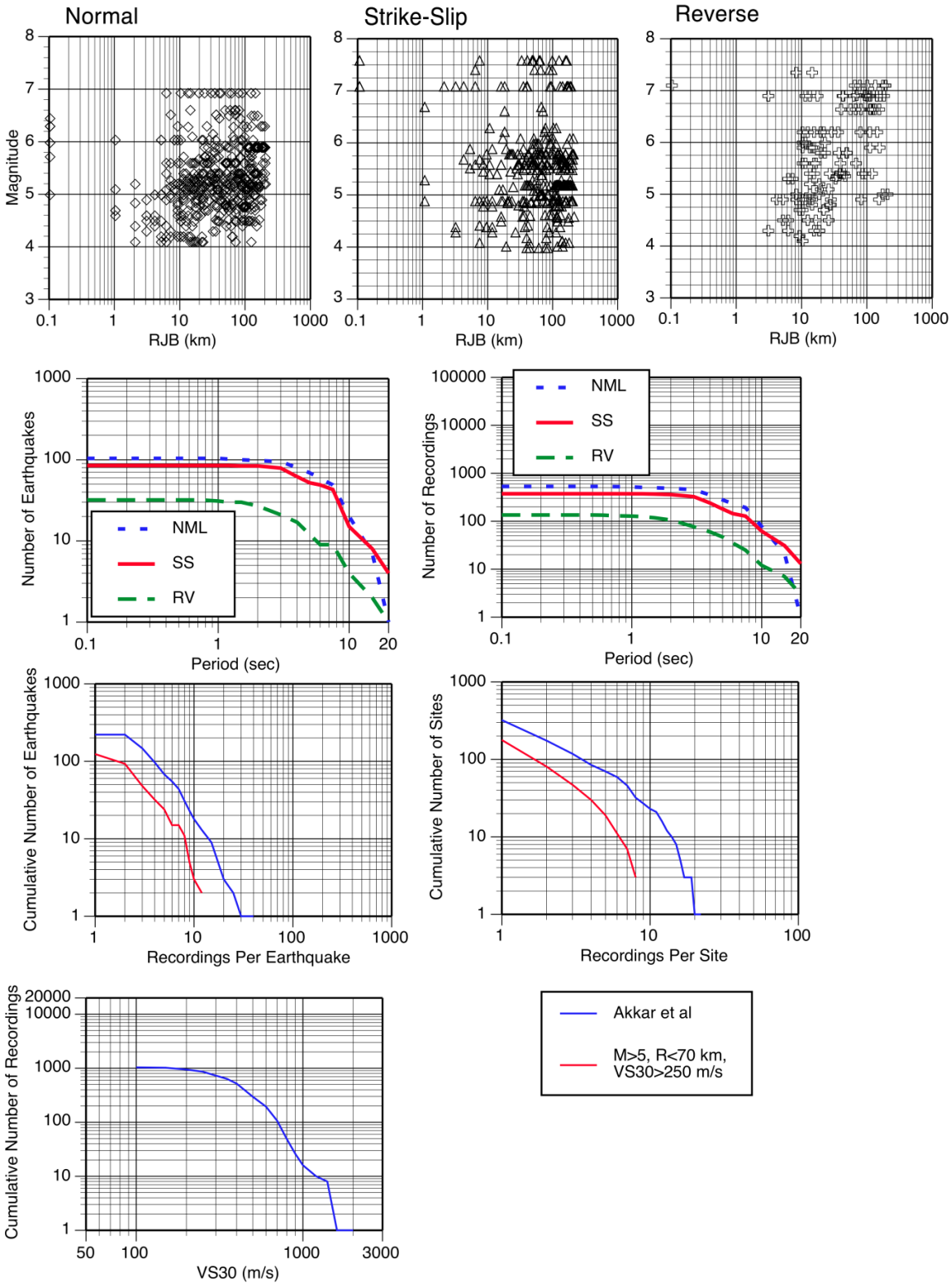

Figure 5.1.3-1: Summary of the data distribution of the European database (Akkar et al, 2014c) using the subset of reliable data selected for the development of the Akkar et al. (2014a and 2014b) model.

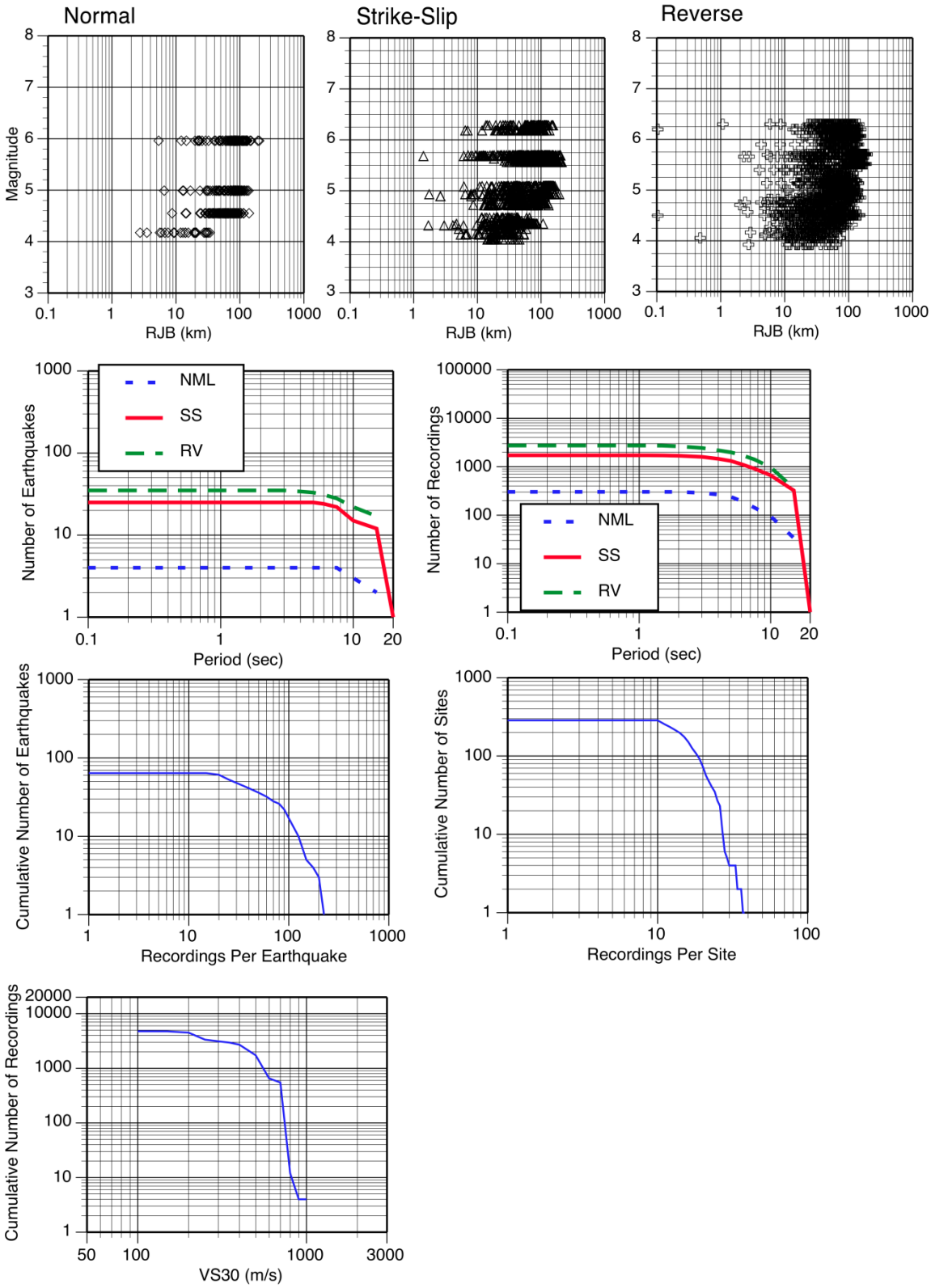

Figure 5.1.4-1: Summary of the data distribution of the Lin et al (2011) Taiwan database.

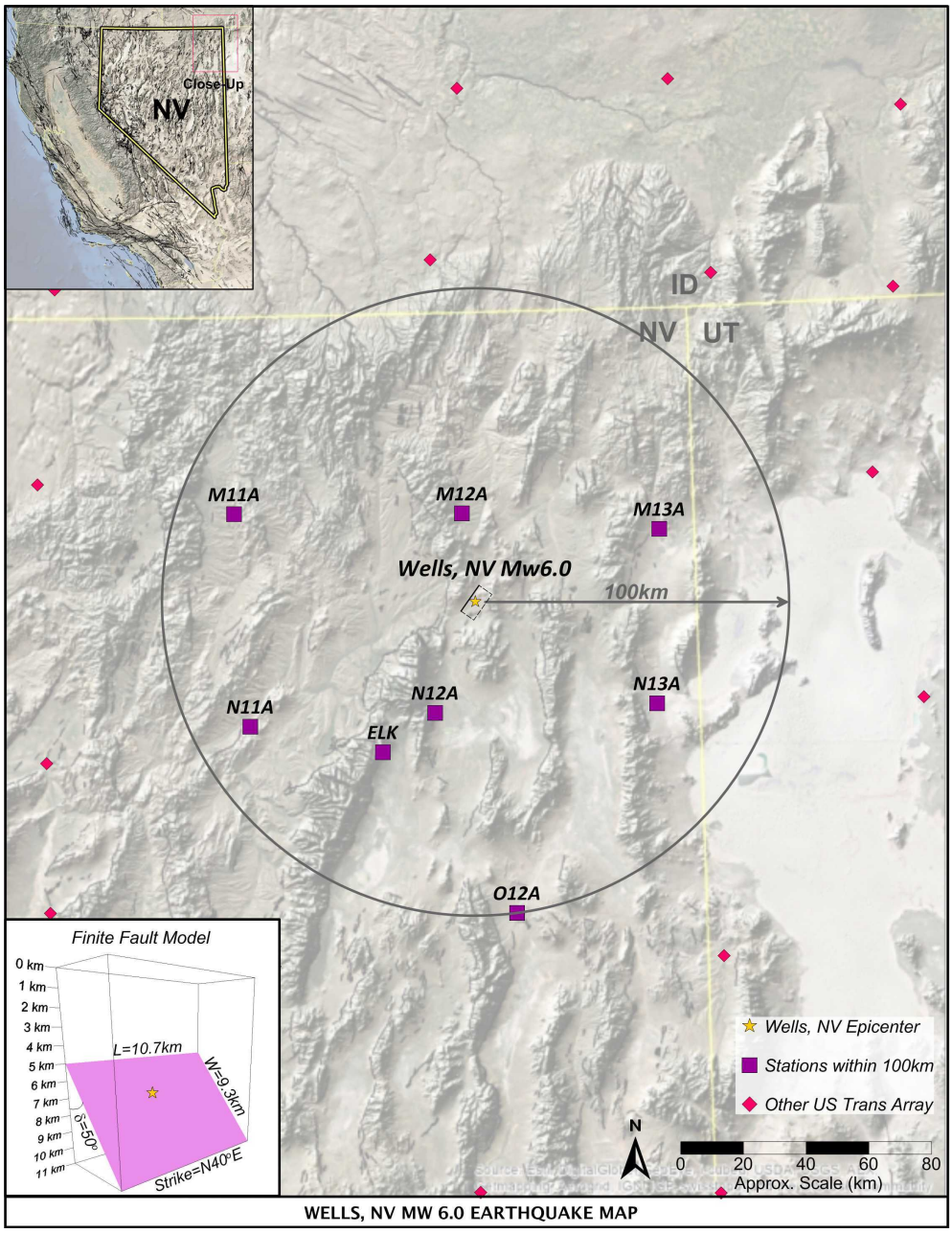

Figure 5.1.5-1: Epicentral location of the Wells (NV) event. Also shown are the stations within 100 km that recorded the event.

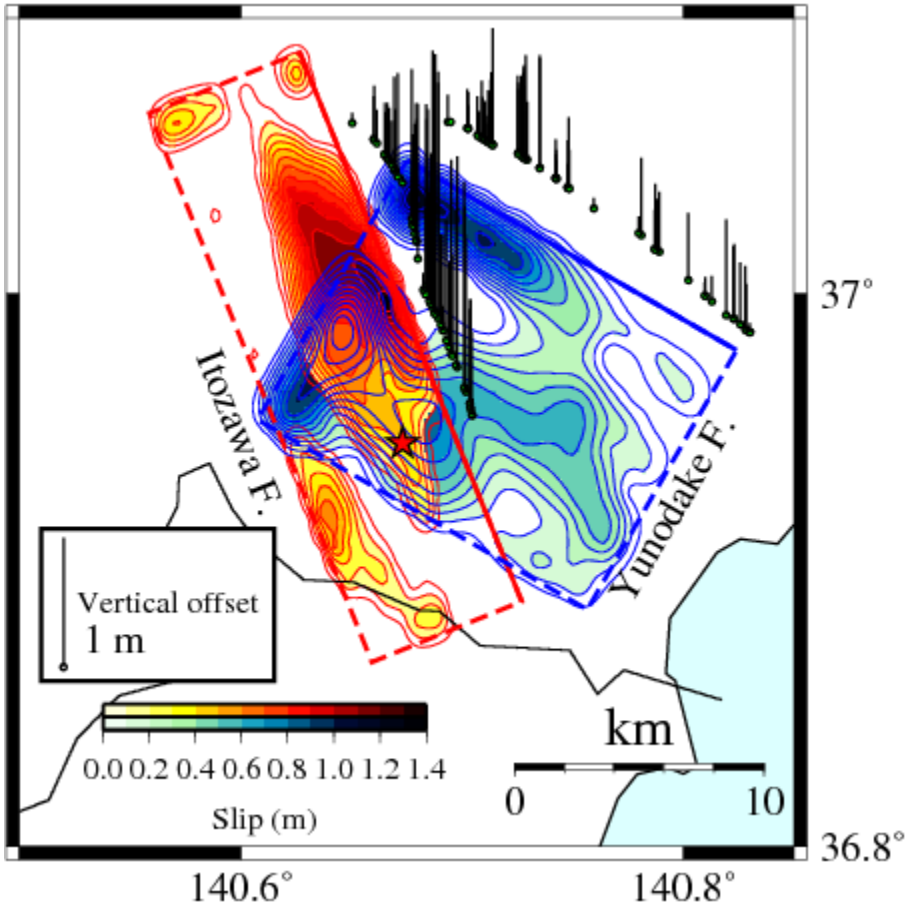

Figure 5.1.5-2: Map showing the slip distribution and the vertical offset associated to the 2011 April 11 Fukushima-Hamadori inland earthquake (Figure from Shiba and Noguchi, 2012).

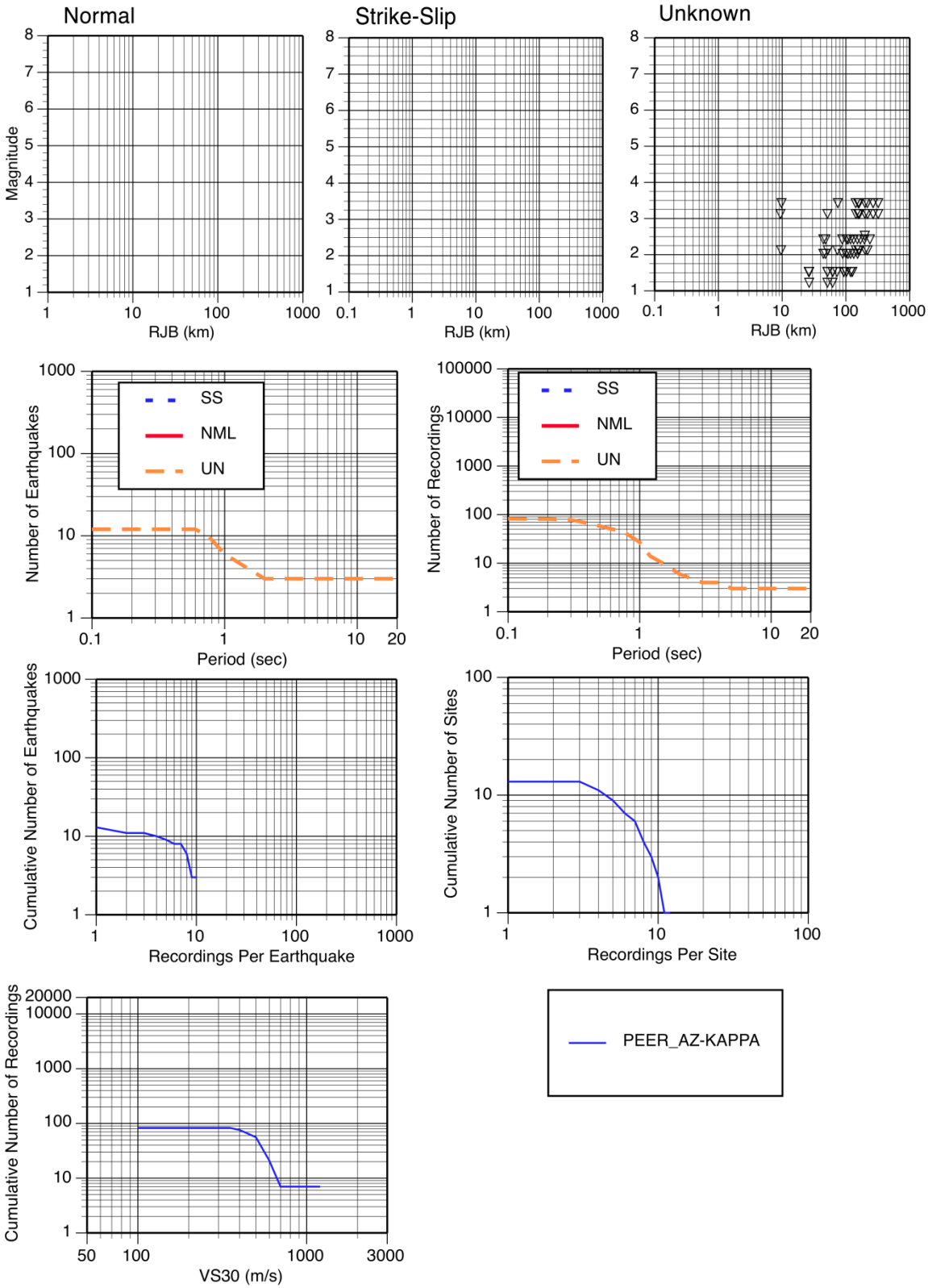

Figure 5.1.7-1: Summary of the distribution of data for the PEER-AZ$_{KAPPA}$ dataset.

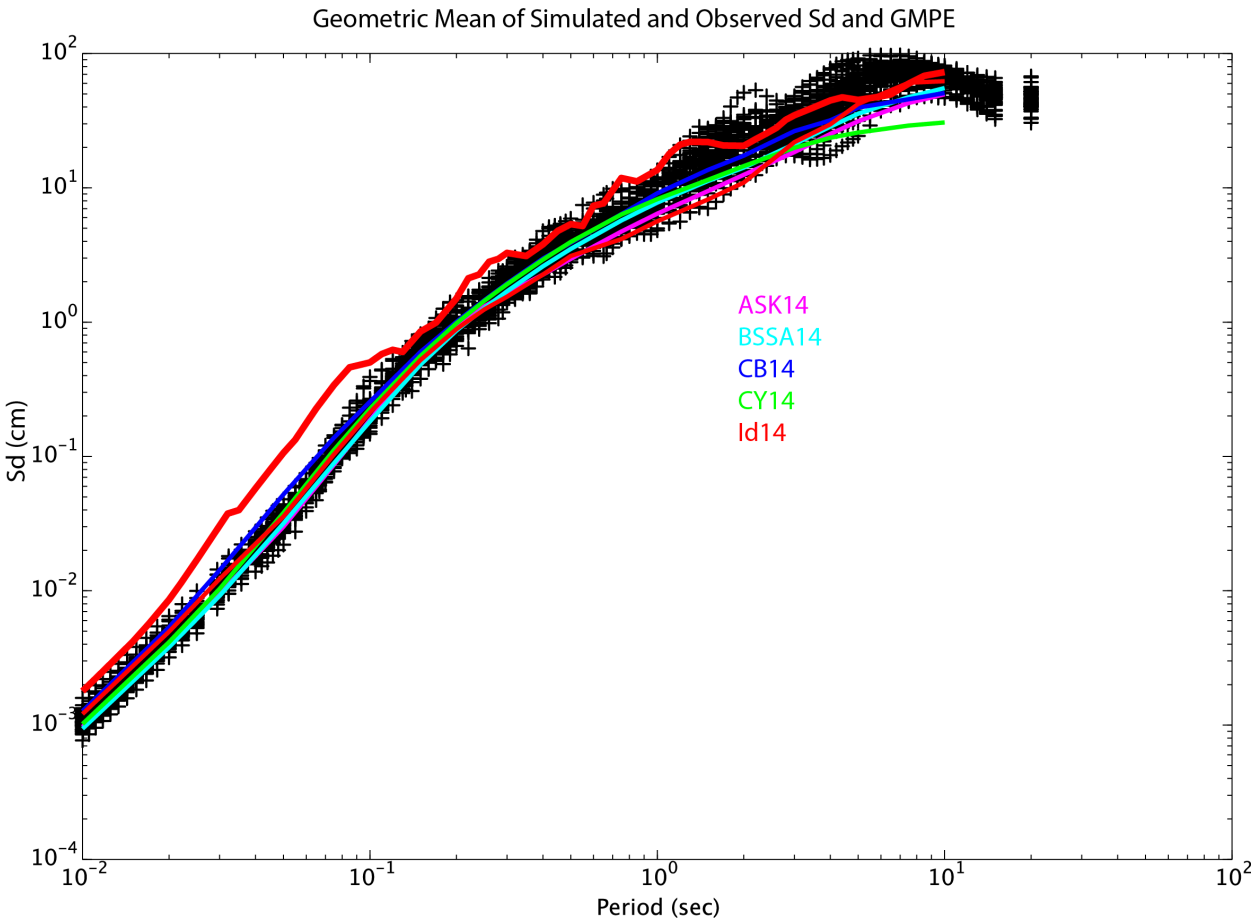

Figure 5.2.1-1: Comparison of the geometric mean of the observed spectral displacement (SD) for the fault normal and fault parallel components (thick red line), the geometric mean of simulated FP and FN SD for the 50 source realizations, and the median SD from the NGA-West2 GMPE relationships (thin colored lines) for station LCN.

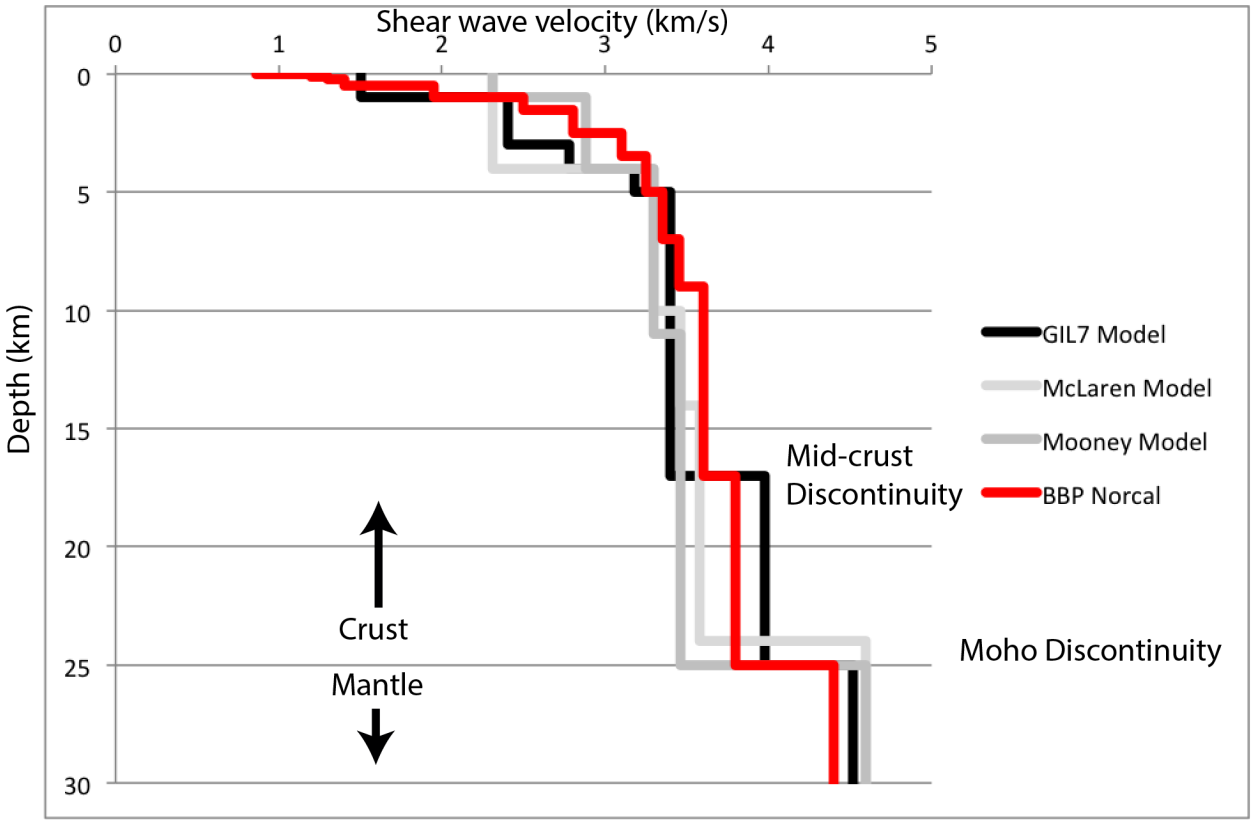

Figure 5.2.2-1: Comparison of 1D velocity models for the Central Coast Region. S-wave velocity is shown in km/s. The red curve show the velocity model used in the SWUS simulations.

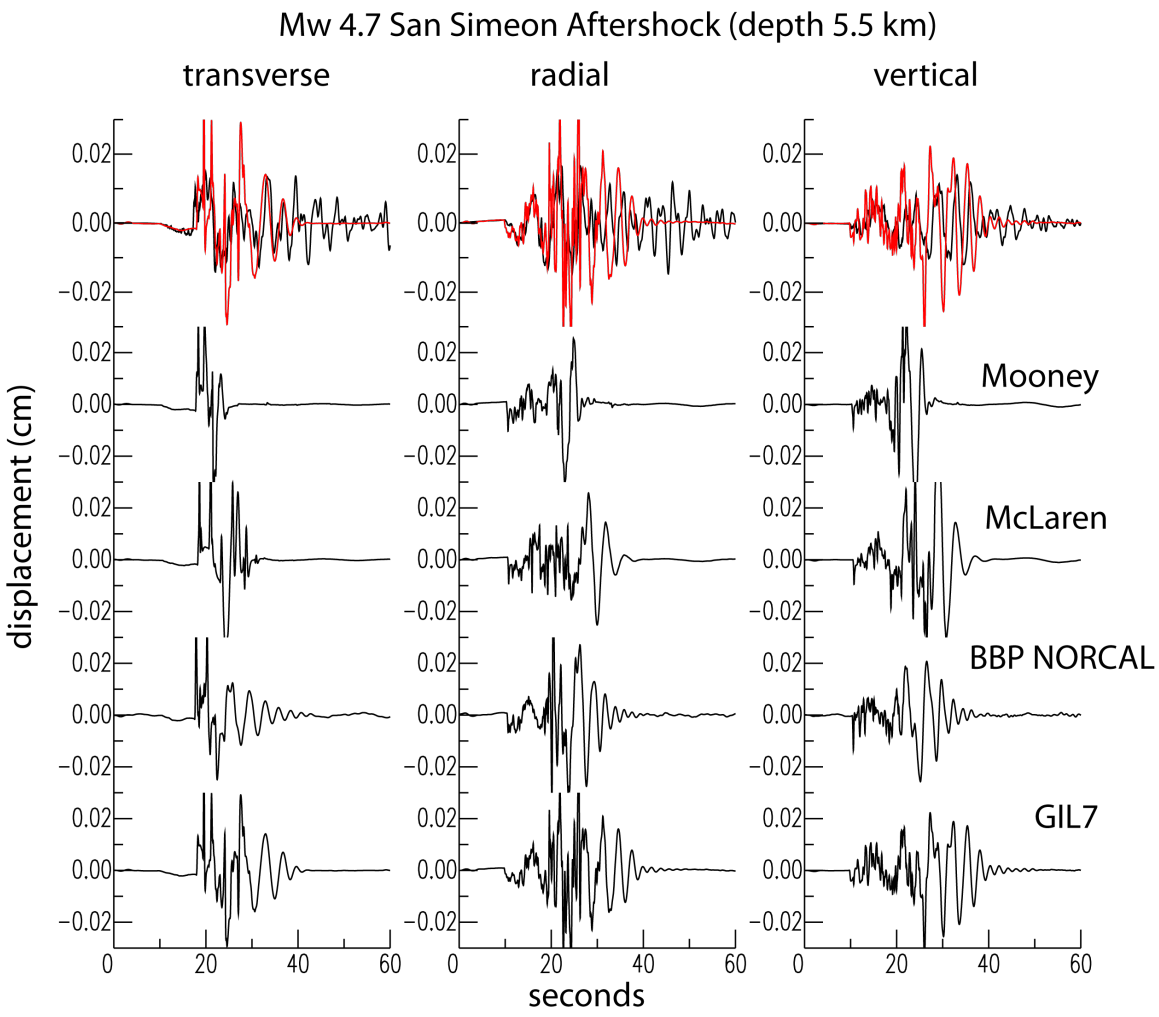

Figure 5.2.2-2: (top row) Comparison of broadband (0 to 25 Hz) data (black) of the **M**4.7 San Simeon aftershock recorded at PKD, and GIL7 synthetic seismogram (red). Rows 2-5 compare the broadband synthetics for three central coast velocity models with the BBP northern California model.

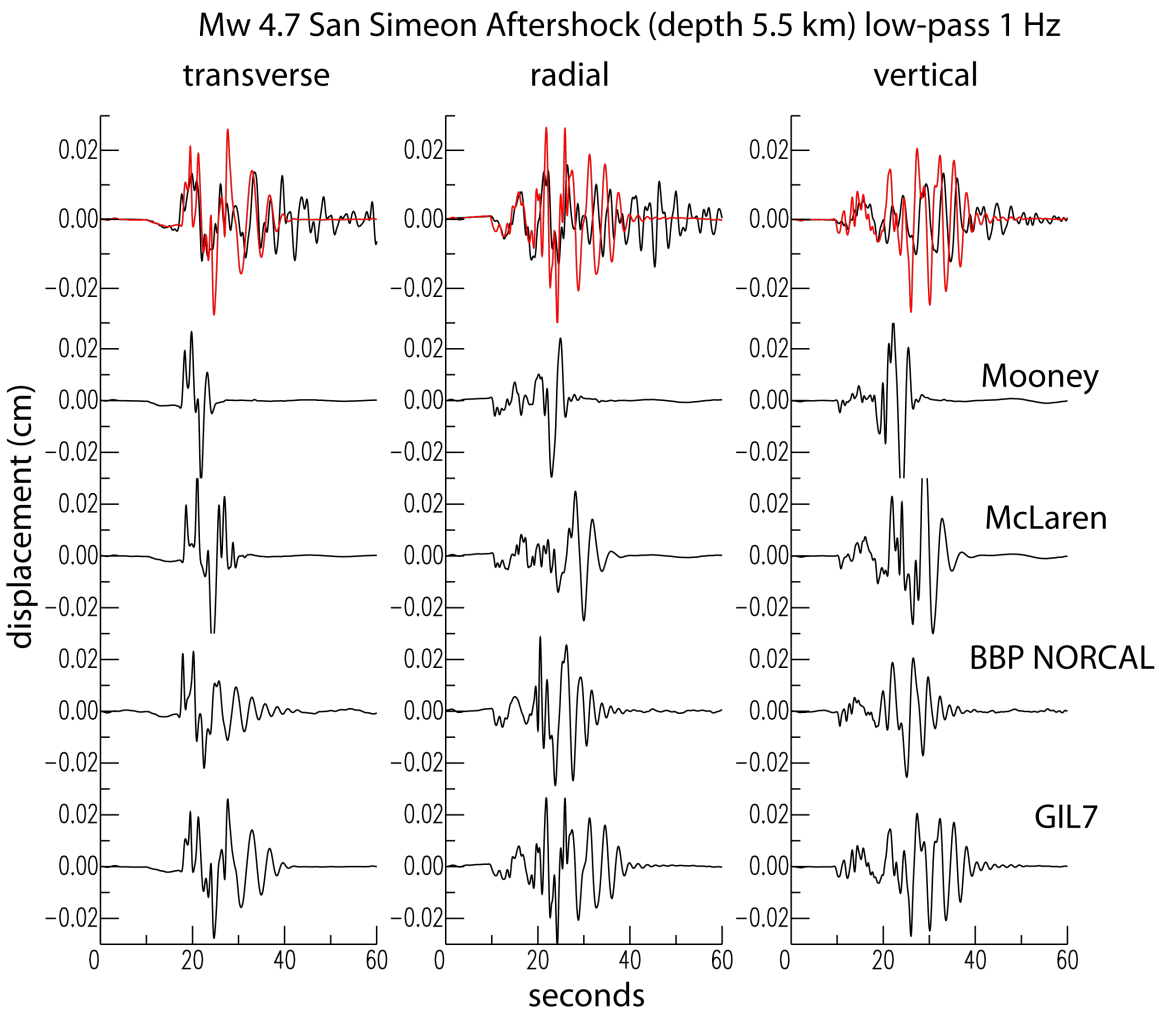

Figure 5.2.2-3: Same as Figure 5.2.2-2 except that the records have been low-pass filtered at 1 Hz with an acausal, 4-pole Butterworth filter.

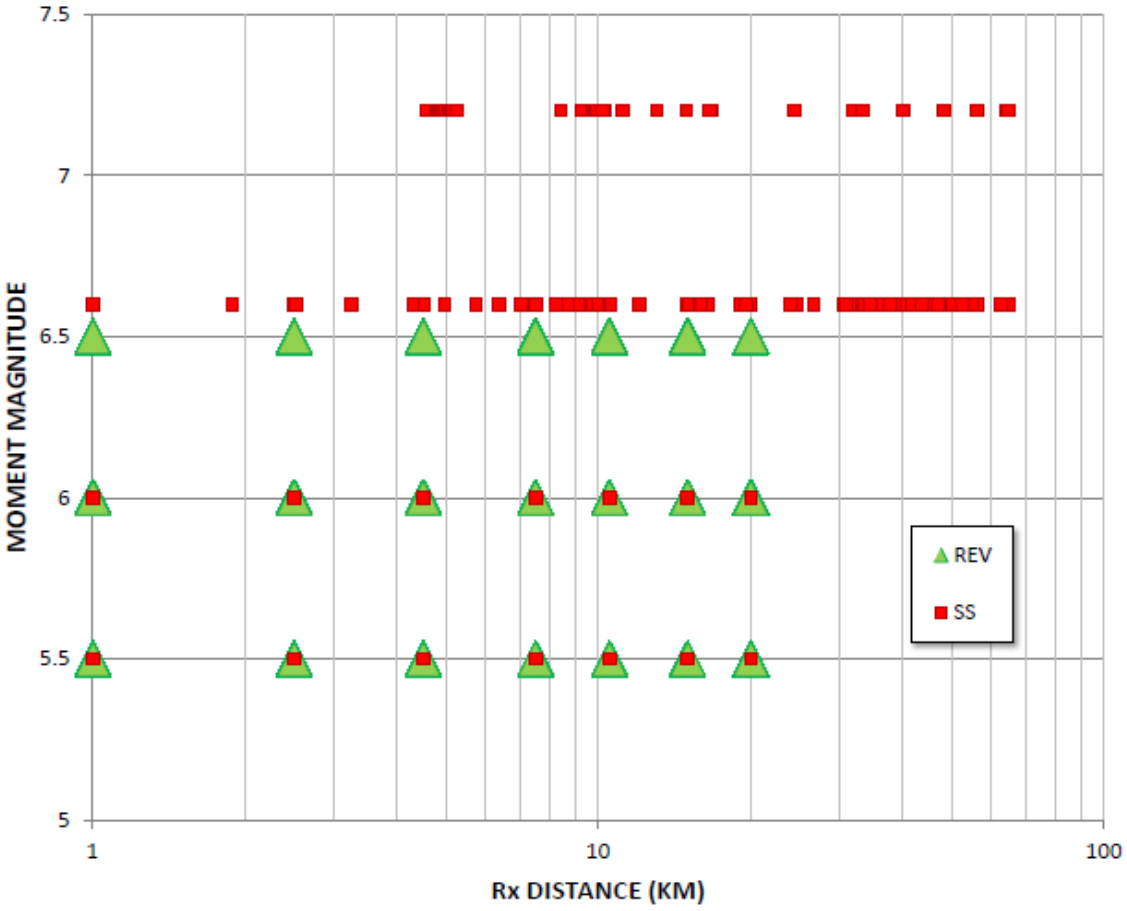

Figure 5.2.3-1: Simulations used in development of the ground-motion models for DCPP.

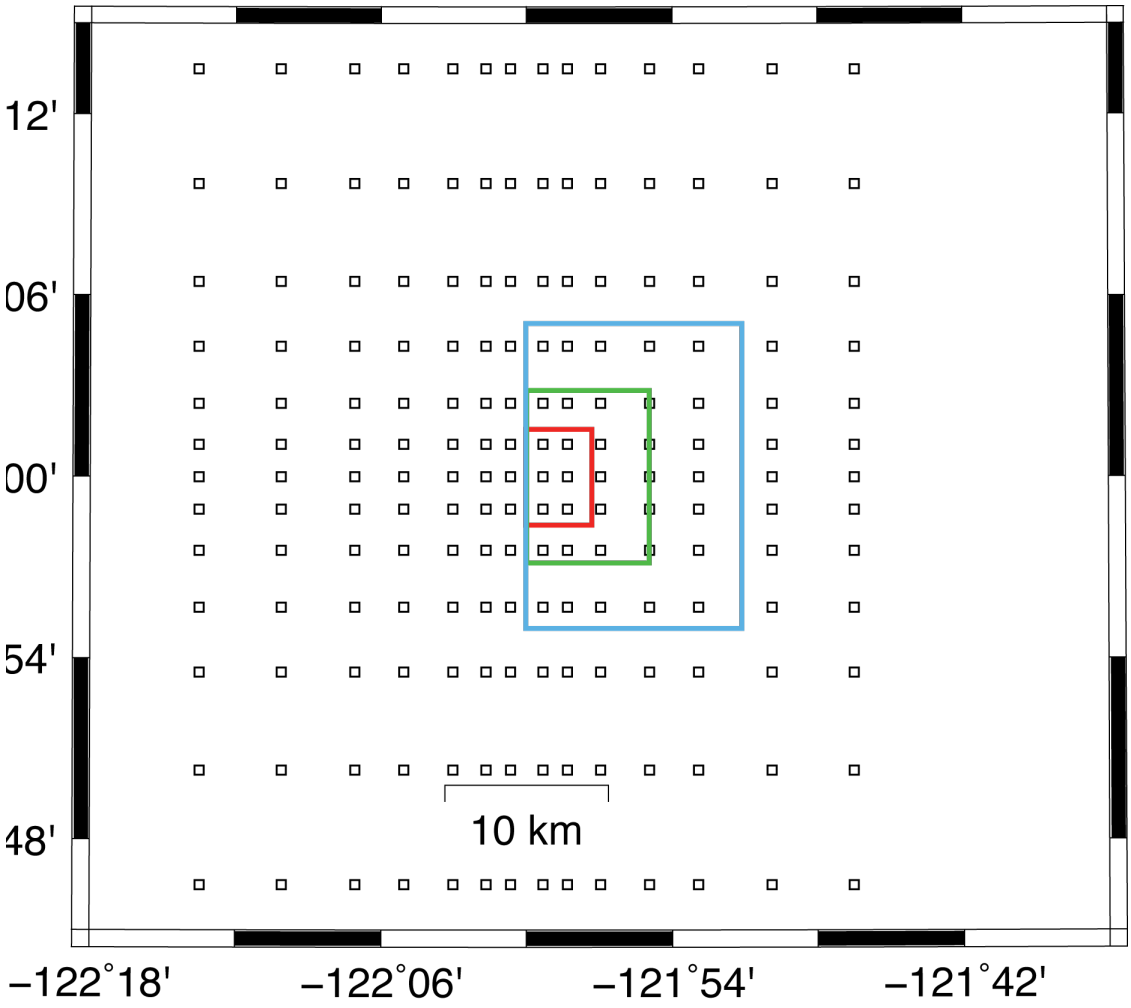

Figure 5.2.3-2: Station Layout for the Simple Planar Ruptures with respect to the **M**5.5 (red), **M**6.0 (green), and **M**6.5 (blue) faults. The rectangles show the surface projection of the faults for the 45-degree dip case.

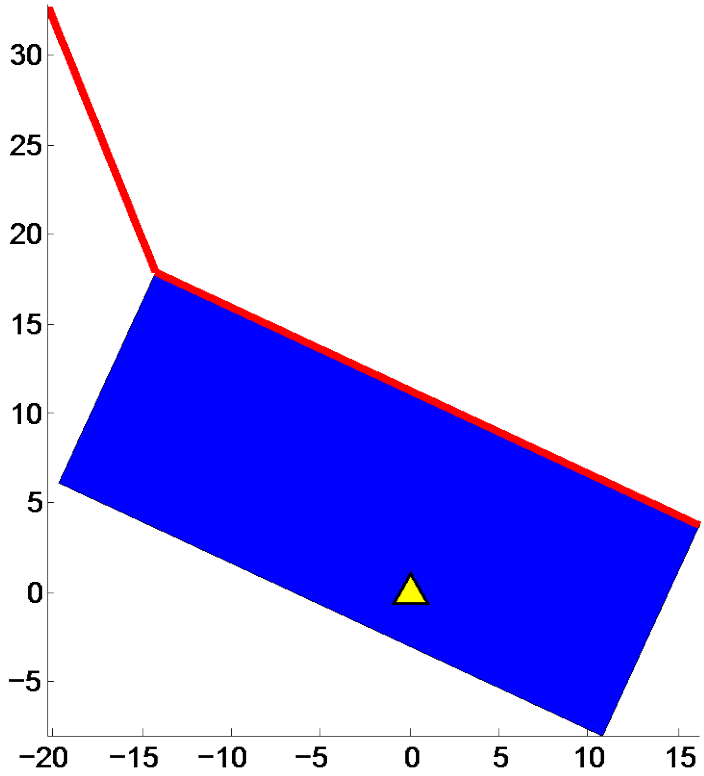

Figure 5.2.3-3: Schematic fault geometry for the Complex Scenario 1, in this case associated to **M**7. The yellow triangle represents a reference site for which to evaluate the ground-motion scaling due to the complex ruptures.

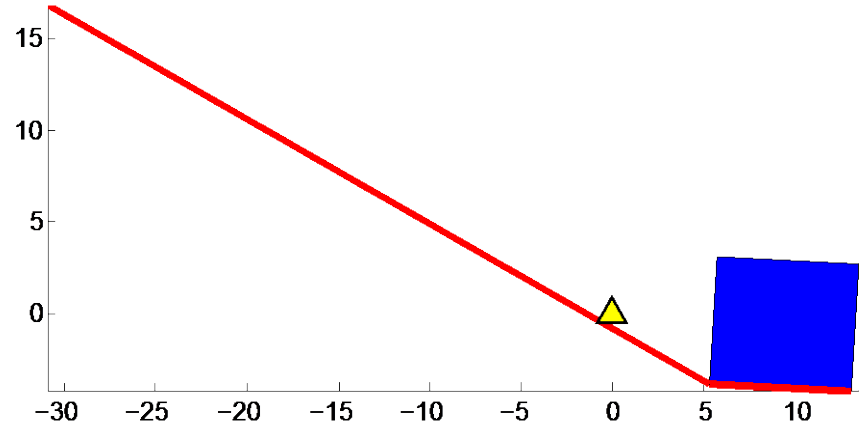

Figure 5.2.3-4: Schematic fault geometry for the Complex Scenario 2, in this case associated to **M**7. The yellow triangle represents a reference site for which to evaluate the ground-motion scaling due to the complex ruptures.

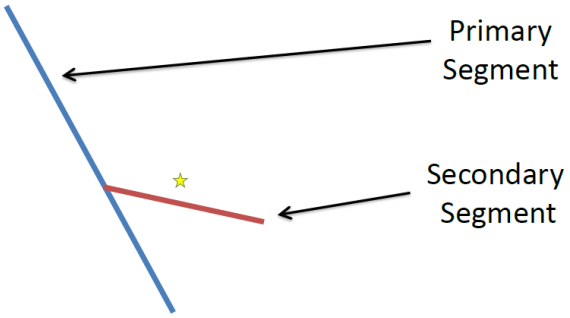

Figure 5.2.3-5: Schematic representation of a splay fault serving for reference on terminology.

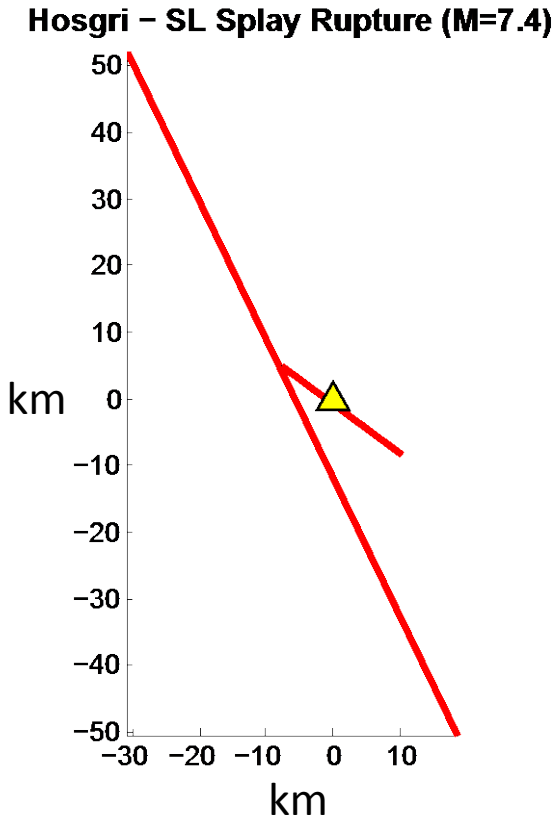

Figure 5.2.3-6: Schematic fault geometry for the Splay Scenario 1, in this case associated to **M**7.4. The yellow triangle represents a reference site for which to evaluate the ground-motion scaling due to the splay ruptures.

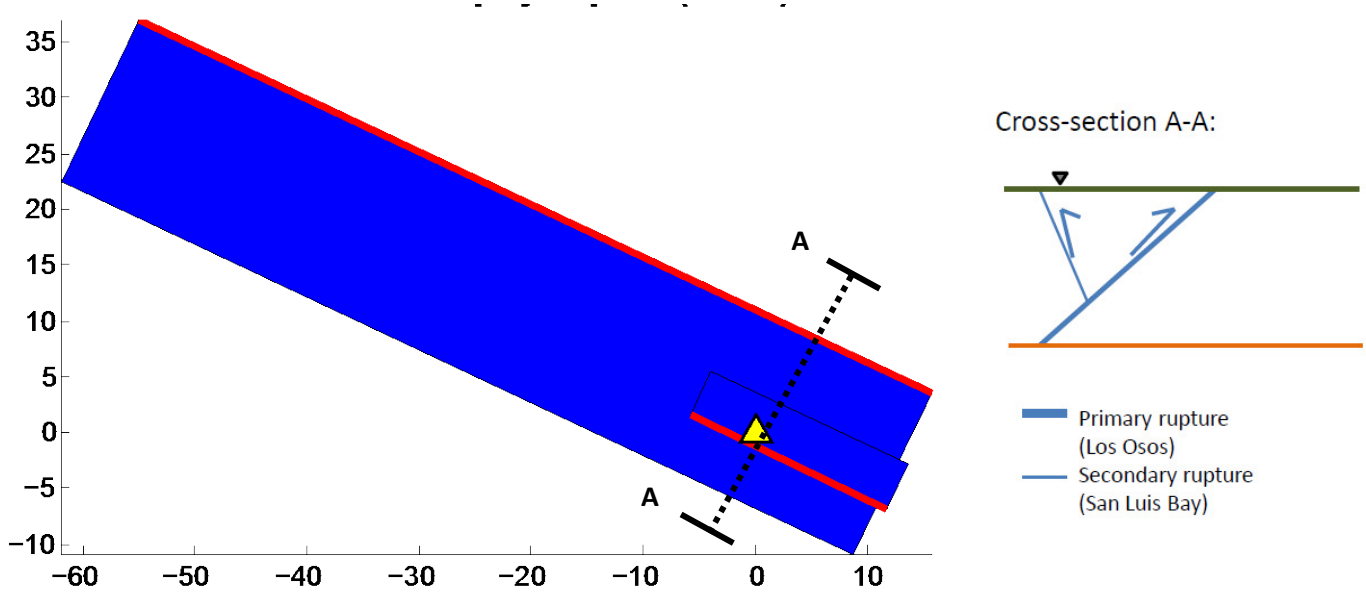

Figure 5.2.3-7: Schematic fault geometry for the Splay Scenario 2, in this case associated to **M**7.4. The yellow triangle represents a reference site for which to evaluate the ground-motion scaling due to the splay ruptures.

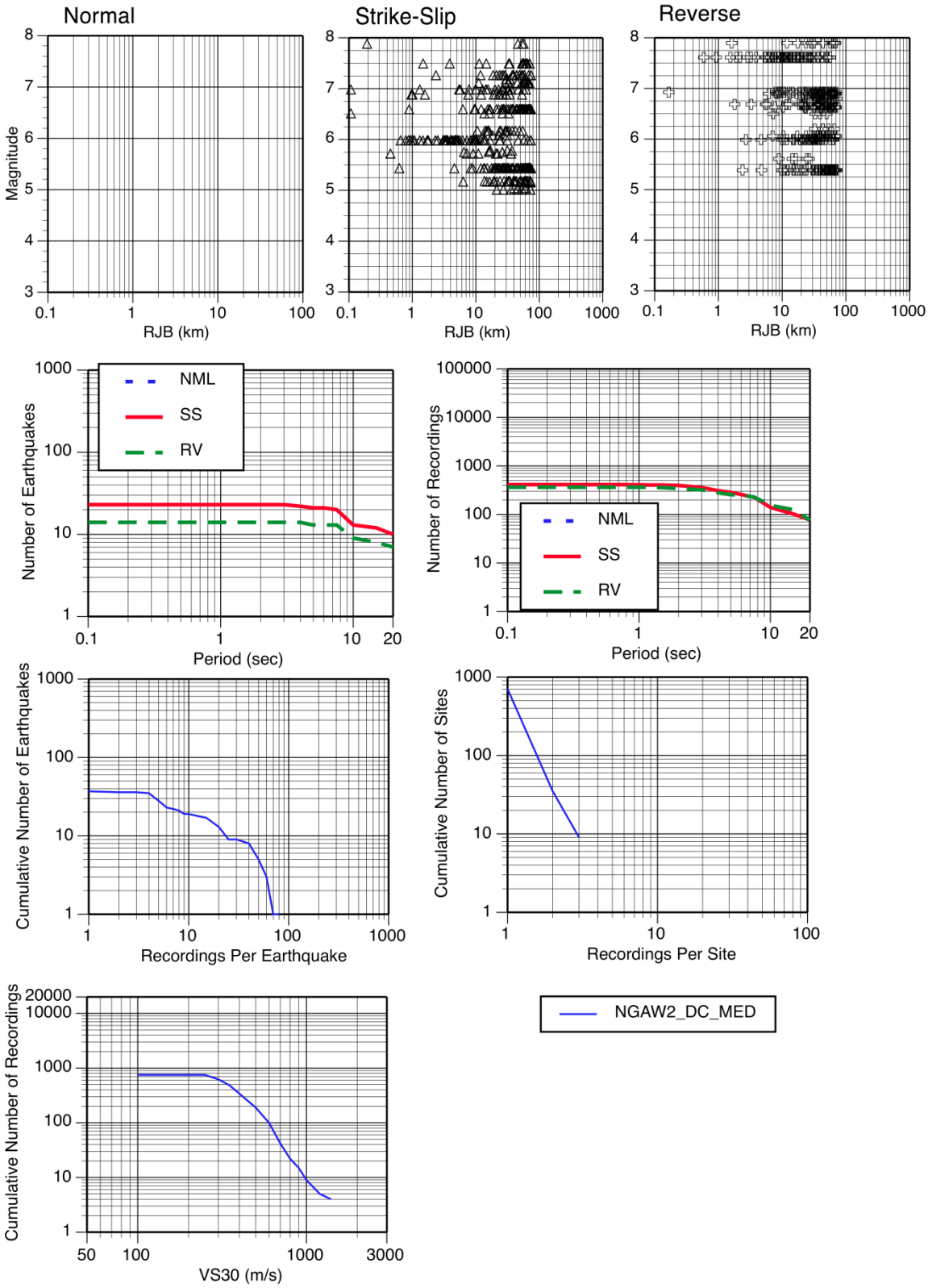

Figure 5.3.1-1: Summary of the data distribution of the NGA-W2$_{DC-MED}$ dataset.

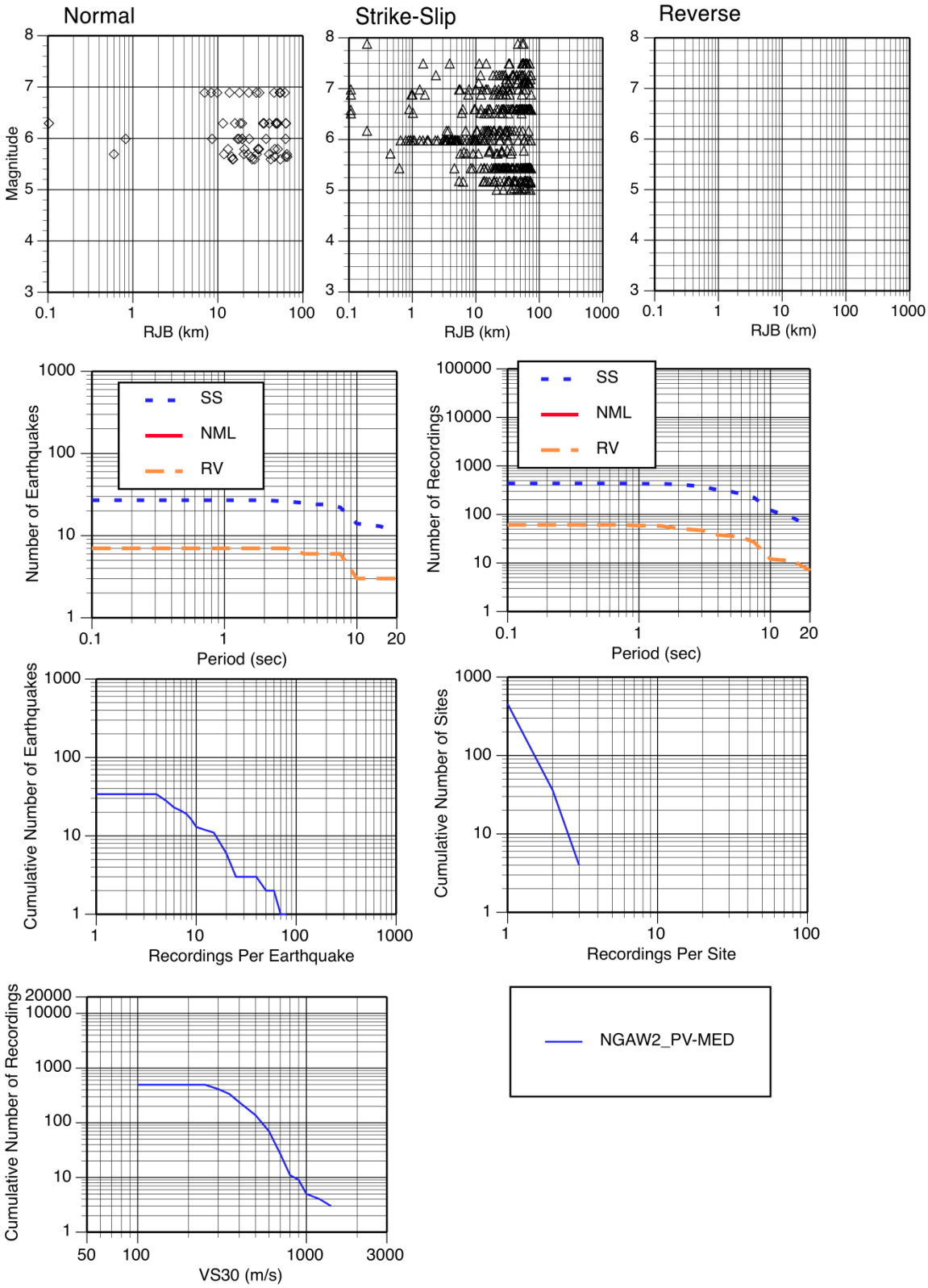

Figure 5.3.2-1: Summary of the data distribution of the NGA-W2$_{PV\text{-}MED}$ dataset.

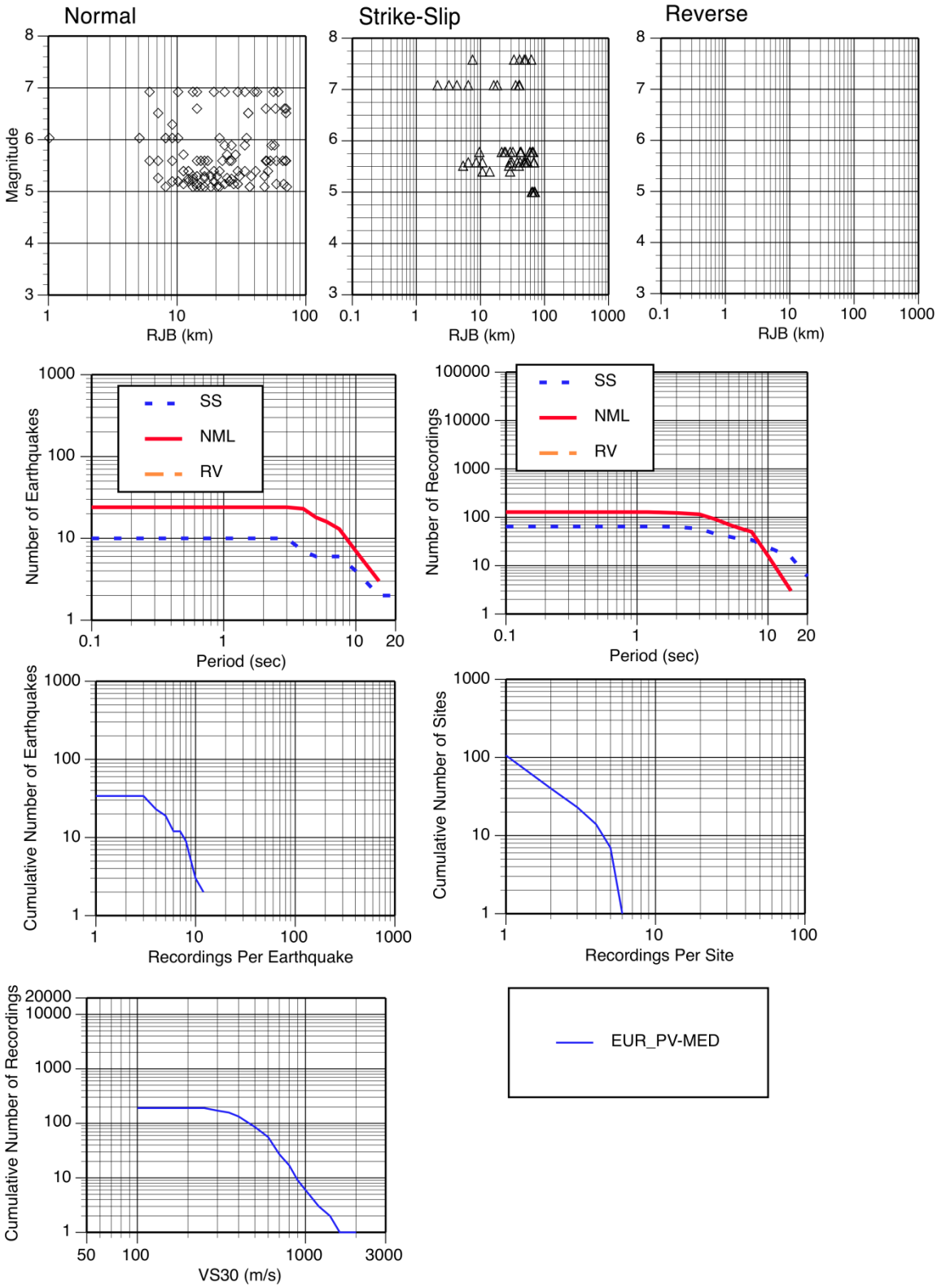

Figure 5.3.2-2: Summary of the data distribution of the $EUR_{PV\text{-}MED}$ dataset.

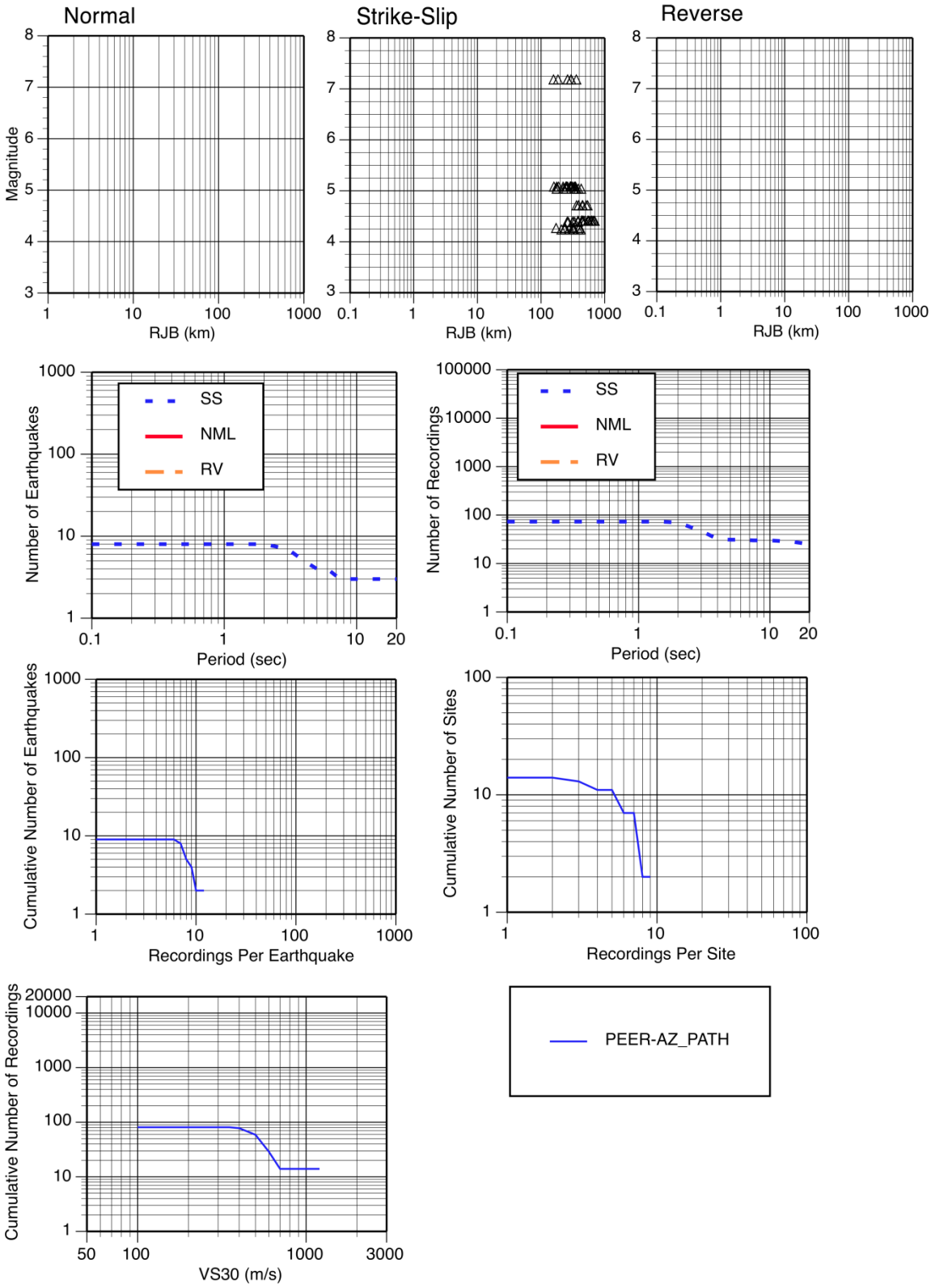

Figure 5.3.3-1: Summary of the data distribution of the PEER-AZ$_{PATH}$ dataset.

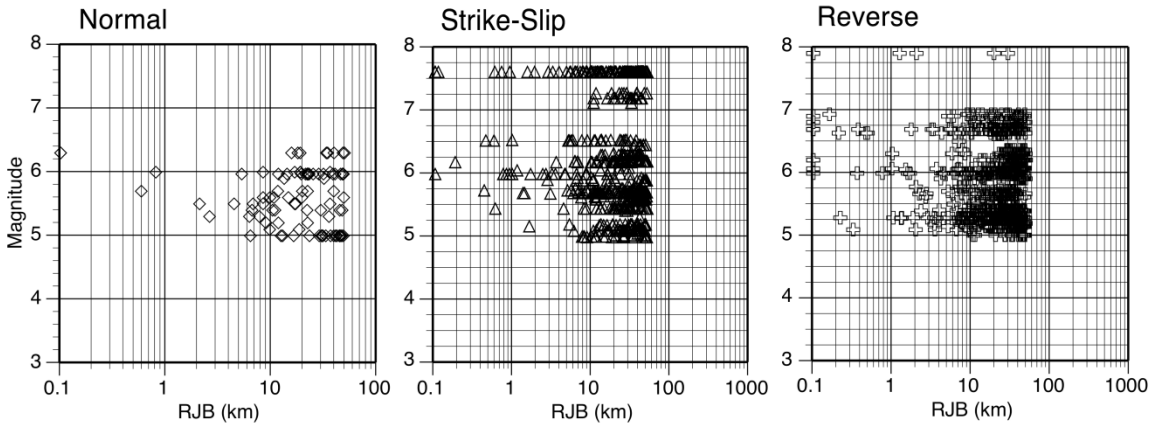

Figure 5.4.1-1: Magnitude-distance distribution of the $GLOBAL_{PHISS\text{-}ASK14}$ dataset.

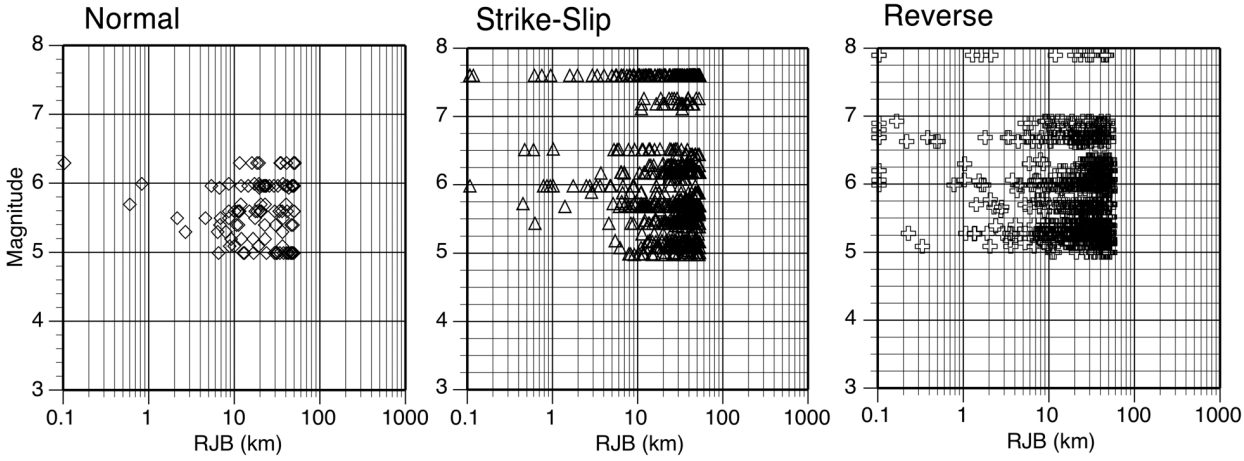

Figure 5.4.1-2: Magnitude-distance distribution of the $GLOBAL_{PHISS\text{-}BSSA14}$ dataset.

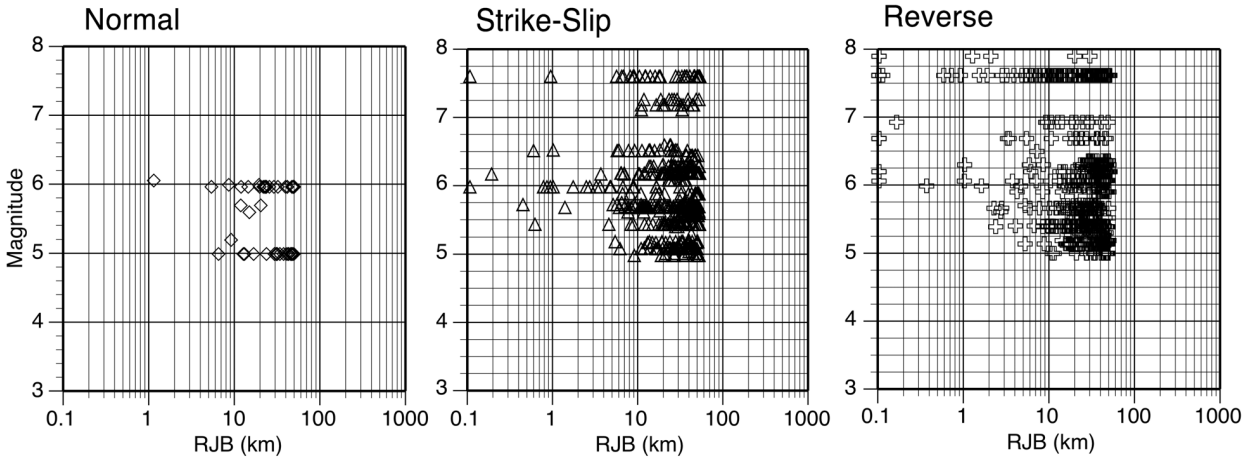

Figure 5.4.1-3: Magnitude-distance distribution of the GLOBAL$_{PHISS\text{-}CB14}$ dataset.

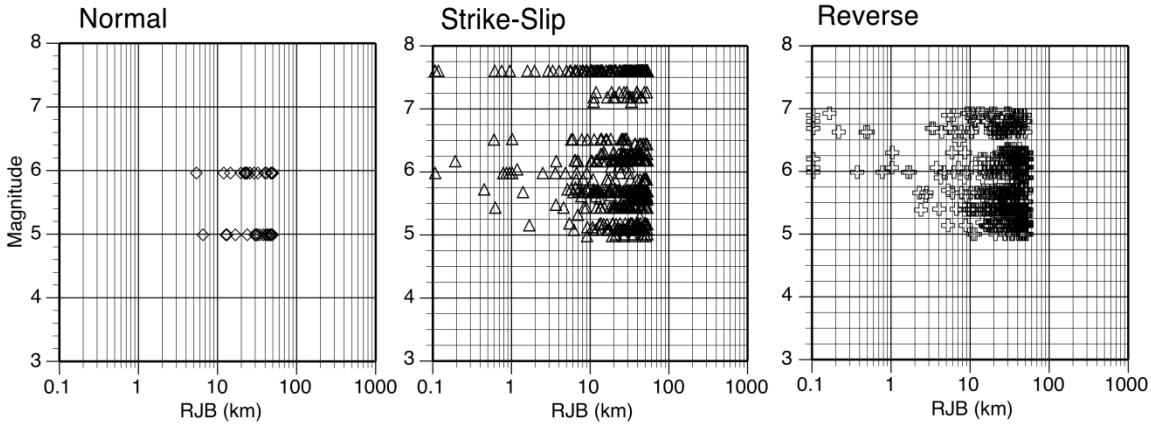

Figure 5.4.1-4: Magnitude-distance distribution of the GLOBAL$_{PHISS\text{-}CY14}$ dataset.

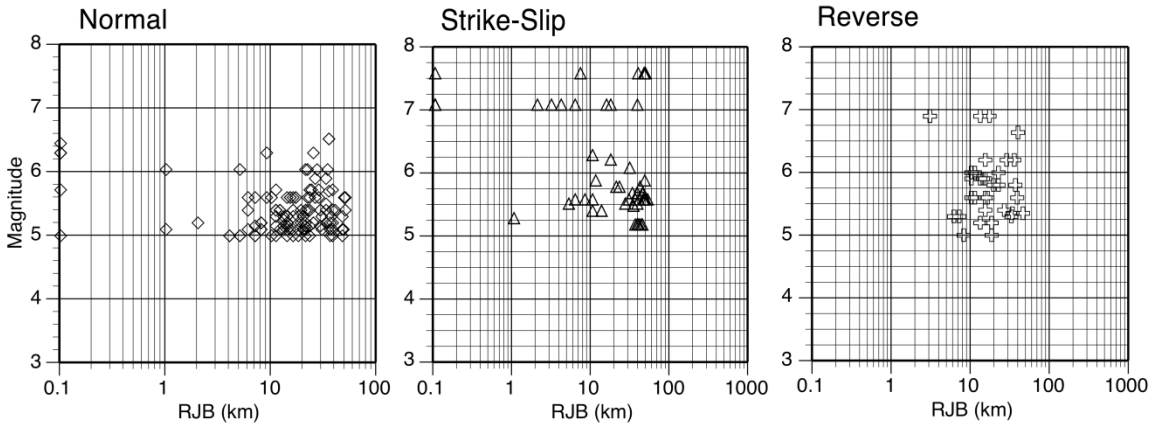

Figure 5.4.2-1: Magnitude-distance distribution of the EUR_{PHISS} dataset. (Note: the minimum of 3 recordings per earthquake and per site is applied to the full data set. This plot only shows the subset for distance less than 50 km and magnitudes greater than 5.0)

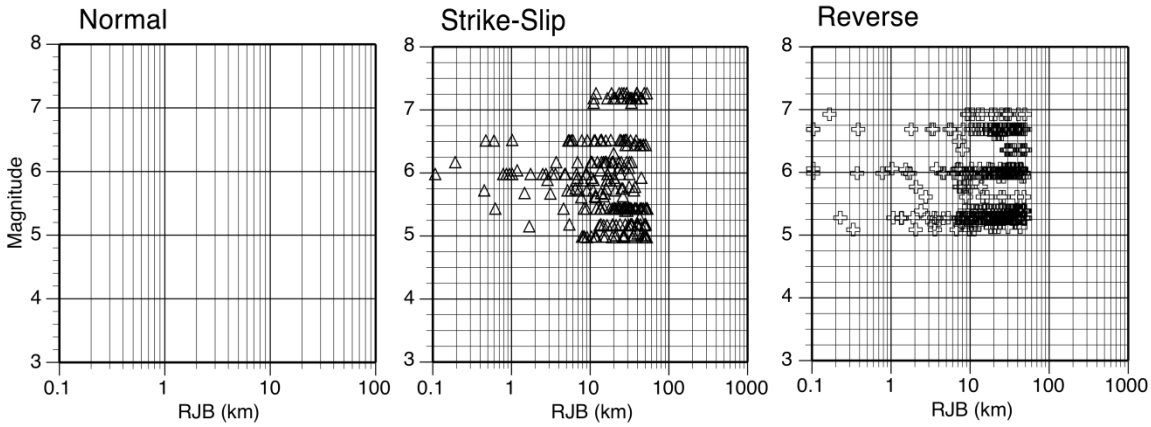

Figure 5.4.3-1: Magnitude-distance distribution of the NGA-W2$_{\text{CA-PHISS-ASK14}}$ dataset.

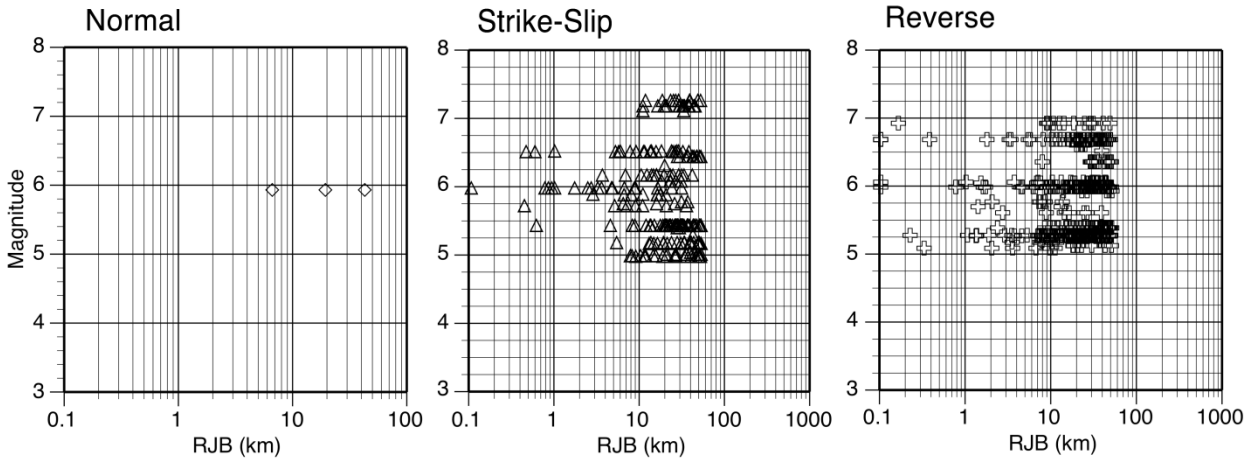

Figure 5.4.3-2: Magnitude-distance distribution of the NGA-W2$_{\text{CA-PHISS-BSSA14}}$ dataset.

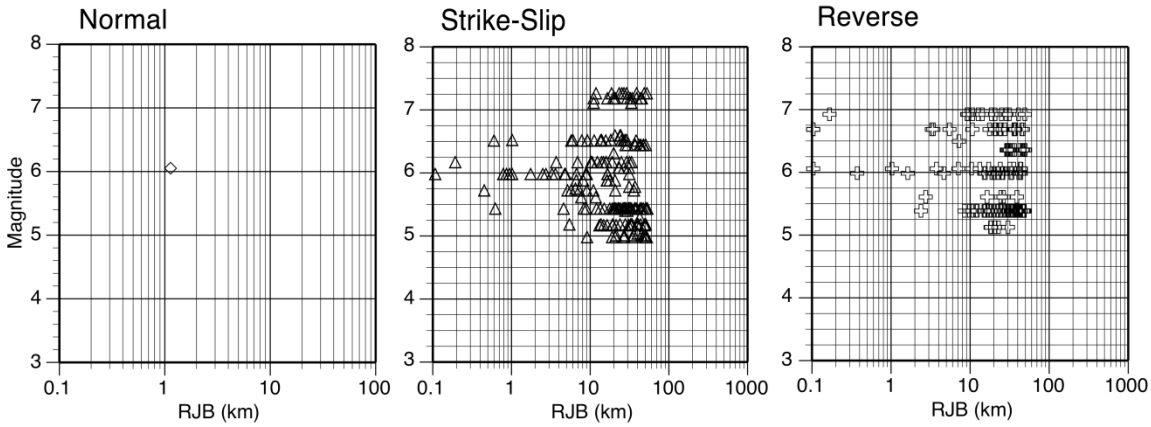

Figure 5.4.3-3: Magnitude-distance distribution of the NGA-W2$_{CA\text{-}PHISS\text{-}CB14}$ dataset.

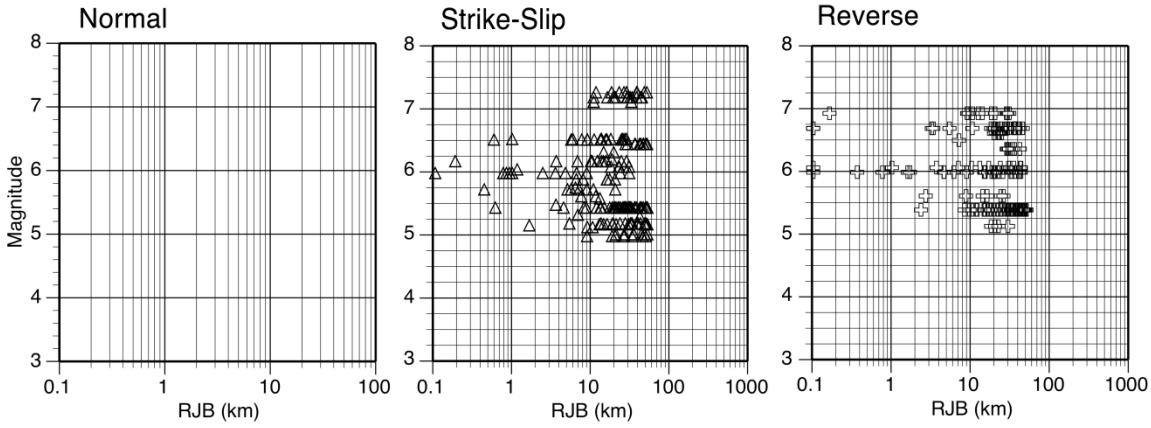

Figure 5.4.3-4: Magnitude-distance distribution of the NGA-W2$_{CA\text{-}PHISS\text{-}CY14}$ dataset.

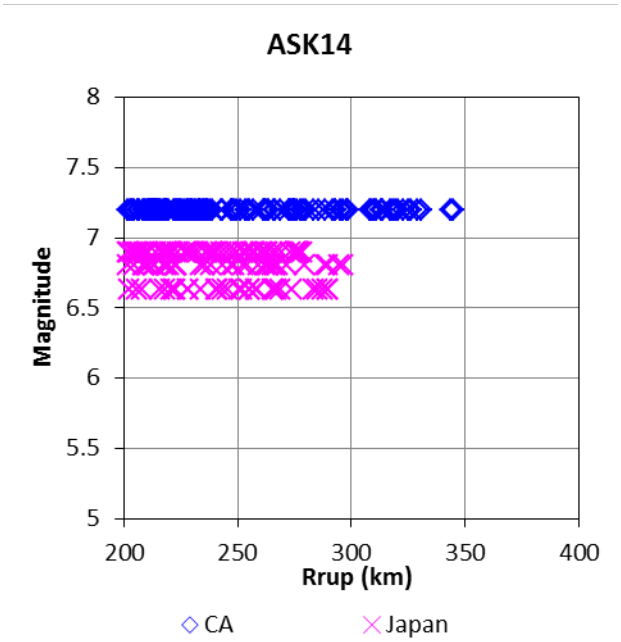

Figure 5.4.4-1: Magnitude-distance distribution of the NGA-W2$_{\text{LD-PHISS-ASK14}}$ dataset.

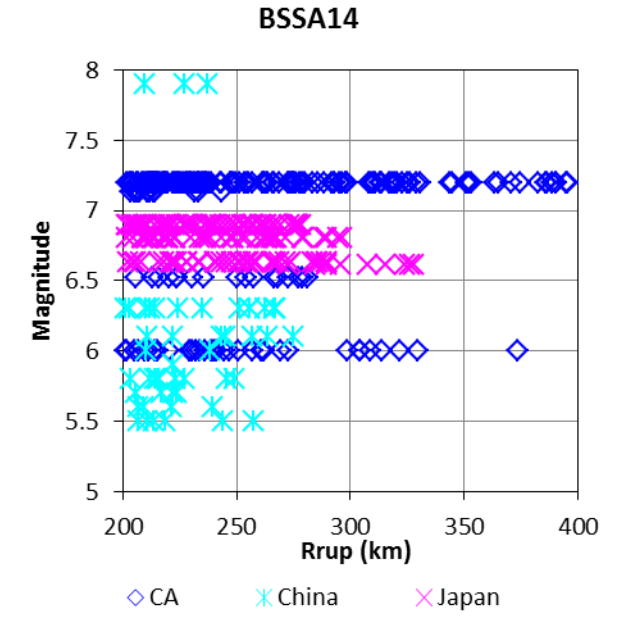

Figure 5.4.4-2: Magnitude-distance distribution of the NGA-W2$_{\text{LD-PHISS-BSSA14}}$ dataset.

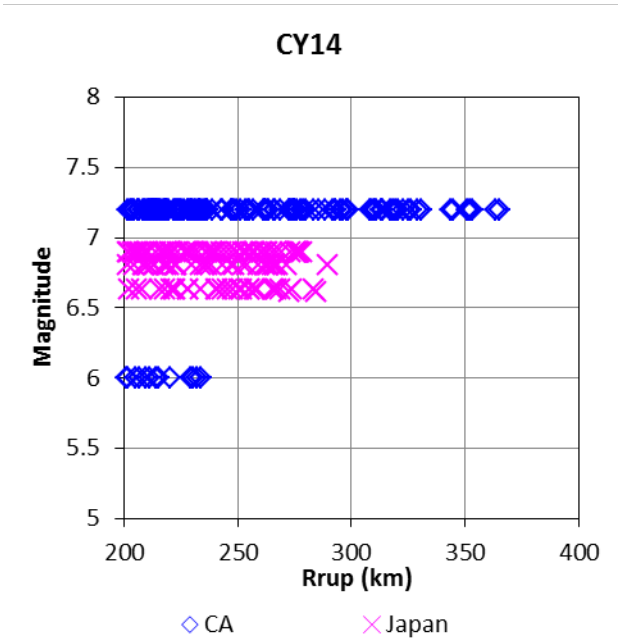

Figure 5.4.4-3: Magnitude-distance distribution of the NGA-W2$_{\text{LD-PHISS-CY14}}$ dataset.

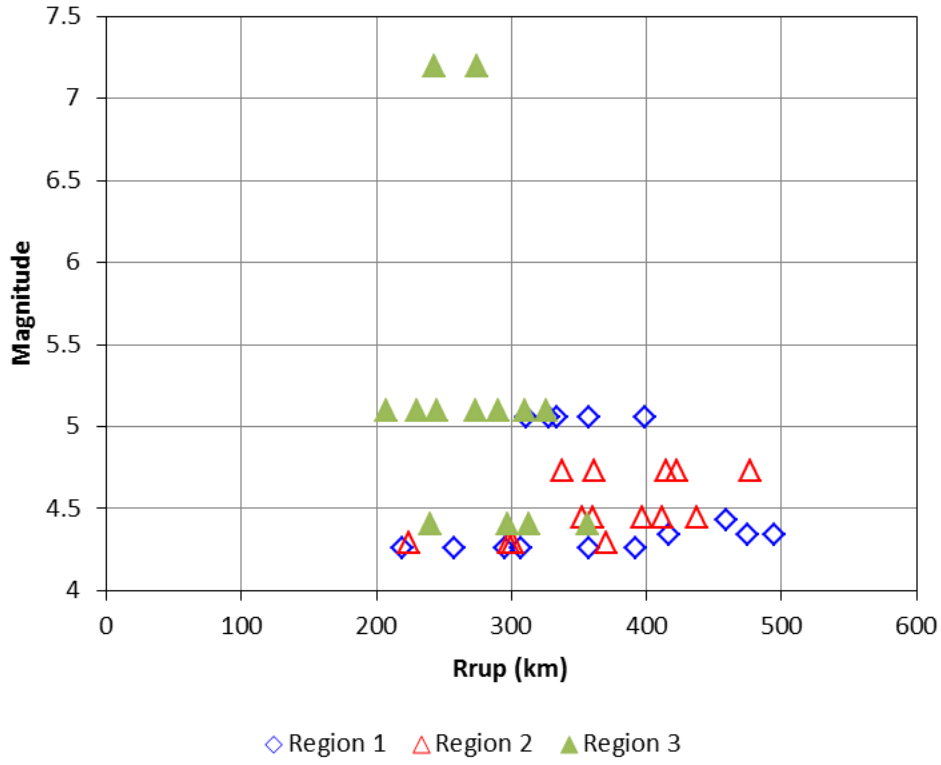

Figure 5.4.5-1: Magnitude-distance distribution of the PEER-AZ$_{\text{PATH}}$ dataset.

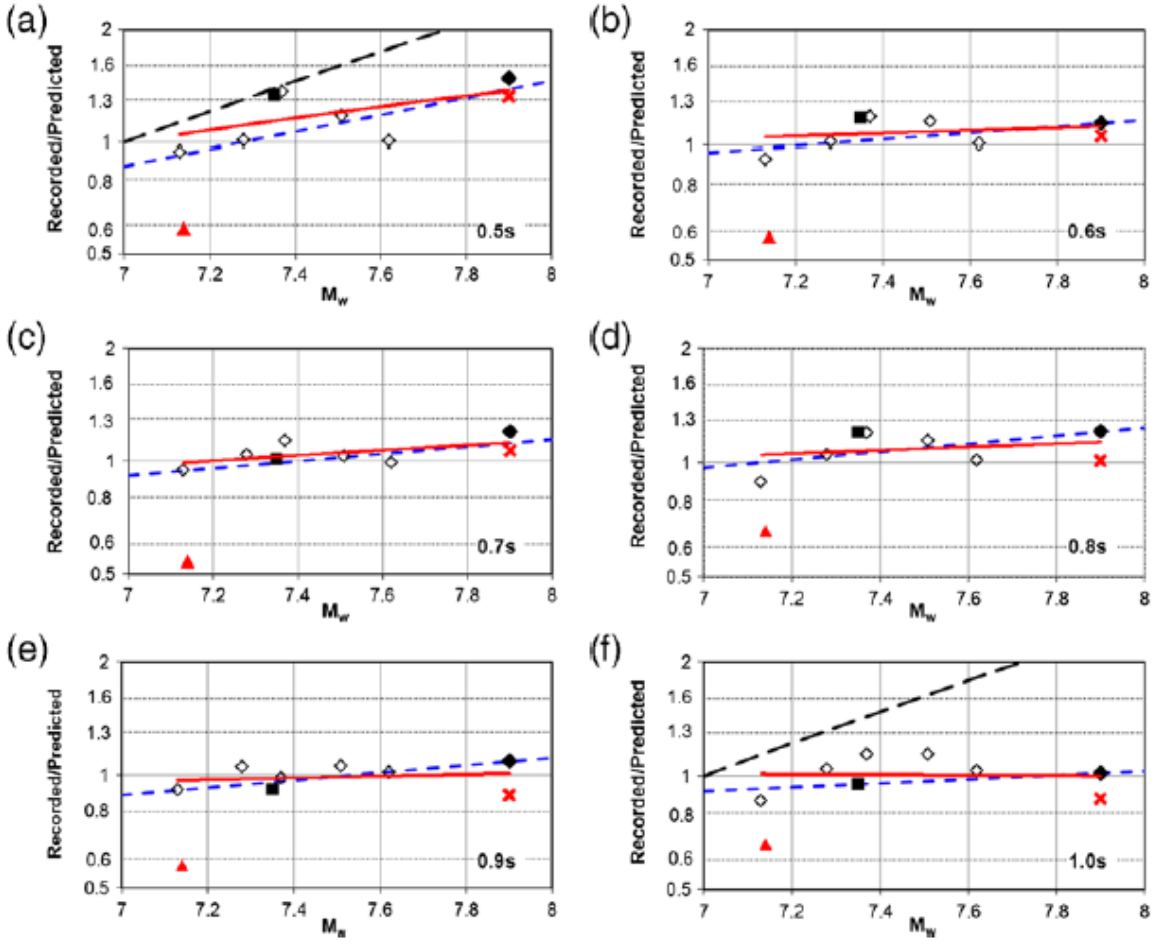

Figure 5.5.1-1: Average residuals for individual earthquakes versus magnitude for periods from 0.5 to 1.0 sec (from Zhao and Lu, 2011, Figure 14). Red triangle is 1999 Duzce earthquake and red X is 2002 Denali, Alaska earthquake. The red curve shows a linear fit to the average residual for each earthquake versus magnitude excluding the Duzce earthquake and the blue dashed line shows a fit including Duzce. The black long dash line is the magnitude scaling from Chiou and Youngs (2008) at a distance of 100 km.

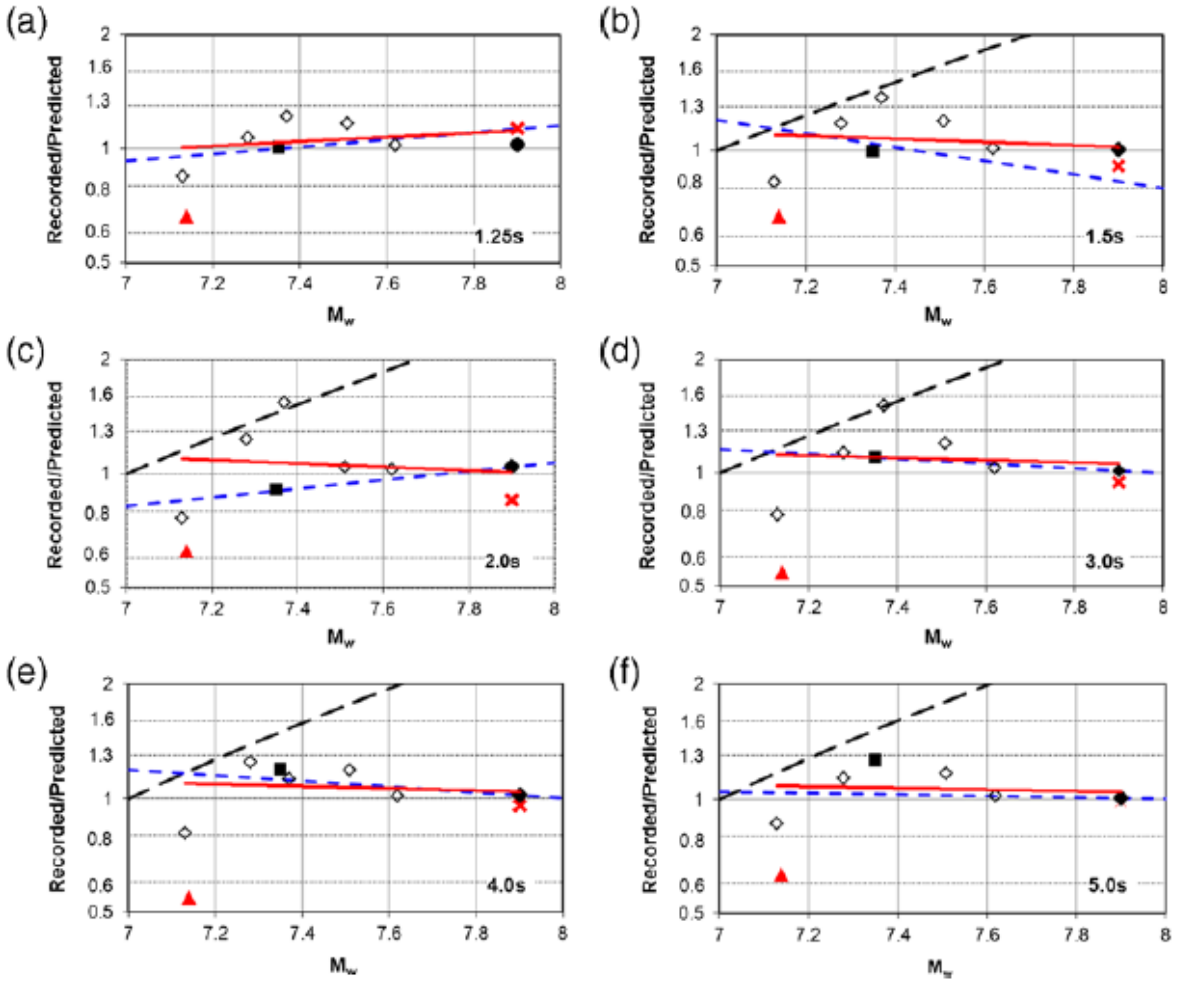

Figure 5.5.1-2: Average residuals for individual earthquakes versus magnitude for periods from 1.25 to 5.0 sec (from Zhao and Lu, 2011, Figure 14). Red triangle is 1999 Duzce earthquake and red X is 2002 Denali, Alaska earthquake. The red curve shows a linear fit to the average residual for each earthquake versus magnitude excluding the Duzce earthquake and the blue dashed line shows a fit including Duzce. The black long dash line is the magnitude scaling from Chiou and Youngs (2008) at a distance of 100 km.

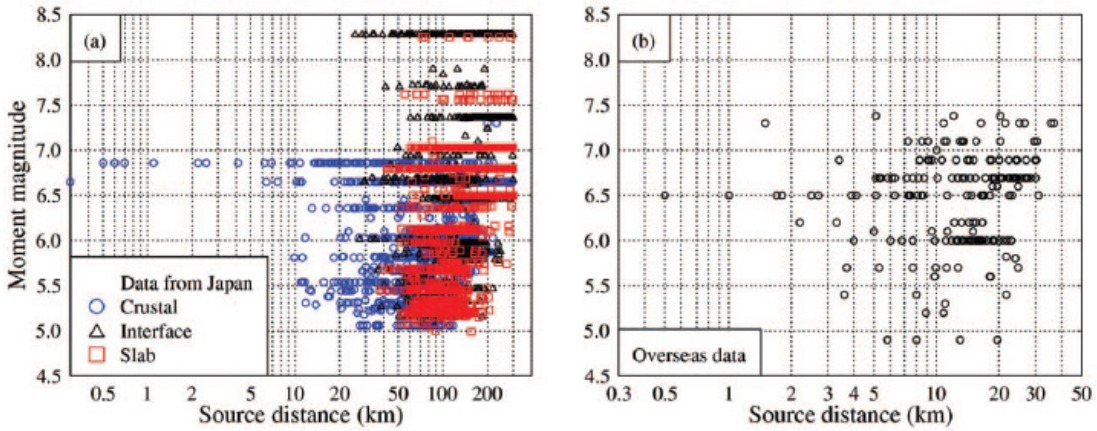

Figure 5.5.1-3: Magnitude distance distribution of data used by Zhao et al. (2006) (from Zhao et al., 2006, Figure 1).

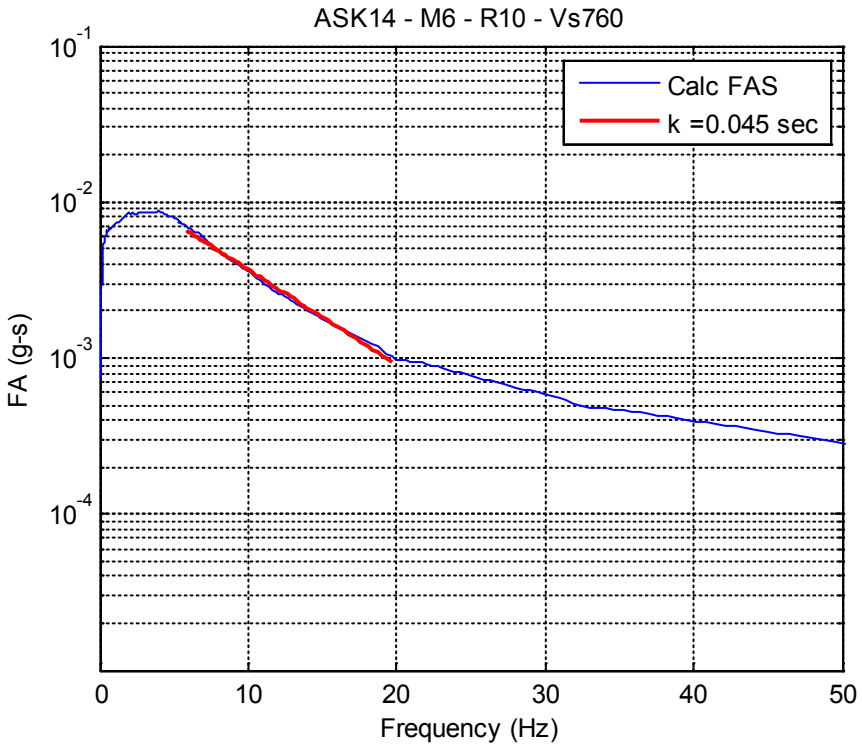

Figure 5.5.3-1: Host kappa value for ASK14 for the **M**6.0 and R_X = 10 km scenario.

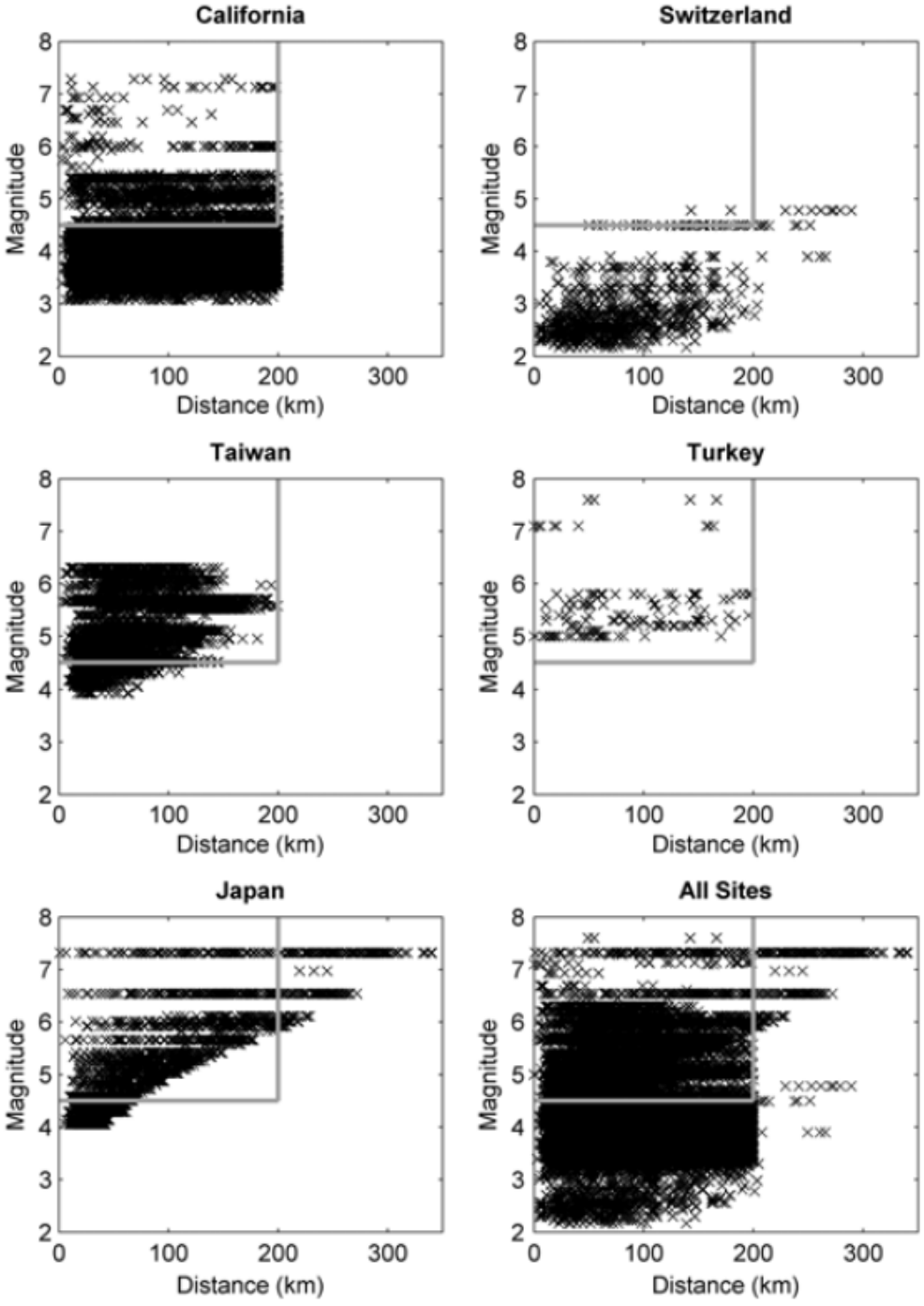

Figure 5.6.2-1: Distribution of data for single-station sigma as compiled by Rodriguez-Marek et al. (2013). (Figure from Rodriguez-Marek et al., 2013.)

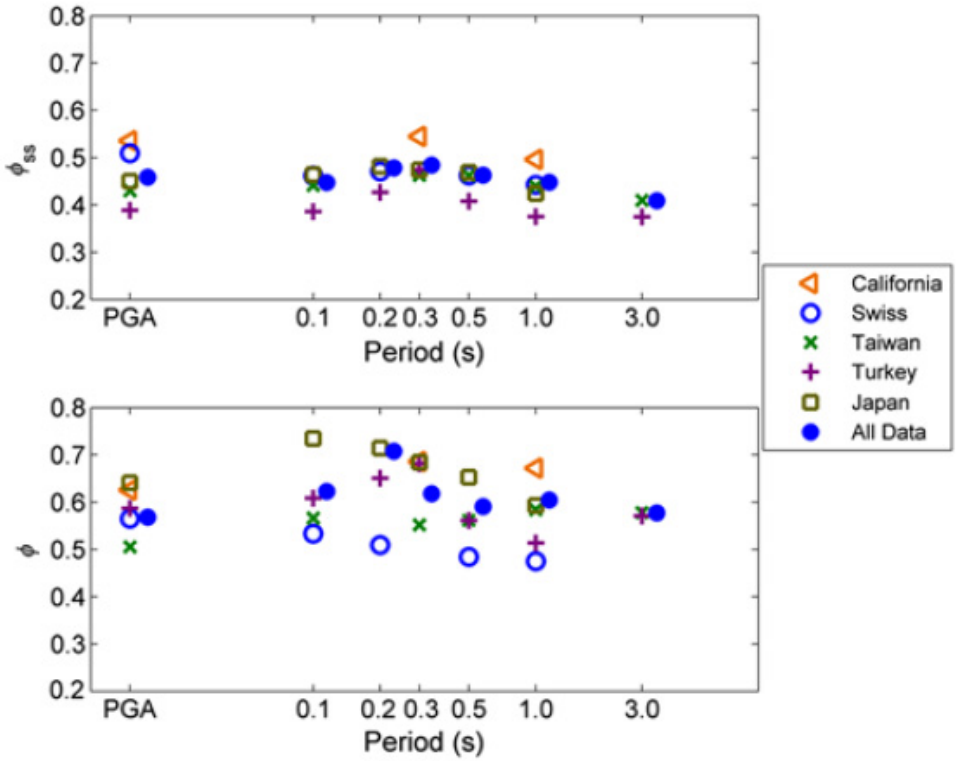

Figure 5.6.2-2: Top: regional dependence of the event-corrected single-station standard deviation ϕ_{SS}. Bottom: regional dependence of the ergodic within-event standard deviations ϕ (from Rodriguez-Marek et al., 2013).

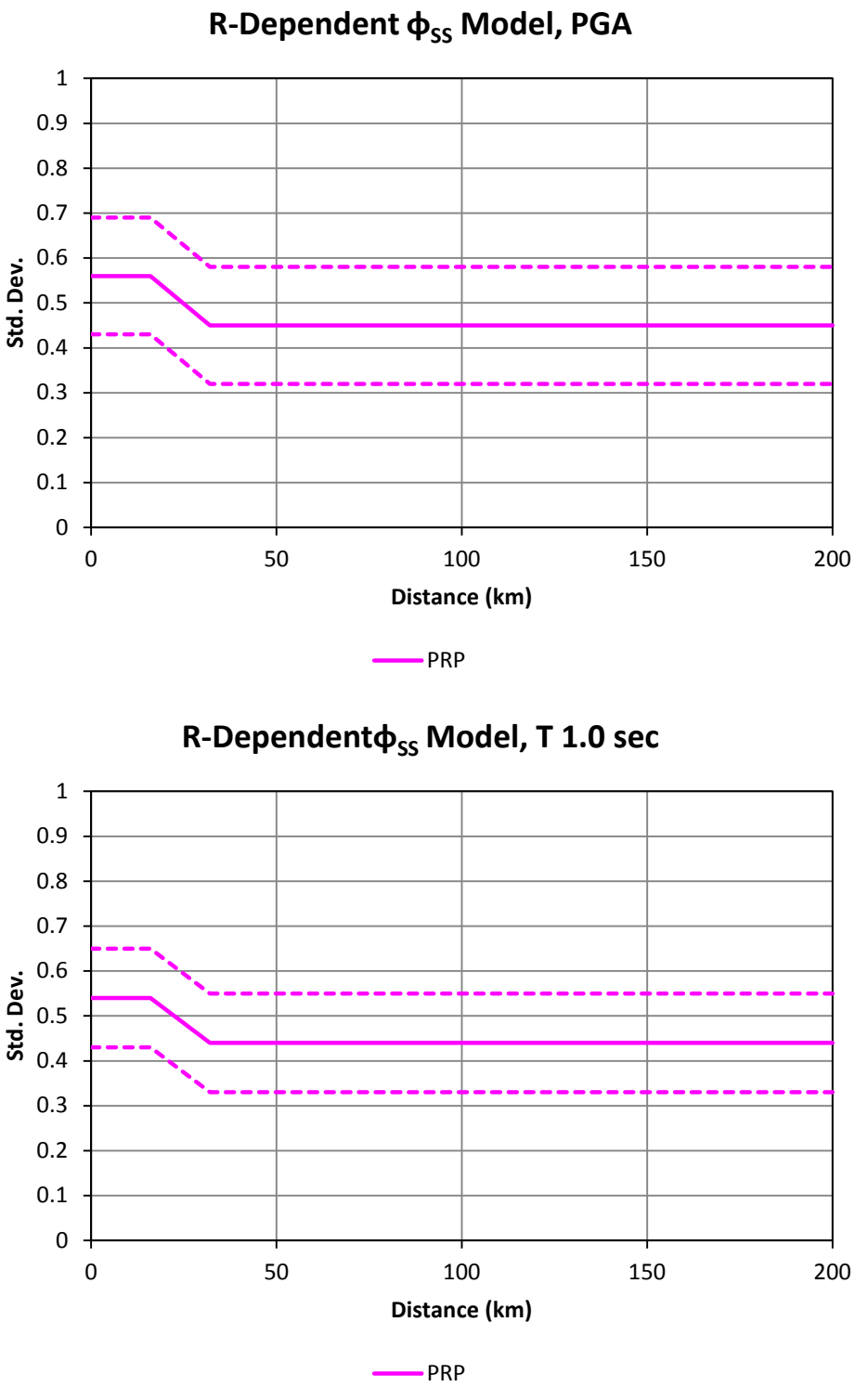

Figure 5.6.2-3: Rodriquez-Marek et al (2013) PRP distance-dependent ϕ_{SS} models (central, upper, and lower branches) for PGA and spectral period of 1.0 seconds.

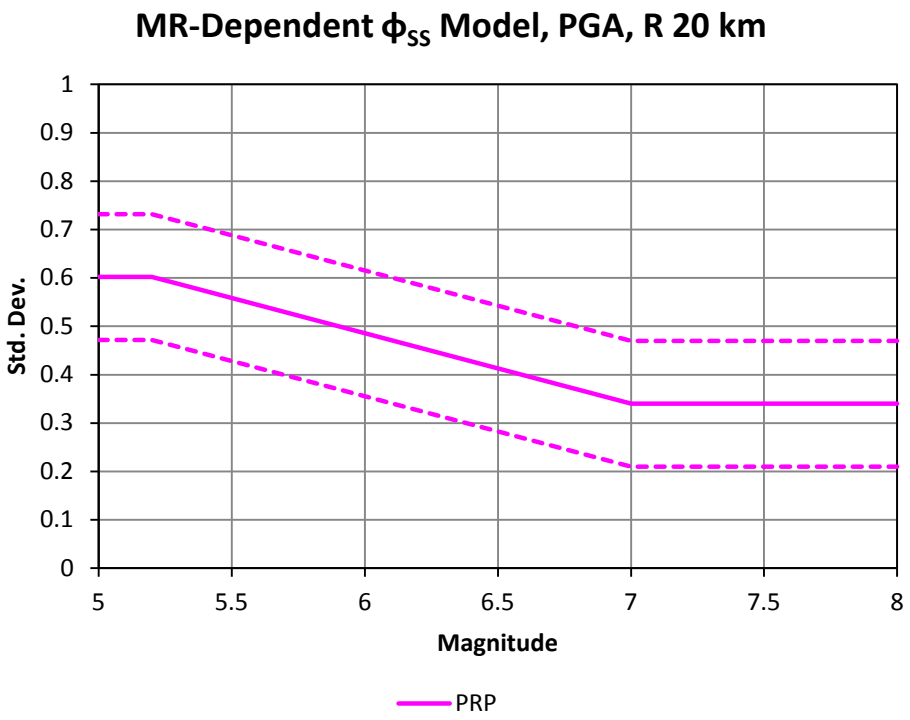

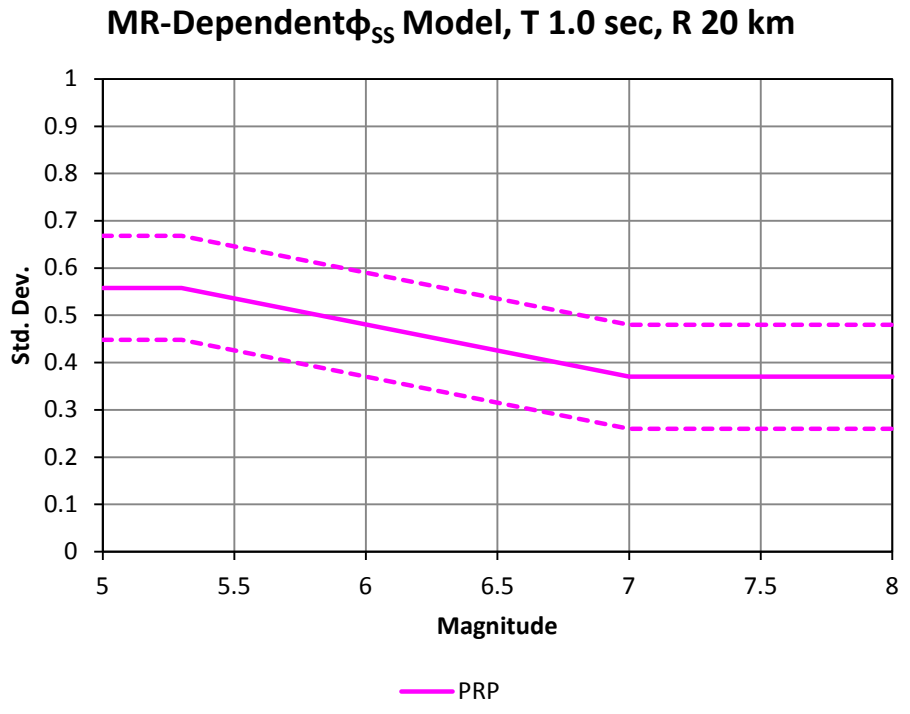

Figure 5.6.2-4: Rodriquez-Marek et al. (2013) PRP magnitude and distance-dependent ϕ_{SS} models (central, upper, and lower branches) shown for a distance of 20 km for PGA and spectral period of 1.0 seconds.

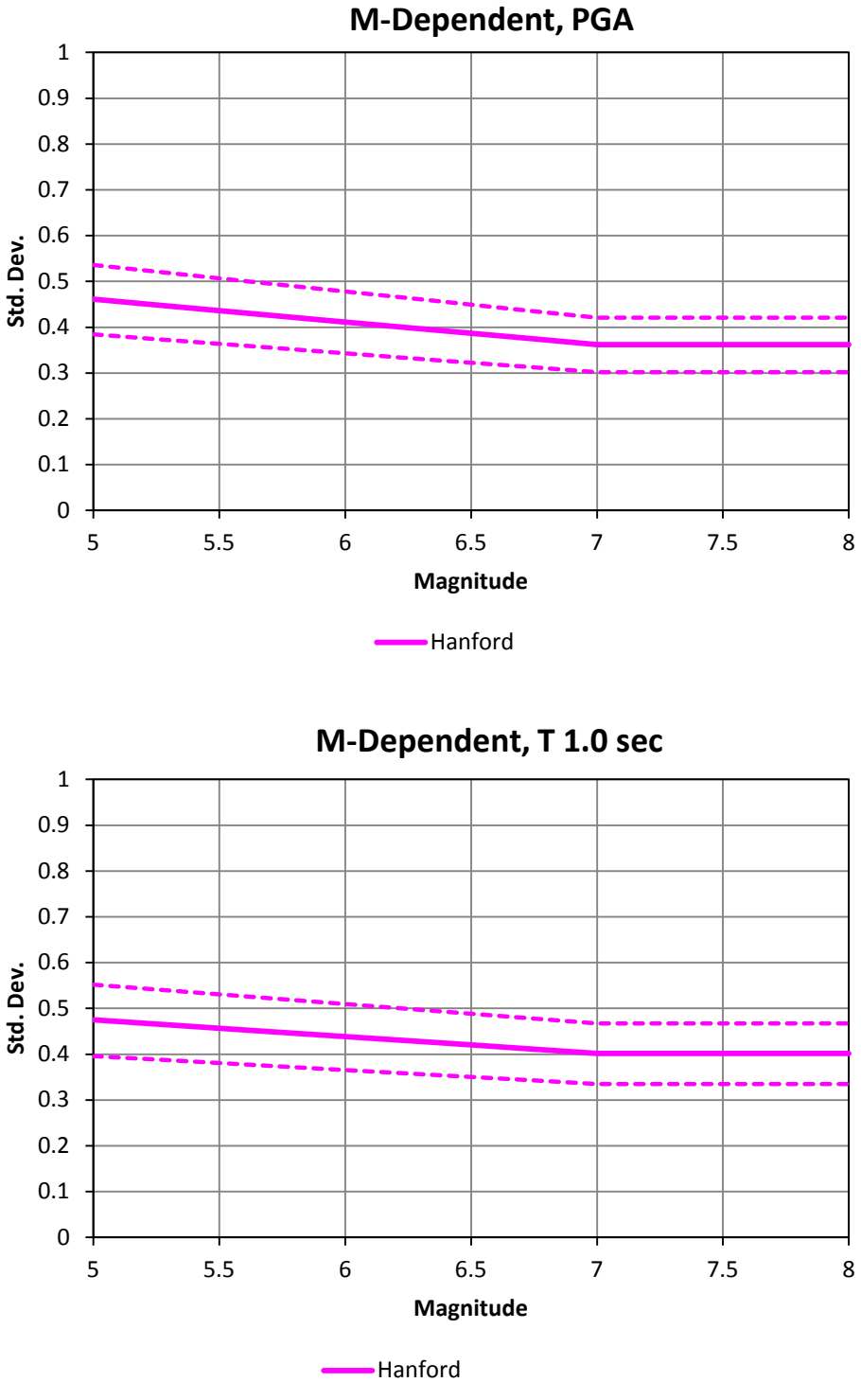

Figure 5.6.3-1: Magnitude-dependent ϕ_{SS} models (central, upper, and lower branches) for the Hanford project for PGA and spectral period of 1.0 seconds.

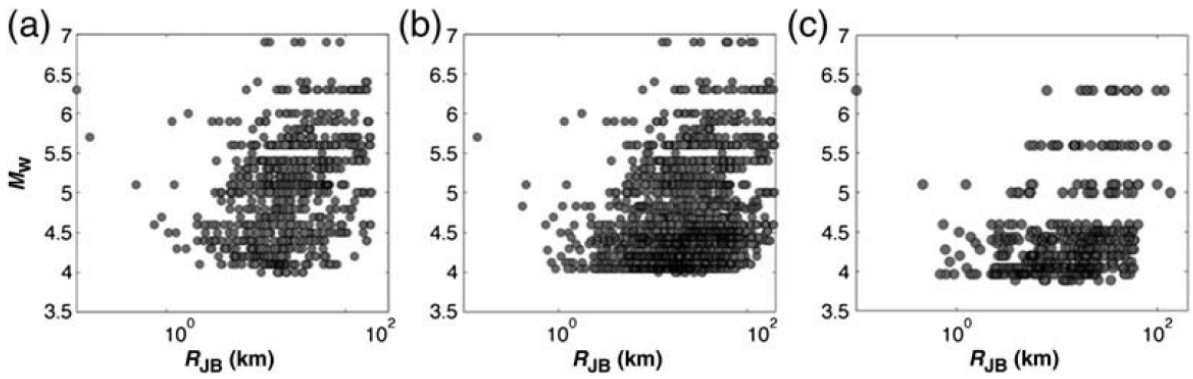

Figure 5.6.4-1: Magnitude – R_{JB} distribution of the three datasets used in Luzi et al. (2014). (From Luzi et al., 2014). (a) is the Bindi et al. (2011) dataset, called BIea; (b) is the extension of the Bindi et al., called BIea2; and (c) is the dataset with the L'Aquila event sequence, called ABR.

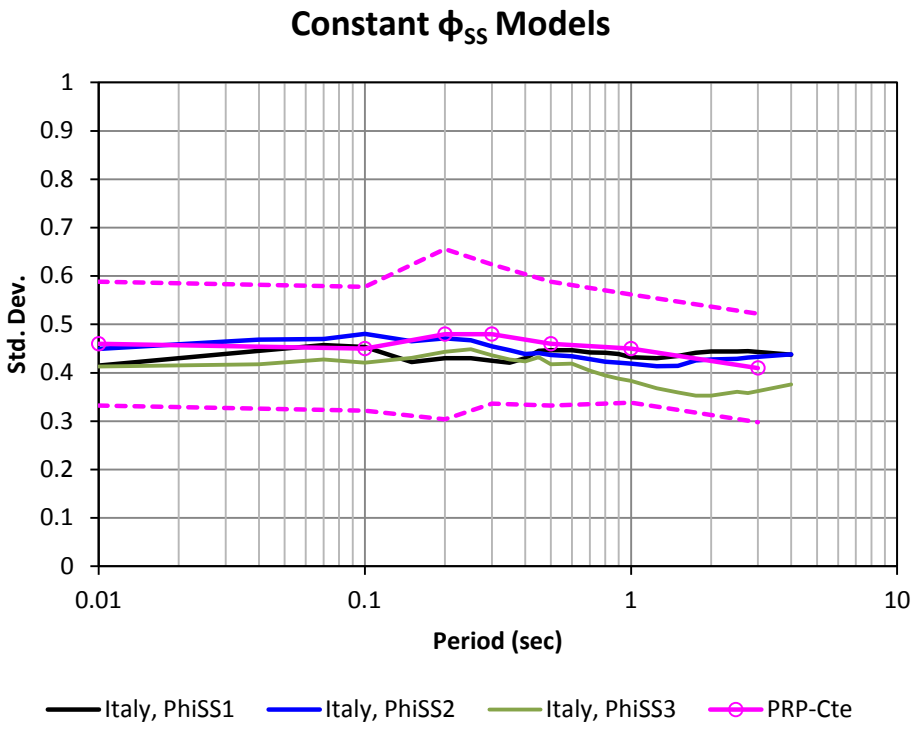

Figure 5.6.4-2: Comparison of Luzi et al. (2014) ϕ_{SS} models using three different Italian datasets with the PRP constant ϕ_{SS} model (called PRP-Cte). The PRP constant ϕ_{SS} model is shown in pink for the central, upper and lower ϕ_{SS} branches.

6 GMC MODELS FOR THE MEDIAN: OVERVIEW AND METHODOLOGY

6.1 Introduction

This Chapter describes the evaluations of the candidate GMPEs selected for the median ground motion compiled in Section 5.5. In addition, the alternative adjustment factors to account for hanging-wall effects, directivity effects, and path effects on the median are described and evaluated. The evaluations of the weights for the logic trees for the median for DCPP and PVNGS are described in Chapters 8 and 9, respectively.

A new methodology is used to develop the suite of alternative median models based on the Sammon's map representation of the alternative magnitude and distance scaling of the GMPEs. Background on the use of the Sammon's map method is given in Appendix H. In this approach, the selected candidate GMPEs are expanded to develop continuous distributions of the median GMPEs which can then be discretized into representative models that are mutually exclusive and collectively exhaustive. This new method, described in Section 6.4, allows the TI Team evaluations to better capture the center, body, and range of median GMPE predictions. The application of the Sammon's map is limited to 17 periods ranging between 0.01 (PGA) and 3 seconds, listed in Table 6.1-1. The spectral accelerations for the suite of median models for periods above 3 seconds are based on the period scaling of NGA-West2 GMPEs beyond 3 seconds, as described in Appendix N.

6.2 Evaluation of Candidate GMPEs for the Median

6.2.1 Evaluation of Candidate GMPEs for DCPP

Section 5.5 described the selection of the candidate GMPEs for the median ground motion. The eight candidate GMPEs selected for application to DCPP are listed below:

- Abrahamson et al. (2014), referred to as ASK14
- Akkar et al. (2014a, 2014b), referred to as ASB14

- Boore et al. (2014), referred to as BSSA14
- Campbell and Bozorgnia (2014) , referred to as CB14
- Chiou and Youngs (2014), referred to as CY14
- Idriss (2014), referred to as Id14
- Zhao et al. (2006), referred to as ZH06
- TI Team implementation of Zhao and Lu (2011), referred to as ZL11 (Section 5.5.1.1)

Based on the discussions in Section 5.5, the eight candidate GMPEs are all considered to be applicable to DCPP for magnitudes 5.0-8.0, distances of 0-30 km, and periods of 0-3 sec for strike-slip and reverse earthquakes for sites on the footwall side with the following exceptions: the Id14 model is not considered applicable for distances less than 3 km for large magnitudes (**M** > 7.5) and the ASB14 model is not considered applicable to magnitudes greater than 7.5. The technical justification for these exceptions is given below.

For the Id14 model, there is a strong distance slope of the short-periods spectral values for large magnitudes for distances less than 5 km. The other candidate GMPEs and two of the finite-fault simulations (GP – Graves and Pitarka, 2015; and SDSU – Olsen and Takedatsu, 2015; see Section 5.2 and Appendix J and references therein for more information) show saturation at short distances for short periods. While the EXSIM method (Atkinson and Assatourians, 2015) in the SCEC validation of broadband simulation methods also showed acceptable saturation with the limited data set, SWUS scenario simulations indicate that it does not saturate as strongly as the other two simulation approaches used nor as strongly as the GMPEs. The developer Gail Atkinson noted at the January 28-29, 2014 Special Working Meeting that, at distances less than 5 km, there may be additional unmodeled saturation effects. Since Gail Atkinson has indicated at the January 28-29, 2014 special working meeting, and also in subsequent email correspondence that the method does not saturate as strongly as observations for distances less than 5 km, the TI Team judges the EXSIM method to be deemed less reliable in this distance range and therefore cannot be used as an argument for accepting Id14 and very near distances. Lastly, EXSIM is not used in the Sammon's map approach to generate a suite of common-form models. Instead, it is used for residuals (together with the other two validated FFS simulations methods) in the weighting scheme. As a result, its behavior to short distance and high frequency does not impact the residuals too much. On the contrary, the Id14 model is used in the generation of the base model via Sammon's map, so the TI Team's assessment of the unreliable magnitude-distance range has important downstream effects in the generation of reliable suite of the common-form models.

Figure 6.2.1-1 shows the median spectra for an **M**7.5 strike-slip earthquake. At 5 km distance, all five models are in a similar range in the short periods, but at 1 km, the Idriss (2014) model is outside the range of the other candidate GMPEs due to the stronger distance scaling in this short distance range.

There is very little empirical data to constrain the short-distance large-magnitude scaling. For **M** ≥ 7.2, R_{RUP} ≤ 10 km, R_X < 0 km (excludes HW sites), V_{S30} > 450 m/s (subset of V_{S30} used by Id14), and requiring more than one recording from an earthquake to constrain the distance scaling, the NGA-West2 data set contains only 19 recordings, all of which are from the Chi-Chi earthquake. If the V_{S30} range is expanded to include soil sites (as used by the other four NGA-West2 modelers), then the short distance, large magnitude data set on the footwall (FW) increases to 35 recordings of which 30 are from Chi-Chi, 3 are from Kocaeli, and 2 are from Landers. While the short-distance scaling in the Id14 model at **M**6.6 is slightly steeper than any other candidate GMPE models (Figure 6.2.1-1 lower panel), it is still in the overall range of the other models and the finite-fault simulations; however, at large magnitudes (**M**7.5, shown in Figure 6.2.1-1 upper panel), the short-distance slope is even steeper than **M**6.6 and does not show saturation. Because the short-distance scaling in the Id14 model leads to a model that is an outlier from the other GMPEs and from the finite-fault simulations, and furthermore, because the Id14 short-distance large-magnitude scaling is based on a more limited data set due to the narrower range of V_{S30} values used by Idriss, the TI Team judged that the Id14 model is not reliable in the short distance range (≤3 km) for larger magnitudes (**M** ≥ 7.5).

For the ASB14 GMPE model, the scaling above **M**7.5 is not well constrained by the empirical data used to derive the model: the only earthquake above **M**7.5 in the ASB14 data is the **M**7.51 Kocaeli earthquake (magnitude from the PEER NGA-West2 database). Because the **M** > 7.5 scaling in the ASB14 model is based on only one earthquake and this earthquake is part of the larger NGA-West2 data set, the ASB14 model does not add information on the large magnitude scaling. Therefore, the TI Team judged that the ASB14 model should not be applied for magnitudes greater than 7.5.

Although previous hazard sensitivity studies (Section 4.1.4) showed that sources at large distances (30-300 km) do not contribute significantly to the hazard at DCPP for hazard levels less than 10^{-3} (the deaggregation for 1 Hz shown in Figure 4.1-4b indicated that there is no contribution to the hazard for distances greater than 50 km), the GMPEs still need to scale in a reasonable way to the large distance for all sources. As long as the large-distance scaling is not unreasonable, then the GMPEs can be used for the distant sources. A comparison of the distance scaling for 0.5 Hz is shown in Figure 6.2.1-2: the ASB14 GMPE model has the weakest attenuation with distance but there is still not a significant effect on the hazard. Figure 6.2.1-2 also shows that the predicted median by ZH06 and ZL11 are much higher than the predicted median by Id14 at short distance. In general, the predicted median by ZH06 and ZL11 are higher than the other GMPEs over a wide distance range, whereas the Id14 model is much higher only at short distance range. The TI Team judged that the overall higher level of ground motion in the ZH06 and ZL11 represented credible alternative scaling models that should be included. As mentioned above, because the Id14 model is based on a much smaller number of near-fault data (due to restricting the data to V_{S30} > 450 m/s), there is much less constraint on the short-distance scaling. The TI Team judged that the short-distance scaling for large magnitudes is not as well constrained in the Id14 model as it is in the other NGA-West2 GMPEs which had the advantage of using the much larger data set that

included soil data at short distances.

The TI Team judged that the large distance scaling in the candidate GMPEs is reasonable for application to DCPP because there is no significant contribution (less than 3% contribution as shown in Figure 4.1-3 for 1 Hz) to the hazard for hazard levels less than 10^{-3} for any of the GMPEs.

Although the Graizer and Kalkan model (Graizer, 2014) was not selected as a candidate GMPE because it had not undergone adequate peer-review, the TI Team included this model for checking its impact on the hazard because of its unique features. In particular, the unique features are the distance scaling at short distances and the spectral-shape approach which fits all frequencies simultaneously.

6.2.2 Evaluation of Candidate GMPEs for PVNGS for Greater Arizona Sources

Section 5.5 described the selection of the candidate GMPEs for the median ground motion. The six candidate GMPEs selected for application to PVNGS for Greater Arizona sources are listed below:

- Abrahamson et al. (2014), referred to as ASK14
- Akkar et al. (2014a, 2014b), referred to as ASB14
- Bindi et al. (2014a, 2014b), referred to as Bi14
- Boore et al. (2014), referred to as BSSA14
- Campbell and Bozorgnia (2014), referred to as CB14
- Chiou and Youngs (2014), referred to as CY14

Based on the data sets used to derive the models, the TI Team judged that the six candidate GMPEs are applicable to normal and strike-slip earthquakes with magnitudes 5 to 7.5 at distances of 0 to 200 km with the exception that the Bi14 model is not considered to be applicable to magnitude greater than 7.0 based on the strong change in the magnitude scaling for 5 Hz. The magnitude scaling of the candidate GMPEs for 5 Hz for strike-slip earthquakes at an R_X distance of 5 km is shown in Figure 6.2.2-1. As evident from the Figure 6.2.2-1, the Bi14 model shows an increase in the magnitude scaling above **M**7, whereas the other candidate GMPEs for DCPP show magnitude saturation. Based on this trend, the TI Team judged that the Bi14 model is not applicable for **M** > 7 for 5 Hz. This feature of the Bi14 model is not seen for all spectral frequencies, but for simplicity of application, the TI Team decided not to use the Bi14 model for **M** > 7 for all spectral frequencies.

6.2.3 Evaluation of Candidate GMPEs for PVNGS for Distant California and Mexico Sources

Previous hazard sensitivity studies (Section 4.2.3) showed that distant California and Mexico earthquakes could have a significant contribution to the low-frequency hazard at PVNGS. The hazard-relevant sources are mainly large magnitude (**M**7 to **M**8.5) strike-slip earthquakes. The issue of the application of the GMPEs to these sources is the large-distance attenuation from California to central Arizona, and, in particular, whether the attenuation from California to central Arizona is different from the attenuation within California.

To compare the large distance attenuation for California sites and central Arizona sites from earthquakes in southern California and Mexico, ground-motion data recorded at Arizona stations from California earthquakes was compiled by Kishida et al. (2014). Although the NGA-West2 data set did not include recordings in Arizona, some of the earthquakes included in the NGA-West2 data set were also recorded at sites in central Arizona in the PVNGS region (see Section 5.1.2).

The best recorded earthquake in the region is the 2010 **M**7.2 El Mayor Cucapah earthquake. Figure 6.2.3-1 shows the PSA at periods of 0.2, 0.5, 1.0 and 2.0 seconds for the El Mayor Cucapah event at stations in California and Mexico in the NGA-West2 dataset, and also the PSA recorded by the Arizona stations. The distance attenuation of the 2014 NGA-West2 ground-motion prediction equations is also shown for comparison. To remove the source-specific effects, the event terms estimated by the NGA-West2 modelers from the California recordings were added to the median values from the ASK14, BSSA14, CB14, and CY14 GMPEs. The Id14 model lacks the event term information and the median is plotted as published (assuming zero event term). Figure 6.2.3-1 shows that the five NGA-West2 GMPEs have distance attenuation that is similar to the attenuation along the path from California sources to the PVNGS site region.

In addition to the El Mayor Cucapah earthquake, Kishida et al. (2014) compared the distance attenuation from the NGA-West2 GMPEs with the attenuation for 13 other earthquakes recorded in central Arizona. They found that there was no systematic bias in the distance attenuation of the within-event residuals for the Arizona sites and concluded that the distance attenuation in the NGA-West2 GMPEs was applicable to the ground motions in central Arizona from distant earthquakes in California and Mexico.

Differences in the distance attenuation can also be evaluated from regional differences in the Q (quality factor) in California and Arizona. As discussed in Section 4.2.1, the Q model of Philips et al. (2014) shows that Q is low in coastal California and high in the Mojave Desert and the Colorado Plateau. To evaluate the potential effects of the Q differences on the ground motions, Kishida et al. (2014) computed the average Q (inverse of the mean of 1/Q along a ray path) for the 14 earthquakes recorded in southern

and central California and the same earthquakes recorded in Arizona. These average Q values are shown in Figures 6.2.3-2 and 6.2.3-3 for the California and Arizona stations, respectively. Over the relevant distance range for PVNGS (200-400 km), the average Q values for the California and Arizona stations are similar: Q of 100 to 300 for frequency of 0.7 to 2 Hz for California stations compared to mean Q values of 150 to 350 for frequency of 0.7 to 2 Hz for Arizona stations. Although there are differences in the Q between California and Arizona, these differences do not lead to a significant discrepancy in the average distance attenuation at distance of 200-400 km in central Arizona as compared to California. The differences in Q between California and Arizona would have a larger effect for larger distances (> 400 km), so the conclusion by Kishida et al. (2014) that the average attenuation is similar for southern California and central Arizona only applies to distances less than 400 km. Figure 4.2-5a shows the hazard deaggregation for PVNGS: there is small contribution (less than 5 %) to the total hazard from the large-magnitude distant sources in California and Mexico.

Based on the evaluation of the candidate GMPEs for application to earthquakes in California and Mexico recorded in central Arizona given in Kishida et al. (2014), the TI Team judged that the NGA-West2 GMPEs are suitable for estimating path terms for the paths from California and Mexico to central Arizona.

6.3 Hanging-Wall Effects Models

Hanging-wall (HW) effects refer to ground motion above the rupture surface of dipping earthquake ruptures that are enhanced compared to what would be expected for equivalent rupture distances on the footwall side of ruptures. The HW effect was first described by Somerville and Abrahamson (1995) and Abrahamson and Somerville (1996) based on data from the 1994 Northridge earthquake. Hanging-wall effects were first introduced into GMPEs by Abrahamson and Silva (1997) and Campbell and Bozorgnia (2003). Chiou et al. (2000) also identified HW effects from analyses of empirical and numerical modeling data for reverse fault ruptures and demonstrated that they could be explained as a geometric effect related to the root mean-squared (RMS) distance measured from the site to the rupture plane.

Numerical simulations conducted for the PEER NGA-West1 project by Somerville et al. (2006) also demonstrated strong HW effects. In the development of the 2008 NGA-West1 models, HW effects were incorporated in the models of Abrahamson and Silva (2008), Campbell and Bozorgnia (2008), and Chiou and Youngs (2008a). More recently, simulations conducted for the PEER NGA-West2 project further demonstrated the presence of strong HW effects. Donahue and Abrahamson (2013, 2014) analyzed the results of these numerical simulations and developed formulations to represent the HW effect for use in GMPE development. The Donahue and Abrahamson (2014) HW formulation was incorporated in the

NGA-West2 GMPEs developed by Abrahamson et al. (2014) and by Campbell and Bozorgnia (2014). Chiou and Youngs (2014) developed a HW formulation from their own analysis of the simulation results.

All of the above referenced studies describe HW effects as enhanced ground motions above what would be observed at similar rupture distances for sites on the footwall of dip-slip ruptures. Thus, the HW effect shows that using the rupture distance metric alone does not capture the distance scaling of the ground motion for sites on the hanging-wall side of the rupture.

The other commonly used distance metric for the distance scaling in GMPEs is the Joyner-Boore distance (Joyner and Boore, 1981), R_{JB}, defined as the shortest horizontal distance to the surface projection of the rupture. Use of the R_{JB} distance metric leads to shorter distances and higher ground motions for sites located over the hanging wall of dipping faults than for sites located on the footwall. Thus, the use of the R_{JB} distance metric implicitly accounts for some of the HW effects, primarily for average dips (near 45 degrees) and for surface-rupturing events (Donahue and Abrahamson, 2013 and 2014).

Chapter 4 summarizes the seismic source characteristics important to the hazard assessment at the two sites. For the DCPP site, HW effects are important for rupture dips in the range of 45 to 84 degrees from magnitudes up to approximately **M**7.5. These are ruptures on specific faults. For the PVNGS site, there are no nearby distinct faults included in the seismic source model. Instead, HW effects are needed for nearby ruptures in the distributed seismicity source zone with dips near 50 degrees.

6.3.1 Candidate Models for Hanging-Wall Effects

Figure 6.3.1-1 shows sets of example **M**7 earthquake rupture scenarios, all extending the rupture to the surface (Z_{TOR} = 0 km). Three ruptures are shown: Rupture 1 is a shallow dipping (30 deg) rupture, Rupture 2 has a moderate dip (45 deg), and Rupture 3 is steeply dipping rupture (60 deg). The dips from the SSC models (see Sections 4.1 and 4.4.2) range from 45 to 90 degrees. For these three rupture scenarios, two sets of site having the same R_{RUP} but located on the opposite side with respect of the fault are considered, as shown in Figure 6.3.1-1. The three R_{RUP}-based NGA-West2 GMPEs that explicitly address HW effects (i.e. ASK14, CB14, and CY14) and the R_{JB}-based Boore et al. (2014) – BSSA14 GMPE were used to compute median spectral accelerations at the sites for each of the three rupture scenarios. Because all R_{JB}-based GMPEs model the HW effects in the same way, the BSSA14 GMPE was used to represent the HW scaling of R_{JB}-based candidate GMPEs for the purpose of evaluating the suitability of the R_{JB} distance metric to capture the HW effects. HW factors were computed as the spectral ratios between the predicted PSA for the hanging-wall and foot-wall sites with the same R_{RUP}. The resulting HW factors for PGA are plotted in Figure 6.3.1-2 for the sites and ruptures of Figure 6.3.1-1. The R_{JB}-based GMPE leads to HW effects that are near constant as dip increases, whereas the R_{RUP}-based GMPEs with HW effects lead to reduced HW effects as the dip increases.

As discussed in Donahue and Abrahamson (2013 and 2014), the empirical data for HW effects remains limited and are insufficient for evaluating if the R_{RUP}-based HW models or the R_{JB}-based models work better. However, the finite-fault simulations described in Donahue and Abrahamson (2013 and 2014) and the simulations conducted in support of the HW evaluation for the SWUS project (Section 5.2.3.3 and Appendix J) clearly show a strong dip dependence that is more consistent with the R_{RUP}-based HW models than with the R_{JB}-based models. The other R_{RUP}-based GMPEs that were selected as candidate models (Id14, ZH06) did not explicitly address HW effects and are not considered for the development of the HW model.

The ASK14, CB14 and CY14 models all have different functional forms for including the HW effects, but they have some common features: (1) the HW effect directly above the rupture depends strongly on dip, (2) the HW effect is reduced as the site moves in the down dip direction beyond the surface projection of the bottom edge of the fault rupture (on the HW side), and (3) the HW effect is reduced as Z_{TOR} increases. The ASK14, CB14 and CY14 HW models differ significantly in the magnitude scaling, particularly how the HW effect is reduced or tapered with respect to magnitude for moderate (**M**5.5 to **M**6.5) events, which is not well constrained in the empirical data, and which was not addressed by Donahue and Abrahamson (2013 and 2014). Appendix J (Section J.5) compares the HW effect for moderate magnitudes based on numerical simulations with the HW effect from the three NGA-West2 models. The comparison with ASK14 and CB14 shows that reducing the magnitude-dependent HW effect to zero at **M**5.5 is too strong a taper for moderate magnitudes (**M** < 6.5). While CY14 does not have an explicit magnitude-dependent taper, its geometry- and distance-based approach does not match moderate magnitude simulations for small R_X. Generally, the **M**5.5 and **M**6.0 numerical simulations display a hanging-wall effect indicating that a magnitude taper to reduce the HW effect to zero at lower magnitudes is not needed, and that either the ASK14, CB14 and CY14 HW functional forms need adjustment, or a new functional form needs to be developed. Although not all simulations show HW effects in the **M**5.5 to **M**6.0 range, the TI Team decided to include the HW effects for the smaller magnitudes for all cases for simplicity. The impact of modifying the magnitude-taper of the hanging wall is discussed in Appendix O, Section O.2. For the example shown for 5Hz and the ASK14 model, the effect of removing the magnitude-dependent hanging-wall taper is 10% in hazard (3% in ground motion). This is small enough that consideration of models with and without the magnitude-dependent hanging-wall taper is not needed. Rather than modifying three different HW effects relationships that the best approach would be to develop a new relationship as described in the next Section.

6.3.2 Development of SWUS Models for Hanging-Wall Effects

This Section presents the development of a model to account for hanging-wall effects in the application of GMPEs in estimating hazard, and is referred to as the Hanging Wall (HW) adjustment model. To create a full set of potential HW adjustment models, a new suite of models was developed by the TI

Team as part of the SWUS GMC project. Drawing on the conclusions from Abrahamson and Donahue (2013 and 2014) and on evaluation of the candidate models for HW effects described in Section 6.3.1, the R_{JB}-based GMPE models were judged by the TI Team not to be applicable for developing HW adjustment models.

The TI Team derived the HW adjustment model from the explicit HW factors presented in the ASK14, CB14, and CY14 models. The ASK14 and CB14 HW characterizations separate the HW effect into five aspects:

1) HW effects directly above the rupture plane for surface rupturing earthquakes ($R_{JB} = 0$, $Z_{TOR} = 0$)
2) The effect of moving off of the HW ($R_{JB} > 0$, $R_X > 0$)
3) The effect of depth to top of rupture ($Z_{TOR} > 0$)
4) The effect of magnitude, and
5) The effect of the dip of the rupture plane.

The two GMPEs provide explicit tapers (functions describing the effect on ground motion due to the specified parameter) to address aspects (2), (3), and (4). In particular, the magnitude taper assumes that the HW effect goes to zero at **M** ≤ 5.5. The CY14 GMPE has tapers that address (2), (3) and (5), however it does not have an explicit magnitude term, instead combines the effects of rupture depth (Z_{TOR}), and location (R_{JB}, R_X, and R_{RUP}) into a single geometric taper function. The above separation of factors employed by ASK14 and CB14 was used to develop the HW factor characterization as it provides the clearest representation of the various modeling results.

The SWUS GMC Model to account for the HW effects has the form given in Eq. 6.3-1, and was developed following the steps described in Sections 6.3.2.1 to 6.3.2.4.

$$f_{HW}(M, Dip, W, R_X, R_{JB}, R_{RUP}, Z_{TOR}) = C_1(T)\cos(dip)\left[C_2(T) + (1 - C_2(T))\tanh\left(\frac{C_3(T)R_X}{W\cos(dip)}\right)\right] \times \left(1 + C_4(T)(M - 7)\right) HWR_{JB}\,\text{Taper}(R_{RUP}, R_{JB})\,\text{HWZ}_{TOR}\,\text{Taper}(Z_{TOR})$$

(Eq. 6.3-1)

The HW model is ln based and is meant to be added to the ln of the median base model predictions.

6.3.2.1 Model for $R_{JB} = 0$, $Z_{TOR} = 0$

The first step was to develop a model for HW effects directly above the rupture plane for surface rupturing earthquakes ($R_{JB} = 0$, $Z_{TOR} = 0$). Figures 6.3.2-1, 6.3.2-2, 6.3.2-3, and 6.3.2-4 show the HW factors from the ASK14, CB14, and CY14 models for spectral periods of 0.01 (PGA), 0.1, 0.3, and 1 sec, respectively. Factors are shown for **M**6.5, **M**7.0, and **M**7.5 earthquakes. Results for smaller magnitudes

are not used as ASK14 and CB14 apply magnitude tapers to HW factors for these magnitudes and the selection of the appropriate taper is addressed separately. The HW factors are presented for Z_{TOR} = 0 km and for a range of dips from 20 to 80 degrees. As can be seen, the HW factors from the three GMPEs have similar trends. All three GMPEs have a non-zero HW factor at R_X = 0, all three show an increase in the HW effect with increasing magnitude and decreasing dip angle. The scaling with R_X is generally similar among the three GMPEs, but the CY14 HW factors show less scaling with R_X at large values of R_X near the down-dip extent of the rupture.

The HW factors from the three GMPEs for R_{JB} = 0 were represented fit by the following functional form:

$$f_{HW}(M, Dip, W, R_X) = C_1 \cos(dip) \times \left[C_2 + (1 - C_2) \tanh\left(\frac{C_3 R_X}{W \cos(dip)} \right) \right] \times \{1 + C_4 (M - 7)\}$$

(Eq. 6.3-2)

The form was motivated by the characterization used in CY14 to capture the shape and trend with dip. As discussed above, the HW effect was interpreted by Chiou et al. (2000) to be primary a geometric effect as a site on the hanging wall will have a smaller average distance or RMS distance to all points on the rupture plane compared to a site located at an equal rupture distance on the footwall site. On the basis that the surface projection of the rupture is directly related to the cosine of dip rather than to the dip angle itself, cos(dip) is used as the predictor variable. Chiou and Youngs (2008b) found that the use of cosine dip or cosine dip squared produced slightly better fits to the limited empirical data than the use of dip angle directly. The formulation allows for an offset at the up-dip tip of the rupture (R_X = 0) and captures the general shape of the quadratic formulation in R_X used in Donahue and Abrahamson (2014). The functional form was fit to the predicted HW factors from the three GMPEs using a mixed effects model in which a random effect was applied to coefficient C_1 using the GMPE as the random effect. Table 6.3-1 lists the fix effects coefficients, the random effect standard deviation and the residual standard error in fitting the factors. The random effect and the residual standard error were combined by summing variances to produce a composite epistemic uncertainty for the overall level of the HW effect, as indicated in the right hand column of Table 6.3-1. A model for the HW factor was not developed for periods longer than 3 sec as the effect essentially goes to zero in the three GMPEs at these longer periods. The resulting fitted model is shown by the solid black lines on Figures 6.3.2-1 through 6.3.2-4.

In order to provide a means of randomly sampling HW factor models in the overall ground-motion characterization (see Section 6.4.3), five equally likely HW factor models were developed assuming that the distribution in the log of HW factors is approximately normal, as explained below. The range in cumulative probability from 0 to 1 was divided into 5 equal intervals with 0.2 probability mass for each. The central model was taken as the model representing the fit of Eq. 6.3-2 to the data, and is considered

to represent the range in cumulative probability from 0.4 to 0.6. To represent the cumulative probability range of 0.2 to 0.4 and 0.6 to 0.8 by a single discrete value of epsilon (the number of standard deviations of a unit normal) in each interval, probability weighted mean epsilons were computed by discretizing the corresponding intervals of epsilons for the unit normal at a fine increment and then weighting each value of epsilon by its corresponding probability mass. When this approach was applied to represent the probability ranges of 0 to 0.2 and 0.8 to 1.0, the resulting probability weighted mean epsilons were ±1.4. However, the resulting 5-point discrete distribution produced a variance less than 1. Therefore, the epsilons of the outer points were increased to ±1.49 in order to achieve a variance of 1. For application to the SWUS GMC Project, the equally weighted factors of -1.49, -0.53, 0, 0.53, and 1.49 were rounded to -1.5, -0.5, 0, 0.5, and 1.5. The HW factor model consists of the fixed effect coefficients listed in Table 6.3-1 plus the epistemic sigma in C_1 multiplied by the equally weighted factors of -1.5, -0.5, 0, 0.5, and 1.5. The resulting SWUS GMC HW adjustment model coefficients are listed in Table 6.3-2 for the five alternative branches (HW1 to HW5) shown by the solid (central model, i.e. HW3) and dashed (HW1, HW2, HW4, and HW5 models) black lines on Figures 6.3.2-1 through 6.3.2-4. In general, the five HW models capturing the range in HW factors predicted by the individual GMPEs as a function of dip and magnitude for the range of magnitudes and dips important to the hazard assessments for the two sites. For a dip angle of 20 degrees, the CB14 HW factors fall above the range of the five HW models in a number of cases. However, this has little impact as rupture dip angles of 20 degrees are not important to the hazard assessment for either site. The HW factors for the CY14 HW factors fall below the range of the five HW models, but this typically occurs where the HW factor is small, and is also not expected to have an important effect on the hazard assessment.

6.3.2.2 Magnitude Taper

Both ASK14 and CB14 applied an external taper to reduce the HW effect to 0 as the magnitude decreased from **M**6.5 to **M**5.5 based on judgment. Other reasons why the ASK14 and CB14 HW models applied a magnitude taper to make the HW factor go to zero at **M**5.5 was the lack of any empirical data or numerical simulations to support a HW effect at smaller magnitudes. However, the limited smaller magnitude simulations conducted in support of the SWUS GMC project showed significant HW effects for **M**5.5 and **M**6 earthquakes. These simulations were insufficient in number to build a specific model for HW effects below **M**6.5. However, it was found that the HW effects at **M** < 6.5 observed in the simulations could be modeled by using the magnitude-scaling effect provided by equations (6.3-1) and (6.3-2) without the need to apply an additional external magnitude taper.

6.3.2.3 Taper for $R_{JB} > 0$

Figure 6.3.2-5 shows the behavior of the HW factors for the three GMPEs as R_{JB} increases from 0 km in a direction parallel to strike (R_X constant). Results are shown for two R_X values, 1 km and 10 km for a fault

rupture with a 45 degree dip and a rupture width of 14.14 km. The comparisons indicate similar behavior for the CB14 and CY14 HW factors while the ASK14 model uses a simple linear trend. It is assessed that the geometry based models of CB14 and CY14 are more appropriate. As parameterized, these models show a smooth, but rapid transition as a function of location around the rupture. The two trends can be represented by the function:

$$HWR_{JB}Taper(R_{RUP},R_{JB}) = 1 - \frac{R_{JB}}{R_{RUP}+0.1} \qquad \text{(Eq. 6.3-3)}$$

The black lines in Figure 6.3.2-5 represent the proposed $HWR_{JB}Taper$ model for the two cases described above.

6.3.2.4 Taper for $Z_{TOR} > 0$

Figure 6.3.2-6 shows the behavior of the HW factors for the three GMPEs as Z_{TOR} increases from 0. Results are again shown for the two cases as the CY14 model would predict different behavior for these two conditions. The three GMPEs show differences in the trends with increasing depth. The ASK14 model is proportional to the square of Z_{TOR}, the CB14 model is linear in Z_{TOR}, and the CY14 model follows the same trend as Eq. (6.3-3). The trends with Z_{TOR} are not well resolved with the existing empirical data and simulations, and the differences represent somewhat arbitrary choices by the GMPE developers. Therefore, a simple linear taper function that represents the general behavior was selected. The depth taper is given by the function:

$$HWZ_{TOR}Taper(Z_{TOR}) = \max\left\{0,\ \ 1 - \frac{Z_{TOR}}{12km}\right\} \qquad \text{(Eq. 6.3-4)}$$

The black line in Figure 6.3.2-6 represents the proposed $HWZ_{TOR}Taper$ model for increasing Z_{TOR}.

6.3.3 Evaluation of SWUS HW Scaling Models

As described above, there are two approaches to modeling HW effects: apply a HW factor to an R_{RUP}-based GMPE or simply use the R_{JB}-based GMPE with its implicit HW effects. These two approaches produce similar HW effects for dips near 45 degrees, but they lead to very different HW effects for small dips. Comparisons with numerical simulations (Donahue and Abrahamson, 2013 and 2014) showed that the R_{RUP}-based GMPEs with HW effects were better able to capture the dip-dependence of the HW effect than the R_{JB}-based GMPEs.

To evaluate its suitability, the proposed HW adjustment model was compared to the ground-motion simulations defined by the TI Team and conducted by the SCEC BBP (Appendix J) in support of the SWUS

GMC project. The footwall motions from the simulations were fit to a log linear R_{RUP} model ($\ln(Y)=a+b*\ln(R_{RUP})$) and then the HW factor was added to the projection of the footwall motions on the HW side of the fault. The approach was first evaluated through comparison with NGA-West2 GMPE motions including the respective HW tapers (Appendix J, Figure J.5.2-2). Figure 6.3.3-1 shows the Z_{TOR} sensitivity for **M**5.5 and a dip of 45 degrees demonstrating good agreement with the simulations. The five equally weighted alternative HW factor models, developed using equal probability of the C_1 coefficient, are compared. Figure 6.3.3-2 shows the same for **M**6.0, and similarly good agreement is observed. For the **M**6.5 cases, only Z_{TOR} values of 0 and 7 km were used, which are shown in Figure 6.3.3-3. Again the agreement is good, and the result of this analysis indicates that magnitude, distance and Z_{TOR} tapers in the proposed HW factor model are consistent with the simulations. For the **M**6.0 case, the sensitivity of the proposed HW factors on fault dip for a fixed Z_{TOR} of 7 km is shown in Figure 6.3.3-4. The dip behavior of the proposed HW factor model is consistent with the simulations.

As described above, five equally weighted alternative HW factor models are developed using equal probability of the C_1 coefficient, and are compared to the simulations in figures 6.3.3-1 to 4. The HW factor model is consistent with the simulations, and the range in the equal probability models reasonably captures the simulation results, particularly for sites located over the surface projection of the dipping fault. The simulations do tend to have values larger than the HW model for sites located off the end of the surface projection of the fault plane, but the TI Team judged that the empirical data should be used for the tapering rather than the simulations. Therefore, the $HWR_{JB}Taper$ (Equation 6.3-3) was designed to be consistent with the empirical observations captured by the published GMPEs (Section 6.3.2.3).

In conclusion, for dips near 45 degrees, the R_{RUP}-based GMPEs and the R_{JB}-based GMPE give similar HW factors and both approaches adequately capture the HW effects. For shallow and steep dips, the comparisons with the numerical simulations showed that the R_{RUP}-based GMPEs with HW factors that account for the scaling with dip adequately capture the HW effect for shallow and steep dips, whereas the R_{JB}-based GMPEs do not capture the HW scaling for shallow and steep dips. Therefore, the TI Team judged that the R_{JB}-based GMPEs are not suitable for developing HW effect models for a wide range of dip angles.

6.4 Approach for Continuous Distributions of the Median Using Visualization Techniques

The traditional approach to ground-motion characterization is to assign weights to candidate GMPEs. A key disadvantage of this approach is that the set of candidate GMPEs may not represent a set of mutually exclusive and collectively exhaustive models. If the weights on logic tree branches are treated

as probabilities, then the branches should be mutually exclusive and collectively exhaustive. If they are not mutually exclusive and collectively exhaustive, then the weights of the branches become relative merits of the models rather than probabilities (Abrahamson and Bommer, 2005). The concept of mutually exclusive and collectively exhaustive is simple for a scalar parameter (such as the ground motion for a single magnitude and distance), but it is more complicated for a vector model such as a GMPE, which provides ground-motion estimates for a range of magnitudes and distances.

Atkinson et al. (2014) introduced the concept of selecting a single "central or backbone GMPE" and scaling it up and down. This concept is here referred to as the "scaled-backbone approach", which provides a method to develop a set of GMPEs that are mutually exclusive and are collectively exhaustive in terms of the amplitudes at a given magnitude and distance, but that do not capture the range of different scaling with magnitude and distance. As an alternative to the scaled-backbone approach, the Sammon's map approach (Sammon, 1969) can be used to develop a continuous distribution of the median GMPE models that are mutually exclusive and collectively exhaustive in terms of the magnitude and distance scaling as well as the amplitude.

In the Sammon's map approach, a large suite of new models are created from existing GMPEs which both interpolate between the existing GMPEs and extrapolate beyond the range of the existing GMPEs. Visualization techniques are used to map the suite of new models into a 2-D plane (Scherbaum et al., 2010). In particular, the Sammon's maps technique is used to calculate a two-dimensional representation of the model space. The model space can then be discretized into a small number of cells with representative models selected for each cell. Subjective weights are then assigned to each cell based on the comparisons with hazard relevant data sets (empirical and/or simulated) and with the density of the representative suite of models within each cell, to represent the center, body and range of median predictions. The representative model for each cell is defined as the model leading to a hazard curve that is the closest to the mean of the hazard curves from all the models within a given cell. In particular, the model is selected by minimizing the variance of the difference in the log hazard for the model and the log of the mean hazard for the cell measured over a range of ground-motion levels. The mean hazard is used because the primary use of the SWUS GMC models will be to develop mean hazard curves for the NPP sites.

The use of the visualization technique for the sampling of the suite of common-form models is applied to the DCPP sources and to the Greater Arizona sources for PVNGS. The ground-motion models addressing the ground motion for PVNGS from sources located in central and southern California and Mexico is treated with a different approach based on as-published GMPEs with path-specific adjustment factor to take advantage of the available ground-motion data in Arizona from these sources (see Section 6.2.3 for details on the approach, and Section 9.2 for the technical justification).

6.4.1 Fitting Candidate GMPEs to a Common Functional Form

In the first step, the candidate GMPEs are fit to a common functional form, which allows an evaluation of the distributions of the coefficients. This step is necessary because the GMPEs use different functional forms and the coefficients cannot be directly compared between GMPEs. By using the common form, the mean and covariance of the resulting sets of coefficients can be estimated. This gives a distribution of the set of coefficients, which can be sampled to generate a large suite of new common-form models. These new models lead to a continuous distribution of median models which fill in between the candidate GMPEs as well as broadening the range of models beyond the range of candidate GMPEs. Based on the evaluation of these new common-form models, which is done by comparing them to data and simulations, a subset of common-form models is selected and weighted appropriately to capture the center, body and range of median PSA predictions.

Two functional forms were used for the common-form models: one based on rupture distance (called Model A) and one based on Joyner-Boore distance (called Model B). The common form for Model A is given in Equation 6.4-1 and was selected based on the magnitude, distance, depth, and style-of-faulting dependence in the candidate GMPEs.

$$\begin{aligned} Ln\left(SA_{BASE}(M,R_{RUP},Z_{TOR},F,T)\right) &= \theta_0(T) - \exp(\theta_7(T))R_{RUP} + \exp(\theta_8(T))Z_{TOR} + \exp(\theta_{10}(T))F_{REV} \\ &+ \left(\theta_4(T) + \theta_5(T)(M-5)\right)\ln\left(\sqrt{R_{RUP}^2 + \theta_6(T)^2}\right) - \exp(\theta_9(T))F_{NML} \\ &+ \begin{cases} \theta_1(T)(5.5-6.5) + \theta_2(T)(M-5.5) & for\, M < 5.5 \\ \theta_1(T)(M-6.5) & for\, 5.5 \le M \le 6.5 \\ \theta_3(T)(M-6.5) & for\, M > 6.5 \end{cases} \end{aligned}$$

(Eq. 6.4-1)

where SA_{BASE} refers to the model without HW effects (called the base model), M is moment magnitude, R_{RUP} is rupture distance in km, Z_{TOR} is the depth to the top of rupture in km. F_{REV} is a flag for the reverse (REV) style-of-faulting (i.e. F_{REV} = 1 for REV sources, and is zero otherwise), and F_{NML} is a flag for the normal (NML) style-of-faulting (i.e. F_{NML} = 1 for NML sources, and is zero otherwise). The coefficients for the linear distance, style of faulting, and rupture depth in the common-form model (θ_7, θ_8, θ_9 and θ_{10}) are fit using the $\exp(\theta_k)$ (for $k = 7,8,9,10$) to ensure that the terms are positive for all four coefficients. A similar form is used for Model B, but with R_{RUP} replaced by R_{JB}. There is no site term (e.g. V_{S30} scaling) in the common form because the application is for a single reference site condition with V_{S30} = 760 m/s.

To focus the common form on the most important sources, the fitting of the common form used different faulting styles for the two sites: for DCPP, the common form is derived for strike-slip (SS) and REV earthquakes only and a single NML factor is added at the end; for PVNGS, the common form is derived for SS and NML earthquakes only and a single REV factor is added at the end. For adding the style-of-faulting (SOF) factors at the end, smoothed average NML factors for DCPP are computed based on the mean style-of-faulting factor for NML earthquakes in the eight candidate GMPEs for **M**6.5, Z_{TOR} = 0 km, R_X = -30 km. Because the NML faulting events do not contribute significantly to the hazard at DCPP (as discussed in Section 4.1), only a single scenario was used to evaluate the NML style-of-faulting factor. For PVNGS, the same approach is used to compute the average REV style-of-faulting factor based on the six candidate GMPEs. Similar to DCPP, only a single scenario was used to evaluate the REV style of faulting factor because the REV faulting events do not contribute significantly to the hazard at PVNGS (as discussed in Section 4.2.2).

For the regression, the $\exp(\theta_k)$ terms (for $k = 7,8,9,10$) are replaced by a_k^2. Thus, the following function is used for the prediction of PSA values using the sampled functions (Eq. 6.4-2):

$$\begin{aligned} Ln\left(SA_{BASE}(M,R_{RUP},Z_{TOR},F,T)\right) = {} & a_0(T) - a_7^2(T)R_{RUP} + a_8^2(T)Z_{TOR} + a_{10}^2(T)F_{REV} \\ & + \left(a_4(T) + a_5(T)(M-5)\right)\ln\left(\sqrt{R_{RUP}^2 + a_6(T)}\right) - a_9^2(T)F_{NML} \\ & + \begin{cases} -a_1(T)(5.5-6.5) + a_2(T)(M-5.5) & for\, M < 5.5 \\ a_1(T)(M-6.5) & for\, 5.5 \le M \le 6.5 \\ a_3(T)(M-6.5) & for\, M > 6.5 \end{cases} \end{aligned}$$

(Eq. 6.4-2)

where $a_k = \theta_k$ for $k = 0,1....6$ and $a_k = \sqrt{\exp\theta_k}$ for $k = 7,8,9,10$. Using the square of the a_k terms for k = 7, 8, 9 and 10 ensures a positive value for these parameters.

To evaluate the suitability of the common form in Eq. 6.4-2 to fit the candidate GMPEs, the TI Team inspected the comparisons of the scaling in the original candidate GMPEs with the scaling in the fitted common-form models. Examples comparing the distance scaling of the candidate GMPEs for DCPP and PVNGS with the fitted common-form models for PGA and T = 1.0 sec are shown in Figures 6.4.1-1 to 6.4.1-3 for the DCPP, PVNGS (Model A) and PVNGS (Model B), respectively. Based on inspections of the fits, the TI Team judged that the function in Eq. 6.4-2 is flexible enough to capture the full range of scaling in the selected candidate GMPEs.

The Z_{TOR} term is included for the R_{RUP}-based common-form models, but not for the R_{JB}-based common-form models, because the candidate GMPEs which use R_{JB} as their primary distance metric (ASB14, BSSA14, Bi14) do not include Z_{TOR} depth-scaling. Therefore, for the R_{JB}-based common-form models,

$a_8 = 0$. For the R_{JB}-based common-form models fit to the candidate GMPEs with Z_{TOR} effects (e.g. ASK14, CB14 and CY14), the Z_{TOR} scaling is not maintained. This is a feature of the R_{JB} metric which does not include depth effects. For the R_{RUP}-based common-form models, the candidate GMPEs are evaluated at three Z_{TOR} values per magnitude, centered on the mean Z_{TOR} from the Z_{TOR}-M relationship developed by CY14. The high and low values are ± 3 km from the mean Z_{TOR}-M relationship of CY14, with the constraint that Z_{TOR} is greater or equal to 0 km. The range of Z_{TOR} values does not represent uncertainty in the mean value of Z_{TOR} for a given magnitude. Rather, the range is included so that the regression of the common-form model can fit the Z_{TOR} dependence.

6.4.1.1 DCPP Fitted Models

For each of the eight selected candidate GMPEs for DCPP listed in Section 6.2.1, median predictions (in ln units) are calculated for **M**5 to **M**8, R_X = -2 to -200 km, V_{S30} = 760m/s, and strike-slip and reverse faulting mechanisms are included. The magnitudes and distances used to define the scenarios for fitting the candidate GMPEs for DCPP are listed below:

- ***M*** *= 5.0, 5.2, 5.4, 5.5, 5.6, 5.8, 6.0, 6.2, 6.4, 6.5, 6.6, 6.8, 7.0, 7.2, 7.4, 7.5, 7.6, 7.8, 8.0*
- R_X *= -200, -100, -70, -65, -60, -55, -50, -45, -40, -35, -30, -28, -26, -25, -24, -22, -20, -18, -16, -15, -14, -12, -10, -8, -6, -5, -4, -2*

The data points are all given equal weights in the regression for the common-form model fit to each candidate GMPE using ordinary least squares.

All other predictor variables are set to the default values recommended by the NGA-West2 developers. For each R_X distance and Z_{TOR} value, the R_{RUP} and R_{JB} distances were computed from specified fault geometry created for the each of the scenarios described above. The sites are all located within the bounds of the ends of the rupture (source-to-site azimuth of -90 degrees). Because only footwall sites are used (R_X <0), R_{JB} equals $|R_X|$ and $R_{RUP} = \sqrt{R_X^2 + Z_{TOR}^2}$ for all scenarios, and the dip is not a factor. Based on the initial evaluations of the candidate GMPEs for DCPP (Section 6.2.1), the model of ASB14 is not used for magnitudes **M** > 7.5, and the model of Id14 is not used for distances $R_X \leq 3$ km. Even though the models are fitted to distances up to 200 km, this large distance is only included to constrain the fitted models at large distances so that they provide reasonable values at large distances. The majority of scenarios are for distances between R_X= -1 and -30 km, since this is the main range of the hazard-relevant scenarios identified in Section 4.1.4. Only a few large-distance data points are used so the fit is more heavily weighted to the short distances.

The total fitted residuals of the median predictions from the candidate GMPEs for DCPP relative to the fitted common-form function are shown in Figures 6.4.1-4 to 6.4.1-5 for PGA and 1.0 sec. In these

figures, residuals for all the scenarios for the fitting are shown, even though, in the actual regression process, some of the predictions from ASB14 and Id14 were not used, as described above.

6.4.1.2 PVNGS Greater Arizona Fitted Models

For each of the six selected candidate GMPEs for PVNGS listed in Section 6.2.2, median predictions are calculated for **M**5 to **M**7.5, R_X = -200 to 18 km, V_{S30} = 760m/s, and strike-slip and normal-faulting mechanisms are included. The magnitudes and distances used to define the scenarios for fitting the candidate GMPEs for PVNGS are listed below:

- ***M*** *= 5.0, 5.2, 5.4, 5.5, 5.6, 5.8, 6.0, 6.2, 6.4, 6.5, 6.6, 6.8, 7.0, 7.2, 7.4, 7.5*
- R_X *= -200, -100, -70, -65, -60, -55, -50, -45, -40, -38, -36, -35, -34, -32, -30, -28, -26, -25, -24, -22, -20, -18, -16, -15, -14, -12, -10, -8, -6, -5, -4, -2, 0, 2, 4, 5, 6, 8, 10, 12, 14, 15, 16, 18*

Other predictor variables are set to the default values recommended by the NGA-West2 developers. For the normal events, a dip of δ = 50° is used based on the preliminary SSC models which had dips from 35 to 65 for the normal-faulting events (the final SSC model also has a mean dip of 50 degrees for the normal-faulting events in the areal sources as shown in Table 4.2-1). Based on the initial evaluations of the candidate GMPEs for PVNGS (Section 6.2.2), the Bi14 model is not used above **M** = 7. The positive R_X values are only used when fitting to R_{JB} for scenarios in which R_{JB} = 0 km. This creates additional data at R_{JB} = 0 km, i.e. above the fault on the hanging wall. This is to ensure that the implicit hanging-wall term for R_{JB} = 0 km captures the mean hanging-wall term of the candidate GMPEs. As for the DCPP case, more scenarios are included for the shorter distances.

The total fitted residuals of the median predictions from the candidate GMPEs for PVNGS relative to the fitted common-form function are shown in Figures 6.4.1-6 to 6.4.1-9 for PGA and 1.0 sec. In these figures, residuals for all the scenarios for the fitting are shown, even though, in the actual regression process, some of the predictions from ASB14 and Bi14 were not used, as described above.

6.4.2 Estimation and Sampling of the Coefficient Covariance Matrix

From the fitted values of the coefficients a_k, the mean and covariance of the coefficient distribution can be calculated. To better capture the correlations between the different coefficients a_k, Equation 6.4-1 is fitted to the candidate GMPEs as well as to interpolated ground motions from the candidate GMPEs. The interpolated versions are created as weighted averages of the candidate GMPEs with the following sets of weights:

w = {1/3, 2/3}, {1/2, 1/2}, {2/3, 1/3}.

For example, for w = {1/3, 2/3}, the interpolated ground motions at each of the scenarios are computed as follows:

$$Interp(\ln SA(M,R)) = \frac{1}{3}\ln(SA_1) + \frac{2}{3}\ln(SA_2) \qquad \text{(Eq. 6.4-3)}$$

For each pair of candidate GMPEs, three interpolated sets of ground motions are created and fitted. The mean and covariance of the coefficient distribution is calculated from the fitted candidate and interpolated GMPEs. Since the interpolation reduces the variance of the marginal coefficient distributions, the entries of the covariance matrix are multiplied by a factor of 2. This factor was determined by comparison of the covariance matrix calculated using all (candidate plus interpolated) GMPEs and the covariance matrix calculated using only the candidate GMPEs. The multiplication increases the marginal variance of each coefficient to account for the correlation of interpolated models, but retains the correlation structure.

To show how the inclusion of the interpolated GMPEs affects the estimate of the covariance matrix, numerical testing was used. Given a population with a known covariance structure, multiple sets with 8 samples per set are selected. For each of the 8 samples, synthetic data is created, and the models are fitted to the common functional form. From the 8 fitted models, the covariance is computed. The covariance of the 8 sampled models is computed for each set. The process is then repeated including the interpolated models, in addition to the 8 sampled models, for computing the covariance following the method described above. Including the interpolated models in the calculation of the covariance matrix results in a mean covariance matrix that is closer to the population covariance than using just 8 sampled models for computing the covariance. Therefore, using the interpolated GMPEs in the estimation of the covariance leads to improved estimates of the covariance.

For both DCPP and PVNGS, the coefficient distributions are calculated for 17 periods, between T = 0.01 sec and T = 3 sec. The primary use of the covariance matrix is to generate a broad range of models. The range of models depends on the size of the covariance and on the number of models being generated. The values of the covariance matrices are given in the electronic attachment to Appendix H.

The sampled common-form models are generated only up to 3 seconds due to limitation in period applicability of some of the candidate GMPEs. Predicted spectral accelerations for periods above 3 seconds are based on the period scaling of NGA-West2 GMPEs beyond 3 seconds. This scaling for long periods is described in Appendix N.

6.4.3 Generation of Ground-Motion Model Maps

To test the required number of models generated, the TI Team used sample sizes of 7500 and 2000 for each of the distance metrics (R_{JB}-based models and R_{RUP}-based models), and computed median ground

motions for selected scenarios (different magnitude and distance combinations), described later in this Section. The standard deviations of the natural log spectral acceleration from the suite of 7500 and 2000 sampled common-form models for a given scenario for DCPP, at PGA, are compared in Figure 6.4.3-1. Based on the comparison in the Figure, the TI Team judged that 2000 models are adequate to capture the distribution of ground-motions, so the subsequent calculations (evaluation and selection of models) are based on a sample of 2000 models.

Figure 6.4.3-2 shows the PGA predictions of the candidate GMPEs for a **M**5 and R_X=-30 scenario, in comparison with the range of the sampled common-form models. The width of the distribution for each candidate GMPE represents the uncertainty model of Al Atik and Youngs (2014). The sampled models cover the range of the candidate GMPEs including their uncertainty.

Figure 6.4.3-3 shows the Sammon's maps (a two-dimensional projection of the model space) of 2000 sampled models for PVNGS for Model A and Model B. The space covered by the two different distance metrics lead to similar distribution and ranges of models. This indicated that either distance metrics can capture the range of the ground-motion models.

For the DCPP application, for each of the 2000 footwall models, the central hanging-wall branch (HW model 3) is applied to all the common-form models. Because the scenarios are all on the FW, this does not affect the Sammon's maps but it does affect the hazard calculation. Although the $NGAW2_{DC\text{-}MED}$ dataset does not include sites over the hanging wall (R_{JB} < 5 km) for dips less than 80 degrees that may have strong HW effects, the central HW term is included in the models for the effect on the hazard (the representative model is selected based on the simplified hazard). Following the selection of the common-form models, the DCPP base models are assigned a random HW model from one of the five HW models that replaces the central HW model initially assigned to each model. A random selection is appropriate because equally likely HW models were developed in Section 6.3. In this way, the epistemic uncertainty in the HW factors is captured. The reason for this two-step treatment of the HW effect for DCPP is to separate the process into an initial selection based on magnitude-distance scaling (without HW effects) and a second step that samples the HW scaling. All combinations of the five HW models and the representative common-form models are not used to reduce the total number for models for the hazard calculation.

For the PVNGS application, there are no known nearby faults, so HW effects are not expected to be critical. Therefore, for PVNGS, each of the 2000 models is randomly assigned one of the five SWUS hanging-wall models for the development of the Sammon's maps.

As mentioned above, for each of the 2000 models developed for the two sites, median ground motions are calculated for the selected scenarios. Independently, for each of the 17 periods used (Table 6.1-1), the ground motions are combined into a high-dimensional vector of ground-motion values, which is then projected into 2 dimensions using principal component analysis for that period (see Appendix H).

The Sammon's maps are then generated for each period using the principal component analysis as the starting solution. Sammon's maps are based on minimizing the misfit between the Euclidean distances of two vectors (i.e. log of the ground-motion values for the models) in high dimensions and 2 dimensions. The Euclidean distances between two vectors m1, m2 is calculated by

$$D(m_1, m_2) = \sqrt{\sum_{i=1}^{N} \left(x_{i,1} - x_{i,2} \right)^2} \qquad \text{(Eq. 6.4-4)}$$

where N is the dimension of the vector (number of scenarios) and x_i is the i^{th} entry of the vector (PSA value for scenario i). Distances calculated by Equation 6.4-4 treat each scenario in the vector equally. For hazard calculations, however, some of the scenarios contribute more to the hazard than others. Therefore, to emphasize those magnitude-distance combinations that contribute most to the hazard, the differences in Equation 6.4-4 are weighted by their contribution to the hazard. Thus, Equation 6.4-4 becomes

$$D(m_1, m_2) = \sqrt{\sum_{i=1}^{N} w_i \left(x_{i,1} - x_{i,2} \right)^2} \qquad \text{(Eq. 6.4-5)}$$

where w_i denotes the weight given to the i^{th} scenario.

For each period, the weights, w_i, are computed from a hazard deaggregation matrix using the mean model of the 2000 common-form models with the simplified source models described in Appendix D. The ground-motion levels used for the deaggregation are given in Table 6.4-1 and Table 6.4-2 for PVNGS and DCPP application, respectively. Plots of the deaggregation are shown in Sections 2.1.1, 3.1.1 and 4.1.1 in Appendix H (Chapters 2, 3 and 4 of Appendix H).

The distance metric chosen for deaggregation is R_X, to separate the contribution from the footwall and hanging-wall scenarios. For DCPP, the following deaggregation bins are used:

- ***M****: 4.5-5, 5-5.5, 5.5-6, 6-6.5, 6.5-7, 7-7.5*
- R_X*: (-10,-5), (-5,-2.5), (-2.5,0), (0,2.5), (2.5,5), (5,10), (10,15), (15,20), (20,30), (30,50), (50,75), (75,100)*

For PVNGS, the following deaggregation bins are used:

- ***M****: 4.5-5, 5-5.5, 5.5-6, 6-6.5, 6.5-7, 7-7.5*
- R_X*: (-100, -75), (-75, -50), (-50, -30), (-30, -20), (-20, -15), (-15, -10), (-10, -5), (-5, 0), (0, 5), (5, 10), (10, 15), (15, 20), (20, 30), (30, 50), (50, 75), (75, 100)*

The magnitude and distance scenarios for which the common-form models are evaluated (predictor variables for the high-dimensional space) are set at the center of these bins. These scenarios are listed

below. Note: these scenarios used for the Sammon's maps are not the same as the scenarios used to fit the candidate GMPEs with the common-form described at Section 6.4.1.

For DCPP, the following magnitude and distance scenarios are used:

- ***M****: 4.75, 5.25, 5.75, 6.25, 6.75, 7.25*
- R_X*: -7.5, -3.75, -1.25, 1.5, 3.75, 7.5, 12.5, 17.5, 25, 40, 62.5, 87.5*

For PVNGS, the following magnitude and distance scenarios are used:

- ***M****: 4.75, 5.25, 5.75, 6.25, 6.75, 7.25*
- R_X*: -87.5, 62.5, -40, -25, -17.5, -12.5, -7.5, -2.5, 2.5, 7.5, 12.5, 17.5, 25, 40, 62.5, 87.5*

The deaggregation weight, $w_{DEAGG_{ik}}$, for a given scenario, at a given ground-motion level, is the value of the deaggregation for the corresponding magnitude-distance bin which contains the scenario. It is given by:

$$w_{DEAGG_{ik}} = DEAGG_k(M_i, R_i) \qquad \text{(Eq. 6.4-6)}$$

where M_i and R_i are the magnitude and distance of the i[th] scenario, k is the ground-motion level, and $DEAGG$ is the value of the hazard deaggregation matrix for the bin containing the M_i and R_i for the k[th] ground-motion level.

The mean deaggregation weight for the i[th] scenario, $\overline{w}_{DEAGG_i}$ is computed by averaging over the number of ground-motion levels, as follows:

$$\overline{w}_{DEAGG_i} = \frac{1}{NG}\sum_k w_{DEAGG_{ik}} \qquad \text{(Eq. 6.4-7)}$$

where NG is the number of ground-motion levels. To avoid putting too much weight on the deaggregation results from the simplified model, the weights are broadened to use the average of the mean deaggregation weight ($\overline{w}_{DEAGG_i}$) and equal weight to each scenario. The renormalized weights are given in Equation 6.4-8:

$$w_i = 0.5\left(\overline{w}_{DEAGG_i} + \frac{1}{NS}\right) \qquad \text{(Eq. 6.4-8)}$$

where NS is the total number of scenarios.

For DCPP, the models are evaluated for SS and REV style-of-faulting, while for PVNGS, the models are evaluated for strike-slip and normal style-of-faulting. The strike-slip events are assumed to be vertically dipping. For the reverse events, a dip of 50° is used for DCPP based on the DCPP SSC model (Table 4.1.1). For the normal events, the same dip of 50° is used for PVNGS based on the PVNGS SSC model (Tables 4.2-1 and 4.2-2). The process is to generate ground motions from the candidate GMPEs and then refit them with a common-form model. To generate the ground motion from the candidate GMPES that use R_{RUP}, a Z_{TOR} value needs to be defined. When the common-form models are derived using the R_{JB} distance metric, there is no Z_{TOR} term in the common-form model. The R_{RUP}-based candidate GMPEs are evaluated for two equally weighted Z_{TOR} values. These are calculated from the model of CY14 – one is the mean value for the magnitude value, the other one is the mean plus 3 km. Only two Z_{TOR} values are needed to capture the Z_{TOR} scaling as this is a linear term in the common-form models (Eq. 6.4-2). For the R_{JB}-based models, only one Z_{TOR} value is used to develop geometries for compatible distance metrics (the mean of the CY14 model), because these models do not include Z_{TOR}-scaling in their functional form.

For each common-form model, the ground-motion values for each of these predictor variable combinations are computed and are combined into a high-dimensional vector, which is used as the basis for calculating Sammon's maps. The dimensions are:

- *DCPP*: 288 for R_{RUP}-based models (Model A) – (6 magnitudes, 12 distances, 2 SOF, and 2 Z_{TOR} values, leading to 6 x 12 x 2 x 2 = 288 dimensions)
- *PVNGS: 3*84 for R_{RUP}-based models (Model A) – (6 magnitudes, 16 distances, 2 SOF, and 2 Z_{TOR} values, leading to 6 x 16 x 2 x 2 = 384 dimensions), and 192 for R_{JB}-based models (Model B) – (6 magnitudes, 13 distances, 2 SOF, and 1 Z_{TOR} value, leading to 6 x 16 x 2 x 1 = 192 dimensions)

The dimensions of the vectors for Model A and Model B are different. Therefore, separate maps are calculated for each case. Thus, each model corresponds to a point in N-dimensional space, where N has values of 288, 384, and 192 for the DCPP, PVNGS Model A, and PVNGS Model B cases, respectively. This space is projected into two dimensions using principal component analysis (PCA), whose output is used as input for Sammon's maps (the first two principal components, however, typically account for about 85-90% of the variance, so the PCA provides a good starting solution). As described above in Equation 6.4-4, the contributions to the difference in the squared Euclidean distances between two vectors are weighted by the weights given by Equation 6.4-8. The deaggregation for PVNGS used ground motions at 10 levels between 0.0004 g and 1.8 g for PGA, as shown in Table 6.4-1, which corresponds to return periods of less than 10 to over 10,000,000 years. The center is at 300 years of return period. The impact of using lower return periods for the deaggregation is to broaden out the magnitudes and distances that contribute to the hazard. For computing the weights, only distances out to 70 km were considered, consistent with the range of distances that control the high-frequency hazard seen in Section 4.2. Figure 6.4.3-4a compares the weights and the deaggregation at 10^{-4} AFE for PVNGS. The weights have a broader range of magnitudes and distances with comparable weights, and they are not as concentrated

at the 15 km distance as seen in the deaggregations. Overall, the weights are generally consistent with the short-distance range seen in the deaggregations.

The deaggregation for DCPP used ground motions at 3 levels (A_4, A_5 and A_6 in Table 6.4-2) between 0.43 g and 1.14 g for PGA, which corresponds to return periods of less than about 1000 to over 100,000 years. The center is at about 10,000 years of return period. Figure 6.4.3-4b compares the weights and the deaggregation at 10^{-4} AFE for DCPP. As intended, the weights have a broader range of magnitudes and distances than the deaggregation: they are not as concentrated at the 3 to 6 km distance range as seen in the deaggregations. Overall, the weights are generally consistent with the short-distance range seen in the deaggregations.

The candidate GMPEs are also projected onto the same map, together with modified versions of themselves that include the additional epistemic uncertainty, which are calculated using the median predictions of the GMPEs ± two times the standard deviation of the epistemic uncertainty model of Al Atik and Youngs (2014). Hence, for each candidate GMPE, the following predictions are calculated:

$$LnY(\mathrm{T})_{ij} = f_i\left(M_j, \mathrm{T}, R_j, ...\right) + \alpha\sigma_{AY14}(T, M, F) \qquad \text{(Eq. 6.4-9)}$$

where f_i is the function for natural log of the median predictions of the j[th] GMPE, α = -2, 0, or 2, σ_{AY14} is the standard deviation of the epistemic uncertainty model of Al Atik and Youngs (2014), and i is the index of the scenario. There is some magnitude and SOF dependence to σ_{AY14}, but the main effect is to shift each candidate GMPE up or down by a constant factor.

6.4.4 Selection of Representative Models

The selection and weighting of models to be used in the hazard calculations is based on their position in the 2D maps, as described below. As an example, the Sammon's map for T = 0.01 sec for PVNGS is shown in Figure 6.4.4-1. The common-form models fit to the candidate GMPEs (called refitted candidate GMPEs) including epistemic uncertainty are shown by the colored points in this figure. The convex hull for these refitted candidate GMPEs is shown by the solid black line in the same figure (the convex hull can be thought of as the shape of a rubber band put around the outermost points). The shape of the convex hull is elongated in the x-axis direction because the additional epistemic uncertainty added to the candidate GMPEs is in the x direction. The convex hull has a general shape of an ellipse. Therefore, the TI Team judged that an ellipse was an adequate representation of the general shape of the convex hull. The best fitting ellipse to the convex hull of all refitted candidate GMPEs including the additional epistemic uncertainty is estimated using least squares. The Sammon's map is rotated such that the x-axis approximates constant scaling between the models, as shown by the orientation of the additional epistemic uncertainty assigned to each refitted candidate GMPEs. Because this is a fit to the convex hull, some refitted candidate GMPEs including the additional epistemic uncertainty may lie outside the

ellipse. From preliminary evaluations, the TI Team found that most of the refitted candidate GMPEs including the additional epistemic uncertainty fall within an ellipse scaled by 1.5 times the best-fitting ellipse. Therefore, a scale factor of 1.5 for the ellipse is used to set the minimum range of the Sammon's map to be sampled. To better define the body of the distribution of the common-form models near the center of the distribution, the fitted ellipse is also scaled by 0.5 to allow for more samples of common-form models around the center of the Sammon's maps (e.g. interpolating between models).

The fitted and scaled ellipses are used to guide the discretization of the Sammon's maps into a small number of regions. The ellipses are plotted on top of a contour plot of the mean-between event residual of each model, as shown in Figure 6.4.4-2. Then, the intersection points of each ellipse and the contours at {-0.3, -0.15, 0, 0.15, 03} are calculated. The +0.3 and -0.3 were selected because they generally captured the outermost range of the candidate GMPEs with epistemic uncertainty. The +0.15 and -0.15 values were selected to sample within the body of the distribution. If the maximum residual of any candidate GMPE (including the additional epistemic uncertainty models) is larger than 0.3 or the minimum residual is less than -0.3, then the range is expanded to capture the position of the candidate GMPEs in the Sammon's map. In addition to the points calculated on the ellipses, the center point of the ellipse is also selected, which roughly corresponds to the center of the candidate GMPEs. Thus, in total up to 31 points can be selected (three ellipses, 5 contours, two intersections for each contour and ellipse, plus the center model), but in practice not all of them are realized. For example, the inner ellipse typically does not reach far enough out to intersect with the -0.3 / 0.3 contour. In our application, the final number of selected representative common-form models for DCPP, PVNGS Model A, and PVNGA Model B for each period ranges from 16 to 25 and is provided in Table 6.4-3.

This approach leads to a suite of common-form models that captures the range of the candidate GMPEs including the ±2 sigma epistemic uncertainty in terms of their position in Sammon's map space. The approach ensures that the suite of models captures the locations of all candidate GMPEs in Sammon's map space. This application of a range of a limit on the mean between-event residuals is a way to screen out some models so that they don't need to be evaluated separately later. If the models had not been removed, they would have been given zero weight in the subsequent TI Team evaluation. As an example, the models that were screened out are shown in Figure 6.4.4-3. The models that are screened out primarily represent too weak or too strong distance scaling shown in the top frame in Figure 6.4.4-3.

The selected points on the ellipses are points in the Sammon's map space, but the objective is to sample the full map. The map is discretized using the Voronoi-diagram (Aurenhammer and Klein, 2000). of the selected points. To calculate the boundaries for the outer models, a fourth ellipse is added (fitted ellipse scaled by a factor of 2), with points at the same azimuth from the ellipse's center as the points on the third ellipse. An example of the Voronoi diagrams and the four ellipses is also shown for PVNGS (Model A) in Figure 6.4.4-2. A full set of these plots is given in Appendix H.

The cell sizes typically span less than 0.2 ln units in any direction, so that difference between common-form models in a cell will be small (less than 20% difference in the ground motion in terms of a constant scale factor). Based on the definition of the Sammon's map, the distance separating the models in the Sammon's map approximates the standard deviation between the predictions for any two models, so models that are close together on the map will have similar magnitude and distance scaling.

A single representative model needs to be selected for each cell. The selection of the representative model for each cell is based on the closeness to the mean hazard for the cell, as described below. Hazard curves are calculated for each common-form model using a simplified SSC model. The mean hazard (arithmetic, not log) is computed for all common-form models that fall within the cell. The mean is computed using equal weights because the cells are small (range less than 0.1 ln units in the Sammon's map).

To assign probabilities would require that the prior is used and in some cases weights are not set based on the prior). The model whose hazard curve is closest to the mean hazard curve of the cell (measured as the standard deviation of the differences in the log hazard values) is selected as a representative common-form model for the cell. The simplified SSC model for the calculation of the hazard curves is the same simplified source model as was used for the deaggregation (Appendix D). Because, as stated above, the difference between common-form models in a cell is small, the difference between the hazard from the common-form models within a cell is also small. An example of the range of hazard curves resulting from two Voronoi polygons is shown in Figure 6.4.4-4. The hazard for points within the cell are generally clustered together, showing that the Sammon's map is associating models that generally lead to similar hazard results. As shown in Figure 6.4.4-4, there can be outlier models within a cell in terms of the impact on the hazard. The single model with much higher hazard, shown in Figure 6.4.4-4, corresponds to a common-form model with stronger magnitude scaling than the other common-form models in the same Voronoi cell. This shows some limitations of the Sammon's map approach for grouping similar models; however, using the representative common-form model that corresponds to the mean hazard for the cell, avoids choosing outlier models.

As described earlier in this Section, for DCPP application, the central HW model was applied to all of the common-form models for the initial selection of the representative common-form model. Once the representative models were selected, the central HW model was replaced by a randomly selected HW model to capture the range of the HW scaling.

As a check of the HW scaling, the distribution of the selection of the HW branches for the selected representative common-form models was evaluated. Figure 6.4.4-5 shows the histogram of the number of each of the five HW models for DCPP and PVNGS at 5 Hz. The distribution of the sampling of the five HW models is close to uniform for DCPP. The mean hazard does not depend on how the hanging-wall models are associated to the cells that lead to high and low hazard because the mean hazard is

controlled by the standard deviation of the fractiles (for approximately log normally distributed hazard fractiles, the mean hazard is given by the median hazard times exp(sigma^2/2), where sigma is the standard deviation of the fractiles); however, the mean hazard will depend on the mean weighted value of the hanging-wall factors where the weights are the weights given to each cell. If more of the cells with higher weights were biased with high or low HW factors, then the mean hazard would be affected. As a check, the mean hanging-wall factor for a **M**7 earthquake with a dip of 45 degrees at R_X 5 km was computed using the hanging-wall factor for each cell and the weights for each cell for 5 Hz. The mean hanging-wall factor of 0.595 ln units is similar to the mean factor of 0.60 ln units, indicating there is not a significant hazard in the mean hazard due to the use of randomly selected hanging-wall models.

For PVNGS, the distribution is more peaked on the central models, but as HW effects are not expected to be a key factor for PVNGS because the virtual faults are randomly oriented, the TI Team judged that the distribution of the selected HW branches is not critical to the hazard.

For DCPP and PVNGS (Model A and Model B, separately), a complete set of maps showing the original GMPEs, their uncertainty and the selection process are shown in Sections 2.1.2, 3.1.2 and 4.1.2 in Appendix H (Chapters 2, 3 and 4 of Appendix H, respectively).

6.4.5 Assigning Weights to Representative Models

Although all candidate GMPEs passed the selection process, they do not lead to complete sampling of the ground-motion space and some of the models may be redundant in their ground-motion estimation. Therefore, the TI Team decided to apply weights to the suite of selected representative common-form model for each cell as of way of discretizing the continuous distribution of possible ground-motion models given in terms of Sammon's map.

The weight for the selected representative common-form model for each cell is based on comparisons to ground-motion data and on the distribution of the covariance matrix for the common-form coefficients. Alternative metrics for estimating weights were evaluated by the TI Team as described below. For each Voronoi cell, the selected metric is computed for all of the models that fall within the cell. The selected metric is averaged over all models that fall within the cell to obtain a mean value of the metric. This mean value is then multiplied by the area of the cell so that the final distribution will not depend on the number or on the size of the cells. The weight given to the representative common-form model selected for a cell is proportional to this area-weighted mean value of the selected metric:

$$w_i \propto A_i \frac{1}{Ni} \sum_{j=1}^{N_i} L_{ji} \qquad \text{(Eq. 6.4-10)}$$

where A_i is the area of the i^{th} Voronoi-cell, N_i is the number of models in cell *i* and L_{ji} is the value of the selected metric of the j^{th} model in the i^{th} cell. This is repeated for all cells and the weights are normalized to one. Tests were carried out calculating weights if cells are merged together. In this case, the weight for the merged cell equals approximately the sum of weights of the individual cells, showing that finer discretization does not change the distribution of weights.

The following alternative metrics were considered by the TI Team for calculating the weights:

- $1/|\mu(\delta B)|$, one over the absolute mean between-event residual;
- $1/\mu(\delta B)^2$, one over the squared mean between-event residual;
- $1/\Delta$, where Δ is the Euclidean distance in ground-motion space between the j^{th} model and the center model;
- $1/\Delta^2$;
- L, the likelihood;
- P, the "prior", which is the value of the probability density function of the coefficient distribution for each model;
- "posterior", which is the prior times the likelihood.

The first two metrics involve an inverse of the mean between-event residual (δB). To avoid a possible singularity if the mean between-event residual is zero, a small value ε is added to each mean residual. The value of ε is ε = 0.0075, which is 1/20 of the width of the residual contours used for selecting points on the ellipses. All of the abovementioned weights are calculated separately for the selected Models A and Models B, based on the respective maps.

6.4.5.1 Effect of Alternative Metrics for the Weights

In Figure 6.4.5-1, all weights are shown for the PVNGS case, based on the weighted $NGAW2_{PV\text{-}MED}$ dataset. The weights based on the different metrics are quite different – in particular, the weights based on likelihood and posterior favor just a few models.

The TI Team evaluation of these alternative metrics is as follows:

1. The squared mean residual was not used because it gave high weight to a few models, similar to the likelihood method, but without the additional information on the standard deviation contained in the likelihood;
2. The Euclidean distance from the center model was not used as this is a measure of the similarity to the average of the common-form models within one cell to the mean common-form model, and is better captured by the prior;
3. For a similar reason as in point (2), the squared Euclidean distance was not used;

4. Finally, the posterior was not used as this is dominated by the likelihood and does not add much to the likelihood approach.

For the final application, the TI Team selected three methods to use for estimating the weights: the inverse of the absolute value of the mean between-event residual, the likelihood, and the prior. In the following, the selected approaches for the weights are called wResidual, wLL and wPrior for the inverse of the absolute mean between-event residual, the likelihood, and the prior, respectively. The residual is an estimate of the absolute bias between model and data, whereas the likelihood also takes into account the variability of the data. The prior incorporates the notion that all original GMPEs are published models which were developed with great care and should be weighted equally. Equal weights refer to assignment of equal weights to the models used to generate the covariance matrix. Once generated, the prior weights reflect how often generated ground-motion models appear in a particular location. The prior weight incorporates the notion that the covariance is correct and fully represents the uncertainty.

For DCPP and PVNGS, examples of contour plots of the relevant mean between-event and the log-likelihood, plotted on top of the maps, and the areas of the cells are shown in Chapter 8 and 9. A full suite of contour plots is available in Sections 2.1.3, 3.1.3 and 4.1.3 in Appendix H (Chapters 2, 3 and 4 of Appendix H) for DCPP Model A, PVNGS Model A, and PVNGS Model B, respectively.

To compare the impact of the three selected approaches to the weights, the TI Team evaluated several plots showing the cumulative distribution and the quantiles of the ln(PSA) for individual scenarios. This provides checks on the centering of the models (50^{th} quantile) and on the body (25^{th} and 75^{th} quantiles) and range of the models (5^{th} and 95^{th} quantiles). In the site-specific applications, the TI Team applied subjective weights based on a weighting scheme logic tree described in Sections 8.3.2 and 9.1.3.2 for the two sites, respectively.

The three methods lead to three different sets of weights for the selected representative common-form models. For the hazard calculation, a single total weight is computed for each selected representative common-form model based on the weighted average of the three sets of weights using the logic tree weights. The TI Team's assessment of the appropriateness of the selected models and model weights in capturing the center, body, and range of the median amplitude are discussed in Section 8.4 for application to DCPP, and in Section 9.1.3 for application to PVNGS (Greater Arizona sources).

6.4.5.2 Cumulative Distribution Functions

Following the approach described above, the weights for the representative suite of common-form models are computed, the median ground-motion predictions from these models are calculated, and the cumulative distribution function (CDF) of the ln(PSA) is then calculated by summing the weights of

the representative common-form models which give a prediction lower than a specified ground-motion value.

Figure 6.4.5-2a shows an example plot of resulting CDF of the selected common-form models, for different approaches to the weights, for a scenario with **M**6.0, R_X = -15 km, normal-faulting case and T = 0.01 sec at PVNGS – Model A. In addition, the CDF of the candidate GMPE distribution is shown. To calculate the CDF of the candidate GMPEs, they are equally weighted, and the weight of an individual GMPE is partitioned 80%/10%/10% into its median and $\pm$ the uncertainty model (using α = -2, 0, and 2 in Eq. 6.4-8). Other examples showing CDF plots for different scenarios are provided in Figures 6.4.5-2b and 6.4.5-2c for **M**6.5, R_X = -10 km, strike-slip faulting case and T = 0.2 sec at DCPP, and for **M**6.5, R_X = -15 km, normal-faulting case and T = 1.0 sec at PVNGS – Model A, respectively.

Using the between-event residual-based weights usually yields to ground-motion distribution broader than the distribution for the candidate GMPEs. In contrast, using the likelihood-based and prior-based weights usually leads to narrow distributions.

A larger suite of plots showing CDF for several scenarios and periods are provided in Appendix H, Sections 2.1.5, 3.1.5 and 4.1.5 (Chapters 2, 3 and 4 of Appendix H), for DCPP, PVNGS Model A and PVNGS Model B, respectively. The information in these plots is used as a check on the weights applied to the residual and likelihood branches.

6.4.5.3 CDF Quantiles

From the CDF of the ground-motion distribution based on the total weights, the 0.05, 0.5 and 0.95 quantiles are calculated, as well as for the candidate GMPE distribution. The candidate GMPEs are equally weighted (as described above), while the common-form model distribution is based on the selected models and total weights. This allows comparing the width and range of the distribution of the representative suite of common-form models and the candidate GMPEs.

Figure 6.4.5-3 shows the 0.05, 0.5 and 0.95 quantiles distributions for Model A and for the PVNGS application, for **M**6.0, normal-faulting cases, at T = 0.01 sec, plotted against distance. Figure 6.4.5-4 shows the quantiles for the PVNGS (Model A) normal-faulting cases, at T = 0.01 sec, plotted against moment magnitude. Figure 6.4.5-5 shows the PSA 0.05, 0.5 and 0.95 quantiles distributions for PVNGS (Model A), for **M**6.0, strike-slip cases, at R_X = -15 km, plotted against periods. The range of the 0.05 to 0.95 quantiles from the representative common-form models is similar to the range from the candidate GMPEs. For some cases, the 0.05 quantile is less stable, leading to a distribution that is skewed to lower values. This is not significant for the hazard because the mean hazard is controlled by the upper tail of the ground-motion distribution.

Appendix H includes several plots showing the 0.05, 0.5 and 0.95 quantiles distributions versus distance and magnitude, for several magnitude and distance values, respectively, in Sections 2.1.6 and 2.1.8 for DCPP (Model A), in 3.1.6 and 3.1.8 for PVNGS (Model A), and 4.1.6 and 4.1.8 for PVNGS (Model B). In addition, the 0.05, 0.5, 0.95 quantiles are plotted against periods, for several scenarios, in Sections 2.1.9, 3.1.9 and 4.1.9 of Appendix H.

6.4.5.4 Range of Distribution

To assess the width of the common-form model distribution, the ratios of the 0.05/0.5 and 0.95/0.5 quantiles are plotted against distance, for several magnitudes. This is an indicator of possible skewness of the model distribution.

Figure 6.4.5-6 shows an example of the 0.05/0.5 and 0.95/0.5 quantiles ratios for Model A and for PVNGS, R_X=-15 km, normal style of faulting, for all periods, and **M**5 (top), **M**6 (center), and **M**7 (bottom).

The quantile ratios show a broadening of the uncertainty as distance increases from 1 to 50 km, which is counter-intuitive as there is more data in the 30-50 km range than the 1-5 km range for constraining GMPEs. The reason for this increase is that the suite of candidate GMPEs has different distance scaling, as discussed in Section 6.4.5.5.

Appendix H includes several plots showing ratios of the 0.05/0.5 and 0.95/0.5 quantiles versus distance for various periods for PVNGS and DCPP, respectively, in Sections 2.1.10, 3.1.10 and 4.1.10.

Although the ranges from the representative suite of common-form models do not bound the ranges from the GMPEs with additional epistemic uncertainty for all scenarios, the ranges of the 5th and 95th fractiles for the representative common-form models are, on average, wider than the ranges of the 5th and 95th fractiles for the GMPEs.

The fractiles for the representative suite of common-form models are based on the weights from the logic trees. The fractiles for the GMPEs with additional epistemic uncertainty are based on using equal weight for each candidate GMPE and using weights of 0.8, 0.1, and 0.1 for the original GMPE and the plus and minus 2 sigma levels for the additional epistemic uncertainty.

The histogram of the ratios of the 95th fractiles from the representative suite of common-form models to the 95th fractiles of the GMPEs for DCPP for strike-slip earthquakes is shown in the top frames of Figure 6.4.5-7. All of the spectral periods are included in the histogram. The lower frame shows the ratios of the 5th fractiles. The histograms for the 95th fractiles are centered on values greater than 0, indicating that the 95th fractiles for the common-form models are, on average, higher than the 95th fractile for the GMPEs. The histograms for the 5th fractile are centered on values less than 0, indicating that the 5th fractiles for the common-form models are, on average, lower than the 5th fractile for the

GMPEs. This indicates that the common-form models are, on average, yielding a wider range than the candidate GMPEs, but they are not broader for every scenario.

Similar histograms of the ratios of the 95th fractiles and 5th fractiles are shown in Figure 6.4.5-8 for DCPP for reverse earthquakes. The histograms for PVNGS are shown in Figures 6.4.5-9 and 6.4.5-10 for R_{RUP}-based models for strike-slip and normal earthquakes, and in Figures 6.4.5-11 and 6.4.5-12 for R_{JB}-based models for strike-slip and normal earthquakes. In all of the plots, the histograms are shifted to wider distributions for the common-form models, but for the R_{JB}-based models, the shift is small.

There are some scenarios for which the GMPEs give a wider range than the representative suite of common-form models in all of the plots. Part of the TI Team's evaluation is to set weights for the common-from models which are not just based on equal weight to each GMPE. Using different weights, the 5th and 95th fractiles for the GMPEs are expected to be different from the fractiles for the common-form models. Also, the shapes of CDFs of the common-form models (e.g. Figures 6.4.5-2 a through c), tend to be smoother than the shapes of the CDFS for the common-form models. The less smooth CDFs of the GMPEs leads to some cases for which the GMPE fractiles are broader than the common-form model fractiles.

6.4.5.5 Epistemic Uncertainty in Distance and Magnitude Scaling

Figures 6.4.5-13 and 6.4.5-14 show range of distance and magnitude scaling in the representative suite of common-form models for PVNGS (Model A), normal style of faulting, and T = 0.01 sec, compared to the scaling of the candidate GMPEs and the candidate GMPEs with epistemic uncertainty. The epistemic uncertainty of magnitude and distance scaling which is contained in the models is assessed by calculating the ratios of ground-motion predictions for different two different magnitudes and distances, and calculating their ratios. The range of the common-form models does not encompass all of the predictions from the candidate GMPEs plus epistemic uncertainty for every scenario. The data sets used for evaluating the alternative weight metrics shift the weights from each weighting each candidate GMPE. In particular, the use of the European data for normal faulting leads to different CBR that what have been by simply assigning equal weights to each candidate GMPE. Here, as shown in Appendix O, the hazard from the common-form models do encompass the hazard from the candidate GMPEs including additional epistemic uncertainty. This indicates that, when considering all scenarios relevant to the hazard, the range of the representative suite of common-form models is broad enough.

Figure 6.4.5-15 and Figure 6.4.5-16 show an example of the epistemic uncertainty in distance and magnitude scaling, respectively, for PVNGS (Model A), normal style of faulting, for T = 0.01 sec. Figure 6.4.5-15 shows the PSA ratio histogram for distance scaling for a **M**6 scenario. Figure 6.4.5-16 shows the PSA ratio histogram for magnitude scaling for a R_X distance of -15 km. These figures show that the range

of magnitude and distance scaling in the representative models is broader than the range of the candidate GMPEs.

Appendix H includes several plots showing epistemic uncertainty in distance and magnitude scaling for various periods for DCPP and PVNGS, respectively, in Sections 2.1.11, 2.1.12, 3.1.11, 3.1.12, 4.1.11 and 4.1.12.

6.5 Directivity Scaling Models

6.5.1 Candidate Models for Directivity Scaling

The most widely used models for incorporating directivity effects into ground motions are the Somerville et al. (1997) model and Abrahamson (2000) modification to this model. These two models parameterize the directivity effect for strike-slip faults using X cos(theta) as the predictive parameter, where X=s/L is the ratio of the rupture length between the epicenter and the site (s), to the total rupture length (L), and theta is the azimuth between the fault strike and the site azimuth from the epicenter.

In 2008, updated directivity models were developed as part of the PEER NGA-West1 ground-motion study. The expanded empirical data sets and numerical simulations for directivity from the 2008 studies showed that the directivity effect depends on the length s and not the normalized length X (Spudich and Chiou (2008). As an example comparison of using normalized versus un-normalized rupture lengths for a **M**8 earthquake, the directivity from the Spudich and Chiou (2008) directivity model is compared to the Abrahamson (2000) directivity model for T=3 seconds in Figure 6.5.1-1. The directivity effects from the Abrahamson (2000) model are similar to the Spudich and Chiou (2008) for the 100 km rupture length for X Cos(theta)>0.2. The Abrahamson (2000) model was based on numerical simulations for **M**7.5 strike-slip earthquakes. This figure shows that for longer or shorter rupture lengths, the older model based on the normalized rupture lengths is not similar to the Spudich and Chiou (2008) model.

In addition to the effect of using un-normalized rupture lengths, Figure 6.5.1-1 also highlights the issue of centering of the directivity. For **M**8, the Spudich and Chiou (2008) directivity model leads to positive directivity effects for almost all rupture locations (all values of X cos(theta)); however, the GMPE models are developed to have near zero mean residual for large magnitudes. This indicates that the 2008 directivity models are not directly applicable to the GMPEs without centering the directivity model.

Chiou and Youngs (2014) addressed the issue of centering the directivity model by considering the sampling of the directivity for stations in the empirical data set compared to the distribution of directivity parameters for randomly located stations. In-depth discussions on the issue of centering can be also found in Spudich et al. (2014) and in Spudich and Chiou (2013). Because the candidate GMPEs

tend to fit the same limited large magnitude data, the centering of the directivity model for the Chiou and Youngs (2014) dataset can be assumed to also represent the centering for the other NGA-West2 candidate GMPEs. For the non-NGA-West2 GMPEs used at DCPP (ASB14, ZH06 and ZL11), there are no available evaluations of the centering of the datasets for directivity parameters. The TI Team judged that directivity effects should be considered in all the models, for application to DCPP, given the short distances and large magnitudes of the controlling events; therefore, the TI Team models apply the Chiou and Youngs (2014) directivity centering to all the common-form models even though they were developed from a combination of NGA-West2 and non-NGA-West2 proponent models.

The key outcome of using this directivity model is that, for sites at the same closest distance, the median of the ground motion will vary for different locations along strike. That is, the GMPEs do not fully capture the scaling of the ground motion for sites located along the rupture (different directivity). Depending on the rupture and the site location, the directivity effect may increase or decrease the ground motion. Randomizing over the hypocenter location for the directivity implies variability in the median ground motions, which impacts the standard deviation.

To simplify the application of the directivity model, Watson-Lamprey (2015) developed scale factors that describe the change in the median and total standard deviation as a function of the position along strike (R_Y) and the distance perpendicular to the strike of the rupture (R_X). The Chiou and Youngs (2014) directivity model could be used, but randomizing over the hypocenter would increase the hazard calculation time, while the Watson-Lamprey's models, which pre-calculated the effect of hypocenter randomization, expedites the calculation. In the Watson-Lamprey (2015) approach, the location of the hypocenter was randomized along the rupture, and the median and variability for the range of hypocenter locations was computed using the directivity effect predicted by Chiou and Youngs (2014), which is based on the directivity parameter DPP described in Chiou and Spudich (2013). The standard deviation reflects the effects of the variability of the random hypocenter on the rupture plane. The median reflects the bias for a particular site and rupture-plane geometry. For example, the site that is located at the end of the rupture plane will have a median which is positive, reflecting a bias compared to the ground-motion models without explicit directivity effects. This simplified model is applicable to both strike slip and dip slip earthquakes.

An additional feature of the Watson-Lamprey model is an adjustment to the standard deviation given by the GMPEs. This reduction is intended to avoid double counting of the variability due to directivity that is implicitly included in the standard deviation from the GMPEs and the variability that is computed from forward modeling due to randomizing the hypocenter locations. This reduction applies only to frequencies below 0.5 Hz.

The Watson-Lamprey simplified method for directivity effects is described in Attachment C, and summarized in the following section. The equations for the preferred directivity model are also provided in the following section.

6.5.1.1 Watson-Lamprey (2015) Directivity Effects Model

The Watson-Lamprey (2015) simplified implementation of directivity is documented in a PEER draft report that will be published in 2015. The basic steps followed by Watson-Lamprey (2015) do develop her model are described here. First, a suite of rupture geometries for strike-slip ruptures up to a moment magnitude of 8 and reverse ruptures up to a moment magnitude of 7.5 was created. Next, the mean and standard deviation of the change in the 5% damped pseudo-spectral acceleration at sites due to directivity by randomizing over hypocenters was calculated for a suite of sites out to a rupture distance of 70 km. The hypocenter randomization model for strike-slip ruptures was from Chiou and Youngs (2008b). For reverse ruptures, a new hypocenter distribution model was developed based on the hypocenters from large magnitude reverse events world-wide (see Attachment C, Section 4).

Using the set of computed directivity factors, the mean and standard deviation of the change in the 5%-damped pseudo-spectral acceleration was used to develop models for both strike-slip and reverse ruptures. The resulting factors for the median and standard deviation were fit to simple parametric models: for strike-slip earthquakes, the model parameters are rupture length, R_X and R_Y; for reverse earthquakes, the model parameters are rupture width, rupture length, dip, R_X and R_Y. Figure 6.5.1-2 shows a schematic representation of the parameters utilized by the directivity model.

An example of the scaling for a strike-slip fault with 80 km rupture length (**M**7) and a site located at an R_X value of 3 km is shown in Figure 6.5.1-3 for two locations of the rupture, representative of the DCPP site and the Hosgri fault. For a rupture centered on the site (R_Y = 0), the median is slightly reduced and the additional standard deviation term (σ_{DIR_SS}) is slightly increased. For a rupture with one end of the rupture plane near the site location (R_Y = 40 km), both the median and standard deviation are increased. This shows that the directivity effects will be strongest if the site is located at the end of the rupture for large strike-slip ruptures. Attachment C has additional example cases.

The functional forms of the directivity adjustment for strike-slip and reverse earthquakes are given below. Although some of the formulas are identical for the two style-of-faulting, the full ensemble of formulas is provided for the two different style-of-faulting for completeness.

$$f_{DIR\_SS}(M, R_{RUP}, R_x, R_y, L) = Factor_{SS}(M, R_{RUP}, R_x, R_y, L)\exp\left(a_M * \left(M - c_{8b}(T)\right)^2\right) \times c_{8\_ratio}(T) T_{DIR\_R}(R_{RUP}) T_{DIR\_M}(M)$$

(Eq. 6.5-1)

and the functional form for reverse earthquakes is given by:

$$f_{DIR\_RV}(M, R_{RUP}, R_x, R_y, W, L, Dip) = Factor_{RV}(M, R_{RUP}, R_x, R_y, W, L, Dip)\exp\left(b_M * \left(M - c_{8b}(T)\right)^2\right) \times c_{8\_ratio}(T) T_{DIR\_R}(R_{RUP}) T_{DIR\_M}(M)$$

(Eq. 6.5-2)

where

$$T_{DIR\_R}(R_{RUP}) = \max\left(1 - \frac{\max\left(R_{RUP} - 40, 0\right)}{30}, 0\right) \quad \text{(Eq. 6.5-3)}$$

$$T_{DIR\_M}(M) = \min\left(\frac{\max\left(M - 5.5, 0\right)}{0.8}, 1\right) \quad \text{(Eq. 6.5-4)}$$

$$Factor_{SS}(M, R_{RUP}, R_x, R_y, L) = a_0 + a_1\left(\max\left(RyRatio * \overline{cos2\theta}, -0.5\right)\right) + a_2\left(\max\left(RyRatio * \overline{cos2\theta}, -0.5\right)\right)^2 + a_3\left(\max\left(RyRatio * \overline{cos2\theta}, -0.5\right)\right)^3 \quad \text{(Eq. 6.5-5)}$$

$$Factor_{REV}(M, R_{RUP}, R_x, R_y, W, L, Dip) = b_0 + b_1\overline{cos2\phi} + b_2\overline{cos2\phi}^2 + b_3\overline{cos2\phi}^3 + b_4\overline{cos2\theta} + b_5\overline{cos2\theta}^2 + b_6\overline{cos2\theta}^3 + b_7 RyRatio + b_8 RyRatio^2$$

(Eq. 6.5-6)

$$RyRatio = \min\left(\frac{|R_y|}{L/2}, 1\right) \quad \text{(Eq. 6.5-7)}$$

For strike-slip sources, $\overline{cos2\theta}$ is the average value of $cos2\theta$ evaluated over the length of the surface projection of the top of rupture and where θ is the angle between the ray from a point on the surface of rupture to the site and the ray from the same point along strike. This is calculated using the following equation:

$$\overline{cos2\theta} = \frac{\left(R_y + L/2 - 2\left|R_x\right| * ArcTangent\left(\frac{R_y + L/2}{\left|R_x\right|}\right)\right)}{L} - \frac{\left(R_y - L/2 - 2\left|R_x\right| * ArcTangent\left(\frac{R_y + L/2}{\left|R_x\right|}\right)\right)}{L} \quad \text{(Eq. 6.5-8)}$$

For reverse sources, $\overline{cos2\phi}$ is the average value of $cos2\phi$ evaluated in the plane perpendicular to rupture over the width of the rupture and where ϕ is the angle between the ray from a point on the rupture to the site and the ray from the same point up dip. This is calculated using the following equation:

$$\overline{cos2\phi} = \frac{\left(R_y + L/2 - 2\left|R_x \cos(Dip)\right| * ArcTangent\left(\frac{R_y + L/2}{\left|R_x \cos(Dip)\right|}\right)\right)}{L} - \frac{\left(R_y - L/2 - 2\left|R_x \cos(Dip)\right| * ArcTangent\left(\frac{R_y + L/2}{\left|R_x \cos(Dip)\right|}\right)\right)}{L} \quad \text{(Eq. 6.5-9)}$$

For reverse sources, $\overline{cos2\theta}$ is the average value of $cos2\theta$ evaluated over the length of the surface projection of the top of rupture and where θ is the angle between the ray from a point on the surface of rupture to the site and the ray from the same point along strike. This is calculated using the following equation:

$$\overline{cos2\theta} = \frac{\left(R_y + L/2 - 2\left|R_x \sin(Dip)\right| * ArcTangent\left(\frac{R_y + L/2}{\left|R_x \sin(Dip)\right|}\right)\right)}{L} - \frac{\left(R_y - L/2 - 2\left|R_x \sin(Dip)\right| * ArcTangent\left(\frac{R_y + L/2}{\left|R_x \sin(Dip)\right|}\right)\right)}{L} \quad \text{(Eq. 6.5-10)}$$

The coefficients for the directivity effects for the median ground motion are listed in Table 6.5-1.

The functional form of the directivity sigma adjustment for strike-slip earthquakes is given by:

$$f_{DIR\_SIG\_SS}(M,R_{RUP},R_x,R_y,L) = Factor_{SS}(M,R_{RUP},R_x,R_y,L)\exp\left(a_M*\left(M-c_{8b}(T)\right)^2\right) \times c_{8\_ratio}(T)T_{DIR\_R}(R_{RUP})T_{DIR\_M}(M)$$

(Eq. 6.5-11)

and the functional form for reverse earthquakes is given by:

$$f_{DIR\_SIG\_RV}(M,R_{RUP},R_x,R_y,W,L,Dip) = Factor_{RV}(M,R_{RUP},R_x,R_y,W,L,Dip)\exp\left(b_M*\left(M-c_{8b}(T)\right)^2\right) \times c_{8\_ratio}(T)T_{DIR\_R}(R_{RUP})T_{DIR\_M}(M)$$

(Eq. 6.5-12)

where

$$T_{DIR\_R}(R_{RUP}) = \max\left(1-\frac{\max\left(R_{RUP}-40,0\right)}{30},0\right) \quad \text{(Eq. 6.5-13)}$$

$$T_{DIR\_M}(M) = \min\left(\frac{\max\left(M-5.5,0\right)}{0.8},1\right) \quad \text{(Eq. 6.5-14)}$$

$$Factor_{SS}(M,R_{RUP},R_x,R_y,L) = a_0 + a_1\left(\max\left(RyRatio*\overline{cos2\theta},-0.5\right)\right) + a_2\left(\max\left(RyRatio*\overline{cos2\theta},-0.5\right)\right)^2 + a_3\left(\max\left(RyRatio*\overline{cos2\theta},-0.5\right)\right)^3 \quad \text{(Eq. 6.5-15)}$$

$$Factor_{REV}(M,R_{RUP},R_x,R_y,W,L,Dip) = b_0 + b_1\overline{cos2\phi} + b_2\overline{cos2\phi}^2 + b_3\overline{cos2\phi}^3 + b_4RyRatio + b_5RyRatio^2 \quad \text{(Eq. 6.5-16)}$$

$$RyRatio = \min\left(\frac{\left|R_y\right|}{L/2},1\right) \quad \text{(Eq. 6.5-17)}$$

For strike-slip sources, $\overline{cos2\theta}$ is the average value of $cos2\theta$ evaluated over the length of the surface projection of the top of rupture and where θ is the angle between the ray from a point on the surface of rupture to the site and the ray from the same point along strike. This is calculated using the following equation:

$$\overline{cos2\theta} = \frac{\left(R_y + L/2 - 2\left|R_x\right| * ArcTangent\left(\frac{R_y + L/2}{\left|R_x\right|}\right)\right)}{L} - \frac{\left(R_y - L/2 - 2\left|R_x\right| * ArcTangent\left(\frac{R_y + L/2}{\left|R_x\right|}\right)\right)}{L} \quad \text{(Eq. 6.5-18)}$$

For reverse sources, $\overline{cos2\phi}$ is the average value of $cos2\phi$ evaluated in the plane perpendicular to rupture over the width of the rupture and where ϕ is the angle between the ray from a point on the rupture to the site and the ray from the same point up dip. This is calculated using the following equation:

$$\overline{cos2\Phi} = \frac{\left(R_y + L/2 - 2\left|R_x \cos(Dip)\right| * ArcTangent\left(\frac{R_y + L/2}{\left|R_x \cos(Dip)\right|}\right)\right)}{L} - \frac{\left(R_y - L/2 - 2\left|R_x \cos(Dip)\right| * ArcTangent\left(\frac{R_y + L/2}{\left|R_x \cos(Dip)\right|}\right)\right)}{L} \quad \text{(Eq. 6.5-19)}$$

For reverse sources, $\overline{cos2\theta}$ is the average value of $cos2\theta$ evaluated over the length of the surface projection of the top of rupture and where θ is the angle between the ray from a point on the surface of rupture to the site and the ray from the same point along strike. This is calculated using the following equation:

$$\overline{cos2\theta} = \frac{\left(R_y + L/2 - 2\left|R_x \sin(Dip)\right| * ArcTangent\left(\frac{R_y + L/2}{\left|R_x \sin(Dip)\right|}\right)\right)}{L} - \frac{\left(R_y - L/2 - 2\left|R_x \sin(Dip)\right| * ArcTangent\left(\frac{R_y + L/2}{\left|R_x \sin(Dip)\right|}\right)\right)}{L} \quad \text{(Eq. 6.5-20)}$$

$$\sigma_{DIR\_SS} = \sqrt{f^2_{DIR\_SIG\_SS}(M, R_{RUP}, R_x, R_y, L) - \sigma^2_{CHANGE}(T)} \quad \text{(Eq. 6.5-21)}$$

$$\sigma_{DIR\_RV} = \sqrt{f^2_{DIR\_SIG\_RV}(M, R_{RUP}, R_x, R_y, L) - \sigma^2_{CHANGE}(T)} \quad \text{(Eq. 6.5-22)}$$

$\sigma^2_{CHANGE}(T)$ is the difference in the variance from the CY14 dataset if directivity effects are explicitly included or excluded in the model functional form. To focus on the range important for directivity, the $\sigma^2_{CHANGE}(T)$ is computed for large magnitudes and short distances (magnitudes greater than **M**6.5 and distances less than 20 km). The coefficients for the directivity effects for the sigma are listed in Tables 6.5-2 (a and b). The improved fit is only seen for frequencies less than 0.5 Hz. The reduction is zero for frequencies less than or equal to 0.5 Hz.

6.5.2 TI Team's Evaluation of Directivity Scaling Models

The TI Team evaluated the simplified approach to directivity described in Section 6.5.1.1 and the evaluations are summarized below.

The advantage of the Watson-Lamprey (2015) model is that it evaluates the net effect of variability in hypocenters on the directivity parameter rather than requiring a direct integration over hypocenter location for the hazard calculation. It has also estimates the impact on the standard deviation of other GMPEs in addition to the CY14 model. The model represents in average effects of directivity over the four NGA-West2 models. The cost of this simplification is that it may not capture all of the features of the CY14 model for the specific site-source geometry for DCPP.

Limitations of the Watson-Lamprey (2015) model are that:

1. It is only for straight faults;
2. It applies the CY14 directivity to other GMPEs;
3. It uses the changes to the standard deviation in the CY14 model to scale the standard deviations from the other GMPEs, and
4. The review of the Watson-Lamprey (2015) model for publication as PEER report is not complete and the model in still draft.

There are two major assumptions that are made in applying the CY14 centered directivity model to the GMPEs used in the DCPP GMC model: (1) that the large-magnitude distribution is similar amongst the NGA-West2 GMPEs so that similar directivity effects can be expected, and (2) that the centered CY14 model can be applied to the NGA-West2 GMPEs to model these effects. Considering the similarities of the large-magnitude short-distance data used by the various modelers, the TI Team's judgment is that the directivity effects will not become significant to hazard if separate centering models were developed for each GMPEs. PEER plans to develop GMPEs including directivity effects which are centered for each individual GMPE. This work is currently scheduled to be completed in 2017. It is beyond the scope of SWUS to develop these models.

6.5.2.1 Evaluation of Alternative Directivity Models

Because the Watson-Lamprey (2015) model is still in a draft report, the TI Team conducted simple checks to show that the results from the recommended model are reasonable in that they are consistent with the range of directivity effects from other directivity models, such as those shown in Figure 6.5.1-1. Because the long-period hazard at DCPP is controlled by the Hosgri fault (Section 4.1.4), the main concern for application of the directivity models is for strike-slip earthquakes at distances less than 10 km. The DCPP site is not located up-dip from the Los Osos fault, so directivity effects from the dip-slip Los Osos fault would not be large.

The TI Team used two simplified approaches to check the Watson-Lamprey directivity model. The first approach evaluates the directivity factors in the Watson-Lamprey model as compared with directivity models in terms of impact on ground motion for a specific scenario. The second approach evaluates the directivity effect on the hazard from the Hosgri fault for the DCPP site.

6.5.2.2 Evaluation of Directivity Effects on Ground Motion for a Specific Scenario

For the first evaluation, the directivity for a **M**7 earthquake at short distances is reviewed. Figure 6.5.1-3 introduced in the previous Section shows the Watson-Lamprey (2015) model for **M**7 earthquakes with an 80 km rupture on a strike-slip fault for two sites at an R_X distance of 3 km: a site located at the end of the rupture ($R_Y = 40$) and a site located at the center of the rupture ($R_Y = 0$). At a period of 3 seconds, the median directivity term for a site located at the end of the rupture is 0.18 (or a factor 1.2). At the center of the rupture, the directivity factor is -0.07 (factor of 0.93). Using the previous directivity models shown in Figure 6.5.1-1, for a 100 km long fault, the Spudich and Chiou (2008) model has a maximum directivity factor for T = 3 sec of 1.5 and a minimum factor of 0.9. If the Spudich and Chiou (2008) model was centered so that the mean factor was about 1.0, then the range would be about 0.7 to 1.3.

The Spudich and Chiou (2008) model is for a specified hypocenter location, while the Watson-Lamprey (2015) model is the average for a randomized hypocenter. The average directivity factor of 1.2 from the Watson-Lamprey model for sites located at the end of the rupture is in the upper range of the Spudich and Chiou model. At the center of the rupture, the Watson-Lamprey model has an average directivity factor of 0.93, which is consistent with sites near the center of the rupture having slightly below average because the ruptures will, on average, be away from the center. The standard deviation of the directivity factor is 0.15 for the site at the end of the rupture. This is consistent with a range of ± 30 % (± 0.28 in ln units) if the full range is taken to be about ± 2 standard deviations.

6.5.2.3 Evaluation of Directivity Effects on Hazard

For the second approach, a sensitivity study was conducted to compare the hazard at DCPP using the full CY14 directivity model and the simplified Watson-Lamprey directivity model.

The distributions of the along-strike and down-dip locations of the hypocenter are based on the distributions shown in Figures 6.5.2-1 and 6.5.2-2. For this sensitivity study, the following hypocenter distributions are used.

For strike-slip earthquakes, the distribution labeled "Appendix D" in Figure 6.5.2-1 is used for the along-strike distribution and the distribution labeled "CY2008" is used for the down-dip distribution. For reverse earthquakes, the uniform distribution is used for the along-strike distribution and the CY2008 distribution is used for the down-dip distribution. For both strike-slip and reverse earthquakes, the hypocenters are restricted to be at least 10% of the rupture length from the ends of the rupture as recommended by Chiou and Spudich (2013).

In the hazard code, these distributions are discretized into 10 locations along strike and 3 locations down dip. The discrete probabilities for these locations are given in Tables 6.5-3 (a and b).

The CY14 directivity model was developed for the CY14 GMPE. The CY14 directivity model uses the difference in the value of the parameter called DPP at the site of interest from the mean value of DPP for sites located at the same R_{RUP} for a given rupture. This difference in the site-specific value and the mean value is called ΔDPP. The hazard was computed using the CY14 GMPE (both the median and standard deviation for the CY14 model are used). Three alternative directivity models are used to compute the hazard:

1) No site-specific directivity added (e.g. $\Delta DPP = 0$);

2) The CY14 directivity model is added using the hypocenter distributions listed in Tables 6.5-3 (a and b);

3) The simplified Watson-Lamprey (2015) directivity model is added.

The hazard was computed for a period of T = 3 sec. At long periods the Hosgri is the main contributor to the hazard: at T=3 sec, the Hosgri contributes about 60% of the hazard at an APE of 10^{-4} and about 75% of the hazard at an APE of 10^{-5}. This contribution is based on the final 2015 DCPP SCC (PG&E, 2015) for the Hosgri fault. Given that the long-period hazard is controlled by the Hosgri fault, the sensitivity study is based on the impacts on the hazard from the Hosgri fault source only.

To show the effect of two directivity models, the ratio of the ground motion for T = 3 sec with directivity to the ground motion for T = 3 without directivity is shown in Figure 6.5.2-3. In the 10^{-3} to 10^{-5} AFE range, the CY14 model and the Watson-Lamprey (2015) model leads to similar directivity factors of 1.01 to 1.05. At lower hazard levels (10^{-6}), the models become more different with the CY14 model showing

increasing directivity effects, up to a factor of 1.08, while the Watson-Lamprey model shows a decrease to back to a factor of 1.00.

From this comparison, the TI Team concludes that the directivity effects based on the simplified Watson-Lamprey (2015) model leads to results consistent with the CY14 directivity model in the 10^{-4} to 10^{-5} range, but the Watson-Lamprey model leads to smaller directivity effects at the 10^{-6} hazard level. The TI Team attributes this difference to the reduction of the standard deviation before adding directivity effects in the Watson-Lamprey model as discussed below in Section 6.5.2.4.

6.5.2.4 Evaluation of Reduction of the Standard Deviation $\sigma^2_{CHANGE}(T)$

The Watson-Lamprey model includes a reduction in the standard deviation for frequencies less than 0.5 Hz to account for the improved fit to the large magnitude (**M** ≥ 6.5) and near-fault (R_{RUP} ≤ 20 km) data if the CY14 directivity parameter (ΔDPP) is included in the functional form of the ground-motion model. The size of the reduction was computed by fitting the data used to develop the CY14 model with two functional forms: one with the ΔDPP parameter and one without the ΔDPP parameter. The difference in the variance of the within-event residuals for **M** ≥ 6.5 and R_{RUP} ≤ 20 km for these two regression analyses provides an estimate of $\sigma^2_{CHANGE}(T)$.

The reduction of the standard deviation is intended to avoid double counting the aleatory variability implicitly included in the aleatory variability for the GMPEs and the computed aleatory variability due to the forward modeling of directivity effects using the CY14 directivity model. To evaluate if this reduction is appropriate, the within-event standard deviation was computed for subsets of the residuals for NGA-west data sets (these are the same residuals that are used to compute the ϕ_{SS}).

The first set of subsets is for **M** ≥ 6.5 and R_{RUP} ≤ 20 km, consistent with the subsets used by Watson-Lamprey (2015). The computed ϕ and the number of recordings for the ASK14, BSSA14, CB14, and CY14 models are listed in Table 6.5-4. The three GMPEs that did not include directivity as a parameter (ASK14, BSSA14, and CB14) have similar values of ϕ (0.54 to 0.57), but the GMPE that included directivity as a parameter (CY14) has the largest ϕ value of 0.63. This is counter-intuitive because adding an additional predictive parameter should, in general, lead to a better fit to the data and a smaller standard deviation. There are differences in the selected subsets for the four GMPEs, but the total number of recordings for the ASK14 and CB14 GMPEs are similar to the number for the CY14 GMPEs, so data set differences are not a likely cause of this counter-intuitive result.

The second set of subsets is for **M** ≥ 6.5 and R_{RUP} ≤ 50 km, consistent with the distance range used for the development of the global ϕ_{SS} models (see Section 5.4.1). The ϕ and the number of recordings for the ASK14, BSSA14, CB14, and CY14 models are also listed in Table 6.5-4. Comparing the ϕ values for

the two distance ranges, there is not a consistent trend between the four GMPEs: two of the GMPEs show no change for the two distance ranges, one GMPE shows slightly larger ϕ values at short distances, and one GMPE shows smaller ϕ values at short distances. If there was a large increase in the ϕ value at short distances due to directivity, then the ϕ values at short distances should be systematically larger than at larger distances for the three GMPEs that did not include directivity as a parameter. This is not seen in the results shown in Table 6.5-4.

Based on the lack of consistent large increase in the ϕ at short distances from the empirical data, there is not clear empirical evidence for a large increase in the standard deviation at short distances. One possible explanation for the lack of an observed increase in the ϕ at short distances may be that the available empirical data do not adequately sample the directivity effects (inadequate station coverage in the empirical data sets). Although the available empirical data may not be a representative sample of the full range of directivity conditions, the empirical data should capture some of the directivity effects on the ϕ value. Without a consistent trend seen in the ϕ values for the two distance ranges, the TI Team judged that the approach used by Watson-Lamprey to avoid double counting the aleatory variability due to directivity is appropriate.

6.5.2.5 Summary of Evaluation of the Watson-Lamprey Directivity Model

Based on the three comparisons given above, the TI Team judged that the directivity scaling in the Watson-Lamprey (2015) simplified implementation are consistent with previous directivity models and are adequate for evaluating the impact of directivity on the hazard for hazard. At a period of 2 seconds, used for the sensitivity studies in Section 14.2.1, the reduction of the standard deviation ($\sigma^2_{CHANGE}(T)$) in the Watson-Lamprey model is zero, so the reduction of the standard deviation is not an issue for the sensitivity studies. At periods longer than 3 seconds, the reduction of the standard error is an issue. For a period of 3 seconds, the results of the CY14 model and Watson-Lamprey model are similar for hazard levels in the 10^{-3} to 10^{-5} AFE, but at hazard levels below 10^{-5}, the Watson-Lamprey simplified model may not fully capture directivity effects.

The primary effect of the directivity using the CY14 model is to increase the standard deviation because the variability due to directivity is added to the standard deviation from the GMPE. In contrast, the Watson-Lamprey model reduces the standard deviation from the GMPE based on the improved fit to the residuals in the CY14 data set to avoid double counting variability for application to other GMPEs that did not directly include directivity effects. There is uncertainty as to which approach is correct. The evaluation of the empirical data, shown in Table 6.5-4, does not support the large difference in the standard deviation at short distances implied by the CY14 model; however, this may reflect the limitations of the available empirical ground motion data close to large magnitude earthquakes.

The epistemic uncertainty in the standard deviation is captured in the GMC model through the logic trees described in Chapter 13. The range of the total sigma from Chapter 13 leads to a broad range (factors of 1.15 to 1.25) on the ground motion for AFE of 10^{-4} to 10^{-6}, as shown in the hazard sensitivity results in Chapter 14 for T = 2 seconds. The same range of epistemic uncertainty will apply for T = 3 seconds. Therefore, the potential effects on the standard deviation due to directivity are well within the range of the total sigma logic trees described in Chapter 13.

The Watson-Lamprey (2015) model has a large advantage over the CY14 model in terms of the required computation time for hazard calculations because the randomization of the hypocenters is done outside of the hazard calculation. This allows for more sensitivity cases to be implemented.

The hazard sensitivity results in Section 14.2.1 showed that including or not including the directivity effect had a small impact on the hazard for a spectral period of 2 seconds. The TI Team's judgment is that, if the CY14 model was fully implemented, the results would fall within the range captured by the total sigma uncertainty.

Because (1) the Watson-Lamprey (2015) model is still under review a PEER, (2) the effect on the hazard at DCPP is small, (3) questions about the applicability of the CY14 centering and directivity models to other GMPEs, and (4) large increase in hazard run times with little expected effect if the CY14 directivity model is implemented in the hazard integral, the TI Team judged that the Watson-Lamprey (2015) directivity model should not be applied for either DCPP or PVNGS.

By excluding the directivity adjustment model in the logic trees for both sites has an implicit assumption that the variability of the ground motion due to directivity is captured by the standard deviation by the GMPEs for the two sites. The basis for this assumption is discussed below.

The standard deviation of GMPEs is due to the simplification of the source, path, and site effects (the single-station sigma approach is used which removes the simplification for site effects, so all that remains is the source and path). A key assumption in using the single-station standard deviation from empirical GMPEs for hazard calculations is that the data used to develop the GMPEs are a representative range of other aspects of the source and path that are not captured in the simple parameters used in the GMPEs. This would include the location of the hypocenter (e.g. directivity), slip distribution, rupture velocity, rise time (or complete slip time function), and 3-D crustal path effects. Directivity is just one of the parameters that is assumed to be representatively sampled in the empirical data.

In magnitude-distance ranges for which there are large numbers of recordings, forward, neutral and backward directivity conditions are all sampled. The TI Team assumes that the sampled distribution is representative of the distribution of future earthquakes.

In magnitude-distance ranges for which there are fewer data (e.g. large magnitudes at short distance), it is less likely that the distribution of directivity effects in available empirical data set is representative of

the distribution of directivity effects for a future earthquake at a specific site. For this reason, the TI Team used the Watson-Lamprey simplified model to check this for DCPP site, which has nearby faults. The results of the sensitivity study indicate that the variability of the ground motion at the DCPP site is consistent with the average variability for all sites.

6.6 Path Effects Models for PVNGS distant California and Mexico Sources

6.6.1 TI Team Models for Path Effects

With the recent large increase in the ground-motion data sets, systematic site, path, and source effects can be seen in the ground-motion residuals. A summary of the size of these systematic effects is given in Lin et al. (2011). The Lin et al. (2011) study showed that the site and path effects lead to similar uncertainties in the estimation of the ground motion at a specific site from an earthquake in a specific region. With data from a region, these path effects can be estimated, removing the path term from the aleatory variability in the traditional ergodic approach for ground-motion models.

The path terms (systematic deviations from the average distance scaling for a given source-site pair) for central Arizona from earthquakes in California and Mexico are based on the Arizona dataset consisting of earthquakes from California and Mexico that have been recorded at the 9 stations in the vicinity of PVNGS (Figure 6.6.1-1). From this dataset, 49 records from 11 earthquakes with rupture distances from 200 to 500 kilometers are evaluated to compute the path terms. Data from one event (NGA EQID 1017, **M**4.6 occurred on September 5, 2008) was an outlier in terms of the within-event residuals for the BSSA14 model. The TI Team found that the data from event 1017 are primarily at large distance. As a result, the event term captures the difference in distance scaling. This leads to an inconsistency for the event-term correction of the within-event residuals of the BSSA14 model. The BSSA14 within-event residuals are a clusters of outliers, leading to path ϕ_{SP-R} estimates that are larger than the ergodic ϕ. The TI Team judged that the trade-off between event terms and distance attenuation made it be unreliable, and removed this event for the path-effects evaluations.

As a result, the available data set includes 4 earthquakes in Region 1, 3 earthquakes in Region 2, and 3 earthquakes in Region 3.

For the development of the path term, first the average path term for all source regions shown in Figure 6.6.1-1 is computed. Next, the path term is evaluated separately by region to determine if there is a difference in the path terms for different source locations. The idea is that there may be differences in the wave propagation from earthquakes located northwest of central Arizona compared to earthquakes located west or southwest of central Arizona.

The development of the TI Team models for the path terms is described in Section 7.4.1. The estimated path terms and the resulting path term models for each of the three regions are shown in Chapter 7 (Figure 7.4.1-6).

6.6.2 Evaluation of Path Effects Models

As shown in Figure 7.4.1-6, the median path terms for Regions 2 and 3 are similar, about -0.6 ln units, whereas the median path terms for Region 1 are about +0.1 ln units (positive path terms correspond to increased ground motion relative to the distance scaling in the reference GMPE, while negative path terms correspond to reduced ground motion relative to the distance scaling in the reference GMPE). The large negative path term for regions 2 and 3 could be due to paths crossing the Gulf of California region where high heat flow would affect attenuation. Because the path terms for Regions 2 and 3 are similar, the path terms for these two regions are combined. The path terms for the combined regions are listed in Table 6.6-1 and shown in Figure 6.6.1-2. The epistemic uncertainty in the path terms shown in Table 6.6-1 is based on the limited sample size. Because the effects of the limited sample size are already captured in the epistemic uncertainty, there is no need for additional epistemic uncertainty in the path terms due to small sample size. Additional epistemic uncertainty for large magnitude scaling is included as described in Section 9.2.4.

The TI Team compared the path terms shown in Table 6.6-1 with the range of path terms estimated by Lin et al. (2011) for Taiwan. The Lin et al. standard deviations of the path terms at long periods range from 0.32 ln units (PSA for T = 1 sec) to 0.35 ln units (PSA for T = 3 sec). The path terms estimated for Regions 1, 2 and 3 are within the 5^{th} to 95^{th} range of the path terms from Lin et al. The TI Team judged that the estimated median path terms are consistent with the range of path terms seen in the Lin et al. data set, and are, therefore, reasonable.

Although there is a small number of events for path effects (3 earthquakes in Region 1 and 7 earthquakes in combined Region 2&3), there is enough to distinguish significant path effects with reduced ground motions for earthquakes in Regions 2&3. Discussion on the weights associated to the branches accounting for the path effects is included in the Section 9.2.3.

6.7 Models for Ground-Motion Computation for Splay and Complex Ruptures

As described in Chapter 4, the SSC for DCPP includes rupture scenarios that involve rupture of multiple fault segments including fault segments with major changes in the rake, dip, and rupture width (called complex ruptures) and ruptures of a splay fault off of a main rupture. While these complex and splay ruptures have very low rates of occurrence in the 2015 DCPP SSC and will, therefore, have little effect on

the hazard, the hazard analysts will require rules for implementing these ruptures using the GMPEs. For complex ruptures, the key issue is how to specify the style-of-faulting parameter which affects the scaling, and how to specify the dip and rupture width which affects the HW scaling.

6.7.1 Alternative Methods

Four alternative methods for using the GMPEs to compute the ground motion for complex and splay ruptures are described in Appendix J (Section J.4). The four methods are listed below:

- METHOD 1: Square Root of the Sum of the Squares (SRSS) of the PSA from Multiple Fault Segments
- METHOD 2: Approximate as a Single Fault using Fault Parameters weighted by the Area of the fault
- METHOD 3: Approximate as a Single Fault using Fault Parameters Averaged using fault parameters weighted by $1/R^2$ where R is the distance from the site to a point on the rupture plane.
- METHOD 4: Approximate as a Single Fault using Closest Segment Parameters

Method 1 takes the approach of computing the square root of the sum of the squares (SRSS) of the PSA values from each of the individual rupture segments (an individual segment is a part of the rupture that has similar rake, and dip and width):

$$PSA_{SRSS} = \sqrt{PSA_{Fault1}^2 + PSA_{Fault2}^2} \qquad \text{(Eq. 6.7-1)}$$

Method 1 is distinct from Methods 2, 3, and 4 in that it is the only method in which the individual rupture segments are treated separately in the GMPEs (separate magnitudes, rakes, dips, widths, and distance metrics for each source) and their ground motions combined in a separate step. Methods 2, 3, and 4 represent different ways of creating a single set of predictor variables (distance, magnitude, rake, dip and down-dip width) that can be used directly in the GMPEs. The motivation behind Method 1 is that the ground motion can be considered to be the combination of the ground motions from separate sub-faults from an extended rupture.

Method 2 calculates the average fault parameters (rake, dip, and down-dip width) along strike weighted by the area of each of the individual participating rupture segments. The distance metrics (R_{RUP}, R_{JB}, and R_X) are based on the distances for the closest point on the rupture plane from the site of interest. The magnitude is the magnitude for the combined ruptures.

Method 3 calculates the average fault parameters (rake, dip, and down-dip width) weighted by $1/R^2$. The fault ruptures are discretized and weighted averages for rake, dip, and down-dip width are computed based on inverse-squared distance to the rupture plane ($1/R^2$) in the following way:

$$Dip_{ave} = \frac{\sum \frac{Dip_i}{R_i^2}}{\sum \frac{1}{R_i^2}} \qquad \text{(Eq. 6.7-2)}$$

Similar weighted averages are used for the rake and the rupture width. The distance metrics (R_{RUP}, R_{JB}, and R_X) are based on the distances for the closest point on the rupture plane from the site of interest. The magnitude is the magnitude for the combined ruptures.

Method 4 is the simplest of the four approaches. The fault parameters and the distance metrics are taken from the closest point along the rupture to the site of interest. The magnitude is the magnitude for the combined ruptures.

The rupture dimensions of the faults are consistent with the Leonard (2010) magnitude-area scaling relations, which was used for the BBP validation scenarios. Details on rules followed for the rupture scenario parameterization are included in Section 5.2.3.1.

6.7.2 Evaluation of Alternative Models

6.7.2.1 Evaluation of Alternative Methods for Complex Ruptures

Although several of the earthquakes in the NGA-West2 database had complex or splay ruptures, Somerville (2011), as part of the DCPP Workshop #1, reviewed the available empirical data and found that there are only a few recordings at close distances (less than 10 km) from these complex and splay rupture scenarios to evaluate the alternative methods listed above. Therefore, the evaluation of the alternative approaches for computing the ground motions for complex ruptures is based on the scaling from finite-fault simulations using the SCEC Broadband Platform (BBP). As described in Appendix J (Section J.4), the ground motions are simulated for each of the ruptures separately and are then combined in the time domain. The ratio of the response spectra from the combined rupture to the response spectra from the primary rupture (the segment with the largest moment release) is used to evaluate the alternative methods.

For complex ruptures, two cases are modeled: (1) a strike-slip rupture and a reverse rupture with similar magnitude, and the site is located close to the dip-slip rupture (Complex Scenario 1B shown in Figure 6.7.2-1), and (2) a strike-slip primary rupture and a smaller reverse secondary rupture, and the site is close to the strike-slip rupture but still near the reverse rupture (Figure 5.2.3-4). Table 6.7-1 lists the fault parameters and distance metrics used for Complex Scenario 1B, which is used as an example of the approach for evaluating the four alternative methods for computing the ground motion for complex ruptures using GMPEs. Figure 6.7.2-2 shows the ln of the complex/primary PSA ratios from the BBP

simulations as a function of frequency. The ratios are generally small (less than 0.2 ln units). For comparison, the ratios for the four methods are shown in Figure 6.7.2-3. Method 1 leads to similar ratios as the simulations, whereas methods 2, 3, and 4 all over-predict the ratios at low frequencies. Similar comparisons were made for the other Complex Scenarios described in Tables 5.2.3-2 and 5.2.3-3 with similar results (described in Appendix J, Section J.4.2). Based on these comparisons, the TI Team selected Method 1 to estimate the ground motions for complex ruptures.

6.7.2.2 Evaluation of Alternative Methods for Splay Ruptures

The evaluation of the alternative approaches for computing the ground motions for splay ruptures is similar to the evaluation for complex ruptures: finite-fault simulations using the SCEC Broadband Platform (BBP) are generated for the separate ruptures and the ground motions are combined in the time domain as described in Appendix J (section J.4). The ratio of the response spectra from the combined rupture to the response spectra from the main rupture is used to evaluate the alternative methods.

For splay ruptures, two cases are modeled: (1) a strike-slip primary rupture with a strike-slip splay, with the site closer to the secondary (splay) segment (Splay Scenario 1C shown in Figure 6.7.2-4), and (2) a dip-slip rupture with a dip-slip splay both intersecting at depth with the primary rupture truncating the secondary rupture, and the site on the hanging-wall side, close the secondary segment surface trace (Figure 5.2.3-7).

Table 6.7-2 lists the fault parameters and distance metrics used for Splay Scenario 1C, which is used as an example of the approach for evaluating the four alternative methods for computing the ground motion for splay ruptures using GMPEs. Figure 6.7.2-5 shows the ln of the ratio of the PSA from the combined primary rupture and splay rupture to the PSA from the primary rupture from the BBP simulations as a function of frequency for each of the three simulation methods. The ratios increase with frequency. For comparison, the ratios for the four methods are also shown in Figure 6.7.2-6. The main difference between the four methods is at the lower frequency range. Method 1 leads to small ratios at low frequencies, consistent with the results from the simulations, whereas the other three methods tend to over-predict the effect at low frequencies. Similar comparisons were made for the other Splay Scenarios described in Tables 5.2.3-4 and 5.2.3-5 with similar results (described in Appendix J, Section J.4.3). Based on these comparisons, the TI Team selected Method 1 to estimate the ground motions for splay ruptures.

6.8 References

Abrahamson, N.A., and Youngs, R.R. (1992). A stable algorithm for regression analysis using the random effects model, *Bull. Seism. Soc. Am.*, Vol. 82, 505-510.

Abrahamson, N.A., and Silva, W.J. (1997). Empirical Response Spectral Attenuation Relations for Shallow Crustal Earthquakes, *Seismol. Res. Letts*, Vol. 68(1), 94-127.

Abrahamson, N.A., and Bommer, J.J. (2005). Probability and Uncertainty in Seismic Hazard Analysis, *Earthquake Spectra*, Vol. 21(2), 603-607, DOI: 10.1193/1.1899158

Abrahamson, N.A., and Silva, W. (2008). Summary of the Abrahamson & Silva NGA Ground-Motion Relations, *Earthquake Spectra*, Vol. 24(1), 67-97.

Abrahamson, N.A., and Somerville, P.G. (1996). Effects of the hanging wall and footwall on the ground motions recorded during the Northridge earthquake, *Bull. Seism. Soc. Am.*, Vol. 86, S93-S99.

Abrahamson, N.A. (2000). Effects of Rupture Directivity on Probabilistic Seismic Hazard Analysis, *Proceedings of the Sixth International Conference on Seismic Zonation: Managing Earthquake Risk in the 21st Century*, Earthquake Engineering Research Institution (EERI), Palm Springs, California, 260 pp.

Abrahamson, N.A., Silva, W.J., and Kamai, R. (2014). Summary of the AKS14 Ground-Motion Relation for Active Crustal Regions, *Earthquake Spectra*, Vol. 30(3), 1025-1055, DOI: 10.1193/070913EQS198M.

Akkar, S., Sandikkaya, M.A., and Bommer, J.J. (2014a). Empirical ground-motion models for point- and extended-source crustal earthquake scenarios in Europe and the Middle East, *Bull. Earthquake Eng.*, Vol. 12(1), 359-387, DOI: 10.1007/s10518-013-9461-4.

Akkar, S., Sandikkaya, M.A., and Bommer, J.J. (2014b). Erratum to: Empirical ground-motion models for point- and extended-source crustal earthquake scenarios in Europe and the Middle East, *Bull. Earthquake Eng.*, Vol. 12(1), 389-390, DOI: 10.1007/s10518-013-9508-6.

Al Atik, L., and Youngs, R.R. (2014). Epistemic Uncertainty for NGA-West2 Models, *Earthquake Spectra*, Vol. 30(3), 1301-1318, DOI: 10.1193/062813EQS173M.

Atkinson, G., Bommer, J., and Abrahamson, N. (2014). Alternative approaches to modeling epistemic uncertainty in ground motions in Probabilistic Seismic Hazard Analysis, *Seismol. Res. Letts*, Vol. 85, 1141-1144, DOI: 10.1785/0220140120.

Atkinson, G.M, and Assatourians, K. (2015). Implementation and validation of EXSIM (a stochastic finite-fault ground-motion simulation algorithm) on the SCEC broadband platform, *Seismol. Res. Letts Letts*., Vol. 86(1), 48-60, DOI: 10.1785/0220140097.

Aurenhammer, F., and Klein, R. (2000). Voronoi Diagrams. Ch. 5 in *Handbook of Computational Geometry* (Ed. J.-R. Sack and J. Urrutia). Amsterdam, Netherlands: North-Holland, 201-290.

Bindi D., Massa M., Luzi L., Ameri G., Pacor F., Puglia R., and Augliera, P. (2014a). Pan-European Ground-Motion Prediction Equations for the Average Horizontal Component of PGA, PGV, and 5%-Damped PSA at Spectral Periods up to 3.0 s using the RESORCE dataset, *Bull. Earthquake Eng*., Vol. 12, 391-430, DOI: 10.1007/s10518-013-9525-5.

Bindi D., Massa M., Luzi L., Ameri G., Pacor F., Puglia R., and Augliera, P. (2014b). Erratum to: Pan-European Ground-Motion Prediction Equations for the Average Horizontal Component of PGA, PGV, and 5%-Damped PSA at Spectral Periods up to 3.0 s using the RESORCE dataset, *Bull. Earthquake Eng*., Vol. 12, 431-448, DOI: 10.1007/s10518-014-9589-x.

Boore, D.M., Stewart, J.P., Seyhan, E., and Atkinson, G.M. (2014). NGA-West 2 Equations for Predicting PGA, PGV, and 5%-Damped PSA for Shallow Crustal Earthquakes, *Earthquake Spectra*, Vol. 30(3), 1057-1085, DOI: 10.1193/070113EQS184M.

Campbell, K.W., and Bozorgnia, Y. (2003). Updated near-source ground motion (attenuation) relations for the horizontal and vertical components of peak ground acceleration and acceleration response spectra, *Bull. Seism. Soc. Am.*, Vol. 93, 314-331.

Campbell, K.W., and Bozorgnia, Y. (2008). NGA Ground Motion Model for the Geometric Mean Horizontal Component of PGA, PGV, PGD and 5% Damped Linear Elastic Response Spectra for Periods Ranging from 0.01 to 10 s, *Earthquake Spectra*, Vol. 24(1), 139-171.

Campbell, K.W., and Bozorgnia, Y. (2014). NGA-West2 Ground Motion Model for the Average Horizontal Components of PGA, PGV, and 5%-Damped Linear Acceleration Response Spectra, *Earthquake Spectra*, Vol. 30(3), 1087-1115, DOI: 10.1193/062913EQS175M.

Chiou, B.S.-J., Makdisi, F.I., and Youngs, R.R. (2000). Style-of-Faulting and Footwall/Hanging Wall Effects on Strong Ground Motion, *FY 1995 NEHRP Award Number 1434-95-G-2614*, final report, 21 pp.

Chiou, B.S.-J., and Youngs, R.R. (2008a). An NGA model for the average horizontal component of peak ground motion and response spectra, *Earthquake Spectra*, Vol. 24(1), 173-215.

Chiou, B.S.-J., and Youngs, R.R. (2008b). NGA model for the average horizontal component of peak ground motion and response spectra, *PEER Report 2008/09*, Pacific Earthquake Engineering Research Center, University of California, Berkeley, CA.

Chiou, B.S.-J., and Youngs, R.R. (2014). Update of the Chiou and Youngs NGA Model for the Average Horizontal Component of Peak Ground Motion and Response Spectra, *Earthquake Spectra*, Vol. 30(3), 1117-1153, DOI: 10.1193/072813EQS219M.

Chiou, B.S.-J., Spudich P. (2013). The Chiou and Spudich NGA-West2 directivity predictor DPP, *PEER Report 2013/09*, Pacific Earthquake Engineering Research Center, University of California, Berkeley, CA.

Donahue, J., and Abrahamson, N.A. (2013). Simulation-based hanging-wall effects, *PEER Report 2013/14*, Pacific Earthquake Engineering Research Center, University of California, Berkeley, CA.

Donahue, J., and Abrahamson, N.A. (2014). Simulation-based hanging-wall effects, *Earthquake Spectra*, Vol. 30(3), 1269-1284, DOI: 10.1193/071113EQS200M.

Dreger, D.S., Beroza, G.C., Day, S.M., Goulet, C.A., Jordan, T. H., Spudich, P.A, and Stewart, J. P. (2013). Evaluation of SCEC Broadband Platform Phase 1 Ground Motion Simulation Results, 33 pp. plus Appendices, Report submitted to SCEC, Aug. 1 2013. Available at http://scec.usc.edu/scecpedia/SCEC_BBP_Phase_1_Evaluation

Graizer, V. (2014). Updated Graizer-Kalkan Ground-motion Prediction Equations for Western United States, *Proceedings for the 10th U.S. National Conference on Earthquake Engineering Frontiers of Earthquake Engineering*, July 21-25, 2014, Anchorage, Alaska, Paper ID 1097, 11 pp.

Graves, R.W. and Pitarka, A. (2015). Refinements of the Graves and Pitarka (2010) Broadband Ground-Motion Simulation Method, *Seismol. Res. Letts*., Vol. 86(1), 75-80, DOI: 10.1785/0220140101.

Idriss, I.M. (2014). An NGA-West2 Empirical Model for Estimating the Horizontal Spectral Values Generated by Shallow Crustal Earthquakes, *Earthquake* Spectra, Vol. 30(3), 1155-1177, DOI: 10.1193/070613EQS195M.

Joyner, W.B., and Boore, D.M. (1981). Peak acceleration and velocity from strong-motion records including records from the 1979 Imperial Valley, California, earthquake, *Bull. Seism. Soc. Am.*, Vol. 71(2), 2011-2038.

Kishida, T., Kayen, R.E., Ktenidou, O.-J., Silva, W., Darragh, R., and Watson-Lamprey, J. (2014). PEER Arizona Strong Motion Database and GMPEs Evaluation, *PEER Report 2014/09*, Pacific Earthquake Engineering Research Center, Berkeley, CA, 135 pp.

Leonard, M. (2010). Earthquake Fault Scaling: Self-Consistent Relating of Rupture Length, Width, Average Displacement, and Moment Release, *Bull. Seismol. Soc. Am.*, Vol. 100, 1971-1988.

Lin, P.-S., Chiou, B., Abrahamson, N., Walling, M., Lee, C.-T., and Cheng, C.-T. (2011). Repeatable source, site, and path effects on the standard deviation for empirical ground-motion prediction models, *Bull. Seismol. Soc. Am.,* Vol. 101(5), 2281-2295, DOI: 10.1785/012009031.

Olsen, K. and Takedatsu, R. (2015). The SDSU Broadband Ground Motion Generation Module BBtoolbox Version 1.5, *Seismol. Res. Letts*., Vol. 86(1), 81-88, DOI: 10.1785/0220140102.

PG&E (2015). Seismic Source Characterization for Probabilistic Seismic Hazard Analysis for the Diablo Canyon Power Plant, San Luis Obispo County, California, Report on the Results of the SSHAC Level 3 Study in Partial Compliance with NRC Letter 50.54(f), March 2015.

Phillips, W.S., Mayeda, K., and Malagnini, L. (2014). How to invert multi-band, regional phase amplitudes for 2-D attenuation and source parameters: Tests using the US Array, *Pure Appl. Geophys.*, Vol. 171, 469-484, DOI: 10.1007/s00024-013-0646-1.

Sammon, J.W. (1969). A nonlinear mapping for data structure analysis, *IEEE Transactions on Computers*, C-18, 401-409.

Scherbaum, F., Kuehn, N.M., Ohrnberger, M., and Koehler, A. (2010). Exploring the Proximity of Ground-Motion Models Using High-Dimensional Visualization Techniques, *Earthquake Spectra*, Vol. 26(4), 1117-1138, DOI: 10.1193/1.3478697.

Somerville, P.G., and Abrahamson, N.A. (1995). Prediction of Ground Motions for Thrust Earthquakes, *Proceedings of the SMIP95 Seminar,* Cal. Div. of Mines and Geology, San Francisco, CA, 11-23.

Somerville, P.G., Smith, N.F., Graves, R.W., and Abrahamson, N.A. (1997). Modification of empirical strong ground motion attenuation relations to include the amplitude and duration effects of rupture directivity, *Seism. Res. Letts*, Vol. 68, 199-222.

Somerville, P., Collins, N., Graves, R., Pitarka, A., Silva, W., and Zeng, Y. (2006). Simulation of ground motion scaling characteristics for the NGA-E project, *Proceedings of the 8th National Conference on Earthquake Engineering*, April 18-22, San Francisco, California, USA, paper No. 1789.

Somerville (2011). Presentation at the DCPP SSHAC Workshop #1 in San Luis Obispo, CA, November 2011.

Spudich, P. and Chiou, B.S.-J. (2008). Directivity in NGA Earthquake Ground Motions: Analysis Using Isochrone Theory, *Earthquake Spectra*, Vol. 24(1), 279-298.

Spudich, P., Rowshandel, B., Shahi, S.K., Baker, J.W., and Chiou, B.S.-J. (2014) Comparison of NGA-West2 Directivity Models, *Earthquake Spectra*, Vol 30 (3), 1199-1221, DOI: 10.1193/080313EQS222M

Spudich and Chiou (2013) Chapter 5 in Final Report of the NGA-West2 Directivity Working Group, *PEER Report 2013/09*, Pacific Earthquake Engineering Research Center, University of California, Berkeley, CA

Watson-Lamprey, J. (2015). Capturing Directivity Effects in the Mean and Aleatory Variability of the NGA-West 2 Ground Motion Prediction Equations, Pacific Earthquake Engineering Research Center PEER Report (in preparation).

Zhao, J.X., Zhang, J., Asano, A., Ohno, Y., Oouchi, T., Takahashi, T., Ogawa, H., Irikura, K., Thio, H.K., Somerville, P.G., Fukushima, Y., and Fukushima, Y. (2006). Attenuation Relations of Strong Ground Motion in Japan Using Site Classification Based on Predominate Period, *Bull. Seism. Soc. Am*., Vol. 96, 898-913.

Zhao, J.X., and Lu, M. (2011). Magnitude-Scaling Rate in Ground-Motion Prediction Equations for Response Spectra from Large, Shallow Crustal Earthquakes, *Bull. Seism. Soc. Am*., Vol. 101, 2643-2661.

Table 6.1-1: 17 periods considered for the Sammon's map application to the SWUS GMC Project. For this application, the PSA at 0.01 sec is considered representative of the PGA.

Period (sec)
0.01 (PGA)
0.02
0.03
0.05
0.075
0.1
0.15
0.2
0.25
0.3
0.4
0.5
0.75
1.0
1.5
2.0
3.0

Table 6.3-1: Fixed and variable coefficients obtained during the derivation of the HW model

Period (sec)	Fixed Effects Coefficients				Variability		
	C_1	C_2	C_3	C_4	*Random* C_1 *Sigma*	Residual Sigma	Epistemic C_1 Sigma
0.01	1.0384	0.2160	2.0289	0.1675	0.1032	0.0474	0.1136
0.02	1.0465	0.2172	2.0260	0.1666	0.1095	0.0477	0.1195
0.03	1.0674	0.2178	2.0163	0.1670	0.1320	0.0488	0.1407
0.05	1.1210	0.2199	1.9870	0.1699	0.1802	0.0515	0.1874
0.075	1.1335	0.2218	1.9906	0.1817	0.1766	0.0531	0.1844
0.1	1.1354	0.2213	1.9974	0.1717	0.1838	0.0533	0.1914
0.15	1.0796	0.2169	2.0162	0.1814	0.1319	0.0506	0.1413
0.2	1.0825	0.2131	1.9746	0.1834	0.1473	0.0486	0.1551
0.25	1.0435	0.1988	1.9931	0.1767	0.1072	0.0462	0.1167
0.3	1.0406	0.2019	2.0179	0.1658	0.1259	0.0462	0.1342
0.4	1.0115	0.2090	2.0249	0.1624	0.1474	0.0456	0.1543
0.5	0.9822	0.2053	2.0041	0.1719	0.1547	0.0438	0.1608
0.75	0.9968	0.1713	1.8697	0.1866	0.2519	0.0439	0.2557
1	0.8719	0.1571	1.8526	0.3143	0.1604	0.0467	0.1671
1.5	0.7402	0.1559	1.8336	0.3195	0.1508	0.0394	0.1559
2	0.6094	0.1559	1.7996	0.3246	0.1421	0.0319	0.1457
3	0.3036	0.1616	1.6740	0.3314	0.1163	0.0151	0.1173

Table 6.3-2: Coefficients for SWUS GMC HW Adjustment Model

Period (s)	Model-dependent C1 Coefficients					Coefficients held Constant for all five models		
	Model HW1	*Model HW 2*	*Model HW 3*	*Model HW 4*	*Model HW 5*	C_2	C_3	C_4
0.01	0.868	0.982	1.038	1.095	1.209	0.2160	2.0289	0.1675
0.02	0.867	0.987	1.046	1.106	1.226	0.2172	2.0260	0.1666
0.03	0.856	0.997	1.067	1.138	1.278	0.2178	2.0163	0.1670
0.05	0.840	1.027	1.121	1.215	1.402	0.2199	1.9870	0.1699
0.075	0.857	1.041	1.133	1.226	1.410	0.2218	1.9906	0.1817
0.1	0.848	1.040	1.135	1.231	1.422	0.2213	1.9974	0.1717
0.15	0.868	1.009	1.080	1.150	1.292	0.2169	2.0162	0.1814
0.2	0.850	1.005	1.082	1.160	1.315	0.2131	1.9746	0.1834
0.25	0.868	0.985	1.044	1.102	1.219	0.1988	1.9931	0.1767
0.3	0.839	0.974	1.041	1.108	1.242	0.2019	2.0179	0.1658
0.4	0.780	0.934	1.011	1.089	1.243	0.2090	2.0249	0.1624
0.5	0.741	0.902	0.982	1.063	1.223	0.2053	2.0041	0.1719
0.75	0.613	0.869	0.997	1.125	1.380	0.1713	1.8697	0.1866
1	0.621	0.788	0.872	0.955	1.123	0.1571	1.8526	0.3143
1.5	0.506	0.662	0.740	0.818	0.974	0.1559	1.8336	0.3195
2	0.391	0.537	0.609	0.682	0.828	0.1559	1.7996	0.3246
3	0.128	0.245	0.304	0.362	0.480	0.1616	1.6740	0.3314
4	0	0.034	0.088	0.138	0.231	0.1616	1.6740	0.3314
5	0	0	0	0	0.040	0.1616	1.6740	0.3314
7.5	0	0	0	0	0	0.1616	1.6740	0.3314
10	0	0	0	0	0	0.1616	1.6740	0.3314

Table 6.4-1: Ground-motion levels (g) for PVNGS R_{RUP}-based (Model A) and R_{JB}-based (Model B) common-form models used in the calculation of hazard curves and deaggregation.

Period (sec)	A_1	A_2	A_3	A_4	A_5	A_6	A_7	A_8	A_9	A_{10}
0.01	0.0004	0.001019	0.002593	0.006604	0.016816	0.042818	0.109027	0.277618	0.706903	1.8
0.02	0.0004	0.001012	0.002561	0.006479	0.016394	0.041479	0.104951	0.265546	0.671884	1.7
0.03	0.0004	0.001025	0.002625	0.006724	0.017224	0.044123	0.113029	0.289541	0.741706	1.9
0.05	0.0004	0.001056	0.00279	0.007368	0.019459	0.05139	0.135721	0.358436	0.94662	2.5
0.075	0.0003	0.000841	0.002356	0.006604	0.018508	0.05187	0.14537	0.407411	1.1418	3.2
0.1	0.0003	0.000846	0.002388	0.006739	0.019013	0.053647	0.151365	0.427081	1.20502	3.4
0.15	0.0003	0.000859	0.002462	0.007054	0.020209	0.057896	0.165863	0.475177	1.36132	3.9
0.2	0.0003	0.000854	0.002434	0.006931	0.019741	0.056227	0.160143	0.456113	1.29908	3.7
0.25	0.0003	0.000846	0.002388	0.006739	0.019013	0.053647	0.151365	0.427081	1.20502	3.4
0.3	0.0003	0.000835	0.002323	0.006463	0.017985	0.050043	0.139248	0.387465	1.07814	3.0
0.4	0.0004	0.001056	0.00279	0.007368	0.019459	0.05139	0.135721	0.358436	0.94662	2.5
0.5	0.0004	0.001036	0.002684	0.006952	0.018008	0.046646	0.120828	0.31298	0.810715	2.1
0.75	0.0003	0.000767	0.001961	0.005013	0.012817	0.032769	0.083777	0.214187	0.547596	1.4
1.0	0.0001	0.000281	0.000791	0.002224	0.006254	0.017588	0.049461	0.139093	0.391155	1.1
1.5	0.0001	0.000267	0.000715	0.001913	0.005116	0.013683	0.036593	0.097866	0.261737	0.7
2.0	0.0001	0.000258	0.000664	0.00171	0.004405	0.01135	0.02924	0.075332	0.194077	0.5
3.0	0.00005	0.000131	0.000346	0.000909	0.002389	0.00628	0.01651	0.043404	0.114111	0.3

Table 6.4-2: Ground-motion levels (g) for DCPP R_{RUP}-based (Model A) common-form models used in the calculation of hazard curves and deaggregation.

Period (sec)	A_1	A_2	A_3	A_4	A_5	A_6	A_7	A_8	A_9	A_{10}
0.01	0.1	0.162725	0.264794	0.430887	0.701161	1.14097	1.85664	3.02121	4.91627	8.0
0.02	0.1	0.162725	0.264794	0.430887	0.701161	1.14097	1.85664	3.02121	4.91627	8.0
0.03	0.1	0.16681	0.278256	0.464159	0.774264	1.29155	2.15444	3.59381	5.99484	10.0
0.05	0.1	0.170224	0.289761	0.493242	0.839616	1.42923	2.43288	4.14134	7.04955	12.0
0.075	0.1	0.174497	0.304492	0.531329	0.927154	1.61786	2.82311	4.92624	8.59614	15.0
0.1	0.2	0.329737	0.543633	0.896281	1.47769	2.43624	4.0166	6.62211	10.9178	18.0
0.15	0.2	0.329737	0.543633	0.896281	1.47769	2.43624	4.0166	6.62211	10.9178	18.0
0.2	0.2	0.329737	0.543633	0.896281	1.47769	2.43624	4.0166	6.62211	10.9178	18.0
0.25	0.1	0.174497	0.304492	0.531329	0.927154	1.61786	2.82311	4.92624	8.59614	15.0
0.3	0.1	0.174497	0.304492	0.531329	0.927154	1.61786	2.82311	4.92624	8.59614	15.0
0.4	0.1	0.170224	0.289761	0.493242	0.839616	1.42923	2.43288	4.14134	7.04955	12.0
0.5	0.09	0.151897	0.256363	0.432675	0.730244	1.23247	2.08008	3.51065	5.92507	10.0
0.75	0.05	0.085112	0.144881	0.246621	0.419808	0.714613	1.21644	2.07067	3.52477	6.0
1.0	0.02	0.037693	0.07104	0.133887	0.252332	0.475563	0.896281	1.6892	3.18358	6.0
1.5	0.01	0.019459	0.037865	0.073681	0.143374	0.27899	0.542884	1.05639	2.05562	4.0
2.0	0.009	0.017162	0.032725	0.062403	0.118993	0.226904	0.432675	0.825052	1.57326	3.0
3.0	0.004	0.007979	0.015916	0.031748	0.063329	0.126325	0.251984	0.502642	1.00264	2.0

Table 6.4-3: Number of common-form models selected for each period for application to DCPP and PVNGS (referred to as representative suite of common-form models).

Period (sec)	Number of representative common-form models		
	DCPP	PVNGS Model A	PVNGS Model B
PGA	23	23	23
0.02	25	23	23
0.03	25	23	22
0.05	24	24	23
0.075	23	23	21
0.1	22	24	21
0.15	23	22	22
0.2	23	21	20
0.25	23	21	20
0.3	22	20	19
0.4	23	17	19
0.5	23	16	19
0.75	26	21	21
1	27	21	22
1.5	27	23	23
2	27	24	23
3	25	25	24

Table 6.5-1: Coefficients for directivity effect adjustments to the media for SS and REV earthquakes.

Median for SS earthquakes					Median for REV earthquakes				
Period-Independent Coefficients		Period-Dependent Coefficients			Period-Independent Coefficients		Period-Dependent Coefficients		
a_0	-0.078101	Period (sec)	c_{8_ratio}	c_{8b}	b_0	-0.13414	Period (sec)	c_{8_ratio}	c_{8b}
a_1	-0.033923	0.01	0.000	0.483	b_1	0.022371	0.01	0.000	0.483
a_2	0.20067	0.02	0.000	1.214	b_2	0.047363	0.02	0.000	1.214
a_3	0.149361	0.03	0.000	1.642	b_3	0.02078	0.03	0.000	1.642
a_M	-0.3004	0.05	0.000	2.181	b_4	0.1042	0.05	0.000	2.181
		0.075	0.000	2.609	b_5	0.00716	0.075	0.000	2.609
		0.1	0.000	2.912	b_6	-0.1239	0.1	0.000	2.912
		0.15	0.000	3.340	b_7	0.069512	0.15	0.000	3.340
		0.2	0.000	3.643	b_8	0.076094	0.2	0.000	3.643
		0.25	0.000	3.879	b_M	-0.26717	0.25	0.000	3.879
		0.3	0.000	4.071			0.3	0.000	4.071
		0.4	0.000	4.375			0.4	0.000	4.375
		0.5	0.460	4.610			0.5	0.460	4.610
		0.75	0.920	5.038			0.75	0.920	5.038
		1	1.000	5.341			1	1.000	5.341
		1.5	1.000	5.769			1.5	1.000	5.769
		2	1.000	6.072			2	1.000	6.072
		3	1.000	6.500			3	1.000	6.500
		4	1.000	6.804			4	1.000	6.804
		5	1.000	7.039			5	1.000	7.039
		7.5	1.000	7.467			7.5	1.000	7.467
		10	1.000	7.770			10	1.000	7.770

Table 6.5-2a: Coefficients for Directivity Adjustment Model for the Sigma

Sigma for SS earthquakes					Sigma for REV earthquakes				
Period-Independent Coefficients		Period-Dependent Coefficients			Period-Independent Coefficients		Period-Dependent Coefficients		
a_0	0.029001	Period (sec)	c_{8_ratio}	c_{8b}	b_0	0.044478	Period (sec)	c_{8_ratio}	c_{8b}
a_1	0.21112	0.01	0.000	0.483	b_1	-0.021982	0.01	0.000	0.483
a_2	0.53116	0.02	0.000	1.214	b_2	-0.025129	0.02	0.000	1.214
a_3	-0.60145	0.03	0.000	1.642	b_3	0.020343	0.03	0.000	1.642
a_M	-0.16960	0.05	0.000	2.181	b_4	-0.022130	0.05	0.000	2.181
		0.075	0.000	2.609	b_5	0.030626	0.075	0.000	2.609
		0.1	0.000	2.912	b_M	0	0.1	0.000	2.912
		0.15	0.000	3.340			0.15	0.000	3.340
		0.2	0.000	3.643			0.2	0.000	3.643
		0.25	0.000	3.879			0.25	0.000	3.879
		0.3	0.000	4.071			0.3	0.000	4.071
		0.4	0.000	4.375			0.4	0.000	4.375
		0.5	0.460	4.610			0.5	0.460	4.610
		0.75	0.920	5.038			0.75	0.920	5.038
		1	1.000	5.341			1	1.000	5.341
		1.5	1.000	5.769			1.5	1.000	5.769
		2	1.000	6.072			2	1.000	6.072
		3	1.000	6.500			3	1.000	6.500
		4	1.000	6.804			4	1.000	6.804
		5	1.000	7.039			5	1.000	7.039
		7.5	1.000	7.467			7.5	1.000	7.467
		10	1.000	7.770			10	1.000	7.770

Table 6.5-2b: Coefficients for Directivity Adjustment Model for the Sigma (from Figure 1.1. of Watson-Lamprey, 2015).

Period (sec)	Frequency (Hz)	σ_{CHANGE}
0.0 - 2.0	≤ 0.5	0
3	0.33	0.1205
4	0.25	0.1535
5	0.20	0.1913
7.5	0.13	0.2285
10	0.1	0.2478

Table 6.5-3a: Discrete distribution used for hypocenter location along strike

Hypocenter location along strike (ratio to rupture length)	Probability for Strike-slip ruptures	Probability for Reverse ruptures
0.10	0.13	0.1
0.19	0.10	0.1
0.28	0.09	0.1
0.37	0.09	0.1
0.46	0.09	0.1
0.54	0.09	0.1
0.63	0.09	0.1
0.72	0.09	0.1
0.81	0.10	0.1
0.90	0.13	0.1

Table 6.5-3b: Discrete distribution used for hypocenter location down dip.

Hypocenter location down dip (ratio to rupture width)	Probability for Strike-slip ruptures	Probability for Reverse ruptures
0.25	0.15	0.15
0.50	0.35	0.35
0.25	0.50	0.50

Table 6.5-4: Comparison of the ϕ from large magnitude earthquakes for two distance ranges.

	ϕ (ln units)				Number of Recordings			
	ASK14	BSSA14	CB14	CY14	ASK14	BSSA14	CB14	CY14
M ≥ 6.5, R_{RUP} ≤ 20 km	0.55	0.57	0.54	0.63	250	197	269	256
M ≥ 6.5, R_{RUP} ≤ 50 km	0.62	0.55	0.54	0.63	629	447	715	682

Table 6.6-1: Median Path Term

	Path Term - Region 1			**Path Term - Region 2&3**		
Period (sec)	Central	High	Low	Central	High	Low
PGA	-0.119	0.1	-0.338	-0.626	-0.387	-0.866
0.02	-0.119	0.1	-0.338	-0.626	-0.387	-0.866
0.03	-0.119	0.1	-0.338	-0.626	-0.387	-0.866
0.05	-0.119	0.1	-0.338	-0.626	-0.387	-0.866
0.075	-0.119	0.1	-0.338	-0.626	-0.387	-0.866
0.1	-0.119	0.1	-0.338	-0.626	-0.387	-0.866
0.15	-0.119	0.1	-0.338	-0.626	-0.387	-0.866
0.2	-0.119	0.1	-0.338	-0.626	-0.387	-0.866
0.25	-0.119	0.1	-0.338	-0.626	-0.387	-0.866
0.3	-0.119	0.1	-0.338	-0.626	-0.387	-0.866
0.4	-0.119	0.1	-0.338	-0.626	-0.387	-0.866
0.5	-0.119	0.1	-0.338	-0.626	-0.387	-0.866
0.75	-0.119	0.1	-0.338	-0.626	-0.387	-0.866
1	-0.119	0.1	-0.338	-0.626	-0.387	-0.866
1.5	-0.119	0.131	-0.369	-0.626	-0.331	-0.921
2	-0.119	0.163	-0.401	-0.626	-0.276	-0.977
3	-0.119	0.184	-0.421	-0.626	-0.256	-0.996
4	-0.119	0.198	-0.436	-0.626	-0.229	-1.023
5	-0.119	0.209	-0.447	-0.626	-0.210	-1.042
7.5	-0.119	0.23	-0.468	-0.626	-0.195	-1.057
10	-0.119	0.245	-0.483	-0.626	-0.168	-1.084

Table 6.7-1: Computed fault parameters and distance metrics for the Complex Scenario 1B: strike-slip primary rupture and a secondary reverse rupture with similar magnitudes.

	R_{RUP} (km)	R_{JB} (km)	R_X (km)	Mag	dip	rake	Down-dip width (km)
Strike-Slip Rupture	22.8	22.8	22.8	6.93	90	180	22
Dip-Slip Rupture	7.8	0	10.2	6.87	50	90	22
Method 2	7.8	0	10.2	7.2	71.5	138.3	22
Method 3	7.8	0	10.2	7.2	55	101.2	22
Method 4	7.8	0	10.2	7.2	50	90	22

Table 6.7-2 Computed fault parameters and distance metrics for the Splay Scenario 1C: Strike-slip main rupture with strike-slip splay.

	R_{RUP} (km)	R_{JB} (km)	R_X (km)	Mag	dip	rake	Down-dip width (km)
Strike-slip main Rupture	5.10	5.10	5.10	7.40	90	180	22.00
Strike-slip splay Rupture	0.66	0.66	0.66	6.43	90	180	11.93
Method 2	0.66	0.66	0.66	7.44	90	180	20.35
Method 3	0.66	0.66	0.66	7.44	90	180	13.06
Method 4	0.66	0.66	0.66	7.44	90	180	11.93

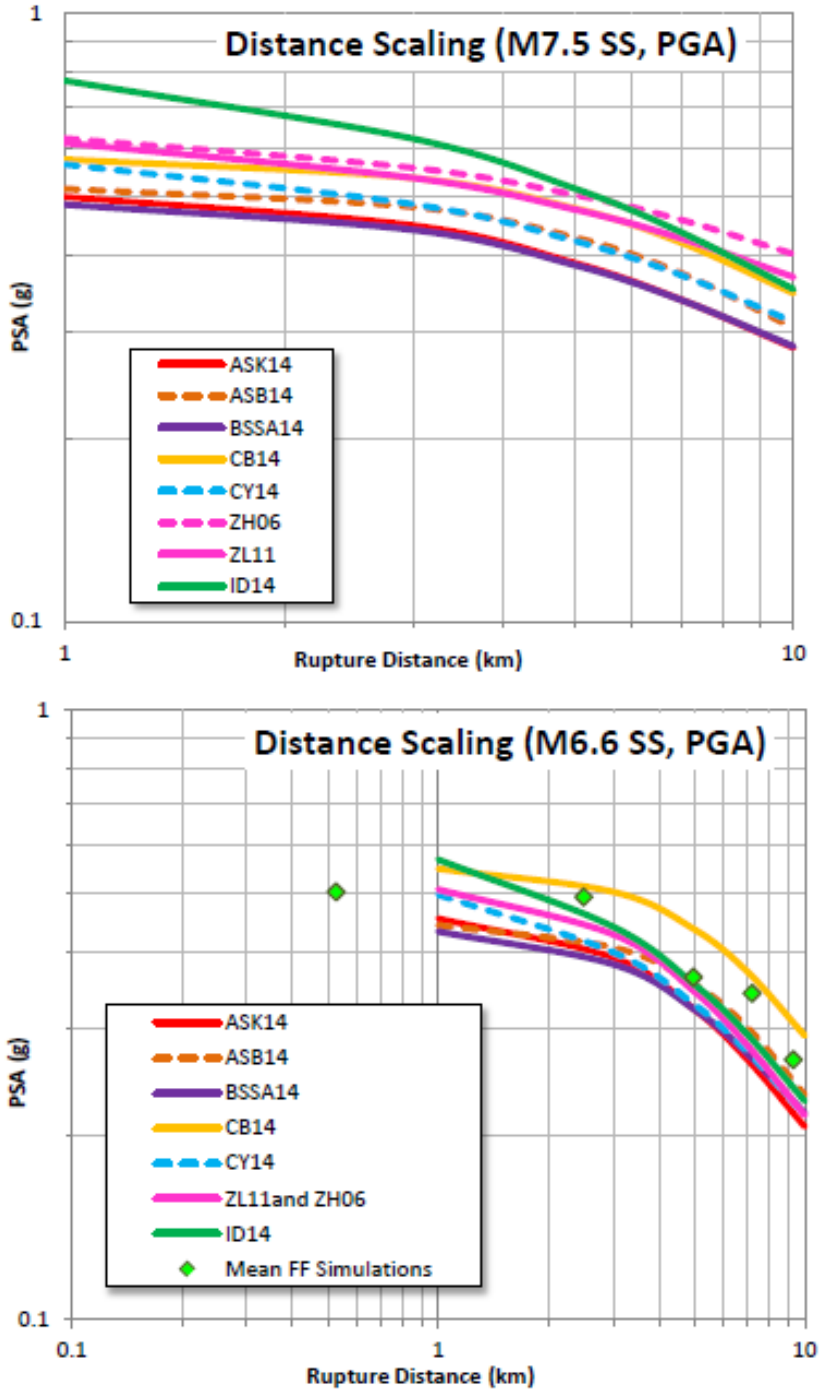

Figure 6.2.1-1: Distance scaling of the 5%-damped response spectra (PSA) at PGA for the candidate GMPEs for a **M**7.5 strike-slip event (top panel) and **M**6.6 strike-slip event (bottom panel). The mean of the finite fault (FF) simulations available for **M**6.6 is also shown in the bottom panel. The ZL11 and ZH06 PSA are identical at **M**6.6.

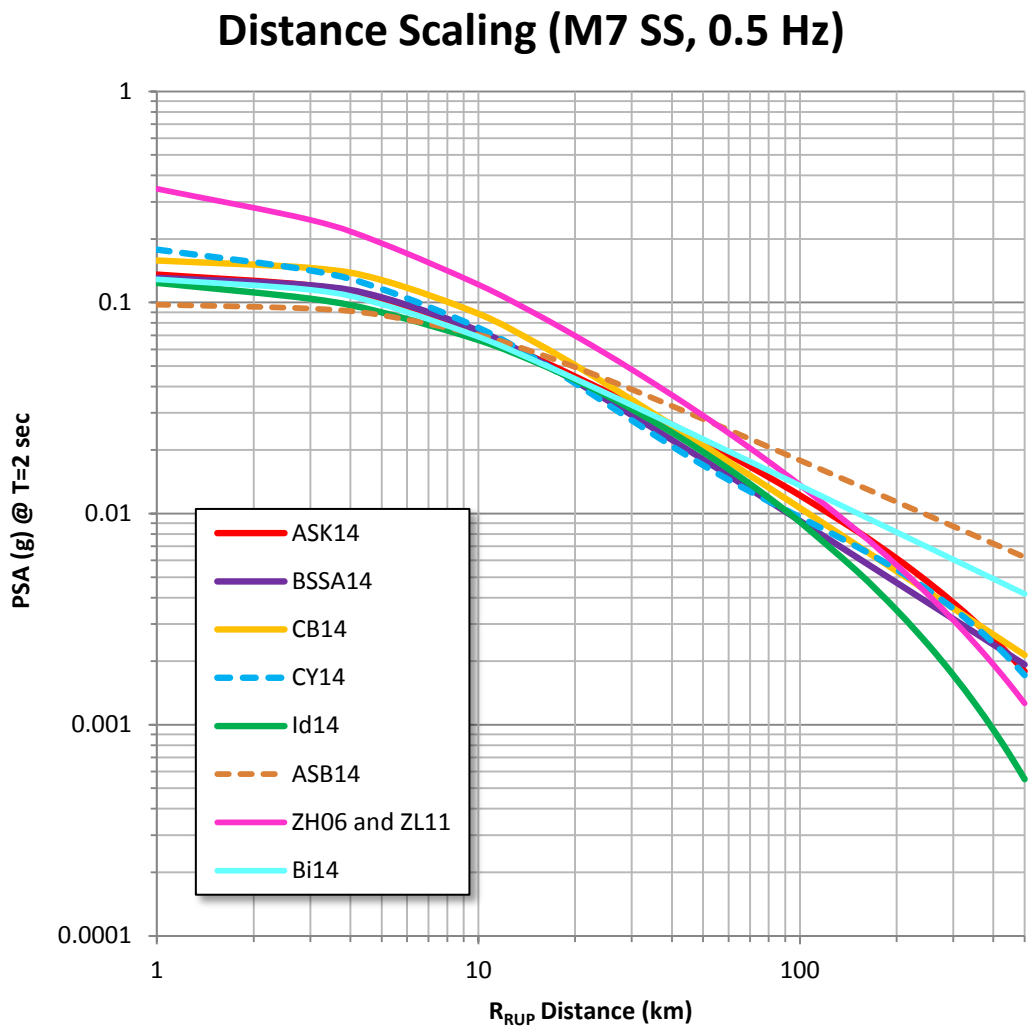

Figure 6.2.1-2: Distance scaling of the candidate GMPEs at 0.5 Hz for a **M**7.0 strike-slip event. The ZL11 and ZH06 PSA are identical at **M**7.0.

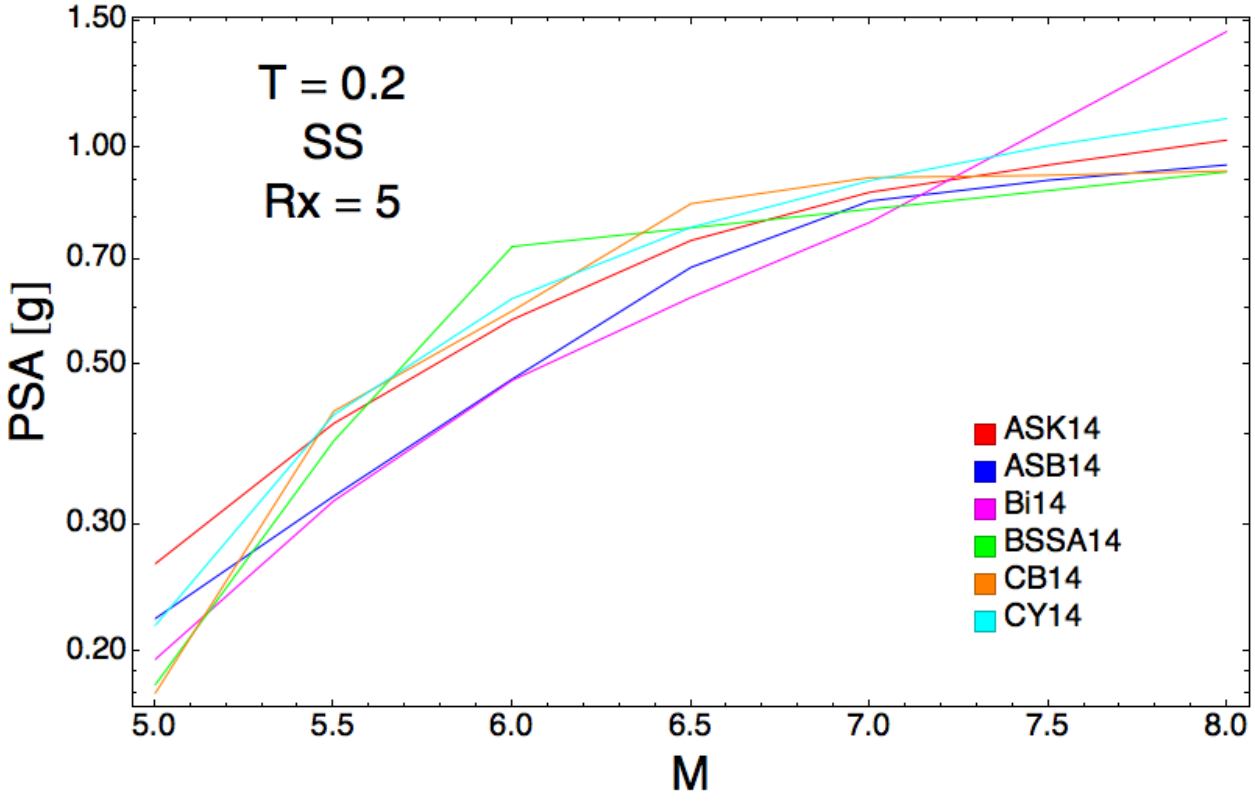

Figure 6.2.2-1: Magnitude scaling of the candidate GMPEs at 5.0 Hz for strike-slip event with R_X distance 5 km. Points in the plot are based on a 0.5 magnitude step.

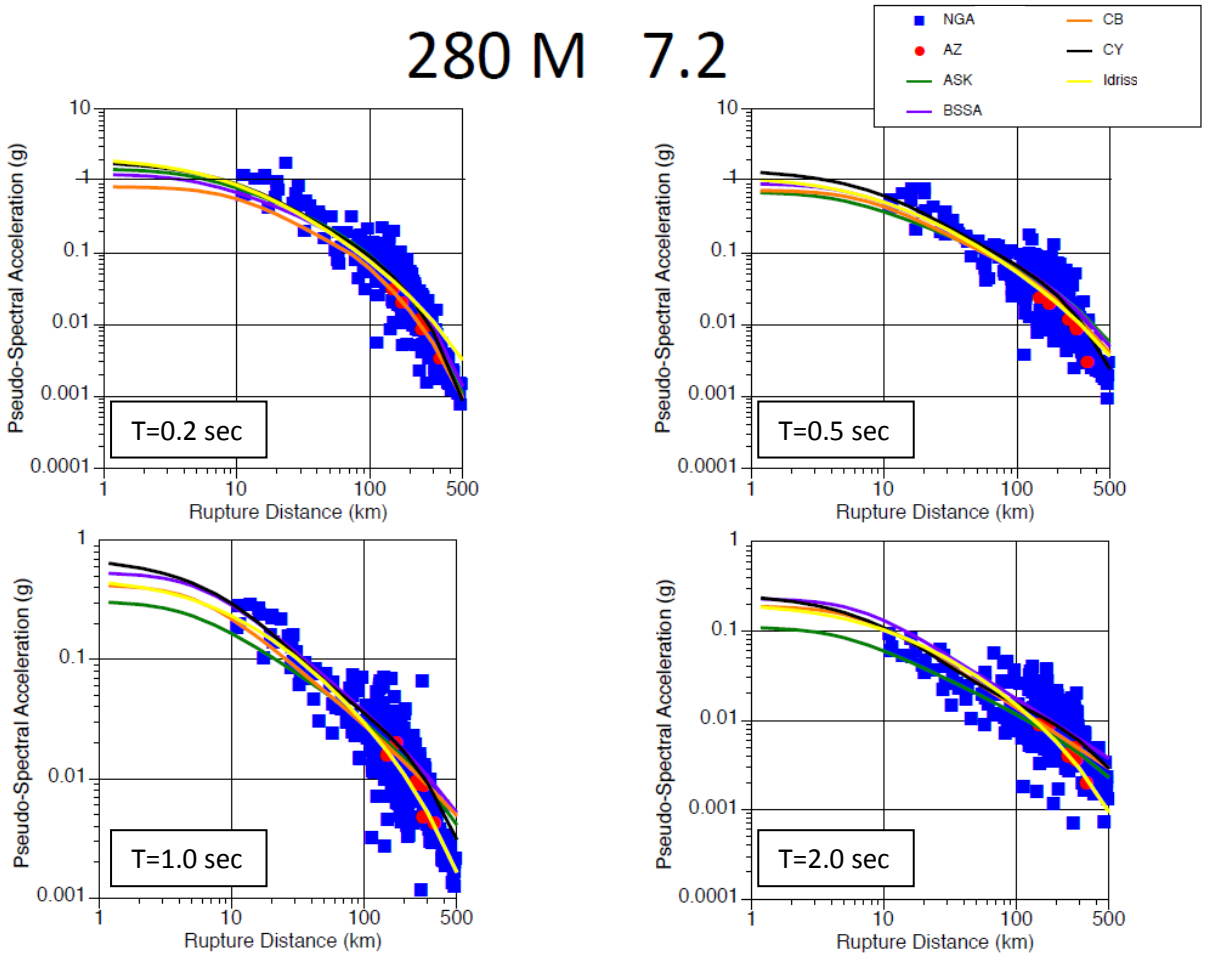

Figure 6.2.3-1: Pseudo-Spectral acceleration (g) at periods of 0.2, 0.5, 1.0 and 2.0 seconds from the El Mayor Cucapah event (NGA EQID 280) recorded by NGA stations in California (blue squares) and by Arizona stations (red circles). The event-term corrected (when event term is available) 2014 NGA-West2 ground-motion prediction equations are also shown.

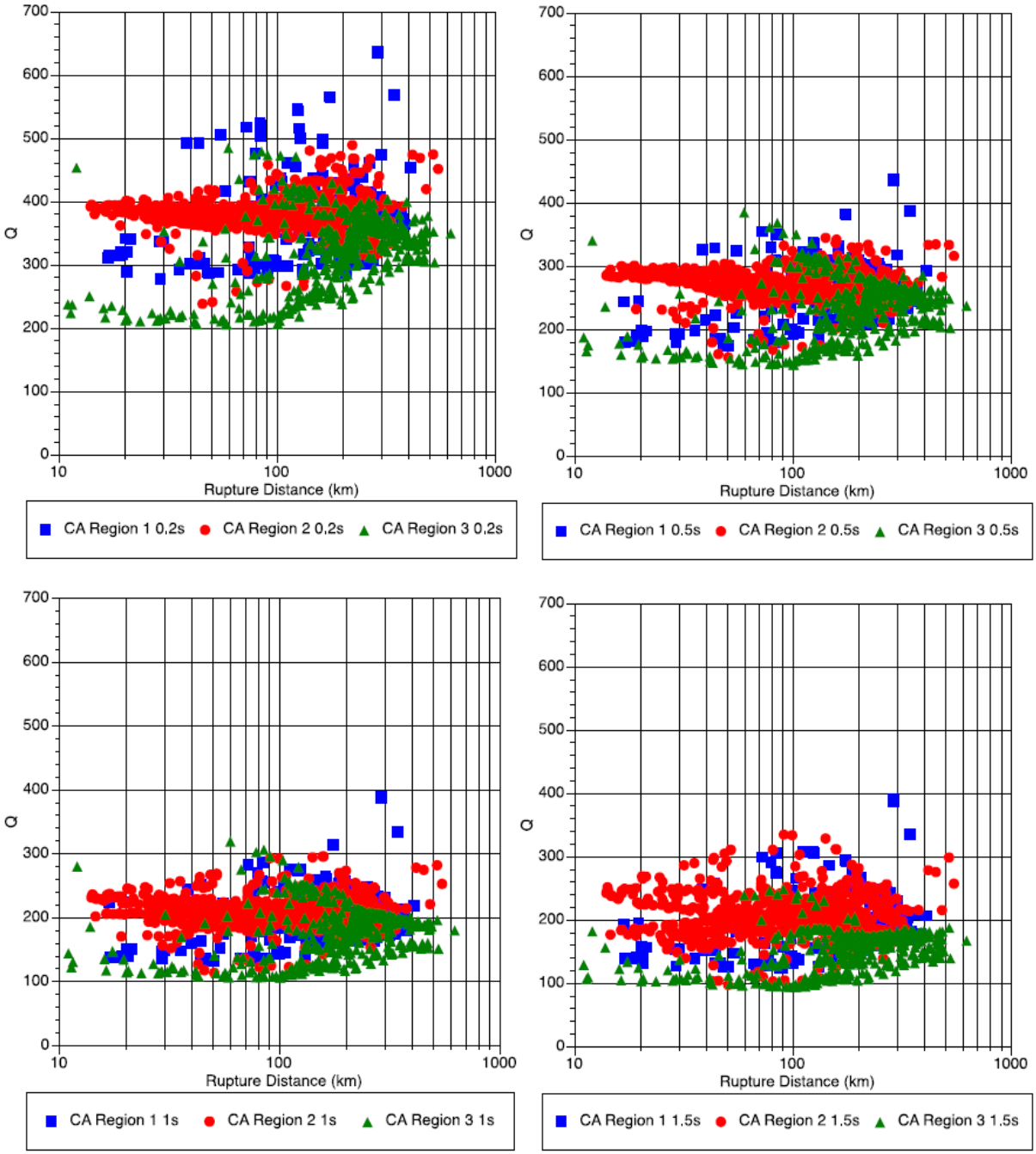

Figure 6.2.3-2: Q values for NGA-West2 data from earthquakes in Region 1, 2, and 3 over frequency ranges with average periods of 0.2, 0.5, 1, and 1.5 sec. (from Figure 5.2 in Kishida et al., 2014).

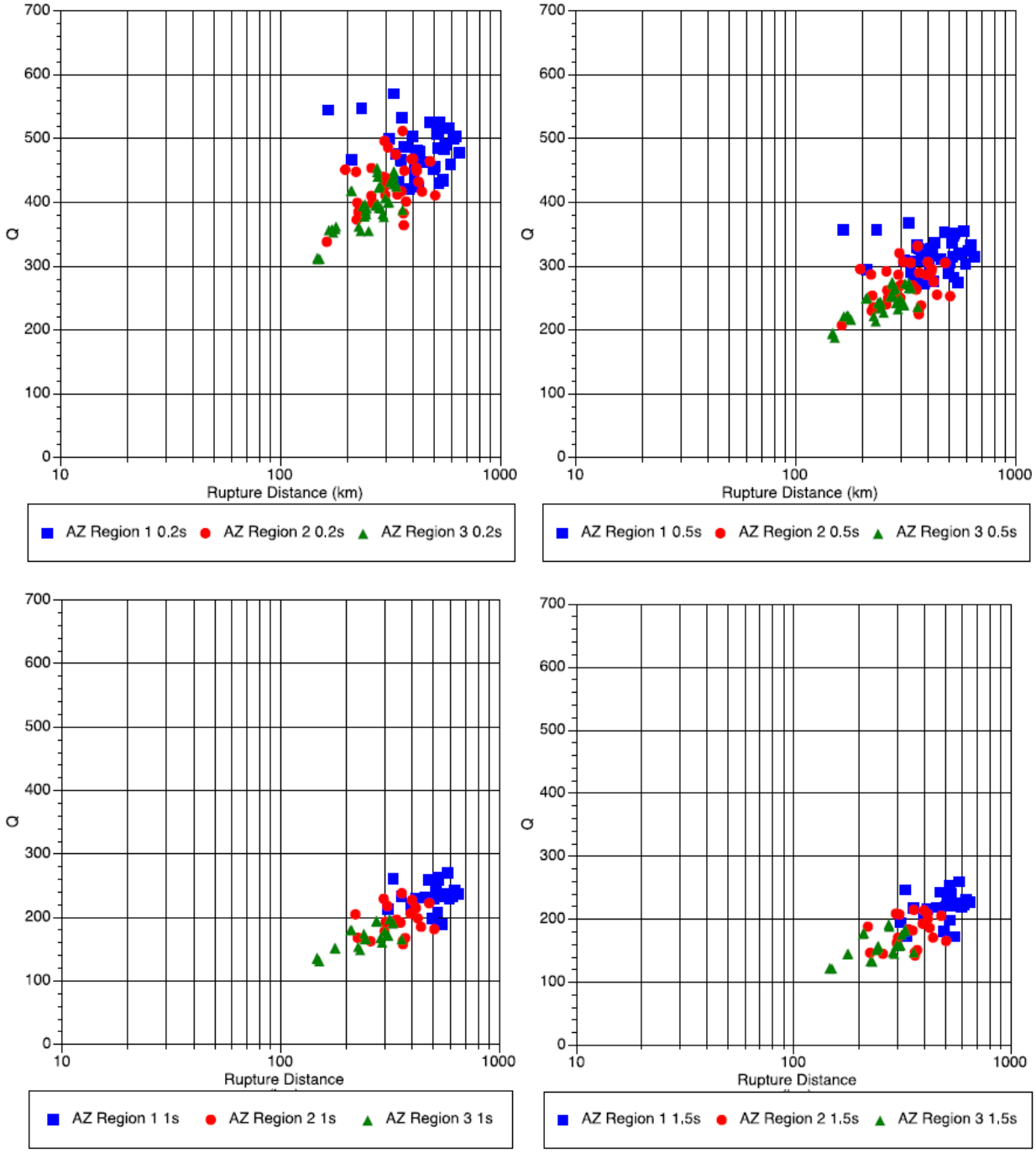

Figure 6.2.3-3: Q values for Arizona data from earthquakes in Region 1, 2, and 3 over frequency ranges with average periods of 0.2, 0.5, 1, and 1.5 sec. (from Figure 5.3 in Kishida et al., 2014).

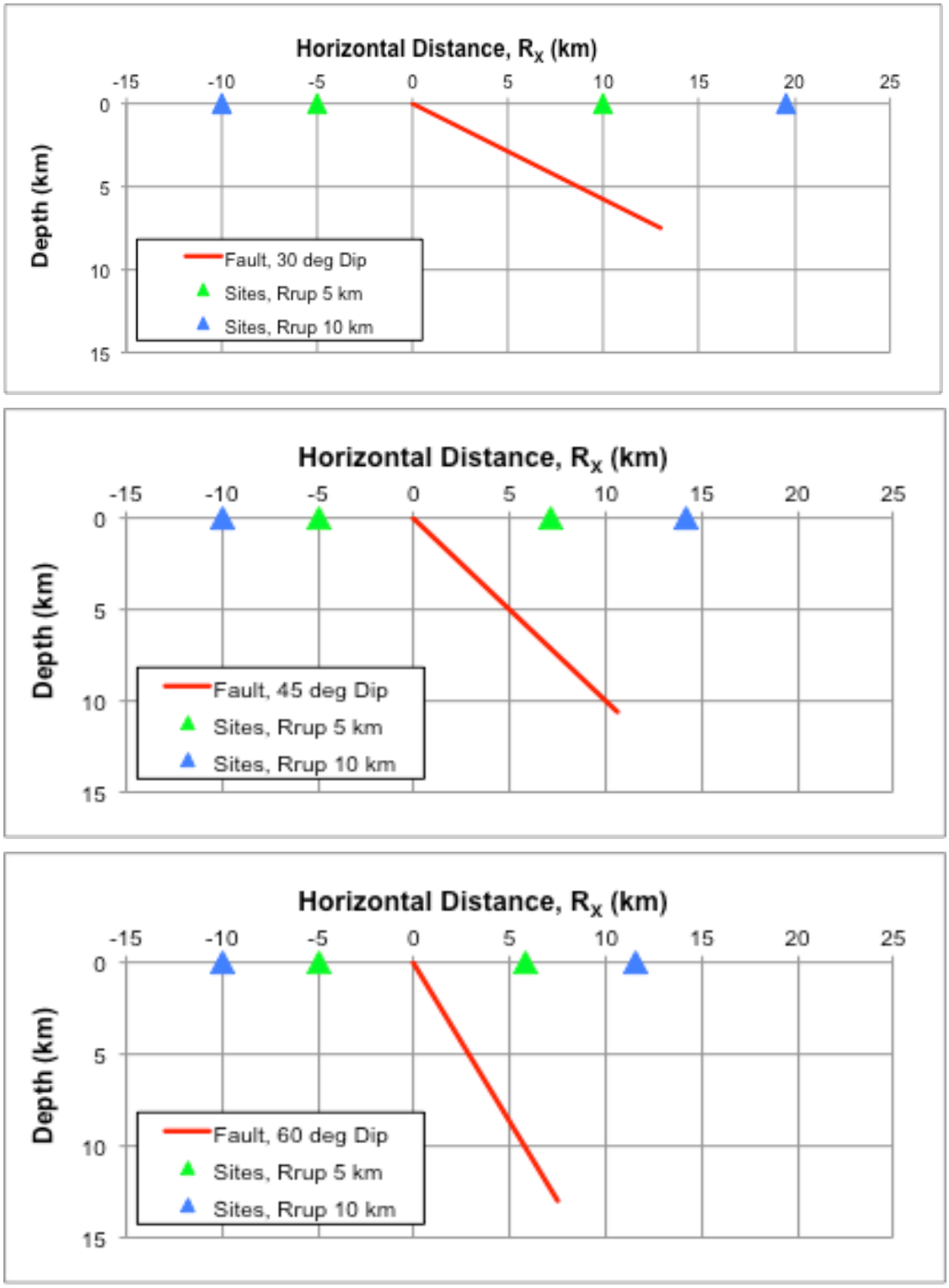

Figure 6.3.1-1: Reverse faulting scenarios used for comparison of HW and FW motions for sites at R_{RUP} of 5 and 10 km.

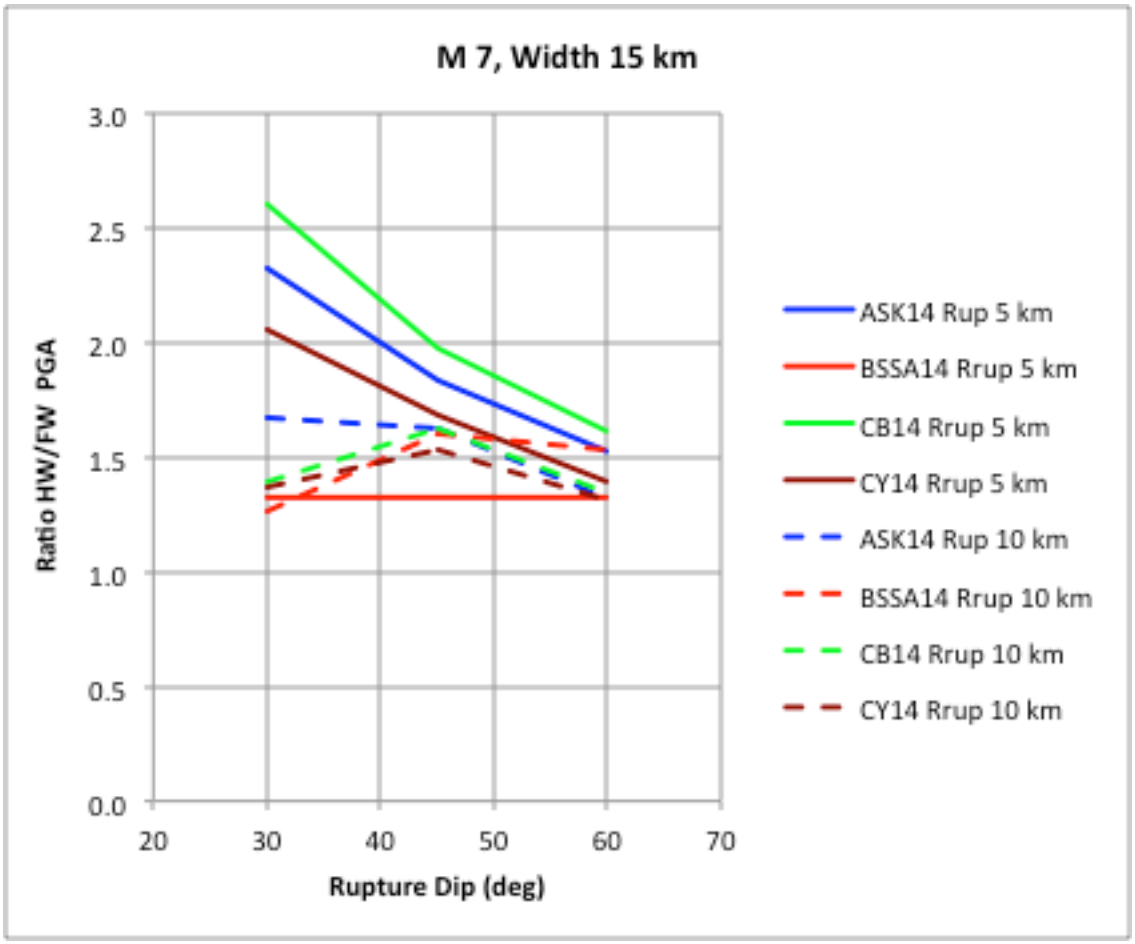

Figure 6.3.1-2: HW/FW PGA ratios for predicted median ground motions at the sites shown in Figure 6.3.1-2.

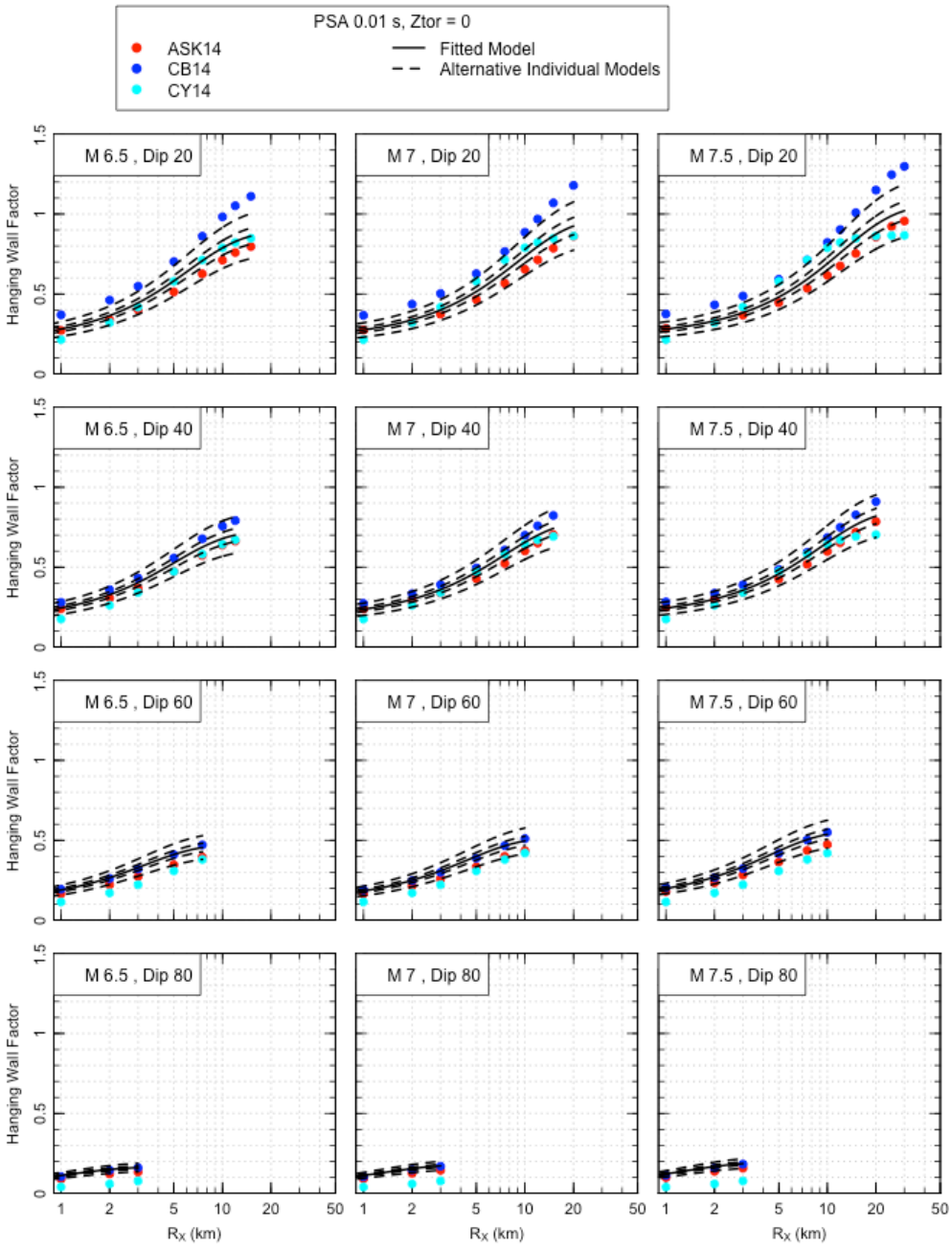

Figure 6.3.2-1: HW factors from ASK14, CB14 and CY14 for PGA, for Z_{TOR} value of 0 km, for **M**6.5, **M**7.0 and **M**7.5, and for fault dip values of 20, 40, 60 and 80 degrees. The solid black line shows the fitted common form in Eq. 6.3-2 (central model), and the dashed black lines show the other four individual models used to approximate the distribution of the modeled HW factors.

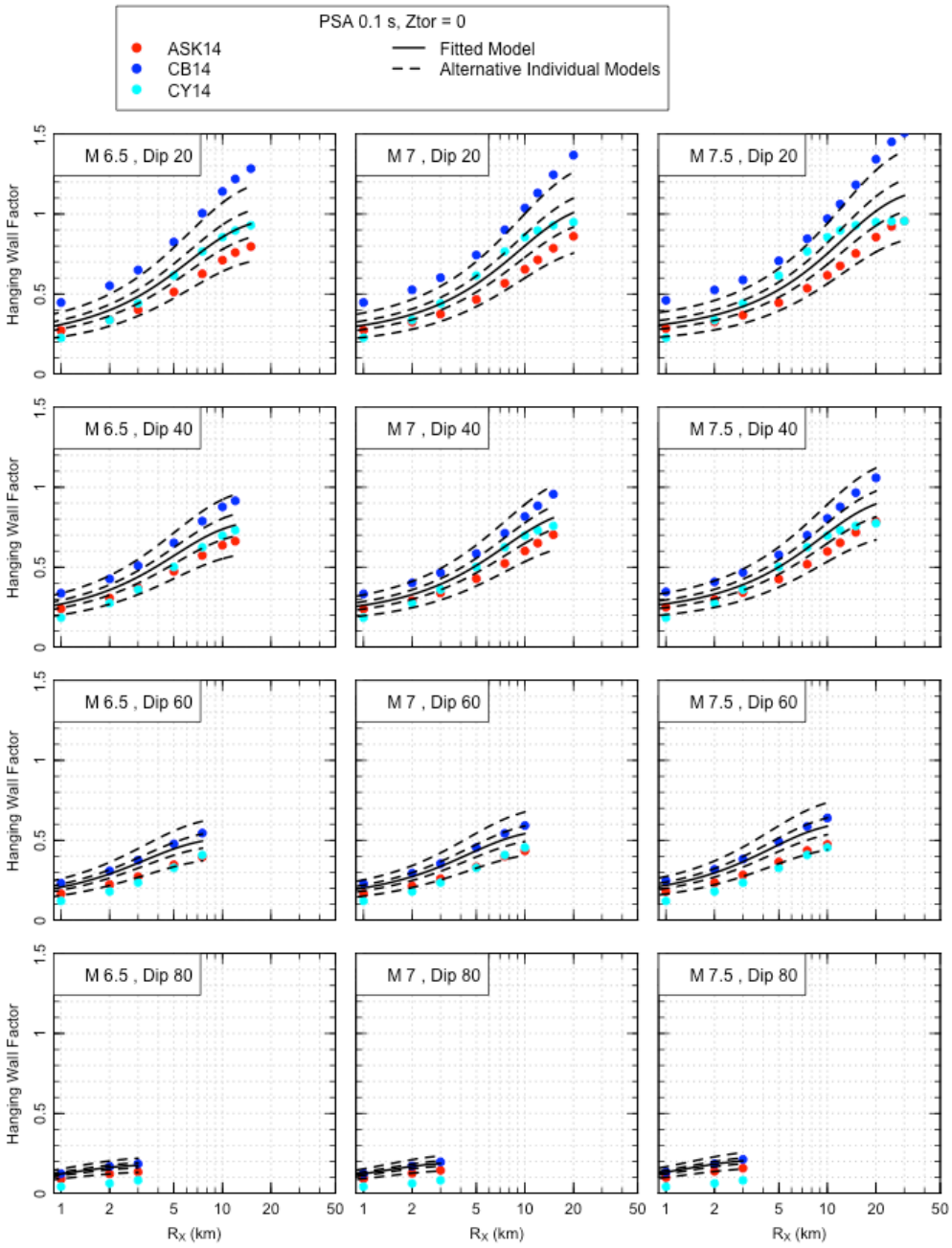

Figure 6.3.2-2: HW factors from ASK14, CB14 and CY14 for 0.1 sec PSA, for Z_{TOR} value of 0 km, for **M**6.5, **M**7.0 and **M**7.5, and for fault dip values of 20, 40, 60 and 80 degrees. The solid black line shows the fitted common form in Eq. 6.3-2 (central model), and the dashed black lines show the other four individual models used to approximate the distribution of the modeled HW factors.

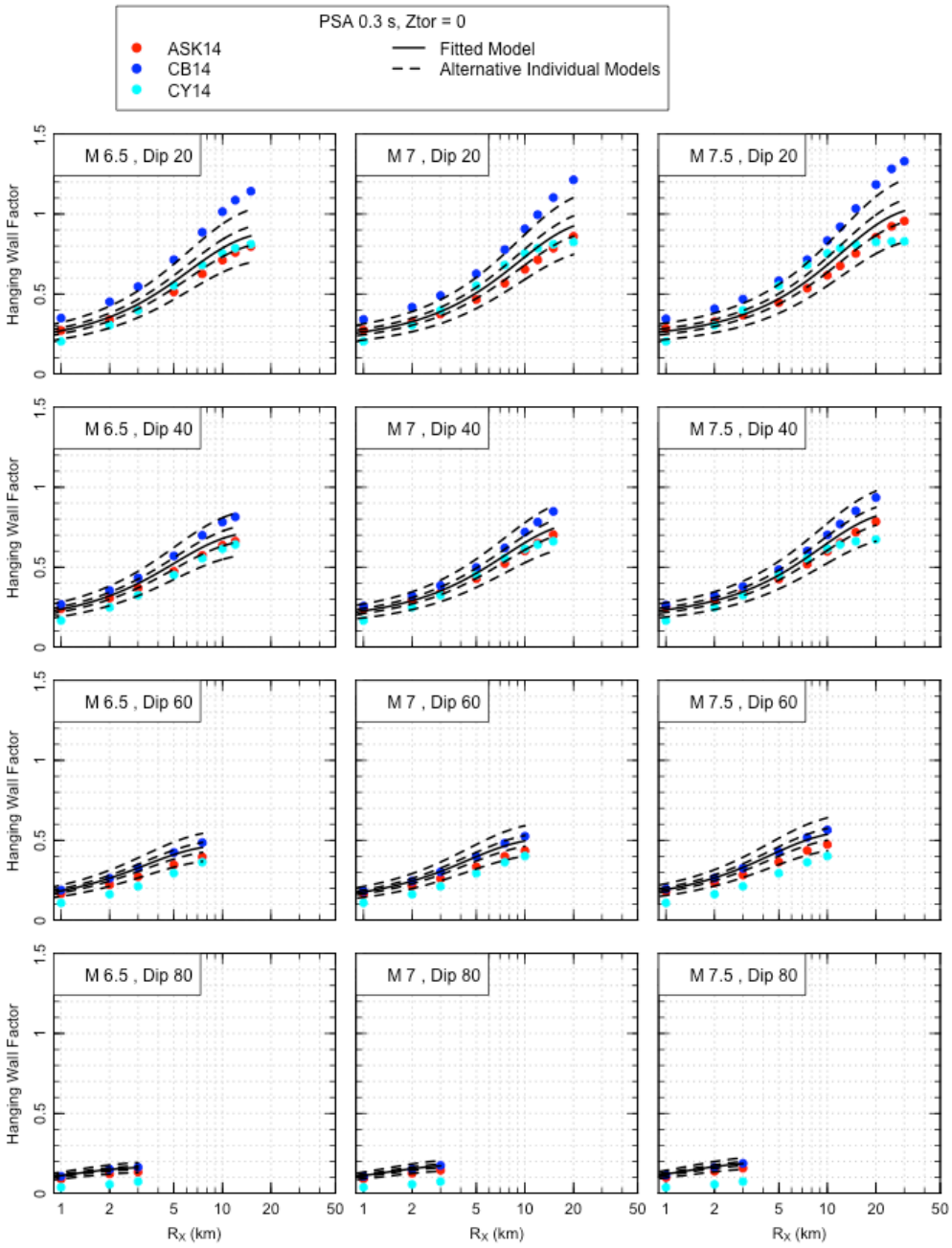

Figure 6.3.2-3: HW factors from ASK14, CB14 and CY14 for 0.3 sec PSA, for Z_{TOR} value of 0 km, for **M**6.5, **M**7.0 and **M**7.5, and for fault dip values of 20, 40, 60 and 80 degrees. The solid black line shows the fitted common form in Eq. 6.3-2 (central model), and the dashed black lines show the other four individual models used to approximate the distribution of the modeled HW factors.

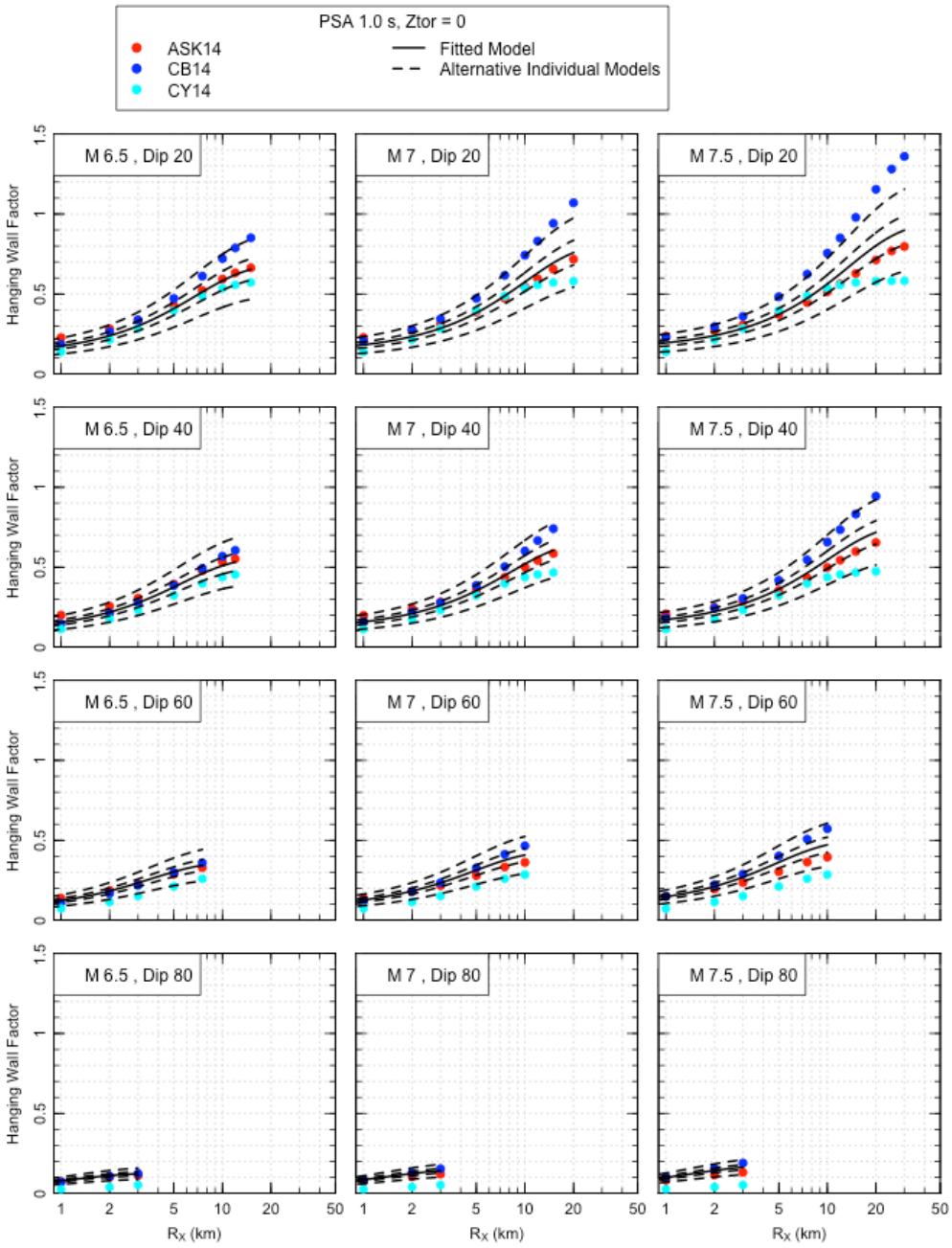

Figure 6.3.2-4: HW factors from ASK14, CB14 and CY14 for 1.0 sec PSA, for Z_{TOR} value of 0 km, for **M**6.5, **M**7.0 and **M**7.5, and for fault dip values of 20, 40, 60 and 80 degrees. The solid black line shows the fitted common form in Eq. 6.3-2 (central model), and the dashed black lines show the other four individual models used to approximate the distribution of the modeled HW factors.

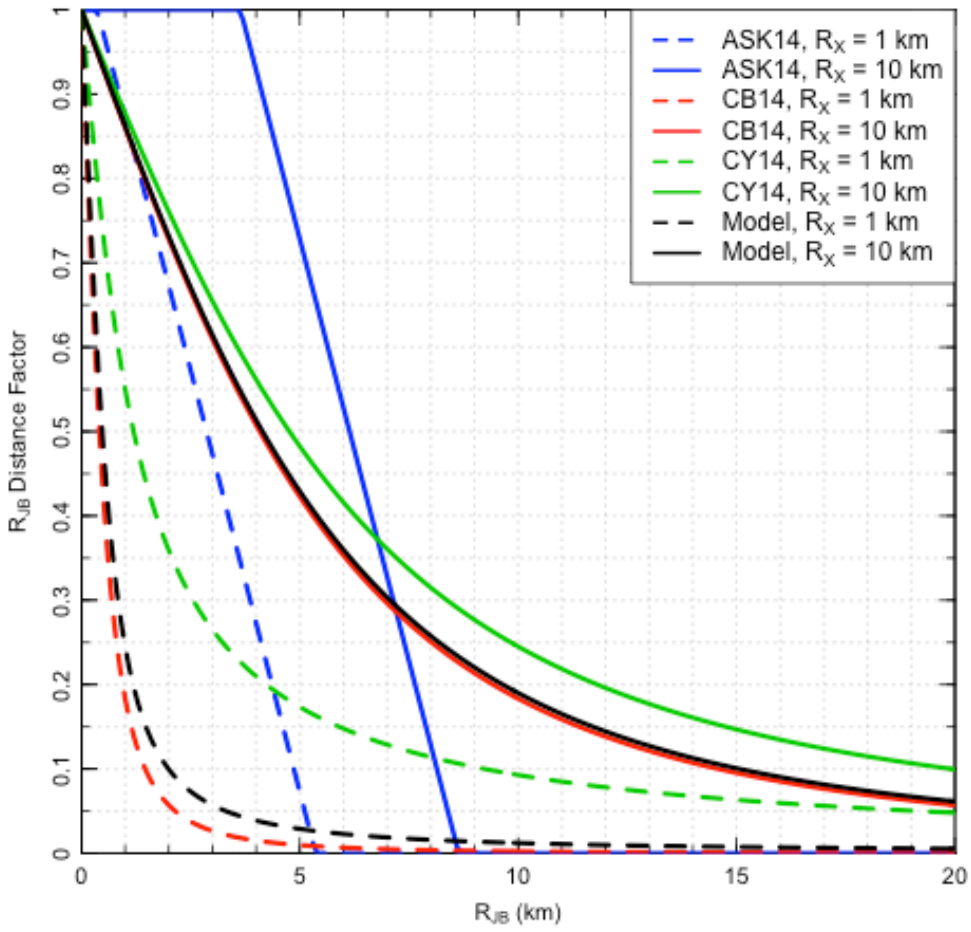

Figure 6.3.2-5: Effect of $R_{JB} > 0$ on HW factor for sites located at two values of R_X, 1 and 10 km adjacent to a rupture with dip 45 degrees, width 14.14 km, and Z_{TOR} of 0 km.

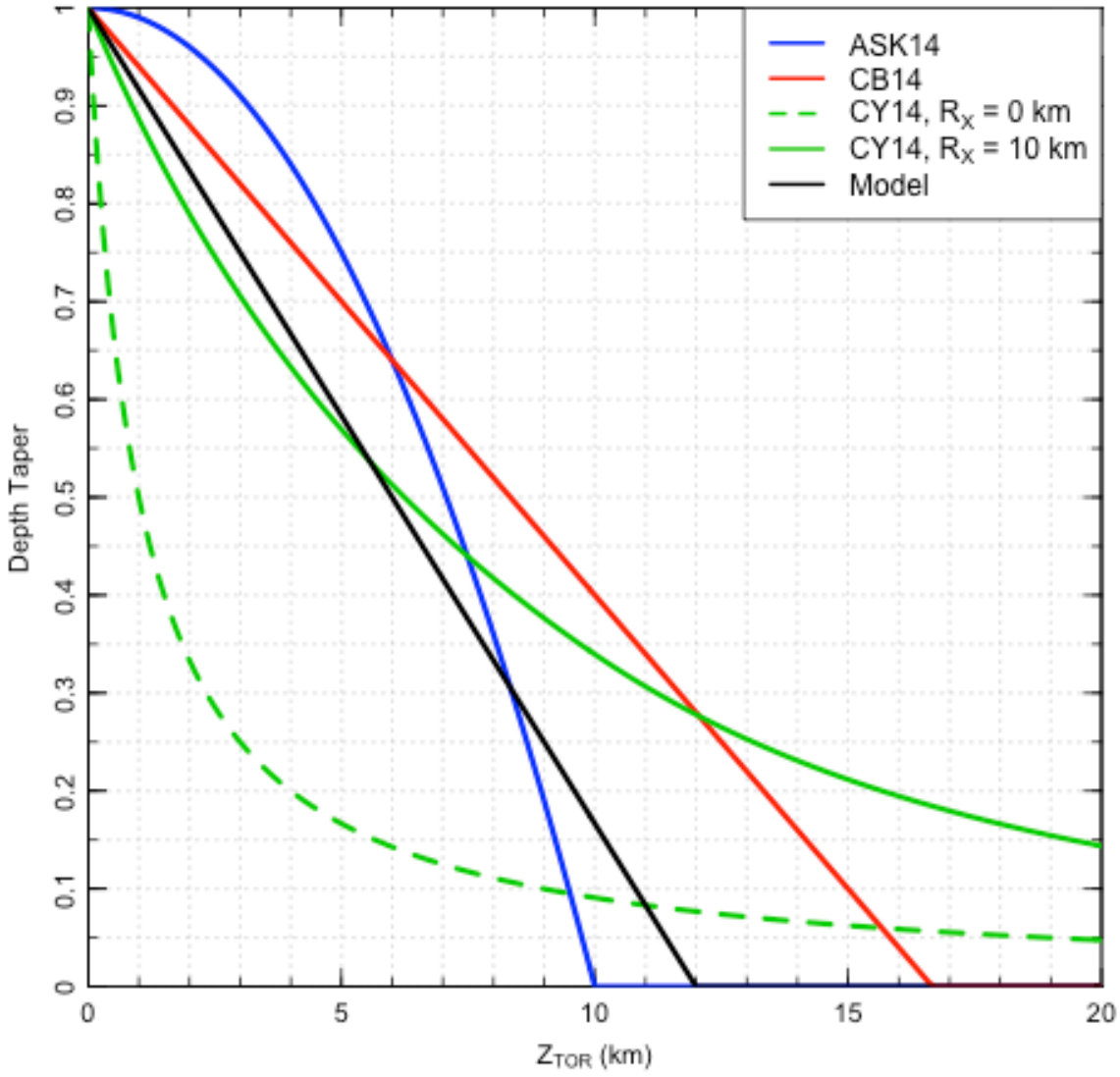

Figure 6.3.2-6: Effect of Z_{TOR} > 0 on HW factor. Rupture dip 45 degrees, rupture width 14.14 km.

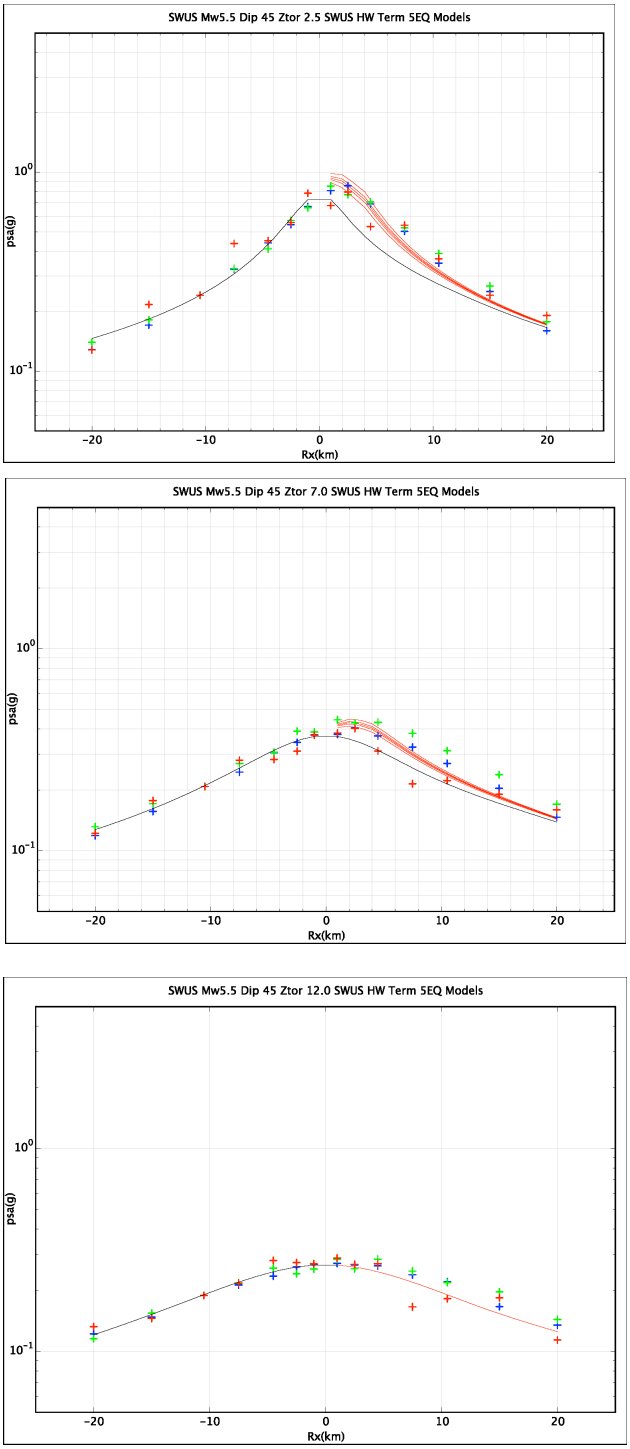

Figure 6.3.3-1: The five equal probability HW factor models (red lines) are compared with simulations (EXSIM: green; GP: blue; SDSU: red) for the **M**5.5, dip = 45 degrees, Z_{TOR} values of 2.5, 7.0, and 12.0 km cases. The black lines show the fitted footwall R_{RUP} model as described in Section 6.3.3.

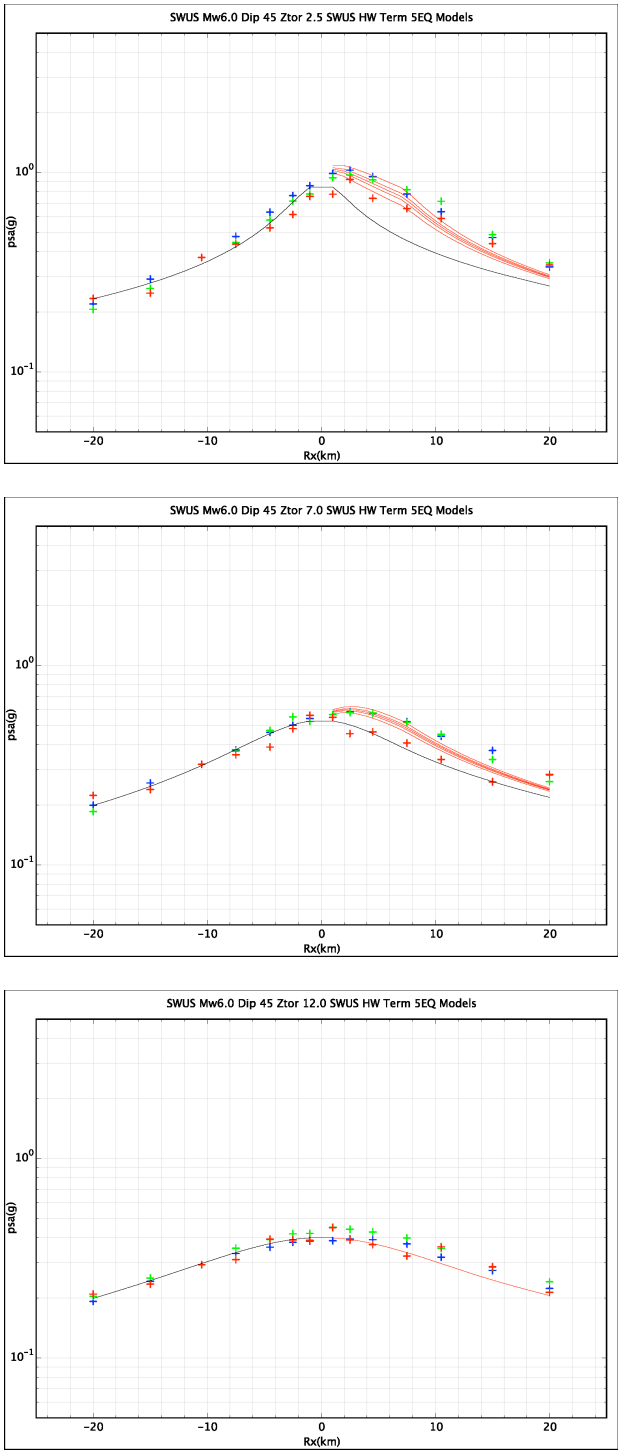

Figure 6.3.3-2: The five equal probability HW factor models (red lines) are compared with simulations (EXSIM: green; GP: blue; SDSU: red) for the **M**6.0, dip = 45 degrees, Z_{TOR} values of 2.5, 7.0, and 12.0 km cases. The black lines show the fitted footwall R_{RUP} model as described in Section 6.3.3.

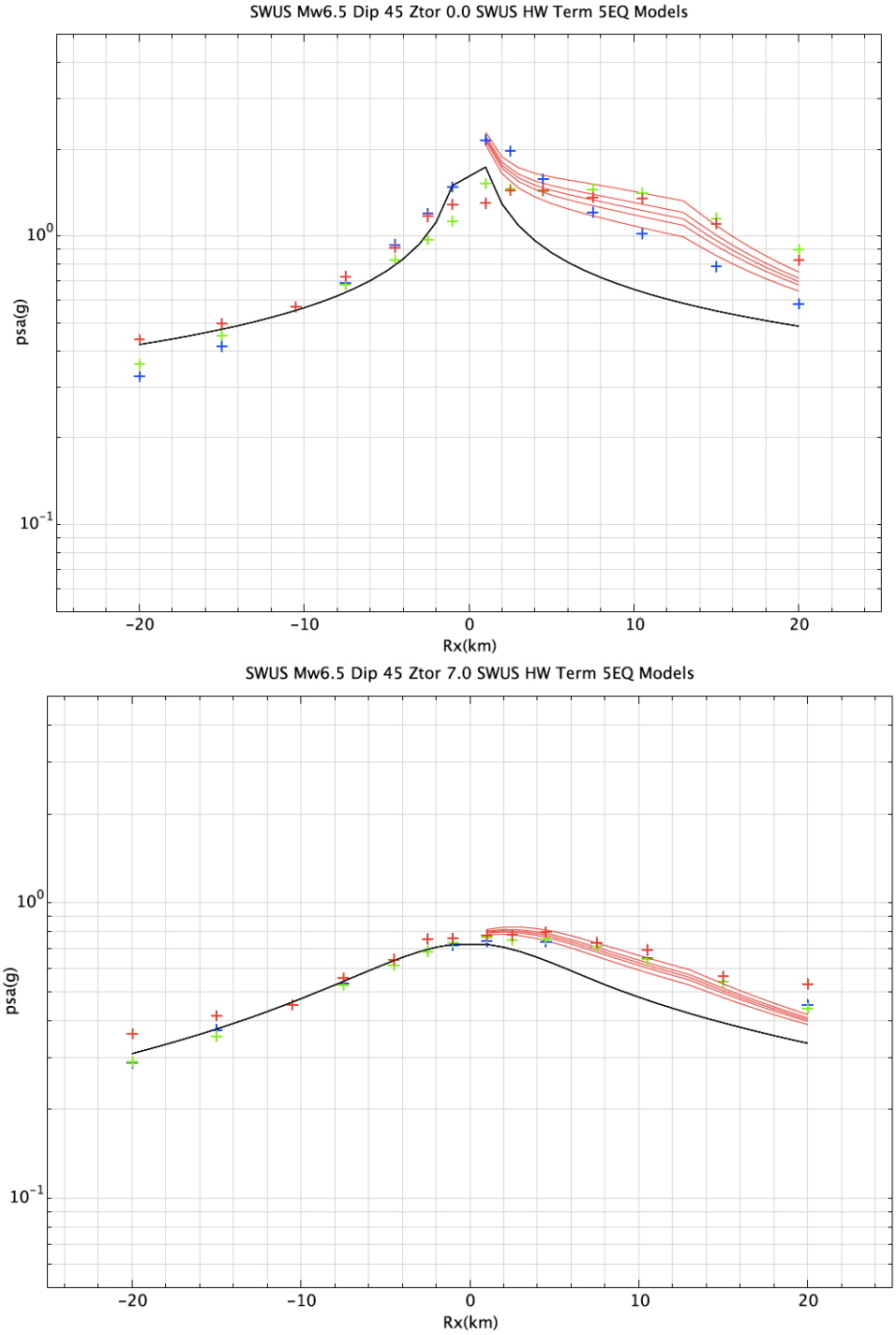

Figure 6.3.3-3: The five equal probability HW factor models (red lines) are compared with simulations (EXSIM: green; GP: blue; SDSU: red) for the **M**6.5, dip = 45 degrees, Z_{TOR} values of 0.0, 7.0 km cases.

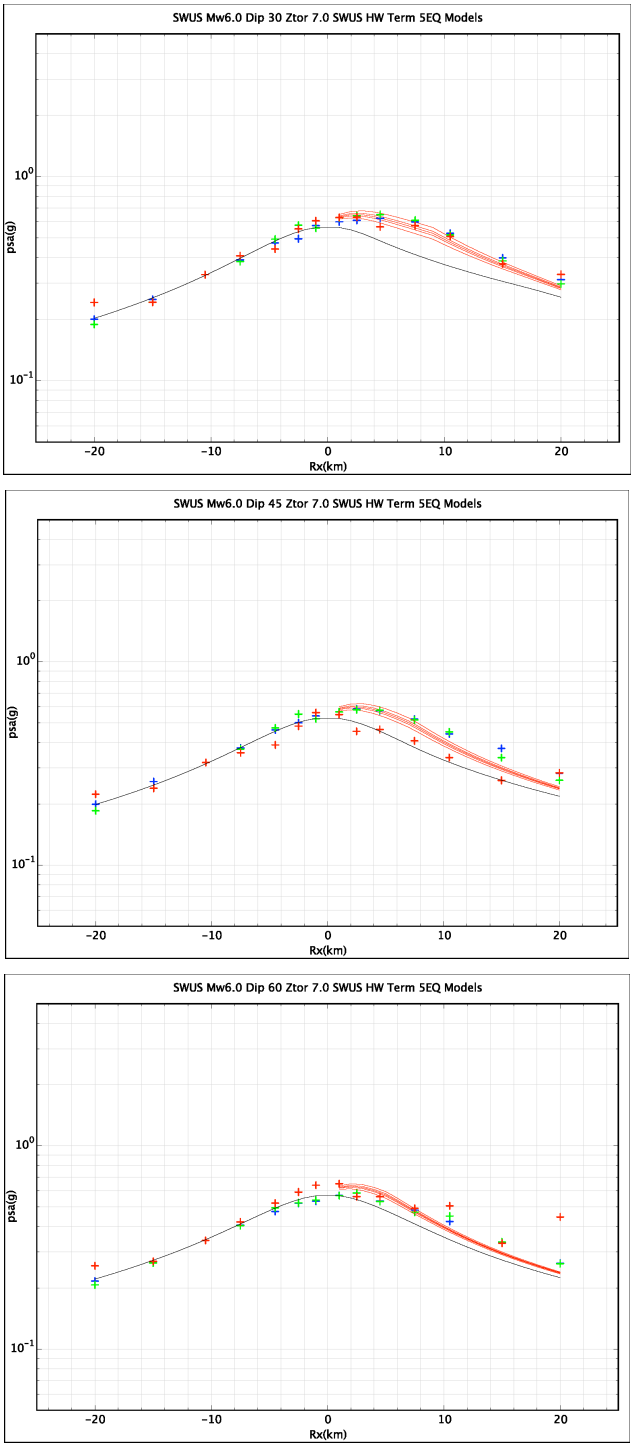

Figure 6.3.3-4: The five equal probability HW factor models (red lines) are compared with simulations (EXSIM: green; GP: blue; SDSU: red) for the **M**6.0, dip values of 30, 45 and 60 degrees, for Z_{TOR} = 7.0 km cases. The black lines show the fitted footwall R_{RUP} model as described in Section 6.3.3.

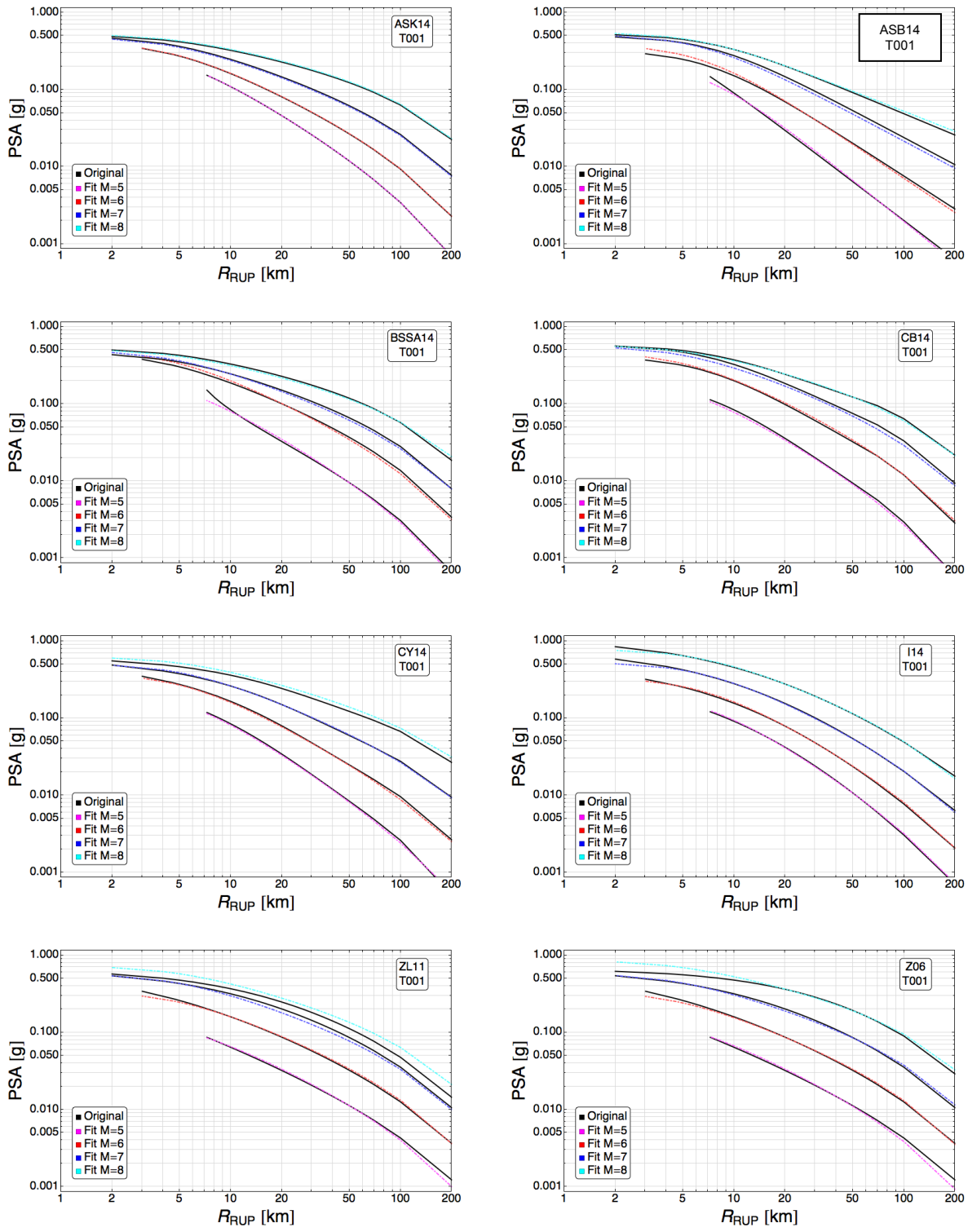

Figure 6.4.1-1a: Fit of the candidate GMPEs for DCPP to the R_{RUP}-based common form plotted versus R_{RUP} for PGA.

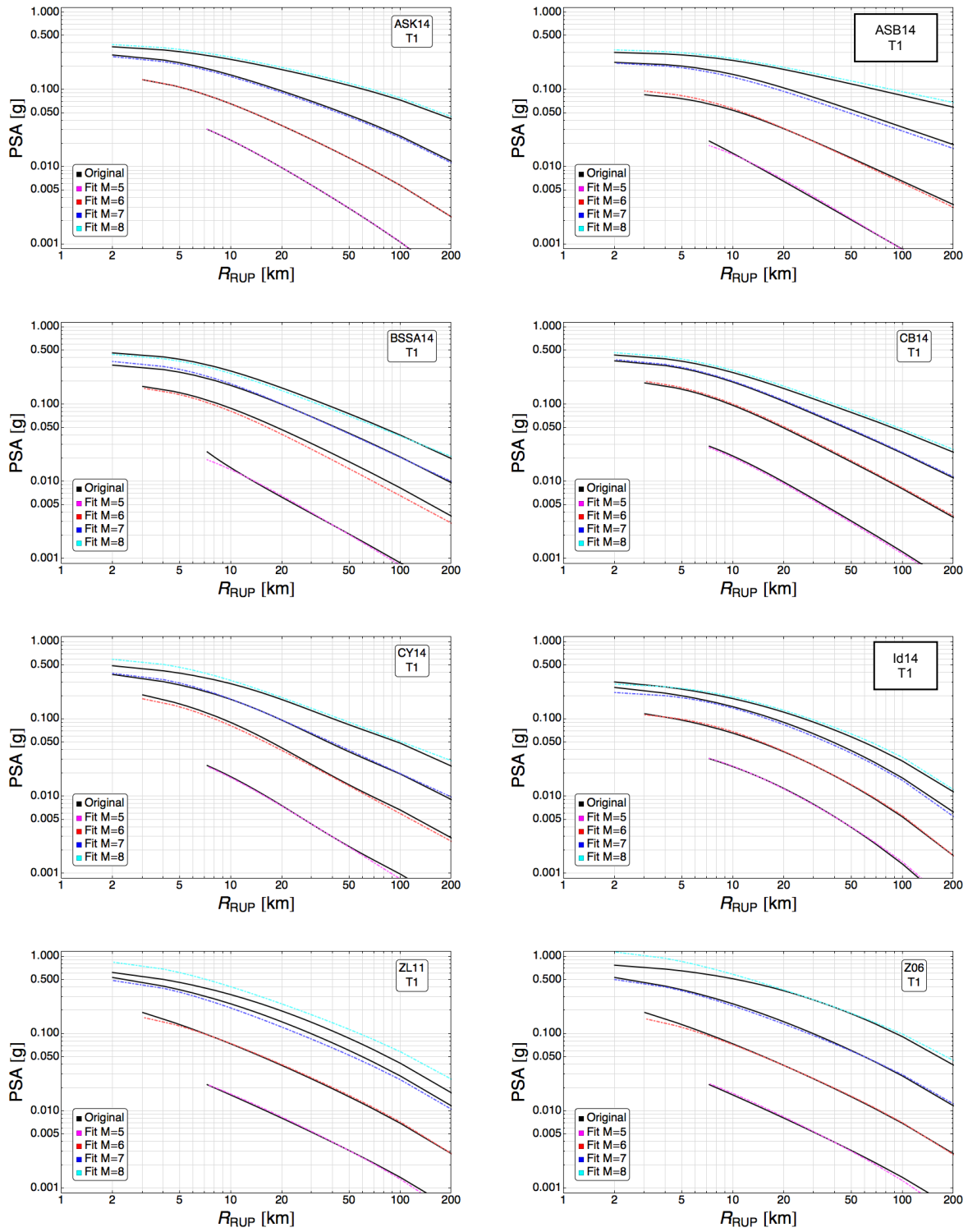

Figure 6.4.1-1b: Fit of the candidate GMPEs for DCPP to the R_{RUP}-based common form plotted versus R_{RUP} for T = 1.0 sec.

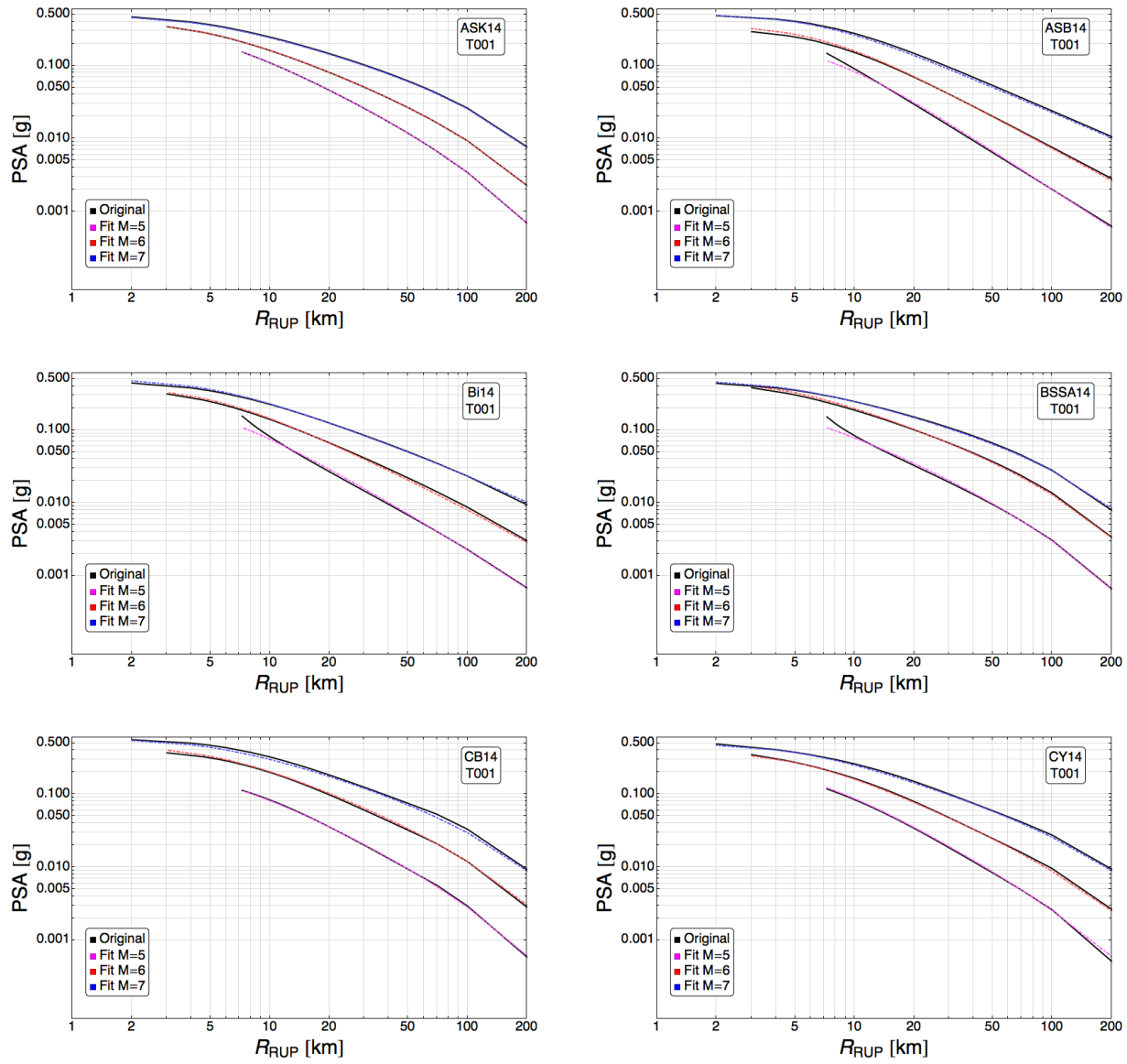

Figure 6.4.1-2a: Fit of the candidate GMPEs for PVNGS (Greater Arizona sources) to the R_{RUP}-based common form plotted versus R_{RUP} for PGA.

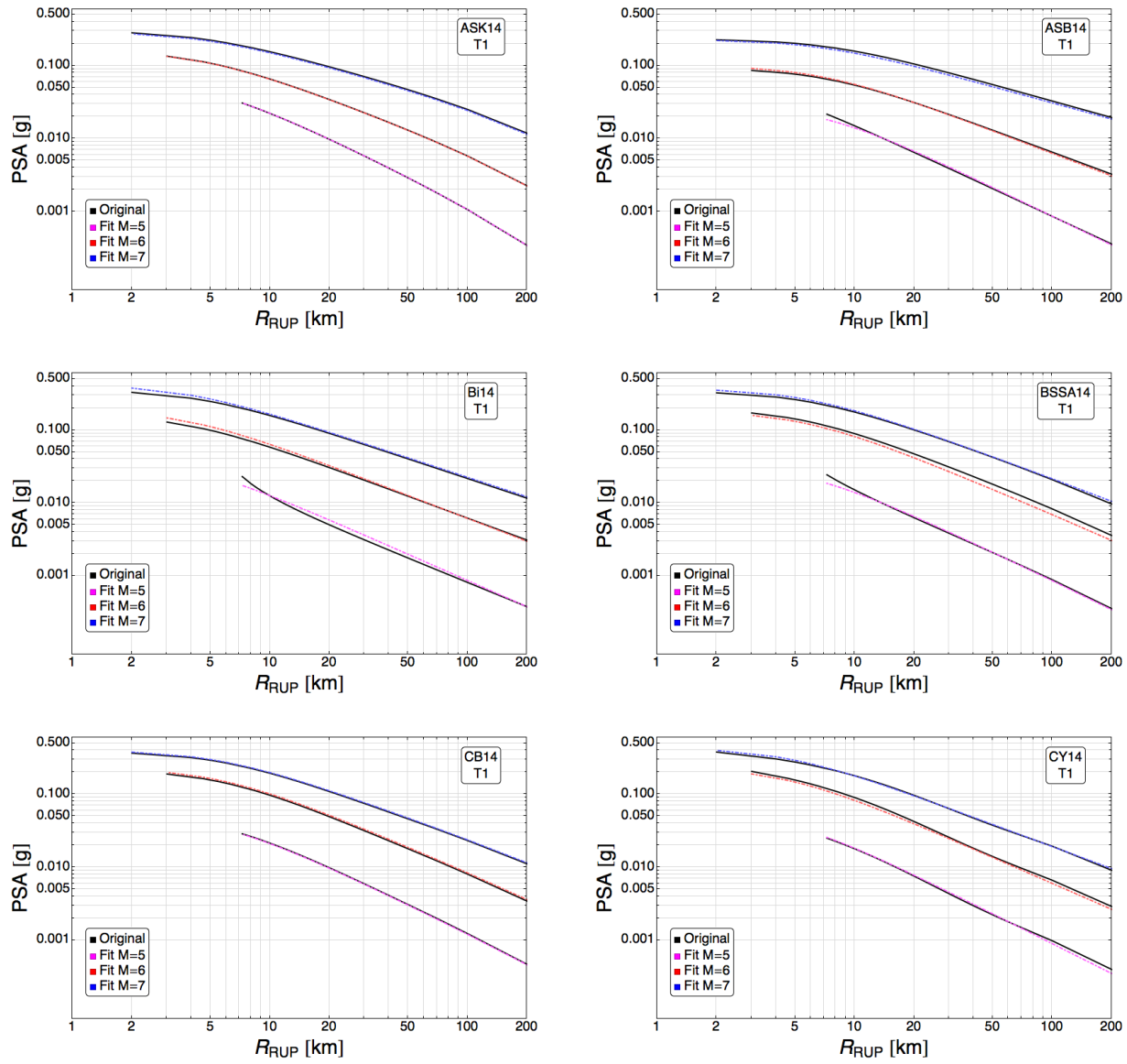

Figure 6.4.1-2b: Fit of the candidate GMPEs for PVNGS (Greater Arizona sources) to the R_{RUP}-based common form plotted versus R_{RUP} for T = 1.0 sec.

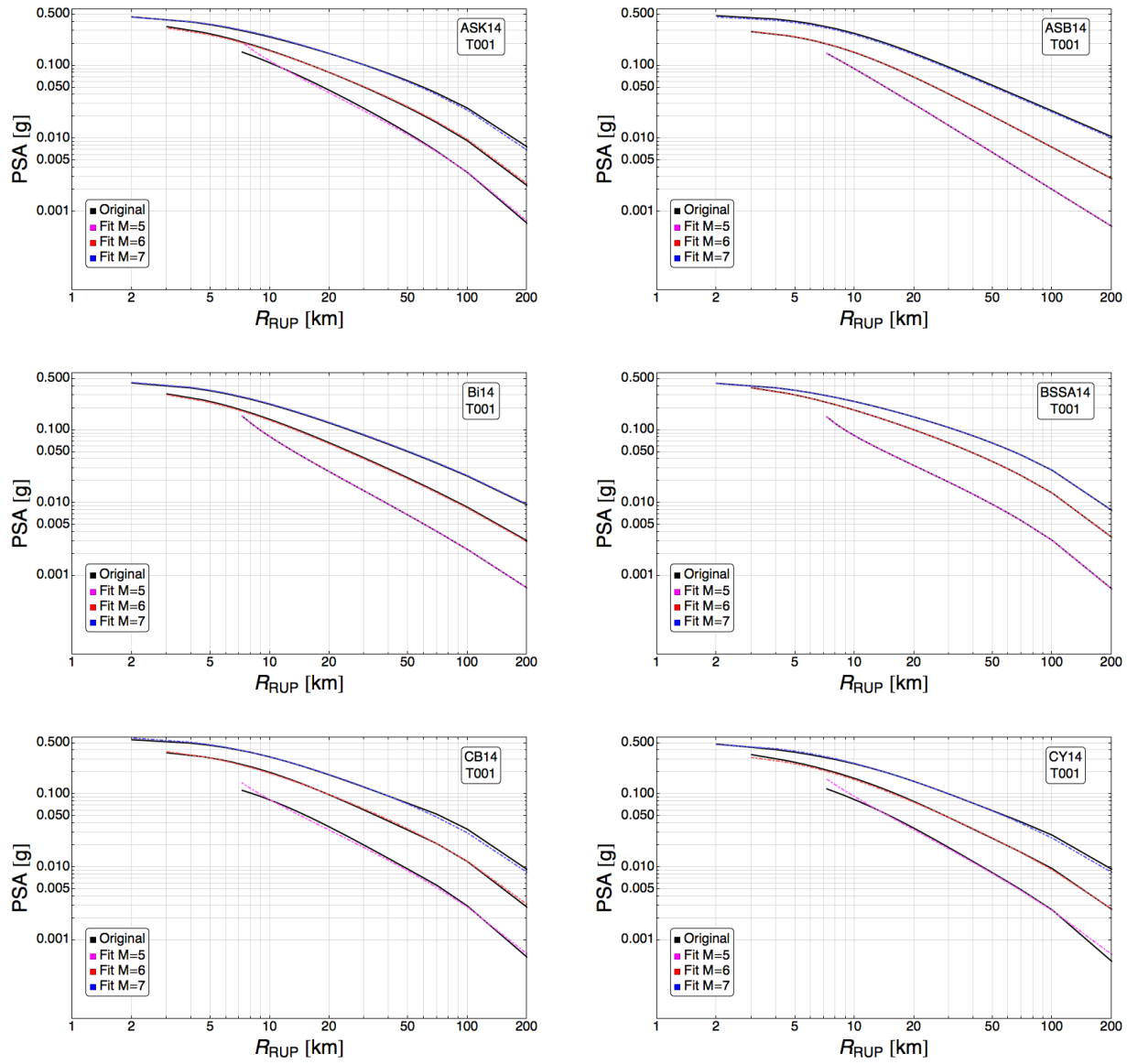

Figure 6.4.1-3a: Fit of the candidate GMPEs for PVNGS (Greater Arizona sources) to the R_{JB}-based common form plotted versus R_{RUP} for PGA.

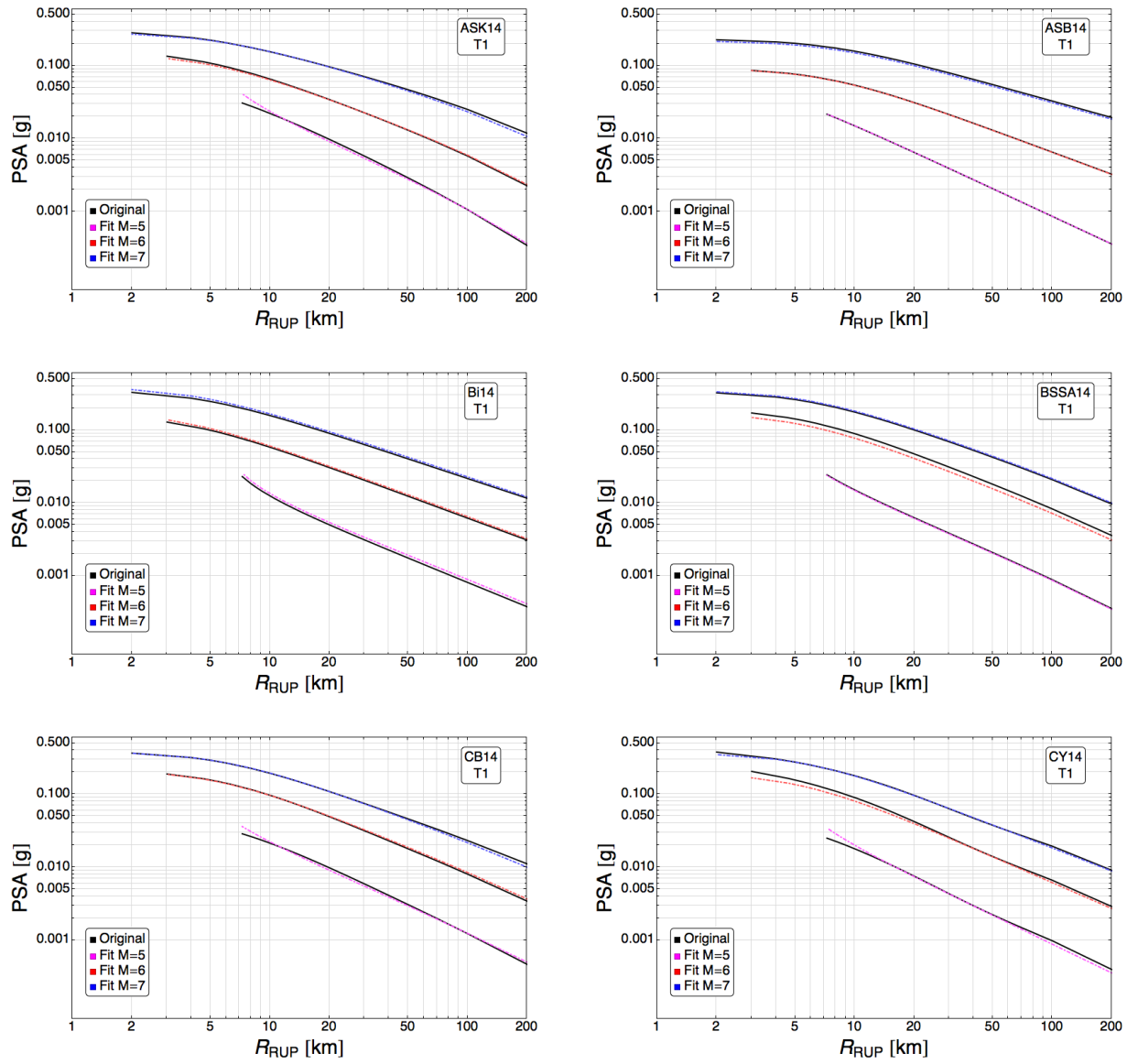

Figure 6.4.1-3b: Fit of the candidate GMPEs for PVNGS (Greater Arizona sources) to the R_{JB}-based common form plotted versus R_{RUP} for T = 1.0 sec.

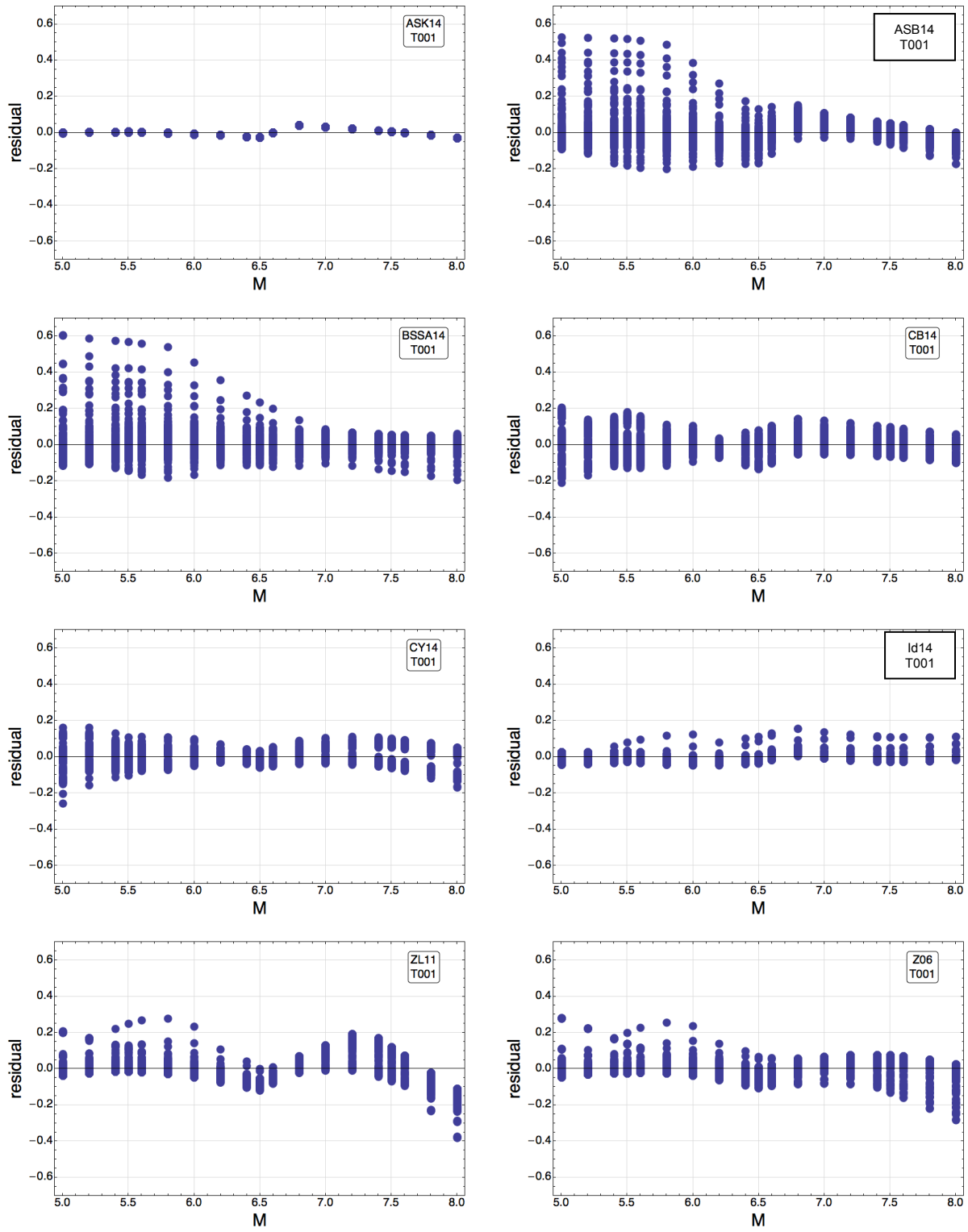

Figure 6.4.1-4a: Total residuals of the candidate GMPEs for DCPP refitted to the R_{RUP}-based common form plotted versus magnitude for PGA.

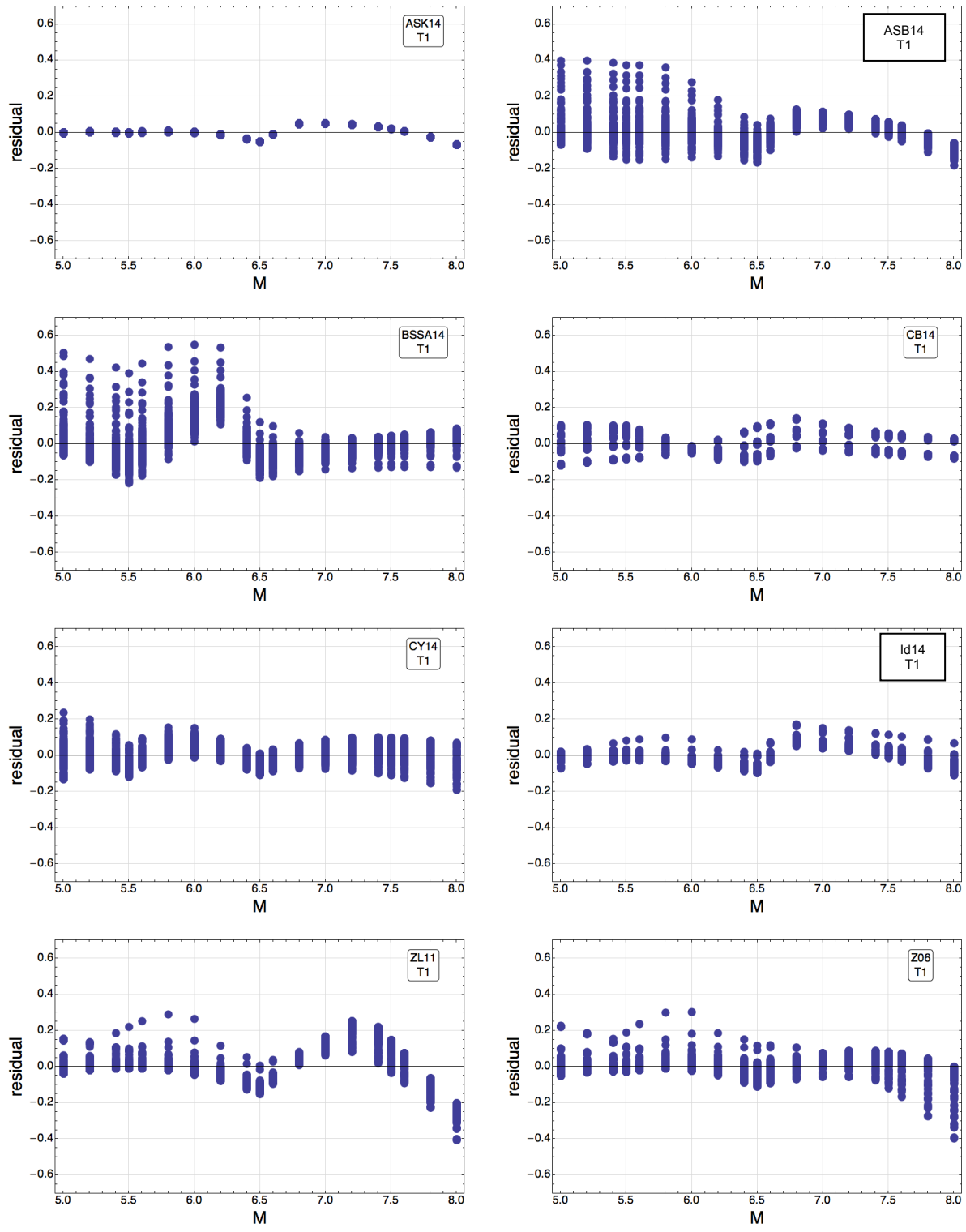

Figure 6.4.1-4b: Total residuals of the candidate GMPEs for DCPP refitted to the R_{RUP}-based common form plotted versus magnitude for T = 1.0 sec.

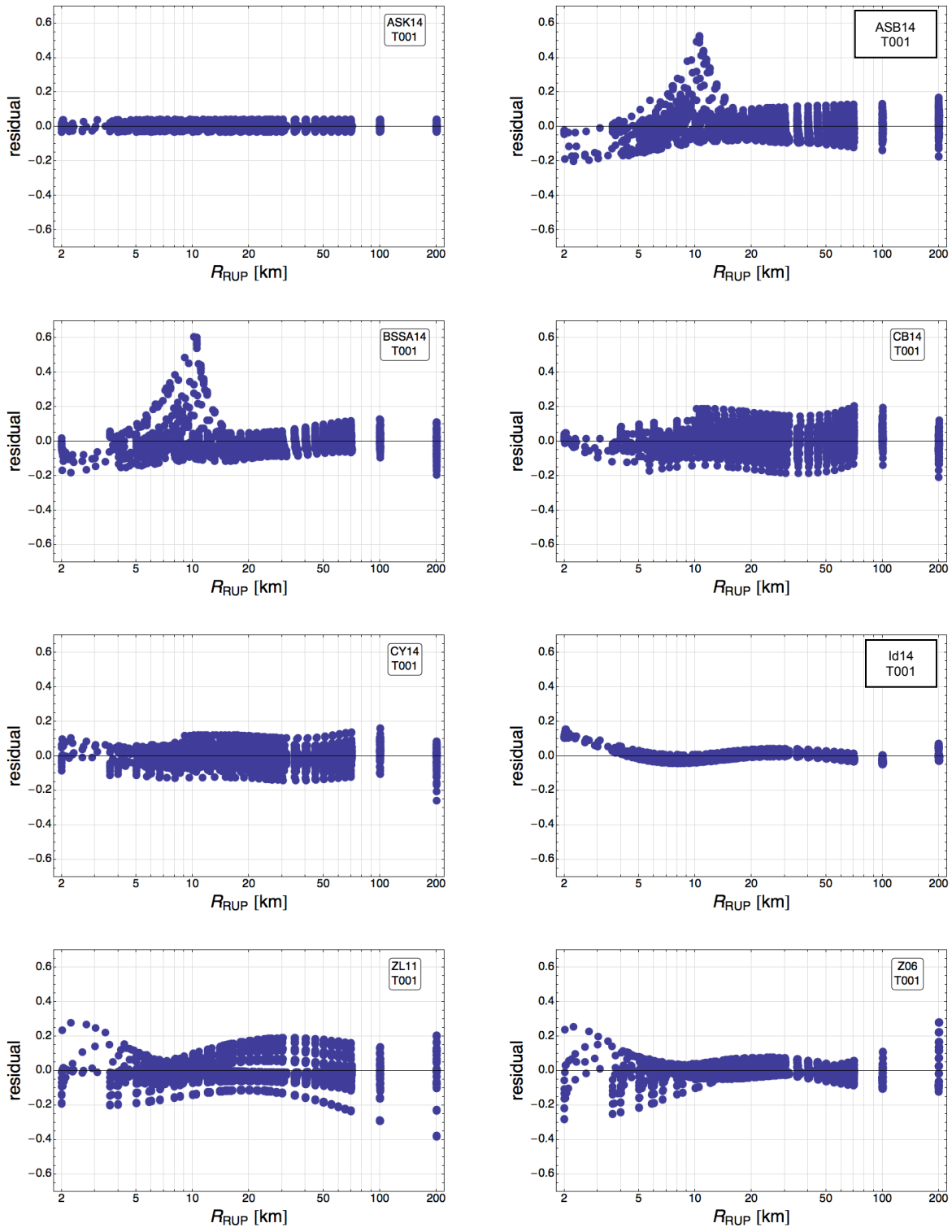

Figure 6.4.1-5a: Total residuals of the candidate GMPEs for DCPP refitted to the R_{RUP}-based common form plotted versus R_{RUP} for PGA.

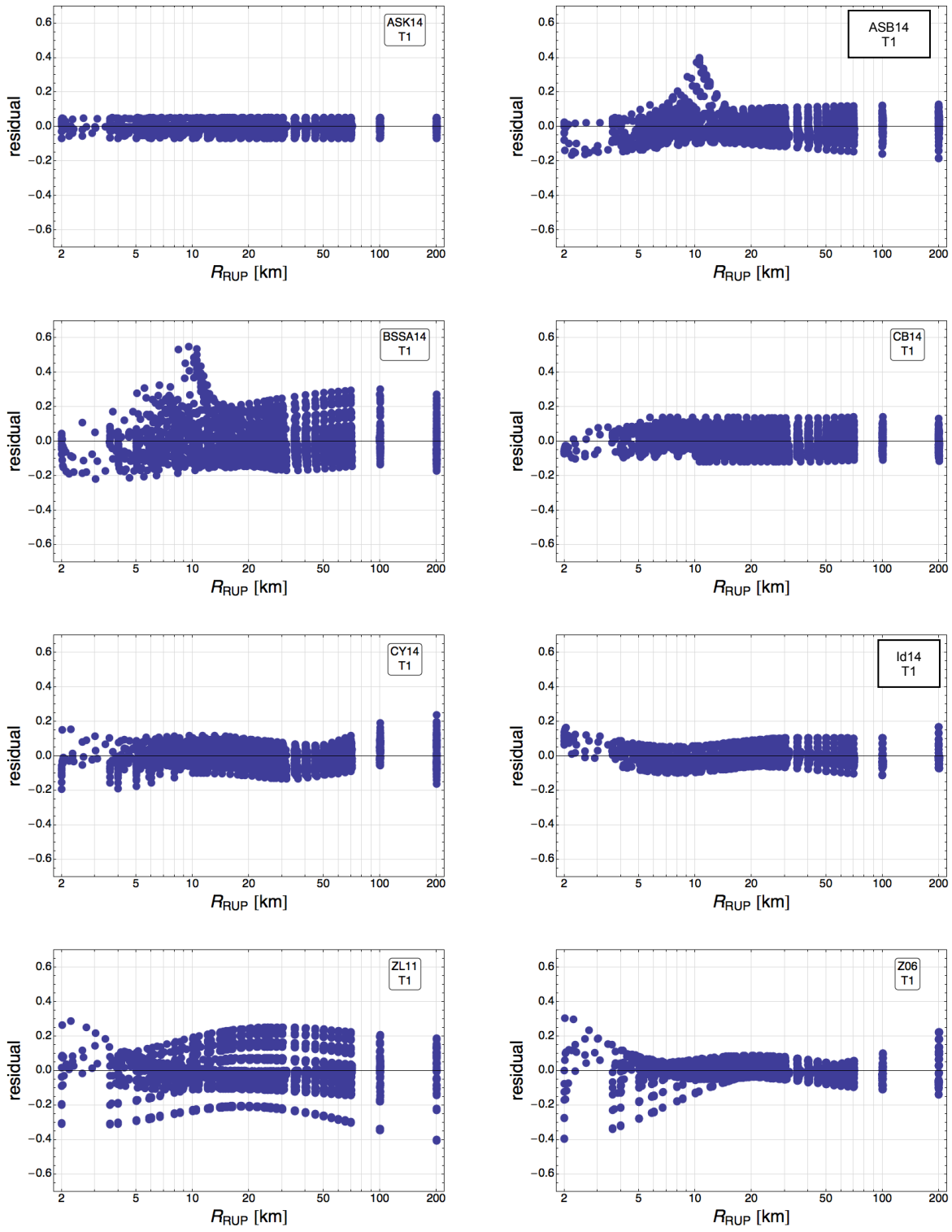

Figure 6.4.1-5b: Total residuals of the candidate GMPEs for DCPP refitted to the R_{RUP}-based common form plotted versus R_{RUP} for T = 1.0 sec.

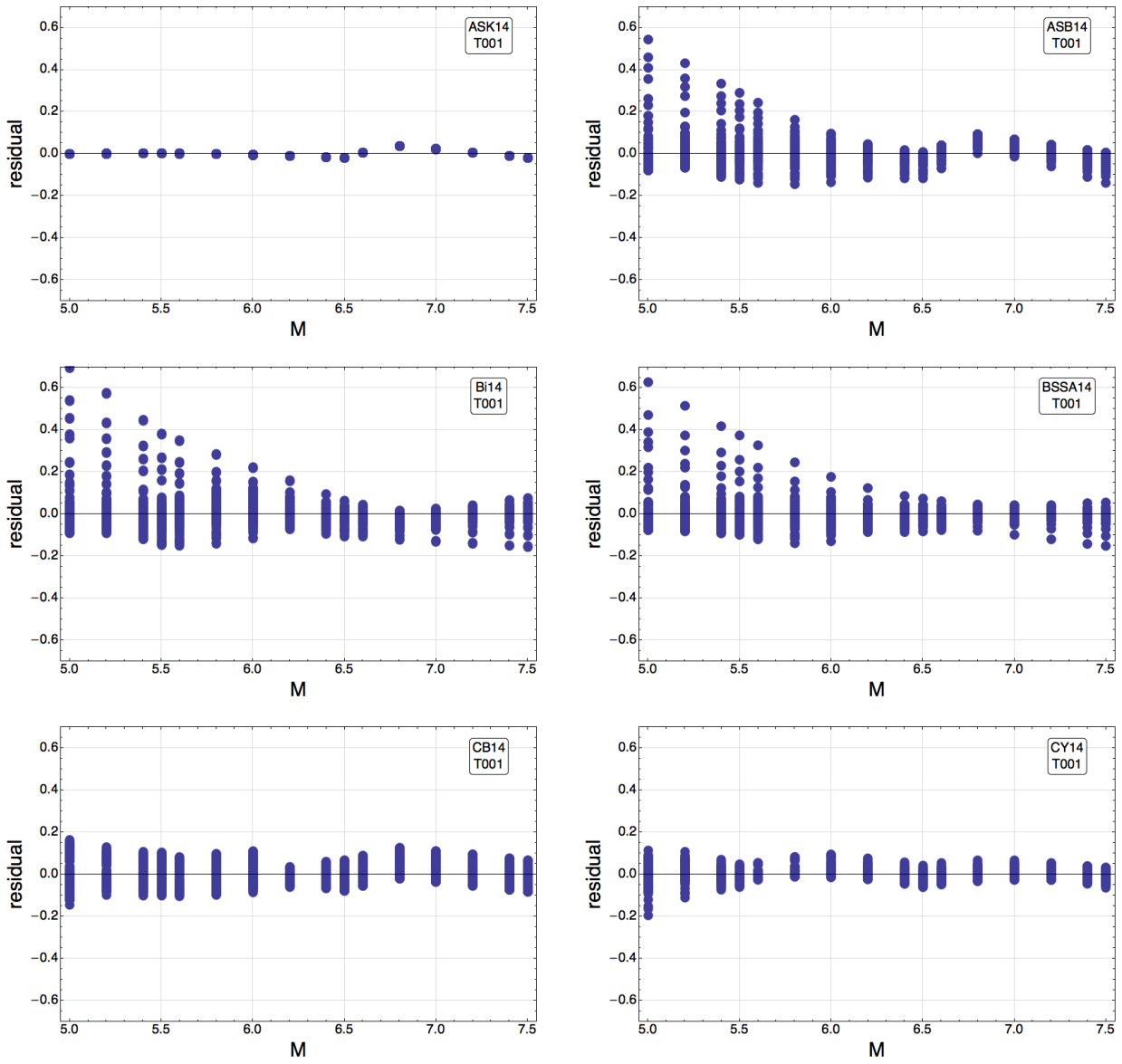

Figure 6.4.1-6a: Total residuals of the candidate GMPEs for PVNGS (Greater Arizona sources) refitted to the R_{RUP}-based common form plotted versus magnitude for PGA.

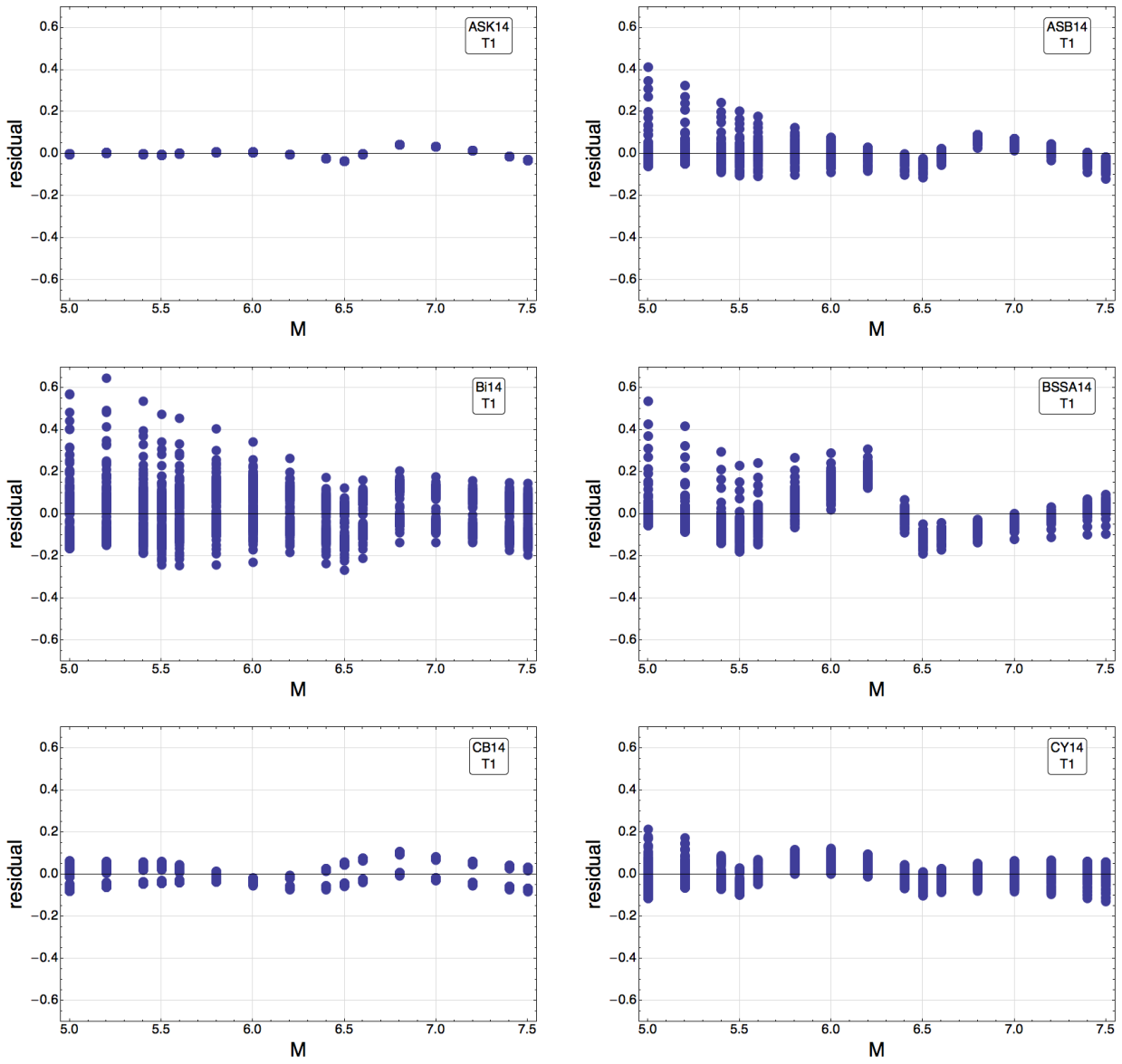

Figure 6.4.1-6b: Total residuals of the candidate GMPEs for PVNGS (Greater Arizona sources) refitted to the R_{RUP}-based common form plotted versus magnitude for T = 1.0 sec.

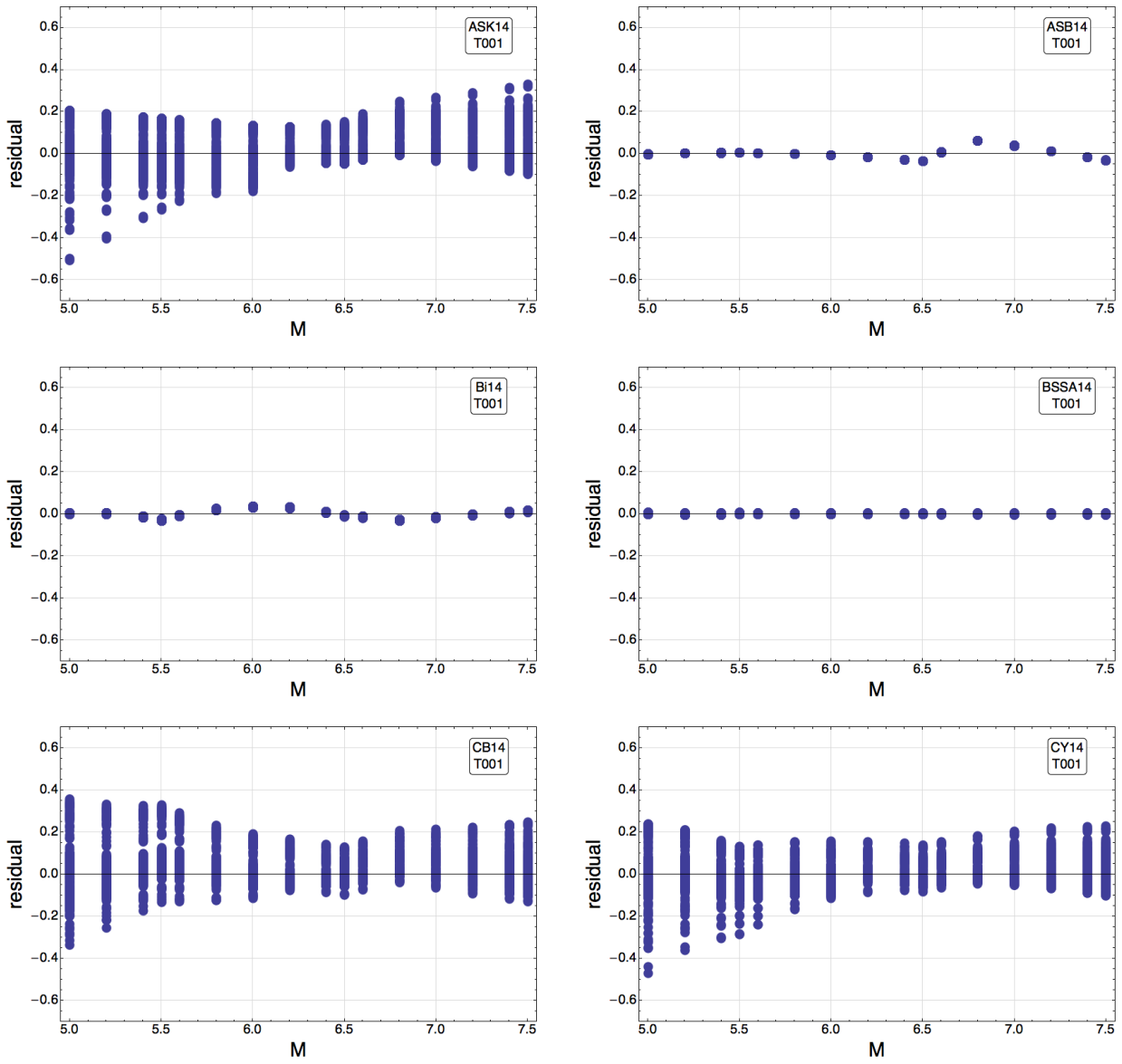

Figure 6.4.1-7a: Total residuals of the candidate GMPEs for PVNGS (Greater Arizona sources) refitted to the R_{JB}-based common form plotted versus magnitude for PGA.

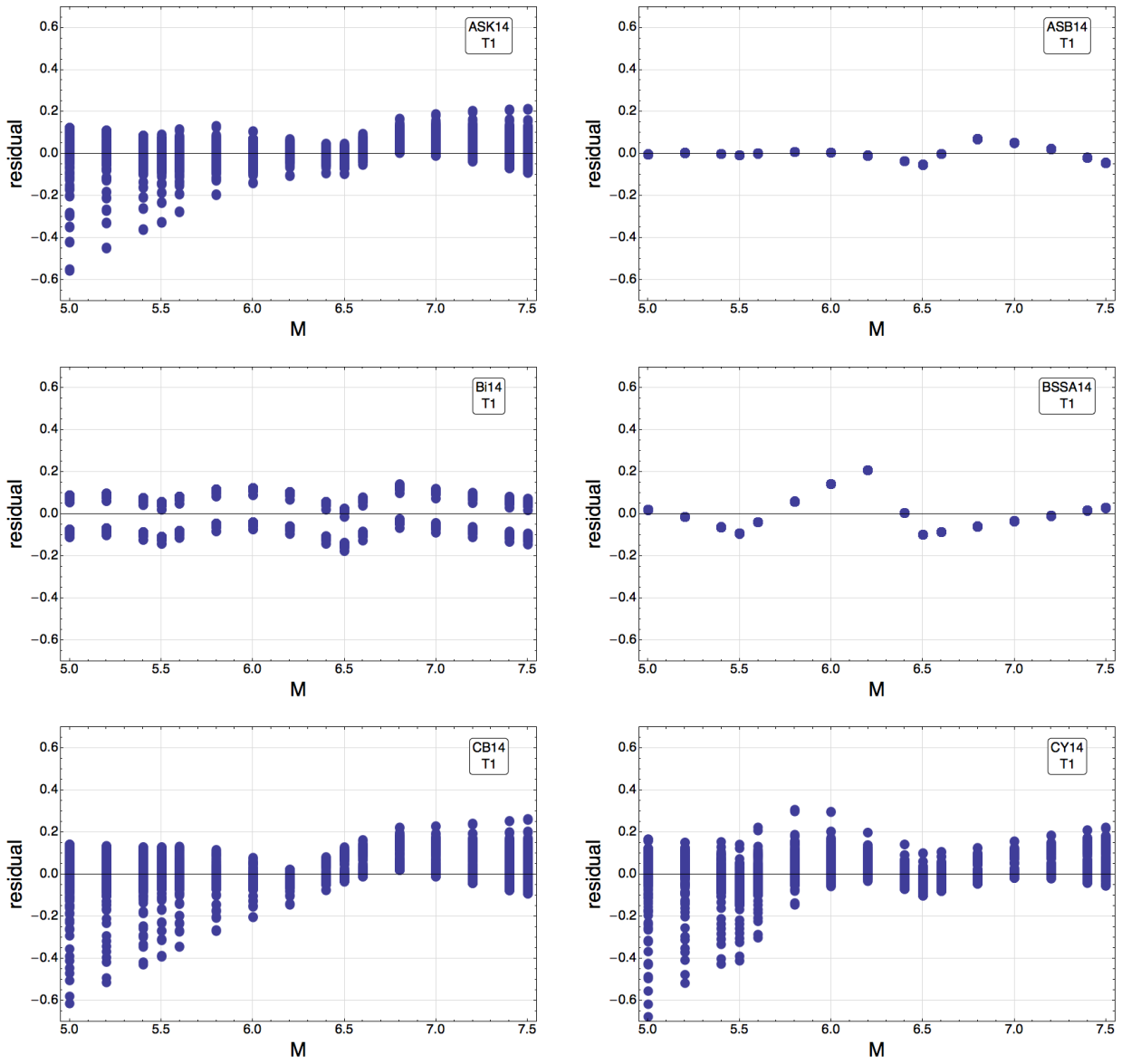

Figure 6.4.1-7b: Total residuals of the candidate GMPEs for PVNGS (Greater Arizona sources) refitted to the R_{JB}-based common form plotted versus magnitude for T = 1.0 sec.

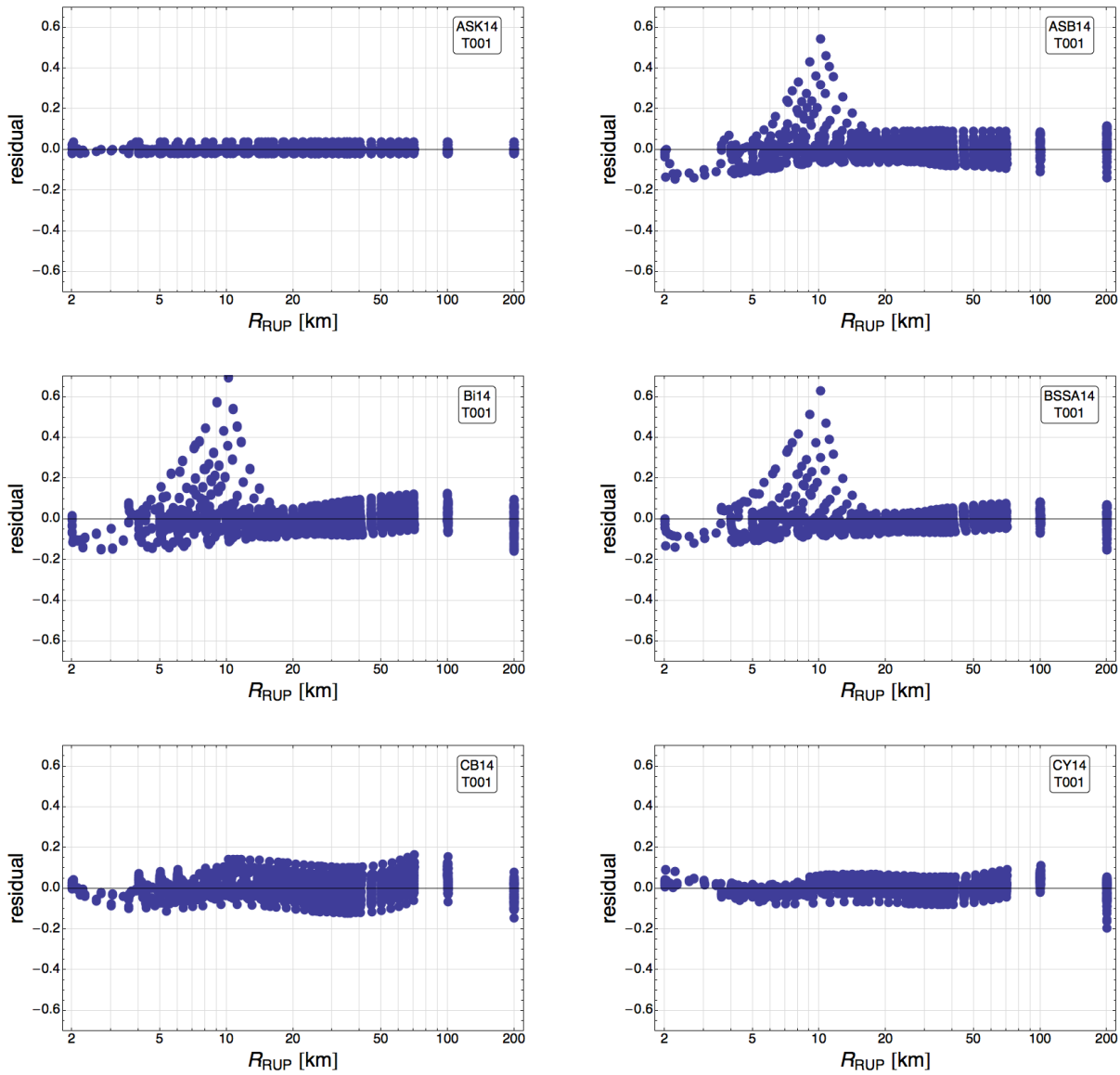

Figure 6.4.1-8a: Total residuals of the candidate GMPEs for PVNGS (Greater Arizona sources) refitted to the R_{RUP}-based common form plotted versus R_{RUP} for PGA.

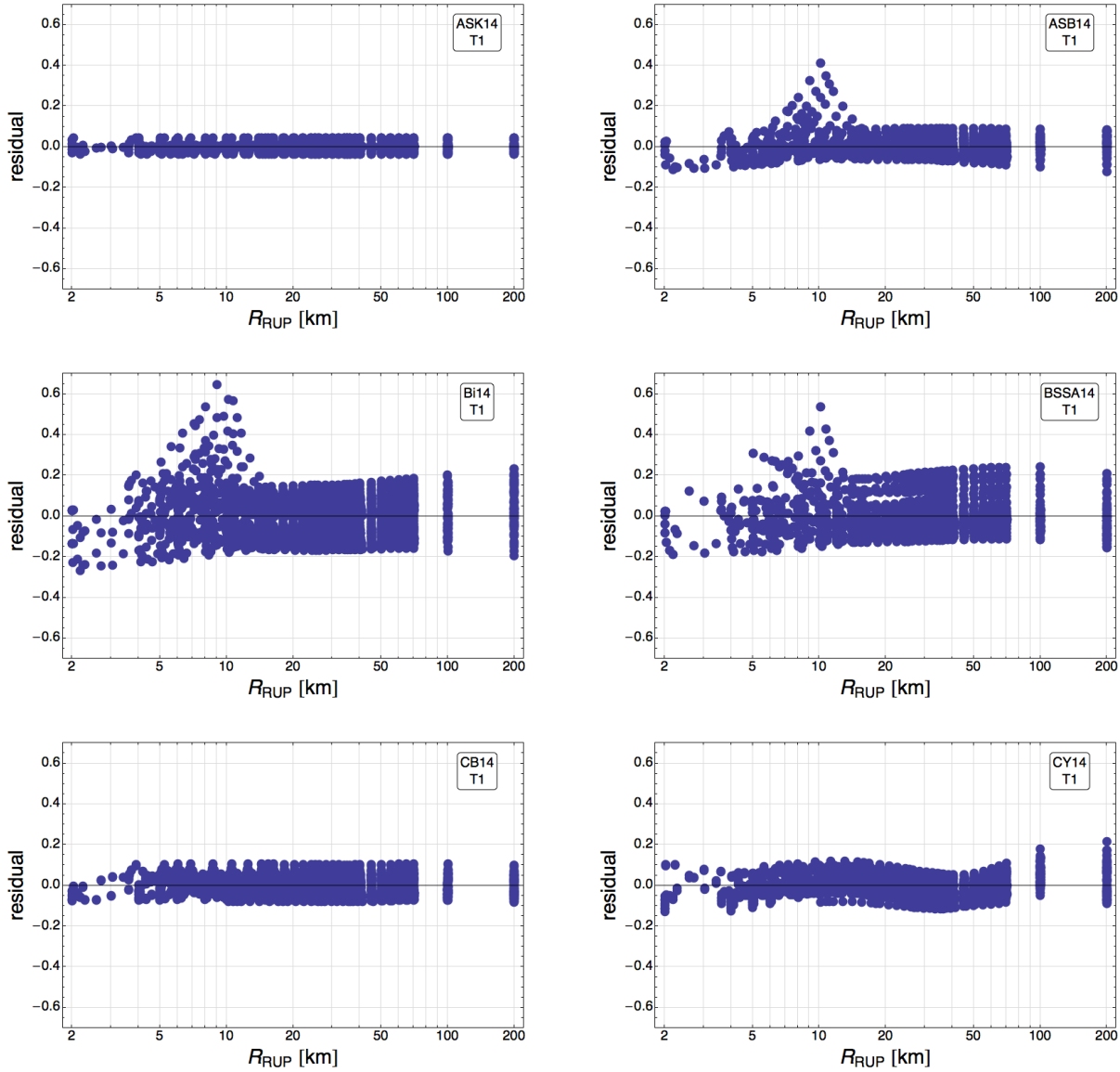

Figure 6.4.1-8b: Total residuals of the candidate GMPEs for PVNGS (Greater Arizona sources) refitted to the R_{RUP}-based common form plotted versus R_{RUP} for T = 1.0 sec.

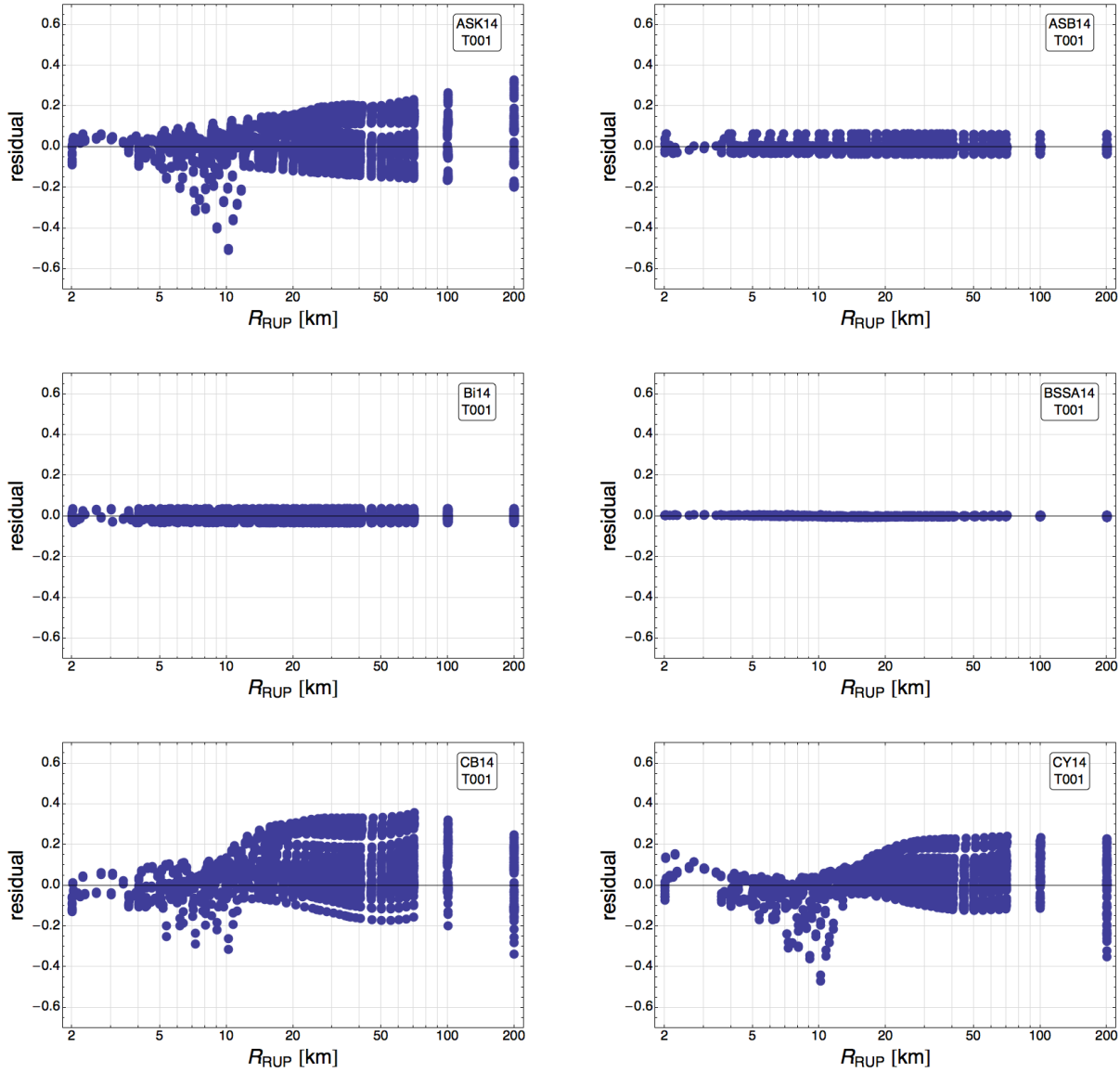

Figure 6.4.1-9a: Total residuals of the candidate GMPEs for PVNGS (Greater Arizona sources) refitted to the R_{JB}-based common form plotted versus R_{RUP} for PGA.

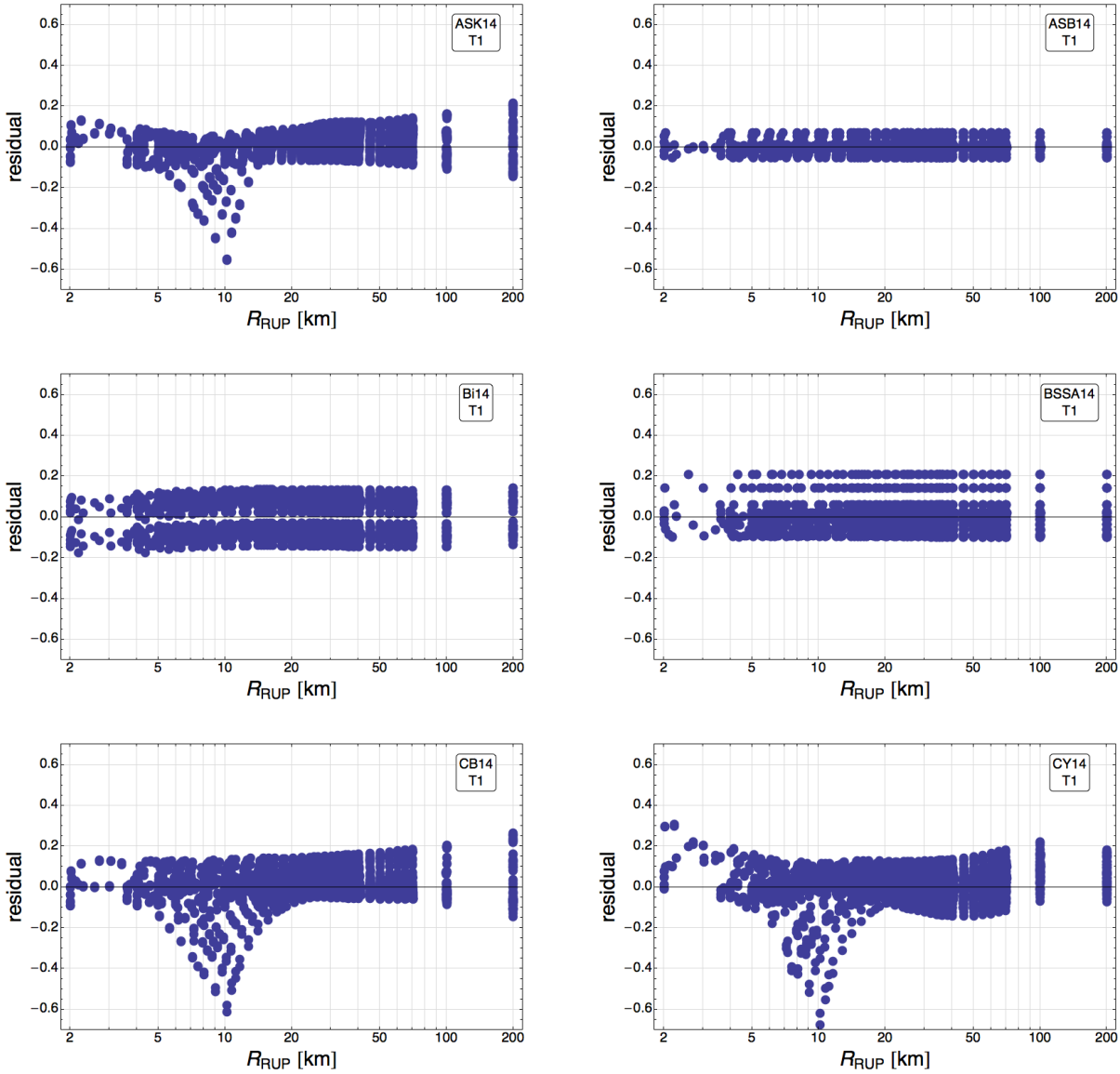

Figure 6.4.1-9b: Total residuals of the candidate GMPEs for PVNGS (Greater Arizona sources) refitted to the R_{JB}-based common form plotted versus R_{RUP} for T = 1.0 sec.

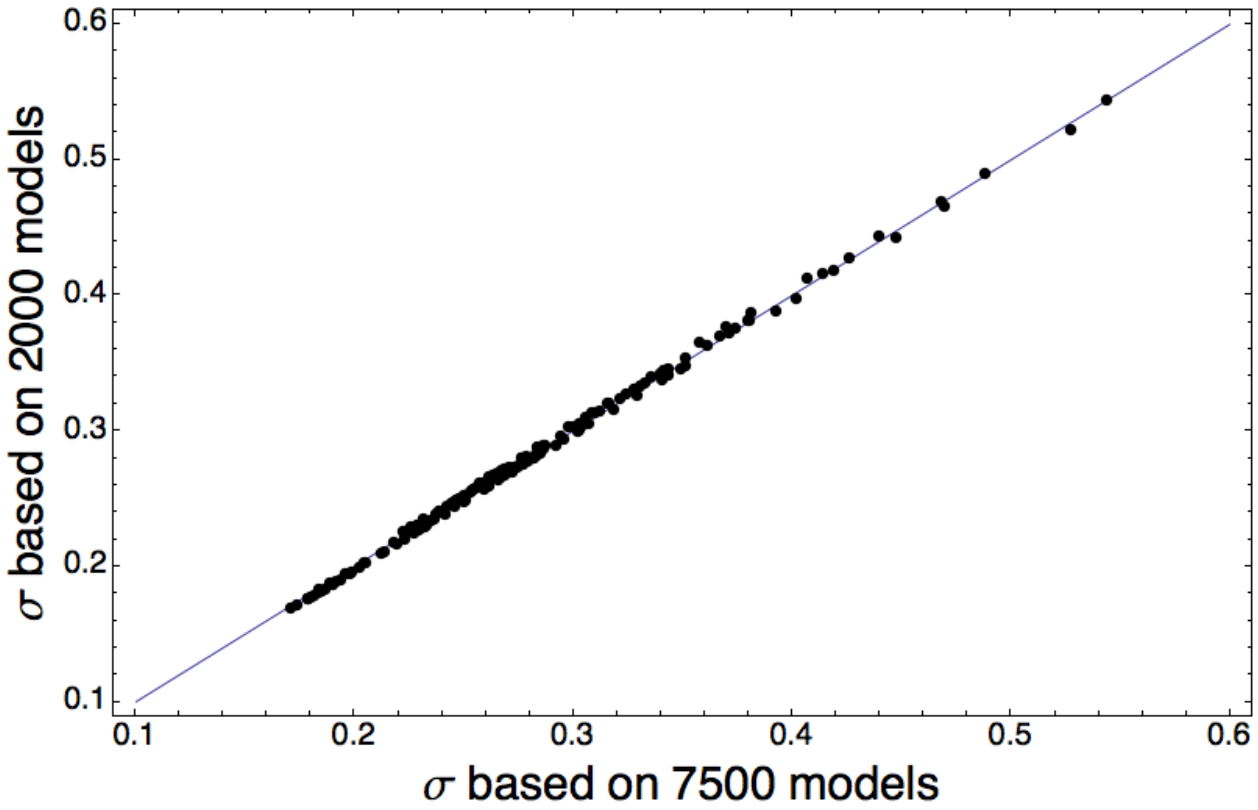

Figure 6.4.3-1: Comparison of the standard deviations of the natural log spectral acceleration, calculated for each scenario discussed in Section 6.4.3, for the 7500 and the 2000 sampled R_{RUP}-based common-form models used to develop the Sammon's map for DCPP, Model A, at PGA. The solid blue line represents the 1-to-1 correlation.

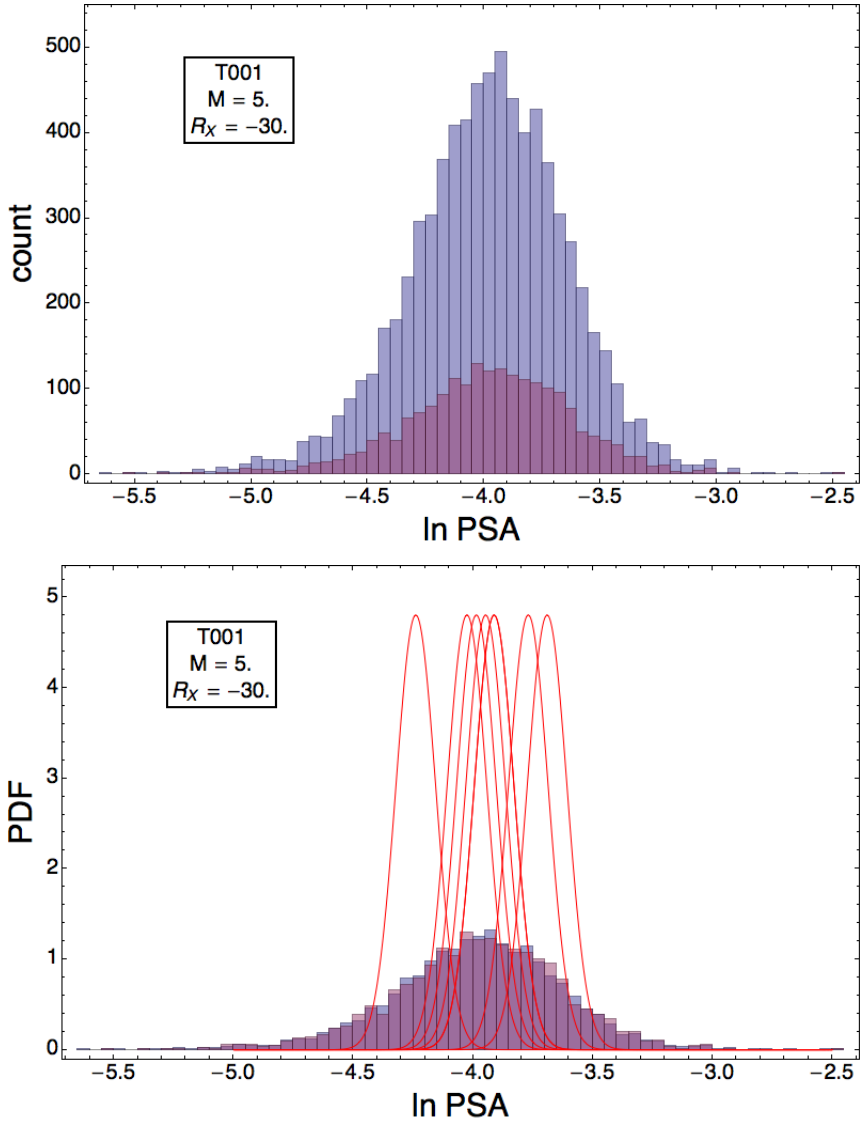

Figure 6.4.3-2: Top panel: Histogram of 7500 and 2000 sampled models for a scenario with **M**5 and R_X = -30 for DCPP (Model A) at T = 0.01 sec. Bottom panel: Normalized histogram for 7500 and 2000 sampled models, showing equivalence in ground-motion range. Also shown are the probability density functions of the original GMPEs with their (epistemic) uncertainty, with their median predictions as mean and standard deviations from the uncertainty model of Al Atik and Youngs (2014).

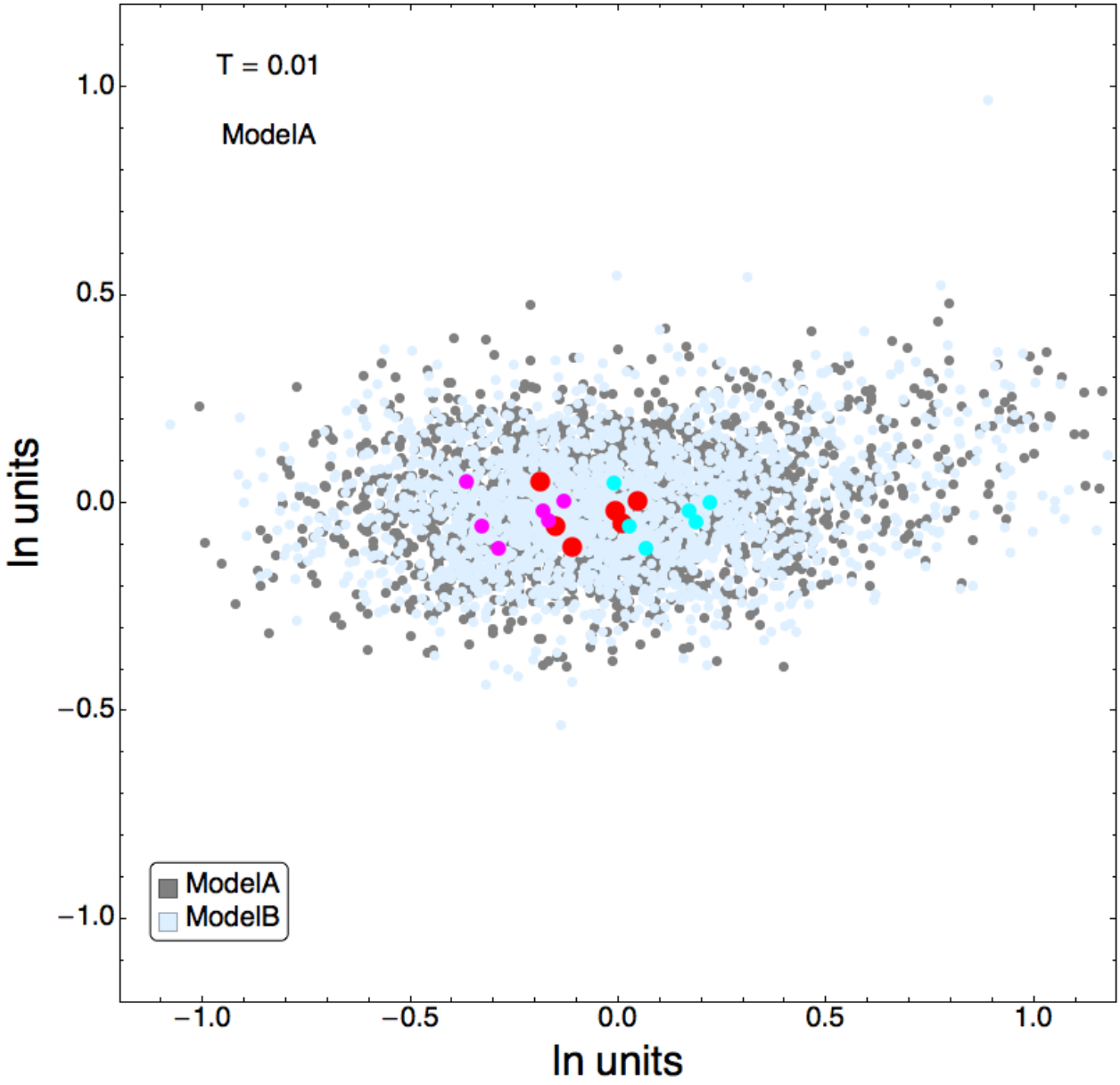

Figure 6.4.3-3: Map of 2000 sampled models using R_{RUP}-based common form (Model A) and R_{JB}-based common form (Model B), for PVNGS at PGA. Red dots show the candidate GMPEs used to develop the ground-motion model distributions. The magenta and cyan dots show plus and minus two sigma epistemic uncertainty, respectively about the candidate GMPEs.

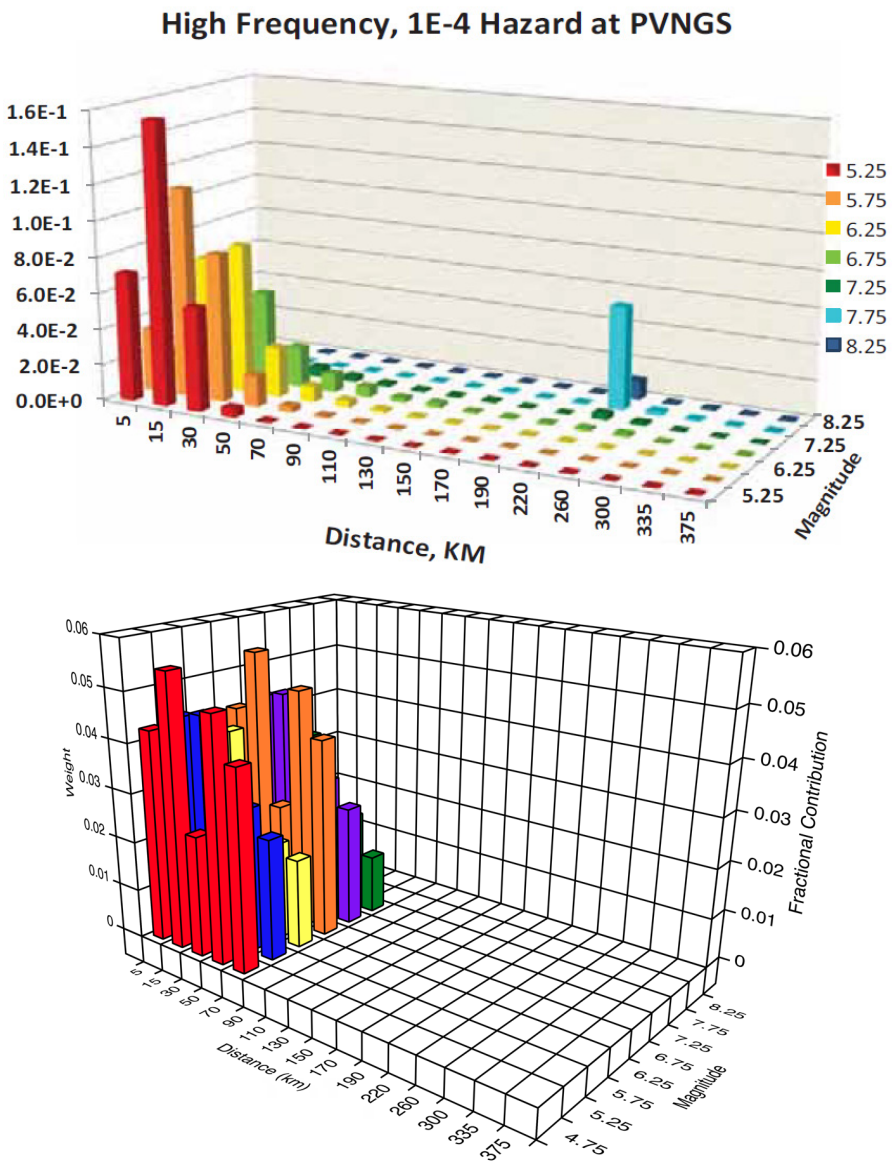

Figure 6.4.3-4a: Comparison of the weights for the vector of scenarios (lower frame) with the deaggregation for the 10^{-4} AFE PGA for PVNGS. The method for the weights spreads out the weights over a broader range of scenarios for the short distances. The large distances (greater than 70 km) are not included in the vector of scenarios.

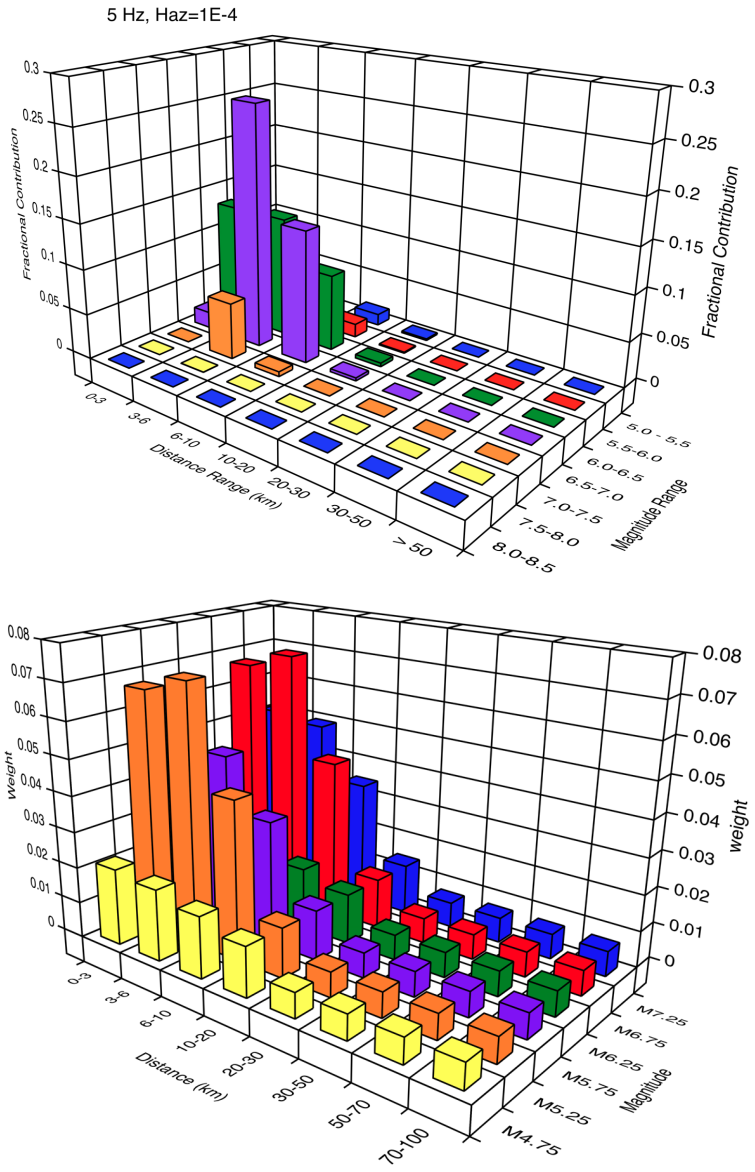

Figure 6.4.3-4b Comparison of the weights for the vector of scenarios (lower frame) with the deaggregation for the 10^{-4} AFE PGA for DCPP. The method for the weights spreads out the weights over a broader range of scenarios.

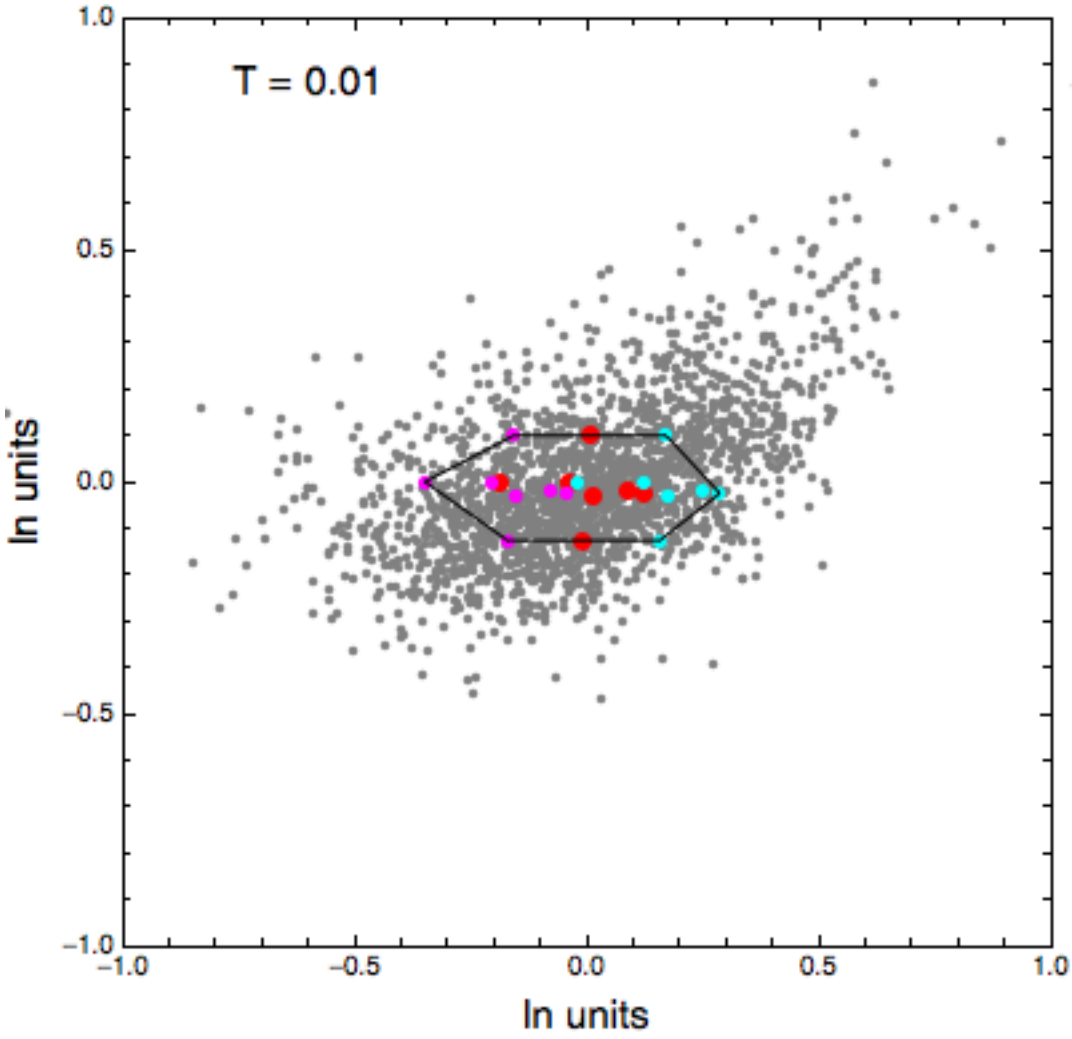

Figure 6.4.4-1: example of a Sammon's map for T = 0.01 sec. The common-form models fit to the candidate GMPEs are show by the red dots, and the ones fit to the candidate GMPEs including plus/minus epistemic uncertainty are shown by the magenta and cyan dots, respectively. The convex hull for these refitted candidate GMPEs is shown by the solid black line.

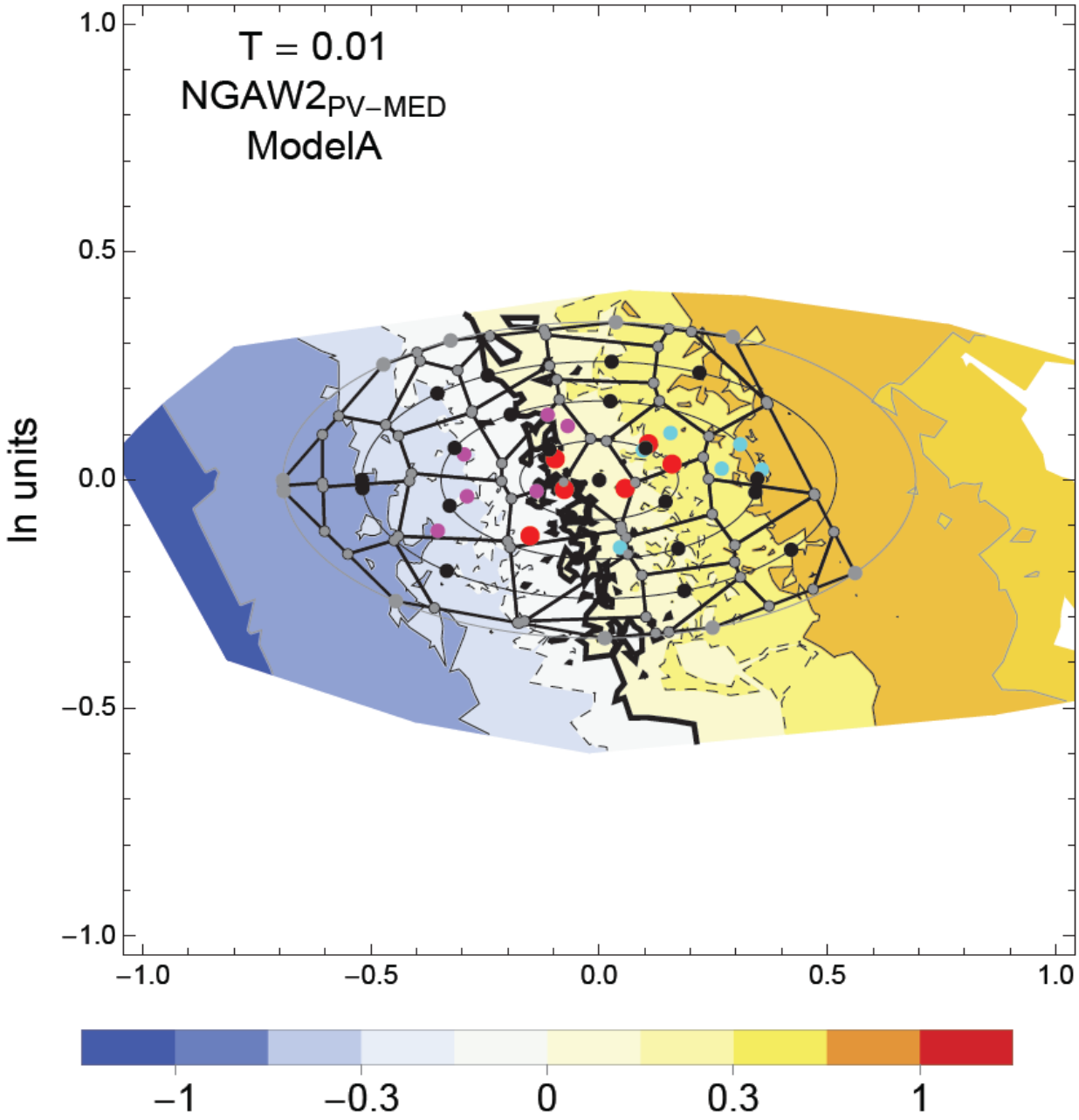

Figure 6.4.4-2: Contour plot of mean between-event residuals for the weighted $NGAW2_{PV-MED}$ dataset (PVNGS, Model A, T = 0.01 sec). The candidate GMPEs are red dots, plus/minus uncertainty as magenta/cyan dots. The Voronoi cells (black closed polygons) are developed based on the locations of the black points on the four concentric ellipses (gray concentric curves), and used for selecting and weighting models. The contour for the zero residual is a thick black line, the ± 0.15 contours are dashed black lines and the ± 0.3 contours are thin black lines.

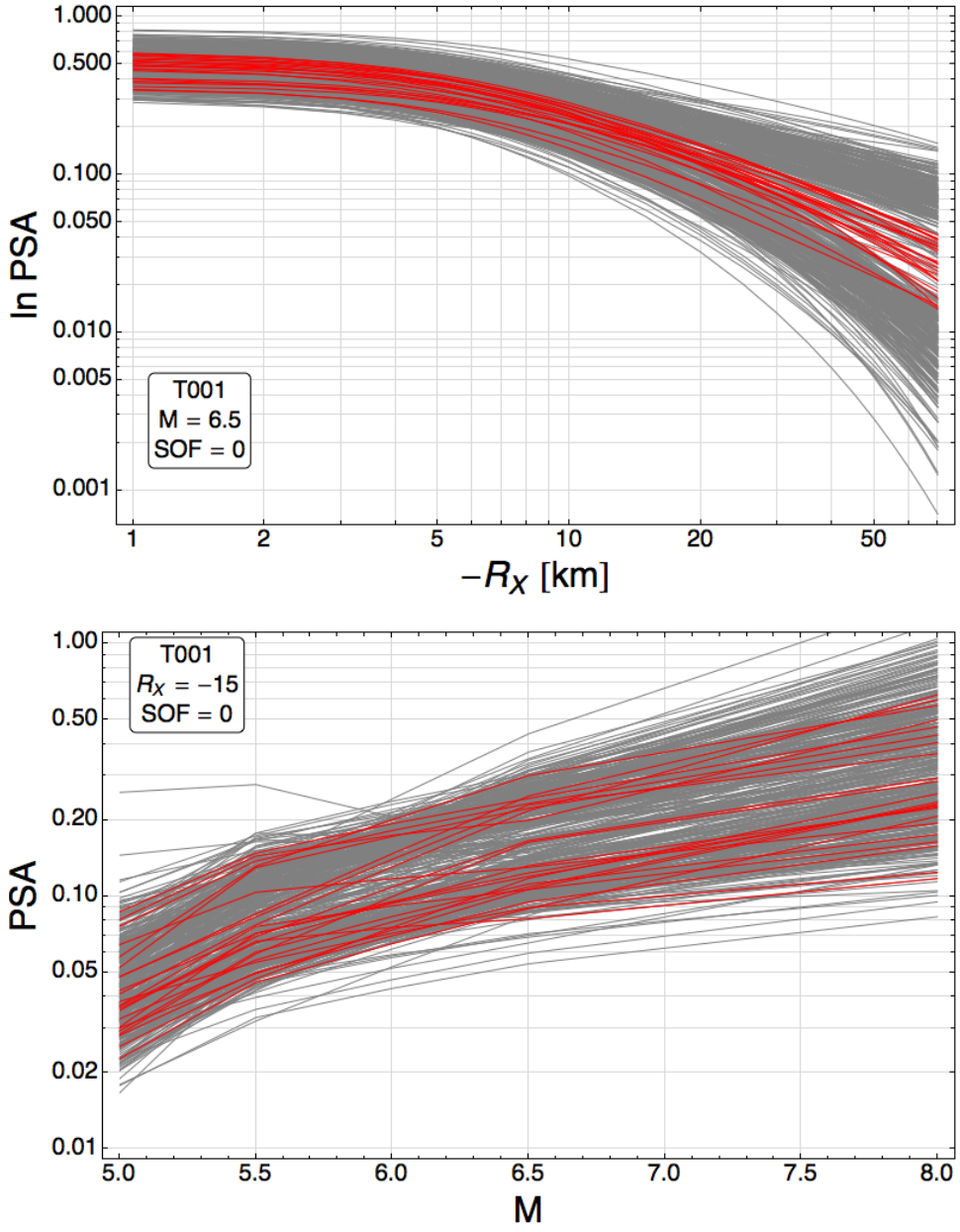

Figure 6.4.4-3: Example of models that have been screened out. The red lines correspond to the representative suite of common-form models that have been selected, and the gray lines correspond to models that have been screened out (outside the outermost ellipse).

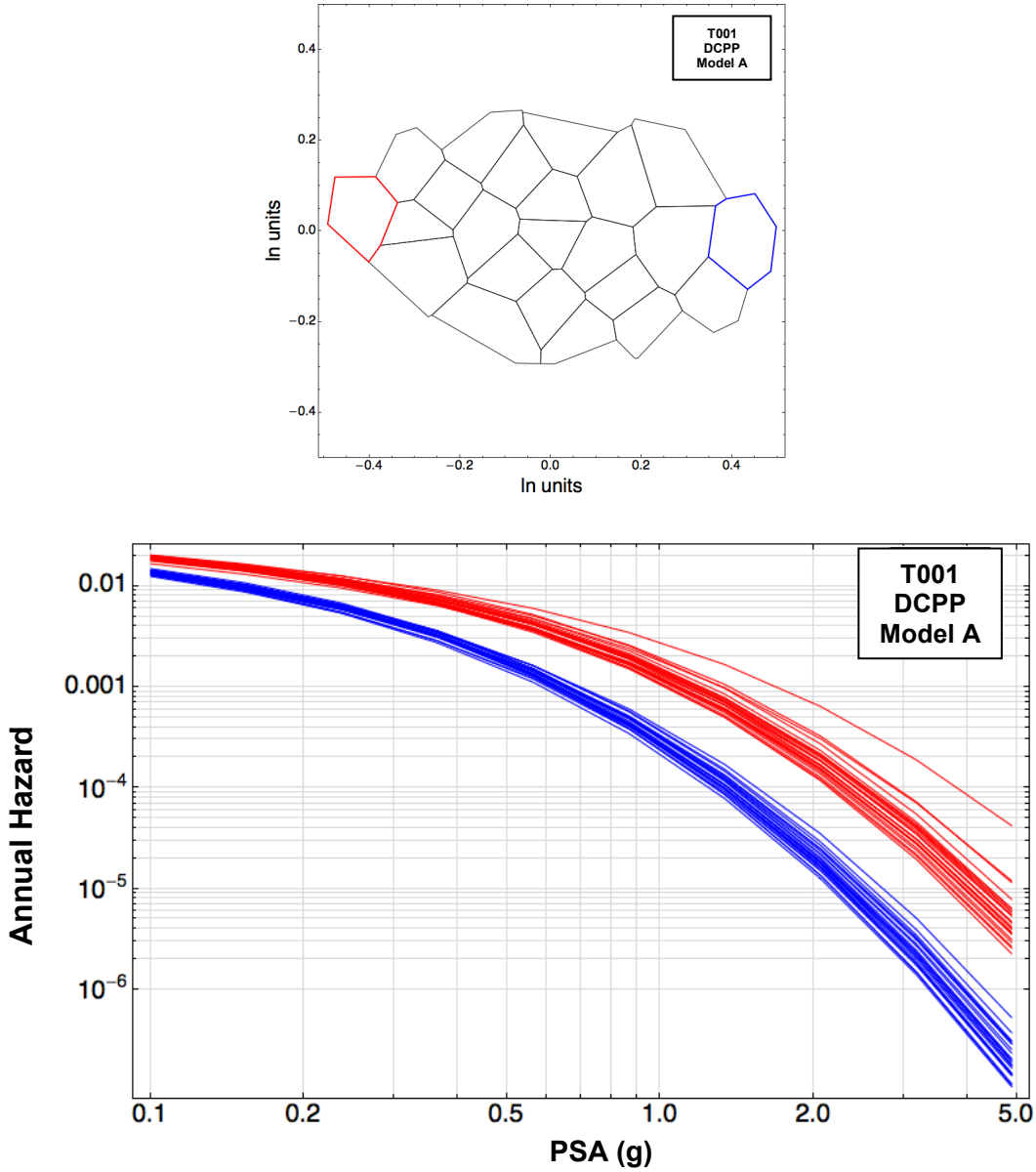

Figure 6.4.4-4: Scatter in the hazard from models in the same cell.

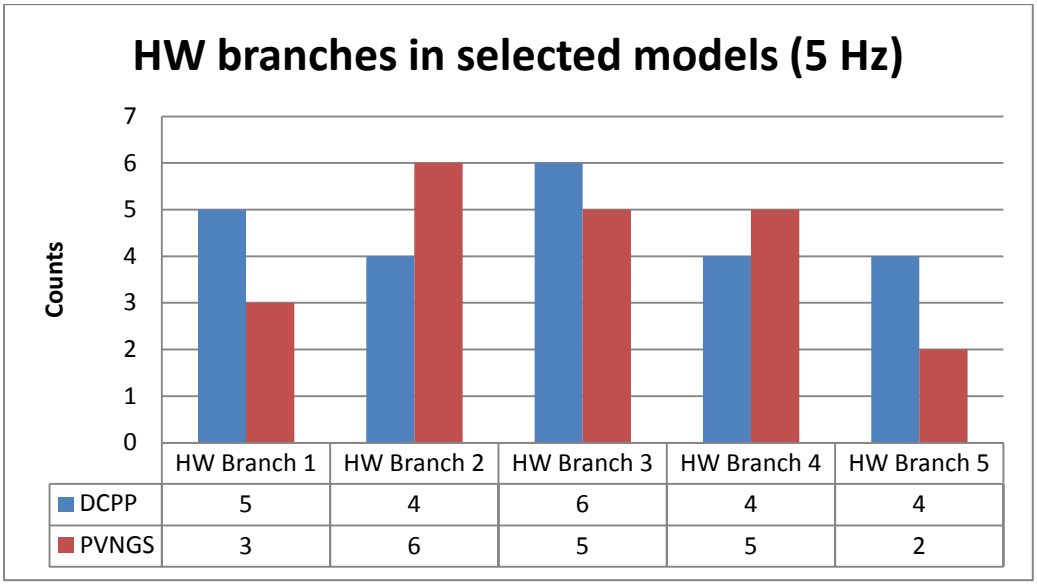

Figure 6.4.4-5: Distribution of the selection of the HW branches for the representative suite of common-form models for PVNGS and DCPP at 5 Hz.

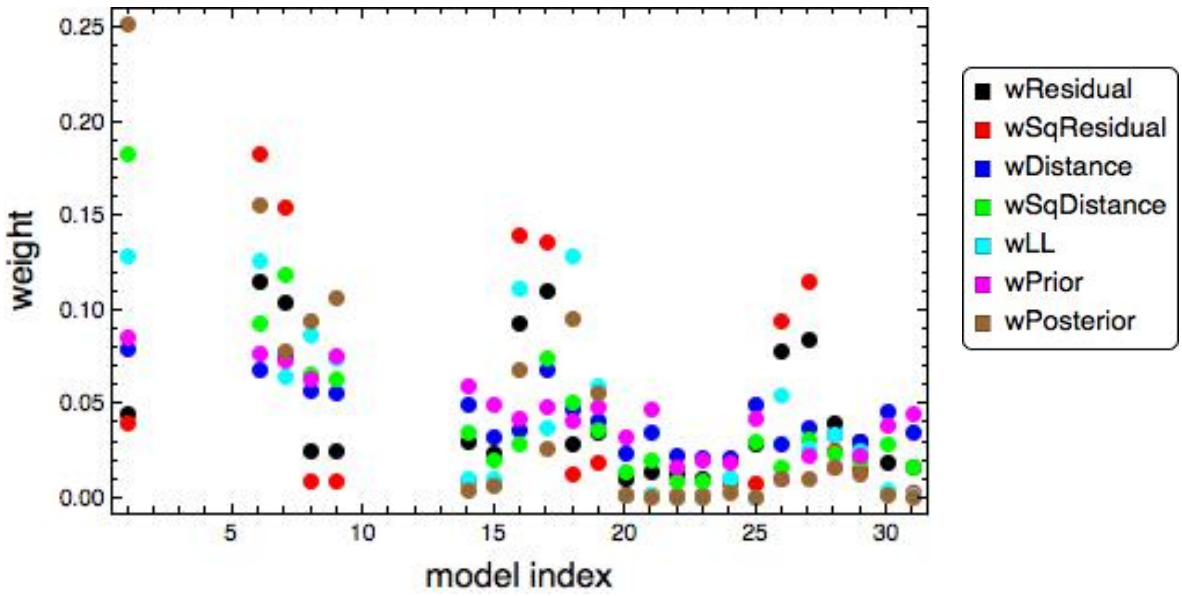

Figure 6.4.5-1: Weights for the representative suite of R_{RUP}–based common-form models (Model A) for PVNGS at T = 0.01 sec, calculated using different statistics based on the weighted $NGAW2_{PV\text{-}MED}$ dataset, versus model index.

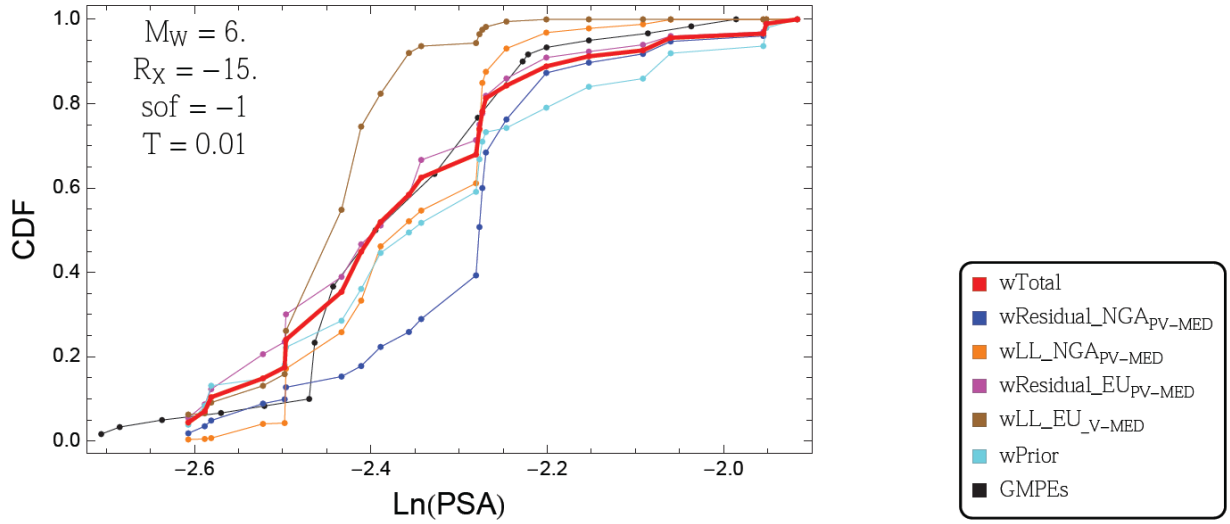

Figure 6.4.5-2a: Cumulative density function of GMPEs (black) and representative suite of common-form models, for different sets of weights, for a scenario with **M**6.0, R_X = -15 Km, NML style-of-faulting, and T = 0.01 sec, for PVNGS Model A (R_{RUP} –based).

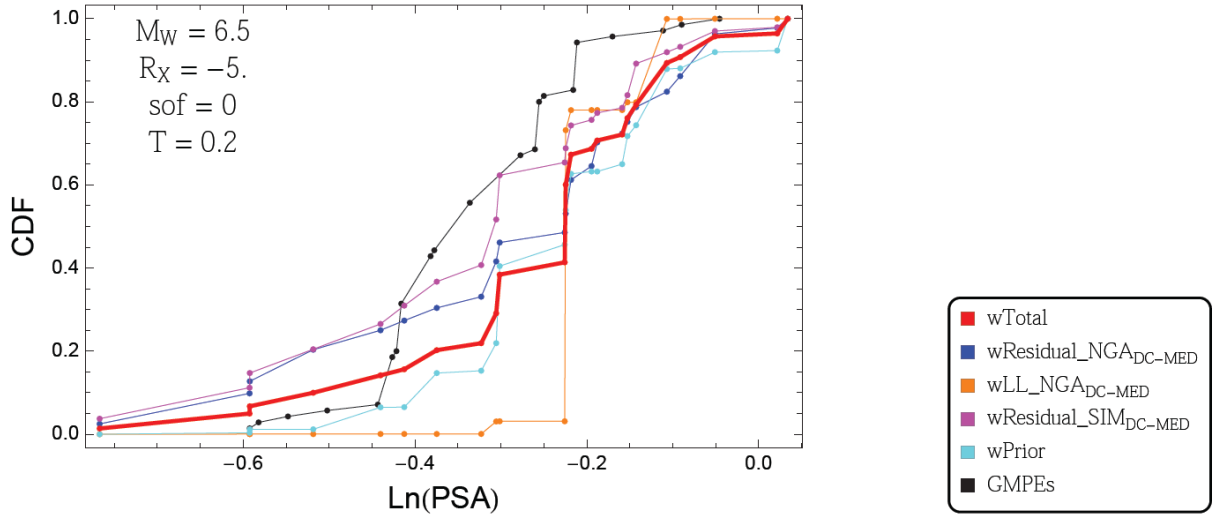

Figure 6.4.5-2b: Cumulative density function of GMPEs (black) and representative suite of common-form models, for different sets of weights, for a scenario with **M**6.5, R_X = -10 Km, SS style-of-faulting, and T = 0.2 sec, for DCPP Model A (R_{RUP} –based).

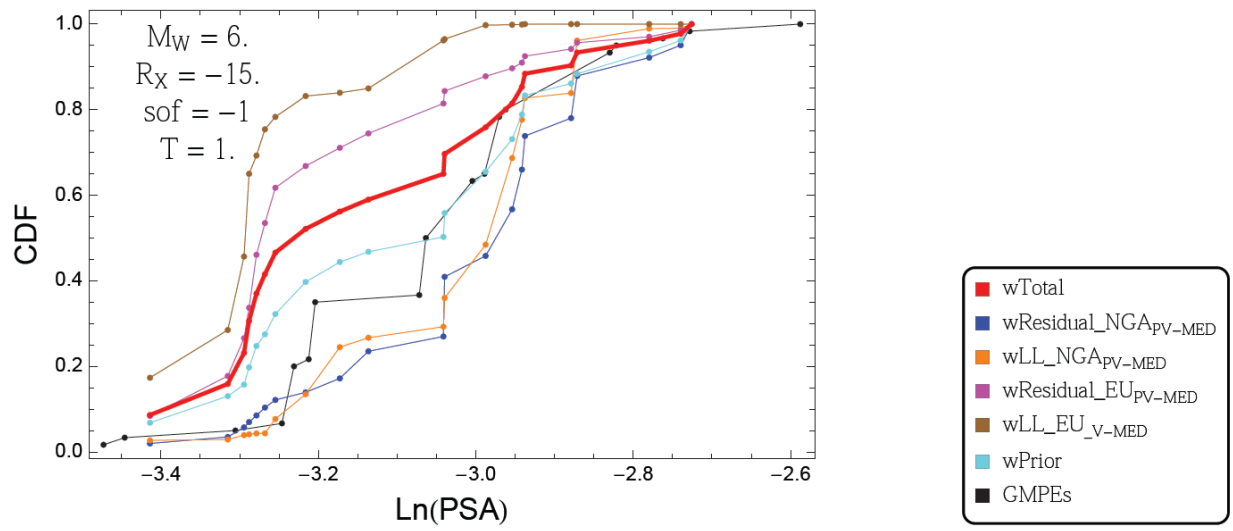

Figure 6.4.5-2c: Cumulative density function of GMPEs (black) and representative suite of common-form models, for different sets of weights, for a scenario with **M**6, R_X = -15 Km, NML style-of-faulting, and T = 1.0 sec, for PVNGS Model A (R_{RUP} –based).

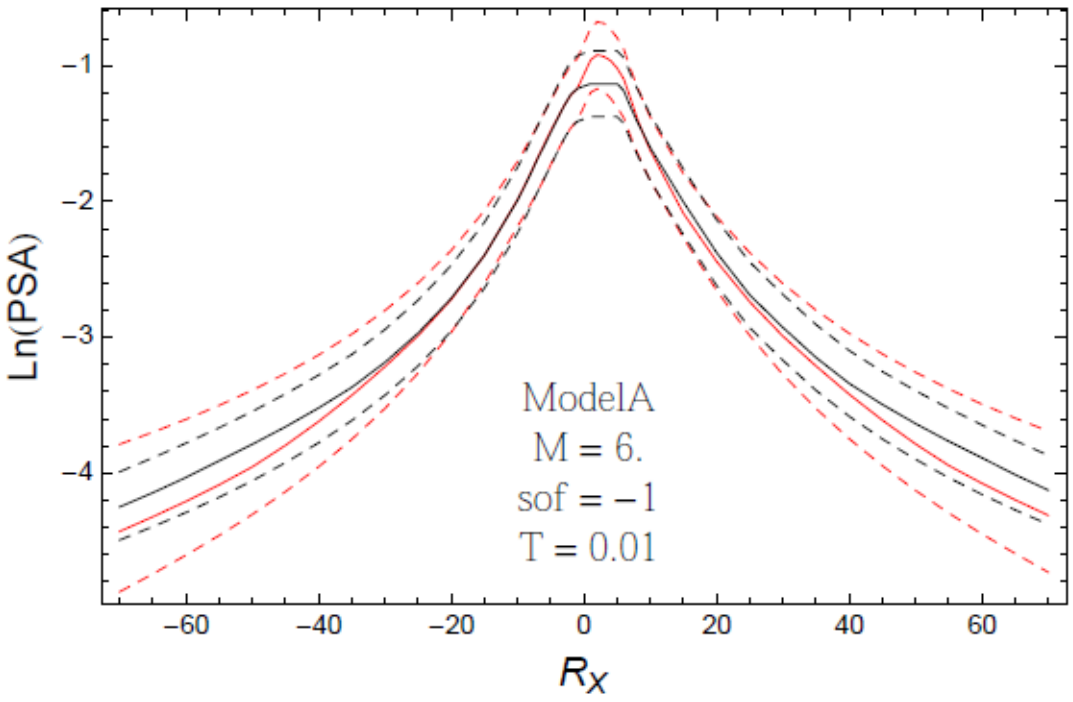

Figure 6.4.5-3: Distance scaling of 0.05, 0.5, and 0.95 quantiles of the GMPE distribution (black) and the representative suite of common-form model distribution (red) with total weights. Plot is for a scenario with **M**6.0, NML style-of-faulting, and T = 0.01 sec, for Model A (R_{RUP} –based) and PVNGS.

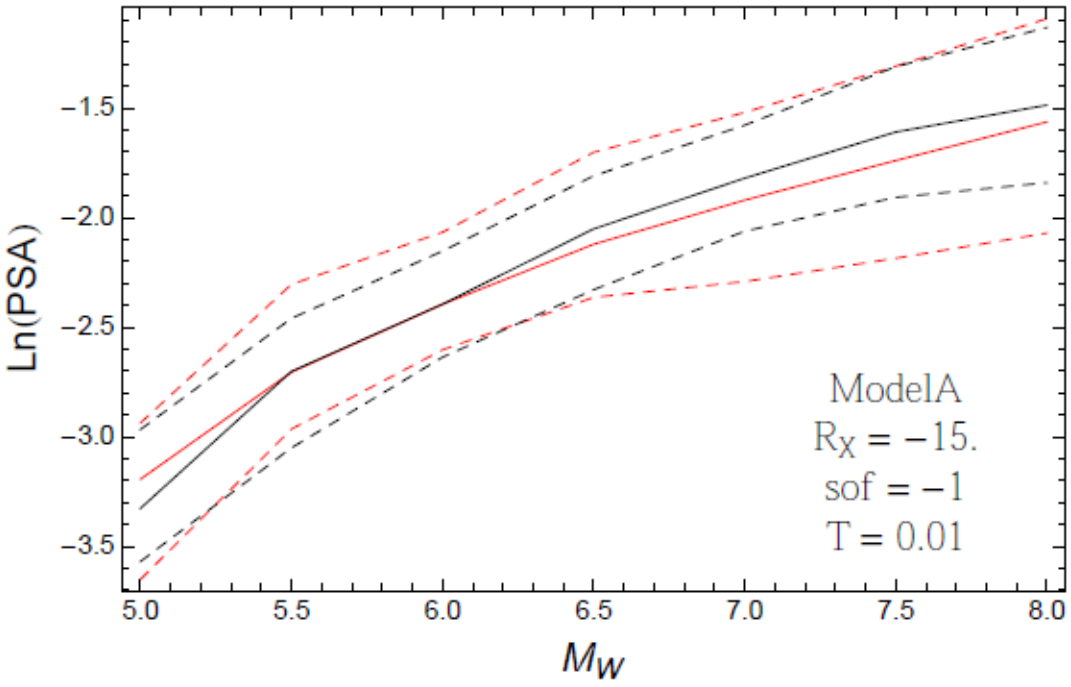

Figure 6.4.5-4: Magnitude scaling of 0.05, 0.5, and 0.95 quantiles of the GMPE distribution (black) and the representative suite of common-form models distribution (red) with total weights. Plot is for a scenario with R_X = -15 km, NML style-of-faulting, and T = 0.01 sec, for Model A (R_{RUP} –based) at PVNGS.

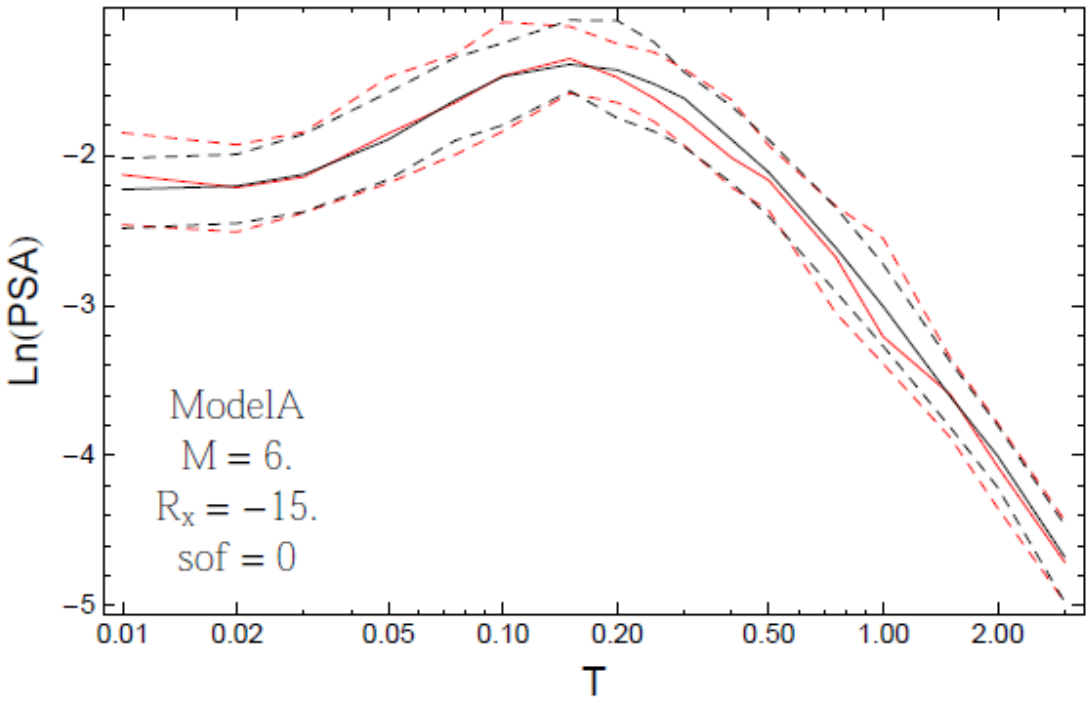

Figure 6.4.5-5: Spectra of 0.05, 0.5, and 0.95 quantiles of the GMPE distribution (black) and the representative suite of common-form models distribution (red) with total weights. Plot is for a scenario with **M**6.0, R_X = -15 km, SS Style-of-faulting, for Model A (R_{RUP} –based) at PVNGS.

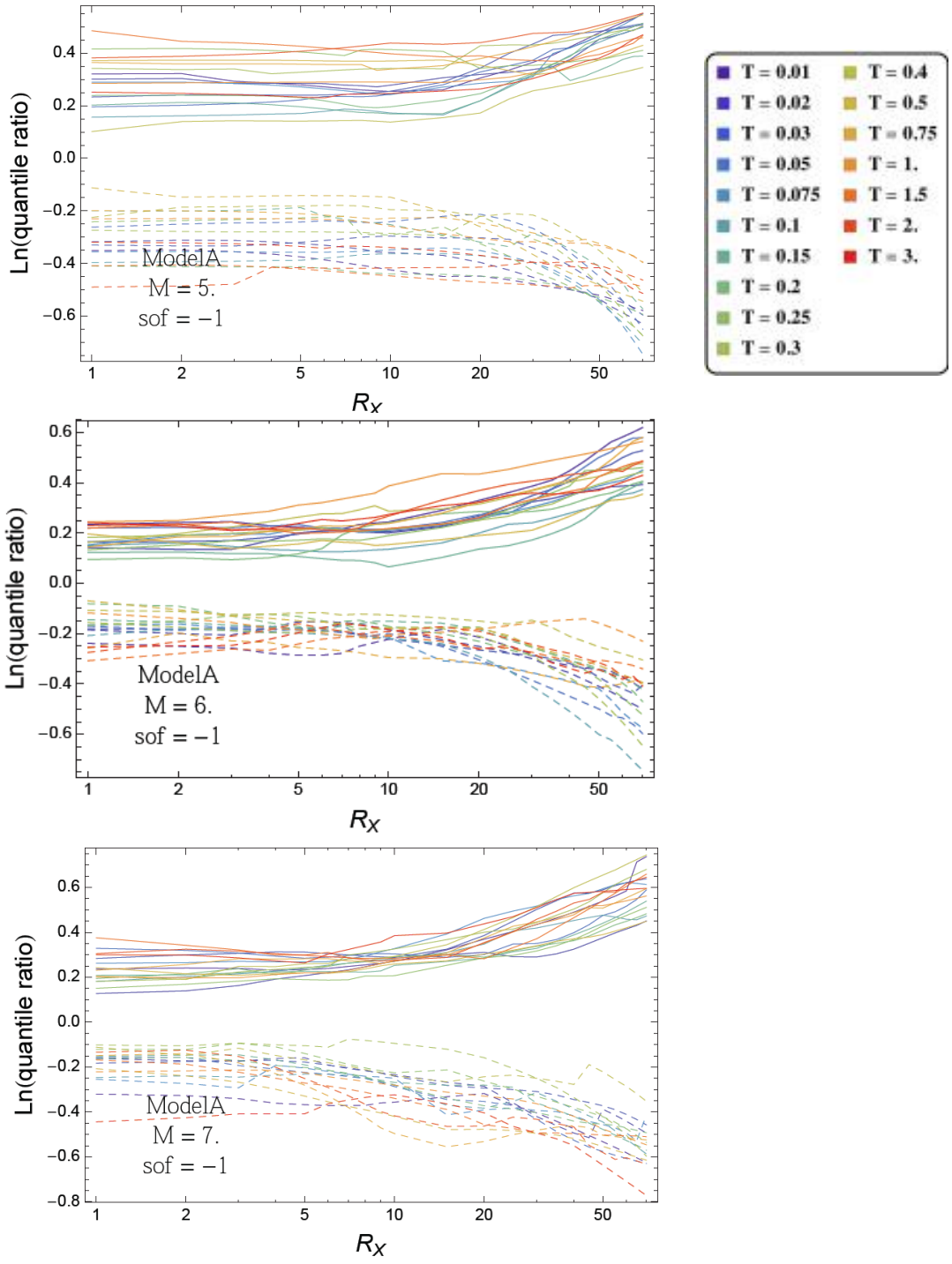

Figure 6.4.5-6: Ratio of 0.05 to 0.5 (dashed) and ratio of 0.95 to 0.5 quantiles (solid) of the representative suite of R_{RUP}-based common-form models distribution with total weights, for a scenario with **M**5 (top), **M**6 (center), and **M**7 (bottom), NML Style-of-faulting, and all periods, for Model A (R_{RUP} – based) at PVNGS.

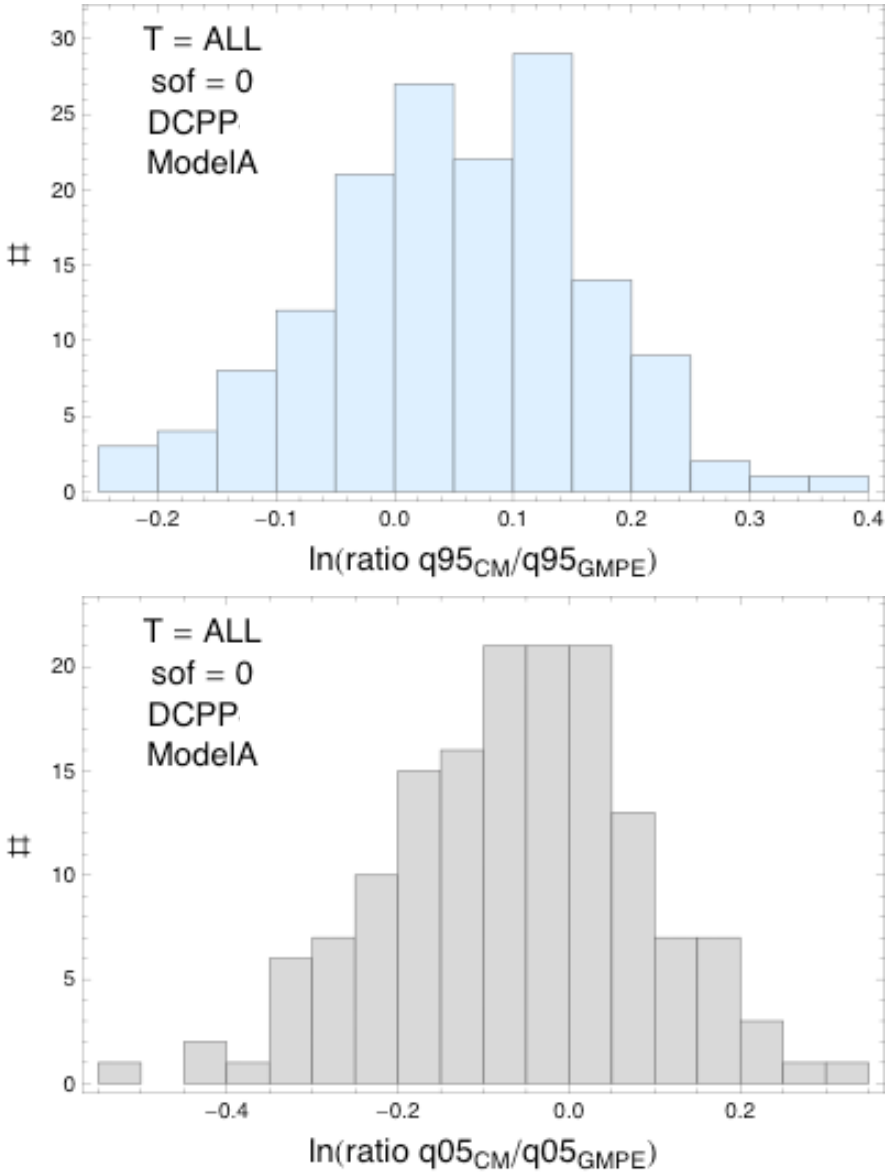

Figure 6.4.5-7: Ln ratio of the 5th and 95th fractile of the median spectral acceleration from the representative suite of common-form models to the 5th and 95th fractile of the median spectral acceleration from the GMPEs with additional epistemic uncertainty (assuming equal weight to each GMPE). Top frame is for the histogram of the ln ratios of the 95th fractile for DCPP for strike-slip earthquakes. Bottom frame is for the histogram of the ln ratios of the 5th fractile for DCPP for strike-slip earthquakes.

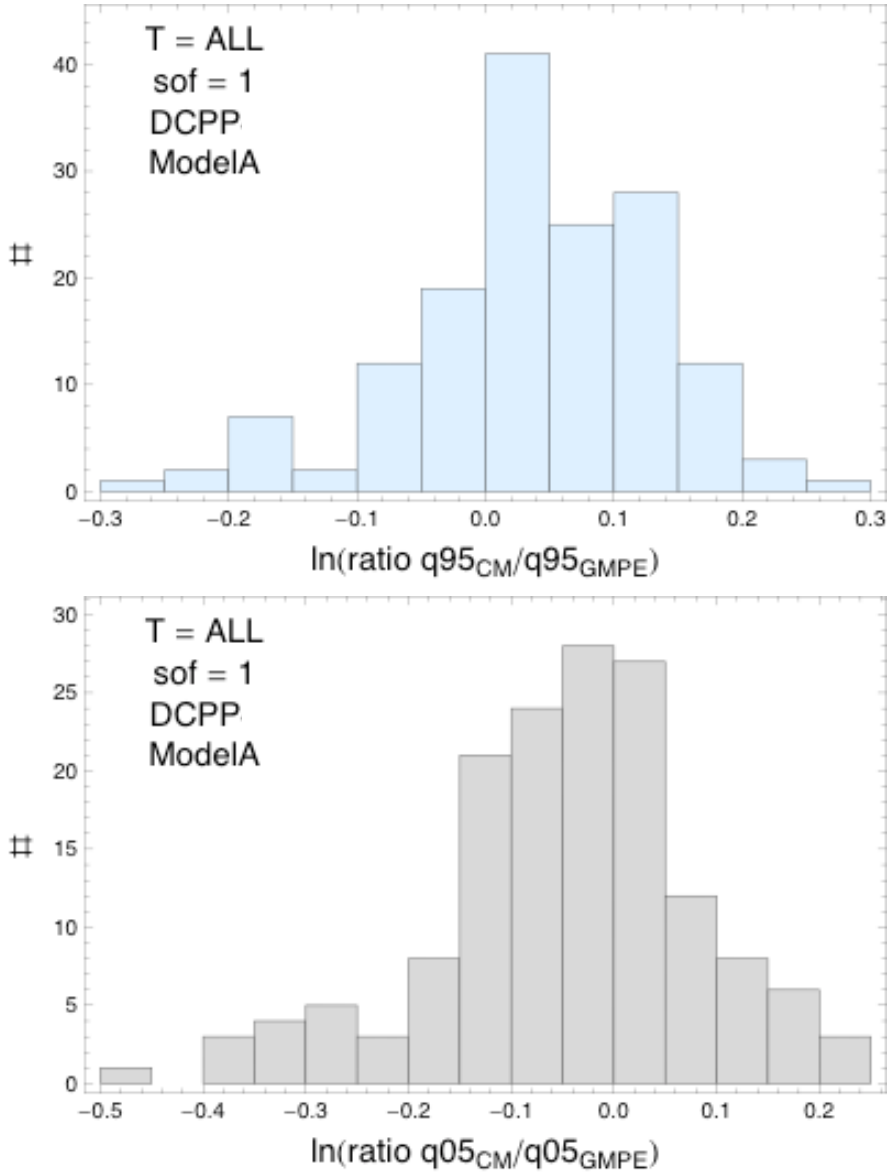

Figure 6.4.5-8: Ln ratio of the 5th and 95th fractile of the median spectral acceleration from the representative suite of common-form models to the 5th and 95th fractile of the median spectral acceleration from the GMPEs with additional epistemic uncertainty (assuming equal weight to each GMPE). Top frame is for the histogram of the ln ratios of the 95th fractile for DCPP from reverse earthquakes. Bottom frame is for the histogram of the ln ratios of the 5th fractile for DCPP for reverse earthquakes.

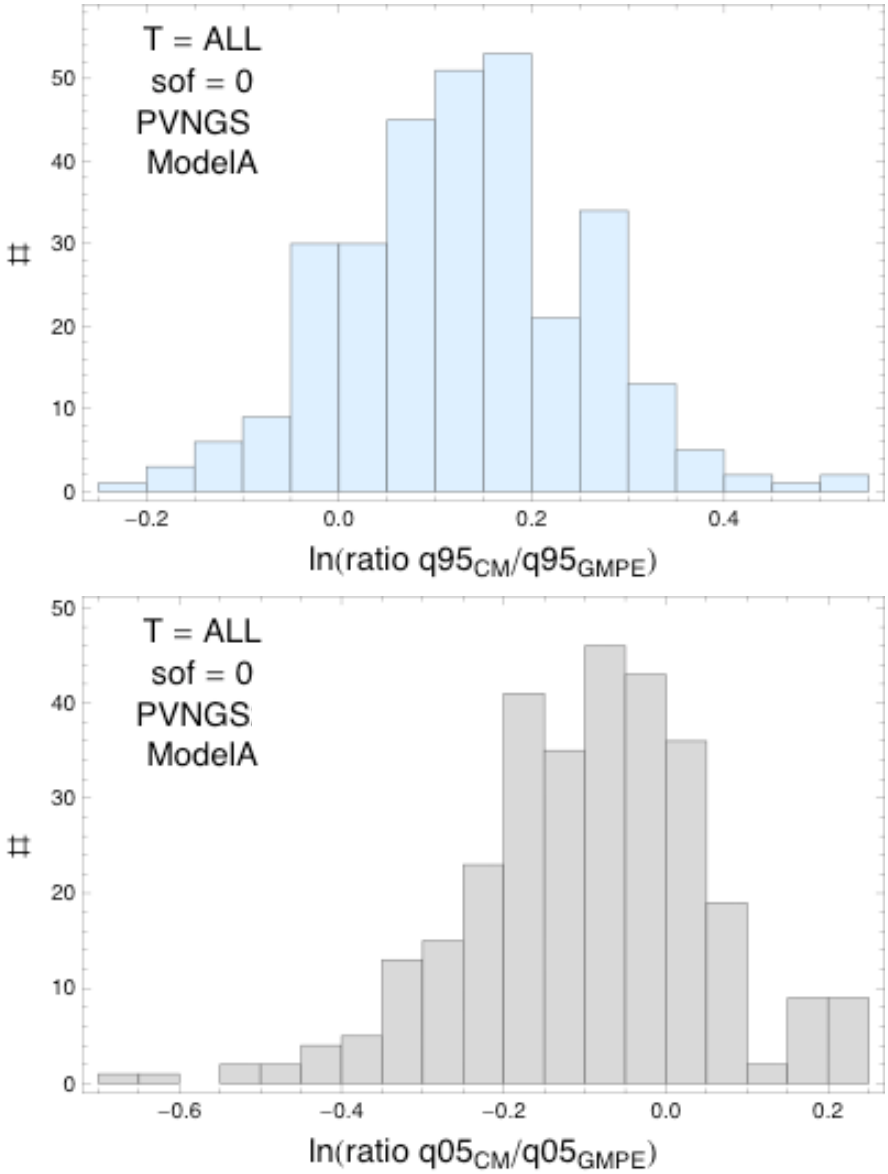

Figure 6.4.5-9: Ln ratio of the 5th and 95th fractile of the median spectral acceleration from the representative suite of common-form models to the 5th and 95th fractile of the median spectral acceleration from the GMPEs with additional epistemic uncertainty (assuming equal weight to each GMPE). Top frame is for the histogram of the ln ratios of the 95th fractile for PVNGS for strike-slip earthquakes, R_{RUP}-based models. Bottom frame is for the histogram of the ln ratios of the 5th fractile for PVNGS for strike-slip earthquakes, R_{RUP}-based models.

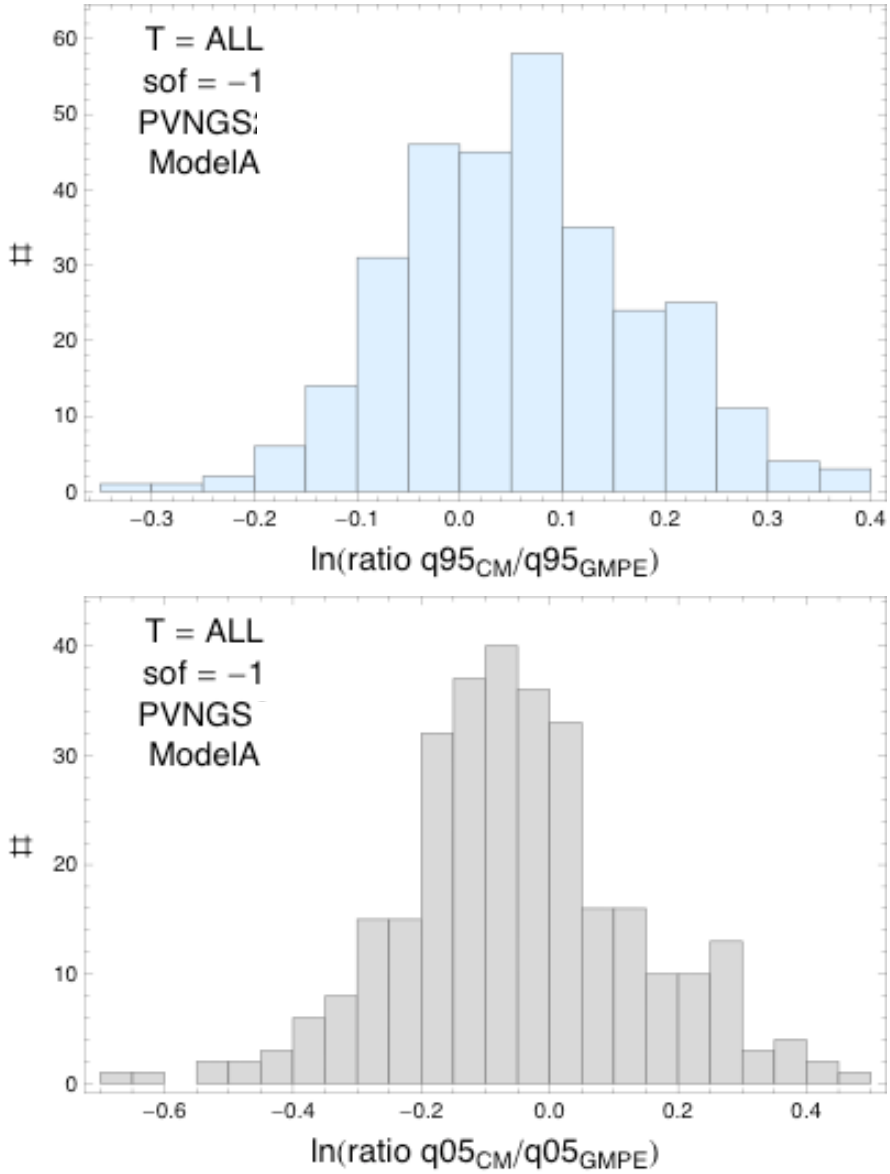

Figure 6.4.5-10: Ln ratio of the 5th and 95th fractile of the median spectral acceleration from the representative suite of common-form models to the 5th and 95th fractile of the median spectral acceleration from the GMPEs with additional epistemic uncertainty (assuming equal weight to each GMPE). Top frame is for the histogram of the ln ratios of the 95th fractile for PVNGS for normal earthquakes, R_{RUP}-based models. Bottom frame is for the histogram of the ln ratios of the 5th fractile for PVNGS for normal earthquakes, R_{RUP}-based models.

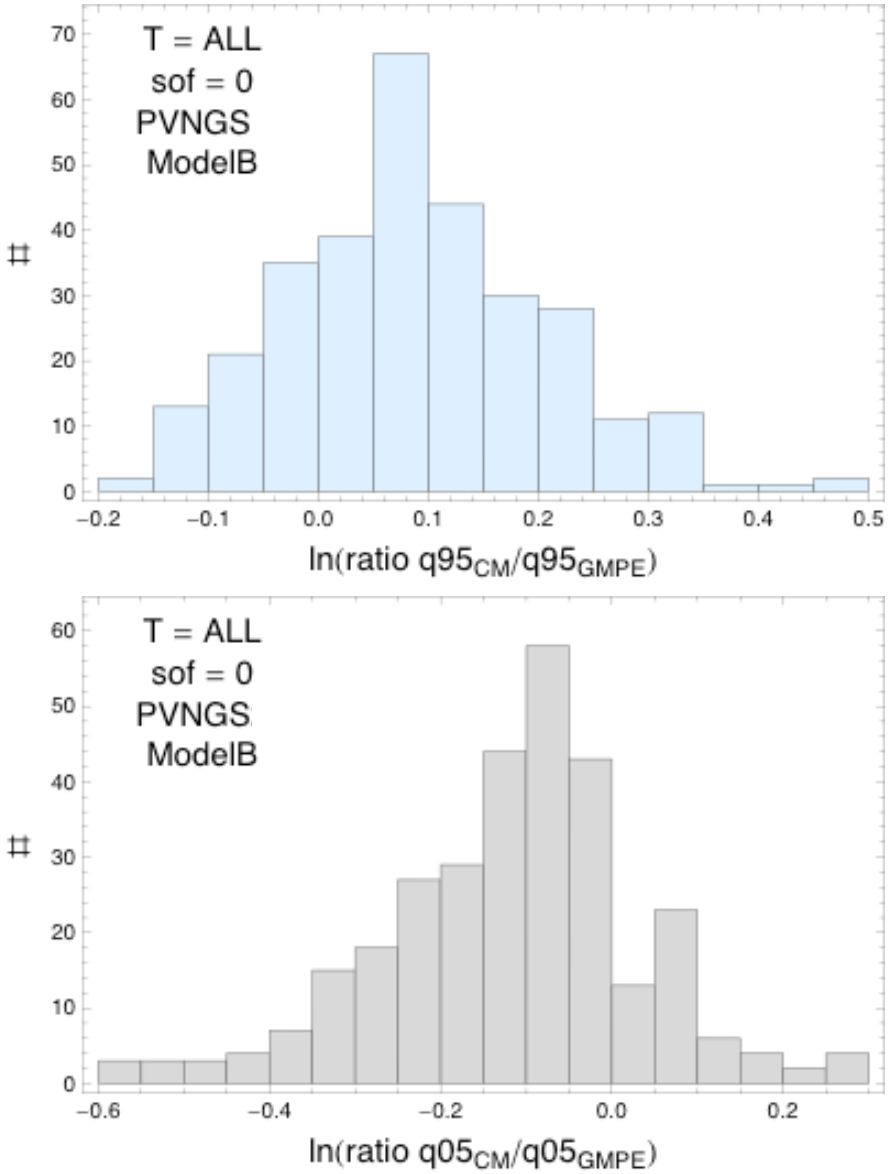

Figure 6.4.5-11: Ln ratio of the 5th and 95th fractile of the median spectral acceleration from the representative suite of common-form models to the 5th and 95th fractile of the median spectral acceleration from the GMPEs with additional epistemic uncertainty (assuming equal weight to each GMPE). Top frame is for the histogram of the ln ratios of the 95th fractile for PVNGS for strike-slip earthquakes, R_{JB}-based models. Bottom frame is for the histogram of the ln ratios of the 5_{th} fractile for PVNGS for strike-slip earthquakes, R_{JB}-based models.

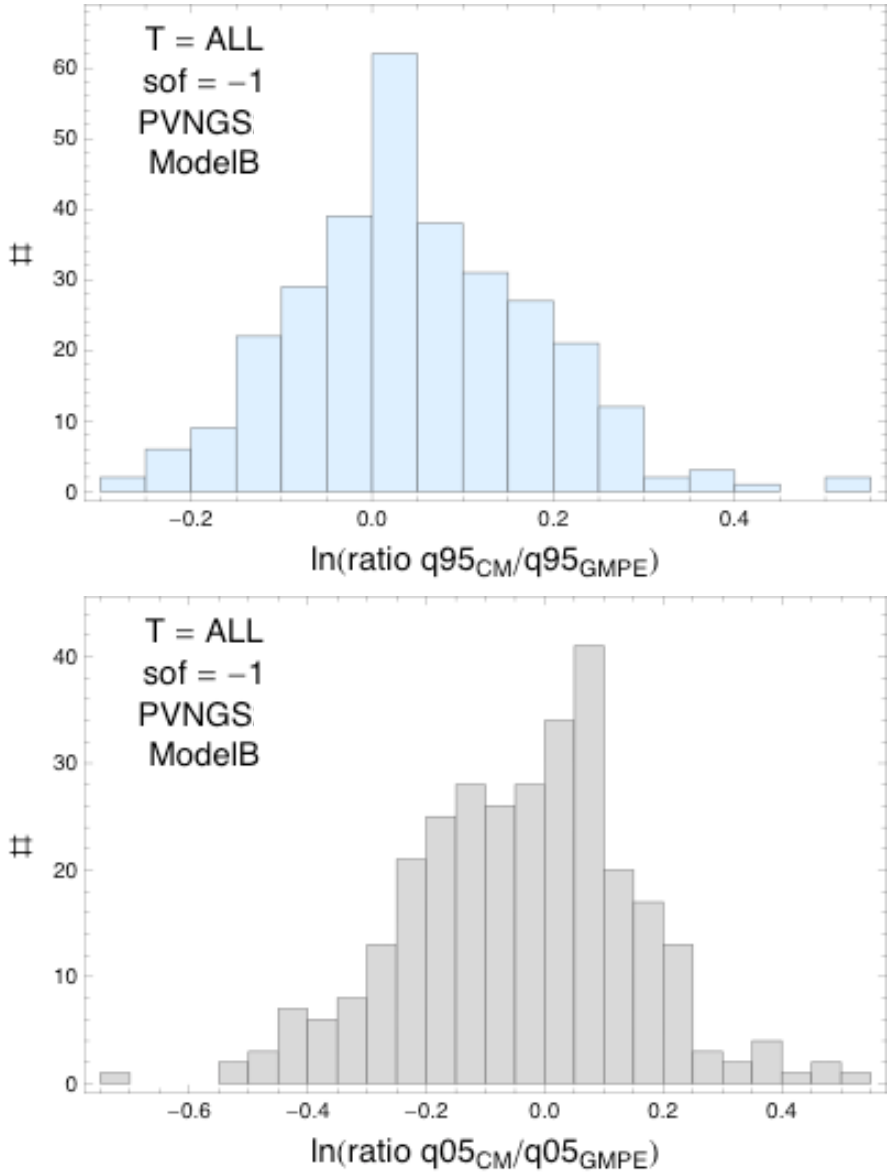

Figure 6.4.5-12: Ln ratio of the 5th and 95th fractile of the median spectral acceleration from the representative suite of common-form models to the 5th and 95th fractile of the median spectral acceleration from the GMPEs with additional epistemic uncertainty (assuming equal weight to each GMPE). Top frame is for the histogram of the ln ratios of the 95th fractile for PVNGS for normal earthquakes, R_{JB}-based models. Bottom frame is for the histogram of the ln ratios of the 5th fractile for PVNGS for normal earthquakes, R_{JB}-based models.

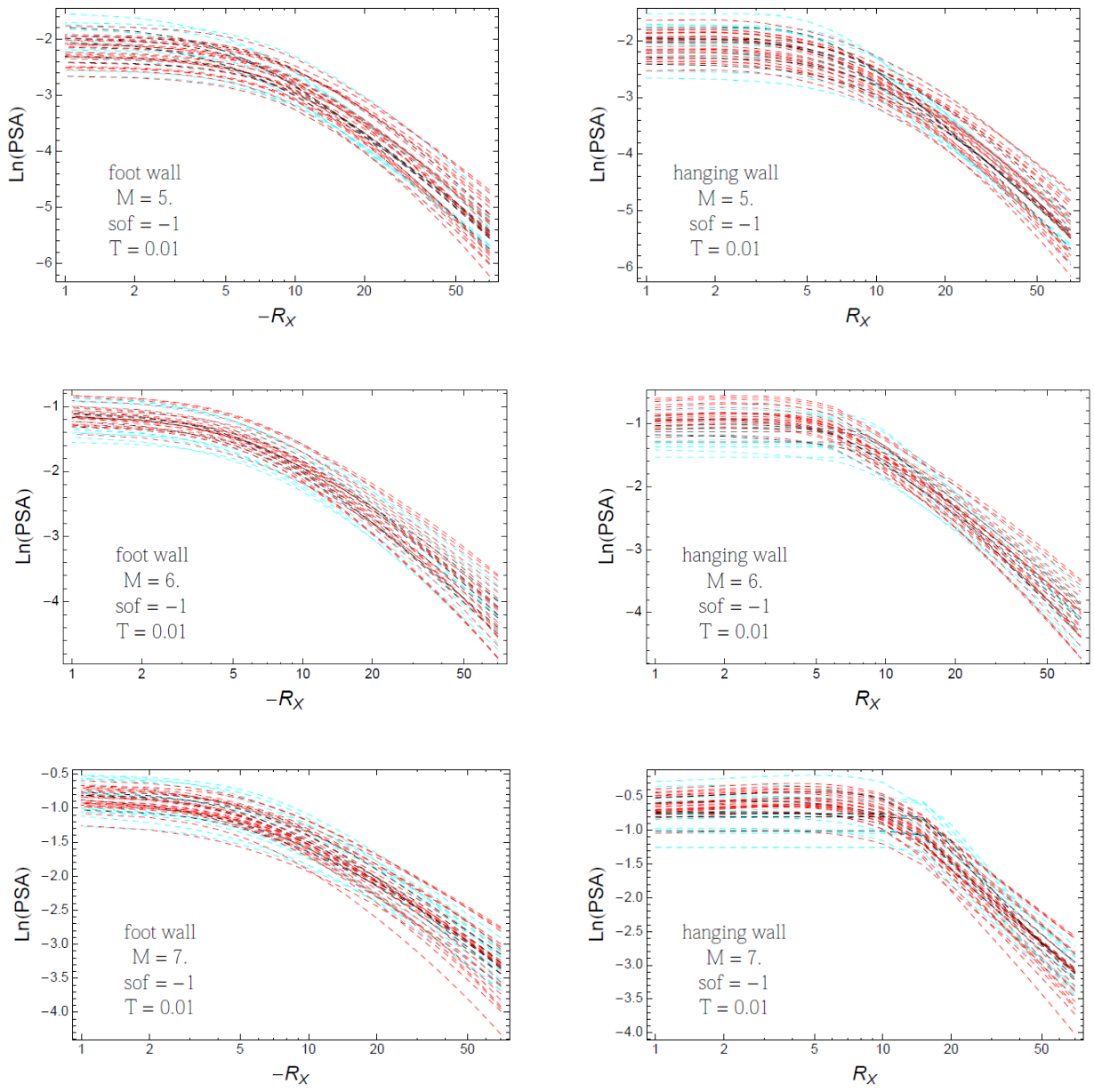

Figure 6.4.5-13: Distance scaling of the candidate GMPEs (dashed black), the candidate GMPEs with uncertainty model (dashed cyan) and the representative suite of common-form models (dashed red), for PVNGS (Model A) and a scenario with **M**5 (top), **M**6 (center) and **M**7 (bottom), normal-faulting style, and T = 0.01 sec. Left: foot-wall scaling; Right: hanging-wall scaling.

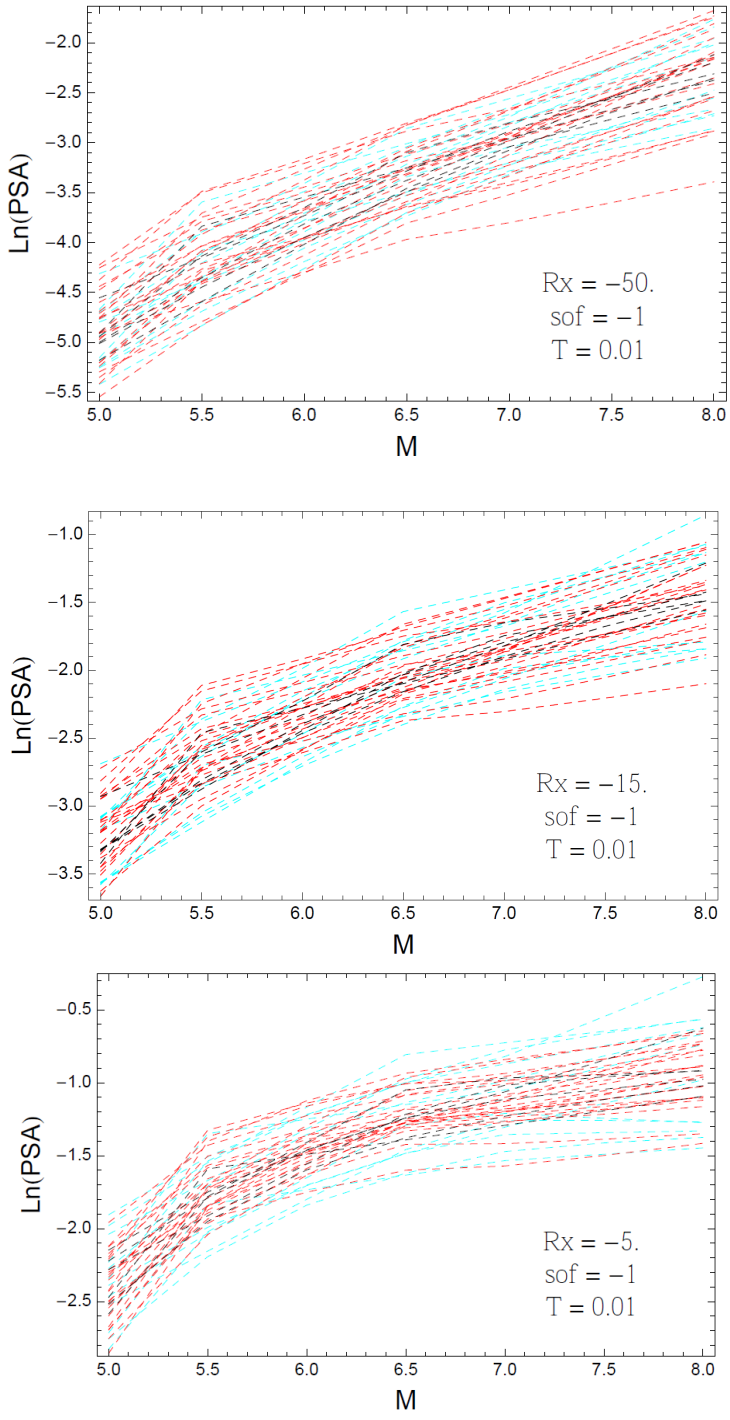

Figure 6.4.5-14: Magnitude scaling of the candidate GMPEs (dashed black), the candidate GMPEs with uncertainty model (dashed cyan) and the representative suite of common-form models (dashed red), for PVNGS (Model A) and a scenario with R_X = -50 (top), R_X = -15 (center) and R_X = -5 (bottom), normal-faulting style, and T = 0.01 sec.

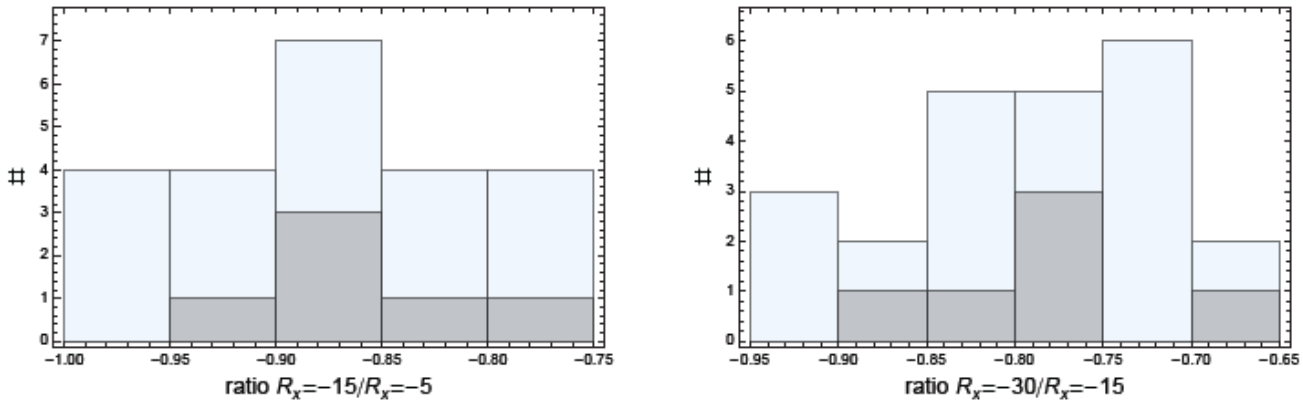

Figure 6.4.5-15: Epistemic uncertainty of distance scaling: Histogram of ratio between model predictions at different distances. Gray histogram is for GMPEs, and blue histogram is for the representative suite of common-form models. Left: Y (R_X= -15)/Y (R_X = -5); Right: Y (R_X = -30)/Y (R_X = -15); for a scenario with **M**6, NML style-of-faulting, and T = 0.01 sec, for Model A (R_{RUP} –based) at PVNGS.

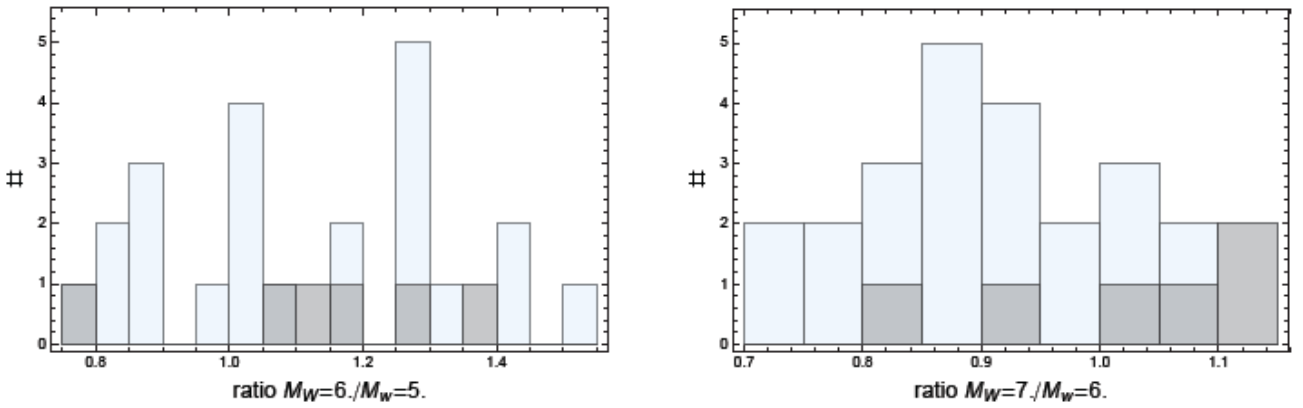

Figure 6.4.5-16: Epistemic uncertainty of magnitude scaling: Histogram of ratio between R_{RUP}-based model (PVNGS) predictions at different magnitudes. Gray histogram is for GMPEs, and blue histogram is for the representative suite of common-form models. Left: Y (**M**6)/Y (**M**5); Right: Y (**M**7)/Y (**M**6); for a scenario with R_X = 15km, NML Style-of-faulting, and T = 0.01 sec.

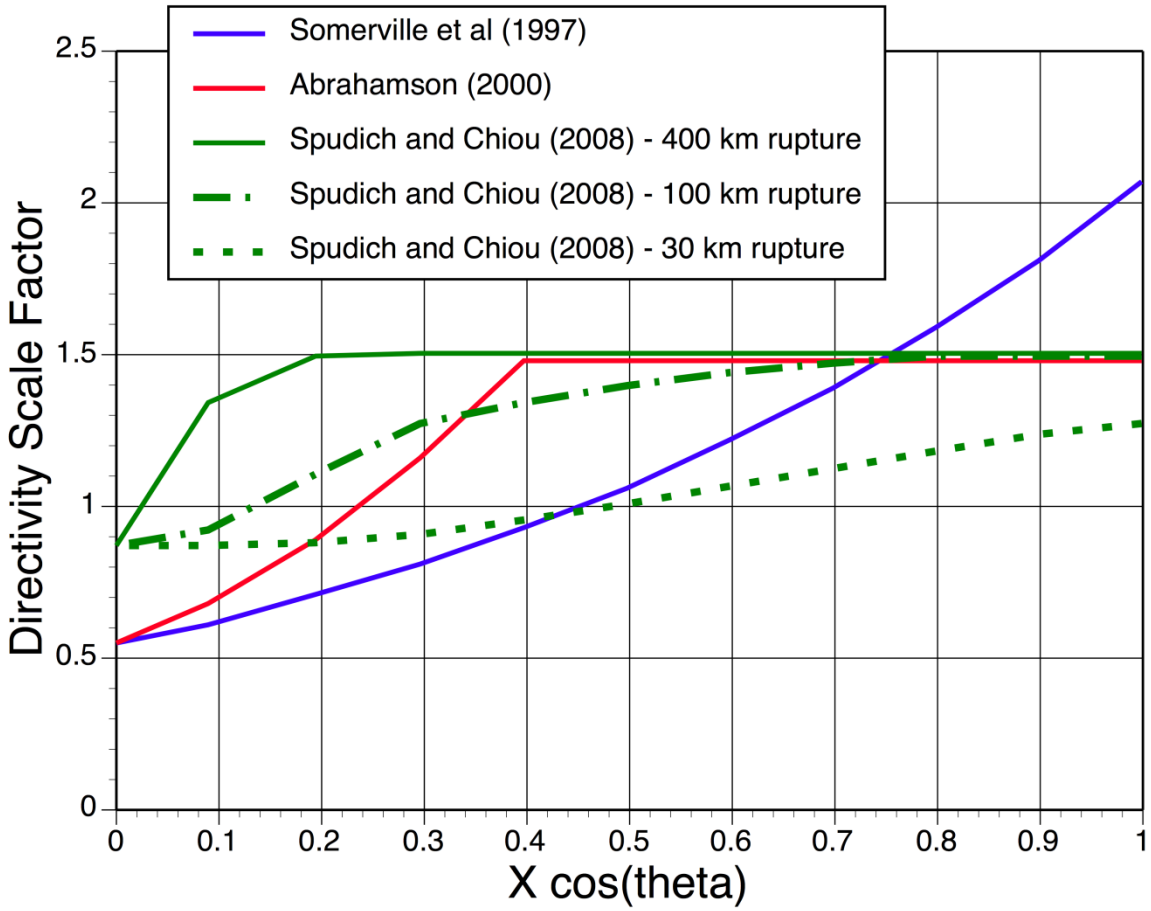

Figure 6.5.1-1: Comparison of directivity from the normalized rupture length models (Somerville et al., 1997; Abrahamson, 2000) and the un-normalized rupture length model of Spudich and Chiou (2008).

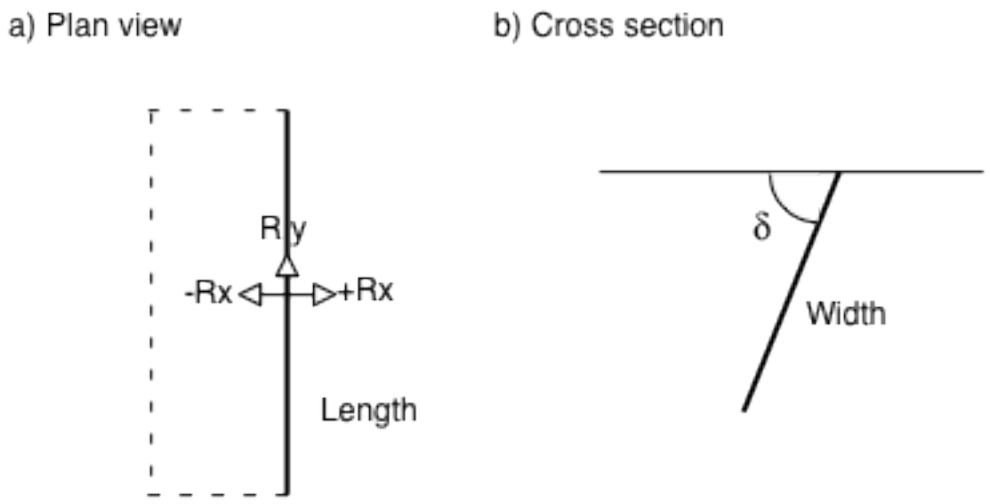

Figure 6.5.1-2: Parameters for the directivity models.

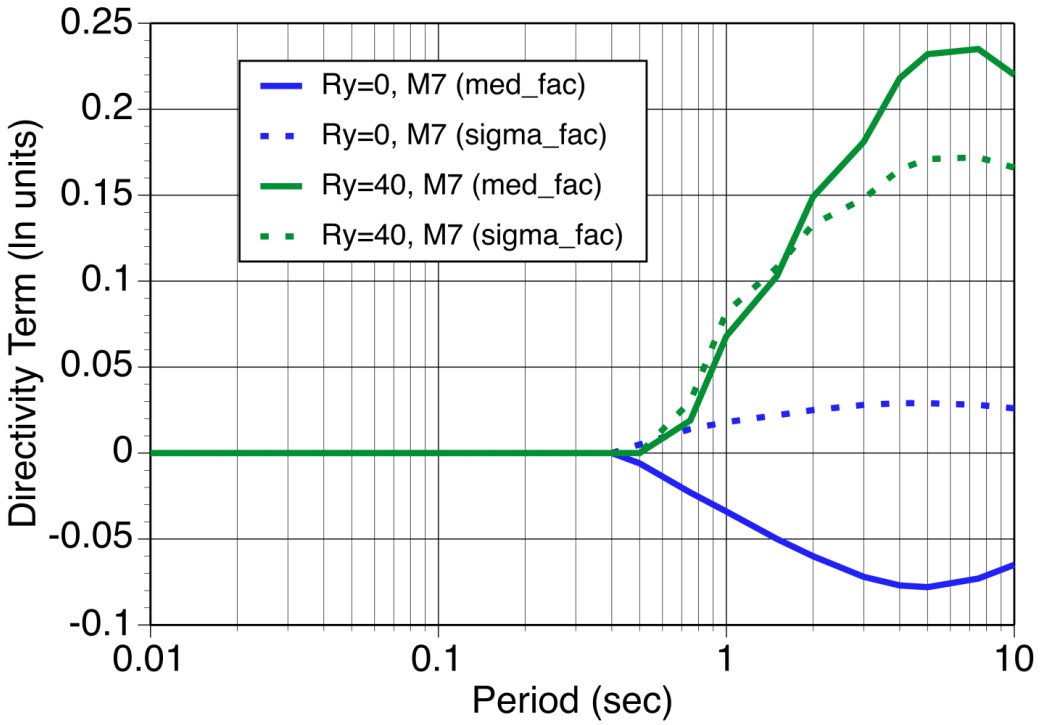

Figure 6.5.1-3: Example of the Watson-Lamprey (2015) directivity model scaling for an 80 km long strike-slip fault and a site located at R_X = 3 km. The randomization of the hypocenters is already included in the Watson-Lamprey (2015) model. The average effects on median ground motion and sigma (σ_{DIR_SS}) are shown for two sites located at the center of the rupture (R_Y = 0 km) and at the end of the rupture (R_Y = 40 km).

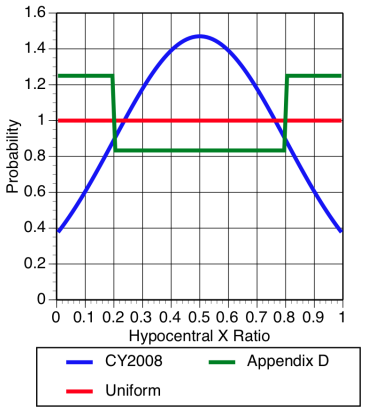

Figure 4.1 Hypocenter distributions along strike for strike-slip ruptures.

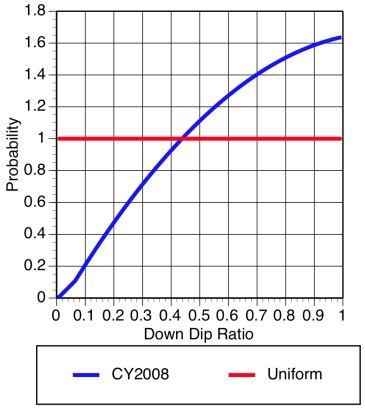

Figure 4.2 Hypocenter distributions down dip for strike-slip ruptures.

Figure 6.5.2-1: Alternative hypocenter distribution models for strike-slip earthquakes given in Watson-Lamprey (2015). The top frame gives the distribution along strike and the bottom frame gives the distribution down dip (Figures from Watson-Lamprey, 2015).

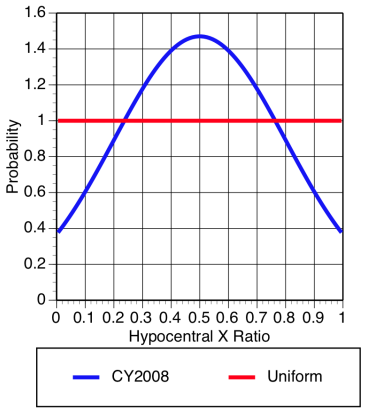

Figure 4.3 Hypocenter distributions along strike for reverse ruptures.

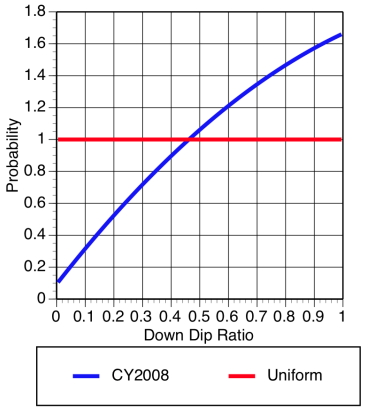

Figure 4.4 Hypocenter distributions down dip for reverse ruptures.

Figure 6.5.2-2: Alternative hypocenter distribution models for reverse earthquakes given in Watson-Lamprey (2015). The top frame gives the distribution along strike and the bottom frame gives the distribution down dip (Figures from Watson-Lamprey, 2015).

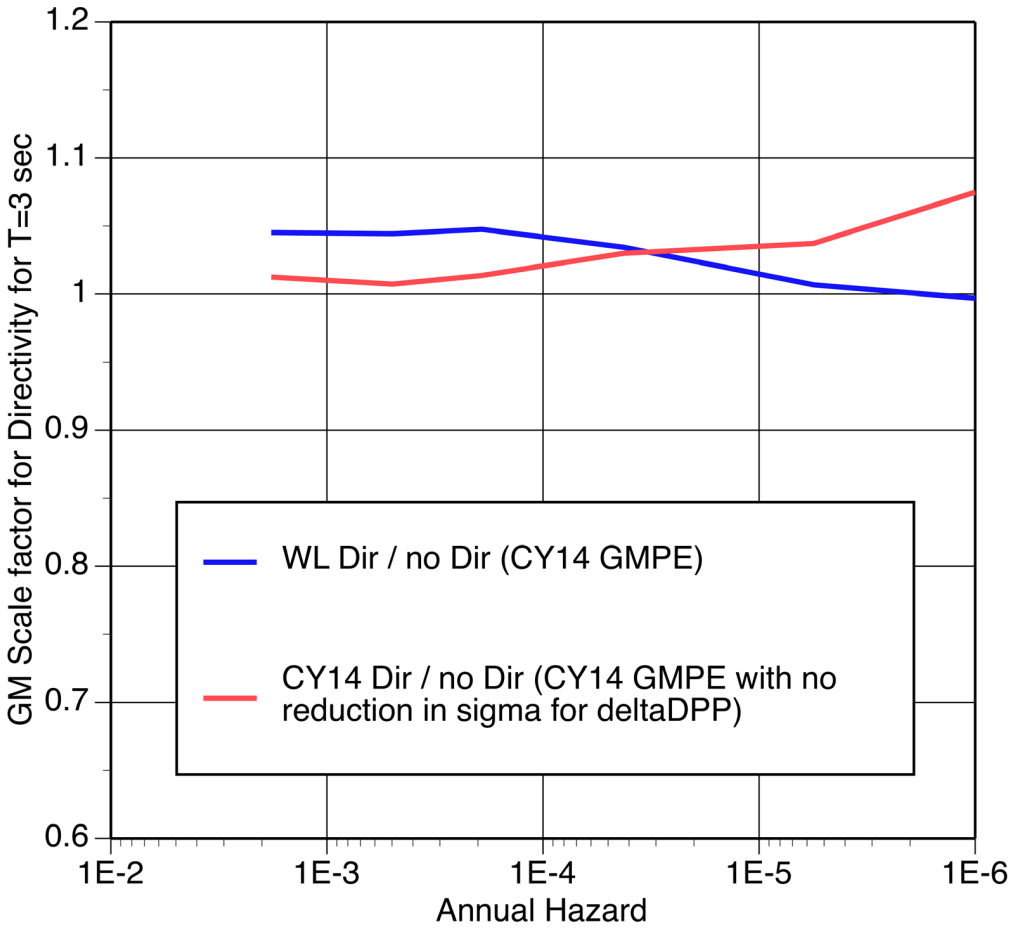

Figure 6.5.2-3: Hazard ratio for directivity effects for the Hosgri fault (using the full Hosgri SSC model in PG&E, 2015) with the CY14 GMPE for both the median and the standard deviation.

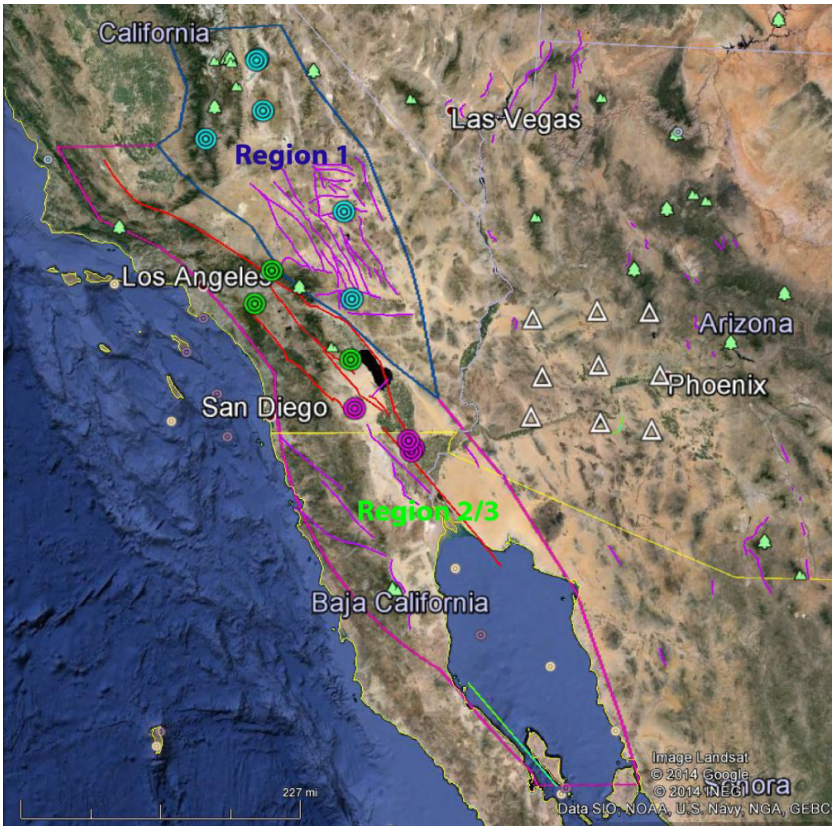

Figure 6.6.1-1: NGA-West2 earthquakes selected for the path effect analysis. Region 1 earthquakes are shown as blue circles, Region 2 earthquakes are shown as green circles, and Region 3 earthquakes are shown as purple circles. Arizona TA recording stations are shown as white triangles. Geographic extensions of Region 1 and Region 2&3 are shown as blue and purple closed polygons, respectively. Purple and red colored lines represent faults in PVNGS SSC Model (Workshop #3, Ross Hartleb, personal communication 2014).

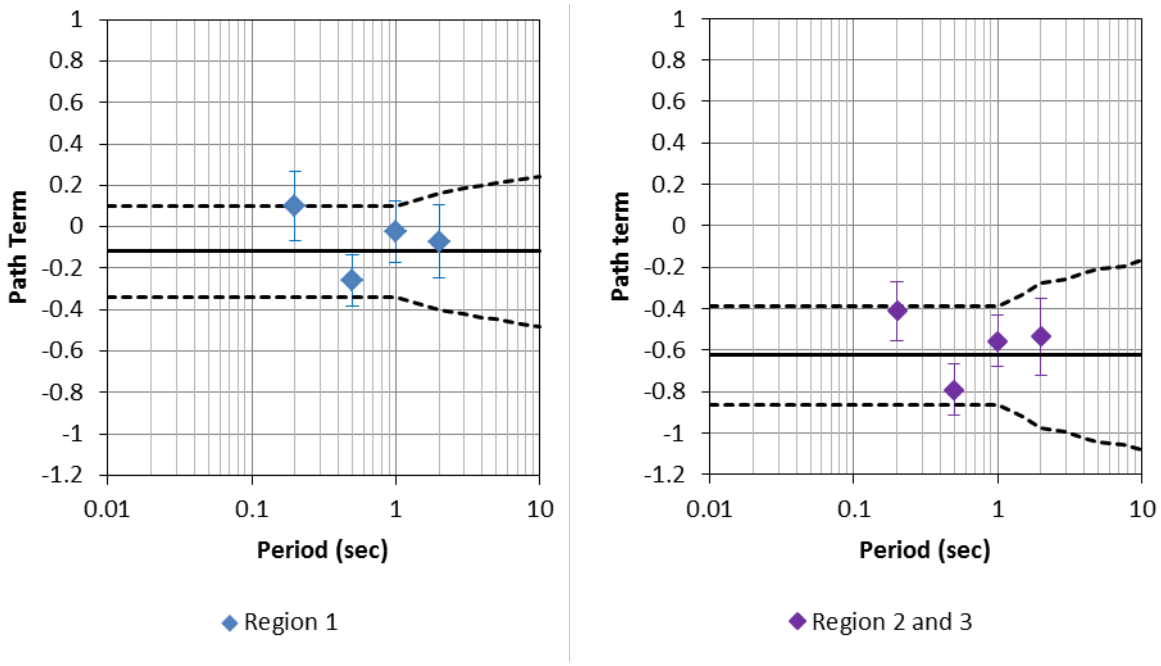

Figure 6.6.1-2: Central, high and low path terms for Regions 1 and combined Region 2&3 compared to the values used to derive them.

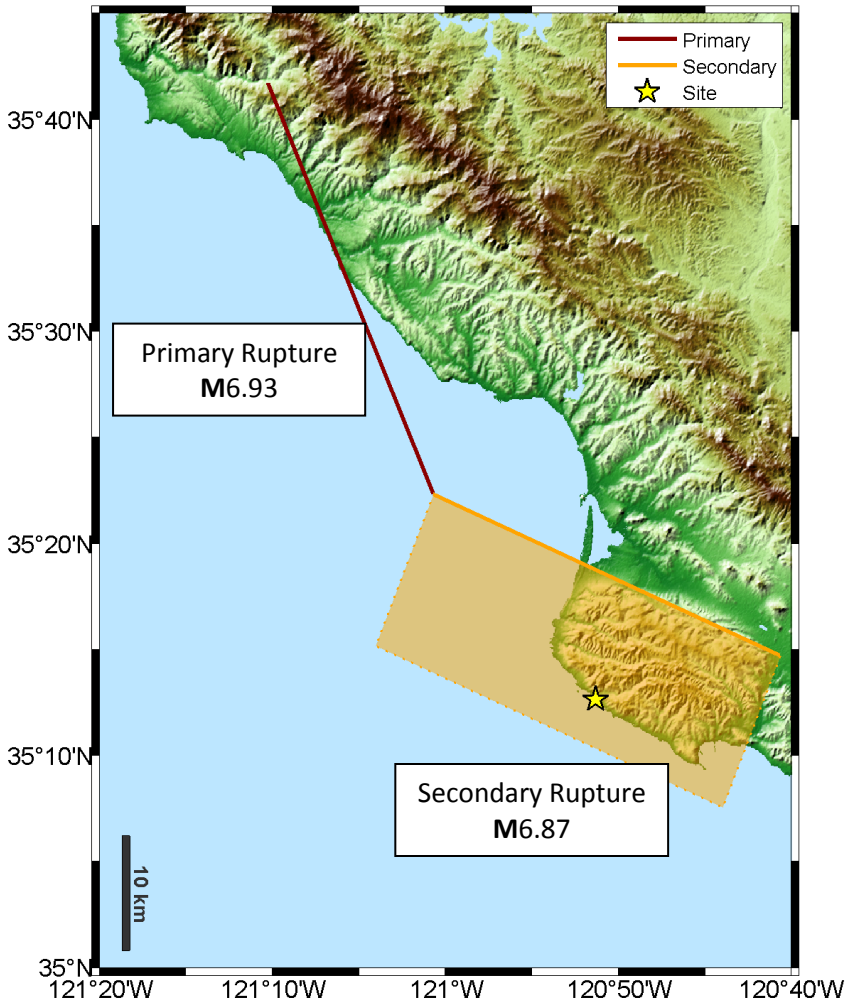

Figure 6.7.2-1: Schematic fault geometry for the Complex Scenario 1B. The yellow star represents a reference site for which to evaluate the ground-motion scaling due to the complex ruptures.

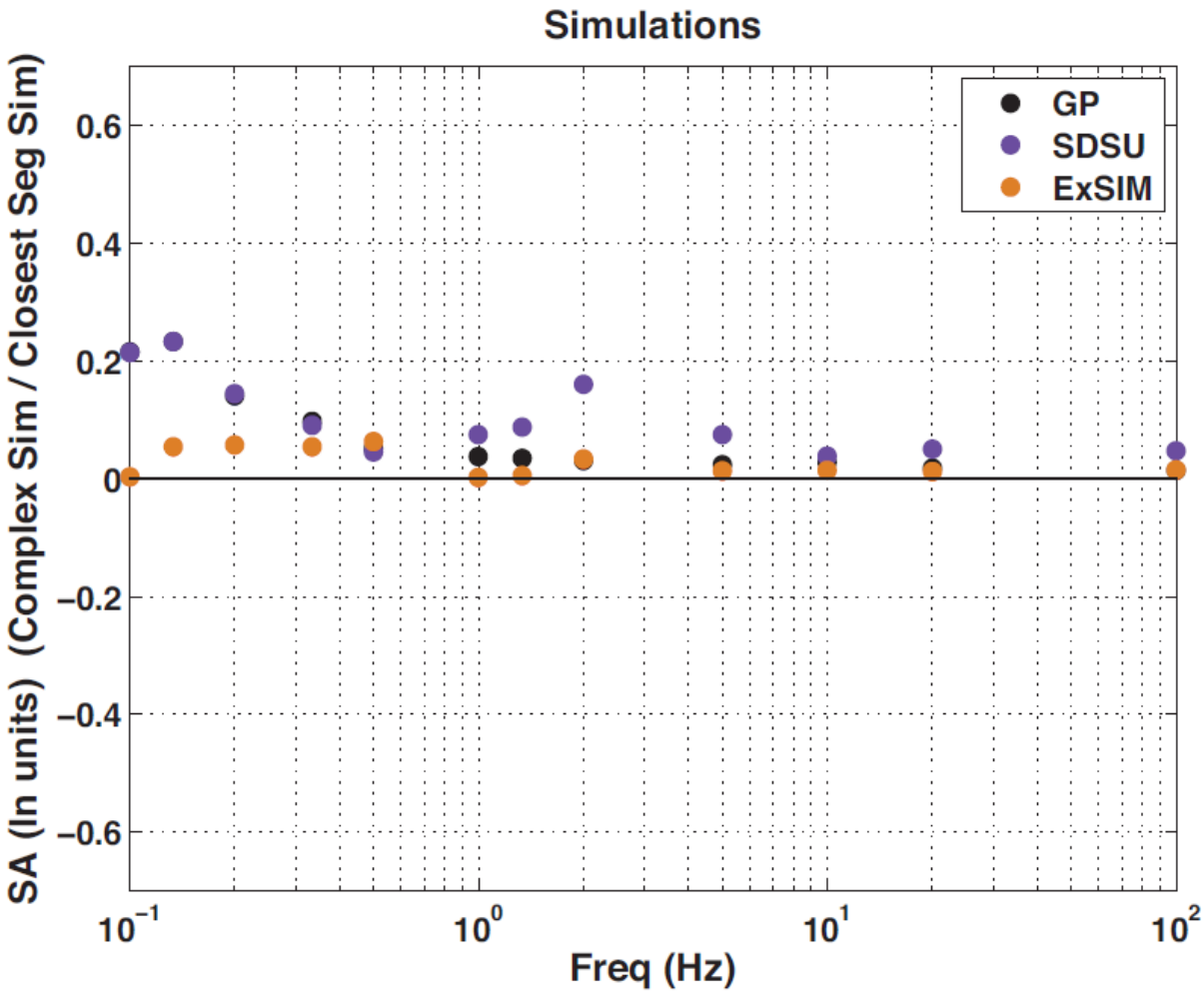

Figure 6.7.2-2: Ground-motion factors (the ratio of the response spectra from the combined rupture to the response spectra from the closest rupture) for the three simulation methods: GP (black), SDSU (violet), and EXSIM (orange).

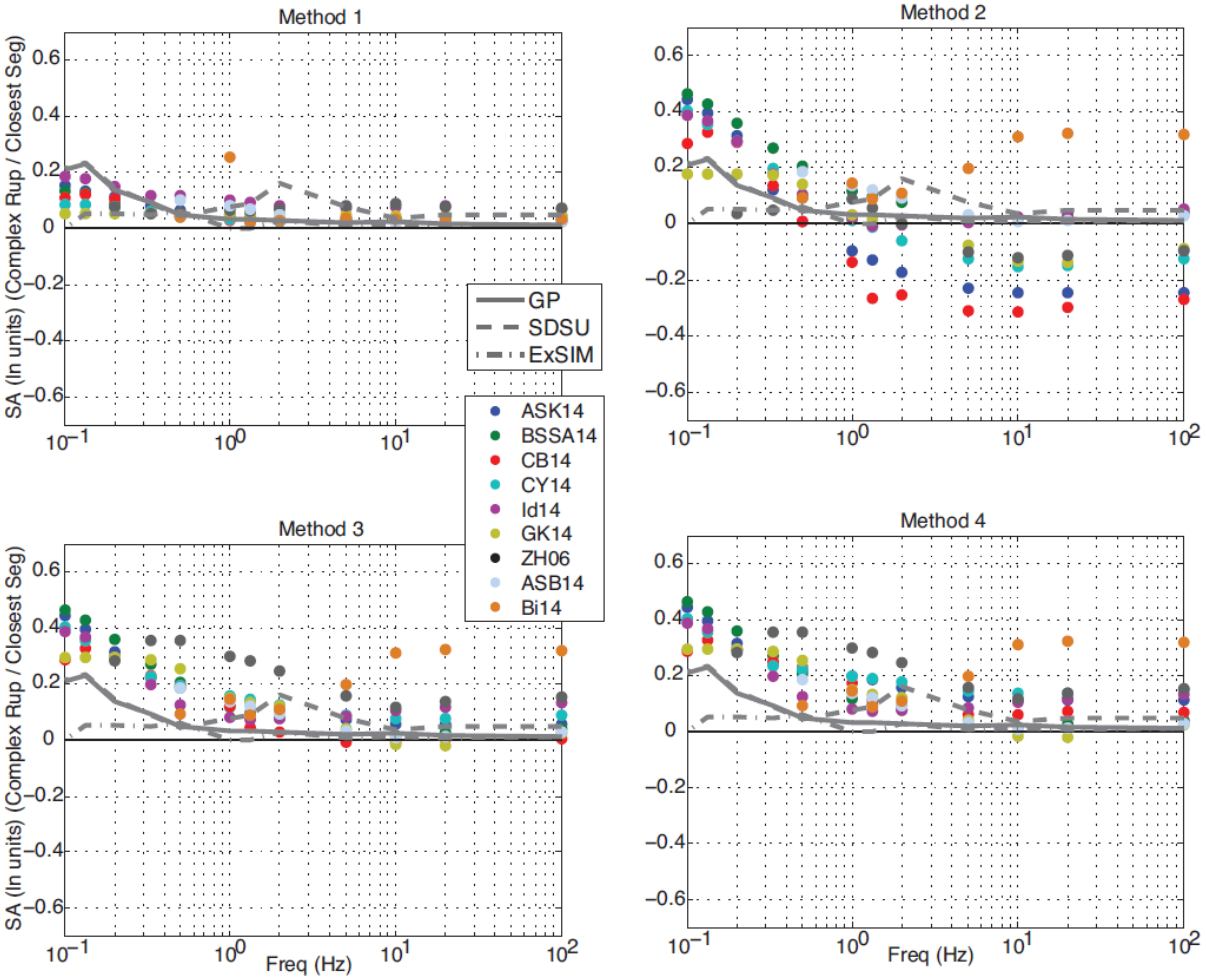

Figure 6.7.2-3: Ground-motion factors (the ratio of the response spectra from the combined rupture to the response spectra from the closest rupture) for the various approaches for computing ground motion for complex ruptures using GMPEs (colored dots), compared to the ground-motion factors for the three simulation methods (grey lines).

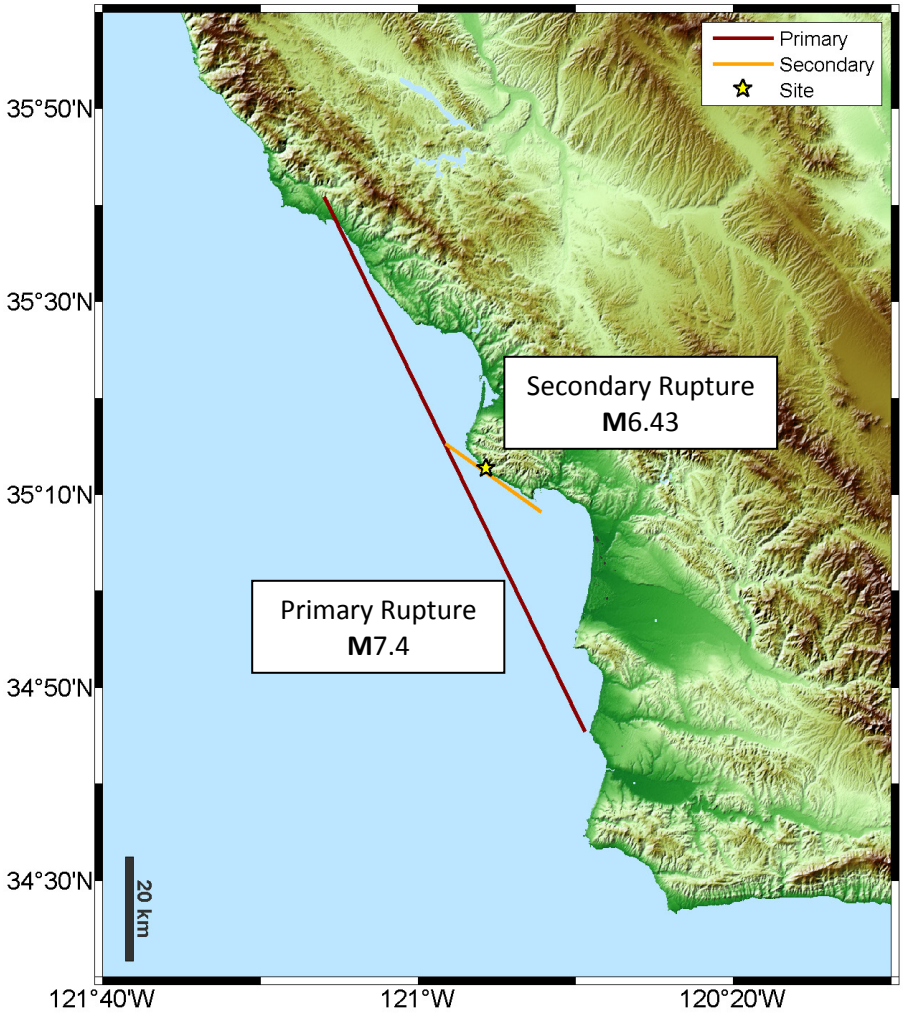

Figure 6.7.2-4: Schematic fault geometry for the Splay Scenario 1C. The yellow star represents a reference site for which to evaluate the ground-motion scaling due to the splay ruptures.

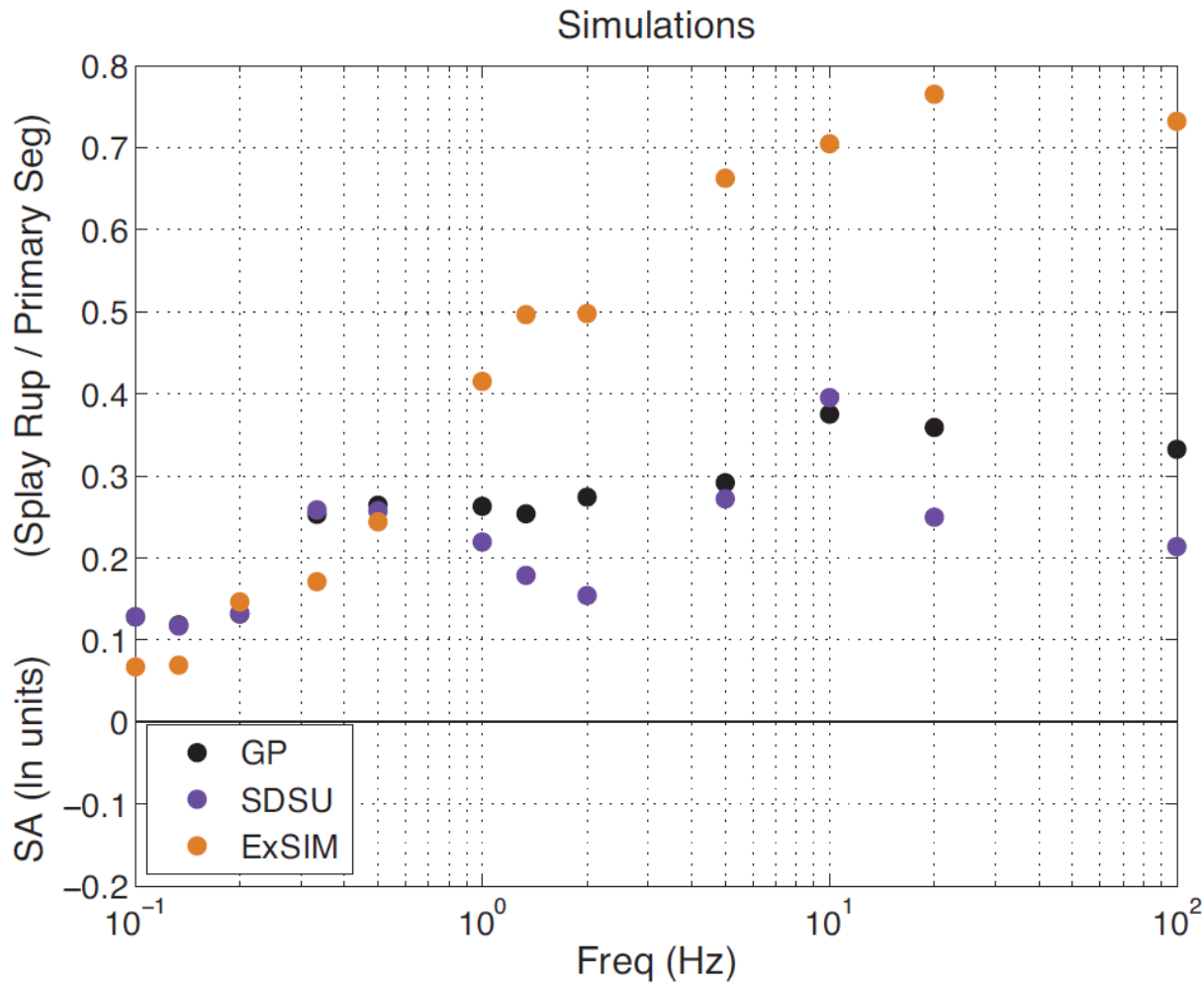

Figure 6.7.2-5: Ground-motion factors (the ratio of the response spectra from the combined rupture to the response spectra from the primary rupture) for the three simulation methods: GP (black), SDSU (violet), and EXSIM (orange).

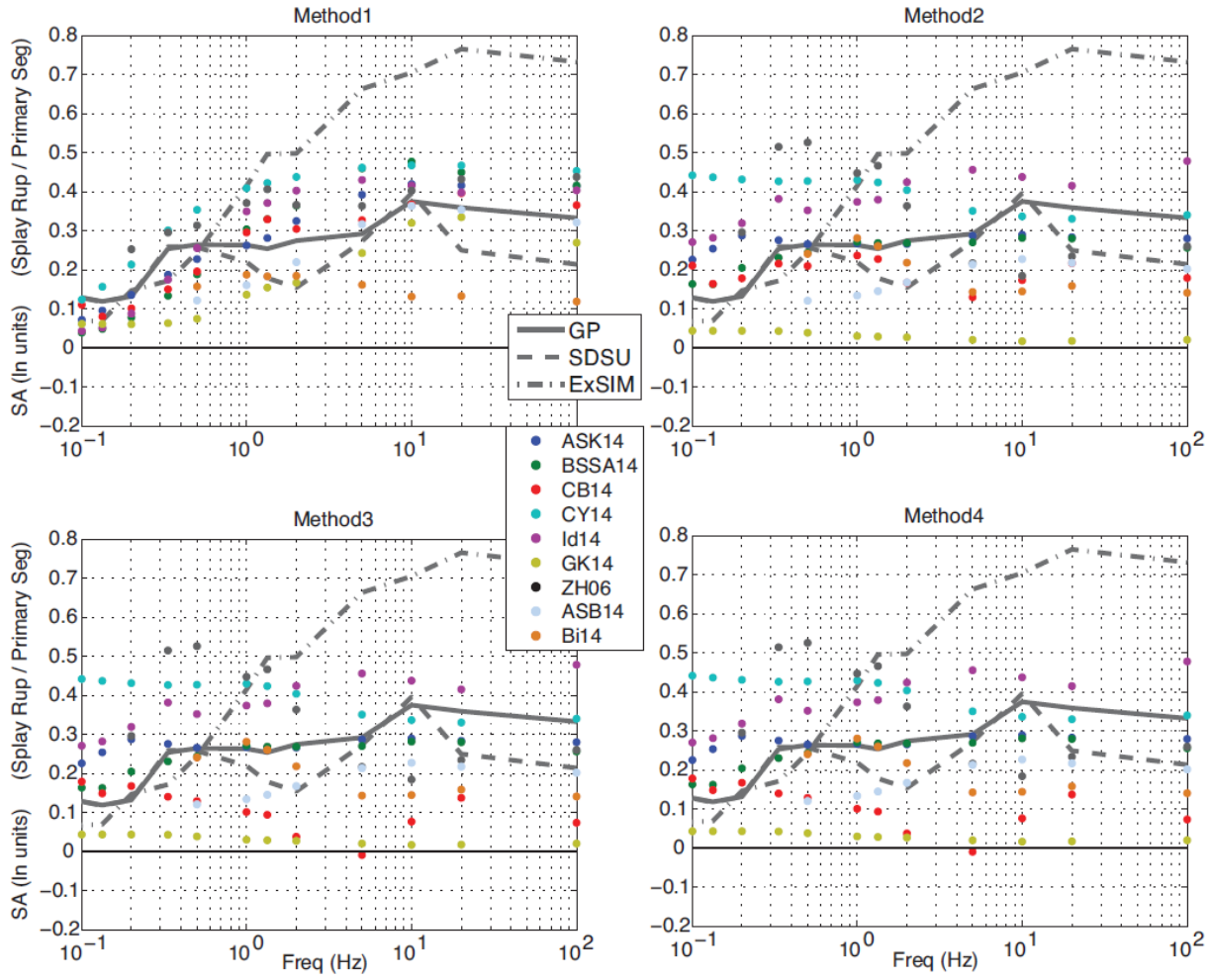

Figure 6.7.2-6: Ground-motion factors (the ratio of the response spectra from the combined rupture to the response spectra from the primary rupture) for the three simulation methods (grey lines) compared with factors from the various approaches for computing ground motion for splay ruptures using GMPEs (colored dots).

7 GMC MODELS FOR THE SIGMA: OVERVIEW AND METHODOLOGY

7.1 Introduction

This Chapter addresses the within-event standard deviation (referred to as ϕ) and between-event standard deviation (referred to as τ) models for the DCPP and PVNGS sites. Section 7.2 addresses the τ models. Sections 7.3 and 7.4 address the ϕ models for the two sites. The ϕ models for DCPP and PVNGS use the concept of partially non-ergodic seismic hazard assessment (Anderson and Brune, 1999). Single-site within-event standard deviation models (ϕ_{SS}) are developed for DCPP. For PVNGS, two alternative and mutually exclusive models are developed, i.e. a single-path for a region within-event standard deviation (ϕ_{SP-R}) model and ϕ_{SS} models. The technical bases for the selection of the weights on the logic trees for ϕ_{SS} and ϕ_{SP-R} are described in Chapters 11 and 12. The branches for ϕ_{SS} (ϕ_{SP-R}) are combined with the τ branches and re-sampled using a smaller number of branches (see Appendix P and Section 13.2) that capture the original distribution of total sigma while reducing the total number of branches for the hazard analysis. Section 7.6 describes the approach to develop a simplified logic tree for the total sigma models that captures both the within-event and between-event components of the aleatory variability. The technical bases for the selection of the weights on the logic trees for the total sigma model are discussed in Chapter 13.

The list of ϕ_{SS} and ϕ_{SP-R} models developed by the TI Team, the data subsets used to develop the models and their application are provided in Table 7.1-1.

7.1.1 Conceptual Background on Partially Non-Ergodic Sigma

The ergodic assumption implies that the variability in ground motion at a single site-source combination is the same as the variability in ground motion observed in a more global dataset (Anderson and Brune, 1999). The availability of multiple recordings at individual sites allows removing the systematic site-specific effects from the ground-motion residuals leading to a reduced aleatory variability. This reduction is more pronounced when there are multiple recordings at single sites from earthquakes in

the same region because the repeatable path effects are also removed in addition to the repeatable site effects (e.g., Lin et al., 2011; Chen and Tsai, 2002; Atkinson, 2006; Morikawa et al., 2008; Anderson and Uchiyama, 2011). To use the reduced aleatory variability requires estimating the repeatable site and path effects, and the epistemic uncertainty in these terms for site-specific applications (see Section 15.4 for more details on the application guidelines and interface with site response).The partially non-ergodic assumption has been applied in multiple studies, such as the PEGASOS Refinement Project (Rodriguez-Marek et al., 2013), the Thyspunt Nuclear Siting Project (Bommer et al., 2013; and Rodriguez-Marek et al., 2014), the BC Hydro Probabilistic Seismic Hazard Assessment Project (Addo et al., 2012), and the Hanford Probabilistic Seismic Hazard Analysis Project (Coppersmith et al., 2014).

In this report, the notation of Al-Atik et al. (2010) is followed, whereby δW_{es} represents the within-event residuals at station s from earthquake e. Having multiple recordings at site s allows estimating the site-to-site residual (also called site term) $\delta S2S_s$ and removing it from δW_{es} to obtain the single-site within-event residual, δWS_{es}, and its standard deviation, ϕ_{SS}. The $\delta S2S_s$ term represents the systematic deviation of the observed amplification at this site from the median amplification predicted by the ground-motion prediction equation (GMPE). For the ϕ_{SS} analysis, stations with a minimum of three recordings were used to obtain a reliable site term. The reason for selecting a minimum of three recordings is based on the sampling on the dataset discussed in Section 5.4. The mixed effects algorithm (Abrahamson and Youngs, 1992) was used to estimate the site-to-site residual and the single-site within-event standard deviation.

7.2 τ Models

7.2.1 Candidate τ Models

The TI Team model for τ was constructed from the τ models of four NGA-West2 models that separated the standard deviation into τ and ϕ, and the Zhao et al. (2006) model.

Other models considered for inclusion are Graizer (2014), Idriss (2014), Akkar et al. (2014a and 2014b) and Bindi et al. (2014a and 2014b). Graizer (2014) and Idriss (2014) were not included because these GMPEs did not provide separate estimates of ϕ and τ. The ϕ and τ could be derived for the Graizer (2014) and Idriss (2014) models but the TI Team decided against this approach because applying a mixed-effect regression would require changing other parts of their model that affect the median (and the authors' judgments), thus requiring the authors to re-evaluate their models.

Akkar et al. (2014a and 2014b) and Bindi et al. (2014a and 2014b) were not included because of the large percentage of small magnitude (**M** < 5) events in their databases. The Akkar dataset has about 60%

of the events from **M** < 5, as shown in Figure 5.1.3.1, and the Bindi et al. 2014a and b dataset has most of the events from **M** < 5 (Figure 5.6.4-1a).

The four NGA-West2 models all report that τ increases as magnitude decreases for **M** ≤ 5.5. Because Akkar et al. (2014a and 2014b) and Bindi et al. (2014a and 2014b) report a magnitude independent value of τ and their databases contain a large percentage of recordings from **M** < 5.5 earthquakes, the TI Team judged that their values of τ would overestimate the values appropriate for the magnitudes of interest to the hazard assessments at the two sites. Therefore, the Akkar and Bindi models were excluded for the τ model, but they were included for the median model as described in Section 6.2. Zhao et al. (2006) also report magnitude-independent values of τ, but their database is almost entirely composed of recordings from earthquakes relevant to hazard assessment, **M** ≥ 5.

The five selected candidate τ models are:

- Abrahamson et al. (2014) - ASK14;
- Boore et al. (2014) - BSSA14;
- Campbell and Bozorgnia (2014) - CB14;
- Chiou and Youngs (2014) - CY14;
- Zhao et al. (2006) – ZH06.

7.2.2 Evaluation of 10 Hz Peak in τ

Figures 7.2.2-1 and 7.2.2-2 compare the published τ values of ASK14, BSSA14, CB14, CY14, and ZH06 for **M**5.5 and **M**7 earthquakes, respectively. The BSSA14 and CB14 τ values show considerable variation with period with a pronounced narrow-band increase at periods near 0.1 sec and a dip or trough at periods near 0.4 sec. In contrast, the τ models of ASK14 and CY14 show no variation or a smooth variation, respectively, with period. The analyses conducted by both ASK14 (as shown in Abrahamson et al., 2013) and CY14 produced variations in τ with period that are similar to those shown by BSSA14 and CB14. Based on point source stochastic ground-motion simulations, CY14 concluded that the peak in τ was likely due to the variation in average site effects among different earthquakes being mapped into the event terms at this period and chose to smooth through the narrow banded variations in τ, as shown on Figures 7.2.2-1 and 7.2.2-2. The ASK14 model smoothed though the peak at 10 Hz because they did not consider the period dependence to be a systematic and repeatable feature of the ground motion, and instead developed a period-independent τ model.

Following the approach used by CY14, the TI Team investigated potential origins of the 10 Hz peak in τ through a series of point-source stochastic ground-motion simulations. The objective of the analysis was to examine how random variations in the simulation parameters that affect the source amplitude and the site amplification effects manifest themselves in the between-event and within-event variability as a function of period. The simulations were conducted using the methodology described by Boore (1983,

1986). The base model consisted of a single corner Brune source spectrum with a median stress parameter of 50 bars along with the generic rock crustal amplification function given in Table 3 of Boore and Joyner (1997), and an average kappa of 0.035 sec were used as the base model. The choice of the median stress parameter, crustal amplification function, and average kappa value are not critical to the analysis as they affect the absolute level of the simulated motions, but not the variability. To simulate random source effects (i.e. random event terms) 200 earthquakes were simulated with the stress parameter sampled from a lognormal distribution with median of 50 bars and a standard deviation of ln(stress parameter) of 0.5. A lognormal distribution was used, consistent with the distribution form for event terms in the analysis of ground-motion data, and the standard deviation of 0.5 was chosen so as to produce a typical standard deviation in between-event residuals (τ) of about 0.4. For each earthquake, ground motions were simulated at 25 sites. The individual kappa values for each site were sampled from a lognormal distribution with a median of 0.035 sec and a standard deviation in ln(kappa) of 0.3. In addition, the base case crustal amplification function for each site was perturbed using a frequency independent random amplification factor with 0 median and standard deviation of ln(amplification adjustment) of 0.4. Again, lognormal distributions were used, consistent with the typically assumed distribution for within-event residuals, and the values of standard deviation were selected to produce a standard deviation of within-event residuals (ϕ) of about 0.4 or more. The resulting ground-motion data for each period were fit with a mixed effects model (e.g. Abrahamson and Youngs, 1992), and values of τ and ϕ were computed for periods from 0.01 to 10 sec. The results, shown on Figure 7.2.2-3 show a peak in ϕ but not in τ. Other simulations with different distributions of kappa and with frequency-dependent random site adjustment factors (increasing variability with decreasing period) were performed with similar results. Doubling the median stress parameter to 100 bars produced nearly identical results, and changing the median kappa from 0.035 to 0.04 sec produced only a slight shift in the period at which the peak in ϕ occurs. It should be noted that the simulation process does not explain the dip in τ near a period of 0.4 sec observed in analyses of empirical data.

A second set of simulations was conducted to model the condition in which there is a degree of correlation in the values of kappa among the sites that record an individual earthquake. This correlation would result if there are regional kappa differences that result in individual earthquakes sampling different distributions of kappa values. The motivation for this case is that τ is the standard deviation of the between-event residuals and it can be related to differences in the source or differences in the average site effects for the data from an individual earthquake that are not accounted for by predictor variables in the regression model. For this case, the variability in kappa at the individual sites was equally partitioned into two components, and event-to-event variability in the median kappa for the 25 sites that recorded each earthquake, and a within-event variability in the kappa at each of the 25 sites. All other parameters were kept the same. The resulting standard deviations are presented in Figure 7.2.2-4 and show that the correlation between the values of kappa at the sites that record an individual earthquake results in peaks occurring in both ϕ and in τ near 0.1 sec period. These results indicate that

the peak in τ could be the result of differences in the average value of kappa at the recording sites from earthquake to earthquake.

Additional evidence that the peak in τ may be due to site effects is obtained from region-specific analysis of residuals. Figure 7.2.2-5 shows estimates of τ for two magnitude ranges using the residuals from Chiou and Youngs (2014) for California earthquakes. Two cases are shown, one in which τ is estimated using only random effects for each earthquake and one in which a random effect for each earthquake and a random effect for each recording station are both included, separating the total ϕ into ϕ_{S2S} (site-to-site) and ϕ_{SS} (single site or single station). In both analyses, only residuals for earthquakes with at least five recordings are included to provide a better estimate of τ. For the 3 < **M** < 5.5 data set, inclusion of random effects for individual stations translates the peak in τ near 0.1 sec into a peak in ϕ_{S2S} at this period. For the **M** ≥ 5.5 data, there is little difference in the estimates of τ for the two cases, although the peak in τ is much less pronounced for the California large magnitude data than it is for the analyses of the global data sets. It should be noted that for the large magnitude California data set there are very few stations that have recorded five or more earthquakes. As a result, ϕ_{S2S} is not well estimated. In the mixed effects formulation, when a particular class (i.e. recording station) has very limited data, its average effect is shifted away from the mean residual towards zero (see discussion by Abrahamson and Youngs, 1992). This can be seen in the plots of the estimated values of ϕ, where ϕ_{S2S} is much smaller than ϕ_{SS} for the large magnitude data set, while they are comparable for the small magnitude data set.

The results of the above analyses indicate that the peak in τ near a period of 0.1 sec likely results from correlations in site effects within earthquakes or within regions. For the τ models used in the SWUS GMC project (Section 7.2.4), the 10 Hz peak is removed from the τ model. To capture the effects of the 10 Hz peak, the epistemic uncertainty in the kappa and site effects for the site needs to be included in the site response studies. More details are provided in Section 15.4.

7.2.3 TI Team τ Model

The central τ branch is based on averaging the between-event variances of the five selected candidate τ models.

Because all selected candidate τ models, with the exception of ZH06, have magnitude-dependent τ, the TI Team adopted a magnitude-dependent form of the τ model. Figure 7.2.3-1 shows τ versus magnitude for the five selected candidate τ models at a period of 1 sec as well their average which has multiple magnitude breakpoints resulting from the selected candidate τ models all having different magnitude breakpoints. For simplicity of implementation, the TI Team's central τ model is anchored to

the average of the five selected candidate τ models at **M**5.5 and **M**7.0, and has only one breakpoint at **M**7 as shown in Figure 7.2.3-1. The model has the following form:

$$\tau(M,T) = \begin{cases} \tau_1(T) + \frac{(M-5)}{2} * \left(\tau_2(T) - \tau_1(T)\right) & for\ M < 7.0 \\ \tau_2(T) & for\ M \geq 7.0 \end{cases} \quad \text{(Eq. 7.2.3-1)}$$

The next issue is the degree to which period dependence is incorporated into the τ_1 and τ_2 terms. As described in Section 7.2.2, the peak in τ near 0.1 sec period is judged by the TI Team to be attributed to differences in average site effects (e.g. kappa) not presently accounted for in standard GMPEs. Because site-specific site effects and their uncertainties will be included in the downstream application of the hazard results, those effects should not be included in the characterization of ground motions for the reference rock condition. Therefore, the TI Team judged that the peak in τ should be removed through smoothing.

No physical mechanism has been suggested for the observed trough in τ near a period of 0.4 sec seen in Figure 7.2.2-1. For the subset of California earthquakes shown on Figure 7.2.2-5, the trough at 0.4 sec is weaker than seen in global data. The TI Team decided to smooth through the trough in τ near 0.4 sec period in the same manner as the peak near 0.1 sec.

Figures 7.2.3-2 and 7.2.3-3 show the average τ versus period for the five selected candidate τ models at the anchoring magnitudes of **M**5.5 and **M**7.0, respectively. The mean τ values shown on these figures are nearly constant with the peak at T = 0.1 sec and with the trough at T = 0.4 sec from the BSSA14 and CB14 models. Therefore, the TI Team adopted a period-independent model for τ. The central values of τ_1 and τ_2 are computed by averaging the between-event variances of the five candidate τ models over the period range of 0.01 to 10 sec. In this approach, the unsmoothed values of BSSA14, CB14, and ZH06 can be combined directly with the smoothed values of ASK14 and CY14, as the averaging across periods is a linear process. The resulting central model for τ is shown on Figures 7.2.3-2 and 7.2.3-3 for **M**5.5 and **M**7.0, respectively.

7.2.4 Epistemic Uncertainty of τ

The standard deviation of τ^2 (σ_{τ^2}) consists of two components: within-model ($\sigma_{\tau_W^2}$) and between-model variability ($\sigma_{\tau_B^2}$) as shown below:

$$\sigma_{\tau^2} = \sqrt{\left(\sigma_{\tau_W^2}\right)^2 + \left(\sigma_{\tau_B^2}\right)^2} \quad \text{(Eq. 7.2.4-1)}$$

The within-model variability, calculated as part of the regressions conducted for the CY14 model, represents the statistical uncertainty in their τ^2 estimates. The between-model variability is the

standard deviation of τ^2 for the five selected candidate τ models. The within-model variability from CY14 reflects the size of the dataset in terms of number of events. The other four candidate τ models are from GMPEs based on datasets with comparable size to the CY14 dataset. Therefore, the TI Team judged that the CY14 within-model variability was representative of the within-model variability for the other candidate τ models. The between-model, within-model, and total variability are shown in Figures 7.2.4-1, 7.2.4-2, and 7.2.4-3, respectively, for **M**5.5 and 7.0. The standard deviation of τ^2 was fitted to a constant, period-independent function. The period-independent constant estimate is similar to the central model.

The high and low τ branches of the logic tree are computed assuming that τ^2 follows a scaled Chi-square distribution with a standard deviation (σ_{τ^2}) and represent the 5th and 95th percentiles of the distribution (see Appendix P for more details). The high and low τ branches are calculated as:

$$\tau_{\text{High}} = \sqrt{c\,\chi^{-1}_{2,k}(0.95)}\,; \qquad \tau_{\text{Low}} = \sqrt{c\,\chi^{-1}_{2,k}(0.05)} \qquad \text{(Eq. 7.2.4-2a and b)}$$

where the scaling parameter $c = \frac{V(\sigma_\tau^2)}{2E(\sigma_\tau^2)}$, the number of degrees of freedom $k = \frac{[E(\sigma_\tau^2)]^2}{V(\sigma_\tau^2)}$, with *E*() and *V*() denoting expectation and variance, respectively, and $\chi^{-1}_{2,k}(x)$ is the inverse of the Chi-square distribution with k degrees of freedom.

In summary, the τ model presented in Equation 7.2.3-1 has parameters τ_1 and τ_2 shown in Table 7.2.4-1 for the central, high and low branches of the logic tree shown in Figure 10-1 in Chapter 10. A comparison of the central, high and low proposed τ branches to the selected candidate τ models is shown in Figure 7.2.4-4 for magnitude **M**5.5 and 7.0. The magnitude dependence of the τ model, as discussed in Section 7.2.3 and Figure 7.2.3-1, is shown in Figure 7.2.4-5 for the central, high, and low branches. The low branch has magnitude-independent τ while the central and high branches have decreasing τ with magnitude between magnitudes 5.0 and 7.0 and a constant τ for magnitude greater than 7.0.

7.2.5 Comparisons to Other τ Models

Figure 7.2.5-1 compares the proposed TI Team τ model to the Akkar et al. (2014a and 2014b) and Bindi et al. (2014a and 2014b) τ models for magnitude **M**5.5 and 7.0. Despite the fact that the τ values from these two GMPEs were not used in deriving the SWUS TI Team τ model, they mostly fall within the uncertainty range.

7.3 ϕ_{SS} Models

7.3.1 Estimation of ϕ_{SS} from Residuals

To estimate ϕ_{SS} requires within-event site corrected residuals. To have enough data to estimate the site terms, the site terms are estimated using the full data set that includes both small and large magnitudes. The ϕ_{SS} is then computed for the sub-set of the within-event site corrected residuals in the desired magnitude and distance range.

The epistemic uncertainty in ϕ_{SS} is estimated using the site-to-site variability of ϕ_{SS} across all sites in the data set. The single-site within-event standard deviation at an individual site is denoted as $\phi_{SS,S}$. The standard deviation of $\phi_{SS,S}$ is denoted SD($\phi_{SS,S}$) and is estimated using the global dataset with magnitude greater than 4.0. The expanded magnitude and distance range of the dataset is used in order to ensure enough recordings for this exercise. The empirical ϕ_{SS} estimates and their standard deviation are, however, biased due to sampling error that decreases as the number of recordings per site increases.

To quantify the sampling error, a statistical exercise was undertaken whereby a large set of single-site within-event residuals was simulated per station for the same number of stations as in the global dataset with all stations having the same $\phi_{SS,S}$ values. A normal distribution was used for the simulations. The $\phi_{SS,S}$ values were then computed at each station using multiple realizations of the dataset and the CV of ϕ_{SS} was calculated for each realization. Figure 7.3.1-1 compares the CV values for the synthetic data set with a population CV of 0 and the CV of ϕ_{SS} from the global dataset (results for $GLOBAL_{PHISS\text{-}ASK14}$ shown for simplicity) with different minimum numbers of recordings per site for PGA and periods of 0.1 and 1.0 sec. The curve in Figure 7.3.1-1 shows the dependence of the SD($\phi_{SS,S}$) bias on the sample sizes and indicates that, for large numbers of recordings per site, the bias decreases and approaches zero. The difference between the blue curve and the CV of $\phi_{SS,S}$ estimated using the empirical data represents the true SD($\phi_{SS,S}$).

The statistical exercise was then repeated with different CV values for the population (0.05, 0.10, and 0.15) assigned for the simulations and the resulting CV for different minimum number of recordings per station are shown in Figure 7.3.1-2. Based on Figure 7.3.1-2, the CV of $\phi_{SS,S}$ for the empirical data fall between the curves for a CV value population of 0.05 and 0.15. Based on this comparison, the TI Team selected a CV value of 0.12 as being representative.

The method for computing the 5th and 95th fractiles for the ϕ_{SS} values based on the CV value is described in Appendix P.

To evaluate the hazard sensitivity to the CV value, a simplified hazard analysis is used considering just a single magnitude (**M**7) at a single distance (15 km) with a recurrence interval of 500 years. First, the hazard sensitivity to the value of ϕ_{SS} is shown in Figure 7.3.1-3. At low hazard levels, the hazard is sensitive to the standard deviation of the ground motion. Next, the mean hazard is computed for different values of the CV of ϕ_{SS}. Plots of the mean hazard for CV values of 0.09, 0.12, and 0.15 are shown in Figure 7.3.1-4. There is very little sensitivity of the mean hazard to the CV value. As there is little sensitivity of the mean hazard to the CV value, more complicated models for the CV, such as magnitude-dependent models, are not evaluated.

7.3.2 TI Team Global ϕ_{SS} Models ($\phi_{SS\text{-}GLOBAL\text{-}R50}$ and $\phi_{SS\text{-}GLOBAL\text{-}LD}$ Models)

7.3.2.1 $\phi_{SS\text{-}GLOBAL\text{-}R50}$ Model

As described in Section 5.4.1, single-site within-event residuals with magnitude greater than or equal to 5.0 and distance less than 50 km were used to evaluate ϕ_{SS} for a global dataset consisting of the four NGA-West2 data sets (datasets for ASK14, BSSA14, CB14 and CY14), each supplemented by the Taiwanese data from Lin et al. (2011). The magnitude and distance ranges used to derive the $\phi_{SS-GLOBAL-R50}$ model were chosen to be applicable to the shorter distance ranges important for both DCPP and PVNGS, yet broad enough to have sufficient data. Other data sets were not available at the time of this project, including the Japanese data (Dawood et al., 2014) used to derive the ϕ_{SS} model for the PEGASOS Refinement Project (Rodriguez-Marek et al., 2013). Existing ϕ_{SS} models, such that the PEGASOS Refinement Project ϕ_{SS} models, were not directly used as candidate models in developing the SWUS $\phi_{SS-GLOBAL-R50}$ model because the NGA-West2 datasets is richer in the magnitude and distance range on interest than the Japanese data of Dawood et al. (2014). Rather than using the Japanese data directly, the TI Team was informed by the PEGASOS Refinement ϕ_{SS} models by comparing them with their ϕ_{SS} models.

The magnitude dependence of the ϕ_{SS} from global data was evaluated by Linda Al Atik for Workshop #3 (see also Appendix K, Section K.1). The global data for ϕ_{SS} do not show a strong magnitude dependence. Example plots showing the global ϕ_{SS} values binned by magnitude are shown in Figure 7.3.2-1 for five available spectral periods (PGA, 0.1, 0.5, 1.0 and 3.0 sec). The TI Team visually inspected the magnitude-binned ϕ_{SS} for the five available periods and found that there was not a strong systematic magnitude

dependence seen consistently across all periods. Therefore, the TI Team judged that a magnitude-independent form for the $\phi_{SS-GLOBAL-R50}$ model is appropriate.

The ϕ_{SS} values, computed for the four sub sets ($GLOBAL_{PHISS\text{-}ASK14}$, $GLOBAL_{PHISS\text{-}BSSA14}$, $GLOBAL_{PHISS\text{-}CY14}$ and $GLOBAL_{PHISS\text{-}CB14}$) were averaged at each period (see Figure 7.3.2-2). A smooth model was developed by fitting the averaged ϕ_{SS} values with a constant function of period (show by the solid line in Figure 7.3.2-2).

The high and low $\phi_{SS-GLOBAL-R50}$ braches are computed using the method described in Appendix P, with the CV (ϕ_{SS}) = 0.12. The resulting central, high, and low $\phi_{SS-GLOBAL-R50}$ branches are shown in Figure 7.3.2-3 and are compared to the ϕ_{SS} values derived for the four sets of within-event site-corrected residuals based on the NGA-West2 GMPEs. The model range encompasses the full range of the ϕ_{SS} values from the four sub sets for all periods. The tabulated values for the $\phi_{SS-GLOBAL-R50}$ model are listed in Table 7.3.2-1.

7.3.2.2 $\phi_{SS\text{-}GLOBAL\text{-}LD}$ Model

As discussed in Section 4.2.3, the distant, large magnitude sources in California and Mexico (Regions 1, 2 and 3 as defined in Section 4.2) can contribute significantly to the low-frequency hazard at PVNGS.

The deaggregation from the previous studies showed the controlling sources were magnitude **M**7 to **M**8.5 and distances of 200 to 300 km. This Section describes the development of the TI Team models for the ϕ_{SS} for sources at long distances ($\phi_{SS-GLOBAL-LD}$ model, where LD indicates long distance).

The datasets used to develop the $\phi_{SS-GLOBAL-LD}$ model are described in Section 5.4.4. There are sparse data from large magnitudes at these distances (see Figure 5.4.4-1). To have enough data to estimate the ϕ_{SS}, the magnitude and distance ranges were broadened to **M** > 5.5 and distances between 200 and 400 km. There are no Taiwanese data in this magnitude and distance range. For the NGA-West2 models, three of the models have event terms and within-event residuals applicable to this distance range, but CB14 does not because they used a maximum distance of 80 km in their regressions for the event terms, and then applied an additional distance scaling term for distances greater than 80 km. Because the event terms for CB14 were only for the shorter distance range, they may not be applicable to 200 to 400 km distance range, and the TI Team decided not to extrapolate the event terms. The remaining datasets are relatively small, consisting primarily of a few California and Japanese earthquakes.

The single-site within-event residuals from the three subsets (NGA-W2$_{LD\text{-}PHISS\text{-}ASK14}$, NGA-W2$_{LD\text{-}PHISS\text{-}BSSA14}$, and NGA-W2$_{LD\text{-}PHISS\text{-}CY14}$) were used to estimate ϕ_{SS} . The average of the ϕ_{SS} values from only three sets of NGA-West2 residuals were used to develop the ϕ_{SS} models. Note that the single-site within-event residuals were calculated using the entire datasets (no magnitude and distance restrictions) as previously mentioned.

The magnitude dependence was evaluated by Linda Al Atik for Workshop #3 (see also Appendix K, Section K.1) and found to not have a strong magnitude dependence. Example plots showing the ϕ_{SS} values binned by magnitude are shown in Figure 7.3.2-4a and b for eight spectral periods (PGA, 0.05, 0.1, and 0.2 sec in Figure 7.3.2-4a; 0.5, 1.0, 2.0, and 5.0 sec in Figure 7.3.2-4b). Large error bars in ϕ_{SS} binned by magnitude are found, due to the relatively small datasets with **M** ≥ 5.5 and 200 ≤ R_{rup} < 400km.

Because the hazard from the sources in Regions 1, 2 and 3 is dominated by large magnitude earthquakes and because no significant magnitude-dependence in ϕ_{SS} was observed in the distance range of 200 to 400 km, a magnitude-independent form for the $\phi_{SS-GLOBAL-LD}$ model was selected by the TI Team.

The average ϕ_{SS} values were smoothed over period smoothed to preserve the general observed trend of the data as shown in Figure 7.3.2-5. The data show a decreasing trend of ϕ_{SS} at the long periods for all three datasets. The TI Team does not have an explanation of this trend, but it is robust in the empirical data. The epistemic uncertainty given by the 5th and 95th percentile was estimated using the method described in Appendix P with a CV(ϕ_{SS}) of 0.12 (Section 7.3.1). Figure 7.3.2-5 also shows the central, high, and low ϕ_{SS} models compared to the ϕ_{SS} values used to derive the central model. The model range encompasses the full range of the ϕ_{SS} values from the three sub sets for all periods. The tabulated values for the $\phi_{SS-GLOBAL-LD}$ model are listed in 7.3.2-2.

7.3.3 TI Team California ϕ_{SS} Models ($\phi_{SS\text{-}CA\text{-}1}$ and $\phi_{SS\text{-}CA\text{-}2}$ Models)

Magnitude-dependent ϕ_{SS} values were calculated in different magnitude bins for magnitude greater than 5.0 and distance less than 50 km from a California only subset (Section 5.4.3) of the NGA-West2 datasets (NGA-W2$_{CA\text{-}PHISS\text{-}ASK14}$, NGA-W2$_{CA\text{-}PHISS\text{-}BSSA14}$, NGA-W2$_{CA\text{-}PHISS\text{-}CB14}$ and NGA-W2$_{CA\text{-}PHISS\text{-}CY14}$). Example plots showing the ϕ_{SS} values binned by magnitude are shown in Figure 7.3.3-1a and b for eight spectral periods (PGA, 0.05, 0.1, and 0.2 sec in Figure 7.3.3-1a; 0.5, 1.0, 2.0, and 5.0 sec in Figure 7.3.3-1b). As shown in those figures, the calculated ϕ_{SS} values are consistent among the four NGA-West2 models. Figures 7.3.3-1a and 7.3.3-1b also show the average ϕ_{SS} for the four NGA-West2 California subset

residuals (averaging the ϕ_{SS}^2 terms). The error bars on the average ϕ_{SS} represent the standard error of the ϕ_{SS} estimates for the individual models combined with the between-model standard deviations.

The distance and V_{S30} dependence of the ϕ_{SS} values was evaluated by Linda Al Atik for Workshop #3 (see also Appendix K, Section K.1) and found to not have a distance or V_{S30} dependence.

The TI Team selected a magnitude-dependent form for the average ϕ_{SS} values and developed two models. The first model ($\phi_{SS-CA-1}$ model) has a magnitude break at **M**7.0 and is constant for **M** ≥ 7.0. It is given by the linear function in Eq. 7.3.3-1a:

$$\phi_{SS-CA-1}(M,T) = \begin{cases} a(T) + \dfrac{M-5}{2}\left(b(T)-a(T)\right) & for\ M < 7 \\ b(T) & for\ M \geq 7 \end{cases} \quad \text{(Eq. 7.3.3-1a)}$$

where coefficient a(T) represents ϕ_{SS} values at **M**5.0 and coefficient b(T) represents ϕ_{SS} values at **M**7.0. Coefficients a(T) and b(T) were obtained at each spectral period less than or equal to 5.0 sec (PGA, 0.030, 0.050, 0.075, 0.100 0.150, 0.200, 0.300, 0.400, 0.500, 0.750, 1.000, 1.500, 2.000, 3.000, and 5.000) by fitting the average ϕ_{SS} values versus magnitude (averaging the binned variances of the four California datasets). At period of 10 sec, no fit was applied to ϕ_{SS} versus magnitude due to the scarcity of the data at this period. Coefficients a(T) and b(T) were then smoothed versus period (up to 5.0 sec) as shown in Figure 7.3.3-2. The adopted smoothing functions (constant for a and inverse hyperbolic cosine function versus ln(T) for b) were chosen to best preserve the overall trend of the derived coefficients versus period. Values of coefficients a and b at T = 5.0 sec were adopted for periods greater than 5.0 sec.

The second model ($\phi_{SS-CA-2}$ model) has a magnitude break at **M**5.5 and has the form described in Eq. 7.3.3-1b)

$$\phi_{SS-CA-2}(M,T) = \begin{cases} a(T) + \dfrac{M-5}{0.5}\left(c(T)-a(T)\right) & for\ M < 5.5 \\ c(T) & for\ M \geq 5.5 \end{cases} \quad \text{(Eq. 7.3.3-1b)}$$

Where coefficient a(T) represents ϕ_{SS} values at **M**5.0 and has the same values derived for the $\phi_{SS-CA-1}$ model, and coefficient c(T) represents ϕ_{SS} values at **M** ≥ 5.5. Derived ϕ_{SS} values for **M** ≥ 5.5 using the four California subsets were averaged at each spectral period (averaging variances) and then smoothed versus period as shown in Figure 7.3.3-3. The inverse hyperbolic cosine function versus ln(T) was adopted for smoothing to best preserve the trend of the coefficient c versus period.

The fits of the $\phi_{SS-CA-1}$ and $\phi_{SS-CA-2}$ models versus magnitudes are shown in Figures 7.3.3-1a and 7.3.3-1b for selected representative periods.

The central, low, and high values of coefficients a(T), b(T), and c(T) are shown in Figure 7.3.3-4 and are listed in Tables 7.3.3-1 and 7.3.3-2 for the $\phi_{SS-CA-1}$ and $\phi_{SS-CA-2}$ models, respectively.

7.3.4 TI Team European ϕ_{SS} Model ($\phi_{SS\text{-}EUR}$ Model)

A magnitude-independent ϕ_{SS-EUR} model was also derived from the European dataset (EUR_{PHISS}, described in Section 5.4.2). The central ϕ_{SS} model was derived by smoothing magnitude-independent ϕ_{SS} values over period using an inverse hyperbolic cosine function versus ln(T), as shown in Figure 7.3.4-1 .

As demonstrated in Appendix P, the high and low ϕ_{SS} branches represent the 5th and 95th percentile of scaled chi-square distribution of ϕ_{SS}^2 with the standard deviation of ϕ_{SS}^2 calculated for CV(ϕ_{SS}) = 0.12. The CV value of 0.12 is from the global data (see Appendix P). The CV value of ϕ_{SS} is related to the differences in the within-event within-site variability between sites. Conceptually, this is related to the complexity of the site conditions in terms of variability about systematic site amplifications. The TI Team judged that there is no obvious reason that the European sites would be more variable in their response than the global sites. Therefore, the global value is assumed to apply to the European data. The central, high, and low ϕ_{SS} branches are also shown in Figure 7.3.4-1 compared to the ϕ_{SS} values used to derive the model. The tabulated values of the ϕ_{SS-EUR} model are listed in Table 7.3.4-1.

The ϕ_{SS} values were analyzed using the European dataset to evaluate magnitude dependence. Figure 7.3.4-2 shows ϕ_{SS} versus magnitude using the entire dataset as well as using only the subset of residuals with distance less than 50 km, for eight spectral periods (PGA, 0.05, 0.1, and 0.2 in Figure 7.3.4-2a; 0.5, 1.0, 2.0, and 4.0 sec in Figure 7.3.4-2b). Figure 7.3.4-2 shows no significant magnitude-dependence of ϕ_{SS} for the European dataset asides from an apparent increase of ϕ_{SS} for magnitude greater than 7.0. It should be noted only two Turkish earthquakes (Duzce and Van) are available in the magnitude 7.0 to 7.5 bin and only one earthquake (Kocaeli) is available in the magnitude 7.5 to 8.0 bin; hence the large error bars on ϕ_{SS} in these two magnitude bins. ϕ_{SS} values were also evaluated by Linda Al Atik (see Appendix K, Section K.2) with respect to distance, V_{S30}, and style-of-faulting for PGA and T=1.0 sec. The results indicated no distance, magnitude, V_{S30} and style-of-faulting dependence. Therefore, a magnitude-dependent ϕ_{SS} model is not developed for the European dataset.

7.4 $\phi_{SP\text{-}R}$ Model ($\phi_{SP\text{-}R123}$ Model)

The availability of recordings from distant California/Mexico earthquakes recorded at a group of sites around PVNGS makes it possible to estimate the repeatable similar path-to-region (SP-R) effects and remove them from the ground-motion variability. The use of ϕ_{SP-R} is coupled with applying an adjustment to the median prediction of GMPEs as discussed in Section 6.6. Section 7.4.1 presents the development of the path terms for Region1 and for combined Regions 2&3. The aleatory variability for these two sub-sets is described in Section 7.4.2 and is called $\phi_{SP-R123}$.

7.4.1 Path Terms

Ground-motion recordings at the Arizona stations from California events with distance range of 200 to 500 km (PEER-AZ_{PATH} subset) were evaluated for their path effects. Event terms (δB) for the California earthquakes, provided by the four NGA-West2 GMPE developers (ASK14, BSSA14, CB14 and CY14), were removed from the total residuals (δ) of the recorded ground motions with respect to the four GMPE predictions to obtain four sets of within-event residuals (δW):

$$\delta W_{ijk}(T) = \delta_{ijk}(T) - \delta B_{ik}(T) \qquad \text{(Eq. 7.4.1-1)}$$

where the indices i, j, and k are for the earthquake, station, and GMPE, respectively. The within-event residuals are shown in Figure 7.4.1-1 to Figure 7.4.1-4. Although the CB14 model was excluded for $\phi_{SS-GLOBAL-LD}$ for large distances (Section 5.4.4), the CB14 model is included for the ϕ_{SP-R} model derivation because ϕ_{SP-R} is estimated from new residuals computed for each GMPE and the Arizona data (not previously included in the NGA-West2 database), whereas for the ϕ_{SS}, the NGA-West2 within-event residuals provided by the developers are used directly. Because the residuals for ϕ_{SP-R} are computed by the TI Team and are not provided by the NGA-West2 developers, all four of the models can be used.

The first step for estimating ϕ_{SP-R} and the path terms for sources in Regions 1, 2, and 3 (as defined in Section 4.2) was to compute the weighted mean bias of the within-event residuals from the four GMPEs (weighted by the number of recordings per GMPE since not all GMPEs used all the available events). This weighted mean bias represents the mean residual for a given path in central Arizona. It is denoted $\delta\bar{W}(T)$ and is given by:

$$\delta\bar{W}(T) = \frac{\sum_{k=1}^{N_{GMPE}} \delta\bar{W}_k(T) N_k}{\sum_{k=1}^{N_{GMPE}} N_k} \quad \text{(Eq. 7.4.1-2)}$$

where $\delta\bar{W}_k$ is the mean bias for the k[th] GMPE and is given in Eq. 7.4.1-3, and N_k is the total number of recordings for the k[th] GMPE. N_{GMPE} is the number of GMPEs. The $\delta\bar{W}_k$ term is the mean of the within-event residuals for a given GMPE:

$$\delta\bar{W}_k(T) = \frac{\sum_{j=1}^{NREC_i} \sum_{i=1}^{NEQK} \delta W_{ijk}(T)\, \mathrm{E}_{ijk}}{N_k} \quad \text{(Eq. 7.4.1-3)}$$

where $NREC_i$ is the number of recordings from the i[th] earthquake, and NEQK is the number of earthquakes and the E_{ijk} is 1 if recording j from earthquake i was used by GMPE k, and zero otherwise.

Next, the mean bias is removed from the within-event residuals to lead to a bias-corrected within-event residual, δW^*_{ijk}, which is given by

$$\delta W^*_{ijk}(T) = \delta W_{ijk}(T) - \delta\bar{W}(T) \quad \text{(Eq. 7.4.1-4)}$$

The goal is to capture the range for large magnitudes whereas the available data are for small magnitude: accordingly, the range of magnitude scaling from the GMPEs is wished to be retained. Correcting for the average bias of the four GMPEs rather than correcting each GMPE separately for its own bias preserves the range of the median spectral amplitudes (PSA) obtained from the four GMPEs.

The standard error of the mean of the path term was approximated as the average standard deviation of the residuals over all four GMPEs (averaging variances) divided by the square root of the average number of recordings for the four GMPEs. Table 7.4.1-1 lists the bias for each GMPE as well as the weighted mean bias ($\delta\bar{W}$) and its standard error.

As discussed in Section 5.3.3, for each station with a minimum of 5 recordings, the site term, $\delta S2S_{jk}$, for each of the GMPEs was computed.

$$\delta S2S_{jk}(T) = \frac{\sum_{i=1}^{NEQK} \delta W^*_{ijk}(T)}{NEQK_k} \quad \text{(Eq. 7.4.1-5)}$$

The weighted mean site term was computed by averaging the site terms over the four GMPEs with the weights proportional to the number of recordings at a given site for a given GMPE. There is a correlation between the average site term and an average path term that cannot be resolved with the available data. Therefore, the site terms computed using Eq. 7.4.1-5 may also contain an average path term.

$$\delta\overline{S}\overline{2}\overline{S}_j(T) = \frac{\sum_{k=1}^{N_{GMPE}} \delta S2S_{jk}(T)\, N_{jk}}{\sum_{k=1}^{N_{GMPE}} N_{jk}} \qquad \text{(Eq. 7.4.1-6)}$$

where N_{jk} is the number of recording from the j^{th} site for GMPE k. This mean site term is removed from the δW^*_{ijk} to obtain the single-site within-event residuals, given below:

$$\delta WS_{ijk}(T) = \delta W^*_{ijk}(T) - \delta S2S_{jk}(T) \qquad \text{(Eq. 7.4.1-7)}$$

The regional path term was then computed for each of the three regions at each spectral period. The path term is given by the mean of the path terms for the four GMPEs. The path term for r^{th} region and k^{th} GMPE is given by

$$\delta P2P_{rk}(T) = \frac{\sum_{i=1}^{NEQK_k} \sum_{j=1}^{NSTA_{ik}} \delta WS_{ijk}(T)\, E_{ir}}{\sum_{i=1}^{NEQK_k} \sum_{j=1}^{NSTA_{ik}} E_{ir}} \qquad \text{(Eq. 7.4.1-8)}$$

where E_{ir} is a dummy variable that is 1 if earthquake i is in region r and 0 otherwise. The mean weighted path term is given by

$$\delta\overline{P}\overline{2}\overline{P}_r(T) = \frac{\sum_{k=1}^{N_{GMPE}} \delta P2P_{rk}(T)\, N_{rk}}{\sum_{k=1}^{N_{GMPE}} N_{rk}} \qquad \text{(Eq. 7.4.1-9)}$$

where N_{rk} is the number of recordings for region r and GMPE k. The standard error of the mean path terms is given by

$$SE(\delta\overline{P}\overline{2}\overline{P}_r(T)) = \frac{\phi_{SP-R}}{\sqrt{N_r}} \qquad \text{(Eq. 7.4.1-10)}$$

where N_r is the average number of recordings in region r (averaged over the GMPEs). Figure 7.4.1-5 shows the mean path terms with the standard error of the mean for the three regions.

For application in the hazard analysis, the sum of the mean bias (average path term for Arizona), $\delta\overline{W}(T)$, and mean regional path term, $\delta\overline{P2P}_r(T)$, is used to derive the total path term for each region:

$$path_r(T) = \delta\overline{W}(T) + \delta\overline{P2P}_r(T) \qquad \text{(Eq. 7.4.1-11)}$$

The $\delta\overline{W}(T)$ term contains both the average site term and the average path term, but the partitioning between the average site term and the average path term cannot be determined.

The central path term for each of the three regions is based on averaging the $path_r(T)$ terms at periods of 0.5, 1.0, and 2.0 sec. The high and low branches around the median are obtained using +/- 1.6*standard error, where the standard error is the square root of the sum of squares of the standard errors of the $\delta\overline{W}(T)$ and $\delta\overline{P2P}_r(T)$ terms. The average standard error for periods 0.5 and 1.0 sec is used for periods less than 1.0 sec. For periods greater than 2 sec, the path term is extrapolated based on the value of the path term at a period of 2 seconds. Additional epistemic uncertainty in the path terms for periods greater than 2 seconds was added to account for the extrapolation by scaling the standard deviation for the 2 sec path term by the ratios of the standard deviations of median motions at longer periods to those at 2 sec from the Al-Atik and Youngs (2014) model. The epistemic uncertainty at periods less than 2 sec is captured by the statistical uncertainty in the path term due to the sample size. The median, high, and low path terms are shown in Figure Eq. 7.4.1-6 and are listed in Table 7.4.1-2.

An issue associated to the path terms is that they are mainly based on small magnitude data. Therefore, the range of the medians from the five NGA-West2 GMPEs is maintained rather than computing a separate path term for each GMPE. This captures the uncertainty in the large magnitude scaling that is present in the range of the five NGA-West2 GMPEs.

7.4.2 TI Team $\phi_{SP\text{-}R}$ Model

The path-corrected site-corrected within-event residual, δWSP_{ijkr}, defined for the recording i at station j for GMPE k in region r, is given by:

$$\delta WSP_{ijkr}(T) = \delta WS_{ijk}(T) - \delta\overline{P2P}_r(T)\,E_{ir} \qquad \text{(Eq. 7.4.2-1)}$$

The standard deviation of the $\delta WSP_{ijkr}(T)$ residuals, denoted $\phi_{SP-R}(\mathrm{T})$, is computed for each of the four NGA-West2 GMPEs. The average $\phi_{SP-R}(T)$ for the four GMPEs for periods 0.5, 1.0, and 2.0 sec

(averaging variances) was used to develop the central $\phi_{SP-R}(T)$ model. The $\phi_{SP-R}(T)$ at a period of 0.2 sec was not used in deriving the central model because sources in Regions 1, 2, and 3 do not contribute significantly to the hazard at short periods (as discussed in Section 4.2.3 and related figures).

An attempt to compute ϕ_{SP-R} at spectral periods of 3, 4 and 5 seconds was unsuccessful due to limitation of usable data at those periods. Accounting for the lowest useable frequency of the recordings in the PEER Arizona dataset for Regions 1, 2 and 3 (Section 5.1.2) and excluding the earthquakes where event terms were not available (events not used in the development of NGA-West2 GMPEs), the total number of recordings per GMPE is listed in Table 7.4.2-1 for periods of 3, 4, and 5 sec. The number of recordings per station for the four NGA-West2 GMPEs at the three spectral periods is also shown in Table 7.4.2-1. Imposing the requirement of a minimum of 5 recordings per station for calculating the site terms, the Table 7.4.2-1 shows that no data is left at period of 3.0 sec. At period of 4.0 sec, only 5 recordings remain for the BSSA14 residuals while no data remain for the rest of the GMPEs. At period of 3.0 sec, all GMPEs have an average of about 5 recordings each at station Y14A. Distributing these recordings among the three regions leaves insufficient data per region for estimating the path terms. Therefore, ϕ_{SP-R} is not shown at periods greater than 2.0 sec due to the data restrictions discussed here.

With the 2.0 seconds limit on the reliable period range for estimating the path effects, the ϕ_{SP-R} model needs to be extrapolated to longer periods. The global long-distance data (NGA-$W2_{LD\text{-}PHISS\text{-}ASK14}$, NGA-$W2_{LD\text{-}PHISS\text{-}BSSA14}$, NGA-$W2_{LD\text{-}PHISS\text{-}CY14}$) used to evaluate PhiSS show a trend of a slight reduction in the **PhiSS** values as the periods increase from 2 to 10 seconds (Figure 7.3.2-5). In addition, the range of **PhiSS** at periods longer than 2 seconds is comparable to the range at 2.0 seconds. Therefore, the TI Team selected a simple model for the extrapolation using a constant ϕ_{SP-R} in both the central value and the range used for periods longer than 2 seconds.

The high and low branches of $\phi_{SP-R}(T)$ represent the 5th and 95th percentile of a scaled chi-square distribution of ϕ^2_{SP-R} (see Appendix P) with a CV(ϕ_{SP-R}) = 0.17 as estimated from the between-model variability of ϕ_{SP-R} and the average standard error of the ϕ_{SP-R} estimates for the individual GMPEs averaged over periods of 0.5, 1.0, and 2.0 sec. The resulting $\phi_{SP-R}(T)$ model is listed in Table 7.4.2-2. Figure 7.4.2-1 shows the central, high and low branches of ϕ_{SP-R} compared to the values for the four GMPEs used to derive the model. For comparison, the value of ϕ_{SP-R} at 1.5 sec from the four NGA-West2 GMPEs is also shown in Figure 7.4.2-1, even though the value at 1.5 sec was not used to derive the $\phi_{SP-R}(T)$ model. The ϕ_{SP-R} value at 1.5 seconds is within the range of the $\phi_{SP-R}(T)$ branches.

7.5 Partially Non-Ergodic Sigma Models Comparisons

The proponent ϕ_{SS} models are compared for DCPP and PVNGS in Figures 7.5-1 and 7.5-2. Overall, the models show the ϕ_{SS} values centered on around 0.35 to 0.45 with an epistemic uncertainty of about 0.1. The models vary about this average range depending on whether they incorporated an M-dependent or period-dependent form. Figure 7.5-2 shows also the comparisons with the SWUS GMC ϕ_{SP-R} model derived from Arizona data. At long periods (T > 2 sec), the ϕ_{SP-R} and the ϕ_{SS} models are similar. The main reduction in ϕ_{SP-R} is seen at 0.5 second value (ϕ_{SP-R} at periods less than 0.5 sec are extrapolated and are not well constrained). Figure 7.5-3 provides comparisons of the DCPP and PVNGS magnitude-independent SWUS GMC ϕ_{SS} models to the PEGASOS Refinement Project (PRP) magnitude-independent ϕ_{SS} model (Rodriguez-Marek et al., 2013). The average values from the GMC TI Team model are consistent with the PRP central model. It should be noted that the PRP did not address the bias in the estimate of the standard deviation of ϕ_{SS} due to sample size; hence the larger epistemic uncertainty observed for the PRP model in Figure 7.5-3. The Hanford project adopted a magnitude-dependent ϕ_{SS} model (Coppersmith et al., 2014). Figure 7.5-4 presents a comparison of the DCPP magnitude-dependent SWUS GMC ϕ_{SS} models and the global magnitude-independent ϕ_{SS} model to the Hanford model. The GMC TI Team M-dependent models are similar to the Hanford models both in the central value and the uncertainty range. Figure 7.5-5 shows the comparison of the magnitude-independent SWUS GMC ϕ_{SS} models to the Luzi et al. (2014) ϕ_{SS} models derived from Italian data. The three models based on the Italian data are consistent with the range from the GMC TI Team model. The lowest model (ϕ_{SS} Italy-3) represents some path effects and is at the lower edge of the uncertainty of the GMC TI Team model for the ϕ_{SS} model.

7.6 Simplified Representation of the Total Sigma Models

Chapters 10, 11, and 12 describe the logic trees for τ, ϕ_{SS} for DCPP, and ϕ_{SS} and ϕ_{SP-R} for PVNGS. The hazard analysis uses the total standard deviation which is computed by combining the τ and ϕ models (see Appendix P for more details). To reduce the number of branches in the ground-motion logic tree, a reduced set of branches for the total sigma, with three representative branches, is developed in Chapter 13.

7.7 References

Abrahamson, N.A., and Youngs, R.R. (1992). A stable algorithm for regression analysis using the random effect model, *Bull. Seism. Soc. Am*., Vol. 82, 505-510.

Abrahamson, N.A., Silva, W.J., and Kamai, R. (2013). Update of the AS08 Ground-Motion Prediction Equations Based on the NGA-West2 Data Set, PEER Report No. 2013/04, Pacific Earthquake Engineering Research Center, University of California, Berkeley, CA.

Abrahamson, N.A., Silva, W.J., and Kamai, R. (2014). Summary of the AKS14 Ground-Motion Relation for Active Crustal Regions, *Earthquake Spectra*, Vol. 30 (3), 1025-1055, DOI: 10.1193/070913EQS198M.

Addo, K.O., Abrahamson, N.A., and Youngs, R.R. (2012). Ground Motion Characterization (GMC) Model, *BC Hydro SSHAC Level 3 Probabilistic Seismic Hazard Analysis (PSHA) Report*, Vol.3, November 2012.

Akkar, S., Sandikkaya, M.A., and Bommer, J.J. (2014a). Empirical ground-motion models for point- and extended-source crustal earthquake scenarios in Europe and the Middle East, *Bull. Earthquake Eng*., Vol. 12(1), 359-387, DOI 10.1007/s10518-013-9461-4.

Akkar, S., Sandikkaya, M.A., and Bommer, J.J. (2014b). Erratum to: Empirical ground-motion models for point- and extended-source crustal earthquake scenarios in Europe and the Middle East, *Bull. Earthquake Eng*, Vol. 12(1), 389-390, DOI 10.1007/s10518-013-9508-6.

Al-Atik, L., Abrahamson, N., Bommer, J., Scherbaum, F., Cotton, F., Kuehn, N. (2010). The variability of ground-motion prediction models and its components, *Seism. Res. Let*., Vol. 81(5), 794-801.

Al Atik, L., and Youngs, R.R. (2014). Epistemic Uncertainty for NGA-West2 Models, *Earthquake Spectra*, Vol. 30(3), 1301-1318, DOI: 10.1193/062813EQS173M.

Anderson, J. G. and Brune, J. (1999). Probabilistic seismic hazard analysis without the ergodic assumption, *Seism. Res. Lett.*, Vol. 70, 19-28.

Anderson, J.G., and Uchiyama, Y. (2011). A methodology to improve ground-motion prediction equations by including path corrections, *Bull. Seism. Soc. Am.,* Vol. 101, 1822-1846.

Atkinson, G.M. (2006). Single-station sigma, *Bull. Seism. Soc. Am*., Vol. 96(2), 446-455.

Bindi D., Massa M., Luzi L., Ameri G., Pacor F., Puglia R., and Augliera, P. (2014a). Pan-European Ground-Motion Prediction Equations for the Average Horizontal Component of PGA, PGV, and 5%-Damped PSA at Spectral Periods up to 3.0 s using the RESORCE dataset, *Bull Earthquake Eng*., Vol. 12, 391–430, DOI 10.1007/s10518-013-9525-5.

Bindi D., Massa M., Luzi L., Ameri G., Pacor F., Puglia R., and Augliera, P. (2014b). Erratum to: Pan-European Ground-Motion Prediction Equations for the Average Horizontal Component of PGA, PGV, and 5%-Damped PSA at Spectral Periods up to 3.0 s using the RESORCE dataset, *Bull Earthquake Eng*., Vol. 12, 431-448, DOI 10.1007/s10518-014-9589-x.

Bommer, J.J., Coppersmith, K.J., Coppersmith, R.T., Hanson, K.L., Mangongolo, A., Neveling, J., Rathje, E.M., Rodriguez-Marek, A., Scherbaum, F., Shelembe, R., Stafford, P.J., and Strasser, F.O. (2013). A SSHAC Level 3 PSHA for a new-build nuclear site in South Africa, *Earthquake. Spectra (in press)*, DOI: 10.1193/060913EQS145M.

Boore, D.M. (1983). Stochastic simulation of high-frequency ground motions based on seismological models of the radiated spectra, *Bull. Seism. Soc. Am*., 73(6), 1865-1894.

Boore, D.M. (1986). Short-period P- and S-wave radiation from large earthquakes: implications for spectral scaling relations, *Bull. Seism. Soc. Am*., 76(1), 43-64.

Boore, D.M., and Joyner, W.B. (1997). Site amplification for generic rock sites, *Bull. Seism. Soc. Am*., Vol. 87, 327-341.

Boore, D.M., Stewart, J.P., Seyhan, E., and Atkinson, G.M. (2014). NGA-West 2 Equations for Predicting PGA, PGV, and 5%-Damped PSA for Shallow Crustal Earthquakes, *Earthquake Spectra*, Vol. 30(3), 1057-1085, DOI: 10.1193/070113EQS184M.

Campbell, K.W., and Bozorgnia, Y. (2014). NGA-West2 Ground Motion Model for the Average Horizontal Components of PGA, PGV, and 5%-Damped Linear Acceleration Response Spectra, *Earthquake Spectra*, Vol. 30(3), 1087-1115, DOI: 10.1193/062913EQS175M.

Chen, Y-H., and Tsai, C-C. P. (2002). A new method for estimation of the attenuation relationship with variance components, *Bull. Seism. Soc. Am*., Vol. 5, 1984-1991.

Chiou, B.S-J., and Youngs, R.R. (2014). Update of the Chiou and Youngs NGA Model for the Average Horizontal Component of Peak Ground Motion and Response Spectra, *Earthquake Spectra*, Vol. 30(3), 1117-1153, DOI: 10.1193/072813EQS219M.

Coppersmith, K.J., Bommer, J., Hanson, K., Coppersmith, R., Unruh, J.R., Wolf, L., Youngs, R., Al Atik, L., Rodriguez-Marek, A., Toro, G., and Montaldo-Falero, V. (2014). Hanford Sitewide Probabilistic Seismic Hazard Analysis, *PNNL-23361*, Pacific Northwest National Laboratory, Richland Washington.

Dawood, H.M., Rodriguez-Marek, A., Bayless, J., Goulet, C., and Thompson E. (2014). The KiK-net database processed using an automated ground motion processing protocol. Available at https://nees.org/resources/7849.

Graizer, V. (2014). Updated Graizer-Kalkan Ground-motion Prediction Equations for Western United States, *Proceedings for the 10th U.S. National Conference on Earthquake Engineering Frontiers of Earthquake Engineering*, July 21-25, 2014, Anchorage, Alaska, Paper ID 1097, 11 pp.

Idriss, I.M. (2014). An NGA-West2 Empirical Model for Estimating the Horizontal Spectral Values Generated by Shallow Crustal Earthquakes, *Earthquake Spectra*, Vol. 30(3), 1155-1177, DOI: 10.1193/070613EQS195M.

Lin, P-S., Chiou, B., Abrahamson, N., Walling, M., Lee, C-T, and Cheng, C-T (2011). Repeatable source, site, and path effects on the standard deviation for empirical ground-motion prediction models, *Bull. Seism. Soc. Am*., Vol. 101(5), 2281-2295.

Luzi, L., Bindi, D., Puglia, R., Pacor, F. and Oth, A. (2014). Single-Station Sigma for Italian Strong-Motion Stations, *Bull. Seism. Soc. Am*., Vol. 104(1), 467-483.

Miller, A.C., and Rice, T.R. (1983). Discrete approximations of probability distributions, *Management Science,* Vol. 29, 352−362.

Morikawa, N., Kanno, T., Narita, A., Fujiwara, H., Okumura, T., Fukushima, Y., and Guerpinar, A. (2008). Strong motion uncertainty determined from observed records by dense network in Japan, *J. Seism*., Vol. 12(4), 529-546.

Rodriguez-Marek, A., Cotton, F., Abrahamson, N., Akkar, S., Al Atik, L., Edwards, B., Montalva, G.A., and Dawood, H.M. (2013). A model for single-station standard deviation using data from various tectonic regions, *Bull. Seismol. Soc. Am.,* Vol. 103, 3149-3163.

Rodriguez-Marek, A., Rathje, E.M., Bommer, J.J., Scherbaum, F., and Stafford, P.J. (2014). Application of Single-Station Sigma and Site-Response Characterization in a Probabilistic Seismic-Hazard Analysis for a New Nuclear Site, *Bull. Seismol. Soc. Am.,* Vol. 104, 1601-1619, DOI: 10.1785/0120130196.

Zhao, J.X., Zhang, J., Asano, A., Ohno, Y., Oouchi, T., Takahashi, T., Ogawa, H., Irikura, K., Thio, H.K., Somerville, P.G., Fukushima, Y., and Fukushima, Y. (2006). Attenuation Relations of Strong Ground Motion in Japan Using Site Classification Based on Predominate Period, *Bull. Seism. Soc. Am*., Vol. 96, 898-913.

Table 7.1-1: ϕ_{SS} and ϕ_{SP-R} models developed by the SWUS GMC TI Team, subset used for their development, and application for different sources. Definition of the subsets is provided in Section 5.4 and illustrated in Table 5.1-4, and is not repeated herein.

SIGMA MODEL	SUBSET USED IN THE DEVELOPMENT	USE OF SIGMA MODEL
ϕ_{SS-EUR}	EUR_{PHISS}	Application to PVNGS sources in Greater Arizona
$\phi_{SS-GLOBAL-R50}$	$GLOBAL_{PHISS\text{-}ASK14}$ $GLOBAL_{PHISS\text{-}BSSA14}$ $GLOBAL_{PHISS\text{-}CY14}$ $GLOBAL_{PHISS\text{-}CB14}$	Application to both DCPP and PVNGS sources in Greater Arizona
$\phi_{SS-GLOBAL-LD}$	$NGA\text{-}W2_{LD\text{-}PHISS\text{-}ASK14}$ $NGA\text{-}W2_{LD\text{-}PHISS\text{-}BSSA14}$ $NGA\text{-}W2_{LD\text{-}PHISS\text{-}CY14}$	Application to PVNGS sources in Regions 1, and 2&3
$\phi_{SS-CA-1}$ and $\phi_{SS-CA-2}$	$NGA\text{-}W2_{CA\text{-}PHISS\text{-}ASK14}$ $NGA\text{-}W2_{CA\text{-}PHISS\text{-}BSSA14}$ $NGA\text{-}W2_{CA\text{-}PHISS\text{-}CY14}$ $NGA\text{-}W2_{CA\text{-}PHISS\text{-}CB14}$	Application to DCPP
$\phi_{SP-R123}$	$PEER\text{-}AZ_{PATH\text{-}ASK14}$ $PEER\text{-}AZ_{PATH\text{-}BSSA14}$ $PEER\text{-}AZ_{PATH\text{-}CY14}$ $PEER\text{-}AZ_{PATH\text{-}CB14}$	Application to PVNGS from earthquakes in Region 1 and Regions 2&3

Table 7.2.4-1: Values of τ_1 and τ_2 for the τ logic tree branches discussed in Chapter 10.

	τ_1	τ_2
Central	0.386	0.338
High	0.539	0.443
Low	0.226	0.226

Table 7.3.2-1: Magnitude-independent $\phi_{SS-GLOBAL-R50}$ model branches.

	$\phi_{SS-GLOBAL-R50}$		
Period (sec)	**Central**	**High**	**Low**
0.01 - 10	0.437	0.522	0.350

Table 7.3.2-2: Magnitude-independent $\phi_{SS-GLOBAL-LD}$ model branches.

Period (sec)	Central	High	Low
PGA	0.517	0.617	0.414
0.02	0.517	0.617	0.414
0.03	0.517	0.617	0.414
0.05	0.517	0.617	0.414
0.075	0.517	0.617	0.414
0.1	0.517	0.617	0.414
0.15	0.517	0.617	0.414
0.2	0.515	0.615	0.412
0.25	0.511	0.610	0.409
0.3	0.508	0.606	0.407
0.4	0.498	0.594	0.399
0.5	0.490	0.585	0.392
0.75	0.476	0.568	0.381
1	0.466	0.556	0.373
1.5	0.452	0.540	0.362
2	0.443	0.529	0.355
3	0.431	0.514	0.345
4	0.423	0.505	0.339
5	0.417	0.498	0.334
7.5	0.407	0.485	0.325
10	0.399	0.476	0.319

Table 7.3.3-1: Magnitude-dependent $\phi_{SS-CA-1}$ model branches.

	$\phi_{SS-CA-1}$ **Model**					
Period (sec)	**a Central**	**b central**	**a High**	**b High**	**a Low**	**b Low**
PGA	0.4850	0.3087	0.5789	0.3685	0.3882	0.2471
0.03	0.4850	0.3183	0.5789	0.3799	0.3882	0.2548
0.05	0.4850	0.3278	0.5789	0.3913	0.3882	0.2624
0.075	0.4850	0.3363	0.5789	0.4014	0.3882	0.2692
0.1	0.4850	0.3425	0.5789	0.4088	0.3882	0.2741
0.15	0.4850	0.3512	0.5789	0.4192	0.3882	0.2811
0.2	0.4850	0.3571	0.5789	0.4262	0.3882	0.2858
0.3	0.4850	0.3648	0.5789	0.4354	0.3882	0.292
0.4	0.4850	0.3699	0.5789	0.4415	0.3882	0.2961
0.5	0.4850	0.3736	0.5789	0.4459	0.3882	0.299
0.75	0.4850	0.3796	0.5789	0.4531	0.3882	0.3038
1	0.4850	0.3835	0.5789	0.4577	0.3882	0.3069
1.5	0.4850	0.3883	0.5789	0.4635	0.3882	0.3108
2	0.4850	0.3913	0.5789	0.4671	0.3882	0.3132
3	0.4850	0.3951	0.5789	0.4716	0.3882	0.3162
5	0.4850	0.3960	0.5789	0.4727	0.3882	0.3169
10	0.4850	0.3960	0.5789	0.4727	0.3882	0.3169

Table 7.3.3-2: Magnitude-dependent $\phi_{SS-CA-2}$ model branches.

	$\phi_{SS-CA-2}$ **Model**					
Period (sec)	**a Central**	**c Central**	**a High**	**c High**	**a Low**	**c Low**
PGA	0.4850	0.3581	0.5789	0.4273	0.3882	0.2865
0.03	0.4850	0.3654	0.5789	0.4357	0.3882	0.2921
0.05	0.4850	0.3725	0.5789	0.4452	0.3882	0.2985
0.075	0.4850	0.3790	0.5789	0.4524	0.3882	0.3033
0.1	0.4850	0.3837	0.5789	0.4583	0.3882	0.3073
0.15	0.4850	0.3902	0.5789	0.4655	0.3882	0.3121
0.2	0.4850	0.3947	0.5789	0.4715	0.3882	0.3161
0.3	0.4850	0.4006	0.5789	0.4786	0.3882	0.3209
0.4	0.4850	0.4044	0.5789	0.4822	0.3882	0.3233
0.5	0.4850	0.4072	0.5789	0.4858	0.3882	0.3257
0.75	0.4850	0.4118	0.5789	0.4918	0.3882	0.3297
1	0.4850	0.4147	0.5789	0.4953	0.3882	0.3321
1.5	0.4850	0.4183	0.5789	0.4989	0.3882	0.3346
2	0.4850	0.4206	0.5789	0.5025	0.3882	0.3370
3	0.4850	0.4234	0.5789	0.5049	0.3882	0.3386
5	0.4850	0.4265	0.5789	0.5085	0.3882	0.3410
10	0.4850	0.4297	0.5789	0.5133	0.3882	0.3442

Table 7.3.4-1: Magnitude-independent ϕ_{SS-EUR} model branches.

	ϕ_{SS-EUR} **Model**		
Period (sec)	**Central**	**High**	**Low**
PGA	0.460	0.549	0.368
0.02	0.462	0.552	0.370
0.03	0.464	0.554	0.371
0.05	0.468	0.559	0.375
0.075	0.471	0.562	0.377
0.1	0.474	0.566	0.379
0.15	0.477	0.569	0.382
0.2	0.480	0.573	0.384
0.25	0.482	0.575	0.386
0.3	0.483	0.577	0.387
0.4	0.485	0.579	0.388
0.5	0.487	0.581	0.390
0.75	0.489	0.584	0.391
1	0.491	0.586	0.393
1.5	0.493	0.588	0.395
2	0.494	0.590	0.395
3	0.496	0.592	0.397
4	0.497	0.593	0.398
5	0.497	0.593	0.398
7.5	0.498	0.595	0.399
10	0.499	0.596	0.399

Table 7.4.1-1: Bias of within-event residuals of the Arizona recordings, $\delta\bar{W}_k$, for the four NGA-West2 GMPEs and their weighted mean, $\delta\bar{W}$, and standard error of the mean.

	$\delta\bar{W}_k$ in ln units				$\delta\bar{W}$ in ln units	
Period (sec)	ASK14	BSSA14	CB14	CY14	Mean	Std Err
0.2	0.042	-0.476	-0.370	-0.063	-0.216	0.100
0.5	-0.548	-0.765	-0.619	-0.401	-0.589	0.087
1.0	-0.053	-0.556	-0.563	-0.260	-0.353	0.087
2.0	-0.219	-0.504	-0.317	-0.303	-0.344	0.096

Table 7.4.1-2: Total path term values, $path_l(T)$, for Regions 1, 2, and 3.

	Path Term - Region 1			Path Term - Region 2			Path Term - Region 3		
Period (sec)	**Central**	**High**	**Low**	**Central**	**High**	**Low**	**Central**	**High**	**Low**
PGA	-0.119	0.100	-0.338	-0.665	-0.433	-0.896	-0.561	-0.309	-0.812
0.02	-0.119	0.100	-0.338	-0.665	-0.433	-0.896	-0.561	-0.309	-0.812
0.03	-0.119	0.100	-0.338	-0.665	-0.433	-0.896	-0.561	-0.309	-0.812
0.05	-0.119	0.100	-0.338	-0.665	-0.433	-0.896	-0.561	-0.309	-0.812
0.075	-0.119	0.100	-0.338	-0.665	-0.433	-0.896	-0.561	-0.309	-0.812
0.1	-0.119	0.100	-0.338	-0.665	-0.433	-0.896	-0.561	-0.309	-0.812
0.15	-0.119	0.100	-0.338	-0.665	-0.433	-0.896	-0.561	-0.309	-0.812
0.2	-0.119	0.100	-0.338	-0.665	-0.433	-0.896	-0.561	-0.309	-0.812
0.25	-0.119	0.100	-0.338	-0.665	-0.433	-0.896	-0.561	-0.309	-0.812
0.3	-0.119	0.100	-0.338	-0.665	-0.433	-0.896	-0.561	-0.309	-0.812
0.4	-0.119	0.100	-0.338	-0.665	-0.433	-0.896	-0.561	-0.309	-0.812
0.5	-0.119	0.100	-0.338	-0.665	-0.433	-0.896	-0.561	-0.309	-0.812
0.75	-0.119	0.100	-0.338	-0.665	-0.433	-0.896	-0.561	-0.309	-0.812
1	-0.119	0.100	-0.338	-0.665	-0.433	-0.896	-0.561	-0.309	-0.812
1.5	-0.119	0.131	-0.369	-0.665	-0.381	-0.948	-0.561	-0.246	-0.875
2	-0.119	0.163	-0.401	-0.665	-0.329	-1.001	-0.561	-0.183	-0.938
3	-0.119	0.184	-0.421	-0.665	-0.304	-1.025	-0.561	-0.155	-0.966
4	-0.119	0.198	-0.436	-0.665	-0.287	-1.043	-0.561	-0.136	-0.986
5	-0.119	0.209	-0.447	-0.665	-0.273	-1.056	-0.561	-0.120	-1.001
7.5	-0.119	0.230	-0.468	-0.665	-0.249	-1.081	-0.561	-0.093	-1.028
10	-0.119	0.245	-0.483	-0.665	-0.231	-1.098	-0.561	-0.073	-1.048

Table 7.4.2-1: Number of recordings per station for the four NGA-West2 GMPEs used to derive the ϕ_{SP-R} model, at periods of 3, 4 and 5 seconds.

		Station ID No.									TOTAL REC.
		Y13A	114A	Z14A	113A	Y14A	115A	Z15A	Z13A	Y15A	
ASK14	T 3.0 sec	0	2	3	1	5	1	0	2	0	14
	T 4.0 sec	0	2	3	1	4	0	0	2	0	12
	T 5.0 sec	0	1	2	0	2	0	0	1	0	6
BSSA14	T 3.0 sec	1	3	4	1	6	2	1	2	1	21
	T 4.0 sec	1	3	4	1	5	1	1	2	1	19
	T 5.0 sec	1	3	4	1	4	1	1	2	1	18
CB14	T 3.0 sec	0	2	3	1	5	1	0	2	0	14
	T 4.0 sec	0	2	3	1	4	0	0	2	0	12
	T 5.0 sec	0	1	2	0	2	0	0	1	0	6
CY14	T 3.0 sec	0	2	3	1	5	1	0	2	0	14
	T 4.0 sec	0	2	3	1	4	0	0	2	0	12
	T 5.0 sec	0	1	2	0	2	0	0	1	0	6

Table 7.4.2-2: Magnitude-independent ϕ_{SP-R} model (Arizona Data) branches for California and Mexico sources in Regions 1, 2, and 3.

Period (sec)	Central	High	Low
PGA	0.304	0.388	0.217
0.02	0.304	0.388	0.217
0.03	0.304	0.388	0.217
0.05	0.304	0.388	0.217
0.075	0.304	0.388	0.217
0.1	0.304	0.388	0.217
0.15	0.304	0.388	0.217
0.2	0.304	0.388	0.217
0.25	0.304	0.388	0.217
0.3	0.304	0.388	0.217
0.4	0.304	0.388	0.217
0.5	0.304	0.388	0.217
0.75	0.339	0.432	0.242
1	0.364	0.464	0.260
1.5	0.399	0.508	0.284
2	0.423	0.540	0.302
3	0.423	0.540	0.302
4	0.423	0.540	0.302
5	0.423	0.540	0.302
7.5	0.423	0.540	0.302
10	0.423	0.540	0.302

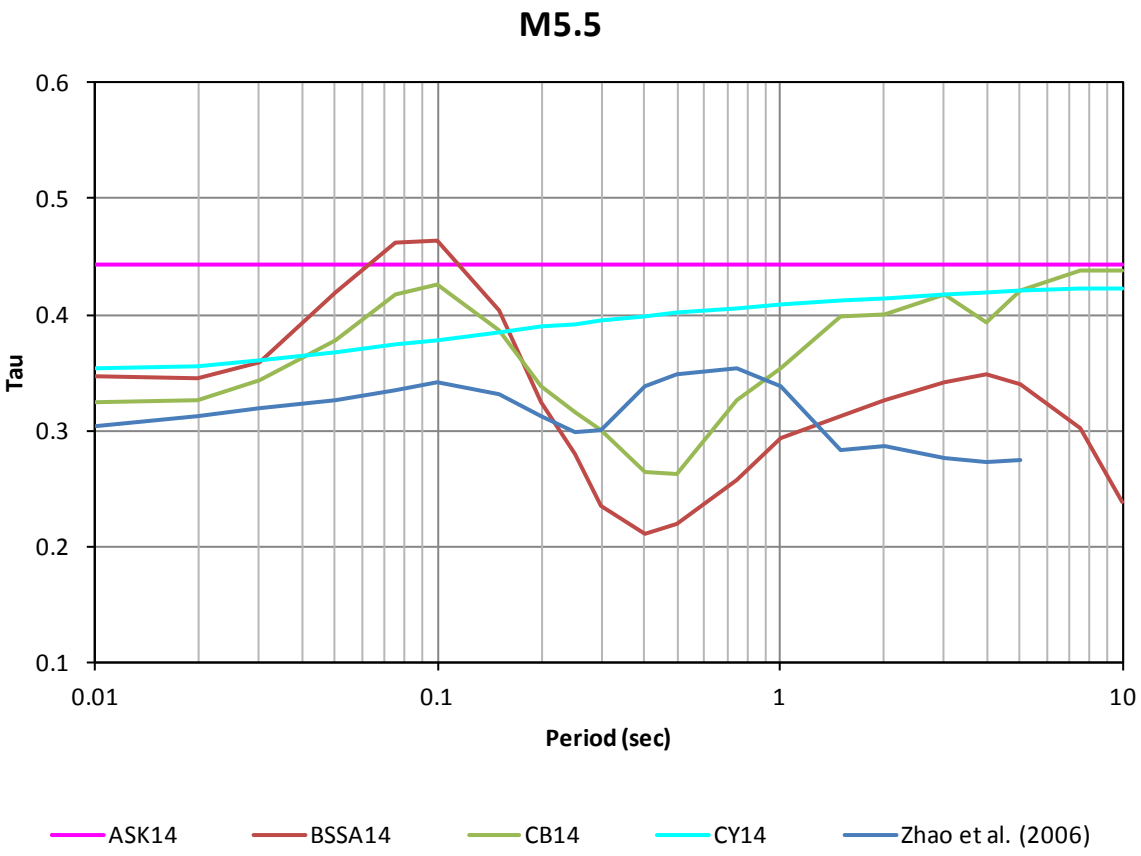

Figure 7.2.2-1: τ versus period at **M**5.5 for the candidate models.

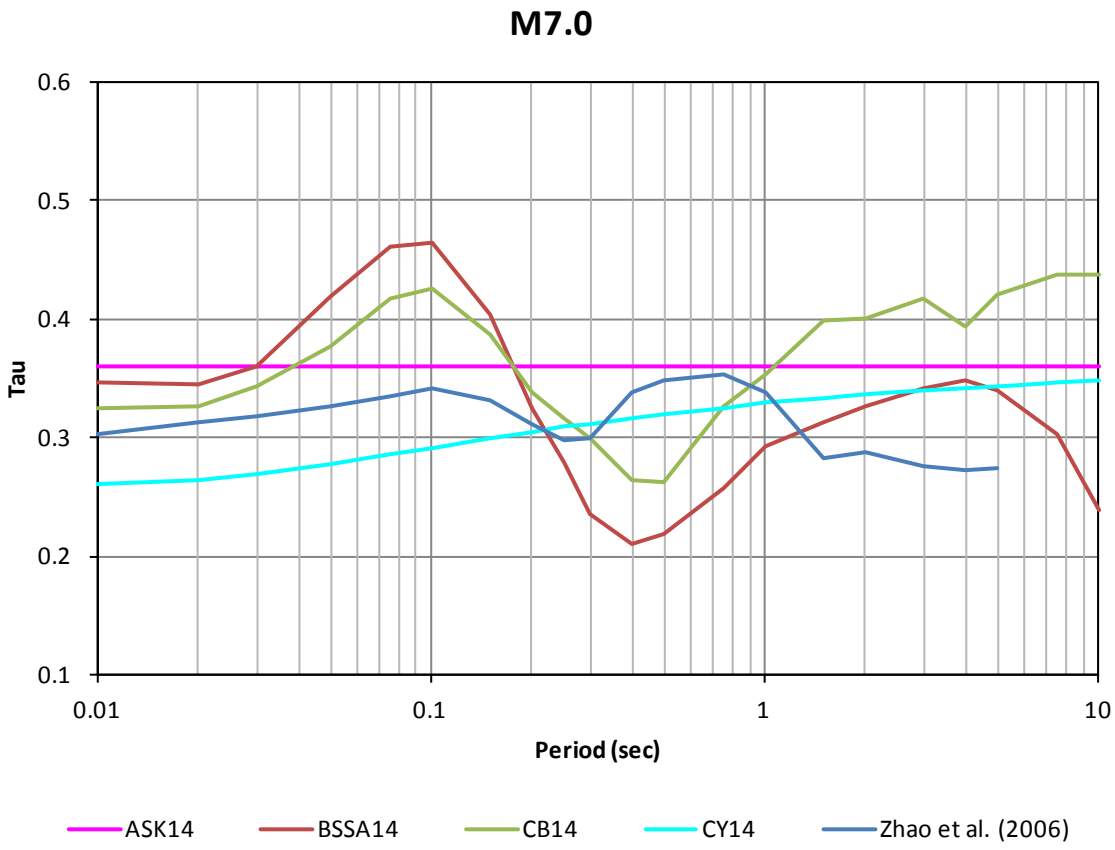

Figure 7.2.2-2: τ versus period at **M**7 for the candidate models.

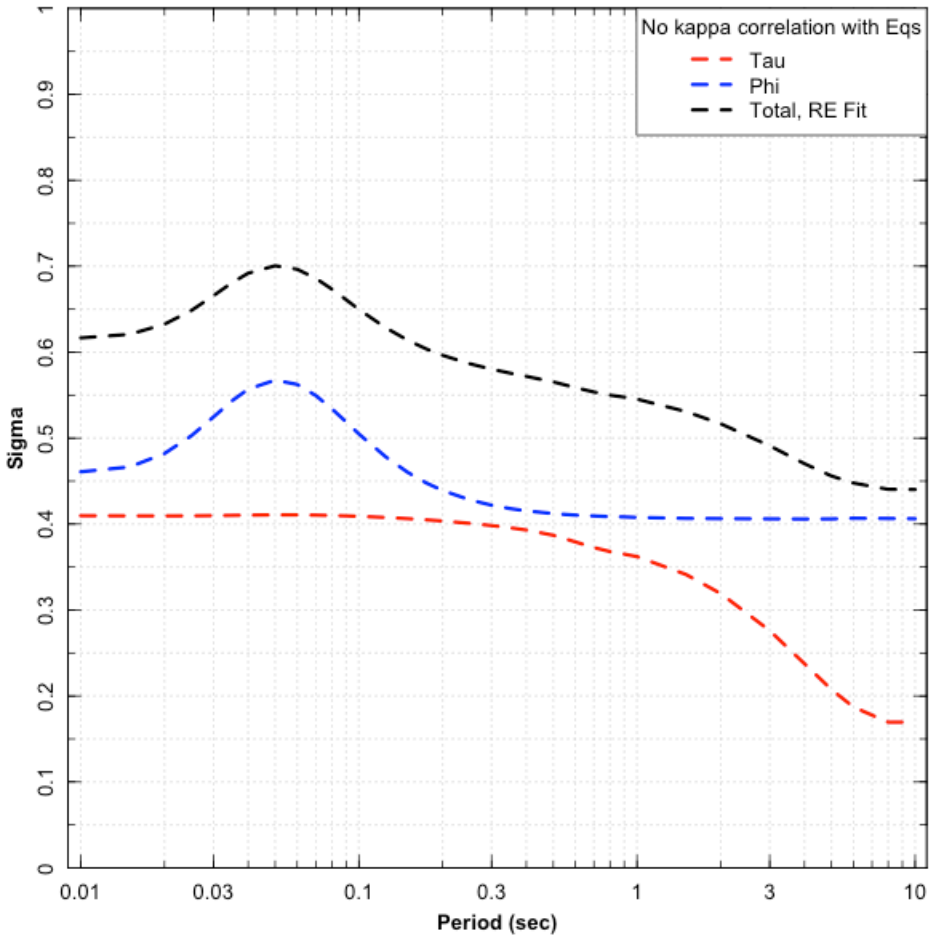

Figure 7.2.2-3: Standard deviations computed using point-source stochastic simulations with random kappa values.

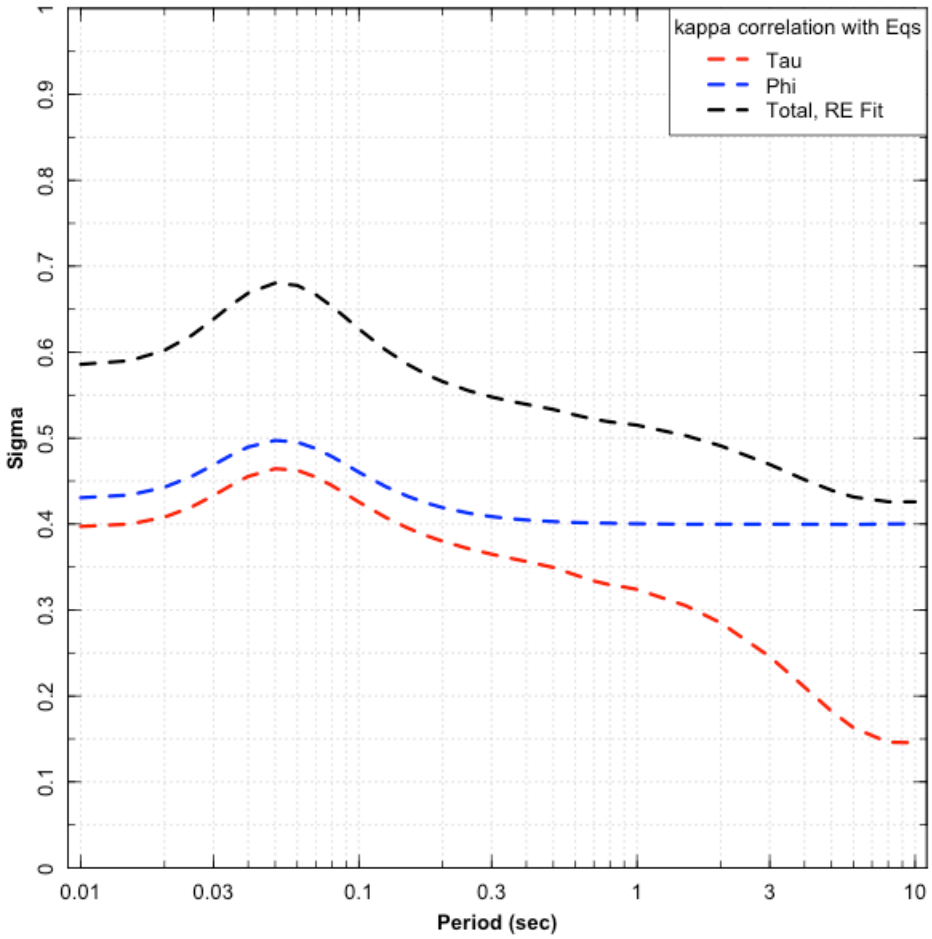

Figure 7.2.2-4: Standard deviations computed using point-source stochastic simulations with correlated kappa values.

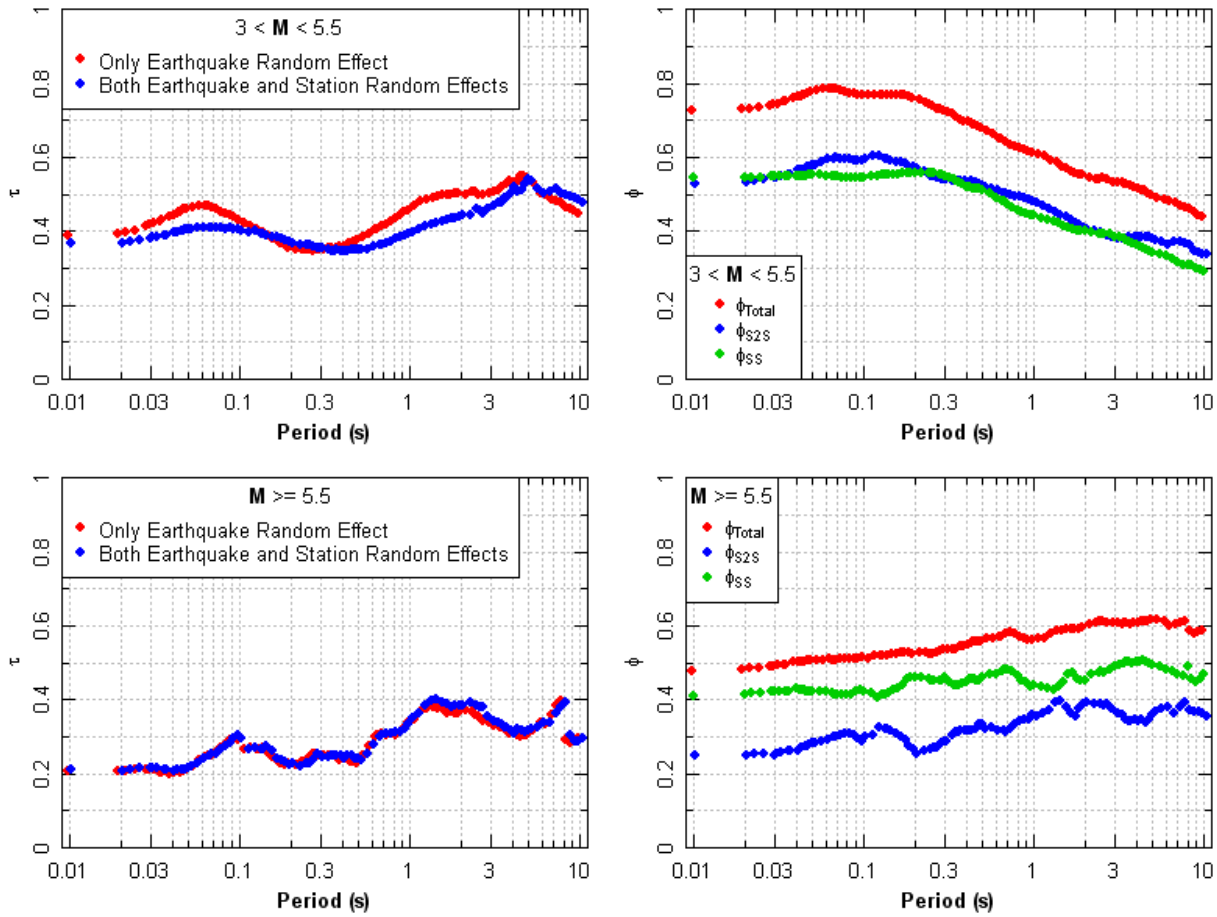

Figure 7.2.2-5: Estimates of τ and ϕ from analysis of the CY14 residuals for California data.

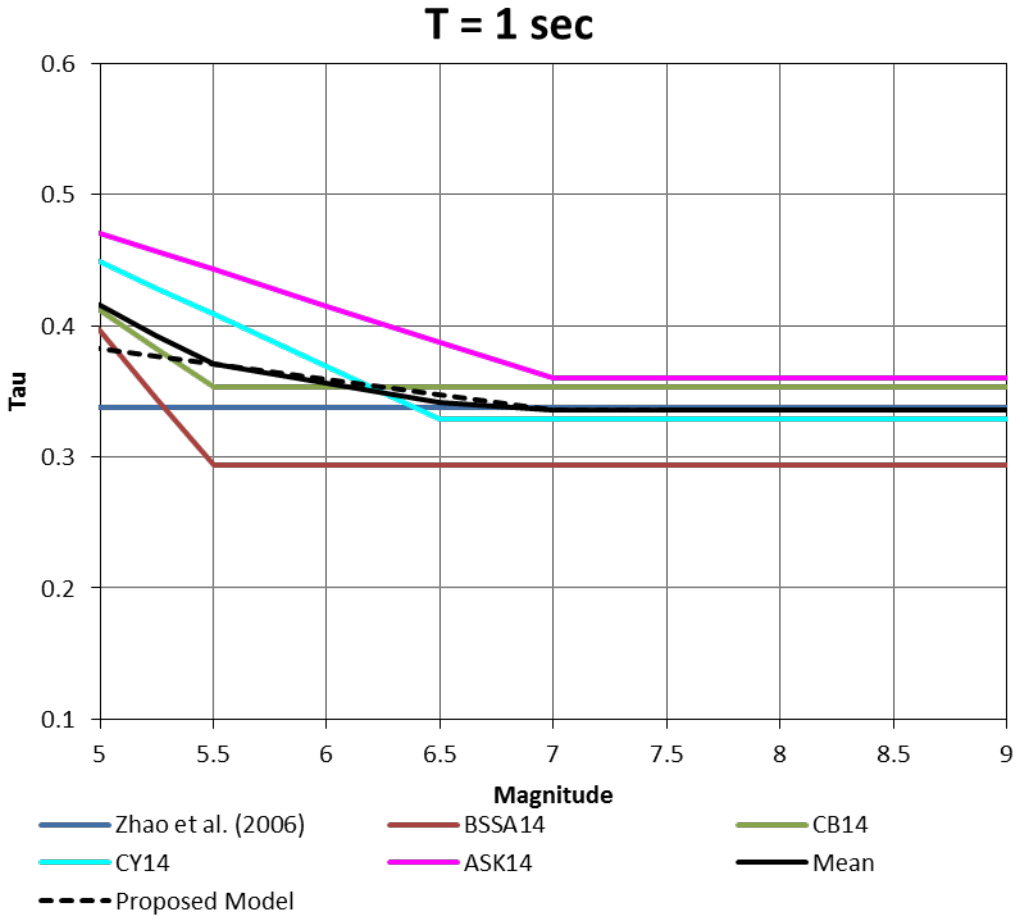

Figure 7.2.3-1: τ versus magnitude at a period of 1 sec.

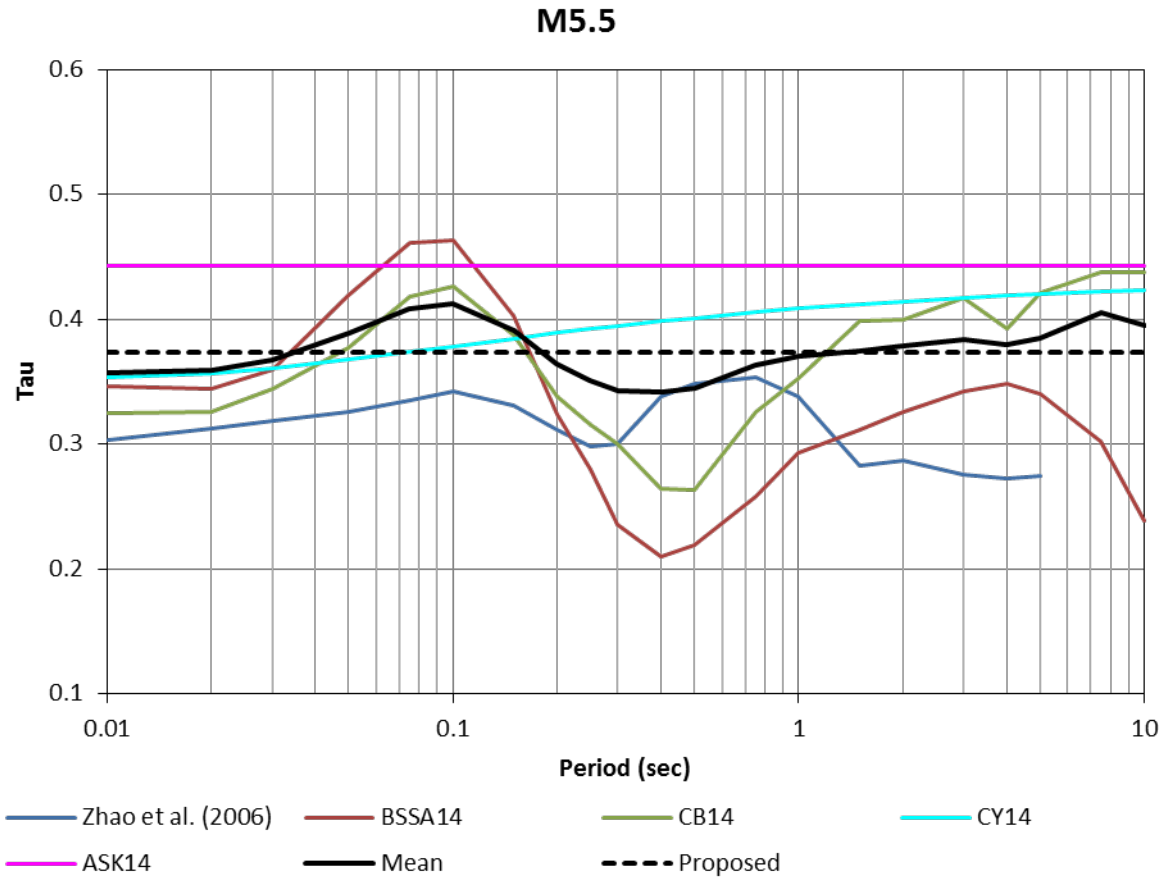

Figure 7.2.3-2: τ versus period at magnitude 5.5.

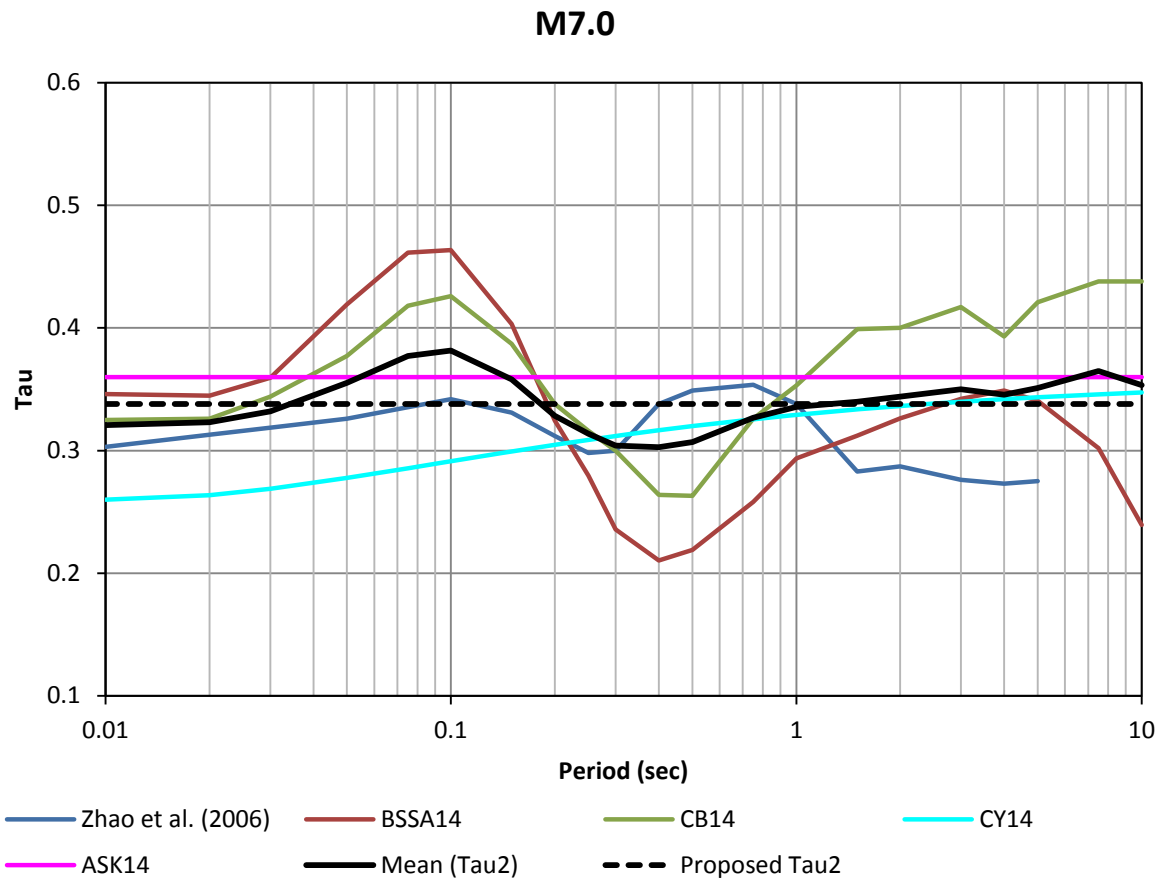

Figure 7.2.3-3: τ versus period at magnitude 7.0.

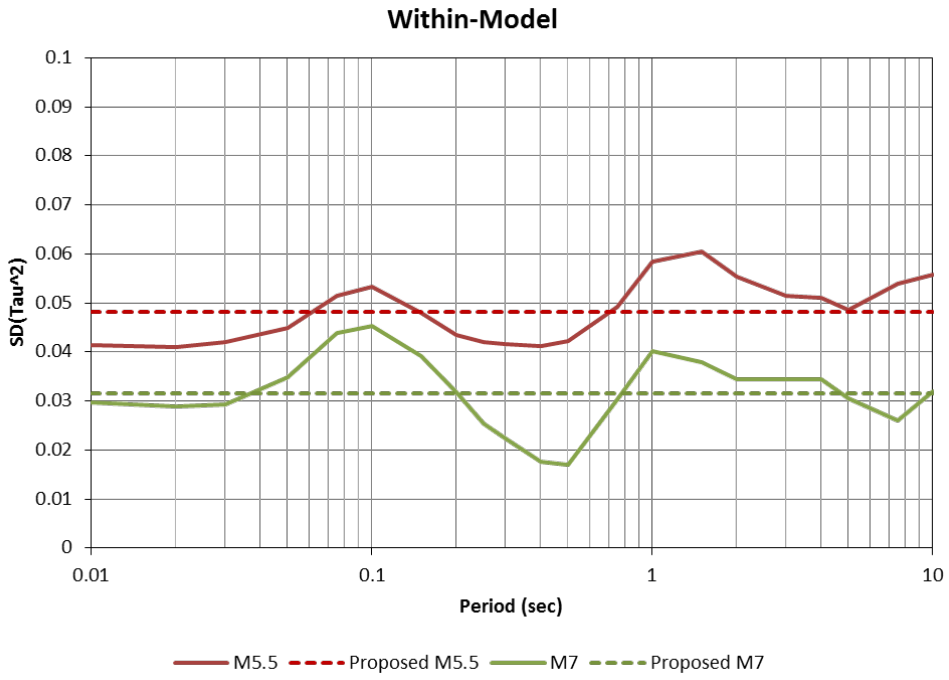

Figure 7.2.4-1: Within-model standard deviation of τ^2 at magnitude 5.5 and 7.0.

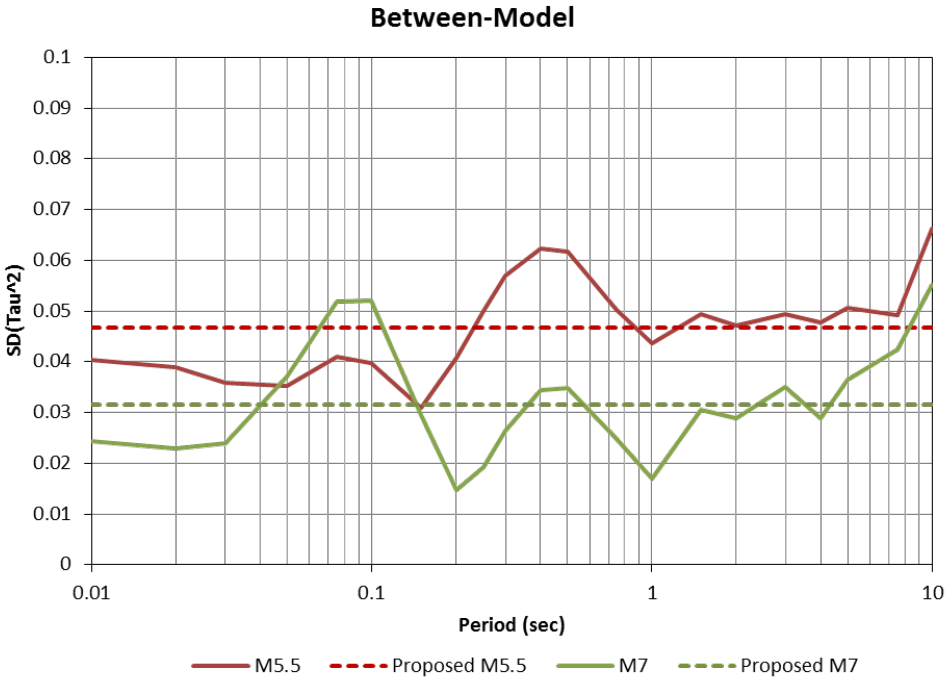

Figure 7.2.4-2: Between-model standard deviation of τ^2 at magnitude 5.5 and 7.0.

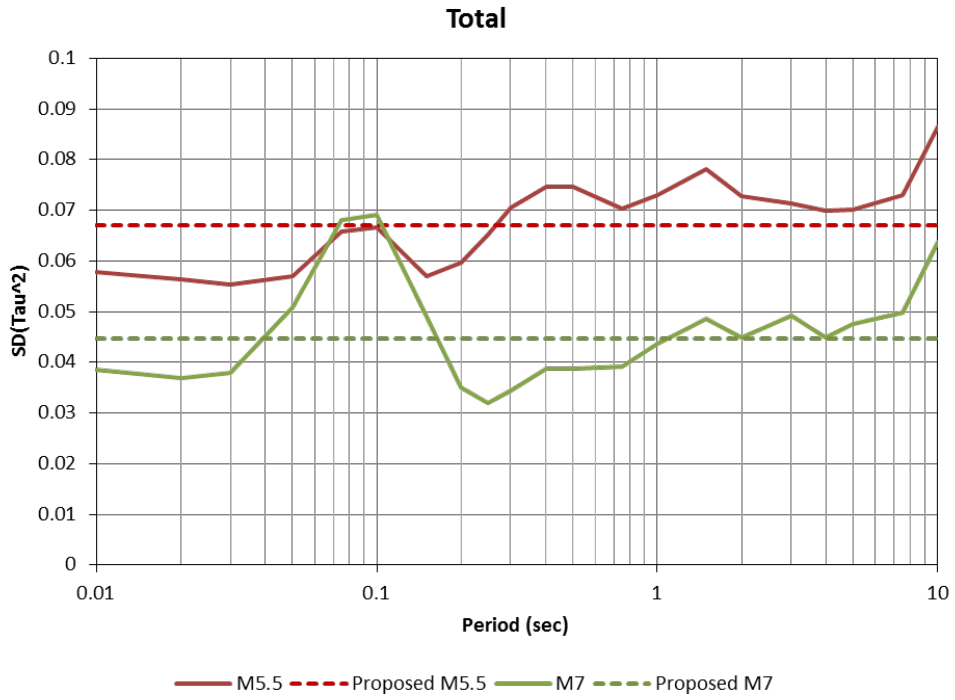

Figure 7.2.4-3: Total standard deviation of τ^2 at magnitude 5.5 and 7.0.

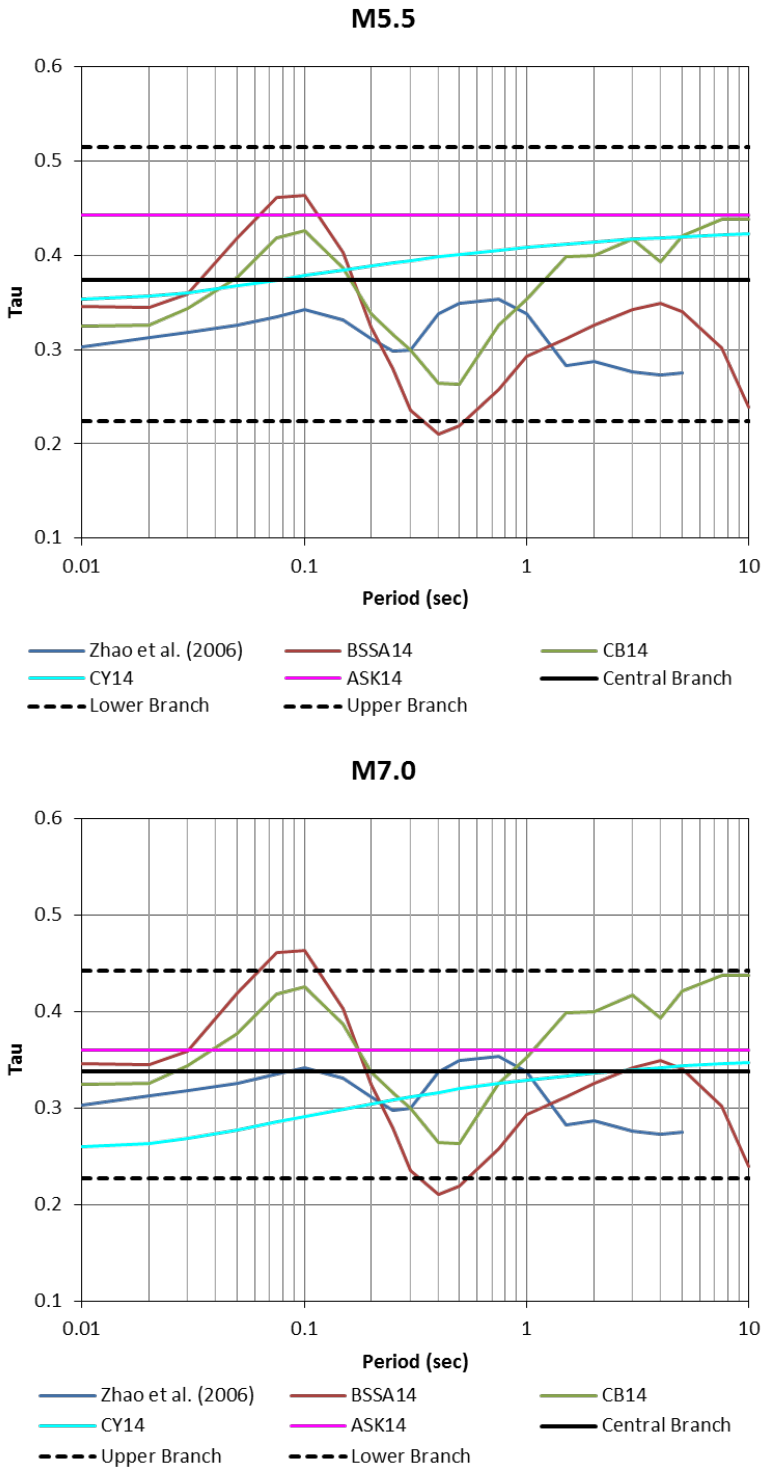

Figure 7.2.4-4: Comparison of the proposed τ model to the τ values for the five selected candidate τ models (four NGA-West2 models and Zhao et al., 2006) at magnitude 5.5 and 7.0.

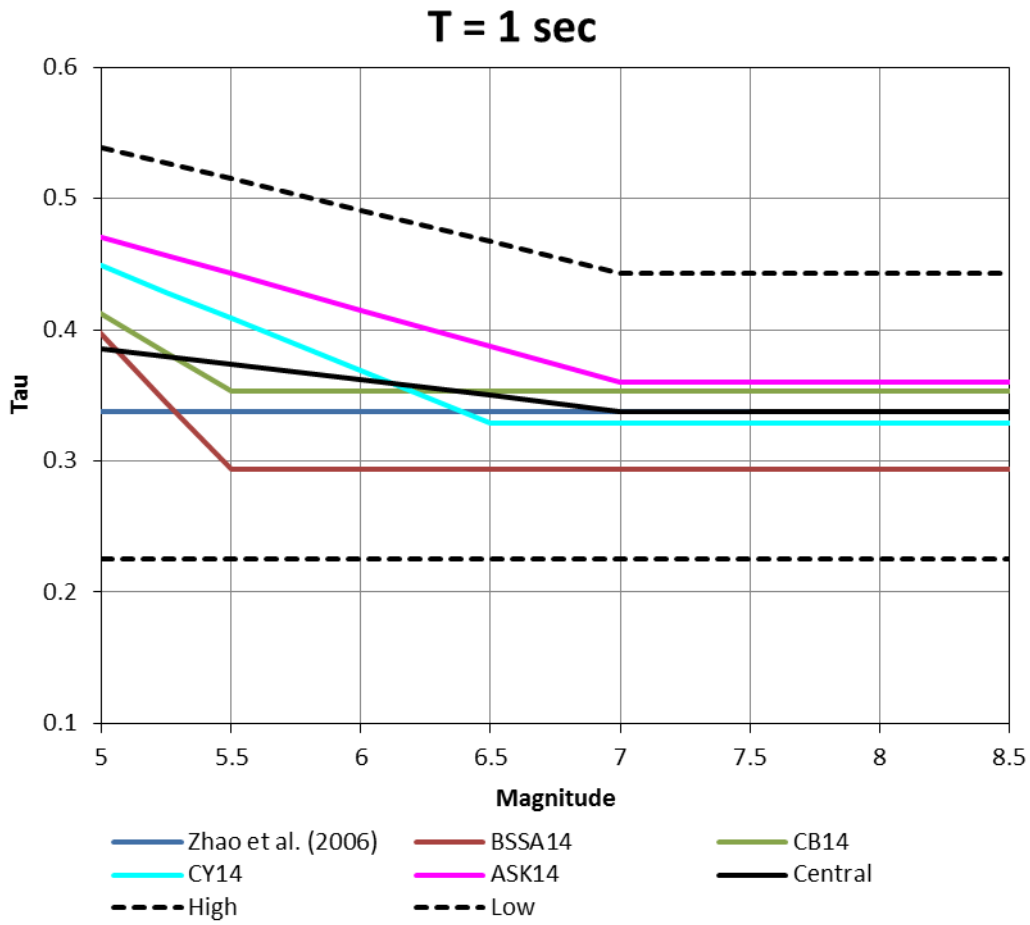

Figure 7.2.4-5: Magnitude dependence of the τ model (central, high and low branches) compared to the candidate τ models at period of 1 second.

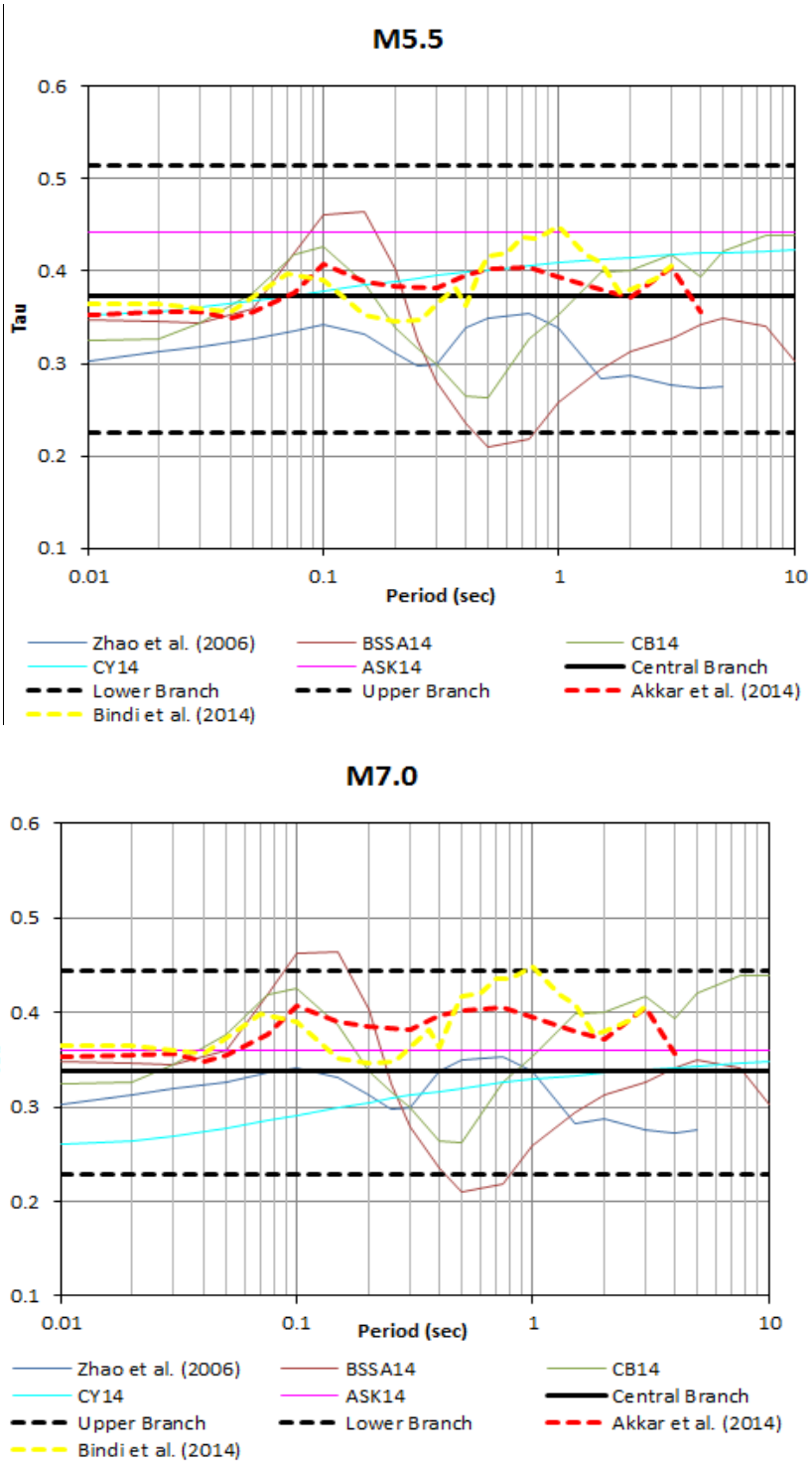

Figure 7.2.5-1: Comparison of the TI Team τ model to the τ values for the five candidate τ models used by the TI Team to derive the τ model (four NGA-West2 models and Zhao et al., 2006), and to the τ model for the Bindi et al. (2014a and 2014b) and Akkar et al. (2014a and 2014b) GMPEs, at magnitude 5.5 and 7.0.

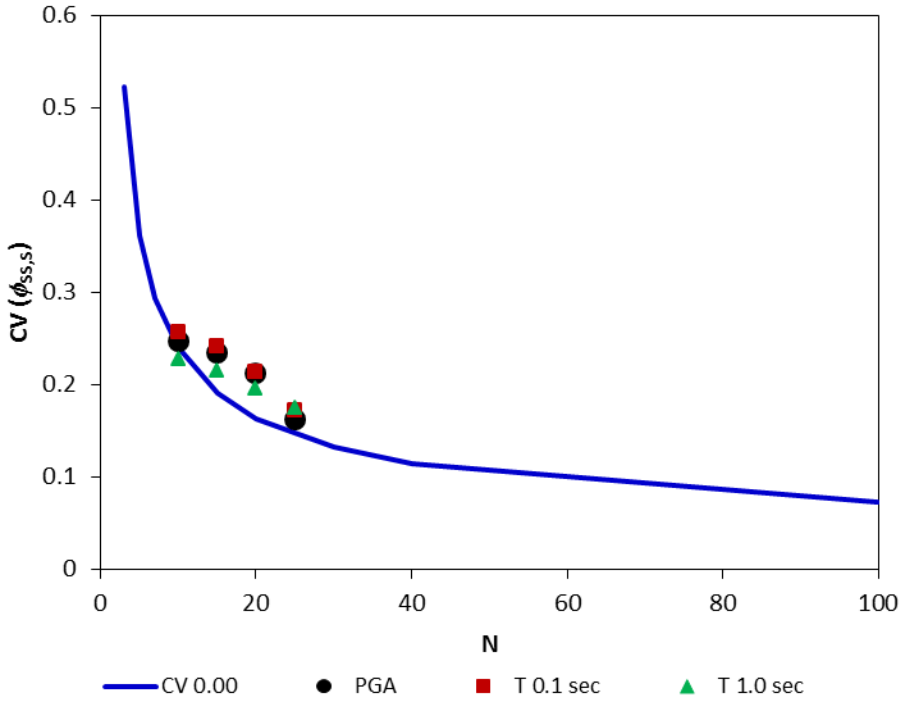

Figure 7.3.1-1: Coefficient of variation (CV) from the global dataset for stations with a minimum of 10 recordings per site (N). The blue line represent the CV for a population with CV = 0.

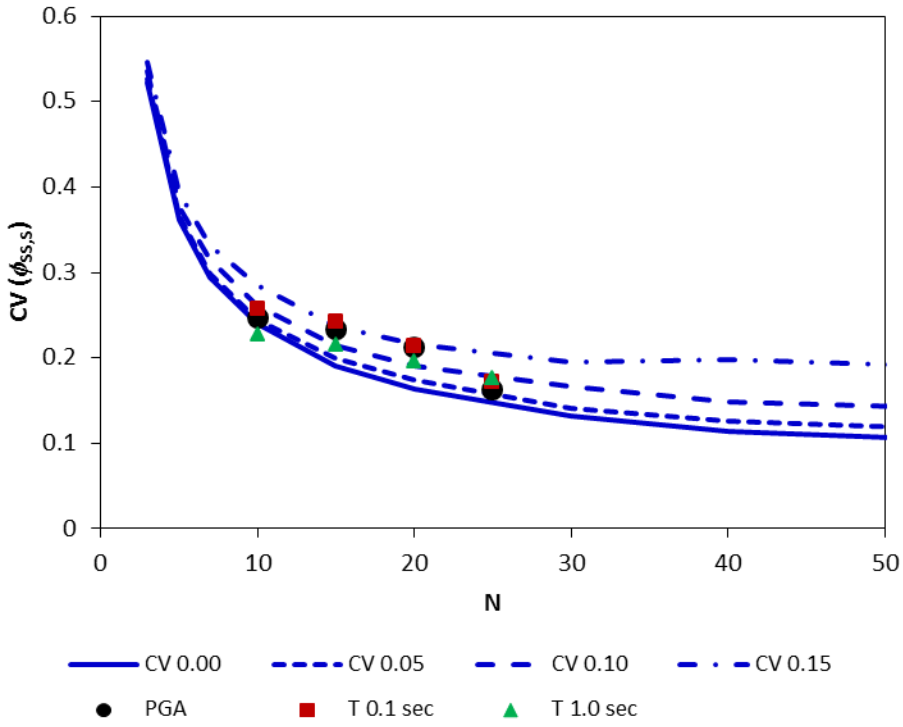

Figure 7.3.1-2: Coefficient of variation (CV) from the global dataset for stations with a minimum of 10 recordings per site (N). The blue lines represent the CV for the simulated datasets with different CV values for the population.

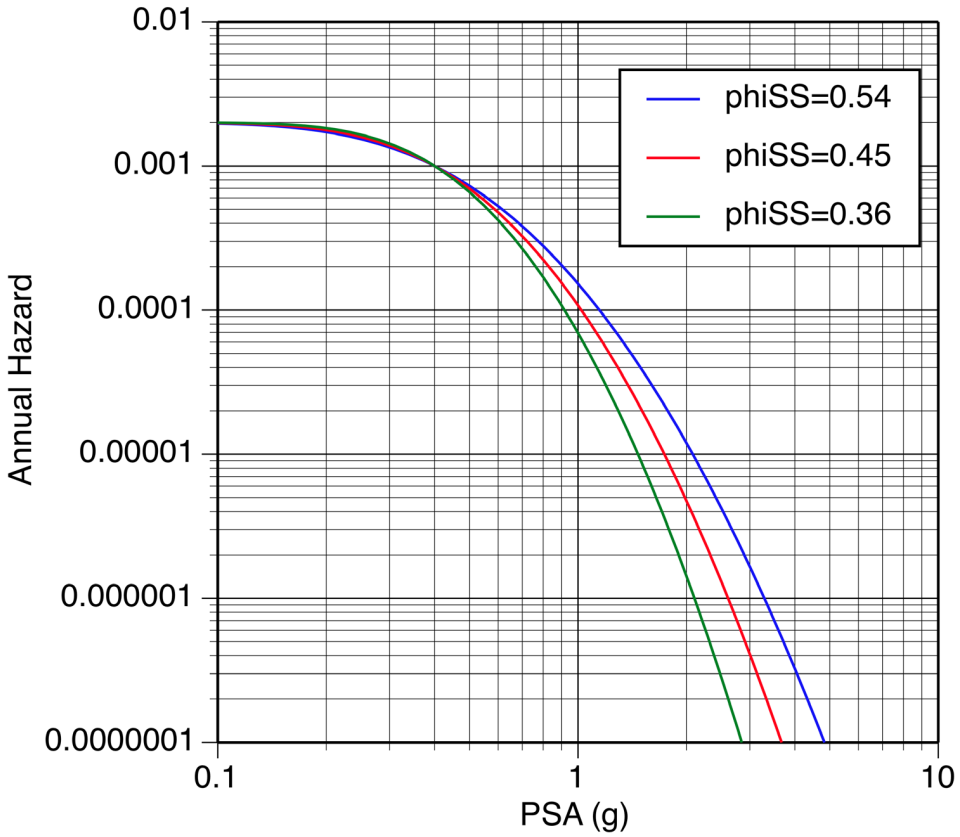

Figure 7.3.1-3: Simplified hazard example (for a **M**7 earthquake at 15 km with a recurrence interval of 500 years) showing the hazard sensitivity to the value of ϕ_{SS} .

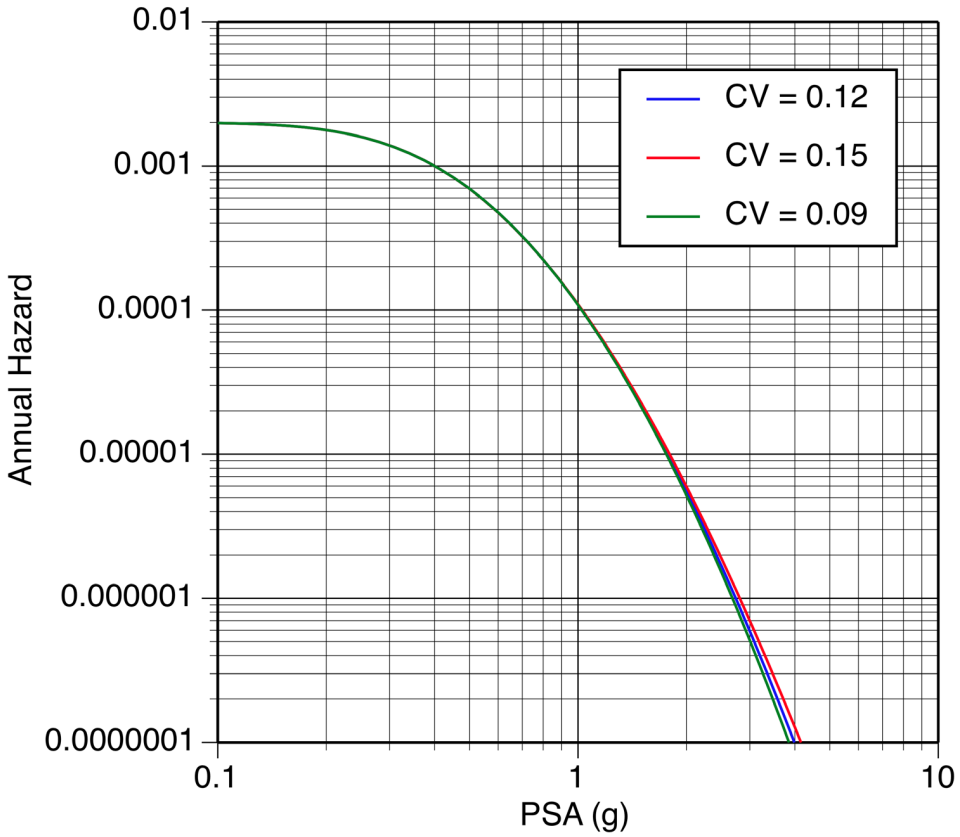

Figure 7.3.1-4: Simplified hazard example (for a **M**7 earthquake at 15 km with a recurrence interval of 500 years) showing the hazard sensitivity to the CV value of ϕ_{SS} .

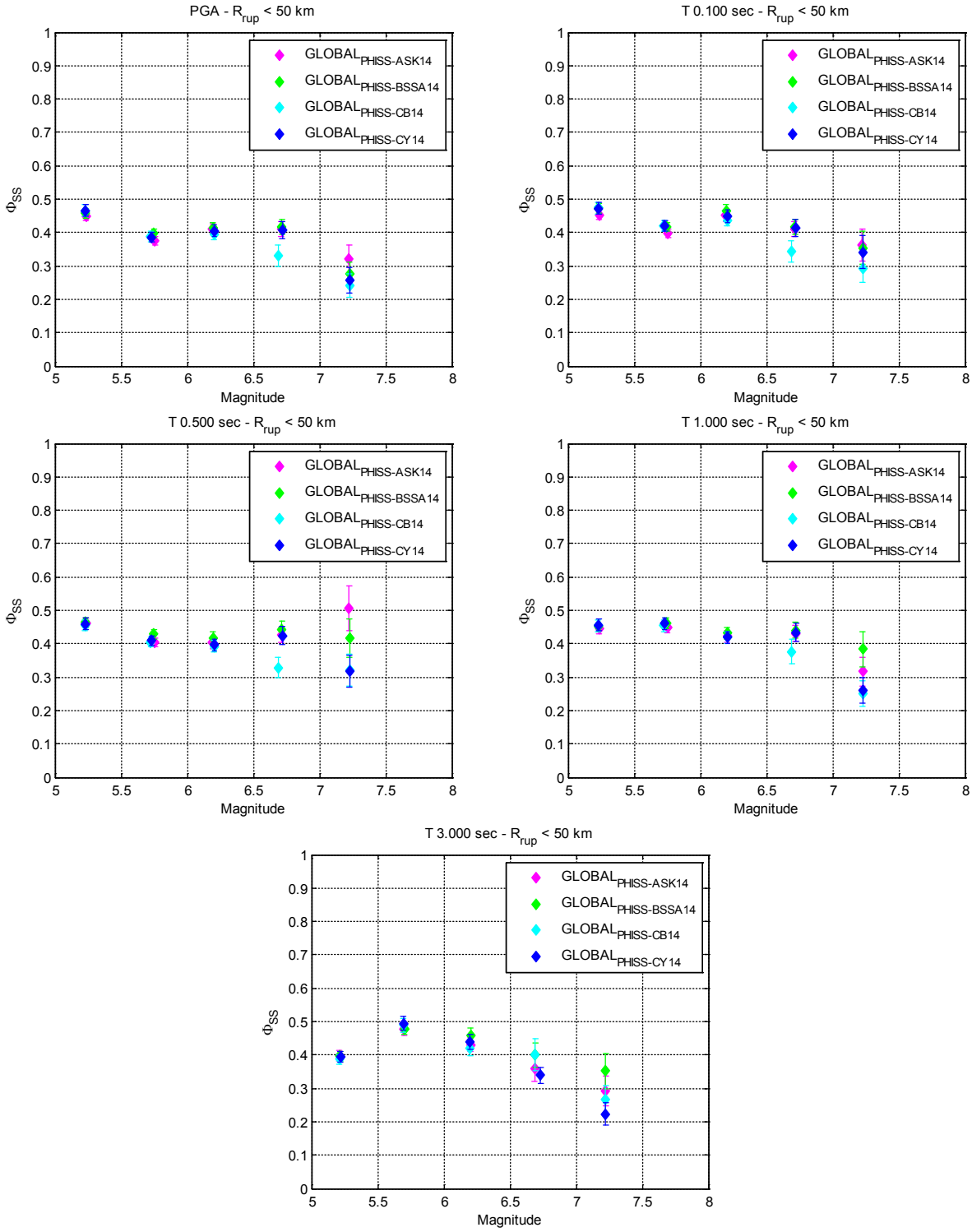

Figure 7.3.2-1: Magnitude-binned ϕ_{SS} values calculated at PGA and spectral periods of 0.1, 0.5, 1.0, and 3.0 sec for the four subsets of global datasets ($GLOBAL_{PHISS\text{-}ASK14}$, $GLOBAL_{PHISS\text{-}BSSA14}$, $GLOBAL_{PHISS\text{-}CY14}$ and $GLOBAL_{PHISS\text{-}CB14}$). The error bars show ± 1 standard error of the empirical estimates.

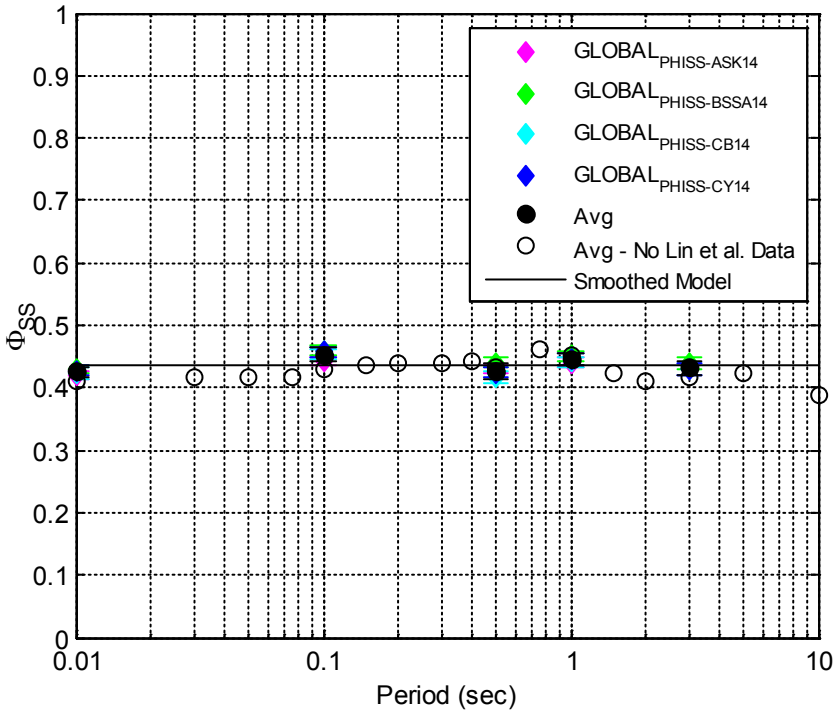

Figure 7.3.2-2: Magnitude-independent $\phi_{SS-GLOBAL-R50}$ values calculated using the four global sub sets ($GLOBAL_{PHISS\text{-}ASK14}$, $GLOBAL_{PHISS\text{-}BSSA14}$, $GLOBAL_{PHISS\text{-}CY14}$ and $GLOBAL_{PHISS\text{-}CB14}$) and proposed central branch. The average values including the Lin et al. (2011) data set are shown for the available periods. The error bars show ± 1 standard error of the empirical estimates.

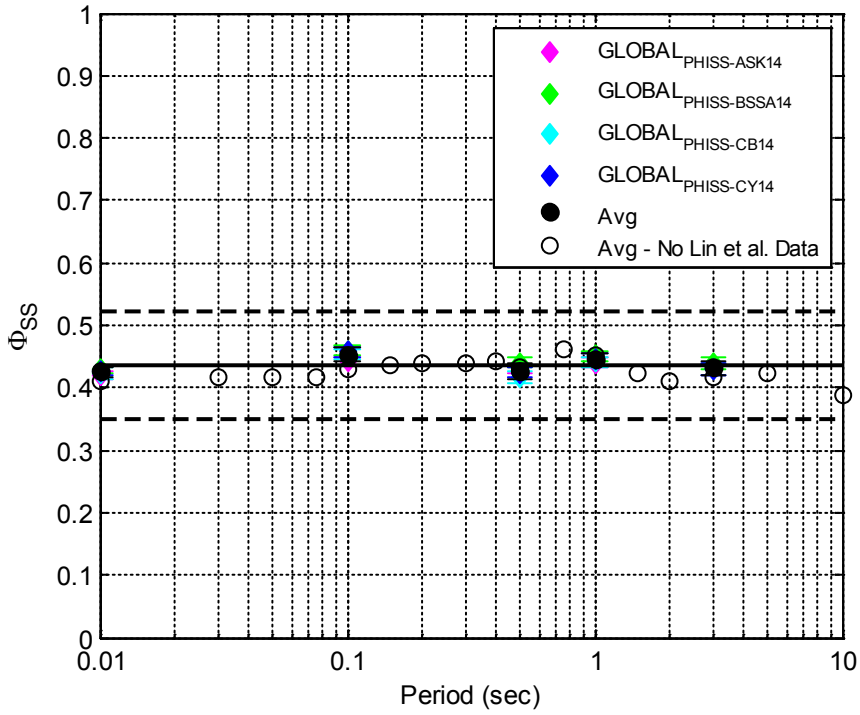

Figure 7.3.2-3: Central, high and low branches of the magnitude-independent $\phi_{SS-GLOBAL-R50}$ model calculated using the four global sub sets ($GLOBAL_{PHISS\text{-}ASK14}$, $GLOBAL_{PHISS\text{-}BSSA14}$, $GLOBAL_{PHISS\text{-}CY14}$ and $GLOBAL_{PHISS\text{-}CB14}$). The average values including the Lin et al. (2011) data set are shown for the available periods. The error bars show ± 1 standard error of the empirical estimates.

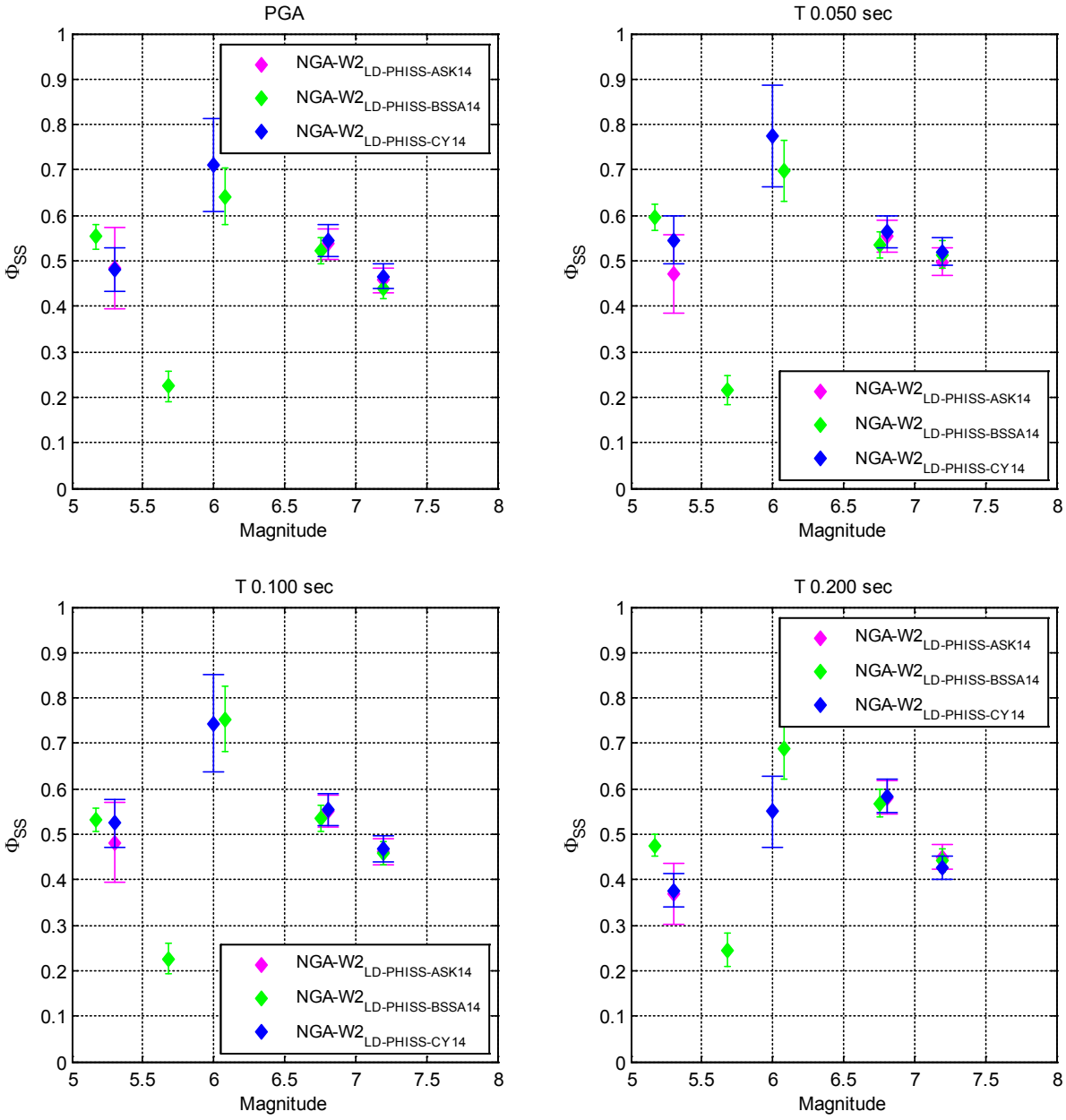

Figure 7.3.2-4a: Magnitude-binned ϕ_{SS} values calculated at PGA and spectral periods of 0.05, 0.1, and 0.2 sec for three subsets of global datasets for long distance (NGA-W2$_{\text{LD-PHISS-ASK14}}$, NGA-W2$_{\text{LD-PHISS-BSSA14}}$, and NGA-W2$_{\text{LD-PHISS-CY14}}$). The error bars show ± 1 standard error of the empirical estimates.

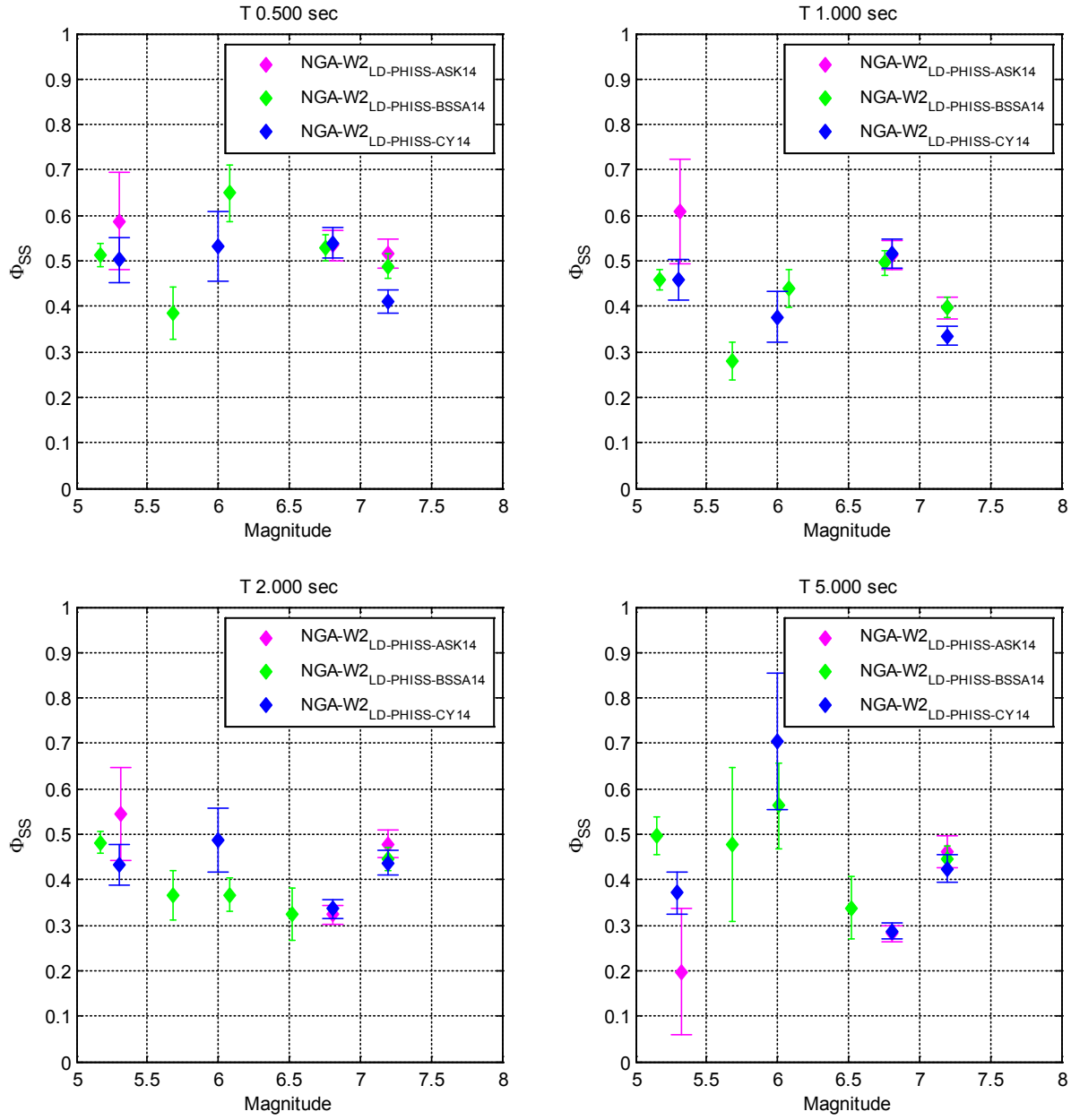

Figure 7.3.2-4b: Magnitude-binned ϕ_{SS} values calculated at spectral periods of 0.5, 1.0, 2.0 and 5.0 sec for three subsets of global datasets for long distance (NGA-W2$_{\text{LD-PHISS-ASK14}}$, NGA-W2$_{\text{LD-PHISS-BSSA14}}$, and NGA-W2$_{\text{LD-PHISS-CY14}}$). The error bars show ± 1 standard error of the empirical estimates.

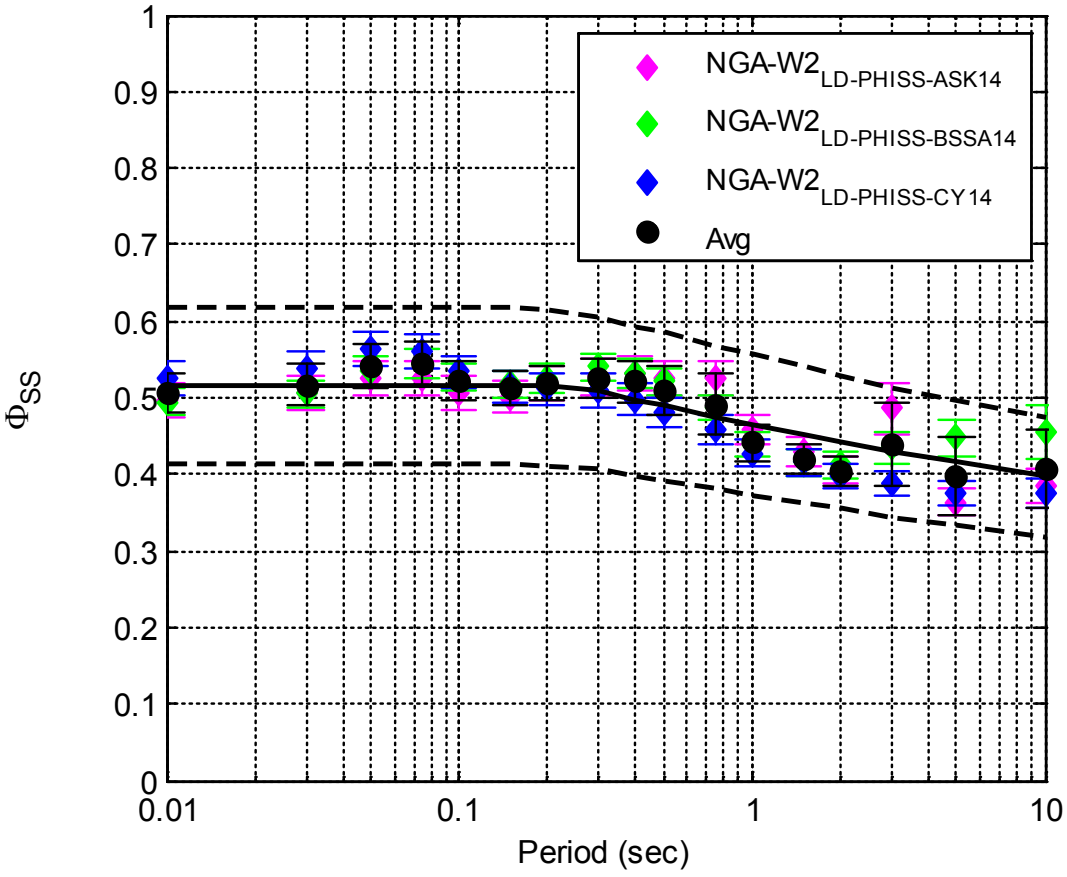

Figure 7.3.2-5: Central, high and low branches (in black) of the magnitude-independent $\phi_{SS-GLOBAL-LD}$ model for PVNGS for California and Mexico sources located in Regions 1, 2, and 3 calculated using the global dataset for long distance (NGA-W2$_{\text{LD-PHISS-ASK14}}$, NGA-W2$_{\text{LD-PHISS-BSSA14}}$, and NGA-W2$_{\text{LD-PHISS-CY14}}$). The error bars show ± 1 standard error of the empirical estimates.

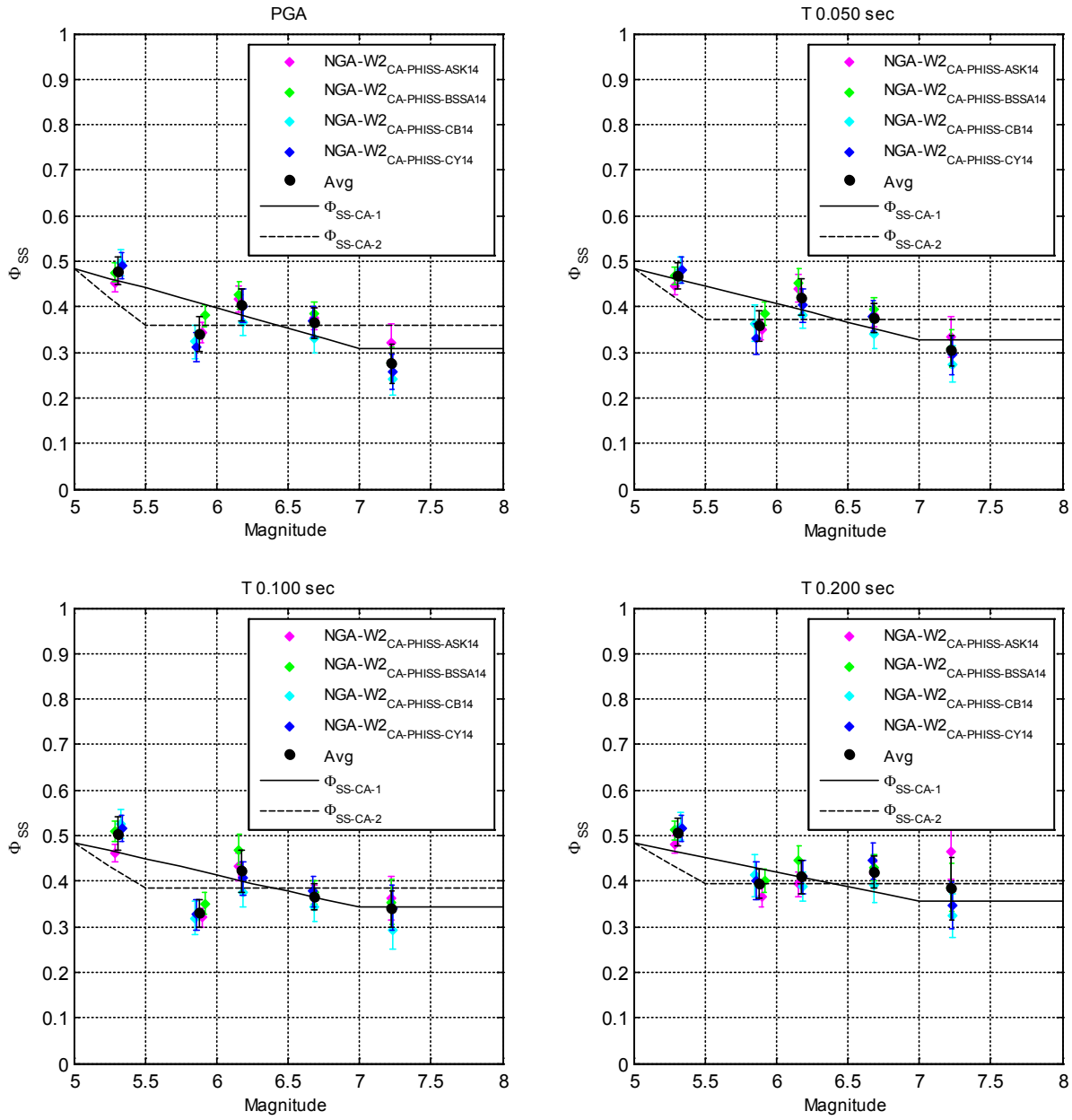

Figure 7.3.3-1a: Magnitude-binned ϕ_{SS} values calculated for PGA and at spectral periods of 0.05, 0.1, and 0.2 sec for four subsets of NGA-West2 California datasets (NGA-W2$_{\text{CA-PHISS-ASK14}}$, NGA-W2$_{\text{CA-PHISS-BSSA14}}$, NGA-W2$_{\text{CA-PHISS-CY14}}$, and NGA-W2$_{\text{CA-PHISS-CY14}}$). The solid and dashed line show the two alternative ϕ_{SS} models based on California data. The error bars show ± 1 standard error of the empirical estimates.

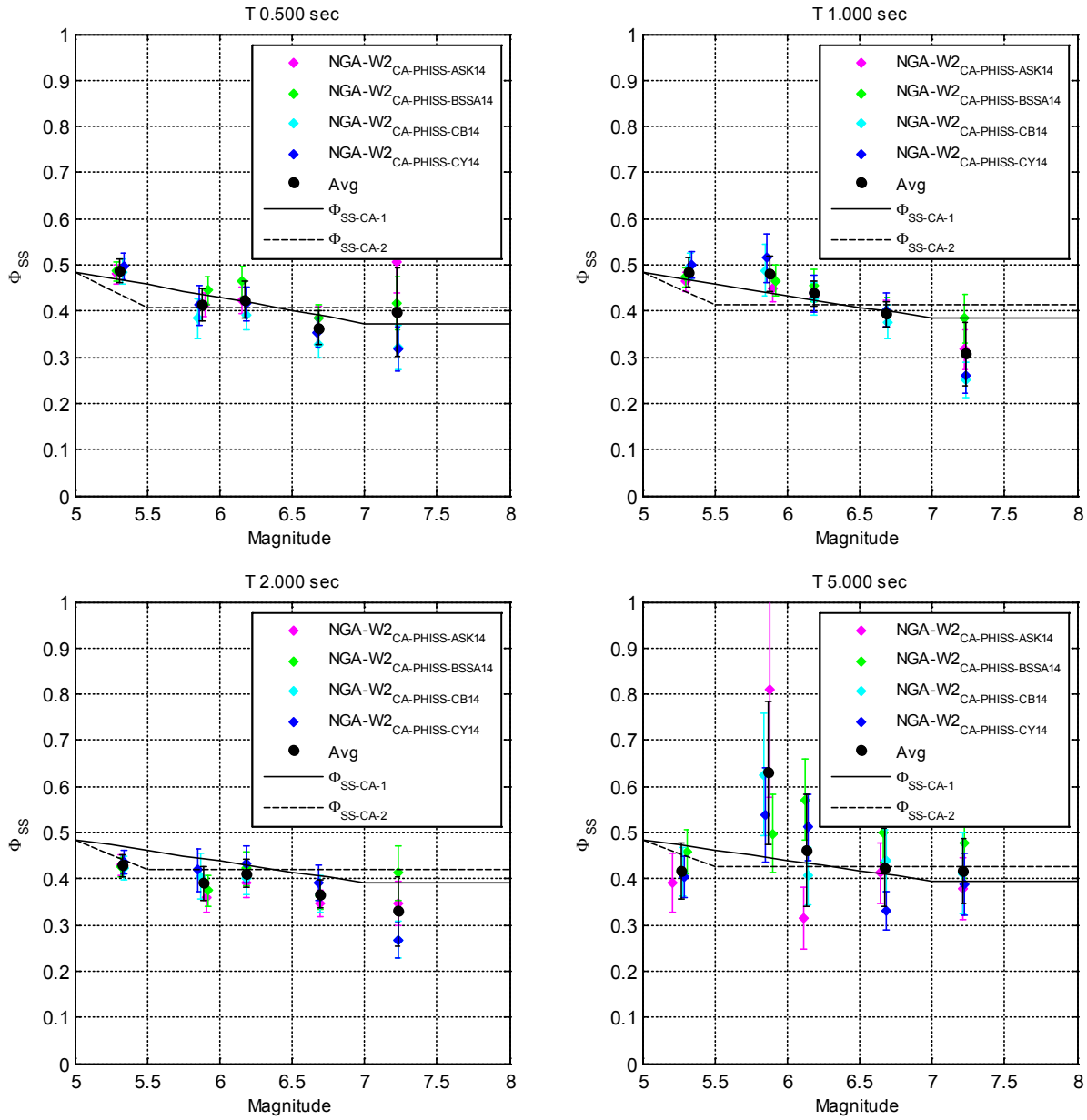

Figure 7.3.3-1b: Magnitude-binned ϕ_{SS} values calculated at spectral periods of 0.5, 1.0, 2.0 and 5.0 sec for four subsets of NGA-West2 California datasets (NGA-W2$_{CA\text{-}PHISS\text{-}ASK14}$, NGA-W2$_{CA\text{-}PHISS\text{-}BSSA14}$, NGA-W2$_{CA\text{-}PHISS\text{-}CY14}$, and NGA-W2$_{CA\text{-}PHISS\text{-}CY14}$). The solid and dashed line show the two alternative ϕ_{SS} models based on California data. The error bars show ± 1 standard error of the empirical estimates.

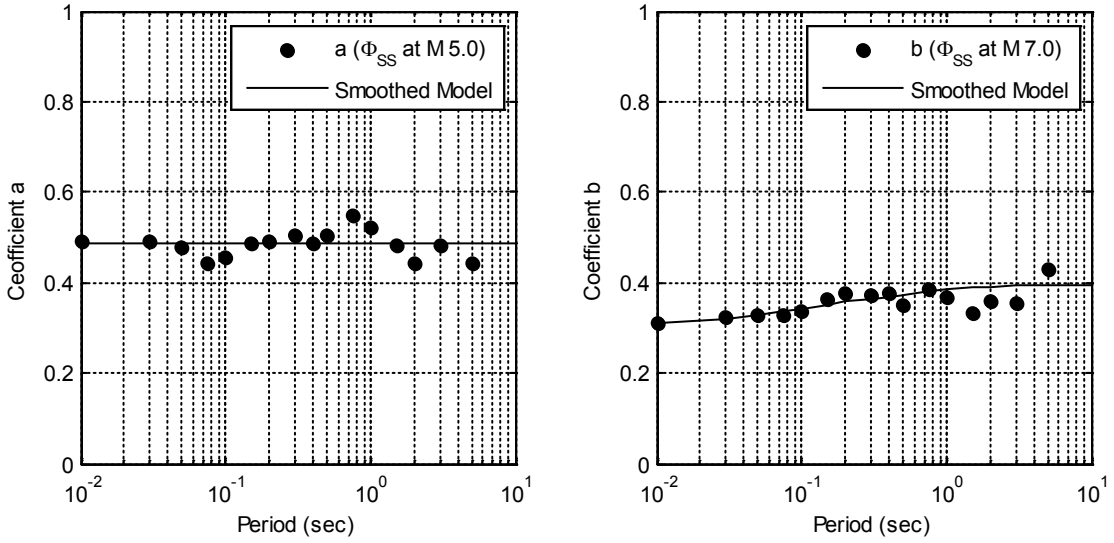

Figure 7.3.3-2: Fit to the coefficients a(T) and b(T) for the central magnitude-dependent $\phi_{SS-CA-1}$ model

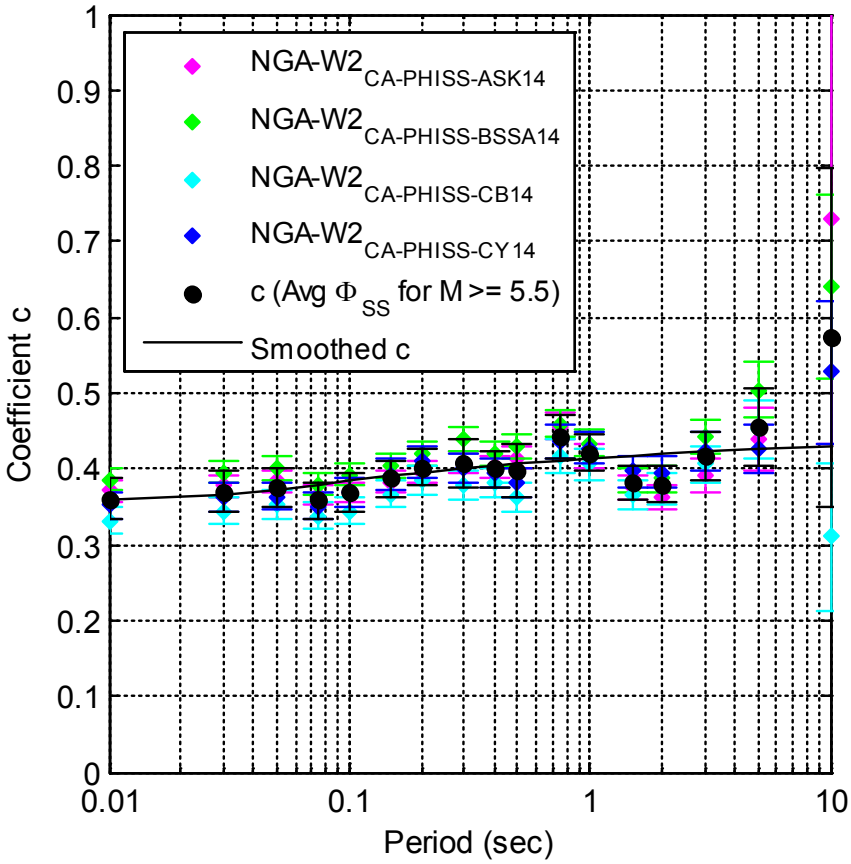

Figure 7.3.3-3: Fit to the coefficient c(T) for the central magnitude-dependent $\phi_{SS-CA-2}$ model. The error bars show ± 1 standard error of the empirical estimates.

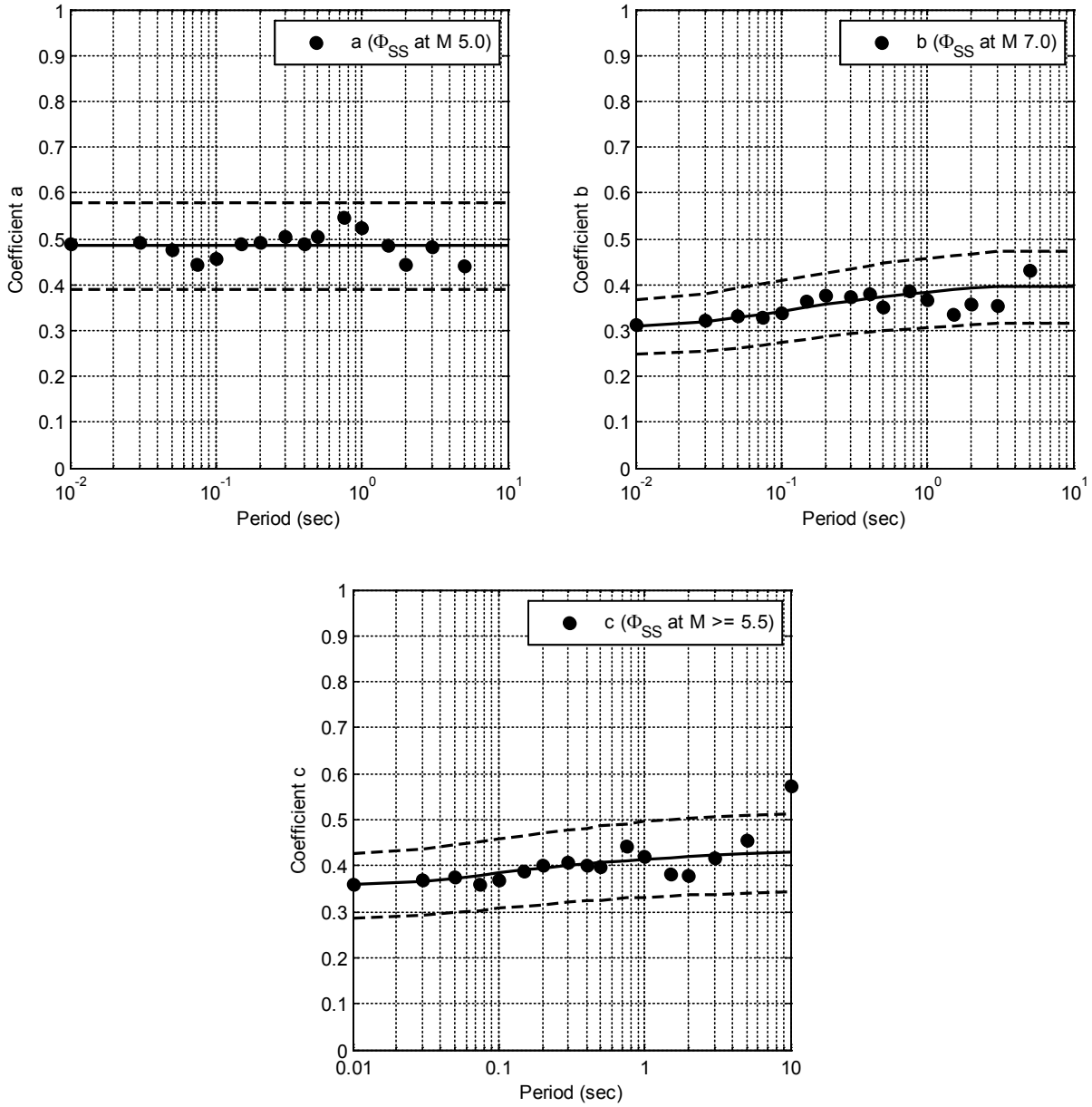

Figure 7.3.3-4: Central, high and low coefficients for the $\phi_{SS-CA-1}$ and $\phi_{SS-CA-2}$ models.

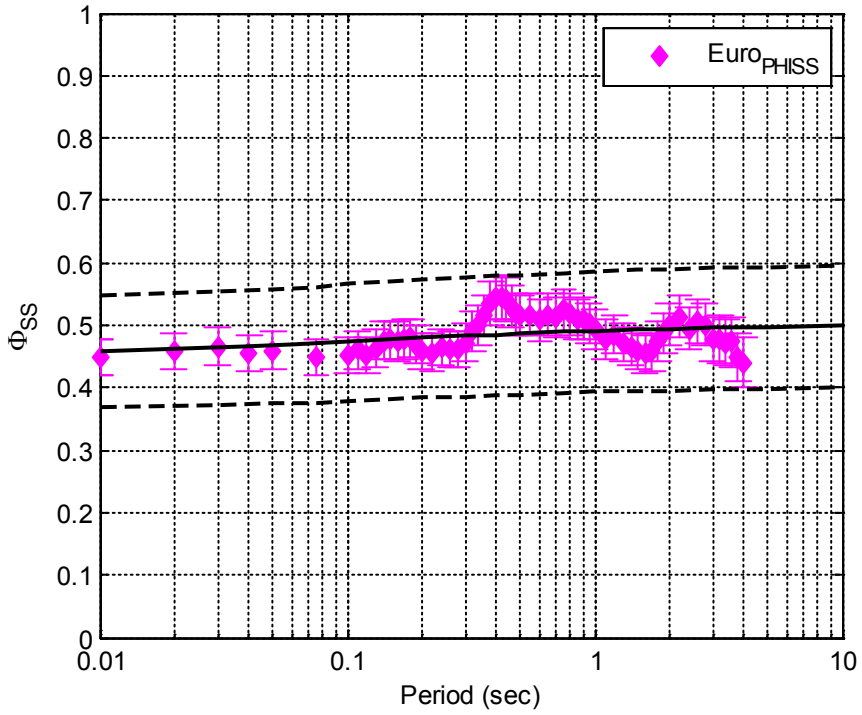

Figure 7.3.4-1: Central, high and low branches (in black) for the magnitude-independent ϕ_{SS-EUR} model using the European dataset (EUR_{PHISS}) compared to the values used to derive the central model. The error bars show ± 1 standard error of the empirical estimates.

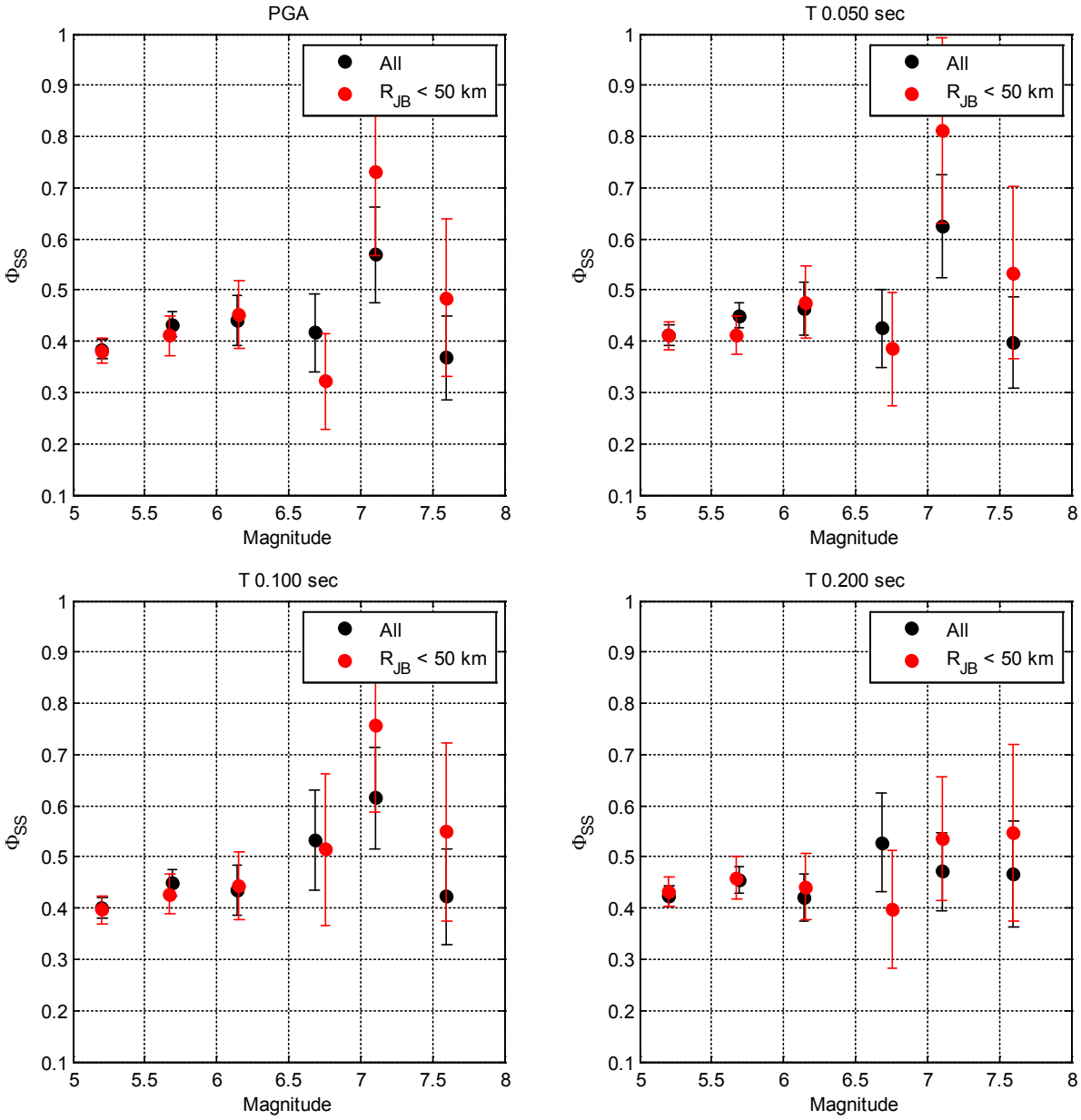

Figure 7.3.4-2a: Magnitude-binned ϕ_{SS} values calculated for PGA and at spectral periods of 0.05, 0.1, and 0.2 sec for the subset of European dataset (EUR_{PHISS}). Values are shown for the entire dataset (black) and for the data with maximum distance of 50km (red). The error bars show ± 1 standard error of the empirical estimates.

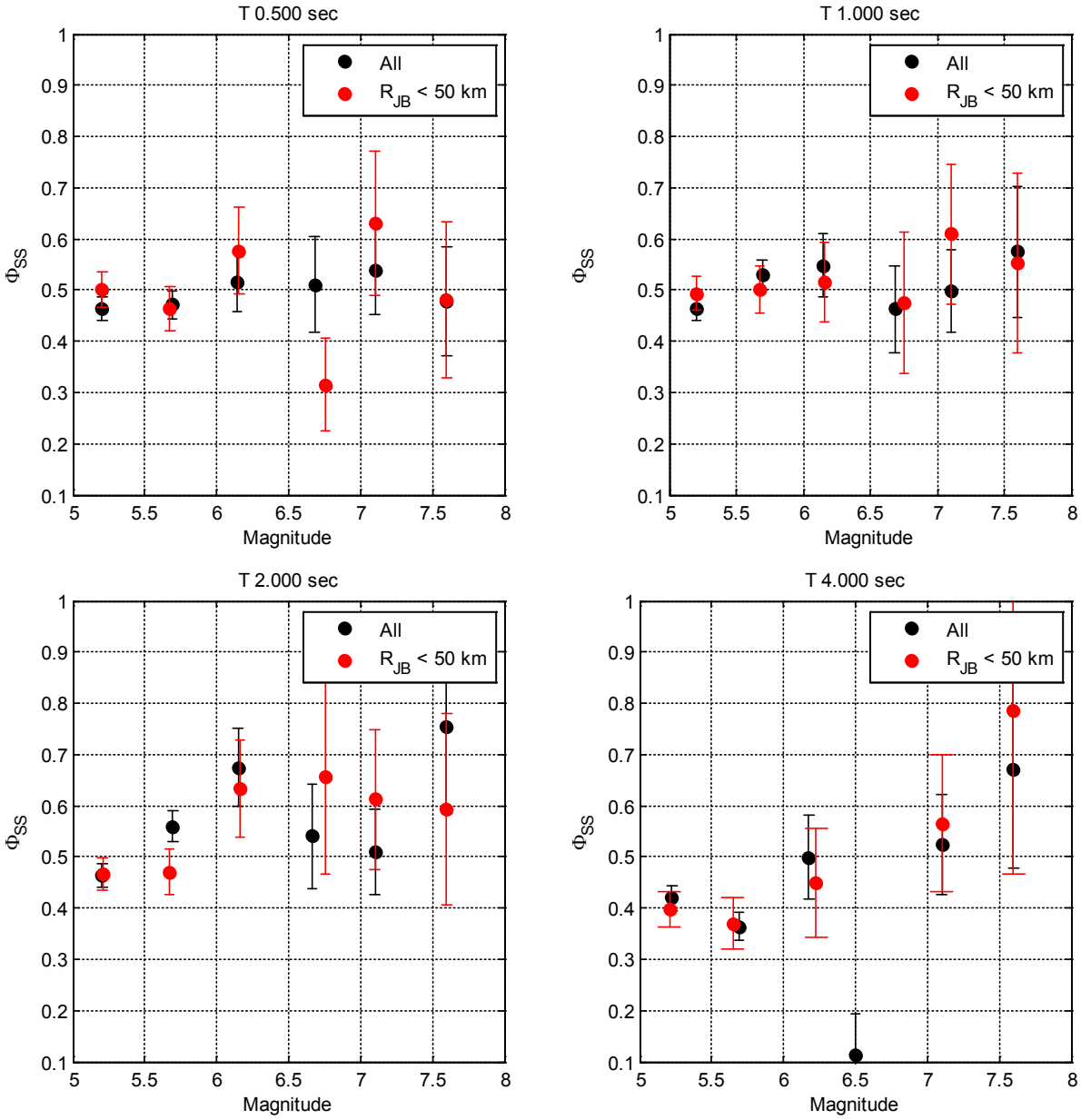

Figure 7.3.4-2b: Magnitude-binned ϕ_{SS} values calculated at spectral periods of 0.5, 1.0, 2.0 and 4.0 sec for the subset of European dataset (EUR_{PHISS}). Values are shown for the entire dataset (black) and for the data with maximum distance of 50km (red). The error bars show ± 1 standard error of the empirical estimates.

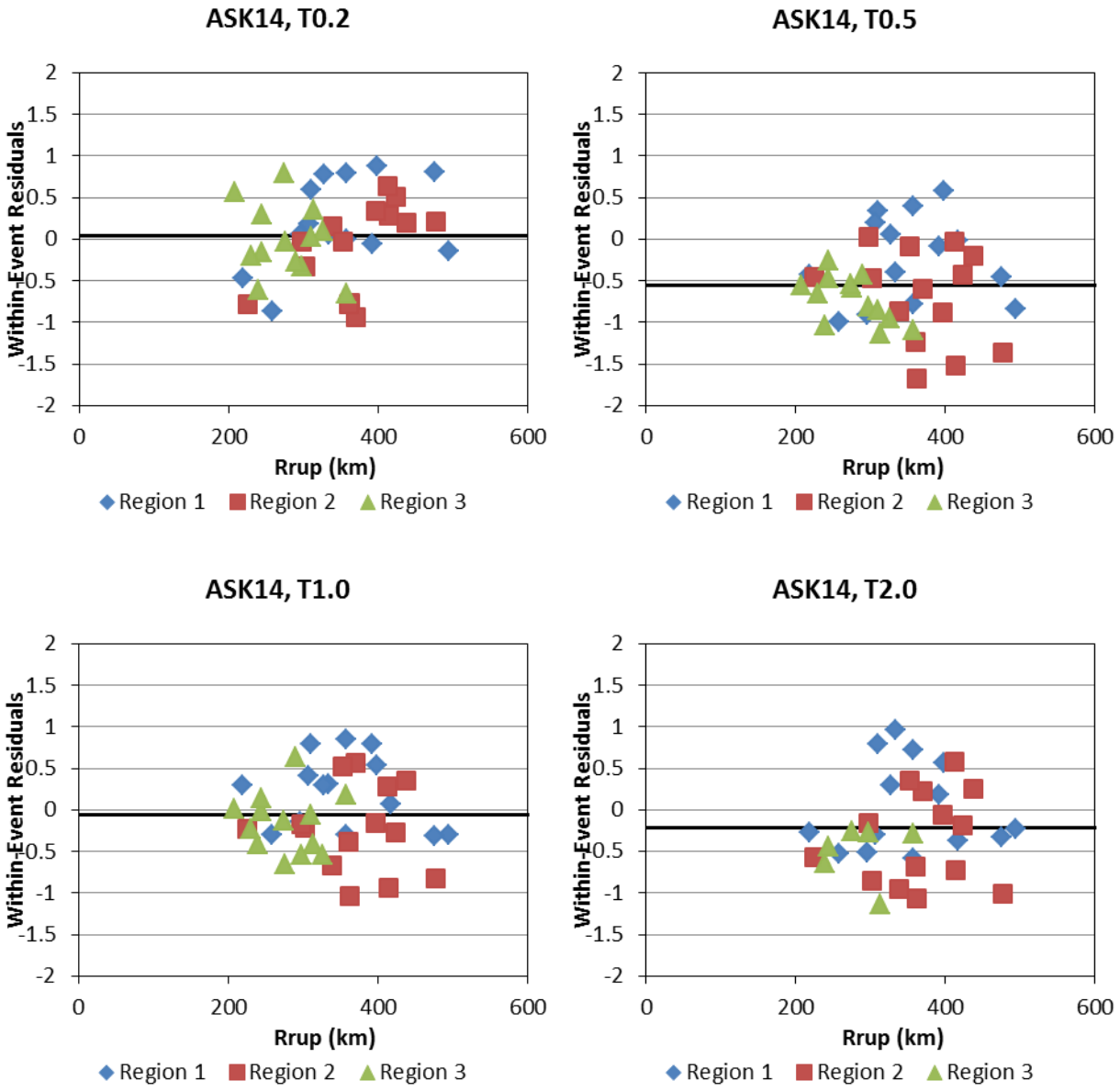

Figure 7.4.1-1: Within-event residuals of the Arizona recordings with respect to ASK14. The mean residual is shown in the plots.

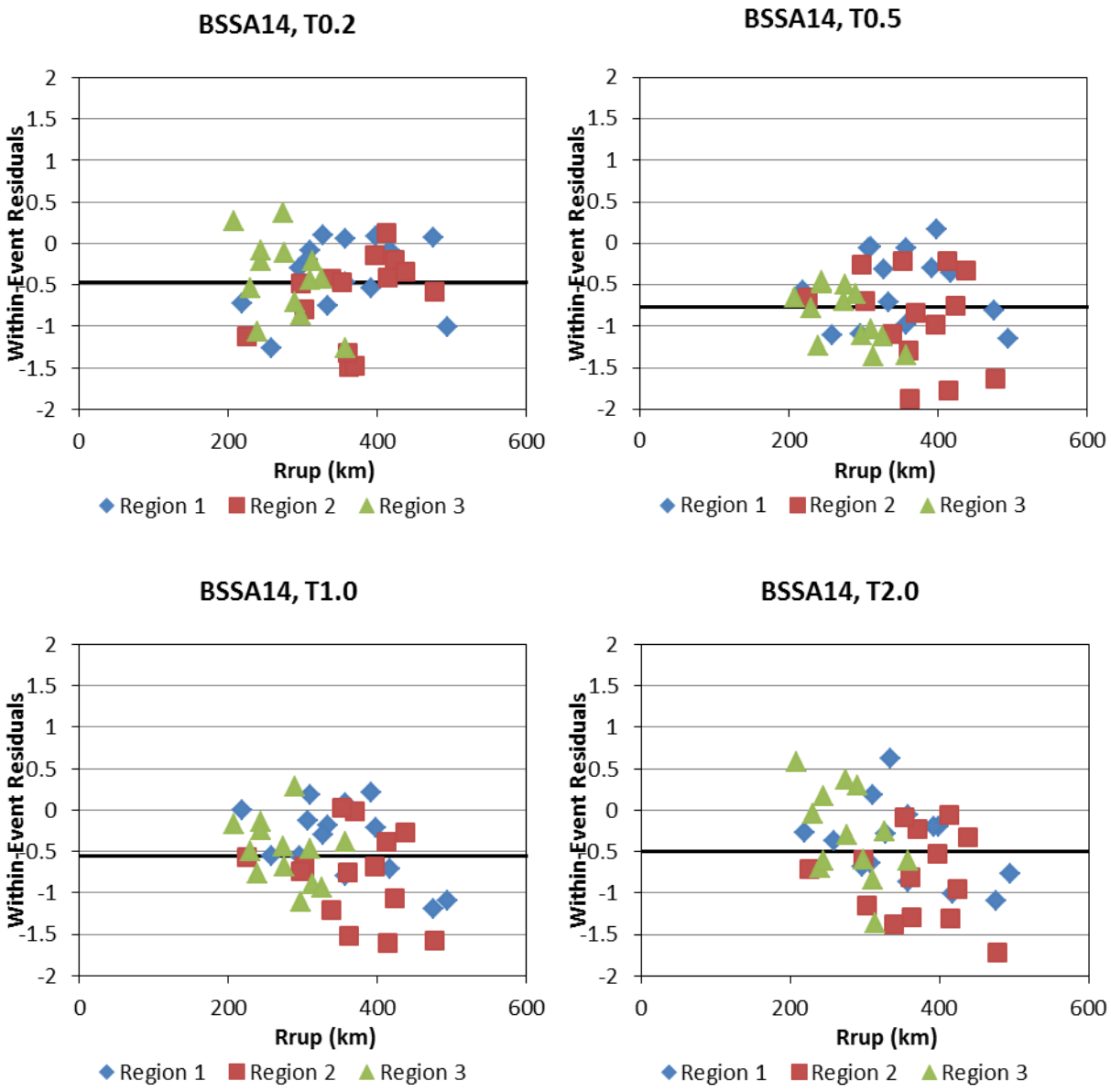

Figure 7.4.1-2: Within-event residuals of the Arizona recordings with respect to BSSA14. The mean residual is shown in the plots.

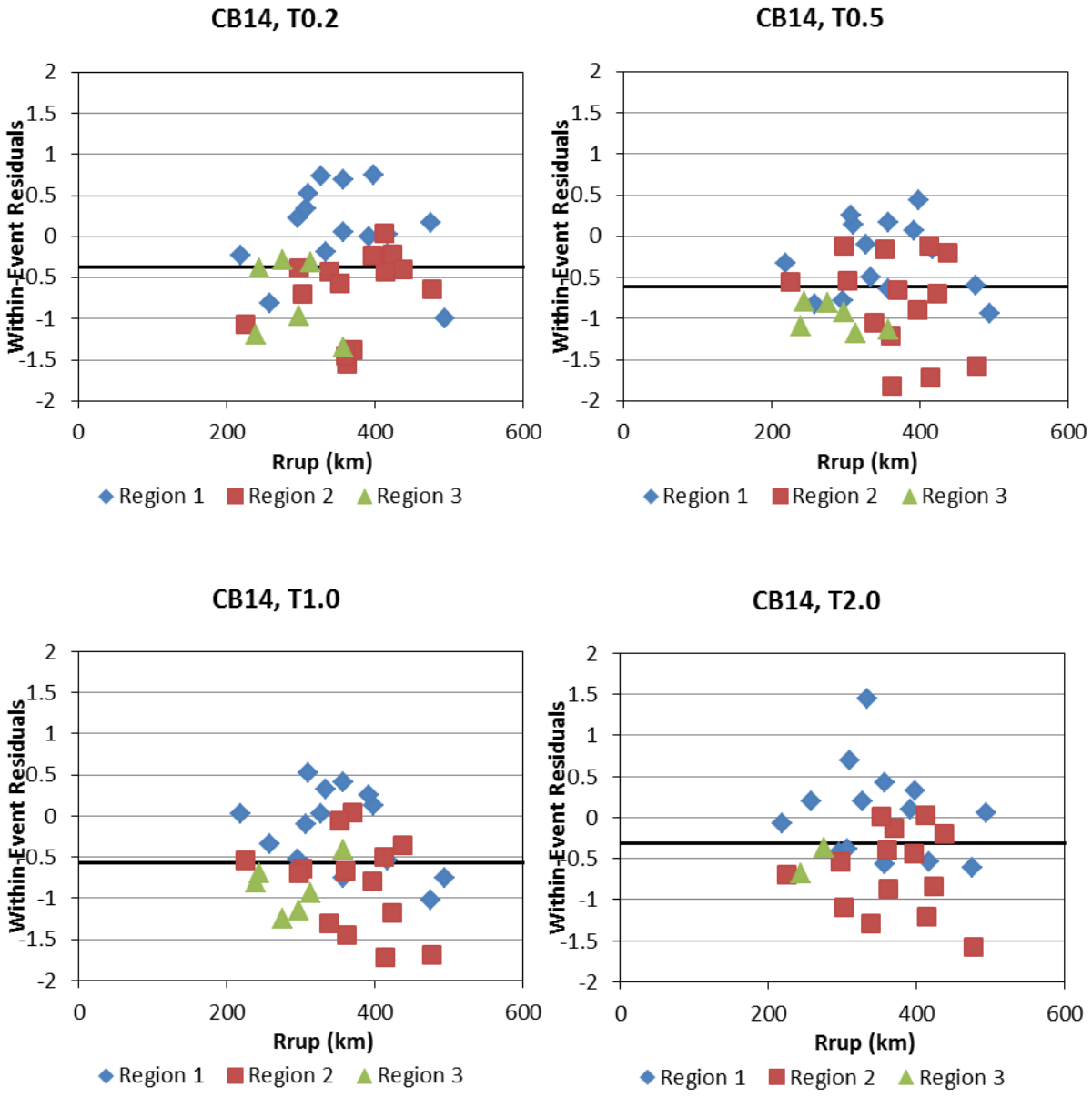

Figure 7.4.1-3: Within-event residuals of the Arizona recordings with respect to CB14. The mean residual is shown in the plots.

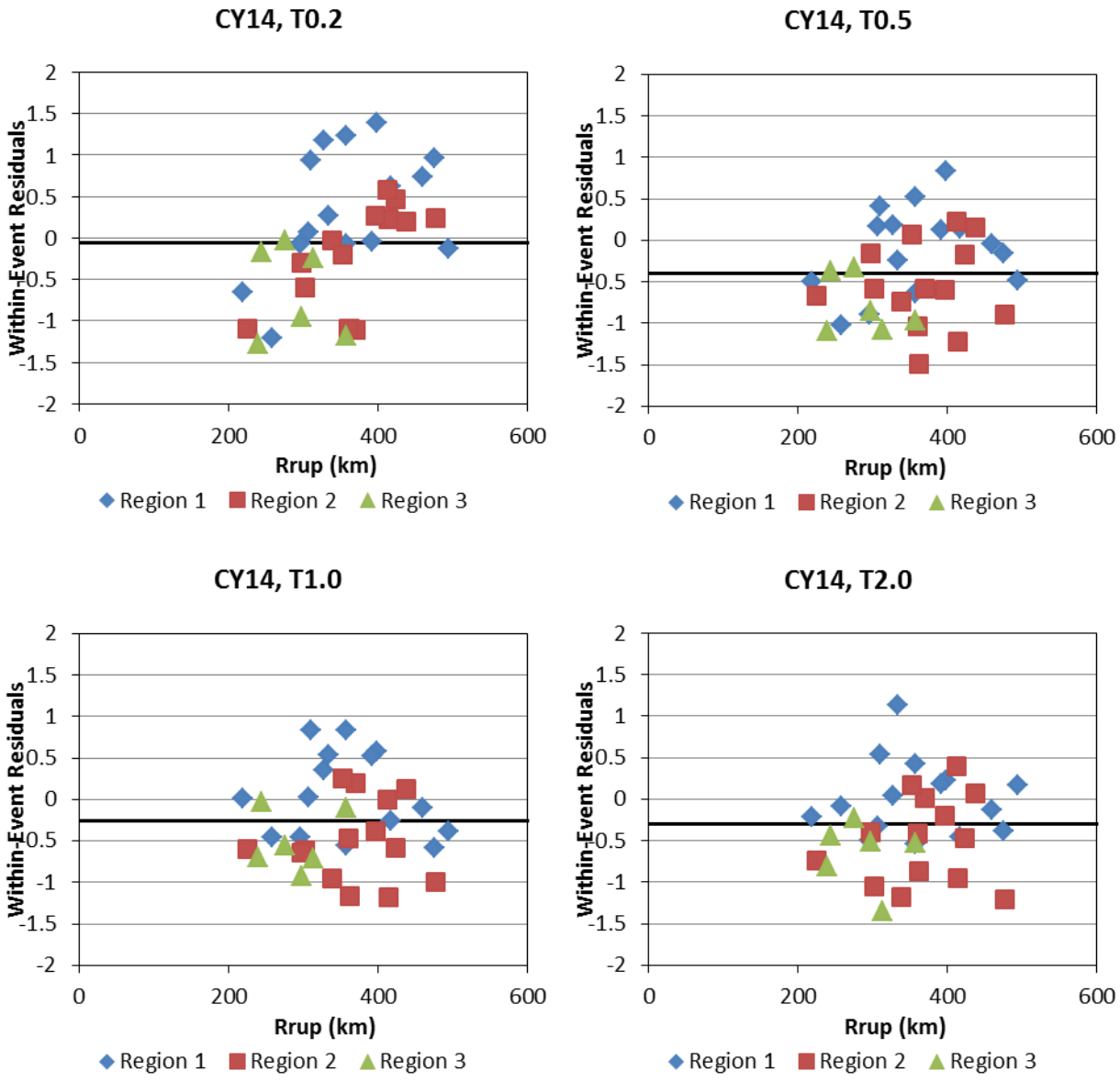

Figure 7.4.1-4: Within-event residuals of the Arizona recordings with respect to CY14. The mean residual is shown in the plots.

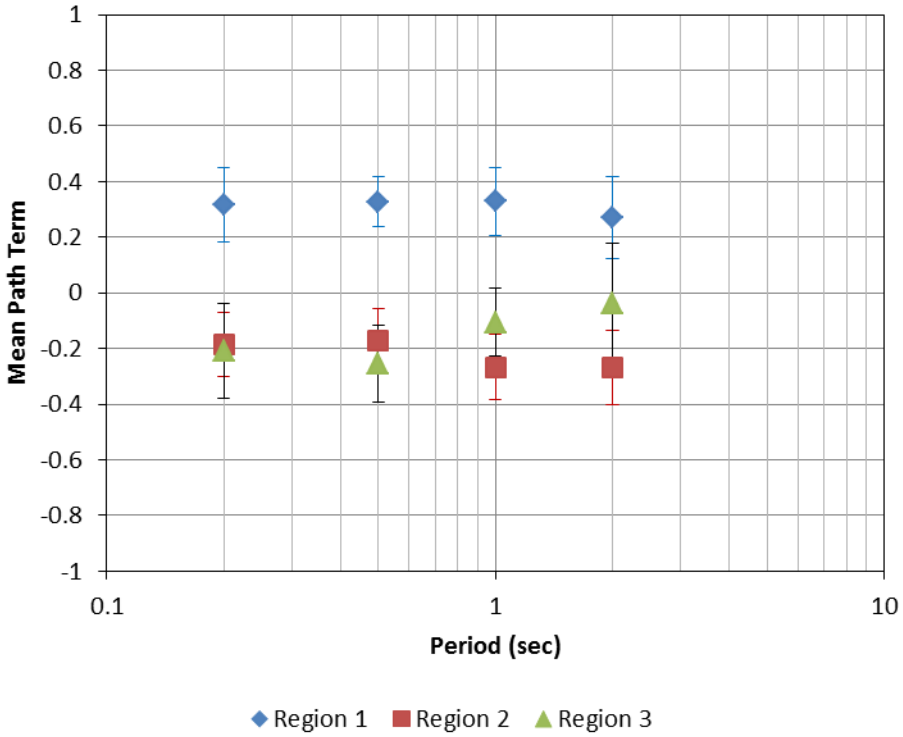

Figure 7.4.1-5: Mean path terms versus period for Regions 1, 2, and 3 averaged over the four NGA-West2 GMPEs. The error bars show ± 1 standard error of the empirical estimates.

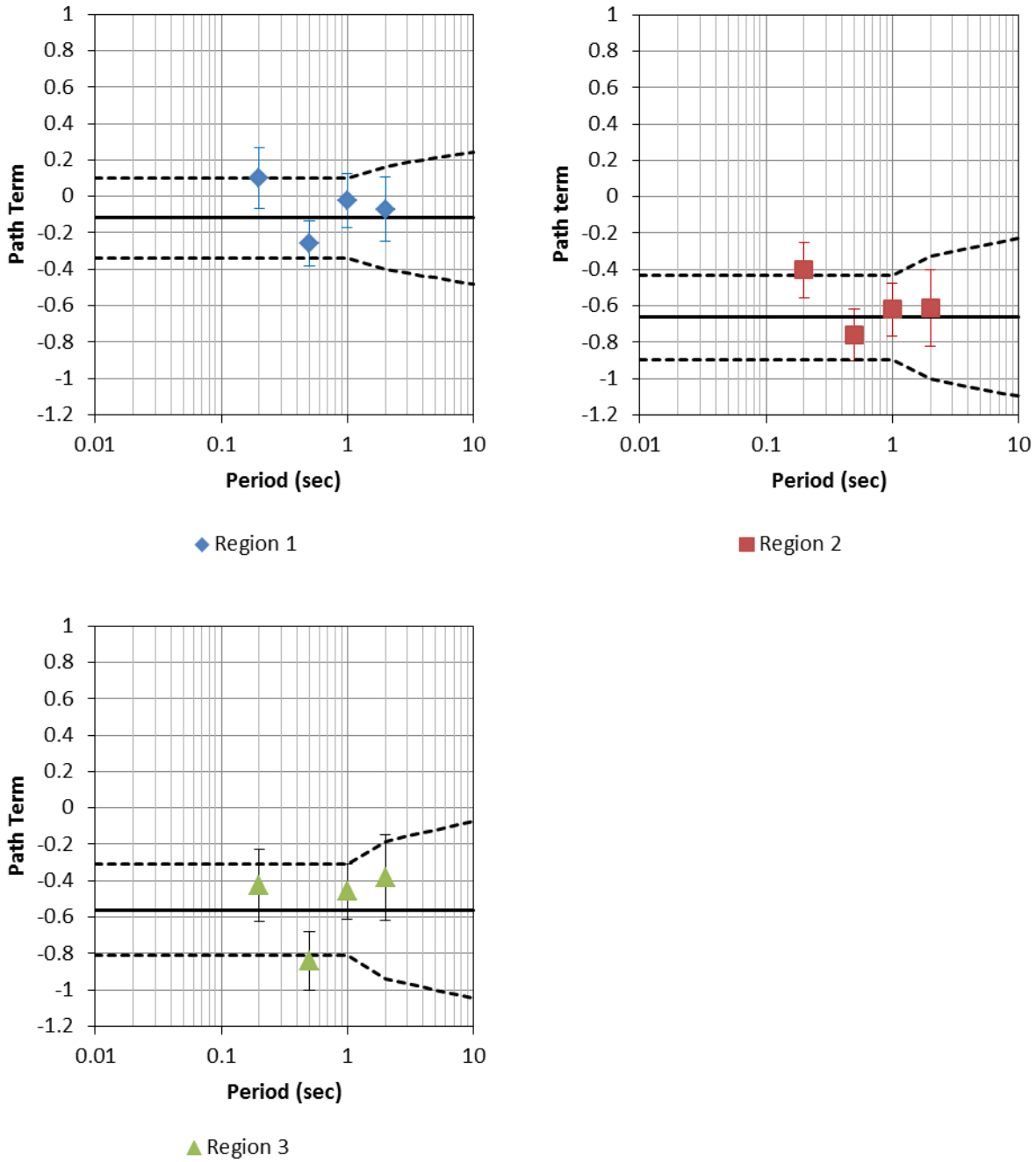

Figure 7.4.1-6: Central, high and low path terms (black lines) for Regions 1, 2, and 3 compared to the values used to derive them. The error bars show ± 1 standard error of the empirical estimates.

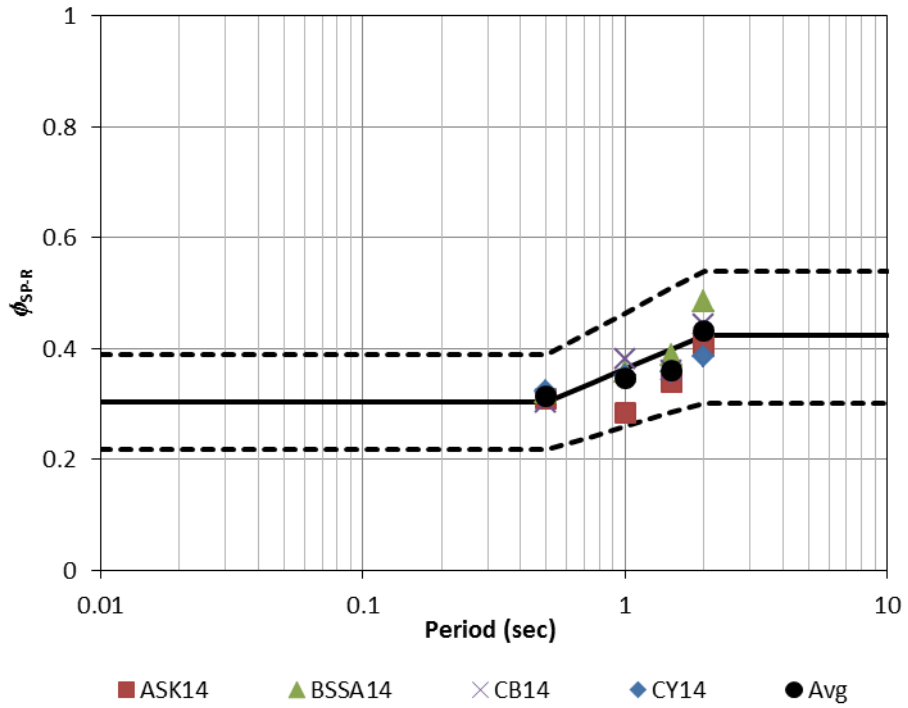

Figure 7.4.2-1: Central, high and low branches (in black) of the magnitude-independent ϕ_{SP-R} model for PVNGS for California and Mexico sources located in Regions 1, 2, and 3.

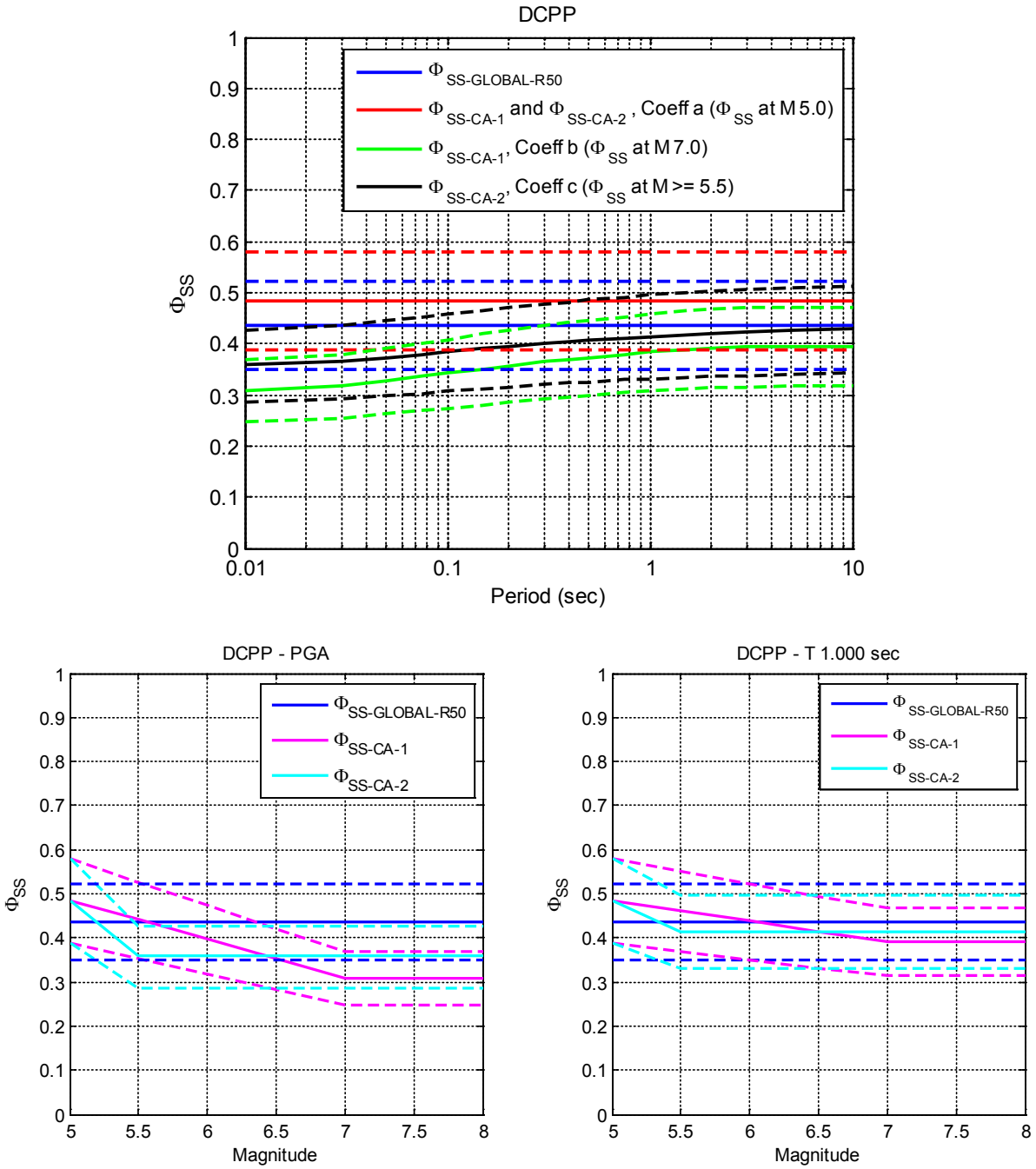

Figure 7.5-1: Comparison of the ϕ_{SS} models for DCPP. The dashed lines show the epistemic uncertainty around the central models shown as solid lines.

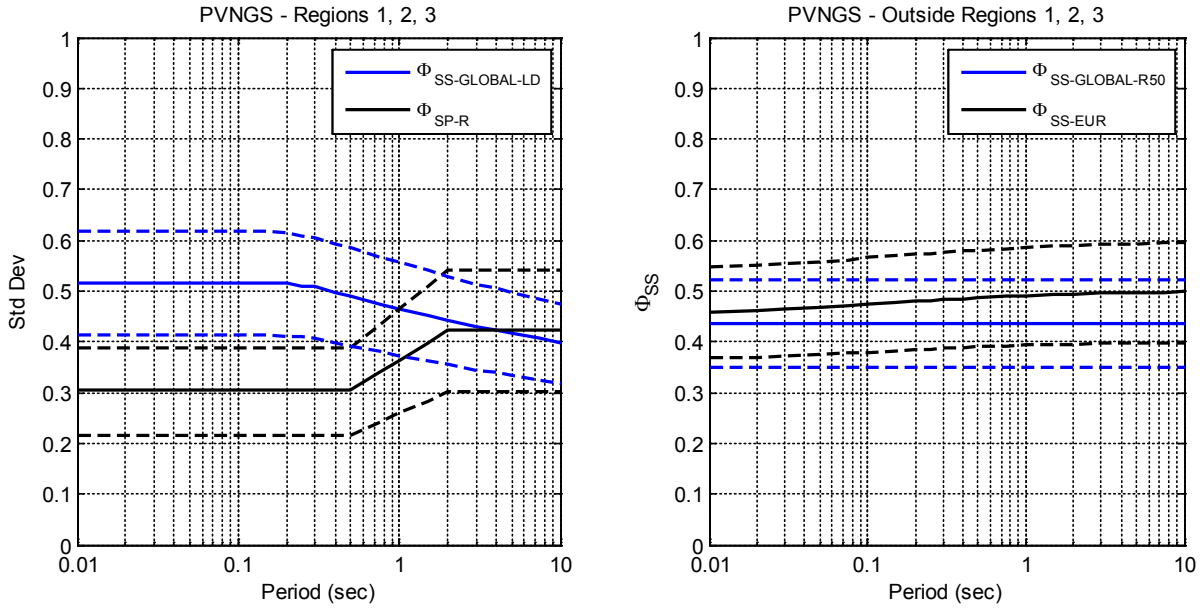

Figure 7.5-2: Comparison of the magnitude-independent ϕ_{SS} and ϕ_{SP-R} models for PVNGS for California and Mexico sources (Regions 1, 2, and 3) and for Greater Arizona sources (outside Regions 1, 2, and 3). The dashed lines show the epistemic uncertainty around the central models shown as solid lines.

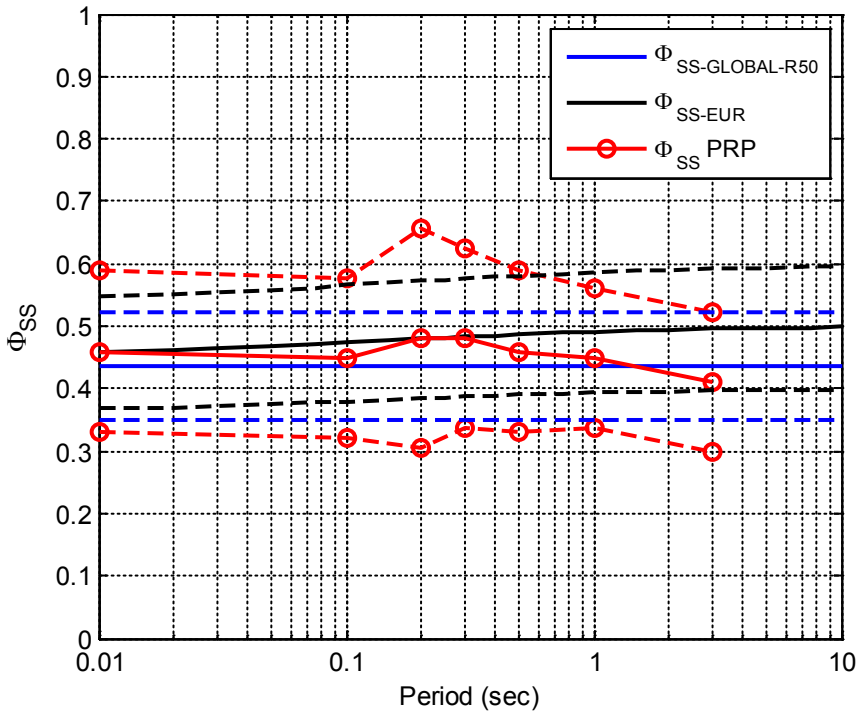

Figure 7.5-3: Comparison of the magnitude-independent ϕ_{SS} models to the magnitude-independent Pegasos Refinement Project (PRP) ϕ_{SS} model. The dashed lines show the epistemic uncertainty around the central models shown as solid lines.

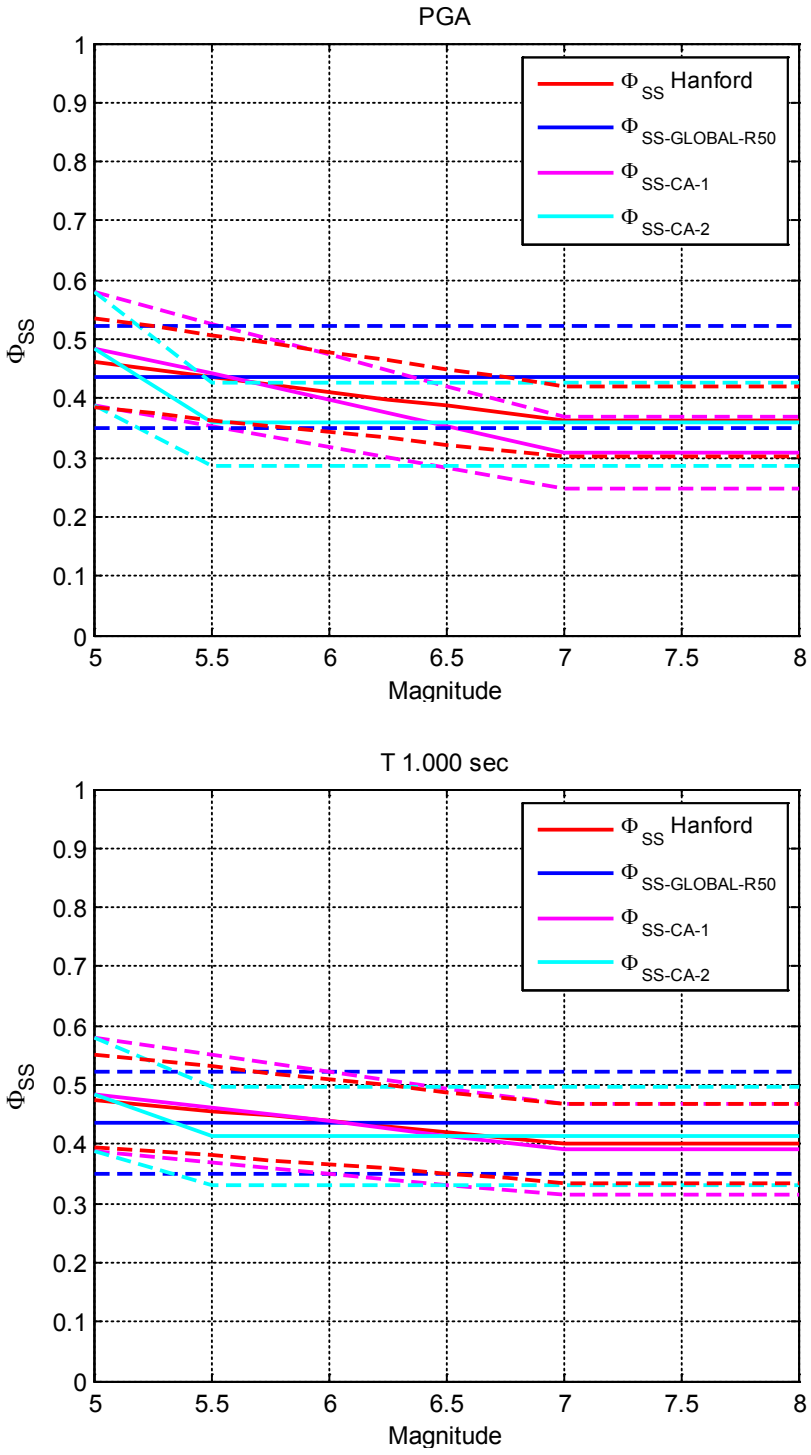

Figure 7.5-4: Comparison of the ϕ_{SS} models to the magnitude-dependent Hanford ϕ_{SS} model at PGA and period of 1 sec. The dashed lines show the epistemic uncertainty around the central models shown as solid lines.

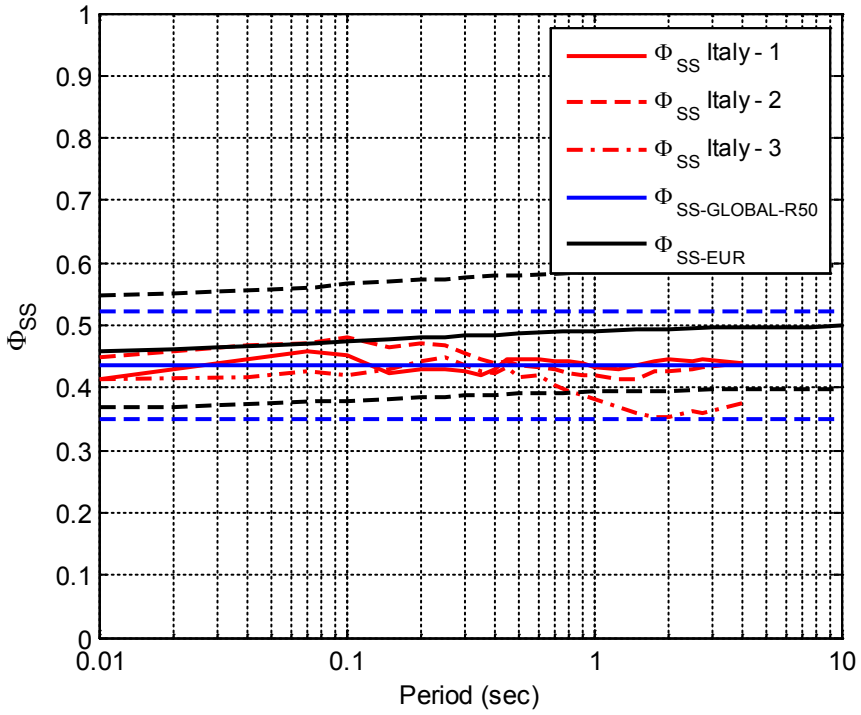

Figure 7.5-5: Comparison of the magnitude-independent SWUS GMC ϕ_{SS} models to the Luzi et al. (2014) ϕ_{SS} models using three different Italian datasets (ϕ_{SS} Italy-1, ϕ_{SS} Italy-2, and ϕ_{SS} Italy-3).

8 MEDIAN GMC MODELS: DCPP SOURCES

8.1 TI Team Approach for the Median Ground Motion

As described in Section 6.4, the TI Team approach used to develop the weighed set of base models (ground motions for strike-slip earthquakes and reverse earthquakes recorded on the footwall) for median ground motions for the local faults consists of the following steps:

1. Fit a common functional form to the GMPEs considered applicable to the assessment of ground motions at the DCPP site.
2. Expand the set of models by interpolating between the candidate models.
3. Develop the covariance matrix for the coefficients in the common-form models.
4. Generate a large suite of ground-motion models by sampling from the multivariate normal distribution defined by the coefficient covariance matrix.
5. Develop a Sammon's map of the generated suite of ground-motion models that approximates the standard deviation of the difference between any two ground-motion predictions from the models by the Sammon's map distance between the two models.
6. Discretize the two-dimensional map space of generated models using Voronoi cells.
7. Select a representative model for each cell based on the mean hazard within the cell.
8. Assign weights to the representative model for each cell that captures the center, body, and range of the ground-motion models to use as the logic tree weight.

For the sources other than the local faults, a simplified approach is used for the median ground motion because these sources contribute less than a few percent to the hazard at the 10^{-3} to 10^{-6} AFE levels at all periods. The simplified approach simply uses the five NGA-West2 GMPEs with the additional epistemic uncertainty for **M**8 earthquakes. The reason for using the candidate NGA-West2 GMPEs rather than the common-form models is that the common-form models were optimized for the controlling sources (local faults) and led to a large epistemic range at large distance (80 km) to the high activity San Andreas Fault.

In this Chapter, the evaluations made by the TI Team to capture the center, body, and range of the median ground motions that are important to hazard at DCPP are described.

8.2 Structure of the Logic Tree

8.2.1 Logic Tree for Local Faults

The master logic tree for characterizing the median ground motion for the local fault sources (within 15 km of DCPP) affecting the hazard at DCPP site is presented in Figure 8.2-1. In Figure 8.2-1 and subsequent figures, weights associated with the TI Team's subjective evaluations are in red, whereas weights associated with statistical sampling are in green.

The first node captures the alternative distance metrics that were considered for developing the common-form models. The second node captures the range of alternative representative base models selected from the large suite of common-form models that were generated. The third node represents the alterative hanging-wall (HW) scaling models. There are five candidate HW models, but to reduce the total number of models, only a single HW effect model is applied to each base model by randomly sampling the five equally weighted alternative HW models (see Section 6.4.3). The fourth node captures the alternatives of either including or excluding adjustments to the base models for directivity effects.

The weights for the base model (second node) are developed independently for each spectral period from 0.01 to 3 seconds. The method for computing the weights, denoted "total weights", uses the logic tree shown in Figure 8.2-2. The first node in Figure 8.2-2 addresses the alternative approaches using either selected empirical dataset (branch called "Data Comparison") or the equally-weighted judgment of the GMPE developers (branch called "GMPE Prior"). The second node addressed the alternative data sets that are considered (empirical and simulated data sets). The third node addresses the two alternative metrics for measuring the difference between the models and the data sets based on the mean between-event residual (branch called "Residual") and the likelihood of the total residual with fixed between-event and within-event standard deviations (branch called "Likelihood").

The evaluations for this second logic tree are the main factors for capturing the center, body, and range of the alternative median ground-motion models for the local faults near DCPP. The T = 3 sec ground-motion models are extrapolated for periods up to 10 seconds, as described in Appendix N, using the same model weights as the T = 3 sec models.

8.2.2 Logic Tree for Distant Sources

The logic tree for the distant sources (all sources other than the local faults) is shown in Figure 8.2-3. In this logic tree, equal weights are used for the five NGA-West2 GMPEs because they are derived for data set that includes California data, and the small contribution to the hazard does not warrant more refined weights. A three-point approximation (Appendix P) for the additional epistemic uncertainty from the Al-Atik and Youngs (2014) model using **M**8 is used to capture the additional epistemic uncertainty on the

large events on the San Andreas fault. The weights for the three branches are based on the statistical sampling of the normal distribution as described in Appendix P.

The basis for using this simplified logic tree is that these sources do not contribute significantly to the hazard (less than a few percent at the 10^{-4} AFE level for long periods). GMPEs that are not based on California data are not used because there are regional differences in the large distance scaling seen in the ground-motion data (e.g. regionalization of the large distance scaling in the NGA-West2 GMPEs). Therefore, the GMPEs developed from other regions may not capture the large distance scaling in California.

8.3 Evaluation of Distance Metric for Common Form

There are two commonly used distance metrics for ground-motion prediction equations: R_{RUP} and R_{JB}. In many applications, both models are applicable, but as discussed in Section 6.3.3, the variation in HW effects over the wide range in dip angles that were initially considered by the SSC TI Team for the DCPP source characterization are difficult to capture in a R_{JB}-based formulation. This was not an issue for developing empirical models (such as BSSA14) because there is sparse sampling of low dip angle earthquakes with sites over the hanging wall, but it is important in the extrapolation of the models required in the PSHA. Simply treating the HW misfits from R_{JB}-based models as aleatory variability is not appropriate because the range in median predictions for these effects is bounded, rather than being log-normally distributed. Therefore, for application to DCPP, the TI Team judged that the R_{JB}-based common-form metric branch shown in Figure 8.2-1 should be given zero weight in developing the common-form ground-motion models for DCPP. The information on magnitude and distance scaling contained in the R_{JB}-based models is still captured by using them to construct ground-motion predictions on the foot-wall side of ruptures, where both distance metrics work well. The R_{JB}-based candidate models are re-parameterized into R_{RUP}-based models which can then be combined with the HW effects models.

We note that the Rev 0 SSC model for DCPP did not include shallow dip angles: the dips for the local reverse faults in the DCPP region range from 45 to 90 degrees (Section 4.1), so there are no local faults with shallow dips in the final model; however, the decision to use only the R_{RUP} distance metric for the common-form models for DCPP was made before the Rev 0 SSC model was available to the GMC TI Team.

8.4 Median Base Models

8.4.1 Evaluation of the Range for the Selected Models

The range of the selected common-form models should capture the range of the candidate GMPEs in the Sammon's map space, and should be representative of the range of the ground motions of the candidate GMPEs in ground-motion space for hazard-relevant earthquake scenarios. In addition, each of the candidate GMPEs has epistemic uncertainty due to the limited data, particularly for large magnitudes and short distances. This epistemic uncertainty for the NGA-West2 GMPEs has been parameterized by Al Atik and Youngs (2014) in terms of the standard error of the (log) mean. A similar evaluation is not available for the non-NGA-West2 GMPEs. A key reason for adding additional epistemic uncertainty is that the NGA-West2 GMPEs were developed from similar datasets and there was significant interaction between the developers, so that the GMPEs are not independent. In contrast, the non-NGA candidate GMPEs (ASB14, ZH06 and ZL11) used different datasets without close interaction, so they are less correlated. The TI Team judged that adding some epistemic uncertainty to these outside models was appropriate even though they are less dependent on each other. The Al Atik and Youngs (2014) model, therefore, was applied to the non-NGA models as well.

To capture the additional uncertainty given by the Al Atik and Youngs (2014) model, the TI Team used the ±2 sigma level, representing the 95% confidence interval for the uncertainty in the median ground motion.

The approach used by the TI Team to generate a large suite of common-form models further expands the range of the candidate GMPEs beyond the ±2 sigma range applied to the candidate GMPEs using the Sammon's maps. The wide range resulting from the 2000 common-form models is overly broad and the range is reduced based on comparisons with the range of the candidate GMPEs with their ± 2 sigma epistemic uncertainty and with the mean residual from the ground-motion data sets. In this section, the check is discussed that the resulting range of common-form models is appropriately wide.

Section 6.4 describes the approach for defining the range of the subset of common-form models that are considered appropriate based on the Sammon's maps. Here, the Sammon's maps for PGA and for T = 1 seconds are used to demonstrate how the range was set. This range is then checked against the range from the original candidate GMPEs to be sure that it is wide enough.

Figures 8.4-1 and 8.4-2 show the Sammon's map for the PGA and T = 1 sec suite of ground-motion common-form models generated for the DCPP site. The distance between two points in the Sammon's map approximates the weighted standard deviation (in ln units) between the ground motions predicted by two different models for the selected sets of magnitudes and distances described in Section 6.4. The weighted standard deviation is the standard deviation between the ln of the ground-motion model amplitudes for two models with the weights being related to the deaggregation using a simplified source

model (eq. 6.4-7). Using these weights focuses the comparison of the amplitudes for two models on the magnitudes and distances that are most important to the hazard at DCPP. The space spanned by the 2000 common-form models is shown by the irregular polygon with the contours in Figure 8.4-1.

The Sammon's maps are rotated such that the x-axis approximates constant scaling between the models, as shown by the orientation of the additional epistemic uncertainty assigned to each candidate GMPEs (orientation of the magenta and cyan dots in Figure 8.4-1). Although magnitude and distance scaling differences are important, the largest map distances between the candidate GMPEs including epistemic uncertainty are in the x-axis direction.

The red dots in Figures 8.4-1 and 8.4-2 denote the locations on the map of the predictions from the eight candidate GMPEs. The magenta and cyan dots show the plus and minus two sigma epistemic uncertainties for each of the candidate GMPEs. As indicated on the plot, the full range from the 2000 common-form models is much broader than the range produced by the eight candidate GMPEs.

As described in Section 6.4, the sampling of the Sammon's map space is based on fitting ellipses to the convex hull of the locations of the candidate GMPEs on the map and scaling the ellipses, as shown in Figures 8.4-1 and 8.4-2. Points on the ellipses were selected to sample the range of representative models (shown by the black points in Figures 8.4-1 and 8.4-2). To put limits on the range of the models, the $NGAW2_{DC\text{-}MED}$ data set (**M** > 5 and R < 50 km as described in Section 5.3.1) was used to compute the mean between-event residual using equations (10) and (7) of Abrahamson and Youngs (1992). The mean between-event residual is shown by the contours in the upper left plot in Figures 8.4-1 and 8.4-2. The small patches on the figures represent the limitations of mapping the differences among the GMPEs into a two-dimensional plane. The sampled points are limited to the region with mean between-event residual between -0.3 and 0.3 or the mean between-event residual given by the candidate GMPEs with ±2 sigma epistemic uncertainties, whichever is larger.

To check that the range of the representative suite of models selected using this approach is broad enough, a simple measure of the range of the candidate GMPEs, defined by the smallest and largest mean between-event residual from the $NGAW2_{DC\text{-}MED}$ data set, is used. Figure 8.4-3 shows the range of mean between-event residuals for the candidate GMPEs and their epistemic uncertainty compared to the range covered by the selected representative suite of common-form models. As indicated in the figure, the selected representative suite of common-form models covers a range of the mean between-event residuals that is at least as wide as the candidate GMPEs and their epistemic uncertainty at every period. In some cases, the range is expanded beyond the range of GMPEs plus epistemic uncertainty, showing that the process of generating the models also extrapolates the candidate set of GMPEs. The range from the Sammon's maps represents the range of the broad features of the candidate GMPEs. It does not lead to bounding models for all magnitude and distance combinations. Only the range of the candidate GMPEs and the mean between-event residuals influence the selection of the range of the

representative suite of common-form models. The likelihood is used only to assign weights to the representative suite of common-form models.

In addition to the between-event residuals, the likelihood of each model given the selected dataset is also calculated using equations (10) and (7) of Abrahamson and Youngs (1992). If a model leads to very large standard deviations (e.g. greater than 1 ln units), the likelihood may still be high; however, the model prediction is not considered to be good because the large standard deviation is inconsistent with the empirical data. To avoid this trade-off between the likelihood and an optimized standard deviation, a fixed value of the standard deviation is used as representative of the typical standard deviation found in empirical GMPEs. For both the between-event and within-event standard deviation, the representative standard deviations are taken from the BSSA14 model. This approach penalizes common-form models that lead to residuals that fit a normal distribution but with a large standard deviation that is inconsistent with the GMPE's standard deviation.

The contour lines underlying the Sammon's map indicate either the value of the mean between-event residual computed for each model or the likelihood for each model. The selection of the data set is discussed in Section 8.4.2. The mean between-event residuals for the large suite of generated models range from about -1 to greater than +1 natural log units, while the range in mean residual for the candidate eight GMPEs ranges from about -0.2 to +0.2, indicating that some of the generated models differ substantially from the candidate GMPEs. For the mean residual (upper left and lower left plots in Figures 8.4-1 and 8.4-2), the contours of zero mean residual extend from the bottom to the top of the map because models with very different magnitude and distance scaling can have a mean residual of zero, but with different standard deviation of the fit. So, while the mean residual is easy to understand and evaluate, it is only part of the evaluation.

The upper right hand plot in Figures 8.4-1 and 8.4-2 shows the contours of the likelihood of the selected data set being generated by each of the common-form models. Using likelihoods with fixed between-event and within-event standard deviations based on the BSSA14 GMPE provides a complementary evaluation of the large suite of 2000 common-form models, which also considers the standard deviation of the between-event residuals and not just the mean value. Models with a high likelihood are more consistent with the data in the selected subset than models with low likelihood. As expected, the models with large absolute mean between-event residuals have much lower relative likelihood than those with small absolute mean between-event residuals, but the models at the top and bottom of the plot near the zero x-axis, which have small mean between-event residuals but poor fits to the BSSA14 standard deviation values, show lower likelihood. Likelihood maps are not shown for the Finite Fault Simulations (FFS) data set because the aleatory variability of the simulations using the SCEC broadband platform was not validated as part of the SCEC broadband validation project: the SCEC validation project only evaluated the methods for the median ground motions.

Similar plots for the other periods are shown in Appendix H (Chapter 2, Section 2.1.3).

The range of selected representative common-form models is intended to represent the range of the candidate GMPEs and their associated ± 2 sigma epistemic uncertainties.

8.4.2 Evaluation of Weights for Selected Models

Two approaches are used to assign weights to the models selected in Section 6.4.4 to represent the distribution of GMPEs. The first approach, called the "prior" approach, utilizes the multivariate normal distribution defined by the coefficient covariance matrix to assign relative weights to the models that occupy each of the Voronoi cells. The second approach utilizes comparisons to ground-motion data to assign relative weights to the models that occupy each of the Voronoi cells. The data comparisons are based on both mean between-event residuals and sample likelihoods.

Two datasets are used to develop the data comparison weights. The first dataset, called $NGAW2_{DC\text{-}MED}$, is a subset of the data taken from the NGA-West2 data set as described in Section 5.3.1. This subset includes **M** ≥ 5, distances less than 70 km, strike-slip and reverse earthquakes, and excludes sites with potential for strong HW effects because these are addressed separately with the addition of the HW model. The $NGAW2_{DC\text{-}MED}$ data set was shown in terms of the magnitude-distance scatter plot and number of earthquakes and number of recordings in Figure 5.3.1-1. The second dataset consists of finite-fault simulations using three different methods (EXSIM – Atkinson and Assatourians, 2015; GP – Graves and Pitarka, 2015; and SDSU – Olsen and Takedatsu, 2015). Details of the finite-fault simulation methods, cases and evaluations are described in Appendix J. The finite-fault simulations are considered for the DCPP evaluations because the hazard is controlled by large magnitude sources at short distances (< 10 km) where the number of empirical data is still limited. The TI Team reviewed the results of the SCEC BBP Validation Project (Dreger et al., 2013 - Attachment B; Appendix J.1), and judged that the three methods identified by the SCEC Review Panel represent technically defensible interpretation of ground motions close to large earthquakes and are suitable for application to the SWUS GMC Project. The finite-fault numerical ground-motion simulations utilized for the Sammon's maps are described in Section 5.2.3.2, and include earthquakes with magnitudes between 5.5 and 7.3 at short distances as shown in Figure 5.2.3-1.

Empirical likelihood-based relative weights (as defined in Section 6.4.5) tend to give much higher weight to a few central models, producing narrower distributions of the ground motion. In contrast, relative weights based on differences in mean between-event residuals tend to produce broad distributions. A balance between these two behaviors was achieved by using a mixture of 60% on mean residual weights and 40% on likelihood weights. The TI Team selected these weights so that the resulting body of the distribution of median base models (as shown by the slope of the CDF plots in Appendix H) are generally consistent with the body of the distribution of the candidate GMPEs (with equal weights) used to develop the covariance matrix of the coefficients for the common-form models.

The subjective logic tree weights on the weighting approach for the DCPP application are based on the following considerations:

1. There is ample empirical data in the NGA-West2 data set for much of the key range (**M**5 - **M**8 at distances less than 70 km). The dataset approach allows the TI Team to put more weights on the magnitude and distances that are relevant to the hazard at DCPP, whereas the GMPE developers tried to capture the full range. However, these same data were considered in the development of the GMPEs, so this is not independent data. This approach just puts more weight of a specific magnitude and distance range of the full data considered by the GMPE developers.

2. The simulations provide a larger set of cases (32 realizations of the source for each scenario) for the large magnitude, short distance cases. The medians are more stable, but the FFS have only been validated for seven large magnitude events. These methods are still relatively new.

3. The "prior" approach implicitly maintains the judgments by the candidate GMPE developers by using the weights from the covariance matrix that is based on the candidate GMPEs, but it is based on equal weight for each selected candidate model and does not consider the correlations in the model due to interaction between the developers. The common-form models fit to the candidate GMPEs maintain the magnitude and distance scaling in the candidate GMPEs as given by the GMPE developers.

The TI Team favors the model weights based on comparisons to data over the model weights based on the common-form parameter distributions (the “prior”) approach by the ratio of 2:1 because of the large amount of relevant data (both empirical and simulated) and because of the limitation that the “prior” was based on applying equal weights to the models without regard to redundancy in the models due to non-independent model development, particularly for the NGA-West2 models. Within the data based approach to weighting, the TI Team strongly favors the use of the empirical data over the simulated data by the ratio of 3:1 because there is a large amount of empirical data in the important magnitude and distance ranges and the FFS methods still need additional validation with more events. Based on these considerations, 1/3 weight is assigned to weights based on the “prior” approach and 2/3 to the comparisons with data. For the data sets, the empirical data is favored strongly (3 to 1) compared to the simulations, thus leading to 0.75 weight assigned to the $NGAW2_{DC\text{-}MED}$ empirical data set, and to 0.25 weight assigned to the finite-fault simulations., as shown on the logic tree in Figure 8.2-2.

The selected weighting scheme is compared to alternative weighting schemes by comparing the cumulative distribution function (CDF) for the ground motion for a given scenario. Examples of the CDF plots are shown in Figures 8.4-4 and 8.4-5 for **M**6.5 strike-slip earthquakes at an R_X distance of 5 km for PGA and T = 1 sec, respectively. For this scenario, the likelihood weighting approach leads to a very narrow range (steeper slope of the CDF) and that the residual weighting approach leads to a broad

range (flatter slope of the CDF). Using a weighted average with 0.4 for the likelihood and 0.6 for the between-event residuals leads to the CDF shown by the red curve. This weighting of the likelihood and mean residual statistics provides a balance between the two different bodies of the distributions from these two approaches. The GMPEs, shown by the brown curves, sometimes have a narrower distribution, and sometimes they have a broader distribution. For the example shown, the selected weighting method leads to models that tend to have a broader body of the distribution than the candidate GMPEs, which is consistent with the concept that some of the GMPEs are correlated and do not represent independent estimates. A large set of CDF plots for a range of **M**, R scenarios and spectral periods are shown in Appendix H (Chapter 2, Section 2.1.5). These additional scenarios and spectral periods show similar trends as discussed above.

8.4.3 Evaluation of Center and Body of the Selected Models

The center and body of the distribution of the medians is evaluated by comparing the CDFs using the weights described in Section 8.4.2 with the CDF from the candidate GMPEs with epistemic uncertainty (see Figures 8.4-4 and 8.4-5 as examples). Figure 8.4-4 shows CDF for PGA for an **M**6.5 strike-slip earthquake for a site at R_X = -5 km (on FW). The selected weights (red curve) has a center (CDF = 0.5) that is about 0.2 ln units greater than the center of the CDF from the finite-fault simulations, about 0.12 units above the GMPEs, and is similar to the CDFs based on the mean residual, prior and likelihood approaches. The average slope of the CDF between CDF = 0.1 and CDF = 0.9 defines the body of the distribution and, overall, is consistent with the slopes from the other methods except for the GMPE and likelihood approaches which are steeper for this example. These comparisons of the center and body of the distribution change for different scenarios and spectral periods.

In addition to the CDF plots, the center and body of the distribution can be evaluated using distance scaling, magnitude scaling, and spectra plots. Figures 8.4-6 and 8.4-7 compare the distance scaling for the 5^{th}, 50^{th}, and 95^{th} fractiles from the logic tree weights with the distance scaling for the candidate GMPEs for PGA and PSA (T = 1 sec), respectively. The 50^{th} percentile for the representative suite of common-from models is not the same as the 50^{th} percentile of the candidate GMPEs. One reason for this difference is that the common-form model weights were partly based on finite-fault simulations that were not part of the dataset used in the candidate GMPEs' derivation.

As seen in these figures, the representative suite of models envelopes the candidate GMPEs for the larger magnitudes (**M**6.5 and **M**7.5) other than at distances less than 3 km. The GMPE that is above the selected model envelope is the Id14 model. As discussed in Section 6.2.1, the TI Team judged the short distance scaling in the Id14 model to be unreliable for large magnitudes and removed the Id14 model at distances less than 3 km from the development of the common-form models. This apparent inconsistency between the range of GMPEs and the range of the representative suite of common-form models reflects the TI Team's judgment with regard to the Id14 GMPE. The shape of the 5% fractiles for

M7.5 shown in Figure 8.4-6 is not smooth due to the relatively small number of common-form models selected (less than 31).

At smaller magnitudes (**M**5.5), the representative suite of common-form models does not envelope all of the candidate GMPEs for **M**5.5 as shown in Figure 8.4-7 (top panel). The differences at **M**5.5 are related to the sharp breaks in the magnitude scaling for the short period ground motion for some of the candidate GMPEs. Figure 8.4-8 shows the magnitude scaling of the candidate GMPEs compared to the 5th, 50th, and 95th fractiles from the representative suite of common-form models using the logic tree weights, for the strike-slip earthquakes and R_X distance of 5 km for PGA, T = 0.2, T = 1, and T = 3 seconds. The candidate GMPEs with additional epistemic uncertainty and the minimum and maximum of the representative common-form models are also shown. The magnitude scaling for the Graizer (2014) model is provided for comparison, because the Graizer (2014) model was not used to generate the large suite of common-form models. The sharp break in the magnitude scaling at **M**5.5 for one of the GMPEs can be seen in this figure. The representative suite of common-form models includes breaks in the magnitude scaling at **M**5.5 and **M**6.5, but the break is not as sharp and leads to a smoother set of models. The TI Team judged that the smoother common-form models are adequate because they cover the CBR of the TDI (i.e. candidate GMPEs) for scenarios that are relevant to the hazard. In some magnitude-distance combinations, the representative suite of common-form models does not fully envelop the prediction of the candidate GMPEs with added epistemic uncertainty, as discussed in the next paragraph. To check that these small exeedances are not at scenarios that control the hazard, the hazard is evaluated using a representative SSC model. These representative hazard results show that the representative suite of common-form models has an appropriate range (shown later in this section).

Examples of the 5th, 50th, and 95th fractiles predictions from the representative suite of common-form models using the logic tree weights are compared to the range of the candidate GMPEs in Figure 8.4-9, for **M**5.5, **M**6.5, and **M**7.5 strike-slip earthquakes at a distance of 5 km. The candidate GMPEs with additional epistemic uncertainty, the minimum and maximum of the representative common-form models, and the GK14 model are also shown. For **M**6.5 and **M**7.5, the selected models envelop the range of the candidate GMPEs plus additional epistemic uncertainty, but at **M**5.5, not all of the models are enveloped due to the sharp breaks in the magnitude scaling at **M**5.5 in one of the GMPE models. This issue of adequate range is evaluated later at the end of Section 8.4.3, using hazard curves as the metric of interest.

An example of the CDF with a broad distribution of the GMPEs is shown in Figure 8.4-10 for a **M**5.5 earthquake at a distance of 1 km. For the spectral acceleration at T = 1 sec, the GMPE distribution is much broader than the distribution for the representative suite of common-form models due to the kink in the magnitude scaling at **M**5.5 for one of the candidate GMPEs. In contrast for PGA, for this same scenario, the GMPE distribution is similar to the representative suite of common-form models as the range of the selected models captures the kink in the magnitude scaling.

The centering of the models can also be evaluated in terms of the influence of the different metrics used for computing the weights for the common-form models. Because the simulations are also used to constrain the center and body of the distribution, differences between the center of the simulations and the center of the candidate GMPEs will affect the centering of the selected models.

A set of CDF plots and ground-motion scaling plots for the scenarios listed in Table 8.4-1 and for a range of spectral periods are shown in Appendix H. The CDFs of the ground motions were reviewed to check the center and body of the distributions. A general result is that the simulations lead to a lower center (PSA at CDF = 0.5) for short periods and a higher center for long periods. The center of the full distribution and the body of the upper tail distribution of the representative suite of common-form models are consistent with the distribution of the GMPEs except at an R_X distance of 1 km from **M**5.5 earthquakes. The lower tail has more variability in the shape of the CDF, but it is not as important to the hazard as the upper tail (the mean hazard is driven by the upper tail because the distribution is skewed).

To summarize the evaluation of the centering of the models based on the CDF plots, the changes in the PSA at CDF = 0.5 for the different metrics and datasets are computed. Specifically, for each scenario listed in Table 8.4-1, the difference in the ground motion for a single metric and the weighted average model is computed. The distribution of the differences of the ln PSA for the 18 scenarios is referred to as an "influence histogram", and is plotted for each statistic and each spectral period. Examples for the R_{RUP}-based models (A models) are shown in Figures 8.4-11, 8.4-12, and 8.4-13 for PGA, and spectral accelerations at T = 1 sec and T = 3 sec, respectively. These plots show the influence of the different metrics on the centering of the distribution with zero residual representing the center based on the TI Team evaluation (shown by the red curves in the CDF plots). For PGA, the simulations are centered lower than the evaluated center (shown by the negative residual compared to the median), whereas, the other metrics are near the evaluated center. For PSA at T = 2 seconds, there is a shift with the simulations along with the $NGAW2_{DC\text{-}MED}$ between-event residuals being slightly above the evaluated center and the likelihood and prior approach being skewed to lower values. For PSA at T = 3 seconds, the simulations lead to higher values than the evaluated center and the other metrics are near the evaluated center. A full set of these influence histograms is given in Appendix H (Section 2.1.15 in Chapter 2 of Appendix H).

The above discussion has focused on the ground-motion levels. The representative suite of models was developed to sample a range of distance scaling and magnitude scaling. An example of the distance scaling for the representative suite of common-form models for **M**6.5 strike-slip earthquakes is shown in Figure 8.4-14 for T = 0.2 sec and T = 2 sec. An example of the magnitude scaling for the representative suite of common-form models for strike-slip earthquakes at a distance of 10 km is shown in Figures 8.4-15 for T = 0.2 sec and T = 2 sec. These figures show that the representative suite of common-form models spans a range of distance and magnitude scaling in addition to changing in the constant value. The differences in the magnitude and distance scaling may also impact the range of the hazard, depending on the source model.

Another key consideration for the center and body of the distribution is that, for each cell, the representative common-form model was selected based on its hazard being close to the mean hazard for the cell. Because the main application of these models is for hazard, it is appropriate to select representative models based on hazard; however, this may not always lead to a selection of models that best samples the range of ground motions for each scenario. That is, checking the center and body of the distribution with respect the candidate GMPEs should be done for hazard, not just ground motion for each scenario.

To evaluate the hazard distribution, the hazard was computed for each selected common-form model and for the candidate GMPEs using the simplified source model that represents a site for which nearby (less than 15 km) strike-slip and reverse sources will dominate the hazard (See Appendix O for details). Because a general near-fault-dominated source model is used, the evaluation of the weights for the representative suite of common-form models is judged, by the TI Team, to be applicable to DCPP as long as the local sources dominate the hazard at the site. Therefore the GMC model does not need to be re-evaluated for new SSC models if the controlling sources remain at distances less than 15 km. A single aleatory standard deviation, based on the central model described in Section 13.2, is used for all of the median models. The range of hazard for spectral acceleration at T = 0.2 sec and T = 2 sec are shown in Figures 8.4-16 and 8.4-17, respectively. Appendix O includes plots showing the range of hazard for three additional periods (PGA, T = 1 sec and T = 0.1 sec).

For the T = 0.2 sec case (Figure 8.4-16), the range of hazard curves from the representative suite of common-form median models is much broader than the range of hazard from the candidate GMPEs, and the mean hazard from the representative suite of common-form models is larger than the hazard from the candidate GMPEs at probability level less than 10^{-4}. The broader uncertainty range increases the mean hazard due to the skewed distribution of hazard (skewed to the higher values). Another cause for this difference between the average hazard from the candidate GMPEs and the mean hazard from the representative suite of common-form models is that the HW effect is included for all common-form models, but there is no HW effect for some of the candidate GMPEs (Id14 [Idriss, 2014), Z06 [Zhao et al., 2006], and ZL11 [Zhao and Lu, 2011] as implemented by the TI Team, see Section 5.5.1.1). Figure 8.4-16 shows that these candidate GMPEs without HW effects have the lowest hazard. An additional difference from the candidate GMPEs is that the magnitude taper for the HW effect was removed, which increases the HW effect for earthquakes with magnitudes less than 6.5. To show the impact of this change, the hazard was also computed for the ASK14 (Abrahamson et al., 2014) model with the HW magnitude taper removed (called ASK modified in Figure 8.4-16). The result of removing the magnitude taper for the HW effect is only a small increase in the hazard.

For the T = 2 sec case (Figure 8.4-17), the range of hazard curves from the candidate GMPEs is much broader than for the T = 0.2 sec case. The range of hazard from the representative suite of common-form median models is broader than the range of hazard from the candidate GMPEs. The mean hazard from the representative suite of common-form models is within the range of the hazard from candidate

GMPEs. Overall, the uncertainty range of the hazard for the T = 2 sec case is much broader than for the T = 0.2 sec case, reflecting the wider uncertainty range of the representative suite of common-form models at long periods as compared to the short periods as seen earlier in Figures 8.4-6, 8.4-7, and 8.4-8.

Figures 8.4-18 shows the 5 Hz mean hazard curves for the representative suite of common-form models, the candidate GMPEs (given equal weight) and the upper and lower bound for the candidate GMPEs with the additional epistemic uncertainty. Figure 8.4-19 shows the same information for the 0.5 Hz hazard. For the 5 Hz case, the mean hazard from the representative suite of common-form models is slightly larger than the mean hazard from the candidate GMPEs. In contrast, for 0.5 Hz, the mean hazard from the candidate GMPEs is slightly larger than the mean hazard from the representative suite of common-form models.

Although the representative suite of common-form models does not fully span the range of the candidate GMPEs for all magnitudes, distances, and spectral periods, the hazard curves from these models do envelope the hazard from the candidate GMPEs for the key hazard levels of 10^{-4} to 10^{-6}, indicating that key median ground-motion features affecting the hazard have been adequately captured by the representative suite of common-form models for the median ground motion.

8.5 Hanging-Wall Adjustment

The five alternative HW models developed in Section 6.3 have equal weight. As described in Section 6.3, a single random HW model is assigned to each base-model GMPE, replacing the central HW model (denoted HW3 in Table 6.3-2) used for the Sammon's maps. The reason for assigning a single HW model rather than all combinations of base models and HW models is to reduce the calculation time for the Sammon's maps. The main use of the maps is to capture the range of base model scaling. The HW effects are then added to the base models to produce a complete set of models that captures both the range of the base models and the range of the HW models.

8.6 Directivity Adjustments on Median Ground Motions

As described in Section 6.5, a single directivity model is considered without epistemic uncertainty because the hazard sensitivity from Section 14.2.1 showed that including the directivity did not have a significant effect on the hazard. The approach to account for directivity adjustments to both median and standard deviation is described in Section 6.5. The model for directivity adjustments accounts for systematic differences in the ground motion (median and standard deviation) based on the location of

the site along the rupture. For a given scenario, there can be significant differences in the ground motion for a specific site-source geometry due to directivity. The DCPP SSC includes large ruptures on the nearby faults (Section 4.1) where defined earthquakes are capable of having large directivity effects. However, the hazard is not significantly affected by directivity, and the TI Team chose not to include directivity effects following the justifications given in Section 6.5.2.

8.7 Rule-based Approach for Complex and Splay Sources

The evaluation of alternative rules is given in Section 6.7 and Appendix J (Section J.4). For complex ruptures (change in dip or rake along strike), the ground motion is given by the square root of the sum of the squares (SRSS) of the ground motions computed for each of the two sub-sources separately. For splay ruptures (overlapping ruptures of two sources), the ground motion is given by the SRSS of the ground motions computed for each of the two sub-sources separately. Epistemic uncertainty on the rule is not incorporated, because these cases have low rates and have a small effect on resulting hazard, as shown in Workshops #2 and #3.

8.8 References

Abrahamson, N.A., and Youngs, R.R. (1992). A stable algorithm for regression analysis using the random effects model, *Bull. Seism. Soc. Am*., Vol. 82, 505-510.

Abrahamson, N.A., Silva, W.J., and Kamai, R. (2014). Summary of the AKS14 Ground-Motion Relation for Active Crustal Regions*, Earthquake Spectra*, Vol. 30(3), 1025-1055, DOI: 10.1193/070913EQS198M

Akkar, S., Sandikkaya, M.A., and Bommer, J.J. (2014a). Empirical ground-motion models for point- and extended-source crustal earthquake scenarios in Europe and the Middle East, *Bull. Earthquake Eng*., Vol. 12, 359–387, DOI: 10.1007/s10518-013-9461-4

Akkar, S., Sandikkaya, M.A., and Bommer, J.J. (2014b). Erratum to: Empirical ground-motion models for point- and extended-source crustal earthquake scenarios in Europe and the Middle East, *Bull. Earthquake Eng*, Vol. 12(1), 389-390, DOI: 10.1007/s10518-013-9508-6

Al Atik, L., and Youngs, R.R. (2014). Epistemic Uncertainty for NGA-West2 Models, *Earthquake Spectra*, Vol. 30, DOI: 10.1193/062813EQS173M

Atkinson, G.M, and Assatourians, K. (2015). Implementation and validation of EXSIM (a stochastic finite-fault ground-motion simulation algorithm) on the SCEC broadband platform, *Seismol. Res. Letts Letts*., Vol. 86(1), 48-60, DOI: 10.1785/0220140097.

Boore, D.M., Stewart, J.P., Seyhan, E., and Atkinson, G.M. (2014). NGA-West 2 Equations for Predicting PGA, PGV, and 5%-Damped PSA for Shallow Crustal Earthquakes, *Earthquake Spectra*, Vol. 30(3), 1057-1085, DOI: 10.1193/070113EQS184M.

Campbell, K.W., and Bozorgnia, Y. (2014). NGA-West2 Ground Motion Model for the Average Horizontal Components of PGA, PGV, and 5%-Damped Linear Acceleration Response Spectra, *Earthquake Spectra*, Vol. 30(3), DOI: 10.1193/062913EQS175M.

Chiou, B.S-J., and Youngs, R.R. (2014). Update of the Chiou and Youngs NGA Model for the Average Horizontal Component of Peak Ground Motion and Response Spectra, *Earthquake Spectra*, Vol. 30(3), 1117-1153, DOI: 10.1193/072813EQS219M.

Graizer, V. (2014). Updated Graizer-Kalkan Ground-motion Prediction Equations for Western United States, *Proceedings for the 10th U.S. National Conference on Earthquake Engineering Frontiers of Earthquake Engineering*, July 21-25, 2014, Anchorage, Alaska, Paper ID 1097, 11 pp.

Graves, R.W. and Pitarka, A. (2015). Refinements of the Graves and Pitarka (2010) Broadband Ground-Motion Simulation Method, *Seismol. Res. Letts.*, Vol. 86(1), 75-80, DOI: 10.1785/0220140101.

Idriss, I.M. (2014). An NGA-West2 Empirical Model for Estimating the Horizontal Spectral Values Generated by Shallow Crustal Earthquakes, *Earthquake* Spectra, Vol. 30(3), 1155-1177, DOI: 10.1193/070613EQS195M.

Olsen, K. and Takedatsu, R. (2015). The SDSU Broadband Ground Motion Generation Module BBtoolbox Version 1.5, *Seismol. Res. Letts*., Vol. 86(1), 81-88, DOI: 10.1785/0220140102.

Zhao, J.X., Zhang, J., Asano, A., Ohno, Y., Oouchi, T., Takahashi, T., Ogawa, H., Irikura, K., Thio, H.K., Somerville, P.G., Fukushima, Y., and Fukushima, Y. (2006). Attenuation Relations of Strong Ground Motion in Japan Using Site Classification Based on Predominate Period, *Bull. Seism. Soc. Am*., Vol. 96, 898-913.

Zhao, J.X., and Lu, M. (2011). Magnitude-Scaling Rate in Ground-Motion Prediction Equations for Response Spectra from Large, Shallow Crustal Earthquakes, *Bull. Seism. Soc. Am*., Vol. 101, 2643-2661.

Table 8.4-1: Scenarios used for the evaluation of the CDF distributions of the representative suite of common-form models for DCPP.

Magnitude	R_X Distance (km)	Style of Faulting (SOF)
5.5	-1	0 (Strike Slip)
5.5	-5	0 (Strike Slip)
5.5	-10	0 (Strike Slip)
6.5	-1	0 (Strike Slip)
6.5	-5	0 (Strike Slip)
6.5	-10	0 (Strike Slip)
7.5	-1	0 (Strike Slip)
7.5	-5	0 (Strike Slip)
7.5	-10	0 (Strike Slip)
5.5	-1	1 (Reverse)
5.5	-5	1 (Reverse)
5.5	-10	1 (Reverse)
6.5	-1	1 (Reverse)
6.5	-5	1 (Reverse)
6.5	-10	1 (Reverse)
7.5	-1	1 (Reverse)
7.5	-5	1 (Reverse)
7.5	-10	1 (Reverse)

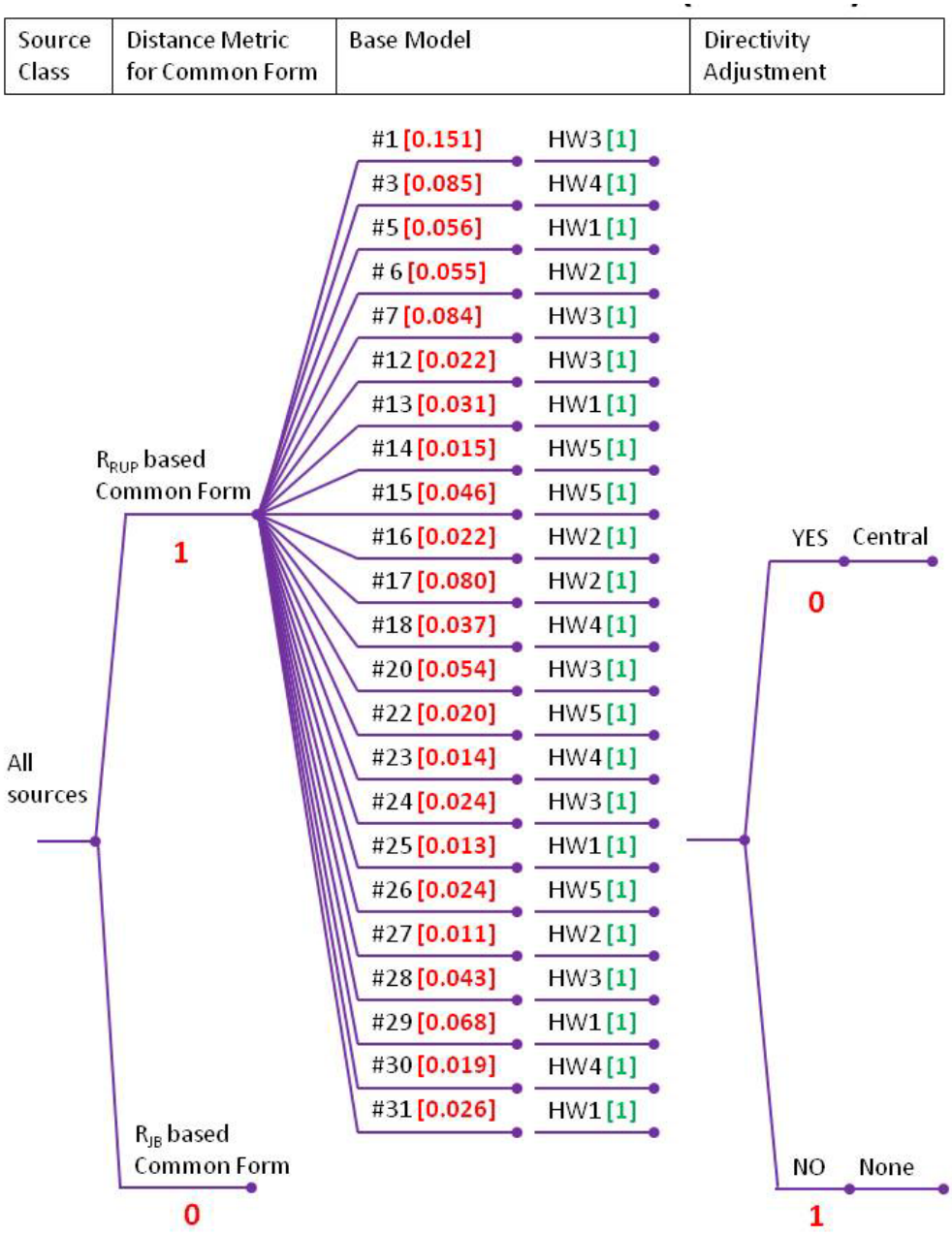

Figure 8.2-1: Logic tree for the median at DCPP for the local faults. The representative suite of common-form models is shown by the unique Model ID # (up to #31), and the models' weights are rounded to the third decimal point. The HW branch name refers to a random sample from one of the five HW models (HW1 to HW5). The weights associated with the TI Team's subjective evaluations are in red, whereas weights associated with statistical sampling are in green. The approach to compute the weights for the models is shown in the logic tree in Figure 8.2-2. The weights shown for the base models and the hanging wall models are for one example case (PGA). The weights for the other periods are listed in the DCPP Hazard Input Document (HID) available in Appendix C – Part II.

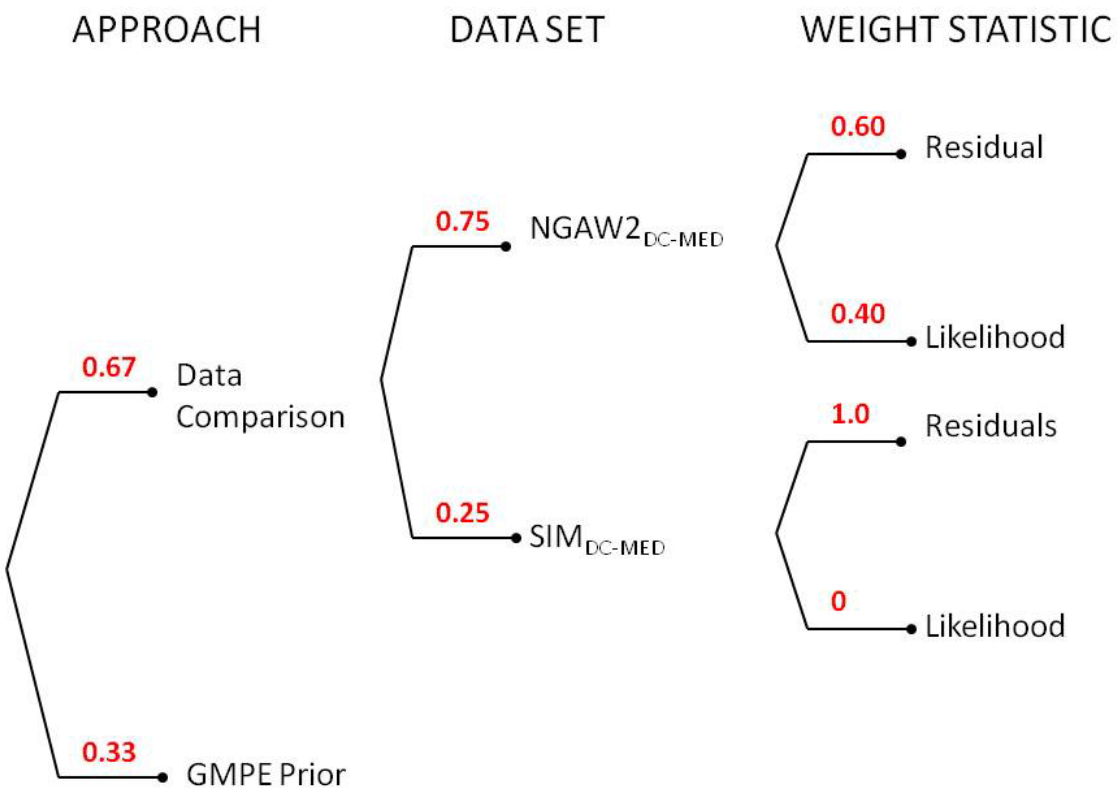

Figure 8.2-2: Weighting scheme for the median base models, involving alternative datasets and alternative weight metrics. The weights associated with the TI Team's subjective evaluations are in red. The description of the data set branches is provided in Section 5.3.1: "$SIM_{DC\text{-}MED}$" and "$NGAW2_{DC\text{-}MED}$" refer to the suite of finite-fault simulations and to the subset of NGA-West2 data used for constraining the median models, respectively.

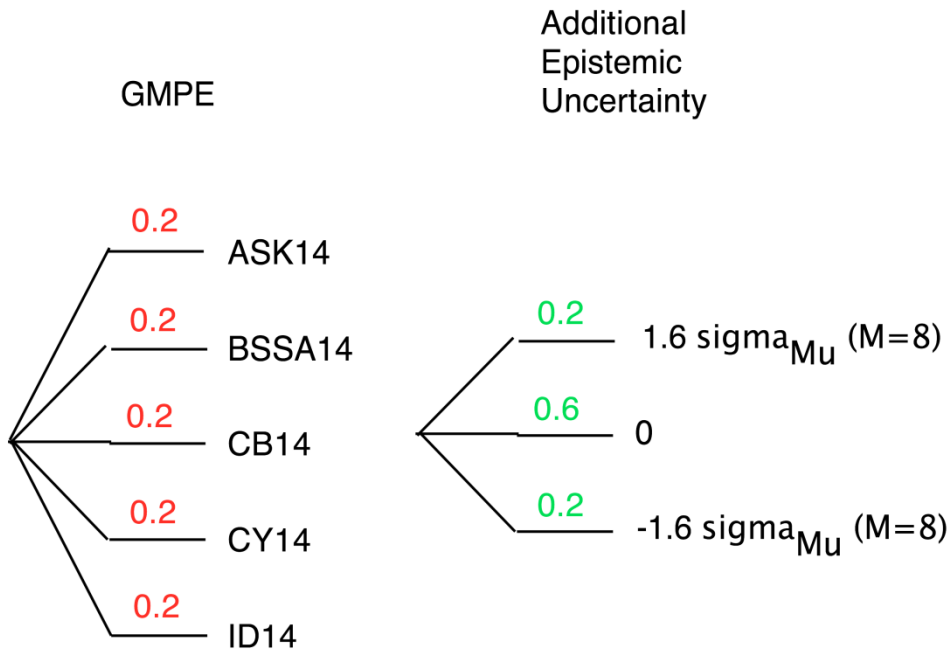

Figure 8.2-3: Logic tree for the median at DCPP for the distant faults. The weights associated with the TI Team's subjective evaluations are in red, whereas weights associated with statistical sampling are in green.

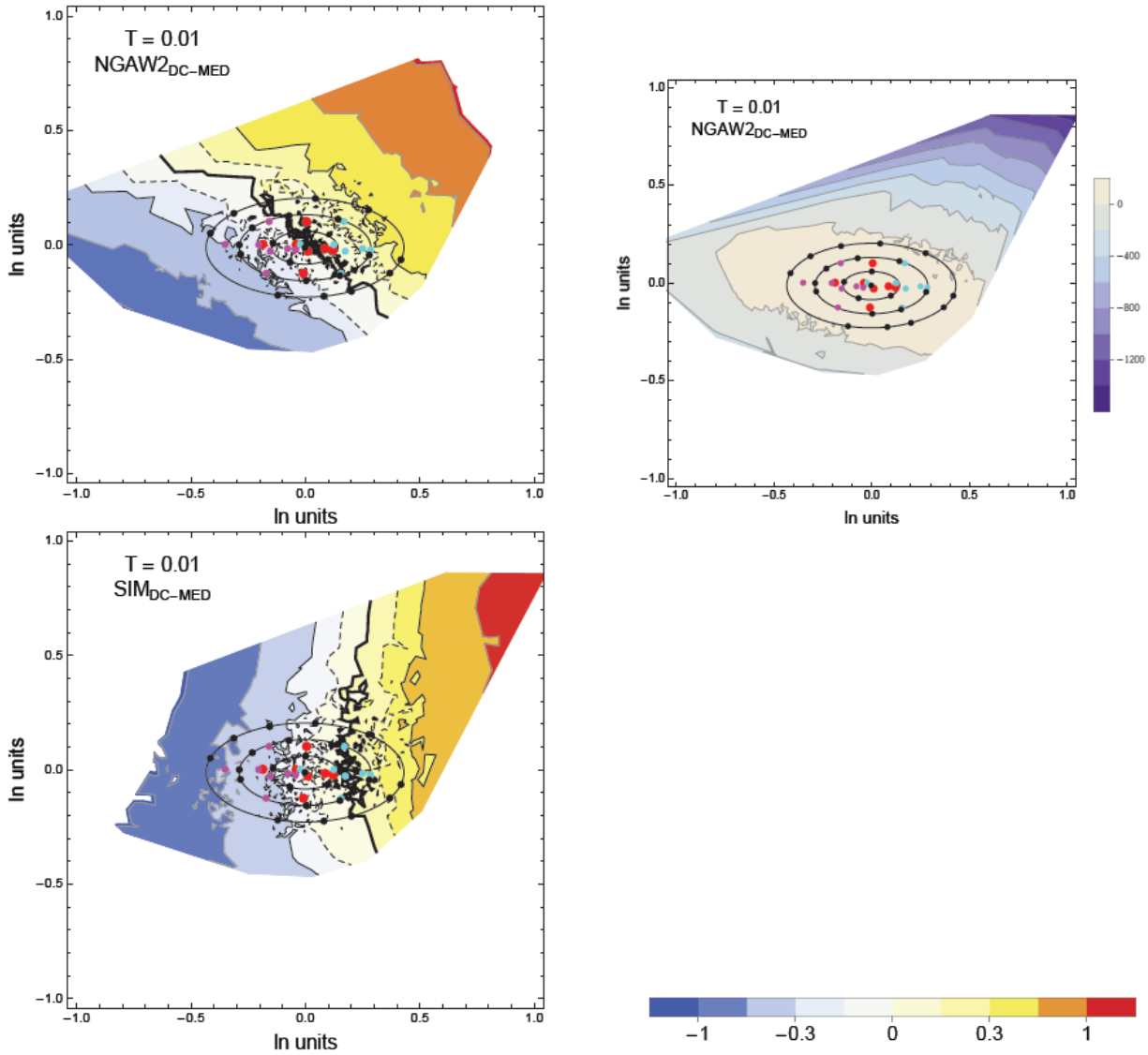

Figure 8.4-1: Range of PGA models generated from sampling the joint distribution of the common-form parameter distribution and the range of representative suite of common-form models (black dots). Red dots show the candidate GMPEs used to develop the ground-motion model distributions. The magenta and cyan dots show plus and minus two sigma epistemic uncertainty, respectively, about the candidate GMPEs. The Voronoi cells (gray closed polygons) are developed based on the locations of the black points on the ellipses (gray concentric curves). The contour for the zero residual is a thick black line, the ± 0.15 contours are dashed black lines and the ± 0.3 contours are thin black lines. Upper left: contour lines indicate the mean between-event residuals for the $NGAW2_{DC\text{-}MED}$ data set. Lower left: contour lines indicate the mean between-event residuals for the simulation data set. Upper right: contour lines indicate the likelihood for the $NGAW2_{DC\text{-}MED}$ data set.

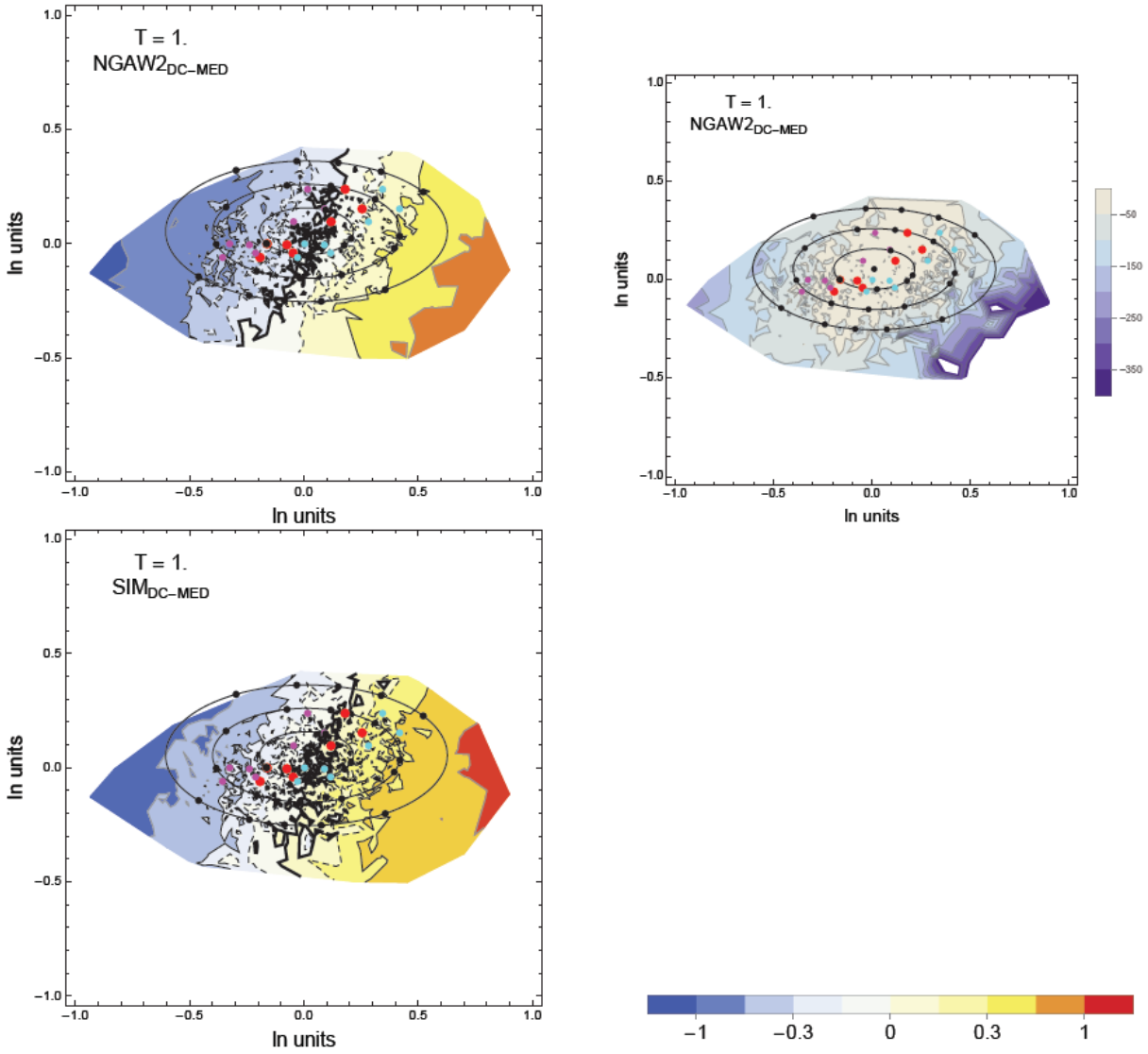

Figure 8.4-2: Range of T = 1 sec models generated from sampling the joint distribution of the common-form parameter distribution and the range of representative suite of common-form models (black dots). Red dots show the candidate GMPEs used to develop the ground-motion model distributions. The magenta and cyan dots show plus and minus two sigma epistemic uncertainty, respectively, about the candidate GMPEs. The Voronoi cells (gray closed polygons) are developed based on the locations of the black points on the ellipses (gray concentric curves). The contour for the zero residual is a thick black line, the ± 0.15 contours are dashed black lines and the ± 0.3 contours are thin black lines. Upper left: contour lines indicate the mean between-event residuals for the $NGAW2_{DC-MED}$ data set. Lower left: contour lines indicate the mean between-event residuals for the simulation data set. Upper right: contour lines indicate the likelihood for the $NGAW2_{DC-MED}$ data set.

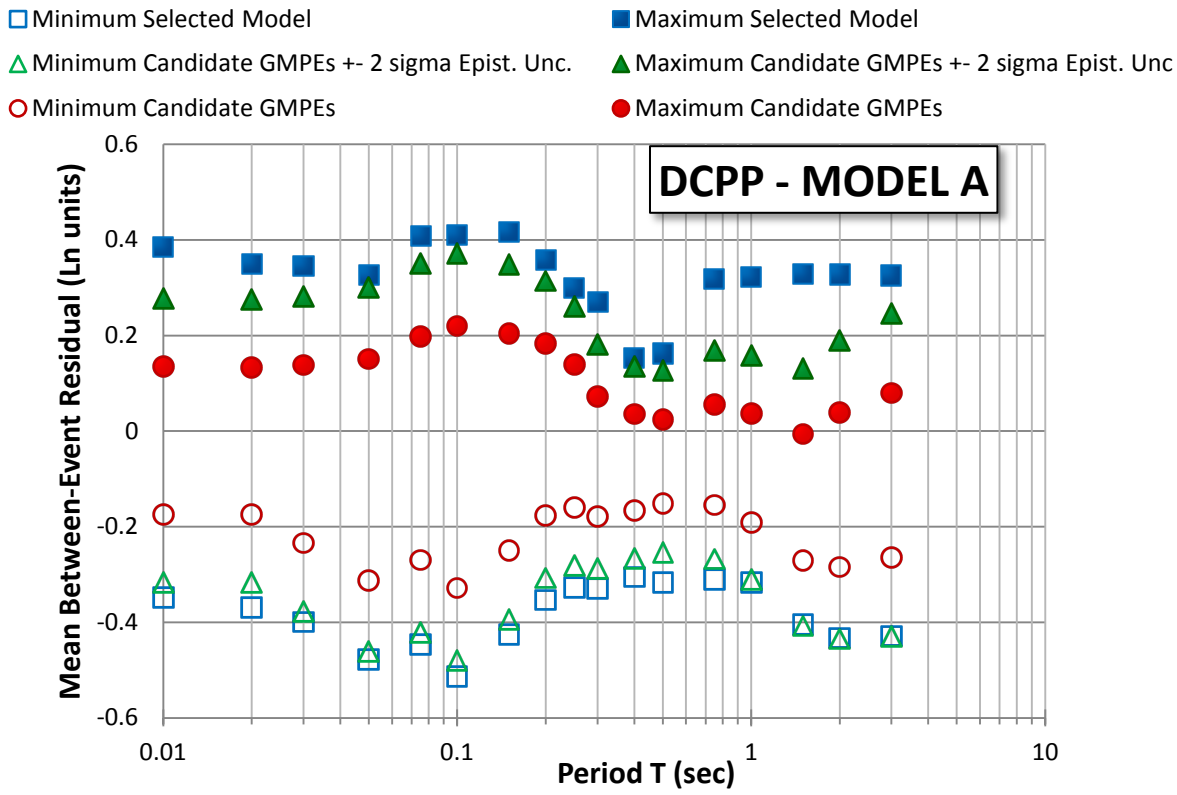

Figure 8.4-3: Range of mean between-event residuals for R_{RUP}-based common-form models (Model A) selected to represent the distribution of ground-motion models for evaluation of hazard at the DCPP site.

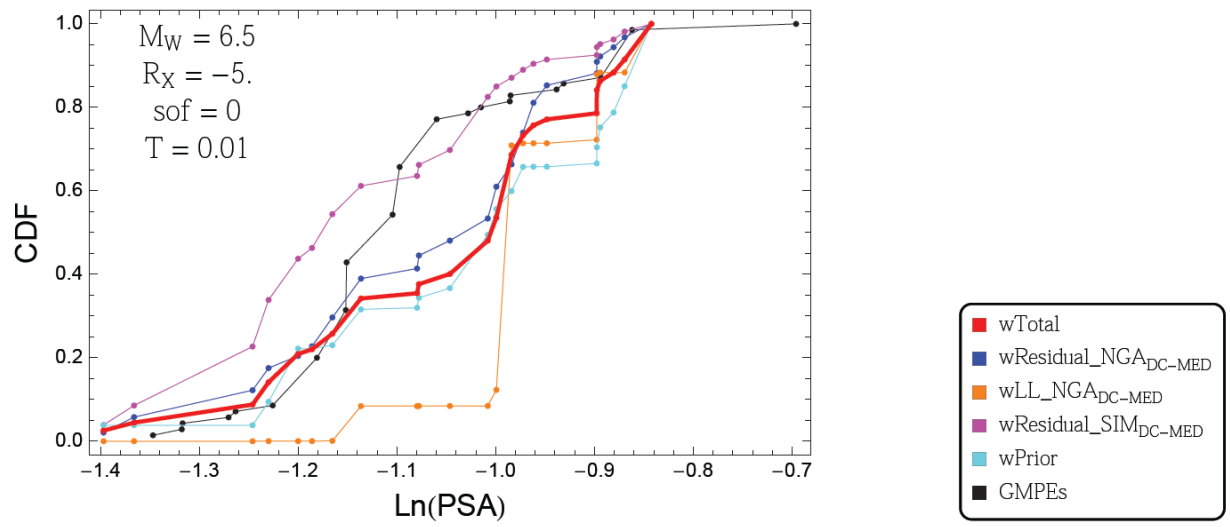

Figure 8.4-4: Example of the cumulative distribution function of the ln PGA for **M** = 6.5, strike-slip earthquakes at a R_X distance of 5 km. The red curve is the weighted average selected by the TI Team. The other curves show what the distribution would be if full weight was assigned to each weighting method. The curves for the GMPEs and the prior are based on equal weight to each candidate GMPE.

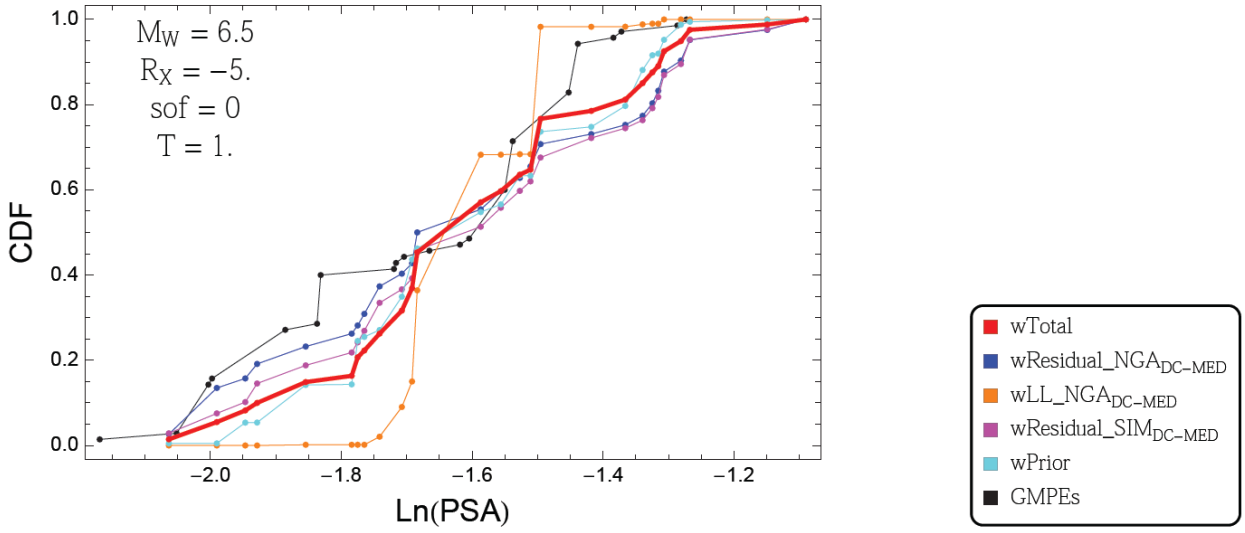

Figure 8.4-5: Example of the cumulative distribution function of the ln PSA (T = 1 sec) for **M** = 6.5, strike-slip earthquakes at a R_X distance of 5 km. The red curve is the weighted average selected by the TI Team. The other curves show what the distribution would be if full weight was assigned to each weighting method. The curves for the GMPEs and the prior are based on equal weight to each candidate GMPE.

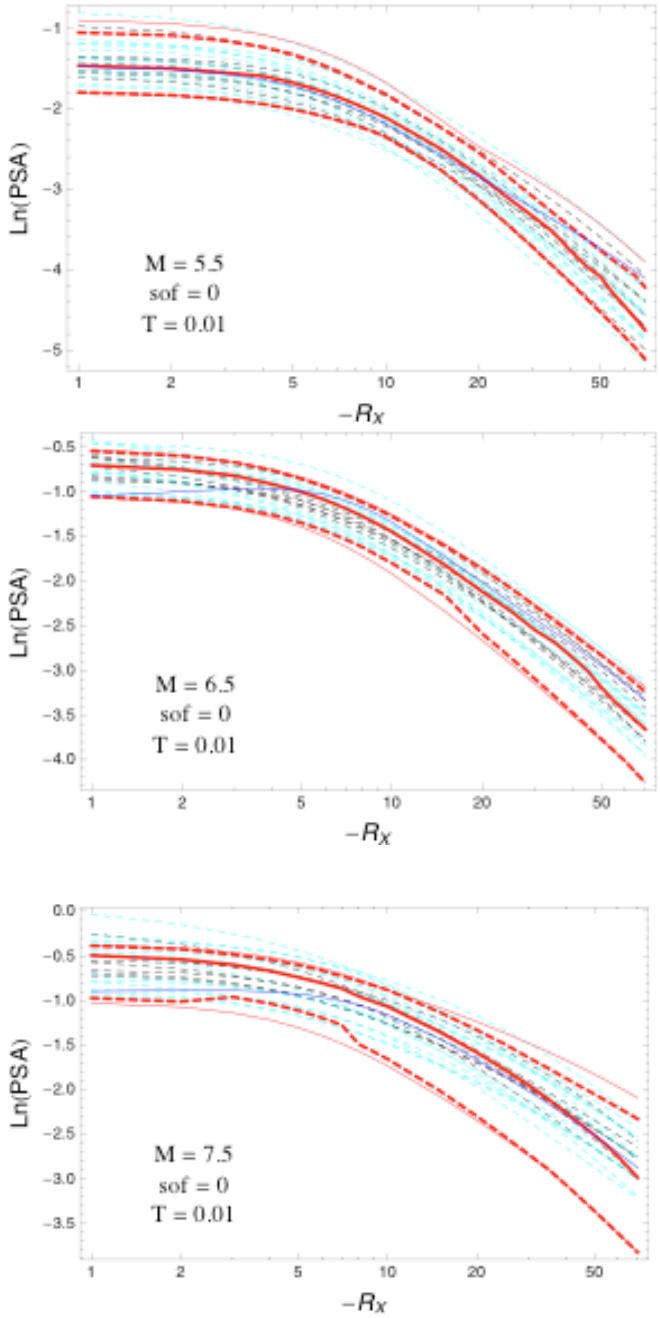

Figure 8.4-6: Example of the distance scaling of the candidate GMPEs (dashed black lines), additional epistemic uncertainty (cyan lines) and 0.05, 0.5, and 0.95 quantiles of the DCPP Model A distribution (red) with total weights obtained from the weighting scheme depicted in Figure 8.2-2. Blue lines are for the GK14 distance scaling, provided for comparison even though the model was not part of the candidate GMPEs. The three panels refer to three scenarios with **M**5.5 (top), **M**6.5 (center) and **M**7.5 (bottom), SS style-of-faulting and T = 0.01 sec. The thin red lines show the minimum and maximum of the representative common-form models.

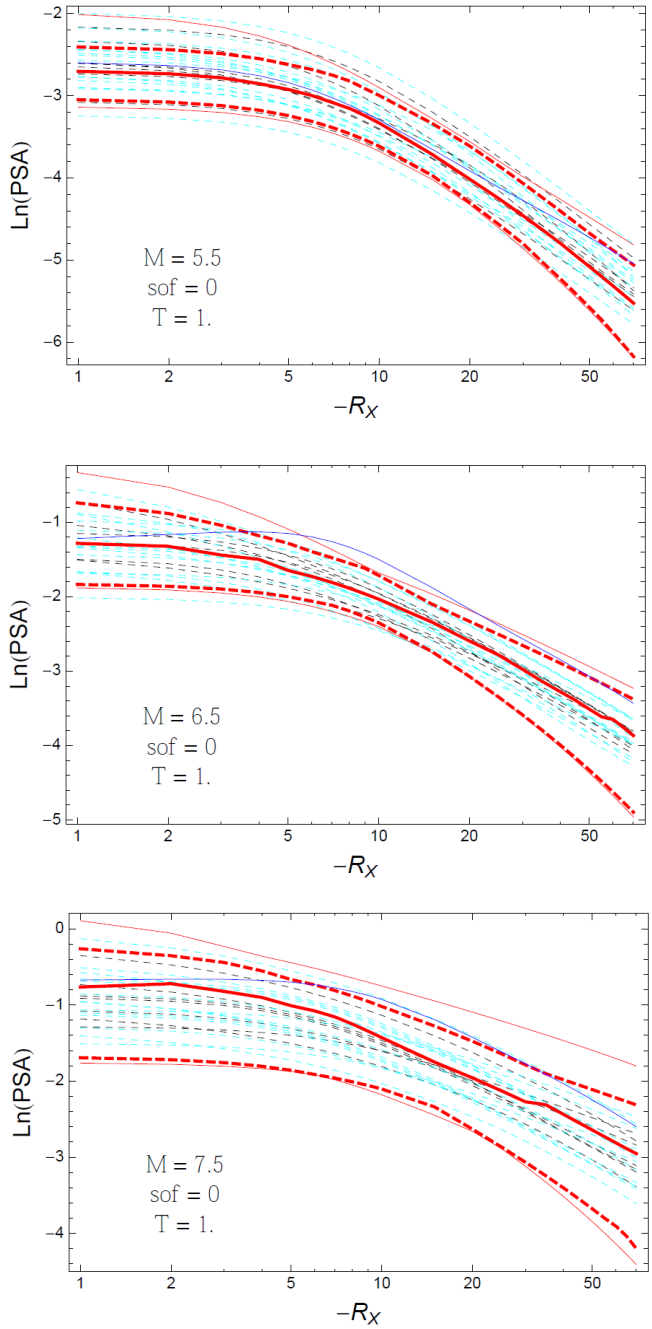

Figure 8.4-7: Example of the distance scaling of the candidate GMPEs (dashed black lines), additional epistemic uncertainty (cyan lines) and 0.05, 0.5, and 0.95 quantiles of the DCPP Model A distribution (red) with total weights obtained from the weighting scheme depicted in Figure 8.2-2. Blue lines are for the GK14 distance scaling, provided for comparison even though the model was not part of the candidate GMPEs. The three panels refer to three scenarios with **M**5.5 (top), **M**6.5 (center) and **M**7.5 (bottom), SS style-of-faulting and T = 1.0 sec. The thin red lines show the minimum and maximum of the representative common-form models.

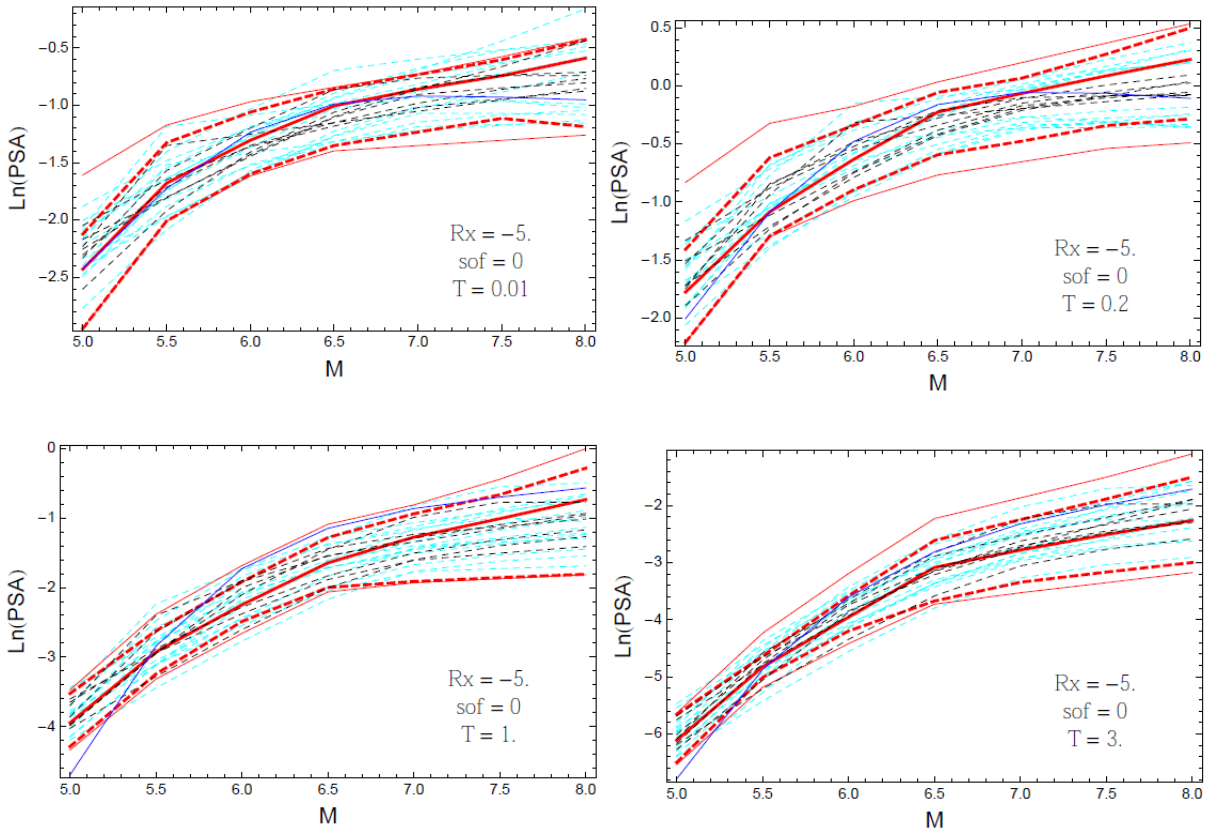

Figure 8.4-8: Example of the magnitude scaling of the candidate GMPEs (dashed black lines), the candidate GMPEs with epistemic uncertainty (dashed cyan lines), and 0.05, 0.5, and 0.95 quantiles of the DCPP Model A distribution (red) with total weights obtained from the weighting scheme depicted in Figure 8.2-2, for a scenario with SS style-of-faulting for an R_X distance of 5 km. Blue lines are for the GK14 distance scaling, provided for comparison even though the model was not part of the candidate GMPEs. The thin red curves are the minimum and maximum of the representative common-form models. The four panels refer to PGA (top left), T = 0.2 sec (top right), T = 1 sec (bottom left) and T = 3 sec (bottom right).

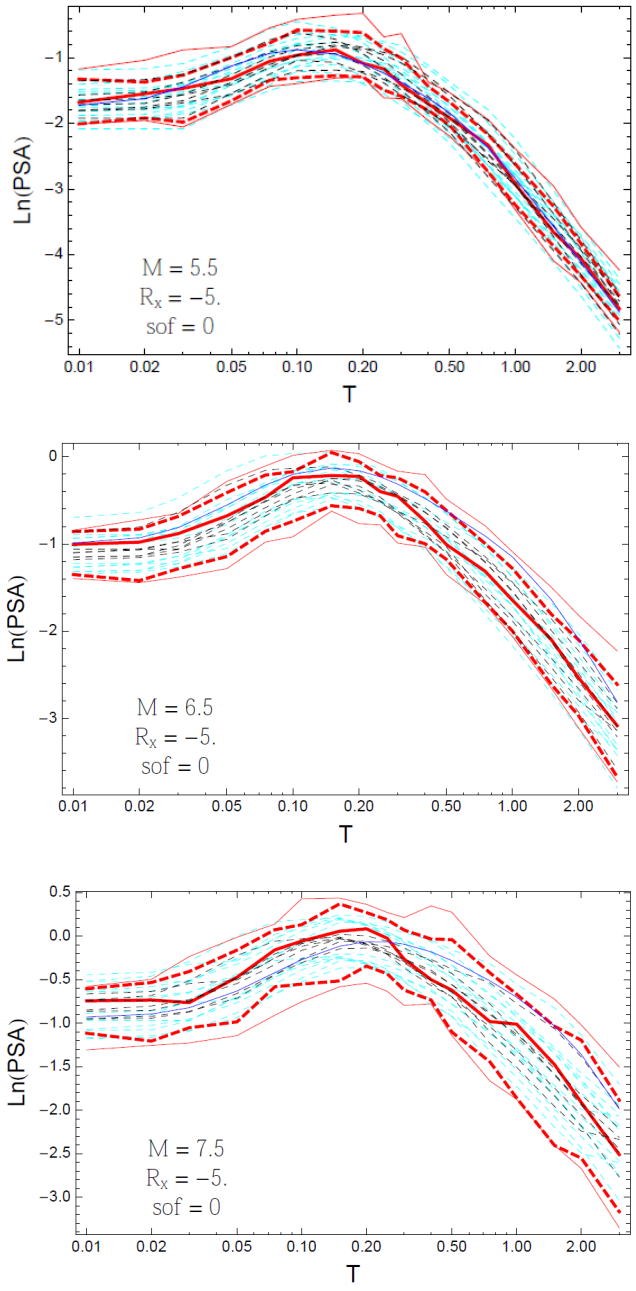

Figure 8.4-9: Example of the spectral shape of the candidate GMPEs (dashed black lines), the candidate GMPEs with epistemic uncertainty (dashed cyan lines), and 0.05, 0.5, and 0.95 quantiles of the DCPP Model A distribution (red) with total weights obtained from the weighting scheme depicted in Figure 8.2-2. The three panels refer to three scenarios with **M**5.5 (top), **M**6.5 (center) and **M**7.5 (bottom), SS style-of-faulting and R_X = -5 km. Blue lines are for the GK14 distance scaling, provided for comparison even though the model was not part of the candidate GMPEs. The thin red lines show the minimum and maximum of the representative common-form models.

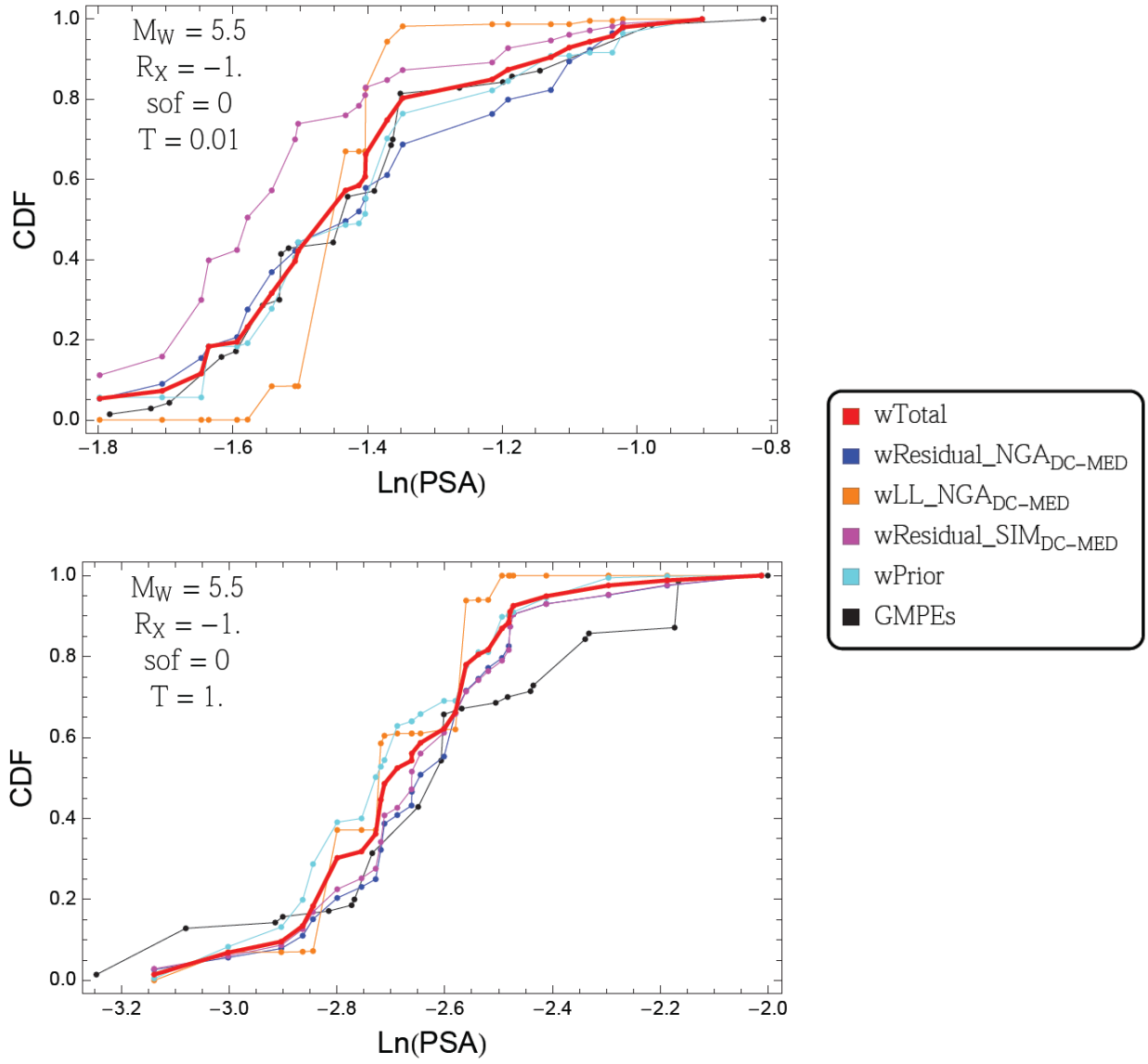

Figure 8.4-10: Example of the cumulative distribution function of the ln PGA for **M** = 5.5, strike-slip earthquakes at a R_x distance of -1 km for PGA (top) and T = 1.0 sec (bottom). The red curve is the weighted average selected by the TI Team. The other curves show what the distribution would be if full weight was assigned to each weighting method. The curves for the GMPEs and the prior are based on equal weight to each candidate GMPE.

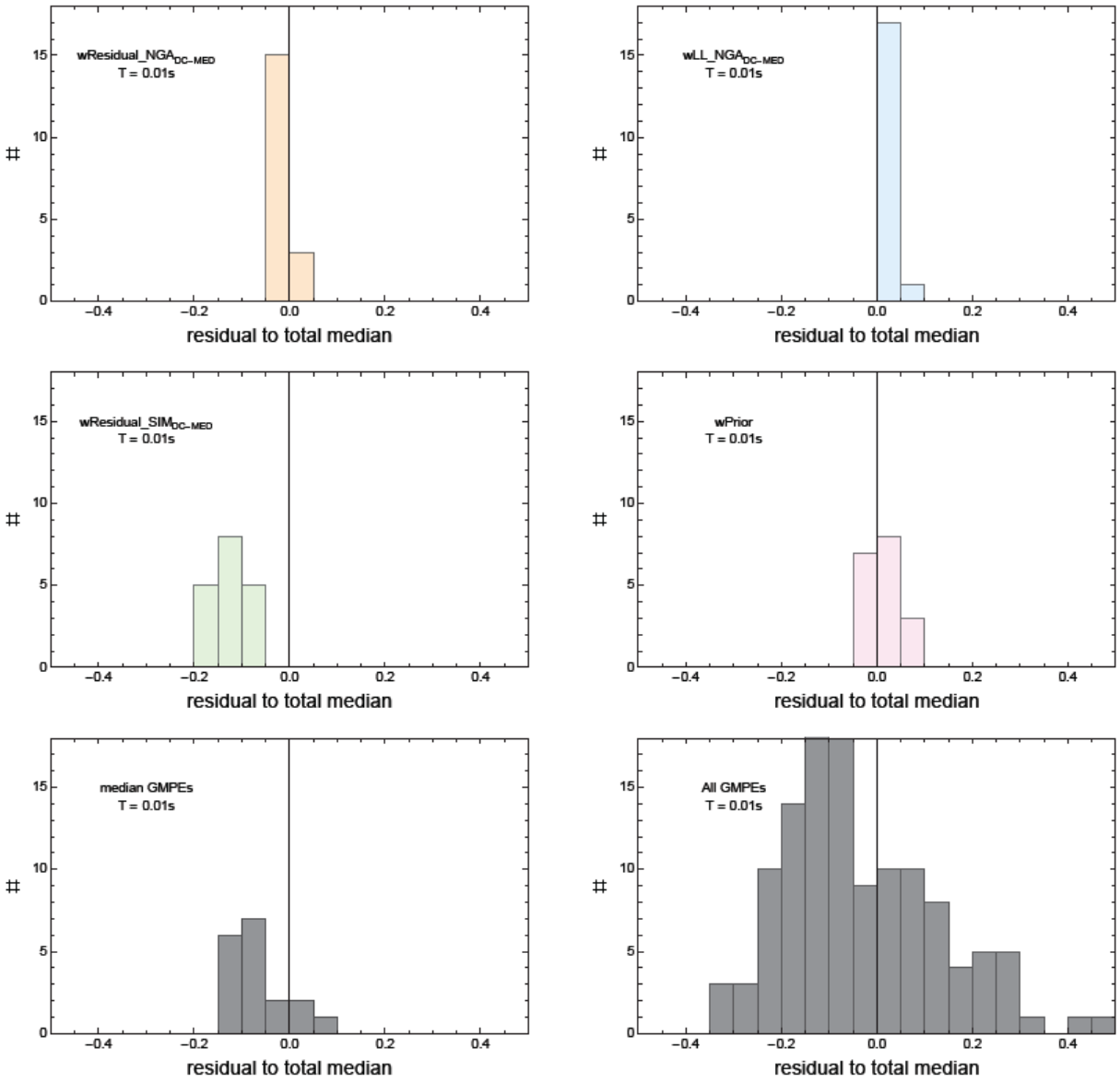

Figure 8.4-11: Example of the influence of the alternative data sets and the prior on the median ground motion for PGA for the scenarios listed in Table 8.4-1. The differences for medians calculated with different weights to median calculated with total weights are plotted in the histograms. The top row shows (left) weights from residual with the $NGA_{DC\text{-}MED}$ data set and (right) weights from the likelihood estimate from the $NGA_{DC\text{-}MED}$ data set. The middle row shows (left) weights from the residual with the $SIM_{DC\text{-}MED}$ data set, and (right) weights from the prior. The zero residual is relative to the PSA at CDF = 0.5 for the weighted common-form models (e.g. red curves in figures showing CDF). Bottom row left shows differences between medians for the GMPE distribution to median calculated with total weights. Bottom row right shows differences between the candidate GMPEs (without uncertainty) to median calculated with total weights.

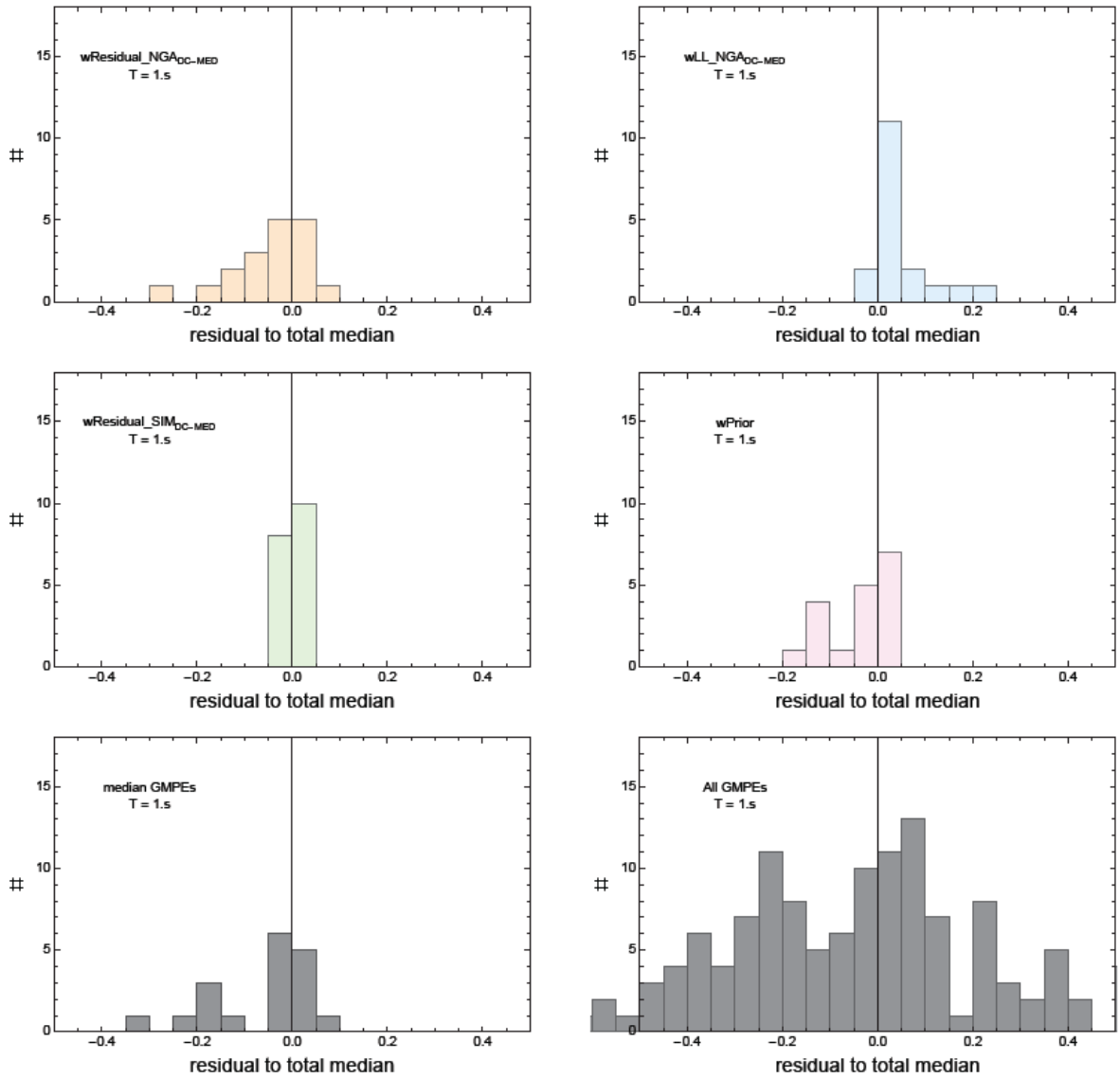

Figure 8.4-12: Example of the influence of the alternative data sets and the prior on the median ground motion for T = 1 sec for the scenarios listed in Table 8.4-1. The differences for medians calculated with different weights to median calculated with total weights are plotted in the histograms. The top row shows (left) weights from residual with the $NGA_{DC\text{-}MED}$ data set and (right) weights from the likelihood estimate from the $NGA_{DC\text{-}MED}$ data set. The middle row shows (left) weights from the residual with the $SIM_{DC\text{-}MED}$ data set, and (right) weights from the prior. The zero residual is relative to the PSA at CDF = 0.5 for the weighted common-form models (e.g. red curves in figures showing CDF). Bottom row left shows differences between medians for the GMPE distribution to median calculated with total weights. Bottom row right shows differences between the candidate GMPEs (without uncertainty) to median calculated with total weights.

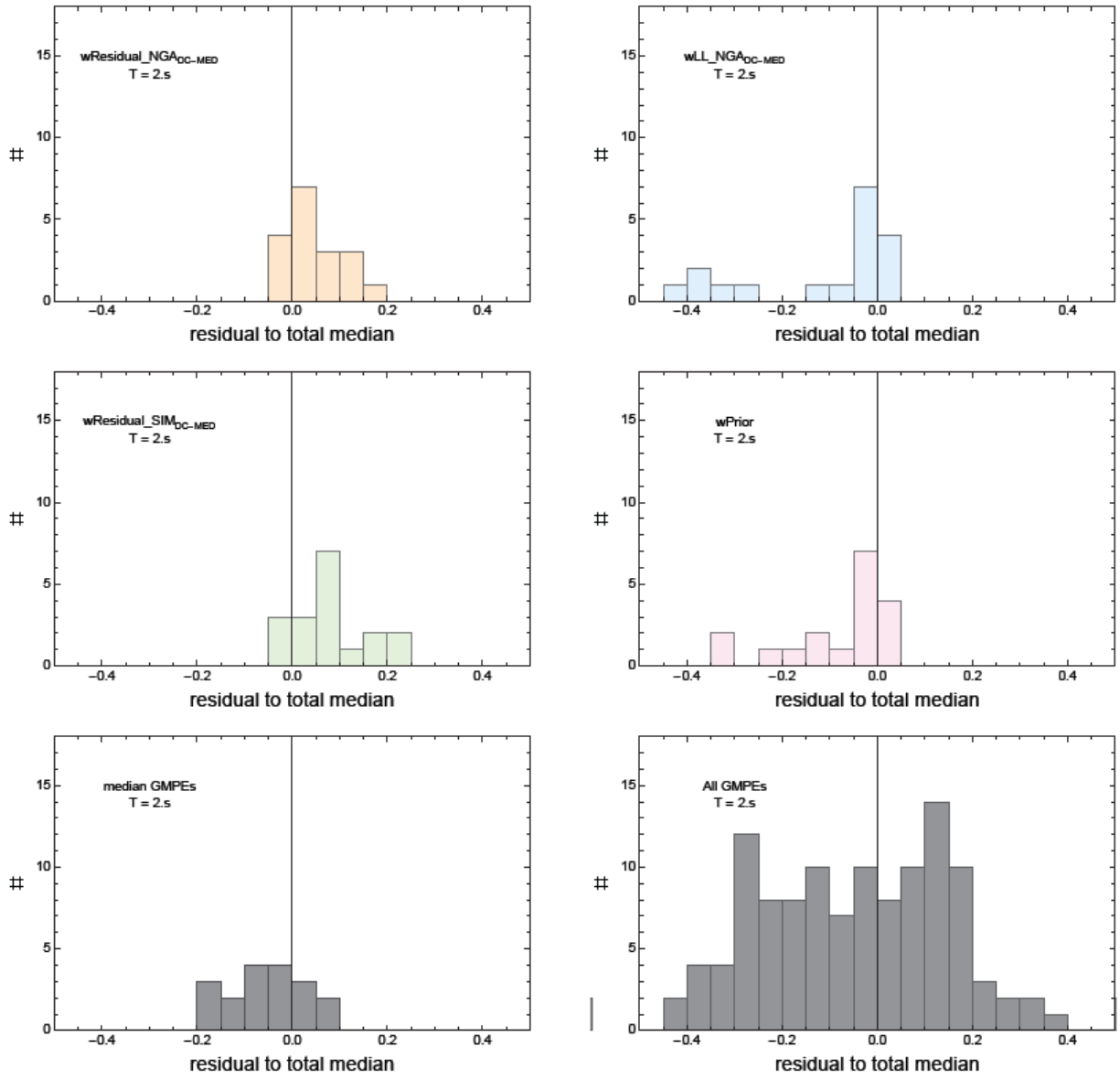

Figure 8.4-13: Example of the influence of the alternative data sets and the prior on the median ground motion for T = 3 sec for the scenarios listed in Table 8.4-1. The differences for medians calculated with different weights to median calculated with total weights are plotted in the histograms. The top row shows (left) weights from residual with the NGA_{DC-MED} data set and (right) weights from the likelihood estimate from the NGA_{DC-MED} data set. The middle row shows (left) weights from the residual with the SIM_{DC-MED} data set, and (right) weights from the prior. The zero residual is relative to the PSA at CDF = 0.5 for the weighted common-form models (e.g. red curves in figures showing CDF). Bottom row left shows differences between medians for the GMPE distribution to median calculated with total weights. Bottom row right shows differences between the candidate GMPEs (without uncertainty) to median calculated with total weights.

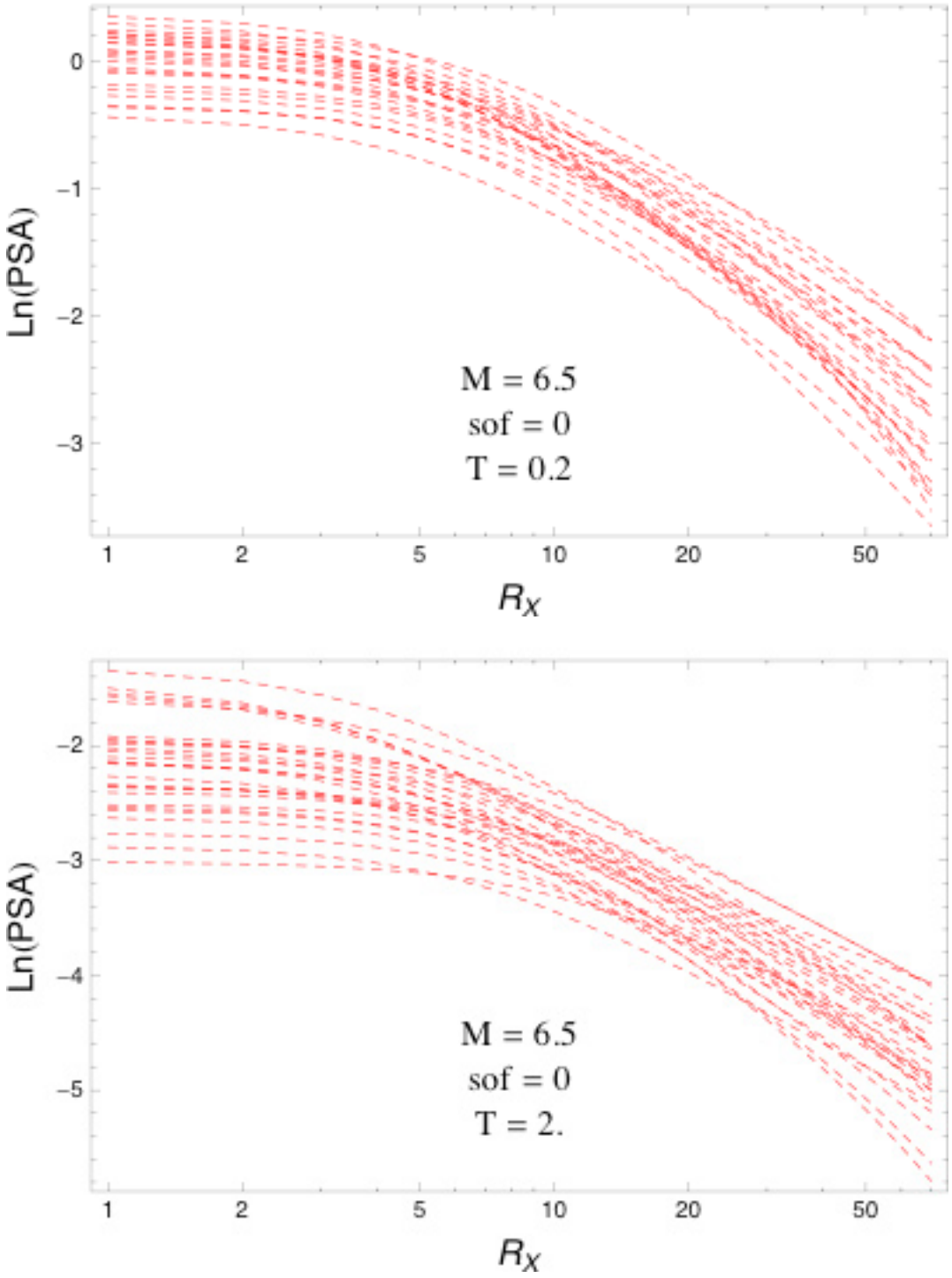

Figure 8.4-14: Example of the distance scaling for the representative suite of common-form models for **M**6.5 vertical strike-slip earthquakes. Top: T = 0.2 sec. Bottom: T = 2 sec.

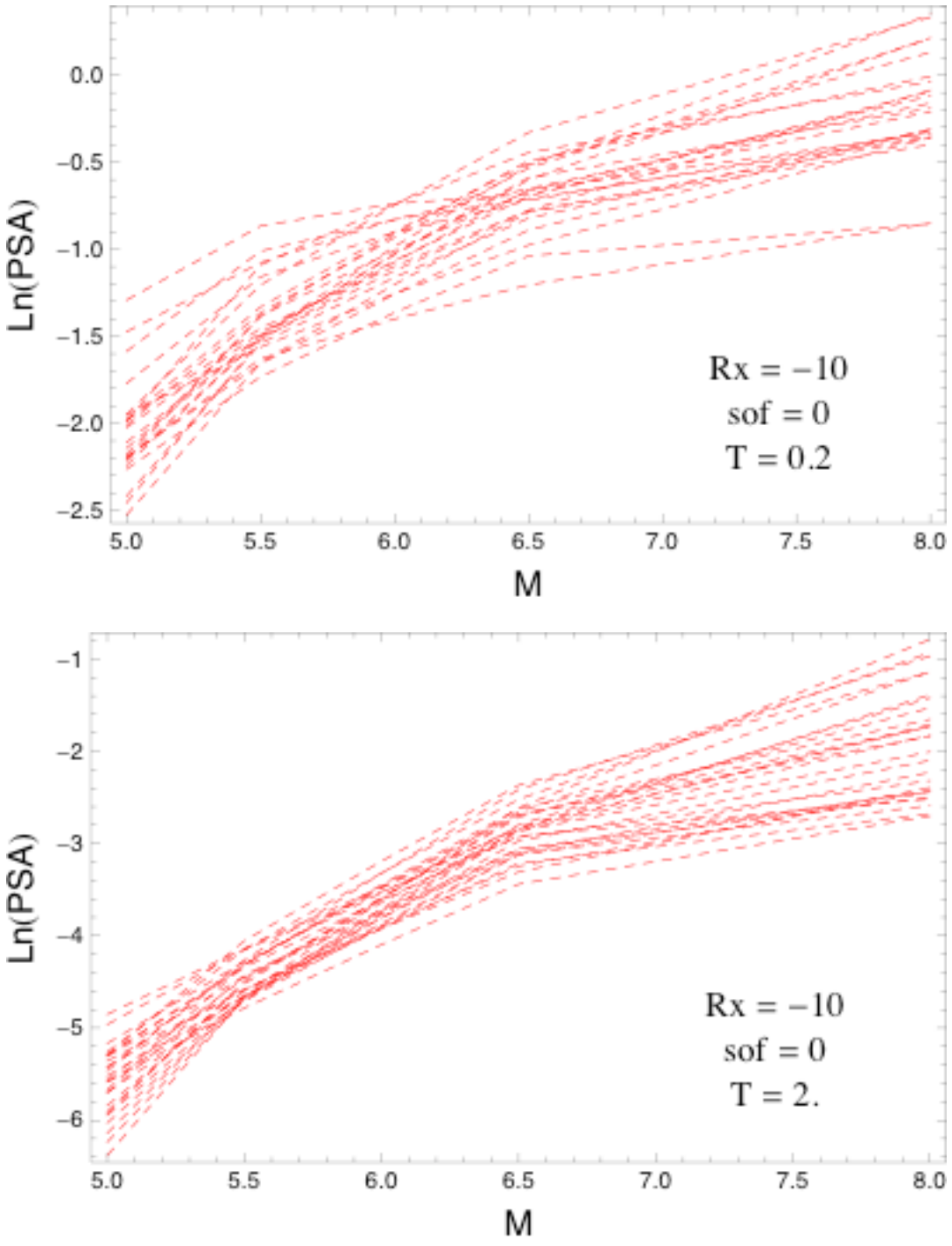

Figure 8.4-15: Example of the magnitude scaling for the representative suite of common-form models for vertical strike-slip earthquakes at an R_X distance of -10 km. Top: T = 0.2 sec. Bottom: T = 2 sec.

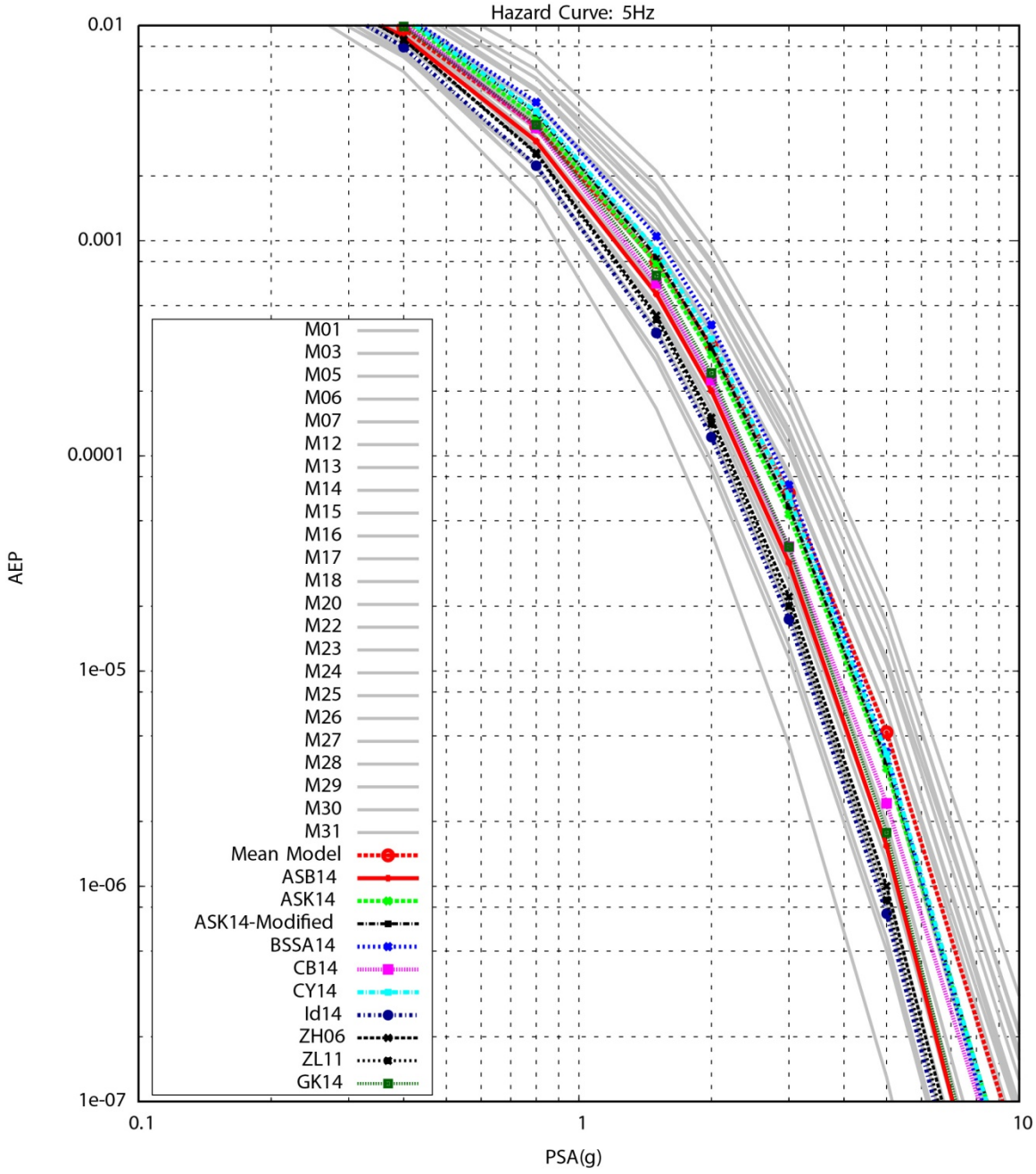

Figure 8.4-16: Comparison of 5 Hz hazard curves using the representative suite of common-form models (grey lines), weighted mean common-form model and the eight empirical GMPE models. For reference, the hazard curves for the GK14 model and for the modified ASK14 model in which the magnitude taper of the HW model is removed are also shown.

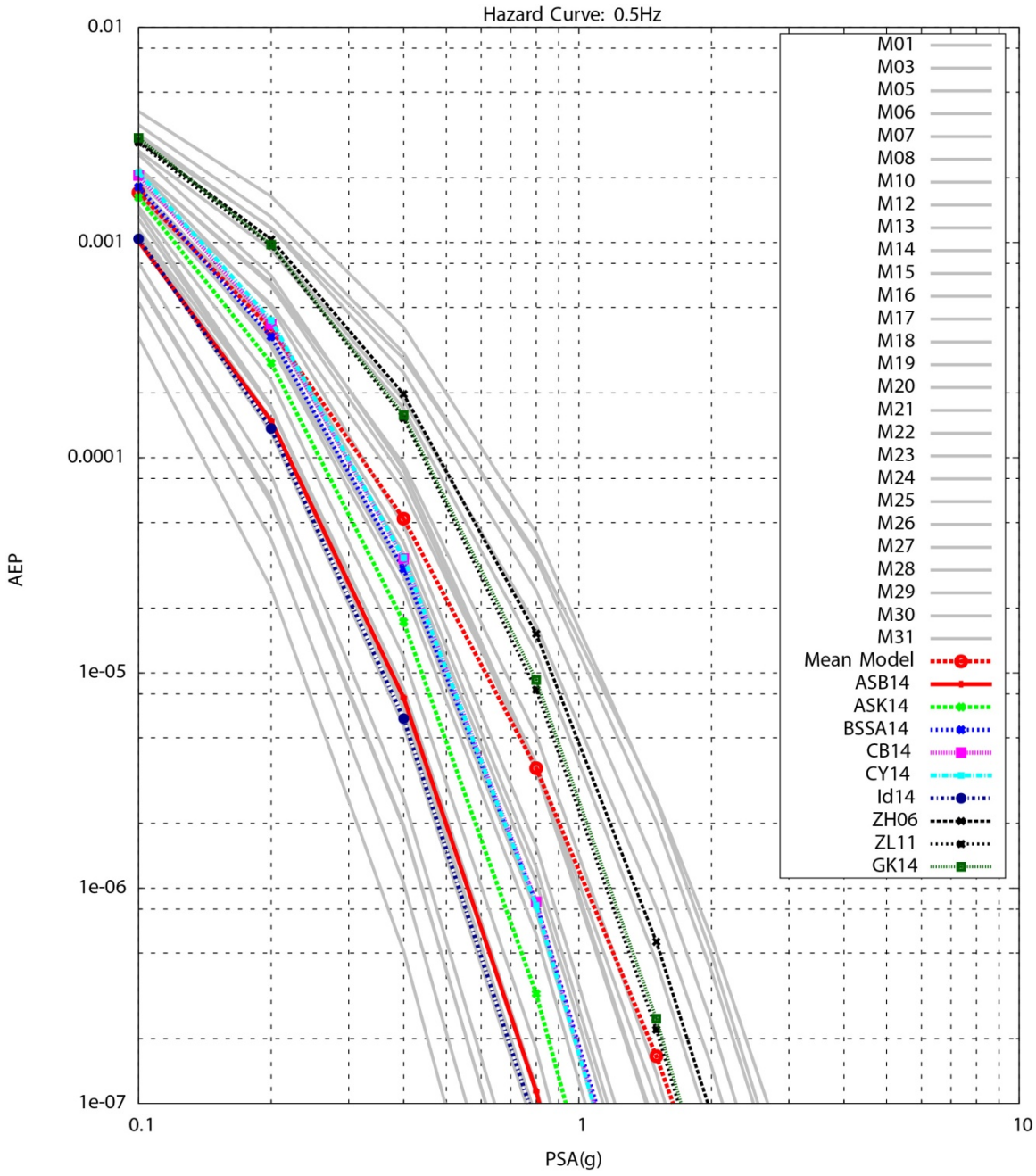

Figure 8.4-17: Comparison of 0.5 Hz hazard curves using the representative suite of common-form models (grey lines), weighted mean common-form model and the eight candidate GMPE models. For reference, the hazard curve for the GK14 model is also shown.

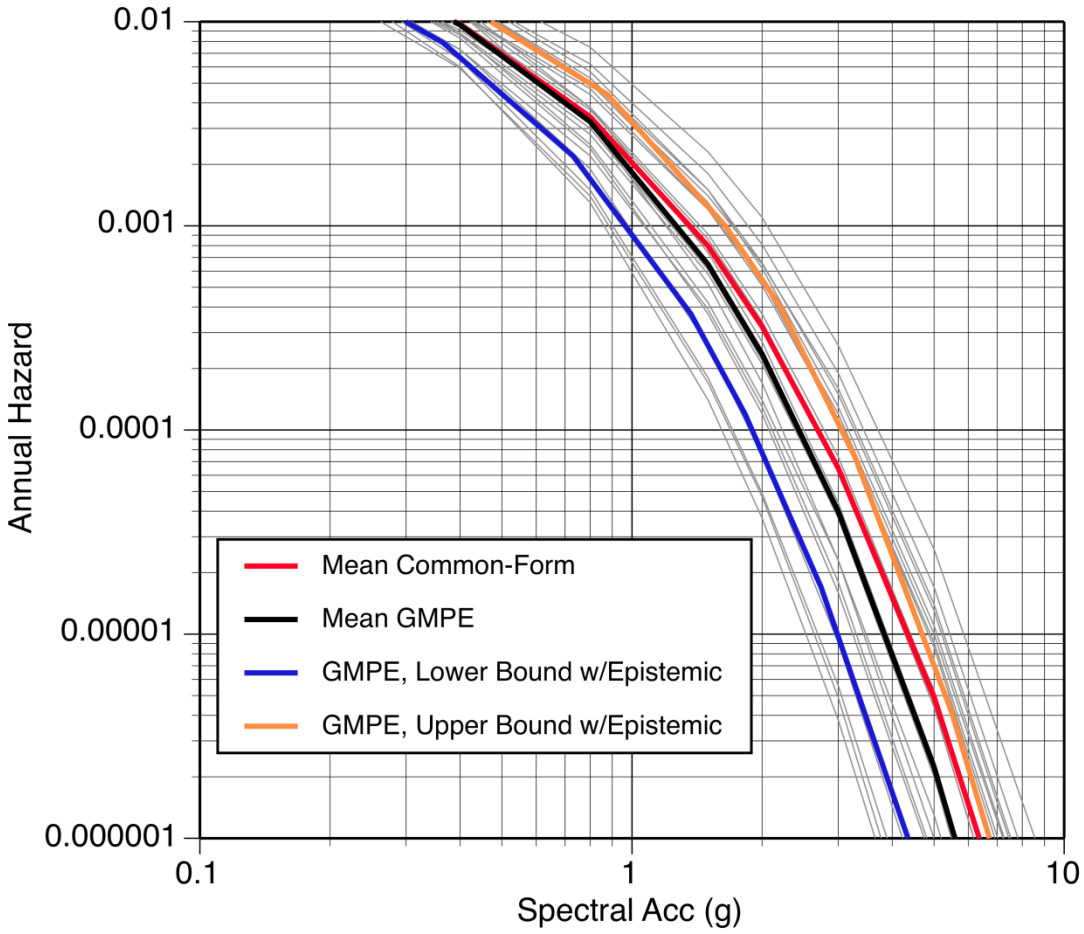

Figure 8.4-18: Comparison of 5 Hz hazard curves using the representative suite of common-form models (grey lines), weighted mean common-form model (red line), mean from the eight candidate GMPE models (black line), and the lower (blue line) and upper (orange line) bounds of the eight candidate GMPE models with the additional epistemic uncertainty (2 sigma level).

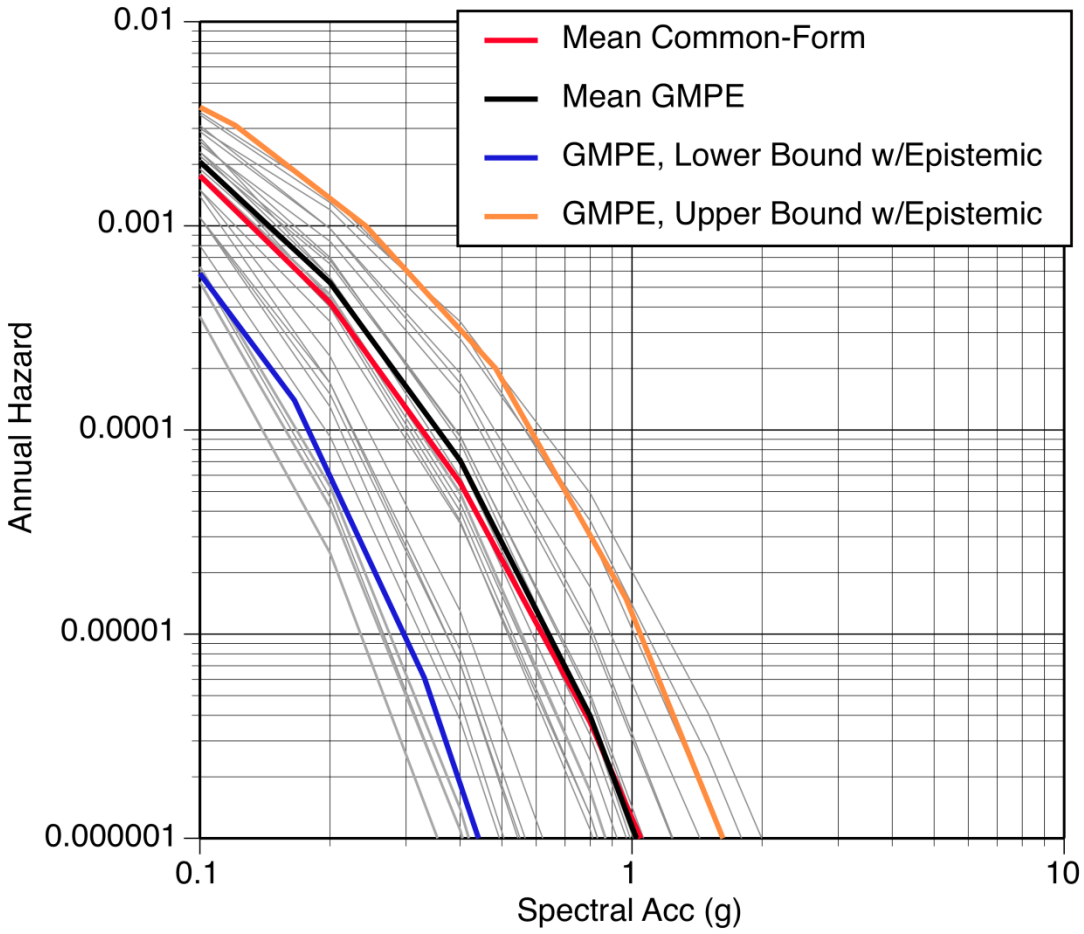

Figure 8.4-19: Comparison of 5 Hz hazard curves using the representative suite of common-form models (grey lines), weighted mean common-form model (red line), mean from the eight candidate GMPE models (black line), and the lower (blue line) and upper (orange line) bounds of the eight candidate GMPE models with the additional epistemic uncertainty (2 sigma level).

9 MEDIAN GMC MODELS: PVNGS SOURCES

Two sets of ground-motion models are developed for use with the PVNGS seismic sources. The first set is used for the Greater Arizona sources, which model the occurrence of primarily normal-faulting earthquakes distributed throughout large regional zones. The second set is used for the distant California sources, which model the occurrence of primarily large, strike-slip earthquakes at distances in excess of 200 km from the PVNGS site. Different approaches, candidate GMPEs, and relevant empirical data are used to develop the ground-motion model characterization for these two source sets.

9.1 Greater Arizona Sources

9.1.1 Structure of the Logic Tree

As described in Section 6.4, the TI Team's approach used to develop the weighted set of base models (ground motions for strike-slip earthquakes and normal earthquakes) for median ground motions consists of the following steps:

1. Fit a common functional form to the GMPEs considered applicable to the assessment of ground motions at the PVNGS site.
2. Expand the set of models by interpolating between the candidate models.
3. Develop the covariance matrix for the coefficients in the common-form models.
4. Generate a large suite of ground-motion models by sampling from the multivariate normal distribution defined by the coefficient covariance matrix.
5. Develop a Sammon's map of the generated suite of ground-motion models that approximates the standard deviation of the difference between any two ground-motion predictions from the models by the map distance between the two models.
6. Discretize the two-dimensional space of generated models using Voronoi cells.
7. Select a representative model for each cell based on the mean hazard within the cell.
8. Assign weights to the representative model for each cell that capture the center, body, and range of the ground-motion models, to use as the logic tree weights.

The logic tree for characterizing the median ground motion for the Greater Arizona sources is presented in Figure 9.1-1. In Figure 9.1-1 and subsequent logic tree figures, weights based on the TI Team's subjective evaluations are in red, whereas weights based on statistical sampling are in green.

The first node in the logic tree is the choice between two alternative distance metrics used in developing the common-form models. The second node captures the range of alternative representative base models selected from the large suite of common-form models that were developed following the approach described in Section 6.4. These common-form models include a specific HW adjustment from one of the five candidate HW models described in Section 6.3. The final node describes the adjustment for directivity effects.

The weights for the base model (second node) are developed independently for each spectral period from 0 to 3 seconds. The method for computing the weights, denoted "total weights", uses the logic tree shown in Figure 9.1-2. The first node in Figure 9.1-2 addresses the alternative approaches using either the selected empirical dataset (branch called "Data Comparison") or the equally-weighted candidate GMPEs (branch called "GMPE Prior"). The second node addresses the alternative data sets that are considered, consisting of a weighted set of NGA-West2 data ($NGAW2_{PV\text{-}MEDV}$), and a European data set ($EUR_{PV\text{-}MED}$), both described in Section 5.3.2. The third node addresses the two alternative methods for measuring the difference between the models and the data sets based on the mean between-event residual (branch called "Residual") and the likelihood of the total residual with fixed between-event and within-event standard deviations (branch called "Likelihood").

The evaluations for this second logic tree are the main factors for capturing the center, body, and range of the alternative median ground-motion models for PVNGS associated with the Greater Arizona sources. The T = 3 sec ground-motion models are extrapolated for periods up to 10 seconds as described in Appendix N, using the same model weights as the T = 3 sec models.

9.1.2 Evaluation of the Distance Metric for the Common Form

Sections 6.3.1 and 6.3.3 discuss the choice of distance metric to be used in a common form. For the PVNGS site, the range in rupture geometries for nearby earthquakes consists of vertical strike-slip ruptures and dip-slip ruptures over the dip range of 50 ± 15 degrees which are modeled as occurring on randomly placed virtual faults rather than on specific geologic structures (Section 4.2). For this range of dip angles, the R_{RUP}-based ground-motion models and the R_{JB}-based ground-motion models both provide reasonable scaling for HW effects (Donahue and Abrahamson, 2014). Therefore, for the PVNGS site, the common-form ground-motion models are developed using both distance metrics. The TI Team judged that the R_{RUP} distance metric is more appropriate (weight = 0.7) than the R_{JB} distance metric (weight = 0.3) because it utilizes additional information on the depth of the rupture that has been shown to be significant in the NGA-West2 data as captured by the 2014 NGA-West2 GMPEs (e.g. Abrahamson et al., 2014; Chiou and Youngs, 2014; and Campbell and Bozorgnia, 2014). These weights

are not related to the fitting of the common form to the candidate GMPEs. The R_{RUP} distance metric models are denoted Model A and the R_{JB} distance metric models are denoted Model B.

9.1.3 Evaluation of the Median Base Models

9.1.3.1 Evaluation of the Range of the Selected Models

The range of the selected common-form models should capture the range of the candidate GMPEs in the Sammon's map space, and should be representative of the range of the ground motions of the candidate GMPEs in ground-motion space for hazard-relevant earthquake scenarios. The approach taken to accomplish this goal is the same as for DCPP as described in Section 8.4.

Figures 9.1-3a and 9.1-3b show the Sammon's map of the range of predicted PGA values from the suite of common-form models generated for the PVNGS site for Model A and Model B, respectively, following the same approach as used for DCPP (Section 8.4.1). The distance between two points in the Sammon's map approximates the weighted standard deviation (in ln units) between the ground motions predicted by two different models for the selected sets of magnitudes and distances described in Section 6.4. The weighted standard deviation is the standard deviation between the ln of the ground-motion model amplitudes for two models with the weights being related to the deaggregation using a simplified source model. Using these weights focuses the comparison of the amplitudes for two models on the magnitudes and distances that are most important to the hazard at PVNGS from the sources located in the Greater Arizona region. The irregular polygon on the figures outlines the region encompassing the large suite of 2000 common-form models. The red dots on the figure denote the locations on the map of the predictions from the six candidate GMPEs used to generate the joint distribution of common-form GMPE parameters. The magenta and cyan dots on the figures show plus and minus two sigma epistemic uncertainty, respectively, about the candidate GMPEs generated using the epistemic uncertainty model of Al Atik and Youngs (2014). As indicated on the plots, the range of predicted motions from the large suite of common-form models is much broader than the range produced by the candidate six GMPEs and much broader than the candidate GMPE range including additional epistemic uncertainty. The additional epistemic uncertainty model of Al Atik and Youngs (2014) was developed for the NGA-West2 GMPEs to account for the dependencies of the data set and the analyses of the NGA-West2 GMPEs. It is likely that the Akkar et al. (2014a, b) and Bindi et al. (2014a, b) GMPEs are also non independent models because they were developed using subsets of the RESORCE strong-motion database under the auspices of the SIGMA project. Therefore, the Al Atik and Youngs (2014) additional epistemic uncertainty model was judged to be applicable to the two European candidate GMPEs as well.

The contour lines underlying the Sammon's map indicate the value of the mean between-event residual computed for each model using two data sets of ground motions selected to represent the range of magnitude-distance scenarios important to the PVNGS hazard from the Greater Arizona sources: a

weighted set of NGA-West2 data ($NGAW2_{PV\text{-}MEDV}$) and a European data set ($EUR_{PV\text{-}MED}$). The selection of the data sets is discussed in Section 9.1.3.2. The mean between-event residuals for the large suite of common-form models range from about -1 to about +0.5 natural log units, while the range in mean residual for the candidate six GMPEs ranges from about -0.2 to +0.2, indicating that some of the generated common-form models differ substantially from the candidate GMPEs.

Figures 9.1-3a and 9.1-3b also show the same Sammons map for predicted PGA values overlaying relative likelihoods of the individual models generating the data sets used to compute the mean residual contours shown on the left side of the same figures. Similar maps for PSA at T = 2 sec are shown in Figures 9.1-4a and 9.1-4b. As is expected, the models with large absolute mean between-event residuals have much lower relative likelihood than those with small absolute mean between-event residuals, but the models at the top and bottom of the map with small mean between-event residuals also show lower likelihood, indicating the usefulness of utilizing relative likelihoods as part of the evaluation.

As described in Section 6.4, the range of the large suite of common-form models was represented by a discrete small set selected to capture the range of the candidate GMPEs and their associated epistemic uncertainty as well as models with mean between-event residuals in the range of at least -0.3 to + 0.3. The sampling of the Sammon's map space is based on fitting ellipses to the envelope of the locations of the candidate GMPEs on the map and scaling the ellipses, as shown in Figures 9.1-3a and 9.1-3b. The Sammon's maps are rotated such that the x-axis approximates constant scaling between the models, as shown by the orientation of the additional epistemic uncertainty assigned to each candidate GMPEs (orientation of the magenta and cyan dots in Figures 9.1-3a and 9.1-3b).

Points on the ellipses were selected to sample the range of models (shown by the black points). To put limits on the range of the models, the $NGAW2_{PV\text{-}MED}$ data set (discussed in Section 5.3.2) was used to compute the mean between-event residual which is shown by the contours in the upper left plots in Figures 9.1-3a, 9.1-3b, 9.1-4a, and 9.1-4b. The small patches and small-scale undulations in the contours on the figures represent the limitations of mapping the differences among the GMPEs into a two-dimensional plane. The sampled points are limited to the region with mean residual between -0.3 and 0.3 or the mean residual given by the candidate GMPEs with ± 2 sigma epistemic uncertainties, whichever is larger.

To check that the range of the representative suite of models selected using this approach is broad enough, a simple measure of the range of the candidate GMPEs, defined by the smallest and largest mean between-event residual from the two data sets ($NGAW2_{PV\text{-}MED}$ and $EUR_{PV\text{-}MED}$) is used. Figure 9.1-5 shows the range of mean between-event residuals for the candidate GMPEs with 2 sigma epistemic uncertainty compared to the range covered by the selected representative suite of common-form models for both the Model A (R_{RUP}-based) and the Model B (R_{JB}-based) cases. Positive between-event residuals represent ground-motion models that have smaller ground motions than the comparison data set, and negative between-event residuals represent ground-motion models that have larger ground

motions than the comparison data set. At every period, the range of the representative suite of common-form models captures the full range of the candidate GMPEs with 2 sigma epistemic uncertainty in the Sammon's map space. At periods of 0.4 and 0.5 seconds, the positive between-event residuals span the smallest range (about +0.25). The range is tighter for these periods because the candidate GMPEs are more similar to each other for this period range.

In addition to the mean residual, the range of the representative suite of common-form models also covers most of the region of highest likelihood, as indicated on Figures 9.1-3 and 9.1-4. As mentioned in Section 8.4.1, models with a high likelihood are more consistent with the data in the selected subset than models with low likelihood. The range of the representative suite of common-form models covers the range of different distance and magnitude scaling as parameterized in the Sammon's map space. A full suite of Sammon's maps for the other periods are shown in Appendix H (Sections 3.1.3 and 4.1.3 in Chapters 3 and 4 of Appendix H, for the Model A and Model B, respectively).

9.1.3.2 Evaluation of the Approach for Weighting the Selected Models

The logic tree used to develop the weights for the common-form models is shown in Figure 9.1-2. Two basic approaches are used to assign weights to the models selected in Section 6.4.4 to represent the distribution of GMPEs. The first approach, called the "prior" approach, utilizes the multivariate normal distribution defined by the coefficient covariance matrix to assign relative weights to the models that occupy each of the Voronoi cells. The second approach utilizes comparisons to ground-motion data to assign relative weights to the models that occupy each of the Voronoi cells. The data comparisons are based on both mean between-event residuals and sample likelihoods.

Two datasets are used to develop the data comparison based weights. The first dataset, called $NGAW2_{PV\text{-}MED}$, is a subset of the data taken from the NGA-West2 data set as described in Section 5.3.2. The second data set is European dataset denoted $EUR_{PV\text{-}MED}$ also described in Section 5.3.2. Both data subsets include **M** ≥ 5, distances less than 70 km, for strike-slip and normal earthquakes with at least 3 recordings per earthquake. The justification for using a minimum of 3 stations per event is given in Section 5.3.2. A minimum of three recordings per earthquake is also applied to the empirical data subset selected for application to PVNGS. The magnitude-distance scatter plot and number of earthquakes and number of recordings for the $NGAW2_{PV\text{-}MED}$ and $EUR_{PV\text{-}MED}$ data sets are shown in Figures 5.3.2-1 and 5.3.2-2, respectively. The European dataset includes the **M**6.3 L'Aquila earthquake. Not all the earthquakes in the European dataset are included in the NGA-West2 database. The TI Team used the databases as provided by PEER and by Dr. Akkar without modification.

The two empirical data sets used for the PVNGS median evaluation included both the footwall and hanging wall sites because all of the candidate GMPEs (both R_{RUP}-based and R_{JB}-based models) are applicable to the range of sources (dip angles) for PVNGS for sites on the footwall and hanging wall.

The $NGAW2_{PV\text{-}MED}$ data set has 25% normal earthquakes and 75% strike-slip earthquakes. Because a greater fraction of normal-faulting events are expected in the source model of PVNGS, but there are many fewer normal-faulting events than strike-slip events in the $NGAW2_{PV\text{-}MED}$ dataset (8 normal and 23 strike-slip earthquakes), the TI Team decided to weight the between-event residuals from normal-faulting and strike-slip events in the $NGAW2_{PV\text{-}MED}$ dataset: the $NGAW2_{PV\text{-}MED}$ between-event residuals are weighted 80% and 20% for normal-faulting and strike-slip events, respectively. In the specifics, the between-event residuals and likelihoods were calculated separately for normal and strike-slip earthquakes and then combined with weights of 0.8 and 0.2, respectively, to be generally consistent with the relative rates of normal and strike-slip mechanisms in the source characterization model for the host zone (see Table 4.2-1). This weighting increases the influence of the normal-faulting earthquakes on the mean residual by about a factor of 3 (80% normal as compared to 25% normal in the $NGAW2_{PV\text{-}MED}$ dataset).

The $EUR_{PV\text{-}MED}$ dataset contains more normal than strike-slip events (71 normal and 45 strike-slip earthquakes) and was not reweighted for the style-of-faulting classes (e.g. no change was made to adjust the sampling of normal and strike-slip earthquakes, and that remained 60% for normal events and 40% for strike-slip events).

As done for the DCPP evaluation (Section 8.4), a mixture of likelihood and mean residual statistics is used to determine the weights. Similar to the DCPP case, the empirical likelihood-based weights tend to produce narrow median ground-motion distributions. In contrast, weights based on mean between-event residuals tend to produce broad median ground-motion distributions. A balance between these two behaviors was achieved by using a mixture of 60% on mean residual weights and 40% on likelihood weights. These weights were selected so that the resulting distribution of median models is generally consistent with the range of the candidate GMPEs (with equal weights) including the additional epistemic uncertainty.

The subjective logic tree weights for the approaches to assigning weights to the selected models for PVNGS (Greater Arizona sources), as shown in Figure 9.1-2, are based on the following considerations:

1. There is ample empirical data in the combined $NGAW2_{PV\text{-}MED}$ and $EUR_{PV\text{-}MED}$ data sets for much of the key range (**M**5 - **M**7 at distances less than 70 km). The dataset approach allows the TI Team to put more weights on the magnitudes and distances that are relevant to the hazard at PVNGS, whereas the GMPE developers tried to capture the full range. However, these same data were considered in the development of the GMPEs, so this is not independent data. This approach just puts more weight of a specific magnitude and distance range of the full data considered by the GMPE developers.

2. The "prior" approach maintains the judgments by the GMPE developers but it gives equal weight to each selected candidate model and does not consider the correlations in the model

due to interaction between the developers. The common-form models fit to the candidate GMPEs maintain the magnitude and distance scaling in the candidate GMPEs as given by the GMPE developers.

3. Some of the NGA-West2 developers constrained the normal factor not to be as large a negative value as given by the center of the data, so the candidate GMPEs from the NGA-West2 models may not all be centered on the available normal-faulting data, depending on the judgment of the GMPE developer.

The TI Team favors the model weights based on comparisons to data over the model weights based on the common-form parameter distributions (the "prior") approach by the ratio of 2:1 because of the relatively large amount of relevant data and because of the limitation that the prior was based on applying equal weights to the models without regard to redundancy in the models due to non-independent model development, particularly for the NGA-West2 models. For the data-based approach to weighting, the TI Team strongly favors use of the $EUR_{PV\text{-}MED}$ data over the $NGAW2_{PV\text{-}MED}$ data by the ratio of 3:1 because of the limited amount of normal-faulting data in the $NGAW2_{PV\text{-}MED}$ data set (8 normal events) compared to $EUR_{PV\text{-}MED}$ data set (23 normal events). The reweighting of the $NGAW2_{PV\text{-}MED}$ greatly increases the weights on this sparse part of the data set.

Based on these considerations, 1/3 weight is assigned to weights based on the prior approach and 2/3 to the comparisons with data. The data based weight is divided between 2/3x3/4 = ½ for model weights based on comparison with the $EUR_{PV\text{-}MED}$ data and 2/3x1/4 = 1/6 for model weights based on comparison with the $NGAW2_{PV\text{-}MED}$ data. The resulting weights (rounded to two significant figures) are 0.50 weight for the $EUR_{PV\text{-}MED}$ dataset approach, 0.17 weight for the $NGAW2_{PV\text{-}MED}$ dataset approach, and 0.33 weight for the "prior" approach, as shown on the logic tree in Figure 9.1-2.

9.1.3.3 Evaluation of the Center and Body of the Distribution of the Selected Models

The center and body of the selected weighting scheme is compared to alternative weighting schemes by comparing the cumulative distribution function (CDF) for the ground motion for a given scenario. Examples of the CDF plots are shown in Figures 9.1-6 and 9.1-7 for **M**6.0 normal earthquakes at an R_X distance of 15 km for PGA and T = 1 sec, respectively. In general, the likelihood approach leads to a narrower range (steeper slope) whereas the residual approach leads to a broader range; however, this is not true in all cases as shown in Figure 9.1-6 top frame (for Model A). The selected approach, shown by the red curve (CDF = 0.5), provides a reasonable balance between these two approaches.

The average slope of the CDF between CDF = 0.1 and CDF = 0.9 defines the body of the distribution. The GMPEs can have narrower or broader body of the distributions than the selected approach. For the examples shown in Figure 9.1-6, the GMPEs have a narrower body of the distribution (steeper slope). A counter example is shown in Figure 9.1-7 for model B. In this case, the GMPE distribution has a much

broader body of the distribution at the upper tail (right side of the plot). This is seen mainly for the **M**5 to **M**6 range. A large suite of CDF plots for a range of **M**, R scenarios and spectral periods are shown in Appendix H (Sections 3.1.5 and 4.1.5 in Chapters 3 and 4 of Appendix H, for the Model A and Model B, respectively). For most scenarios, the selected models have a similar slope (body of the distribution) as the candidate GMPEs.

In addition to the CDF plots, the center and body of the distribution can be evaluated using distance scaling, magnitude scaling, and response spectra plots. Figures 9.1-8 and 9.1-9 compare the distance scaling for the 5^{th}, 50^{th}, and 95^{th} fractiles from the logic tree weights with the distance scaling for the candidate GMPEs for PGA and PSA (T = 1 sec), respectively. For some scenarios, the median of the representative suite of common-form models is near the lower end of the range of the GMPEs (e.g. see Fig 9.1-9, **M**6 at R_X ranging 15 to 50 km). The reason for this shift in the center of the distribution from the center of the GMPEs is that the $EUR_{PV\text{-}MED}$ dataset has much lower ground motions. The CDF plot in Figure 9.1-7 for model A shows that the selected model (red curve) is between the curves for the European data and the NGA-West2 data.

Figure 9.1-10 shows examples of the magnitude scaling from the GMPEs and the representative suite of common-form models for PGA and PSA (T = 1 sec). Figure 9.1-11 shows examples of the response spectra for **M**5, **M**6, and **M**7 normal-faulting events for a distance of 15 km. This figure also shows that the median of the representative suite of common-form models is near the lower range of the GMPEs for **M** > 6. The influence of the different statistics used for setting the weights for the common-form models is discussed below.

A set of CDF plots and ground-motion scaling plots for the scenarios listed in Table 9.1-1 and for a range of spectral periods are shown in Appendix H. The CDFs of the ground motions were reviewed to check the center and body of the distributions. A general result is that the between-event residuals and likelihood from the $EUR_{PV\text{-}MED}$ data set has significantly lower ground motions for long periods than the GMPEs. With a high weight of 0.5 given to the $EUR_{PV\text{-}MED}$ data set, the median of the models is lower than the median for the GMPEs.

To summarize the evaluation of the centering of the models based on the CDF plots, the change in the PSA at CDF = 0.5 for the different metrics and datasets are computed. Specifically, for each scenario listed in Table 9.1-1, the difference in the ground motion for a single statistic and the weighted average model is computed. The distribution of the differences of the ln PSA for the 36 scenarios is referred to as an "influence histogram", and is plotted for each statistic and each spectral period. Examples for the R_{RUP}-based models (A models) are shown in Figures 9.1.12a-e for PGA, and spectral accelerations at T = 0.2 sec, T = 1 sec, T = 2 sec, and T = 3 sec, respectively. These plots show the influence of the different statistics on the centering of the distribution with zero residual representing the center based on the TI Team evaluation (shown by the red curves in the CDF plots). For the European data set, the residual and likelihood weighting methods have negative between-event residuals (weaker ground motions than the

average from the selected method), and for the NGA data set, the residual and likelihood weighting methods have positive between-event residuals (stronger ground motions). At longer periods, this difference becomes greater. Overall, the centering of the selected method is a balance between these two different sets of data. A full set of these influence histograms are given in Appendix H (Sections 3.1.15 and 4.1.15 in Chapters 3 and 4 of Appendix H, for the Model A and Model B, respectively).

The above discussion has focused on the ground-motion levels. The selected models were developed to sample a range of distance scaling and magnitude scaling. An example of the distance scaling for the representative suite of common-form models for **M**6 strike-slip earthquakes is shown in Figures 9.1-13 and 9.1-14 for T = 0.2 sec and T = 2 sec, respectively. An example of the magnitude scaling for the representative suite of common-form models for strike-slip earthquakes at a distance of 15 km is shown in Figures 9.1-15 and 9.1-16 for T = 0.2 sec and T = 2 sec, respectively. These figures show that the representative suite of common-form models span a range of distance and magnitude scaling in addition to changing in the constant value. The differences in the magnitude and distance scaling will also impact the range of the hazard.

Another consideration for the center and body of the distribution is that, for each cell, the representative common-form model was selected based on its hazard being close to the mean hazard for the cell. Because the main application of these models is for hazard, it is appropriate to select representative models based on hazard; however, this may not always lead to the selection of models that best sample the range of ground motions for each scenario. Thus, checking the center and body of the distribution with respect to the candidate GMPEs should also be done for hazard, not just ground motion for each scenario.

The goal of the SSHAC evaluation is develop a representative suite of common-form ground-motion models that captures the CBR of TDI for scenarios that are relevant to the hazard. If the representative ground-motion models capture the CBR for all scenarios, then it will also capture the range of the hazard.

If the range of the representative suite of common-form ground-motion models does not fully capture the range for all scenarios, then the range of hazard may or may not be captured. Because the SWUS GMC base model does not capture the full range of the ground motion from the candidate GMPEs with additional epistemic uncertainty (2 sigma) for every scenario, there is the need to check that the range of hazard is captured.

The main evaluation was in the ground-motion space. In developing the TI Team's weights for the alternative weights approaches (prior, residual, likelihood, data sets), GM-based CDF were explicitly evaluated and the TI Team chose a weighting scheme for the weighting approaches that lead to a CDF with an appropriate shape of the CDF (body of the distribution) in addition to the 5^{th} and 95^{th} fractiles (range of the CDF).

The range of the hazard was then evaluated as a check that the range of the hazard-significant scenarios is captured. The hazard evaluation is just a check that the approach used to set the weights for weighting approaches, which control the full distribution (CBR), does not miss the range of a key contributor to the hazard.

To evaluate the hazard distribution, the hazard was computed for each of the representative suite of common-form models` and for the candidate GMPEs using the simplified source model (See Appendix O for details). A single aleatory standard deviation, based on the central model described in Section 13.3, is used for all of the median models. The mean hazard from the distant sources in California and Mexico is added to the hazard for each model for Greater Arizona sources. The range of hazard for spectral acceleration at T = 0.2 sec is shown in Figure 9.1-17a and 9.1-17b for R_{RUP}-based models (Model A) and R_{JB}-based models (Model B), respectively. Similar plots are shown in Figures 9.1-18a and 9.1-18b for spectral acceleration at T = 2 sec. Appendix O includes plots showing the range of hazard for three additional periods (PGA, T = 1 sec and T = 0.1 sec).

For the T = 0.2 sec case (Figures 9.1-17a and 9.1-17b), the mean hazard curves from the representative suite of R_{RUP}-based and R_{JB}-based common-form models are both similar to the average from the candidate GMPEs, but the range of the hazard curves for the R_{RUP}-based models is broader than for the R_{JB}-based models because the R_{RUP}-based models include alternative depth-scaling effects which are not included in the R_{JB}-based models. Overall, the range of hazard curves from the representative suite of common-form models is much broader than the range of hazard from the candidate GMPEs.

For the T = 2 sec case (Figures 9.1-18a and 9.1-18b), the range of the hazard curves from the representative suite of common-form models is broader than for the T = 0.2 sec case. The mean hazard from the R_{RUP}-based models and R_{JB}-based models are similar to each other but are higher than the average from the candidate GMPEs. The broader uncertainty range increases the mean hazard due to the skewed distribution of hazard (skewed to the higher values).

Figure 9.1-19a compares the center and range of the T = 0.2 sec hazard based on the R_{RUP}-based common-form ground-motion models with the center and range of the hazard based on the candidate GMPEs with the additional epistemic uncertainty. The mean hazard curves are similar between the representative suite of common-form ground-motion models and the candidate GMPEs. In addition, the range of the hazard using the representative suite of common-form models is similar to the range from adding the additional epistemic uncertainty to the candidate GMPEs.

A similar comparison is made in Figure 9.1-19b for the T = 2 sec hazard. As seen for the T = 0.2 sec hazard, the mean hazard curves are similar between the representative suite of common-form ground-motion models and the candidate GMPEs; however, the upper range of the hazard from the representative suite of common-form models is wider than the upper range found by adding the additional epistemic uncertainty to the candidate GMPEs. The hazard curves from these models

envelope the hazard from the candidate GMPEs, indicating that range of key median ground-motion features affecting the hazard have been adequately captured by the representative suite of common-form models for the median ground motion and their weights.

9.1.4 Evaluation of Directivity Adjustments

There are no known faults nearby (less than 20 km) the NPP site such that specific rupture orientations can be identified. The directivity effects model, described in Section 6.5, provides adjustments to the median and standard deviation of the ground motion based on the location of the site along the rupture. As described in Section 4.2, the PVNGS SSC model for the nearby sources uses randomly oriented pseudo-faults. Therefore, there is no information on the expected location of the site along the fault ruptures. As discussed in Section 6.5.2, the TI Team judged that the directivity effects from more distant (greater than 20 km) sources are adequately captured by the standard deviation from the GMPEs because this distance range is well sampled by the empirical data. Therefore, there is no need to include directivity adjustments and zero weight is applied to the directivity adjustment branch.

9.1.5 Evaluation of Other Normal-Faulting Earthquake Ground Motions

As noted in Section 5.1.5, the SWUS GMC project investigated if there were additional moderate to large magnitude normal-faulting earthquakes that were well recorded and may be useful in the evaluation of the ground-motion models. Two events were identified: the 2008 Wells, Nevada earthquakes (**M**6) and the 2011 Fukushima-Hamadori, Japan earthquake (**M**6.7). The magnitudes and focal mechanisms of these two earthquakes are consistent with the types of seismic sources that contribute significantly to the hazard at PVNGS. The Wells earthquake is located in the Basin and Range, so it is from the same tectonic regime as for the PVNGS site region. The Fukushima-Hamadori Japan earthquake is from a different tectonic regime, but it is one of the largest normal-faulting earthquakes with extensive ground-motion data. The evaluation of the data from these two events is given below.

9.1.5.1 Evaluation of the 2008 Wells, Nevada Earthquake Ground Motions

The available strong ground motions from this event are described in Appendix I. These data were evaluated to determine if they could provide additional information for normal-faulting earthquakes that is not well captured by the strong motion data sets used to evaluate the GMPEs. In particular, the Wells data was evaluated for any significant deviations in the scaling from the candidate GMPEs for the Greater Arizona sources.

The Wells earthquake had seven useable recordings within a distance of 100 km. The peak ground velocities recorded by nearby stations do not show an azimuthally-dependent trend (Figures I-4 and I-5). In terms of average scaling, the total residuals from the Wells ground motions with respect to the six

candidate GMPEs applicable for PVNGS (Greater Arizona sources) for a range of period were computed (see Figure I-16). Mean total residuals versus period were also computed with respect to the same six candidate GMPEs (see Figure I-17). Overall, the short period (less than 0.2 sec) data are in general agreement with the GMPEs with an average residual between -0.3 and 0.3 natural log units, which is about one standard deviation of the between-event variability seen in the candidate GMPEs. In particular, the total residuals from the NGA-West2 models are systematically lower than the total residuals from the European models, reflecting the reduced ground motions for normal-faulting earthquakes in the European GMPEs. At this short-period range, the NGA-West2 total residuals are negative or near zero whereas the European model total residuals are positive, indicating that, on average, the NGA-West2 models are a better fit the short periods. At intermediate periods (T = 0.2 to 0.5 sec), both the NGA-West2 and European models show a trend of the mean residuals becoming more negative as the period increases. In this period range, the NGA-West2 models over-predict the ground motions and the European models are closer to the zero residual line than the NGA-West2 models. At long periods (greater than 0.5 sec), both the NGA-West2 models and the European models strongly over-predict the ground motions, and the total residuals become more negative (-0.5 to -1.2 natural log units).

In conclusion, the TI Team judged that this single event did not provide a strong enough basis for correcting for this bias in the candidate GMPEs for normal-faulting ground motion at long periods.

9.1.5.2 Evaluation of the 2011 Fukushima-Hamadori, Japan Earthquake

As noted in Section 5.1.5.2, the Fukushima Hamadori earthquake involved ruptures of the Itozawa fault and the Yunodake fault (Shiba and Noguchi, 2012 in Japanese; Tanaka et al., 2014), which were also responsible for surface ruptures (Mizoguchi et al., 2012). With both overlapping ruptures and extensions along the length of the rupture, this earthquake is a mixture of the complex and splay rupture types as defined in Section 5.1.5.2. As the square root of the sum of the squares (SRSS) method described in Section 6.7 was found to be reasonable for both complex and splay ruptures, the TI Team assumed that the SRSS method can also be applied to this earthquake.

Using the source parameters for each of the two ruptures listed in Section 5.1.5.2 (M6.5 for each rupture and normal style-of-faulting), the ground motion was computed using the SRSS method. Japan-specific terms of ASK14, BSSA14, CB14, and CY14 were used to evaluate the median motions used as inputs for the SRSS method. Residuals were not computed with respect of other candidate GMPEs such as Bindi et al. (2014a and 2014b) and Akkar et al. (2014a and 2014b) because these models do not have Japan-specific adjustments, which the NGA developers found necessary. Japan regional factors in the NGA-West2 GMPES were used to. The mean total residuals for the ASK14, BSSA14, CB14, and CY14 GMPEs are shown in Figure 9.1-20 for data within 300 km and within 100 km. The mean total residual (i.e. the event term) is large (about 1) at short periods and decreases with increasing period. The mean

total residuals for CY14 are somewhat larger than for the other three NGA-West2 GMPEs, especially at longer periods, where the predictions from CY14 are typically lower than those of the other three.

Event terms of 1.0 or larger are not common for large magnitude events. The standard deviation of the event terms (τ) is about 0.4 (See Section 7.2.4). An event term of greater than 1.0 is more than 2.5 standard deviations above the mean, and appears as an outlier. This event, however, indicates that normal-faulting earthquakes can have very large strong ground motions.

The applicability of this event to the tectonic environment of the basin and range is an additional issue. Hardebeck (2012) has separated the normal-faulting events occurring shortly after the Tohoku earthquake into two groups: shallow on-shore normal-faulting events that occurred in areas that had a normal-faulting stress regime prior to the Tohoku event, and normal-faulting events near the subduction interface, which are most likely the result of large stress changes due to near-complete stress drop. The Fukushima-Hamadori earthquake is associated to the first case according to Hardebeck (2012). Toda et al. (2011) also suggest that there are patches of normal-faulting stress regimes along the subduction zone corresponding to local stress heterogeneities. The TI Team judged the stress regime of the Fukushima-Hamadori earthquake to be fundamentally different from the stress regime in the Greater Arizona region where normal-faulting is the main tectonic regime.

For application to the ground-motions models for PVNGS, the TI Team judged that the range of ground motions from the Wells and Fukushima-Hamadori earthquakes (low long-period PSA values for Wells and high short-period PSA for Fukushima-Hamadori) represent variability in the event terms that is already captured in the aleatory variability terms, and do not warrant a modification to the median ground-motion models.

9.2 Distant California and Mexico Sources in Regions 1, 2 and 3

9.2.1 Structure of the Logic Tree

The hazard deaggregation in Section 4.2.3 shows that a limited distance range from California and Mexico sources contributes to the hazard at long periods. This simplifies the range of ground-motion models to considering the amplitude (constant term) and the magnitude scaling. Therefore, the Sammon's map procedure is not required and a simpler approach is used based on scaling the candidate GMPEs which have appropriate distance attenuation and are applicable to large (**M**7 to **M**8.5) magnitudes.

The master logic tree for characterizing the median ground motion for the sources in central and southern California and Mexico (also referred to as Regions 1, 2, and 3) affecting the hazard at PVNGS site is presented in Figure 9.2-1.

The first node in the logic tree is the choice among the five alternative GMPEs for the median model. The second node is the choice between two alternative approaches to encompass the effect of the path into the median ground motion. The third node captures the alternative models for the additional epistemic uncertainty for the selected GMPEs. The fourth node is the alternative estimates of the median path term adjustment. The final node is the adjustment for directivity effects.

In Figure 9.2-1, weights based on the TI Team's evaluations are in red, whereas weights based on statistical sampling are in green.

9.2.2 Evaluation of Median Models

In section 6.2.3, the five candidate GMPEs (consisting of the five NGA-West2 models) were found to be consistent with observed attenuation from California earthquakes recorded in Arizona, indicating that they all have appropriate large distance scaling for application to PVNGS. As all five models have acceptable large distance scaling, they are all given equal weight.

9.2.3 Evaluation of Approach for Path Terms

Recent studies of ground motions from multiple earthquakes in a small region recorded at a suite of sites have shown that there are large path effects that are systematic and repeatable (e.g. Morikawa et al., 2008 and Lin et al., 2011). In most applications, however, the data are not available to constrain the path effects. The TI Team evaluation considers that systematic path effects are real, but may have large uncertainties in the estimates. Including path effects leads to better partitioning of epistemic and aleatory variability. Even though the TI Team favors the path effect branch because it is believed the ground motion to be strongly path-specific, there is limited data available to estimate the effect. Therefore, the TI Team retains the ergodic (no-path) model as well and chose a weighting ratio of 4 to 1. The TI Team assigned a weight of 0.8 to the branch where path effects are accounted and a weight of 0.2 for the branch without path effects.

9.2.4 Evaluation of Additional Epistemic Uncertainty

Additional epistemic uncertainty is included to address the uncertainty in the median estimates of the individual NGA-West2 GMPEs. A model for the minimum epistemic uncertainty in the NGA-West2 models was developed by Al Atik and Youngs (2014). It is based on the statistical constraints on the empirical model predictions provided by the empirical data for distances up to 300 km. The controlling distances are at distances of 200 to 300 km (Section 4.2.3). Although the controlling sources are at the edge of the applicable distance range of the Al Atik and Youngs (2014) model, the TI Team judged that the Al Atik and Youngs (2014) model is the best available model.

The Al Atik and Youngs (2014) model contains increasing uncertainty for magnitudes larger than 7 and periods larger than 1 sec. This model is applied to add additional epistemic uncertainty to ground-motion estimates from each GMPE for **M** ≥ 7. The application depends upon the approach used to address path effects, as described below.

9.2.4.1 Branches with Path Effects

The epistemic uncertainty for small magnitude (**M**4 to **M**6) is already captured in the epistemic uncertainty of the path terms as described in Section 7.4.1. To incorporate additional epistemic uncertainty at larger magnitudes and longer periods, separate models for the magnitude scaling uncertainty and the long period scaling uncertainty are used. As mentioned in Section 7.4.1, for longer periods, additional epistemic uncertainty was added to the range of the median path terms (the plus and minus values) by scaling the standard deviation for the 2 sec path term by the ratios of the standard deviations of median motions at longer periods to those at 2 sec from the Al Atik and Youngs (2014) model. This broadens the epistemic uncertainty at periods above 2 seconds to be as large as the Al Atik and Youngs (2014) epistemic uncertainty.

The remaining model is an increase in the uncertainty at larger magnitudes (**M** > 7). This effect is introduced by including an increasing epistemic uncertainty with increasing magnitude, computed as the square root of the additional variance occurring for **M** > 7 as given in Eq. 9.2-1:

$$\sigma_{\mu\_ADD\_path}(M) = \sqrt{\left[\sigma_{\mu}(M > 7, T = 2\,\text{sec})\right]^2 - \left[\sigma_{\mu}(M = 7, T = 2\,\text{sec})\right]^2} \qquad \text{Eq. 9.2-1)}$$

Substituting Eq. (9) from Al Atik and Youngs (2014) into Eq. 9.2-1 gives

$$\sigma_{\mu\_ADD\_path}(M) = \sqrt{\left[0.083 + 0.056\max(0, M-7)\right]^2 - 0.083^2} \qquad \text{(Eq. 9.2-2)}$$

The logic tree branches for this node in the tree are set to approximate a normal distribution with a three point estimate using the standard deviation given in Eq. 9.2-2. The values are taken as the 5th, 50th, and 95th values with weights of 0.2, 0.6, and 0.2. These represent statistical-based weights, following the technical justifications and bases provided in Appendix P.

9.2.4.2 Branches without Path Effects

For the branch where no path effects are applied, the minimum epistemic uncertainty model given in Eq. (10) of Al Atik and Youngs (2014) is applied to each of the five NGA-West2 models as described in Eq. (9.2-3):

$$\sigma_{\mu\_ADD\_\text{no}\,path}(M) = \left[0.083 + 0.056\max(0, M-7)\right] + 0.0171\max(0, \ln(T)) \qquad \text{(Eq. 9.2-3)}$$

The logic tree branches for this node in the tree are set to approximate a normal distribution with a three point estimate using the standard deviation given in Eq. 9.2-3. The values are taken as the 5th, 50th, and 95th values with weights of 0.2, 0.6, and 0.2. These represent statistical-based weights, following the technical justifications and bases provided in Appendix P.

9.2.5 Median Path Terms

The estimates of the median path terms for Region 1 and Regions 2&3 combined are given in Section 6.6 and are fully described in Section 7.4.1. The median path term is a constant to be added to the median prediction.

The range of median ground motions (PSA at T = 2 sec) at distances of 100 to 300 km resulting from applying the median path term terms to NGA-West2 GMPEs for a **M**7.5 strike-slip event is shown in Figure 9.2-2 for Region 1 (left panel) and Regions 2&3 (right panel). At a distance of 200 km, the total range (GMPE differences and path term uncertainty) corresponds to about a factor of 5 in PSA, with the GMPE between-model uncertainties and the path term uncertainties being similar (each a little more than a factor of 2). This range reflects both the uncertainty in the path terms and the uncertainty in the large magnitude scaling. The total uncertainty is about twice as large as the uncertainty given by the Al-Atik and Youngs (2014) uncertainty model.

The logic tree branches for this node in the tree are the 5th, 50th, and 95th values with weights of 0.2, 0.6, and 0.2. These represent statistical-based weights (Appendix P).

9.2.6 Directivity Adjustments to Median

The directivity model in the CY14 GMPE has a distance taper resulting in no directivity effects at these large distances. In addition, the distant California strike-slip sources are located at distances for which there is adequate empirical data to capture the directivity as part of the aleatory variability. Therefore, the TI Team judged that the GMPEs do not need to be modified to incorporate additional directivity effects.

9.3 References

Abrahamson, N.A., Silva, W.J., and Kamai, R. (2014). Summary of the AKS14 Ground-Motion Relation for Active Crustal Regions, *Earthquake Spectra*, Vol. 30(3), 1025-1055, DOI: 10.1193/070913EQS198M.

Akkar, S., Sandikkaya, M.A., and Bommer, J.J. (2014a). Empirical ground-motion models for point- and extended-source crustal earthquake scenarios in Europe and the Middle East, *Bull. Earthquake Eng*., Vol. 12, 359-387, DOI: 10.1007/s10518-013-9461-4.

Akkar, S., Sandikkaya, M.A., and Bommer, J.J. (2014b). Erratum to: Empirical ground-motion models for point- and extended-source crustal earthquake scenarios in Europe and the Middle East, *Bull. Earthquake Eng*, Vol. 12(1), 389-390, DOI: 10.1007/s10518-013-9508-6.

Al Atik, L., and Youngs, R.R. (2014). Epistemic Uncertainty for NGA-West2 Models, *Earthquake Spectra*, Vol. 30(3), 1301-1318, DOI: 10.1193/062813EQS173M.

Bindi D., Massa M., Luzi L., Ameri G., Pacor F., Puglia R., and Augliera, P. (2014a). Pan-European Ground-Motion Prediction Equations for the Average Horizontal Component of PGA, PGV, and 5%-Damped PSA at Spectral Periods up to 3.0 s using the RESORCE dataset, *Bull. Earthquake Eng*., Vol. 12, 391-430, DOI: 10.1007/s10518-013-9525-5.

Bindi D., Massa M., Luzi L., Ameri G., Pacor F., Puglia R., and Augliera, P. (2014b). Erratum to: Pan-European Ground-Motion Prediction Equations for the Average Horizontal Component of PGA, PGV, and 5%-Damped PSA at Spectral Periods up to 3.0 s using the RESORCE dataset, *Bull. Earthquake Eng*., Vol. 12, 432-448, DOI: 10.1007/s10518-014-9589-x.

Boore, D.M., Stewart, J.P., Seyhan, E., and Atkinson, G.M. (2014). NGA-West 2 Equations for Predicting PGA, PGV, and 5%-Damped PSA for Shallow Crustal Earthquakes, *Earthquake Spectra*, Vol. 30(3), 1057-1085, DOI: 10.1193/070113EQS184M.

Campbell, K.W., and Bozorgnia, Y. (2014). NGA-West2 Ground Motion Model for the Average Horizontal Components of PGA, PGV, and 5%-Damped Linear Acceleration Response Spectra, *Earthquake Spectra*, Vol. 30(3), 1087-1115, DOI: 10.1193/062913EQS175M.

Chiou, B.S.-J., and Youngs, R.R. (2014). Update of the Chiou and Youngs NGA Model for the Average Horizontal Component of Peak Ground Motion and Response Spectra, *Earthquake Spectra*, Vol. 30(3), 1117-1153, DOI: 10.1193/072813EQS219M.

Donahue, J., and Abrahamson, N.A. (2014). Simulation-based hanging-wall effects, *Earthquake Spectra*, Vol. 30(3), 1269-1284, DOI: 10.1193/071113EQS200M.

Graizer, V. (2014). Updated Graizer-Kalkan Ground-motion Prediction Equations for Western United States, *Proceedings for the 10th U.S. National Conference on Earthquake Engineering Frontiers of Earthquake Engineering*, July 21-25, 2014, Anchorage, Alaska, Paper ID 1097, 11 pp.

Hardebeck, J.L. (2012). Coseismic and postseismic stress rotations due to great subduction zone earthquakes, *Geophys. Res. Lett.*, Vol. 39, L21313, DOI: 10.1029/2012GL053438.

Lin, P.-S., Chiou, B., Abrahamson, N., Walling, M., Lee, C.-T., and Cheng, C.-T. (2011). Repeatable source, site, and path effects on the standard deviation for empirical ground-motion prediction models, *Bull. Seismol. Soc. Am.,* Vol. 101(5), 2281-2295, DOI: 10.1785/012009031.

Mizoguchi, K., Uehara, S., and Ueta, K. (2012). Surface fault ruptures and slip distributions of the Mw 6.6 11 April 2011 Hamadoori, Fukushima, northeast Japan, earthquake, *Bull. Seism. Soc. Am.* Vol. 102(5), 1949-1956, DOI: 10.1785/0120110308.

Morikawa, N., Kanno, T., Narita, A., Fujiwara, H., Okumura, T., Fukushima, Y., and Guerpinar, A. (2008). Strong motion uncertainty determined from observed records by dense network in Japan, *J. Seismol.,* Vol. 12(4), 529-546.

Shiba, Y., and Noguchi, S. (2012). Statistical characteristics of seismic source parameters controlling broadband strong ground motions -Investigation based on source inversion analysis-. *CRIEPI REPORT.* N11054 (in Japanese with English abstract).

Tanaka, M., Asano, K., Iwata, T., and Kubo, H. (2014). Source rupture process of the 2011 Fukushima-ken Hamadori earthquake: how did the two subparallel faults rupture? *Earth, Planets and Space*, Vol. 66:101, DOI:10.1186/1880-5981-66-101

Toda, S., Stein, R.S., and Lin, J. (2011). Widespread seismicity excitation throughout central Japan following the 2011 M=9.0 Tohoku earthquake and its interpretation by Coulomb stress transfer, *Geophys. Res. Lett*. Vol. 38(7), L00G03, DOI: 10.1029/2011GL047834.

Table 9.1-1: Scenarios used for the evaluation of the CDF distributions of the representative suite of common-form models for PVNGS.

Magnitude	R_X Distance (km)	Style of Faulting (SOF)
5.0	-50	0 (Strike Slip)
5.0	-30	0 (Strike Slip)
5.0	-15	0 (Strike Slip)
5.0	-5	0 (Strike Slip)
5.0	5	0 (Strike Slip)
5.0	15	0 (Strike Slip)
6.0	-50	0 (Strike Slip)
6.0	-30	0 (Strike Slip)
6.0	-15	0 (Strike Slip)
6.0	-5	0 (Strike Slip)
6.0	5	0 (Strike Slip)
6.0	15	0 (Strike Slip)
7.0	-50	0 (Strike Slip)
7.0	-30	0 (Strike Slip)
7.0	-15	0 (Strike Slip)
7.0	-5	0 (Strike Slip)
7.0	5	0 (Strike Slip)
7.0	15	0 (Strike Slip)
5.0	-50	-1 (Normal)
5.0	-30	-1 (Normal)
5.0	-15	-1 (Normal)
5.0	-5	-1 (Normal)
5.0	5	-1 (Normal)
5.0	15	--1 (Normal)
6.0	-50	-1 (Normal)
6.0	-30	-1 (Normal)
6.0	-15	-1 (Normal)
6.0	-5	-1 (Normal)
6.0	5	-1 (Normal)
6.0	15	-1 (Normal)
7.0	-50	-1 (Normal)
7.0	-30	-1 (Normal)
7.0	-15	-1 (Normal)
7.0	-5	-1 (Normal)
7.0	5	-1 (Normal)
7.0	15	-1 (Normal)

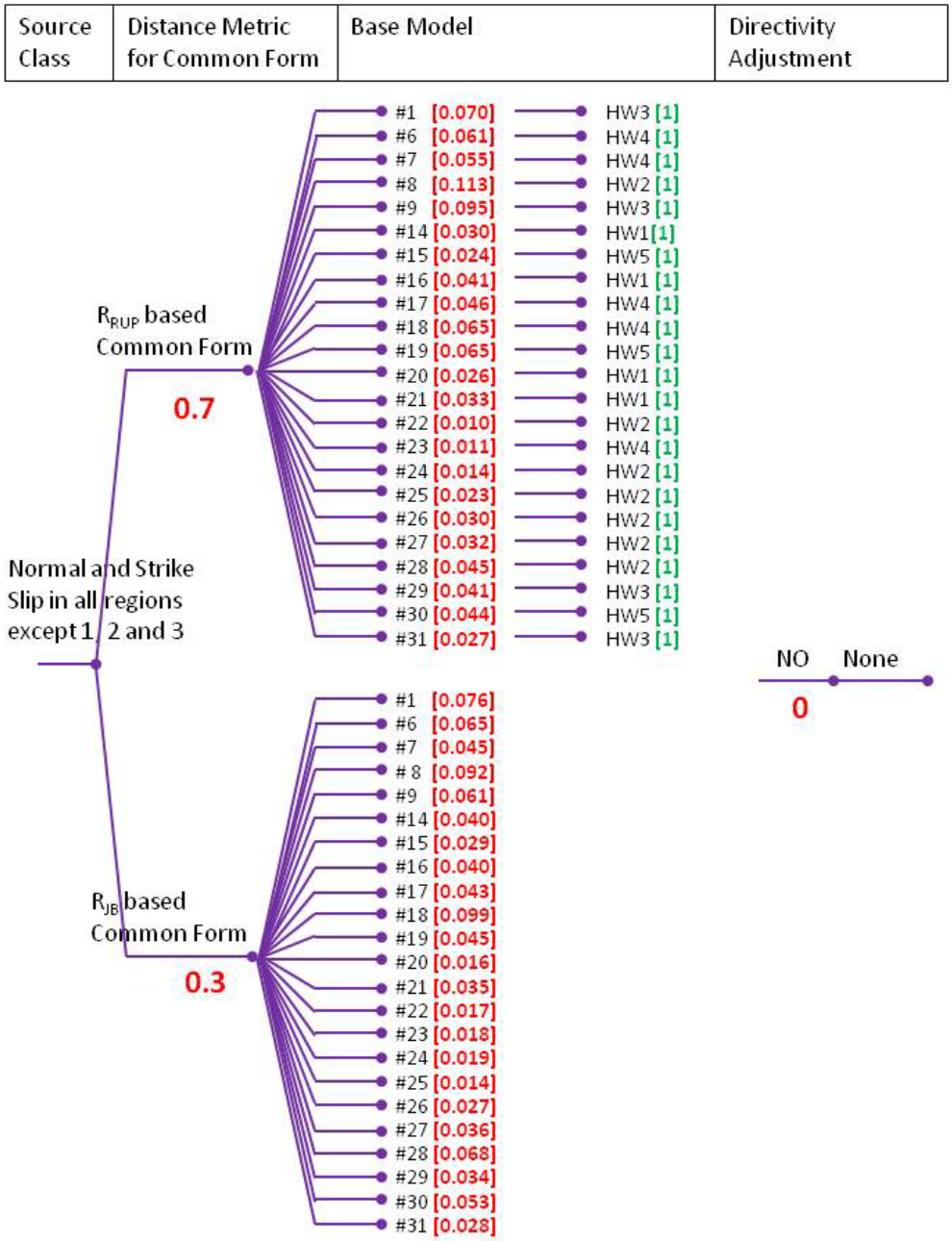

Figure 9.1-1: Logic Tree for median ground motion for Greater Arizona sources affecting the hazard at PVNGS. The representative suite of common-form models is shown by the unique Model ID # (up to #31), and their weights are rounded to the third decimal point. The HW branch name refers to a random sample from one of the five HW models (HW1 to HW5). The weights based on the TI Team's subjective evaluations are in red, whereas weights based on statistical sampling are in green. The approach to compute the weights for the models is shown in the logic tree in Figure 9.1-2. The weights shown for the base models and the hanging wall models are for one example case (PGA). The weights for the other periods are listed in the PVNGS Hazard Input Document (HID) available in Appendix C – Part I.

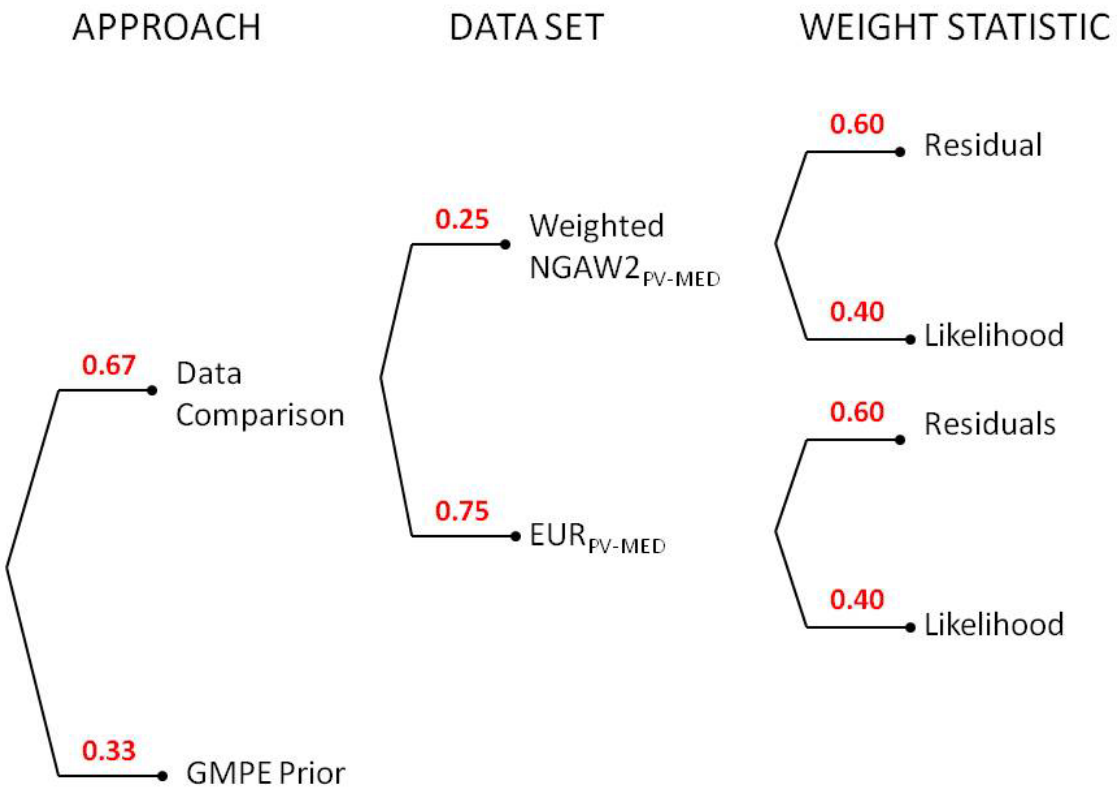

Figure 9.1-2 Weighting scheme for the median base models, involving alternative datasets and alternative weight metrics. The weights based on the TI Team's subjective evaluations are in red. The description of the data set branches is provided in Section 5.3.2: "Weighted $NGAW2_{PV\text{-}MED}$" and "$EUR_{PV\text{-}MED}$" refer to the weighed subset of NGA-West2 data and to the subset of the Akkar et al.'s dataset used for constraining the median models for PVNGS, respectively.

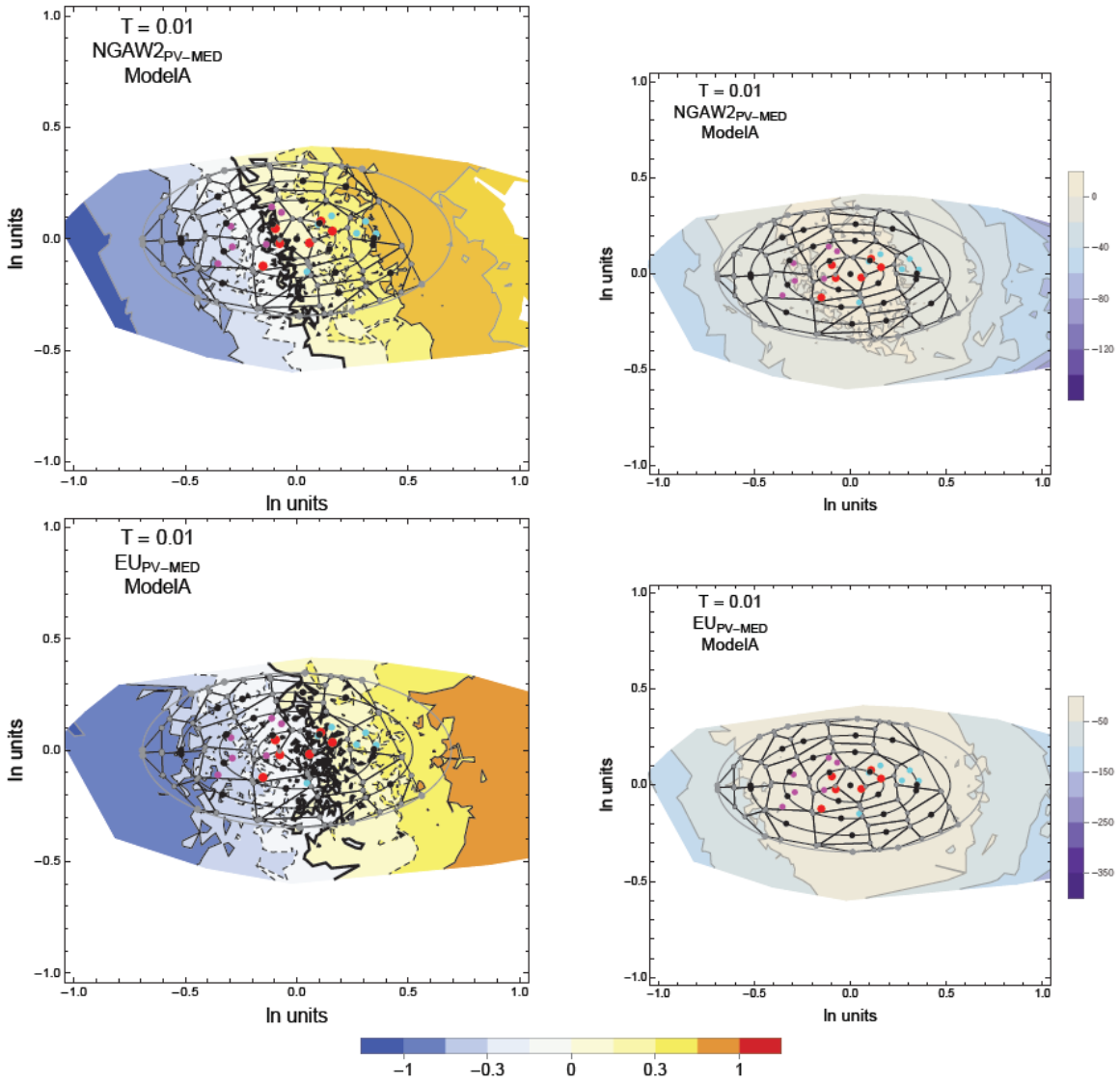

Figure 9.1-3a: Range of PGA models generated from sampling the joint distribution of the Model A common-form parameter distribution and range of representative suite of common-form models (black dots). Red dots show the candidate GMPEs used to develop the ground-motion model distributions. The magenta and cyan dots show plus and minus two sigma epistemic uncertainty, respectively about the candidate GMPEs. The Voronoi cells (gray closed polygons) are developed based on the locations of the black points on the ellipses (gray concentric curves). The contour for the zero residual is a thick black line, the ± 0.15 contours are dashed black lines and the ± 0.3 contours are thin black lines. Upper left: contour lines indicate the range in mean between-event residuals for the weighted NGA ($NGAW2_{PV\text{-}MED}$). Lower left: contour lines indicate the mean between-event residuals for the European ($EUR_{PV\text{-}MED}$) data sets selected for the PVNGS evaluation. Upper right: contour lines indicate the likelihood for the weighted $NGAW2_{PV\text{-}MED}$ data set. Lower right: contour lines indicate the likelihood for the $EUR_{PV\text{-}MED}$ data set.

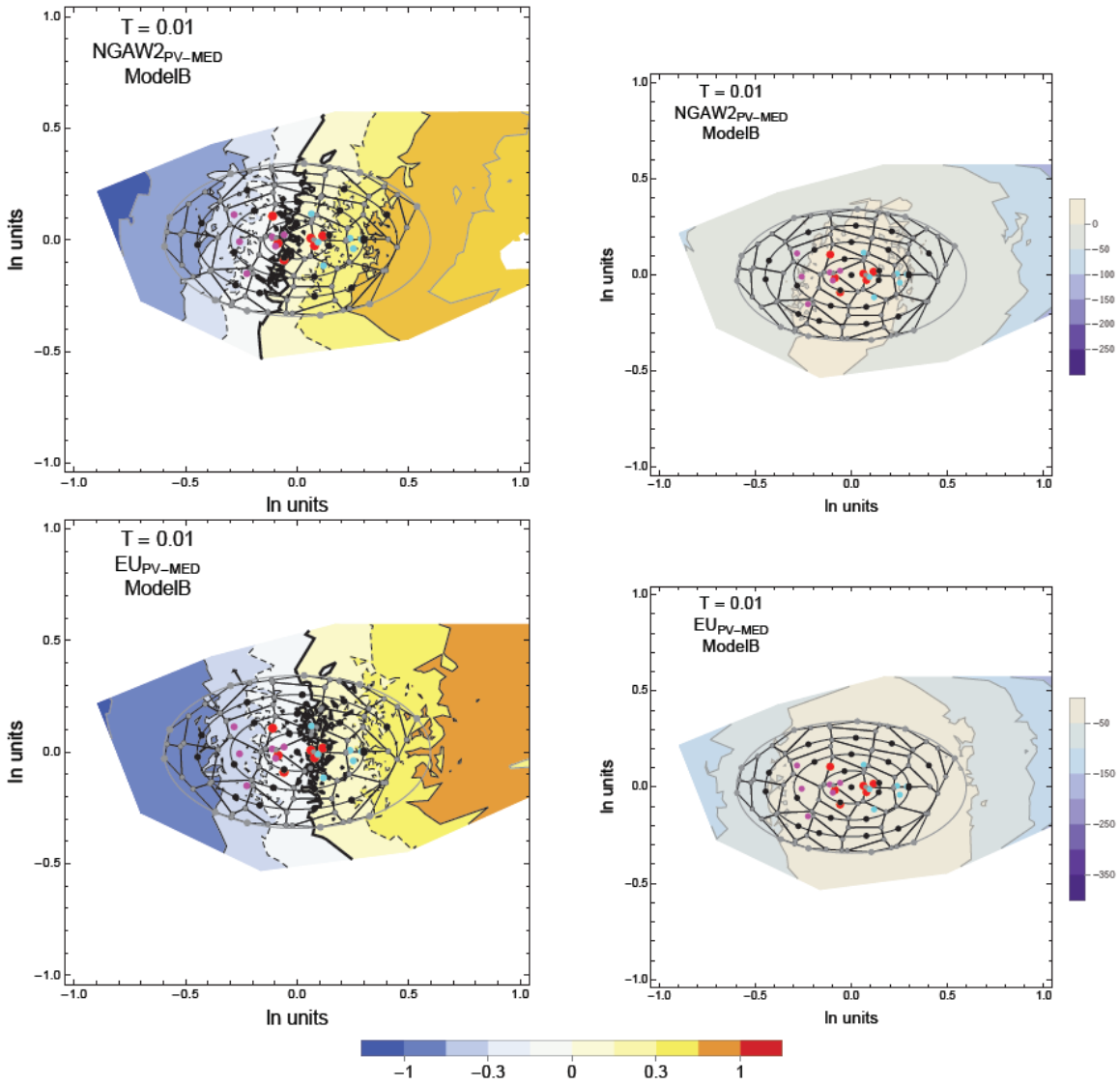

Figure 9.1-3b: Range of PGA models generated from sampling the joint distribution of Model B common-form parameter distribution and range of representative suite of common-form models (black dots). Red dots show the candidate GMPEs used to develop the ground-motion model distributions. The magenta and cyan dots show plus and minus two sigma epistemic uncertainty, respectively about the candidate GMPEs. The Voronoi cells (gray closed polygons) are developed based on the locations of the black points on the ellipses (gray concentric curves). The contour for the zero residual is a thick black line, the ± 0.15 contours are dashed black lines and the ± 0.3 contours are thin black lines. Upper left: contour lines indicate the range in mean between-event residuals for the weighted NGA ($NGAW2_{PV\text{-}MED}$). Lower left: contour lines indicate the mean between-event residuals for the European ($EUR_{PV\text{-}MED}$) data sets selected for the PVNGS evaluation. Upper right: contour lines indicate the likelihood for the weighted $NGAW2_{PV\text{-}MED}$ data set. Lower right: contour lines indicate the likelihood for the $EUR_{PV\text{-}MED}$ data set.

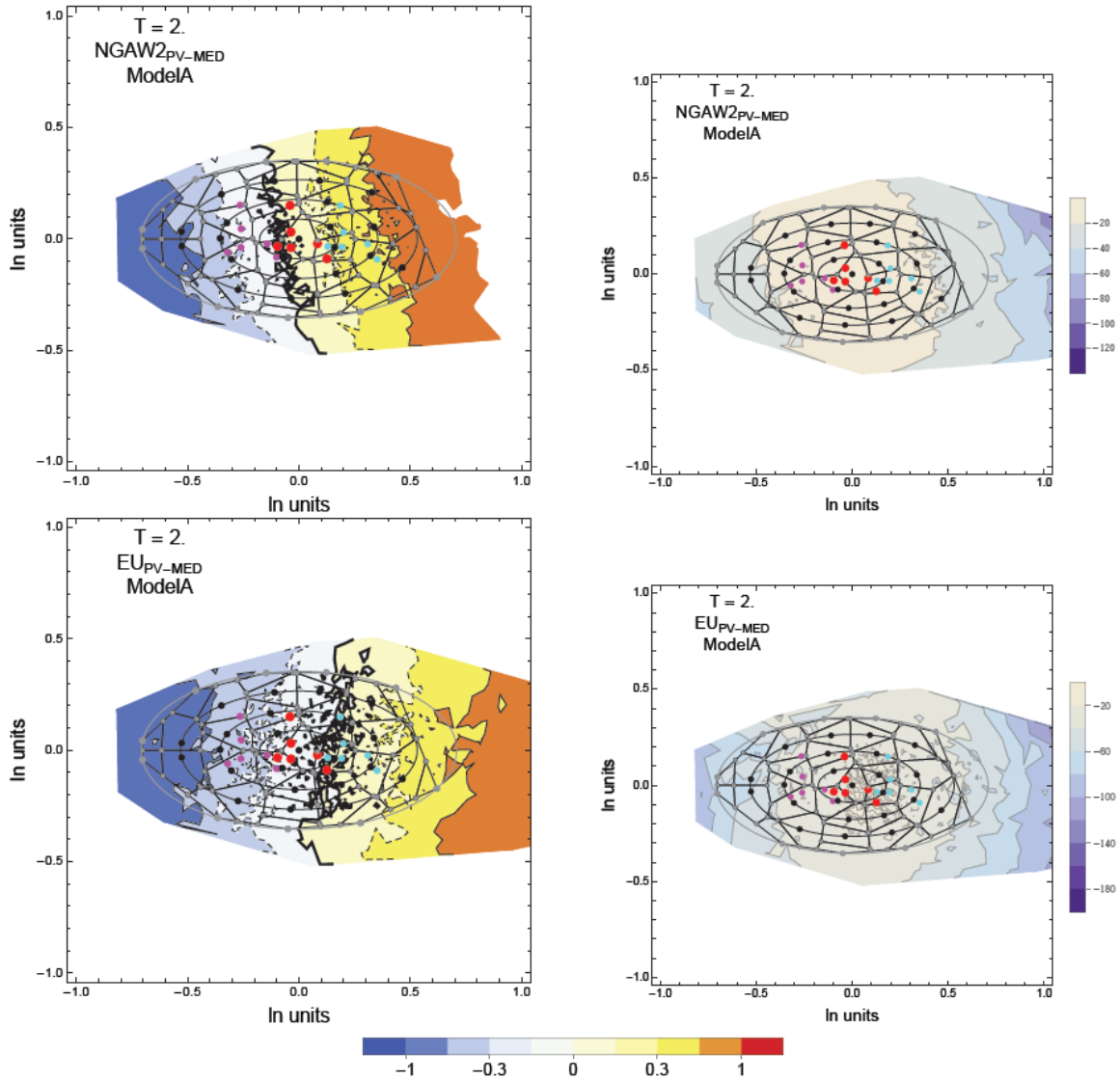

Figure 9.1-4a: Range of T = 2 sec models generated from sampling joint distribution of Model A common-form parameter distribution and range of representative suite of common-form models (black dots). Red dots show the candidate GMPEs used to develop the ground-motion model distributions. The magenta and cyan dots show plus and minus two sigma epistemic uncertainty, respectively about the candidate GMPEs. The Voronoi cells (gray closed polygons) are developed based on the locations of the black points on the ellipses (gray concentric curves). The contour for the zero residual is a thick black line, the ± 0.15 contours are dashed black lines and the ± 0.3 contours are thin black lines. Upper left: contour lines indicate the range in mean between-event residuals for the weighted NGA ($NGAW2_{PV\text{-}MED}$). Lower left: contour lines indicate the mean between-event residuals for the European ($EUR_{PV\text{-}MED}$) data sets selected for the PVNGS evaluation. Upper right: contour lines indicate the likelihood for the weighted $NGAW2_{PV\text{-}MED}$ data set. Lower right: contour lines indicate the likelihood for the $EUR_{PV\text{-}MED}$ data set.

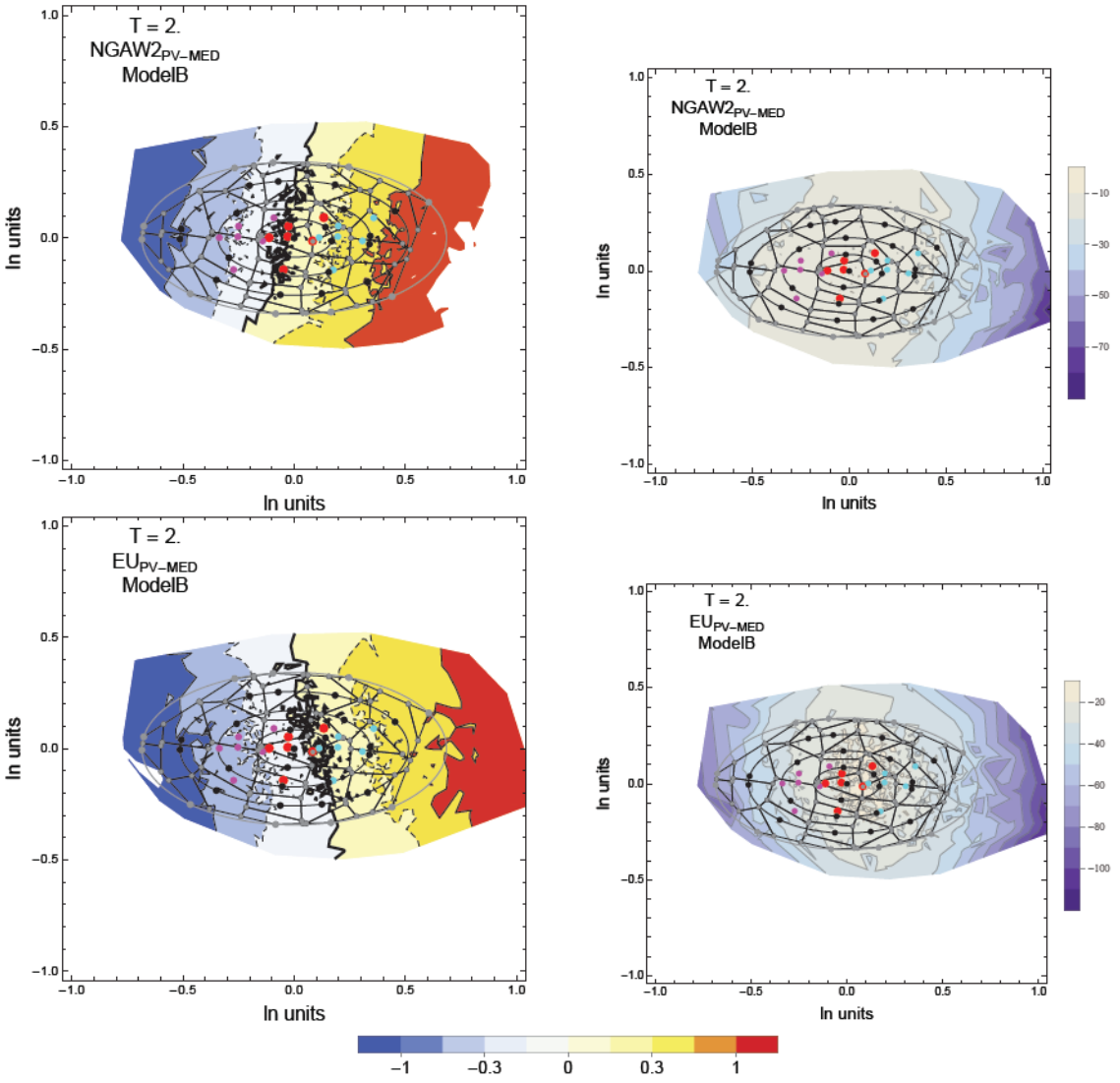

Figure 9.1-4b: Range of T = 2 sec models generated from sampling joint distribution of Model B common-form parameter distribution and range of representative suite of common-form models (black dots). Red dots show the candidate GMPEs used to develop the ground-motion model distributions. The magenta and cyan dots show plus and minus two sigma epistemic uncertainty, respectively about the candidate GMPEs. The Voronoi cells (gray closed polygons) are developed based on the locations of the black points on the ellipses (gray concentric curves). The contour for the zero residual is a thick black line, the ± 0.15 contours are dashed black lines and the ± 0.3 contours are thin black lines. Upper left: contour lines indicate the range in mean between-event residuals for the weighted NGA ($NGAW2_{PV\text{-}MED}$). Lower left: contour lines indicate the mean between-event residuals for the European ($EUR_{PV\text{-}MED}$) data sets selected for the PVNGS evaluation. Upper right: contour lines indicate the likelihood for the weighted $NGAW2_{PV\text{-}MED}$ data set. Lower right: contour lines indicate the likelihood for the $EUR_{PV\text{-}MED}$ data set.

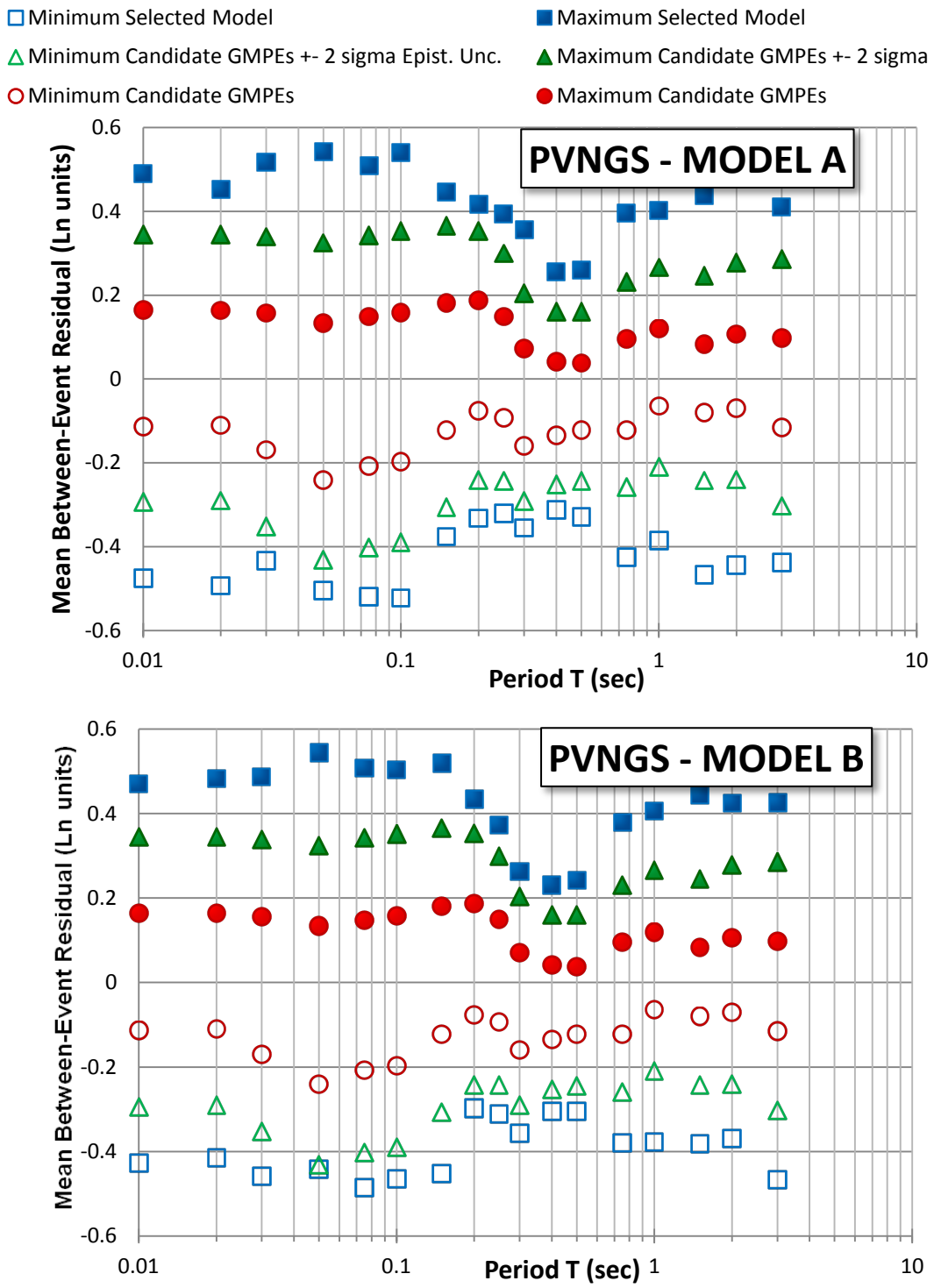

Figure 9.1-5: Range of mean between-event residuals for R_{RUP}-based (Model A) and R_{JB}-based (Model B) common-form models selected to represent the distribution of ground-motion models for evaluation hazard at the PVNGS site from the Greater Arizona sources.

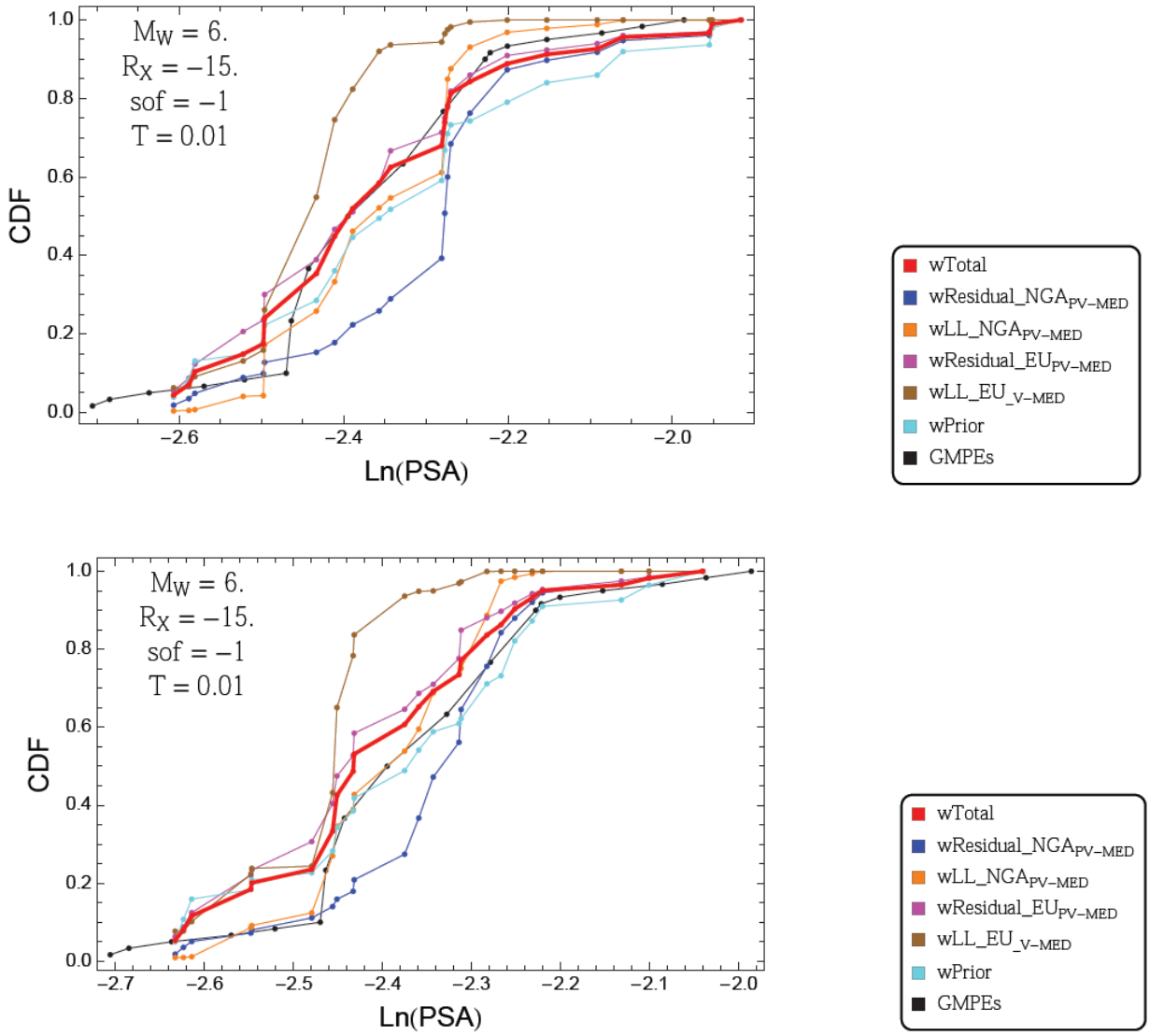

Figure 9.1-6: Example of the cumulative distribution function of the ln PGA for **M** = 6.0, normal earthquakes at a R_X distance of 5 km. The red curve is the distribution used the TI Team approach. The other curves show what the distribution would be if full weight was assigned to each weighting method. The curves for the GMPEs and the prior are based on equal weight to each candidate GMPE. Top: R_{RUP}-based (Model A). Bottom: R_{JB}-based (Model B).

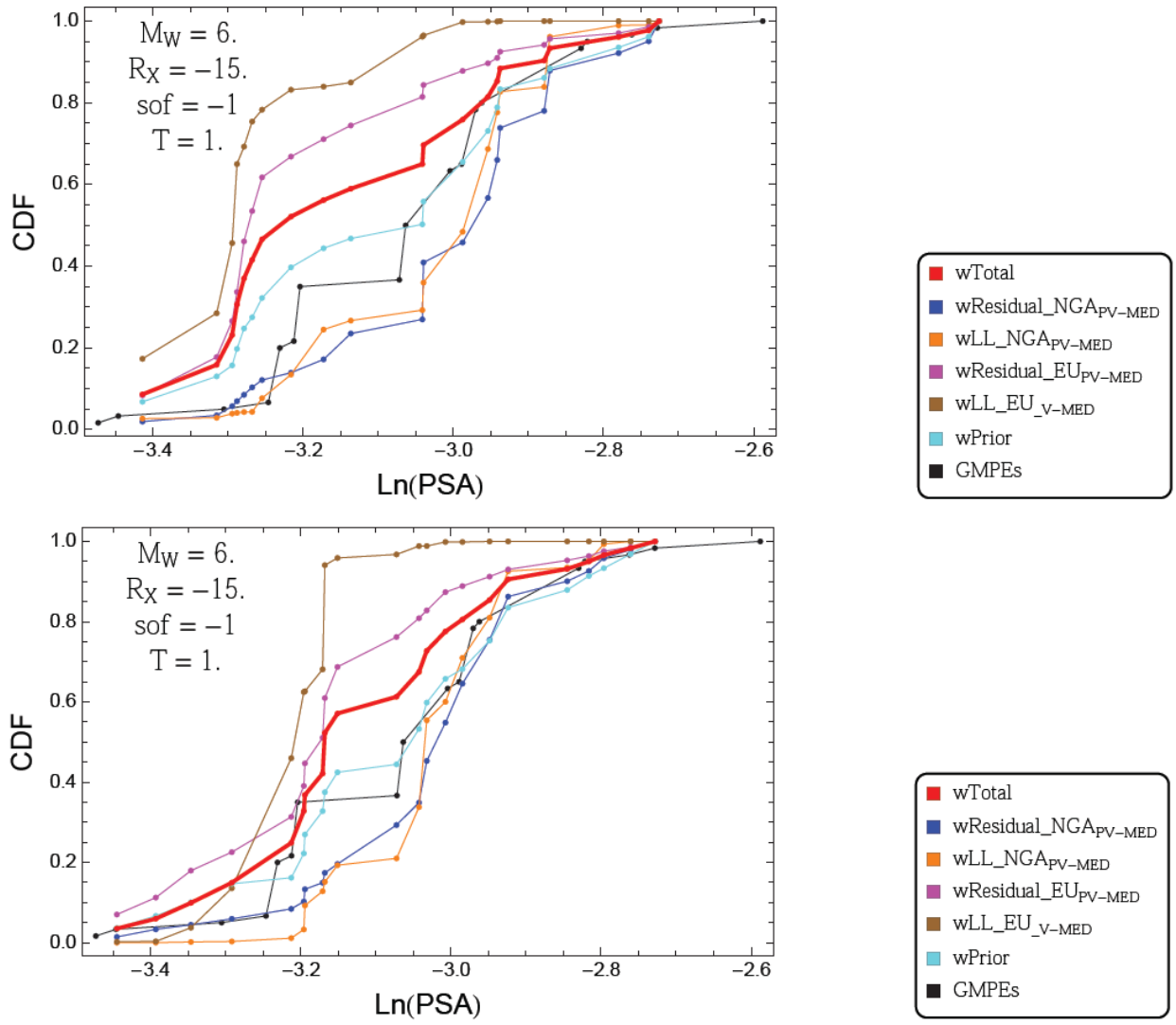

Figure 9.1-7: Example of the cumulative distribution function of the ln PSA (T = 1 sec) for **M** = 6.0, normal earthquakes at a R_X distance of 5 km. The red curve is the distribution used the TI Team approach. The other curves show what the distribution would be if full weight was assigned to each weighting method. The curves for the GMPEs and the prior are based on equal weight to each candidate GMPE. Top: R_{RUP}-based (Model A). Bottom: R_{JB}-based (Model B).

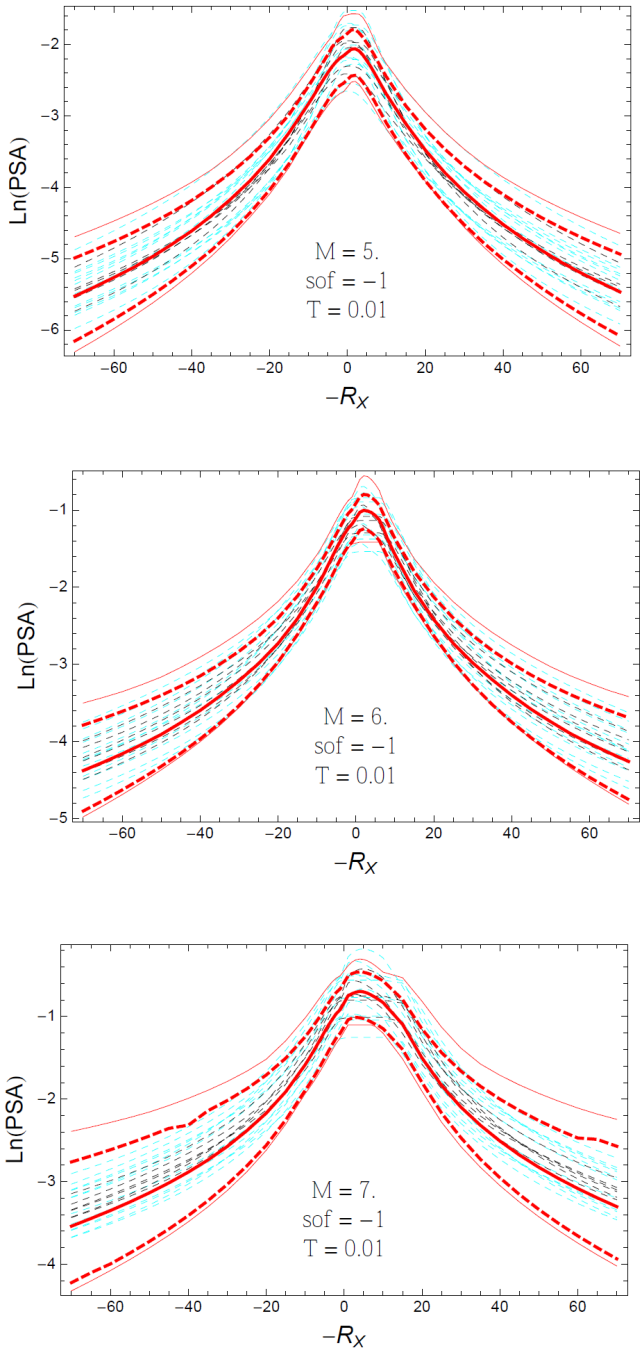

Figure 9.1-8: Example of the distance scaling of PGA for normal faulting. The candidate GMPEs are shown by the dashed black lines, the candidate GMPES with additional epistemic uncertainty are shown by the dashed cyan lines, and the 0.05, 0.5, and 0.95 quantiles of the representative suite of common-form models (combined Models A&B distribution) are shown by the red curves. The thin red lines show the minimum and maximum of the representative common-form models.

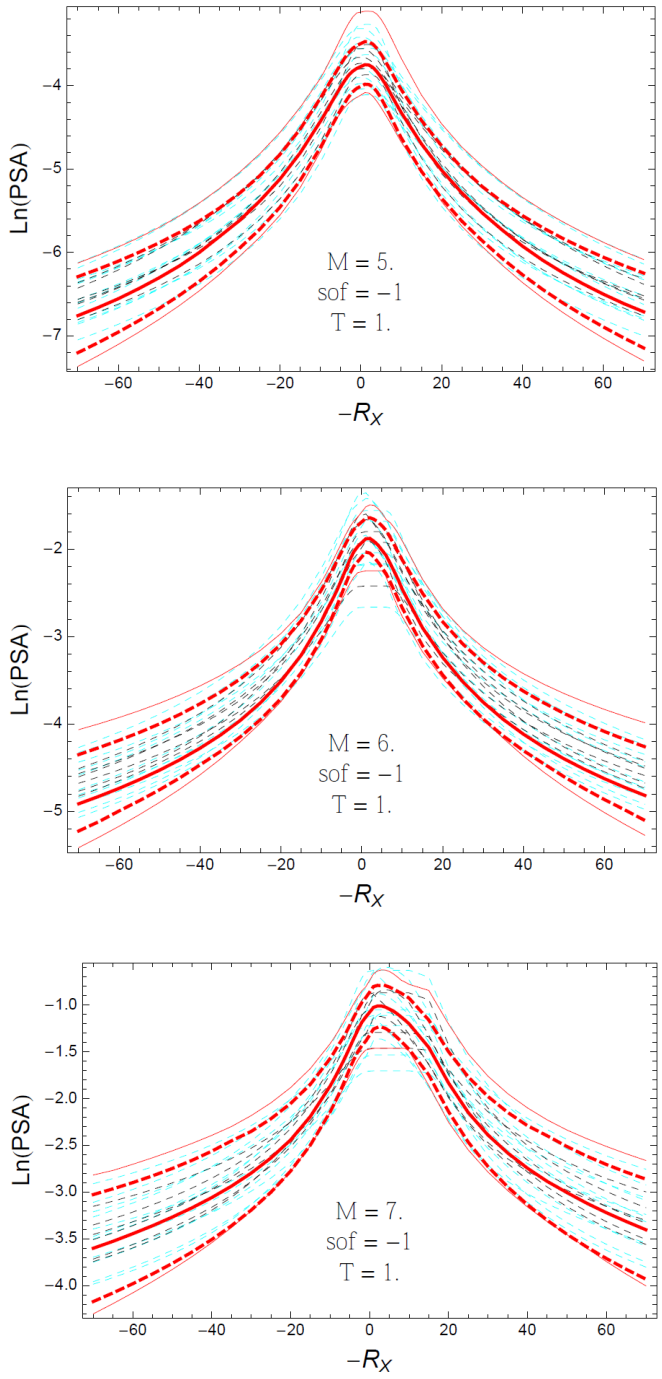

Figure 9.1-9: Example of the distance scaling of PSA for T = 1 sec for normal faulting. The candidate GMPEs are shown by the dashed black lines, the candidate GMPES with additional epistemic uncertainty are shown by the dashed cyan lines, and the 0.05, 0.5, and 0.95 quantiles of the representative suite of common-form models (combined Models A&B distribution) are shown by the red curves. The thin red lines show the minimum and maximum of the representative common-form models.

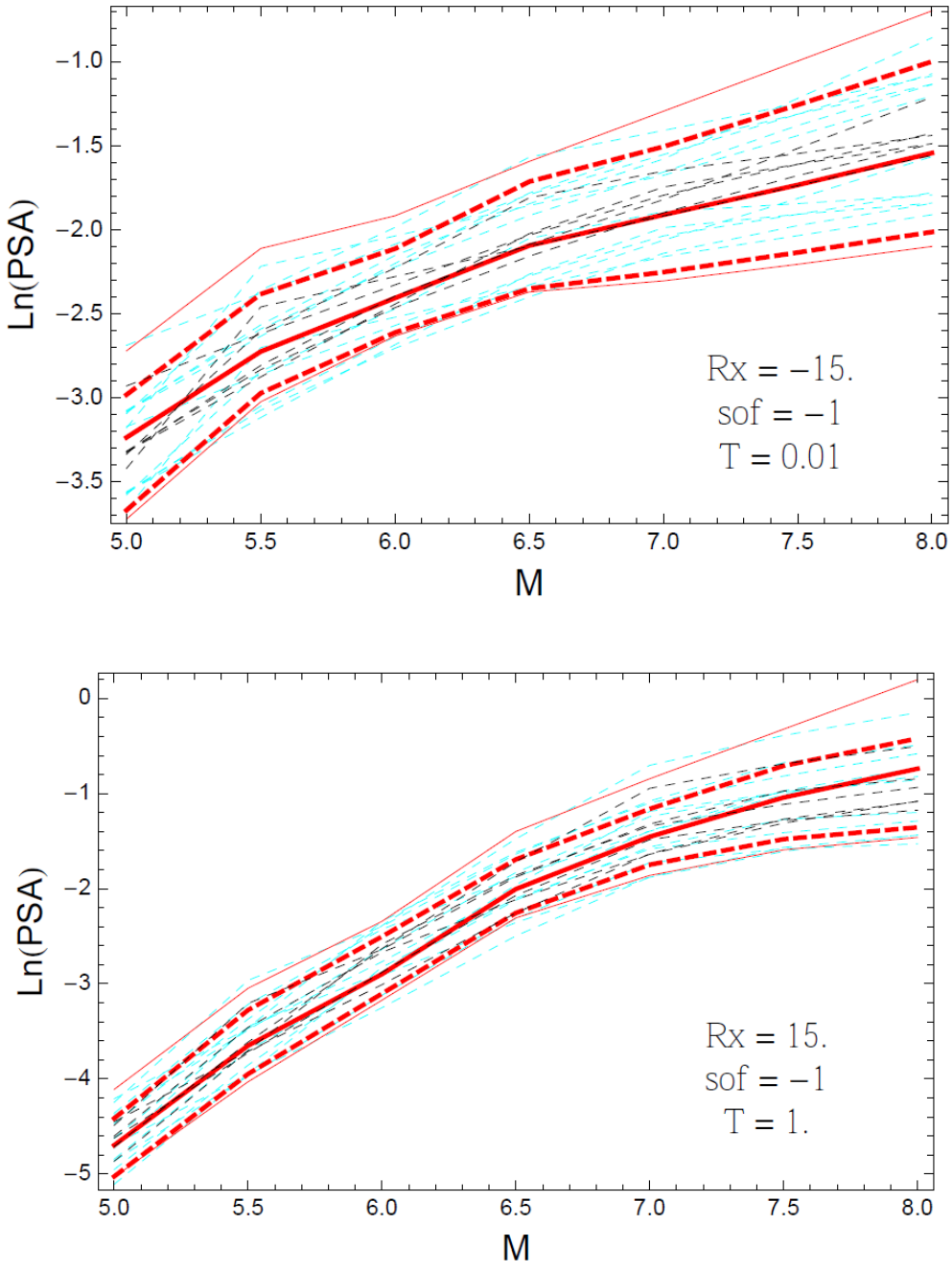

Figure 9.1-10: Example of the magnitude scaling for normal faulting. The candidate GMPEs are shown by the dashed black lines, the candidate GMPES with additional epistemic uncertainty are shown by the dashed cyan lines, and the 0.05, 0.5, and 0.95 quantiles of the representative suite of common-form models (combined Models A&B distribution) are shown by the red curves. The thin red lines show the minimum and maximum of the representative common-form models. Top: PGA. Bottom: PSA for T = 1 sec.

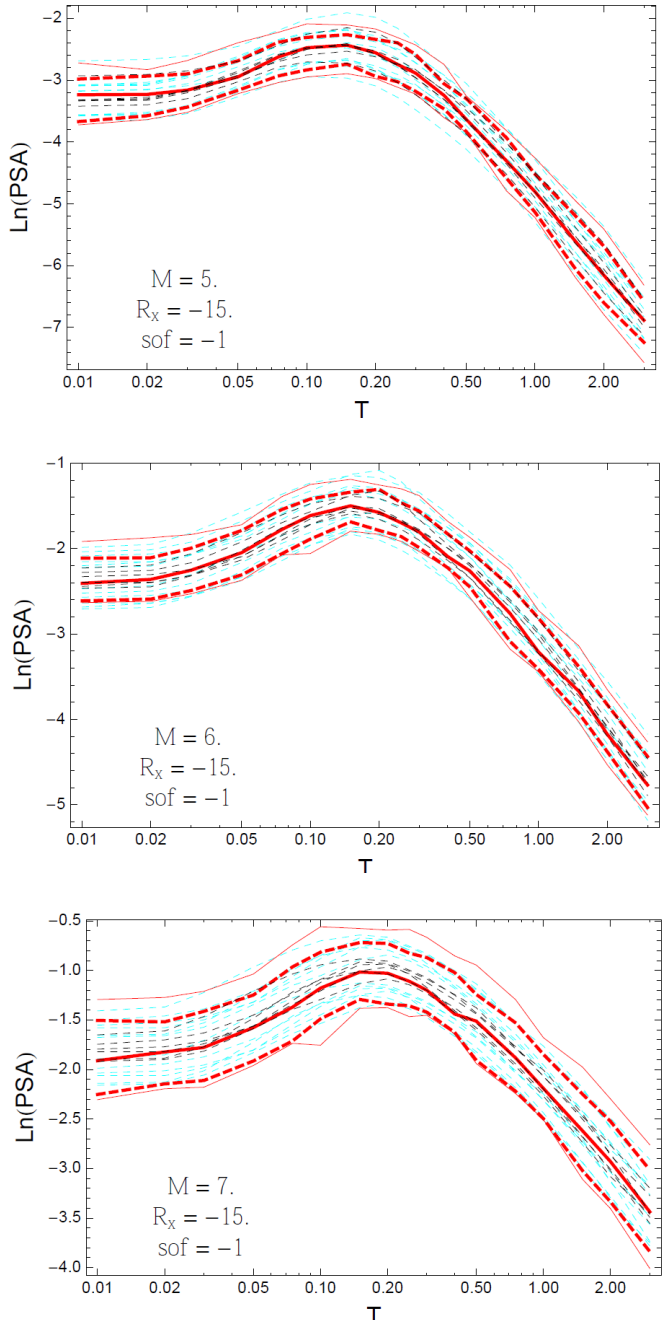

Figure 9.1-11: Example of the response spectra for normal faulting for **M**5, **M**6, and **M**7 at an R_X distance of -15 km. The candidate GMPEs are shown by the dashed black lines, the candidate GMPES with additional epistemic uncertainty are shown by the dashed cyan lines, and the 0.05, 0.5, and 0.95 quantiles of the representative suite of common-form models (combined Models A&B distribution) are shown by the red curves. The thin red lines show the minimum and maximum of the representative common-form models.

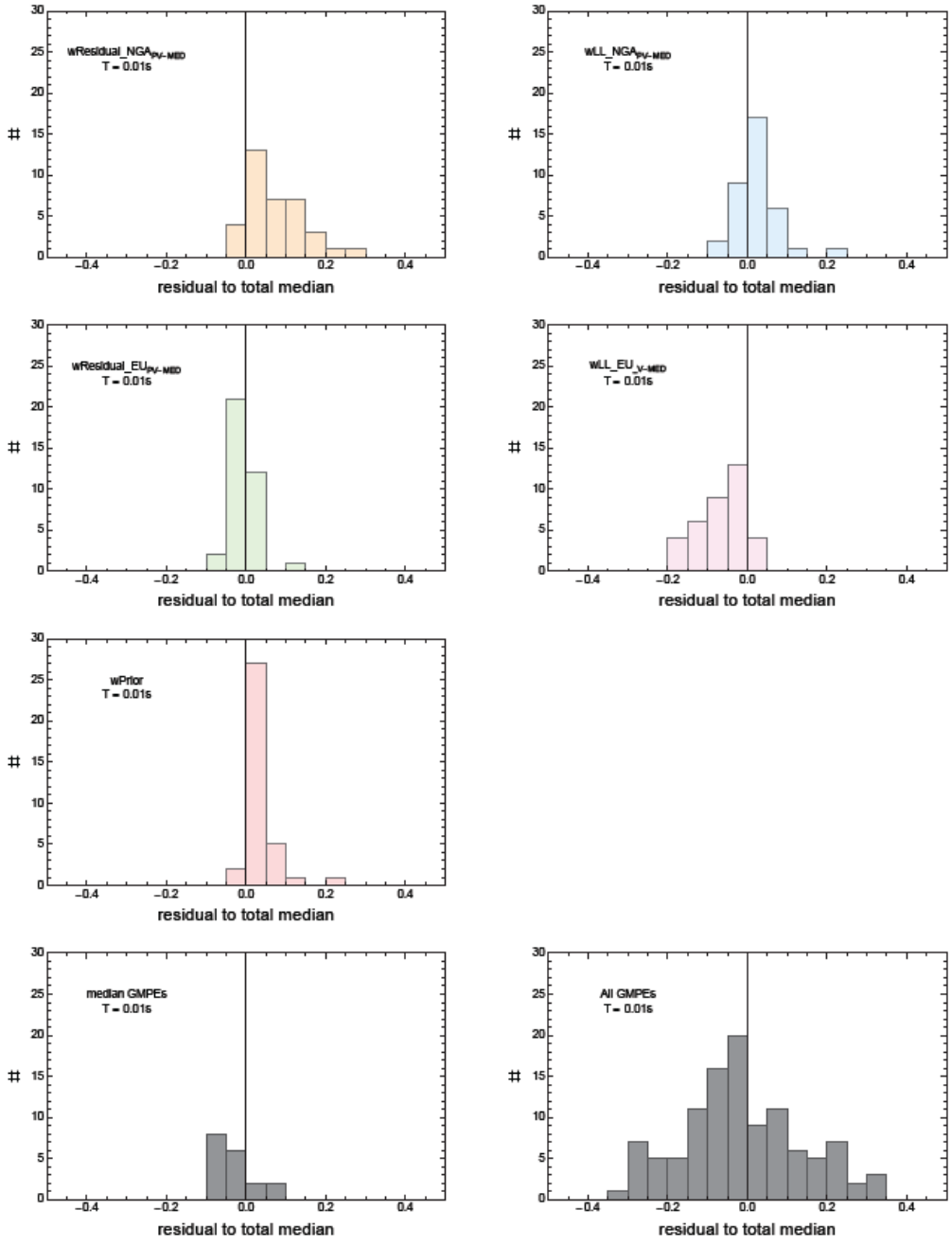

Figure 9.1-12a: Example of the influence of the alternative data sets and the prior on the median ground motion for Model A at PGA for the scenarios listed in Table 9.1-1. The differences for medians calculated with different weights to median calculated with total weights are plotted in the histograms. The zero residual is relative to the PSA at CDF = 0.5 for the weighted common-form models (e.g. red curves in figures showing CDF). Bottom row left shows differences between medians for the GMPE distribution to median calculated with total weights. Bottom row right shows differences between the candidate GMPEs (without uncertainty) to median calculated with total weights.

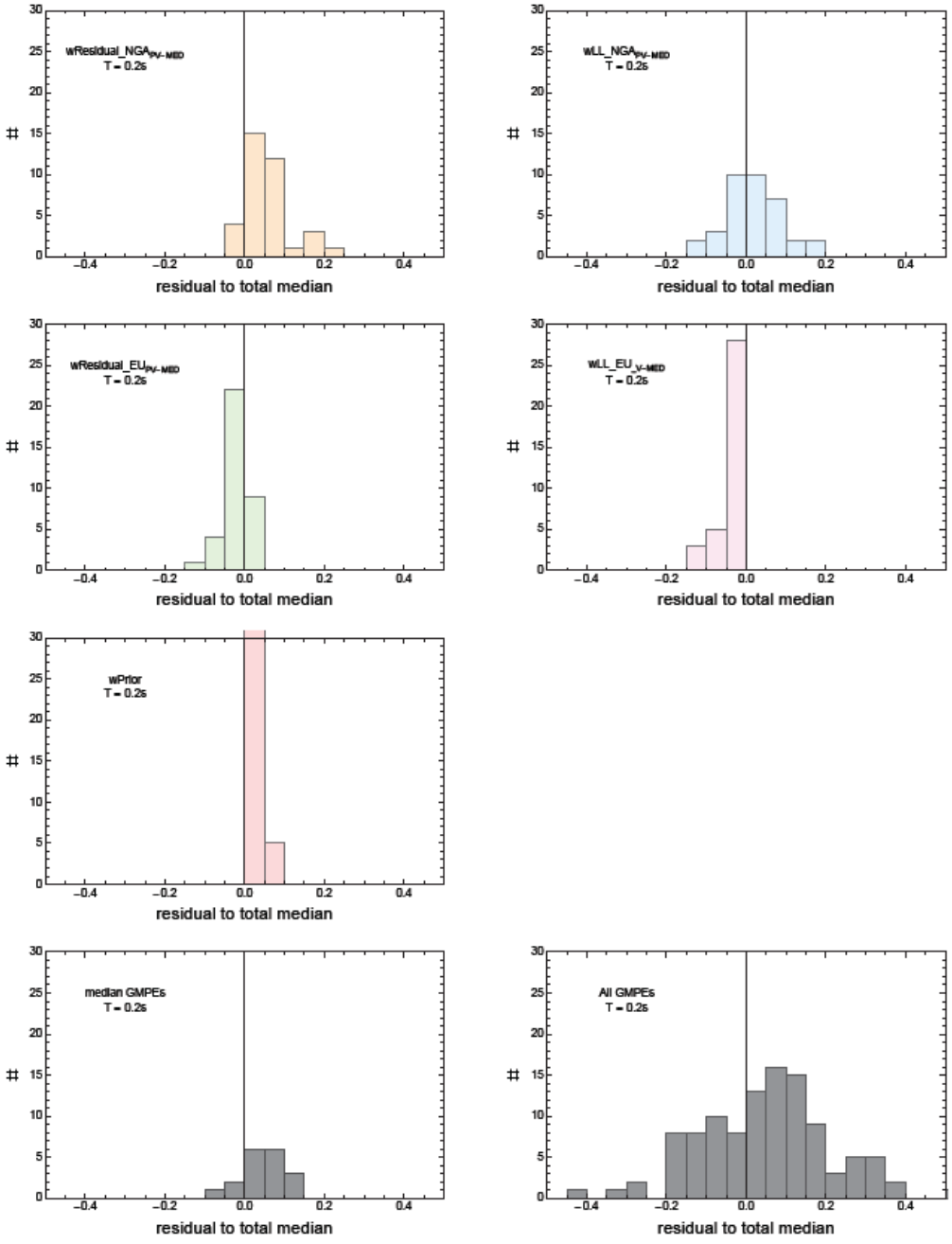

Figure 9.1-12b: Example of the influence of the alternative data sets and the prior on the median ground motion for Model A at T = 0.2 sec for the scenarios listed in Table 9.1-1. The differences for medians calculated with different weights to median calculated with total weights are plotted in the histograms. The zero residual is relative to the PSA at CDF = 0.5 for the weighted common-form models (e.g. red curves in figures showing CDF). Bottom row left shows differences between medians for the GMPE distribution to median calculated with total weights. Bottom row right shows differences between the candidate GMPEs (without uncertainty) to median calculated with total weights.

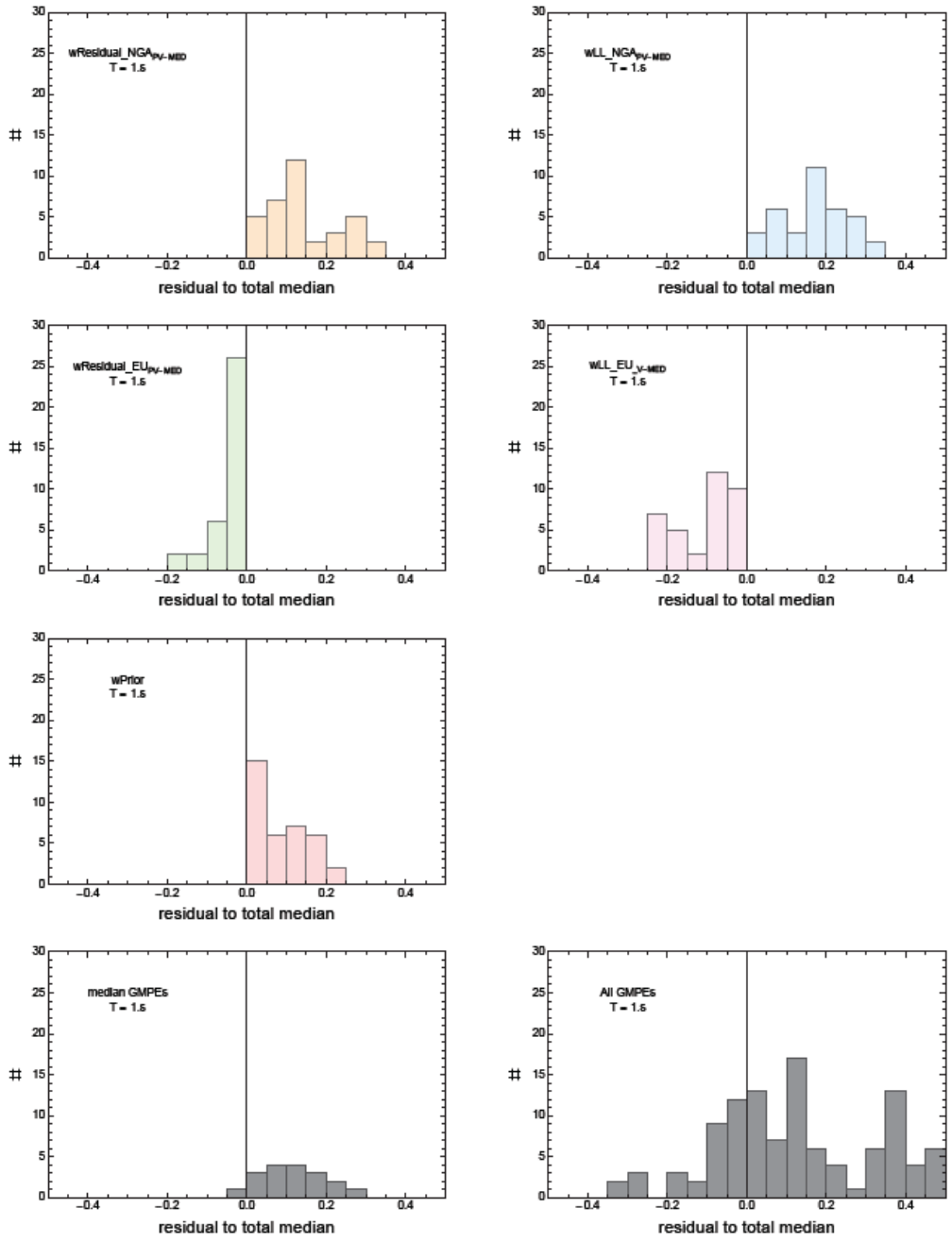

Figure 9.1-12c: Example of the influence of the alternative data sets and the prior on the median ground motion for Model A at T = 1 sec for the scenarios listed in Table 9.1-1. The differences for medians calculated with different weights to median calculated with total weights are plotted in the histograms. The zero residual is relative to the PSA at CDF = 0.5 for the weighted common-form models (e.g. red curves in figures showing CDF). Bottom row left shows differences between medians for the GMPE distribution to median calculated with total weights. Bottom row right shows differences between the candidate GMPEs (without uncertainty) to median calculated with total weights.

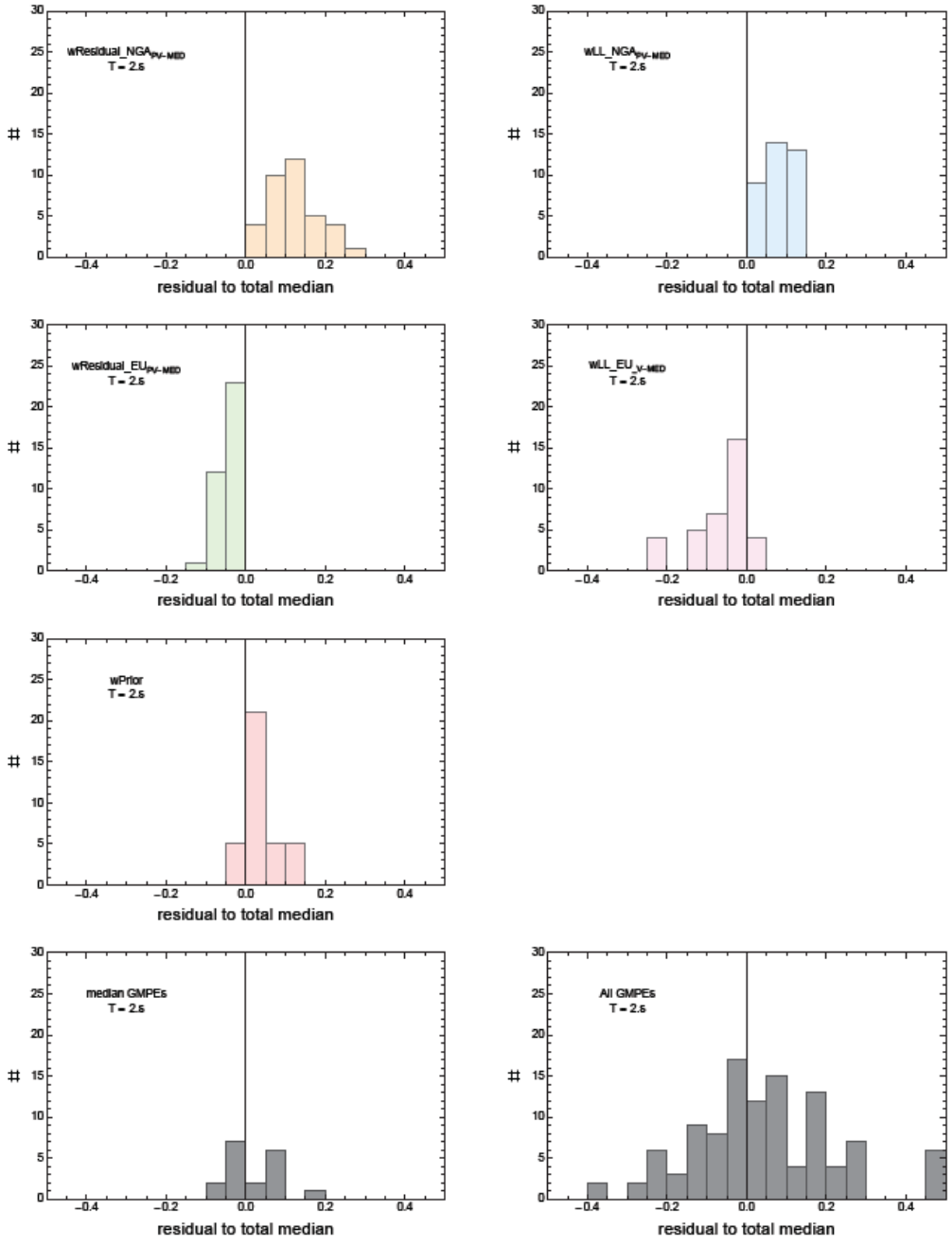

Figure 9.1-12d: Example of the influence of the alternative data sets and the prior on the median ground motion for Model A at T = 2 sec for the scenarios listed in Table 9.1-1. The differences for medians calculated with different weights to median calculated with total weights are plotted in the histograms. The zero residual is relative to the PSA at CDF = 0.5 for the weighted common-form models (e.g. red curves in figures showing CDF). Bottom row left shows differences between medians for the GMPE distribution to median calculated with total weights. Bottom row right shows differences between the candidate GMPEs (without uncertainty) to median calculated with total weights.

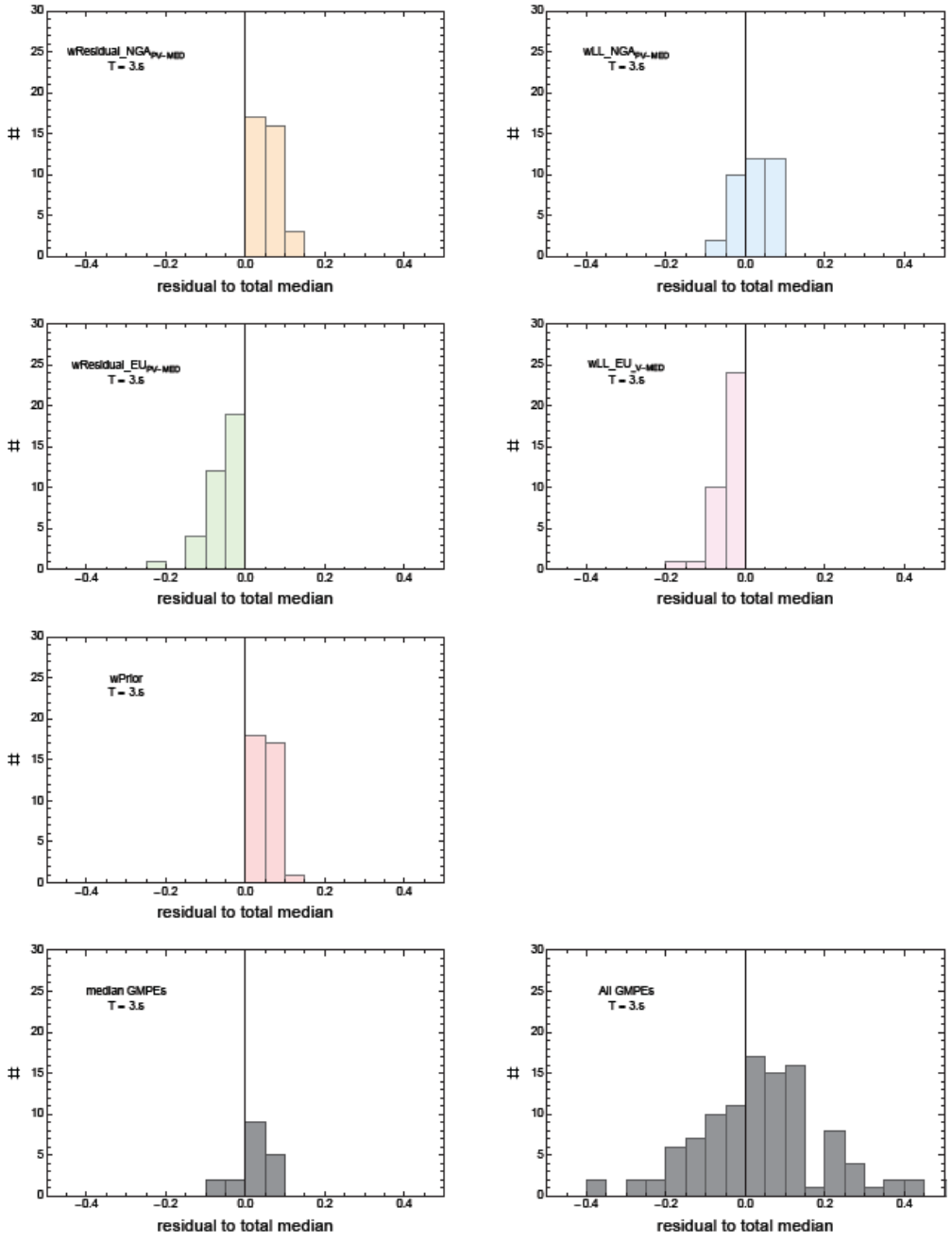

Figure 9.1-12e: Example of the influence of the alternative data sets and the prior on the median ground motion for Model A at T = 3 sec for the scenarios listed in Table 9.1-1. The differences for medians calculated with different weights to median calculated with total weights are plotted in the histograms. The zero residual is relative to the PSA at CDF = 0.5 for the weighted common-form models (e.g. red curves in figures showing CDF). Bottom row left shows differences between medians for the GMPE distribution to median calculated with total weights. Bottom row right shows differences between the candidate GMPEs (without uncertainty) to median calculated with total weights.

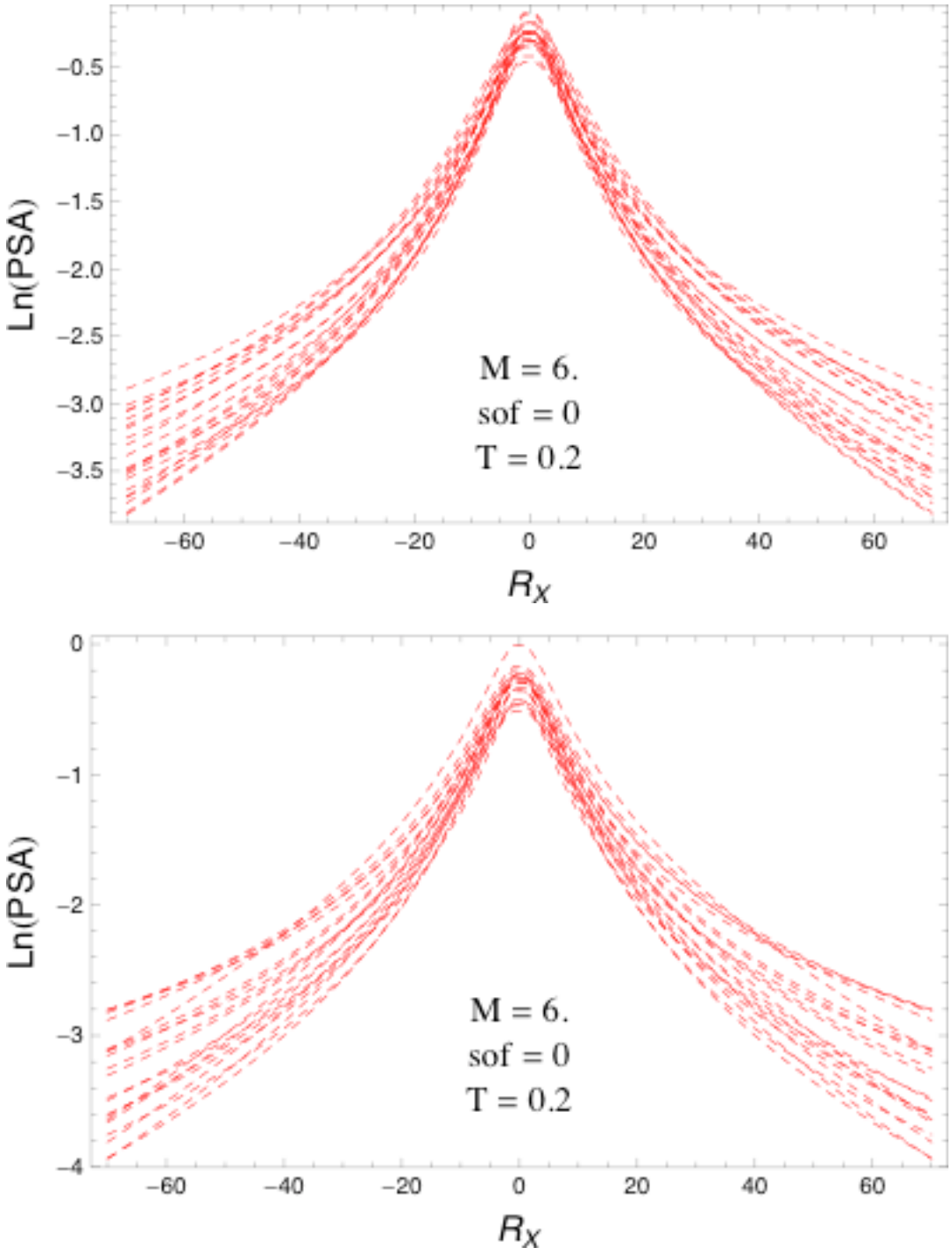

Figure 9.1-13: Example of the distance scaling for the representative suite of common-form models for **M**6 vertical strike-slip earthquakes for T = 0.2 sec. Top: R_{RUP}-based models. Bottom: R_{JB}-based models.

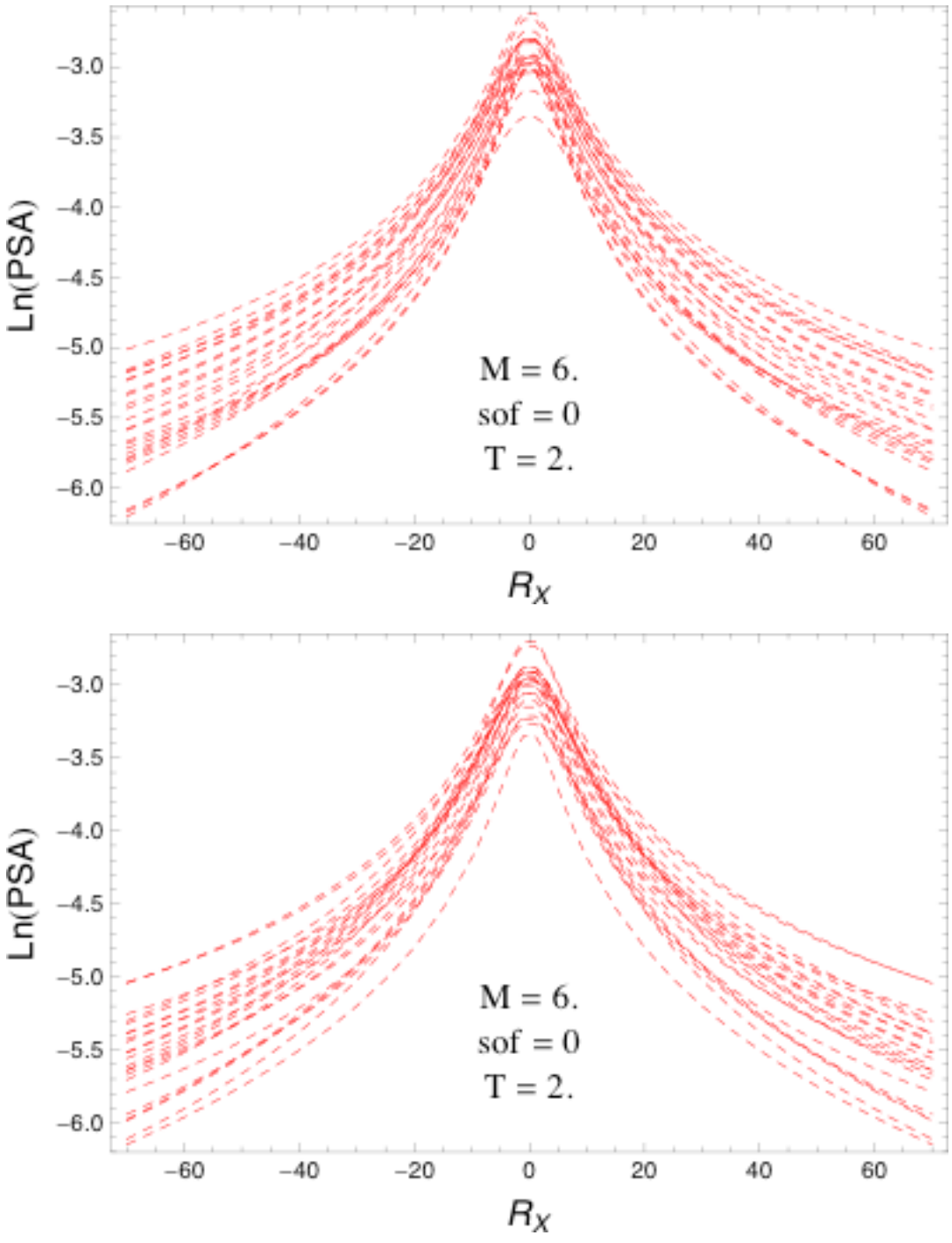

Figure 9.1-14: Example of the distance scaling for the representative suite of common-form models for **M**6 vertical strike-slip earthquakes for T = 2 sec. Top: R_{RUP}-based models. Bottom: R_{JB}-based models.

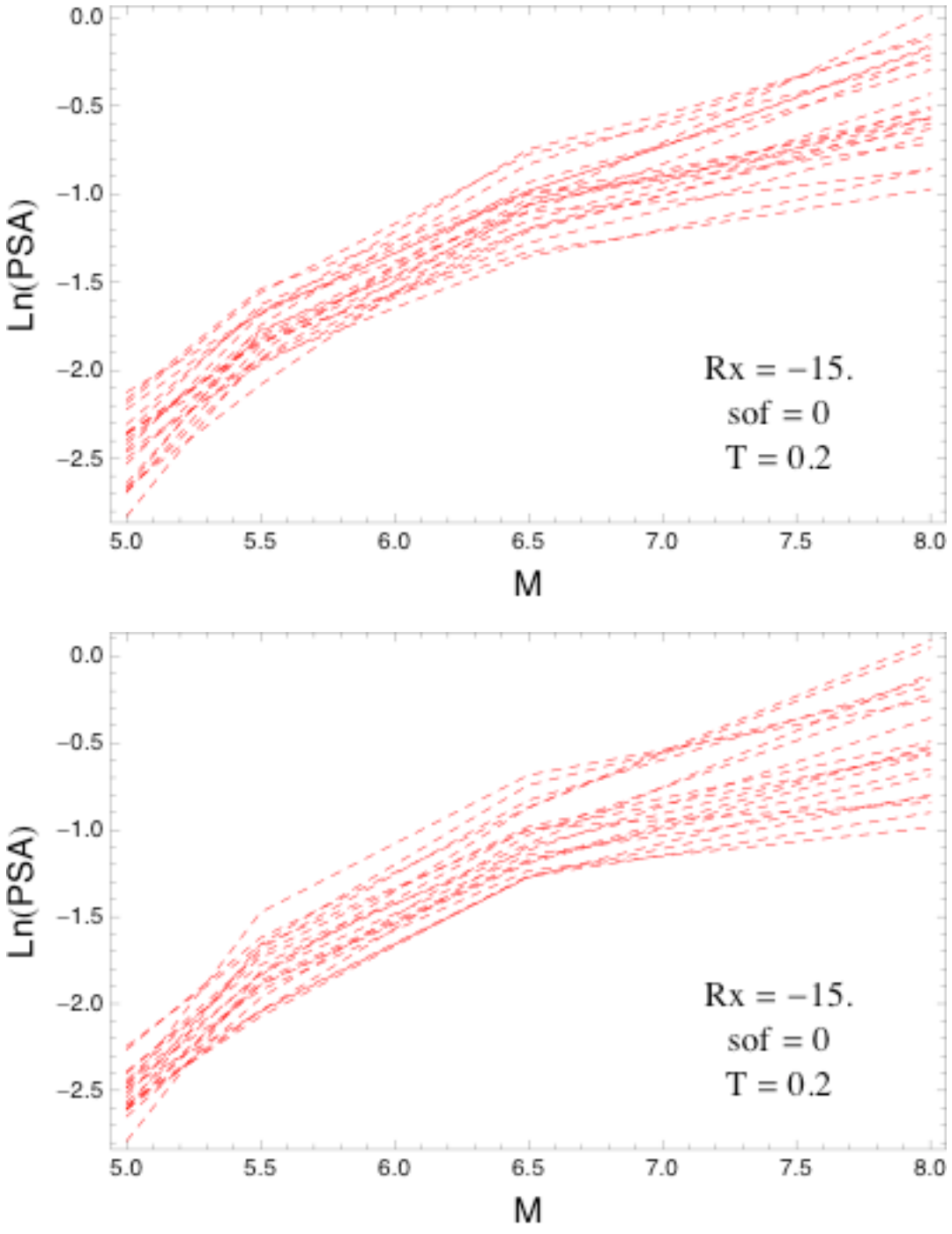

Figure 9.1-15: Example of the magnitude scaling for the representative suite of common-form models for vertical strike-slip earthquakes at an R_X distance of -15 km for T = 0.2 sec. Top: R_{RUP}-based models. Bottom: R_{JB}-based models.

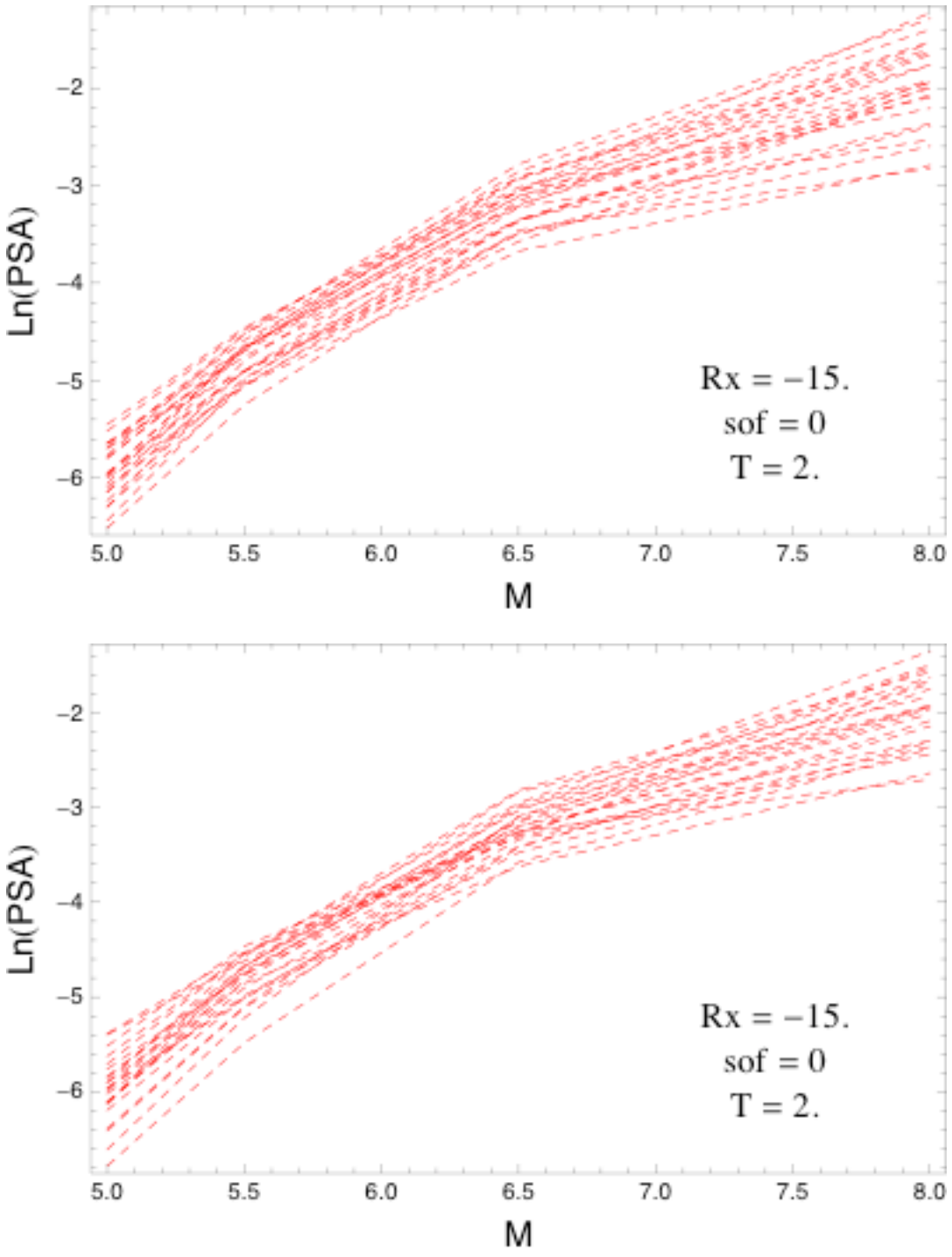

Figure 9.1-16: Example of the magnitude scaling for the representative suite of common-form models for vertical strike-slip earthquakes at an R_X distance of -15 km for T = 2 sec. Top: R_{RUP}-based models. Bottom: R_{JB}-based models.

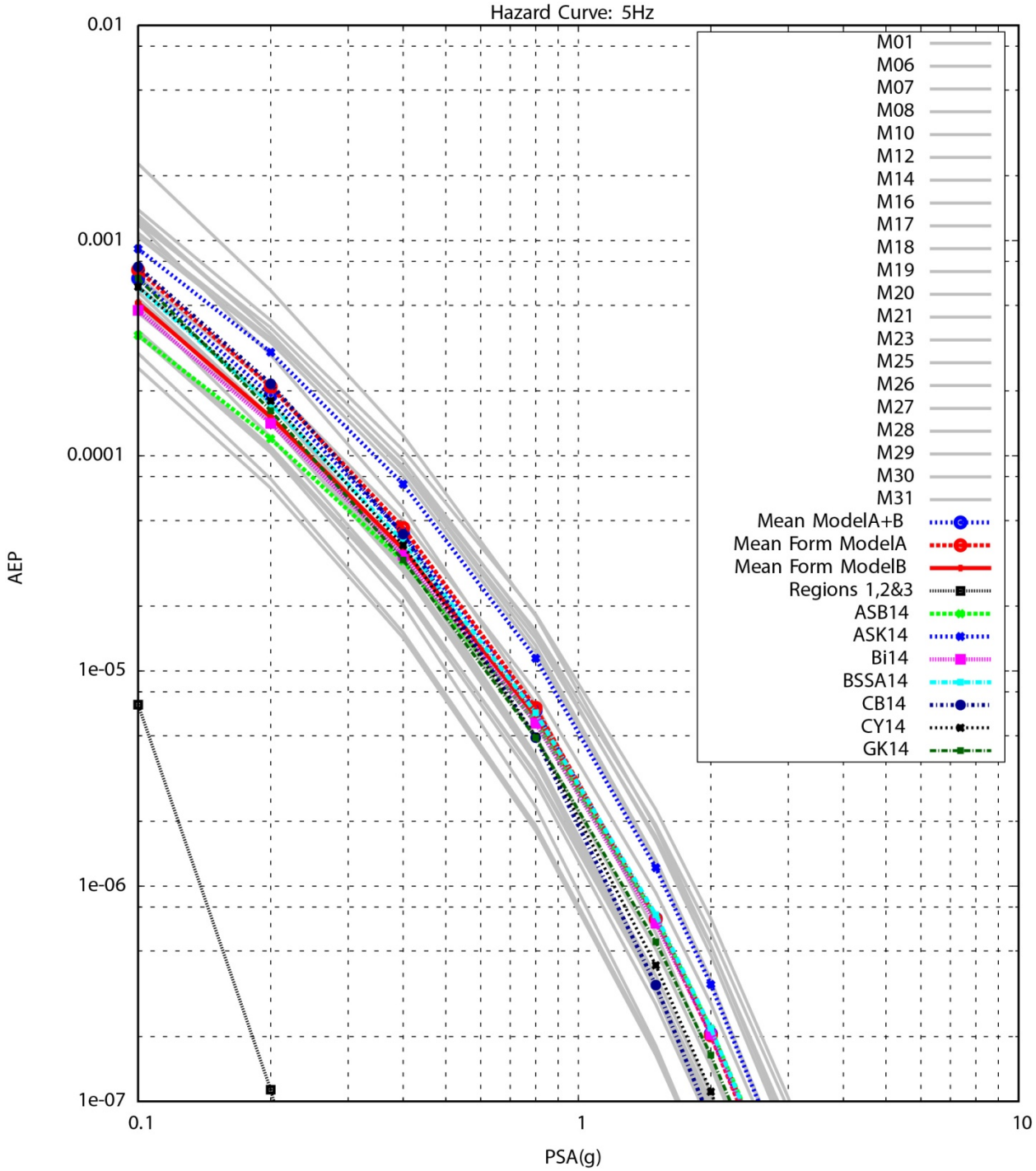

Figure 9.1-17a: Example of hazard for PSA at T = 0.2 sec for the candidate GMPEs and the hazard for the representative suite of R_{RUP}-based common-form models (Model A). The contribution from the distant California and Mexico sources is shown by the lowest curve (curve labeled Regions 1, 2&3). The hazard curve from the GK14 model is shown as well for comparison, although the GK14 model is not part of the candidate GMPEs for PVNGS.

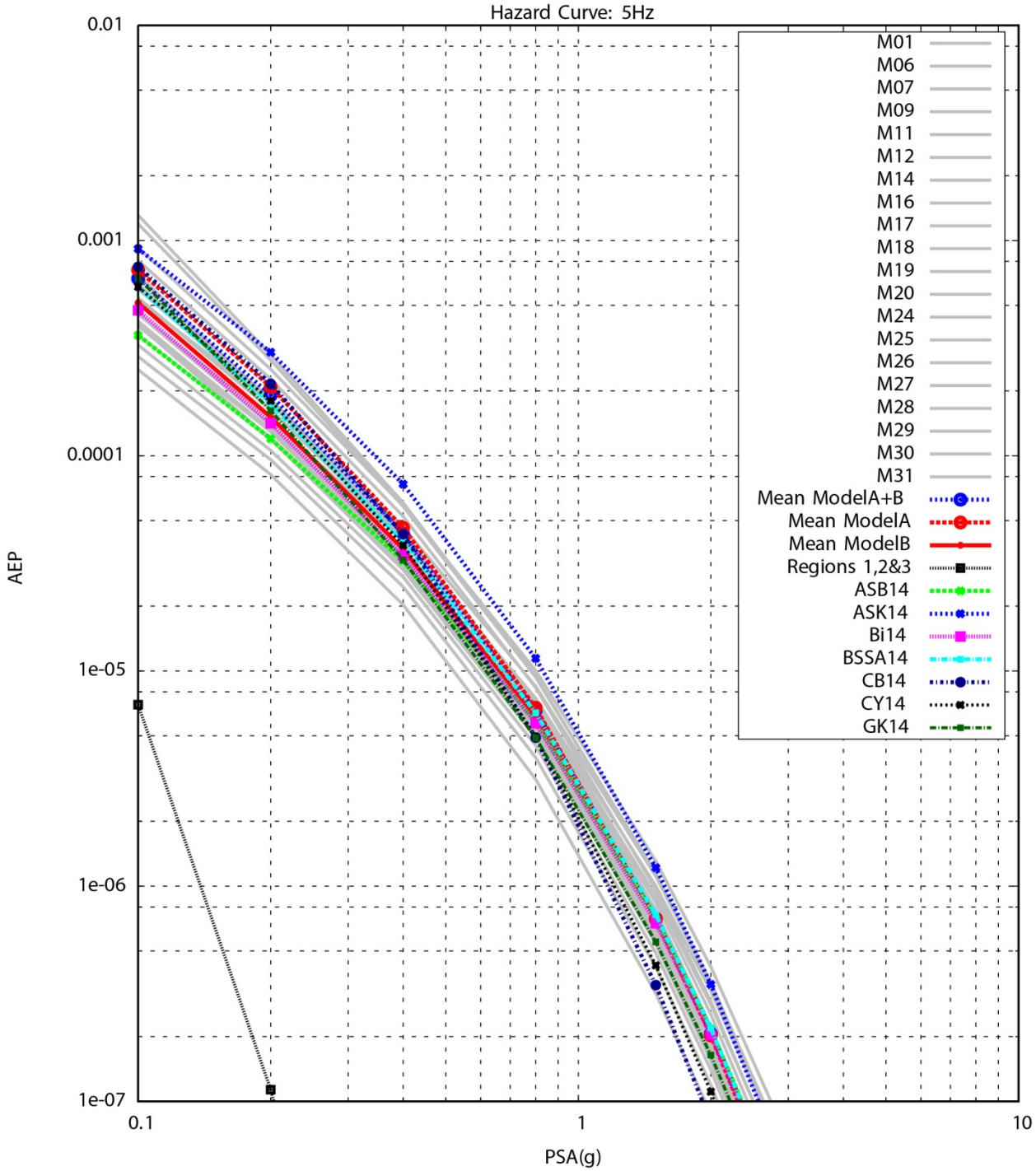

Figure 9.1-17b: Example of hazard for PSA at T = 0.2 sec for the candidate GMPEs and the hazard for the representative suite of R_{JB}-based common-form models (Model B). The contribution from the distant California and Mexico sources is shown by the lowest curve (curve labeled Regions 1, 2&3). The hazard curve from the GK14 model is shown as well for comparison, although the GK14 model is not part of the candidate GMPEs for PVNGS.

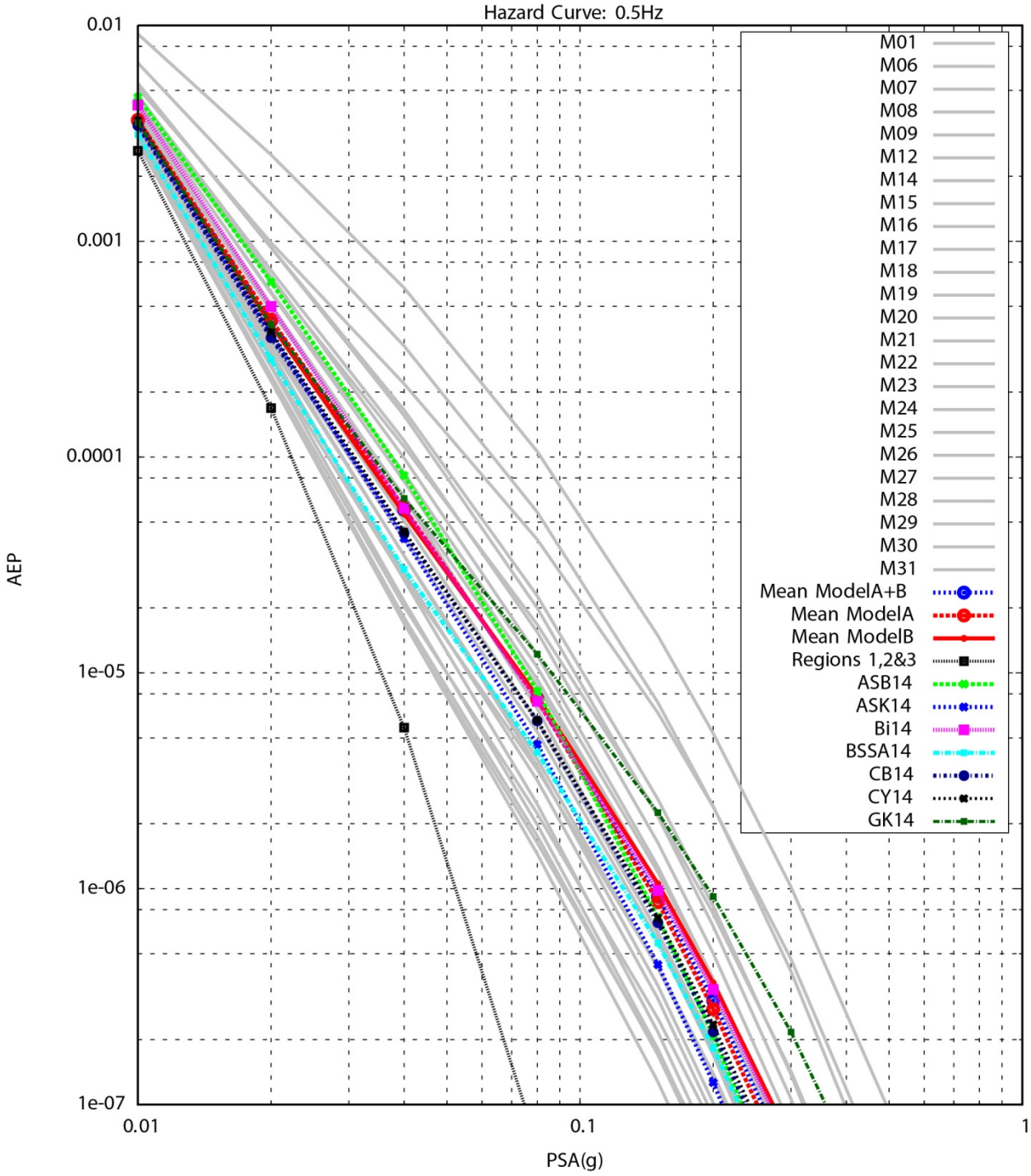

Figure 9.1-18a: Example of hazard for PSA at T = 2 sec for the candidate GMPEs and the hazard for the representative suite of R_{RUP}-based common-form models (Model A). The contribution from the distant California and Mexico sources is shown by the lowest curve (curve labeled Regions 1, 2&3). The hazard curve from the GK14 model is shown as well for comparison, although the GK14 model is not part of the candidate GMPEs for PVNGS.

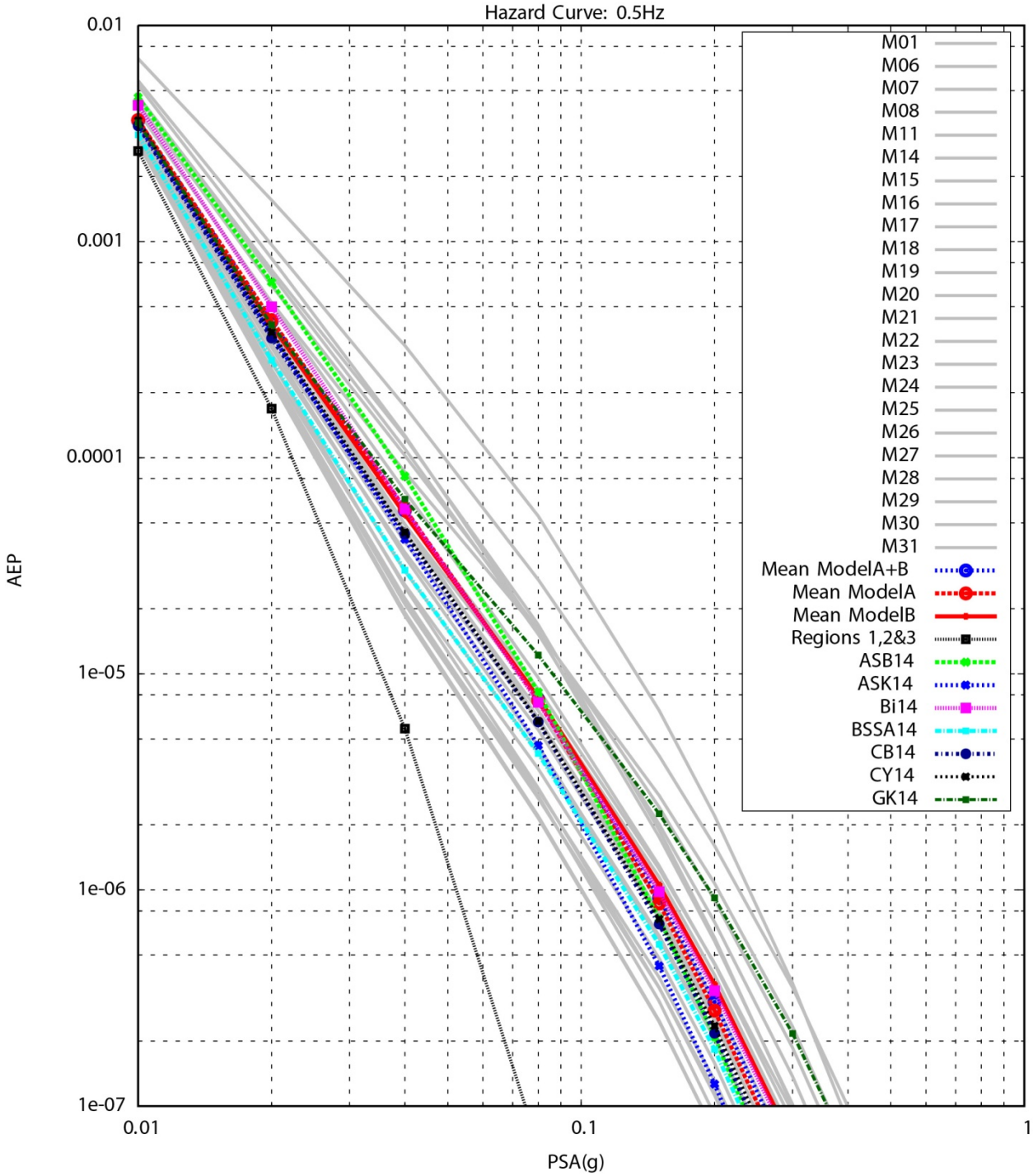

Figure 9.1-18b: Example of hazard for PSA at T = 2 sec for the candidate GMPEs and the hazard for the representative suite of R_{JB}-based common-form models (Model B). The contribution from the distant California and Mexico sources is shown by the lowest curve (curve labeled Regions 1, 2&3). The hazard curve from the GK14 model is shown as well for comparison, although the GK14 model is not part of the candidate GMPEs for PVNGS.

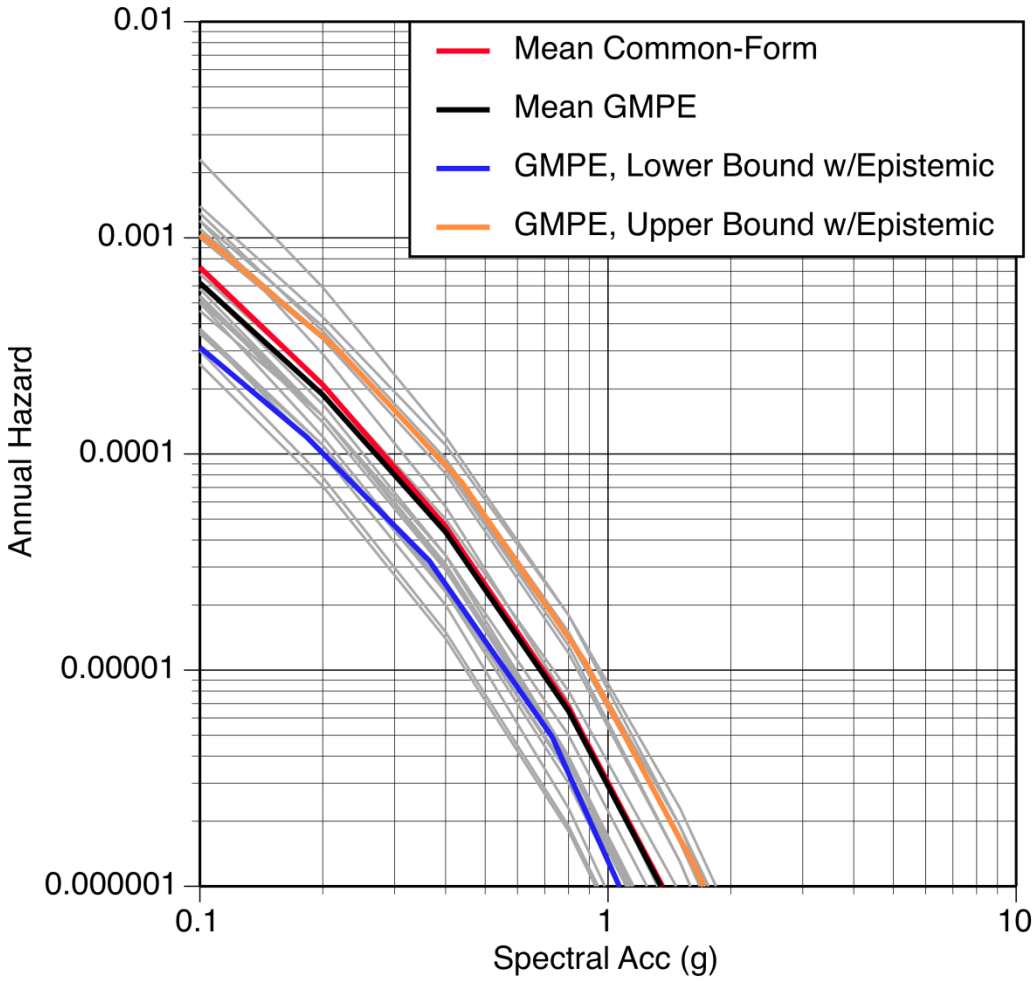

Figure 9.1-19a: Comparison of the hazard for PSA at T = 0.2 sec using the representative suite of common-form models (grey lines), the weighted mean common-form model (red line), mean from the six candidate GMPE models (black line), and the lower (blue line) and upper (orange line) bounds of the six candidate GMPE models with the additional epistemic uncertainty (2 sigma level).

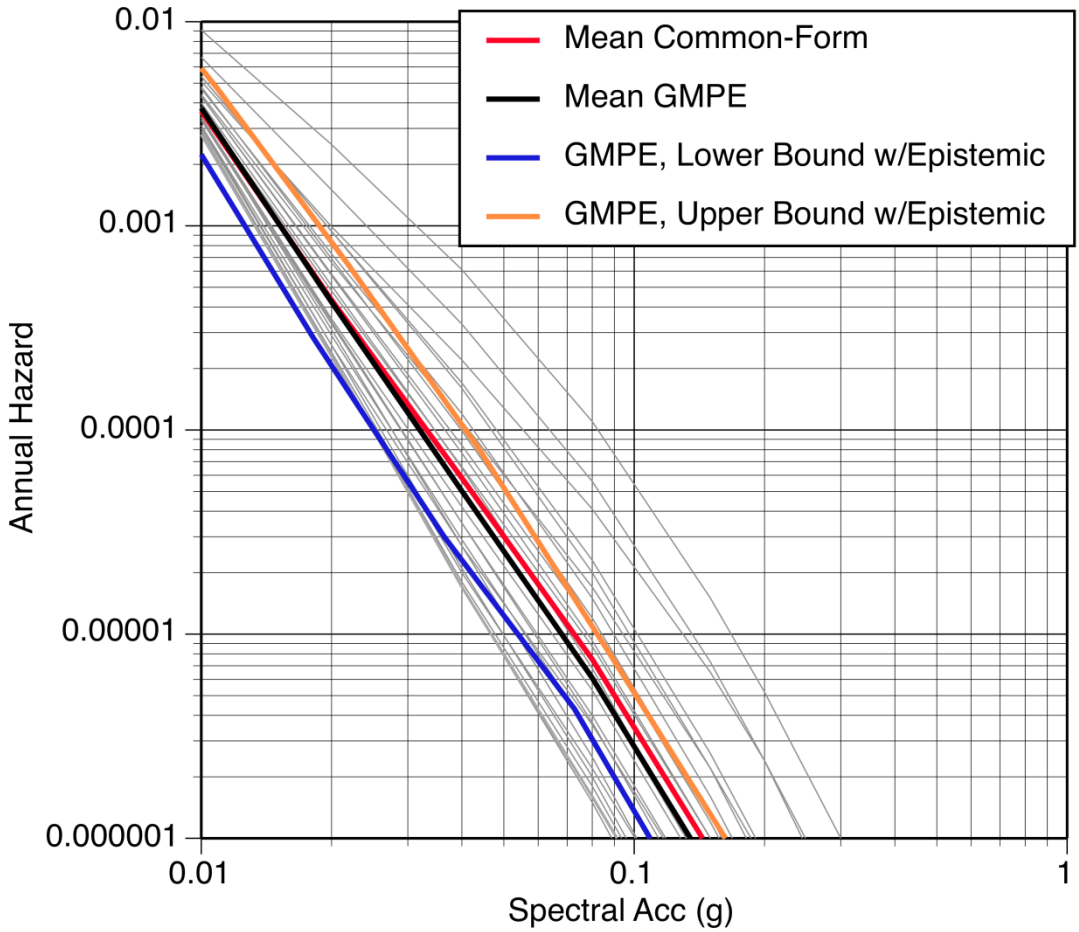

Figure 9.1-19b: Comparison of the hazard for PSA at T = 2.0 sec using the representative suite of common-form models (grey lines), the weighted mean common-form model (red line), mean from the six candidate GMPE models (black line), and the lower (blue line) and upper (orange line) bounds of the six candidate GMPE models with the additional epistemic uncertainty (2 sigma level).

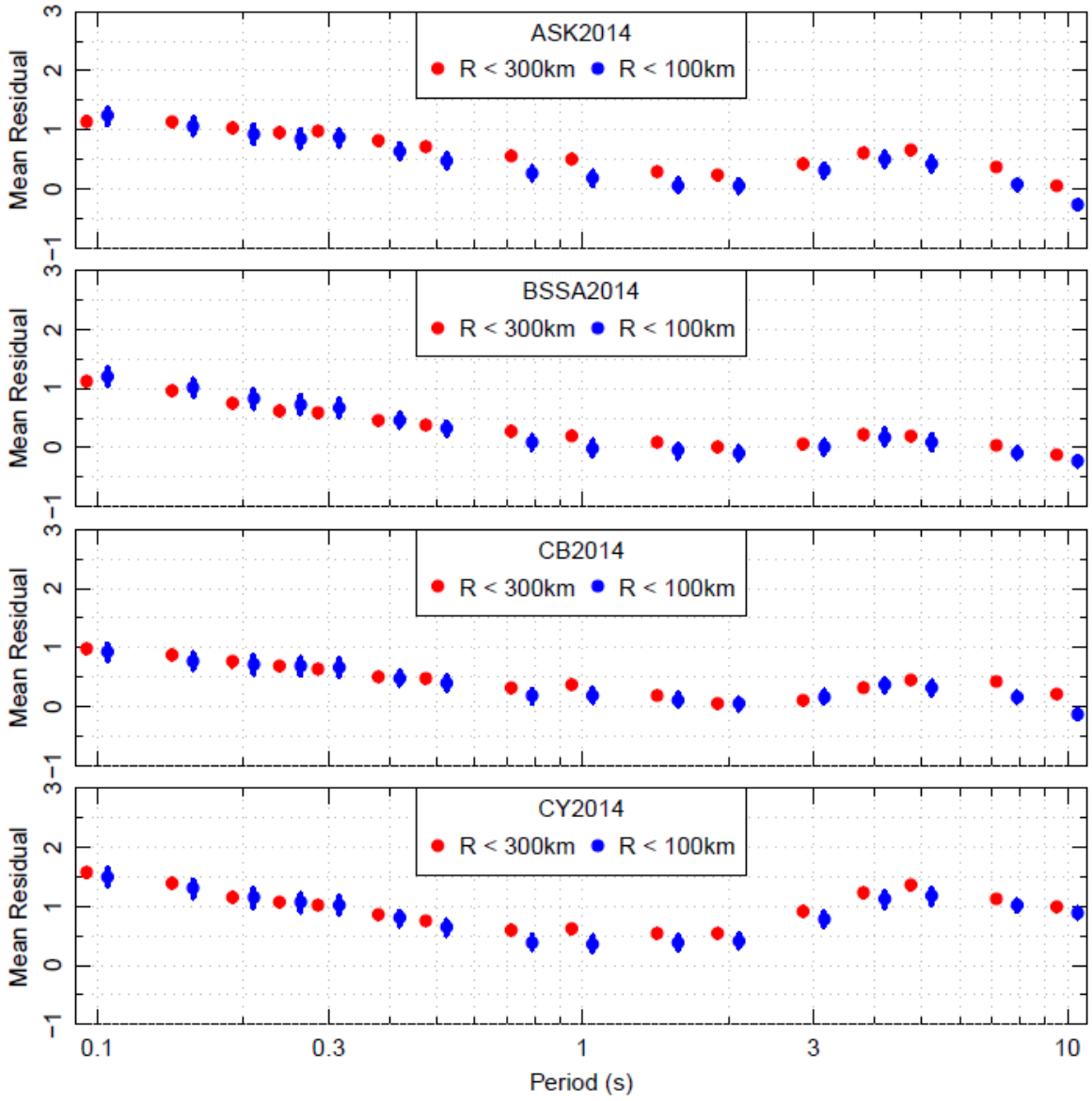

Figure 9.1-20: Mean total residuals for the Fukushima-Hamadori data computed using the NGA-West2 GMPEs of ASK14, BSSA14, CB14, and CY14.

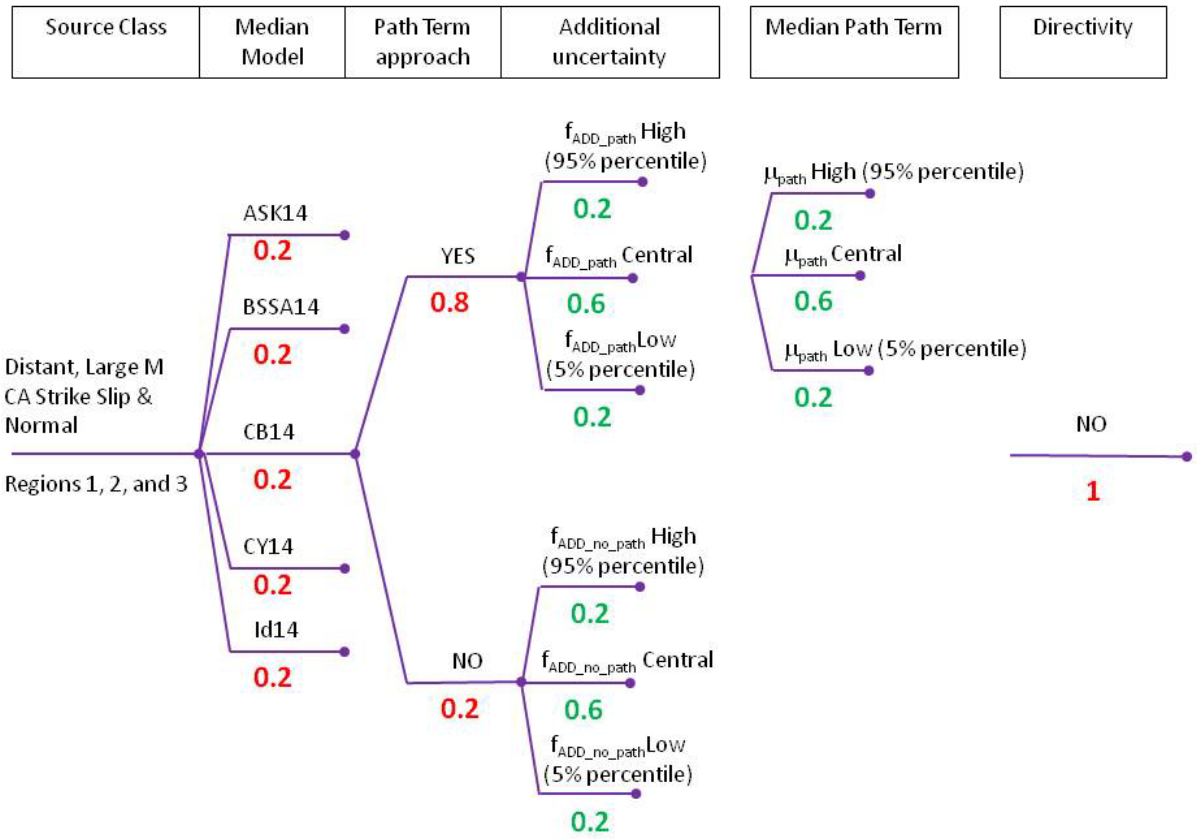

Figure 9.2-1: Logic Tree scheme for the median ground motion at PVNGS from sources in Regions 1, 2, and 3. The weights associated to the TI Team's subjective evaluations are in red, whereas weights associated to statistical sampling are in green

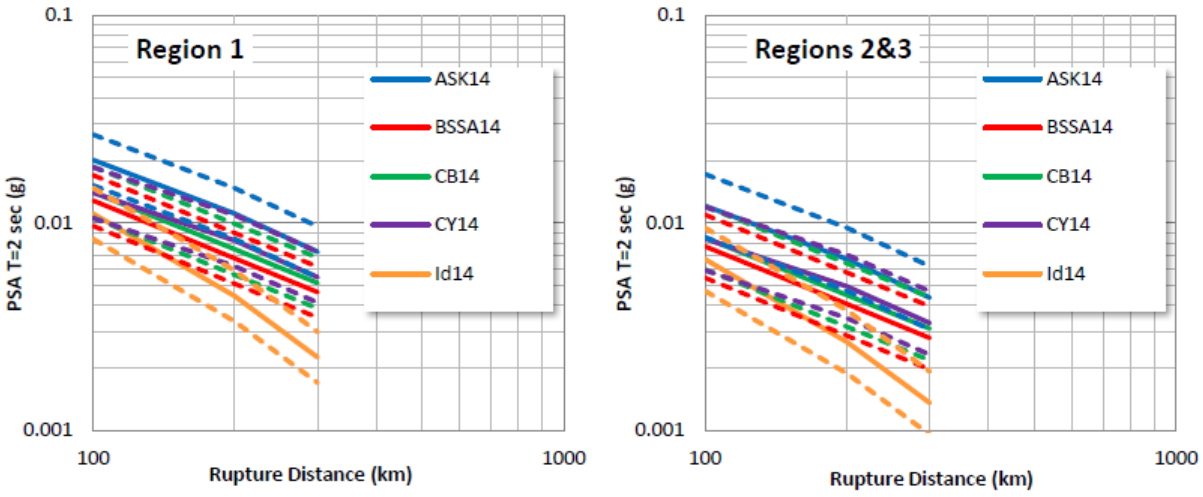

Figure 9.2-2: Ranges of ground motions for distances between 100 and 300 km, resulting from applying the path terms to the median PSA (T = 2 sec) from the NGA-West2 models for an **M**7.5 event with strike-slip style of faulting. Left panel: distance scaling for the median ground motions for events originated in Region 1. Right panel: distance scaling for the median ground motions for events originated in Regions 2&3.Central branches are shown as solid lines, while high and low branches are shown as dotted lines.

10 τ MODEL LOGIC TREE FOR BOTH DCPP AND PVNGS

This Chapter presents the τ model logic tree that applies to both DCPP and PVNGS sites based on the τ models that were developed in Section 7.2.3 and the uncertainty in the τ model described in Section 7.2.4. This chapter also addresses the technical justifications for the weights associated to the alternative branches in the logic tree. As described in Section 7.6, the logic tree for τ is combined with the corresponding logic tree for ϕ_{SS} to develop a single logic tree for total sigma σ_{SS} to reduce the total number of models for the hazard calculation.

10.1 τ Model Logic Tree

Figure 10.1-1 shows the logic tree for τ along with the associated weights. The logic tree is very simple with just two nodes: one node for the form of τ model (magnitude dependent or magnitude independent); and one node for the epistemic uncertainty in the estimates of τ .

In Figure 10.1-1, weights associated to the TI Team's subjective evaluations are in red, whereas weights associated to statistical sampling are in green.

10.2 Evaluation of Weights for Magnitude Dependence of τ

The first node addresses the alternative functional forms for the τ model in terms of the magnitude dependence. As part of the evaluation of the need for a magnitude-dependent τ model, the TI team considered the following assessments:

1. The hazard at DCPP is controlled by sources with **M** > 5.5, and the hazard at PVNGS is controlled by sources with **M** > 5.

2. Three magnitude-independent τ models (Akkar et al., 2014a and 2014b; Bindi et al., 2014a and 2014b; and Zhao et al., 2006), were considered. The TI Team judged that the first two models should be rejected because their databases contain a large percentage of recordings from **M** <

5.5 earthquakes, and, because they use magnitude-independent τ, their values of τ would overestimate the τ appropriate for the magnitudes of interest to the hazard assessments at the two sites (**M** > 5). The TI Team also judged that the Zhao et al. (2006) magnitude-independent proponent τ model is applicable because their database is almost entirely composed of recordings from earthquakes with **M** ≥ 5. Although this model is magnitude independent, it can be used in developing the magnitude-dependent τ model because two of the magnitude-dependent τ models had constant τ above **M** > 5.5, so there is little bias by incorporating the Zhao et al. (2006) magnitude-independent τ model.

3. The four NGA-West2 GMPEs that provide τ models (Boore et al., 2014; Campbell and Bozorgnia, 2014; Abrahamson et al., 2014; and Chiou and Youngs, 2014) all use a magnitude-dependent model, with τ decreasing to a constant level as magnitude increases. For the NGA-West2 that provide τ models, the threshold for reaching a constant τ is at **M** = 5.5 for BSSA14 and CB14, **M** = 6.5 for CY14, and **M** = 7 for ASK14.

Of the five candidate τ models, four are magnitude-dependent; however, for two of the four models (BSSA14 and CB14), the magnitude-dependence is only below **M**5.5. The magnitude-independent model of Zhao et al. (2006) is similar to the magnitude-dependent model of the BSSA14 and CB14.

Therefore, only a magnitude-dependent branch is used to simplify the logic tree. A weight of 1.0 is assigned to the magnitude-dependent τ branch.

10.3 Evaluation of Weights for Epistemic Uncertainty of τ

The second node of the logic tree captures the alternative values of parameters in the τ model based on the uncertainty of the estimation of τ. The high and low τ branches of the logic tree are computed using a scaled Chi-square distribution for τ^2 as described in Appendix P. The weights of 0.2, 0.6 and 0.2 are statistically-based weights associated to the low (5^{th}), central (mean), and high (95^{th}) τ branches, respectively. They are computed by discretizing the Chi-square distribution into a three-point distribution that approximates the mean and variance of the full distribution (Appendix P).

The central, high, and low branches represent the mean, 95^{th} and 5^{th} percentile of a scaled Chi-square distribution (this is described in Appendix P). The TI Team central τ model with its uncertainty is shown in Figure 10.3-1.

10.4 References

Abrahamson, N.A., Silva, W.J., and Kamai, R. (2014). Summary of the AKS14 Ground-Motion Relation for Active Crustal Regions, *Earthquake Spectra*, Vol. 30(3), 1025-1055, DOI: 10.1193/070913EQS198M

Akkar, S., Sandikkaya, M.A., and Bommer, J.J. (2014a). Empirical ground-motion models for point- and extended-source crustal earthquake scenarios in Europe and the Middle East, *Bull. Earthquake Eng*., Vol. 12(1), 359-387, DOI: 10.1007/s10518-013-9461-4.

Akkar, S., Sandikkaya, M.A., and Bommer, J.J. (2014b). Erratum to: Empirical ground-motion models for point- and extended-source crustal earthquake scenarios in Europe and the Middle East, *Bull. Earthquake Eng.*, Vol. 12(1), 389-390, DOI: 10.1007/s10518-013-9508-6.

Bindi D., Massa M., Luzi L., Ameri G., Pacor F., Puglia R., and Augliera, P. (2014a). Pan-European Ground-Motion Prediction Equations for the Average Horizontal Component of PGA, PGV, and 5%-Damped PSA at Spectral Periods up to 3.0 s using the RESORCE dataset, *Bull. Earthquake Eng*., Vol. 12, 391-430, DOI: 10.1007/s10518-013-9525-5.

Bindi D., Massa M., Luzi L., Ameri G., Pacor F., Puglia R., and Augliera, P. (2014b). Erratum to: Pan-European Ground-Motion Prediction Equations for the Average Horizontal Component of PGA, PGV, and 5%-Damped PSA at Spectral Periods up to 3.0 s using the RESORCE dataset, *Bull. Earthquake Eng*., Vol. 12, 431-448, DOI: 10.1007/s10518-014-9589-x.

Boore, D.M., Stewart, J.P., Seyhan, E., and Atkinson, G.M. (2014). NGA-West 2 Equations for Predicting PGA, PGV, and 5%-Damped PSA for Shallow Crustal Earthquakes, *Earthquake Spectra*, Vol. 30(3), 1057-1085, DOI: 10.1193/070113EQS184M.

Campbell, K.W., and Bozorgnia, Y. (2014). NGA-West2 Ground Motion Model for the Average Horizontal Components of PGA, PGV, and 5%-Damped Linear Acceleration Response Spectra, *Earthquake Spectra*, Vol. 30(3), 1087-1115, DOI: 10.1193/062913EQS175M

Chiou, B.S.-J., and Youngs, R.R. (2014). Update of the Chiou and Youngs NGA Model for the Average Horizontal Component of Peak Ground Motion and Response Spectra, *Earthquake Spectra*, Vol. 30(3), 1117-1153, DOI: 10.1193/072813EQS219M

Zhao, J.X., Zhang, J., Asano, A., Ohno, Y., Oouchi, T., Takahashi, T., Ogawa, H., Irikura, K., Thio, H.K., Somerville, P.G., Fukushima, Y., and Fukushima, Y. (2006). Attenuation Relations of Strong Ground Motion in Japan Using Site Classification Based on Predominate Period, *Bull. Seism. Soc. Am*., Vol. 96, 898-913.

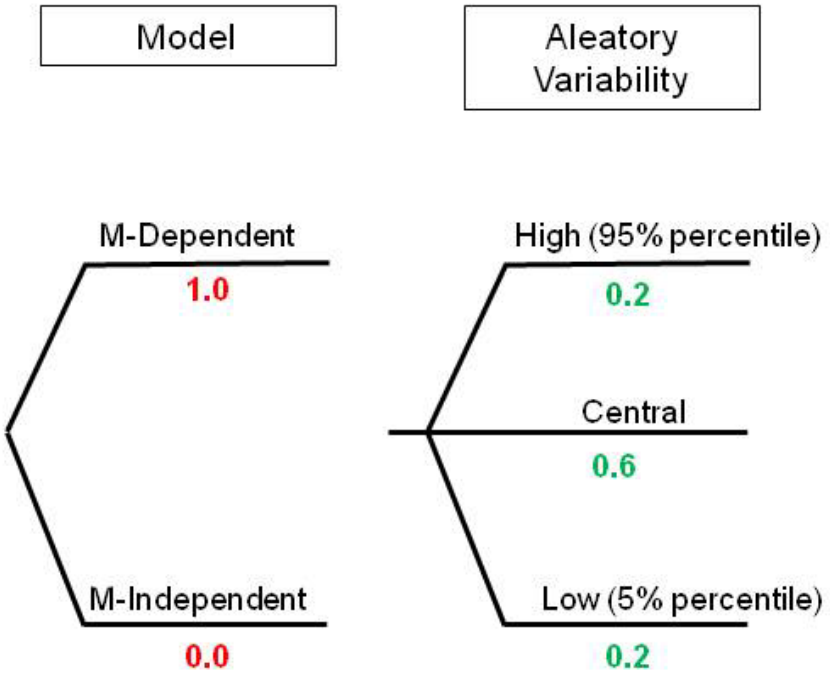

Figure 10.1-1: Logic tree for τ . Weights associated to the TI Team's subjective evaluations are in red, whereas weights associated to statistical sampling are in green.

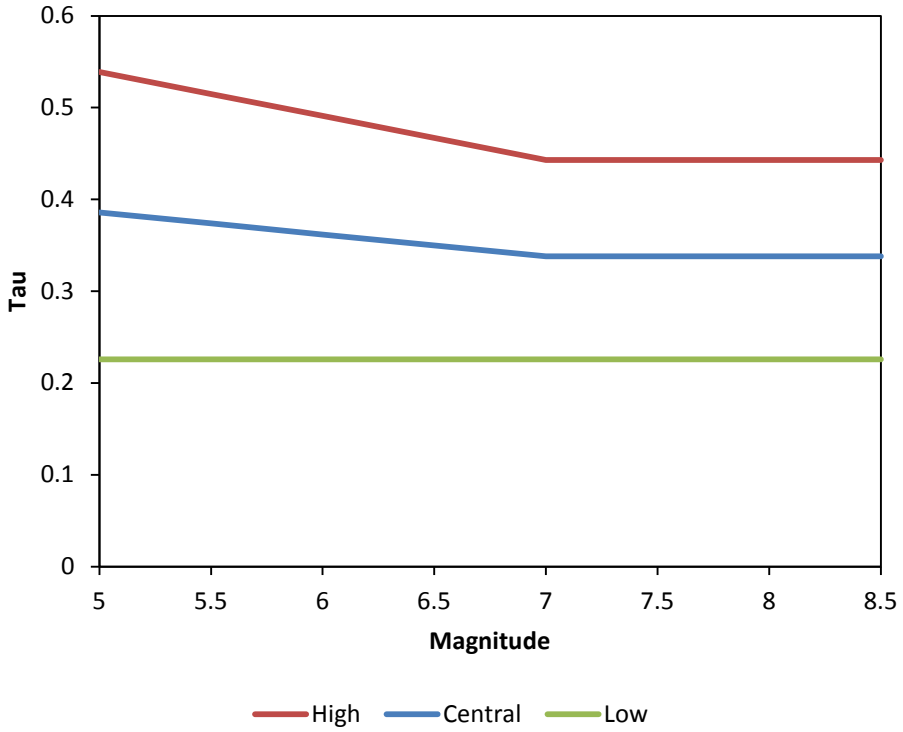

Figure 10.3-1: Magnitude dependence of the τ model (central, low and high branches) at period of 1 second.

11 ϕ MODEL LOGIC TREE: DCPP

11.1 ϕ_{SS} Logic Tree for DCPP

Figure 11.1-1 shows the ϕ_{SS} logic tree for DCPP. There are five nodes in the logic tree. The weights for the branches for the nodes are shown in two colors to distinguish between subjective evaluations by the TI Team (shown in red) and statistical sampling of continuous distributions (shown in green).

The first node captures the alternative datasets used to derive the ϕ_{SS} models. The second node captures the alternative functional forms of ϕ_{SS} models. The third node captures the epistemic uncertainty in the estimated value of ϕ_{SS} for a single site. The fourth node is associated to the TI Team's evaluation of the applicability of directivity adjustments for ϕ_{SS}. Finally, the last node is associated with alternative forms of the upper tail for the single-site within-event residual distribution. The description of the datasets used to develop the ϕ_{SS} models is provided in Section 5.4. Details of the ϕ_{SS} model derivation for DCPP are provided in Sections 7.3.2 and 7.3.3. The notation of Al Atik et al. (2010) is followed.

11.2 Evaluation of Weights for Alternative Datasets for ϕ_{SS}

As mentioned in Section 5.4.1 and 5.4.3, two datasets of single-site within-event residuals with magnitude greater than or equal to 5.0 and distance less than 50 km were used to evaluate ϕ_{SS} for DCPP: a global dataset consisting of the NGA-West2 data (datasets for ASK14 [Abrahamson et al., 2014], BSSA14 [Boore et al., 2014], CB14 [Campbell and Bozorgnia, 2014] and CY14 [Chiou and Youngs, 2014]) supplemented by the Taiwanese data from Lin et al. (2011) and a California only subset of the NGA-West2 data.

The global dataset is dominated by the recordings from Taiwan, which comprises 50% to 70% of the recordings depending on the subset used by the GMPE developer. The California set comprises 30% to 40% of the recordings of the global data set. A limitation of the Taiwan data is that the residual analysis

by Lin et al. (2011) was only conducted for five spectral periods (PGA, 0.1, 0.5, 1.0, and 3.0 sec), hence, requiring interpolation and extrapolation for the rest of the spectral periods for this project. Such limitation does not exist for the California set.

Although the California data set is about a third of the total number of recordings in the global data set, it still has enough data to constraint the ϕ_{SS} : there are 342 to 372 recordings from earthquakes with **M** > 5.5 and R_{RUP} < 50 km. The TI Team judged the California data set to be more applicable to DCPP because it is from the same region as the NPP. The California data set was assigned a weight of 0.67 compared to 0.33 for the global dataset.

11.3 Evaluation of Weights for Magnitude-Dependence of ϕ_{SS}

For the California data set, two alternative magnitude-dependent ϕ_{SS} models were developed by the TI Team ($\phi_{SS-CA-1}$ and $\phi_{SS-CA-2}$ models, described in Section 7.3.3). To evaluate the relative merits of the two $\phi_{SS-CA-1}$ and $\phi_{SS-CA-2}$ models, the first with a magnitude-break at **M**7 and the second with a magnitude-break at **M**5.5, the TI Team considered the magnitude-dependence in ϕ given in the NGA-West2 models. All four NGA-West2 models that separate the residuals into within-event and between-event terms have a magnitude-dependent ϕ for **M** greater than 3, but only two of them (ASK14 and CY14) have a magnitude-dependent ϕ for **M** > 5.5, whereas two models (CB14 and BSSA14) have a constant ϕ for **M** > 5.5. Based on half of the NGA-West2 models using a break at **M**5.5 and half at **M**7, the TI Team assigned equal weights to the two alternative magnitude-dependent branches for the California data set.

For the global data set, a magnitude-dependence in the ϕ_{SS} is not seen (Appendix K, Section 7.3.2, and figures therein). Therefore, the magnitude-independent branch ($\phi_{SS-GLOBAL-R50}$ model, described in Section 7.3.2.1) is given full weight (weight = 1.0).

11.4 Evaluation of Weights for Epistemic Uncertainty in Site-specific ϕ_{SS}

For each alternative data set and model combination, the ϕ_{SS} is an average value for the full data set. At an individual site, the value of ϕ_{SS} may vary from the average. The site-specific value is denoted $\phi_{SS,S}$. The epistemic uncertainty in the site-specific $\phi_{SS,S}$ is captured in the third branch of the logic

tree. It represents the site-to-site differences in the $\phi_{SS,S}$ and not the standard error of the average ϕ_{SS} of the data set. The site-specific value of ϕ_{SS} at DCPP is denoted DCPP ϕ_{SS}. The central branch of the DCPP ϕ_{SS} is based on the average for the data set, and the high and low branches account for the site-to-site variation about this average.

The evaluation of the epistemic uncertainty in the DCPP ϕ_{SS} estimate, for a given data set, is based on a Chi-square distribution of $\phi^2_{SS,S}$, as described in Appendix P. The statistical evaluation of the standard error of $\phi_{SS,S}$, given in Section 7.3.1, showed that the estimated standard error is biased due to small number of observations per site. The bias-corrected coefficient of variation (CV) of $\phi_{SS,S}$ is 0.12. Using this CV value, high and low epistemic uncertainty branches were computed corresponding to the 5th and 95th percentile of $\phi_{SS,S}$, respectively.

Statistical weights of 0.6, 0.2, and 0.2 are assigned to the central, high, and low branches, respectively to approximate the mean and variance of the underlying distribution.

11.5 Evaluation of Weights for Directivity Adjustment to the ϕ_{SS}

The directivity factors described in Section 6.5.1 have two parts: and adjustment to the median ln(PSA) and an adjustment to the within-event standard deviation. These two terms are correlated so they both need to be in the model. That is, the adjustment to the within-event standard deviation can only be used if the directivity adjustments are used for the median ground-motion model. For DCPP, the directivity adjustment for the median model is given zero weight (Section 8.4). Therefore, to be consistent with the application of directivity factors for the median model, this branch is given zero weight (weight = 0.0).

11.6 Evaluation of Weights for the Aleatory Distribution Form for ϕ_{SS}

An evaluation of the appropriate form to represent the extreme tails of the aleatory distribution was presented in Workshop #3 (see Appendix G). Figure 11.6-1 shows an analysis conducted on the within-event residuals for the ASK14 model. The residuals are shown in terms of a quantile plot (Q-Q plot) which compares the observed data density at various values of epsilon (normalized residual, e.g. residual divided by the standard deviation) on the vertical axis with what is expected from the assumed distribution, in this case normal, on the horizontal axis. A Q-Q plot maps the normal distribution into a straight line, such that, if the data follow a normal distribution, they would fit along the 1:1 line. The

dashed lines show a 95% confidence interval on the normal distribution residuals given the size of the data sample. A departure of the residuals from these lines indicates departure from a normal distribution. The TI Team used the 95% confidence intervals as a guide for the significance of the departure from normality, and not as a formal statistical test. In particular, the TI Team's evaluation considered multiple points falling outside of the 95% confidence interval as an indication that there was a significant deviation from normality.

The deviation from normality, in this case, is described as "heavy tailed" because there is a higher probability of extremes (at both high and low epsilon) than predicted by the normal distribution. Heavy tails are observed in the ASK14 data for a wide range of oscillator periods at values of epsilon higher than 2. The same deviation from normality is observed for site- and event-corrected residuals (e.g., for single-station sigma) as shown in Figure 11.6-2. Similar results are seen when magnitudes are restricted to $\mathbf{M} \geq 5.5$, so this is not just a small magnitude issue. Similar deviations from normality are not seen in the between-event residuals.

Similar analyses to those presented in Figures 11.6-1 and 11.6-2 are conducted on the CY14 residuals. The results of these analyses are similar to the results for the ASK14 data. The Q-Q plots showed that the observed distribution of epsilon fall outside the 95^{th} percentile confidence limits, indicating a significant deviation from a normal distribution. The deviation from normality is observed at nearly all periods for epsilons greater than 2.5 for the within-event term. On the other hand, the normality assumption holds for between-event residuals with the exception of very long periods and an epsilon of 3.5 (the highest epsilon with sufficient number of events to test). In addition, the Anderson-Darling test for normality (Anderson and Darling, 1952) was applied to the CY14 residuals. The test results indicated a statistically significant departure from normality (p-value that the non-normality occurred by chance < 5%) for the CY14 within-event residuals. The same tests did not find a statistically significant departure from normality for the between-event residuals. Coppersmith et al. (2014) also report evidence of heavy-tailed distributions in analyses of ground-motion data from shallow crustal earthquakes in Japan and in a global database of subduction zone earthquake ground motions.

The approach selected to represent a heavy tailed aleatory distribution was to use a mixture model. In general, a mixture model is a composite distribution computed by summing multiple normal distributions with different means and standard deviations. For the SWUS GMC application, the CY14 residuals were analyzed using the statistical package MIXTOOLS (Benaglia et al., 2009). The results indicated that the residuals were adequately fit by an equal mixture of two normal distributions with means of zero (centered on the same PSA median as from GMPEs) and standard deviations of 0.8 and 1.2 times the standard deviation of the within-event residuals from the GMPEs. The same mixture model was found to provide an adequate fit to the ASK14 residuals: tests of this mixture using the ASK14 data produced Q-Q plots that did not show a significant deviation from the mixture model, indicating that the observed heavy tails are captured.

While there are alternative ways of capturing heavy-tailed distributions, this form of the mixture model is attractive because the only parameters that need to be calibrated are the weights and the scale factors for the standard deviations used for the two normal distributions. As indicated above, the mixture model parameters were calibrated using the ASK14 and CY14 residuals. The selected model assigns 50% weight to each of the two distributions with standard deviation scale factors of 1.2 and 0.8. Figure 11.6-3 shows the resulting fit of the tails of the distribution using this mixture model. Using the mixture model adequately captures the heavy tails for the large epsilons. For very small epsilons (≤-3) there is still a heavy tail but this range of epsilons does not contribute to the seismic hazard. Similar results were obtained for the BSSA14, CB14, and CY14 within-event residuals. Figures 11.6-4, 11.6-5 and 11.6-6 show the comparisons of Q-Q plots for the traditional normal distribution and the proposed mixture model for BSSA14, CB14, and CY14, respectively, for PSA at 5 Hz. All three sets of residuals show fat tails and are consistent with the proposed mixture model.

For this mixture model, the conditional probability of exceeding a ground-motion level Z is given by:

$$P(Z > z) = w_{Mix1}\left\{1 - \Phi\frac{(z-\mu)}{\sigma_{Mix1}}\right\} + w_{Mix2}\left\{1 - \Phi\frac{(z-\mu)}{\sigma_{Mix2}}\right\} \qquad \text{(Eq. 11-1)}$$

where Φ is a standard normal cumulative distribution function, w_{Mix1} and w_{Mix2} are the weights in this case, (0.5 and 0.5), and σ_{Mix1} and σ_{Mix2} are the standard deviations obtained by combining 1.2ϕ and 0.8ϕ with the values of τ derived in Section 7.2. The value of ϕ used is either ϕ_{SS} or ϕ_{SP-R} derived above, depending on the application.

In the GMC logic tree, the TI Team assigned the mixture model a weight of 0.8 and the traditional normal distribution a weight of 0.2. The mixture model is strongly favored because the most of the data sets tested showed statistically significant evidence of heavy tails in the within-event residuals and improved fits of the residuals were found with very similar mixtures. While the TI Team strongly favors the mixture model, this is a new approach and the TI Team maintained the traditional normal distribution model with small weight because the traditional normal distribution is the most widely used model in current practice.

11.7 References

Abrahamson, N.A., Silva, W.J., and Kamai, R. (2014). Summary of the AKS14 Ground-Motion Relation for Active Crustal Regions, *Earthquake Spectra*, Vol. 30(3), 1025-1055, DOI: 10.1193/070913EQS198M

Al Atik, L., Abrahamson, N., Bommer, J., Scherbaum, F., Cotton, F., Kuehn, N. (2010). The variability of ground-motion prediction models and its components, *Seismol. Res. Letts*, Vol. 81(5), 794-801.

Anderson, T.W., D.A. Darling. (1952). Asymptotic theory of certain goodness-of-fit criteria based on stochastic processes, *Ann. Math. Statistics,* Vol. 23, 193–212.

Benaglia, T., D. Chauveau, D.R. Hunter, and D.S. Young. (2009). Mixtools: An R package for analyzing finite mixture models, *J. of Statistical Software*, Vol. 32(6), http://www.jstatsoft.org/

Boore, D.M., Stewart, J.P., Seyhan, E., and Atkinson, G.M. (2014). NGA-West 2 Equations for Predicting PGA, PGV, and 5%-Damped PSA for Shallow Crustal Earthquakes, *Earthquake Spectra*, Vol. 30(3), 1057-1085, DOI: 10.1193/070113EQS184M

Campbell, K.W., and Bozorgnia, Y. (2014). NGA-West2 Ground Motion Model for the Average Horizontal Components of PGA, PGV, and 5%-Damped Linear Acceleration Response Spectra, *Earthquake Spectra*, Vol. 30(3), 1087-1115, DOI: 10.1193/062913EQS175M

Chiou, B.S-J., and Youngs, R.R. (2014). Update of the Chiou and Youngs NGA Model for the Average Horizontal Component of Peak Ground Motion and Response Spectra, *Earthquake Spectra*, Vol. 30(3), 1117-1153, DOI: 10.1193/072813EQS219M

Coppersmith, K.J., Bommer, J., Hanson, K., Coppersmith, R., Unruh, J.R., Wolf, L., Youngs, R., Al Atik, L., Rodriguez-Marek, A., Toro, G., and Montaldo-Falero, V. (2014). Hanford Sitewide Probabilistic Seismic Hazard Analysis, *PNNL-23361*, Pacific Northwest National Laboratory, Richland Washington.

Dawood, H.M., Rodriguez-Marek, A., Bayless, J., Goulet, C., and Thompson E. (2014). The KiK-net database processed using an automated ground motion processing protocol. Available at https://nees.org/resources/7849.

Lin, P.-S., Chiou, B., Abrahamson, N., Walling, M., Lee, C.-T., and Cheng, C.-T. (2011). Repeatable source, site, and path effects on the standard deviation for empirical ground-motion prediction models, *Bull. Seism. Soc. Am*., Vol. 101(5), 2281-2295, DOI: 10.1785/012009031.

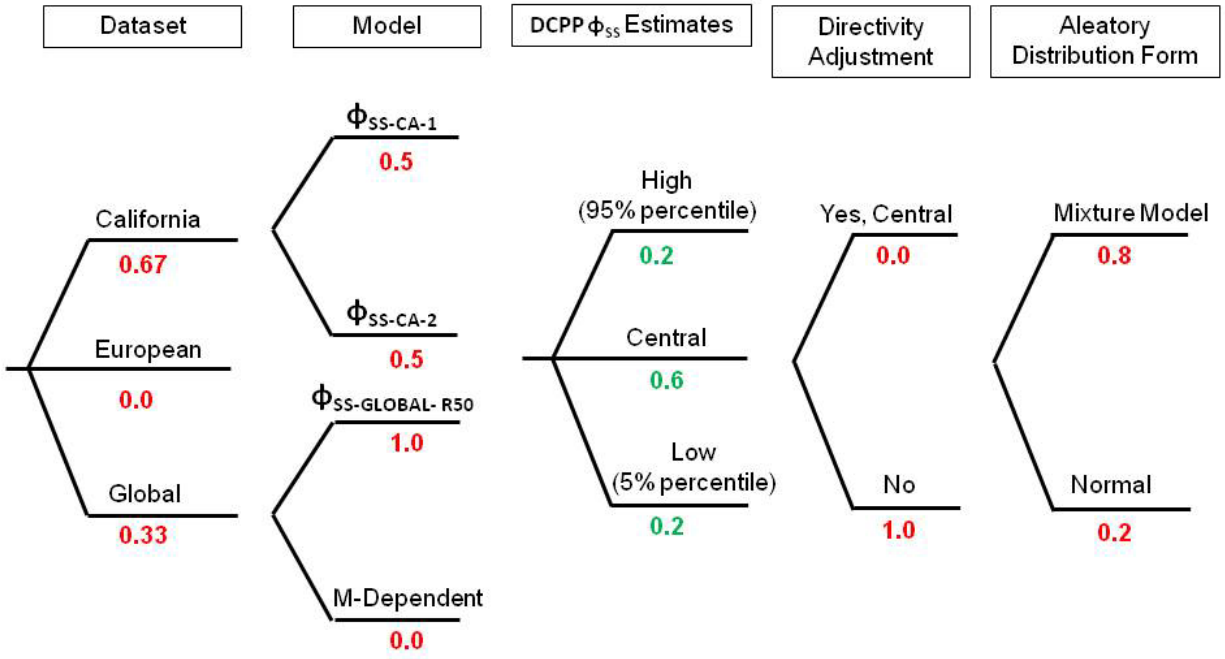

Figure 11.1-1: DCPP ϕ_{SS} Logic Tree. Weights associated to the TI Team's subjective evaluations are in red, whereas weights associated to statistical sampling are in green.

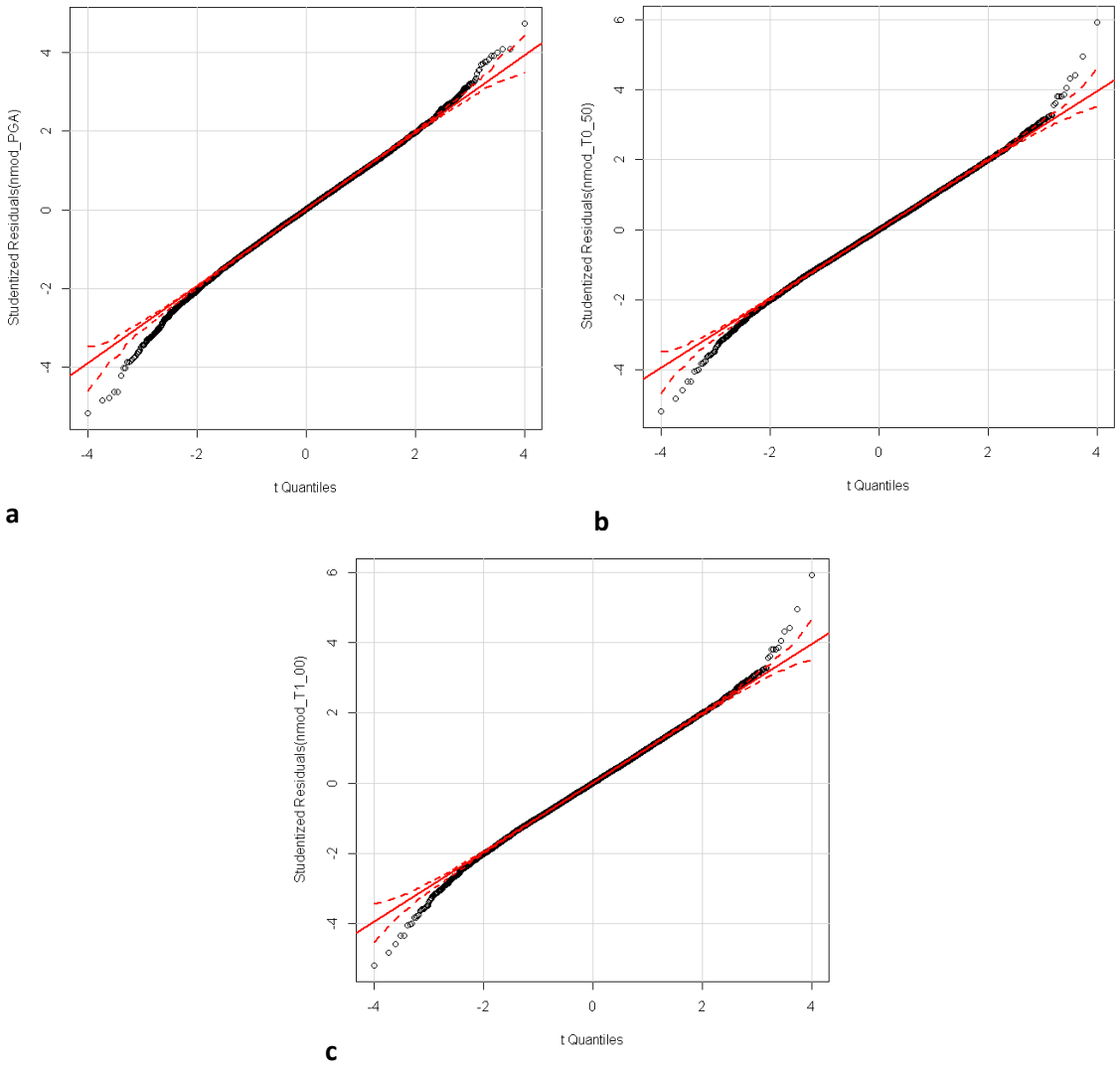

Figure 11.6-1: Q-Q plots for ASK14 within-event normalized residuals for **M** ≥ 5. a) PGA, b) T = 0.5 sec, c) T = 1 sec. The solid red straight line maps the normal distribution if the data follow a normal distribution, and the dashed red lines show a 95% confidence interval on the normal distribution residuals given the size of the data sample.

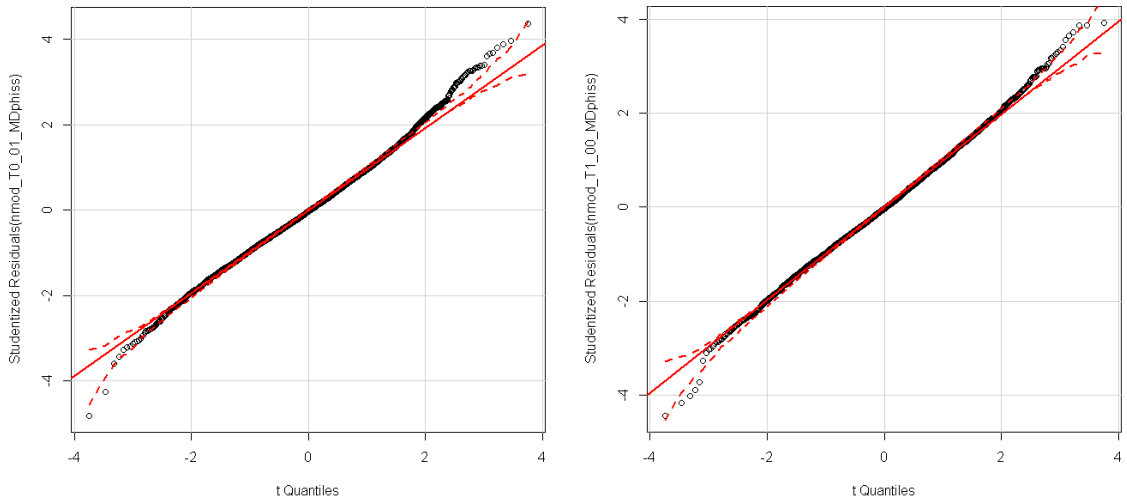

Figure 11.6-2: Q-Q plots for normalized site- and event-corrected within-event residuals for the ASK14 database for two periods (PGA in the left panel, and T = 1 sec in the right panel). The solid red straight line maps the normal distribution if the data follow a normal distribution, and the dashed red lines show a 95% confidence interval on the normal distribution residuals given the size of the data sample.

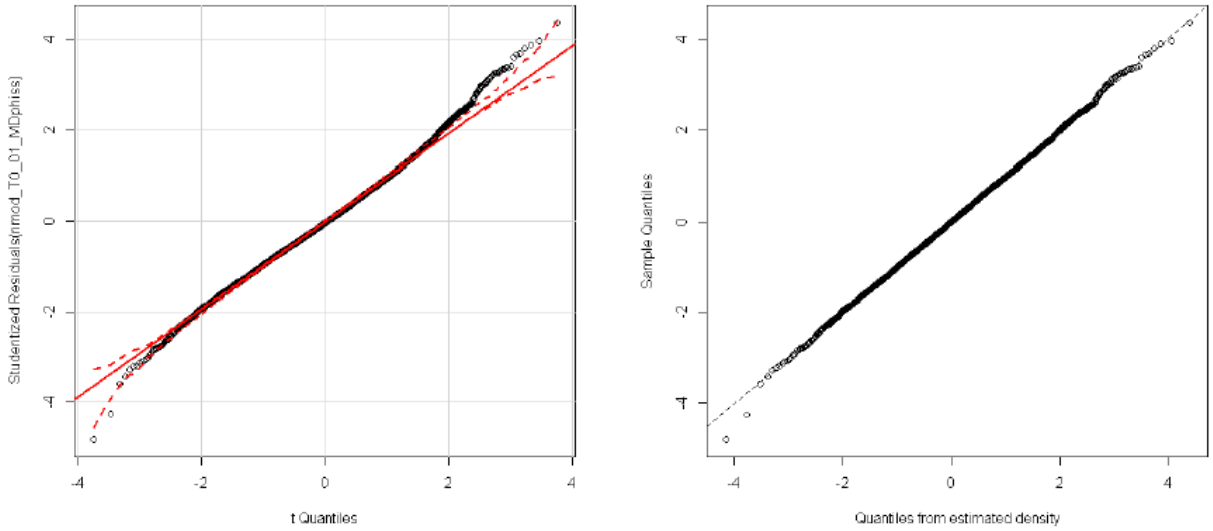

Figure 11.6-3: The plot on the left shows the event- and site-corrected within-event residuals of the ASK14 relationship using a normal distribution. The plot on the right shows the same residuals fitted to a mixture model that uses two distributions with sigma ratios of 1.2 and 0.8 with 50% weight to each distribution.

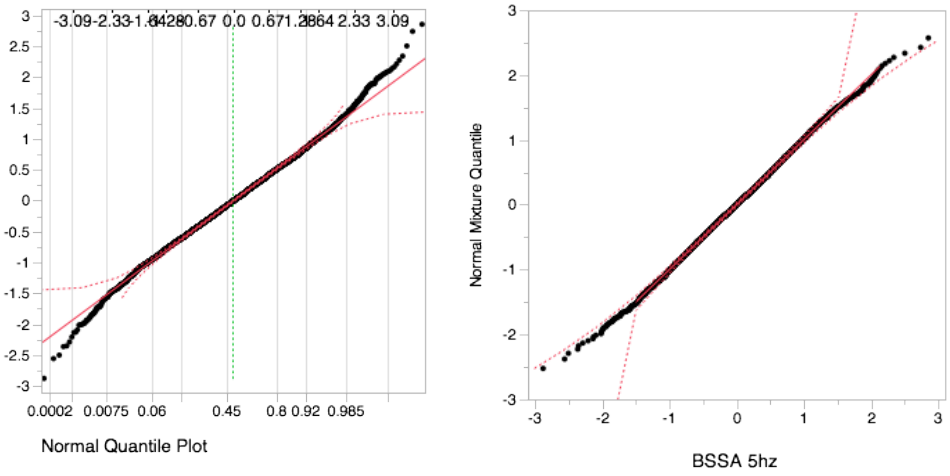

Figure 11.6-4: The plot on the left shows the 5 Hz within-event residuals of the BSSA14 relationship using a normal distribution. The plot on the right shows the same residuals fitted to a mixture model that uses two distributions with sigma ratios of 1.2 and 0.8 with 50% weight to each distribution.

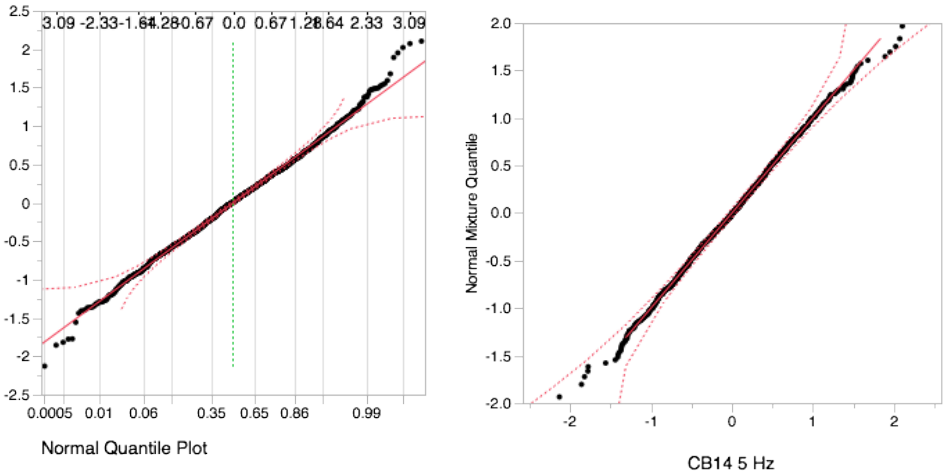

Figure 11.6-5: The plot on the left shows the 5 Hz within-event residuals of the CB14 relationship using a normal distribution. The plot on the right shows the same residuals fitted to a mixture model that uses two distributions with sigma ratios of 1.2 and 0.8 with 50% weight to each distribution.

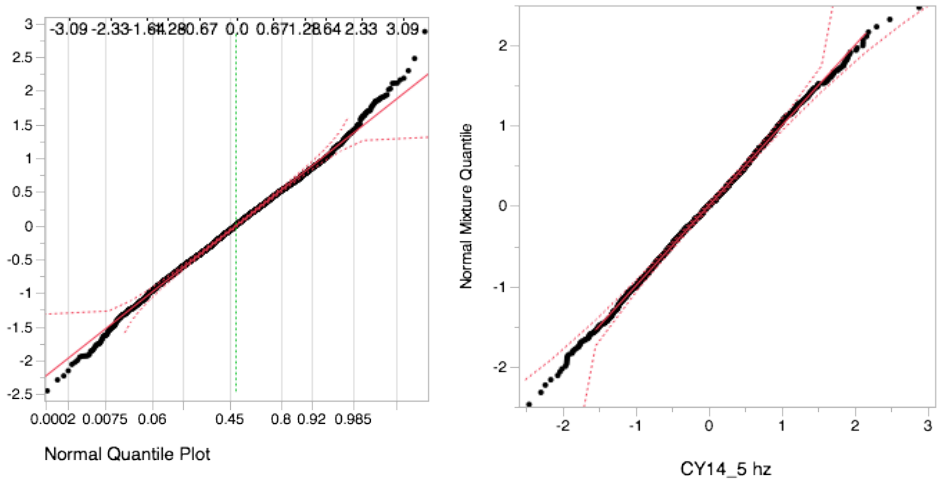

Figure 11.6-6: The plot on the left shows the 5 Hz within-event residuals of the CY14 relationship using a normal distribution. The plot on the right shows the same residuals fitted to a mixture model that uses two distributions with sigma ratios of 1.2 and 0.8 with 50% weight to each distribution.

12 ϕ MODELS LOGIC TREE: PVNGS

Two logic trees were constructed for PVNGS conditioned on the source location: (1) a ϕ_{SS} and a ϕ_{SP-R} logic tree for sources located in Regions 1, and combined Regions 2&3 (distant California and Mexico sources) of Figure 6.6.1-1; and (2) a ϕ_{SS} logic tree for sources outside Regions 1, and 2&3 (Greater Arizona sources).

The use of ϕ_{SP-R} is correlated with the path adjustments to the median prediction of GMPEs as discussed in Section 6.6. That is, ϕ_{SP-R} can only be used if the median path effects, including the epistemic uncertainty in the path effects, are used for the median ground-motion model.

The use of two different logic trees for the ϕ models for PVNGS is motivated by the availability of recordings from distant California earthquakes recorded at a group of sites around PVNGS, which allows estimation of the repeatable similar path-to-region effects which can be removed from the aleatory ground-motion variability. In addition, these two sources have different controlling distances (< 50 km for the Greater Arizona sources and > 200 km for the distant California sources).

12.1 ϕ_{SS} for Greater Arizona Sources

12.1.1 ϕ_{SS} Logic Tree

The ϕ_{SS} logic tree for PVNGS for sources outside Regions 1, and 2&3 is presented in Figure 12.1-1. There are four nodes in the logic tree. The weights for the branches for the nodes are shown in two colors to distinguish between subjective evaluations by the TI Team (shown in red) and statistical sampling of continuous distributions (shown in green).

The first node captures the alternative datasets used to derive the ϕ_{SS} model. The second node is associated to the evaluation of the magnitude–dependence of the ϕ_{SS} models. The third node captures the range of the ϕ_{SS} values applicable to a single site based on sample size. Finally, the last node is associated with alternative forms of the upper tail for the aleatory residual distribution.

12.1.2 Evaluation of Weights for Alternative Databases for ϕ_{SS}

Two groups of datasets are available for evaluating ϕ_{SS} model: a global dataset which combines the NGA-West2 and Taiwanese data in Lin et al. (2011), and the European dataset used in Akkar et al. (2014a, 2014b). Both the global and European data sets were included because they represent different sampling of recordings. The European data set is more heavily weighted to the normal events which are important to the hazard at PVNGS, but this is not a key factor because the aleatory variability has not been seen to depend on the style-of-faulting.

The description of these two alternative datasets was given in Sections 5.4.1 and 5.4.2. Some of the earthquakes in the European dataset (mainly with **M** > 6) are contained in the global dataset so there is some overlap between the two data sets, but the European data set has earthquakes in the **M**5 to **M**6 range that are not included in the NGA-West2 data set.

The evaluation of the two data sets for estimating ϕ_{SS} is primarily based on the relative number of recordings. The global datasets in this magnitude and distance range (**M** ≥ 5, distance ≤ 50 km) with at least three recordings per earthquake ($GLOBAL_{PHISS\_ASK14}$, $GLOBAL_{PHISS\_BSSA14}$, $GLOBAL_{PHISS\_CB14}$, and $GLOBAL_{PHISS\_CY14}$) consists of an average of 1,460 recordings from about 90 earthquakes, depending on the selected subset used by each NGA-West2 developer. The subset of European data for this same magnitude and distance range (EUR_{PHISS}) consists of 223 recordings from 73 earthquakes. So the global data sets have about 6 times as many recordings as the European data.

The global datasets are more abundant in data with magnitude greater than 6.0 than the European data (Figures 5.4.1-1 and 5.4.2-1). The large magnitudes are important for the hazard calculations as shown by the deaggregation in Section 4.2.3 for PVNGS. The European dataset generally has smaller numbers of recordings per earthquake leading to less stable τ estimates which affects the estimates of ϕ and the within-event residuals. Finally, the rupture dimension information used to compute the closest distances in the EUR_{PHISS} dataset are, in general, not as well constrained as for the NGA-west2 data set.

Based on six times more recordings in the global data sets, the global data sets would be given about 2.5 times the weight than for the EUR_{PHISS} data set based on 1/sqrt(N) weighting. Taking the other limitations into account, the TI Team increased the relative weight of 2.5 based on the number of recordings to 3.0, leading to subjective weights of 0.75 and 0.25 for the global and the European datasets, respectively. The ϕ_{SS} values are computed for each of the four global data sets ($GLOBAL_{PHISS\_ASK14}$, $GLOBAL_{PHISS\_BSSA14}$, $GLOBAL_{PHISS\_CB14}$, and $GLOBAL_{PHISS\_CY14}$) and the results from the four subsets are then averaged (using equal weights) to develop the ϕ_{SS} model.

12.1.3 Evaluation of Weights for Magnitude-Dependence of ϕ_{SS}

As discussed in Section 7.3.4, no significant magnitude-dependence of ϕ_{SS} for the European dataset was noticed while evaluating the entire dataset as well as using only data with maximum distance of 50 km. Therefore, no magnitude-dependent ϕ_{SS} model was developed by the TI Team for the European dataset. Therefore, the magnitude-independent ϕ_{SS} model (ϕ_{SS-EUR} model) was selected for the European dataset with weight of 1.0.

As discussed in Section 7.3.2.1, no magnitude-dependence was observed for ϕ_{SS} using the global dataset for magnitude greater than 5.0 and distance less than 50 km. Therefore, only a magnitude-independent ϕ_{SS} model ($\phi_{SS-GLOBAL-R50}$ model) was developed by the TI Team for the global dataset. Therefore, the magnitude-independent $\phi_{SS-GLOBAL-R50}$ model was also selected with weight of 1.0.

12.1.4 Evaluation of Weights for Epistemic Uncertainty of ϕ_{SS}

The discussion of the epistemic uncertainty of ϕ_{SS} is addressed in Section 11.4 for the DCPP ϕ_{SS} models. The same considerations apply in this case. The same bias-corrected CV value of 0.12 for ϕ_{SS} (developed in Section 7.3.1) is used for the PVNGS ϕ_{SS} models. Using this CV value, high and low epistemic uncertainty branches were computed corresponding to the 5th and 95th percentile of $\phi_{SS,S}$. Statistical weights of 0.6, 0.2, and 0.2 are assigned to the central, high, and low branches, respectively, to approximate the mean and variance of the underlying distribution (see Appendix P for the basis for the these weights for a three point distribution).

12.1.5 Evaluation of Weights for the Aleatory Distribution Form for ϕ_{SS}

The discussion of the aleatory distribution form was addressed in Section 11.6 for the DCPP ϕ_{SS} models. The same considerations apply in this case and the same weights are used for the logic tree: the mixture model is assigned a weight of 0.8 and the normal model is assigned a weight of 0.2.

12.2 ϕ_{SS} and $\phi_{SP\text{-}R}$ for Sources in California and Mexico

12.2.1 ϕ_{SS} and $\phi_{SP\text{-}R}$ Logic Tree

The logic tree for PVNGS for sources in California and Mexico (Regions 1, 2, and 3) is shown in Figure 12.2-1 and consists of both ϕ_{SS} and ϕ_{SP-R} models.

The use of ϕ_{SP-R} requires that the median ground-motion estimation includes the path effect adjustments and the epistemic uncertainty in the path effects. In this case, the median and aleatory variability of the path term for Regions 1, 2, and 3 (see Section 6.6) are used to modify the GMPEs. The ϕ_{SS} branch is only used for the median ground-motion branch that does not include path effect adjustments.

The first node captures the alternative datasets used to derive the ϕ_{SS} and ϕ_{SP-R} models. The second node is associated to the evaluation of the magnitude–dependence of the ϕ_{SS} and ϕ_{SP-R} models. The third node captures the range of ϕ_{SS} and ϕ_{SP-R} values applicable to a single site based on the between-model variability of ϕ_{SP-R} and the average standard error of the ϕ_{SP-R} estimates for the individual GMPEs (Section 7.4.2). Finally, the last node is associated with alternative forms of the upper tail for the aleatory residual distribution. Description of the datasets used to build the central branches and their associate epistemic uncertainties is provided in Sections 5.4.4 and 5.4.5 for the ϕ_{SS} and ϕ_{SP-R} models, respectively. Details on the ϕ_{SS} model derivation for PVNGS ($\phi_{SS-GLOBAL-LD}$ model) are provided in Section 7.3.2.2. Details on the ϕ_{SP-R} model derivation for PVNGS ($\phi_{SP-R123}$ models for Region1 and Regions 2&3) are provided in Section 7.4.

12.2.2 Evaluation of Weights for Alternative Datasets for ϕ_{SS} and $\phi_{SP\text{-}R}$

For the no path-term median model, three alternative data sets are used for the development of the $\phi_{SS-GLOBAL-LD}$ model based on the single-site within-event residuals of global datasets (NGA-W2$_{\text{LD-PHISS-ASK14}}$, NGA-W2$_{\text{LD-PHISS-BSSA14}}$, and NGA-W2$_{\text{LD-PHISS-CY14}}$). The datasets contain the single-site within-event residuals with magnitude larger than 5.5 and distance range of 200 to 400 kilometers. Within this magnitude and distance range, the three global datasets contain 4-23 earthquakes and 264-415 records depending on the NGA-West2 developer subset (see Table 5.4.4-1). About half of the data are from Japan and half from California. The ϕ_{SS} values are computed for each of the three NGA-West2 data sets and the results from the three subsets are then averaged (using equal weights) to develop the

$\phi_{SS-GLOBAL-LD}$ model. The European data set is not used for the long distance ($\phi_{SS-GLOBAL-LD}$) model because it only includes data up to 200 km.

For the median model with a path term, the magnitude-independent $\phi_{SP-R123}$ model is based on the PEER Arizona dataset consisting of earthquakes from California and Mexico that have been recorded at the 9 stations in the vicinity of PVNGS (PEER-$AZ_{PATH\text{-}ASK14}$, PEER-$AZ_{PATH\text{-}BSSA14}$, PEER-$AZ_{PATH\text{-}CB14}$, and PEER-$AZ_{PATH\text{-}CY14}$). This is the only data set available for this evaluation. These four data sets contain up to 49 records from 11 earthquakes with rupture distances from 200 to 500 km, depending on which earthquakes were selected by each NGA-West2 developer (the event terms from the NGA-Developer based on the recordings in the NGA-West2 data set are used). The single-site, within-event residuals corrected to remove systematic source-region to site-region bias for each of the three regions: Region 1 (4 earthquakes), Region 2 (3 earthquakes), and Region 3 (3 earthquakes). The ϕ_{SP-R} values are then computed for the residuals for each of the four NGA-West2 data sets and the results from the four subsets are then averaged (using equal weights) to develop the $\phi_{SP-R123}$ model.

12.2.3 Evaluation of Weights for Magnitude-dependence of ϕ_{SS} and $\phi_{SP\text{-}R}$

As shown in Sections 7.3.2 and 7.3.4, there is no magnitude dependence seen for the global dataset or for the European dataset for **M** > 5. Therefore, only magnitude-independent ϕ_{SS} models were developed.

For the ϕ_{SP-R} model, the main contribution to the hazard is from large magnitude earthquakes (**M** > 7.5 shown in Figure 4.2-5). The global data set used for developing the ϕ_{SP-R} model is for **M** > 5.5. As no magnitude dependence was seen in the global ϕ_{SS} model, only a magnitude-independent model is developed for the ϕ_{SP-R}.

12.2.4 Evaluation of Weights for Epistemic Uncertainty of ϕ_{SS} and $\phi_{SP\text{-}R}$

The discussion of the epistemic uncertainty of ϕ_{SS} is addressed in Section 11.4 for the DCPP ϕ_{SS} models. The same considerations apply in this case. The same biased-corrected CV value of 0.12 for ϕ_{SS} (developed in Section 7.2.4) is used for the PVNGS ϕ_{SS} models. Using this CV value, high and low epistemic uncertainty branches were computed corresponding to the 5th and 95th percentile of $\phi_{SS,S}$. Statistical weights of 0.6, 0.2, and 0.2 are assigned to the central, high, and low branches, respectively, to approximate the mean and variance of the underlying distribution.

For ϕ_{SP-R}, the bias-corrected CV value was estimated to be 0.17 in Section 7.4.2. Using this CV value, high and low epistemic uncertainty branches were computed corresponding to the 5th and 95th percentile of ϕ_{SP-R}. Statistical weights of 0.6, 0.2, and 0.2 are assigned to the central (mean), high, and low branches, respectively, to approximate the mean and variance of the underlying distribution (see Appendix P for the basis for the these weights for a three point distribution).

12.2.5 Evaluation of Weights for the Aleatory Distribution Form for ϕ_{SS} and ϕ_{SP-R}

The discussion of the aleatory distribution form was addressed in Section 11.6. The same considerations apply in this case. The heavy tails were observed for a wide range of magnitudes and distances. There is no reason to expect that this feature would not be applicable to large distance data. The TI Team judged that the heavy tail model is applicable to the large magnitude earthquakes from California and Mexico. Therefore, the same weights of 0.8 and 0.2 are assigned for the mixture and the normal model, respectively. As discussed in Section 11.6, the traditional normal distribution was maintained with a low weight of 0.2 because this model is still widely used in PSHA applications.

12.3 References

Akkar, S., Sandikkaya, M.A., and Bommer, J.J. (2014a). Empirical ground-motion models for point- and extended-source crustal earthquake scenarios in Europe and the Middle East, *Bull. Earthquake Eng*., Vol. 12(1), 359-387, DOI: 10.1007/s10518-013-9461-4.

Akkar, S., Sandikkaya, M.A., and Bommer, J.J. (2014b). Erratum to: Empirical ground-motion models for point- and extended-source crustal earthquake scenarios in Europe and the Middle East, *Bull. Earthquake Eng.*, Vol. 12(1), 389-390, DOI: 10.1007/s10518-013-9508-6.

Abrahamson, N.A., Silva, W.J., and Kamai, R. (2014). Summary of the AKS14 Ground-Motion Relation for Active Crustal Regions, *Earthquake Spectra*, Vol. 30(3), 1025-1055, DOI: 10.1193/070913EQS198M

Lin, P.-S., Chiou, B., Abrahamson, N., Walling, M., Lee, C.-T., and Cheng, C.-T. (2011). Repeatable source, site, and path effects on the standard deviation for empirical ground-motion prediction models, *Bull. Seismol. Soc. Am.,* Vol. 101(5), 2281-2295, DOI: 10.1785/012009031.

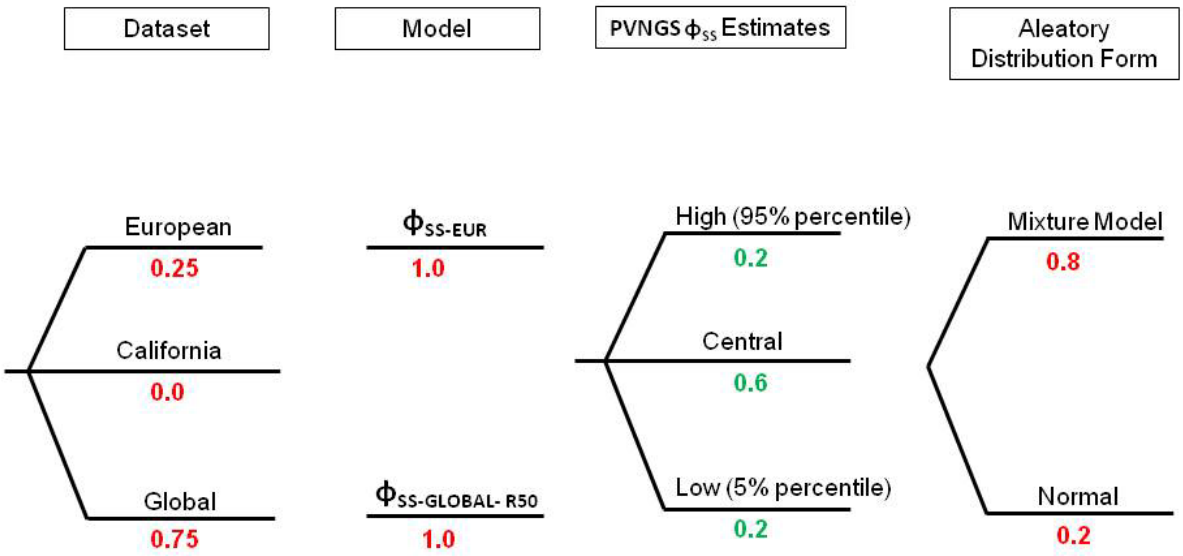

Figure 12.1-1: ϕ_{SS} Logic tree for PVNGS for Greater Arizona sources (outside Regions 1, 2, and 3). Weights associated to the TI Team's subjective evaluations are in red, whereas weights associated to statistical sampling are in green.

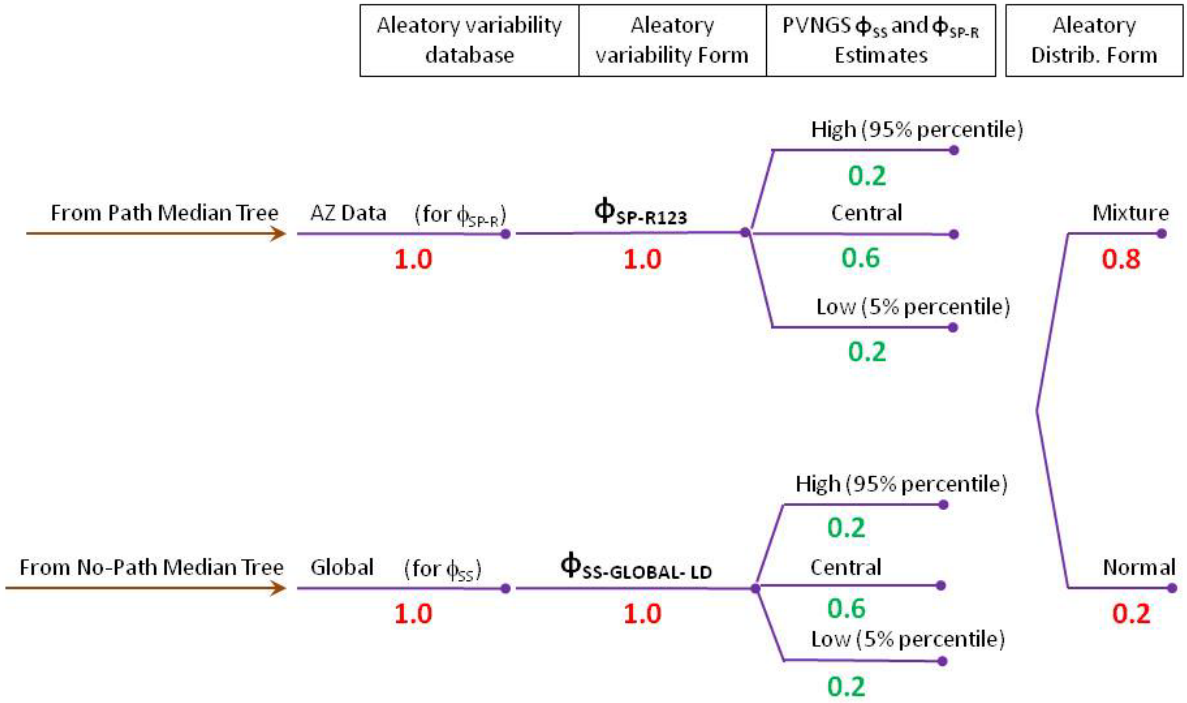

Figure 12.2-1:1 ϕ_{SS} and ϕ_{SP-R} Logic tree for PVNGS for sources in California and Mexico (Regions 1, 2, and 3). Weights associated to the TI Team's subjective evaluations are in red, whereas weights associated to statistical sampling are in green.

13 TOTAL SIGMA MODEL

13.1 Introduction

The assessment of seismic hazard at a single point location utilizes the total aleatory variability, which is composed of the between-event and within-event components (e.g. Al-Atik et al., 2010). Chapters 10, 11, and 12 present the characterization of the components in terms of uncertainty models for the between-event standard deviation τ, and the within-event standard deviation ϕ. The two components are combined to produce the total aleatory standard deviation, σ, by summing variances:

$$\sigma^2 = \tau^2 + \phi^2 \qquad \text{(Eq. 13.1-1)}$$

As discussed in Chapter 7, the within-event component may be characterized in terms of the variability in ground motions at a single site from all earthquakes, single-station ϕ_{SS}, or variability in ground motions from earthquakes that have a similar path to the site region, ϕ_{SP-R}. Each of these is combined with the between event standard deviation using Eq. (13.1-1) to form the corresponding total aleatory variability standard deviation. These are denoted as σ_{SS} or σ_{SP-R}, depending on the type of within-event variability appropriate for the specific application.

The epistemic uncertainty distributions for τ, ϕ_{SS}, and ϕ_{SP-R} developed in Chapters 10, 11, and 12 are in the form of continuous scaled χ^2 distributions (Ang and Tang, 2007) as described in Appendix P. These continuous distributions were represented discretely by logic trees, such as the τ logic tree shown in Figure 10.1-1. Epistemic uncertainty distributions for total sigma could be developed by combining the τ and ϕ logic trees to form a composite logic tree for σ. This approach was followed in developing the EPRI (2006) model for aleatory variability for ground motions in the central and eastern United States. The PEGASOS Refinement Project (PRP) developed separate logic trees for τ and ϕ and then used all possible combinations of the two logic trees for hazard analyses. Similarly, Rodriguez-Marek et al. (2014) constructed separate logic trees for τ and ϕ and then combined them, although they assumed full correlation between the two epistemic uncertainty distributions, which limited the number of alternative models. However, it is more computationally efficient to use the underlying

continuous distributions for τ and ϕ to construct a continuous distribution for σ, and then represent that continuous epistemic distribution discretely in a logic tree for use in hazard computation. This approach was followed in the SSHAC Level 3 study recently completed for the Hanford Washington site (Coppersmith et al., 2014) and is adopted for use in this study. Conceptually, the only difference between the two approaches is the point at which the continuous distributions are represented discretely. The motivation for the choice made here is reduction in computation burden – the use of three alternative discrete values representing the composite continuous distribution for σ instead of nine alternative discrete values representing the combination of three alternative discrete values for τ with three alternative discrete values for ϕ.

Section 13.2 describes the process used to develop the uncertainty distribution for total sigma for the DCPP site from the uncertainty distributions for between-event and within-event aleatory variability components and then represents that distribution discretely for use in PSHA calculations. Additional details are provided in Appendix P. The result is the total sigma logic tree shown on Figure 13.1-1. The same process was used to develop the total sigma logic trees for the PVNGS site for the Greater Arizona sources and for the distant sources in California and Mexico, shown in Figures 13.1-2 and 13.1-3, respectively.

13.2 Total Sigma Model for DCPP

As discussed in Chapter 7, the appropriate form of within-event variability for assessing seismic hazard at the DCPP site is the partially non-ergodic single-station ϕ_{SS}. Using Eq. (13.1-1), the corresponding total aleatory variability is denoted as σ_{SS}^2, and is given by:

$$\sigma_{SS}^2 = \tau^2 + \phi_{SS}^2 \qquad \text{(Eq. 13.2-1)}$$

Chapter 10 develops a continuous epistemic uncertainty distribution for τ and Chapter 11 develops a continuous epistemic uncertainty distribution for ϕ_{SS} at DCPP. These two distributions are used to develop a continuous epistemic uncertainty distribution for σ_{SS}. As described in Appendix P, the uncertainty distribution for the variance of a normally distributed random variable can be represented by a scaled χ^2 distribution (Ang and Tang, 2007). Because of the monotonic one-to-one relationship between σ and σ^2, the cumulative distribution function for σ, $F(\sigma)$, is given by:

$$F_{\sigma_{SS}}(\sigma_i) = F_{\sigma_{SS}^2}(\sigma_i^2) = \int_0^{\sigma_i^2} \chi_k^2\left(\frac{\sigma_{SS}^2}{c}\right) d(\sigma_{SS}^2) \qquad \text{(Eq. 13.2-2)}$$

The cumulative distribution function is used to develop the discrete approximation used in the logic tree formulation to represent the uncertainty in the variance parameter.

The scale parameter *c* is given by:

$$c = \frac{V(\sigma_{SS}^2)}{2E(\sigma_{SS}^2)} \quad \text{(Eq. 13.2-3)}$$

and the degress of freedom *k* is given by:

$$k = \frac{2[E(\sigma_{SS}^2)]^2}{V(\sigma_{SS}^2)} \quad \text{(Eq. 13.2-4)}$$

The results of maximum likelihood estimation of the variance terms τ^2 and ϕ^2 (Appendix P, Section P.3) have shown that there is only a very weak negative correlation (between -0.01 and -0.03) between the errors in estimation for each. Therefore, it is assumed that the two are uncorrelated. Given this assumption, the expected value of σ_{SS}^2 is given by:

$$E(\sigma_{SS}^2) = E(\tau^2) + E(\phi_{SS}^2) \quad \text{(Eq. 13.2-5)}$$

and the variance in σ_{SS}^2 is given by:

$$V(\sigma_{SS}^2) = \sigma_{\sigma_{SS}^2}^2 = \sigma_{\tau^2}^2 + \sigma_{\phi_{SS}^2}^2 \quad \text{(Eq. 13.2-6)}$$

Values for the central estimate and the standard deviation of τ^2 are developed in Chapter 10. Because τ is magnitude dependent, values are developed for **M**5 and **M**7. The logic tree for ϕ_{SS} at DCPP presented in Figure 11.1-1 contains three discrete alternatives, two alternative magnitude-dependent models based on the California dataset, and a magnitude-independent model for the global dataset. Each alternative model provides values of $E(\sigma_{SS}^2)$ and $V(\sigma_{SS}^2)$. These values were used to develop cumulative distribution functions (CDF) for σ_{SS}^2. Because of the monotonic one-to-one relationship between σ_{SS}^2 and σ_{SS}, the CDF for σ_{SS}^2 can be directly translated into a CDF for σ_{SS}. The two ϕ_{SS} models based on the California data are bi-linear with magnitude break points at **M**7 for $\phi_{SS-CA-1}$ model and **M**5.5 for $\phi_{SS-CA-2}$ model. Combining these with the bi-linear model for τ leads to break points at **M**5.5 and **M**7 in the relationship between magnitude and σ_{SS}. As a result, CDFs for σ_{SS} were developed for **M**5.0, **M**5.5, and **M**7. Appendix P presents typical examples of the calculations.

Figure 13.2-1 shows examples developed for PGA and **M**7 for the three cases of ϕ_{SS}. For each case, Equations (13.2-2) through (13.2-6) were used to develop a continuous CDF for σ_{SS}. The three CDFs

were then combined to develop a weighted composite CDF. The process used was to numerically compute a probability mass function (PMF) for σ_{SS} from each of the three CDFs. A weighted sum of the PMFs was then computed using the weights assigned to the ϕ_{SS} models. The composite PMD is then used to develop the composite CDF shown on Figure 13.2-1. The resulting composite continuous distribution is then represented by three discrete points selected at the 5th, 50th, and 95th percentiles. The distributions for σ_{SS} show only a small degree of skewness and the nominal weights of 0.2, 0.6, and 0.2 on the 5th, 50th, and 95th percentiles, respectively, produce values for the mean and standard deviation of σ_{SS} that adequately represent those computed from the continuous distribution. Table 13.2-1 compares the mean and standard deviation for σ_{SS} of PGA computed from the continuous and discrete distributions. As indicated, the means are identical to three digits and the standard deviation from the discrete model is slightly greater by less than 5 percent.

For ease of use in hazard computation, a bi-linear model for $\sigma_{SS}(M)$ was developed as follows. Initial estimates of σ_{SS} were obtained at **M**5, **M**5.5, and **M**7. Examples of the values for four periods are shown in Figure 13.2-2. Then a bi-linear relationship $\sigma_{SS}(M)$ defined by Equation (13.2-7) was fit to the results as follows. The form for the bi-linear model was chosen to be consistent with the model for τ and the most magnitude dependent version of ϕ_{SS}. Values of $\sigma_{SS}(M)$ at magnitudes between **M**5 and **M**7 spaced at 0.1 magnitude units were obtained by from the tri-linear form with break points at **M**5, **M**5.5, and **M**7. The value of σ_2 was set to the value of σ_{SS} obtained at **M**7. Parameter σ_1 was set to the value that minimized the difference between $\sigma_{SS}^2(M)$ obtained using Equation (13.2-7) and the interpolated values. Minimization of the difference in σ_{SS}^2 was used because the probability of exceedance in hazard is more directly proportional to the variance (e.g. Appendix I of EPRI, 2004). Table 13.2-2 lists the resulting discrete distributions for σ_1 and σ_2 for DCPP.

$$\sigma_{SS}(M) = \begin{cases} \sigma_1 + \frac{(M-5)}{2} * (\sigma_2 - \sigma_1) & for\ M < 7.0 \\ \sigma_2 & for\ M \geq 7.0 \end{cases} \qquad \text{(Eq. 13.2-7)}$$

13.3 Total Sigma Model for PVNGS

Sections 7.3.2.1 and 7.3.4 addressed the models for ϕ_{SS} developed for the PVNGS site for the Greater Arizona sources; Sections 7.3.2.2 and 7.4.2 addressed the models for ϕ_{SS} and ϕ_{SP-R} developed for the PVNGS site for the distant sources in California and Mexico (Regions 1, 2 and 3). Separate models are

developed for the Greater Arizona sources and for distant California and Mexico sources because different magnitude ranges and paths are important for the different sources.

13.3.1 Model for Greater Arizona Sources

To characterize ϕ_{SS} for ground motions from the Greater Arizona sources, two alternative ϕ_{SS} models were developed in Chapter 7, one based on European data (ϕ_{SS-EUR} model) and one based on Global data ($\phi_{SS-GLOBAL-R50}$). Both of these models are magnitude independent. However, because the model for τ developed in Section 7.2 is magnitude dependent, the model for σ_{SS} is magnitude dependent. Using the process described above in Section 13.2, a composite distribution was developed for σ_{SS} as a weighted combination of the distributions for the two discrete alternatives for ϕ_{SS}. Figure 13.3-1 shows an example of the CDFs for σ_{SS} for the Greater Arizona sources. Table 13.3-1 lists the resulting epistemic distribution for σ_{SS}.

13.3.2 Models for Distant California and Mexico Sources

To characterize ϕ_{SS} for ground motions from the distant sources in California and Mexico, two models were developed. One model is for the case when path specific adjustments are applied, designated to as $\phi_{SP-R123}$ model, and the second model is for the case when path adjustments are not applied and is designated $\phi_{SS-GLOBAL-LD}$. Both of these models are magnitude independent, in part because the earthquake magnitudes that contribute to the hazard at the PVNGS site from the distant California and Mexico sources are for the most part **M**7 and larger. Because of this, the total σ_{SS} model for these sources was developed using only the values of τ from Section 7.2 for **M** ≥ 7 and the models are magnitude independent. The process described above in Section 13.1 was used to develop epistemic uncertainty distributions for single station σ for each of the two cases. The resulting values of the single station σ models, denoted σ_{SP-R} and σ_{SS}, are listed in Tables 13.3-2 and 13.3-3, respectively. Note that each of the total sigma models uses only one ϕ model, therefore, the step of developing a weighted composite CDF is not needed.

The results in Tables 13.3-2 and 13.3-3 indicate that, for the large distance data set (200-400 km), the standard deviation decreases with period while the results presented in Tables 13.2-2 and 13.3-1 for shorter distances indicate the opposite trend. These differences are the result of differences in the data set that are relevant to assessing the hazard from the different sources. On average, ϕ_{SP-R} is expected

to be lower than ϕ_{SS} for many data sets. However, for an individual path, ϕ_{SP-R} may be larger if the crustal structure is more variable than average.

13.4 Effect of Spatial Correlation

Within-event residuals have been observed to be spatially-correlated (Jayaram and Baker, 2010). They found that accounting for this spatial correlation has negligible effects on the derived coefficients of the GMPEs and their median predictions, but found that it leads to an increase in the ϕ estimates and decrease in the τ estimates. The impact of including spatial-correlation of within-event residuals on the ϕ, τ, and total σ estimates of the CY14 (Chiou and Youngs, 2014) was evaluated by Shahi et al. (2015) – See Attachment D. Figure 13.4-1 shows the impact of including the spatial correlation on ϕ, τ, and total σ for homoskedastic and heteroskedastic models (magnitude-independent and magnitude-dependent, respectively). The ϕ and τ are negatively correlated, so an increase in ϕ leads to a decrease in τ. The net effect is still an increase in the total sigma, particularly for large magnitudes at periods of 0.3 sec and longer. Semivariogram analyses of the single-site within-event residuals of ASK14 (Abrahamson et al., 2014) and CY14 (Chiou and Youngs, 2014) versus stations separation distance conducted for the project using the method of Jayaram and Baker (2009) shows that the single-site within-event residuals are spatially correlated as presented in Figure 13.4-2. The variogram was normalized by the variance of the selected data. The increase in the variance (ϕ_{SS}^2) is about 10 percent (the normalized variogram at large separation distance is about 1.1). This increase corresponds to an increase in ϕ_{SS} of 5%. With a small reduction in τ (in the range of 0 to 7 percent), the total σ_{SS} would increase by about 4%. These results are for a magnitude-independent model (homoskedastic). Figure 13.4-1 shows that, for a magnitude-dependent τ and ϕ, the effect of the spatial correlation is larger for large magnitudes (tau2, phi2 and sigma2) and smaller for small magnitudes (tau1, phi1 and sigma1). The large variability of the estimated factors for large magnitudes for different periods indicates that the large-magnitude factors are not as reliable compared to the magnitude-independent factors (tau, phi and sigma). Given that is a new issue that has not been addressed in previous hazard studies, the TI Team judged that the adjustments to the traditional standard deviations should be based on the smoother magnitude-independent results.

The available studies (Jayaram and Baker, 2010; and Shahi et al., 2015) indicate that the spatial correlation leads to underestimation of the ϕ and ϕ_{SS}. The TI Team's evaluation concluded that the bias in the ϕ values in traditional studies exists, but because these models are relatively new and the bias has not been estimated for all of the available data sets, the TI Team decided to account for the bias by applying extra weight to the high branch of the sigma uncertainty model, rather than making specific

adjustments to individual values of sigma on the logic tree branches. This approach is motivated by the concept that the uncertainty distribution for ϕ_{SS}, and as a result σ_{SS}, should be biased toward larger values as the current empirically based values that do not consider spatial correlation may be under estimated. Although the bias shown in Figure 13.4-3 is period-dependent, the change in weights was applied to all periods. Jayaram and Baker (2010) and Shahi et al. (2015) found differing trends with period, but the average of the two analysis results is approximately constant with period. Given the small effect of the adjustment, a simple period independent adjustment was adopted. The re-sampled sigma branches have modified weights of 0.15, 0.55, and 0.3 from low to high branches, respectively. Using these weights increases the mean value of sigma by 3-4%. The adopted solution has the desired effect on the mean value of sigma and only a minor effect on the epistemic standard deviation on sigma (less than a 5 percent increase). Given the early state of the evaluation of these effects, the adopted solution is considered to adequately capture the minor impact on the total standard deviation. The modification in weights is applied to both the magnitude-dependent models for DCPP and PVNGS, and to the magnitude-independent models for the distant California and Mexico sources used for PVNGS, as the latter are essentially the large-magnitude end of the general magnitude-dependent models, as only large magnitudes on the distant California and Mexico sources contribute to the hazard at the PVNGS site.

The resulting total sigma models are shown in figures 13.4-4 to 13.4-7 for DCCP, PVNGS sources in Greater Arizona, PVNGS sources in California and Mexico with path effects, and PVNGS sources in California and Mexico without path effects, respectively. In these plots, the three alternative total sigma branches are shown along with the weighted mean and the adjusted sigma applying the Jayaram and Baker (2010) and Shahi et al. (2015) factors to the central estimate. The high range of the sigma model captures the range for these adjusted sigma models.

13.5 Implementation of the Mixture Model

As discussed in Section 11.6, two alternatives are developed to represent the shape of the distribution for the within-event residuals: the traditional log normal (on the natural log of ground-motion amplitude) with weight 0.2 and a mixture of two normal distributions with weight 0.8. The analyses that identified the mixture were based on ϕ. Extending the analysis to ϕ_{SS} becomes difficult as the sample size decreases, thus limiting the amount of data in the extreme tails. Therefore, the findings for ϕ were applied to ϕ_{SS}. The mixture model consists of an equally weighted mixture with one component having 0.8 times the normal ϕ_{SS} and one component having 1.2 times the normal ϕ_{SS}. For simplicity in application, this ϕ_{SS} mixture model is applied to the total σ_{SS} values. This is conservative as the

between-event residuals have not demonstrated heavy tails to the same extent as the within-event residuals, but because the values of ϕ_{SS} are larger than those of τ, the tail of the total residual distribution will be dominated by ϕ_{SS}. In addition, the sample size for estimation of τ is much smaller that that for estimation of ϕ or ϕ_{SS}, limiting the ability to evaluate the shape of the tails in the distribution of event terms.

13.6 References

Abrahamson, N.A., Silva, W.J., and Kamai, R. (2014). Summary of the AKS14 Ground-Motion Relation for Active Crustal Regions, *Earthquake Spectra*, Vol. 30(3), 1025-1055, DOI: 10.1193/070913EQS198M

Ang, A.H.-S., and Tang, W.H. (2007). *Probability Concepts in Engineering: Emphasis on Applications to Civil and Environmental Engineering (Vol. 1)*. John Wiley and Sons, New York, 409 pp.

Campbell, K.W., and Bozorgnia, Y. (2008). NGA Ground Motion Model for the Geometric Mean Horizontal Component of PGA, PGV, PGD and 5% Damped Linear Elastic Response Spectra for Periods Ranging from 0.01 to 10 s, *Earthquake Spectra*, Vol. 24(1), 139-171.

Chiou, B.S-J., and Youngs, R.R. (2014). Update of the Chiou and Youngs NGA Model for the Average Horizontal Component of Peak Ground Motion and Response Spectra, *Earthquake Spectra*, Vol. 30(3), 1117-1153, DOI: 10.1193/072813EQS219M

Electric Power Research Institute – EPRI (2004). CEUS Ground Motion Project Final Report, *EPRI Report 1009684*, December, Palo Alto, Calif.

Electric Power Research Institute – EPRI (2006). Program on Technology Innovation: Truncation of the Lognormal Distribution and Value of the Standard Deviation for Ground Motion Models in the Central and Eastern United States, *EPRI Report 1013105*, Technical Update, February, Palo Alto, Calif.

Jayaram, N., and Baker, J.W. (2009). Correlation model for spatially distributed ground-motion intensities, *Earthq. Eng. Struct. Dynam*., Vol 38(15), 1687–1708.

Jayaram, N., and Baker, J.W. (2010). Considering spatial correlation in mixed-effects regression and the impact on ground-motion models, *Bull. Seism. Soc. Am*., Vol. 100(6), 3295-3303.

Rodriguez-Marek, A., Rathje, E.M., Bommer, J.J, Scherbaum, F., and Stafford, P.J. (2014). Application of single-station sigma and site-response characterization in a probabilistic seismic-hazard analysis for a new nuclear site, *Bull. Seism. Soc. Am*., Vol. 104(4), 1601-1619.

Shahi K.S, Baker J.W., and Rodriguez-Marek, A. (2015). Effect of Spatial Correlation on the Model Standard Deviations of CY14 Model, Deliverable submitted to GeoPentech, January 2015, 9 pp.

Table 13.2-1: Mean and standard deviation for σ_{SS} of PGA computed from the continuous and discrete distributions.

Magnitude	Mean of σ_{SS}		Standard Deviation of σ_{SS}	
	Continuous	Discrete	Continuous	Discrete
5	0.596	0.596	0.073	0.076
5.5	0.547	0.547	0.073	0.076
7	0.498	0.498	0.068	0.071

Table 13.2-2: Epistemic Distribution for σ_{SS} for DCPP

Period (sec)	Low Branch		Central Branch		High Branch	
	σ_1	σ_2	σ_1	σ_2	σ_1	σ_2
0.01	0.456	0.390	0.576	0.495	0.699	0.614
0.02	0.457	0.394	0.577	0.498	0.699	0.614
0.03	0.458	0.396	0.577	0.499	0.700	0.615
0.05	0.460	0.402	0.578	0.504	0.700	0.616
0.075	0.461	0.407	0.578	0.507	0.701	0.617
0.1	0.462	0.411	0.579	0.510	0.702	0.618
0.15	0.464	0.416	0.580	0.514	0.703	0.620
0.2	0.465	0.419	0.581	0.517	0.703	0.621
0.25	0.465	0.422	0.581	0.519	0.704	0.622
0.3	0.466	0.424	0.581	0.520	0.704	0.623
0.4	0.466	0.427	0.582	0.522	0.704	0.625
0.5	0.467	0.429	0.582	0.524	0.705	0.626
0.75	0.468	0.432	0.583	0.527	0.705	0.628
1	0.468	0.434	0.583	0.529	0.706	0.629
1.5	0.469	0.437	0.584	0.531	0.706	0.631
2	0.469	0.439	0.584	0.532	0.707	0.632
3	0.470	0.441	0.585	0.534	0.707	0.633
4	0.470	0.441	0.585	0.534	0.707	0.634
5	0.470	0.441	0.585	0.535	0.707	0.634
7.5	0.471	0.442	0.585	0.535	0.708	0.635
10	0.471	0.442	0.586	0.536	0.708	0.635

Table 13.3-1: Epistemic Distribution for σ_{SS} for PVNGS – Greater Arizona Sources

Period (sec)	Low Branch		Central Branch		High Branch	
	σ_1	σ_2	σ_1	σ_2	σ_1	σ_2
0.01	0.461	0.459	0.573	0.553	0.694	0.652
0.02	0.461	0.459	0.574	0.553	0.695	0.653
0.03	0.461	0.460	0.574	0.553	0.695	0.653
0.05	0.462	0.460	0.575	0.554	0.696	0.655
0.075	0.462	0.460	0.576	0.555	0.697	0.656
0.1	0.463	0.461	0.576	0.555	0.698	0.657
0.15	0.463	0.461	0.577	0.556	0.699	0.658
0.2	0.463	0.461	0.577	0.556	0.700	0.659
0.25	0.463	0.461	0.578	0.557	0.701	0.660
0.3	0.463	0.461	0.578	0.557	0.701	0.661
0.4	0.464	0.461	0.578	0.557	0.702	0.662
0.5	0.464	0.461	0.579	0.558	0.702	0.662
0.75	0.464	0.462	0.579	0.558	0.703	0.664
1	0.464	0.462	0.579	0.558	0.704	0.664
1.5	0.464	0.462	0.580	0.559	0.705	0.665
2	0.464	0.462	0.580	0.559	0.705	0.666
3	0.464	0.462	0.580	0.559	0.706	0.667
4	0.464	0.462	0.580	0.559	0.706	0.667
5	0.464	0.462	0.580	0.559	0.707	0.667
7.5	0.464	0.462	0.581	0.560	0.707	0.668
10	0.464	0.462	0.581	0.560	0.707	0.668

Table 13.3-2: Epistemic Distribution for σ_{SP-R} for PVNGS – Distant California Sources, Path Effects Modeled Case Using ϕ_{SP-R}

Period (sec)	Low Branch	Central Branch	High Branch
0.01	0.354	0.449	0.552
0.02	0.354	0.449	0.552
0.03	0.354	0.449	0.552
0.05	0.354	0.449	0.552
0.075	0.354	0.449	0.552
0.1	0.354	0.449	0.552
0.15	0.354	0.449	0.552
0.2	0.354	0.449	0.552
0.25	0.354	0.449	0.552
0.3	0.354	0.449	0.552
0.4	0.354	0.449	0.552
0.5	0.354	0.449	0.552
0.75	0.375	0.473	0.579
1	0.390	0.491	0.600
1.5	0.410	0.517	0.631
2	0.425	0.535	0.655
3	0.425	0.535	0.655
4	0.425	0.535	0.655
5	0.425	0.535	0.655
7.5	0.425	0.535	0.655
10	0.425	0.535	0.655

Table 13.3-3: Epistemic Distribution for σ_{SS} for PVNGS – Distant California Sources, Path Effects Not Modeled Case Using ϕ_{SS}

Period (sec)	Low Branch	Central Branch	High Branch
0.01	0.512	0.613	0.720
0.02	0.512	0.613	0.720
0.03	0.512	0.613	0.720
0.05	0.512	0.613	0.720
0.075	0.512	0.613	0.720
0.1	0.512	0.613	0.720
0.15	0.512	0.613	0.720
0.2	0.511	0.612	0.718
0.25	0.508	0.609	0.715
0.3	0.506	0.606	0.712
0.4	0.499	0.598	0.702
0.5	0.493	0.591	0.694
0.75	0.483	0.579	0.681
1	0.476	0.571	0.672
1.5	0.467	0.561	0.660
2	0.460	0.553	0.652
3	0.452	0.544	0.641
4	0.446	0.537	0.634
5	0.442	0.532	0.629
7.5	0.435	0.525	0.620
10	0.430	0.519	0.614

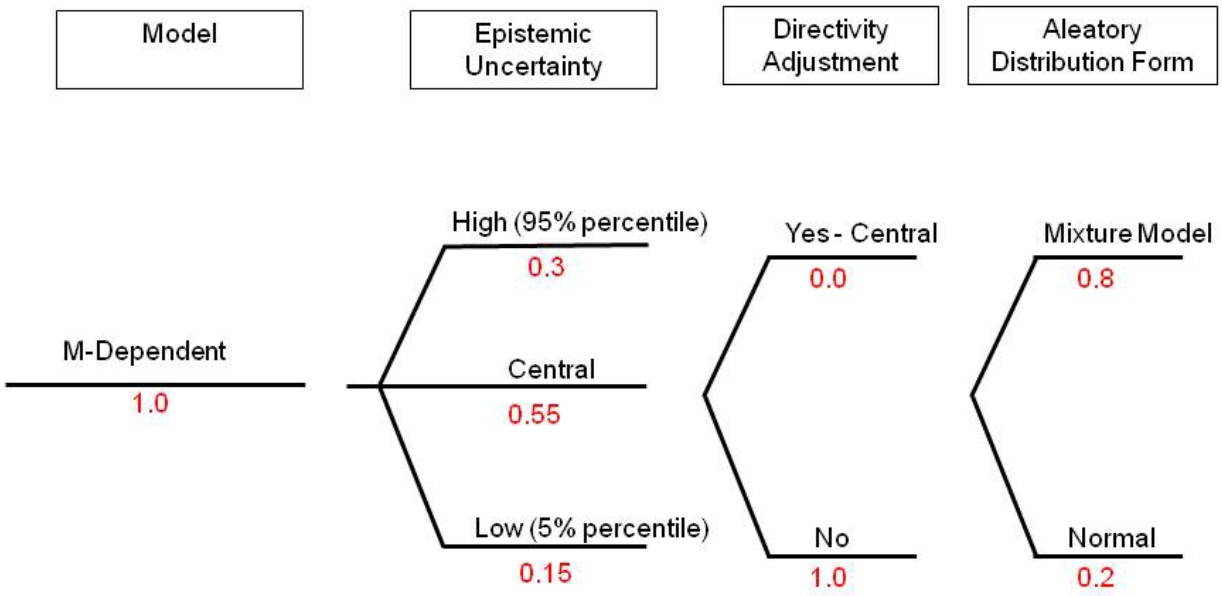

Figure 13.1-1: Logic Tree for Total Sigma at DCPP.

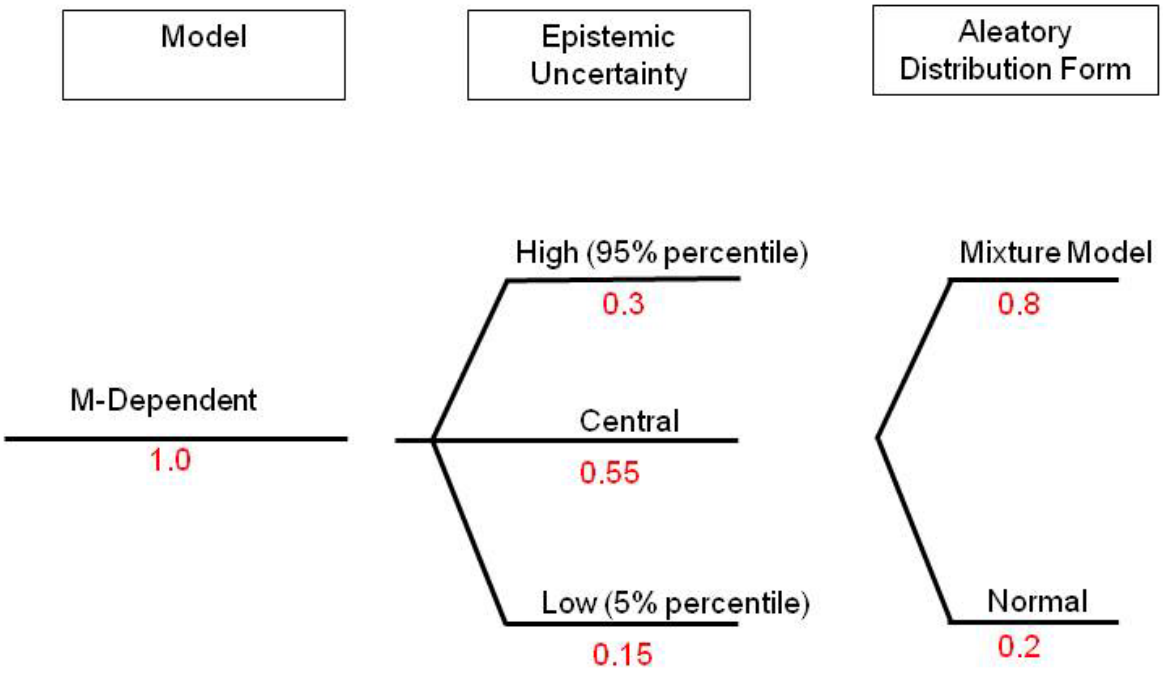

Figure 13.1-2: Logic Tree for Total Sigma at PVNGS (Greater Arizona Sources).

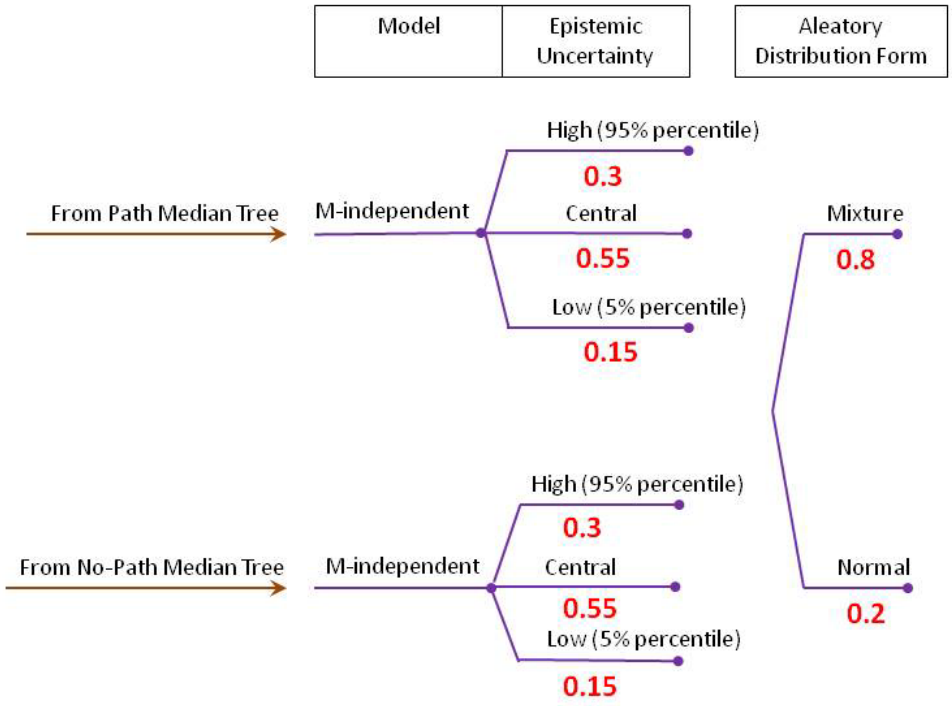

Figure 13.1-3: Logic Tree for Total Sigma at PVNGS (Sources in California and Mexico).

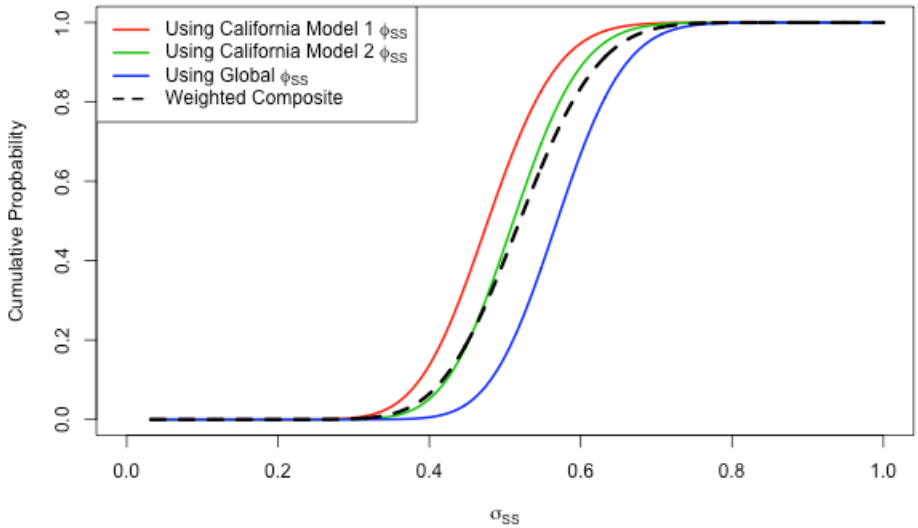

Figure 13.2-1: Example cumulative distribution functions for total σ_{SS} for **M**7 for DCPP computed using different ϕ_{SS} models.

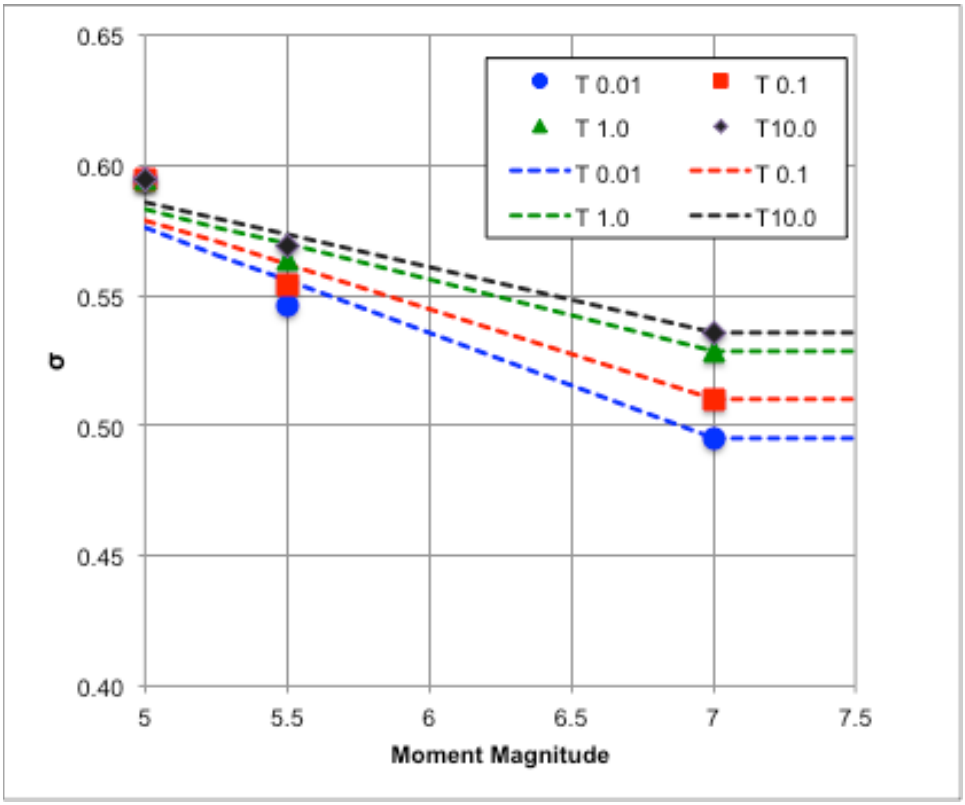

Figure 13.2-2: Individual values of σ_{SS} at **M**5, **M**5.5, and **M**7 for DCPP and fitted bi-linear relationship.

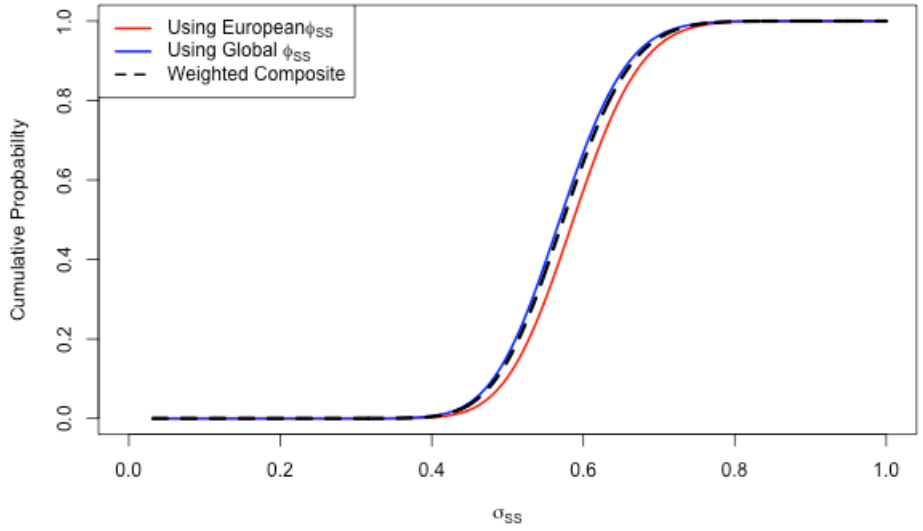

Figure 13.3-1: Example cumulative distribution functions for total σ_{SS} for **M**5 for PVNGS, Greater Arizona source, computed using different ϕ_{SS} models.

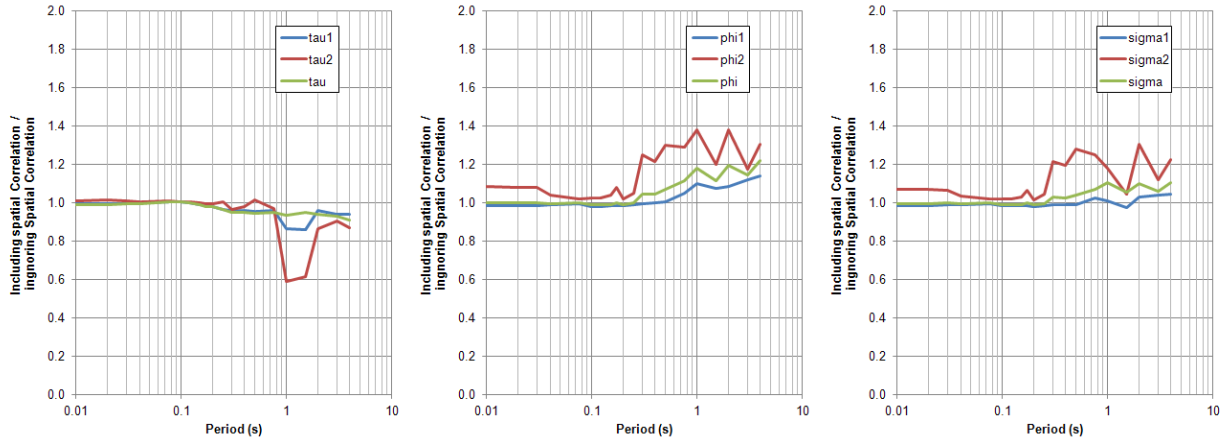

Figure 13.4-1: Impact of including spatial-correlation effects on the ϕ, τ, and σ estimates of CY14. Tau1, phi1, and sigma1 are for magnitude less than or equal to 5.0. Tau2, phi2, and sigma2 are for magnitude greater than or equal to 7.25. Tau, phi and sigma are for a homoscedastic model. Results from Shahi et al. (2015).

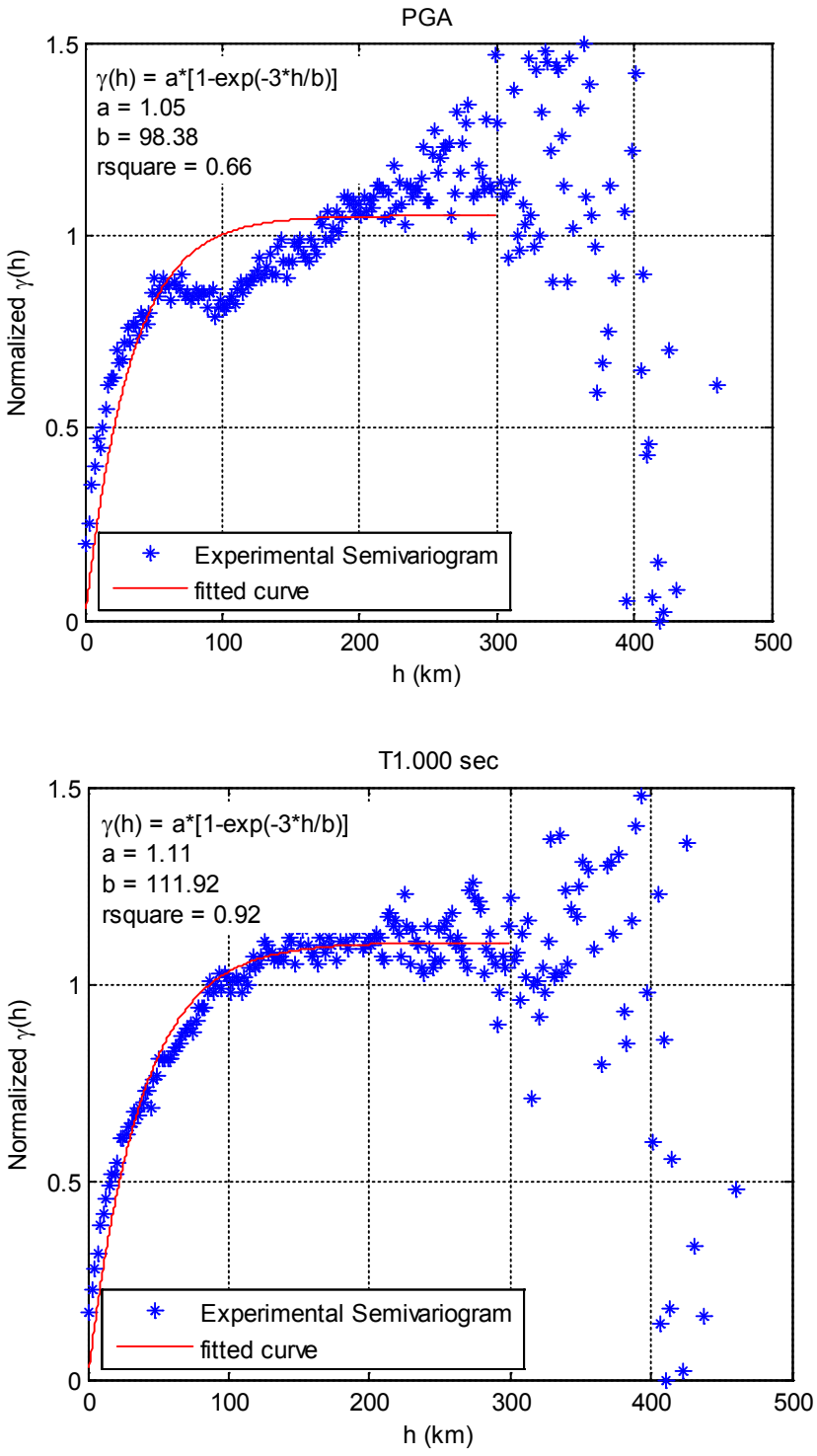

Figure 13.4-2: Semivariogram of the ASK14 single-site within-event residuals versus station separation distance. All residuals (all magnitudes and distances) were used here.

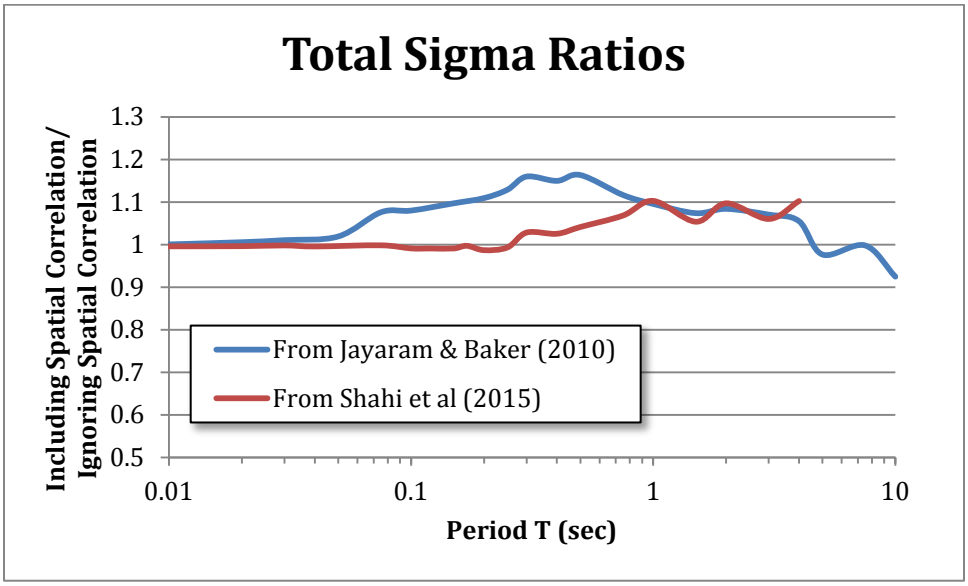

Figure 13.4-3: Examples of the effect of including spatial-correlation effects on the total sigma. The Jayaram and Baker (2010) results are based on the residuals from CB08 (Campbell and Bozorgnia, 2008). The Shahi et al. (2015) results are based on the residuals from the CY14 model (Chiou and Youngs, 2014).

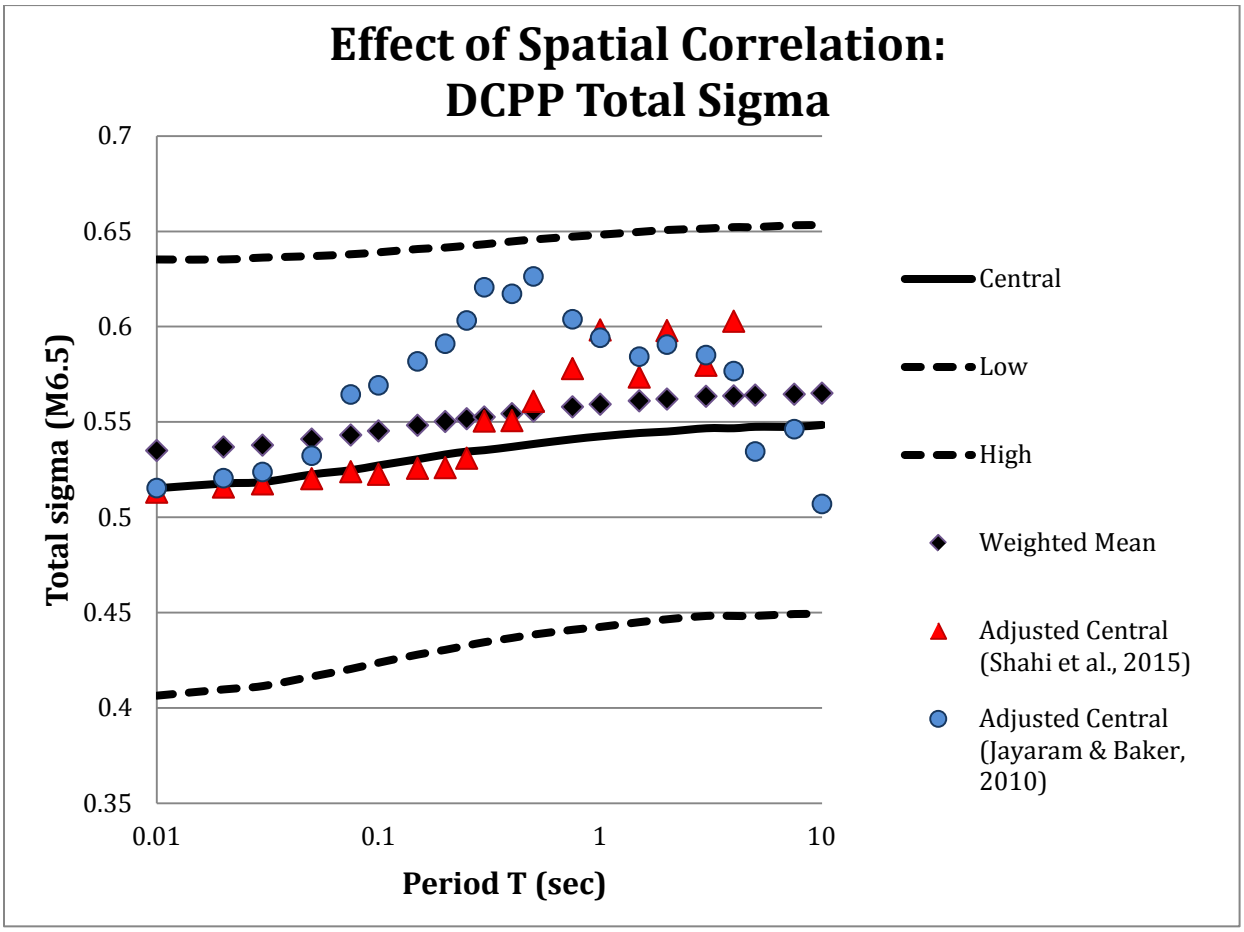

Figure 13.4-4: Example of the total sigma range and the effect of spatial correlation applied to the central estimate for DCPP.

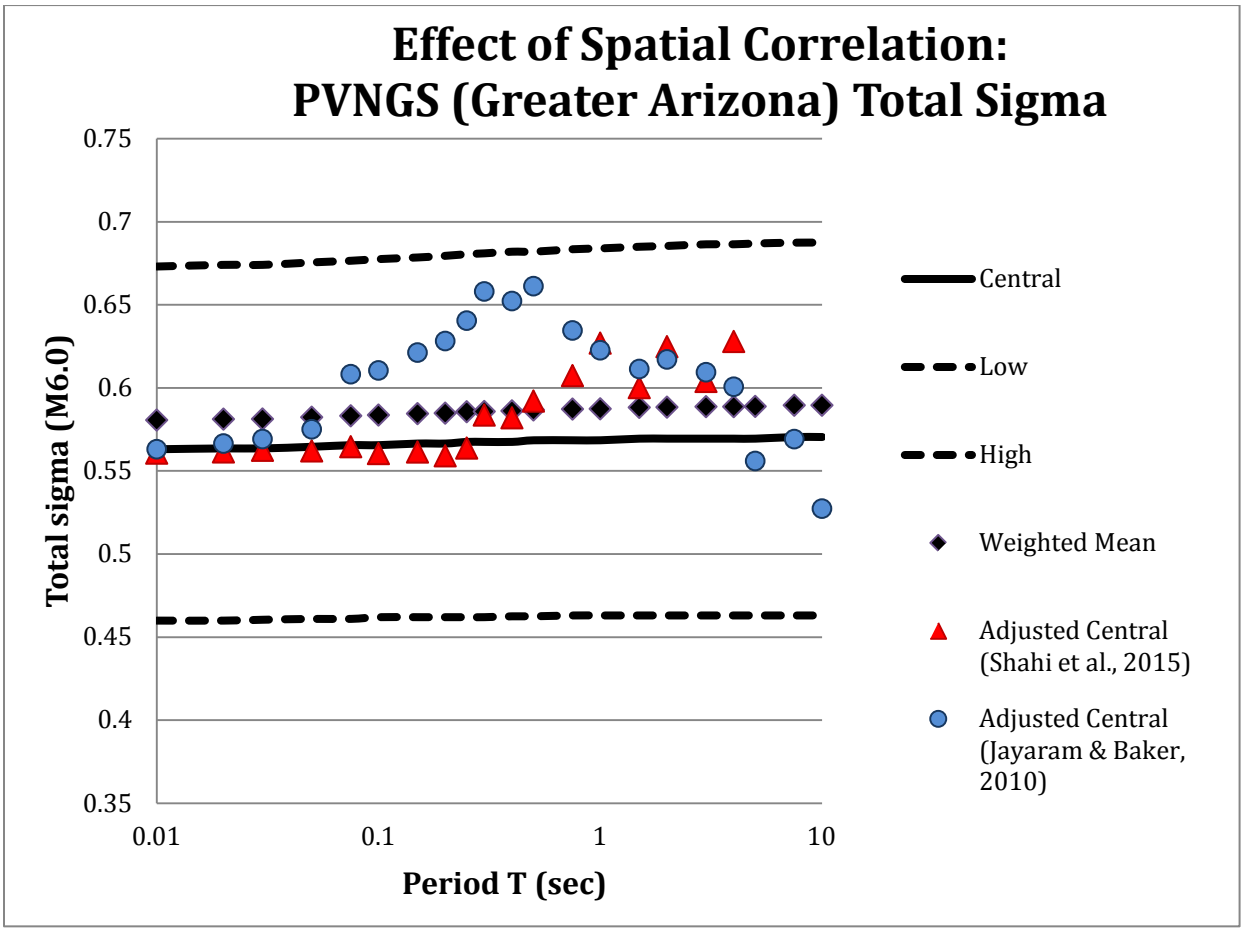

Figure 13.4-5: Example of the total sigma range and the effect of spatial correlation applied to the central estimate for PVNGS Greater Arizona sources.

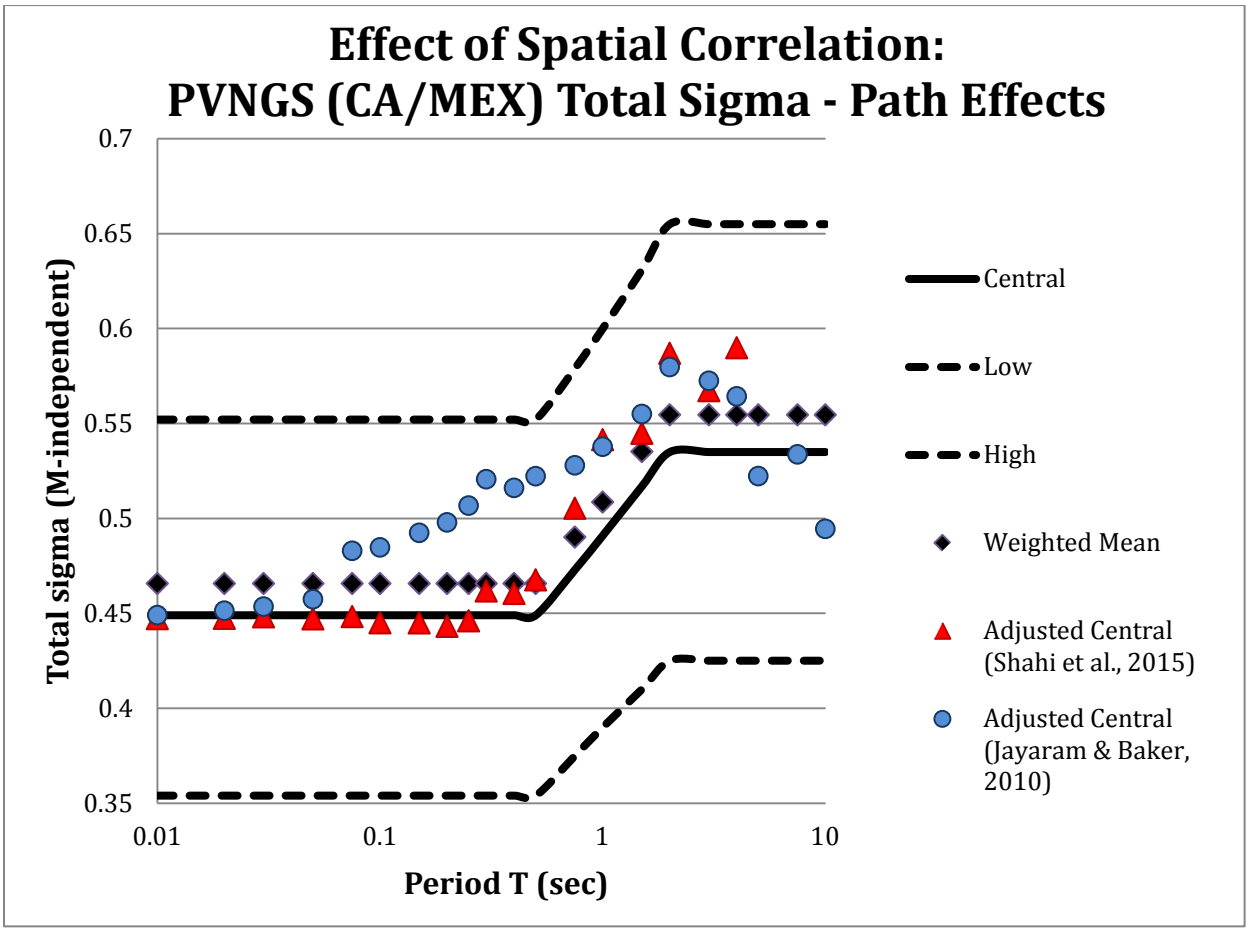

Figure 13.4-6: Example of the total sigma range and the effect of spatial correlation applied to the central estimate for PVNGS sources in California and Mexico with path effects.

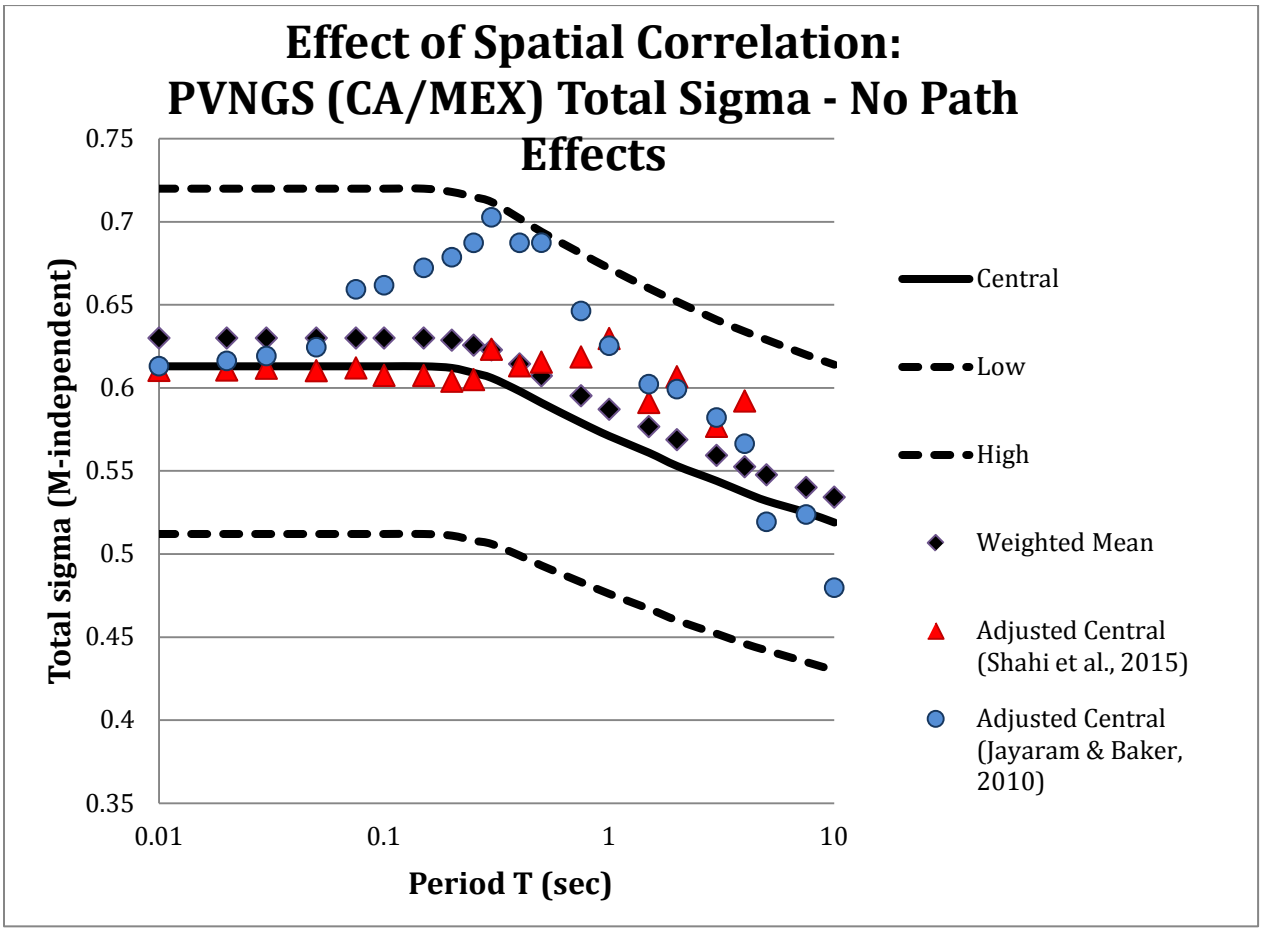

Figure 13.4-7: Example of the total sigma range and the effect of spatial correlation applied to the central estimate for PVNGS sources in California and Mexico without path effects.

14 HAZARD SENSITIVITY

14.1 Hazard Sensitivity Runs

Hazard sensitivity feedback was provided throughout the project (Table 14.1-1) to focus the TI Team's evaluations on the uncertainties that are most important for the hazard at the two nuclear power plant (NPP) sites. In this Chapter, the hazard sensitivities using the final set of logic tree weights for the two sites are shown. For the hazard sensitivity, simplified versions of the previously published Seismic Source Characterization (SSC) models for the two sites were used (PG&E, 2011 and LCI, 2013 for DCPP and PVNGS, respectively). These simplified versions of the previous SSC models, described in Sections 14.2 for DCPP and 14.3 for PVNGS, capture the key aspects of the controlling sources for each of the two sites. For each of the two sites, hazard deaggregation results for the simplified versions of the previous SSC models are also presented. The deaggregations show the contribution to the hazard by magnitude and distance bins for spectral accelerations corresponding to mean hazard level of 10^{-4} and of 10^{-6}, for 5Hz and 0.5 Hz spectral frequencies. The final SSHAC Level 3 SSC models were not used because these hazard sensitivities were computed before the SSC models were finalized. The curves shown in this Section correspond to the mean hazard, are only intended for demonstration purposes, and to provide insights for parameter sensitivity for making hazard-informed decisions. The hazard curves shown herein do not represent the final hazard levels at either of the two NPP sites, because it is the responsibility of the individual NPPs to conduct thorough sensitivity analyses for their individual sites.

The hazard sensitivity was conducted for two frequencies: a high frequency of 5 Hz and a low frequency of 0.5 Hz. These two spectral frequencies were selected to be representative of the expected range of importance for the two nuclear power plant sites, as well as to provide informative feedback for the development of the GMC logic trees.

The hazard sensitivity was conducted by isolating each node of the GMC logic trees. For the node of interest, one branch is given full weight and the mean hazard is computed by sampling every combination of branches for the other nodes. The results of the hazard sensitivity are presented in the form of tornado plots for a given hazard level (y-axis value). Tornado plots are a representation of the hazard sensitivity to the alternative models and/or parameter values in the logic tree. They can show either the sensitivity of the hazard level at a given ground motion, or the sensitivity of the ground-motion level at a given hazard. The tornado plots are constructed such that the parameters leading to

the largest uncertainty are at the top, and parameters leading to the smallest uncertainty are at the bottom, giving these plots the shape of a tornado.

For this project, the tornado plots show the ratio of the ground motion from the isolated branch to the ground motion for the mean hazard obtained with the full logic tree weights (called the base case). These computed ratio values for each branch of the logic tree are then normalized by the logic-tree branch weights to center the individual tornado results about the center line of unity. Tornado plots are computed for the two spectral frequencies of 5 Hz and 0.5 Hz and for the mean annual frequency of exceedance of 10^{-4} and 10^{-6}. The points on the sensitivity tornado plots are plotted as circles with their radii proportional to the logic tree weight. The center point of each weight-based circle is shown as a small point. In addition, the color scheme is consistent with the previous presentation of the GMC logic tree (i.e., green weights are based on statistical sampling, whereas red weights are based on TI Team's judgment).

The hazard sensitivities for the median ground-motion branches and for the sigma ground-motion branches are shown using tornado plots. For median ground-motion model sensitivity, the aleatory sigma value is taken as the central sigma model. Using the central sigma model simplified the hazard calculations while still capturing the effects of the different median models. For the sigma model sensitivity, only the central GMPE model is used and the individual sigma branches are evaluated. Because the sensitivity studies are not based on the final SSC models, the hazard results presented in this Chapter are for GMC sensitivity only and should not be considered as representative of the final hazard results in terms of the ground-motion level, but they are representative of the expected contribution of the different magnitude and distance ranges to the hazard.

Table 14.1-1: Hazard sensitivity feedback occurred during the SWUS GMC project.

HAZARD FEEDBACK	HAZARD ANALYST	TOPIC
Kick-off Meeting (August 27, 2012)	K. Wooddell	Hazard significant sources, hazard curves and SSC sensitivity from the Shoreline Fault Report Study (PG&E, 2011)
	A. Dinsick	Hazard significant sources, hazard curves, SSC and GMC sensitivity from the SONGS 2010 PSHA study (GeoPentech, 2010)
	M. Walling	Hazard significant sources, hazard curves, SSC and GMC sensitivity from the PVNGS SSHAC L.2 study (LCI, 2013)
Preparation and execution of SWUS GMC Workshop #1 (March 19-21, 2013) - Sensitivities to GMC Model V0	N. Gregor	Hazard curves and deaggregation from the Shoreline Fault Report Study; GM sensitivity to other available GMPEs for active crustal regions with shallow seismicity (ACR)
	A. Dinsick	Hazard curves and deaggregation from the SONGS 2010 PSHA study; GM sensitivity to other available GMPEs for ACR; sensitivity to HW effects
	M. Walling	Hazard curves and deaggregation from the PVNGS SSHAC L.2 study
Preparation and execution of SWUS GMC Workshop #2 (October 22-24, 2013) - Sensitivities to GMC Model V1.0	N. Gregor	Hazard curves and deaggregation using simplified SSC model; mean hazard curves for median and sigma; tornado plots for base case (equally weighted NGA-West1 GMPEs) and other available GMPEs for ACR, with emphasis on the style of faulting and single station sigma uncertainty impact
	M. Walling	Base case hazard by source contribution and deaggregation; hazard sensitivity results using simplified SSC model and other GMPEs for ACR; tornado plots with emphasis on the style of faulting and single station sigma uncertainty impact
Preparation and execution of SWUS GMC Workshop #3 (March 10-12, 2014) - Sensitivities to GMC Model V2.0	M. Walling	Sensitivity to GMPEs for local sources and distant sources, separately, using simplified SSC model; hazard curves and tornado plots showing sensitivity to median model and standard deviation model (sigma mixture model, tau model, single-station sigma models, and single path-to-region sigma model)
	N. Gregor	Sensitivity to GMPEs for GM model using simplified SSC model; hazard curves and tornado plots showing sensitivity to individual candidate GMPEs, common-form models, directivity effects to median and sigma, tau model, single-station sigma models, and sigma mixture model
PPRP Closure Briefing (July 17-18, 2014) - Sensitivities to GMC Model V3.1	N. Gregor	Tornado plots for two freq (5 Hz and 0.5 Hz) showing ratio of ground-motion values, not hazard, at three hazard levels (10^{-4}, 10^{-5}, and 10^{-6}); sensitivity to median and standard deviation models for the majority of nodes and branches included in the Preliminary GMC Logic Tree for DCPP
	M. Walling	Tornado plots for two freq (5 Hz and 0.5 Hz) showing ratio of ground-motion values, not hazard, at two hazard levels (10^{-4} and 10^{-6}); sensitivity to median and standard deviation models for the majority of nodes and branches included in the Preliminary GMC Logic Tree for PVNGS
SWUS GMC Report - Sensitivities to Final GMC Model V4.0	N. Gregor	This Chapter; hazard deaggregation by sources using simplified SSC models for DCPP and PVNGS; tornado plots for the majority of nodes and branches included in the Final GMC Logic Tree for application to DCPP and PVNGS sites.

14.2 Deaggregation and Sensitivity Analyses - DCPP

Previous studies have shown that the hazard at DCPP is controlled by the four closest faults to the site: Hosgri fault, Shoreline fault, Los Osos fault and San Luis Bay fault (PG&E, 2011). Figures 14.2-1 and 14.2-2 plot the fractional contribution of the different seismic sources to the total mean hazard for DCPP. This fractional contribution was computed by dividing the hazard from a single source by the total hazard. These curves are computed based on the weighted combination of the selected common model using the central branch of the Total Sigma model. For both the 5 and 0.5 Hz spectral acceleration cases, the individual curves for the Hosgri fault (solid red line), Shoreline fault (solid green line), Los Osos fault (solid purple line), San Luis Bay fault (solid blue line), the combination of these four local faults (dashed green line), regional faults (dotted black line) and background source zone (dashed blue line) are plotted. For the 5 Hz spectral acceleration case shown in Figure 14.2-1, the combined local faults contribute more than 90% of the total hazard for ground motions greater than about 0.3 g. For 0.5 Hz spectral acceleration, the ground-motion value for the 90% contribution is about 0.08 g. Therefore, for the sensitivity analysis, the source model was simplified to only include the foul local faults as described in the PGE (2011) Shoreline Report.

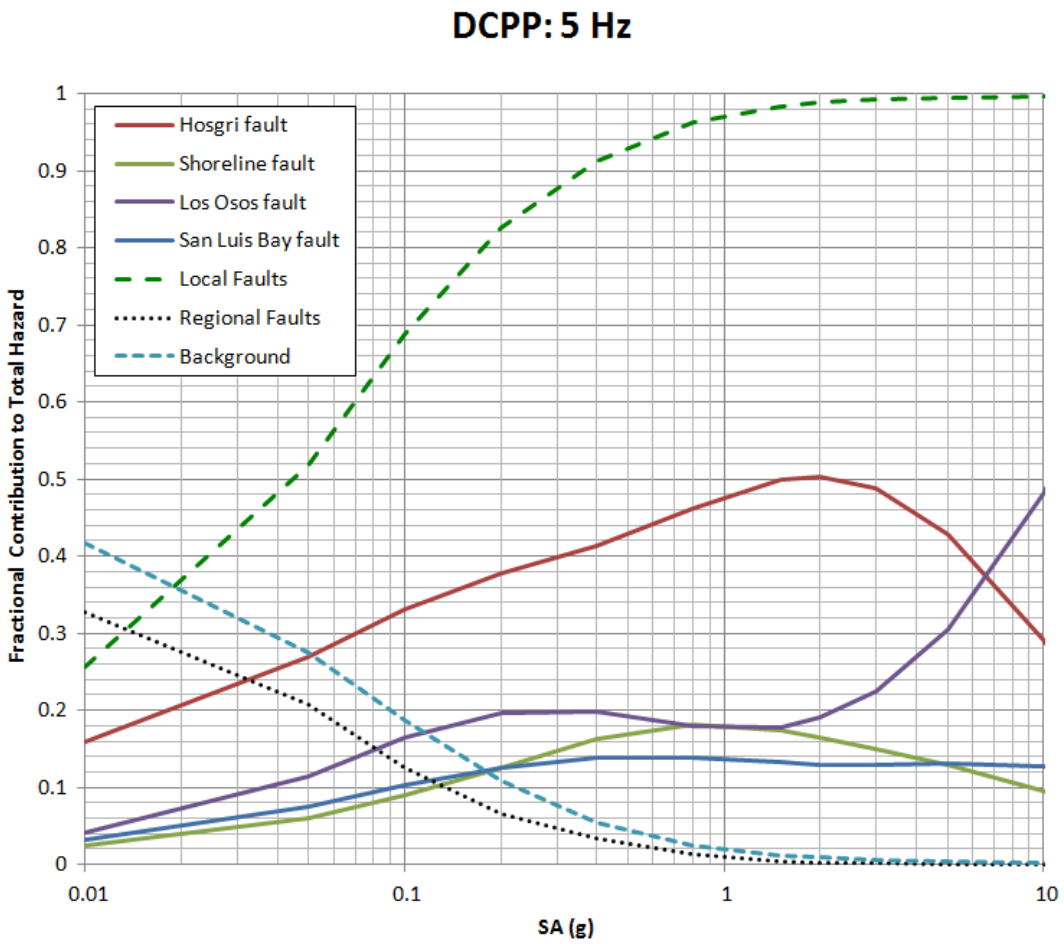

Figure 14.2-1: Deaggregation by source as a function of ground motions for 5 Hz spectral acceleration.

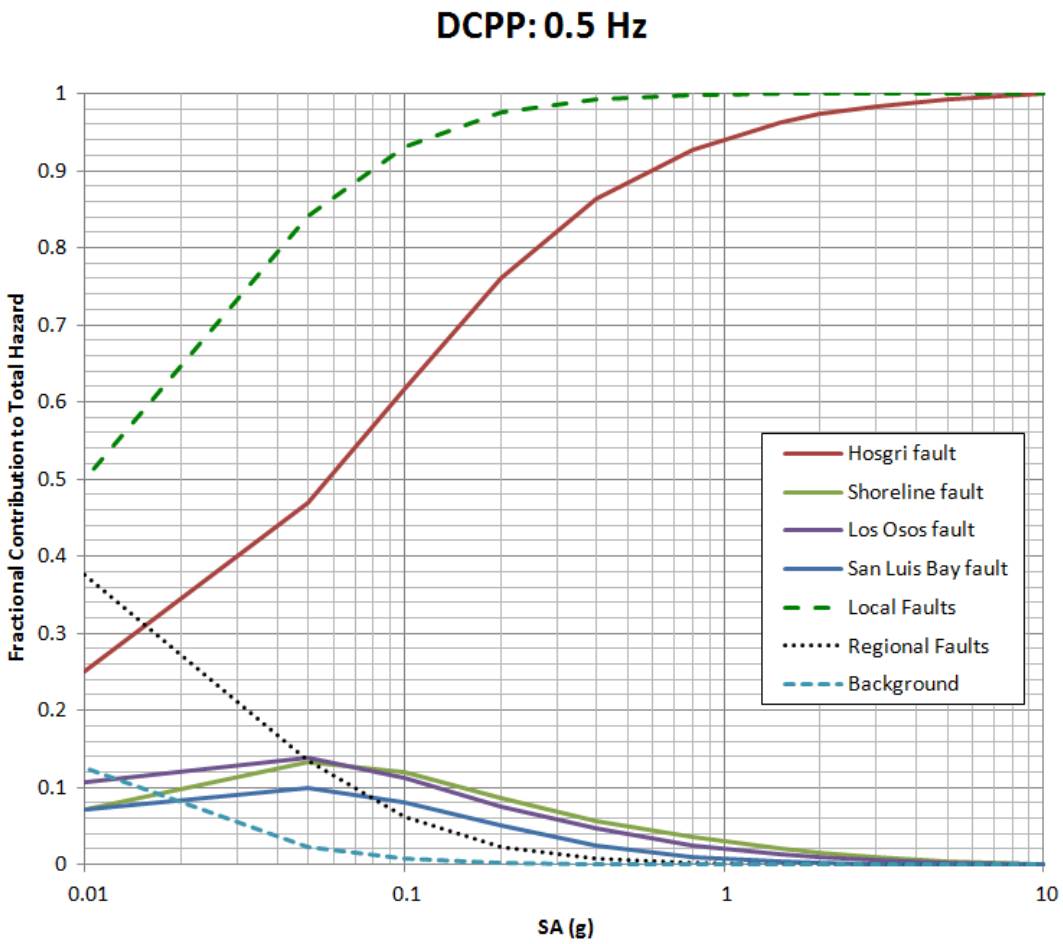

Figure 14.2-2: Deaggregation by source as a function of ground motions for 0.5 Hz spectral acceleration.

Figures 14.2-3a and 14.2-4a show deaggregation results by magnitude and distance for a mean hazard level of 10^{-4} for 5 Hz and 0.5 Hz spectral accelerations, respectively. Figures 14.2-3b and 14.2-4b show deaggregation results by magnitude and distance for a hazard level of 10^{-6} for 5 Hz and 0.5 Hz spectral accelerations, respectively. The deaggregation is computed from the mean hazard. Deaggregation plots show that the hazard at DCPP for spectral acceleration at both 5 Hz and 0.5 Hz is controlled by earthquakes within 10 km, which coincides with the shortest distances to the four local faults: Hosgri fault, Shoreline fault, Los Osos fault and San Luis Bay fault.

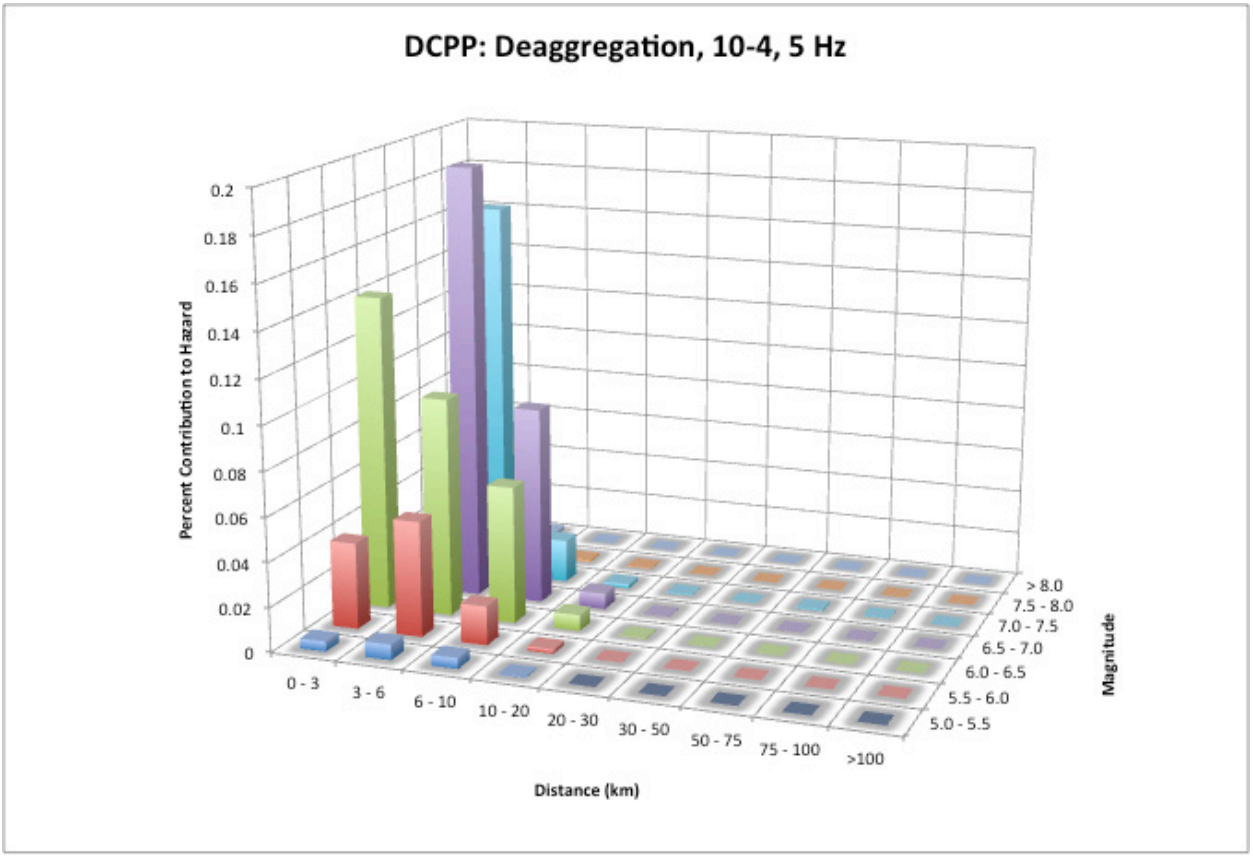

Figure 14.2-3a: Deaggregation of reference site condition (V_{S30} of 760 m/s) hazard at mean annual frequency of exceedance of 10^{-4} and at a spectral frequency of 5 Hz.

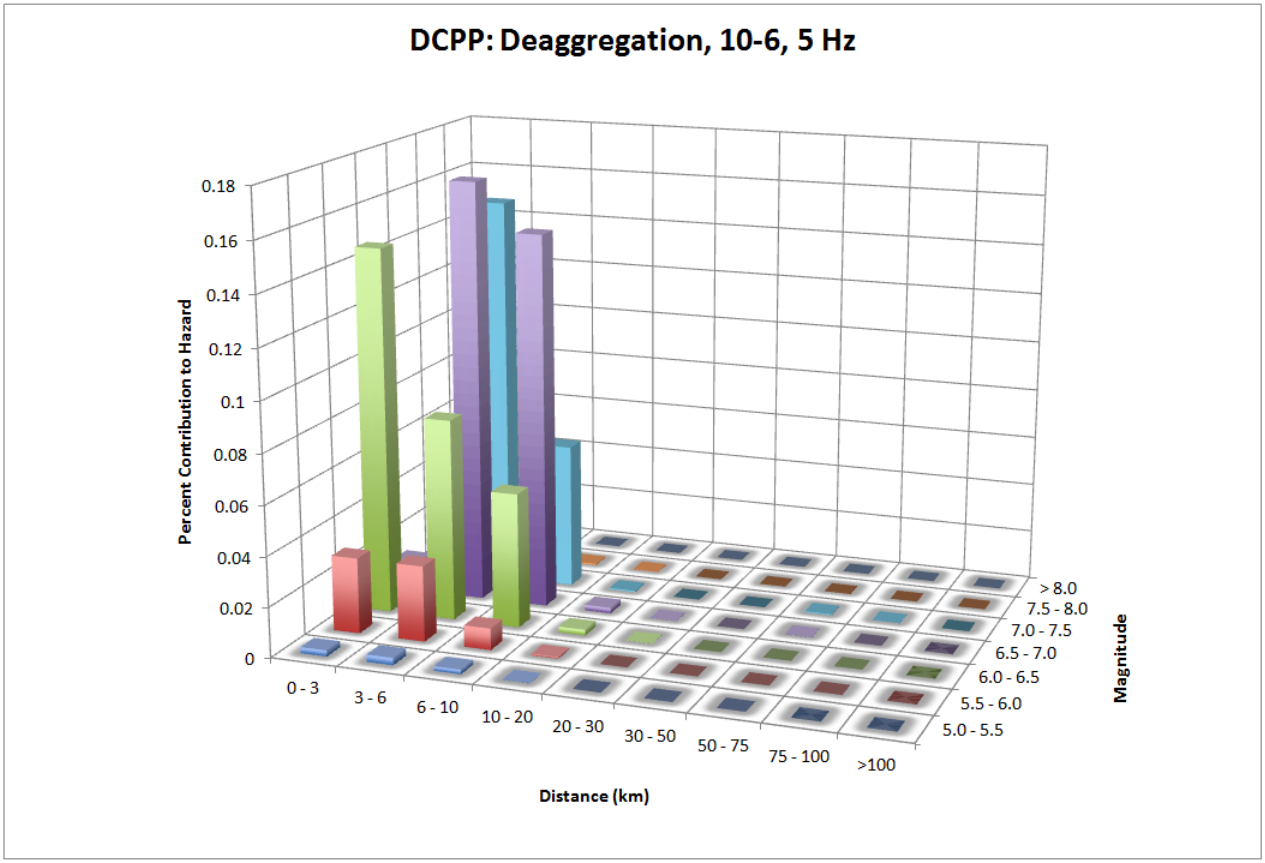

Figure 14.2-3b: Deaggregation of reference site condition (V_{S30} of 760 m/s) hazard at mean annual frequency of exceedance of 10^{-6} and at a spectral frequency of 5 Hz.

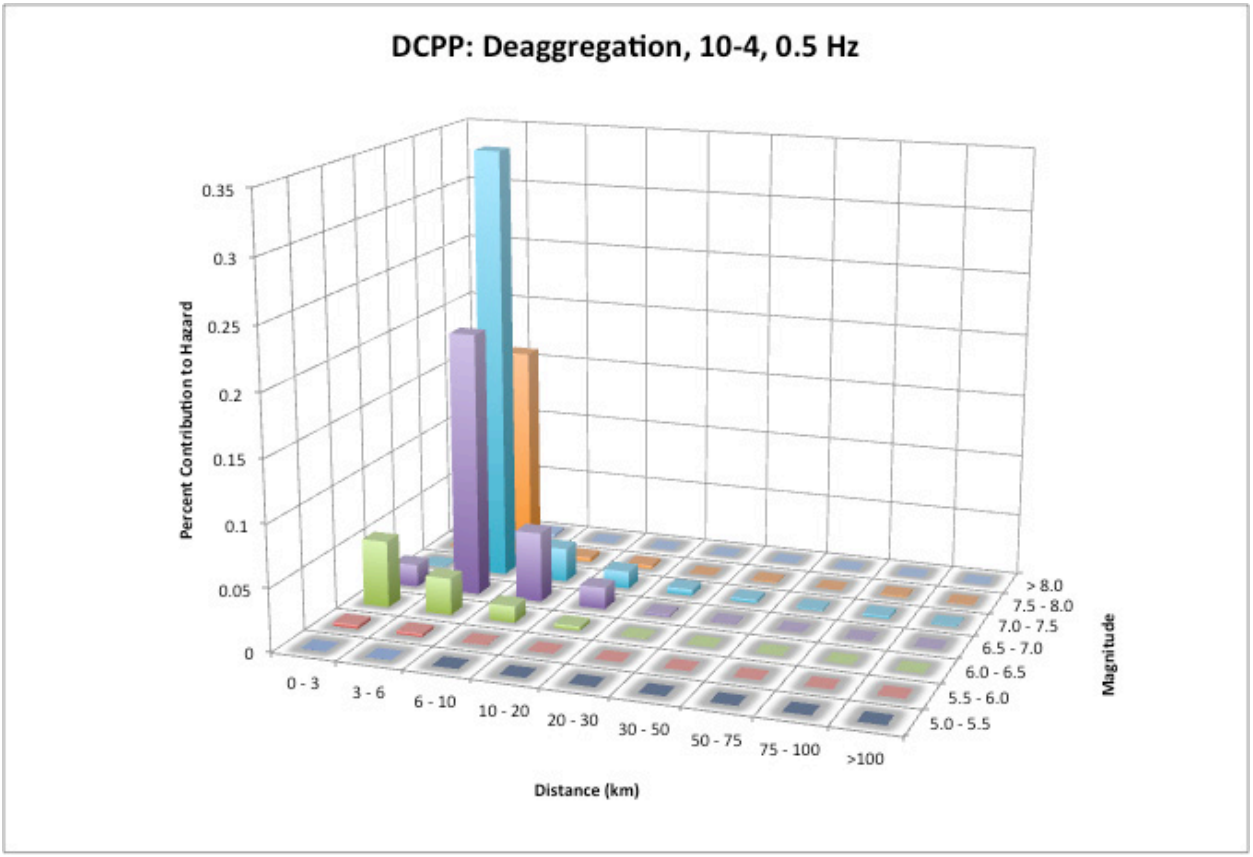

Figure 14.2-4a: Deaggregation of reference site condition (V_{S30} of 760 m/s) hazard at mean annual frequency of exceedance of 10^{-4} and at spectral frequencies of 0.5 Hz.

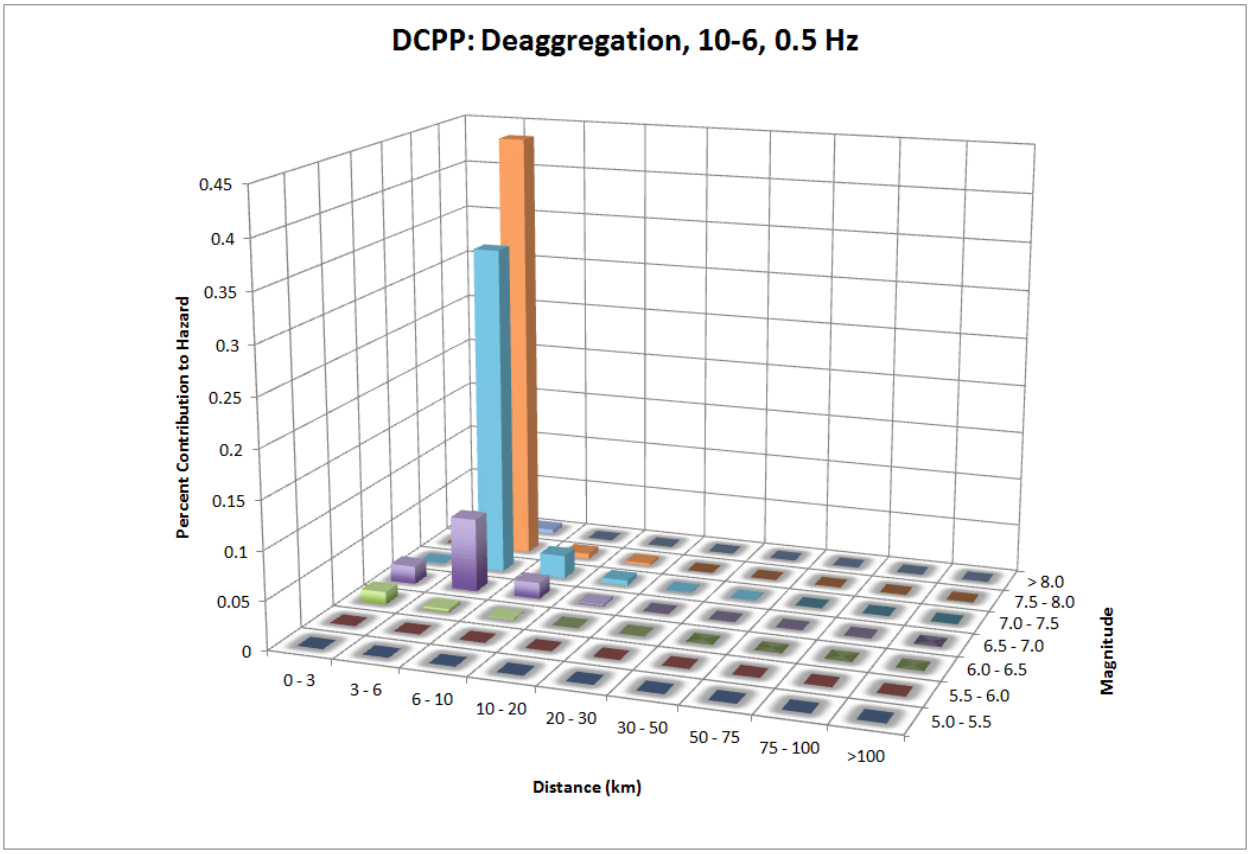

Figure 14.2-4b: Deaggregation of reference site condition (V_{S30} of 760 m/s) hazard at mean annual frequency of exceedance of 10^{-6} and at spectral frequencies of 0.5 Hz.

14.2.1 Median Models

The logic tree for the median ground motions at DCPP is shown in Chapter 8, Figure 8.2-1. The common functional form of the models developed for DCPP is based on the R_{RUP} distance metric (see Section 8.3). The hazard sensitivity results for the DCPP median ground motions in terms of normalized ground-motion ratios for 5 Hz spectral acceleration at the 10^{-4} and 10^{-6} hazard level are shown in the tornado plots in Figures 14.2-5a and 14.2-5b, respectively. The results for 0.5 Hz spectral acceleration are shown in Figures 14.2-6a and 14.2-6b. Each line in these figures represents one sensitivity case in which the single node of the logic tree is isolated.

The first sensitivity case shown in Figures 14.2-5 and 14.2-6 is for the representative suite of common-form median models. The number of models varies due to the sampling on the Sammon's maps. A total of 23 representative common-form models are selected for the 5 Hz case and 27 representative common-form models for the 0.5 Hz case. The sensitivity to the common-form models is plotted on the

top line of the tornado plots. The results for 5 Hz are similar between the 10^{-4} and 10^{-6} hazard levels. For the 0.5 Hz case, the spread is larger between the common-form models at the 10^{-6} hazard level than at the 10^{-4} hazard level.

The second sensitivity case addressed both the approach (comparison to data or prior) and the alternative datasets evaluated during the development of weights for the common-form model. NGA-West2 and simulation datasets were used in the development of the weights for the median common-form models for DCPP as presented in Figure 8.2-2. The sensitivity results are shown in the second line in the tornado plots.

The third to fifth lines in the tornado plots show the sensitivity to the suite of five hanging wall models. To reduce the calculations for these sensitivity cases, three representative common-form models were selected to represent models selected from the inner, middle and outer ellipses. For the 5 Hz case the three selected models were Model 5 (inner), 13 (middle), and 23 (outer) and for the 0.5 Hz case the three selected models were Model 5 (inner), 11 (middle), and 21 (outer). The five alternative HW models were then each given full weight for each of the three common-form models. The range of the HW sensitivities is small for all three common-form models used.

The last three lines in the tornado plots show the sensitivity to the directivity adjustment. As indicated in Figure 8.2-1, the directivity adjustment model is assigned a weight of 0 indicating that the directivity adjustment is never applied. For the sensitivity case, the hazard was also computed with the directivity adjustments to show the impact of the adjustment, even though the logic tree does not include the directivity case. The directivity adjustment affects both the median and the standard deviation. The hazard sensitivity shown in the tornado plots represents the total effect from directivity including both the median and standard deviation changes. For speed of calculation, the same three selected common-form models as used for the hanging wall comparison are used here. Note that the directivity adjustment is a low spectral frequency adjustment and for 5 Hz spectral acceleration there is no adjustment based on the directivity model. The range of the directivity effect is small and similar for each of the three common-form models used.

Based on these sensitivity cases for the median ground-motion logic tree, the uncertainty is dominated by the representative suite of common-form models, while the other parameters lead to a much smaller spread in the hazard values.

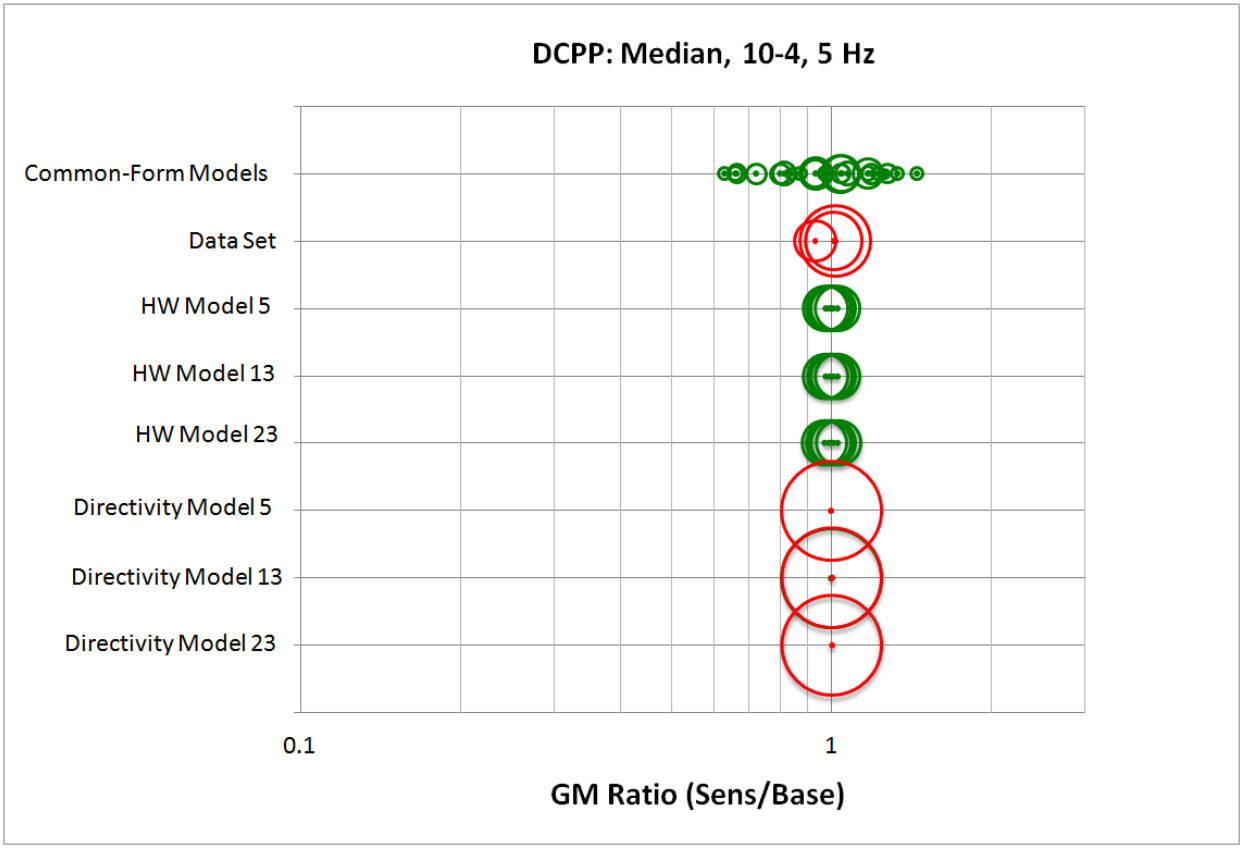

Figure 14.2-5a: Tornado plot for the median ground-motion logic tree for DCPP for 5 Hz spectral acceleration at the 10^{-4} hazard level.

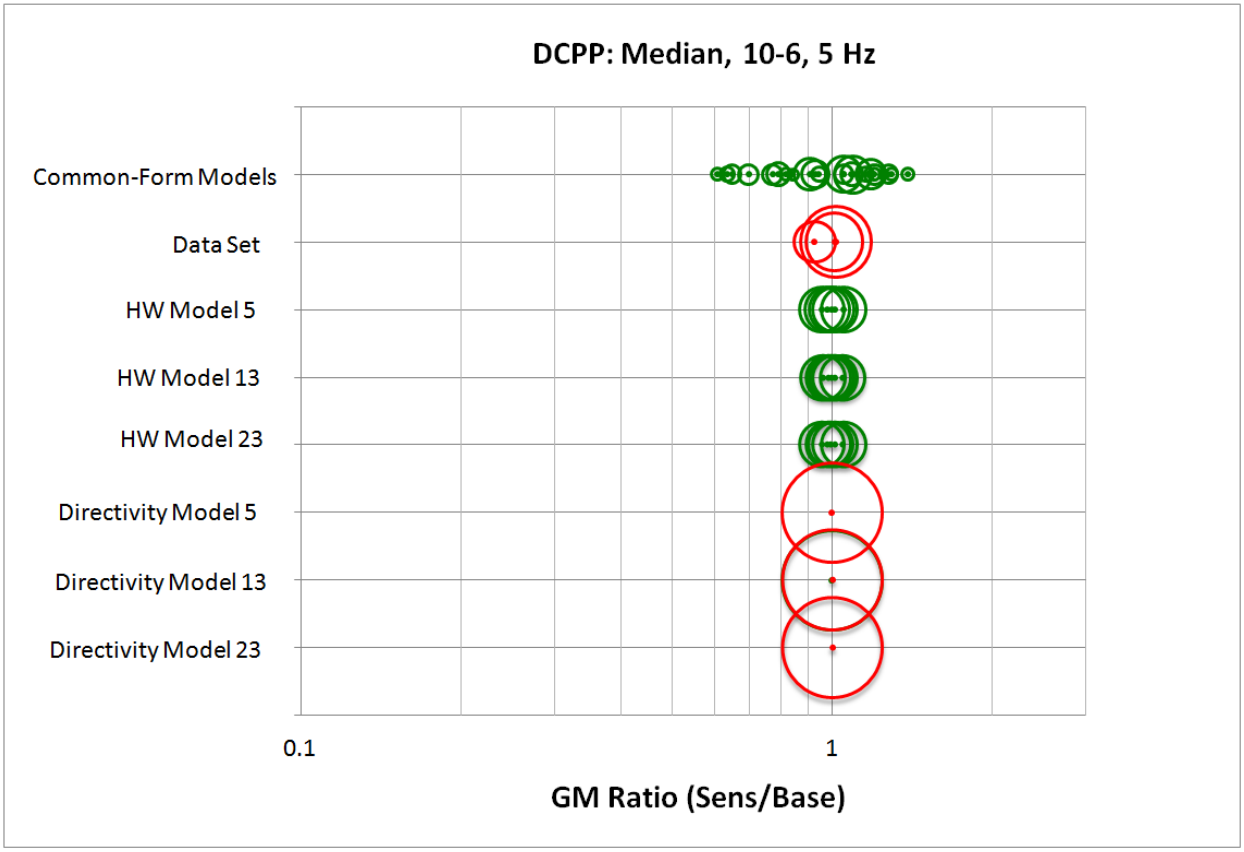

Figure 14.2-5b: Tornado plot for the median ground-motion logic tree for DCPP for 5 Hz spectral acceleration at the 10^{-6} hazard level.

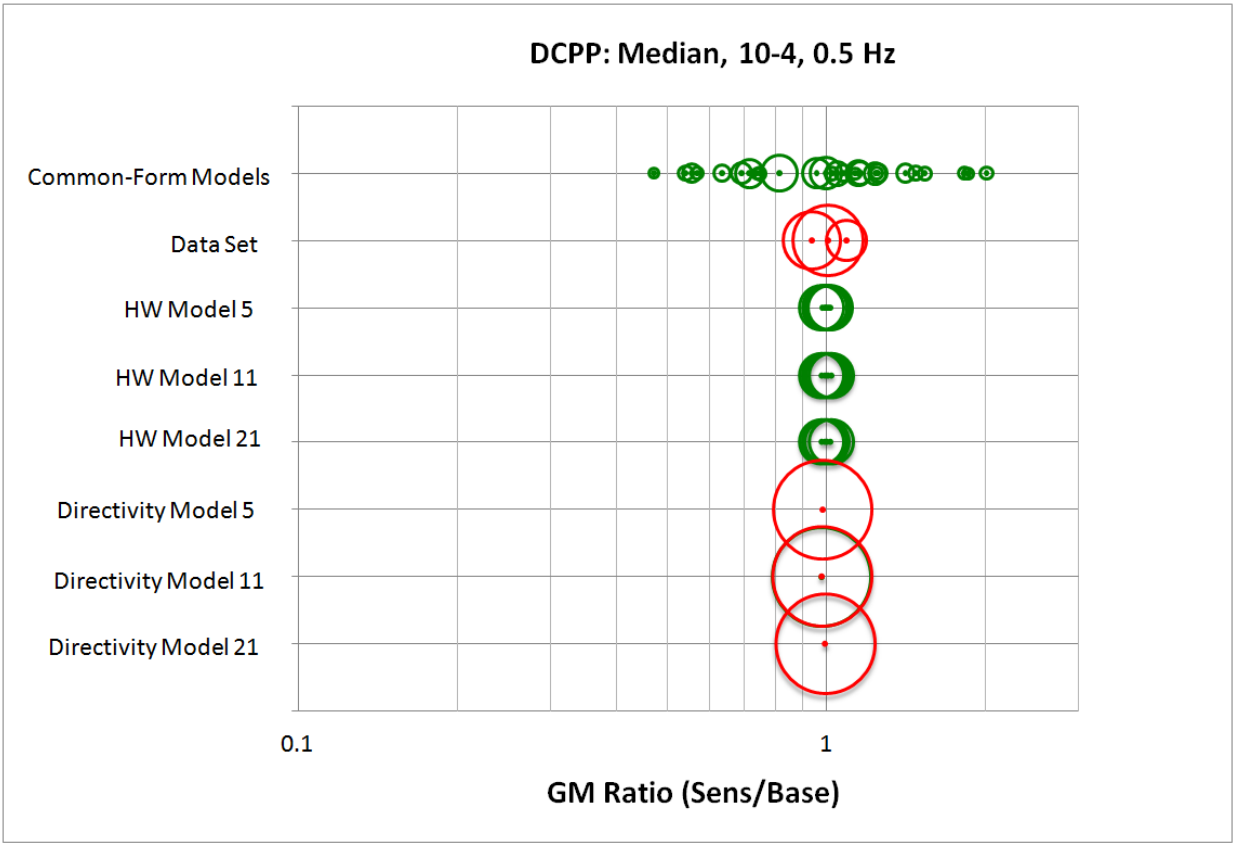

Figure 14.2-6a: Tornado plot for the median ground-motion logic tree for DCPP for 0.5 Hz spectral acceleration at the 10^{-4} hazard level.

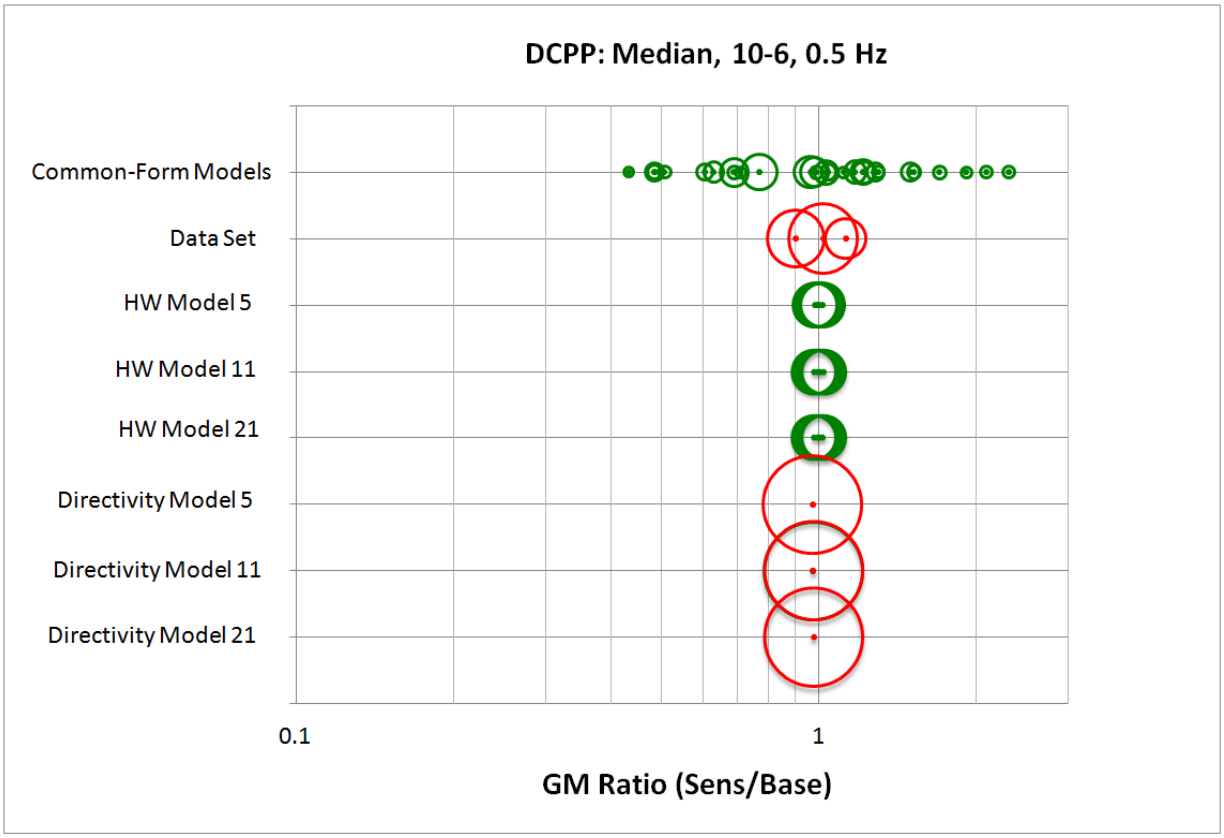

Figure 14.2-6b: Tornado plot for the median ground-motion logic tree for DCPP for 0.5 Hz spectral acceleration at the 10^{-6} hazard level.

14.2.2 Sigma Models

The sigma model described in Chapter 13 consists of a logic tree (see Figure 13.1-1) for the total sigma (combined between-event and within-event variability). For this hazard sensitivity, the separate logic tree for the τ (see Figure 10.1-1) and ϕ_{SS} (see Figure 11.1-1) terms, described in Chapters 10 and 11, are used rather than the total sigma logic tree to provide additional insights into the key contributors to the uncertainty. While the total sigma logic tree is more efficient for hazard calculations, the logic trees given in Chapters 10 and 11 provide all of the information for users of the model to conduct their own sensitivity studies for the contributions of ϕ and τ to the uncertainty in the hazard.

For all of the sensitivity analyses of the sigma models, only the central model (which is always denoted as Model 1) from the common functional-form model is used. For all of the cases except the mixture model, the standard normal distribution was used in the analyses. The same seismic source model used for the sensitivity analyses for the median ground motions is used in this case. The hazard sensitivity

results for the DCPP sigma models in terms of normalized ground-motion ratios for 5 Hz spectral acceleration at the 10^{-4} and 10^{-6} hazard level are shown in the tornado plots in Figures 14.2-7a and 14.2-7b, respectively. The results for 0.5 Hz spectral acceleration are shown in Figures 14.2-8a and 14.2-8b.

The logic tree for the τ model is given in Figure 10.1-1 and consists of a single magnitude-dependent model with three branches for the aleatory variability. For the sensitivity analyses, the individual branches of the τ model were combined with the weighted average of the ϕ_{SS} models, including only the central aleatory-variability branch on ϕ (see Figure 11.1-1). The sensitivity results for τ are shown in the second line of the tornado plots.

The logic tree for ϕ_{SS} for DCPP is presented in Figure 11.1-1. This logic tree contains several nodes, and sensitivity results will be presented for the different nodes and branches. For all of these analyses the central τ model (see Figure 10.1-1) was applied and the mixture model was only used for the specific analyses of the mixture model branch.

The first sensitivity analysis addresses the two alternative datasets used to compute ϕ_{SS} . The sensitivity results are shown in the fifth line from the top of the tornado plots in Figures 14.2-7 (a and b) and 14.2-8 (a and b), and they are based on using only the central branch of the ϕ_{SS} models. The California data set corresponds to the lower ratio point in the fifth line and the Global data set corresponds to the higher ratio point in the same line.

The second sensitivity analysis for the ϕ_{SS} addresses the two alternative functional forms for the California model, which has one magnitude-independent and one magnitude-dependent form (see Figure 11.1-1). The sensitivity results are shown in the bottom line of the tornado plots in Figures 14.2-7 (a and b) and 14.2-8 (a and b). As before, these results are based on the central τ model along with the central ϕ_{SS} value for the specific cases. These sensitivity results indicate that both the magnitude-independent and magnitude-dependent models for California produce very similar ground-motion ratios.

The next sensitivity analysis on the ϕ_{SS} logic tree addresses the epistemic uncertainty of the ϕ_{SS} models due to the sample-size limitations. The epistemic uncertainty is developed for the California and Global models separately. The sensitivity results for the three branches are shown in the third and fourth lines in the tornado plots, respectively, in Figures 14.2-7 (a and b) and 14.2-8 (a and b). Note that for the California case these results include the equal weighting of the magnitude-independent and magnitude-dependent models.

The last sensitivity analysis on the ϕ_{SS} logic tree addresses the aleatory distribution form, which includes a mixture and a normal model as alternatives. The sensitivity results are shown in the sixth and seventh

lines in the tornado plots in Figures 14.2-7 (a and b) and 14.2-8 (a and b). For these sensitivity analyses, the two end member ϕ_{SS} models were selected. Specifically, the Global model with the high epistemic uncertainty branch (i.e., Mixture High) and the California model with the low epistemic uncertainty branch (i.e., Mixture Low) were selected. For the τ values, the high τ model was combined with the Global-high ϕ_{SS} model and the low τ model was combined with the California-low ϕ_{SS} model. Thus, the sensitivity results represent the expected end member cases and not the average or full distribution of cases. The relative difference between the normal and mixture model ratio values indicates the impact on the ground motions using either the normal or mixture distribution for these end cases. In general, at the 10^{-4} hazard level, the sensitivity due to the mixture model is less than the sensitivity due to the other parameters; however, at the 10^{-6} hazard level, the sensitivity due to the mixture model is similar to the sensitivity range due to the other parameters. The expected full weighted impact of the aleatory distribution form would be less than the results for these two bounding end member cases.

The final sensitivity shown in the tornado plots addresses the total sigma model for DCPP shown in Figure 13.1-1, which is a magnitude-dependent model with central, low, and high epistemic uncertainty branches. The hazard sensitivity results shown in the top line of the tornado plots in Figures 14.2-7 (a and b) and 14.2-8 (a and b) are based on the use of the central common-form model (Model 1). These results are also computed only using the traditional normal-distribution model (without the mixture distribution model). Overall, the tornado plots show that most of the branches in the ϕ_{SS} and τ models lead to similar ranges of the hazard. There is no single dominant contributor to uncertainty as was seen in the median sensitivity analyses. The alternative magnitude-dependences for the California models lead to the smallest impact on the hazard.

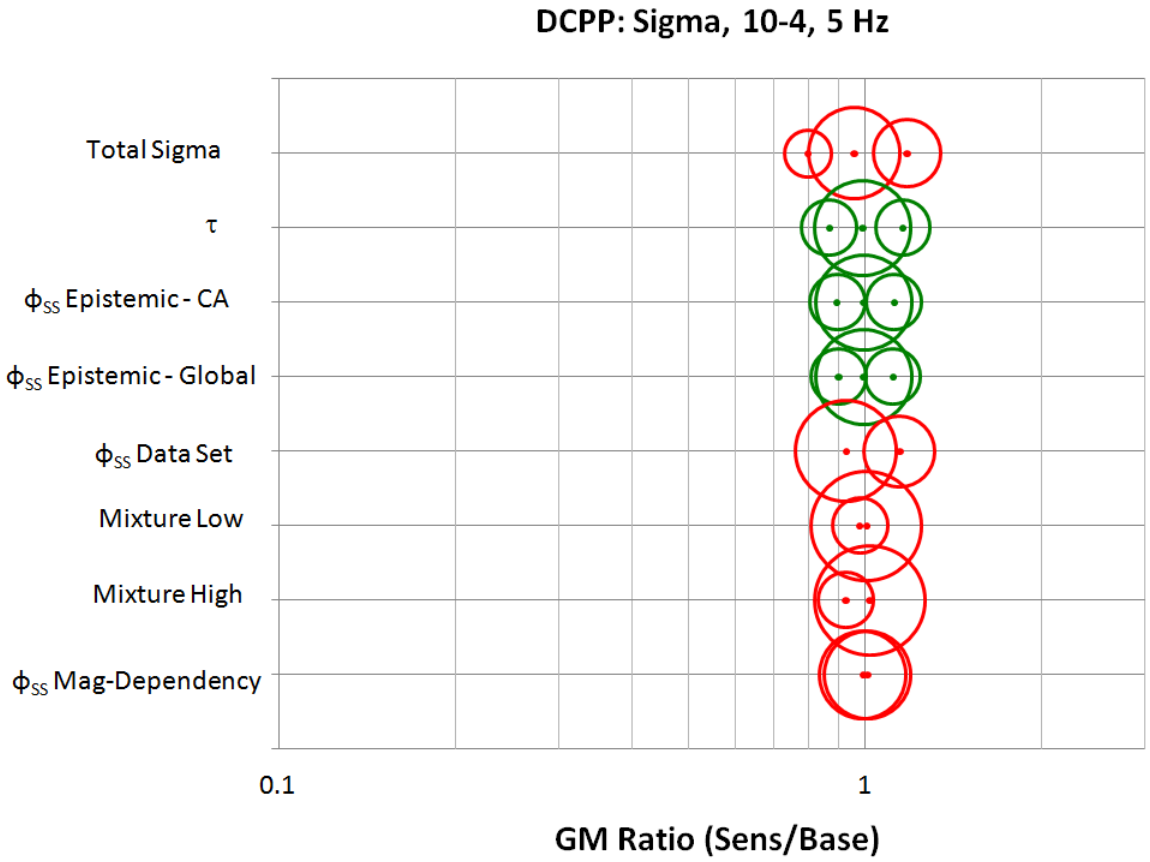

Figure 14.2-7a: Tornado plot for the sigma model logic tree for DCPP for 5 Hz spectral acceleration at the 10^{-4} hazard level.

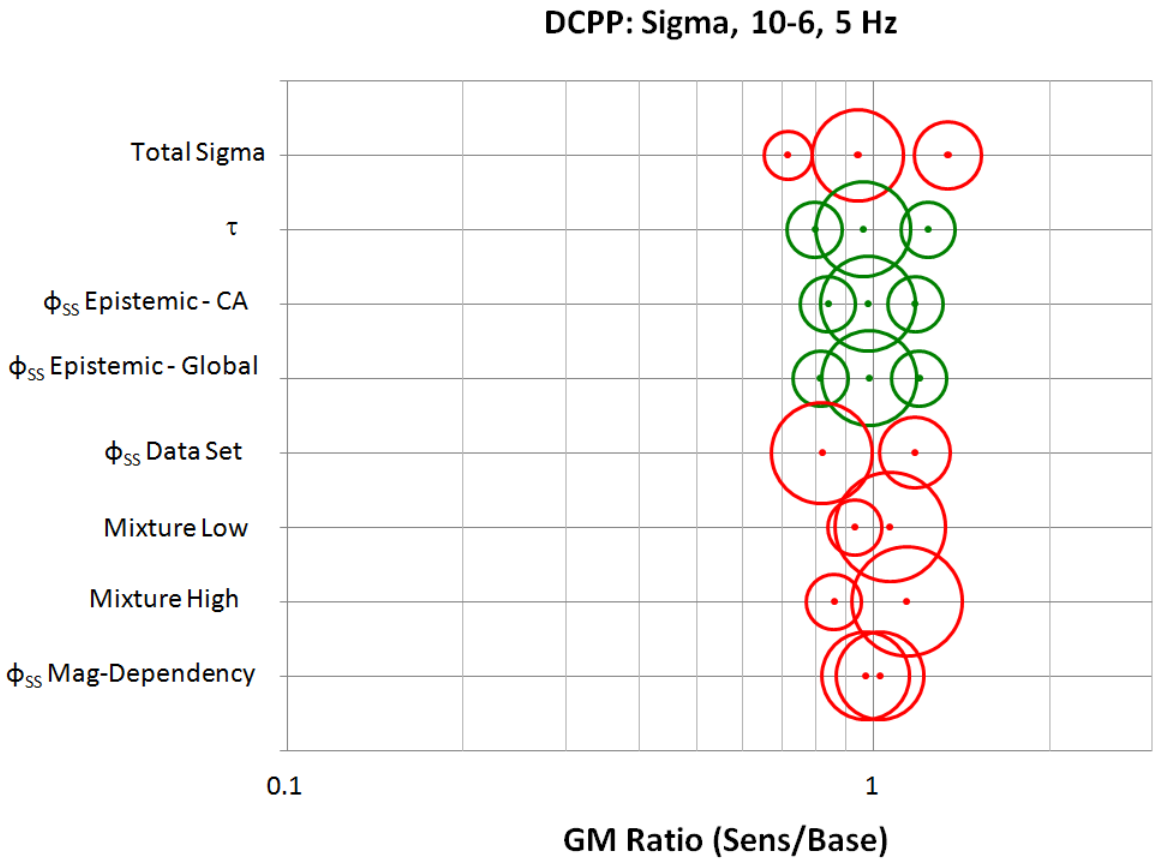

Figure 14.2-7b: Tornado plot for the sigma model logic tree for DCPP for 5 Hz spectral acceleration at the 10^{-6} hazard level.

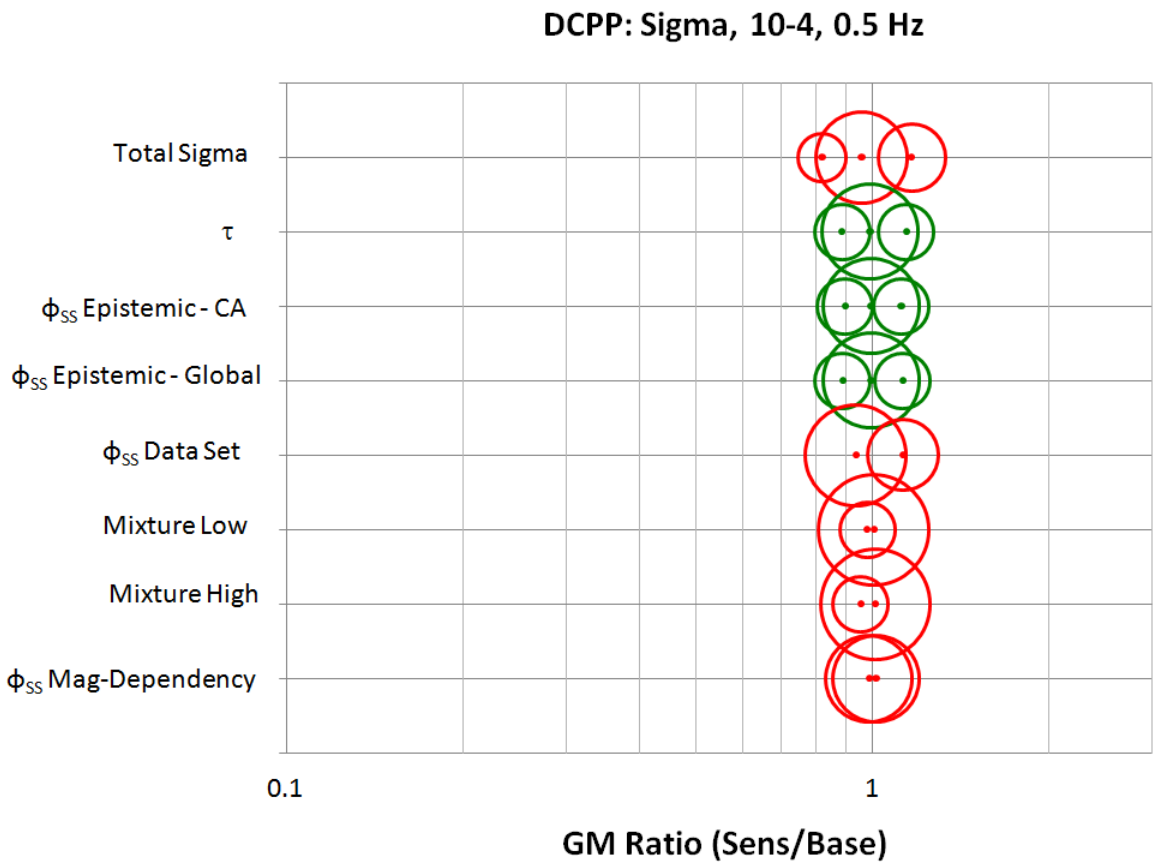

Figure 14.2-8a: Tornado plot for the sigma model logic tree for DCPP for 0.5 Hz spectral acceleration at the 10^{-4} hazard level.

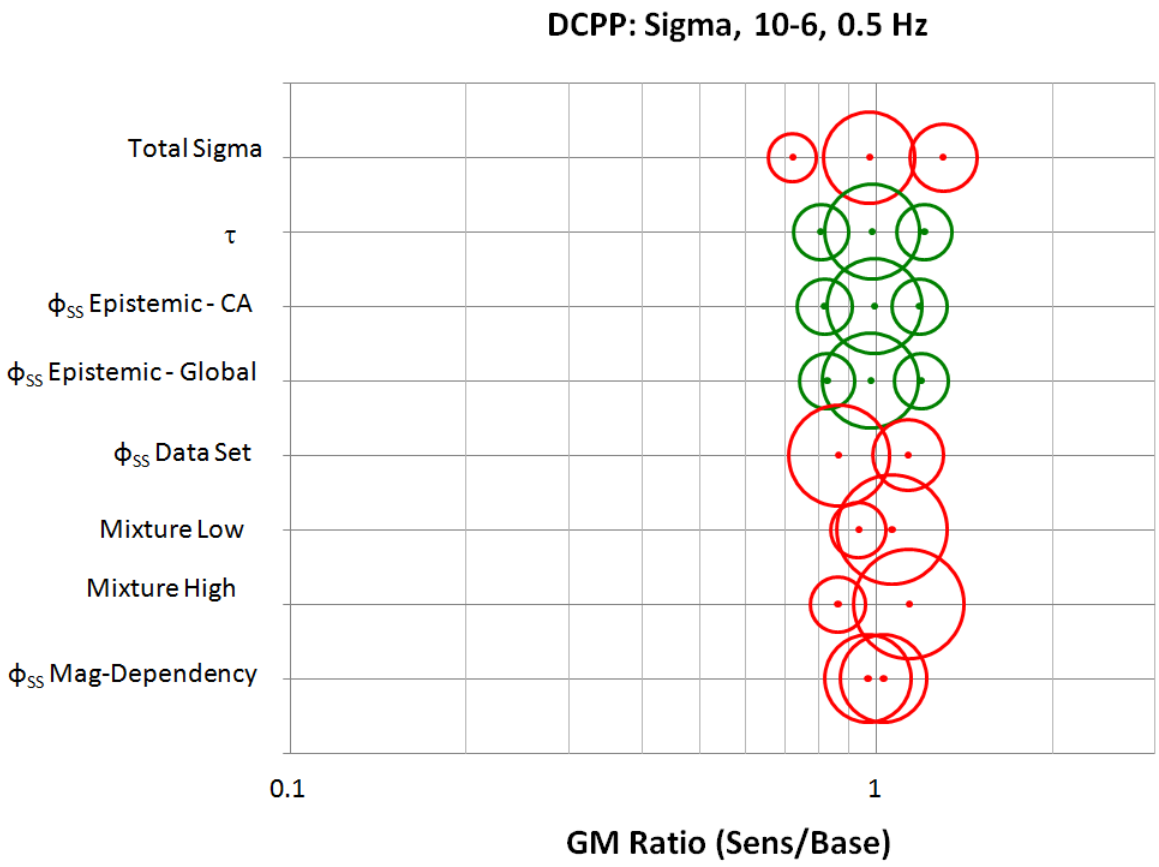

Figure 14.2-8b: Tornado plot for the sigma model logic tree for DCPP for 0.5 Hz spectral acceleration at the 10^{-6} hazard level.

14.2.3 Summary of Sensitivity Analyses for DCPP

Based on these sensitivity analyses, summary tornado plots are provided for the two spectral frequencies of 5 and 0.5 Hz at the two hazard levels of 10^{-4} and 10^{-6}. The DCPP hazard sensitivity results, in terms of normalized ground-motion ratios for 5 Hz spectral acceleration at the 10^{-4} and 10^{-6} hazard level, are shown in the tornado plots in Figures 14.2-9a and 14.2-9b, respectively. The results for 0.5 Hz spectral acceleration are shown in Figures 14.2-10a and 14.2-10b. In these plots, the symbol size is constant and not scaled as a function of the individual weights for a specific branch of the logic tree. Similar to the previous plots, however, the green symbols are for statistically based weights and the red symbols are for the judgment based weights.

The sensitivity analyses results summarized in the plots indicate that the largest uncertainty is for the selection of the representative common-form models, followed by the sigma models.

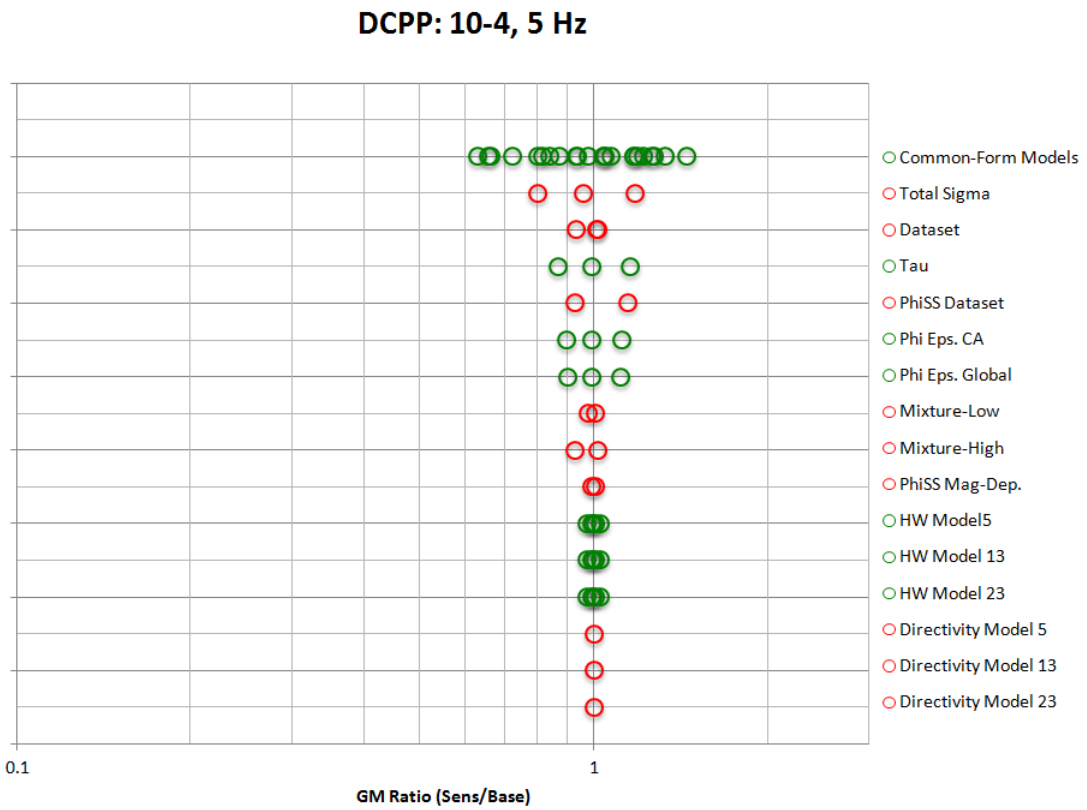

Figure 14.2-9a: Summary tornado plot for DCPP for 5 Hz spectral acceleration at the 10^{-4} hazard level.

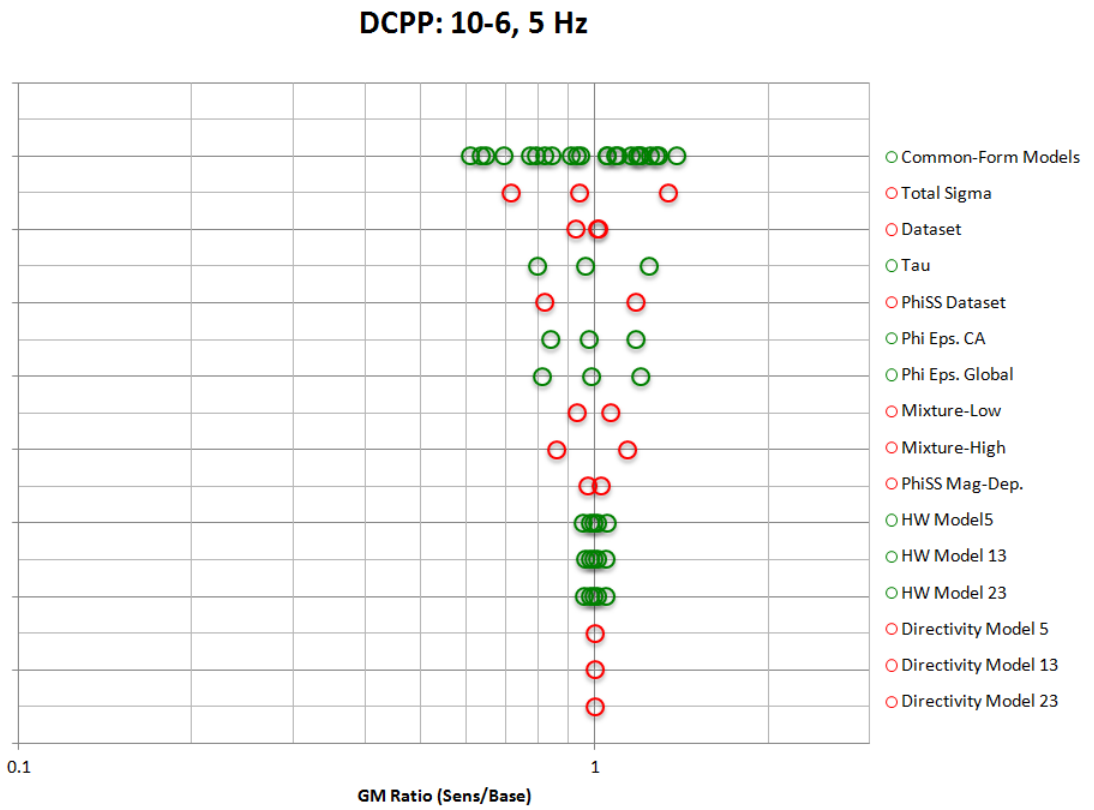

Figure 14.2-9b: Summary tornado plot for DCPP for 5 Hz spectral acceleration at the 10^{-6} hazard level.

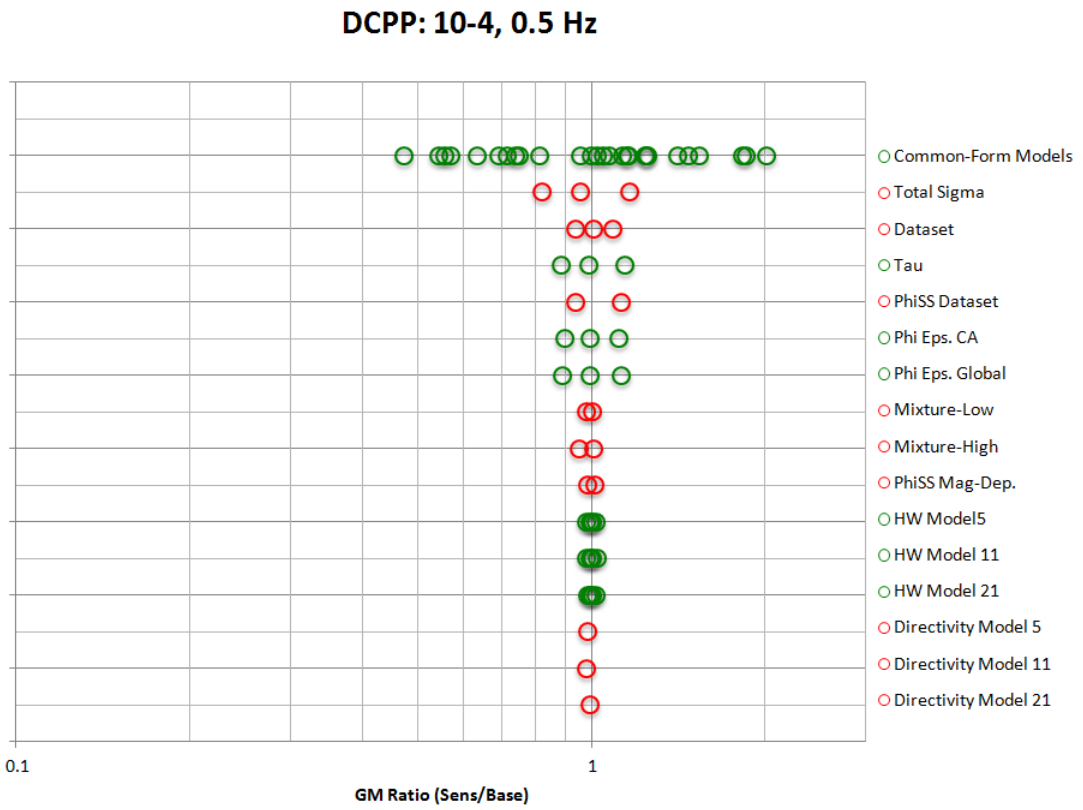

Figure 14.2-10a: Summary tornado plot for DCPP for 0.5 Hz spectral acceleration at the 10^{-4} hazard level.

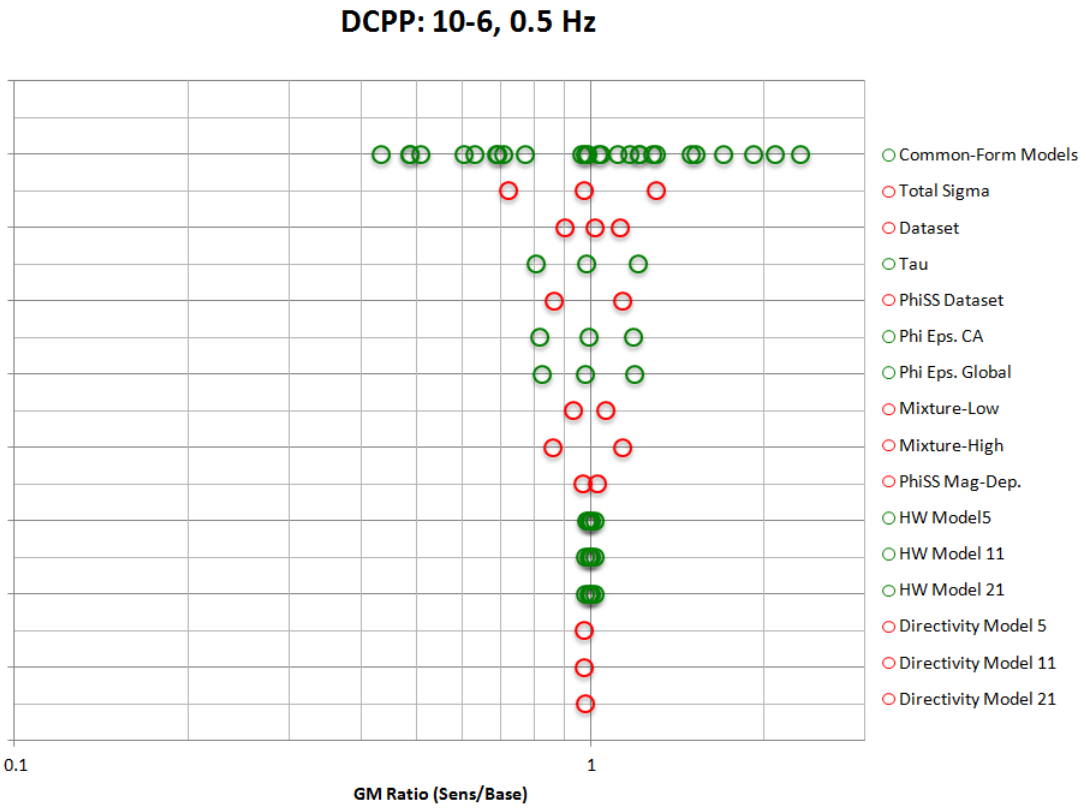

Figure 14.2-10b: Summary tornado plot for DCPP for 0.5 Hz spectral acceleration at the 10^{-6} hazard level.

14.3 Deaggregation and Sensitivity Analyses - PVNGS

The seismic source model given in LCI (2013) consists of areal sources and fault sources. The seismic source inputs to the hazard sensitivity calculations performed here using a simplified version of the PVNGS SSHAC Level 2 Seismic Source Characterization (SSC) model (LCI, 2013). The areal source model was reduced from the two-alternative zonation ('fine' and 'coarse' models) to just the 'fine' zonation areal source model for these sensitivity analyses. The fine zonation approach, which had a higher associated weight, is based on uniform seismicity rates within each zone and included eleven areal sources that were based on seismicity, geology, fault activity, topography and structural style. Previous results also indicated that the fine zonation model was the primary contributor to the PVNGS background source hazard.

The fine sources, all of which lie within 320 km of the PVNGS site, are identified according to the following 11 physiographic provinces whose names are consistent with the nomenclature applied to the fine zonation in the PVNGS SSHAC Level 2 project (LCI, 2013, and Figure 3.17 therein):

1. Colorado Plateau (CP)
2. Northern Arizona Seismic Belt (NASB)
3. Arizona Transition Zone A (TZA)
4. Arizona Transition Zone B (TZB)
5. Arizona Transition Zone C (TZC)
6. Sonora Basin and Range (SBR [1])
7. Nevada Basin and Range (NBR)
8. Mexican Highland Basin and Range (MHBR)
9. Gulf of California (GULF)
10. Baja California (B)
11. Southern California (SC)

In addition to the suite of background areal source zones, a total of 26 fault sources were identified in the PVNGS SSHAC Level 2 project that, when combined with the background zone, account for 99% of the total hazard (see Table 3.1 in LCI, 2013 for more details on the source zone characterization). The same faults were utilized as fault source inputs to the hazard sensitivity calculations performed here. The 26 faults included in the hazard calculations were the following:

1. Cerro Prieto fault (CP - F)
2. San Andreas fault (SA)
3. San Jacinto fault (SJ)

[1] According to the PVNGS SSHAC Level 2 project for PVNGS (LCI, 2013), the host source is called Sonoran Basin and Range, but in the SSHAC Level 3 project (LCI, 2014) it is called the Southern Basin and Range

4. Imperial fault (IMP)
5. Laguna Salada fault (LS)
6. Agua Blanca fault (AB)
7. Elsinore fault (EL)
8. Calico-Hidalgo fault (CH)
9. Pinto Mountain fault (PM)
10. Canada David Detachment (CD)
11. Libertad fault (LI)
12. San Pedro Martir Escarpment (SPME)
13. Lenwood-Lockhart-Old Women Spring fault (LLOWS)
14. Pisgah-Bullion Mountain-Mesquite Lake fault (PBMML)
15. Big Chino Little Chino fault (BCLC)
16. Superstition Hills fault (SH)
17. Landers fault (LA)
18. Vallecitos fault (VA)
19. San Miguel fault (SM)
20. Hurricane fault (Central) (HC)
21. Hurricane fault (Southern) (HS)
22. Helendale-South Lockhart fault (HSL)
23. Sand Tank fault (ST)
24. Williamson Valley Grabens (WVG)
25. Horseshoe fault zone (HS)
26. Carefree fault zone (CF)

These fault sources (1 to 26 listed above) fall mainly within either Region 1 or Regions 2&3 (Figure 4.2-2) as defined for the GMC logic trees (distant sources in California and Mexico). The GMC TI Team selected the boundaries for Region 1 and Region 2&3 based on the path-effects evaluation using the PEER-AZ_{PATH} dataset, and on the boundaries of the source zone from the preliminary PVNGS SSC SSHAC Level 3 model. The Hurricane faults (Central and Southern), Sand Tank fault, Williamson Valley Grabens, Horseshoe fault zone and Carefree fault zone fall instead into the Greater Arizona source region. All fault sources have estimated distributions of slip rate from which the frequency of occurrence of large earthquakes is calculated. Additionally, distributions on the potential sizes of those large earthquakes have been assessed. For the purpose of these hazard sensitivity calculations, a single maximum magnitude with a pure characteristic earthquake magnitude distribution (delta function for the magnitude probability density function) has been used. Also, each fault source has a fault width distribution and several sources have dip distributions with alternative fault-types.

Figures 14.3-1 and 14.3-2 plot the fractional contribution of the different seismic sources to the total mean hazard. This fractional contribution was computed by dividing the hazard from a single source by

the total hazard. These curves are computed based on the weighted combination of the representative suite of common-form models (i.e., Model A and Model B) for the Greater Arizona sources and the weighted models for the other distant sources in Regions 1 and 2&3. For these results, a common sigma value given by the BSSA14 model was used. For 5 Hz spectral acceleration, the curves shown in Figure 14.3-1 indicate that the host areal source zone (SBR) is the significant contributor to the total hazard for ground motions greater than about 0.04g. For ground-motion values greater than about 0.1g (about 10^{-3} AFE) this host zone controls more than 90% of the total hazard. For ground motions less than 0.04g, the Region 1 and 2&3 sources are the controlling sources for the total hazard. The other sources have a minimal contribution to the total hazard.

The results for 0.5 Hz spectral acceleration are shown in Figure 14.3-2. For ground motions less than about 0.1g (corresponding to hazard level of about 10^{-5} AFE), the Region 1 and 2&3 sources are the controlling sources for the total hazard with the host zone source having the next significant contribution to the total hazard. For ground motions greater than 0.1g, the relative contribution to the total hazard switches with the host source zone being the main contributing source to the total hazard while the Region 1 and 2&3 sources contribute less.

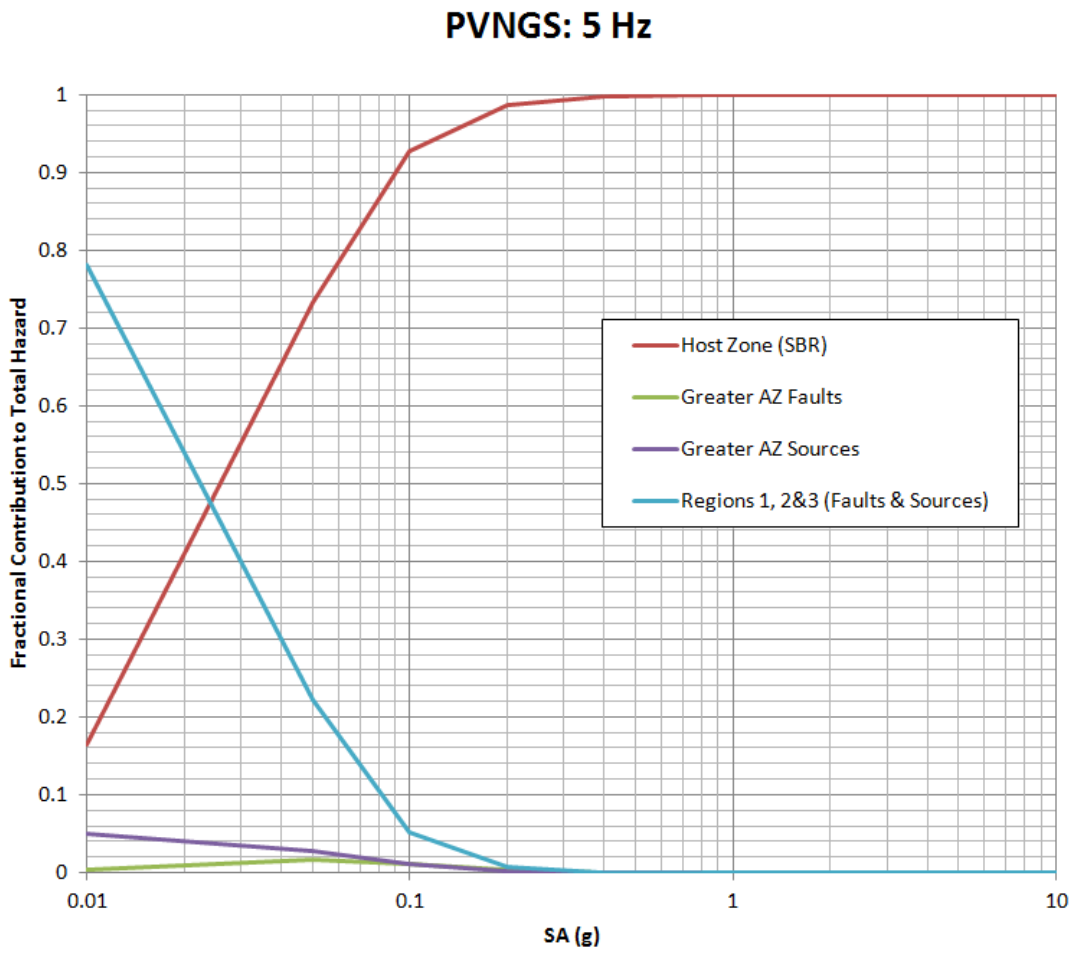

Figure 14.3-1: Deaggregation by source as a function of ground motions for 5 Hz spectral acceleration.

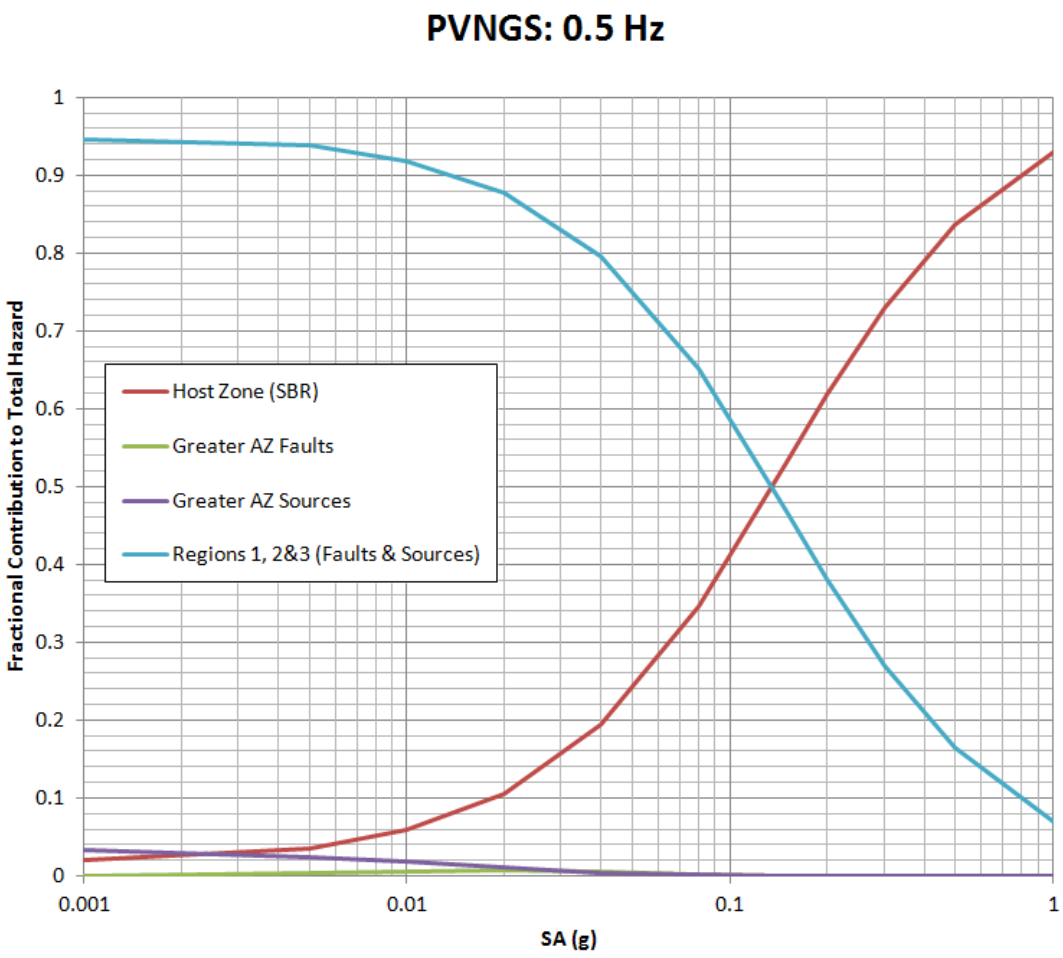

Figure 14.3-2: Deaggregation by source as a function of ground motions for 0.5 Hz spectral acceleration.

Based on the results of previous studies (LCI, 2013) at PVNGS, the local areal sources are the dominant contributor to hazard at the higher spectral frequencies and a smaller percentage of the hazard at the low spectral frequencies. The distant fault sources are the dominant contributor to hazard at lower spectral frequencies (for hazard levels greater than 10^{-5}), but they are expected to contribute only a small percentage of the hazard at the higher spectral frequencies.

Figures 14.3-3a and 14.3-4a show deaggregation results by magnitude and distance for spectral accelerations corresponding to hazard level of 10^{-4} for 5 Hz and 0.5 Hz spectral accelerations, respectively. Figures 14.3-3b and 14.3-4b show deaggregation results by magnitude and distance for spectral accelerations corresponding to hazard level of 10^{-6} for 5 Hz and 0.5 Hz spectral accelerations, respectively. For hazard level of 10^{-4} and 5 Hz spectral acceleration, local magnitude earthquakes (i.e. with **M**5 to **M**7 at distances less than 50 km) dominate the hazard. For hazard level of 10^{-4} and 0.5 Hz spectral acceleration, distant large earthquakes (i.e. with **M**6.5 to **M**8 at distances above 200 km) on the

San Andreas, San Jacinto, and Cerro Prieto faults represent an important contribution to seismic hazard. The low-frequency deaggregation plot shows these contributions at magnitudes around 8 and distances of about 220 km. The deaggregation plots for the 10^{-6} hazard level lead to similar conclusions with the noted exception of a reduction of the relative contribution from the distant sources for the 0.5 Hz spectral acceleration case with an increase relative contribution from the local Greater Arizona sources.

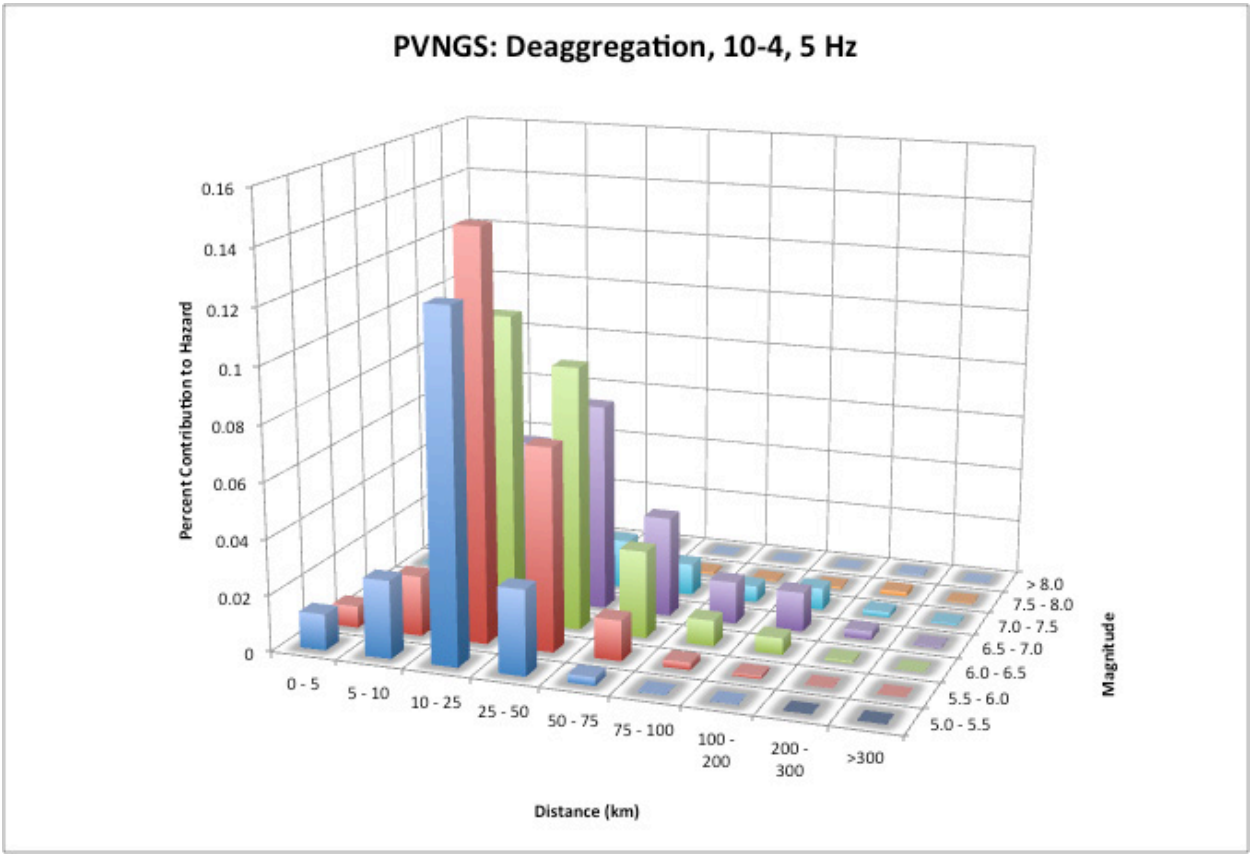

Figure 14.3-3a: Deaggregation of reference site condition (V_{S30} of 760 m/s) hazard at mean annual frequency of exceedance of 10^{-4} and at spectral frequencies of 5 Hz.

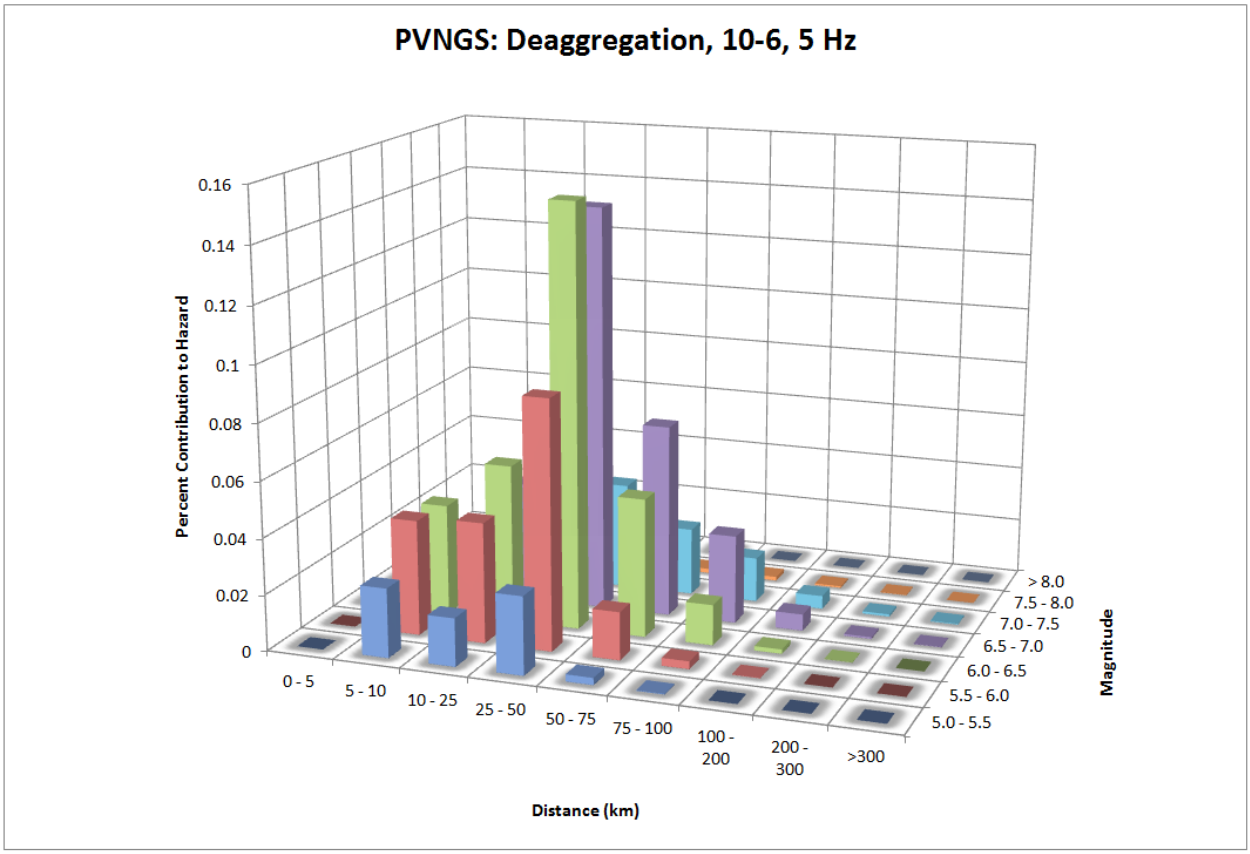

Figure 14.3-3b: Deaggregation of reference site condition (V_{S30} of 760 m/s) hazard at mean annual frequency of exceedance of 10^{-6} and at spectral frequencies of 5 Hz.

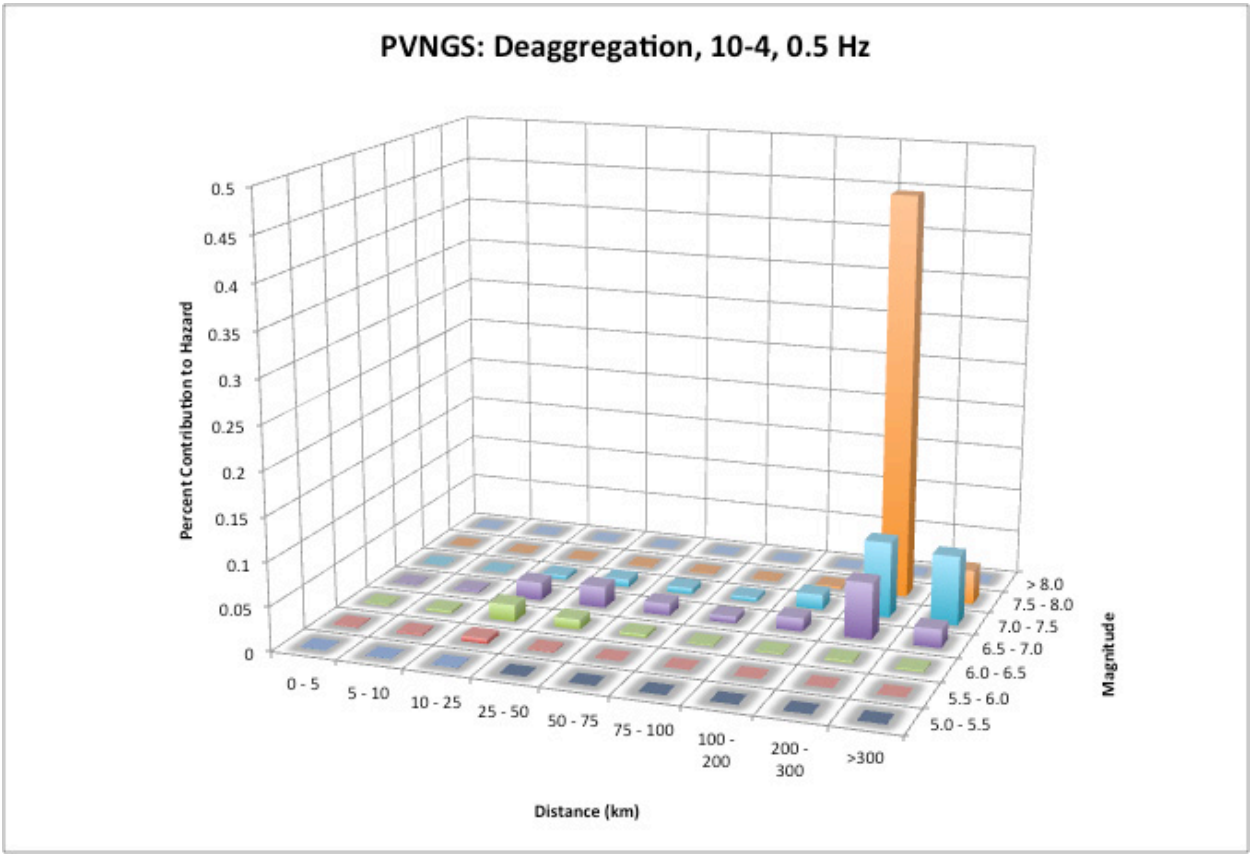

Figure 14.3-4a: Deaggregation of reference site condition (V_{S30} of 760 m/s) hazard at mean annual frequency of exceedance of 10^{-4} and at spectral frequencies of 0.5 Hz.

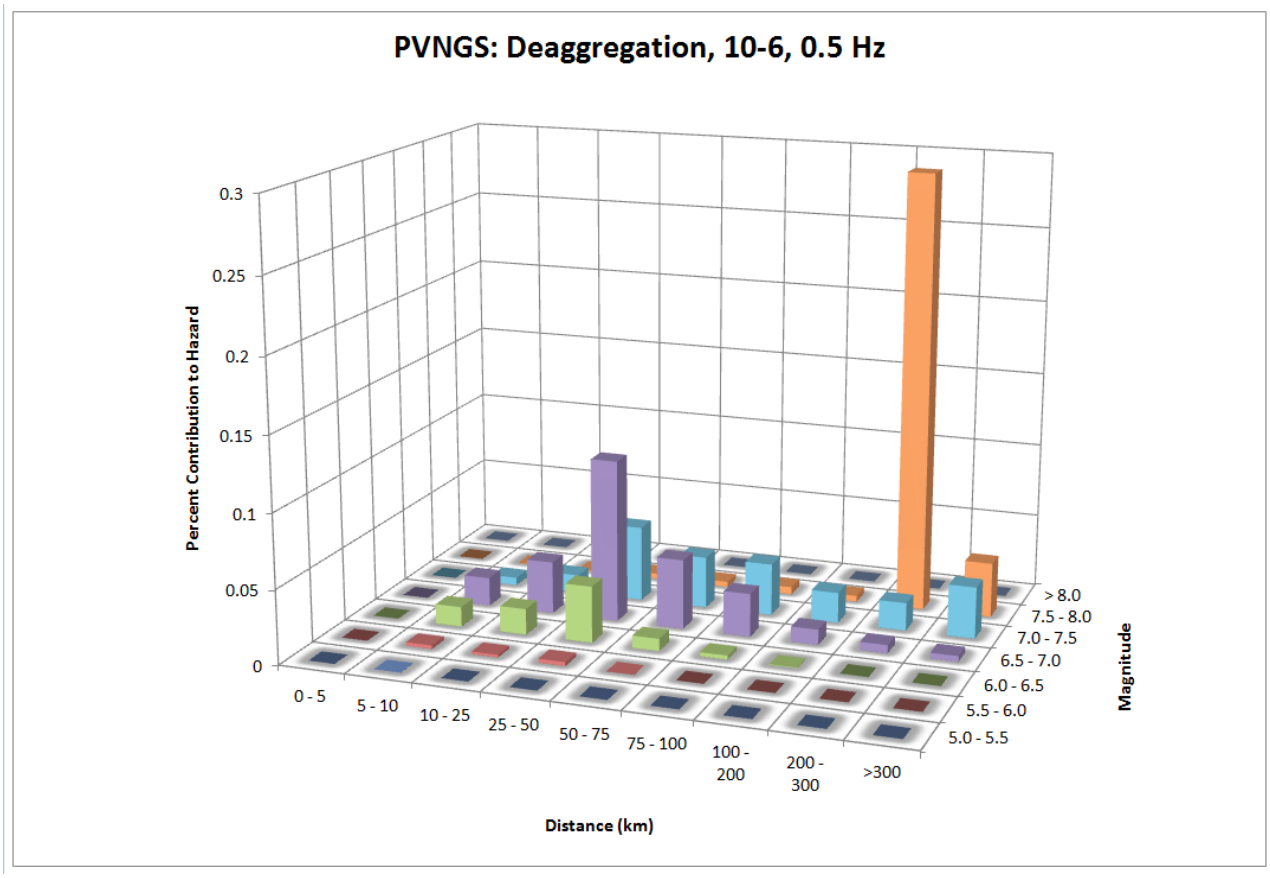

Figure 14.3-4b: Deaggregation of reference site condition (V_{S30} of 760 m/s) hazard at mean annual frequency of exceedance of 10^{-6} and at spectral frequencies of 0.5 Hz.

14.3.1 Median Base Models – Greater Arizona Sources

In the sensitivity analysis for the PVNGS site, separate logic trees were developed for the Greater Arizona seismic sources and for the more distant seismic sources located in Southern California and Mexico (i.e., referred to as Regions 1 and 2&3). As such, the number of logic-tree nodes is twice the number for the DCPP site. As was the case for the DCPP cases, different base case results were used for the sensitivity analysis associated with different branches of the logic trees. In the results that follow, the hazard includes both the Greater Arizona sources and the sources in Regions 1 and 2&3.

The logic tree for the median ground motions at PVNGS from the Greater Arizona sources is shown in Figure 9.1-1. The hazard sensitivity results for the PVNGS median ground motions in terms of normalized ground-motion ratios for 5 Hz spectral acceleration at the 10^{-4} and 10^{-6} hazard levels are shown in the tornado plots in Figures 14.3-5a and 14.3-5b, respectively. The results for 0.5 Hz spectral accelerations

are shown in Figures 14.3-6a and 14.3-6b. The directivity model was not applied to PVNGS because there are no known active faults close to the site (see Section 9.1.4). Therefore, the directivity model was not included in the sensitivity analysis.

The first sensitivity analysis addresses the alternative distance metric for the development of the common-form models: the R_{RUP} distance associated to common-form Model A and the R_{JB} distance associated to common-form Model B. The sensitivity results shown in the fourth line of the tornado plots in Figures 14.3-5 (a and b) and 14.3-6 (a and b) indicate that there is relatively little impact of the distance-metric choice as compared to the other logic-tree branches.

The second sensitivity analysis addresses the alternative median ground-motion models for the Greater Arizona sources. Model A includes 21 representative common-form models for 5 Hz spectral frequency and 24 representative common-form models for 0.5 Hz spectral frequency. Model B includes 20 representative common-form models for 5 Hz spectral frequency and 23 representative common-form models for 0.5 Hz spectral frequency. The sensitivity results shown in the first and second line of the tornado plots in Figures 14.3-5 (a and b) and 14.3-6 (a and b) indicate that the largest uncertainty is due to the median ground-motion models for both the 5 Hz and 0.5 Hz spectral frequencies. The uncertainty range is larger at 5 Hz spectral acceleration than at 0.5 Hz spectral acceleration. These results are expected, as the higher frequency spectral acceleration is controlled by the Greater Arizona sources, unlike at the lower frequency spectral acceleration, which is also affected by the distant sources. The ground-motion range is greater for the 10^{-4} hazard level than for the 10^{-6} hazard level, reflecting the additional uncertainty from the depth scaling in the Model A case. The R_{RUP}-based GMPEs often include a scale factor for rupture depth. The alternative models for the depth scaling in the different GMPEs leads to a wider range of the GMPEs than for the R_{JB}-based GMPEs which generally do not include depth scaling.

Because the 0.5 Hz spectral acceleration case is affected by a wider range of sources (see the deaggregation plots in Figure 14.3-2), the 0.5 Hz spectral acceleration hazard is less sensitive to the parameters for any individual source. The 0.5 Hz spectral acceleration tornado plots for the median ground motion have a broader range on the high side. This skewed behavior occurs because the distant sources in Regions 1 and 2&3 contribute significantly to the hazard and produce a floor for the hazard estimate (as the hazard from the Greater Arizona source is reduced, the total hazard cannot be less than the hazard from the Regions 1 and 2&3 sources). This effect is seen at both 10^{-4} and 10^{-6} hazard levels because the fractional contribution from Regions 1 and 2&3 sources is about 0.8 at 10^{-4} and 0.5 at 10^{-6}.

The final sensitivity performed for the Greater Arizona sources median motions addressed both the approach (comparison to data or prior) and the alternative datasets evaluated during the development of weights for the common-form models: the weighted NGA dataset and the European dataset. The weighting scheme for the median base models, involving alternative datasets and alternative weight metrics, is shown in Figure 9.1-5. The sensitivity results for the alternative datasets for the weights are

shown in the third and fifth lines of the tornado plots in Figures 14.3-5 (a and b) and 14.3-6 (a and b). There is only a small sensitivity in hazard due to the weighting scheme.

Based on the sensitivity results for the median ground motions for the Greater Arizona sources shown in Figures 14.3-5 (a and b) and 14.3-6 (a and b), the largest range is associated with the representative suite of common-form models related to Model A and Model B.

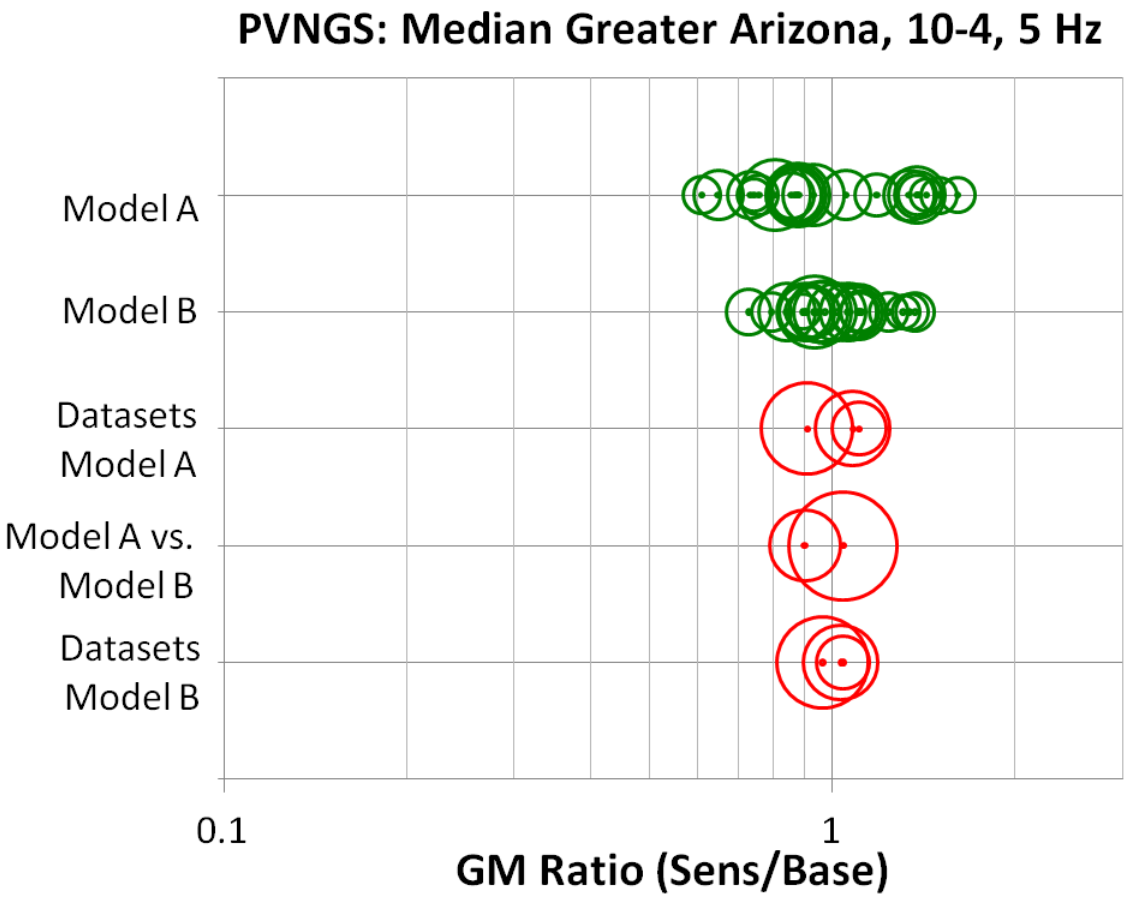

Figure 14.3-5a: Tornado plot for the median ground-motion logic tree for Greater Arizona sources for PVNGS for 5 Hz spectral acceleration at the 10^{-4} hazard level.

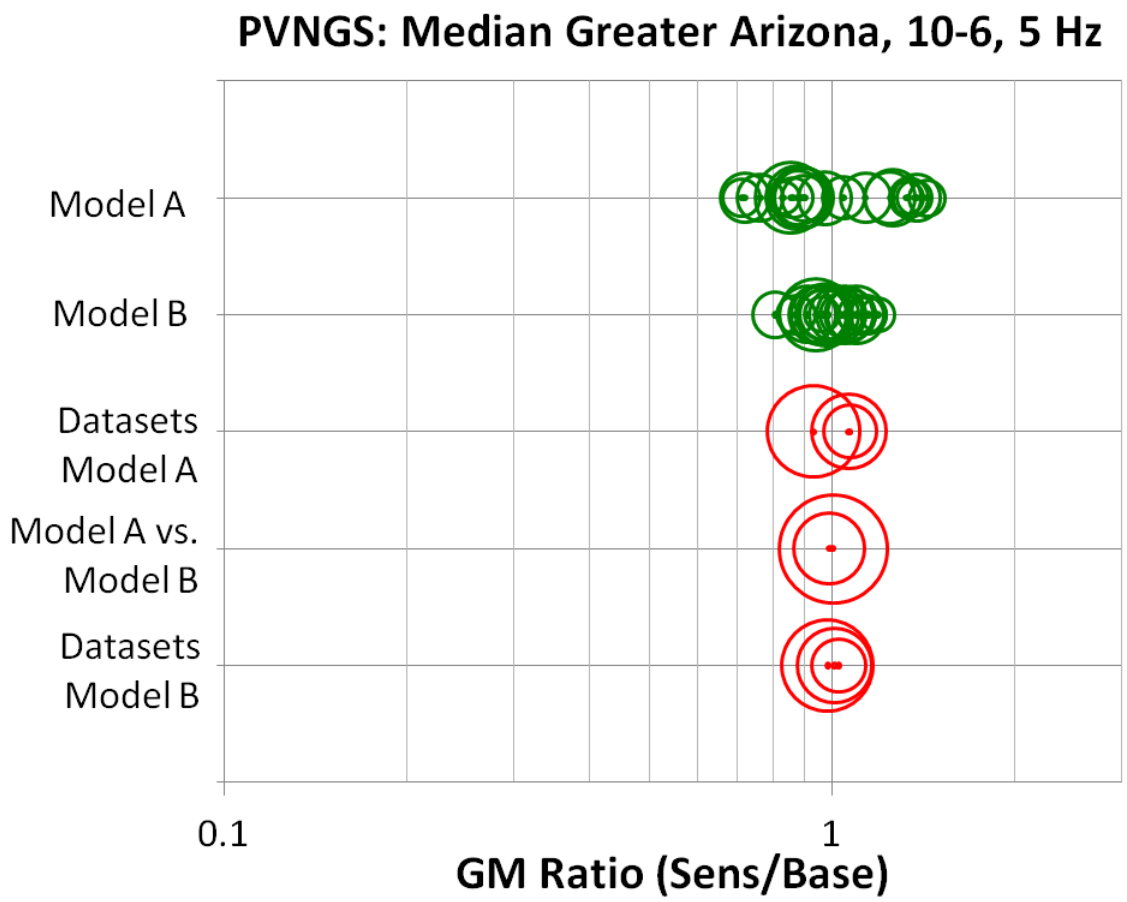

Figure 14.3-5b: Tornado plot for the median ground-motion logic tree for Greater Arizona sources for PVNGS for 5 Hz spectral acceleration at the 10^{-6} hazard level.

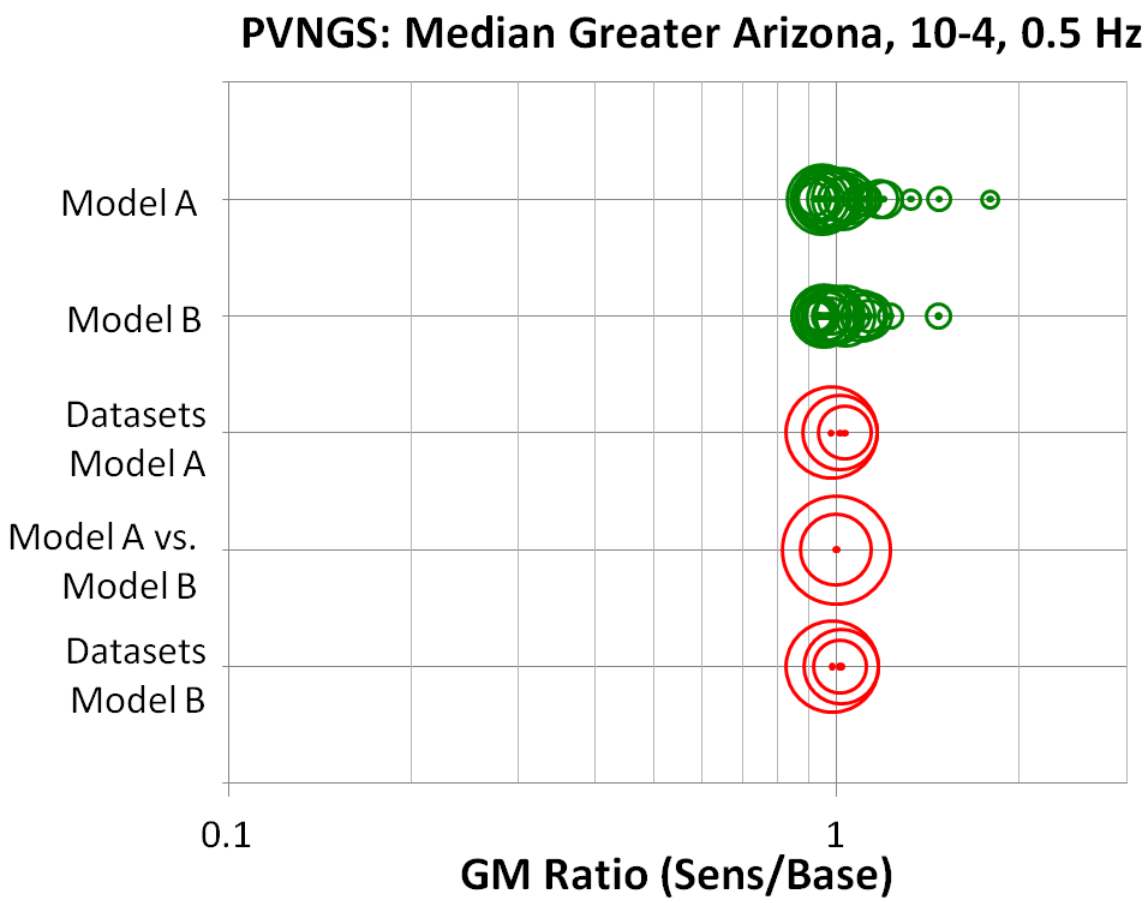

Figure 14.3-6a: Tornado plot for the median ground-motion logic tree for Greater Arizona sources for PVNGS for 0.5 Hz spectral acceleration at the 10^{-4} hazard level.

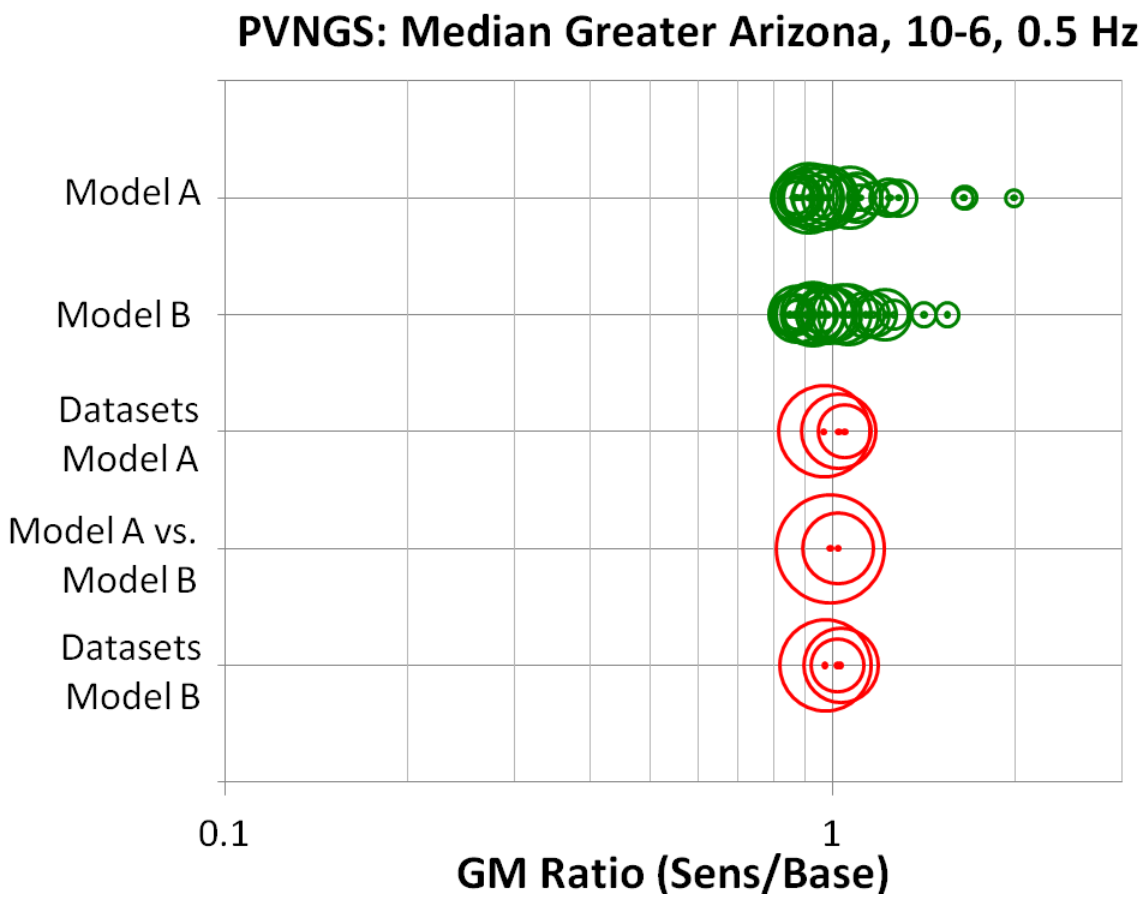

Figure 14.3-6b: Tornado plot for the median ground-motion logic tree for Greater Arizona sources for PVNGS for 0.5 Hz spectral acceleration at the 10^{-6} hazard level.

14.3.2 Median Base Models – Region 1 and Regions 2&3 Sources

The distant source (i.e., both Regions 1 and 2&3) logic tree associated with the median ground motions is shown in Figure 9.2-1. Similar to the Greater Arizona source logic tree, directivity is not deemed applicable for Region 1 and Regions 2&3 sources (as discussed in Section 9.2.4). In the sensitivities associated with the distant Region 1 and Regions 2&3 sources, five branches of the logic tree are presented. The contribution from the Greater Arizona sources for each case was taken as the weighted average from the two sets of common-form models. The hazard sensitivity results for the Regions 1 and 2&3 median base model in terms of normalized ground-motion ratios for 5 Hz spectral acceleration at the 10^{-4} and 10^{-6} hazard levels are shown in the tornado plots in Figures 14.3-7a and 14.3-7b, respectively. The results for 0.5 Hz spectral acceleration are shown in Figures 14.3-8a and 14.3-8b. For all sensitivities, there is no impact on the 5 Hz spectral acceleration hazard from the Regions 1 and 2&3

sources as shown in Figure 14.3-7. Therefore the following discussion only addresses the 0.5 Hz spectral acceleration sensitivities.

The first sensitivity analysis shown in Figure 14.3-8 (a and b) addresses the five alternative NGA-West2 GMPE models. In these sensitivity cases, the results from the individual NGA-West2 GMPE models were used with the weighted mean of the path term approach and the central values for the additional uncertainty and path term branches. The sensitivity results are shown in the first line of the tornado plots in Figures 14.3-8 (a and b) for the 0.5 Hz spectral acceleration case. At 10^{-4} hazard level, the selection of the GMPE has the largest impact on the hazard, but at 10^{-6} hazard level, the selection of the GMPE has a much smaller impact on the hazard. The reduced sensitivity at the lower 10^{-6} hazard level is expected because there is an increased contribution to the hazard from the local Greater Arizona sources for the 10^{-6} hazard level compared to the 10^{-4} hazard level.

The next sensitivity analysis for the distant Region 1 and Regions 2&3 source logic tree addressed the treatment of the path approach, which has two alternatives according to whether the path effects are included or not. The sensitivity results are shown in the second line of the tornado plots in Figures 14.3-8 (a and b) for the 0.5 Hz spectral acceleration case.

The next sensitivity analysis for the logic tree addresses the additional epistemic uncertainty in the magnitude scaling including or excluding the path effects (Section 9.2.4). The sensitivity results are shown in the third and fourth lines of the tornado plots in Figures 14.3-8 (a and b) for the 0.5 Hz spectral acceleration case. In this sensitivity case (i.e., numerator) the weighted mean from the Greater Arizona sources based on the two types of common-form models was combined with the individual branch results (i.e., with and without path term and three epistemic cases) using only the Campbell and Bozorgnia (2014 – referred to as CB14) NGA-West2 GMPE model. This simplification was based on the CB14 model being representative of the central model of the five NGA-West2 GMPEs and it reduced the number of calculations for the sensitivity. The sensitivity analysis for the path term approach application used only the central median path term branch (i.e., the sensitivity to this branch will be presented with the next case). Similar to the results from the previous branches, the 0.5 Hz spectral accelerations have the largest deviation from unity for the 10^{-4} hazard level cases and smaller deviations for the 10^{-6} hazard level.

The final sensitivity performed for Region 1 and Regions 2&3 sources addresses the median path correction terms, whose results are shown in the bottom line of the tornado plots in Figures 14.3-8 (a and b) for the 0.5 Hz spectral acceleration case. This node only applies to the case that applies the path term approach. Only a single reference median GMPE is used (CB14 NGA-West2 GMPE model). The hazard sensitivity is similar to magnitude scaling uncertainty and to the path approach results.

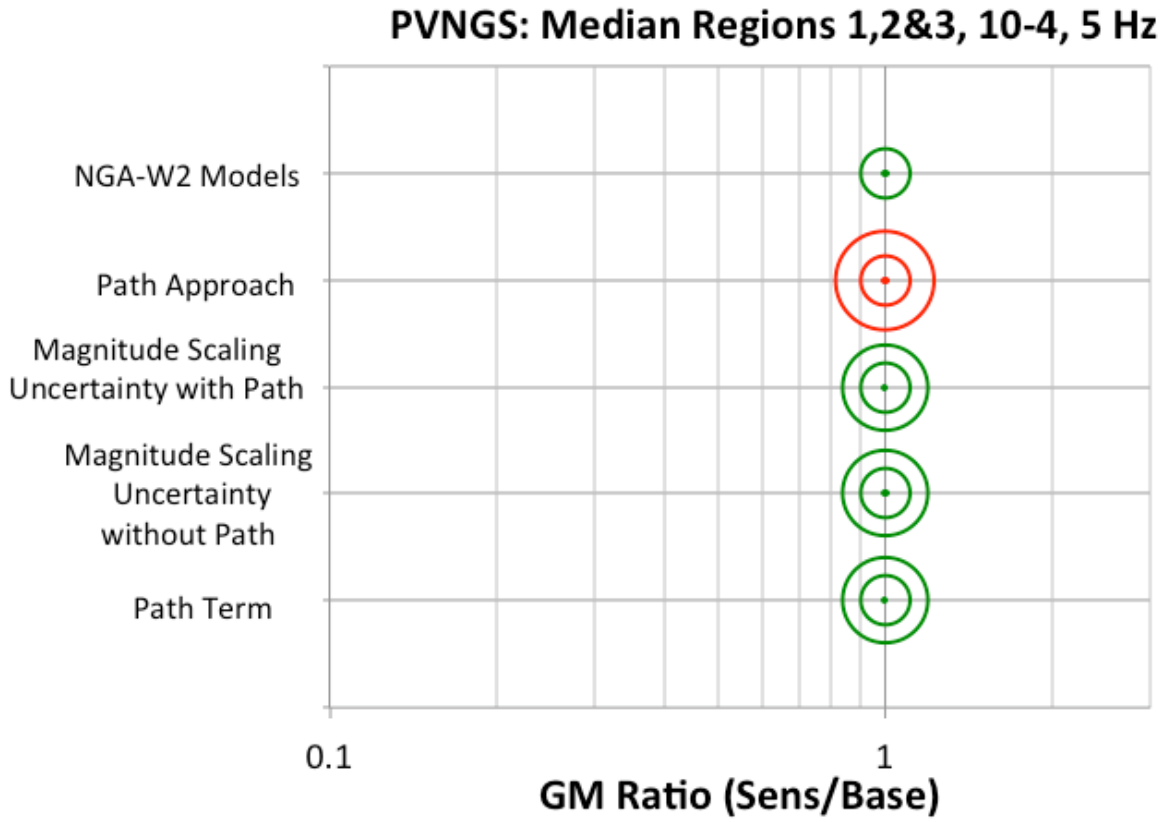

Figure 14.3-7a: Tornado plot for the median ground-motion logic tree for distant Region 1 and Regions 2&3 sources for PVNG for 5 Hz spectral acceleration at the 10^{-4} hazard level.

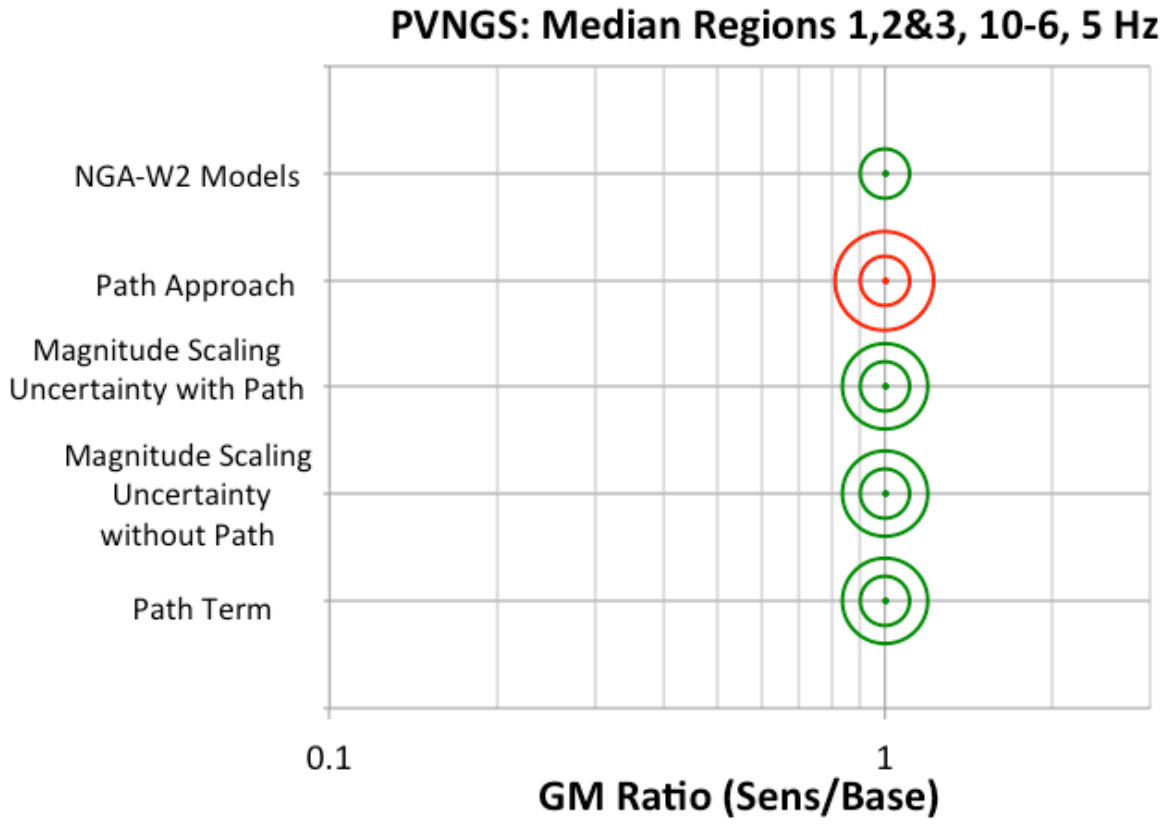

Figure 14.3-7b: Tornado plot for the median ground-motion logic tree for distant Region 1 and Regions 2&3 sources for PVNGS for 5 Hz spectral acceleration at the 10^{-6} hazard level.

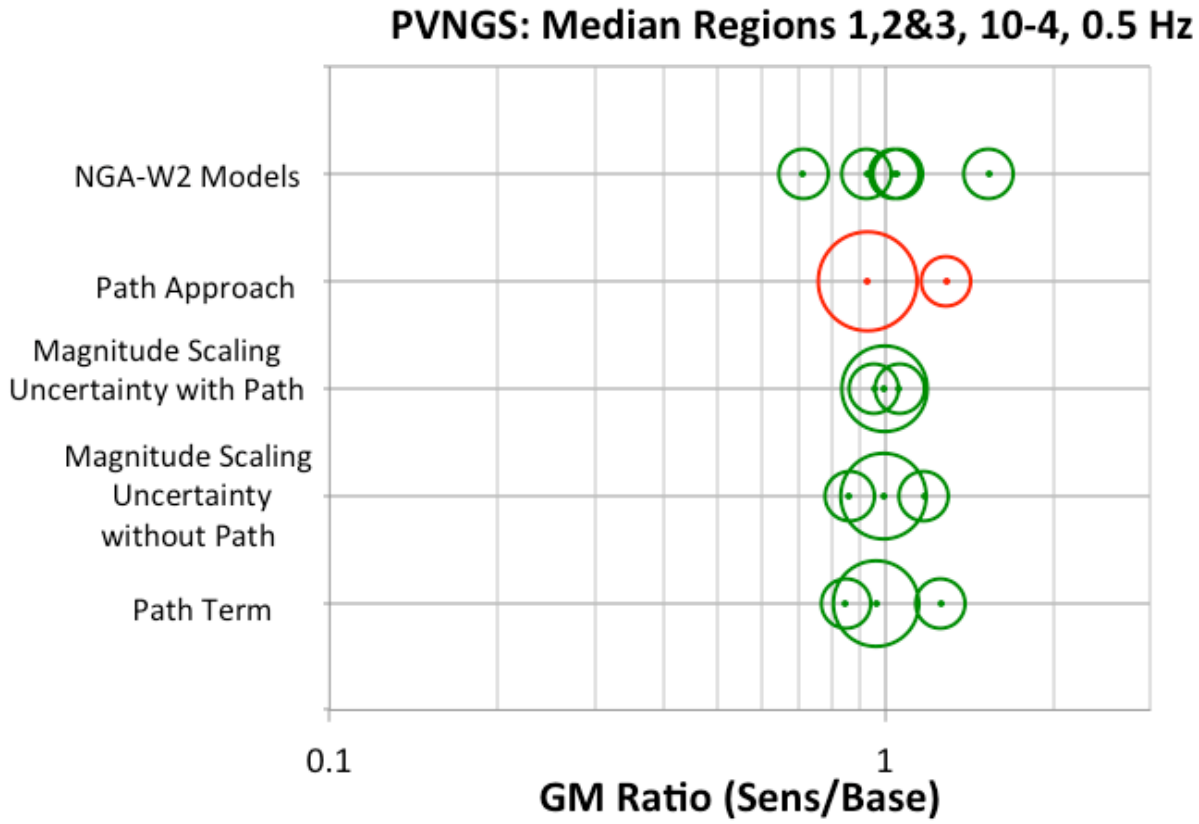

Figure 14.3-8a: Tornado plot for the median ground-motion logic tree for distant Region 1 and Regions 2&3 sources for PVNGS for 0.5 Hz spectral acceleration at the 10^{-4} hazard level.

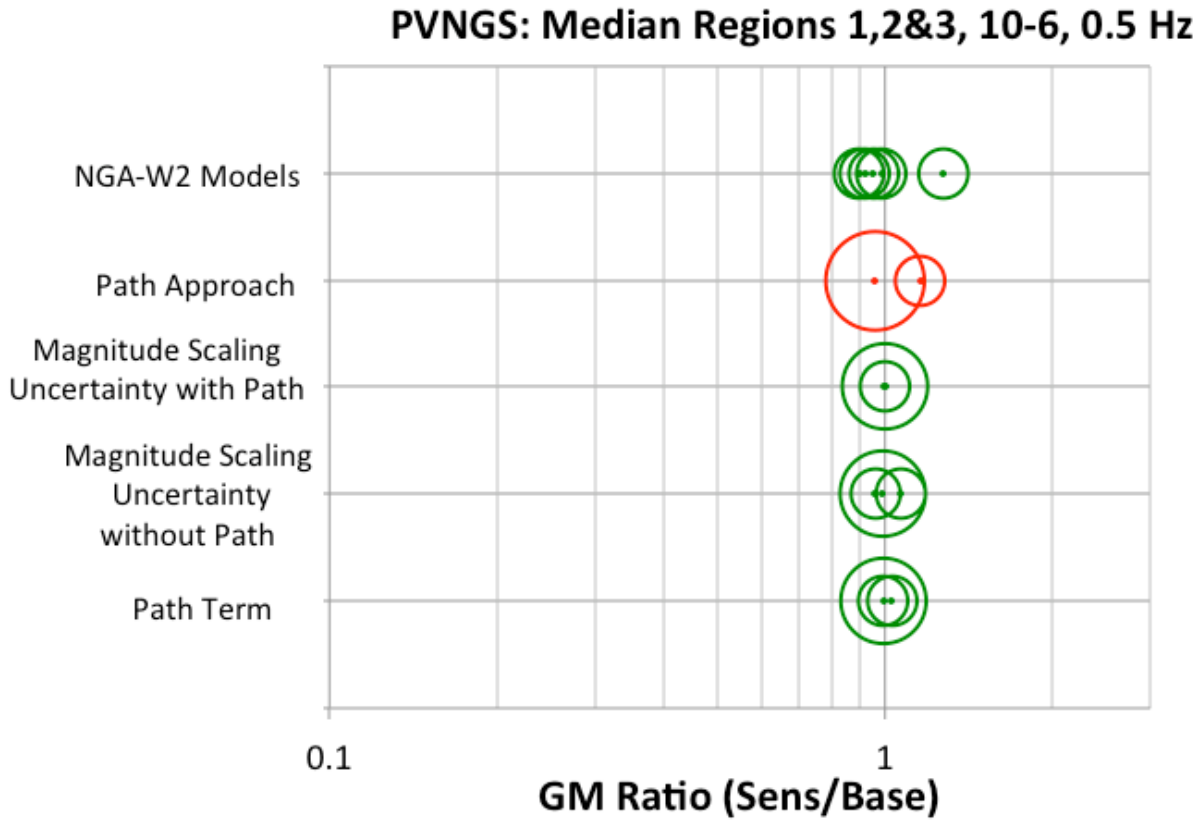

Figure 14.3-8b: Tornado plot for the median ground-motion logic tree for distant Region 1 and Regions 2&3 sources for PVNGS for 0.5 Hz spectral acceleration at the 10^{-6} hazard level.

14.3.3 Sigma Models – τ

The sigma model consists of a separate logic tree for the τ (see Figure 10.1-1) and ϕ_{SS} (see Figure 12.1-1) terms for the Greater Arizona sources. A separate logic tree for the ϕ_{SS} and ϕ_{SP-R} models is given in Figure 12.2-1 for the distant sources in Region 1 and 2&3. In the sensitivity analyses of the τ models, only the weighted mean from the two central models (i.e., Model 1 selected from the inner ellipse, as discussed in Section 14.2.1) from the representative suite of common functional-form models using R_{RUP} (Model A) and R_{JB} (Model B) distance metrics were used. For the distant sources in Region 1 and 2&3, the Boore et al. (2014 – referred to as BSSA14) NGA-West2 GMPE model with the mean path effects was used in these sensitivity analyses. The BSSA14 median model was selected because it is representative of the mean GMPE for the distant sources in Regions 1 and 2&3.

The sensitivity analyses for the τ model are shown in the tornado plots in Figures 14.3-9a and 14.3-9b for 5 Hz spectral acceleration at the 10^{-4} and 10^{-6} hazard levels, respectively, for the Greater Arizona sources (top line) and for the distant Region 1 and Regions 2&3 sources both with and without path terms (second and third lines, respectively). For the 5 Hz spectral acceleration cases, the τ sensitivity is strongest for the Greater Arizona sources. For the Region 1 and Regions 2&3 cases, there is no sensitivity to τ for short periods because of the small contribution from these sources to the total hazard. The sensitivity analyses for the τ model are shown in the tornado plots in Figures 14.3-10a and 14.3-10b for 0.5 Hz spectral acceleration at the 10^{-4} and 10^{-6} hazard levels, respectively. For the 0.5 Hz spectral acceleration cases, the τ sensitivity for the distant sources shows the largest range at the 10^{-4} hazard level but the τ sensitivity for the Greater Arizona sources show the largest range at the 10^{-6} hazard level. This reflects the increased contribution from the Greater Arizona sources at the low hazard level (as shown in the hazard deaggregation by source plot in Figure 14.3-2).

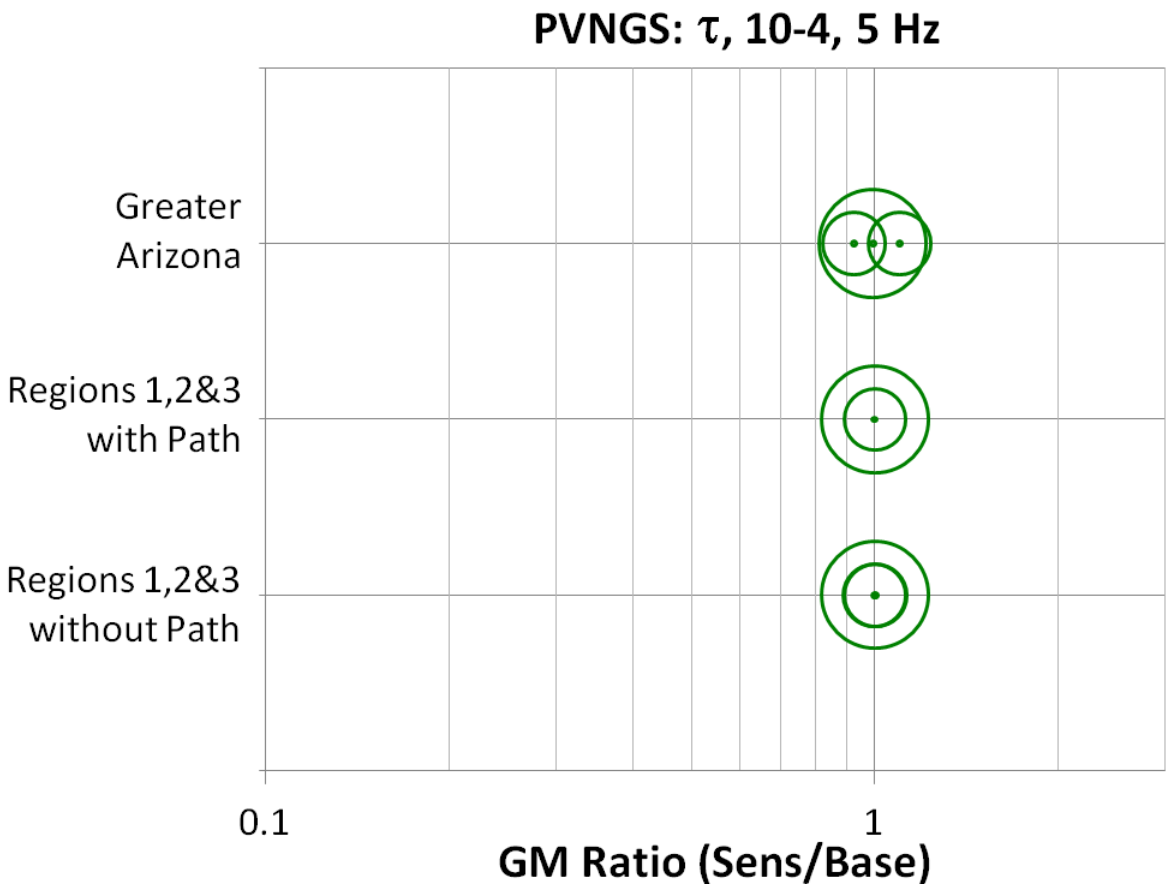

Figure 14.3-9a: Tornado plot for the τ logic tree PVNGS for 5 Hz spectral acceleration at the 10^{-4} hazard level.

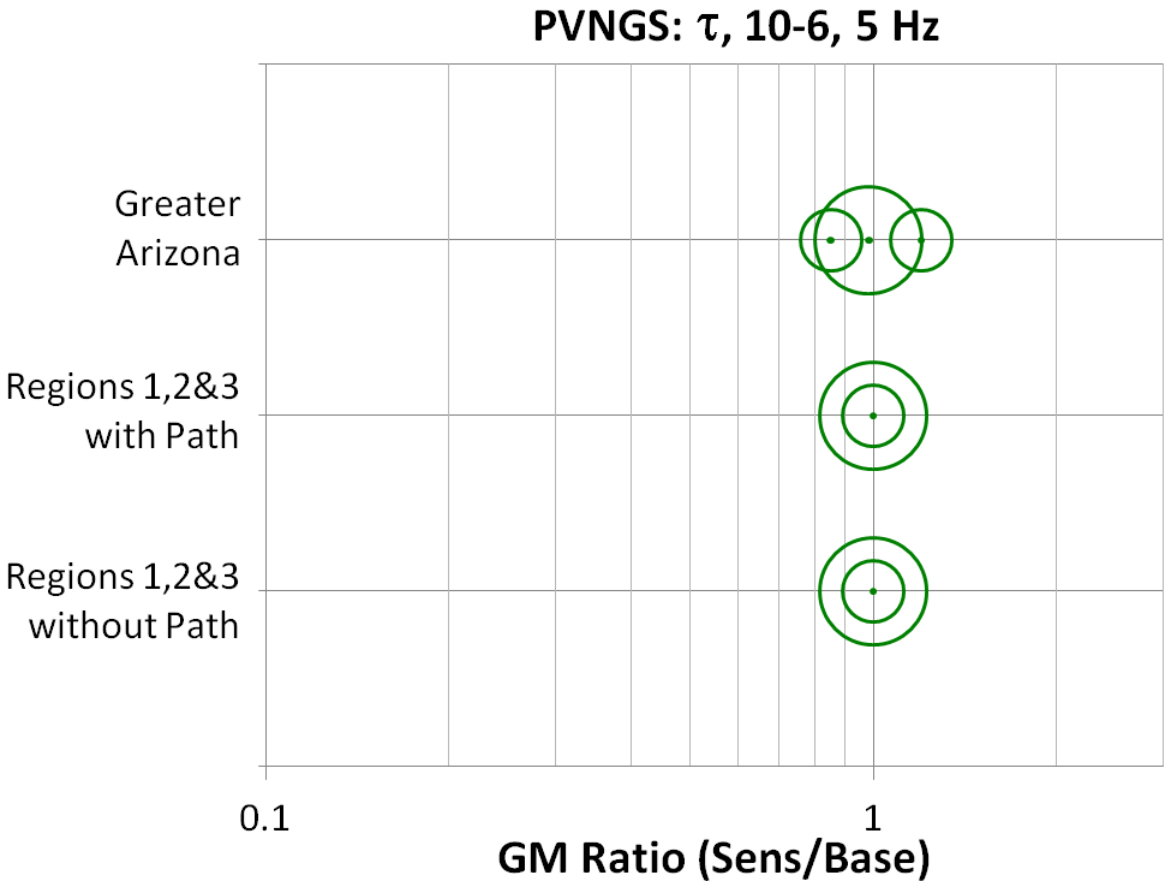

Figure 14.3-9b: Tornado plot for the τ logic tree for PVNGS for 5 Hz spectral acceleration at the 10^{-6} hazard level.

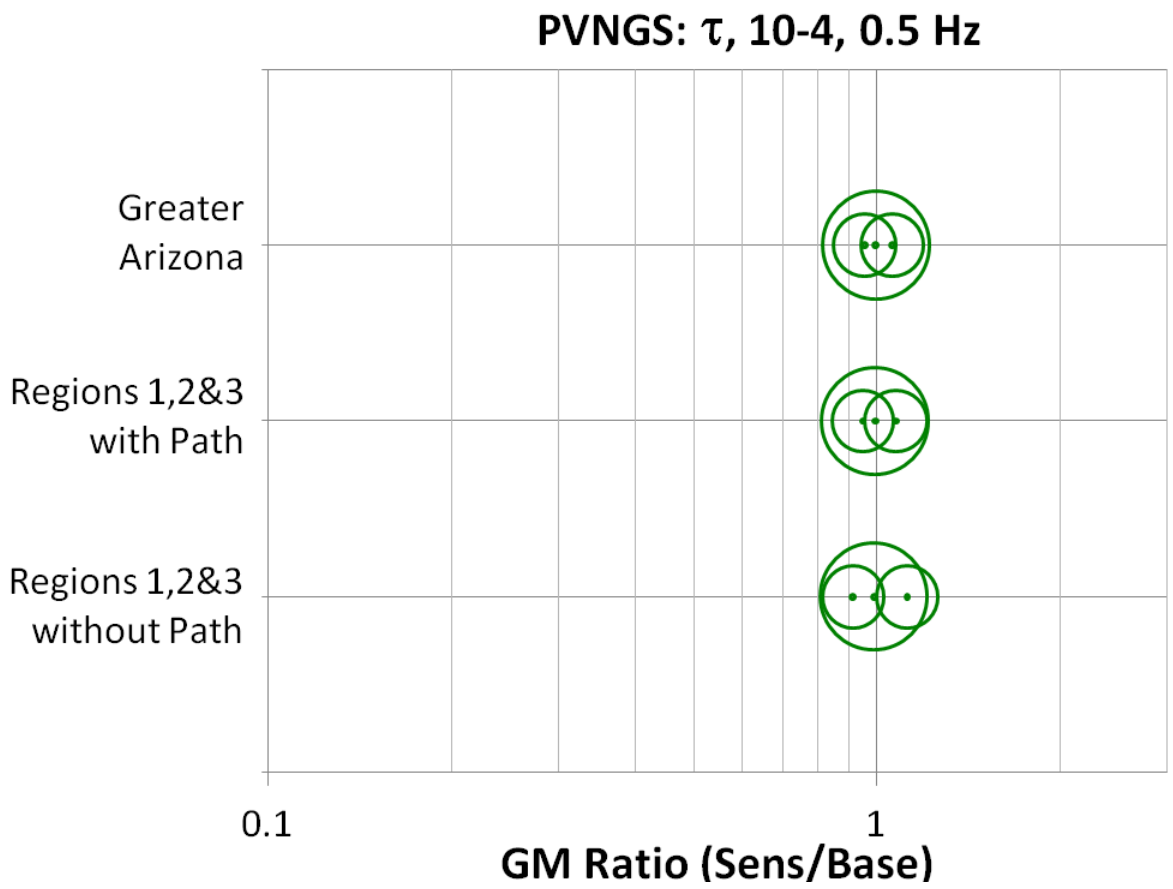

Figure 14.3-10a: Tornado plot for the τ logic tree for PVNGS for 0.5 Hz spectral acceleration at the 10^{-4} hazard level.

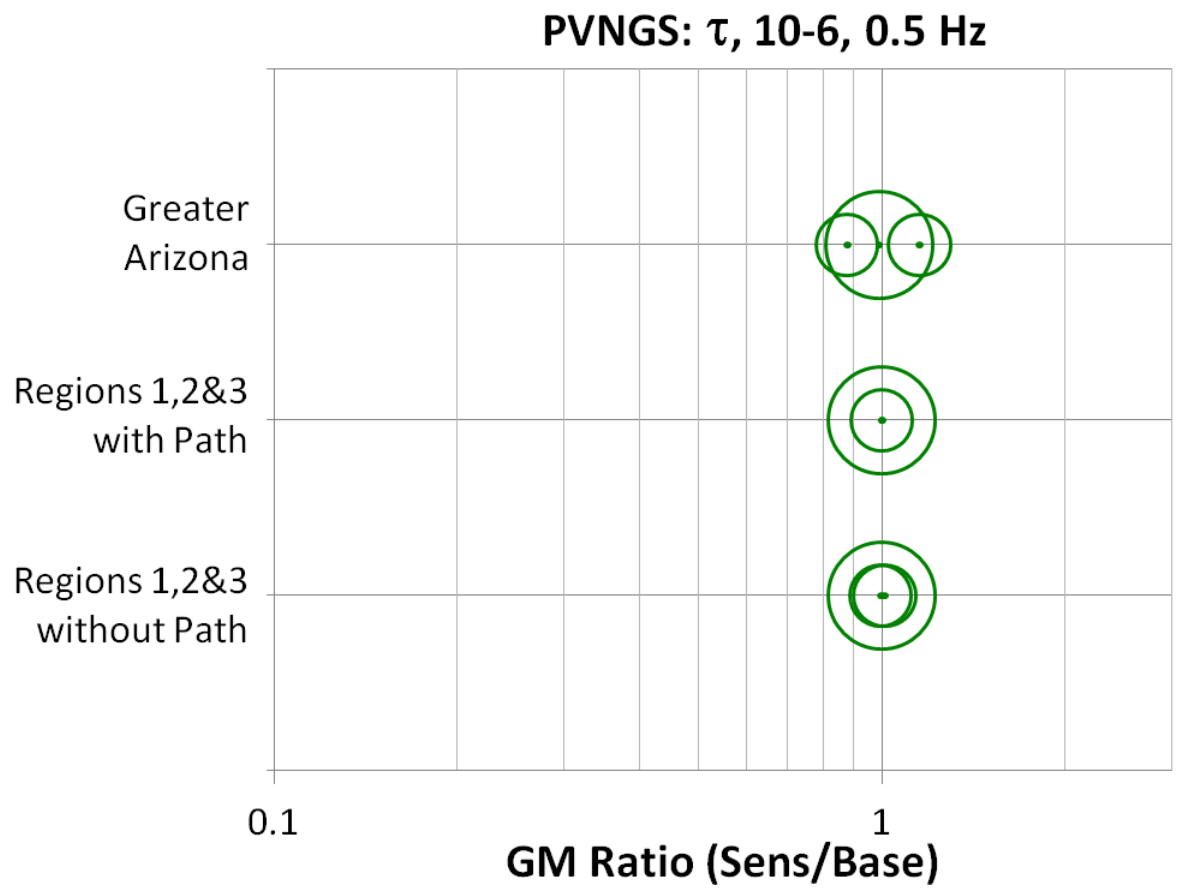

Figure 14.3-10b: Tornado plot for the τ logic tree for PVNGS for 0.5 Hz spectral acceleration at the 10^{-6} hazard level.

14.3.4 ϕ_{SS} Models – Greater Arizona Sources

Separate ϕ_{SS} logic trees are presented for the Greater Arizona sources (see Figure 12.1-1) and the distant Region 1 and Regions 2&3 sources (see Figure 12.2-1). Similar to the sensitivity cases for the τ logic tree, the weighted mean of the two central models from the R_{RUP} (Model A) and R_{JB} (Model B) common-form models were used for the Greater Arizona sources. For the distant Region 1 and Regions 2&3 sources, the weighted mean from the BSSA14 NGA-West2 GMPE model was used. These models were all used with the central τ branch of the τ logic tree.

The hazard sensitivity results for the ϕ_{SS} model in terms of normalized ground-motion ratios for 5 Hz spectral acceleration at the 10^{-4} and 10^{-6} hazard level are shown in the tornado plots in Figures 14.3-11a

and 14.3-11b, respectively. The results for 0.5 Hz spectral acceleration are shown in Figures 14.3-12a and 14.3-12b.

The first sensitivity analysis for the Greater Arizona source logic tree addresses the two alternative data sets – European and Global. The sensitivity results are plotted in the third line on the tornado plots in Figures 14.3-11 (a and b) and 14.3-12 (a and b). The sensitivity to the data set is small at the 10^{-4} hazard level but increases at the 10^{-6} hazard level.

The next sensitivity addresses the epistemic uncertainty of ϕ_{SS} due to the sample size limitations. The ground-motion ratios are plotted in the first and second lines of the tornado plots in Figures 14.3-11 (a and b) and 14.3-12 (a and b) for the European and Global data sets, respectively. The epistemic uncertainty due to the data-set size has the largest impact on the hazard at both 5 and 0.5 Hz and for both the 10^{-4} and 10^{-6} hazard levels.

The final two sensitivity cases for the ϕ_{SS} associated with the logic tree for the Greater Arizona sources address the different aleatory distribution forms, i.e. the mixture model and the standard normal model. To simplify the sensitivity cases for the mixture model, two representative end members were selected. These two end members are the high τ and high ϕ_{SS} model and the low τ and low ϕ_{SS} models. The sensitivity results are shown in the lower two lines of the tornado plots in Figures 14.3-11 (a and b) and 14.3-12 (a and b). The relative difference between the normal and mixture model ratio values indicates the impact on the ground motions using either the normal or mixture distribution for these end member cases. In general, the sensitivity due to the mixture model is less than the sensitivity due to the other parameters. The expected full weighted impact of the aleatory distribution form would be less than the results for these two bounding end member cases.

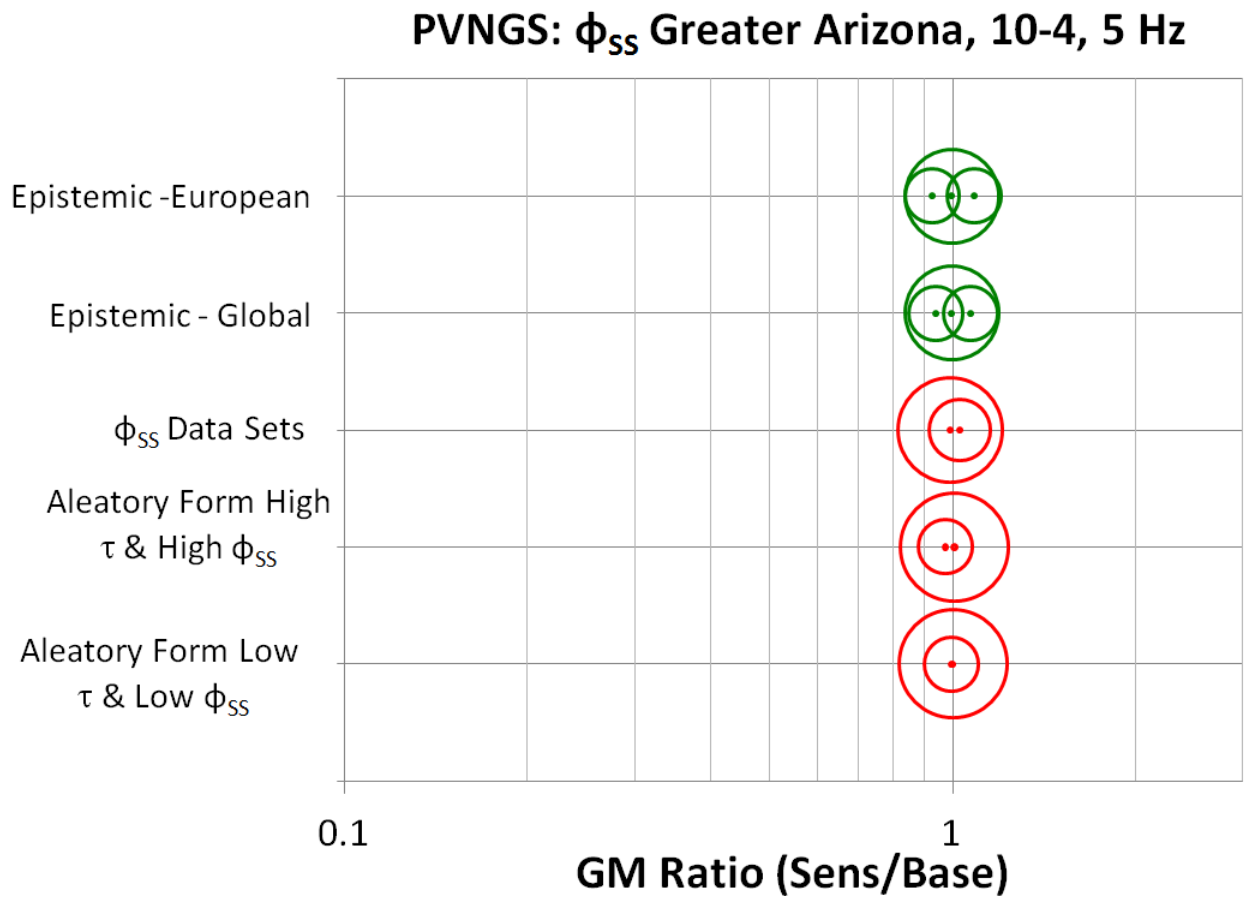

Figure 14.3-11a: Tornado plot for the ϕ_{SS} logic tree for Greater Arizona sources for PVNGS for 5 Hz spectral acceleration at the 10^{-4} hazard level.

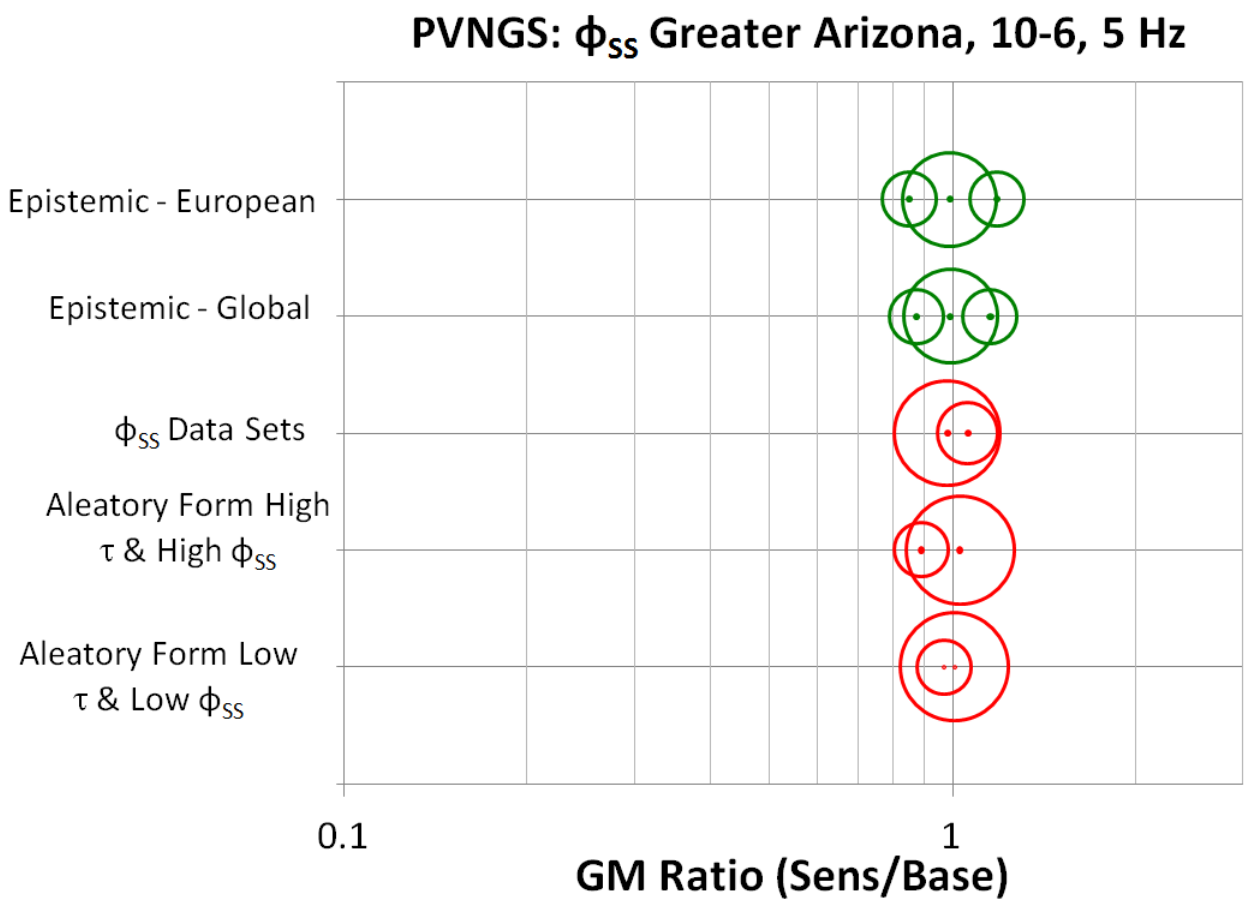

Figure 14.3-11b: Tornado plot for the ϕ_{SS} logic tree for Greater Arizona sources for PVNGS for 5 Hz spectral acceleration at the 10^{-6} hazard level.

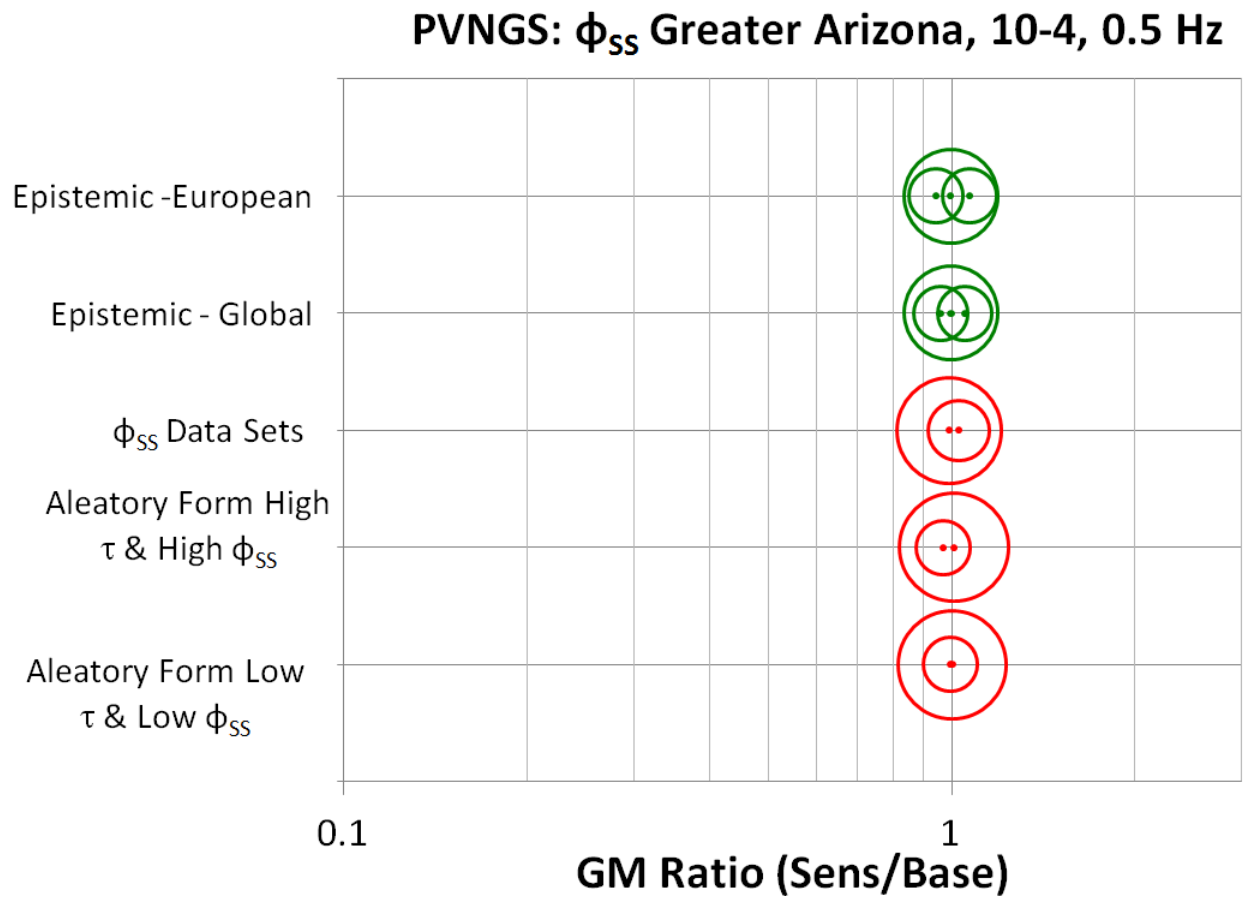

Figure 14.3-12a: Tornado plot for the ϕ_{SS} logic tree for Greater Arizona sources for PVNGS for 0.5 Hz spectral acceleration at the 10^{-4} hazard level.

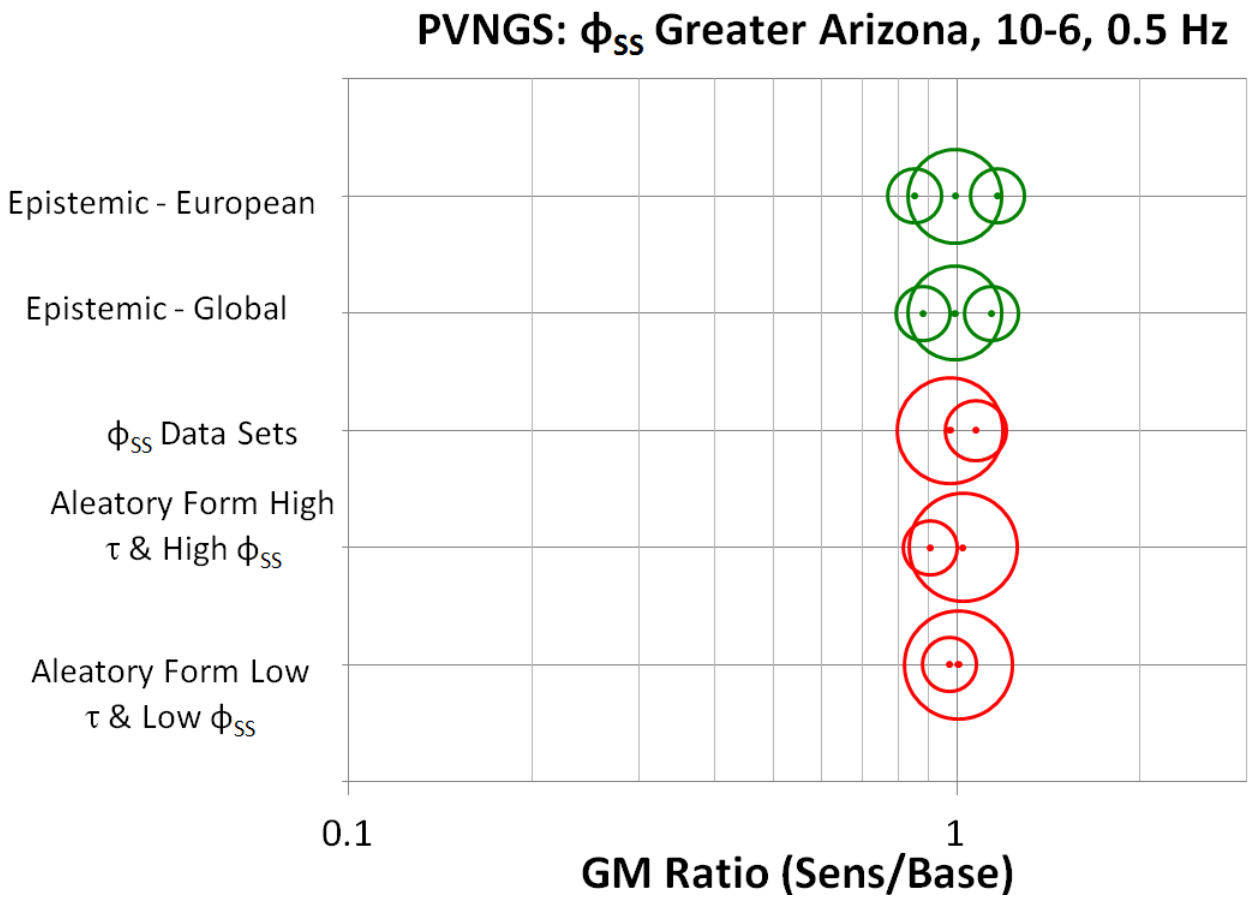

Figure 14.3-12b: Tornado plot for the ϕ_{SS} logic tree for Greater Arizona sources for PVNGS for 0.5 Hz spectral acceleration at the 10^{-6} hazard level.

14.3.5 ϕ_{SS} and $\phi_{SP\text{-}R}$ Models – Distant Region 1 and Regions 2&3 Sources

A separate logic tree for the ϕ_{SS} and ϕ_{SP-R} models associated with the distant Region 1 and Regions 2&3 sources is shown in Figure 12.2-2. In these sensitivities, the denominator was based on the contribution from the Greater Arizona sources using the weighted mean from the central model from the two types of common-form models, the weighted mean based on the ϕ_{SS} logic tree (see Figure 12.1-1) and the central τ value. The contribution from the distant Region 1 and Regions 2&3 sources was computed based on the BSSA14 NGA-West2 GMPE model and the weighted combination of the "with path" and "without path" components with the central τ model.

The hazard sensitivity results for the ϕ_{SS} and ϕ_{SP-R} models in terms of normalized ground-motion ratios for 5 Hz spectral acceleration at the 10^{-4} and 10^{-6} hazard level are shown in the tornado plots in Figures 14.3-13a and 14.3-13b, respectively. The results for 0.5 Hz spectral acceleration are shown in Figures 14.3-14a and 14.3-14b.

As discussed earlier, there is no sensitivity at 5 Hz spectral acceleration due to the small contributions from the Regions 1 and 2&3, so these are not discussed further.

The first sensitivity addresses the three epistemic uncertainty branches in the ϕ_{SS} and ϕ_{SP-R} models, with the upper and lower branches based on the statistical uncertainty due to limited sampling, as described in Sections 7.3.1 and 7.4.2. The sensitivity results are shown in the first and second lines of the tornado plots in Figures 14.3-14 (a and b) for ϕ_{SS} and ϕ_{SP-R}, respectively. For this 0.5 Hz spectral acceleration case, the ground-motion ratios vary less at the 10^{-6} level than at the 10^{-4} hazard level because of the relative contribution from the Greater Arizona sources at these hazard levels.

The final two sensitivity cases for the ϕ_{SS} and ϕ_{SP-R} associated with the logic tree for the distant sources address the different aleatory distribution forms. To simplify the sensitivity case for the mixture model, two representative end members were selected. These two end members are the high τ and high ϕ model and the low τ and low ϕ models. For the ϕ model, the weighted combination of the ϕ_{SS} and ϕ_{SP-R} branches are used. The sensitivity results are shown in the last two lines of the tornado plots in Figures 14.3-14 (a and b) for the 0.5 Hz spectral acceleration case. The relative difference between the normal and mixture model ratio values indicates the impact on the ground motions using either the normal or mixture distribution for these end cases. In general, the sensitivity due to the mixture model is less than the sensitivity due to the other parameters. The expected full weighted impact of the aleatory distribution form would be less than the results for these two bounding end member cases.

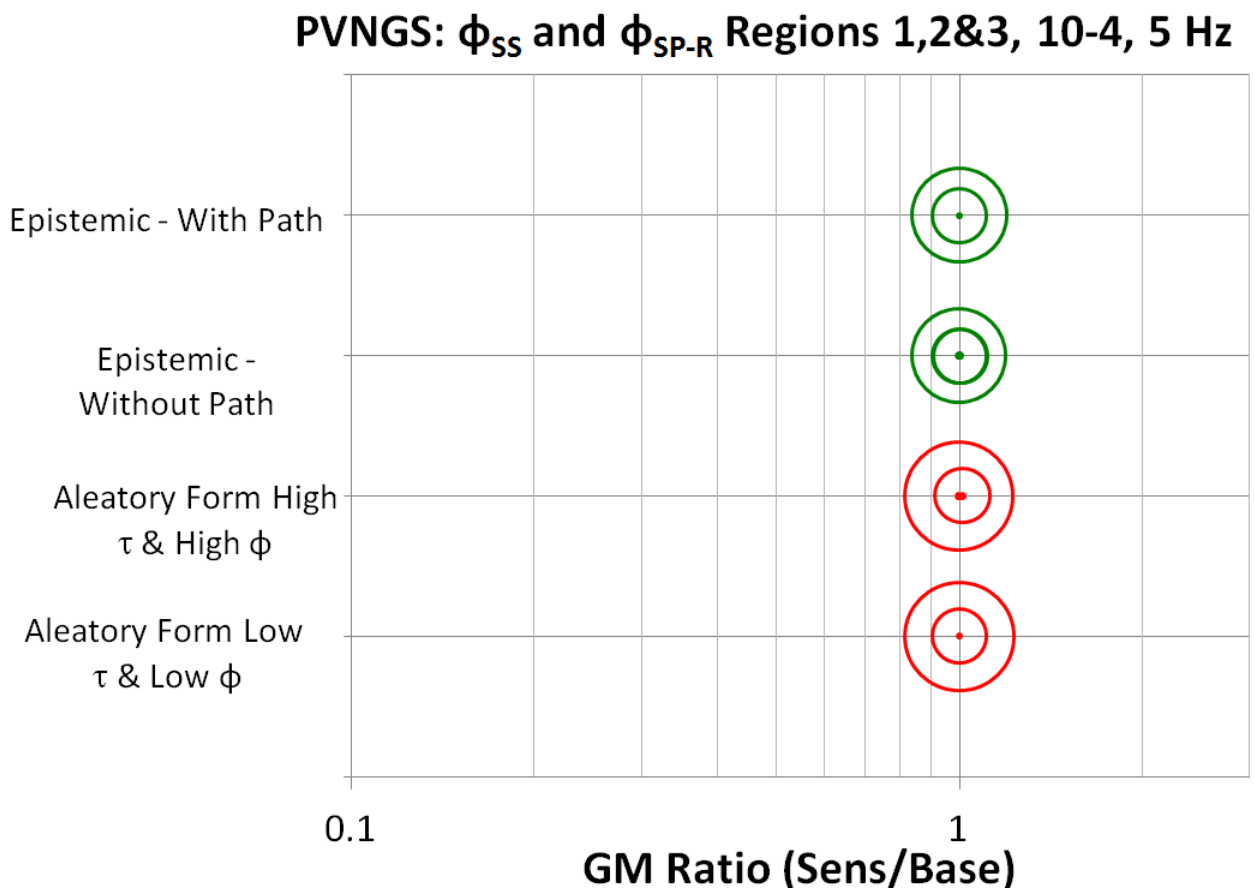

Figure 14.3-13a: Tornado plot for the ϕ_{SS} and ϕ_{SP-R} logic tree for distant Region 1 and Regions 2&3 sources for PVNGS for 5 Hz spectral acceleration at the 10^{-4} hazard level.

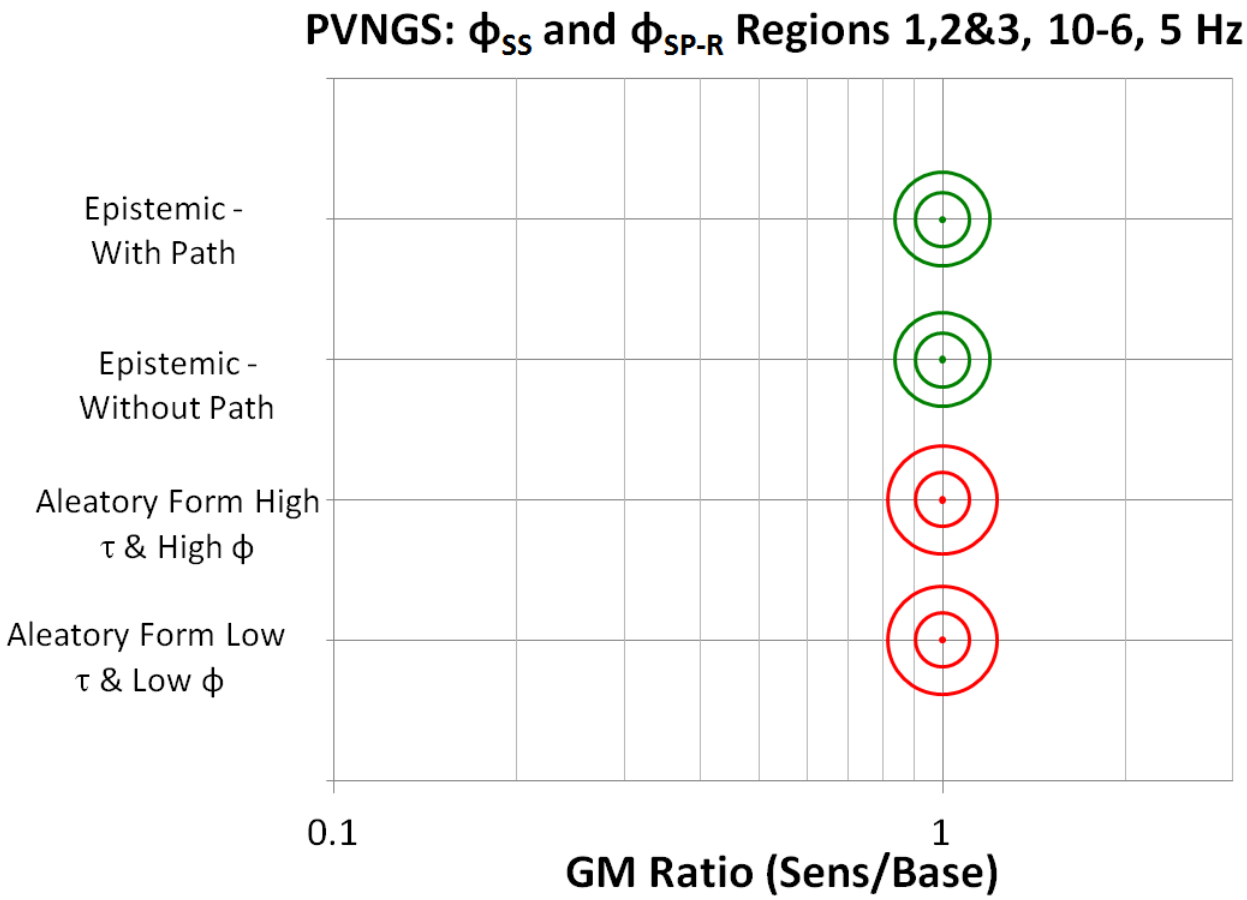

Figure 14.3-13b: Tornado plot for the ϕ_{SS} and ϕ_{SP-R} logic tree for distant Region 1 and Regions 2&3 sources for PVNGS for 5 Hz spectral acceleration at the 10^{-6} hazard level.

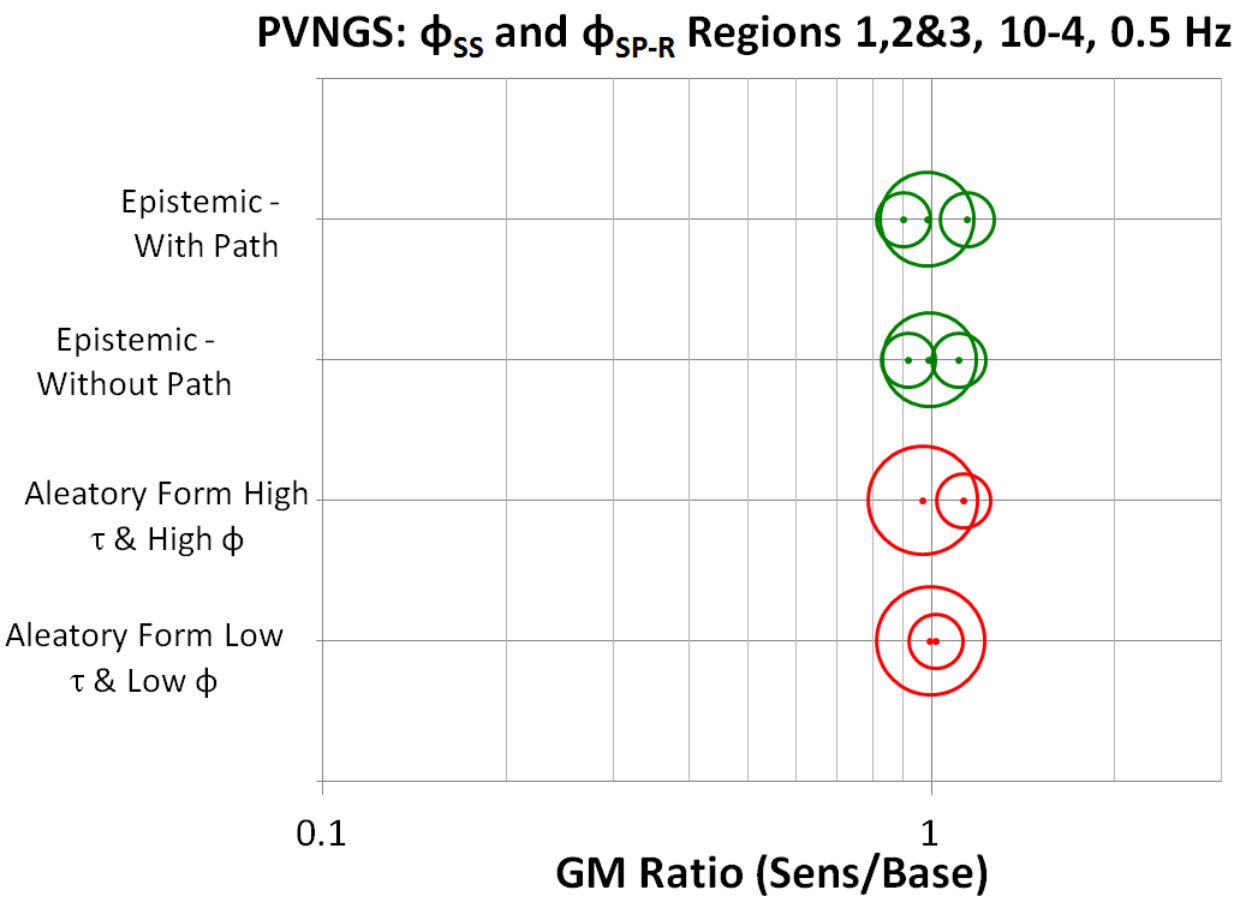

Figure 14.3-14a: Normalized tornado plot for the ϕ_{SS} and ϕ_{SP-R} logic tree for distant Region 1 and Regions 2&3 sources for PVNGS for 0.5 Hz spectral acceleration at the 10^{-4} hazard level.

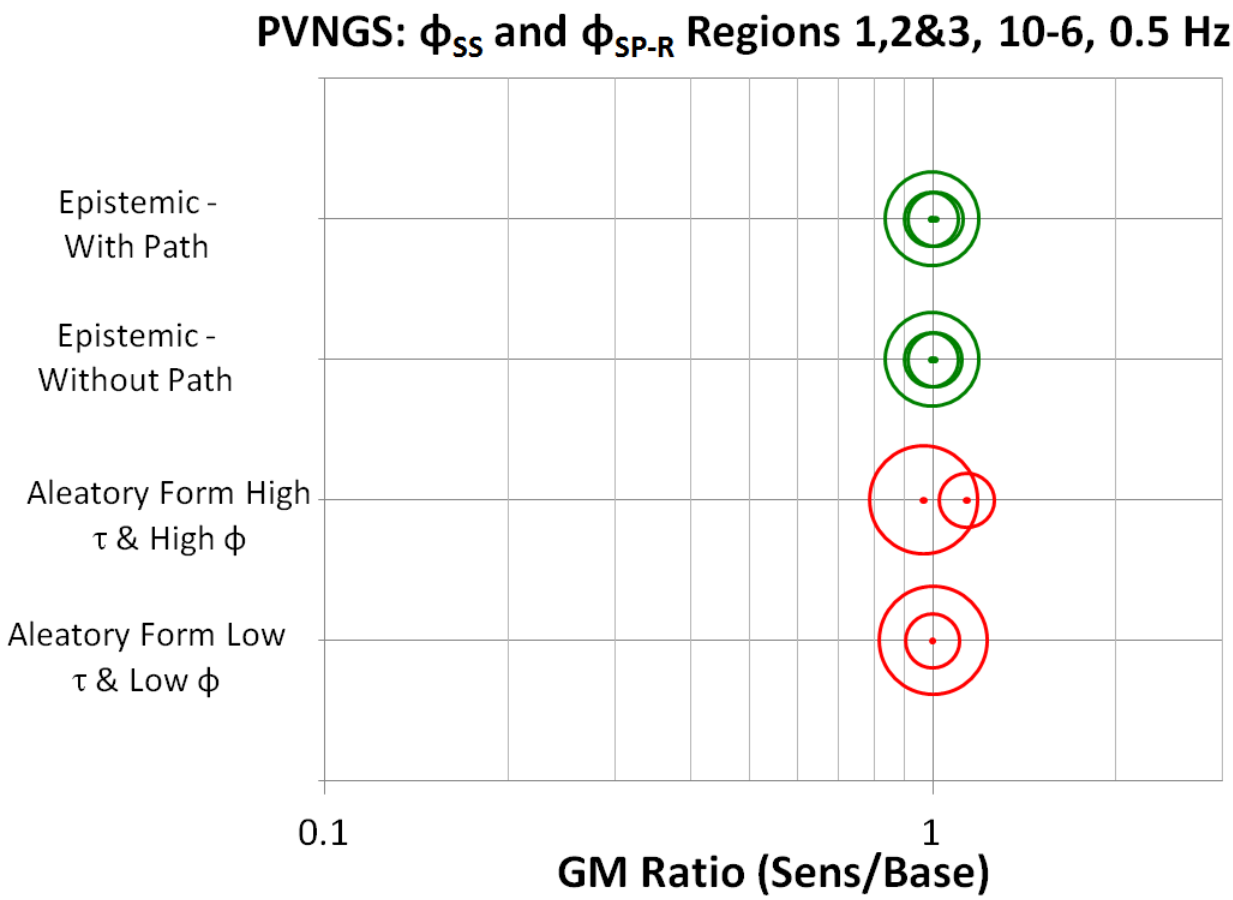

Figure 14.3-14b: Tornado plot for the ϕ_{SS} and ϕ_{SP-R} logic tree for distant Region 1 and Regions 2&3 sources for PVNGS for 0.5 Hz spectral acceleration at the 10^{-6} hazard level.

14.3.6 Total Sigma Models

The final logic tree sensitivity is for the recommended total sigma model for PVNGS. Separate total sigma models are recommended for the Greater Arizona sources (Figure 13.1-2) and the distant Region 1 and Regions 2&3 sources both with and without path effects (Figure 13.1-3). Each recommended total sigma model has three epistemic uncertainty branches. In these sensitivity cases, the hazard is based on the weighted mean of the common-form models for the Greater Arizona sources and the weighted mean of the NGA-West2 GMPE models for the distant Region 1 and Regions 2&3 sources using the central path and no path terms.

The hazard sensitivity results for the PVNGS total sigma model in terms of normalized ground-motion ratios for 5 Hz spectral acceleration at the 10^{-4} and 10^{-6} hazard levels are shown in the tornado plots in

Figures 14.3-15a and 14.3-15b, respectively. The results for 0.5 Hz spectral acceleration are shown in Figures 14.3-16a and 14.3-16b. These results, along with the median logic tree results shown earlier in this Chapter, are part of the hazard informed feedback used in the development of the GMC logic trees for PVNGS.

For 5 Hz spectral acceleration, the sensitivity is seen only for the Greater Arizona sources (first line in the tornado plot shown in Figures 14.3-15 a and b) while at 0.5 Hz spectral acceleration the Regions 1 and 2&3 sources have the largest sensitivity at 10^{-4} hazard level, but have only a small sensitivity at 10^{-6} hazard level similar to the ϕ_{SS} sensitivities (Section 14.3.4).

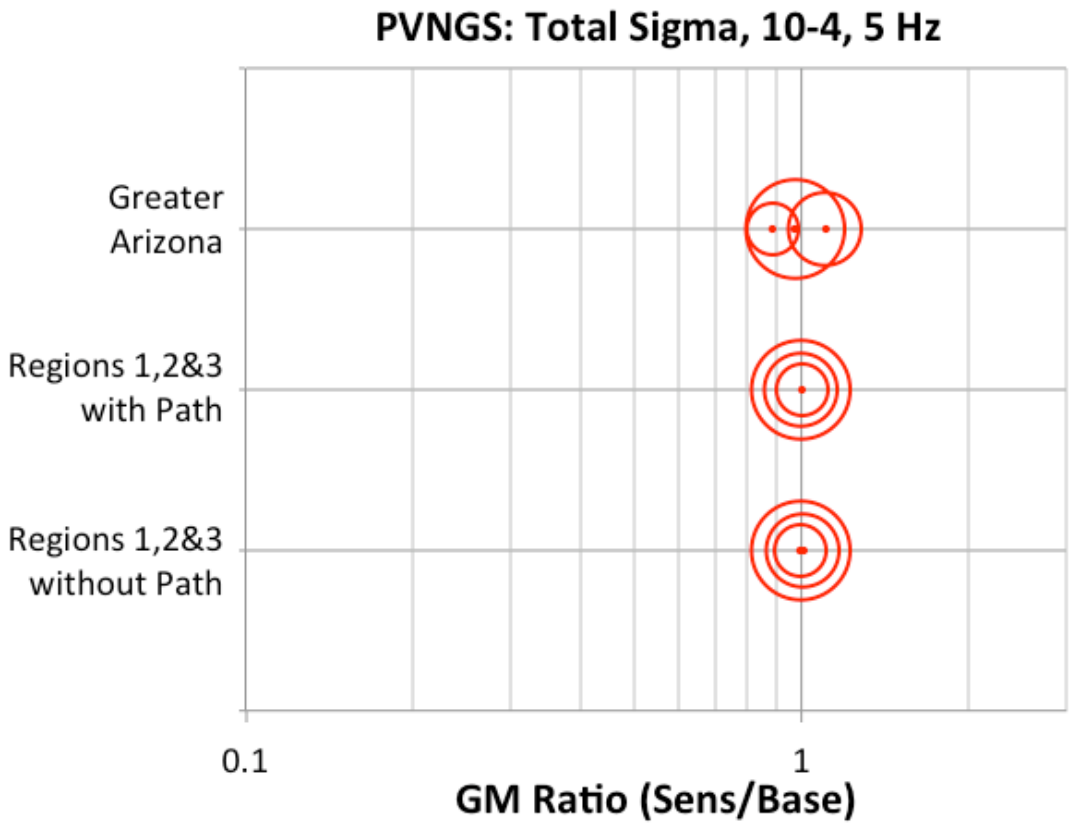

Figure 14.3-15a: Tornado plot for the total sigma logic tree for PVNGS for 5 Hz spectral acceleration at the 10^{-4} hazard level.

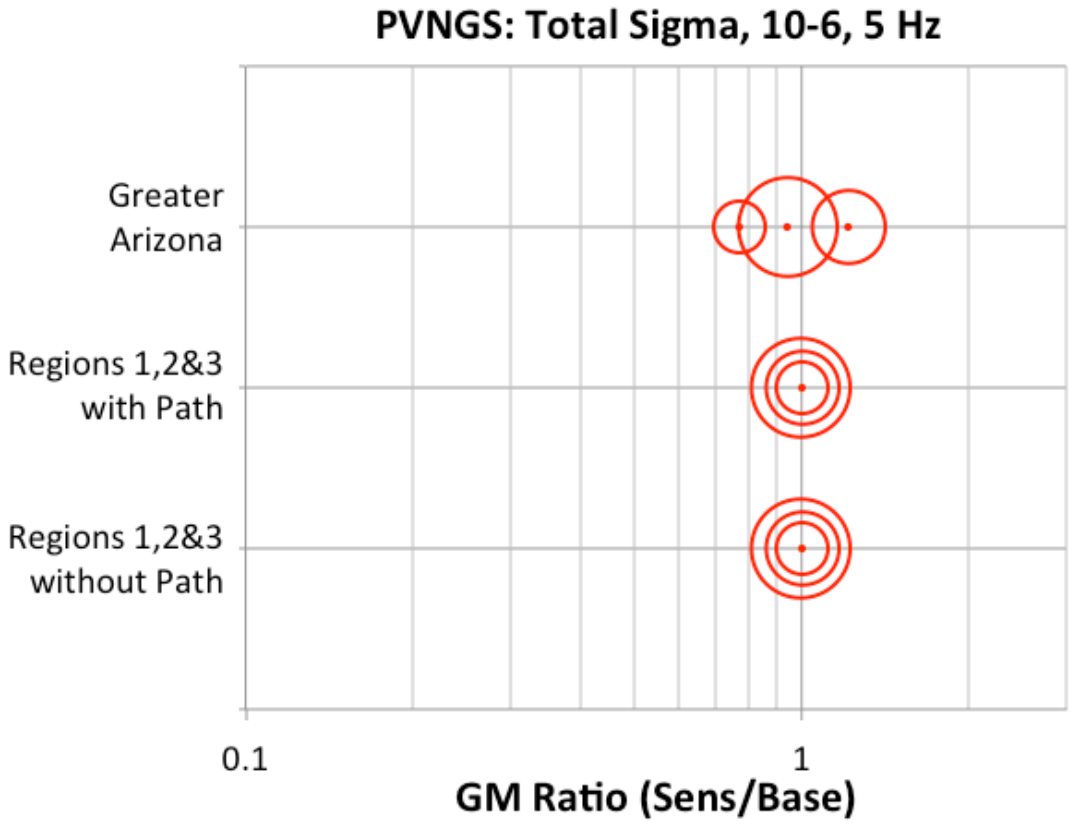

Figure 14.3-15b: Tornado plot for the total sigma logic tree for PVNGS for 5 Hz spectral acceleration at the 10^{-6} hazard level.

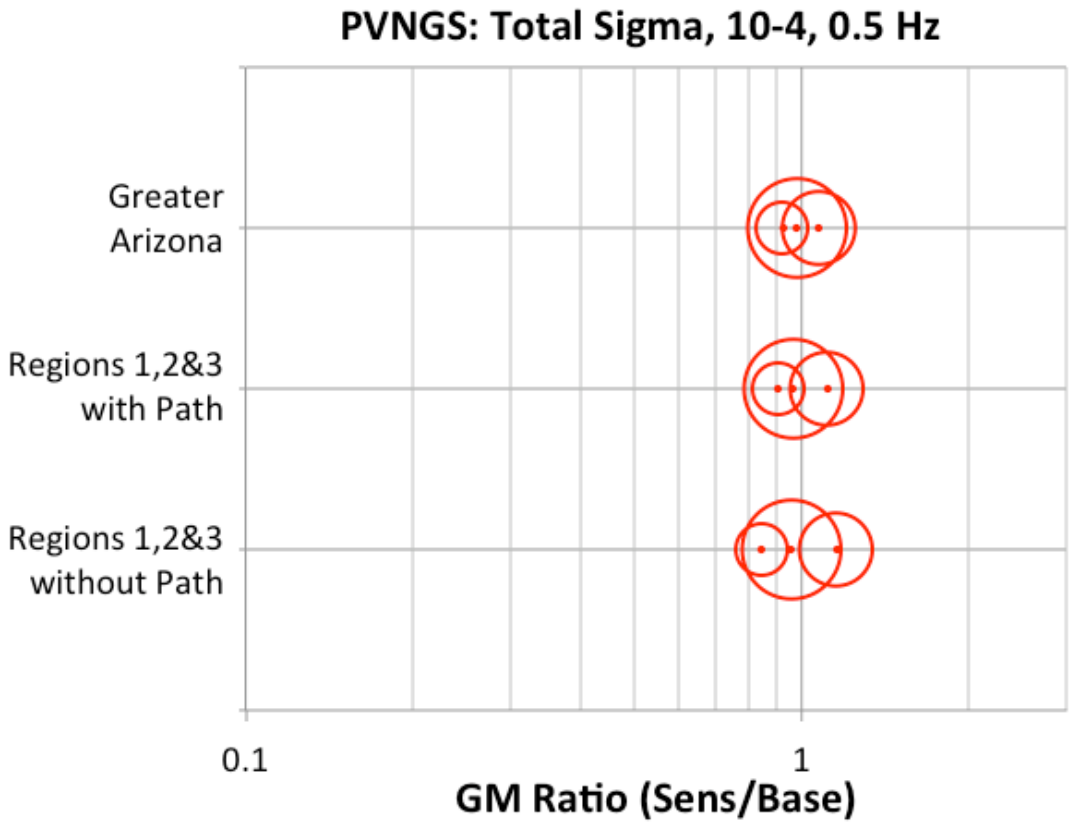

Figure 14.3-16a: Tornado plot for the total sigma logic tree for PVNGS for 0.5 Hz spectral acceleration at the 10^{-4} hazard level.

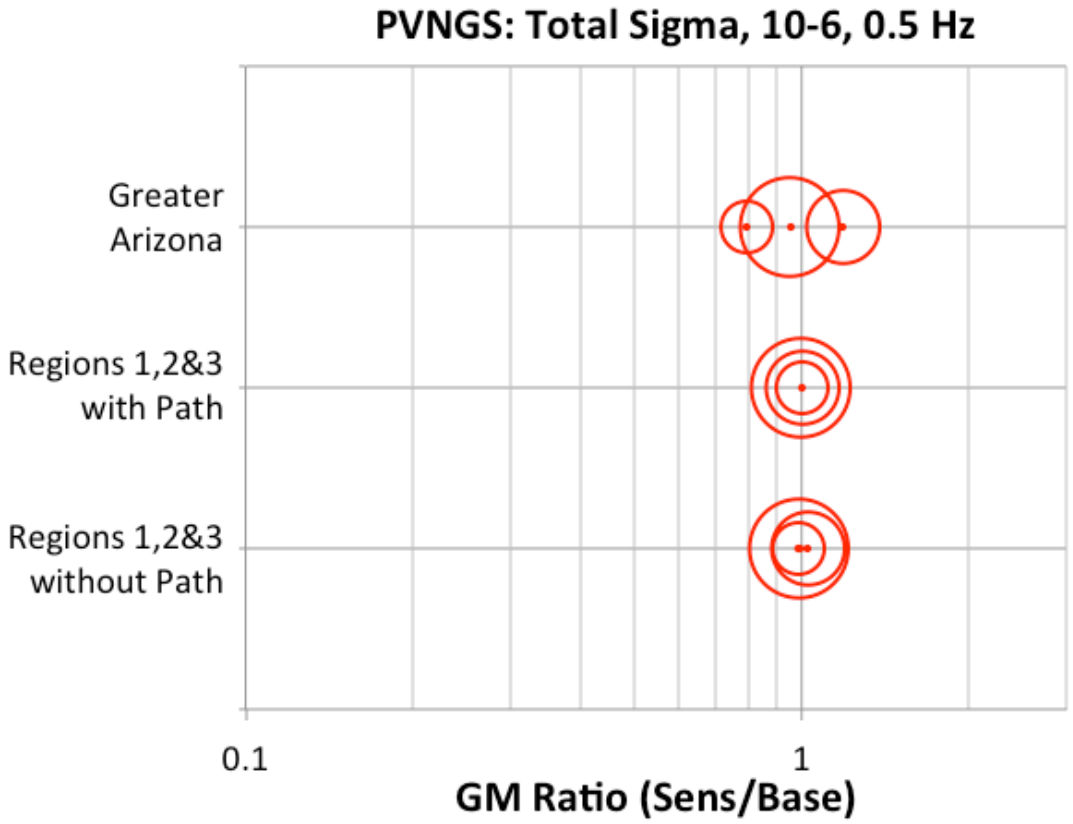

Figure 14.3-16b: Tornado plot for the total sigma logic tree for PVNGS for 0.5 Hz spectral acceleration at the 10^{-6} hazard level.

14.3.7 Summary of Sensitivity Analyses for PVNGS

Based on the sensitivity analyses for PVNGS, a summary normalized tornado plot is provided for the two spectral frequencies of 5 and 0.5 Hz at the two hazard levels of 10^{-4} and 10^{-6}. The PVNGS hazard sensitivity results, in terms of normalized ground-motion ratios for 5 Hz spectral acceleration at the 10^{-4} and 10^{-6} hazard levels, are shown in the tornado plots in Figure 14.3-17a and 14.3-17b, respectively. The results for 0.5 Hz spectral acceleration are shown in Figures 14.3-18a and 14.3-18b. In these plots the symbol size is constant and not scaled as a function of the individual weights for a specific branch of the logic tree. Similar to the previous plots, however, the green symbols are for statistically based weights and the red symbols are for the judgment based weights. The sensitivity analyses results summarized in the plots indicate that the largest sensitivity to the normalized ground-motion ratio values is from the selection of the base model cases and from the NGA-West2 models. In particular, at 5 Hz spectral acceleration, the biggest impact is from the selected base models, whereas at 0.5 Hz spectral acceleration, the biggest impact is from the selection of NGA-West2 models. At 5 Hz spectral

acceleration, the τ and ϕ_{SS} epistemic uncertainties (due to limited sample size) for the Greater Arizona sources are the second largest contributors to the hazard sensitivity. At 0.5 Hz spectral acceleration, the path terms are the second largest contributors to the hazard uncertainty at 10^{-4} hazard level, but the τ and ϕ_{SS} epistemic uncertainties (due to limited sample size) for the Greater Arizona sources are the second largest contributors to the hazard uncertainty at 10^{-6} hazard level.

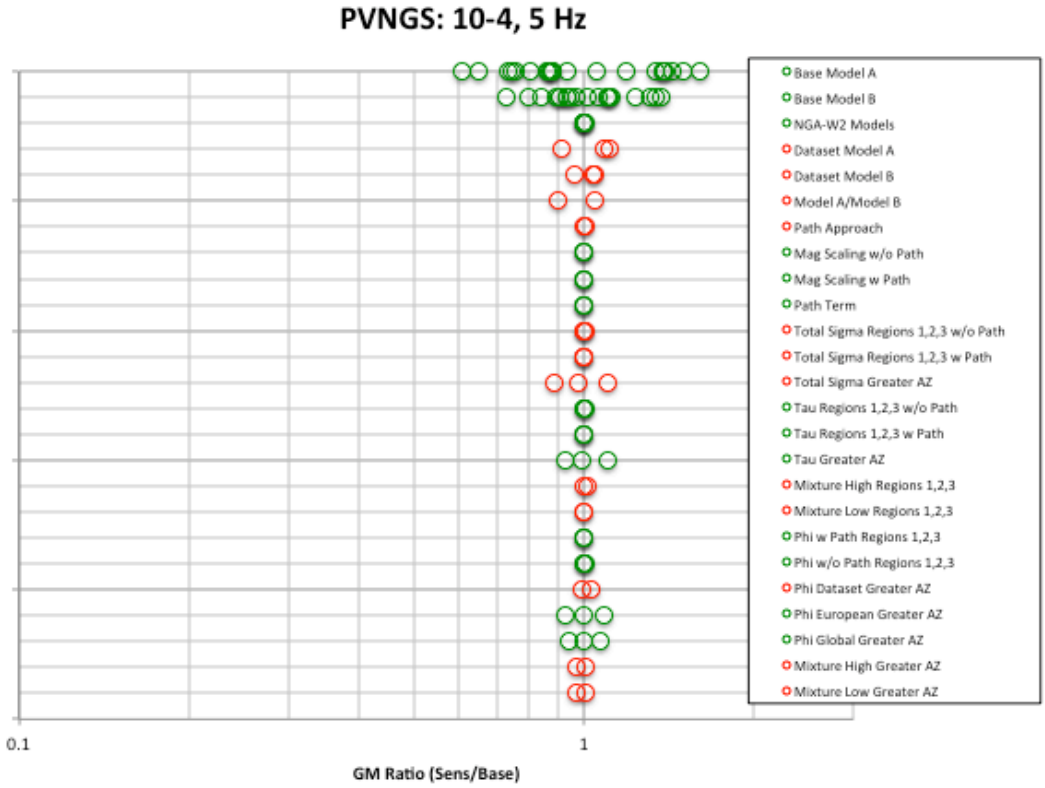

Figure 14.3-17a: Summary tornado plot for PVNGS for 5 Hz spectral acceleration at the 10^{-4} hazard level.

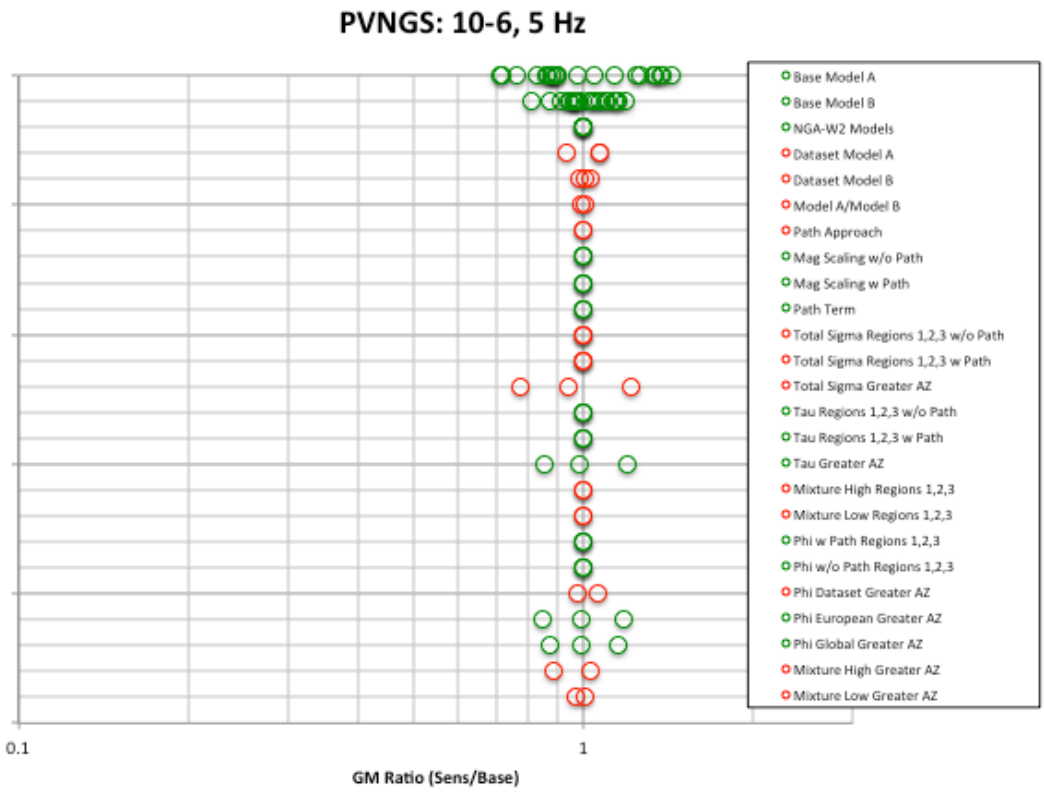

Figure 14.3-17b: Summary tornado plot for PVNGS for 5 Hz spectral acceleration at the 10^{-6} hazard level.

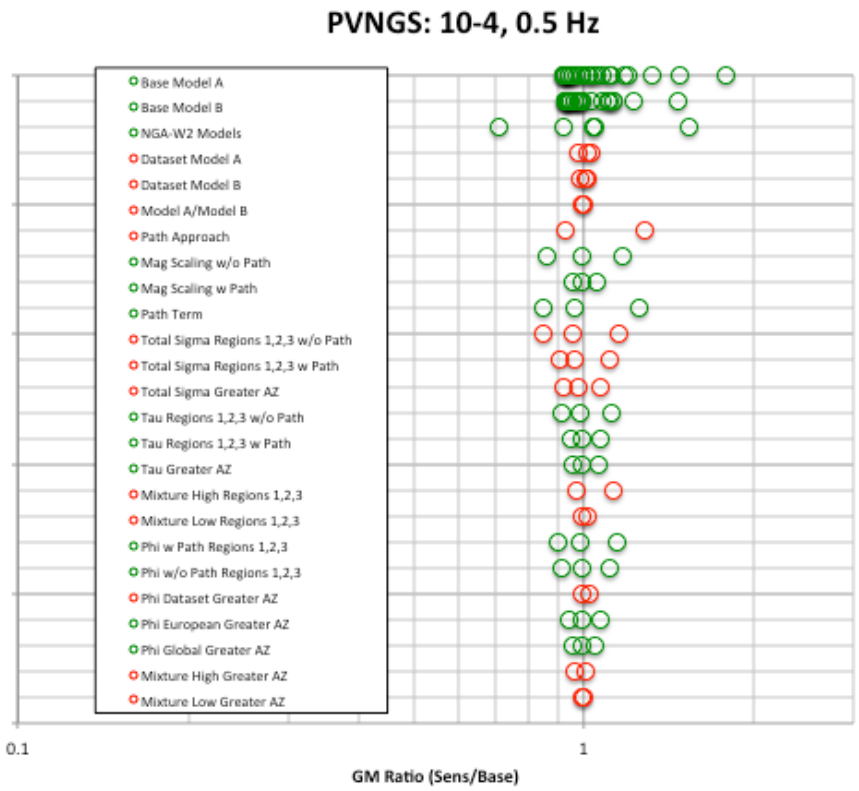

Figure 14.3-18a: Summary tornado plot for PVNGS for 0.5 Hz spectral acceleration at the 10^{-4} hazard level.

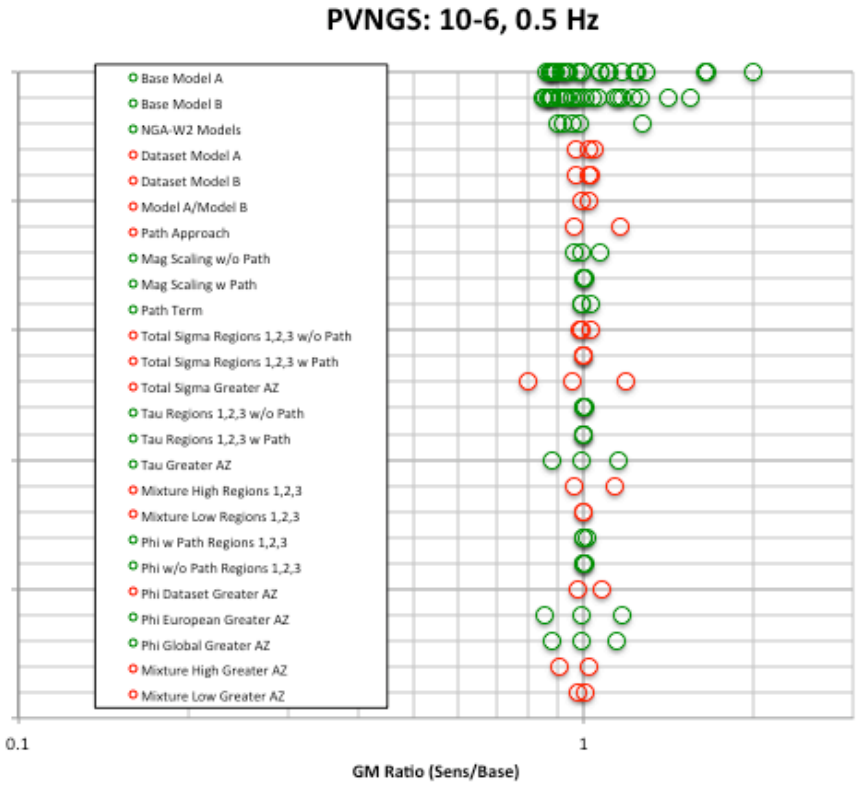

Figure 14.3-18b: Summary tornado plot for PVNGS for 0.5 Hz spectral acceleration at the 10^{-6} hazard level.

14.4 References

Boore, D.M., Stewart, J.P., Seyhan, E., and Atkinson, G.M. (2014). NGA-West 2 Equations for Predicting PGA, PGV, and 5%-Damped PSA for Shallow Crustal Earthquakes, Earthquake Spectra, Vol. 30(3), 1057-1085, DOI: 10.1193/070113EQS184M.

Campbell, K.W., and Bozorgnia, Y. (2014). NGA-West2 Ground Motion Model for the Average Horizontal Components of PGA, PGV, and 5%-Damped Linear Acceleration Response Spectra, *Earthquake Spectra*, Vol. 30(3), 1087-1115, DOI: 10.1193/062913EQS175M.

GeoPentech, Inc. (2010). San Onofre Nuclear Generating Station Seismic Hazard Assessment Program: 2010 Seismic Hazard Analysis Report, prepared by GeoPentech, Inc. for Southern California Edison Co., 74 pp. plus appendices.

Lettis Consultants International – LCI (2013). Seismic Hazard Evaluation for the Palo Verde Nuclear Generating Station Wintersburg, Arizona, Final Report (Revision 4), Arizona Public Service Co., August 2013.

PG&E (2011). Report on the Analysis of the Shoreline Fault Zone, Central Coastal California, January 2011.

15 APPLICATION GUIDELINES AND LIMITATIONS

15.1 Reference Site Conditions

The Ground Motion (GM) Models for both sites are applicable to a reference site condition with V_{S30} = 760 m/s with an average kappa value of 0.041 seconds (Section 5.3.3 and Appendix M). The kappa values estimated for the candidate GMPEs for DCPP range from 0.037 sec to 0.045 sec. For PVNGS, the kappa values from the candidate GMPEs cover the same range of 0.037 sec to 0.045 sec. This range of implied kappa values in the candidate GMPEs will lead to a similar range of implied kappa values for the suite of common-form models. Given this range of implied kappa values, no epistemic uncertainty in the host kappa value should be considered in the calculation of adjustment factors from reference-rock to PVNGS rock because this uncertainty is captured by the range of the implied kappa values within the SWUS GMC common-form based models. For the distant sources, the kappa does not have a significant effect on the hazard as these sources are significant contributors to the long period hazard only (see deaggregation in Section 4.1.4).

An issue is the representative V_S and density profiles for the reference site condition that are consistent with the representative suite of common-form models. Because the common-form models represent samples of the covariance distribution of the entire candidate GMPEs, the common-form models are not associated to a single candidate GMPE and, therefore, they are not associated to the V_S profile implied by the candidate GMPE. If several alternative V_S profiles are assigned to every common-form model, then there may be combinations of ground-motion models and Vs profiles that don't go together, which would lead to an over-estimate of the uncertainty. The other approach is to select a single representative V_S profile for all of the ground-motion models and capture the uncertainty in the site-specific site profiles for the site response study. The TI Team selected the single representative V_S profile approach. Because most of the candidate GMPEs for DCPP and PVNGS are based on the NGA-West2 data set, a representative profile for V_{S30}=760 m/s, shown in Appendix M, is selected. The digital values of the profiles are listed in the digital attachments in Appendix L (the excel file labeled “WUS_VsProfile-10272014.xls”).

The representative density values can be computed from the above Vs values using the approach recommended by Dr. David Boore of the USGS. This approach is documented in the following URL:

http://daveboore.com/daves_notes/daves_notes_on_relating_density_to_velocity_v1.2.pdf

A detailed evaluation of the density profiles was not part of the SWUS GMC TI Team's scope of work.

15.2 SWUS GMC Model Applicability for DCPP

The DCPP ground-motion models are separated into two sets: one set of models for the nearby faults and one set of models for the distant faults. The common-form models are optimized for large magnitues (**M**5.5 to **M**7.5) strike-slip and reverse events at short distances(< 10 km) that dominate the hazard at DCPP (Section 4.2.3). The common-form models are applicable to the following sources nearby DCPP (from Table 4.1-1): Hosgri fault, Shoreline fault, San Luis Bay fault, Oceano Fault, Wilmar fault, Los Osos fault, Oceano and SWBZ faults, and the Irish Hills background zone. The representative suite of common-form ground-motion models capture the Center, Body and Range (CBR) for the scenarios that dominate the hazard, but they may not capture the full CBR for the very long distances and normal-faulting events. For the other more distant sources, the NGA-West2 GMPEs are applicable. These distant sources do not contribute significantly to the hazard at DCPP. The NGA-West2 GMPEs are used for these sources rather than the common-form models because the common-form models were not well constrained for larger distances (the focus was on the short distances).

Because a general near-fault-dominated source model is used to develop the weights for the representative suite of common-form models, the weights are applicable to DCPP as long as the local sources dominate the hazard at the site. Therefore the GMC model does not need to be re-evaluated for new SSC models if the controlling sources remain at distances less than 15 km.

15.3 SWUS GMC Model Applicability for PVNGS

The PVNGS ground-motion models are separated into two types of sources: the earthquakes in the Greater Arizona regions, and the earthquakes in California and Mexico in Regions 1, 2 and 3.

For the Greater Arizona regions, the ground-motion models are optimized for magnitues **M**5.0 to **M**7.0 normal and strike-slip events at a distance less that 70 km that dominate the hazard at PVNGS for the short period; however, the GM models were constrained to extrapolate in a reasonable way for mangitudes up to **M**8.0, and for distances as large as 320 km. GM models are also applicable to reverse-faulting events. The GM models capture the CBR for the scenarios that dominate the hazard, but they may not capture the full CBR for the very long distances and reverse-faulting events.

For the sources in California and Mexico in Regions 1, 2 and 3, the GM models are optimized for the path effects from southern California to central Arizona. The GM model is based on the NGA-West2 GMPEs which can be extrapolated reasonably up to **M**8.5. The GM models capture the CBR for the scenarios that dominate the low-frequency hazard.

Branches associated to path effects from distant California sources to Arizona are applicable in the broad region where recorded data was available to constrain the effect (i.e. approximately 100 km radius from the PVNGS site, in the quadrangle comprising the nine closest Transportable Array (TA Array) stations around the PVNGS site), but are not site-specific path effects due to the lack of currently available recordings at the PVNGS that can be used for the path-effect analysis.

15.4 Interface with Site Response

The aleatory variability uses the single-station sigma (ϕ_{SS}) approach. The reduction of aleatory variability in this method requires that epistemic uncertainty in the site amplification be included in the site response studies at the sites. An additional interface issue is the effect of the kappa on the aleatory variability. In particular, the peak in the τ near 10 Hz was attributed to regional differences in kappa, and was removed from the GM model by smoothing through the peak. This uncertainty should be captured in the site response analyses by considering the epistemic uncertainty in the kappa for rock sites in the DCPP and PVNGS regions.

16 REFERENCES

Abercrombie, R.E. (2000). Crustal attenuation and site effects at Parkfield, California. *J. Geophys. Res.*, Vol. 105 (B3), 6277-6286.

Abrahamson, N.A. (2000). Effects of Rupture Directivity on Probabilistic Seismic Hazard Analysis, *Proceedings of the Sixth International Conference on Seismic Zonation: Managing Earthquake Risk in the 21st Century*, Earthquake Engineering Research Institution (EERI), Palm Springs, California, 260 pp.

Abrahamson, N.A. (2012). DCPP SSC Workshop 2 presentation [available at http://www.pge.com/mybusiness/edusafety/systemworks/dcpp/SSHAC/workshops/ws2.shtml]

Abrahamson, N.A., and Silva, W. (2008). Summary of the Abrahamson & Silva NGA Ground-Motion Relations, *Earthquake Spectra*, Vol. 24(1), 67-97.

Abrahamson, N.A., and Silva, W.J. (1997). Empirical Response Spectral Attenuation Relations for Shallow Crustal Earthquakes, *Seismol. Res. Letts*, Vol. 68(1), 94-127.

Abrahamson, N.A., and Silva, W.J. (2009). Errata for 'Summary of the Abrahamson & Silva NGA ground-motion relations' [available at http://peer.berkeley.edu/products/abrahamson-silva_nga_report_files/AS08_NGA_errata.pdf]

Abrahamson, N.A., and Somerville, P.G. (1996). Effects of the hanging wall and footwall on the ground motions recorded during the Northridge earthquake, *Bull. Seism. Soc. Am.*, Vol. 86, S93-S99.

Abrahamson, N.A., and Youngs, R.R. (1992). A stable algorithm for regression analysis using the random effects model, *Bull. Seism. Soc. Am.*, Vol. 82, 505-510.

Abrahamson, N.A., Silva, W.J., and Kamai, R. (2013). Update of the AS08 Ground-Motion Prediction Equations Based on the NGA-West2 Data Set, PEER Report No. 2013/04, Pacific Earthquake Engineering Research Center, University of California, Berkeley, CA.

Abrahamson, N.A., Silva, W.J., and Kamai, R. (2014). Summary of the AKS14 Ground-Motion Relation for Active Crustal Regions, *Earthquake Spectra*, Vol. 30(3), 1025-1055, DOI: 10.1193/070913EQS198M.

Addo, K.O., Abrahamson, N.A., and Youngs, R.R. (2012). Ground Motion Characterization (GMC) Model, *BC Hydro SSHAC Level 3 Probabilistic Seismic Hazard Analysis (PSHA) Report*, Vol.3, November 2012.

Abrahamson, N.A., and Bommer, J.J. (2005). Probability and Uncertainty in Seismic Hazard Analysis, *Earthquake Spectra*, Vol. 21(2), 603-607, DOI: 10.1193/1.1899158

Akkar, S. and Bommer, J.J. (2010). Empirical Equations for the Prediction of PGA, PGV, and Spectral Accelerations in Europe, the Mediterranean Region, and the Middle East, *Seism. Res. Letters*, Vol. 81, 195-206.

Akkar, S. and Çagnan, Z. (2010). A Local Ground-Motion Predictive Model for Turkey, and Its Comparison with Other Regional and Global Ground-Motion Models, *Bull. Seism. Soc. Am.*, Vol. 100(6), 2978-2995.

Akkar, S., Sandikkaya, M.A., and Bommer, J.J. (2014a). Empirical ground-motion models for point- and extended-source crustal earthquake scenarios in Europe and the Middle East, *Bull. Earthquake Eng*., Vol. 12(1), 359–387, DOI 10.1007/s10518-013-9461-4.

Akkar, S., Sandikkaya, M.A., and Bommer, J.J. (2014b). Erratum to: Empirical ground-motion models for point- and extended-source crustal earthquake scenarios in Europe and the Middle East, *Bull. Earthquake Eng*., Vol. 12(1), 389-390, DOI 10.1007/s10518-013-9508-6.

Akkar S., Sandıkkaya M.A., Şenyurt M., Azari Sisi A., Ay B.Ö., Traversa P., Douglas J., Cotton F., Luzi L., Hernandez B., Godey S. (2014). Reference database for seismic ground-motion in Europe (RESORCE), *Bull. Earthquake Eng.*, Vol.12(1), 311-339, DOI 10.1007/s10518-013-9506-8.

Al Atik, L. (2011). Summary of updated kappa-fpeak relationships, Report submitted to PEGASOS Refinement Project.

Al Atik, L. and Abrahamson, N. (2012). Kappa scaling using empirical ground motion data, Report prepared for the PEGASOS Refinement Project.

Al Atik, L. Kottke, A., Abrahamson, N.A, and Hollenback, J. (2013). Kappa (κ) Scaling of Ground-Motion Prediction Equations Using an Inverse Random Vibration Theory Approach, *Bull. Seismol. Soc. Am.* Vol. 14, 336-346. DOI: 10.1785/0120120200.

Al Atik, L., Abrahamson, N., Bommer, J., Scherbaum, F., Cotton, F., Kuehn, N. (2010). The variability of ground-motion prediction models and its components, *Seismol. Res. Letts*, Vol. 81(5), 794-801.

Al Atik, L., Abrahamson, N., Cotton, F., Scherbaum, F., Bommer, J., and Kuehn, N. (2010). The variability of ground-motion prediction models and its components, *Seismol. Res. Letts*, Vol. 81(5), 794-801.

Al Atik, L., and Youngs, R.R. (2013). Epistemic Uncertainty for NGA-West2 Models, *PEER Report No. 2013/11*, Pacific Earthquake Engineering Research Center, University of California, Berkeley, CA, 59 pp.

Al Atik, L., and Youngs, R.R. (2014). Epistemic Uncertainty for NGA-West2 Models, Earthquake Spectra, Vol. 30, DOI: 10.1193/062813EQS173M

Al Atik, L., Kottke, A., Abrahamson, N., and Hollenback, J. (2013). Kappa scaling of ground motion prediction equations using IRVT approach, *Bull. Seism. Soc. Am.* (Submitted).

Allen, C.R., Silver, L.T., and Stehli, F.G. (1960). Agua Blanca fault – a major transverse structure of northern Baja California, Mexico, *Bull. Seism. Soc. Am.*, Vol. 71(4), 467-482.

Allen, T.I. and Wald, D.J. (2009). On the Use of High-Resolution Topographic Data as a Proxy for Seismic Site Conditions (V_{S30}), *Bull. Seism. Soc. Am*., Vol. 99(2A), 935-943

Ancheta, T.D., Darragh, R.B., Stewart, J.P., Seyhan, E., Silva, W.J., Chiou, B., Wooddell, K., Graves, R., Kottke, A., Boore, D.M., Kishida, T. and Donahue, J.L. (2013). PEER NGA-West2 Database, *PEER Report 2013/01*, Pacific Earthquake Engineering Research Center, University of California, Berkeley, CA.

Ancheta, T.D., Darragh, R.B, Stewart, J.P., Seyhan, E., Silva, W.J, Chiou, B.S-J., Wooddell, K.E., Graves, R.W., Kottke, A.R., Boore, D.M., Kishida, T., and Donahue J.L. (2014). NGA-West 2 Database, *Earthquake Spectra*, Vol. 30(3), 989-1005, DOI: 10.1193/070913EQS197M.

Anderson, J. (2010). Source and site characteristics of earthquakes that have caused exceptional ground accelerations and velocities, *Bull. Seism. Soc. Am.,* Vol. 100, 1-36.

Anderson, J., Brune, J.N., Biasi, G., Anooshehpoor, A., and Purvance, M. (2011). Workshop Report: Application of Precarious Rocks and Related Fragile Geological Features to U.S. National Hazard Maps, *Seismological Research Letters*, Vol. 82, 431-441.

Anderson, J., Koketsu, K., and Miyake, H. (2013). Expanded Compilation and Statistics of Exceptional Ground Motions, USGS *External Grant G12AP20024 Final Technical Report*.

Anderson, J.G. (1991). A preliminary descriptive model for the distance dependence of the spectral decay parameter in southern California, *Bull. Seism. Soc. Am.*, Vol. 81, 2186–2193.

Anderson, J.G. and Brune, J. (1999). Probabilistic seismic hazard analysis without the ergodic assumption, *Seism. Res. Lett.*, Vol. 70, 19-28.

Anderson, J.G., and Brune, J.N. (1999). Methodology for using precarious rocks in Nevada to test seismic hazard models, *Bull. Seism. Soc. Am.,* Vol. 89, 456-467.

Anderson, J.G., and Heaton, T.H. (1980). Aftershock accelerograms recorded on a temporary array in Johnson, C.E., Sharp, R., and Rohan, C., eds., The Imperial Valley Earthquake: *U.S. Geological Survey Professional Paper* No. 1254, pp 443-451.

Anderson, J.G., and Hough, S E. (1984). A model for the shape of the Fourier amplitude spectrum of acceleration at high frequencie, Bulletin of the Seismological Society of America, 74(5), 1969–1993.

Anderson, J.G., and Hough, S.E. (1984). A model for the shape of the Fourier amplitude spectrum of acceleration at high frequencies, *Bull. Seism. Soc. Am*., Vol. 74(5), 1969–1993.

Anderson, J.G., and Hough, S.E. (1984). A model for the shape of the Fourier amplitude spectrum of acceleration at high frequencies, *Bull. Seismol. Soc. Am.* Vol. 74, 1969-1993.

Anderson, J.G., and Uchiyama, Y. (2011). A methodology to improve ground-motion prediction equations by including path corrections, *Bull. Seism. Soc. Am.,* Vol. 101, 1822-1846.

Anderson, J.G., Brune, J., Biasi, G., Anooshehpoor, A., and Purvance, M., (2011). Workshop Report: Applications of Precarious Rocks and Related Fragile Geological Features to U.S. National Hazard Maps, *Seismological Research Letters*, Vol. 82(3), 431-441

Anderson, J.G., Wesnousky, S.G., and Stirling, M.W. (1996). Earthquake Size as a Function of Fault Slip Rate, *Bull. Seism. Soc. Am.*, Vol. 86(3), 683-690.

Anderson, T.W., D.A. Darling. (1952). Asymptotic theory of certain goodness-of-fit criteria based on stochastic processes, *Ann. Math. Statistics* Vol.23, 193–212.

Ang, A.H.-S., and Tang, W.H. (2007). *Probability Concepts in Engineering: Emphasis on Applications to Civil and Environmental Engineering (Vol. 1)*. John Wiley and Sons, New York, 409 pp.

Aoi, S., Kunugi, T., and Fujiwara H. (2009). Trampoline effect in extreme ground motion, *Science*, Vol. 322, 727-730.

Arabasz, W. J., Pechmann, J. C., and Brown, E. D. (1987). Observational seismology and the evaluation of earthquake hazards and risk in the Wasatch Front area, Utah, in Gori, P. L., and Hays, W. W., eds., Assessment of regional earthquake hazards and risk along the Wasatch Front, Utah: *U. S. Geological Survey Open-File Report* 87-585, D1-D58.

Arizona Database: ground motions processed at PEER (2014). [http://peer.berkeley.edu/ngawest2/wp-content/uploads/2010/09/Arizona_Database.zip]

Atkinson, G., Bommer, J., and Abrahamson, N. (2014). Alternative approaches to modeling epistemic uncertainty in ground motions in Probabilistic Seismic Hazard Analysis, *Seismol. Res. Letts*, Vol. 85, 1141-1144, DOI: 10.1785/0220140120.

Atkinson, G.M, and Assatourians, K. (2015). Implementation and validation of EXSIM (a stochastic finite-fault ground-motion simulation algorithm) on the SCEC broadband platform, *Seismol. Res. Letts Letts*., Vol. 86(1), 48-60, DOI: 10.1785/0220140097.

Atkinson, G.M. (2015). Ground-Motion Prediction Equation for Small-to-Moderate Events at Short Hypocentral Distances, with Application to Induced-Seismicity Hazards, *Bull. Seismol. Soc. Am.*, Vol. 105, DOI: 10.1785/0120140142.

Atkinson, G.M. (2006). Single-station sigma, *Bull. Seism. Soc. Am*., Vol. 96(2), 446-455.

Atkinson, G.M., and Boore, D.M. (2000). Reply to comment by R. A. W. Haddon on evaluation of models for earthquake source spectra in eastern North America by Gail M. Atkinson and David M. Boore, *Bull. Seism. Soc. Am.*, Vol. 90, 1339-1341.

Atkinson, G.M., and Boore, D.M. (2006). Earthquake ground-motion prediction equations for eastern north America, *Bull. Seism. Soc. Am.*, Vol. 97(3), 2181- 2205.

Atkinson, G.M., and Silva, W. (1997). An empirical study of earthquake source spectra for California earthquakes, *Bull. Seism. Soc. Am.,* Vol. 87, 97–113.

Atkinson, G.M., Boore, D.M., Assatourians, K., Campbell K., and Motazedian, D. (2009). A guide to differences between stochastic point-source and stochastic finite-fault simulations, *Bull. Seism. Soc. Am.,* Vol. 99, 3192-3201.

Atkinson, G.M., Boore, D.M., Assatourians, K., Campbell K., and Motazedian, D. (2009). A guide to differences between stochastic point-source and stochastic finite-fault simulations, *Bull. Seism. Soc. Am*., Vol. 99, 3192-3201.

Atwater, T.M. (1970). Implications of plate tectonics for the Cenozoic tectonic evolution of western North America, *Bull. Seism. Soc. Am.,* Vol. 81, 3513-3536.

Aurenhammer, F., and Klein, R. (2000). Voronoi Diagrams. Ch. 5 in Handbook of Computational Geometry (Ed. J.-R. Sack and J. Urrutia). Amsterdam, Netherlands: North-Holland, 201-290.

Balco G., Purvance, M., Rood, D. (2011). Exposure dating of precariously balanced rocks, Quaternary Geochronology Vol. 6, 295-303

Baltay, A.S., and Hanks, T.C. (2013). Magnitude Dependence of PGA and PGV in NGA-West2 Data: Parameterization of the Model for Use by NGA-Developers, Report provided to PEER

Baltay, A.S., and Hanks, T.C. (2014). Understanding the Magnitude Dependence of PGA and PGV in NGA-West2 Data, , *Bull. Seism. Soc. Am*., Vol. 104(6), 2851–2865.

Barall, M. (2009). A grid-doubling technique for calculating dynamic three-dimensional spontaneous rupture on an earthquake fault, *Geophysical Journal International* Vol. 178, 845–859.

Barall, M. (2013). Branch fault benchmarks TPV24 and TPV25. Dynamic Rupture Code Validation Workshop, Menlo Park, CA. Conference presentation.

Base Maps: PG&E Civil Site Facilities Layout Plan (modified 1994)

Bashir, L., Gao, S.S., Liu, K.H., and Mickus, K. (2011). Crustal structure and evolution beneath the Colorado Plateau and the southern Basin and Range Province: Results from receiver function and gravity studies, *Geochem. Geophys. Geosyst.*, Vol. 12, Q06008.

Bausch, D.B., and Brumbaugh, D.S. (1994). Seismic Hazards in Arizona: Arizona Ground Shaking Intensity and 100-year Acceleration Contour Maps, Prepared for Arizona Division of Emergency Management and FEMA by the Arizona Earthquake Information Center.

Bausch, D.B., and Brumbaugh, D.S. (1997). Flagstaff Community Earthquake Hazard Evaluation, Coconino County, Arizona. Flagstaff, AZ, *Northern Arizona University Arizona Earthquake Information Center*.

Bazzurro, P. and Cornell, C. A. (1999). Disaggregaion of seismic hazard, *Bull. Seism. Soc. Am.,* Vol. 89(2), 501-520.

Beard, L.S., Karlstrom, K.E., Young, R.A., and Billingsley, G.H., eds. (2011). CRevolution 2— Origin and evolution of the Colorado River system, workshop abstracts: *U.S. Geological Survey Open-File Report* 2011–1210, 300 p., [available at http://pubs.usgs.gov/of/2011/1210/]

Beavan, J., Samsonov, S., Motagh, M., Wallace, L., Ellis, S., and Palmer, N. (2010). The Darfield (Canterbury) earthquake: geodetic observations and preliminary source model, *Bulletin of the New Zealand Society for Earthquake Engineering*, Vol. 43 (4), 228-235

Beck, S., Linkimer, L., Zandt, G., and Holland, A. (2013). Focal Mechanisms and Preliminary Attenuation Measurements in Arizona, *Arizona Geological Survey Contributed Report* C-13, 21 p. [available at http://repository.azgs.az.gov/sites/default/files/dlio/files/nid1496/cr-13-c_az_seismic.pdf]

Bell, J.W., Brune, J.N., Liu, T., Zreda, M., and Yount, J.C. (1998). Dating precariously balanced rocks in seismically active parts of California and Nevada, *Geology,* Vol. 26, 495-498.

Benaglia, T., D. Chauveau, D.R. Hunter, and D.S. Young. (2009). Mixtools: An R package for analyzing finite mixture models, *J. of Statistical Software*, Vol. 32(6), http://www.jstatsoft.org/

Bennett, R. A., Rodi, W., and Reilinger, R.E. (1996). Global Positioning System constraints on fault slip rates in southern California and northern Baja, Mexico, *Journal of Geophysical Research*, Vol. 101(B10), 21943–21960.

Beresnev, I., and Atkinson, G. (1998a). FINSIM: a FORTRAN program for simulating stochastic acceleration time histories from finite faults, *Seism. Res. Lett.*, Vol. 69, 27–32.

Berglund, H.T., Sheehan, A.F., Murray, M.H., Roy, M., Lowry, A.R., Nerem, R.S., and Blume, F. (2012). Distributed deformation across the Rio Grande Rift, Great Plains and Colorado Plateau, *Geology*, Vol. 40(1), 23-26.

Bernreuter, D.L., Savy, J.B., Mensing, R.W., Chen, J.C., and Davis, B.C. (1989). Seismic hazard characterization of 69 nuclear plant sites east of the Rocky Mountains, NUREG/CR-5250, Volumes 1-8, U.S. Nuclear Regulatory Commission, Washington D.C.

Biasi, G., and Anderson, J.G. (2007). Measurement of the parameter kappa, and reealuation of kappa for small to moderate earthquakes at seismic stations in the vicinity of Yucca Mountain, Nevada, TR-07-007, Task ORD-FY04-006, Nevada System of Higher Education, Las Vegas.

Biasi, G.P., and Smith, K.D. (2001). Site effects for seismic monitoring stations in the vicinity of Yucca Mountain, Nevada, MOL20011204.0045, Report prepared for the US DOE/University and Community College System of Nevada (UCCSN) Cooperative Agreement.

Bindi D., Massa M., Luzi L., Ameri G., Pacor F., Puglia R., and Augliera, P. (2014a). Pan-European Ground-Motion Prediction Equations for the Average Horizontal Component of PGA, PGV, and 5%-Damped PSA at Spectral Periods up to 3.0 s using the RESORCE dataset, *Bull. Earthquake Eng*., Vol. 12, 391-430, DOI: 10.1007/s10518-013-9525-5.

Bindi D., Massa M., Luzi L., Ameri G., Pacor F., Puglia R., and Augliera, P. (2014b). Erratum to: Pan-European Ground-Motion Prediction Equations for the Average Horizontal Component of PGA, PGV, and 5%-Damped PSA at Spectral Periods up to 3.0 s using the RESORCE dataset, *Bull. Earthquake Eng*., Vol. 12, 431-448, DOI: 10.1007/s10518-014-9589-x.

Bindi, D., Luzi, L., Massa, M., and Pacor, F. (2009). Horizontal and Vertical ground motion prediction equations derived from the Italian Accelerometric Archive (ITACA), *Bull. Earthquake Eng*., Vol. 8(5), 1209-1230.

Bindi, D., Pacor, F., Luzi, L., Puglia, R., Massa, M., Ameri, G., and Paolucci, R. (2011). Ground motion prediction equations derived from the Italian strong motion database, *Bull Earthquake Eng*., Vol. 9, 1899-1920.

Bird, P. (1998). Kinematic history of the Laramide orogeny in latitudes 35° -49° N, western United States, *Tectonics*, Vol. 17, 780-801.

Bird, P. (2003). An updated digital model of plate boundaries, *Geochemistry Geophysics Geosystems*, Vol. 4(3), 1027 p., doi:10.1029/2001GC000252.

Blackwell, D., Richards, M., Frone, Z., Batir, J., Ruzo, A., Williams, M., and Dingwall, R. (2011). Enhanced Geothermal Resources of the United States, *Geothermal Resources Council Transactions*, 35 pp.

Blank, H.R., Butler, W.C., and Saltus, R.W. (1998). Neogene Uplift and Radial Collapse of the Colorado Plateau--Regional Implications of Gravity and Aeromagnetic Data, in Friedman, J. D., and Huffman, A.C., Jr, eds., Laccolith Complexes of Southeastern Utah: Tectonic Control and Time of Emplacement - *Workshop Proceedings*: U.S. Geological Survey Bulletin 2158, 9-32.

Bommer, J.J. (2010). Sigma: What it is, why it matters and what we can do with it, *NGA-East workshop presentation*, February 10, 2010.

Bommer, J.J., and Abrahamson, N.A. (2006). Why do modern probabilistic seismic-hazard analyses often lead to increased hazard estimates?, *Bull. Seism. Soc. Am.,* Vol. 96, 1967–1977.

Bommer, J.J., Coppersmith, K.J., Coppersmith, R.T., Hanson, K.L., Mangongolo, A., Neveling, J., Rathje, E.M., Rodriguez-Marek, A., Scherbaum, F., Shelembe, R., Stafford, P.J., and Strasser, F.O. (2013). A

SSHAC Level 3 PSHA for a new-build nuclear site in South Africa, *Earthquake Spectra*, DOI: 10.1193/060913EQS145M, *in press*

Boore, D.M. (2003). Simulation of ground motion using the stochastic method, *Pure and Applied Geophysics*, Vol. 160, 635-675.

Boore, D.M. (1983). Stochastic simulation of high-frequency ground motions based on seismological models of the radiated spectra, *Bull. Seism. Soc. Am*., 73(6), 1865-1894.

Boore, D.M. (1986). Short-period P- and S-wave radiation from large earthquakes: implications for spectral scaling relations, *Bull. Seism. Soc. Am*., 76(1), 43-64.

Boore, D.M. (2005). SMSIM--Fortran Programs for Simulating Ground Motions from Earthquakes: Version 2.3--A Revision of OFR 96-80-A, U.S. Geological Survey Open-File Report, 59 pp.

Boore, D.M. (2009). Comparing stochastic point-source and finite-source ground-motion simulations: SMSIM and EXSIM, *Bull. Seism. Soc. Am.*, Vol. 99(6), 3202-3216.

Boore, D.M., and Atkinson, G.M. (2008). Ground-Motion Prediction Equations for the Average Horizontal Component of PGA, PGV, and 5%-Damped PSA at Spectral Periods between 0.01s and 10.0s, *Earthquake Spectra*, Vol. 24(1), 99-138.

Boore, D.M., and Joyner, W.B. (1997). Site amplification for generic rock sites, *Bull. Seism. Soc. Am*., Vol. 87, 327-341.

Boore, D.M., Azari, A., and Akkar, S. (2012). Using pad-stripped acausally filtered strong-motion data, *Bull. Seism. Soc. Am.* (Submitted).

Boore, D.M., Joyner, W.B., and Fumal, T.E. (1997). Equations for estimating horizontal response spectra and peak acceleration from western North American earthquakes: A summary of recent work, *Seism. Res. Letters*, Vol. 68, 128-153.

Boore, D.M., Stewart, J.P., Seyhan, E., and Atkinson, G.M. (2013). NGA-West2 Equations for Predicting Response Spectral Accelerations for Shallow Crustal Earthquakes, *Pacific Earthquake Engineering Research Center report* 2013/05.

Boore, D.M., Stewart, J.P., Seyhan, E., and Atkinson, G.M. (2014). NGA-West 2 Equations for Predicting PGA, PGV, and 5%-Damped PSA for Shallow Crustal Earthquakes, *Earthquake Spectra*, Vol. 30(3), 1057-1085, DOI: 10.1193/070113EQS184M.

Boore, D.M., Watson-Lamprey, J., and Abrahamson, N.A. (2006). Orientation-independent measures of ground motion, *Bull. Seism. Soc. Am*., Vol. 96 (4A), 1502-1511.

Bora, S.S., Scherbaum, F., Kuehn, N., and Stafford, P. (2013). Fourier spectral- and duration models for the generation of response spectra adjustable to different source-, propagation-, and site conditions, *Bull. Earthquake Eng*., Vol. 12(1), 467-493, DOI: 10.1007/s10518-013-9482-z.

Boumediene, D., Bard, P.Y., and Cotton, F. (2013). Towards fully data driven ground-motion prediction models for Europe, *Bulletin of Earthquake Engineering*, DOI 10.1007/s10518-013-9481-0

Bozorgnia, Y., Abrahamson, N.A., Al Atik, L., Ancheta, T.D., Atkinson, G.M., Baker, J.W., Baltay, A., Boore, D.M., Campbell, K.W., Chiou, B.S.-J., Darragh, R., Day, S., Donahue, J., Graves, R.W., Gregor, N., Hanks, T., Idriss, I.M., Kamai, R., Kishida, T., Kottke, A., Mahin, S.A., Rezaeian, S., Rowshandel, B.,

Seyhan, E., Shahi, S., Shantz, T., Silva, W., Spudich, P., Stewart, J.P., Watson-Lamprey, J., Wooddell, K., and Youngs, R. (2014). NGA-West2 research project, *Earthquake Spectra* Vol. 30(3), 973-987.

Bradley, B.A. (2010). NZ-Specific Pseudo-Spectral Acceleration Ground Motion Prediction Equations Based on Foreign Modes, Department of Civil Engineering, University of Canterbury, Christchurch, New Zealand, Sept. 2010.

Bradley, B.A. (2013). A New Zealand-Specific Pseudospectral Acceleration Ground-Motion Prediction Equation for Active Shallow Crustal Earthquakes Based on Foreign Models, *Bull. Seism. Soc. Am.*, Vol. 103(3), 1801-1822, DOI: 10.1785/0120120021.

Brown, L.G. (1978). Recent fault scarps along the eastern escarpment of the Sierra San Pedro Martir, Baja California. *MS thesis*, San Diego State University, San Diego, California, 88 p.

Brumbaugh, D.S. (1987). A tectonic boundary for the southern Colorado Plateau, *Tectonophysics*, Vol. 136, 125–136.

Brumbaugh, D.S. (2008). Seismicity and tectonics of the Blue Ridge area of the Mogollon Plateau, Arizona, *Bull. Seism. Soc. Am.,* Vol. 98(3), 1527–1534

Brune, J.N. (1970). Tectonic stress and the spectra of seismic shear waves from earthquakes, *J. Geophys. Res*., Vol. 76, 4997-5009.

Brune, J.N. (1971). Correction, *J. Geophys. Res.,* Vol. 76, 5002.

Brune, J.N. (1996). Precariously balanced rocks and ground motion maps for southern California, *Bull. Seism. Soc. Am.*, Vol. 86, 43-54.

Brune, J.N. and Whitney, J.W. (2000). Precarious Rocks and Seismic Shaking at Yucca Mountain, Nevada: in Whitney, J.W. and Keefer, W.R., eds., Geologic and geophysical studies of Yucca mountain, Nevada, A potential high-level radioactive-waste repository, *USGS Digital Data Series 058*, Chapter M, 19 p.

Brune, J.N., and Whitney, J.W. (1992). Precariously balanced rocks with rock varnish: paleoindicators of maximum ground acceleration? *Seism. Res. Lett*., Vol. 63, 1-21.

Budnitz, R.J., Apostolakis, G., Boore, D.M., Cluff, L.S., Coppersmith, K.J., Cornell, C.A., and Morris, P.A. (1997). Recommendations for Probabilistic Seismic Hazard Analysis: Guidance on Uncertainty and Use of Experts: Washington, D.C., US Nuclear Regulatory Commission, NUREG/CR-6372, 278 pp.

Bull, W.B., and Pearthree, B.A. (1988). Frequency and size of Quaternary surface ruptures of the Pitaycachi fault, northeastern Sonora, Mexico, *Bull. Seism. Soc. Am.,* Vol. 78, 956-978.

Campbell, K.W. (1997). Empirical near-source attenuation relations for horizontal and vertical components of peak ground acceleration, peak ground velocity, and pseudo-absolute acceleration response spectra, *Seismol. Res. Lett.*, Vol. 68, 154-179.

Campbell, K.W. (2003). Prediction of strong ground motion using the hybrid empirical method and its use in the development of ground-motion (attenuation) relations in eastern North America, *Bull. Seismol. Soc. Am.*, Vol. 93, 1012-1033.

Campbell, K.W. (2004). Erratum to Prediction of strong ground motion using the hybrid empirical method and its use in the development of ground-motion (attenuation) relations in Eastern North America, *Bull. Seism. Soc. Am.,* Vol. 94(6), 2418.

Campbell, K.W. (2009). Estimates of shear-wave Q and κ0 for unconsolidated and semiconsolidated sediments in Eastern North America, *Bull. Seismol. Soc. Am.*, Vol. 99(4), 2365−2392.

Campbell, K.W., and Bozorgnia, Y. (2003). Updated near-source ground motion (attenuation) relations for the horizontal and vertical components of peak ground acceleration and acceleration response spectra, *Bull. Seism. Soc. Am.*, Vol. 93, 314-331.

Campbell, K.W., and Bozorgnia, Y. (2008). NGA Ground Motion Model for the Geometric Mean Horizontal Component of PGA, PGV, PGD and 5% Damped Linear Elastic Response Spectra for Periods Ranging from 0.01 to 10 s, *Earthquake Spectra*, Vol. 24(1), 139-171.

Campbell, K.W., and Bozorgnia, Y. (2013). NGA-West2 Campbell-Bozorgnia Ground Motion Model for the Horizontal Components of PGA, PGV, and 5%-Damped Elastic Pseudo-Acceleration Response Spectra for Periods Ranging from 0.01 to 10 sec, *PEER Report 2013/06*.

Campbell, K.W., and Bozorgnia, Y. (2014). NGA-West2 Ground Motion Model for the Average Horizontal Components of PGA, PGV, and 5%-Damped Linear Acceleration Response Spectra, *Earthquake Spectra*, Vol. 30(3), 1087-1115, DOI: 10.1193/062913EQS175M

Campbell, K.W., and Bozorgnia, Y. (2014). NGA-West2 Ground Motion Model for the Average Horizontal Components of PGA, PGV, and 5%-Damped Linear Acceleration Response Spectra, *Earthquake Spectra*, Vol. 30(3), 1087-1115, DOI: 10.1193/062913EQS175M.

Campbell, K.W., Hashash, Y.M.-A., Kim, B., Kottke, A.R., Rathje, E., Silva, W.J., and Stewart, J.P. (2014) Reference-Rock Site Conditions for Central and Eastern North America: Part II - Attenuation (Kappa) Definition, *PEER Report 2014/12*, Pacific Earthquake Engineering Research (PEER) Center, University of California, Berkeley, CA, August 2014, 54 pp.

Castro, R.R., Acosta, J.G., Wong, V.M. (2011a). Location of Aftershocks of the 4 April 2010 Mw 7.2 El Mayor-Cucapah Earthquake of Baja California, Mexico, *Bull. Seism. Soc. Am.,* Vol. 101, 3072-3080.

Castro, R.R., Shearer, P.M., Astiz L., Suter M., Jacques-Ayala, C., and Vernon, F. (2010). The Long-Lasting Aftershock Series of the 3 May 1887 Mw 7.5 Sonora Earthquake in the Mexican Basin and Range Province, *Bull. Seismol. Soc. Am.*, Vol. 100(3), 1153-1164.

Castro, R.R., Valdes-Gonzalez, C., Shearer, P., Wong, V., Astiz, L., Vernon, F., Perez-Vertti, A., and Mendoza, A. (2011b). The 3 August 2009 Mw 6.9 Canal de Ballenas region, Gulf of California, earthquake and its aftershocks, *Bull. Seism. Soc. Am.,* Vol. 101(3), 929-939.

CEUS (2012). Central and Eastern United States Seismic Source Characterization for Nuclear Facilities, Report published by NRC Report NUREG-2115, DOE Report NE-0140, EPRI Report 1021097, 6 Volumes.

Chandler, A.M., Lam, N.T.K., and Tsang, H.H. (2006). Near-surface attenuation modeling based on rock shear-wave velocity profile, *Soil Dyn. Earthq. Eng.,* Vol. 26, 1004–1014.

Chapman, M.C., and Godbee, R.W. (2012). Modeling Geometrical Spreading and the Relative Amplitudes of Vertical and Horizontal High-Frequency Ground Motions in Eastern North America, *Bull. Seism. Soc. Am.,* Vol. 102, 1957-1975, doi:10.1785/0120110081

Chen, Y-H., and Tsai, C-C.P. (2002). A new method for estimation of the attenuation relationship with variance components, *Bull. Seism. Soc. Am.,* Vol. 92, 1984-1991.

Chiou B.S.-J., Spudich P. (2013). The Chiou and Spudich NGA-West2 directivity predictor DPP, *PEER Report 2013/09*, Pacific Earthquake Engineering Research Center, University of California, Berkeley, CA.

Chiou, B., Darragh, R., Gregor, N., and Silva, W. (2008). NGA project strong-motion database, *Earthquake Spectra*, Vol. 24(1), 23-44.

Chiou, B.S.-J., and Youngs, R.R. (2008). An NGA Model for the Average Horizontal Component of Peak Ground Motion and Response Spectra, *Earthquake Spectra*, Vol. 24(1), 173-215.

Chiou, B.S.-J., and Youngs, R.R. (2013). Update of the Chiou and Youngs NGA Ground Motion Model for Average Horizontal Component of Peak Ground Motion and Response Spectra. May 2013, *PEER Report 2013/07*, Pacific Earthquake Engineering Research Center, University of California, Berkeley, CA.

Chiou, B.S.-J., and Youngs, R.R. (2014). Update of the Chiou and Youngs NGA Model for the Average Horizontal Component of Peak Ground Motion and Response Spectra, *Earthquake Spectra*, Vol. 30(3), 1117-1153, DOI: 10.1193/072813EQS219M.

Chiou, B.S.-J., Darragh, R., and Silva, W. (2008). An overview of the NGA database, *Earthquake Spectra,* Vol. 24, 23–44.

Chiou, B.S.-J., Youngs, R.R., Abrahamson, N.A., and Addo, K. (2010). Ground-motion attenuation model for small-to-moderate shallow crustal earthquakes in California and its implications on regionalization of ground-motion prediction models, *Earthquake Spectra,* Vol. 26(4), 907-926.

Chiou, S.-J., Makdisi, F.I., and Youngs, R.R. (2000). Style-of-Faulting and Footwall/Hanging Wall Effects on Strong Ground Motion, *FY 1995 NEHRP Award Number 1434-95-G-2614*, final report, 21 pp.

Community Fault Model (CFM), 2012, SCEC Community Fault Model version 4.0, accessed and downloaded January 2013, available at [http://structure.harvard.edu/cfm/modelaccess.html].

Community Velocity Model – Harvard (CVM-H), 2012, SCEC Community Velocity Model version 11.9.1, accessed January 2013, available at [http://www.data.scec.org/researchtools/3d-velocity.html].

Community Velocity Model (CVM), 2012, SCEC Community Velocity Model version 4.0, accessed January 2013, available at [http://www.data.scec.org/research-tools/3dvelocity. html].

Conrad, J.E., Ryan, H.F., and Sliter, R.W. (2010). Tracing active faulting in the Inner Continental Borderland, Southern California, using new high-resolution seismic reflection and bathymetric data [abstract]: Seismological Society of America 2010 Annual Meeting, *Seismological Research Letters*, Vol. 81(2), 347.

Coppersmith, K.J., Bommer, J., Hanson, K., Coppersmith, R., Unruh, J.R., Wolf, L., Youngs, R., Al Atik, L., Rodriguez-Marek, A., Toro, G., and Montaldo-Falero, V. (2014). Hanford Sitewide Probabilistic Seismic Hazard Analysis, *PNNL-23361*, Pacific Northwest National Laboratory, Richland Washington.

Coppersmith, K.J., Bommer, J.J., Kammerer, A.M., and Ake, J. (2010). Implementation guidance for SSHAC Level 3 and 4 processes; 10th International Probabilistic Safety and Management Conference, Seattle, Washington, June 7-11, 2010.

Darragh R.B., Silva W.J., Gregor N. (2004). Strong motion record processing procedures for the PEER center, *Proceedings of COSMOS Workshop on Strong-Motion Record Processing*, Richmond, California, pp. 1–12.

Dawood, H.M., Rodriguez-Marek, A., Bayless, J., Goulet, C., and Thompson E. (2014). The KiK-net database processed using an automated ground motion processing protocol. Available at https://nees.org/resources/7849.

Day, S.M., Graves, R., Bielak, J., Dreger, D., Larsen, S., Olsen, K.B., Pitarka, A. and Ramirez-Guzman, L. (2008). Model for basin effects on long-period response spectra in Southern California, *Earthquake Spectra*, Vol. 24 (1), 257-277.

DeCelles, P.G. (2004). Late Jurassic to Eocene Evolution of the Cordilleran, Thrust Belt and Foreland Basin Systems, Western U.S.A., *American Journal of Science*, Vol. 304, 105-168.

DeMets, C., and Dixon, T. (1999). New kinematic models for Pacific-North America motion from 3 Ma to present, I: Evidence for steady motion and biases in the NUVEL-1A model, *Geophysical Research Letters*, Vol. 26(13), doi: 1029/1999GL900405.

Demsey, K.A., and Pearthree, P.A. (1990). Late Quaternary Surface-Rupture History Of The Sand Tank Fault, And Associated Seismic Hazard For The Proposed Superconducting Super Collider Site, Maricopa County, Arizona, *Arizona Geological Survey, Open-File Report* 90-01, 46 p.

DePolo, C.M., and LaPointe, D.D - Editors (2011). The 21 February 2008 Mw 6.0 Wells, Nevada Earthquake - A compendium of earthquake-related investigations prepared by the University of Nevada, Reno*, Nevada Bureau of Mines and Geology Special Publication* Vol. 36

Derras, B., Bard, P-Y, and Cotton, F. (2013) Towards fully data driven ground-motion prediction models for Europe, *Bull Earthquake Eng*., Vol. 12, 391–430, DOI: 10.1007/s10518-013-9481-0.

Di Alessandro, C. and Abrahamson, A. (2013). Ground motion for complex multi-fracture, *Proceedings of IASPEI General Assembly*, Goteborg, July 2013 – Paper S201bS1.04

Dixon, T.H., Robaudo, S., Lee, J., and Reheis, M.C. (1995). Constraints on present-day Basin and Range deformation from space geodesy, *Tectonics*, Vol. 14(4), 755–772.

Donahue, J. (2013). Data to Constrain GMPEs in Critical Ranges –Multi-Fault Ruptures, Presentation to SWUS GMC Workshop #1.

Donahue, J., and Abrahamson, N.A. (2013). Simulation-based hanging-wall effects, *PEER Report 2013/14*, Pacific Earthquake Engineering Research Center, University of California, Berkeley, CA.

Donahue, J., and Abrahamson, N.A. (2014). Simulation-based Hanging-Wall Effects, Earthquake Spectra, Vol. 30(3), 1269-1284, DOI: 10.1193/071113EQS200M.

Dor, O., Ben-Zion, Y., Rockwell, T.K., and Brune, J.N. (2006a). Pulverized Rocks in the Mojave section of the San Andreas FZ, *Earth Planet. Sci. Lett*., Vol. 245, 642–654, doi:10.1016/j.epsl.2006.03.034.

Dor, O., Chester, J.S., Ben-Zion, Y., Brune, J.N., and Rockwell, T.K. (2009). Characterization of damage in sandstones along the Mojave section of the San Andreas Fault: Implications for the shallow extent of damage generation, *Pure Appl. Geophys*., Vol. 166, 1747–1773, doi:10.1007/s00024-009-0516-z.

Dor, O., Rockwell, T.K., and Ben-Zion, Y. (2006b). Geologic observations of damage asymmetry in the structure of the San Jacinto, San Andreas and Punchbowl faults in southern California: A possible indicator for preferred rupture propagation direction, *Pure Appl. Geophys*., Vol. 163, doi 10.1007/s00024-005-0023-9.

Dor, O., Yildirim, C., Rockwell, T.K., Ben-Zion, Y., Emre, O., Sisk, M., and Duman, T.Y. (2008). Geological and geomorphologic asymmetry across the rupture zones of the 1943 and 1944 earthquakes on the North Anatolian Fault: Possible signals for preferred earthquake propagation direction, *Geophys. J. Int*., Vol. 173, 483–504, doi:10.1111/j.1365-246X.2008.03709.x.

Dorsey, R.J. and Umhoefer, P J. (2012). Influence of sediment input and plate motion obliquity on basin development along an active oblique-divergent plate boundary: Gulf of California and Salton Trough. In: Tectonics of Sedimentary Basins: Recent Advances (C. Busby and A. Azor, Editors), Blackwell Publishing, p. 209-225.

Douglas, J., Akkar, S., Ameri, G., Bard. P-J, Bindi, D., Bommer, J.J, Bora, S.S., Cotton, F., Derras, B., Hermkes, M., Kuehn, N.M., Luzi, L., Massa, M., Pacor, F., Riggelsen, C., Sandıkkaya, M.A., Scherbaum, F., Stafford, P.J., Traversa, P. (2013). Comparisons among the five ground-motion models developed using RESORCE for the prediction of response spectral accelerations due to earthquakes in Europe and the Middle East, *Bulletin of Earthquake Engineering*, DOI 10.1007/s10518-013-9522-8

Douglas, J., Gehl, P., Bonilla, L.F., and Gelis, C. (2010). A kappa model for mainland France, *Pure Appl. Geophys*., Vol. 167, 1303–1315.

Douglas, J.P., and Boore, D.M. (2011). High-frequency filtering of strong-motion records, *Bulletin of Earthquake Engineering*, Vol. 9, 395-409.

Dreger, D., Tinti, E., and Cirella, A. (2005). Slip velocity function parameterization for broadband ground motion simulation, *Seismol. Soc. Am. 2007 Annual Meeting*, Waikoloa, Hawaii, 11-13 April 2007.

Dreger, D.S. Dreger, Ford, S.R, and Ryder, I. (2011). "Preliminary Finite-Source Study of the February 21, 2008 Wells, Nevada Earthquake". Nevada Bureau of Mines and Geology Special Publication 36, 147-156.

Dreger, D.S., Beroza, G.C., Day, S.M., Goulet, C.A., Jordan, T.H., Spudich, P.A, and Stewart, J.P. (2013). Evaluation of SCEC Broadband Platform Phase 1 Ground Motion Simulation Results, 33 pp. plus Appendices, Report submitted to SCEC, Aug. 1 2013 and available at http://scec.usc.edu/scecpedia/SCEC_BBP_Phase_1_Evaluation

Dreger, D. S., G. C. Beroza, S. M. Day, C. A. Goulet, T. H. Jordan, P. A. Spudich, and J. P. Stewart (2015). Validation of the SCEC broadband platform v14.3 simulation methods using pseudospectral acceleration data, *Seismol. Res. Lett.*, Vol. 86(1), 39-47, DOI: 10.1785/0220140118.

Drouet S., Cotton F., and Gueguen, P. (2010). v_{S30}, κ, regional attenuation and Mw from accelerograms: application to magnitude 3–5 French earthquakes, *Geophys. J. Int*., Vol. 182, 880–898.

DuBois, S.M., Smith, AW., Nye, N.K., and Nowak, T.A, Jr. (1982). Arizona earthquakes, 1776-1980, *Arizona Bureau of Geology and Mineral Technology Bulletin* Vol. 193, 456 p., 1 sheet, scale 1:1,000,000.

Edwards B., Fah, D., and Giardini, D. (2011). Attenuation of seismic shear wave energy in Switzerland. *Geophys. J. Int.,* Vol. 185, 967–984

Electric Power Research Institute – EPRI (1993). Guidelines for determining design basis ground motions. Palo Alto, Calif: Electric Power Research Institute, Vol. 1‑5, *EPRI TR‑102293*.

Electric Power Research Institute – EPRI (2004). CEUS Ground Motion Project Final Report, *EPRI Report 1009684*, December, Palo Alto, Calif.

Electric Power Research Institute – EPRI (2006). Program on Technology Innovation: Truncation of the Lognormal Distribution and Value of the Standard Deviation for Ground Motion Models in the Central and Eastern United States, *EPRI Report 1013105*, Technical Update, February, Palo Alto, Calif.

EPRI-SOG (1988). Seismic hazard methodology for the central and eastern United States, *EPRI NP-4726A*, Revision 1, Volumes 1-11, Electric Power Research Institute, Palo Alto, California

Erickson, D., McNamara, D.E., and Benz, H.M. (2004). Frequency-dependent Lg Q within the continental United States, *Bull. Seism. Soc. Am*., Vol. 94, 1630-1643.

Euge, K.M., Schell, B.A., and Lam, I.P. (1992). Development of seismic acceleration maps for Arizona, *Arizona Department of Transportation Report* AZ92-344, 327 p., 5 sheets, scale1:1,000,000.

Faccioli, E., Bianchini, A., and Villani, M. (2010). New ground motion prediction equations for T > 1 s and their influence on seismic hazard assessment, *Proc. Univ. Tokyo Sym. on Long-Period Ground Motion and Urban Disaster Mitigation*, March 17-18, 2010.

Fenton, C.R., Webb, R.H., Pearthree, P.A., Cerling, T.E., and Poreda, R.J. (2001). Displacement rates on the Toroweap and Hurricane faults--Implications for Quaternary downcutting in the Grand Canyon, Arizona, *Geology*, Vol. 29, 1035-1038.

Field, E. H., Jordan, T.H., and Cornell, C. A. (2003). OpenSHA: A developing community-modeling environment for seismic hazard analysis, *Seism. Res. Letters*, Vol. 74(4), 406-419.

Field, E., Dawson, T., Ellsworth, W., Felzer, V., Frankel, A., Gupta, V., Jordan, T., Parsons, T., Petersen, M., Stein, R., Weldon, R., and Wills, C. (2008). The Uniform California Earthquake Rupture Forecast, Version 2 (UCERF 2): U.S. Geological Survey Open-File Report and California Geological Survey Special Report Vol. 203, 97p.

Field, E.H., Dawson, T.E., Felzer, K.R., Frankel, A.D. Gupta, V., Jordan, T.H., Parsons, T., Petersen, M.D., Stein, R.S., Weldon R.J. II, and Wills C.J. (2009). Uniform California earthquake rupture forecast, version 2 (UCERF2.0). *Bull. Seism. Soc. Am*., Vol. 99, 2053-2107.

Fletcher, J.M. and Spelz, R.M. (2009). Patterns of Quaternary deformation and rupture propagation associated with an active low-angle normal fault, Laguna Salada, Mexico: Evidence of a rolling hinge?, *Geosphere*, Vol. 5, 385-407.

Frankel, A., Carver, D., Cranswick, E., Bice, T., Sell, R., and Hanson, S. (2001). Observation of basin ground-motions from a dense seismic array in San Jose, California, *Bull. Seism. Soc. Am*., Vol. 91, 1-12.

Frassetto, A., Gilbert, H., Zandt, G., Beck, S., and Fouch, M. (2006). Support of high elevation in the southern Basin and Range based on the composition and architecture of the crust in the Basin and Range and Colorado Plateau, *Earth and Planetary Science Letters,* Vol. 249(1-2), 62-73.

Fugro Consultants (2010). Initial assessment of precariously balanced rocks in the DCPP area (Ground Motion Task GM-3), draft letter report submitted to N. Abrahamson, PG&E, dated September 11, 2010. [Selected publications provided therein.]

Fukushima ground motions processed at PEER (2014). [http://peer.berkeley.edu/ngawest2/wp-content/uploads/2010/09/Fukushima_Flatfile_RotD50_d050_04112014.zip]

Gastil, R.G. and Krummenacher, D. (1977). Reconnaissance geology of coastal Sonora between Puerto Lobos and Bahía Kino, *Geological Society of America Bulletin*, Vol. 88, 189-198.

GeoPentech, Inc. (2010). San Onofre Nuclear Generating Station Seismic Hazard Assessment Program: 2010 Seismic Hazard Analysis Report, prepared by GeoPentech, Inc. for Southern California Edison Co., 74 pp. plus appendices.

GeoPentech, Inc. (2013). San Onofre Nuclear Generating Station Long Term SONGS Seismic Setting Research Program: Site Characterization Report, prepared by GeoPentech, Inc. for Southern California Edison Co., Draft Report version October 2012, 53 pp. plus appendices.

GeoPentech, Inc. (2013). Southwester United States Ground Motion Characterization SSHAC Level 3 Workshop #1 Proceedings, prepared by GeoPentech, Inc. for Arizona Public Service Co., Pacific Gas and Electric Co. and Southern California Edison Co., 69 pp., [available at http://www.pge.com/includes/docs/pdfs/shared/edusafety/systemworks/dcpp/SSHAC/sugmworkshops/WS1_Proceedings.pdf].

Geusebroek, J., Burghouts, G., and Smeulders, A. (2005). The Amsterdam library of object images, *Int. J. Comput. Vision*, Vol. 61, 103-112.

Gibbard, P. L., Head, M. J., Walker, M. J. C., and the Subcommission on Quaternary Stratigraphy (2010). Formal ratification of the Quaternary System/Period and the Pleistocene Series/Epoch with a base at 2.58 Ma, *Journal of Quaternary Science*, Vol. 25, 96–102.

Gilbert, H., Velasco, A.A., and Zandt, G. (2007). Preservation of Proterozoic Terrane Boundaries Within the Colorado Plateau and Implications for Its Tectonic Evolution, *Earth and Planetary Science Letters*, Vol. 258, 237-248.

Gledhill, K., Ristau, J., Reyners, M., Fry, B, and Holden, C. (2011). The Darfield (Canterbury, New Zealand) Mw 7.1 Earthquake of September 2010: A Preliminary Seismological Report, *Seismological Research Letters*, Vol. 82(3), 378-386

Goda, K., and Hong, H. P. (2008). Spatial Correlation of Peak Ground Motions and Response Spectra *Bull. Seismol. Soc. Am.,* Vol. 98(1), 354–365.

Goldstein, P., Dodge, D., Firpo, M., and Minner, L. (2003). SAC2000: Signal processing and analysis tools for seismologists and engineers, *The IASPEI International Handbook of Earthquake and Engineering Seismology*, W.H.K. Lee, H. Kanamori, P.C. Jennings, C. Kisslinger (Editors), Academic Press, London.

Gonzales-Leon, C.M., Solari, L., Sole, J., Ducea, M.H., Lawton, T.F., Bernal, J.P., Becuar, E.G., Gray, F., Martinez, M.L., and Santacruz, R.L. (2011). Stratigraphy, geochronology, and geochemistry of the Laramide magmatic arc in north-central Sonora, Mexico, *Geosphere*, Vol. 7(6), 1392-1418.

Goulet, C.A., Abrahamson, N.A., Somerville, P.G., and Wooddell, K.E. (2015). The SCEC Broadband Platform Validation Exercise: Methodology for Code Validation in the Context of Seismic-Hazard Analyses, *Seismological Research Letters*, Vol. 86(1), 17-26, DOI: 10.1785/0220140104.

Graizer, V. (2012), "Effects of low-pass filtering and re-sampling on spectral and peak ground acceleration in strong-motion records", *Proc. 15th World Conference of Earthquake Engineering*, Lisbon, Portugal, 24-28 Sep., 10 pp.

Graizer, V. and Kalkan, E. (2007). Ground-motion Attenuation Model for Peak Horizontal Acceleration from Shallow Crustal Earthquakes, *Earthquake Spectra*, Vol. 23 (3), 585-613.

Graizer, V. and Kalkan, E. (2009). Prediction of response spectral acceleration ordinates based on PGA attenuation, *Earthquake Spectra*, Vol. 25 (1), 39-69.

Graizer, V. and Kalkan, E. (2011). Modular filter-based approach to ground-motion attenuation modeling, *Seism. Res. Lett.*, Vol. 82(1), 21-31.

Graizer, V. (2014). Updated Graizer-Kalkan Ground-motion Prediction Equations for Western United States, *Proceedings for the 10th U.S. National Conference on Earthquake Engineering Frontiers of Earthquake Engineering*, July 21-25, 2014, Anchorage, Alaska, Paper ID 1097, 11 pp.

Graizer, V., Kalkan, E., and Lin, K.W. (2013). Global ground-motion prediction equation for shallow crustal regions, *Earthquake Spectra*, Vol. 29 (3), 1-15.

Graizer, V., Shakal, A., Scrivner, C., Hauksson, E., Polet J., and Jones, L. (2002). TriNet strong-motion data from the M 7.1 Hector Mine, California, earthquake of 16 October 1999, *Bull. Seism. Soc. Am*., Vol. 92, 1525-1541.

Grant, L. B., and Rockwell, T.K. (2002). A northward-propagating earthquake sequence in coastal southern California, *Seismological Research Letters*, Vol. 73(4), 461–469.

Graves, R. (2012). Broadband Simulation Results for Footwall/Hanging Wall and Rupture Directivity Analysis – Deliverable in Subaward Agreement 000007598, Memorandum dated February 23 2012, submitted to Pacific Earthquake Engineering Research Center (PEER), University of California - Berkeley, CA, USA

Graves, R. W. and Pitarka, A. (2010). Broadband Ground-Motion Simulation Using a Hybrid Approach, *Bull. Seism. Soc. Am*., Vol. 100 (5a), 2095-2123.

Graves, R. W., Aagaard, B. T., and Hudnut, K. W. (2011). The ShakeOut earthquake source and ground motion simulations, *Earthquake Spectra*, Vol. 27(2), 273-291.

Graves, R., Jordan, T.H., Callaghan, S., Deelman, E., Field, E.H., June, G., Kesselman, C., Maechling, P., Mehta, G., Okaya, D. , Small, P., and Vahi K. (2010). CyberShake: A Physics-Based Seismic Hazard Model for Southern California, *Pure Appl. Geophys*., Vol. 168(3-4), 367-381.

Graves, R.W. and Pitarka, A. (2015). Refinements of the Graves and Pitarka (2010) Broadband Ground-Motion Simulation Method, *Seismol. Res. Letts*., Vol. 86(1), 75-80, DOI: 10.1785/0220140101.

Gregor, N. (2013). Fortran implementation of the NGA-West 2 GMPEs.

Gregor, N. (2014). Fortran implementation of the NGA-West 2 GMPEs.

Gregor, N., Silva, W.J, and Darragh R. (2002). Development of attenuation relations for peak particle velocity and displacement" A PEARL Report to PG&E/CEC/Caltrans and available online at http://www.pacificengineering.org/rpts_page1.shtml.

Haddad, D. (2013). Precariously balanced rocks near Palo Verde Nuclear Generating Station. Resource Expert presentation at PVNGS SSC SSHAC Level 3 Workshop #1.

Haddad, D.E., Zielke O, Arrowsmith, J.R., Purvance, M.D., Haddad, A.G., and Landgraf, A. (2012). Estimating two-dimensional static stabilities and geomorphic settings of precariously balanced rocks from unconstrained digital photographs, *Geosphere*, Vol. 8(5), 1042–1053; doi:10.1130/GES00788.1

Hall, C.A. Jr., Ernest, W.G., Prior, S.W., and Siese, J.W. (1979). Geologic map of the San Luis Obispo-San Simeon region, *U.S. Geological Survey Miscellaneous Investigation* I-1097.

Hall, C.A. (1973). Geologic map and map database of the Morro Bay South and Port San Luis Quadrangles, San Luis Obispo County, California, U.S. Geological Survey Miscellaneous Field Studies Map MF-511, 1:24,000 scale.

Hall, D.B. (1996). Modelling failure of natural rock columns, *Geomorphology*, Vol. 15, 123-134

Hanks, T.C., Abrahamson, N.A., Boore, D.M., Coppersmith, K.J., and Knepprath, N.E. (2009). Implementation of the SSHAC Guidelines for Level 3 and 4 PSHAs—Experience Gained from Actual Applications, U.S. Geological Survey, Open File Report 2009-1093, 66 pp.

Hanson, K., Wesling, J., Lettis, W., Kelson, K., and Mezger, L., (1994). Correlation, ages, and uplift rates of Quaternary marine terraces: South-central coastal California, in Alterman, I., McMullen, R., Cluff, L., and Slemmons, D., eds., Seismotectonics of the Central California Coast Ranges, *Geological Society of America Special Paper* 292, 45-71.

Hardebeck, J.L. (2010). Seismotectonics and fault structure of the California central coast, *Bull. Seism. Soc. Am*., Vol. 100(1), 031-1050, and electronic supplement [available at: http://www.seismosoc.org/publications/BSSA_html/bssa_100-3/2009307-esupp/index.html]

Hardebeck, J.L. (2010). Seismotectonics and fault structure of the California central coast, *Bull. Seismol. Soc. Am.,* Vol. 100, 1031-1050, DOI: 10.1785/0120090307.

Hardebeck, J.L. (2012). Coseismic and postseismic stress rotations due to great subduction zone earthquakes, *Geophys. Res. Lett.*, Vol. 39, L21313, DOI: 10.1029/2012GL053438.

Hardebeck, J.L. (2013). Geometry and Earthquake Potential of the Shoreline Fault, Central California, *Bull. Seism. Soc. Am.*, Vol. 103(1), 447-462, doi: 10.1785/0120120175

Harris, R. (2013). Splays and linkage: dynamic rupture modeling. SWUS GMC Workshop #1, Oakland, CA. Conference presentation.

Harris, R.A., M. Barall, D.J. Andrews, B. Duan, E.M. Dunham, S. Ma, A.-A. Gabriel, Y. Kaneko, Y. Kase, B. Aagaard, D. Oglesby, J.-P. Ampuero, T.C. Hanks, N. Abrahamson (2011). Verifying a computational method for predicting extreme ground motion, *Seism. Res. Lett*., Vol. 82(5), 638-644, doi: 10.1785/gssrl.82.5.638.

Harris, R.A., M. Barall, R. Archuleta, E. Dunham, B. Aagaard, J.P. Ampuero, H. Bhat, V. Cruz-Atienza, L. Dalguer, P-. Dawson, S. Day, B. Duan, G. Ely, Y. Kaneko, Y. Kase, N. Lapusta, Y. Liu, S. Ma, D. Oglesby, K. Olsen, A. Pitarka, S. Song, E. Templeton (2009). The SCEC/USGS Dynamic Earthquake Rupture Code Verification Exercise, *Seism. Res. Lett.*, Vol. 80(1), 119-126, doi: 10.1785/gssrl.80.1.119.

Hashash, Y.M.-A., Kottke, A.R., Stewart, J.P., Campbell, K.W., Kim, B., Moss, C., Nikolaoy, S., Rathje, E., and Silva, W.J. (2014) Reference Rock Site Condition for Central and Eastern North America, *Bull. Seismol. Soc. Am.*, Vol.104(2), 684–701.

Hatayama, K. and Kalkan, E. (2012). Spatial Amplification of Long-Period (3 to 16 s) Ground Motions in and around the Los Angeles Basin during the 2010 M7.2 El Mayor-Cucapah Earthquake, *Proc. of the 15th World Conf. on Earthquake Engineering*, Lisbon, Portugal.

Hauksson, E. (2000). Crustal structure and seismicity distribution adjacent to the Pacific and North America plate boundary in southern California, *Journal of Geophysical Research*, Vol. 105, 13875-13903.

Hauksson, E., Stock, J., Hutton, K., Yang, W., Vidal-Villegas, J.A., and Kanamori, H. (2011).The 2010 Mw7.2 El Mayor-Cucapah earthquake sequence, Baja California, Mexico and southernmost California, USA; active seismotectonics along the Mexican Pacific margin, *Pure and Applied Geophysics*, Vol. 168, 1255–1279.

Hauksson, E., Yang, W., and Shearer, P.M. (2012). Waveform Relocated Earthquake Catalog for Southern California (1981 to June 2011), *Bull. Seism. Soc. Am*., Vol. 102(5), 2239-2244.

Hendricks, J.D., and Plescia, J.B. (1991). A Review of the Regional Geophysics of the Arizona Transition Zone, *Journal of Geophysical Research*, Vol. 96(B7), 12351–12373, DOI: 10.1029/90JB01781

Hermkes, M., Kuehn, N.M., and Riggeslen, C. (2013). Simultaneous quantification of epistemic and aleatory uncertainty in GMPEs using Gaussian process regression, *Bull. Earthquake Eng*., DOI: 10.1007/s10518-013-9507-7.

Hirabayashi, C.K., Rockwell, T.K., Wesnowsky, S.G., Stirling, M.W., and Suárez, F. (1996). A neotectonic study of the San Miguel-Vallecitos Fault, Baja California, Mexico, *Bull. Seism. Soc. Am*., Vol. 86(6), 1770-1783.

Hirschberg, D.M., and Pitts, G.S. (2000). Digital geologic map of Arizona: a digital database derived from the 1983 printing of the Wilson, Moore, and Cooper 1:500,000-scale map: *U.S. Geological Survey Open-File Report* 00-409.

Hole, J.A. (1992). Non-linear high resolution three-dimensional seism travel time tomography, *J. Geophys. Res.,* Vol. 97, 6553-6562.

Hotelling H. (1933). Analysis of a complex of statistical variables into principal components, *J. Educ. Psychol.*, Vol. 24(6), 417–441.

Hough, S.E., and Anderson, J.G. (1988). High-frequency spectra observed at Azna, California: Implications for Q structure, *Bull. Seism. Soc. Am*., Vol. 78, 692-707.

Hough, S.E., Anderson, J.G., Brune, J., Vernon, F., Berger, J., Fletcher, J., Haar, L., Hanks, T., and Baker, L. (1988). Attenuation near Anza, California, *Bull. Seism. Soc. Am*., Vol. 78, 672-691.

Hruby, C.E., and Beresnev, I.A. (2003). Empirical corrections for basin effect in stochastic ground-motion prediction, based on the Los Angeles basin analysis, *Bull. Seism. Soc. Am.,* Vol. 93, 1679-1690.

Idriss, I.M. (2008). An NGA Empirical Model for Estimating the Horizontal Spectral Values Generated By Shallow Crustal Earthquakes, *Earthquake Spectra*, Vol. 24(1), 217-242.

Idriss, I.M. (2014). An NGA-West2 Empirical Model for Estimating the Horizontal Spectral Values Generated by Shallow Crustal Earthquakes, Earthquake Spectra, Vol. 30(3), 1155-1177, DOI: 10.1193/070613EQS195M.

Irikura, K. and Miyake, H. (2010). Recipe for Predicting Strong Ground Motion from Crustal Earthquake Scenarios, *Pure and Applied Geophysics*, Vol. 168, 85-104, DOI 10.1007/s00024-010-0150-9.

IRIS, DMC (2013). Incorporated Research Institutions for Seismology Data Management Center. http://www.iris.edu/dms/dmc/ accessed March 2013.

Irwin, W.P. (1991). Geology and plate-tectonic development, in The San Andreas Fault System, California, Wallace, R.E. (Editor), *U.S. Geological Survey Professional Paper* 1515, 61-80.

Jackson, G.W. (1990). Tectonic geomorphology of the Toroweap fault, western Grand Canyon, Arizona: Implications for transgression of faulting on the Colorado Plateau, *Arizona Geological Survey Open-File Report* 90-4, 1–66.

Jayaram, N., and Baker, J.W. (2009). Correlation model for spatially distributed ground-motion intensities, *Earthquake Engineering & Structural Dynamics*, Vol. 38(15), 1687–1708.

Jayaram, N., and Baker, J.W. (2010). Considering spatial correlation in mixed-effects regression and the impact on ground-motion models, *Bull. Seism. Soc. Am.,* Vol. 100, 3295-3303.

Jennings, C.W., and Bryant, W.A. (2010), Fault activity map of California, California Geological Survey Geologic Data Map No. 6, map scale 1:750,000.

Joyner, W.B., and Boore, D.M. (1981). Peak acceleration and velocity from strong-motion records including records from the 1979 Imperial Valley, California, earthquake, *Bull. Seism. Soc. Am.*, Vol. 71(2), 2011-2038.

Joyner, W.B., and Boore, D.M. (1986). On simulating large earthquakes by Green's function addition of smaller earthquakes, in Earthquake Source Mechanics, *Geophysical Monograph* 37, Maurice Ewing Vol. 6, Eds S. Das, J. Boatwright, and C.H. Scholz.

Kamai, R., Abrahamson, N.A., and Silva, W.J. (2013). Nonlinear Horizontal Site Response for the NGA-West2 Project, *PEER Report 2013/12*, Pacific Earthquake Engineering Research (PEER) Center, University of California, Berkeley, CA, May 2013, 70 pp.

Kame, N., Rice, J., and Dmowska, R. (2003). Effects of pre-stress state and rupture velocity on dynamic fault branching, *Journal of Geophysical Research* Vol. 108, 2265, doi: 10.1029/2002JB002189.

Kanno, T., Narita, A., Morikawa, N., Fujiwara, H. and Fukushima, Y. (2006) A New Attenuation Relation for Strong Ground Motion in Japan Based on Recorded Data, *Bull. Seism. Soc. Am*., Vol. 96, 879-897.

Keefer, D.L., and Bodily, S. E. (1983). Three-point approximations for continuous random variables, *Management Science*, Vol. 29, 595-609.

Kenney, J.F., and Keeping, E.S. (1951). The Distribution of the Standard Deviation. §7.8 in Mathematics of Statistics, Pt. 2, 2nd ed. Princeton, NJ: Van Nostrand, 170-173, 1951.

Kilb D., Biasi, G., Anderson, J.G., Brune, J., Peng, Z., and Vernon F.L. (2012). A Comparison of Spectral Parameter Kappa from Small and Moderate Earthquakes Using Southern California ANZA Seismic Network Data, *Bull. Seism. Soc. Am*., Vol. 102, 284-300.

Kishida, T., Kayen, R.E., Ktenidou, O.-J., Silva, W., Darragh, R., and Watson-Lamprey, J. (2014a). PEER Arizona Strong Motion Database and GMPEs Evaluation, Pacific Earthquake Engineering Research Center PEER Report 2014/09, 135 pp.

Kishida, T., Ktenidou, O.-J., Darragh, R., and Silva, W. (2014b). Data processing for Fourier amplitude spectrum (FAS) estimation from NGA-West2 processed accelerations, Chapter 7 in the PEER NGA-East Database Report Pacific Earthquake Engineering Research Center, pp. 50 (in review).

Kohonen, T. (2001). Self-organizing maps, Springer 2001, 501 pages.

Kottke, A.R., and Rathje, E.M. (2008). Technical manual for Strata, *PEER Report 2008/10*, Pacific Earthquake Engineering Research (PEER) Center, University of California, Berkeley, CA.

Krantz, R.W. (1989). Orthorhombic fault patterns: the odd axis model and slip vector orientations, *Tectonics*, Vol. 8, 483-495.

Kreemer, C., Blewitt, G., and Bennett, R. A. (2010). Present-day motion and deformation of the Colorado plateau, *Geophysical Research Letters*, Vol. 37(10), DOI: 10.1029/2010GL043374

Ktenidou O.-J., Drouet, S., Theodulidis, N., Chaljub, M., Arnaouti, S., Cotton, F. (2012). Estimation of kappa (κ) for a sedimentary basin in Greece (EUROSEISTEST) - Correlation to site characterisation parameters. *Proc. 15th World Conference of Earthquake Engineering*, Lisbon, Portugal, 24-28 Sep., 10 pp.

Ktenidou O.-J., Gelis, C., Bonilla, F. (2013). A study on the variability of kappa in a borehole: implications of the computation process, *Bull. Seism. Soc. Am*., Vol. 103(2A), 1048-1068.

Ktenidou, O.-J., Cotton, F., Abrahamson, N.A., and Anderson, J.G. (2014). Taxonomy of kappa: a review of definitions and estimation methods targeted to applications. *Seismol. Res. Letts,* Vol. 85(1), 135-146, DOI: 10.1785/0220130027.

Lee, V. W., Trifunac, M. D., Todorovska, M. I. and Novikova, E. I. (1995). Empirical equations describing attenuation of peak of strong ground-motion, in terms of magnitude, distance, path effects and site conditions, *Report No. CE 95-02*. Los Angeles, California. 268 pp.

Leonard, M. (2010). Earthquake Fault Scaling: Self-Consistent Relating of Rupture Length, Width, Average Displacement, and Moment Release, *Bull. Seism. Soc. Am.*, Vol. 100(5A), 1971-1988.

Lermo, J., and Chávez-García, F.-J. (1993). Site effect evaluation using spectral ratios with only one station, *Bull. Seism. Soc. Am.*, Vol. 83 1574-1594.

Lettis Consultants International – LCI (2012). Characterization of Ground Motion Propagation for Palo Verde SSHAC Level 2 PSHA, Internal Project Report.

Lettis Consultants International – LCI (2013). Seismic Hazard Evaluation for the Palo Verde Nuclear Generating Station Wintersburg, Arizona, Final Report (Revision 4), Arizona Public Service Co., August 2013.

Lettis Consultants International – LCI (2014). Hazard Input Document (HID) for Palo Verde Final SSC Model, PR No. PV001-PR-01 - Revision 0, November 7, 2014

Lettis, W. (2012). Diablo Canyon SSC Workshop 2 presentation [available at http:// www.pge.com/mybusiness/edusafety/systemworks/dcpp/SSHAC/workshops/ws2.shtml]

Lettis, W.R., and Unruh, J.R. (2009). Quaternary Tectonic Setting of South-Central Coastal California, SSA 2009 Annual Meeting Abstract, *Seismological Research Letters*, Vol. 80(2), 323.

Levander, A., Niu, F., Miller, M.S. (2008). The Moho and the lithosphere-asthenosphere boundary under the western U.S. from USArray PdS receiver functions, Eos Transactions, American Geophysical Union, Vol. 89(53), Fall Meeting Supplemental, Abstract 231D-05, and supplemental information accessed 3/26/2012 at http://terra.rice.edu/department/faculty/levander/downloads.

Lewis, J.L., Day, S.M., Magistrale, H., Castro, R.R., Astiz, L., Rebollar, C., Eakins, J., Vernon, F.L., and Brune, J.N. (2001). Crustal thickness of the Peninsular Ranges and Gulf Extensional Province in the Californias, *Journal of Geophysical Research*, Vol. 106, 13,599–13,611.

Lin, G., Shearer, P.M., Hauksson, E., and Thurber, C.H. (2007). A three-dimensional crustal seismic velocity model for southern California from a composite event method, *J. Geophys. Res*., Vol. 112, B11306, doi:10.1029/2007JB004977

Lin, P.-S., Chiou, B., Abrahamson, N., Walling, M., Lee, C.-T., and Cheng, C.-T. (2011). Repeatable source, site, and path effects on the standard deviation for empirical ground-motion prediction models, *Bull. Seism. Soc. Am*., Vol. 101(5), 2281-2295, DOI: 10.1785/012009031.

Liu, P., Archuleta, R.J., and Hartzell, S.H. (2006). Prediction of broadband ground-motion time histories: Hybrid low/high-frequency method with correlated random source parameters, *Bull. Seism. Soc. Am*., Vol. 96, 2118-2130, doi: 10.1785/0120060036.

Lockridge, J., Fouch, M., and Arrowsmith, J.R. (2012). Seismicity within Arizona during the deployment of the EarthScope USArray Transportable Array, *Bull. Seism. Soc. Am*., Vol. 12(102), 1850-1863.

Lockridge, J.S. (2011). Seismicity within Arizona during the deployment of the EarthScope USArray Transportable Array, *Arizona State University, Master's Thesis*, 112 pp.

Lockridge, J.S., Fouch, M.J., Arrowsmith, J R., and Linkimer L. (2012). Analysis of seismic activity near Theodore Roosevelt Dam, Arizona, during the occupation of the EarthScope / USArray Transportable Array, *Seis. Res. Lett*., Vol. 83(6), 1014-1022, doi: 10.1785/0220120034.

Loth, C., and Baker, J.W. (2013). A spatial cross-correlation model for ground motion spectral accelerations at multiple periods. *Earthquake Engineering & Structural Dynamics,* Vol. 42(3), 397–417.

Lozos, J. (2013). Dynamic rupture and ground motion modeling on realistically complex strike-slip faults, *PhD dissertation*, University of California, Riverside.

Lozos, J., Oglesby, D., Duan, B., and Wesnousky, S. (2011). The effects of double fault bends on rupture propagation: a geometrical parameter study, *Bull. Seism. Soc. Am*., Vol. 101, 385-398.

Lund, W.R. (2005). Consensus preferred recurrence interval and vertical slip rate estimates - Review of Utah paleoseismic-trenching data by the Utah Quaternary Fault Parameters Working Group, *Utah Geological Survey Bulletin* Vol. 134.

Luzi, L., Bindi, D., Puglia, R., Pacor, F. and Oth, A. (2014). Single-Station Sigma for Italian Strong-Motion Stations, *Bull. Seism. Soc. Am*., Vol. 104(1), 467-483.

Ma, S. (2008). A physical model for widespread near-surface and fault zone damage induced by earthquakes, *Geochemistry Geophysics Geosystems*, Vol. 9, 1-9.

Machette, M.N. (1998). Contrasts between short-term and long-term records of seismicity, in The Rio Grande Rift: Important Implications for Seismic-Hazard Assessments in Areas of Slow Extension, Basin and Range Province Seismic-Hazards Summit, W. R. Lund (Editor), *Utah Geological Survey Misc. Publ*. Vol. 98(2), 84–95.

Maechling, P.J., Silva, F., Callaghan, S., and Jorda, T.H. (2015). Broadband Platform: System Architecture and Software Implementation, *Seismol. Res. Letts*., Vol. 86(1),27-38, DOI:10.1785/0220140125

Magistrale, H., S. M. Day, R. W. Clayton, and R. W. Graves (2000). The SCEC Southern California reference three-dimensional seismic velocity model version 2, *Bull. Seism. Soc. Am*., Vol. 90(6B), S65-S76.

Mai, P., and Beroza, G. (2010). A spatial random field model to characterize complexity in earthquake slip, *J. Geophys. Res.*, Vol. 107(B11), doi:10.1029/2001JB000588.

Mai, P.M., and Beroza, G.C. (2003). A hybrid method for calculating near-source, broadband seismograms: Application to strong motion prediction, *Phys. Earth Planet. In.* Vol. 137(1-4), 183-199.

Mai, P.M., Imperatori, W., Olsen, K.B. (2010), Hybrid Broadband Ground-Motion Simulations: Combining Long-Period Deterministic Synthetics with High-Frequency Multiple S-to-S Backscattering, *Bull. Seism. Soc. Am*., Vol. 100(5A), 2124-2142.

Mayeda, K., and Malagnini, L. (2010). Source radiation invariant property of local and near-regional shear-wave coda: Application to source scaling for the Mw 5.9 Wells, Nevada sequence, *Geophysical Research Letters*, Vol. 37, L07306.

McGuire, R.K., Silva, W.J., and Costantino, C.J. (2001). Technical basis for revision of regulatory guidance on design ground motions: Hazard- and Risk- consistent ground motion spectra guidelines. *NUREG/CR-6728* Prepared for the U.S. NRC, Washington DC.

McLaren, M. (2011). DCPP SSC Workshop 1 presentation [available at http://www.pge.com/mybusiness/edusafety/systemworks/dcpp/SSHAC/workshops/ws1.shtml]

McLaren, M.K., and Savage, W.U. (2001). Seismicity of South-Central Coastal California: October 1987 through January 1997, *Bull. Seism. Soc. Am*., Vol. 91, 1629-1658.

McLaren, M.K., Hardebeck, J.L., van der Elst, N., Unruh, J.R., Bawden, G.W., and Blair, J.L. (2008). Complex faulting associated with the 22 December 2003 Mw 6.5 San Simeon, California, earthquake, aftershocks and postseismic surface deformation, *Bull. Seismol. Soc. Am*., Vol. 98, 1659-1680.

McVerry, G.H., Zhao, J.X., Abrahamson, N.A., Somerville, P.G. (2006). New Zealand acceleration response spectrum attenuation relations for crustal and subduction zone earthquakes, *Bulletin of the New Zealand Society for Earthquake Engineering*, Vol. 39, 1-58.

Mena, B., Mai, P.M., Olsen, K.B., Purvance, M.D., and Brune, J.N. (2010). Hybrid Broadband Ground-Motion Simulation Using Scattering Green's Functions: Application to Large-Magnitude Events, *Bull. Seism. Soc. Am*., Vol. 100, 2143-2162.

Menges, C.M., and Pearthree, P.A. (1989). Late Cenozoic tectonism in Arizona and its impact on regional landscape evolution. In Geologic Evolution of Arizona, edited by J.P. Jenney and S.J. Reynolds, pp. 649–680. Digest No. 17. Tucson, Arizona: Arizona Geological Society.

Miller, A.C., and Rice, T.R. (1983). Discrete approximations of probability distributions, *Management Science,* Vol. 29, 352-362.

Mitchell, B.J., and Hwang, H.J. (1987) Effect of low Q sediments and Crustal Q on Lg attenuation in the United States, *Bull. Seism. Soc. Am*., Vol. 77, 1197-1210.

Mizoguchi, K., Uehara, S., and Ueta, K. (2012). Surface fault ruptures and slip distributions of the Mw 6.6 11 April 2011 Hamadoori, Fukushima, northeast Japan, earthquake, *Bull. Seism. Soc. Am.* Vol. 102(5), 1949-1956, DOI: 10.1785/0120110308.

Mooney, W. (2011). DCPP SSC Workshop 1 presentation [available at http://www.pge.com/mybusiness/edusafety/systemworks/dcpp/SSHAC/workshops/ws1.shtml]

Morikawa, N., Kanno, T., Narita, A., Fujiwara, H., Okumura, T., Fukushima, Y., and Guerpinar, A. (2008). Strong motion uncertainty determined from observed records by dense network in Japan, *J. Seism*., Vol. 12(4), 529-546.

Motozedian, D. and Atkinson, G.M. (2005). Stochastic finite-fault modeling based on a dynamic corner frequency, *Bull. Seism. Soc. Am*., Vol. 95(3), 995-1010.

Mueller, K.J. and Rockwell, T.K. (1991). Late Quaternary structural evolution of the western margin of the Sierra Cucapa, Baja California Norte, in The Gulf and Peninsular province of the Californias, Dauphin, J.P. and Simoneit, B.T. (Editors), *American Association of Petroleum Geologists, Memoir* 47, 249-260.

Mueller, K.J. and Rockwell, T.K. (1995). Late Quaternary activity of the Laguna Salada fault in northern Baja California, Mexico, *Geological Society of America Bulletin*, Vol. 107(1), 8-18.

Nagy, E.A., and Stock, J.M. (2000). Structural controls on the continent-ocean transition in the northern Gulf of California, *Journal of Geophysical Research*, Vol. 105(B7), 16251-16269.

Nazareth, J.J., and Hauksson, E. (2004). The seismogenic thickness of the southern California crust, *Bull. Seism. Soc. Am*., Vol. 94(3), 940-960.

Ness, G.E. and Lyle, M.W. (1991). A Seismo-Tectonic map of the Gulf and Peninsular Province of the Californias, Chapter 5: Part II Geological and Geophysical Maps, in *AAPG Special Volume* Book M47, pub ID A114

NGA-West2 Flatfile (2013). [http://peer.berkeley.edu/ngawest2/databases/]

Nodal Zland Earthquake Database (2011). [http://www.pge.com/mybusiness/edusafety/systemworks/dcpp/SSHAC/legacy_documents/datasets/index.shtml]

Olsen, K. and Takedatsu, R. (2015). The SDSU Broadband Ground Motion Generation Module BBtoolbox Version 1.5, *Seismol. Res. Letts*., Vol. 86(1), 81-88, DOI: 10.1785/0220140102.

Olsen, K.B. (2000). Site amplification in the Los Angeles basin from three-dimensional modeling of ground motion. *Bull. Seism. Soc. Am*., Vol. 90(6B), S77-S94.

Oth, A., Bindi, D., Parolai, S., and Di Giacomo, D. (2011). Spectral Analysis of K-NET and KiK-net Data in Japan, Part II: On Attenuation Characteristics, Source Spectra, and Site Response of Borehole and Surface Stations, *Bull. Seism. Soc. Am*., Vol. 101, 667-687.

Pacheco, M., Martín-Barajas, A., Eldres, W., Espinosa-Cardeña, J.M., Belenes, J., and Segura, A. (2006). Stratigraphy and structure of the Altar basin of NW Sonora: implications for the history of the Colorado River delta and the Salton Trough, *Revista Mexicana de Ciencias Geológicas*, Vol. 23(1), 1–22.

Pacific Gas and Electric Company (2011). Shoreline Fault Report.

Pacific Northwest National Laboratory – PNNL (2014). Hanford Site-Wide Probabilistic Seismic Hazard Analysis. Prepared for the U.S. Department of Energy, under Contract DE-AC06076RL01830, and Energy Northwest. Report PNNL-SA-23361, November 2014.

Pacor, F., Paolucci, R., Luzi, L., Sabetta, F., Spinelli, A., Gorini, A., Nicoletti, M., Marcucci, S., Filippi, L., and Dolce, M. (2011). Overview of the Italian strong motion database ITACA 1.0, *Bull. Earthq. Eng.,* Vol. 9(6), 1723–1739, DOI: 10.1007/s10518-011-9327-6.

Pancha, A., Anderson, J.G., and Kreemer, C. (2006). Comparison of seismic and geodetic scalar moment rates across the Basin and Range Province, *Bull. Seism. Soc. Am*., Vol. 96, 11-32.

Pankow, K.L., and Pechmann, C. (2004). The SEA99 ground-motion predictive relations for extensional tectonic regimes: Revisions and a new peak ground velocity relation, *Bull. Seism. Soc. Am*., Vol. 94(1), 341-348.

Parolai, S., and Bindi, D. (2004). Influence of soil-layer properties on k evaluation, *Bull. Seismol. Soc. Am*., Vol. 94, 349–356.

Pasyanos, M., Dreger, D.S., and Romanowicz, B. (1996). Toward real-time estimation of regional moment tensors, *Bull. Seism. Soc. Am*., Vol. 86, 1255-1269.

Pasyanos, M.E. (2013). A lithospheric attenuation model of North America, *Bull. Seismol. Soc. Am.,* Vol. 103, 3321-3333.

Pearthree, P. A., and Bausch, D. B. (1999). Earthquake hazards in Arizona. *Arizona Geological Survey*, Map 34, scale 1:1,000,000.

Pearthree, P.A., Amoroso, L., Fenton, C.R., and Stenner, H.D. (2002). Paleoseismology of the Hurricane fault zone in northwestern Arizona, *Geological Society of America Abstracts with Program*, Vol. 34(4), 4.

Pearthree, P.A., compiler, (1998). Quaternary fault data and map for Arizona, *Arizona Geological Survey Open-File Report* 98-24, scale 1:750,000, 122 p.

Pearthree, P.A., Menges, C.M., and Mayer, L. (1983). Distribution, recurrence, and possible tectonic implications of late Quaternary faulting in Arizona, *Arizona Geological Survey Open-File Report* 83-20, 53 p.

Pearthree, P.A., Vincent, K.R., Brazier, R., and Hendricks, D.M. (1996). Pilo-Quaternary Faulting and Seismic Hazard in the Flagstaff Area, Northern Arizona, *Arizona Geological Survey, Bulletin* 200, 31p.

PEER GM Database (2011). Accessed and downloaded January 2013, available at [http://peer.berkeley.edu/peer_ground_motion_database/site].

PEER GM Processing. Resources available at [http://peer.berkeley.edu/smcat/process.html] and [http://www.cosmoseq.org/EVENTS/wkshop_records_processing/papers/Darragh_Silva_Gregor_Paper.pdf]

Persaud, P., Perez-Campos, X., and Clayton, R. (2007). Crustal thickness variations in the margins of the Gulf of California from receiver functions, *Geophysical Journal International*, Vol. 170(2), 687-699.

Persaud, P., Stock, J.M., Steckler, M.S., Martín-Barajas, A., Diebold, J.B., González-Fernández, A., and Mountain, G.S. (2003). Active deformation and shallow structure of the Wagner, Consag, and Delfín Basins, northern Gulf of California, Mexico, *Journal of Geophysical Research*, Vol. 108(B7), 2355.

Petersen, M.D., Dawson, T.E., Chen, R., Cao, T, Wills, C.J., Schwartz, D.P., Frankel, A.D (2011). Fault Displacement Hazard for Strike-Slip Faults, *Bull. Seism. Soc. Am*., Vol. 101(2), 805-825

Petersen, M.D., Frankel, A.D., Harmsen, S.C., Mueller, C.S., Haller, K.M., Wheeler, R.L., Wesson, R.L., Zeng, Y., Boyd, O.S., Perkins, D.M., Luco, N., Field, E.H., Wills, C.J., and Rukstales, K.S. (2008). Documentation for the 2008 Update of the United States National Seismic Hazard Maps, *U.S. Geological Survey Open-File Report* 2008–1128, 61 p.

PG&E (1988). Final report of the Diablo Canyon long-term seismic program, U.S. Nuclear Regulatory Commission Docket No. 50-275 and No. 50-323.

PG&E (2011). Report on the Analysis of the Shoreline Fault Zone, Central Coastal California, January 2011.

PG&E (2015). Seismic Source Characterization for Probabilistic Seismic Hazard Analysis for the Diablo Canyon Power Plant, San Luis Obispo County, California, Report on the Results of the SSHAC Level 3 Study in Partial Compliance with NRC Letter 50.54(f), March 2015.

Phillips, W.S., Mayeda, K., and Malagnini, L. (2014). How to invert multi-band, regional phase amplitudes for 2-D attenuation and source parameters: Tests using the US Array, *Pure Appl. Geophys.*, Vol. 171, 469-484, DOI: 10.1007/s00024-013-0646-1.

Phillips, W.S., Mayeda, K.M., and Malagnini, L. (2013). How to Invert a Multi-Band, Regional Phase Amplitudes for 2-D Attenuation and Source Parameters: Tests Using the USArray, *PAGEOPH,* DOI 10.1007/s00024-013-0646-1.

Pitarka, A. (2009). Simulating forward and backward scattering in viscoelastic 3D media with random velocity variations and basin structure, *Tech. Rep., USGS, award number 06HQGR0042*.

Plesch, A., Shaw J.H., Benson, C., Bryant, W.A., Carena, S., Cooke, M., Dolan, J., Fuis, G., Gath, E., Grant, L., Hauksson, E., Jordan, T., Kamerling, M., Legg, M., Lindvall, S., Magistrale, H., Nicholson, C., Niemi, N., Oskin, M., Perry, S., Planansky, G., Rockwell, T., Shearer, P., Sorlien, C., Süss, M.P., Suppe, J., Treiman, J., and Yeats, R. (2007). Community Fault Model (CFM) for Southern California, *Bull. Seism. Soc. Am*., Vol. 97, 1793-1820.

Purvance, M. D., and Brune J.N. (2008). Fragile Geomorphic Features on Yucca Mountain, Nevada, *Seismol. Res. Lett.*, Vol. 79(2), 296

Purvance, M.D., and Anderson, J.G. (2003). A comprehensive study of the observed spectral decay in strong-motion accelerations recorded in Guerrero, Mexico, *Bull. Seism. Soc. Am*., Vol. 93, 600–611.

Purvance, M.D., Anooshehpoor, A., and Brune, J.N. (2008). Freestanding block overturning fragilities: Numerical simulation and experimental validation, *Earthquake Eng & Struct. Dynamics*, Vol.37, 791-808.

Renault, P., Heuberger, S., and Abrahamson, N.A. (2010). PEGASOS Refinement Project: An improved PSHA for Swiss nuclear power plants, *Proc. 14th European Conference of Earthquake Engineering*, Ohrid, Republic of Macedonia, 30 August-3 September 2010, Paper ID 991.

Replogle, C.T. (2011). Corestone and saprock development in a zone of precariously balanced rocks, Peninsular Ranges, southern California: Speculations on the effects of ground shaking during earthquakes, *M.S. thesis*, 67 pp., San Diego State Univ., San Diego, Calif.

Richard, S.M., Shipman, T.C., Greene, L.C., Harris, R.C. (2007). Estimated Depth to Bedrock in Arizona, *Digital Geologic Map Series* DGM-52, Version 1.0, prepared by Arizona Geological Survey

Rockwell, T., Sisk, M., Girty, G., Dor, O., Wechsler, N., and Ben-Zion, Y. (2009). Chemical and physical characteristics of pulverized Tejon Lookout Granite adjacent to the San Andreas and Garlock Faults: Implications for earthquake physics, *Pure Appl. Geophys*., Vol. 166, 1725–1746, doi: 10.1007/s00024-009-0514-1.

Rockwell, T.K., Schug, D.L., and Hatch, M.E. (1993). Late Quaternary slip rates along the Agua Blanca fault, Baja California, Mexico: in (P.L. Abbott, ed.) Geological Investigations of Baja California: South Coast Geological Society, Annual Field Trip Guidebook, 21, 53-92.

Rocscience (2005). Phase2, Elasto-plastic finite element stress analysis program for underground or surface excavations in rock or soil. Rocscience Inc., Toronto.

Rodriguez-Marek, A. (2012). Addendum to "Single Station Sigma", EXT-TN-1225 / prepared for PRP - Pegasos Refinement Project.

Rodriguez-Marek, A. (2014). Crustal Sigma Model, SSHAC Level-3 Site-Wide PSHA for the Hanford Site, WA. TI Team Presentation.

Rodriguez-Marek, A., and Cotton, F. (2011). Final report: Single-station sigma project prepared for PEGASOS Refinement Project, *EXT-TB-1058*, Publisher name and location, OR a better reference for the model – waiting feedback from Adrian

Rodriguez-Marek, A., Cotton, F., Abrahamson, N., Akkar, S., Al Atik, L., Edwards, B., Montalva, G.A., and Dawood, H.M. (2013). A model for single-station standard deviation using data from various tectonic regions, *Bull. Seism. Soc. Am*., Vol. 103(6), 3149-3163

Rodriguez-Marek, A., Rathje, E.M., Bommer, J.J., Scherbaum, F., and Stafford, P.J. (2014). Application of Single-Station Sigma and Site-Response Characterization in a Probabilistic Seismic-Hazard Analysis for a New Nuclear Site, *Bull. Seismol. Soc. Am.,* Vol. 104(4), 1601-1619, DOI: 10.1785/0120130196.

Rodriguez-Marek. A., Montalva, G.A., Cotton, F. and Bonilla, F. (2011). Analysis of Single-Station Standard Deviation Using the KiK-net Data, *Bull. Seism. Soc. Am*., Vol. 101, 1242–1258.

Rolandone, F., D. Dreger, M. Murray, and R. Burgmann (2006). Coseismic slip distribution of the 2003 Mw6.6 San Simeon earthquake, California, determined from GPS measurements and seismic waveform data, *Geophys. Res. Lett.*, Vol. 33, L16315, doi:10.1029/2006GL027079.

Roy, M., Jordan, T.H., and Pederson, J. (2009). Colorado Plateau magmatism and uplift by warming of heterogeneous lithosphere, *Nature*, Vol. 459, 978-982.

Rymer, M.J., Treiman, J.A., Kendrick, K.J., Lienkaemper, J.J., Weldon, R.J., Bilham, R., Wei, M., Fielding, E.J., Hernandez, J.L., Olson, B.P.E., Irvine, P.J., Knepprath, N., Sickler, R.R., Tong, .X., and Siem, M.E. (2011). Triggered surface slips in southern California associated with the 2010 El Mayor-Cucapah, Baja California, Mexico, earthquake, *U.S. Geological Survey Open-File Report* 2010–1333 and California Geological Survey Special Report 221, 62 p.

Sadigh, K., Chang, C., Egan, J., Makdisi, F., and Youngs, R. (1997). Attenuation relationships for shallow crustal earthquakes based on California strong motion data, *Seism. Res. Lett*., Vol. 68, 180–189.

Sammon, J.W. (1969). A nonlinear mapping for data structure analysis, *IEEE Transactions on Computers*, C-18, 401-409.

Sandıkkaya, M. A., Yılmaz, M.T., Bakır, B.B., and Yılmaz, Ö. (2010). Site classification of Turkish national strong-motion stations, *Journal of Seismology*, Vol. 14, 543–563.

Scarborough, R.B., Menges, C.M., and Pearthree, P.A. (1986), Late Pliocene-Quaternary (post 4 m.y.) faults, folds, and volcanic rocks in Arizona, *Arizona Geological Survey*, Map 22, scale 1:1,000,000.

SCE (1995). Seismic Hazard at San Onofre Nuclear Generating Station, prepared by Risk Engineering, Inc. for Southern California Edison Co., 2244 Walnut Grove Avenue, Rosemead, California 91770, 25 August 1995, 340 pp.

SCE (2001). San Onofre Nuclear Generating Station Units 2 and 3 Seismic Hazard Study of Postulated Blind Thrust Faults, prepared by Geomatrix Consultants, GeoPentech, and Southern California Edison for the Nuclear Regulatory Commission, 26 December 2001, 165 pp.

SCEC (Southern California Earthquake Center), information accessed 4/13/2012 at http://www.data.scec.org/significant/cerroprieto.html.

SCEC Seismogram Transfer Program – STP (2007) accessed and downloaded January 2013, available at [http://www.data.scec.org/research-tools/stp-index.html].

Schellart, W.P., Stegman, D.R., Farrington, R.J., Freeman, J., and Moresi, L. (2010). Cenozoic tectonics of western North America controlled by evolving width of Farallon slab, *Science*, Vol. 329 (5989), 316-319.

Scherbaum F. (2010). Determination of Vs-k correction factors, *Report for PEGASUS Refinement Project (PRP*), TP2-TB-1036.

Scherbaum F., Cotton, F., and Staedtke, H. (2006). The estimation of minimum-misfit stochastic models from empirical ground-motion prediction equations, *Bull. Seism. Soc. Am*., Vol. 96, 427–445.

Scherbaum, F., Kuehn, N.M., Ohrnberger, M., and Koehler, A. (2010). Exploring the Proximity of Ground-Motion Models Using High-Dimensional Visualization Techniques, *Earthquake Spectra*, Vol. 26(4), 1117-1138. DOI: 10.1193/1.3478697.

Schmedes J., Archuleta R.J. (2008). Near-source ground motion along strike-slip faults: insights into magnitude saturation of PGV and PGA, *Bull. Seism. Soc. Am*., Vol. 98, 2278-2290.

Schmedes, J., Archuleta, R.J., and Lavallée, D. (2010). Correlation of earthquake source parameters inferred from dynamic rupture simulations, *J. Geophys. Res*., Vol. 115, B03304, DOI: 10.1029/2009JB006689.

Schmedes, J., Archuleta, R.J., and Lavallée, D. (2010). Dependency of supershear transition and ground motion on the autocorrelation of initial stress, *Tectonophysics*, Vol. 493, 222-235, doi: 10.1016/j.tecto.2010.05.013

Schmedes, J., Archuleta, R.J., and Lavallée, D. (2012). A kinematic rupture model generator incorporating spatial interdependency of earthquake source parameters, *Geophys. J. Int.*, Vol. 192(3), 1116-1131.

Searle, S. R. (1971). *Linear Models*, John Wiley and Sons, New York.

Seiler, C. (2009). Structural and thermal evolution of the Gulf Extensional Province in Baja California, Mexico: implications for Neogene rifting and opening of the Gulf of California, *PhD thesis*, Faculty of Science, Earth Sciences, The University of Melbourne.

Senior Seismic Hazard Analysis Committee – SSHAC (1997). Recommendations for Probabilistic Seismic Hazard Analysis — Guidance on Uncertainty and Use of Experts, Prepared by SSHAC, NUREG/CR-6372.

Seyhan, E., Stewart, J.P., Ancheta, T.D., Darragh, R.B., and Graves, R.W. (2014). NGA-West2 Site Database, *Earthquake Spectra*, Vol. 30(3), 1007-1024.

Shahi, S. K. (2013). A probabilistic framework to include the effects of near-fault directivity in seismic hazard assessment. *PhD Thesis*, Dept. of Civil and Environmental Engineering, Stanford University, Stanford, CA. http://purl.stanford.edu/hb804nv7861

Shahi, S.K., Baker, J.W., and Rodriguez-Marek, A. (2015). Effect of Spatial Correlation on the Standard Deviations of CY14 Model, Report submitted to GeoPentech, Inc., January 2015, 9 pp.

Shaw, J.H., Plesch, A., Tape, C., Suess, M.P., Jordan, T., Hauksson, E., Tromp, J., Tanimoto, T., Maechling, P., Ely, G., Graves, R., Rivero, C., Lovely, P., Brankman, C., Munster, J. (2014). Unified Structural Representation of the southern California crust and upper mantle, EPSL submitted, July 2014).

Shi, B., Anooshehpoor, A., Zeng, Y., and Brune, J.N. (1996). Rocking and overturning of precariously balanced rocks by earthquakes, *Bull. Seism. Soc. Am*., Vol. 86, 1364–1371.

Shiba, Y., and Noguchi, S. (2012). Statistical characteristics of seismic source parameters controlling broadband strong ground motions -Investigation based on source inversion analysis-. *CRIEPI REPORT.* N11054 (in Japanese with English abstract).

Silva, W. J. (2008). Site Response Simulations for the NGA project, Report prepared for the Pacific Earthquake Engineering Research Center, University of California, Berkeley, CA

Silva, W., Darragh, R.B., Gregor, N., Martin, G., Abrahamson, N., and Kircher, C. (1998). Reassessment of site coefficients and near-fault factors for building code provisions, Technical Report Program Element II: 98-HQ-GR-1010, Pacific Engineering and Analysis, El Cerrito, USA.

Silva, W.J. and Darragh, R. (1995). Engineering characterization of earthquake strong ground motion recorded at rock sites, Palo Alto, Electric Power Research Institute, TR-102261.

Silva, W.J., Abrahamson, N., Toro, G., and Costantino, C. (1997). Description and validation of the stochastic ground motion model, Report submitted to Brookhaven National Laboratory, Associated Universities, Inc., Upton, New York 11973, Contract No. 770573.

Sjogreen, B., and Petersson, N.A. (2010). A fourth order accurate finite difference scheme for the elastic wave equation in second order formulation. *J. Sci. Comput*., Vol. 52, 17–48, 2012. DOI 10.1007/s10915-011-9531-1.

Sleep, N.H. (2011). Seismically damaged regolith as self-organized fragile geological feature, *Geochem. Geophys. Geosyst*., Vol. 12, Q12013, doi:10.1029/2011GC003837.

Smith, R.B., and Sbar, M.L. (1974). Contemporary tectonics and seismicity of the western United States with emphasis on the intermountain seismic belt, *Geologic Society of American Bulletin*, Vol. 85, 1205-1218.

Somerville (2011). Presentation at the DCPP SSHAC Workshop #1 in San Luis Obispo, CA, November 2011.

Somerville, P. G., Callaghan, S., Maechling, P., Graves, R. W., Collins, N., Olsen, K. B., Imperatori, W., Jones, M., Archuleta, R., Schmedes, J., And Jordan, T.H. (2011). The SCEC Broadband Ground Motion Simulation Platform, *Seismol. Res. Let.*, Vol. 82(2), p. 275, 10.1785/gssrl.82.2.273.

Somerville, P., Collins, N., Graves, R., Pitarka, A., Silva, W., and Zeng, Y. (2006). Simulation of ground motion scaling characteristics for the NGA-E project, *Proceedings of the 8th National Conference on Earthquake Engineering*, April 18-22, San Francisco, California, USA, paper No. 1789.

Somerville, P.G., and Abrahamson, N.A. (1995). Prediction of Ground Motions for Thrust Earthquakes, *Proceedings of the SMIP95 Seminar*, Cal. Div. of Mines and Geology, San Francisco, CA, 11-23.

Somerville, P.G., Callaghan, S., Maechling, P., Graves, R.W., Collins, N., Olsen, K.B., Imperatori, W., Jones, M., Archuleta, R., Schmedes, J., and Jordan, T.H. (2011). The SCEC Broadband Ground Motion Simulation Platform, *Seismol. Res. Letts.*, Vol. 82(2), p. 275, 10.1785/gssrl.82.2.273.

Somerville, P.G., Smith, N.F., Graves, R.W., and Abrahamson, N.A. (1997). Modification of empirical strong ground motion attenuation relations to include the amplitude and duration effects of rupture directivity, *Seismol. Res. Let.*, Vol. 68(1), 199-222.

Sonder, L.J., and Jones, C.H. (1999). Western United States extension: How the West was widened, *Annual Review of Earth and Planetary Sciences*, Vol. 27, 417-466.

Sorlien, C.C., Campbell, B.A., and Seeber, L., (2009b). Geometry, kinematics, and activity of a young mainland-dipping fold and thrust belt: Newport Beach to San Clemente, California, USDI/USGS Award No. 08HQGR0103 Final Technical Report, 25 pp.

Southwestern U.S. Ground Motion Characterization Project Plan, November 16, 2012 [available at www.swus-gmc.com/docs/SWUS_GMC_SSHAC_Plan.pdf]

Spelz, R.M., Fletcher, J.M., Owen, L.A., and Caffee, M.W. (2008). Quanternary alluvial-fan development, climate and morphologic dating of fault scarps in Laguna Salada, Baja California, Mexico, *Geomorphology*, Vol. 102, 578-594.

Spencer, J.E., and Reynolds, S. J. (1989). Middle Tertiary Tectonics of Arizona and Adjacent Areas, in Geologic Evolution of Arizona, edited by J. P. Jenney and S. J. Reynolds, *Arizona Geological Society Digest*, 17, 539-574.

Springer, A. (2010). Constraining basin geometry and fault kinematics on the Santo Tomás segment of the Agua Blanca Fault through a combined geophysical and structural study, *Theses and Dissertations*, Paper 1779.

Spudich, P. and Chiou, B.S.-J. (2008). Directivity in NGA Earthquake Ground Motions: Analysis Using Isochrone Theory, *Earthquake Spectra*, Vol. 24(1), 279-298.

Spudich, P., Bayless, J.R., Baker, J.W., Chiou, B.S-J., Rowshandel, B., Shay, S.K., and Somerville, P. (2013). Final Report of the NGA-West2 Directivity Working Group, *PEER Report 2013/09*, Pacific Earthquake Engineering Research Center, University of California, Berkeley, CA

Spudich, P., Rowshandel, B., Shahi, S.K., Baker, J.W., and Chiou, B.S.-J. (2014) Comparison of NGA-West2 Directivity Models, *Earthquake Spectra*, Vol 30 (3), 1199-1221, DOI: 10.1193/080313EQS222M

Spudich, P., Joyner, W.B., Lindh, A.G., Boore, D.M., Margaris, B.M., and Fletcer, J.B. (1999). SEA99: A revised ground motion prediction relation for use in extensional tectonic regimes, *Bull. Seism. Soc. Am*., Vol. 89(5), 1156-1170.

Stenner, H.D., Lund, W.R., Pearthree, P.A., and Everitt, B.L. (1999). Paleoseismic investigation of the Hurricane fault in northwestern Arizona and southwestern Utah, *Arizona Geological Survey, Open-File Report* 99-8, 137 p.

Stidham, C., Antolik, M., Dreger, D., Larsen, S., and Romanowicz, B. (1999). Three-Dimensional Structure Influences on the Strong Motion Wavefield of the 1989 Loma Prieta Earthquake, *Bull. Seism. Soc. Am.*, Vol. 89, 1184-1202.

Stirling, M., Rhoades, D., and Berryman, K. (2002). Comparison of earthquake scaling relations derived from data of the instrumental and preinstrumental era, *Bull. Seism. Soc. Am*., Vol. 92(2), 812-830.

Stirling, M.W. (2013). Diablo Canyon Power Plant: Field Reconnaissance of Fragile Geologic Features, August 2013. *GNS Science Letter Report 229LR*.

Stirling, M.W., and Anooshehpoor, R. (2006). Constraints on Probabilistic Seismic-Hazard Models from Unstable Landform Features in New Zealand, *Bull. Seism. Soc. Am.,* Vol. 96, 404-414.

Stirling, M.W., Ledgerwood, J., Liu, T., Apted, M. (2010). Age of unstable bedrock landforms southwest of Yucca Mountain, Nevada, and implications for past ground motions, *Bull. Seism. Soc. Am.,* Vol. 100(1), 74-86; doi: 10.1785/0120080359

Stock, J.M. and Hodges, K. V. (1989). Pre-Pliocene extension around the Gulf of California and the transfer of Baja California to the Pacific Plate, *Tectonics*, Vol. 8, 99-115.

Stover, C.W., and Coffman, J.L. (1993). Seismicity of the United States, 1568-1989 (Revised), *U.S. Geological Survey Professional Paper* 1527, 418p.

Strasser, F.O., Abrahamson, N.A., and Bommer, J.J. (2009). Sigma: Issues, insights and challenges, *Seism. Res. Let*., Vol. 80(1), 40-54

Suarez, G., and Hough, S.E. (2008). Reevaluation of the macroseismic effects of the 1887 Sonora, Mexico earthquake and its magnitude estimation, accessed 9/14/2012 at http://usuarios.geofisica.unam.mx/cruz/Sismociones_Libres/Biblio_Sismocion/Sonora_v5.p df.

Suess, M.P., and Shaw, J.H. (2003). P-wave seismic velocity structure derived from sonic logs and industry reflection data in the Los Angeles basin, California, J. Geoph. Res., Vol. 108(B3), 2170, doi 10.1029/2001JB001628

Suter, M. (2008a). Structural configuration of the Otates fault (southern Basin and Range Province) and its rupture in the 3 May 1887 Mw 7.5 Sonora, Mexico, earthquake, *Bull. Seism. Soc. Am*., Vol. 98, 2879–2893.

Suter, M. (2008b). Structural configuration of the Teras fault (southern Basin and Range Province) and its rupture in the 3 May 1887 Mw 7.5 Sonora, Mexico earthquake, *Revista Mexicana de Ciencias Geológicas*, Vol. 25, 179–195.

Suter, M., and Contreras J. (2002). Active tectonics of northeastern Sonora, Mexico (Southern Basin and Range Province) and the 3 May 1887 Mw 7.4 Earthquake, *Bull. Seism. Soc. Am*., Vol. 92 (2), 581–589.

Sweeney, R.E., and Hill, P.L. (2001). Arizona aeromagnetic and gravity maps and data: A web site for distribution of data, *U.S. Geological Survey Open-File Report* 01-0081.

Tanaka, M., Asano, K., Iwata, T., and Kubo, H. (2014). Source rupture process of the 2011 Fukushima-ken Hamadori earthquake: how did the two subparallel faults rupture? *Earth, Planets and Space*, Vol. 66:101, DOI:10.1186/1880-5981-66-101

Thompson, G.A., and Zoback, M.L. (1979). Regional geophysics of the Colorado Plateau, *Tectonophysics*, Vol. 61, 149–181.

Thompson, S. (2012). DCPP SSC Workshop 2 presentation [available at http://www.pge.com/mybusiness/edusafety/systemworks/dcpp/SSHAC/workshops/ws2.shtml]

Till, C.B., Gans, P.B., Spera, F.J., MacMillan, I., and Blair, K.D. (2009). Perils of petrotectonic modeling: A view from southern Sonora, Mexico, *Journal of Volcanology and Geothermal Research*, Vol. 186, 160-168.

Toda, S., Stein, R.S., and Lin, J. (2011). Widespread seismicity excitation throughout central Japan following the 2011 M=9.0 Tohoku earthquake and its interpretation by Coulomb stress transfer, *Geophys. Res. Lett*. Vol. 38(7), L00G03, DOI: 10.1029/2011GL047834.

Toro, G.R. (2002). Modification of the Toro et al. (1997) attenuation equations for large magnitudes and short distances, *Technical Report*, Risk Engineering.

Toro, G.R. (2012). Characterization of Ground Motion Propagation for Palo Verde SSHAC Level 2 Probabilistic Seismic Hazard Assessment Report, Lettis Consultants International, Inc.

Trifunac, M.D. (1994). Q and high-frequency strong motion spectra, *Soil Dynamics and Earthquake Engineering*, Vol. 13, 149-161.

U.S. NRC (1997). Recommendations for probabilistic seismic hazard analysis: Guidance on uncertainty and use of experts, prepared by Senior Seismic Hazard Analysis Committee, Lawrence Livermore National Laboratory, Volume 1, Main Report, NUREG/CR-6372, UCRL-ID-122160, 280 pp.

U.S. NRC (2007). Regulatory Guide 1.208: A Performance-Based Approach to Define the Site-Specific Earthquake Ground Motion, US Nuclear Regulatory Commission, 53 pp.

U.S. NRC (2012). Practical Implementation Guidelines for SSHAC Level 3 and 4 Hazard Studies: Washington D.C., US Nuclear Regulatory Commission, NUREG-2117.

U.S. NRC (2012a). Near-Term Task Force, "Request For Information Pursuant To Title 10 Of The Code Of Federal Regulations 50.54(F) Regarding Recommendations 2.1, 2.3, and 9.3, Of The Near-Term Task Force Review Of Insights From The Fukushima Dai-Ichi Accident."

UCB (2014). Moment tensor solutions, available at http://seismo.berkeley.edu/mt/

United States Geologic Survey – USGS (2007). Preliminary integrated geologic map databases for the United States: Western States, California, Nevada, Arizona, Washington, Oregon, Idaho, and Utah, Version 1.3, Open File Report 2005-1305, available at [http://pubs.usgs.gov/of/2005/1305/], updated December 2007.

United States Geologic Survey – USGS (2008). Documentation for the 2008 update of the United States National Seismic Hazard Maps, prepared by Petersen, M. D., et al., *U.S. Geological Survey Open File Report* 2008-1128.

United States Geologic Survey – USGS (2009). Quaternary fault and fold database for the United States, accessed 25 October 2010, from USGS website, [http//earthquakes.usgs.gov/regional/qfaults/].

United States Geologic Survey – USGS (2014). Magnitude 6.0 – NEVADA: Earthquake Summary, available at [http://earthquake.usgs.gov/earthquakes/eqinthenews/2008/us2008nsa9/#summary]; page last modified July 2014.

US Array (2003). [http://www.usarray.org/researchers/obs/transportable] (Last accessed Dec. 15, 2013)

Van Houtte, C., Drouet, S., and Cotton, F. (2011). Analysis of the origins of κ (kappa) to compute hard rock to rock adjustment factors for GMPEs, *Bull. Seism. Soc. Am*., Vol. 101, 2926-2941.

Villani, M., and Abrahamson, N. (2013). Repeatable site and path effects on the ground motion sigma based on empirical data from Southern California and simulated waveforms from the CyberShake platform. Poster at SCEC 2013 annual meeting and draft paper for Earthquake Spectra.

Vucetic, M., and Dobry, R. (1991). Effects of Soil Plasticity on Cyclic Response, *Journal of Geotechnical Engineering*, ASCE, Vol. 117(1), 89-107.

Wald, D.J., and Allen, T.I. (2007). Topographic slope as a proxy for seismic site conditions and amplification, *Bull. Seism. Soc. Am*., Vol. 97(5), 1379-1395.

Walker, J.D., and Geissman, J.W., compilers (2009). Geologic Time Scale, *Geological Society of America*, doi: 10.1130/2009.CTS004R2C.

Walling, M.A. (2009). Non-Ergodic Probabilistic Seismic Hazard Analysis and Simulation Spatial of Variation in Ground Motion, *PhD. Thesis*, University of California, Berkeley, Department of Civil and Environment Engineering.

Walter, A.W., and Mooney, W.D. (1982). Crustal structure of the Diablo Gabilan Ranges, Central California; a reinterpretation of existing data, *Bull. Seism. Soc. Am*., Vol. 72, 1567-1590.

Watson-Lamprey, J. (2015). Capturing Directivity Effects in the Mean and Aleatory Variability of the NGA-West 2 Ground Motion Prediction Equations, Pacific Earthquake Engineering Research Center PEER Report (in preparation).

Wdowinski, S. (2006). Current crustal movements across the southern San Andreas Fault and the southern Dead Sea Fault systems: A comparative study, MARGINS-RCL Workshop on "Lithospheric rupture in the Gulf of California – Salton Trough region", Ensenada, Mexico, Abstracts.

Wechsler, N., Rockwell, T.K., and Ben-Zion, Y. (2009). Application of high resolution DEM data to detect rock damage from geomorphic signals along the central San Jacinto Fault, *Geomorphology*, Vol. 113, 82–96, doi:10.1016/j.geomorph.2009.06.007.

Wei, M., Sandwell, D.T., Fialko, Y., and Bilham, R. (2011). Slip on faults in the Imperial Valley triggered by the 4 April 2010 Mw 7.2 El Mayor-Cucapah earthquake revealed by InSAR, *Geophysical Research Letters*, Vol. 38, L01308.

Wells, D.L., and Coppersmith, K.J. (1994). New empirical relationships among magnitude, rupture length, rupture width, rupture area, and surface displacement, *Bull. Seism. Soc. Am.*, Vol. 84, 974-1002.

Wesnousky, S.G. (2005). The San Andreas and Walker Lane Fault systems, western North America: transpression, transtension, cumulative slip and the structural evolution of a major transform plate boundary, *Journal of Structural Geology*, Vol. 27, 1505-1512.

Wessel, P., and Smith, W.H.F. (1998). New, improved version of the Generic Mapping Tools Released, *EOS Trans. AGU* Vol. 79, 579.

Wills, C.J., and Clahan, K.B. (2006). Developing a map of geologically defined site- condition categories for California, *Bull. Seismol. Soc. Am*., Vol. 96, 1483-1501.

Wills, C.J., Weldon, R.J., II, and Bryant, W.A. (2008). California fault parameters for the National Seismic Hazard Maps and Working Group on California Earthquake Probabilities, Appendix A in The Uniform California Earthquake Rupture Forecast, version 2 (UCERF 2), *U.S. Geological Survey Open-File Report* 2007-1437A, and *California Geological Survey Special Report* 203A, 48 p.

Wooddell, K.E., and Abrahamson, N.A. (2012). New earthquake classification scheme for mainshocks and aftershocks in the NGA-West2 ground motion prediction equations, *Proceedings, 15th World Conference on Earthquake Engineering,* Lisbon, Portugal.

Working Group on California Earthquake Probabilities – WGCEP (1995). Seismic hazards in southern California: probable earthquakes, 1994–2024, *Bull. Seism. Soc. Am*., Vol. 85, 379–439.

Working Group on California Earthquake Probabilities – WGCEP (2008). The Uniform California Earthquake Rupture Forecast, Version 2 (UCERF2), prepared by 2007 Working Group on California Earthquake Probabilities, *U.S. Geological Survey Open File Report* 2007-1437 and *California Geological Survey Special Report* 203.

Working Group on California Earthquake Probabilities – WGCEP (2012, in review). The Uniform California Earthquake Rupture Forecast, Version 3.1 (UCERF3.1), prepared by Working Group on California Earthquake Probabilities, accessed 5 February 2013 at [http://wgcep.org/UCERF3pt1].

Yamada, M., K. Mori, and T. Heaton, 2009, Slapdown phase in high acceleration records of large earthquakes, *Seismol. Res. Letts*, Vol. 80, 559-564.

Yamada, M., Olsen, A., and Heaton, T. (2009). Statistical features of short- and long-period near-source ground motions, *Bull. Seism. Soc. Am*., Vol. 99, 3264 -3274.

Yan, Z., and R. W. Clayton (2007). Regional mapping of the crustal structure in southern California from receiver functions, *J. Geophys. Res*., Vol. 112, B05311, doi:10.1029/2006JB004622

Yang, W., Hauksson, E., and Shearer, P.M. (2012). Computing a Large Refined Catalog of Focal Mechanisms for Southern California (1981- 2010): Temporal Stability of the Style of Faulting, *Bull. Seism. Soc. Am*., Vol. 102(3), 1179-1194.

Yoo, S.H., and Mayeda, K. (2013). Validation of non-self-similar source scaling using ground motions from the 2008 Wells, Nevada, earthquake sequence, *Bull. Seism. Soc. Am*., Vol. 103, 2508-2519.

Youngs R.R. (2009). Epistemic uncertainty in the NGA models, Appendix D in Ground Motion Models for the Pacific Northwest, Report to B.C. Hydro, December 2010.

Youngs, R.R. (2006). Epistemic Uncertainty Model for Use of PEER-NGA Ground Motion Models in National Hazard Mapping. Presented to Next Generation Attenuation Relationships Workshop, PEER, Richmond, CA, September, available at http://earthquake.usgs.gov/hazards/about/workshops/nga_workshop/1D--Youngs_Epistemic.pdf (last accessed 8/05/2014).

Youngs, R.R. (2011). Near Source Data from NGA (2008) and NGAW2 Datasets - Data Quantity and Implication for Uncertainty in GMPEs, DCPP Seismic Hazard Update, Workshop #1 (Nov. 29, 2011)

Youngs, R.R., and Coppersmith, K.J. (1985). Implications of fault slip rates and earthquake recurrence models to probabilistic seismic hazard estimates, *Bull. Seism. Soc. Am*., Vol. 58, 939–964.

Zeng, Y., Anderson, J.G. and Yu, G. (1994). A composite source model for computing realistic synthetic strong ground motions, *Geophysical Research Letters*, Vol. 21, 725-728.

Zeng, Y.H., Aki, K., and Teng, T.L. (1993). Mapping of the high-frequency source radiation for the Loma Prieta earthquake, California, *J. Geophys. Res. Vol.* 98(B7), 11981-11993.

Zeng, Y.H., Su, F., and Aki, K. (1991). Scattering wave energy propagation in a random isotropic scattering medium 1. Theory, *J. Geophys. Res.* Vol. 96 (B1), 607-619.

Zhang, X., Paulssen, H., Lebedev, S., and Meier, T. (2007). Surface wave tomography of the Gulf of California, *Geophysical Research Letters*, Vol. 34(15), doi:10.1029/2007GL030631.

Zhao, J.X., and Lu, M. (2011). Magnitude-Scaling Rate in Ground-Motion Prediction Equations for Response Spectra from Large, Shallow Crustal Earthquakes, *Bull. Seism. Soc. Am*., Vol. 101, 2643-2661.

Zhao, J.X., Irikura, K., Zhang, J., Fukushima, Y., Somerville, P.G., Asano, A., Ohno, Y., Oouchi, T., Takahashi, T., and Ogawa, H. (2006). An empirical site-classification method for strong-motion stations in Japan using H/V response spectral ratio, *Bull. Seism. Soc. Am*., Vol. 96(3), 914-925.

Zhao, J.X., Zhang, J., Asano, A., Ohno, Y., Oouchi, T., Takahashi, T., Ogawa, H., Irikura, K., Thio, H.K., Somerville, P.G., Fukushima, Y., and Fukushima, Y. (2006). Attenuation Relations of Strong Ground Motion in Japan Using Site Classification Based on Predominate Period, *Bull. Seism. Soc. Am*., Vol. 96, 898-913.

Zhu, L., and Rivera, L.A. (2002). A note on the dynamic and static displacements from a point source in multilayered media, *Geophysical Journal International*, Vol. 148(3), 619-627.